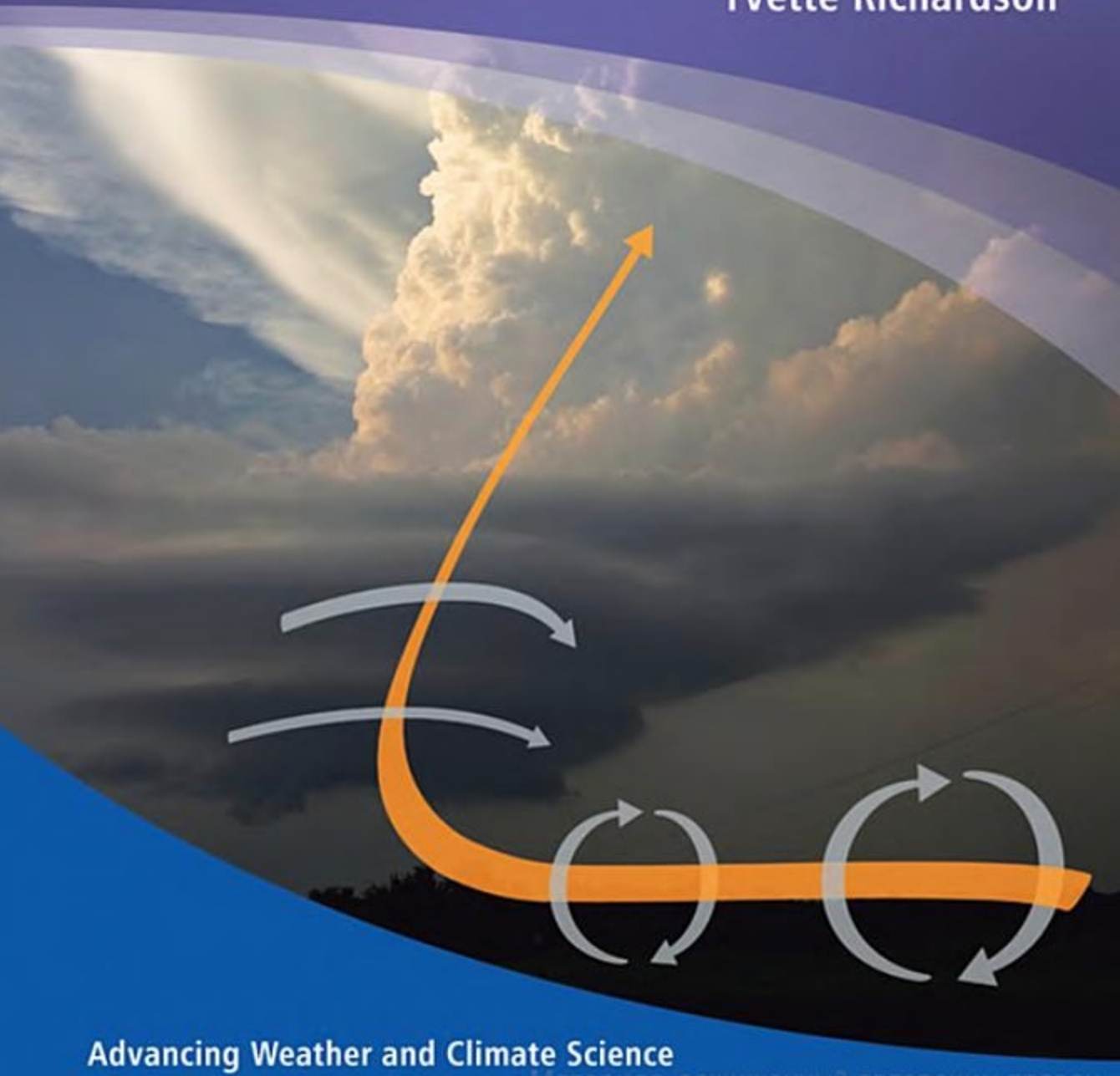


Mesoscale Meteorology in Midlatitudes

Paul Markowski
Yvette Richardson



Mesoscale Meteorology in Midlatitudes

Paul Markowski and Yvette Richardson,

Penn State University, University Park, PA, USA

 **WILEY-BLACKWELL**

A John Wiley & Sons, Ltd., Publication

This edition first published 2010, © 2010 by John Wiley & Sons, Ltd

Wiley-Blackwell is an imprint of John Wiley & Sons, formed by the merger of Wiley's global Scientific, Technical and Medical business with Blackwell Publishing.

Registered office: John Wiley & Sons Ltd, The Atrium, Southern Gate, Chichester, West Sussex, PO19 8SQ, UK

Other Editorial Offices:

9600 Garsington Road, Oxford, OX4 2DQ, UK
111 River Street, Hoboken, NJ 07030-5774, USA

For details of our global editorial offices, for customer services and for information about how to apply for permission to reuse the copyright material in this book please see our website at www.wiley.com/wiley-blackwell

The right of the author to be identified as the author of this work has been asserted in accordance with the Copyright, Designs and Patents Act 1988.

All rights reserved. No part of this publication may be reproduced, stored in a retrieval system, or transmitted, in any form or by any means, electronic, mechanical, photocopying, recording or otherwise, except as permitted by the UK Copyright, Designs and Patents Act 1988, without the prior permission of the publisher.

Wiley also publishes its books in a variety of electronic formats. Some content that appears in print may not be available in electronic books.

Designations used by companies to distinguish their products are often claimed as trademarks. All brand names and product names used in this book are trade names, service marks, trademarks or registered trademarks of their respective owners. The publisher is not associated with any product or vendor mentioned in this book. This publication is designed to provide accurate and authoritative information in regard to the subject matter covered. It is sold on the understanding that the publisher is not engaged in rendering professional services. If professional advice or other expert assistance is required, the services of a competent professional should be sought.

Library of Congress Cataloguing-in-Publication Data

Record on file

ISBN: 978-0-470-74213-6

A catalogue record for this book is available from the British Library.

Set in 9.75/11.75 Minion by Laserwords Private Ltd, Chennai

Printed in Spain by Grafos S.A., Barcelona

First impression—2010

*We dedicate this book to our families
Marisa, Nolan, & Shane
and
Scott, Nick, & Sydney*

Contents

Series Foreward	xi
Preface	xiii
Acknowledgments	xv
List of Symbols	xvii
PART I General Principles	1
1 What is the Mesoscale?	3
1.1 Space and time scales	3
1.2 Dynamical distinctions between the mesoscale and synoptic scale	5
2 Basic Equations and Tools	11
2.1 Thermodynamics	11
2.2 Mass conservation	16
2.3 Momentum equations	17
2.4 Vorticity and circulation	21
2.5 Pressure perturbations	25
2.6 Thermodynamic diagrams	32
2.7 Hodographs	34
3 Mesoscale Instabilities	41
3.1 Static instability	41
3.2 Centrifugal instability	48
3.3 Inertial instability	49
3.4 Symmetric instability	53
3.5 Shear instability	58
PART II Lower Tropospheric Mesoscale Phenomena	71
4 The Boundary Layer	73
4.1 The nature of turbulent fluxes	73
4.2 Surface energy budget	82
4.3 Structure and evolution of the boundary layer	83
4.4 Boundary layer convection	88

4.5	Lake-effect convection	93
4.6	Urban boundary layers	103
4.7	The nocturnal low-level wind maximum	105
5	Air Mass Boundaries	115
5.1	Synoptic fronts	117
5.2	Drylines	132
5.3	Outflow boundaries	140
5.4	Mesoscale boundaries originating from differential surface heating	149
6	Mesoscale Gravity Waves	161
6.1	Basic wave conventions	161
6.2	Internal gravity wave dynamics	165
6.3	Wave reflection	170
6.4	Critical levels	172
6.5	Structure and environments of ducted mesoscale gravity waves	173
6.6	Bores	175
PART III Deep Moist Convection		181
7	Convection Initiation	183
7.1	Requisites for convection initiation and the role of larger scales	183
7.2	Mesoscale complexities of convection initiation	189
7.3	Moisture convergence	195
7.4	Elevated convection	197
8	Organization of Isolated Convection	201
8.1	Role of vertical wind shear	201
8.2	Single-cell convection	206
8.3	Multicellular convection	209
8.4	Supercellular convection	213
9	Mesoscale Convective Systems	245
9.1	General characteristics	245
9.2	Squall line structure	249
9.3	Squall line maintenance	253
9.4	Rear inflow and bow echoes	260
9.5	Mesoscale convective complexes	265

10 Hazards Associated with Deep Moist Convection	273
10.1 Tornadoes	273
10.2 Nontornadic, damaging straight-line winds	292
10.3 Hailstorms	306
10.4 Flash floods	309
PART IV Orographic Mesoscale Phenomena	315
11 Thermally Forced Winds in Mountainous Terrain	317
11.1 Slope winds	317
11.2 Valley winds	320
12 Mountain Waves and Downslope Windstorms	327
12.1 Internal gravity waves forced by two-dimensional terrain	327
12.2 Gravity waves forced by isolated peaks	332
12.3 Downslope windstorms	333
12.4 Rotors	342
13 Blocking of the Wind by Terrain	343
13.1 Factors that govern whether air flows over or around a terrain obstacle	343
13.2 Orographically trapped cold-air surges	346
13.3 Lee vortices	351
13.4 Gap flows	358
PART V Appendix	367
A Radar and Its Applications	369
A.1 Radar basics	369
A.2 Doppler radar principles	371
A.3 Applications	374
References	389
Index	399

Series Foreword

Advances in Weather and Climate

Meteorology is a rapidly moving science. New developments in weather forecasting, climate science and observing techniques are happening all the time, as shown by the wealth of papers published in the various meteorological journals. Often these developments take many years to make it into academic textbooks, by which time the science itself has moved on. At the same time, the underpinning principles of atmospheric science are well understood but could be brought up to date in the light of the ever increasing volume of new and exciting observations and the underlying patterns of climate change that may affect so many aspects of weather and the climate system.

In this series, the Royal Meteorological Society, in conjunction with Wiley–Blackwell, is aiming to bring together both the underpinning principles and new developments

in the science into a unified set of books suitable for undergraduate and postgraduate study as well as being a useful resource for the professional meteorologist or Earth system scientist. New developments in weather and climate sciences will be described together with a comprehensive survey of the underpinning principles, thoroughly updated for the 21st century. The series will build into a comprehensive teaching resource for the growing number of courses in weather and climate science at undergraduate and postgraduate level.

Series Editors

Peter Inness, University of Reading, UK

William Beasley,
University of Oklahoma, USA

Preface

This text originated from course notes used in the undergraduate mesoscale meteorology class at Pennsylvania State University. We assume that students have already had courses in atmospheric dynamics, thermodynamics, and synoptic meteorology. A mesoscale meteorology textbook likely will always be a “work in progress”, given that so much of what we teach is constantly evolving as observing and numerical modeling capabilities continually improve. Another obvious challenge in preparing a reference on mesoscale meteorology is that the specialty is extraordinarily broad, and in a way a catch-all for essentially all atmospheric phenomena that are not dominated at one extreme by quasigeostrophic dynamics or at the other extreme by the effects of small-scale turbulence. Thus, it is perhaps impossible to write a truly comprehensive mesoscale meteorology textbook that can adequately address all of the mesoscale processes that influence the weather in every corner of the world in important ways.

Our focus is midlatitude mesoscale phenomena. The thermodynamics and dynamics of tropical convective clusters and hurricanes are therefore not included, nor is a comprehensive treatment of polar lows. It is our experience that these topics tend to be covered in tropical meteorology and synoptic meteorology courses, respectively, rather than in mesoscale meteorology courses. Other perhaps surprising omissions include jet streaks and lee cyclogenesis, and the treatment of fronts and frontogenesis might be considered by some to be rather abridged. Again, in our experience these topics also tend to be covered in courses on synoptic meteorology. We also did not include chapters on upslope precipitation events or mesoscale modeling. The most interesting aspects of the former topic are probably the microphysical aspects (e.g. the seeder-feeder process) rather than the mesoscale dynamical aspects. Regarding mesoscale modeling, even though numerous figures throughout the text are derived from numerical simulations, we felt that this topic deserves an entire course by itself. It is possible that we might reconsider including these topics in an expanded future edition. We also caution the reader that the subject of atmospheric convection, particularly deep,

moist convection, is what drew us to meteorology in the first place and its study is what puts food on our tables. It will be obvious to the casual reader that this bias has not been well concealed.

The book is divided into four parts. Part I, General Principles, begins by defining what is meant by the term *mesoscale* (Chapter 1). This requires the introduction of some basic dynamical concepts, such as the Rossby number, hydrostatic approximation, and pressure perturbations. In Chapter 2 we present a more detailed review of the tools that will be needed for the rest of the book. Some readers may wish to skip Chapter 2. It might seem somewhat awkward to introduce some dynamics in Chapter 1 and then review the basic governing equations more thoroughly in Chapter 2, but the alternative – forcing readers to trudge through a lengthy review chapter to open a book before getting to a description of the types of phenomenon that are the focus of the book – seemed even less attractive. One of the concepts in Chapter 1 is that mesoscale phenomena can be driven by a variety of instabilities, unlike synoptic-scale motions, which are driven almost exclusively by baroclinic instability, at least in midlatitudes. Chapter 3 discusses these mesoscale instabilities.

The remaining chapters in the book (Parts II–IV) deal with mesoscale phenomena. The phenomena can be attributed to either instabilities, topographic forcing, or, in the case of air mass boundaries such as fronts and drylines, frontogenesis. There no doubt are a number of ways to organize mesoscale meteorology topics, as is evidenced by the fact that we did things differently at least the first four times we taught the course at Penn State. In Part II we explore mesoscale phenomena that are confined principally to the lower troposphere, for example, boundary layer convection, air mass boundaries (e.g. fronts, drylines, sea breezes, outflow boundaries), and ducted gravity waves. Part III treats the subject of deep moist convection, including its initiation, organization, and associated hazards. Part IV contains mountain meteorology topics. The basic idea in Part IV is to treat each of the following in a separate chapter, in this order: (i) the simplest case – no ambient flow and only heating/cooling of sloped

terrain, which results in thermally forced mountain and valley circulations; (ii) the case of wind flowing over a topographic barrier, which excites gravity waves and occasionally leads to severe, dynamically induced downslope winds; (iii) phenomena resulting when winds that impinge on a topographic barrier experience significant blocking, such as cold-air damming, wake vortices, and gap winds.

We lament that each of Parts II–IV themselves could be the basis for entire textbooks. The scope of each chapter purposely has been limited somewhat to facilitate the examination of a wide range of mesoscale topics within the course

of a typical semester. In part for this reason, a “further reading” list also appears at the end of each chapter, which contains supplemental references not specifically cited in the bibliography. We speculate that these listings might be most valuable to graduate students seeking to supplement the contents herein with more advanced readings. Finally, a “crash course” on radar meteorology is provided in an appendix. Radars are arguably the most important instrument in the observation of mesoscale phenomena. After all, the term *mesoscale* originated in a review paper on radar meteorology.

Acknowledgments

We are grateful for all of the discussions with our friends and colleagues over the years: Mark Askelson, Peter Bannon, Howie Bluestein, Harold Brooks, George Bryan, Don Burgess, Fred Carr, John Clark, Bill Cotton, Bob Davies-Jones, Chuck Doswell, David Dowell, Kelvin Droegemeier, Dale Durran, Evgeni Fedorovich, Bill Frank, Mike Fritsch, Kathy Kanak, Petra Klein, Sukyoung Lee, Doug Lilly, Matt Parker, Erik Rasmussen, Dave Schultz, Alan Shapiro, Nels Shirer, Todd Sikora, Dave Stensrud, Jerry Straka, Jeff Trapp, Hans Verlinde, Tammy Weckwerth, Morris Weisman, Lou Wicker, Josh Wurman, John Wyngaard, George Young, and Conrad Ziegler. We are especially appreciative of those who reviewed earlier versions of this book: George Bryan, John Clark, Chuck Doswell, Dale Durran, Evgeni Fedorovich, Bart Geerts, Thomas Haiden, Jerry Harrington, Steve Koch, Dennis Lamb, Sukyoung Lee, Doug Lilly, Matt Parker, Dave Schultz, Russ Schumacher, Alan Shapiro, Nels Shirer, Todd Sikora, Hans Verlinde, Dave Whiteman, Josh Wurman, John Wyngaard, George Young, and Fuqing Zhang.

We also thank those who provided us with their original photographs or figures (all photographs are copyrighted by the those credited in the figure captions): Nolan Atkins, Peter Blottman, Harold Brooks, George Bryan, Fernando Caracena, Brian Colle, Chris Davis, Chuck Doswell, Jim Doyle, Dale Durran, Charles Edwards, Roger Edwards, Craig Epifanio, Marisa Ferger, Brian Fiedler, Jeff Frame, Bart Geerts, Roberto Giudici, Joel Gratz, Vanda Grubisic, Jessica Higgs, Richard James, Dave Jorgensen, Pat Kennedy, Jim LaDue, Bruce Lee, Dave Lewellen, Amos Magliocco, Jim Marquis, Brooks Martner, Al Moller, Jerome Neufeld, Eric Nguyen, Matt Parker, Erik Rasmussen, Chuck Robertson, Paul Robinson, Chris Rozoff, Thomas S{a}vert, Dave Schultz, Jim Steenburgh, Herb Stein, Jeff Trapp, Roger Wakimoto, Nate Winstead, Josh Wurman, Ming Xue, and Conrad Ziegler. A number of staff at Penn State helped us acquire several archived datasets that were used to construct some of the figures within the book, in addition to providing virtually “24/7” computer support: Chad Bahrmann, Chuck Pavloski, Art Person, and Bill Syrett. We also are grateful for the support and patience of Wiley, especially Rachael Ballard and Robert Hambrook. Some of

the figures contain numerical model output generated by the Advanced Regional Prediction System (ARPS), developed by the Center for the Analysis and Prediction of Storms at the University of Oklahoma, and the Bryan Cloud Model, developed by George Bryan. Much of the radar imagery appearing in figures was displayed using the SOLOII software from the National Center for Atmospheric Research.

Paul Markowski
Yvette Richardson

Work on this book began in the spring of 2001 when I began preparing to teach the undergraduate mesoscale meteorology course at Penn State for the first time. Much of the inspiration at that time came from reviewing Greg Forbes' lecture notes from the class, which I took from Dr. Forbes in 1995 as an undergraduate meteorology major at Penn State. Dr. Forbes' influence on my early development—through his formal classroom lectures, undergraduate honors thesis mentorship, and simply shared interests in convective storms—cannot be overstated. I also likely would not be where I am today if not for the opportunity to spend the summer after my junior year in Norman, Oklahoma, as a Research Experiences for Undergraduates (REU) student. My mentor there, Dave Stensrud, is one of the reasons I decided to pursue a Ph.D. Another important aspect of my REU experience in Norman was the opportunity to participate in the Verification of the Origins of Rotation in Tornadoes Experiment (VORTEX). My experience in the field forever sealed my fate to follow a career path to research. It was through VORTEX that I met Jerry Straka and Erik Rasmussen, who convinced me to attend the University of Oklahoma and who served as my advisors. They were superb advisors, and it's hard to say what their biggest contribution was. It was either their trust in me to allow me to work so independently right from the start, or it was their tireless and selfless willingness to discuss pretty much any aspect of my research or theirs at virtually any hour of the day. I also single-out Bob Davies-Jones, with whom I chased storms

for a number of years while doing field work as a part of my graduate research. Hours upon hours of watching the sky and listening to Bob's assessments, in addition to discussing dynamics problems, benefited me in immeasurable ways. Finally, I am forever grateful for the support of my wife (also a meteorologist) throughout the project.

Paul Markowski

My path to authoring this book was somewhat circuitous. I majored in physics as an undergraduate at the University of Wisconsin-River Falls. The professors I had there were incredible teachers and mentors, and I will always be indebted to Drs. Shepherd, Larson, Paulson, and Blodgett for providing me with a solid foundation. My journey into meteorology began with the Summer Institute on Atmospheric Science at NASA-Goddard Space Flight Center between my junior and senior year. It was there that my husband (also a physics major) and I both realized that atmospheric science was an extremely interesting application of our physics backgrounds, and it is where we met Kelvin Droegemeier, who represented the University of Oklahoma graduate program with such enthusiasm we could not help but go there! I am grateful to Fred Carr who served as the thesis advisor for my masters degree and

did his best to teach a physics student to understand actual weather! For my Ph.D., I decided to study severe storms with Kelvin, and I am ever grateful for his undying support and encouragement. It was through him that I learned to be a numerical modeler, and his markups of my manuscripts taught me the essence of scientific writing. I also will never forget having the opportunity to sit at the feet of theoretical giants Douglas Lilly and Robert Davies-Jones, both of whom always were willing to discuss difficult concepts and pass along their incredible insight. As I was finishing my Ph.D., the University of Oklahoma allowed me to get my feet wet in teaching as a Visiting Assistant Professor, and through this I determined that was the career path for me. Following my Ph.D., I had the wonderful opportunity of a post-doc position with Joshua Wurman, who did his best to help a numerical modeler become an observationalist, before landing at the Pennsylvania State University as an assistant professor. It has been an interesting path, and one made possible through the support of family and all of the friendships developed along the way. In particular, this path was possible because of my husband who started out as my study partner in my Freshman year of college and has fully supported my endeavors ever since.

Yvette Richardson

List of Symbols

α	specific volume, angle a parcel displacement makes with respect to the horizontal, angle of axis of dilatation with respect to the x axis, inclination angle of sloping terrain	$\bar{\theta}_a$	mean potential temperature at anemometer level
α_0	constant reference specific volume	θ'	potential temperature perturbation
α_d	specific volume of dry air	$\hat{\theta}$	amplitude of potential temperature perturbation
β	angle between \mathbf{v} and $d\mathbf{l}$, latitudinal variation of Coriolis parameter, angle between isentropes and the axis of dilatation, between-beam angle	θ_0	constant reference potential temperature, potential temperature at the height of the roughness length
γ	environmental lapse rate	θ_c	potential temperature in well-mixed region between split streamlines in flow over a barrier
Γ_d	dry adiabatic lapse rate	θ_e	equivalent potential temperature
Γ_m	moist adiabatic lapse rate	θ_e^*	equivalent potential temperature if air is saturated at its current temperature and pressure
Γ_p	parcel lapse rate	$\bar{\theta}_e^*$	mean (environmental) equivalent potential temperature if air is saturated at its current temperature and pressure
Γ_{ps}	pseudoadiabatic lapse rate	θ_{ep}	pseudoequivalent potential temperature
Γ_{rm}	reversible moist adiabatic lapse rate	θ_v	virtual potential temperature
δ	horizontal divergence, displacement of a streamline	$\bar{\theta}_v$	mean (environmental) virtual potential temperature
δ_c	displacement of the dividing streamline	θ'_v	virtual potential temperature perturbation
$\bar{\delta}$	vertically averaged horizontal divergence	θ_w	wet-bulb potential temperature
ε	ratio of gas constants for dry air and water vapor, dissipation	θ_ρ	density potential temperature
ζ	vertical vorticity component	$\bar{\theta}_\rho$	mean (environmental) density potential temperature
$\bar{\zeta}$	mean (environmental) vertical vorticity	θ'_ρ	density potential temperature perturbation
ζ'	vertical vorticity perturbation	κ	wave vector
η	meridional vorticity component	κ	thermal diffusivity
$\langle \eta \rangle$	cross-section-averaged meridional vorticity	κ_e	moisture diffusivity
$\bar{\eta}$	mean (environmental) meridional vorticity	λ	longitude, wavelength
ξ	zonal vorticity component	λ_x	zonal wavelength
$\bar{\xi}$	mean (environmental) zonal vorticity	λ_z	vertical wavelength
θ	potential temperature, radar beam azimuth angle	μ	a real number
$\bar{\theta}$	mean (environmental) potential temperature	ν	kinematic viscosity
$\langle \bar{\theta} \rangle$	layer-averaged environmental potential temperature	π	3.141 592 65, Exner function

$\bar{\pi}$	mean (environmental) Exner function	A_e	projection of A onto the equatorial plane
π'	perturbation Exner function	a	radius of Earth, shape parameter for terrain profile
ρ	air density	B	buoyancy
ρ_0	constant reference density	Bu	Burger number
ρ_a	density of an adiabatic reference state	C	circulation, condensation rate, speed of bore relative to upstream density current, radar constant
ρ_d	density of dry air	C_a	absolute circulation
ρ_i	density of ice hydrometeor	C_p	heat capacity at constant pressure
ρ_v	density of water vapor	\mathbf{c}	storm motion vector
$\bar{\rho}$	mean (environmental) air density	c_g	group velocity
ρ'	air density perturbation	c	phase speed, speed of light
σ	static stability parameter, growth rate of isentropic surface	c^*	complex conjugate of the phase speed
τ	lifetime of a convective cell	c_d	drag coefficient
ϕ	latitude, radar beam elevation angle, phase of radar transmission	c_e	bulk transfer coefficient for moisture
Φ	geopotential	c_{gx}	zonal group velocity component
$\bar{\Phi}$	mean geopotential	c_{gz}	vertical group velocity component
Φ'	geopotential perturbation	c_h	bulk transfer coefficient for heat
Φ'_i	imaginary part of the geopotential perturbation	c_i	imaginary part of phase speed
Φ'_r	real part of geopotential perturbation	c_l	specific heat of liquid water for a constant pressure process
Φ'^*	complex conjugate of the geopotential perturbation	c_p	specific heat for a constant-pressure process
ψ	streamfunction	c_{pd}	specific heat at constant-pressure for dry air
ψ_0	angular constant designating the orientation of the ageostrophic wind at the start of the inertial oscillation that leads to the nocturnal low-level wind maximum	c_{pv}	specific heat at constant-pressure for water vapor
$\bar{\psi}$	mean streamfunction	c_r	real part of phase speed
ψ'	streamfunction perturbation	c_v	specific heat for a constant-volume process
$\hat{\psi}$	complex amplitude of streamfunction perturbation	c_{vd}	specific heat at constant-volume for dry air
$\boldsymbol{\Omega}$	Earth's angular velocity vector	c_{vv}	specific heat at constant volume for water vapor
Ω	angular rotation rate of Earth, intrinsic frequency	D	characteristic depth scale, resultant deformation, depth of wave duct, depth of fluid layer, depth of outflow, duration of precipitation, hailstone diameter
ω	relative vorticity vector	D_1	stretching deformation
ω_h	horizontal vorticity vector	D_2	shearing deformation
ω	frequency	d	depth of control volume
ω_c	crosswise vorticity component	dA	element of an arbitrary surface having an area A
ω_k	frequency of k th mode	dl	element of a circuit about which circulation is evaluated
ω_s	streamwise vorticity component	E	evaporation rate, precipitation efficiency
A	area of an arbitrary surface bounded by the circuit about which circulation is computed	e	vapor pressure, Euler's number

\bar{e}	mean vapor pressure, turbulent kinetic energy	L_x	distance between mountain crests
e_{ij}	deformation tensor	l	meridional wavenumber, mixing length, cross-gap length scale, Scorer parameter
e_s	saturation vapor pressure	l_f	specific latent heat of fusion
\mathbf{F}	viscous force	l_s	specific latent heat of sublimation
F_h	sum of horizontal forces acting on an air parcel	l_v	specific latent heat of vaporization
F_u	viscous force acting on u	M	angular momentum, absolute (or pseudoangular) momentum
F_v	viscous force acting on v , sum of vertical forces acting on an air parcel	\overline{M}	mean angular momentum
F_w	viscous force acting on w	M'	angular momentum perturbation
Fr	Froude number	M_g	geostrophic absolute (or geostrophic pseudoangular) momentum
Fr_m	mountain Froude number	m	vertical wavenumber
f	Coriolis parameter, frequency	N	Brunt-Väisälä frequency, refractivity
f_0	constant reference Coriolis parameter	N_m	moist Brunt-Väisälä frequency
\mathbf{g}	gravitational acceleration vector	N_0	constant Brunt-Väisälä frequency
g	gravitational acceleration	\mathbf{n}	unit vector that points to the left of the horizontal wind velocity
g'	reduced gravity	n	coordinate in the \mathbf{n} direction, an integer, refractive index
H	scale height of atmosphere, undisturbed depth of fluid layer, far-field depth of cold pool	P_r	received backscattered power
H_0	original height of dividing streamline	p	pressure
H_1	nadir height of dividing streamline	\overline{p}	mean (environmental) pressure
h	specific enthalphy, height above ground	p_0	reference pressure
h_0	depth of stable layer	p_d	pressure of dry air
h_1	depth of bore	p^*	saturation pressure
h_l	inertial height scale	p'	pressure perturbation
h_m	height of mountain summit	\hat{p}	amplitude of pressure perturbation
h_t	height of terrain	p'_b	buoyancy pressure perturbation
I_δ	vertical integral of the displacement of potential temperature surfaces	p'_d	dynamic pressure perturbation
\mathbf{i}	unit vector in positive x direction	p'_h	hydrostatic pressure perturbation
i	$\sqrt{-1}$	p'_{nh}	nonhydrostatic pressure perturbation
\mathbf{j}	unit vector in positive y direction	p'_{dl}	linear dynamic pressure perturbation
K_e	eddy diffusivity for moisture	p'_{dnl}	nonlinear dynamic pressure perturbation
K_h	eddy diffusivity for heat	\hat{p}	complex amplitude of pressure perturbation
K_m	eddy viscosity	p_∞	ambient far-field pressure away from a tornado
\mathbf{k}	unit vector in positive z direction	PV	Ertel's potential vorticity
k	zonal wavenumber, von Karman's constant, wave mode	PV_g	geostrophic potential vorticity
KE	kinetic energy	Q	heating rate
L_R	Rossby radius of deformation	Q_e	surface latent heat flux
L_{Rm}	mountain Rossby radius of deformation		

Q_h	surface sensible heat flux	T_0	constant reference absolute temperature
Q_g	ground heat flux	T_d	dew-point temperature
q	specific heating rate	T_e	equivalent temperature
R	gas constant, radius of circulation circuit, reflection coefficient, rainfall rate	T_v	virtual temperature
R^*	complex conjugate of reflection coefficient	\bar{T}_v	mean (environmental) virtual temperature
R_d	gas constant for dry air	T'_v	virtual temperature perturbation
R_f	flux Richardson number	T_w	wet-bulb temperature
R_n	net radiation	T^*	saturation temperature
R_t	radius of curvature of a trajectory	T_ρ	density temperature
R_v	gas constant for water vapor	t	time
\mathbf{r}	position vector	U	along-gap wind speed
r	distance to center of Earth, radial coordinate, range to radar target, linear correlation coefficient, aspect ratio of a mountain	u	zonal wind component, radial wind component, cross-mountain wind component, cross-gap wind speed
r_h	hydrometeor mixing ratio	\bar{u}	mean (environmental) zonal wind component
r_t	total water mixing ratio	\bar{u}_a	mean zonal wind at anemometer level
r_v	water vapor mixing ratio	u'	zonal wind perturbation
r_{v0}	water vapor mixing ratio at the height of the roughness length	\hat{u}	amplitude of zonal wind perturbation
\bar{r}_v	mean water vapor mixing ratio	u_*	friction velocity
\bar{r}_{va}	mean water vapor mixing ratio at anemometer level	u_a	zonal ageostrophic wind component
r'_v	water vapor mixing ratio perturbation	u_0	constant reference zonal wind component, wind speed far upstream of a mountain
r_{vs}	saturation water vapor mixing ratio	u_{a0}	zonal ageostrophic wind at the start of the inertial oscillation that leads to the nocturnal low-level wind maximum
Ra	Rayleigh number	u_g	zonal geostrophic wind component
Ra_c	critical Rayleigh number	u_{gc}	along-front geostrophic wind component on cold side of front
Re	Reynolds number	u_{gw}	along-front geostrophic wind component on warm side of front
Ri	Richardson number	V	characteristic velocity scale, horizontal wind speed, volume of air
Ro	Rossby number	V_g	geostrophic wind speed
RH	relative humidity	\mathbf{v}	wind velocity vector
\mathbf{S}	mean vertical wind shear vector	$\bar{\mathbf{v}}$	mean (environmental) wind velocity vector
S	swirl ratio	\mathbf{v}'	perturbation wind velocity vector
S_i	sources and sinks of water vapor	\mathbf{v}_a	ageostrophic wind vector
\mathbf{s}	unit vector that points in the direction of the horizontal wind velocity	\mathbf{v}_{a0}	ageostrophic wind vector at the start of the inertial oscillation that leads to the nocturnal low-level wind maximum
s	coordinate in the \mathbf{s} direction	\mathbf{v}_g	geostrophic wind vector
T	absolute temperature, characteristic timescale		
\bar{T}	mean (environmental) absolute temperature		
T'	absolute temperature perturbation		

\mathbf{v}_h	horizontal wind velocity vector	\tilde{w}	complex amplitude of the vertical velocity perturbation
\mathbf{v}_T	thermal wind vector	\tilde{w}_k	k th mode of the complex amplitude of the vertical velocity perturbation
v	meridional wind component, tangential wind component, mountain-parallel wind component	\tilde{w}_{k_i}	imaginary part of the k th mode of the complex amplitude of the vertical velocity perturbation
\bar{v}	mean (environmental) meridional wind component	\tilde{w}_{k_r}	real part of the k th mode of the complex amplitude of the vertical velocity perturbation
\bar{v}_a	mean meridional wind at anemometer level	x	coordinate in the \mathbf{i} direction
v'	meridional wind perturbation	y	coordinate in the \mathbf{j} direction
v_R	radial velocity	Z	impedance, logarithmic reflectivity factor
v_a	meridional ageostrophic wind component	Z_{hh}	reflectivity factor associated with horizontally polarized transmitted and backscattered pulses
v_{a0}	meridional ageostrophic wind at the start of the inertial oscillation that leads to the nocturnal low-level wind maximum	Z_{vv}	reflectivity factor associated with vertically polarized transmitted and backscattered pulses
v_g	meridional geostrophic wind component	Z_{DR}	differential reflectivity factor
v_t	hydrometeor fall speed	z	coordinate in the \mathbf{k} direction, reflectivity factor
W	work, width, sum of vertical velocity of air plus hydrometeor fall speed	z'	characteristic distance a parcel travels before mixing with its surroundings
W_\downarrow	work required to displace parcel downward	z_0	roughness length, height of a streamline far upstream of a mountain
W_\uparrow	work required to displace parcel upward	z_i	height of the inversion at the top of the boundary layer
w	vertical wind component	z_{inv}	height of inversion
\bar{w}	mean vertical wind component	z_r	height of interface separating two layers of fluid
w'	vertical velocity perturbation		
\hat{w}	amplitude of vertical velocity perturbation		

PART I

General Principles

1

What is the Mesoscale?

1.1 Space and time scales

Atmospheric motions occur over a broad continuum of space and time scales. The mean free path of molecules (approximately 0.1 μm) and circumference of the earth (approximately 40 000 km) place lower and upper bounds on the space scales of motions. The timescales of atmospheric motions range from under a second, in the case of small-scale turbulent motions, to as long as weeks in the case of planetary-scale Rossby waves. Meteorological phenomena having short temporal scales tend to have small spatial scales, and vice versa; the ratio of horizontal space to time scales is of roughly the same order of magnitude for most phenomena ($\sim 10 \text{ m s}^{-1}$) (Figure 1.1).

Before defining the mesoscale it may be easiest first to define the synoptic scale. Outside of the field of meteorology, the adjective *synoptic* (derived from the Greek *synoptikos*) refers to a “summary or general view of a whole.” The adjective has a more restrictive meaning to meteorologists, however, in that it refers to large space scales. The first routinely available weather maps, produced in the late 19th century, were derived from observations made in European cities having a relatively coarse characteristic spacing. These early meteorological analyses, referred to as *synoptic maps*, paved the way for the Norwegian cyclone model, which was developed during and shortly after World War I. Because only extratropical cyclones and fronts could be resolved on the early synoptic maps, *synoptic* ultimately became a term that referred to large-scale atmospheric disturbances.

The debut of weather radars in the 1940s enabled phenomena to be observed that were much smaller in scale than the scales of motion represented on synoptic weather maps. The term *mesoscale* appears to have been

introduced by Ligda (1951) in an article reviewing the use of weather radar, in order to describe phenomena smaller than the synoptic scale but larger than the *microscale*, a term that was widely used at the time (and still is) in reference to phenomena having a scale of a few kilometers or less.¹ The upper limit of the mesoscale can therefore be regarded as being roughly the limit of resolvability of a disturbance by an observing network approximately as dense as that present when the first synoptic charts became available, that is, of the order of 1000 km.

At least a dozen different length scale limits for the mesoscale have been broached since Ligda’s article. The most popular bounds are those proposed by Orlanski (1975) and Fujita (1981).² Orlanski defined the mesoscale as ranging from 2 to 2000 km, with subclassifications of meso- α , meso- β , and meso- γ scales referring to horizontal scales of 200–2000 km, 20–200 km, and 2–20 km, respectively (Figure 1.1). Orlanski defined phenomena having scales smaller than 2 km as microscale phenomena, and those having scales larger than 2000 km as macroscale phenomena. Fujita (1981) proposed a much narrower range of length scales in his definition of mesoscale, where the mesoscale ranged from 4 to 400 km, with subclassifications of meso- α and meso- β scales referring to horizontal scales of 40–400 km and 4–40 km, respectively (Figure 1.1).

¹ According to Ligda (1951), the first radar-detected precipitation area was a thunderstorm observed using a 10-cm radar in England on 20 February 1941. Organized atmospheric science research using radars was delayed until after World War II, however, given the importance of the relatively new technology to military interests and the secrecy surrounding radar development.

² In addition to Orlanski and Fujita, scale classifications and/or subclassifications also have been introduced by Petterssen (1956), Byers (1959), Tepper (1959), Ogura (1963), and Agee *et al.* (1976), among others.

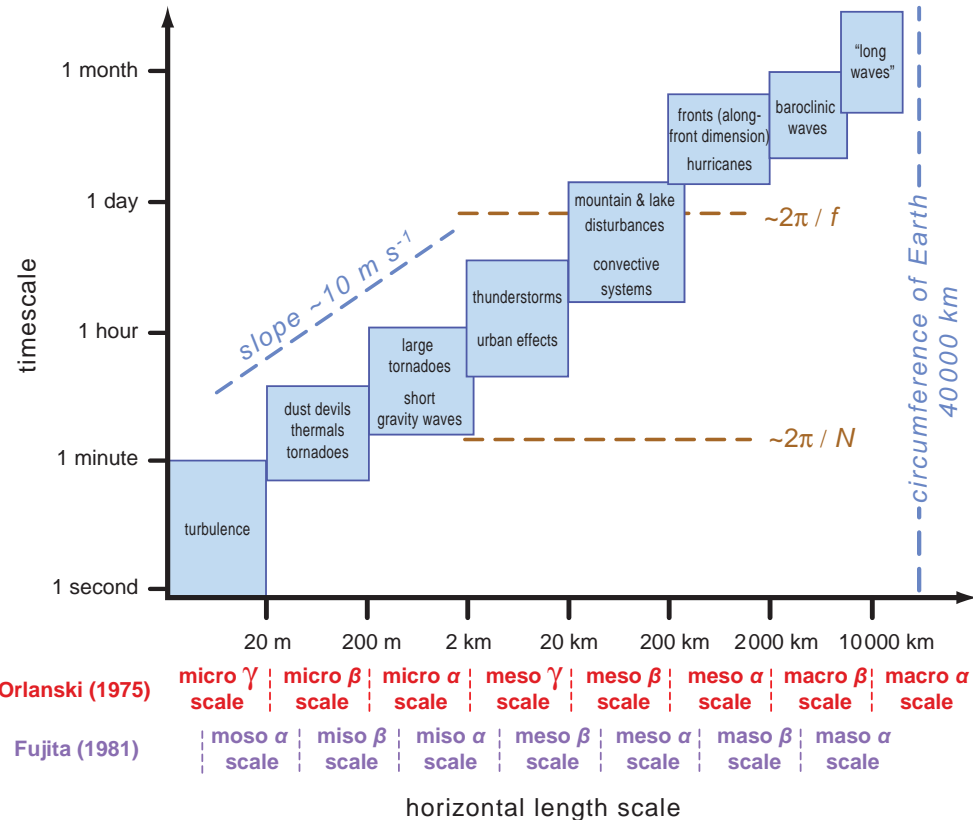


Figure 1.1 Scale definitions and the characteristic time and horizontal length scales of a variety of atmospheric phenomena. Orlanski's (1975) and Fujita's (1981) classification schemes are also indicated.

Fujita's overall scheme proposed classifications spanning two orders of magnitude each; in addition to the mesoscale, Fujita proposed a 4 mm–40 cm musoscale, a 40 cm–40 m mososcale, a 40 m–4 km misoscale, and a 400–40 000 km masoscale (the vowels A, E, I, O, and U appear in alphabetical order in each scale name, ranging from large scales to small scales). As was the case for Fujita's mesoscale, each of the other scales in his classification scheme was subdivided into α and β scales spanning one order of magnitude.

The specification of the upper and lower limits of the mesoscale does have some dynamical basis, although perhaps only coincidentally. The mesoscale can be viewed as an intermediate range of scales on which few, if any, simplifications to the governing equations can be made, at least not simplifications that can be applied to *all* mesoscale phenomena.³ For example, on the synoptic scale, several

terms in the governing equations can safely be disregarded owing to their relative unimportance on that scale, such as vertical accelerations and advection by the ageostrophic wind. Likewise, on the microscale, different terms in the governing equations can often be neglected, such as the Coriolis force and even the horizontal pressure gradient force on occasion. On the mesoscale, however, the full complexity of the unsimplified governing equations comes into play. For example, a long-lived mesoscale convective system typically contains large pressure gradients and horizontal and vertical accelerations of air, and regions of substantial latent heating and cooling and associated positive and negative buoyancy, with the latent heating and cooling profiles being sensitive to microphysical processes. Yet even the Coriolis force and radiative transfer effects have been shown to influence the structure and evolution of these systems.

The mesoscale also can be viewed as the scale on which motions are driven by a variety of mechanisms rather than by a single dominant instability, as is the case on

³ This is essentially the same point as made by Doswell (1987).

the synoptic scale in midlatitudes.⁴ Mesoscale phenomena can be either entirely topographically forced or driven by any one of or a combination of the wide variety of instabilities that operate on the mesoscale, such as thermal instability, symmetric instability, barotropic instability, and Kelvin-Helmholtz instability, to name a few. The dominant instability on a given day depends on the local state of the atmosphere on that day (which may be heavily influenced by synoptic-scale motions). In contrast, midlatitude synoptic-scale motions are arguably solely driven by baroclinic instability; extratropical cyclones are the dominant weather system of midlatitudes on the synoptic scale. Baroclinic instability is most likely to be realized by disturbances having a horizontal wavelength roughly three times the Rossby radius of deformation, L_R , given by $L_R = NH/f$, where N , H , and f are the Brunt-Väisälä frequency, scale height of the atmosphere, and Coriolis parameter, respectively.⁵ Typically, L_R is in the range of 1000–1500 km. In effect, the scale of the extratropical cyclone can be seen as defining what synoptic scale means in midlatitudes.

In contrast to the timescales on which extratropical cyclones develop, mesoscale phenomena tend to be shorter lived and also are associated with shorter Lagrangian timescales (the amount of time required for an air parcel to pass through the phenomenon). The Lagrangian timescales of mesoscale phenomena range from the period of a pure buoyancy oscillation, equal to $2\pi/N$ or roughly 10 minutes on average, to a pendulum day, equal to $2\pi/f$ or roughly 17 hours in midlatitudes. The former timescale could be associated with simple gravity wave motions, whereas the latter timescale characterizes inertial oscillations, such as the oscillation of the low-level ageostrophic wind component that gives rise to the low-level wind maximum frequently observed near the top of nocturnal boundary layers.

The aforementioned continuum of scales of atmospheric motions and associated pressure, temperature, and moisture variations is evident in analyses of meteorological

⁴ See, for example, Emanuel (1986).

⁵ In addition to being related to the wavelength that maximizes the growth rate of baroclinic instability, L_R also is important in the problem of geostrophic adjustment. Geostrophic adjustment is achieved by relatively fast-moving gravity waves. The horizontal scale of the influence of the gravity waves is dictated by L_R , which physically can be thought of as the distance a gravity wave can propagate under the influence of the Coriolis force before the velocity vector is rotated so that it is normal to the pressure gradient, at which point the Coriolis and pressure gradient forces balance each other. For phenomena having a horizontal scale approximately equal to L_R , both the velocity and pressure fields adjust in significant ways to maintain/establish a state of balance between the momentum and mass fields. On scales much less than (greater than) L_R , the pressure (velocity) field adjusts to the velocity (pressure) field during the geostrophic adjustment process.

variables. Figure 1.2 presents one of Fujita's manual analyses (i.e., a hand-drawn, subjective analysis) of sea level pressure and temperature during an episode of severe thunderstorms.⁶ Pressure and temperature anomalies are evident on a range of scales: for example, a synoptic-scale low-pressure center is analyzed, as are smaller-scale highs and lows associated with the convective storms. The magnitude of the horizontal pressure and temperature gradients, implied by the spacing of the isobars and isotherms, respectively, varies by an order of magnitude or more within the domain shown.

The various scales of motion or scales of atmospheric variability can be made more readily apparent by way of filters that preferentially damp select wavelengths while retaining others. For example, a *low-pass* filter can be used to remove relatively small scales from an analysis (*low-pass* refers to the fact that low-frequency [large-wavelength] features are retained in the analysis). A *band-pass* filter can be used to suppress scales that fall outside of an intermediate range. Thus, a low-pass filter can be used to expose synoptic-scale motions or variability and a band-pass filter can be used to expose mesoscale motions. (A *high-pass* filter would be used to suppress all but the shortest wavelengths present in a dataset; such filters are rarely used because the smallest scales are the ones that are most poorly resolved and contain a large noise component.) The results of such filtering operations are shown in Figure 1.3, which serves as an example of how a meteorological field can be viewed as having components spanning a range of scales. The total temperature field comprises a synoptic-scale temperature field having a southward-directed temperature gradient plus mesoscale temperature perturbations associated with thunderstorm outflow.

1.2 Dynamical distinctions between the mesoscale and synoptic scale

1.2.1 Gradient wind balance

On the synoptic scale, phenomena tend to be characterized by a near balance of the Coriolis and pressure gradient forces (i.e., geostrophic balance) for straight flow, so accelerations of air parcels and ageostrophic motions tend to be very small. For curved flow, the imbalance between these forces on the synoptic scale results in a centripetal acceleration such that the flow remains nearly parallel to the curved

⁶ Fujita called these mesoscale meteorological analyses *mesoanalyses*. The analyses he published over the span of roughly five decades are widely regarded as masterpieces.

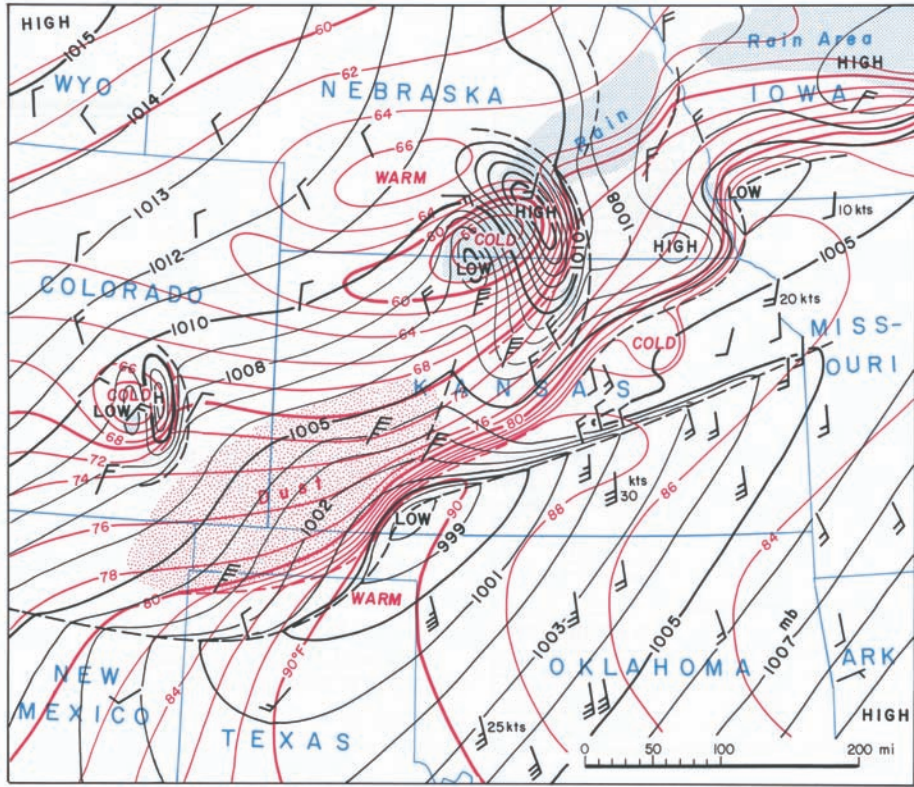


Figure 1.2 Sea-level pressure (black contours) and temperature (red contours) analysis at 0200 CST 25 June 1953. A squall line was in progress in northern Kansas, eastern Nebraska, and Iowa. (From Fujita [1992].)

isobars (i.e., gradient wind balance). Gradient wind balance is often a poor approximation to the air flow on the mesoscale. On the mesoscale, pressure gradients can be considerably larger than on the synoptic scale, whereas the Coriolis acceleration (proportional to wind velocity) is of similar magnitude to that of the synoptic scale. Thus, mesoscale systems are often characterized by large wind accelerations and large ageostrophic motions.

As scales decrease below ~ 1000 km the Coriolis acceleration becomes increasingly important compared with the pressure gradient force, and as scales increase beyond ~ 1000 km ageostrophic motions become increasingly significant. Let us consider a scale analysis of the horizontal momentum equation (the x equation, without loss of generality):

$$\frac{du}{dt} = -\frac{1}{\rho} \frac{\partial p}{\partial x} + fv + F_u, \quad (1.1)$$

where u , v , ρ , p , f , d/dt , and F_u are the zonal wind speed, meridional wind speed, air density, pressure, Coriolis

parameter, Lagrangian time derivative, and viscous effects acting on u , respectively. We shall neglect F_u for now, but we shall find later that effects associated with the F_u term are often important.

On the synoptic scale and mesoscale, for $O(v) \sim 10 \text{ m s}^{-1}$, the Coriolis acceleration fv is of order

$$O(fv) \sim (10^{-4} \text{ s}^{-1}) (10 \text{ m s}^{-1}) \sim 10^{-3} \text{ m s}^{-2}.$$

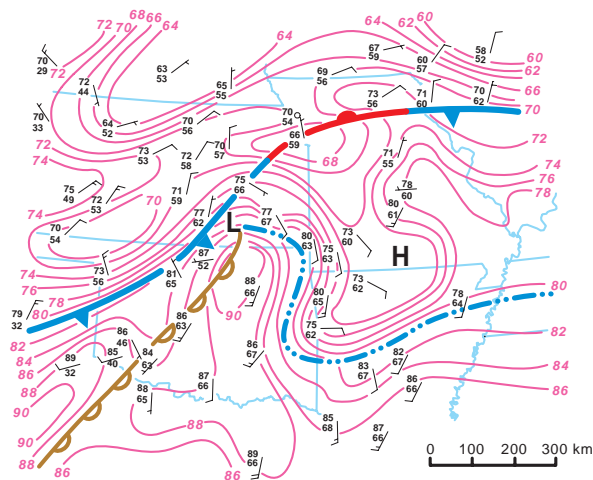
On the synoptic scale, the pressure gradient force has a scale of

$$O\left(-\frac{1}{\rho} \frac{\partial p}{\partial x}\right) \sim \frac{1}{1 \text{ kg m}^{-3}} \frac{10 \text{ mb}}{1000 \text{ km}} \sim 10^{-3} \text{ m s}^{-2};$$

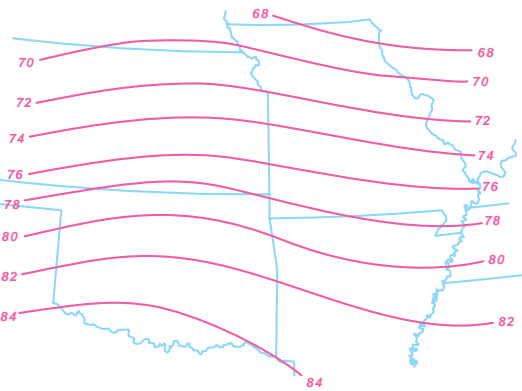
thus, the Coriolis and pressure gradient forces are of similar scales and, in the absence of significant flow curvature, we can infer that accelerations (du/dt) are small. Furthermore, because $v = v_g + v_a$ and $v_g = \frac{1}{\rho f} \frac{\partial p}{\partial x}$, where v_g and v_a are the geostrophic and ageostrophic meridional winds, respectively, (1.1) can be written as (ignoring F_u)

2100 UTC 24 April 1975

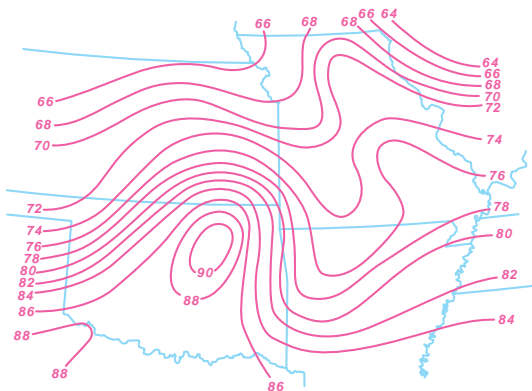
(a) manual analysis



(c) synoptic temperature field



(b) objectively analyzed temperature field



(d) mesoscale temperature perturbations

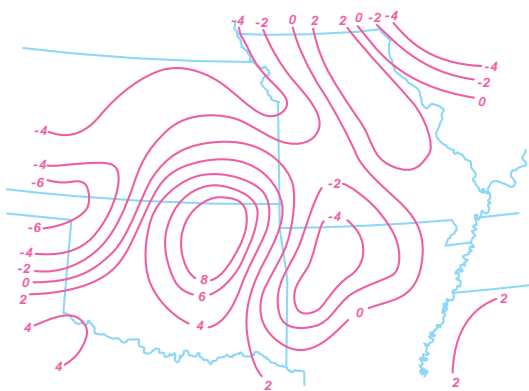


Figure 1.3 (a) Manual surface analysis for 2100 UTC 24 April 1975. Isotherms are drawn at 2°F intervals and fronts and pressure centers are also shown. A thunderstorm outflow boundary is indicated using a blue dashed line with double dots. The brown boundary with open scallops denotes a dryline. (The symbology used to indicate outflow boundaries and drylines has varied from analyst to analyst; different symbols for outflow boundaries and drylines appear in other locations within this book.) (b) Computer-generated ('objective') analysis of the total temperature field, i.e., the sum of the synoptic-scale temperature field and the mesoscale temperature perturbations. The objectively analyzed total temperature field is fairly similar to the manually produced temperature analysis in (a), although some small differences can be seen. (c) The synoptic-scale temperature field (°F). This was obtained using a low-pass filter that significantly damped wavelengths smaller than approximately 1500 km. (d) Mesoscale temperature perturbation field (°F). This was obtained using a band-pass filter that had its maximum response for wavelengths of 500 km, and damped wavelengths much longer and much shorter than 500 km. (Adapted from Maddox [1980].)

$f v_a = -\frac{1}{\rho} \frac{\partial p}{\partial x} + fv$. Therefore, ageostrophic motions are also small on the synoptic scale (particularly for fairly straight flow), owing to the approximate balance between the Coriolis and pressure gradient forces, referred to as *quasigeostrophic balance*.

On the mesoscale, the horizontal pressure gradient, $\partial p / \partial x$, can range from 5 mb/500 km (e.g., in quiescent conditions) to 5 mb/5 km (e.g., beneath a thunderstorm). At the small end of this range, the Coriolis and pressure gradient forces may be approximately in balance, but at the large end of this range, the pressure gradient force is two orders of magnitude larger than on the synoptic scale (i.e., 10^{-1} m s $^{-2}$ versus 10^{-3} m s $^{-2}$). On these occasions, the pressure gradient force dominates, the Coriolis force is relatively unimportant, and accelerations and ageostrophic motions are large.

A dimensionless number, called the *Rossby number*, assesses the relative importance of the Coriolis force and air parcel accelerations (the magnitude of the acceleration is directly related to the magnitude of the ageostrophic wind). The Rossby number can be used to distinguish synoptic-scale weather systems from subsynoptic-scale phenomena and is defined as

$$\text{Ro} = \frac{O(\mathbf{d}\mathbf{v}/dt)}{O(-f\mathbf{k} \times \mathbf{v})} \sim \frac{V/T}{fV} \sim \frac{V^2/L}{fV} \sim \frac{V}{fL}, \quad (1.2)$$

where \mathbf{k} is the unit vector in the positive z direction, T is a timescale (generally the advective timescale), V is the magnitude of a characteristic wind velocity, \mathbf{v} , and L is a characteristic horizontal length scale. On the synoptic scale, where the quasigeostrophic approximation usually can be made, $\text{Ro} \ll 1$. For mesoscale systems, $\text{Ro} \gtrsim 1$.

1.2.2 Hydrostatic balance

In many atmospheric applications (e.g., synoptic meteorology, large-scale dynamics) we assume that the atmosphere is in hydrostatic balance, that is, the vertical pressure gradient force per unit mass and gravitational acceleration are nearly balanced, resulting in negligible vertical accelerations. The vertical momentum equation can be written as

$$\frac{dw}{dt} = -\frac{1}{\rho} \frac{\partial p}{\partial z} + 2\Omega u \cos \phi - g + F_w, \quad (1.3)$$

where w , g , Ω , ϕ , and F_w are the vertical velocity, gravitational acceleration, angular rotation rate of the earth, latitude, and viscous effects acting on w , respectively. The scale of g is 10 m s $^{-2}$ and the scale of $|\frac{1}{\rho} \frac{\partial p}{\partial z}|$ is also $\sim (1 \text{ kg m}^{-3})^{-1} \cdot 100 \text{ mb/1000 m} \sim (1 \text{ kg m}^{-3})^{-1} \cdot 10^4$

Pa/10 3 m ~ 10 m s $^{-2}$. We neglect F_w in this simple analysis, although F_w can be important, particularly near the edges of clouds and in rising thermals. Moreover, the vertical component of the Coriolis force, $2\Omega u \cos \phi$, can be shown to be negligible compared with the size of the gravitational acceleration and the vertical pressure gradient, with a scale of 10 $^{-3}$ m s $^{-2}$. Thus, we neglect this term as well, which gives us

$$\frac{dw}{dt} = -\frac{1}{\rho} \frac{\partial p}{\partial z} - g. \quad (1.4)$$

If dw/dt is negligible, then (1.4) becomes the so-called *hydrostatic approximation*,

$$\frac{\partial p}{\partial z} = -\rho g. \quad (1.5)$$

In which types of phenomenon can we assume that dw/dt is negligible compared with $|\frac{1}{\rho} \frac{\partial p}{\partial z}|$ and g ? In other words, what determines whether a phenomenon is regarded as a hydrostatic or nonhydrostatic phenomenon?

It turns out we cannot simply scale the terms in (1.4) to determine which are significant, because the two terms on the rhs are nearly equal in magnitude but opposite in sign, and thus we must compare dw/dt with their residual. (Note that even small values of dw/dt [in comparison to g] can lead to vertical velocities of significance to mesoscale weather.) We do this by defining a base state (e.g., an average over a large horizontal area) density and a base state pressure, defined to be in hydrostatic balance with it. We then express the total pressure and density as the sum of the base state value (\bar{p} and $\bar{\rho}$, respectively) and a perturbation (p' and ρ' , respectively), that is,

$$p = \bar{p}(z) + p'(x, y, z, t) \quad (1.6)$$

$$\rho = \bar{\rho}(z) + \rho'(x, y, z, t), \quad (1.7)$$

and we require

$$0 = -\frac{\partial \bar{p}}{\partial z} - \bar{\rho}g. \quad (1.8)$$

Multiplying (1.4) by ρ , subtracting (1.8), dividing by ρ , and incorporating the definitions of \bar{p} and $\bar{\rho}$ yields

$$\frac{dw}{dt} = -\frac{1}{\rho} \frac{\partial p'}{\partial z} - \frac{\rho' g}{\rho}. \quad (1.9)$$

The relative importance of dw/dt compared with $|\frac{1}{\rho} \frac{\partial p'}{\partial z}|$ (and $|\frac{\rho' g}{\rho}|$) is

$$\frac{O\left(\frac{dw}{dt}\right)}{O\left(-\frac{1}{\rho} \frac{\partial p'}{\partial z}\right)}. \quad (1.10)$$

The scale of w can be obtained from scaling the continuity equation (the two-dimensional Boussinesq approximation is used for simplicity; see Chapter 2 for a review),

$$O\left(\frac{\partial w}{\partial z}\right) \sim O\left(\frac{\partial u}{\partial x}\right); \quad (1.11)$$

thus,

$$O(w) \sim \frac{VD}{L}, \quad (1.12)$$

where $O(w)$ is the scale of w , and V , D , and L are the characteristic horizontal velocity scale, depth scale, and horizontal length scale of the phenomenon, respectively. From (1.12) the scale of dw/dt is therefore

$$O\left(\frac{dw}{dt}\right) \sim \frac{VD}{LT}, \quad (1.13)$$

where T is the characteristic timescale for accelerations within the phenomenon.

The scale of $|\frac{1}{\rho} \frac{\partial p'}{\partial z}|$ may be written as

$$O\left(-\frac{1}{\rho} \frac{\partial p'}{\partial z}\right) \sim \frac{\delta p'}{\rho D}, \quad (1.14)$$

where $\delta p'$ is the characteristic pressure perturbation within the phenomenon. We want to eliminate $\delta p'$ and ρ in favor of the characteristic scales of the phenomenon (e.g., V , D , L , and T). We do this by scaling the horizontal momentum equation as follows:

$$\frac{du}{dt} \approx -\frac{1}{\rho} \frac{\partial p'}{\partial x} \quad (1.15)$$

$$O\left(\frac{du}{dt}\right) \sim O\left(-\frac{1}{\rho} \frac{\partial p'}{\partial x}\right) \quad (1.16)$$

$$\frac{V}{T} \sim \frac{\delta p'}{\rho L} \quad (1.17)$$

$$\frac{VL}{T} \sim \frac{\delta p'}{\rho}; \quad (1.18)$$

therefore, using (1.14),

$$O\left(-\frac{1}{\rho} \frac{\partial p'}{\partial z}\right) \sim \frac{VL}{TD}. \quad (1.19)$$

Using (1.13) and (1.19), (1.10) becomes

$$\frac{O\left(\frac{dw}{dt}\right)}{O\left(-\frac{1}{\rho} \frac{\partial p'}{\partial z}\right)} \sim \frac{\frac{VD}{LT}}{\frac{VL}{TD}} = \left(\frac{D}{L}\right)^2. \quad (1.20)$$

The quantity D/L is known as the *aspect ratio* of the phenomenon—the ratio of the characteristic depth scale

of the phenomenon to the horizontal length scale (or width) of the phenomenon. When a phenomenon is much wider than it is deep ($D/L \ll 1$), dw/dt is relatively small compared with the vertical perturbation pressure gradient force and the phenomenon can be considered a *hydrostatic phenomenon*; that is, the hydrostatic approximation is justified. When a phenomenon is approximately as wide as it is deep ($D/L \sim 1$), dw/dt is similar in magnitude to the vertical perturbation pressure gradient force, and the phenomenon is considered a *nonhydrostatic phenomenon*; that is, the hydrostatic approximation should not be made (Figure 1.4). Note that we have assumed equivalent timescales for the horizontal and vertical accelerations (i.e., T is equivalent in (1.13) and (1.17)). This assumption is equivalent to (1.11), which dictates that D/W (the vertical advective timescale) is equal to L/V (the horizontal advective timescale). There may be cases in which $\partial u/\partial x$ is balanced by $\partial v/\partial y$ such that the scaling in (1.11) is not appropriate. In that case, even phenomena with a large aspect ratio may be nearly hydrostatic. For convective motions, (1.11) is considered a good assumption.

On the synoptic scale, $D/L \sim 10 \text{ km}/1000 \text{ km} \sim 1/100 \ll 1$. On the mesoscale, D/L can be ~ 1 or $\ll 1$, depending on the phenomenon. For example, in a thunderstorm updraft, $D/L \sim 10 \text{ km}/10 \text{ km} \sim 1$ (i.e., the thunderstorm updraft can be considered to be a nonhydrostatic phenomenon). However, for the rain-cooled outflow that the thunderstorm produces, $D/L \sim 1 \text{ km}/10 \text{ km} \sim 1/10 \ll 1$ (i.e., the outflow can be considered to be an approximately hydrostatic phenomenon).

In a hydrostatic atmosphere, pressure can be viewed essentially as being proportional to the weight of the atmosphere above a given point. Pressure changes in a hydrostatic atmosphere arise from changes in the density of air vertically integrated over a column extending from the location in question to $z = \infty$ ($p = 0$). This interpretation of pressure will be useful for some mesoscale phenomena. For a nonhydrostatic phenomenon, we cannot relate pressure fluctuations solely to changes in the weight of the overlying atmosphere. Instead, significant *dynamic* effects may contribute to pressure perturbations. Examples include the low pressure found in the core of a tornado and above the wing of an airplane in flight, and the high pressure found beneath an intense downburst and on the upwind side of an obstacle. The relationship between the pressure field and wind field is discussed in much greater depth in Section 2.5.

In the next chapter we review some of the basic equations and tools that will be relied upon in the rest of the book. The experienced reader may wish to skip ahead to Chapter 3.

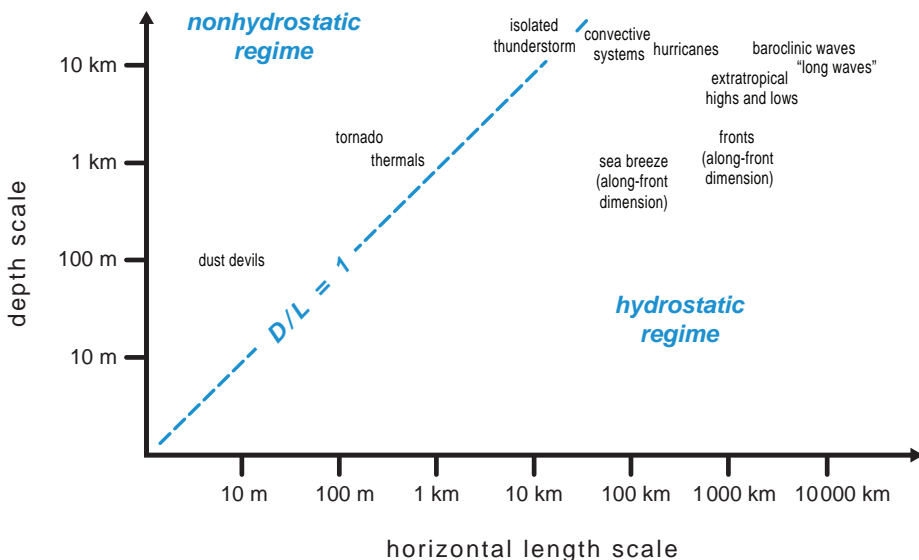


Figure 1.4 We can infer that a phenomenon is hydrostatic when its horizontal length scale is significantly larger than its vertical depth scale. Shown above are some examples of nonhydrostatic and approximately hydrostatic phenomena plotted as a function of depth versus horizontal length (i.e., width) scale.

Further reading

- Emanuel (1986).
- Fujita, T. T., 1963: Analytical mesometeorology: A review. *Severe Local Storms, Meteor. Monogr.*, No. 27, 77–125.
- Fujita (1981).
- Fujita, T. T., 1986: Mesoscale classifications: Their history and their application to forecasting. *Mesoscale Meteorology and Forecasting*, P. S., Ray, Ed., Amer. Meteor. Soc., 18–35.
- Lilly, D. K., 1983: Stratified turbulence and mesoscale variability of the atmosphere. *J. Atmos. Sci.*, **40**, 749–761.
- Maddox (1980).
- Orlanski (1975).
- Tepper, M., 1959: Mesometeorology—the link between macroscale atmospheric motions and local weather. *Bull. Amer. Meteor. Soc.*, **40**, 56–72.
- Thunis, P., and R. Bornstein, 1996: Hierarchy of mesoscale flow assumptions and equations. *J. Atmos. Sci.*, **53**, 380–397.
- Vinnichenko, N. K., 1970: Kinetic energy spectrum in the free atmosphere—one second to five years. *Tellus*, **22**, 158–166.

2

Basic Equations and Tools

In this chapter, we examine the equations necessary for the study of mesoscale phenomena. This equation set must ensure the conservation of momentum, mass, and energy, and must also allow exchanges between different forms of energy. We also introduce the useful concepts of vorticity and circulation, and we examine the relationship between pressure perturbations and the wind and temperature fields. Finally, we cover the basics of soundings and hodographs, which are important tools for assessing atmospheric conditions with regard to the development or sustenance of mesoscale phenomena.

2.1 Thermodynamics

2.1.1 Ideal gas law and first law of thermodynamics

We begin with the *ideal gas law* or *equation of state*, which can be expressed as

$$p = \rho RT, \quad (2.1)$$

where p is the pressure, ρ is the air density, R is the gas constant (which depends on the composition of the air), and T is absolute temperature. If we consider only the pressure of dry air, p_d , then we can write (2.1) as

$$p_d = \rho_d R_d T \quad (2.2)$$

where ρ_d is the density of the dry air (i.e., the mass of dry air per unit volume) and $R_d = 287.04 \text{ J kg}^{-1} \text{ K}^{-1}$ is the gas constant for dry air.

One of the fundamental laws governing the behavior of atmospheric gases and the exchange of energy between

a volume of air and its environment is the *first law of thermodynamics*, given by

$$q = c_v \frac{dT}{dt} + p \frac{d\alpha}{dt}, \quad (2.3)$$

where q is the specific heating rate, c_v is the specific heat for a constant volume process, α is the specific volume ($=\rho^{-1}$), t is time, and d/dt is a material derivative such that

$$\frac{d}{dt} = \frac{\partial}{\partial t} + u \frac{\partial}{\partial x} + v \frac{\partial}{\partial y} + w \frac{\partial}{\partial z} = \frac{\partial}{\partial t} + \mathbf{v} \cdot \nabla, \quad (2.4)$$

where $\mathbf{v} = u \mathbf{i} + v \mathbf{j} + w \mathbf{k}$ is the velocity vector, u , v , and w are the velocity components in the east (x), north (y), and upward (z) directions, respectively, \mathbf{i} , \mathbf{j} , and \mathbf{k} are unit vectors in the east, north, and upward directions, respectively, and $\nabla = \mathbf{i}\partial/\partial x + \mathbf{j}\partial/\partial y + \mathbf{k}\partial/\partial z$. For a scalar χ , $\partial\chi/\partial t$ represents the *local tendency* of χ and $-\mathbf{v} \cdot \nabla \chi$ represents the *advection* of χ .

The specific heating rate q can include heating and cooling due to phase changes of water, radiation, and molecular diffusion. The terms on the rhs of (2.3) represent the change in internal energy and the work done on the environment through expansion, respectively. Alternatively, (2.3) can be written as

$$q = c_p \frac{dT}{dt} - \alpha \frac{dp}{dt}, \quad (2.5)$$

where c_p is the specific heat for a constant pressure process ($R = c_p - c_v$). The two terms on the rhs of (2.5) do not have the same interpretation as the terms on the rhs of (2.3); $c_p dT/dt$ represents the change in specific enthalpy, h ($=c_v T + p\alpha$), and $-\alpha dp/dt$ represents the effects of changing pressure.

We can derive the *dry adiabatic lapse rate* from (2.5), that is, the rate at which an air parcel cools (warms) owing to expansion (compression) if ascending (descending) dry adiabatically. If we let $q = 0$ (i.e., no heat is exchanged between the parcel and its environment), assume T and p are functions of z only, such that $\frac{dT}{dt} = \frac{dT}{dz} \frac{dz}{dt}$ and $\frac{dp}{dt} = \frac{dp}{dz} \frac{dz}{dt}$ via the chain rule, and assume that $dp/dz = -\rho g$ (in effect, we are assuming that the pressure in the displaced parcel is equal to the pressure within the environment, which we also assume is hydrostatic), then (2.5) can be rearranged to yield

$$\Gamma_d \equiv -\frac{dT}{dz} = \frac{g}{c_p}, \quad (2.6)$$

where $\Gamma_d \approx 9.8 \text{ K km}^{-1}$ is the dry adiabatic lapse rate.

Along similar lines, by integrating (2.3) from p to a reference pressure p_0 (generally taken to be 1000 mb) and assuming $q = 0$, we obtain *Poisson's equation*,

$$\theta = T \left(\frac{p_0}{p} \right)^{R/c_p}, \quad (2.7)$$

where θ is known as the *potential temperature*. The potential temperature is the temperature of an air parcel if the parcel is expanded or compressed adiabatically to p_0 ; θ is conserved for adiabatic displacements of unsaturated air.¹

The definition of potential temperature given by (2.7) allows us to recast (2.5) as

$$\frac{d \ln \theta}{dt} = \frac{q}{c_p T}; \quad (2.8)$$

thus, local potential temperature changes are governed by

$$\frac{\partial \theta}{\partial t} = -u \frac{\partial \theta}{\partial x} - v \frac{\partial \theta}{\partial y} - w \frac{\partial \theta}{\partial z} + \frac{q \theta}{c_p T}. \quad (2.9)$$

2.1.2 Moisture variables and moist processes

The most interesting (in our view) meteorological phenomena could not occur without water vapor and its phase changes. Unlike the other major constituents of air, the

¹ Quantities that are conserved following parcel motions are useful in many applications. In such cases, one need not integrate all forcings along trajectories to obtain a final value. Instead, with knowledge of the initial state (e.g., θ at the initial pressure level) and partial knowledge of the final state (e.g., to what pressure level the parcel moved), one can often solve for an unknown final property (e.g., the temperature of the parcel at the final pressure level).

concentration of water vapor is highly variable in space and time. Below our focus is on the thermodynamics of the liquid phase. For a rigorous treatment of the thermodynamics of the ice phase, we refer the reader to the work of Bohren and Albrecht (1998).

The equation of state for water vapor is

$$e = \rho_v R_v T, \quad (2.10)$$

where e is the vapor pressure, ρ_v is the density of the water vapor (i.e., the mass of water vapor per unit volume), and $R_v = 461.51 \text{ J kg}^{-1} \text{ K}^{-1}$ is the gas constant for water vapor. Note that $\rho = \rho_d + \rho_v$. Moreover, from Dalton's law, the total pressure is just the sum of the pressure of dry air and the vapor pressure, that is, $p = p_d + e$.

The water vapor mixing ratio, r_v , is defined as

$$r_v = \frac{\rho_v}{\rho_d} = \frac{\varepsilon e}{p_d} = \frac{\varepsilon e}{p - e}, \quad (2.11)$$

where $\varepsilon = R_d/R_v \approx 0.622$. The water vapor mixing ratio is conserved for dry adiabatic processes (i.e., $dr_v/dt = 0$), because no mass is exchanged between a parcel and its environment and there is no phase change. In general, the conservation of water vapor is governed by

$$\frac{dr_v}{dt} = \frac{\partial r_v}{\partial t} + u \frac{\partial r_v}{\partial x} + v \frac{\partial r_v}{\partial y} + w \frac{\partial r_v}{\partial z} = S_i, \quad (2.12)$$

where S_i are sources and sinks of water vapor attributable to phase changes (e.g., condensation is a water vapor sink, whereas evaporation is a water vapor source).

A dimensionless measure of water vapor, the relative humidity, RH (often expressed as a percentage), is defined as either the quotient of the vapor pressure and saturation vapor pressure, e_s , or as the quotient of the water vapor mixing ratio and saturation water vapor mixing ratio, r_{vs} , that is,

$$RH = \frac{e}{e_s} \quad (2.13)$$

or

$$RH = \frac{r_v}{r_{vs}}, \quad (2.14)$$

where e_s is a function of temperature only. Slight differences between e/e_s and r_v/r_{vs} exist for $0\% < RH < 100\%$; when $RH = 0\%$ or $RH = 100\%$, $e/e_s = r_v/r_{vs}$.

The *Clausius–Clapeyron equation* relates e_s to T ,

$$\frac{de_s}{dT} = \frac{l_v e_s}{R_v T^2}, \quad (2.15)$$

where l_v is the specific latent heat of vaporization (l_v is a function of T ; $l_v = 2.501 \times 10^6 \text{ J kg}^{-1}$ at 0°C). To a good approximation,²

$$e_s \approx 6.112 \exp\left(\frac{17.67T}{T + 243.5}\right), \quad (2.16)$$

where e_s is in millibars, and T is in degrees Celsius.

Because R in (2.1) depends on the composition of the air and because water vapor is so variable, the ideal gas law for moist air often is expressed more conveniently in terms of R_d using

$$R = R_d \frac{1 + r_v/\varepsilon}{1 + r_v}, \quad (2.17)$$

together with a *virtual temperature*, T_v , that accounts for the presence of water vapor, that is,

$$p = \rho R_d T_v, \quad (2.18)$$

where

$$T_v = T \frac{1 + r_v/\varepsilon}{1 + r_v} \approx T(1 + 0.61r_v). \quad (2.19)$$

The virtual temperature can be interpreted as the temperature that a sample of dry air must have so that its density is equivalent to a sample of moist air at the same pressure.

The *virtual potential temperature*, θ_v , is simply the virtual temperature of an air parcel if expanded or compressed adiabatically to a reference pressure of p_0 , that is,

$$\theta_v = \theta \frac{1 + r_v/\varepsilon}{1 + r_v} \approx \theta(1 + 0.61r_v). \quad (2.20)$$

Because θ and r_v are both conserved for dry adiabatic motions, θ_v also is conserved for dry adiabatic motions.

The effects of condensate on air density can be accommodated in a similar manner via the *density temperature*, T_ρ , where

$$T_\rho = T \left(\frac{1 + r_v/\varepsilon}{1 + r_t} \right) \approx T(1 + 0.61r_v - r_h). \quad (2.21)$$

Here r_h is the hydrometeor mixing ratio (i.e., the mass of hydrometeors per unit mass) and $r_t = r_v + r_h$ is the total water mixing ratio (i.e., the mass of water vapor plus condensate per unit mass). Likewise, the density potential temperature, θ_ρ , is

$$\theta_\rho = \theta \frac{1 + r_v/\varepsilon}{1 + r_t} \approx \theta(1 + 0.61r_v - r_h). \quad (2.22)$$

² See Bolton (1980). His formula is accurate to within 0.3% in the range $-35^\circ\text{C} \leq T \leq 35^\circ\text{C}$.

Not only does the water vapor concentration affect R , but it also affects c_p and c_v . The specific heats at constant pressure and volume for dry air, c_{pd} and c_{vd} , respectively, are related to c_p and c_v via

$$c_p = c_{pd} \left(\frac{1 + r_v \frac{c_{pv}}{c_{pd}}}{1 + r_v} \right) \approx c_{pd}(1 + 0.85r_v) \quad (2.23)$$

$$c_v = c_{vd} \left(\frac{1 + r_v \frac{c_{vv}}{c_{vd}}}{1 + r_v} \right) \approx c_{vd}(1 + 0.94r_v), \quad (2.24)$$

where c_{pv} and c_{vv} are the specific heats at constant pressure and volume for water vapor. Approximate values of c_{pd} , c_{vd} , c_{pv} , and c_{vv} are 1005, 719, 1870, and $1410 \text{ J kg}^{-1} \text{ K}^{-1}$, respectively. For most practical purposes, the effects of water vapor on the specific heats can be neglected without serious errors, as will be done in subsequent chapters.

The *dewpoint temperature*, T_d , is the temperature at which saturation is achieved if air is cooled while holding pressure and water vapor mixing ratio constant; that is, $e = e_s(T_d)$. By inverting (2.16), to a good approximation,

$$T_d \approx \frac{243.5}{\left[\frac{17.67}{\ln(e/6.112)} \right] - 1}, \quad (2.25)$$

where e is in millibars and T_d is in degrees Celsius. In contrast, the *wet-bulb temperature*, T_w , is the temperature to which air can be cooled, at constant pressure, by evaporating water into the air until the air becomes saturated. It can be computed either graphically on a thermodynamic diagram (Figure 2.2) or iteratively via the relation

$$[c_{pd} + r_{vs}(T_w)c_l](T - T_w) = l_v(T_w)r_{vs}(T_w) - l_v(T)r_v, \quad (2.26)$$

where c_l is the specific heat of liquid water at constant pressure ($\sim 4200 \text{ J kg}^{-1} \text{ K}^{-1}$). The *wet-bulb potential temperature*, θ_w , is simply the potential temperature that a parcel would have if cooled by evaporation during saturated descent to the reference pressure p_0 .

Because potential temperature is conserved for dry adiabatic motion, air parcels cool as they ascend dry adiabatically to lower pressures. If the vertical displacement is sufficiently large, saturation occurs. In a *moist or saturated adiabatic process*, air is saturated and may contain condensate. A distinction is made between a reversible moist adiabatic process, in which total water (vapor plus condensate) is conserved (i.e., $dr_t/dt = 0$), and an irreversible

moist adiabatic process, called a *pseudoadiabatic process*, in which condensate is assumed to be removed as soon as it forms.

In the case of a reversible moist adiabatic process, the specific heating rate is

$$q = -T \frac{d}{dt} \left(\frac{l_v r_v}{T} \right), \quad (2.27)$$

where $r_v = r_{vs}$ because the parcel is saturated and $d(l_v r_v)/dt < 0 (>0)$ if condensation (evaporation) is occurring. Furthermore, in (2.5), c_p is replaced with $c_{pd} + r_t c_1$, p is replaced with p_d , and α is replaced with $\alpha_d (= \rho_d^{-1})$. Substituting (2.27) into (2.5), modified as described above, and assuming that T , p_d , and $l_v r_v$ are functions of z only, (2.5) becomes

$$(c_{pd} + r_t c_1) \frac{dT}{dz} - \alpha_d \frac{dp_d}{dz} = -\frac{d(l_v r_v)}{dz} + \frac{l_v r_v}{T} \frac{dT}{dz}. \quad (2.28)$$

From the Clausius–Clapeyron equation and the fact that $p = p_d + e$,

$$-\alpha_d \frac{dp_d}{dz} = -\alpha_d \frac{dp}{dz} + \frac{l_v r_v}{T} \frac{dT}{dz}. \quad (2.29)$$

Furthermore, if we assume that $-\alpha_d dp/dz = \rho g / \rho_d \approx g$, then we can rearrange (2.28) to obtain the *reversible moist adiabatic lapse rate*, Γ_{rm} (Figure 2.1), where

$$\Gamma_{rm} \equiv -\frac{dT}{dz} = \frac{g}{c_{pd} + r_t c_1} + \frac{1}{c_{pd} + r_t c_1} \frac{dl_v r_v}{dz}. \quad (2.30)$$

Note that $\Gamma_{rm} < \Gamma_d = g/c_p$ because $r_t > 0$ and $d(l_v r_v)/dz < 0$.

We can integrate the first law of thermodynamics with $q = -T d(l_v r_v/T)/dt$ and the above substitutions for c_p , p , and α to obtain another conserved variable, the *equivalent potential temperature*, θ_e , given by

$$\theta_e = T \left(\frac{p_0}{p_d} \right)^{R_d/(c_{pd} + r_t c_1)} \times \exp \left[\frac{l_v r_v}{(c_{pd} + r_t c_1)T} \right]. \quad (2.31)$$

The equivalent potential temperature is the potential temperature an air parcel would attain if all its water vapor were to condense in an adiabatic process. (Similarly, the *equivalent temperature*, T_e , is defined as the temperature an air parcel would attain if all its water vapor were to condense in an adiabatic, *isobaric* process.) In the case of unsaturated air, T is replaced with T^* , the temperature at which a lifted parcel becomes saturated, known as the *saturation temperature* [note that $l_v = l_v(T)$; for unsaturated

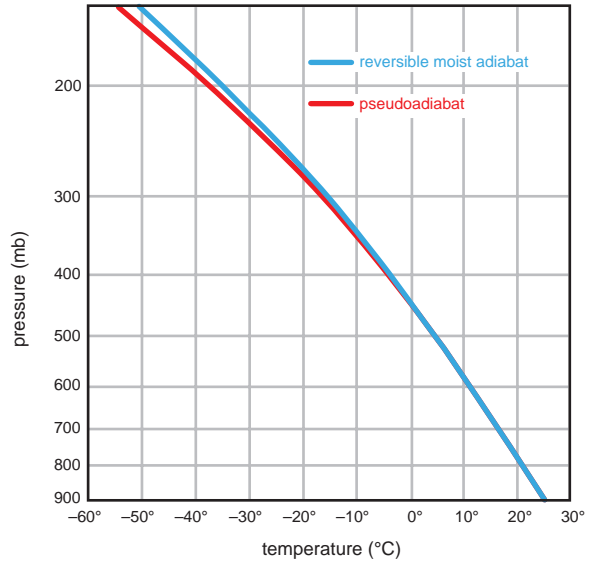


Figure 2.1 Temperature as a function of pressure for reversible moist adiabatic and pseudoadiabatic ascent from saturated initial conditions of $p = 900$ mb and $T = 25^\circ\text{C}$.

air, $l_v(T^*)$ should be used]. To a good approximation,³

$$T^* = \frac{2840}{3.5 \ln T - \ln e - 4.805} + 55. \quad (2.32)$$

Note that $\theta_e = \theta$ for $r_v = 0$.

At the other extreme, if we assume that the condensate is removed immediately from the parcel as it forms, in which case the latent heat from condensation is absorbed only by the gaseous portion of the parcel (i.e., the condensate does not absorb any heat), then we have what is said to be a *pseudomoist adiabatic* or *pseudoadiabatic process*. Substituting (2.27) into (2.5), again replacing p with p_d and α with α_d , but replacing c_p with $c_{pd} + r_v c_1$, we can obtain the *pseudoadiabatic lapse rate*, Γ_{ps} , where

$$\Gamma_{ps} \equiv -\frac{dT}{dz} = \frac{g}{c_{pd} + r_v c_1} + \frac{1}{c_{pd} + r_v c_1} \frac{dl_v r_v}{dz}. \quad (2.33)$$

Note that $\Gamma_{ps} > \Gamma_{rm}$ because $r_v < r_t$. Sometimes Γ_{ps} is generically referred to as the *saturated adiabatic lapse rate* or (irreversible) *moist adiabatic lapse rate*, Γ_m . The curves representing moist adiabatic processes on a thermodynamic diagram do not account for the heat carried by condensate; thus, the curves are called *pseudoadiabats* (Figures 2.1 and 2.2).

³ See Bolton (1980).

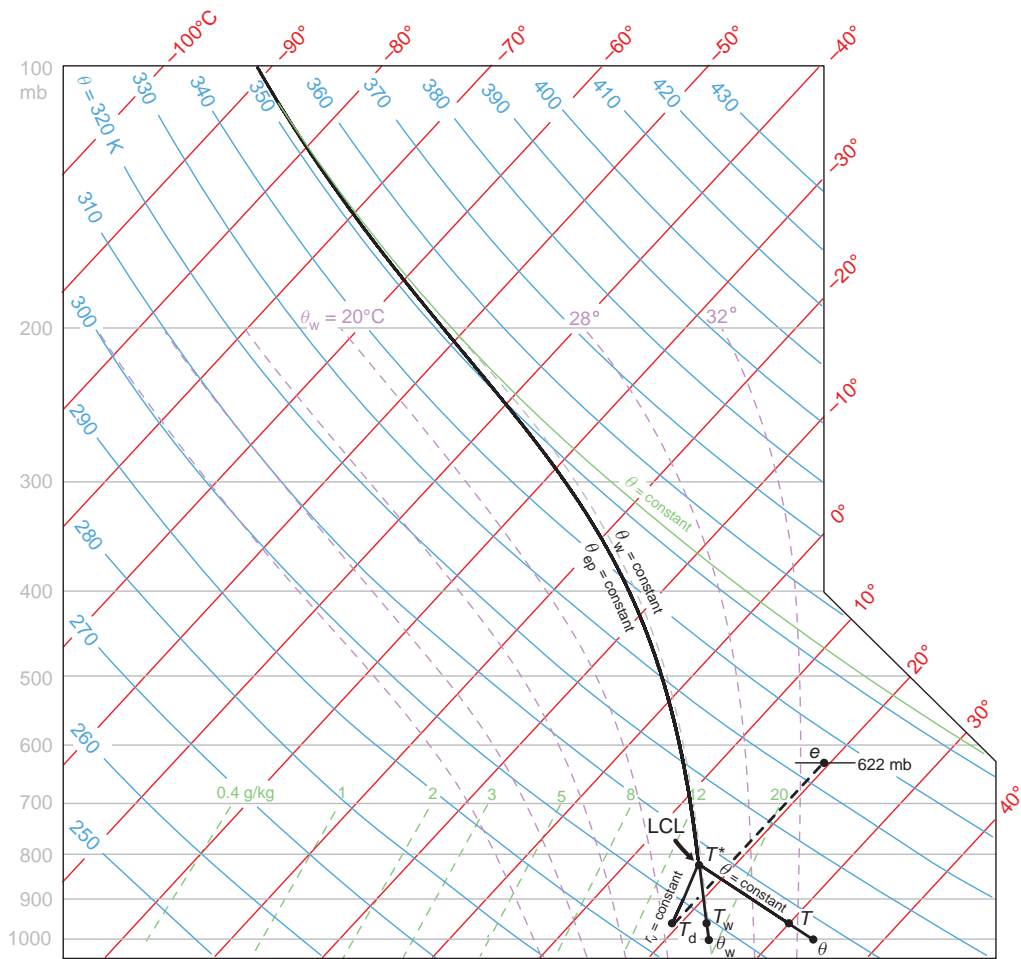


Figure 2.2 Skew T -log p diagram illustrating how to compute θ , θ_w , θ_{ep} , T_w , T^* , e , and the lifting condensation level (LCL) from observations of T and T_d . Isobars are gray (labeled in mb), isentropes (dry adiabats) are blue (labeled in K), isotherms are red (labeled in °C), water vapor mixing ratio lines are green (dashed; labeled in g kg⁻¹), and pseudoadiabats are purple (dashed; labels in °C indicate θ_w values corresponding to the pseudoadiabats). The LCL and T^* are found by finding the intersection of the dry adiabat and constant mixing ratio line that pass through the potential temperature and mixing ratio, respectively, of the parcel to be lifted. The potential temperature is found by following a dry adiabat to 1000 mb through the temperature of the parcel. The wet-bulb temperature (wet-bulb potential temperature) is found by following a pseudoadiabat from a parcel's T^* value back to the parcel's pressure (1000 mb). The equivalent potential temperature is found by following a pseudoadiabat from T^* to a pressure (high altitude) where the pseudoadiabat is parallel to the dry adiabats, and then identifying the potential temperature associated with the pseudoadiabat at this pressure (the solid green line identifies the θ_{ep} of a parcel located at the surface). The vapor pressure is found by locating the intersection of the isotherm passing through the parcel's water vapor mixing ratio and the $p = 622 \text{ mb}$ isobar. The water vapor mixing ratio line passing through this intersection point (dashed black line) represents e in millibars. (The saturation vapor pressure can be found via the same exercise but by following the isotherm that passes through the temperature rather than water vapor mixing ratio of the parcel.) For the parcel shown ($T \approx 30^\circ\text{C}$, $T_d \approx 19^\circ\text{C}$, $r_v \approx 15 \text{ g kg}^{-1}$), the θ , θ_w , θ_{ep} , T_w , T^* , e , and LCL are as follows: 307.5 K, 23.5°C, 352 K, 22.5°C, 17°C, 22 mb, and 825 mb.

The *pseudoequivalent potential temperature*, θ_{ep} , is the temperature achieved by an air parcel that is lifted pseudoadiabatically to 0 mb, followed by a dry adiabatic descent to $p_0 = 1000 \text{ mb}$ (Figure 2.2). An expression⁴ for θ_{ep} (in our experience, this is how the field identified as ‘ θ_e ’ is usually computed in computer-generated weather analyses and forecasts) is

$$\theta_{\text{ep}} = T \left(\frac{p_0}{p} \right)^{0.2854(1-0.28r_v)} \times \exp \left[r_v(1 + 0.81r_v) \left(\frac{3376}{T^*} - 2.54 \right) \right] \quad (2.34)$$

The θ_{ep} computed using the expression above is conserved for dry adiabatic processes and approximately conserved for pseudoadiabatic processes. For dry adiabatic and moist reversible processes, the θ_e given by (2.31) is conserved. The evaporation of rain into unsaturated air (an irreversible process) causes θ_e to increase slightly; the melting of ice has the opposite effect.

The differences between θ_e and θ_{ep} are small for most practical purposes. Hereafter we shall not make a distinction between the two. We shall treat θ_e , regardless of the details of how it is computed, as being approximately conserved for dry and moist adiabatic processes. We also note that θ_w is approximately conserved for dry and moist adiabatic motions as well. For this reason, θ_e and θ_w are sometimes used as tracers of air.

2.2 Mass conservation

Our equation set must ensure the conservation of mass through a *mass continuity equation*, which we shall often use in future chapters to provide a link between the horizontal and vertical wind fields (e.g., when air is rising within a column, we expect net convergence below the level of maximum vertical velocity and net divergence above). This will prove to be useful to our later conceptual models.

For strict conservation of mass, any net three-dimensional convergence following a parcel must be accompanied by an increase in the density of that parcel. This principle is expressed in equation form as

$$\frac{d\rho}{dt} + \rho (\nabla \cdot \mathbf{v}) = 0. \quad (2.35)$$

Similarly, if we were to examine a fixed volume of space, the density within that volume must change given a net

⁴ See Bolton (1980).

divergence of mass within the volume. Thus, the local change in density is given by

$$\frac{\partial \rho}{\partial t} + \nabla \cdot (\rho \mathbf{v}) = 0. \quad (2.36)$$

Though the above equations satisfy mass conservation exactly, it is often difficult to gain physical insight when all of the terms are retained. Therefore, it is helpful to simplify these equations under those conditions for which certain terms dominate. Although mass is not strictly conserved in the new equations, we shall be able to use them much more easily to understand the behavior of the atmosphere.

When the square of the speed of motion is much less than the square of the speed of sound (a good approximation for nearly all atmospheric phenomena), we can make what is known as the *anelastic approximation*. If the atmosphere is assumed to have only small deviations from a constant reference potential temperature, the continuity equation can be expressed as⁵

$$\nabla \cdot (\rho_a \mathbf{v}) = 0, \quad (2.37)$$

where $\rho_a(z)$ is the density of the adiabatic reference state. For qualitative purposes, we shall use (2.37) at times with a vertical profile of density $\bar{\rho} = \bar{\rho}(z)$ that does not necessarily correspond to a constant potential temperature atmosphere. (For quantitative purposes, we would need to modify the thermodynamic equation to maintain energy conservation.)

If the anelastic conditions are met and the depth of the flow (D) is much less than the scale height of the atmosphere ($H \sim 8 \text{ km}$), it can be shown that the *incompressible* or *Boussinesq*⁶ form of the mass continuity equation,

$$\nabla \cdot \mathbf{v} = 0, \quad (2.38)$$

can be used. It should be noted that incompressibility is satisfied if density is not a function of pressure (e.g., if one squeezes a water balloon, it will change shape but will not tend to occupy a smaller volume overall). In addition, to obtain (2.38), changes in density due to heating following the flow must be ignored. This form of the continuity equation conserves volume rather than mass (although the two are equivalent if density is constant), and is the easiest

⁵ See Ogura and Phillips (1962).

⁶ Joseph Boussinesq (1842–1929) was a French mathematician and physicist. He is probably best known for his contributions to the study of turbulence.

form to use for linking the horizontal and vertical motions. This is clear if (2.38) is written in component form as

$$\frac{\partial u}{\partial x} + \frac{\partial v}{\partial y} + \frac{\partial w}{\partial z} = 0. \quad (2.39)$$

The vertical velocity at any height (z_1) can be related to the net horizontal convergence below that level by integrating (2.39) from $z = 0$ to $z = z_1$. Then,

$$\int_0^{z_1} \left(\frac{\partial u}{\partial x} + \frac{\partial v}{\partial y} \right) dz = - \int_0^{z_1} \frac{\partial w}{\partial z} dz \quad (2.40)$$

Defining horizontal divergence as $\delta = \partial u / \partial x + \partial v / \partial y$, and $\bar{\delta}$ as the average of δ over the depth from 0 to z_1 , we can write (2.40) as

$$\bar{\delta} z_1 = -w(z_1) + w(0). \quad (2.41)$$

For a flat surface, $w(0) = 0$; therefore, (2.41) reduces to

$$w(z_1) = -\bar{\delta} z_1, \quad (2.42)$$

and it is clear that positive (negative) vertical motion at z_1 must be accompanied by mean convergence (divergence) between the surface and z_1 .

2.3 Momentum equations

2.3.1 Conservation of momentum

Even though we have already, somewhat unavoidably, introduced some forms of the momentum equations in Chapter 1, at the risk of being redundant, we again present the momentum equations. In vector form, the momentum equations can be expressed in rotating coordinates as

$$\frac{dv}{dt} = -2\Omega \times v - \frac{1}{\rho} \nabla p + g + F, \quad (2.43)$$

where $\Omega = \Omega \cos \phi \mathbf{j} + \Omega \sin \phi \mathbf{k}$ is the earth's angular velocity, ϕ is latitude, $\mathbf{g} = -g\mathbf{k}$ is the gravitational acceleration (the centrifugal force has been combined with gravitation in \mathbf{g}), and $\mathbf{F} = F_u \mathbf{i} + F_v \mathbf{j} + F_w \mathbf{k}$ represents frictional forces. Equation (2.43) represents Newton's second law applied to the airflow on earth. Regarding \mathbf{F} , it can be related to either molecular viscosity or turbulence. The contribution to \mathbf{F} from molecular viscosity is proportional to $v \nabla^2 v$, where v is the *kinematic viscosity* (assuming constant ρ). The relative importance of molecular viscosity is

related to the inverse of the *Reynolds number*,⁷ $Re = VL/v$, where V is a characteristic velocity scale and L is a characteristic length scale. Because the kinematic viscosity of air is small ($v \approx 1.5 \times 10^{-5} \text{ m}^2 \text{ s}^{-1}$), Re is very large except within a few millimeters of the ground; thus, molecular viscosity is negligible except within the lowest few millimeters. Turbulent eddies, however, can produce an *eddy viscosity* with respect to the mean flow, especially in the atmospheric boundary layer. This topic is dealt with in considerably greater detail in Chapter 4.

In spherical coordinates, (λ, ϕ, z) , the components of \mathbf{v} are defined as

$$u \equiv r \cos \phi \frac{d\lambda}{dt} = \frac{dx}{dt} \quad (2.44)$$

$$v \equiv r \frac{d\phi}{dt} = \frac{dy}{dt} \quad (2.45)$$

$$w \equiv \frac{dz}{dt} \quad (2.46)$$

where λ is longitude and r is the distance to the center of the earth, which is related to z by $r = a + z$, with a being the radius of the earth (we shall assume that $r \approx a$). Note that the (x, y, z) coordinate system defined by the above relationships is not a Cartesian coordinate system because the \mathbf{i}, \mathbf{j} , and \mathbf{k} unit vectors are not constant. Instead,

$$\frac{d\mathbf{i}}{dt} = \frac{u}{a \cos \phi} (\mathbf{j} \sin \phi - \mathbf{k} \cos \phi) \quad (2.47)$$

$$\frac{d\mathbf{j}}{dt} = -\frac{u \tan \phi}{a} \mathbf{i} - \frac{v}{a} \mathbf{k} \quad (2.48)$$

$$\frac{d\mathbf{k}}{dt} = \mathbf{i} \frac{u}{a} + \mathbf{j} \frac{v}{a}; \quad (2.49)$$

thus,

$$\begin{aligned} \frac{dv}{dt} = & \left(\frac{du}{dt} - \frac{uv \tan \phi}{a} + \frac{uw}{a} \right) \mathbf{i} + \left(\frac{dv}{dt} + \frac{u^2 \tan \phi}{a} + \frac{vw}{a} \right) \mathbf{j} \\ & + \left(\frac{dw}{dt} - \frac{u^2 + v^2}{a} \right) \mathbf{k}. \end{aligned} \quad (2.50)$$

The momentum equations in the x , y , and z directions, respectively, can therefore be expressed as

$$\begin{aligned} \frac{du}{dt} - \frac{uv \tan \phi}{a} + \frac{uw}{a} = & -\frac{1}{\rho} \frac{\partial p}{\partial x} + 2\Omega v \sin \phi \\ & - 2\Omega w \cos \phi + F_u \end{aligned} \quad (2.51)$$

⁷ Osborne Reynolds (1842–1912) was an Irish mathematician and engineer best known for his fluid dynamics contributions, specifically, his study of the conditions in which the flow in pipes transitioned from laminar flow to turbulent flow.

$$\frac{dv}{dt} + \frac{u^2 \tan \phi}{a} + \frac{vw}{a} = -\frac{1}{\rho} \frac{\partial p}{\partial y} - 2\Omega u \sin \phi + F_v \quad (2.52)$$

$$\frac{dw}{dt} - \frac{u^2 + v^2}{a} = -\frac{1}{\rho} \frac{\partial p}{\partial z} + 2\Omega u \cos \phi - g + F_w. \quad (2.53)$$

We will assume that the vertical component of the Coriolis acceleration can be neglected, as can the $-2\Omega w \cos \phi$ contribution to the Coriolis acceleration in the u momentum equation. The metric terms (terms with an a in the denominator) are small in midlatitudes (the $\tan \phi$ terms, however, become significant near the poles). Under these assumptions, the momentum equations can be expressed reasonably accurately as

$$\frac{du}{dt} = -\frac{1}{\rho} \frac{\partial p}{\partial x} + fv + F_u \quad (2.54)$$

$$\frac{dv}{dt} = -\frac{1}{\rho} \frac{\partial p}{\partial y} - fu + F_v \quad (2.55)$$

$$\frac{dw}{dt} = -\frac{1}{\rho} \frac{\partial p}{\partial z} - g + F_w \quad (2.56)$$

where $f = 2\Omega \sin \phi$ is the Coriolis parameter. The above forms probably are most familiar to readers and will be the forms most often used throughout this book. In vector form, we can write these as

$$\frac{d\mathbf{v}}{dt} = -\frac{1}{\rho} \nabla p - g\mathbf{k} - f\mathbf{k} \times \mathbf{v} + \mathbf{F}. \quad (2.57)$$

In a few locations in the book it will be advantageous to use pressure as a vertical coordinate. In isobaric coordinates, the horizontal momentum equation can be written as

$$\frac{d\mathbf{v}_h}{dt} = -\nabla_p \Phi - f\mathbf{k} \times \mathbf{v}_h + \mathbf{F}, \quad (2.58)$$

where $\mathbf{v}_h = (u, v)$ is the horizontal wind, $d/dt = \partial/\partial t + u\partial/\partial x + v\partial/\partial y + w\partial/\partial p$, $w = dp/dt$ is the vertical velocity, $\Phi = gz$ is the geopotential, and horizontal derivatives in d/dt and ∇_p are evaluated on constant pressure surfaces.

2.3.2 Balanced flow

In many situations the forces in the momentum equations are in balance or near balance. It will be useful to draw upon knowledge of such equilibrium states later in the text. For example, equilibrium states are the starting point for the study of many dynamical instabilities.

In the horizontal, *geostrophic balance* results when horizontal accelerations are zero owing to a balance between the horizontal pressure gradient force and the Coriolis force. If du/dt and dv/dt vanish from (2.54) and (2.55), respectively, then, neglecting F_u and F_v , we obtain the geostrophic wind relations

$$u_g = -\frac{1}{\rho f} \frac{\partial p}{\partial y} \quad (2.59)$$

$$v_g = \frac{1}{\rho f} \frac{\partial p}{\partial x} \quad (2.60)$$

where $\mathbf{v}_g = (u_g, v_g, 0) = \frac{1}{\rho f} \mathbf{k} \times \nabla_h p$ is the *geostrophic wind*. In isobaric coordinates,

$$u_g = -\frac{1}{f} \frac{\partial \Phi}{\partial y} \quad (2.61)$$

$$v_g = \frac{1}{f} \frac{\partial \Phi}{\partial x}, \quad (2.62)$$

and $\mathbf{v}_g = \frac{1}{f} \mathbf{k} \times \nabla_p \Phi$. Using the above definitions, (2.58) can be written as

$$\frac{d\mathbf{v}_h}{dt} = -f\mathbf{k} \times \mathbf{v}_a + \mathbf{F}. \quad (2.63)$$

where $\mathbf{v}_a = \mathbf{v}_h - \mathbf{v}_g$ is the *ageostrophic wind*. Neglecting the variation of f with latitude, it is easily shown that the geostrophic wind is nondivergent; thus, the ageostrophic part of the wind field contains all of the divergence.

In the vertical, *hydrostatic balance* occurs when gravity and the vertical pressure gradient force are equal and opposite. If dw/dt is negligible (and also assuming F_w is negligible), then we readily obtain the hydrostatic equation from (2.56). In height coordinates it takes the form

$$\frac{\partial p}{\partial z} = -\rho g, \quad (2.64)$$

and in isobaric coordinates,

$$\frac{\partial \Phi}{\partial p} = -\frac{RT}{p}. \quad (2.65)$$

Integration of (2.65) over a layer yields the *hypsometric equation*, which relates the thickness of the layer to the temperature within the layer, that is,

$$\begin{aligned} z(p_t) - z(p_b) &= \int_{p_t}^{p_b} \frac{RT}{g} d \ln p = \frac{R_d}{g} \int_{p_t}^{p_b} T_v d \ln p \\ &= \frac{R_d \bar{T}_v}{g} \ln \left(\frac{p_b}{p_t} \right), \end{aligned} \quad (2.66)$$

where p_t and p_b are the pressures of the top and bottom of the layer, respectively, $z(p_t)$ and $z(p_b)$ are the heights of the top and bottom of the layer, respectively, and \bar{T}_v is the log-pressure-weighted mean virtual temperature of the layer. We replaced RT with $R_d T_v$ in (2.65) so that R_d could be pulled outside of the integral. The thickness of a layer, $z(p_t) - z(p_b)$, is proportional to \bar{T}_v .

As discussed in Chapter 1, phenomena having a small aspect ratio can be regarded as being in approximate hydrostatic balance. We shall exploit the hydrostatic equation in the study of a number of mesoscale phenomena later in the book, particularly phenomena near the upper limit of the mesoscale.

We can relate the geostrophic wind to the temperature field by taking $\partial \mathbf{v}_g / \partial p$ and substituting (2.65). This results in the *thermal wind equation*,

$$-\frac{\partial \mathbf{v}_g}{\partial p} = -\frac{\partial}{\partial p} \left(\frac{1}{f} \mathbf{k} \times \nabla_p \Phi \right) = \frac{R}{fp} \mathbf{k} \times \nabla_p T, \quad (2.67)$$

which implies that the shear in the vertical profile of the geostrophic wind is proportional to the horizontal temperature gradient. (The thermal wind relation in height coordinates has a less friendly form.) The geostrophic wind shear vector, $-\partial \mathbf{v}_g / \partial p$, is parallel to the isotherms and is oriented such that cold air is on its left (right) in the northern (southern) hemisphere. Similarly, the *thermal wind*, \mathbf{v}_T , is a geostrophic wind vector difference between two levels. For example, the thermal wind defined by the geostrophic winds at an upper level u and a lower level l is $\mathbf{v}_T = \mathbf{v}_{gu} - \mathbf{v}_{gl}$; \mathbf{v}_T points along the isotherms characterizing the mean temperature in the layer bounded by the two levels, with cold air to the left of \mathbf{v}_T . By adding the thermal wind vector to a low-level wind associated with warm advection, one notes immediately from the upper-level wind vector that the wind profile has ‘veering’ (i.e., clockwise turning) of \mathbf{v}_g with height, whereas cold advection is associated with ‘backing’ (i.e., counterclockwise turning) of \mathbf{v}_g with height in the northern hemisphere. In the southern hemisphere, clockwise (counterclockwise) turning of \mathbf{v}_g with height signifies cold (warm) advection.

Geostrophic balance is technically only valid for straight isobars. A more general wind balance among the horizontal forces acting on a parcel of air is known as *gradient wind balance*. It is most easily demonstrated by expressing the horizontal momentum equation in natural coordinates, that is,

$$\frac{d\mathbf{v}_h}{dt} = \frac{dV}{dt} \mathbf{s} + \frac{V^2}{R_t} \mathbf{n}, \quad (2.68)$$

where \mathbf{s} is a unit vector that points in the direction of \mathbf{v}_h (i.e., along a streamline), \mathbf{n} is the unit vector that points 90°

to the left of \mathbf{v}_h , $V = |\mathbf{v}_h|$ is the horizontal wind speed, and R_t is the radius of curvature of the trajectory followed by a parcel of air (defined to be positive [negative] for cyclonic [anticyclonic] flow; the curvature of the flow increases with decreasing $|R_t|$), and V^2/R_t is the centripetal acceleration.

We now consider the forces acting in the along-wind (\mathbf{s}) and cross-wind (\mathbf{n}) directions. In the \mathbf{s} direction, accelerations are driven by the along-wind pressure gradient, that is,

$$\frac{dV}{dt} = -\frac{1}{\rho} \frac{\partial p}{\partial s}. \quad (2.69)$$

A *gradient wind* is a wind that blows parallel to the isobars; thus, $\partial p / \partial s = 0$ for a gradient wind. We therefore only need to consider the force balance in the \mathbf{n} direction. The Coriolis and pressure gradient forces in the \mathbf{n} direction are $-fV$ and $-\frac{1}{\rho} \frac{\partial p}{\partial n}$, respectively, where n is the coordinate in the \mathbf{n} direction. In most situations $-\frac{1}{\rho} \frac{\partial p}{\partial n} > 0$, that is, high pressure usually is to the right of the wind direction. Thus, the force balance in the \mathbf{n} direction is

$$0 = -fV - \frac{1}{\rho} \frac{\partial p}{\partial n} - \frac{V^2}{R_t}. \quad (2.70)$$

The three-way balance among the Coriolis, pressure gradient, and centrifugal forces implied by (2.70) is commonly recognized as the gradient wind balance relation.

The geostrophic wind is the gradient wind that results when $|R_t| \rightarrow \infty$ (i.e., straight flow). In natural coordinates, $\mathbf{v}_g = -\frac{1}{\rho f} \frac{\partial p}{\partial n}$, which allows us to write (2.70) as

$$\frac{V_g}{V} = 1 + \frac{V}{f R_t}, \quad (2.71)$$

from which it is apparent that anticyclonic ($R_t < 0$) gradient winds are supergeostrophic (i.e., $V > V_g$) and cyclonic ($R_t > 0$) gradient winds are subgeostrophic (i.e., $V < V_g$).

When the Coriolis force is negligible relative to the centrifugal and pressure gradient forces in (2.70), as is the case in strong mesoscale vortices, *cyclostrophic balance* is present. In this case, the pressure gradient force is directed toward the axis of rotation and balances the centrifugal force.

2.3.3 Buoyancy

The dynamics of many mesoscale phenomena are often more intuitive if the vertical momentum equation is written in terms of a *buoyancy force* and a *vertical perturbation pressure gradient force*. The buoyancy force is a vertical pressure gradient force that is not balanced with gravity and is attributable to variations in density within a column.

The origin of the buoyancy force can be elucidated by first rewriting (2.56), neglecting F_w , as

$$\rho \frac{dw}{dt} = -\frac{\partial p}{\partial z} - \rho g. \quad (2.72)$$

Let us now define a horizontally homogeneous base state pressure and density field (denoted by overbars) that is in hydrostatic balance, such that

$$0 = -\frac{\partial \bar{p}}{\partial z} - \bar{\rho}g. \quad (2.73)$$

Subtracting (2.73) from (2.72) yields

$$\rho \frac{dw}{dt} = -\frac{\partial p'}{\partial z} - \rho'g, \quad (2.74)$$

where the primed p and ρ variables are the deviations of the pressure and density field from the horizontally homogeneous, balanced base state [i.e., $p = \bar{p}(z) + p'$, $\rho = \bar{\rho}(z) + \rho'$]. Rearrangement of terms in (2.74) yields

$$\frac{dw}{dt} = -\frac{1}{\rho} \frac{\partial p'}{\partial z} - \frac{\rho'}{\rho} g \quad (2.75)$$

$$= -\frac{1}{\rho} \frac{\partial p'}{\partial z} + B \quad (2.76)$$

where $B (= -\frac{\rho'}{\rho}g)$ is the buoyancy and $-\frac{1}{\rho} \frac{\partial p'}{\partial z}$ is the vertical perturbation pressure gradient force. The vertical perturbation pressure gradient force arises from velocity gradients and density anomalies. A more thorough examination of pressure perturbations is undertaken in Section 2.5.

When the Boussinesq approximation is valid (Section 2.2), $\rho(x, y, z, t)$ is replaced with a constant ρ_0 everywhere that ρ appears in the momentum equations except in the numerator of the buoyancy term in the vertical momentum equation. Similarly, when the anelastic approximation is valid, $\rho(x, y, z, t)$ is replaced with $\bar{\rho}(z)$ in the momentum equations except in the numerator of the buoyancy term in the vertical momentum equation.

It is often sufficiently accurate to replace ρ with $\bar{\rho}$ in the denominator of the buoyancy term, that is,

$$B = -\frac{\rho'}{\bar{\rho}} g \approx \left(\frac{T'_v}{\bar{T}_v} - \frac{p'}{\bar{p}} \right) g, \quad (2.77)$$

where we also have made use of the equation of state and have assumed that perturbations are small relative to the mean quantities. In many situations, $|p'/\bar{p}| \ll |T'_v/\bar{T}_v|$, in which case $B \approx T'_v/\bar{T}_v$ (it can be shown that $|p'/\bar{p}| \ll |T'_v/\bar{T}_v|$ when $u^2/c^2 \ll |T'_v/\bar{T}_v|$, where $c = \sqrt{c_p R_d \bar{T}_v / c_v}$ is

the speed of sound). Furthermore, it is often customary to regard the reference state virtual temperature as that of the ambient environment, and the virtual temperature perturbation as the temperature difference between an air parcel and its surrounding environment, so that

$$B \approx \frac{T_{v_p} - T_{v_{env}}}{T_{v_{env}}} g, \quad (2.78)$$

where T_{v_p} is the virtual temperature of an air parcel and $T_{v_{env}}$ is the virtual temperature of the environment. When an air parcel is warmer than the environment, a positive buoyancy force exists, resulting in upward acceleration.

When hydrometeors are present and assumed to be falling at their terminal velocity, the downward acceleration due to drag from the hydrometeors is equal to gr_h , where r_h is the mass of hydrometeors per kg of air (maximum values of r_h within a strong thunderstorm updraft typically are $8-18 \text{ g kg}^{-1}$). The effect of this *hydrometeor loading* on an air parcel can be incorporated into the buoyancy; for example, we can rewrite (2.77) as

$$\begin{aligned} B &\approx \left(\frac{T'_v}{\bar{T}_v} - \frac{p'}{\bar{p}} - r_h \right) g = \left[\frac{\theta'_v}{\bar{\theta}_v} + \left(\frac{R}{c_p} - 1 \right) \frac{p'}{\bar{p}} - r_h \right] g \\ &= \left[\frac{\theta'_\rho}{\bar{\theta}_\rho} + \left(\frac{R_d}{c_p} - 1 \right) \frac{p'}{\bar{p}} \right] g, \end{aligned} \quad (2.79)$$

where $\theta'_\rho = \theta_\rho - \bar{\theta}_\rho$ ($\bar{\theta}_\rho = \bar{\theta}_v$ if the environment contains no hydrometeors).⁸ Examination of (2.79) reveals that the positive buoyancy produced by a 3 K virtual temperature excess (i.e., how warm a parcel is compared to its environment) is offset entirely (assuming $\bar{\theta}_v \sim 300 \text{ K}$) by a hydrometeor mixing ratio of 10 g kg^{-1} . In many applications throughout this book, we can understand the essential

⁸Sometimes the pressure gradient force is expressed in terms of a nondimensional pressure, $\pi = (p/p_0)^{R/c_p}$, often referred to as the *Exner function*. In that case, the rhs of (2.75) can be written as $-c_p \theta_\rho \frac{\partial \pi}{\partial z} + g \frac{\theta'_\rho}{\bar{\theta}_\rho}$, where π' is the perturbation Exner function and $\bar{\theta}_\rho = \bar{\theta}_v$ if the base state is unsaturated, as is typically the case. Notice that the buoyancy term $g \theta'_\rho / \bar{\theta}_\rho$ has the base state density potential temperature in its denominator, in contrast to the buoyancy term $-g \rho' / \rho$ in (2.75). When the Exner function is used in the pressure gradient force and buoyancy is written as $g \theta'_\rho / \bar{\theta}_\rho$, part of the pressure perturbation that contributes to ρ' is absorbed by θ'_ρ , and the remainder of the pressure perturbation is absorbed by π' . On the other hand, if the vertical pressure gradient and buoyancy are written as $-\frac{1}{\rho} \frac{\partial p'}{\partial z}$ and $-g \rho' / \rho$, respectively, as on the rhs of (2.75), and if the buoyancy is approximated as $-g \rho' / \rho \approx -g \rho' / \bar{\rho} \approx g \theta'_\rho / \bar{\theta}_\rho$, then only part of the contribution of p' to ρ' is included. In summary, replacing $-g \rho' / \rho$ with $g \theta'_\rho / \bar{\theta}_\rho$ is an approximation if the pressure gradient force is expressed in terms of ρ and p' , and is exact if the pressure gradient force is expressed in terms of θ_ρ and π' .

dynamics without considering the effects of hydrometeors, water vapor, or pressure perturbations on the buoyancy. In those instances we commonly will approximate the buoyancy as $B \approx g\theta'/\bar{\theta}$.

2.4 Vorticity and circulation

2.4.1 Vector form of the vorticity equation

The *vorticity* of a fluid is a vector field that provides a microscopic measure of the rotation at any location in the fluid, and is equal to twice the instantaneous rotation rate for a solid body. Although we do not need vorticity to explain atmospheric motions, the use of vorticity is often desirable because pressure is absent from vorticity equations governing barotropic flows, making it very easy to conceptualize dynamical processes that might not be so obvious from consideration of the momentum equations alone.

The vorticity, ω , is defined as the curl of the velocity field, that is,

$$\omega = \nabla \times \mathbf{v} = \begin{vmatrix} \mathbf{i} & \mathbf{j} & \mathbf{k} \\ \frac{\partial}{\partial x} & \frac{\partial}{\partial y} & \frac{\partial}{\partial z} \\ u & v & w \end{vmatrix} \quad (2.80)$$

$$= \left(\frac{\partial w}{\partial y} - \frac{\partial v}{\partial z} \right) \mathbf{i} + \left(\frac{\partial u}{\partial z} - \frac{\partial w}{\partial x} \right) \mathbf{j} + \left(\frac{\partial v}{\partial x} - \frac{\partial u}{\partial y} \right) \mathbf{k} \quad (2.81)$$

$$= \xi \mathbf{i} + \eta \mathbf{j} + \zeta \mathbf{k} \quad (2.82)$$

where ξ , η , and ζ are the x , y , and z vorticity components, respectively. To derive a vorticity equation (i.e., a prognostic equation for ω), it will be convenient to express (2.43) in a slightly different form. Using the identity $\mathbf{v} \cdot \nabla \mathbf{v} = \nabla \frac{|\mathbf{v}|^2}{2} + \omega \times \mathbf{v}$, expressing the gravitational acceleration as $\mathbf{g} = -\nabla(gz)$, and neglecting the components of the Coriolis acceleration in which w appears, (2.43) can be written as

$$\frac{\partial \mathbf{v}}{\partial t} + \nabla \left(\frac{|\mathbf{v}|^2}{2} - gz \right) + \omega \times \mathbf{v} = -\frac{1}{\rho} \nabla p - f \mathbf{k} \times \mathbf{v} + \mathbf{F}. \quad (2.83)$$

If we neglect the small metric terms (i.e., assume that the coordinate system is Cartesian), taking the curl of (2.83) leads to

$$\frac{\partial \omega}{\partial t} + \nabla \times \omega \times \mathbf{v} = -\nabla \left(\frac{1}{\rho} \right) \times \nabla p + \nabla \times (-f \mathbf{k} \times \mathbf{v}) + \nabla \times \mathbf{F}, \quad (2.84)$$

where $\nabla \times \nabla \left(\frac{|\mathbf{v}|^2}{2} - gz \right) = 0$ and $-\frac{1}{\rho} \nabla \times \nabla p = 0$ from the identity $\nabla \times \nabla \chi = 0$, where χ is any scalar. By way of vector identities it also can be shown that

$$\begin{aligned} \nabla \times \omega \times \mathbf{v} &= \omega(\nabla \cdot \mathbf{v}) - \mathbf{v}(\nabla \cdot \omega) \\ &\quad + (\mathbf{v} \cdot \nabla)\omega - (\omega \cdot \nabla)\mathbf{v} \\ &= \omega(\nabla \cdot \mathbf{v}) + (\mathbf{v} \cdot \nabla)\omega - (\omega \cdot \nabla)\mathbf{v}, \end{aligned} \quad (2.85)$$

where $\mathbf{v}(\nabla \cdot \omega) = \mathbf{v}(\nabla \cdot \nabla \times \mathbf{v}) = 0$. Similarly,

$$\begin{aligned} \nabla \times (-f \mathbf{k} \times \mathbf{v}) &= -f \mathbf{k}(\nabla \cdot \mathbf{v}) - (\mathbf{v} \cdot \nabla)f \mathbf{k} \\ &\quad + \mathbf{v}(\nabla \cdot f \mathbf{k}) + f(\mathbf{k} \cdot \nabla)\mathbf{v}. \end{aligned} \quad (2.86)$$

Using (2.85) and (2.86), and noting that $-\nabla \rho^{-1} = \rho^{-2} \nabla \rho$ and $\mathbf{v}(\nabla \cdot f \mathbf{k}) = 0$, (2.84) can be written as

$$\begin{aligned} \frac{\partial \omega}{\partial t} + (\omega + f \mathbf{k})(\nabla \cdot \mathbf{v}) + (\mathbf{v} \cdot \nabla)(\omega + f \mathbf{k}) \\ = [(\omega + f \mathbf{k}) \cdot \nabla] \mathbf{v} + \frac{1}{\rho^2} \nabla \rho \times \nabla p + \nabla \times \mathbf{F}. \end{aligned} \quad (2.87)$$

If incompressibility is assumed ($\nabla \cdot \mathbf{v} = 0$), (2.87) can be expressed as

$$\begin{aligned} \frac{d(\omega + f \mathbf{k})}{dt} &= \underbrace{\frac{\partial \omega}{\partial t}}_{\text{local tendency}} + \underbrace{(\mathbf{v} \cdot \nabla)(\omega + f \mathbf{k})}_{\text{advection}} \\ &= \underbrace{[(\omega + f \mathbf{k}) \cdot \nabla] \mathbf{v}}_{\text{tilting/stretching}} + \underbrace{\frac{1}{\rho^2} \nabla \rho \times \nabla p}_{\text{baroclinic generation}} \\ &\quad + \underbrace{\nabla \times \mathbf{F}}_{\text{viscous effects}}. \end{aligned} \quad (2.88)$$

The terms on the lhs of (2.88) are the local tendency and advective parts of $d\omega/dt$, and the terms on the rhs of (2.88) represent tilting and stretching of vorticity, baroclinic generation, and viscous effects, respectively.

2.4.2 Horizontal and vertical vorticity equations

From (2.88) we can obtain equations for the horizontal and vertical vorticity components:

$$\begin{aligned} \mathbf{i} \cdot \frac{\partial \omega}{\partial t} &= \frac{\partial \xi}{\partial t} = -\mathbf{v} \cdot \nabla \xi + \omega \cdot \nabla u + f \frac{\partial u}{\partial z} \\ &\quad + \frac{1}{\rho^2} \left(\frac{\partial \rho}{\partial y} \frac{\partial p}{\partial z} - \frac{\partial \rho}{\partial z} \frac{\partial p}{\partial y} \right) + \mathbf{i} \cdot \nabla \times \mathbf{F} \end{aligned} \quad (2.89)$$

$$\begin{aligned} \mathbf{j} \cdot \frac{\partial \boldsymbol{\omega}}{\partial t} &= \frac{\partial \eta}{\partial t} = -\mathbf{v} \cdot \nabla \eta + \boldsymbol{\omega} \cdot \nabla v + f \frac{\partial v}{\partial z} \\ &\quad + \frac{1}{\rho^2} \left(\frac{\partial \rho}{\partial z} \frac{\partial p}{\partial x} - \frac{\partial \rho}{\partial x} \frac{\partial p}{\partial z} \right) + \mathbf{j} \cdot \nabla \times \mathbf{F} \end{aligned} \quad (2.90)$$

$$\begin{aligned} \mathbf{k} \cdot \frac{\partial \boldsymbol{\omega}}{\partial t} &= \frac{\partial \zeta}{\partial t} = -\mathbf{v} \cdot \nabla (\zeta + f) + \boldsymbol{\omega} \cdot \nabla w + f \frac{\partial w}{\partial z} \\ &\quad + \frac{1}{\rho^2} \left(\frac{\partial \rho}{\partial x} \frac{\partial p}{\partial y} - \frac{\partial \rho}{\partial y} \frac{\partial p}{\partial x} \right) + \mathbf{k} \cdot \nabla \times \mathbf{F}. \end{aligned} \quad (2.91)$$

The terms on the rhs of (2.89)–(2.91), in order, are the advection of ξ , η , and $\zeta + f$, respectively, the stretching and/or reorientation of vorticity in/into the x , y , and z directions, respectively, tilting (in the ξ and η equations) and stretching (in the ζ equation) of earth's vorticity, baroclinic generation, and viscous effects. Note that the baroclinic generation term has a much larger effect on ξ and η than on ζ owing to the fact that ρ and p vary much more in the vertical than in the horizontal.

When the vertical momentum equations are expressed in terms of pressure perturbations and buoyancy under the Boussinesq approximation, (2.88) can be written as

$$\begin{aligned} \frac{\partial \boldsymbol{\omega}}{\partial t} &= -\mathbf{v} \cdot \nabla (\boldsymbol{\omega} + f\mathbf{k}) + (\boldsymbol{\omega} + f\mathbf{k}) \cdot \nabla \mathbf{v} \\ &\quad + \nabla \times B\mathbf{k} + \nabla \times \mathbf{F}. \end{aligned} \quad (2.92)$$

Similarly, (2.89)–(2.91) can be written as

$$\begin{aligned} \frac{\partial \xi}{\partial t} &= -\mathbf{v} \cdot \nabla \xi + \boldsymbol{\omega} \cdot \nabla u + f \frac{\partial u}{\partial z} + \frac{\partial B}{\partial y} \\ &\quad + \mathbf{i} \cdot \nabla \times \mathbf{F} \end{aligned} \quad (2.93)$$

$$\begin{aligned} \frac{\partial \eta}{\partial t} &= -\mathbf{v} \cdot \nabla \eta + \boldsymbol{\omega} \cdot \nabla v + f \frac{\partial v}{\partial z} - \frac{\partial B}{\partial x} \\ &\quad + \mathbf{j} \cdot \nabla \times \mathbf{F} \end{aligned} \quad (2.94)$$

$$\begin{aligned} \frac{\partial \zeta}{\partial t} &= -\mathbf{v} \cdot \nabla (\zeta + f) + \boldsymbol{\omega} \cdot \nabla w + f \frac{\partial w}{\partial z} \\ &\quad + \mathbf{k} \cdot \nabla \times \mathbf{F}. \end{aligned} \quad (2.95)$$

Notice that there is no direct generation of vertical vorticity by baroclinic effects because $\nabla \times B\mathbf{k}$ has no vertical component.

One also can combine (2.93) and (2.94) into one equation for the horizontal vorticity vector $\boldsymbol{\omega}_h = (\xi, \eta)$:

$$\frac{\partial \boldsymbol{\omega}_h}{\partial t} = -\mathbf{v} \cdot \nabla \boldsymbol{\omega}_h + (\boldsymbol{\omega} + f\mathbf{k}) \cdot \nabla \mathbf{v}_h + \nabla \times B\mathbf{k}, \quad (2.96)$$

where $\mathbf{v}_h = (u, v)$ is the horizontal wind velocity and viscous effects have been neglected. The horizontal vorticity also can be partitioned into components aligned with the flow and normal to the flow, referred to as *streamwise* and *crosswise* components, respectively. More will be said of this

decomposition in Section 2.7. This partitioning will prove useful in our discussion of severe storms in later chapters.

2.4.3 Circulation theorems

Circulation is another measure of rotation within a fluid. In contrast to vorticity, circulation is a scalar and it provides a macroscopic measure of the rotation within a finite region of the fluid. The circulation, C , is defined as the line integral around a circuit of the wind component locally tangent to the circuit, that is

$$C = \oint \mathbf{v} \cdot d\mathbf{l} = \oint |\mathbf{v}| \cos \beta dl, \quad (2.97)$$

where $d\mathbf{l}$ is an element of the circuit, β is the angle between \mathbf{v} and $d\mathbf{l}$, and the loop through the integral signs indicates that the circuit is closed (Figure 2.3). By convention, C is evaluated by counterclockwise integration around the circuit. *Stokes's theorem* states that

$$\oint \mathbf{v} \cdot d\mathbf{l} = \int \nabla \times \mathbf{v} \cdot d\mathbf{A}, \quad (2.98)$$

where $d\mathbf{A}$ is an element of an arbitrary surface having an area A , bounded by the circuit about which C is computed. Therefore,

$$C = \int \boldsymbol{\omega} \cdot d\mathbf{A}, \quad (2.99)$$

which implies that the circulation around a circuit is equal to the surface integral of vorticity, sometimes called the *vorticity flux*. Equivalently, the circulation per unit area is equal to the average vorticity within the area. In the case of a circular circuit of radius R centered on a vertical vortex having a tangential velocity V at radius R , the circulation is $C = 2\pi RV$ and the mean vorticity is $\bar{\omega} = \bar{\zeta} = C/A = 2\pi RV/\pi R^2 = 2V/R$. Although we have centered the circuit on the axis of rotation in the preceding example, circulation need not be computed around a circuit centered on the axis of rotation, and in many situations an axis of rotation is not even easily identified.

Bjerknes' circulation theorem can be obtained by taking the line integral of the inviscid form of (2.43), and making use of (2.97) and the fact that the line integral about a closed circuit of a perfect differential is zero:

$$\frac{dC}{dt} = - \oint \frac{dp}{\rho} - 2\Omega \frac{dA_e}{dt}. \quad (2.100)$$

The $-\oint \frac{dp}{\rho}$ term represents the *solenoidal* or *baroclinic generation* of circulation, and the $-2\Omega \frac{dA_e}{dt}$ term represents the change in circulation due to the rotation of the earth,

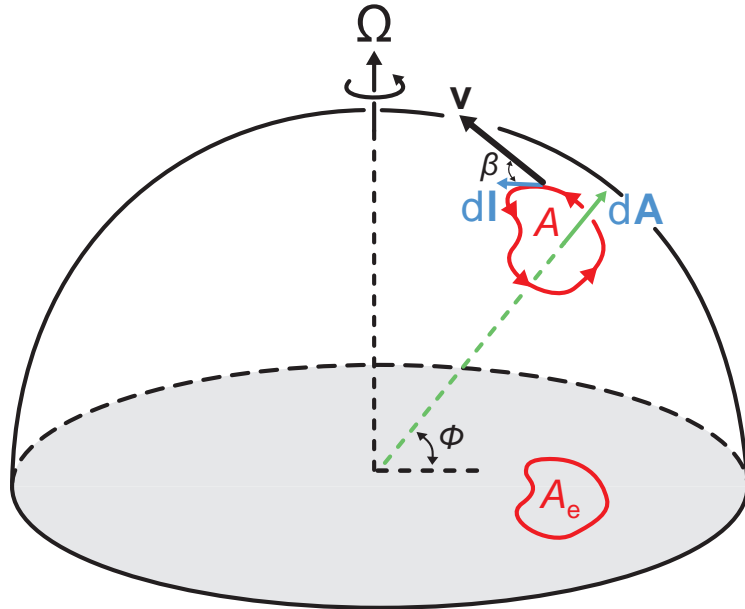


Figure 2.3 The relationship among dl , v , β , dA , A , and A_e in the calculation of circulation around a closed circuit (red). The arrows along the circuit indicate the direction of integration.

where A_e is the projection of A onto the equatorial plane, and changes in A_e modulate C (Figure 2.3). One common way by which A_e can change is by latitudinal motion of the circuit about which circulation is evaluated. For example, a horizontal circuit that moves northward acquires anticyclonic (negative) circulation because A_e increases as the circuit moves northward, assuming that A does not change. This is a reflection of the Coriolis force acting to the right of the winds as the circuit moves north.

Sometimes the $-2\Omega \frac{dA_e}{dt}$ term is combined with dC/dt such that (2.100) is written as

$$\frac{dC_a}{dt} = - \oint \frac{dp}{\rho}, \quad (2.101)$$

where $C_a = C + 2\Omega A_e$ is the *absolute circulation*. In inviscid, barotropic conditions (i.e., density is a function of pressure only), the absolute circulation is conserved following the motion of the circuit, that is,

$$\frac{dC_a}{dt} = 0, \quad (2.102)$$

which is also known as *Kelvin's circulation theorem*.⁹

⁹ William Thomson (1824–1907) was a British physicist and engineer who was given the title Baron Kelvin (and is most commonly referred to

Below we present an example of how Bjerknes' circulation theorem can be used to predict the circulation induced by a horizontal temperature gradient such as might be found along a mesoscale air mass boundary. If the Earth's rotation can be neglected, (2.100) can be written as

$$\frac{dC}{dt} = - \oint R_d T_v d \ln p. \quad (2.103)$$

Consider the case shown in Figure 2.4. Only the vertical segments of the loop contribute to the line integral because the quasihorizontal segments are along constant pressure surfaces. Thus, (2.103) becomes

$$\frac{dC}{dt} = R_d \ln \left(\frac{p_b}{p_t} \right) (\bar{T}_w - \bar{T}_c) > 0, \quad (2.104)$$

where p_b and p_t are the pressures along the bottom and top of the circuit, respectively (Figure 2.4), and \bar{T}_w and \bar{T}_c are the log-pressure-weighted mean virtual temperatures along the vertical segments of the circuit on the warm and cold sides of the circuit, respectively. For $p_t = 900$ mb,

as Lord Kelvin) in honor of his achievements in electricity, thermodynamics, and modern physics. The title refers to the River Kelvin, which runs through Glasgow, Scotland, where Lord Kelvin was on the faculty at the University of Glasgow.

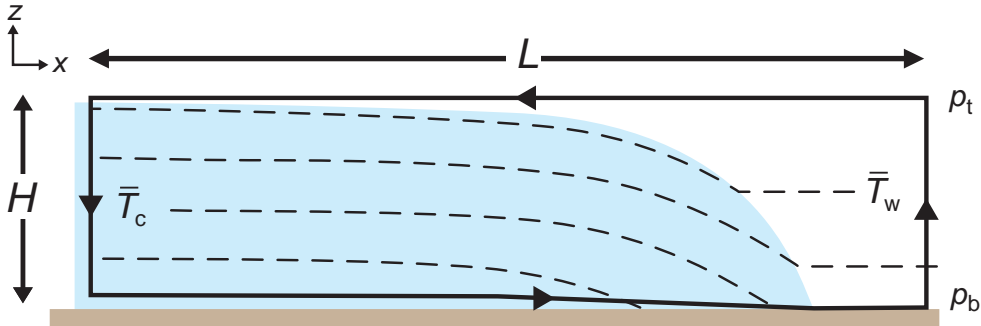


Figure 2.4 An example of how Bjerknes' circulation theorem can be applied to a mesoscale air mass boundary associated with a horizontal temperature gradient. The relatively cold air mass is shaded blue, and dashed lines indicate surfaces of constant density. The closed solid line is the loop about which the circulation is to be evaluated (its quasihorizontal segments follow constant pressure surfaces). The mean virtual temperature in the warm air mass along the circuit is \bar{T}_w , and in the cold air mass it is \bar{T}_c .

$p_b = 1000 \text{ mb}$, $\bar{T}_w = 300 \text{ K}$, and $\bar{T}_c = 290 \text{ K}$, (2.104) yields $dC/dt = 302 \text{ m}^2 \text{ s}^{-2}$, which implies an increase in C of $1.09 \times 10^6 \text{ m}^2 \text{ s}^{-1}$ in 1 h.

The mean tangential wind speed acceleration about the circuit is $(dC/dt)/P$, where $P [\approx 2(L + H)]$ is the perimeter of the quasirectangular circuit shown in Figure 2.4, L is the horizontal dimension of the circuit, and H is the mean vertical dimension of the circuit. (The circuit is not a perfect rectangle because at least one of the pressure surfaces along which the circuit is drawn must be sloped if a horizontal density gradient is present; the vertical dimension of the circuit is shorter in the cold air.) For a circuit that is 30 km wide and has an average depth of 0.9 km (this is approximately the mean thickness of a layer bounded by the 1000 mb and 900 mb pressure surfaces for the given temperatures), a mean tangential wind acceleration about the circuit of $4.89 \times 10^{-3} \text{ m s}^{-2}$ is implied. Thus, a mean tangential wind speed of 17.6 m s^{-1} is generated in 1 h. The actual mean tangential speed attained for such a horizontal temperature gradient might be as little as half this value owing to the effects of friction.

The average horizontal vorticity generated in 1 h within the region enclosed by the circuit (Figure 2.4 shows the x - z plane) is

$$\Delta \langle \eta \rangle = -\frac{\Delta C}{HL}, \quad (2.105)$$

where $\langle \eta \rangle$ is the average meridional vorticity component ($\eta < 0$ implies that the horizontal vorticity vector points out of the page in Figure 2.4) and HL is the area enclosed by the circuit in the x - z plane. An increase in C of $1.09 \times 10^6 \text{ m}^2 \text{ s}^{-1}$ implies a change in $\langle \eta \rangle$ of $-4.03 \times 10^{-2} \text{ s}^{-1}$.

Alternatively, the above result could have been obtained from the meridional horizontal vorticity equation, which,

neglecting viscosity and the earth's rotation, and assuming two-dimensionality (i.e., $\partial/\partial y = 0$), can be written as [cf. (2.94)]

$$\frac{d\eta}{dt} = -\frac{\partial B}{\partial x} = -\frac{g}{\bar{T}_v} \frac{\partial T'_v}{\partial x}, \quad (2.106)$$

where the buoyancy force B is assumed to be $B = gT'_v/\bar{T}_v$ and T'_v is the virtual temperature perturbation relative to a mean virtual temperature $\bar{T}_v = \bar{T}_v(z)$. Letting $\bar{T}_v = \bar{T}_w$ and $T'_v = T_v - \bar{T}_w$, the area-averaged vorticity equation is

$$\frac{d\langle \eta \rangle}{dt} = -\frac{g}{H\bar{T}_v} \int_0^H \int_0^L \frac{\partial T'_v}{\partial x} dx dz \approx \frac{g}{L} \left(\frac{\bar{T}_c}{\bar{T}_w} - 1 \right), \quad (2.107)$$

where the approximation is due to the fact that \bar{T}_c and \bar{T}_w were defined to be log-pressure averages rather than simple vertical averages. For $\bar{T}_w = 300 \text{ K}$ and $\bar{T}_c = 290 \text{ K}$ as before, we obtain $d\langle \eta \rangle/dt \approx -1.09 \times 10^{-5} \text{ s}^{-2}$, which implies a change in $\langle \eta \rangle$ of $-3.92 \times 10^{-2} \text{ s}^{-1}$ in 1 h. This result differs slightly from that obtained via (2.104) and (2.105) because of the substitution of \bar{T}_w for \bar{T}_v in (2.107) and the fact that the P used to convert the circulation obtained via (2.104) to a mean tangential wind acceleration is not exactly equal to $2(L + H)$.

2.4.4 Vortex lines

A *vortex line* is a curve in the fluid such that its tangent at any given point gives the direction of the local vorticity. A vortex line is related to the vorticity vector in the same way that a streamline is related to the velocity vector. Vortex lines cannot be broken and they can only terminate at solid surfaces (e.g., the ground). Moreover, as a result

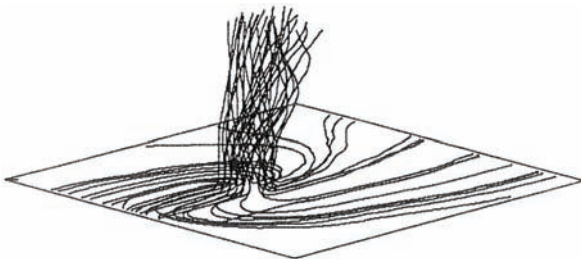


Figure 2.5 Vortex lines associated with a tornado in a simulation by Walko (1993). Courtesy of the American Geophysical Union.

of Helmholtz's theorem, in an inviscid, barotropic fluid (i.e., one in which baroclinic effects and viscosity can be neglected), vortex lines are 'frozen' in the fluid, that is, they are material lines that move with the flow.¹⁰ Vortex lines near a simulated tornado are shown in Figure 2.5. As one would probably expect, the vortex lines are nearly erect in the tornado, turn horizontally at the base of the tornado, and then extend horizontally several kilometers from the tornado along the surface.

Vortex lines can aid the visualization of the three-dimensional vorticity field. The three-dimensional perspective provided by vortex lines can expose dynamics that may not be as apparent in inspections of only one vorticity component at a time. For example, in Chapter 8 we shall find that the dynamics of midlevel mesocyclogenesis in supercell thunderstorms is easily demonstrated by way of vortex lines. The presence of horizontal buoyancy gradients can complicate vortex line analyses in phenomena such as thunderstorms owing to the virtually unavoidable baroclinic generation of vorticity by the horizontal buoyancy gradients that accompany the precipitation regions and vertical drafts of thunderstorms. In the presence of significant baroclinic vorticity generation, vortex lines may not even closely approximate material lines. Nonetheless, vortex line analyses can still be enlightening in that they can suggest plausible methods of vorticity generation and reorientation (e.g., observations of vortex rings might lead one to surmise that a local buoyancy extremum is present and responsible for the generation of the rings).

¹⁰ A number of vector calculus, classical mechanics, and fluid mechanics theorems have been attributed to the German physician and physicist Hermann von Helmholtz (1821–1894). The theorem that vortex lines move as material lines in inviscid, barotropic fluids is sometimes referred to as Helmholtz's *second theorem* of fluid mechanics. Helmholtz's fluid mechanics (1858) theorems actually were published prior to Lord Kelvin's circulation theorem (1867), which proved Helmholtz's theorems.

2.4.5 Ertel's potential vorticity

A state variable is one that can be expressed as a function of p and ρ (or p and T) only. If a conservative state variable, λ , exists (i.e., $d\lambda/dt = 0$) and the flow is inviscid, then the vorticity equation can be used to derive an expression for the conservation of *Ertel's potential vorticity*:

$$\frac{d}{dt} \left[\frac{(\boldsymbol{\omega} + f\mathbf{k}) \cdot \nabla \lambda}{\rho} \right] = 0. \quad (2.108)$$

Equation (2.108) is obtained by adding the dot product of $d[(\boldsymbol{\omega} + f\mathbf{k})/\rho]/dt$ and $\nabla \lambda$ to the dot product of $(\boldsymbol{\omega} + f\mathbf{k})/\rho$ and $d(\nabla \lambda)/dt$. We can obtain $d[(\boldsymbol{\omega} + f\mathbf{k})/\rho]/dt$ by combining the inviscid form of (2.87) with the continuity equation given by (2.36).

Unfortunately, there are no state variables for both dry and moist adiabatic motions. For dry adiabatic motions, θ is a state variable and $d\theta/dt = 0$, whereas θ_e is not a state variable (because it is a function of T , p , and r_v), although $d\theta_e/dt = 0$. For moist adiabatic motions, $d\theta/dt \neq 0$, but θ_e is a state variable (because $r_v = r_{vs}$, which is a function of T only) and $d\theta_e/dt = 0$. Therefore, for dry adiabatic motions using $\lambda = \theta$ would be appropriate, and for moist adiabatic motions using $\lambda = \theta_e$ would be appropriate.

The application of (2.108) can lead to dynamical insight in a variety of phenomena [e.g., Section 8.4 applies (2.108) to the problem of mesocyclogenesis in a supercell thunderstorm]. For example, suppose that $\lambda = \theta$ and we know that $\zeta = 0$ at some time, in which case $\boldsymbol{\omega}$ is oriented horizontally. Also suppose that $\nabla \theta$ is directed downward in a horizontally uniform, unstable environment. Then the potential vorticity, proportional to $\boldsymbol{\omega} \cdot \nabla \theta$, is zero; that is, vortex lines are located *within* θ surfaces. Moreover, they are located within θ surfaces for *all time* (neglecting the effects of viscosity), since potential vorticity is conserved. Thus, if we know the future evolution of θ surfaces, we automatically know the future distribution of vortex lines, and from this we can make inferences about a number of things, such as the nature of air motions through the phenomenon and the distribution of pressure perturbations within the phenomenon.

2.5 Pressure perturbations

Considerable dynamical insight can be gained from being able to relate the wind and temperature fields to the pressure field, and vice versa. At many times throughout the remainder of this book, we shall use the wind and temperature fields to make inferences about the pressure field, and this knowledge of the pressure field can then be exploited to gain understanding of the accelerations that influence the structure and evolution of a variety of

mesoscale phenomena. We begin by reviewing pressure changes in a hydrostatic atmosphere, which can be interpreted as changes in the weight of the overlying atmosphere. We then investigate the more general relationship between pressure and the wind and temperature (buoyancy) fields, applicable even when the atmosphere may depart significantly from hydrostatic balance.

2.5.1 Pressure changes in a hydrostatic atmosphere

In a hydrostatic atmosphere, that is, one in which $-\frac{1}{\rho} \frac{\partial p}{\partial z}$ and g are approximately in balance so that dw/dt is very small, the pressure at some level can be viewed as essentially the weight (per unit horizontal area) of the atmosphere above this level. In other words,

$$p(z) = g \int_z^\infty \rho \, dz. \quad (2.109)$$

To investigate what leads to pressure changes in a hydrostatic atmosphere, we differentiate (2.109) with respect to time,

$$\frac{\partial p}{\partial t} = g \int_z^\infty \frac{\partial \rho}{\partial t} \, dz, \quad (2.110)$$

where it is understood that p is the pressure at height z . However, mass conservation mandates that

$$\frac{\partial \rho}{\partial t} = -\frac{\partial(\rho u)}{\partial x} - \frac{\partial(\rho v)}{\partial y} - \frac{\partial(\rho w)}{\partial z}. \quad (2.111)$$

Substituting (2.111) into (2.110) gives

$$\begin{aligned} \frac{\partial p}{\partial t} &= -g \int_z^\infty \left[\frac{\partial(\rho u)}{\partial x} + \frac{\partial(\rho v)}{\partial y} \right] dz \\ &\quad - g \int_z^\infty \frac{\partial(\rho w)}{\partial z} \, dz \end{aligned} \quad (2.112)$$

$$\begin{aligned} &= -g \int_z^\infty \left[\frac{\partial(\rho u)}{\partial x} + \frac{\partial(\rho v)}{\partial y} \right] dz \\ &\quad - g \int_z^\infty d(\rho w) \end{aligned} \quad (2.113)$$

$$\begin{aligned} &= -g \int_z^\infty \left[\frac{\partial(\rho u)}{\partial x} + \frac{\partial(\rho v)}{\partial y} \right] dz \\ &\quad - [g(\rho w)|_\infty - g(\rho w)|_z]. \end{aligned} \quad (2.114)$$

But $\rho = 0$ at $z = \infty$, therefore $\rho w = 0$ at $z = \infty$, and

$$\frac{\partial p}{\partial t} = -g \int_z^\infty \left[\frac{\partial(\rho u)}{\partial x} + \frac{\partial(\rho v)}{\partial y} \right] dz + g\rho w, \quad (2.115)$$

where w is the vertical velocity at height z . Therefore, hydrostatic pressure changes at height z , which are attributable

to changes in the weight of the atmosphere above height z , are caused by net mass divergence in the column above height z [first term on the rhs of (2.115)] and the vertical advection of mass into or out of the column through the bottom of the column at height z [second term on the rhs of (2.115)]. At the ground, where $w = 0$ (if the ground is level), the second term on the rhs of (2.115) vanishes.

Another perspective into hydrostatic pressure fluctuations can be obtained by differentiating the hypsometric equation (2.66) with respect to time, which gives

$$\frac{\partial z(p_b)}{\partial t} - \frac{\partial z(p_t)}{\partial t} = -\frac{R_d}{g} \int_{p_t}^{p_b} \frac{\partial T_v}{\partial t} \, d \ln p, \quad (2.116)$$

where p_t and p_b are pressure levels at the top and bottom, respectively, of a layer of arbitrary thickness. From the first law of thermodynamics, we can obtain an expression for the local virtual temperature tendency on an isobaric surface,

$$\frac{\partial T_v}{\partial t} = -\mathbf{v} \cdot \nabla_p T_v + \omega\sigma + \frac{q}{c_p}, \quad (2.117)$$

where σ ($= -\frac{T_v}{\theta_v} \frac{\partial \theta_v}{\partial p}$) is a static stability parameter. Substitution of (2.117) into (2.116) leads to

$$\begin{aligned} \frac{\partial z(p_b)}{\partial t} &= -\frac{R_d}{g} \int_{p_t}^{p_b} \left(-\mathbf{v} \cdot \nabla_p T_v + \omega\sigma + \frac{q}{c_p} \right) d \ln p \\ &\quad + \frac{\partial z(p_t)}{\partial t}. \end{aligned} \quad (2.118)$$

If we choose the upper pressure level to be very high in the atmosphere, then we can reasonably assume that $\partial z(p_t)/\partial t \approx 0$, which then gives

$$\frac{\partial z(p_b)}{\partial t} = -\frac{R_d}{g} \int_{p_t}^{p_b} \left(-\mathbf{v} \cdot \nabla_p T_v + \omega\sigma + \frac{q}{c_p} \right) d \ln p. \quad (2.119)$$

If we define p_b to be near the surface, then we can use (2.119) to anticipate surface pressure changes qualitatively, owing to the relationship between surface pressure tendency and height tendency near the ground (height falls are associated with pressure falls). From (2.119), falling surface pressure would be anticipated when the mean virtual temperature of the overlying column of air increases owing to warm advection, adiabatic warming associated with subsidence, or diabatic heating such as that due to radiation or latent heat release. Rising surface pressure would be anticipated when the mean virtual temperature of the overlying column of air decreases owing to cold advection, adiabatic cooling associated with ascent, or diabatic cooling. Some examples of mesoscale pressure changes that can be considered to be due to hydrostatic effects include the lowering of surface pressure in regions of

compensating subsidence, where adiabatic warming lowers the density in the column (e.g., the wake depressions and inflow lows of mesoscale convective systems), and the increase of surface pressure in regions where evaporative cooling increases density (e.g., mesohighs within mesoscale convective systems).

2.5.2 Hydrostatic and nonhydrostatic pressure perturbations

There are many mesoscale phenomena for which the hydrostatic approximation is not a good one (i.e., dw/dt is significant). In such instances, pressure perturbations cannot be deduced accurately using an integrated form of the hydrostatic equation like that used above. Moreover, it is often more intuitive to partition variables into base state values and perturbations from the base state. In principle, *any* base state can be specified, but we typically choose a base state that is representative of some average state of the atmosphere in order to facilitate interpretation of what the deviations from the base state imply. For example, a horizontally homogeneous, hydrostatic base state is the most common choice.

Let us describe the total pressure p and density ρ as the sum of a horizontally homogeneous base state pressure and density, and a deviation from this base state, that is,

$$p(x, y, z, t) = \bar{p}(z) + p'(x, y, z, t) \quad (2.120)$$

$$\rho(x, y, z, t) = \bar{\rho}(z) + \rho'(x, y, z, t), \quad (2.121)$$

where the base state is denoted with overbars, the deviation from the base state is denoted with primes, and the base state is defined such that it is in hydrostatic balance ($\frac{\partial \bar{p}}{\partial z} = -\bar{\rho}g$).

The perturbation pressure, p' , can be represented as the sum of a hydrostatic pressure perturbation p'_h and a nonhydrostatic pressure perturbation p'_{nh} , that is,

$$p' = p'_h + p'_{nh}. \quad (2.122)$$

The former arises from density perturbations by way of the relation

$$\frac{\partial p'_h}{\partial z} = -\rho' g, \quad (2.123)$$

which allows us to rewrite the inviscid form of (2.56) as

$$\frac{dw}{dt} = -\frac{1}{\rho} \frac{\partial p'_{nh}}{\partial z}. \quad (2.124)$$

Hydrostatic pressure perturbations occur beneath buoyant updrafts (where $p'_h < 0$) and within the latently cooled precipitation regions of convective storms (where $p'_h > 0$) (e.g., Figure 5.23). The nonhydrostatic pressure

perturbation is simply the difference between the total pressure perturbation and hydrostatic pressure perturbation and is responsible for vertical accelerations. An alternate breakdown of pressure perturbations is provided below.

2.5.3 Dynamic and buoyancy pressure perturbations

Another common approach used to partition the perturbation pressure is to form a diagnostic pressure equation by taking the divergence ($\nabla \cdot$) of the three-dimensional momentum equation. We shall use the Boussinesq momentum equation for simplicity, which can be written as [cf. (2.43)]

$$\frac{\partial \mathbf{v}}{\partial t} + \mathbf{v} \cdot \nabla \mathbf{v} = -\alpha_0 \nabla p' + B \mathbf{k} - f \mathbf{k} \times \mathbf{v} \quad (2.125)$$

where $\alpha_0 \equiv 1/\rho_0$ is a constant specific volume and the Coriolis force has been approximated as $-f \mathbf{k} \times \mathbf{v}$. The use of the fully compressible momentum equations results in a few additional terms upon taking the divergence, but the omission of these terms does not severely hamper a qualitative assessment of the relationship between pressure perturbations and the wind and buoyancy fields derived from the Boussinesq momentum equations.

The divergence of (2.125) is

$$\frac{\partial(\nabla \cdot \mathbf{v})}{\partial t} + \nabla \cdot (\mathbf{v} \cdot \nabla \mathbf{v}) = -\alpha_0 \nabla^2 p' + \frac{\partial B}{\partial z} - \nabla \cdot (f \mathbf{k} \times \mathbf{v}). \quad (2.126)$$

Using $\nabla \cdot \mathbf{v} = 0$, we obtain

$$\alpha_0 \nabla^2 p' = -\nabla \cdot (\mathbf{v} \cdot \nabla \mathbf{v}) + \frac{\partial B}{\partial z} - \nabla \cdot (f \mathbf{k} \times \mathbf{v}). \quad (2.127)$$

After evaluating $\nabla \cdot (\mathbf{v} \cdot \nabla \mathbf{v})$ and $\nabla \cdot (f \mathbf{k} \times \mathbf{v})$, we obtain

$$\begin{aligned} \alpha_0 \nabla^2 p' = & - \left[\left(\frac{\partial u}{\partial x} \right)^2 + \left(\frac{\partial v}{\partial y} \right)^2 + \left(\frac{\partial w}{\partial z} \right)^2 \right] \\ & - 2 \left(\frac{\partial v}{\partial x} \frac{\partial u}{\partial y} + \frac{\partial w}{\partial x} \frac{\partial u}{\partial z} + \frac{\partial w}{\partial y} \frac{\partial v}{\partial z} \right) \\ & + \frac{\partial B}{\partial z} + f \zeta - \beta u, \end{aligned} \quad (2.128)$$

where $\zeta = \frac{\partial v}{\partial x} - \frac{\partial u}{\partial y}$ and $\beta = df/dy$. The last term on the rhs of (2.128) is associated with the so-called β effect and is small, even on the synoptic scale. The second-to-last term on the rhs of (2.128) is associated with the Coriolis force. The remaining terms will be discussed shortly.

On the synoptic scale, the Coriolis force tends to dominate (2.128) and, neglecting the β effect, we obtain

$$\alpha_0 \nabla^2 p' = f \zeta. \quad (2.129)$$

The Laplacian of a wavelike variable away from boundaries tends to be positive (negative) where the perturbations of the variable itself are negative (positive). Thus, $\nabla^2 p' \propto -p'$ and

$$p' \propto -f \zeta, \quad (2.130)$$

which is the familiar synoptic-scale relationship between pressure perturbations and flow curvature: anticyclonic flow is associated with high pressure and cyclonic flow is associated with low pressure.

Hereafter, we shall neglect the terms in (2.128) associated with the Coriolis force and β effect. Also, it will be helpful to rewrite (2.128) in terms of vorticity (ω) and the *deformation tensor* (also known as the *rate-of-strain tensor*), e_{ij} , such that

$$\alpha_0 \nabla^2 p' = -e_{ij}^2 + \frac{1}{2} |\omega|^2 + \frac{\partial B}{\partial z}, \quad (2.131)$$

where

$$e_{ij}^2 = \frac{1}{4} \sum_{i=1}^3 \sum_{j=1}^3 \left(\frac{\partial u_i}{\partial x_j} + \frac{\partial u_j}{\partial x_i} \right)^2 \quad (2.132)$$

and $u_1 = u$, $u_2 = v$, $u_3 = w$, $x_1 = x$, $x_2 = y$, and $x_3 = z$. Deformation describes the degree to which a fluid element changes shape as a result of spatial variations in the velocity field (e.g., fluid elements can be stretched or sheared by velocity gradients).

For well-behaved fields (i.e., $\nabla^2 p' \propto -p'$),

$$p' \propto \underbrace{e_{ij}^2}_{\text{dynamic pressure perturbation}} - \underbrace{\frac{1}{2} |\omega|^2}_{\text{splat}} - \underbrace{\frac{\partial B}{\partial z}}_{\text{buoyancy pressure perturbation}}. \quad (2.133)$$

We see that deformation is always associated with high perturbation pressure via the e_{ij}^2 term, sometimes known as the *splat* term.¹¹ Rotation (of any sense) is always associated with low pressure by way of the $|\omega|^2$ term, sometimes referred to as the *spin* term. We know that, hydrostatically, warming in a column leads to pressure falls in the region below the warming. The $\partial B / \partial z$ or *buoyancy pressure* term partly accounts for such hydrostatic effects.

¹¹ The informal, and perhaps a bit humorous, name of the splat term originates from the field of fluid dynamics, presumably because the term is large when fluid elements are deformed by velocity gradients in a way that is similar to how a fluid element would flatten if impacted against an obstacle.

Low- (high-) pressure perturbations occur below (above) regions of maximum buoyancy (e.g., below and above a region of maximum latent heat release). Although it is tempting to regard the terms on the rhs of (2.133) as *forcings* for p' , (2.133) is a *diagnostic* equation rather than a *prognostic* equation. In other words, the terms on the rhs of (2.133) are *associated with* pressure fluctuations, rather than being the *cause* of the pressure fluctuations.

Pressure fluctuations associated with the first two terms on the rhs of (2.133) are sometimes referred to as *dynamic pressure perturbations*, p'_d , whereas pressure perturbations associated with the third term on the rhs of (2.133) sometimes are referred to as *buoyancy pressure perturbations*, p'_b , where

$$p' = p'_d + p'_b, \quad (2.134)$$

and

$$\alpha_0 \nabla^2 p'_d = -e_{ij}^2 + \frac{1}{2} |\omega|^2 \quad (2.135)$$

$$\alpha_0 \nabla^2 p'_b = \frac{\partial B}{\partial z}. \quad (2.136)$$

Comparison of the partitioning of pressure perturbations in this section with that performed in the previous section [compare (2.122) with (2.134)] reveals that the nonhydrostatic pressure perturbation, p'_{nh} , comprises the dynamic pressure perturbation, p'_d , and *a portion of* the buoyancy pressure perturbation, p'_b . The hydrostatic pressure perturbation, p'_h , comprises the remainder of p'_b . It can be shown that $-\frac{1}{\rho} \frac{\partial p'_b}{\partial z} + B$ is *independent of* the specification of the somewhat arbitrary base state $\bar{p}(z)$ profile, unlike B and $-\frac{1}{\rho} \frac{\partial p'_b}{\partial z}$, which individually depend on the base state. For this reason, diagnostic studies often evaluate $-\frac{1}{\rho} \frac{\partial p'_b}{\partial z} + B$ collectively and refer to it as the *buoyancy forcing*. In such instances, B is sometimes referred to as the *thermal buoyancy*.¹²

Examples of the pressure perturbation fields associated with a density current (Section 5.3.2) and a buoyant, moist updraft are presented in Figures 2.6 and 2.7. In the case of the density current (Figure 2.6), positive p'_h and p'_b are found within the cold anomaly, with the maxima at the ground. A discrete excess in total pressure is present at the leading edge of the density current. This high pressure is a consequence of $p'_{nh} > 0$ and $p'_d > 0$ and the fact that $(\frac{\partial u}{\partial x})^2$ is large there. There is also a prominent area of $p' < 0$ (and $p'_d < 0$) centered behind the leading edge of the density current, near the top of the density current, associated with the horizontal vorticity that has been generated baroclinically. In the case of the moist, buoyant updraft (Figure 2.7),

¹² Additional discussion is provided by Doswell and Markowski (2004).

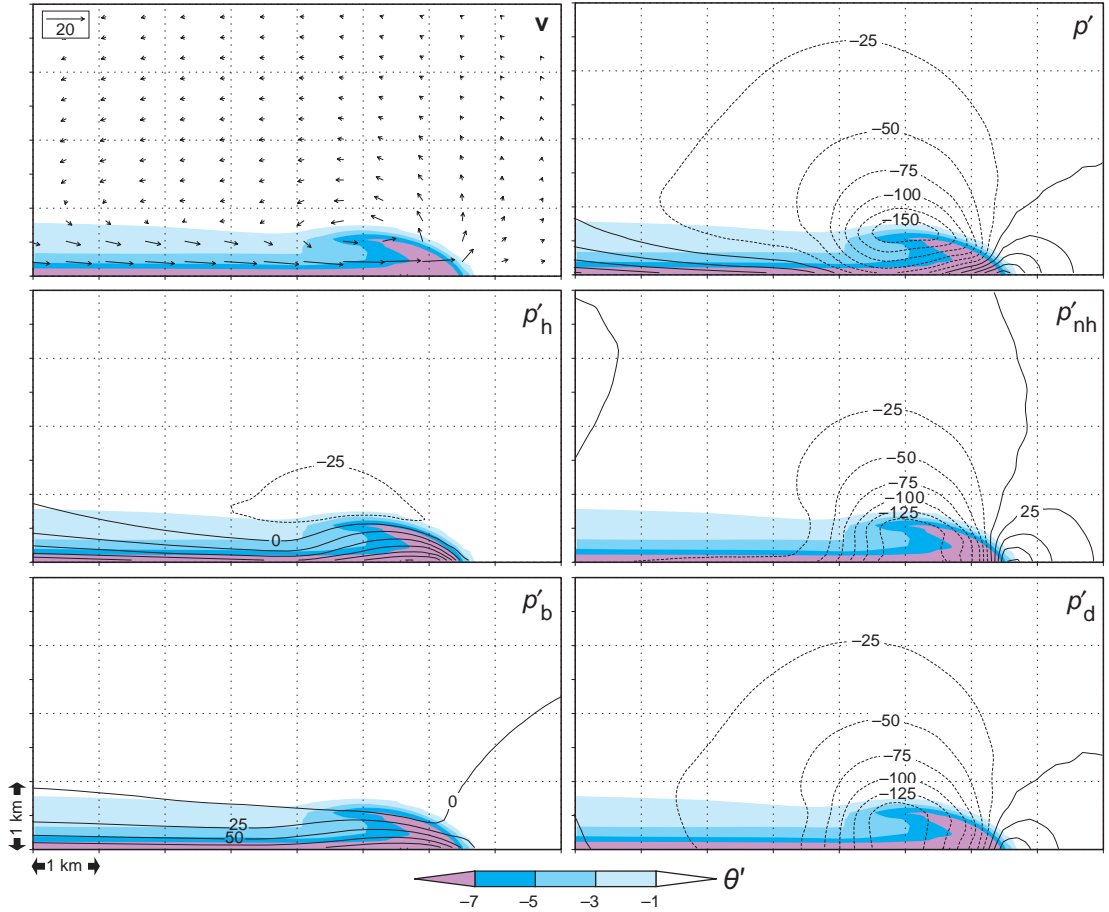


Figure 2.6 The pressure perturbations associated with a numerically simulated density current. The horizontal and vertical grid spacing of the simulation is 100 m. The ambient environment is unstratified. The domain shown is much smaller than the actual model domain used in the simulation. Potential temperature perturbations (θ') are shown in each panel (refer to the color scale). Wind velocity (v) vectors in the x - z plane are shown in the top left panel (a reference vector is shown in the corner of this panel). Pressure perturbations are presented in the other panels. Units are Pa; the contour interval is 25 Pa = 0.25 mb (dashed contours are used for negative values). Note that $p' = p'_h + p'_{nh} = p'_d + p'_b$. The p'_b field was obtained by solving $\nabla^2 p'_b = \frac{\partial(\bar{p}B)}{\partial z}$, where \bar{p} is the base state density, using periodic lateral boundary conditions and assuming $\frac{\partial p'_b}{\partial z} = 0$ at the top and bottom boundaries. (Regarding the boundary conditions, all that is known is that $\frac{\partial p'}{\partial z} = \bar{p}B$ at the top and bottom boundaries, owing to the fact that $dw/dt = 0$ at these boundaries, but it is somewhat arbitrary how one specifies the boundary conditions for $\frac{\partial p'_b}{\partial z}$ and $\frac{\partial p'_d}{\partial z}$ individually.) Because of the boundary conditions used, the retrieved p'_b field is not unique. A constant was added to the retrieved p'_b field so that the domain-averaged p'_b field is zero. The p'_d field was then obtained by subtracting p'_b from the total p' field.

a region of $p'_h < 0$ (and $p'_{nh} > 0$) is located beneath the buoyant updraft. A region of $p'_d > 0$ exists above (below) the maximum updraft where horizontal divergence (convergence) is strongest; $(\frac{\partial u}{\partial x})^2$ is large in both regions. On the flanks of the updraft, $p'_d < 0$ as a result of the horizontal vorticity that has been generated baroclinically by the horizontal buoyancy gradients. The total p' field opposes

the upward-directed buoyancy force, in large part as a result of the p'_b field (i.e., the p' and p'_b fields are well-correlated).

It is often useful to partition the wind field into a mean flow with vertical wind shear representing the environment (denoted with overbars) and departures from the mean (denoted with primes); i.e., let $u = \bar{u} + u'$, $v = \bar{v} + v'$, and

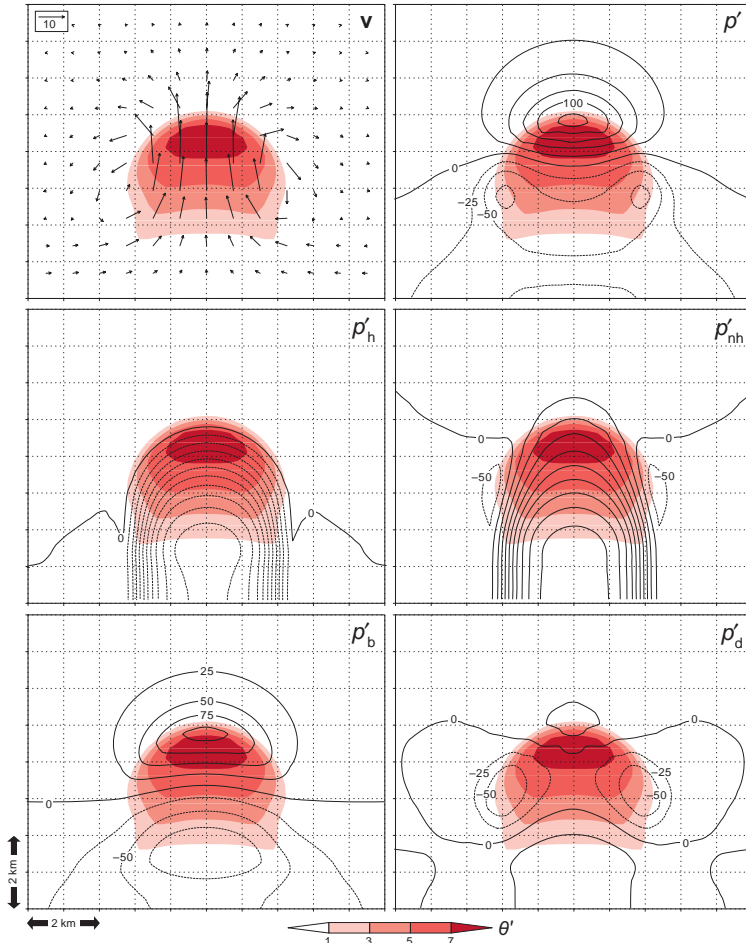


Figure 2.7 As in Figure 2.6, but for the case of a warm bubble released in a conditionally unstable environment. The bubble had an initial potential temperature perturbation of 2 K, a horizontal radius of 5 km, and a vertical radius of 1.5 km. The bubble was released 1.5 km above the ground. The fields shown above are from 600 s after the release of the bubble. The environment has approximately 2200 J kg^{-1} of CAPE and is the environment used in the simulations of Weisman and Klemp (1982). The horizontal and vertical grid spacing is 200 m (the domain shown above is much smaller than the actual model domain). The contour interval is 25 Pa (0.25 mb) for p' , p'_h , and p'_d . The contour interval is 50 Pa (0.50 mb) for p'_b and p'_{nh} .

$w = w'$. Then (2.133) becomes

$$p' \propto \underbrace{e_{ij}'^2 - \frac{1}{2}|\omega'|^2}_{\text{nonlinear dynamic pressure perturbation}} + \underbrace{2 \left(\frac{\partial w'}{\partial x} \frac{\partial \bar{u}}{\partial z} + \frac{\partial w'}{\partial y} \frac{\partial \bar{v}}{\partial z} \right)}_{\text{linear dynamic pressure perturbation}} - \underbrace{\frac{\partial B}{\partial z}}_{\text{buoyancy pressure perturbation}} \quad (2.137)$$

where e_{ij}' and ω' are the deformation and vorticity perturbations, respectively. The dynamic pressure terms

involving spin and splat are referred to as *nonlinear dynamic pressure* terms, whereas the remaining dynamic pressure terms are referred to as *linear dynamic pressure* terms because they include only one perturbation quantity per term.

The linear dynamic pressure terms can be written as

$$2 \left(\frac{\partial w'}{\partial x} \frac{\partial \bar{u}}{\partial z} + \frac{\partial w'}{\partial y} \frac{\partial \bar{v}}{\partial z} \right) = 2\mathbf{S} \cdot \nabla_h w' \quad (2.138)$$

where $\mathbf{S} = (\partial \bar{u} / \partial z, \partial \bar{v} / \partial z)$ is the mean vertical wind shear and $\nabla_h w'$ is the horizontal gradient of the vertical velocity

perturbation. From (2.138) it is apparent that high- (low-) pressure perturbations are found upshear (downshear) of an updraft, such that a high-low pressure couplet is aligned with the vertical wind shear vector at a given level. We can relate this to (2.131) by noting that the pressure field depends on the squares of both the total (i.e., base state plus perturbation) deformation and the total vorticity. Noting that $(a + b)^2 = a^2 + 2ab + b^2$, and relating a to the base state terms and b to the perturbation terms, we see that the dynamic part of the rhs of (2.131) can be interpreted as the perturbation quantities squared plus the base state quantities squared (which do not appear explicitly because a base state consisting of only vertical shear is a combination of deformation and vorticity that leads to cancellation of the purely base state dynamic terms), with the remaining linear term representing the net result of the ' $2ab$ '-type terms in the squares of total deformation and total vorticity. These ' $2ab$ ' terms cause the square of either total field to be greater (less) than the sum of the square of the base state field and the square of the perturbation field if the base state and perturbation fields have the same (opposite) sign. Thus, when the perturbation fields are added to the

base state, on the upshear (downshear) side of the updraft, the deformation due to the gradient in w' acts in the same (opposite) sense as the deformation inherent to the base state shear (Figure 2.8a). Conversely, on the upshear (downshear) side of the updraft, the vorticity is of the opposite (same) sense as that of the base state shear (Figure 2.8b). Thus, on the upshear (downshear) side, the linear term accounts for increased (decreased) deformation squared and decreased (increased) rotation squared for the total wind field compared to that predicted by summing only the separate squares of the base state and the perturbation terms. These influences on deformation squared and vorticity squared both lead to a higher (lower) pressure on the upshear (downshear) flank. (It is worth noting that the linear term is only one influence on the pressure. For example, if the perturbation horizontal vorticity associated with the vortex ring surrounding the updraft is sufficiently large, a low pressure could still exist in both the upshear and downshear directions. However, assuming this vortex ring is fairly symmetric it would not result in a pressure gradient across the updraft, and the linear term would still dominate the direction of this pressure gradient, in this

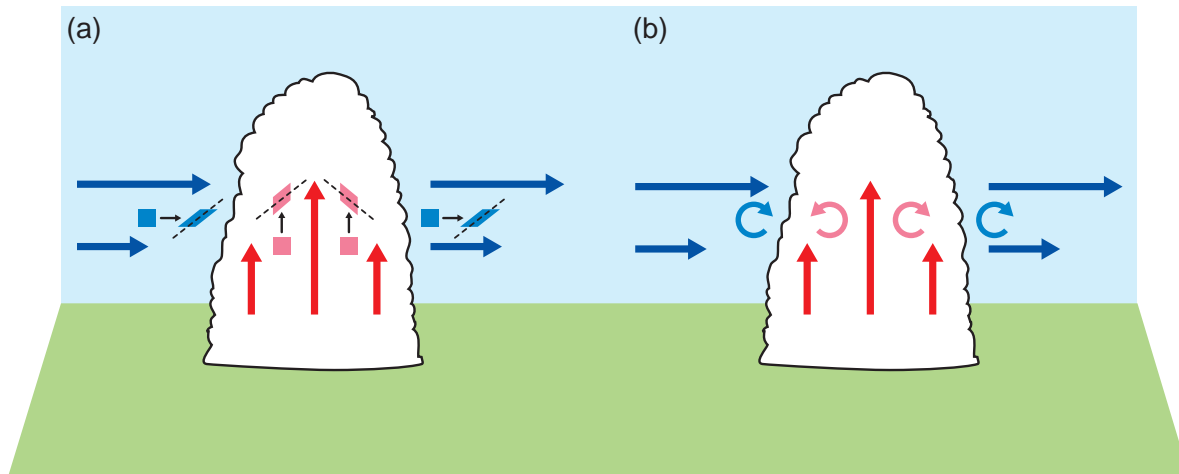


Figure 2.8 (a) Illustration showing the deformation associated with the mean vertical wind shear acts in the same (opposite) sense as that associated with the gradient of w' on the upshear (downshear) flank of an updraft. The blue vectors give a sense of the increase in westerly winds with height (the shear points toward the right, thus the upshear flank is the left flank, and the downshear flank is the right flank), and the red vectors give a sense of the horizontal gradient of (perturbation) vertical velocity. The sense of how a fluid element would be deformed by the mean and perturbation wind gradients is shown schematically via the light blue and pink polygons, respectively. The black dashed lines indicate the axes along which the fluid elements are elongated by the shear. (b) Illustration showing how the vorticity associated with the mean vertical wind shear points in the opposite (same) direction as that associated with the gradient of w' on the upshear (downshear) flank of an updraft. The light blue curved arrows indicate the sense of rotation associated with the mean wind shear, and the pink curved arrows indicate the sense of rotation associated with the updraft (i.e., the perturbation wind field).

case from low pressure on the upshear flank toward even lower pressure on the downshear flank.)

2.5.4 Bernoulli equations

The assumption that $\nabla^2 p' \propto -p'$ generally is satisfactory for well-behaved fields and away from the ground, but near the ground (a physical boundary) the diagnostic pressure equation we derived in the previous section may not necessarily predict the correct pressure perturbation, owing to a lack of consideration of boundary conditions in making the $\nabla^2 p' \propto -p'$ assumption. Pressure perturbations must be inferred using some other means, and a class of equations called *Bernoulli equations* is often useful. Bernoulli equations can be formulated if the flow is steady or if it is irrotational (the flow must also be inviscid and in an inertial reference frame, i.e., no friction or Coriolis force). Here we shall look at the steady-flow case ($\partial/\partial t = 0$).

Let us again write the momentum equation, this time as

$$\frac{\partial \mathbf{v}}{\partial t} + \mathbf{v} \cdot \nabla \mathbf{v} = -\frac{1}{\rho} \nabla p - g\mathbf{k}. \quad (2.139)$$

If the flow is steady, then $\partial \mathbf{v}/\partial t = 0$. Also, we can use vector identities to express $\mathbf{v} \cdot \nabla \mathbf{v}$ as $\nabla |\mathbf{v}|^2/2 + \boldsymbol{\omega} \times \mathbf{v}$. Furthermore, we can write $g\mathbf{k}$ as ∇gz . We thus obtain

$$\nabla \frac{|\mathbf{v}|^2}{2} + \boldsymbol{\omega} \times \mathbf{v} + \frac{1}{\rho} \nabla p + \nabla gz = 0. \quad (2.140)$$

Hereafter we shall write $|\mathbf{v}|$ as v . If we take $d\mathbf{r} \cdot$ (2.140), where $d\mathbf{r} = (dx \mathbf{i} + dy \mathbf{j} + dz \mathbf{k})$ ($d\mathbf{r}$ is an infinitesimal distance along a streamline), and note that $d\mathbf{r} \cdot \boldsymbol{\omega} \times \mathbf{v} = 0$ because $\boldsymbol{\omega} \times \mathbf{v}$ points normal to a streamline, then (2.140) becomes

$$d\left(\frac{v^2}{2}\right) + \frac{dp}{\rho} + d(gz) = 0 \quad (2.141)$$

along a streamline, and integrating (2.141) gives

$$\frac{v^2}{2} + \int \frac{dp}{\rho} + gz = \text{constant} \quad (2.142)$$

along a streamline, such that the lhs of (2.142) is conserved along streamlines (which are also trajectories because $\partial/\partial t = 0$). Equation (2.142) is called a Bernoulli equation. If ρ is constant and equal to ρ_0 (incompressibility assumed), then (2.142) can be written as

$$\frac{v^2}{2} + \frac{p}{\rho_0} + gz = \text{constant}, \quad (2.143)$$

which is another Bernoulli equation.

If the equation of motion is written in terms of the perturbation pressure gradient and buoyancy forces, i.e.,

$$\frac{\partial \mathbf{v}}{\partial t} + \mathbf{v} \cdot \nabla \mathbf{v} = -\frac{1}{\rho} \nabla p' + B\mathbf{k}, \quad (2.144)$$

then instead of (2.142) we obtain a Bernoulli equation of the form

$$\frac{v^2}{2} + \int \frac{dp'}{\rho} - \int B dz = \text{constant}. \quad (2.145)$$

Because θ rather than ρ tends to be conserved along trajectories, it is sometimes useful to express the pressure gradient force in terms of nondimensional pressure (i.e., the Exner function), $\pi = (p/p_0)^{R/c_p} = T/\theta$, such that $\rho^{-1} \nabla p = -c_p \theta \nabla \pi$. The corresponding Bernoulli equation derived in the same manner as (2.143), assuming θ is a constant along a streamline/trajecotry (dry adiabatic motion), is

$$\begin{aligned} \frac{v^2}{2} + c_p \theta \pi + gz &= \frac{v^2}{2} + c_p T + gz \\ &= \frac{v^2}{2} + RT + c_v T + gz \\ &= \frac{v^2}{2} + \frac{p}{\rho} + c_v T + gz \\ &= \text{constant}. \end{aligned} \quad (2.146)$$

2.6 Thermodynamic diagrams

The analysis of soundings is important in many mesoscale meteorology and forecasting applications treated in this book, such as the evolution of the atmospheric boundary layer, convection initiation, the organization of thunderstorms, lake-effect snow, phenomena related to the blocking of winds by topographic barriers, and severe downslope winds. A thermodynamic diagram plots pressure, temperature, and moisture observations from a sounding such that the equation of state, the Clausius-Clapeyron equation, and the first law of thermodynamics for dry adiabatic and moist or pseudoadiabatic processes are satisfied. Cyclic processes can be represented on thermodynamic diagrams by a closed curve, and on many thermodynamic diagrams the area enclosed is directly proportional to the work done in the process.¹³ Although a large number of individual thermodynamic diagrams accomplish this general task, the most

¹³ For example, the amount of energy associated with a parallelogram bounded by isobars and isotherms on a skew $T-\log p$ diagram is given by $R_d \Delta(\ln p) \Delta T$, where $\Delta(\ln p)$ and ΔT are the dimensions of the parallelogram. Also see Doswell (1991b).

widely used diagram, especially within the United States, is the skew T -log p diagram. Only a brief review appears below; we assume that readers have been introduced to thermodynamic diagrams elsewhere.

It is essential that the reader be familiar with the different thermodynamic processes that can be represented on a thermodynamic diagram (Figure 2.2). For example, because potential temperature and water vapor mixing ratio are conserved in a dry adiabatic process, the *lifting condensation level* (LCL) or *saturation point* (defined by T^* and p^* , the saturation pressure) of a parcel lifted from a particular pressure level can be found by locating the intersection of the dry adiabat (isentrope) and the constant mixing ratio line that pass through the potential temperature and mixing ratio, respectively, of the parcel to be lifted (Figures 2.2 and 2.9). The temperature of a parcel that is lifted moist adiabatically beyond its saturation pressure is found by following the pseudoadiabat that passes through the saturation point of the lifted parcel. The lifted parcel approximately conserves its θ_e and θ_w for both the unsaturated and saturated portions of its ascent. The *level of free convection* (LFC) is where the lifted parcel becomes warmer than the environmental temperature, and if an LFC exists the *equilibrium level* (EL) is defined to be the height at which a buoyant lifted parcel becomes neutrally buoyant, that is, the height above the LFC at which the parcel temperature is equal to the environmental temperature (Figure 2.9).

The area bounded by the environmental temperature trace and pseudoadiabat followed by a saturated parcel lifted from its LFC to EL is often referred to as the *positive area* and is proportional to the *convective available potential energy* (CAPE; Figure 2.9). Conversely, the area bounded by the environmental temperature trace and the path taken on a thermodynamic diagram by a negatively buoyant air parcel, usually from the surface to the LFC, is often referred to as the *negative area* and is proportional to the *convective inhibition* (CIN). CAPE and CIN are defined as

$$\text{CAPE} = \int_{\text{LFC}}^{\text{EL}} B \, dz \approx g \int_{\text{LFC}}^{\text{EL}} \frac{T'_v}{\bar{T}_v} \, dz \quad (2.147)$$

$$\text{CIN} = - \int_0^{\text{LFC}} B \, dz \approx -g \int_{\text{SFC}}^{\text{LFC}} \frac{T'_v}{\bar{T}_v} \, dz, \quad (2.148)$$

where $z = 0$ at the surface, the buoyancy B has been expressed in terms of the virtual temperature perturbation of the lifted parcel (T'_v) relative to the virtual temperature of the environment (\bar{T}_v), and the virtual temperature of the lifted parcel is $T_v = \bar{T}_v + T'_v$. CAPE is proportional to the kinetic energy that a parcel can gain from its environment as a result of the contribution of buoyancy to the vertical acceleration. CIN is equal to the

work that must be done against the stratification to lift a parcel of air to its LFC. In typical severe storm environments, CAPE values $\lesssim 1000 \text{ J kg}^{-1}$ are usually considered small, whereas values $\gtrsim 2500 \text{ J kg}^{-1}$ are usually considered large. CIN values $\lesssim 10 \text{ J kg}^{-1}$ are usually considered small, whereas values $\gtrsim 50 \text{ J kg}^{-1}$ are usually considered large.

One often underappreciated aspect of computing CIN and CAPE is the effect of moisture on the calculation.¹⁴ In contrast to (2.147) and (2.148), CAPE and CIN frequently are computed using temperature instead of virtual temperature (or potential temperature instead of virtual potential temperature). The amount of CIN and CAPE computed using virtual temperature can differ significantly from the CIN and CAPE computed using temperature. For example, in Figure 2.9, which displays the positive and negative areas both with and without the inclusion of moisture, the CAPE increases by roughly 10% when virtual temperature effects are included, but, even more importantly, the CIN is reduced from 35 J kg^{-1} to 1 J kg^{-1} —this is the difference between having a virtually insurmountable amount of CIN (and thus almost no chance of thunderstorm initiation) versus practically no CIN at all (and thunderstorm initiation very likely)—when virtual temperature is considered in the calculations. In typical daytime temperature and moisture profiles, CAPE (CIN) values are increased (decreased) when the effects of moisture are included.

Along similar lines, a quantity known as *downdraft CAPE* or DCAPE is related to the amount of kinetic energy that can be realized by a saturated downdraft en route to the ground. For an air parcel descending from height $z = h$ to the surface ($z = 0$), DCAPE is computed by cooling and saturating the parcel to the wet-bulb temperature at $z = h$, following a pseudoadiabat from the wet-bulb temperature of the parcel at $z = h$ to $z = 0$, and then integrating the negative buoyancy along the path, that is,

$$\text{DCAPE} = g \int_h^0 \frac{T'_v}{\bar{T}_v} \, dz, \quad (2.149)$$

where the effects of water vapor on the negative buoyancy have been included, as in (2.147) and (2.148) (Figure 2.10). One difficulty in using the above expression to predict downdraft speeds is the fact that the depth of the layer over which DCAPE should be integrated is usually not obvious, and downdraft parcels are often unsaturated for part of their excursions (i.e., parcels may not follow a pseudoadiabat all the way to the ground). For these reasons and others that will not be discussed until convective outflows and

¹⁴ For example, see Doswell and Rasmussen (1994).

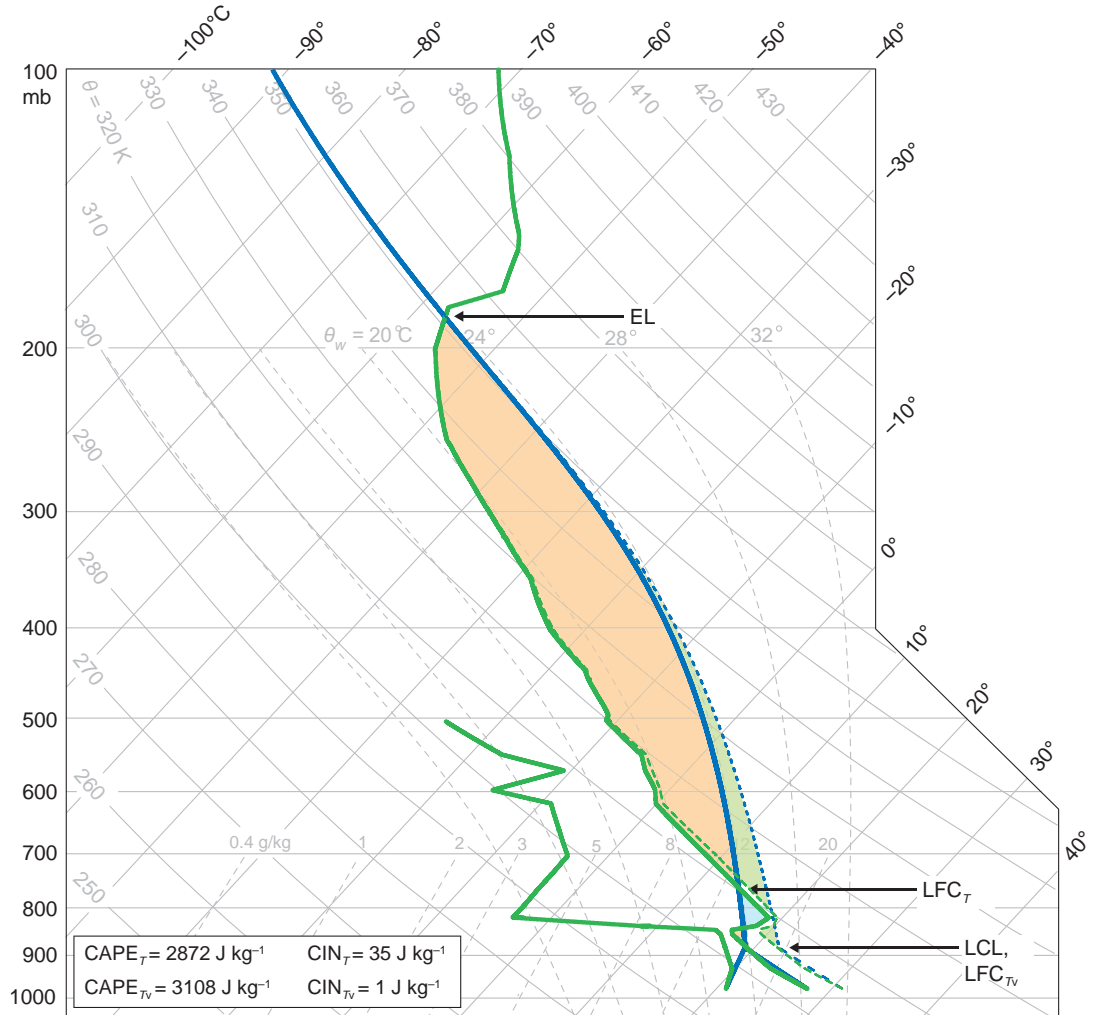


Figure 2.9 Skew T -log p diagram obtained from the Del Rio, Texas, sounding at 1800 UTC 14 May 2008. The temperature and dewpoint profiles are solid green (dewpoints are not plotted above 500 mb because they were unreliable above 500 mb). The virtual temperature profile is indicated with the dashed green line. The solid blue line indicates the temperature of a parcel of air lifted from the surface to its lifting condensation level (LCL), level of free convection (LFC), and equilibrium level (EL). The dashed blue line indicates the virtual temperature of the parcel. The LFC, CAPE, and CIN computed by including virtual temperature effects are LFC_{T_v} , CAPE_{T_v} , and CIN_{T_v} , respectively. The LFC, CAPE, and CIN based on temperature alone (the effect of moisture on buoyancy is neglected) are LFC_T , CAPE_T , and CIN_T , respectively. The positive and negative areas for the solid blue parcel trajectory (proportional to CAPE_T and CIN_T , respectively) are shaded light orange and light blue, respectively. The positive area for the dashed blue parcel trajectory (proportional to CAPE_{T_v} ; the negative area is virtually nonexistent) encompasses both the orange area and the area that is shaded light green.

downdrafts are discussed later in the book (Sections 5.3.1 and 10.3.1), DCAPE is generally not as good at predicting the maximum downdraft speed as CAPE is at predicting the maximum updraft speed (although, as will be discussed in Section 3.1.2, CAPE also has its limits in predicting maximum updraft speeds).

2.7 Hodographs

2.7.1 Hodograph basics

The specification of a vector requires at least two quantities; for wind vectors, this often takes the form of speed ($|\mathbf{v}|$)

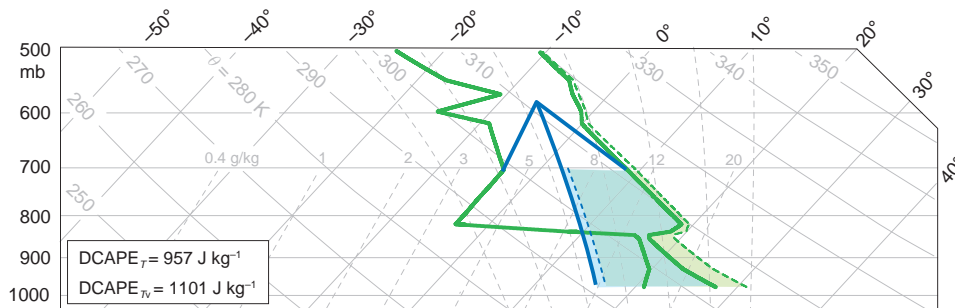


Figure 2.10 Skew T -log p diagram obtained from the Del Rio, Texas, sounding at 1800 UTC 14 May 2008 (this is the same sounding as appeared in Figure 2.9). The temperature and dewpoint profiles are solid green. The virtual temperature profile is indicated with the dashed green line. The solid blue line indicates the temperature of a parcel descending moist adiabatically from 700 mb, and the dashed blue line indicates the virtual temperature of the descending parcel. $DCAPE_T$ and $DCAPE_{TV}$ are the DCAPE values computed based on temperature alone and including the effects of both temperature and moisture on buoyancy, respectively. The negative area for the solid blue parcel trajectory (proportional to $DCAPE_T$) is shaded light blue. The negative area for the dashed blue parcel trajectory (proportional to $DCAPE_{TV}$) encompasses both the light blue area and the area shaded light green.

and direction (θ). A vertical wind profile consists of a set of wind speeds and directions at various heights. The vectors composing the vertical wind profile are commonly plotted in $|\mathbf{v}| - \theta$ space or $u - v$ space. A plot of the curve connecting the tips of the wind vectors defining the vertical wind profile is called a *hodograph* (Figure 2.11).¹⁵

In looking at the hodograph in Figure 2.11, it is apparent that it provides information about how the wind changes with height, that is, the vertical wind shear. For any two points along the hodograph, the vector wind difference ($\Delta\mathbf{v}$) between those heights is a vector connecting the points (Figure 2.11). Thus, long hodographs imply a large vertical wind shear magnitude. As the difference between the two heights (Δz) becomes infinitesimally small, $\Delta\mathbf{v}/\Delta z \rightarrow \partial\mathbf{v}/\partial z$, which defines the vertical wind shear vector $\mathbf{S} = \partial\mathbf{v}/\partial z$ at any given height, and this vector is tangent to the hodograph. Thus, the curvature of a hodograph provides information about how the vertical shear changes direction with height. When the wind direction itself turns counterclockwise with height, the wind is said to be *backing* with height. When the wind direction turns clockwise with height, the wind is said to be *veering* with height. Note that

¹⁵ The use of hodographs is believed to have originated with the Irish mathematician and physicist Sir William Hamilton (1805–1865) (Goodstein and Goodstein 1996), who is probably best known for his reformulation of classical mechanics and the use of Hamiltonians (Hamiltonians also have been employed in quantum mechanics). Hamilton used hodographs in his explanation of planetary motions such that the hodograph was used to depict the velocity of a planet moving around the sun as a function of time. Such a hodograph traces an ellipse.

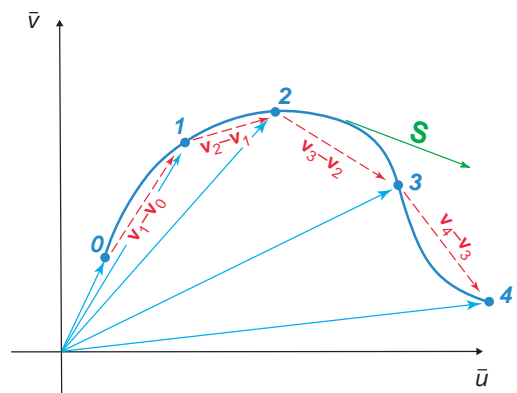


Figure 2.11 A hodograph (blue curve) and its relationship to the horizontal winds (blue vectors), which are drawn at five different levels (the labels along the hodograph indicate heights above ground level in kilometers). The point on the hodograph labeled “0” is the lowest altitude where the wind is measured, which typically is a few meters above the ground rather than $z = 0$ m (the horizontal wind goes to zero at $z = 0$). The vector wind difference between the winds at the top and bottom of each layer also are shown (red vectors). The shear vector at a point between 2 and 3 km also is shown (green vector); it lies tangent to the hodograph.

veering and backing of winds with height do not imply anything about the *curvature* of a hodograph.

If the horizontal gradient of vertical velocity is small relative to the vertical wind shear, then the horizontal

vorticity ω_h can be written as

$$\omega_h \approx \left(-\frac{\partial v}{\partial z}, \frac{\partial u}{\partial z} \right) = \mathbf{k} \times \mathbf{s}; \quad (2.150)$$

that is, ω_h has the same magnitude as the vertical shear and points 90° to the left of $\partial v / \partial z$ (Figure 2.12). A hodograph often is assumed to depict a base state (i.e., the ‘environment’) having horizontal wind components of \bar{u} and \bar{v} , just as temperature measurements from a sounding are used as values of \bar{T} in calculations of CAPE. The base state vertical velocity (\bar{w}) usually is assumed to be very small, if not zero, such that its horizontal gradients are negligible compared to the vertical gradients of \bar{u} and \bar{v} .

A significant fraction of the vertical wind shear present in a hodograph is the result of the large-scale horizontal temperature gradient via the thermal wind relation given by (2.67). However, vertical wind shear also can be present in the absence of large-scale baroclinity. For example, friction plays a role in creating vertical wind shear within the boundary layer, owing to the fact that the effects of friction decrease with height, becoming negligible at the top of the boundary layer. An analytical wind profile containing vertical wind shear—the *Ekman spiral*—can be derived by assuming the presence of boundary layer friction and no ambient baroclinity (Section 4.1.4). Large accelerations of the horizontal wind, which imply a significant ageostrophic wind, also can contribute to vertical wind shear in ways not predicted by the thermal wind relation. For example, near jet streaks or rapidly moving and/or intensifying cyclones,

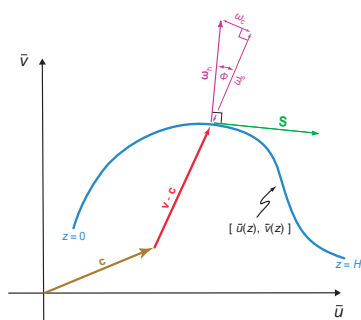


Figure 2.12 Diagram of a hodograph $[\bar{u}(z), \bar{v}(z)]$ depicting the storm motion vector \mathbf{c} , storm-relative wind vector $\mathbf{v} - \mathbf{c}$, shear vector \mathbf{s} , and environmental horizontal vorticity vector ω_h . When \mathbf{s} is a good representation of the thermal wind (i.e., when winds are close to geostrophic), ω_h points toward the cold air and $\mathbf{v} \cdot \omega_h$ is proportional to temperature advection. The streamwise and crosswise vorticity components, ω_s and ω_c , respectively, are also indicated.

the observed vertical wind shear can differ substantially from the geostrophic vertical wind shear.¹⁶

2.7.2 Mean wind on a hodograph and storm-relative winds

Although it is generally difficult to obtain the exact mean wind velocity within a layer without numerically averaging the wind data obtained within the layer, the mean wind velocity within a layer can usually be estimated reasonably well from a casual inspection of the hodograph. If a hodograph is straight in the layer within which the mean wind velocity is desired, the mean wind must lie somewhere on the hodograph. The position of the mean wind velocity on the hodograph can be estimated by interpolating between wind observations at specific heights along the hodograph (e.g., the mean wind must lie between the points that correspond to the minimum and maximum wind speeds within the layer). If the hodograph is curved in the layer within which the mean wind velocity is desired, the mean wind must lie on the concave side of the hodograph. The position of the mean wind velocity on the concave side of the hodograph can also be estimated by considering the minimum and maximum wind components within the layer.

Hodographs are most often used in the forecasting of convective storms (both their movement and organization can be predicted by the hodograph characteristics). In their early stages, convective storms tend to move with roughly the mean wind velocity averaged over the depth of the storm. Thus, if a hodograph is straight, the storm motion tends to be on the hodograph. For a curved hodograph, initial storm motion tends to be on the concave side of the hodograph. When convective storms have reached maturity (e.g., large evaporatively-driven cold pools exist at the ground, precipitation regions are extensive), storm motions may deviate from the mean wind velocity owing to *propagation* effects, such as new updrafts being triggered by a gust front moving with a velocity different from the velocity of individual convective elements, or perhaps strong dynamic pressure gradients forcing new updrafts on the flank of a storm. For example, many severe storms actually move to the right of the mean wind velocity during their mature phase.

In convective storm applications, we shall also find later that it is most appropriate to consider the winds in the reference frame moving with the convection. Consider the flow as seen by an observer moving along with a storm. Given a particular wind vector \mathbf{v} , for a storm moving with a vector velocity \mathbf{c} , the wind in a storm-relative reference frame can be obtained by subtracting the storm motion;

¹⁶ A more lengthy discussion of the processes contributing to vertical wind shear is provided by Doswell (1991).

thus, the *storm-relative wind* is $\mathbf{v} - \mathbf{c}$. Storm-relative winds are easy to obtain from a hodograph if the storm motion is known or predicted from the hodograph (Figure 2.12) by simply moving the hodograph origin to the (u, v) location corresponding to storm motion.

2.7.3 Directional shear versus speed shear

Although the definition of vertical wind shear does not distinguish between wind shear that results primarily from wind direction variations with height versus wind speed variations with height, vertical wind shear commonly is identified as being either *directional* or *speed* shear. Directional shear usually refers to variations of the ground-relative wind direction with height (expressed in degrees per vertical distance), whereas speed shear most commonly refers to variations in ground-relative wind speed with height. However, directional shear has also occasionally referred to the change in direction of the wind *shear* vector, rather than the horizontal wind vector, with height, and the terms *unidirectional* or *one-directional* shear have commonly been used to describe a shear vector that does not change direction with height. These classifications of the vertical wind shear, which describe whether a hodograph is curved (directional or directionally varying shear) or straight (unidirectional shear), have been used extensively within the convective storm community because the shape and length of the hodograph, which determine the vertical profiles of wind shear and storm-relative winds, are much more dynamically relevant than the vertical profile of ground-relative winds. Furthermore, in some contexts, directional shear and speed shear refer to variations in the storm-relative wind direction and speed with height, respectively.

Consider the idealized hodographs depicted in Figure 2.13. Hodographs A and A' are identical in length and shape (both are straight), but hodograph A' has been shifted by adding -5 m s^{-1} (10 m s^{-1}) to the zonal (meridional) wind speeds of the points comprising hodograph A. Hodographs A and A' both have unidirectional shear as defined by the variation of the wind shear vector with height (the shear is westerly at all levels), but have very different degrees of directional wind shear if directional shear is defined as the angular turning of the ground-relative wind vector with height (0° of veering in the case of hodograph A; $\sim 90^\circ$ of veering in the case of hodograph A'). Likewise, hodographs B and B' are identical in length and shape (both are half-circles), but hodograph B' has been shifted by adding 20 m s^{-1} (8 m s^{-1}) to the zonal (meridional) wind speeds of the points comprising hodograph B. Hodographs B and B' have identical amounts of directional shear if directional shear is defined as the veering of the shear vector with height or veering of the

storm-relative winds with height. However, if directional shear is defined as the veering of the ground-relative wind vector with height, then hodographs B and B' have very different degrees of directional shear ($\sim 180^\circ$ of veering in the case of hodograph B; $\sim 45^\circ$ of veering in the case of hodograph B'). Furthermore, hodograph B has no speed shear yet hodograph B' has 25 m s^{-1} of speed shear, if speed shear is defined as the variation of ground-relative wind speed with height. The storm-relative wind profiles are identical within each pair of hodographs (Figure 2.13), assuming that the storm motion is the same function of the environmental wind profile in each case.

Directional and speed shear of the ground-relative wind depend on the mean wind velocity, which determines where a hodograph is positioned relative to the origin, as well as the thermal wind representative of a deep layer, which largely controls the orientation of a hodograph. The hodographs shown in Figure 2.14, which have roughly similar shapes, span a variety of mean wind velocities and thermal wind orientations. Hodographs that are confined to the first quadrant (i.e., $u, v > 0$ at all levels) are commonly observed during outbreaks of severe convection in the eastern United States (Figures 2.14a and 2.14b), whereas hodographs commonly span the first and second quadrants (i.e., $v > 0$ at all levels, but u changes sign from negative to positive in the lower troposphere) in severe weather outbreaks in the United States Great Plains region (Figure 2.14d). Hodographs occasionally span more than two quadrants, as in ‘northwest-flow’ events, so called because the upper-tropospheric winds are usually from the northwest (in the northern hemisphere) (Figure 2.14c). Ground-relative veering is smaller when hodographs are confined to a single quadrant compared to when hodographs span multiple quadrants, yet the magnitude of storm-relative wind speeds and veering is largely independent of hodograph orientation and position with respect to the origin (storm motions tend to be faster given the same hodograph length when hodographs are confined to a single quadrant). In the specific examples of Figure 2.14, the cases with the *smallest* ground-relative wind veering (Figures 2.14a and 2.14b) are actually associated with the *largest* storm-relative wind veering.

We shall revisit the importance of wind shear and storm-relative winds in Part III in our treatment of deep moist convection. The bottom line is that one needs to be careful about directional and speed shear terminology because they can have different meanings in different contexts. For example, the ground-relative wind profile might be of greater interest when surface friction or terrain is important, as in the study of boundary layer phenomena (Chapter 4), whereas wind shear and storm-relative wind profiles are usually of greater interest in studies of phenomena for which the effects of surface

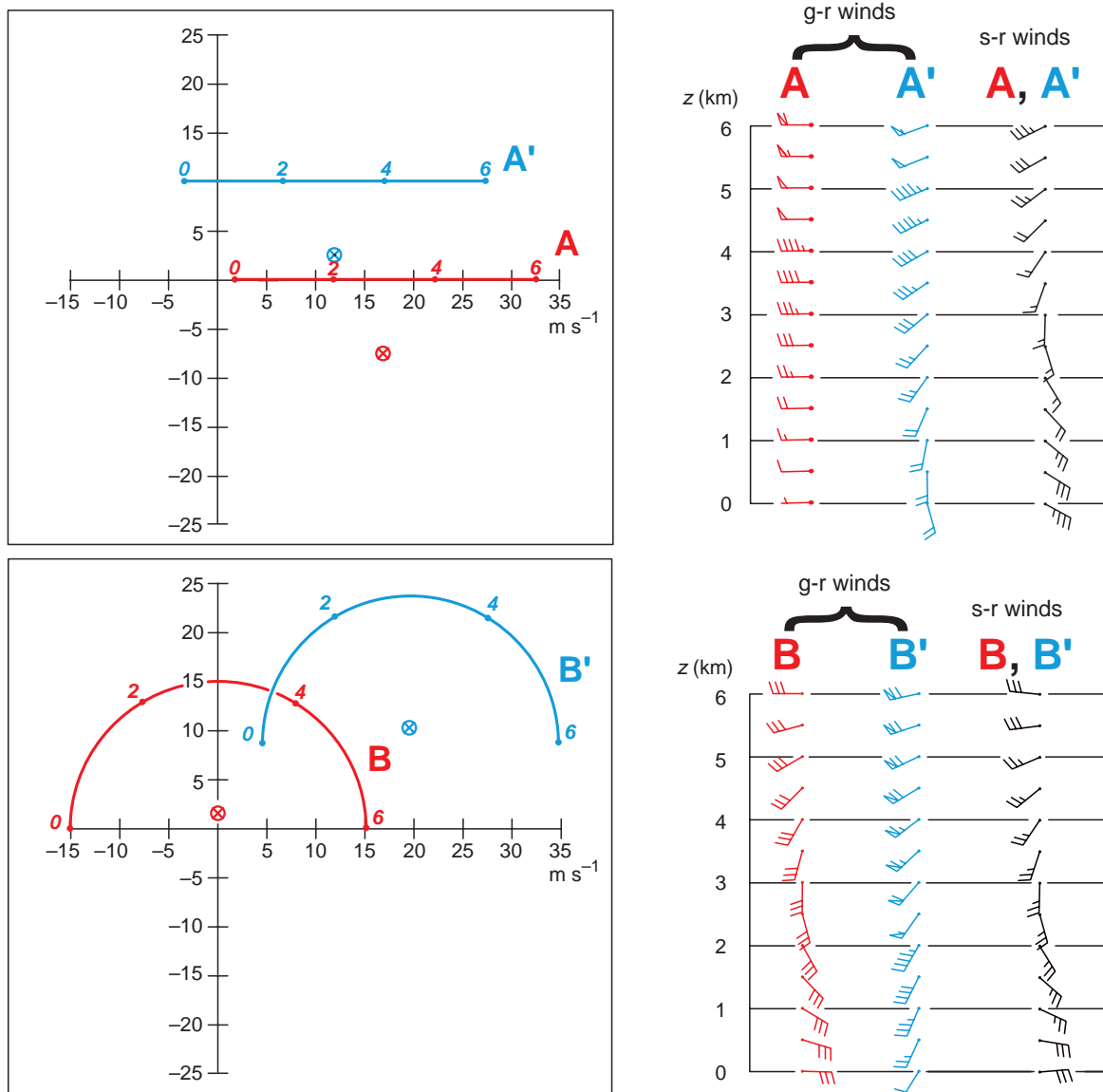


Figure 2.13 Idealized straight (top left) and curved (bottom left) hodographs and their corresponding ground-relative (g-r) and storm-relative (s-r) wind profiles (top and bottom right; half barb — $2.5 m s^{-1}$, full barb — $5 m s^{-1}$, flag — $25 m s^{-1}$). Labels along the hodographs indicate heights above ground level in kilometers. The \otimes symbols indicate the assumed storm motions (a mature convective storm would likely have a motion to the right of the mean wind in these environments, as we shall later find in Chapter 8). Hodographs A and A' are identical, but hodograph A' has been shifted by adding $-5 m s^{-1}$ ($10 m s^{-1}$) to the zonal (meridional) wind components of the points comprising hodograph A. Hodographs B and B' are identical, but hodograph B' has been shifted by adding $20 m s^{-1}$ ($8 m s^{-1}$) to the zonal (meridional) wind components of the points comprising hodograph B. The storm-relative wind profiles are identical for the A and A' hodographs and the B and B' hodographs. (Adapted from Markowski and Richardson [2006].)

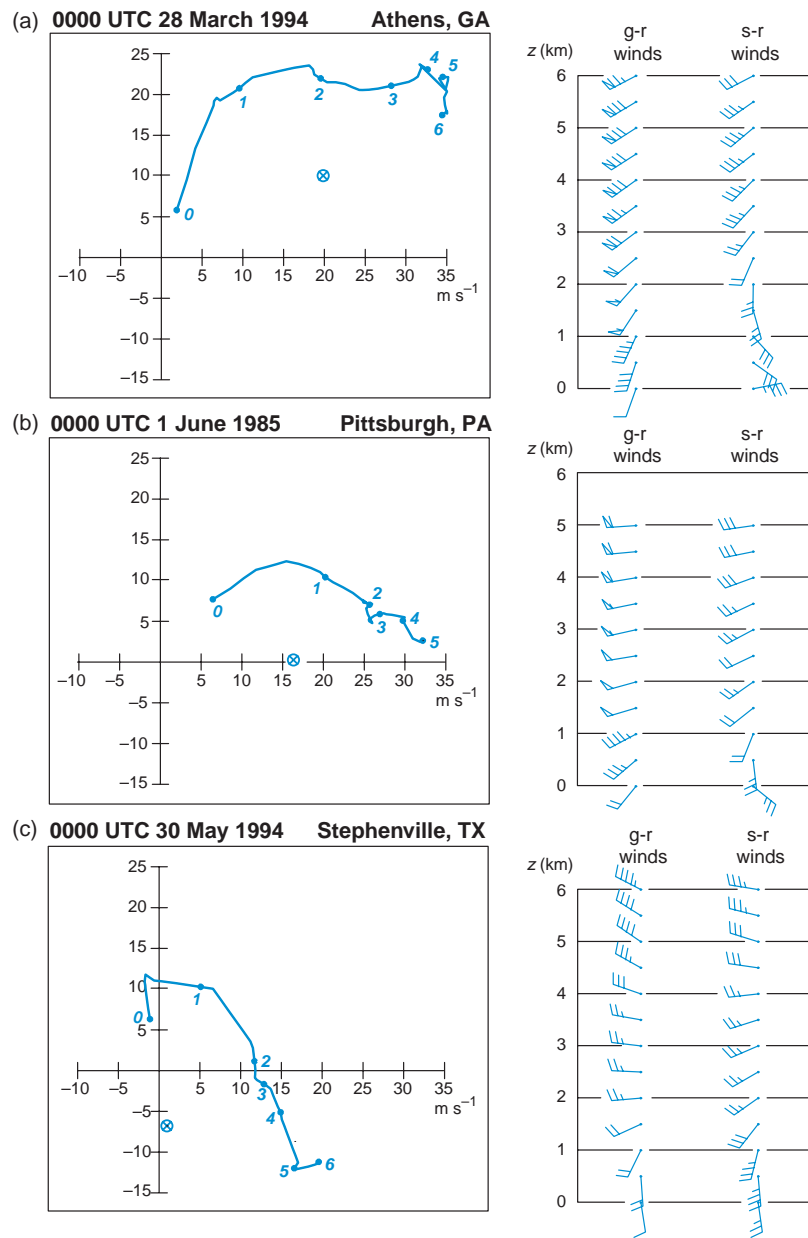


Figure 2.14 (a)–(d) Hodographs observed in relative proximity to outbreaks of severe convection and tornadoes having a wide variety of mean wind velocities and deep-layer shear (thermal wind) orientations. Labels along the hodographs indicate heights above ground level in kilometers. The \otimes symbols indicate the approximate average storm motions observed on each day. Profiles of ground-relative (g-r) and storm-relative (s-r) winds (half barb— 2.5 m s^{-1} , full barb— 5 m s^{-1} , flag— 25 m s^{-1}) are displayed to the right of each hodograph. (Although wind data in only the lowest 6 km are plotted [the winds are missing above 5 km in (b)], it is not implied that the winds above 6 km are unimportant.) (Adapted from Markowski and Richardson [2006].)

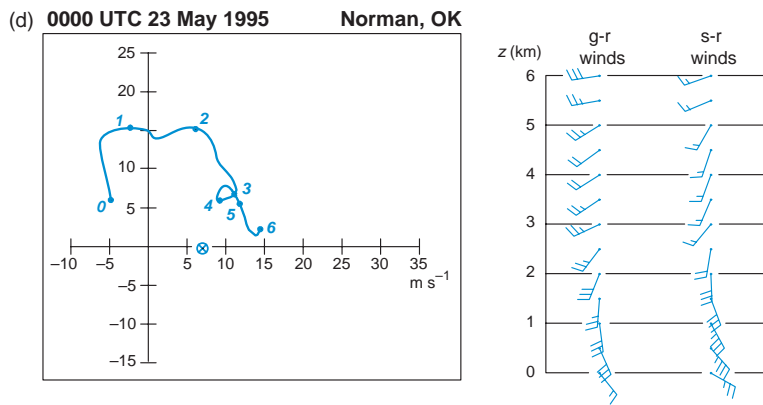


Figure 2.14 *Continued*

friction and terrain are not of primary importance, as in the study of deep moist convection (Chapter 8).

2.7.4 Streamwise and crosswise vorticity

A useful way to partition the horizontal vorticity ω_h is into *streamwise* (parallel to the storm-relative velocity) and *crosswise* (normal to storm-relative velocity) components, ω_s and ω_c , respectively (Figure 2.12): Streamwise vorticity is equal to the storm-relative wind speed times the rate at which the storm-relative winds veer with height (storm-relative *directional shear*). Crosswise vorticity is simply the rate of increase of the storm-relative wind speed with height (storm-relative *speed shear*).

When storm-relative winds are unidirectional with height (the hodograph must be straight), then the horizontal vorticity is entirely crosswise. When storm-relative winds veer with height (the hodograph may be straight or curved), then the horizontal vorticity has a streamwise component.¹⁷ Streamwise vorticity is important because, when ingested by an updraft, the updraft acquires net cyclonic rotation.¹⁸ The sense of rotation for parcels containing mainly crosswise vorticity is like that of an American football rotating end-over-end, whereas for parcels containing mainly streamwise vorticity, the sense of rotation is like that of a football thrown as a spiral. Flows containing streamwise vorticity are said to be helical (Figure 2.15), or contain (storm-relative) helicity, which is

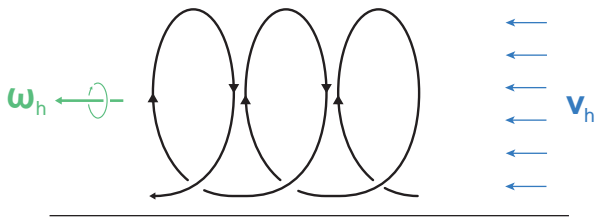


Figure 2.15 Schematic showing how the superposition of horizontal vorticity parallel to the horizontal flow produces a helical flow and is associated with streamwise vorticity. (Adapted from Doswell [1991].)

given by the product of the streamwise vorticity and the storm-relative wind speed.

The importance of streamwise and crosswise vorticity will be more apparent in the discussion of the dynamics of supercell thunderstorms that appears in Chapter 8. We hope that the presentation in Chapter 8 will be more easily grasped by having introduced these concepts here.

Further reading

- Bohren and Albrecht (1998).
- Doswell (1991a).
- Emanuel, K. A., 1994: *Atmospheric Convection*. Oxford University Press.
- Houze, R. A., Jr., 1993: *Cloud Dynamics*. Academic Press, 573 pp.
- List, R. and E. P. Lozowski, 1970: Pressure perturbations and buoyancy in convective clouds. *J. Atmos. Sci.*, **27**, 168–170.
- Ogura and Phillips (1962).

¹⁷ When storm-relative winds back with height (the hodograph may be straight or curved), then the horizontal vorticity is said to have an *antistreamwise* component.

¹⁸ When antistreamwise vorticity is ingested by an updraft, the updraft acquires net anticyclonic rotation.

3

Mesoscale Instabilities

As discussed in Chapter 1, one of the characteristics of the mesoscale is that mesoscale motions can be driven by a number of instabilities, possibly even acting at the same time, rather than by a single dominant instability (e.g., in contrast, midlatitude synoptic-scale motions are dominated by the release of baroclinic instability). This chapter treats a variety of instabilities that can drive or constrain the mesoscale phenomena studied in the remainder of the book. The instabilities are ultimately a result of the characteristics of the governing equations reviewed in Chapter 2. Although our focus is mesoscale meteorology, the development and/or release of mesoscale instabilities frequently is governed by synoptic-scale processes, such as temperature advection, moisture advection, and the formation or intensification of fronts that accompanies extratropical cyclogenesis.

3.1 Static instability

Static or *gravitational instability* is usually the first instability to which a meteorology student, or even a nonmajor taking an introductory meteorology class, is exposed. Static instability is determined by the buoyancy force experienced by an air parcel that is displaced vertically. In a statically unstable (stable) environment, a vertically displaced air parcel is accelerated away from (returned to) its equilibrium position by the buoyancy force.

Buoyancy is what drives the thermally direct circulations sometimes referred to as *free convection*, in contrast to *forced convection*, which is driven by large dynamic vertical perturbation pressure gradients. Buoyancy-driven convection is also sometimes referred to as *gravitational convection* or *upright convection*, in contrast to *slantwise convection*, in

which the release of symmetric instability (to be discussed in Section 3.4) leads to accelerations along a slanted path.

Convection, as used in most fields, refers to the bulk movement of fluid parcels and is one of the principal means by which heat is transferred (radiation and conduction are the other two ways). In meteorology, we typically restrict the use of the term to vertical motions that ensue owing to an imbalance of forces in the vertical. Convection can occur in the absence of condensation or it may lead to condensation, and in certain circumstances (as we shall find in Part III), condensation produced by convective overturning can feed back to convective overturning.

The approach undertaken to assess static instability is to begin with the vertical momentum equation written as

$$\frac{dw}{dt} = B, \quad (3.1)$$

where w is the vertical velocity component and B is the buoyancy force. Pressure perturbations, viscosity, and the Coriolis force have been neglected. By neglecting pressure perturbations, we are effectively assuming that we shall displace a parcel having no dimensions, such that the parcel does not disturb the surrounding air when it is displaced. These assumptions, made in (3.1), are sometimes referred to as *parcel theory*.

Let us approximate the buoyancy force as $B = g(T - \bar{T})/\bar{T}$, which neglects the effects of pressure perturbations [consistent with their neglect in (3.1)], water vapor, and condensate on the density of an air parcel. It is customary to regard \bar{T} as the environmental temperature and T as the temperature of an individual air parcel. We shall displace a parcel vertically from an initial level, z_0 , where the parcel is in equilibrium with its environment, that is,

$\bar{T}(z_0) = T_0$, where T_0 is the temperature of both the parcel and the environment at the equilibrium position. Because $w = dz/dt$, we can rewrite (3.1) as

$$\frac{d^2\Delta z}{dt^2} = g \frac{T - \bar{T}}{\bar{T}}, \quad (3.2)$$

where Δz is the distance of the vertical displacement ($z = z_0 + \Delta z$ at some future time; thus, dw/dt can be written as $d^2\Delta z/dt^2$).

The temperature of the displaced parcel at its new position is (using a first-order Taylor series approximation)

$$T = T_0 - \Gamma_p \Delta z, \quad (3.3)$$

where $\Gamma_p = -\partial T/\partial z$ is the parcel lapse rate. If the parcel is unsaturated during its displacement, $\Gamma_p = \Gamma_d$, the dry adiabatic lapse rate. If the parcel is saturated during its displacement, $\Gamma_p = \Gamma_m$, the moist adiabatic lapse rate.

The temperature of the environment at the new position of the displaced parcel is (using a first-order Taylor series approximation)

$$\bar{T} = T_0 - \gamma \Delta z, \quad (3.4)$$

where $\gamma = -\partial \bar{T}/\partial z$ is the environmental lapse rate. Therefore, we can write (3.2) as

$$\frac{d^2\Delta z}{dt^2} = -g \frac{\Gamma_p - \gamma}{T_0 - \gamma \Delta z} \Delta z. \quad (3.5)$$

But $T_0 \gg \gamma \Delta z$ if the vertical displacement is relatively small; therefore, with reasonable accuracy, we can write (3.5) as

$$\frac{d^2\Delta z}{dt^2} + \frac{g}{T_0} (\Gamma_p - \gamma) \Delta z = 0. \quad (3.6)$$

Equation (3.6) is a second-order ordinary differential equation having the general solution

$$\Delta z(t) = C_1 e^{i \left[\frac{g}{T_0} (\Gamma_p - \gamma) \right]^{1/2} t} + C_2 e^{-i \left[\frac{g}{T_0} (\Gamma_p - \gamma) \right]^{1/2} t}, \quad (3.7)$$

where C_1 and C_2 are constants that depend on the magnitude and direction of the initial parcel displacement.

For $\gamma < \Gamma_p$, $i \left[\frac{g}{T_0} (\Gamma_p - \gamma) \right]^{1/2}$ is imaginary and the real part of (3.7) can be written as

$$\Delta z(t) = C \cos \left\{ \left[\frac{g}{T_0} (\Gamma_p - \gamma) \right]^{1/2} t \right\}; \quad (3.8)$$

that is, the parcel oscillates about its initial position (z_0), which implies that the environmental lapse rate is *statically stable*. The amplitude of the oscillations is

$C = C_1 + C_2 = (\Delta z)_0$, although in reality this would decrease in time due to viscous effects. In an unsaturated environment, the frequency of the oscillations can be written as $\left[\frac{g}{T_0} (\Gamma_d - \gamma) \right]^{1/2} = \left(\frac{g}{\theta_0} \frac{\partial \bar{\theta}}{\partial z} \right)^{1/2} = N$, where θ_0 is the potential temperature of the environment at z_0 and N is the Brunt-Väisälä frequency at z_0 . More generally, $N = \left(\frac{g}{\theta_v} \frac{\partial \bar{\theta}_v}{\partial z} \right)^{1/2}$, where the frequency of the buoyancy oscillation also depends on the contribution of water vapor to the buoyancy. In many applications throughout this book, we shall use $N \approx \left(\frac{g}{\theta} \frac{\partial \bar{\theta}}{\partial z} \right)^{1/2}$, just as we shall frequently approximate the buoyancy as being proportional to temperature or potential temperature perturbations.¹

In a saturated environment (e.g., displacements occurring within a cloud), the displaced parcel oscillates according to the *moist* Brunt-Väisälä frequency, N_m . Neglecting the effects of water vapor or condensate on buoyancy (i.e., assuming that buoyancy is only affected by latent heating and cooling), $N_m = \left(\frac{g}{\theta_e} \frac{\Gamma_m}{\Gamma_d} \frac{\partial \bar{\theta}_e}{\partial z} \right)^{1/2}$. If the full buoyancy is used (i.e., if we include the effect of water vapor and condensate on the density of an air parcel, in addition to the temperature perturbations associated with latent heating and cooling), then a much more complicated expression results,² where

$$N_m^2 = \frac{1}{1 + r_t} \left\{ \Gamma_m \frac{\partial}{\partial z} \left[(c_p + c_l r_t) \ln \bar{\theta}_e \right] - (c_l \Gamma_m \ln \bar{T} + g) \frac{\partial r_t}{\partial z} \right\}. \quad (3.9)$$

Here c_p and c_l are the specific heats at constant pressure of dry air and liquid water, and $r_t (= r_{vs} + r_h)$ is the total water mixing ratio (the sum of the saturation water vapor mixing ratio, r_{vs} , and the hydrometeor mixing ratio, r_h).

A parcel displaced vertically in a statically stable environment triggers gravity waves that propagate away from the location of the displacement; N (N_m) is the intrinsic frequency of the gravity waves in the case of purely horizontal wave propagation (which results in purely vertical parcel displacements as waves pass by a location) in an unsaturated (saturated) atmosphere. Here our goal is only to evaluate the net acceleration experienced by a

¹ The neglect of water vapor in buoyancy calculations has its largest impact when buoyancy is integrated, in which case the water vapor contribution to buoyancy accumulates. For example, the calculations of convective inhibition (CIN) and convective available potential energy (CAPE) in Section 2.6 were shown to be very sensitive to whether or not buoyancy was expressed in terms of a temperature or virtual temperature perturbation.

² See Lalas and Einaudi (1974), Durran and Klemp (1982), Emanuel (1994, p. 168), and Kirshbaum and Durran (2004).

displaced parcel as a function of the environmental lapse rate; gravity waves are discussed in much greater detail in Chapter 6.

For $\gamma > \Gamma_p$, $i\left[\frac{g}{T_0}(\Gamma_p - \gamma)\right]^{1/2}$ is real, and as t becomes large, (3.7) becomes

$$\Delta z(t) = C_1 e^{\left[\frac{g}{T_0}(\gamma - \Gamma_p)\right]^{1/2} t}. \quad (3.10)$$

The displacement of the parcel increases exponentially with time, implying instability, although (3.10) fails to tell us how far a parcel will rise. The assumed linear profile of environmental temperature does not extend to infinity; (3.10) is only valid for relatively small Δz .

An environmental lapse rate for which $\gamma > \Gamma_d$ is said to be *absolutely unstable*, and when $\gamma < \Gamma_m$ the environmental lapse rate is said to be *absolutely stable*. When $\Gamma_m < \gamma < \Gamma_d$, the environmental lapse rate is *conditionally unstable* (stable with respect to unsaturated vertical displacements, unstable with respect to saturated vertical displacements). When $\gamma = \Gamma_d$ ($\gamma = \Gamma_m$) the environmental lapse rate is said to be *neutral* with respect to dry (saturated) vertical displacements. Lastly, when $\gamma_m > \Gamma_m$, where $\gamma = \gamma_m$ when the atmosphere is saturated, the environmental lapse rate is regarded as *moist absolutely unstable*. In terms of the environmental potential temperature and equivalent potential temperature, absolute instability is present when $\partial\bar{\theta}/\partial z < 0$, conditional instability is present when $\partial\bar{\theta}_e^*/\partial z < 0$, and absolute stability is present when $\partial\bar{\theta}_e^*/\partial z > 0$, where $\bar{\theta}_e^*$ is the equivalent potential temperature that the environment would have if it were saturated at its current temperature and pressure. Dry (moist) neutral conditions are present when $\partial\bar{\theta}/\partial z = 0$ ($\partial\bar{\theta}_e^*/\partial z = 0$). Moist absolute instability is present when $\partial\bar{\theta}_e/\partial z < 0$ in a saturated atmosphere.

There is often confusion between the aforementioned *lapse rate* definition of stability, which involves *infinitesimal* displacements and depends on the local lapse rate compared with the dry and moist adiabatic lapse rates, and what sometimes is referred to as the *available-energy* definition of stability, which depends on whether a parcel, if given a sufficiently large *finite* displacement, acquires positive buoyant energy (i.e., an acceleration due to buoyancy acting in the direction of the displacement).³ Finite-amplitude displacements are often of greater interest in the release of mesoscale instabilities. For example, a sounding with convective inhibition (CIN) requires a finite upward displacement of a surface parcel to its level of free convection (LFC), after which convective available potential energy

(CAPE) is released and the parcel freely accelerates away from its initial location. The parcel keeps accelerating upward as long as $B > 0$, regardless of the environmental lapse rate at any particular level where $B > 0$. Another example is the release of symmetric instability, wherein frontogenesis drives circulations believed to provide finite-amplitude slantwise displacements that enable air parcels to reach a point where they are accelerated in the same direction as their initial displacements.

3.1.1 Vertical velocity of an updraft

If we multiply both sides of (3.1) by $w \equiv dz/dt$, we obtain

$$w \frac{dw}{dt} = B \frac{dz}{dt} \quad (3.11)$$

$$\frac{d}{dt} \left(\frac{w^2}{2} \right) = B \frac{dz}{dt} \quad (3.12)$$

Next, we integrate (3.12) over the time required to travel from the LFC to the equilibrium level (EL). We assume $w = 0$ at the LFC, since the only force considered here is the buoyancy force, which, by definition, does not become positive until the LFC is reached. Also, we assume that the maximum vertical velocity, w_{\max} , occurs at the EL, which is consistent with the assumption that $dw/dt = B$ (neglecting the weight of hydrometeors in B). Integration of (3.12) yields

$$\int_{LFC}^{EL} dw^2 = 2 \int_{LFC}^{EL} B dz \quad (3.13)$$

$$w_{EL}^2 - w_{LFC}^2 = 2 \int_{LFC}^{EL} B dz \quad (3.14)$$

$$w_{\max}^2 = 2 \int_{LFC}^{EL} B dz \quad (3.15)$$

$$w_{\max} = \sqrt{2 \text{ CAPE}}. \quad (3.16)$$

For $\text{CAPE} = 2000 \text{ J kg}^{-1}$, which corresponds to an average temperature (or virtual temperature) excess of $\approx 5 \text{ K}$ over a depth of 12 km, parcel theory predicts $w_{\max} = 63 \text{ m s}^{-1}$. The prediction of w_{\max} in a convective updraft by (3.16) typically is too large, for several reasons discussed in the next section. Therefore, the value of w_{\max} predicted by (3.16) can be interpreted as an upper limit for vertical velocity when buoyancy is the only force; w_{\max} sometimes is called the *thermodynamic speed limit*.⁴

³ Sherwood (2000) and Schultz *et al.* (2000) discuss at length the potential confusion surrounding these definitions.

⁴ We leave it as an exercise for the reader to show that (3.16) can also be obtained by applying the Bernoulli equation given by (2.146) along a trajectory from the LFC to EL, neglecting pressure perturbations.

3.1.2 Limitations of parcel theory

Recall that we have neglected perturbation pressures in the preceding analysis of instability and maximum updraft velocity via (3.7) and (3.16), respectively (actually, we have neglected pressure perturbations *twice*—once in the vertical momentum equation, and once in the approximation for buoyancy). In general, the vertical perturbation pressure gradient is not negligible, and it tends to partially offset the acceleration induced by the buoyancy force.⁵ As shown in Section 2.5.3, relatively high (low) pressure tends to be located above a warm (cold) bubble, and relatively low (high) pressure tends to be located beneath a warm (cold) bubble, causing a vertical gradient of the buoyancy pressure perturbation, p'_b (recall Figure 2.7). An *upward-directed* buoyancy force associated with a warm bubble tends to be associated with a *downward-directed* perturbation pressure gradient force, and a *downward-directed* buoyancy force associated with a cold bubble tends to be associated with an *upward-directed* perturbation pressure gradient force as dictated by (2.134).

A physical explanation for such perturbation pressures and their gradients is that a positive perturbation pressure (relatively high pressure) must exist above a rising bubble in order to push air laterally out of the way of the rising bubble, and a negative perturbation pressure (relatively low pressure) must exist beneath a rising bubble in order to draw air into the wake of the rising bubble and preserve mass continuity. Conversely, a cold bubble tends to have relatively high (low) pressure beneath (above) it for the same reasons. Furthermore, the presence of a temperature anomaly alone, regardless of whether or not it is rising or sinking, leads to pressure perturbations, owing to the fact that temperature anomalies are associated with thickness changes; that is, pressure surfaces are perturbed by temperature anomalies (thereby giving rise to pressure anomalies) in a hydrostatic atmosphere. In short, when considering the effect of the perturbation pressure gradient, isolated warm (cold) bubbles tend not to rise (sink) as fast as one would expect based on the consideration of the buoyancy force alone.

If the cold or warm anomaly is relatively narrow, then the buoyancy force is larger in magnitude than the perturbation pressure gradient forces, and warm (cold) air does in fact rise (sink). However, as a warm (cold) bubble increases in width, more air must be pushed out of its way in order for it to rise (sink), and more air must be drawn

⁵ An exception is for updrafts occurring in environments containing large vertical wind shear, in which the perturbation pressure gradient force may act in the same direction as buoyancy, especially at low levels, thereby augmenting the vertical acceleration. This effect will be discussed in greater detail in Chapter 8.

in below (above) to compensate for the wider region of ascent (descent). Thus, the opposing perturbation pressure gradient increases in magnitude with respect to the buoyancy force as a warm or cold bubble increases in width (Figure 3.1). When a warm or cold bubble becomes very wide, the opposing vertical perturbation pressure gradient becomes so large that it entirely offsets the buoyancy force, and the net acceleration is zero. This is the hydrostatic limit; in other words, the width scale of the temperature anomaly is very large compared with the depth scale, and the vertical pressure gradient and gravity are in balance. This is equivalent to setting $\nabla_h^2 p'_b = 0$ in (2.137), indicating a parcel of infinite horizontal extent, in which a case (2.137) reduces to

$$\alpha_0 \frac{\partial^2 p'_b}{\partial z^2} = -\frac{\partial}{\partial z} \left(\frac{\rho' g}{\rho_0} \right), \quad (3.17)$$

which can be simplified and integrated to yield

$$\frac{\partial p'_b}{\partial z} = -\rho' g, \quad (3.18)$$

in which case $p'_b = p'_h$, where p'_h is the hydrostatic pressure perturbation (recall Section 2.5.2). In this case, one could simply redefine the base state so that there are no density and pressure perturbations.

Parcel theory also neglects the exchange of momentum, moisture, and temperature between the parcel and its environment. Mixing of environmental air into a rising air parcel typically slows the parcel by reducing its buoyancy and upward momentum. This process is called *entrainment*. Entrainment can be viewed as a parcel dilution process, because the θ_e of a rising parcel typically is reduced by entrainment, leading to the realization of less CAPE and smaller w_{max} than predicted by (3.16) (Figure 3.2).

Updraft dilution increases with the tilt of an updraft, which increases the surface area of the updraft exposed to the hostile (subsaturated) environment. The entrainment into the sides of an updraft also increases as the vertical acceleration within the updraft increases, owing to mass continuity. It is possible to estimate the entrainment rate from *in situ* thermodynamic measurements within a cloud. As updraft width increases, the core of the updraft can become better shielded from the effects of entrainment. For this reason, skinny updrafts are more susceptible to the detrimental effects of entrainment than are wide updrafts. In simple one-dimensional cloud models, the entrainment rate is often parameterized in terms of updraft width. Updrafts are often wider in the presence of strong mesoscale ascent (e.g., ascent along an air mass boundary), which might be one reason why regions of mesoscale ascent are the most favorable locations for the initiation and maintenance of deep moist convection.

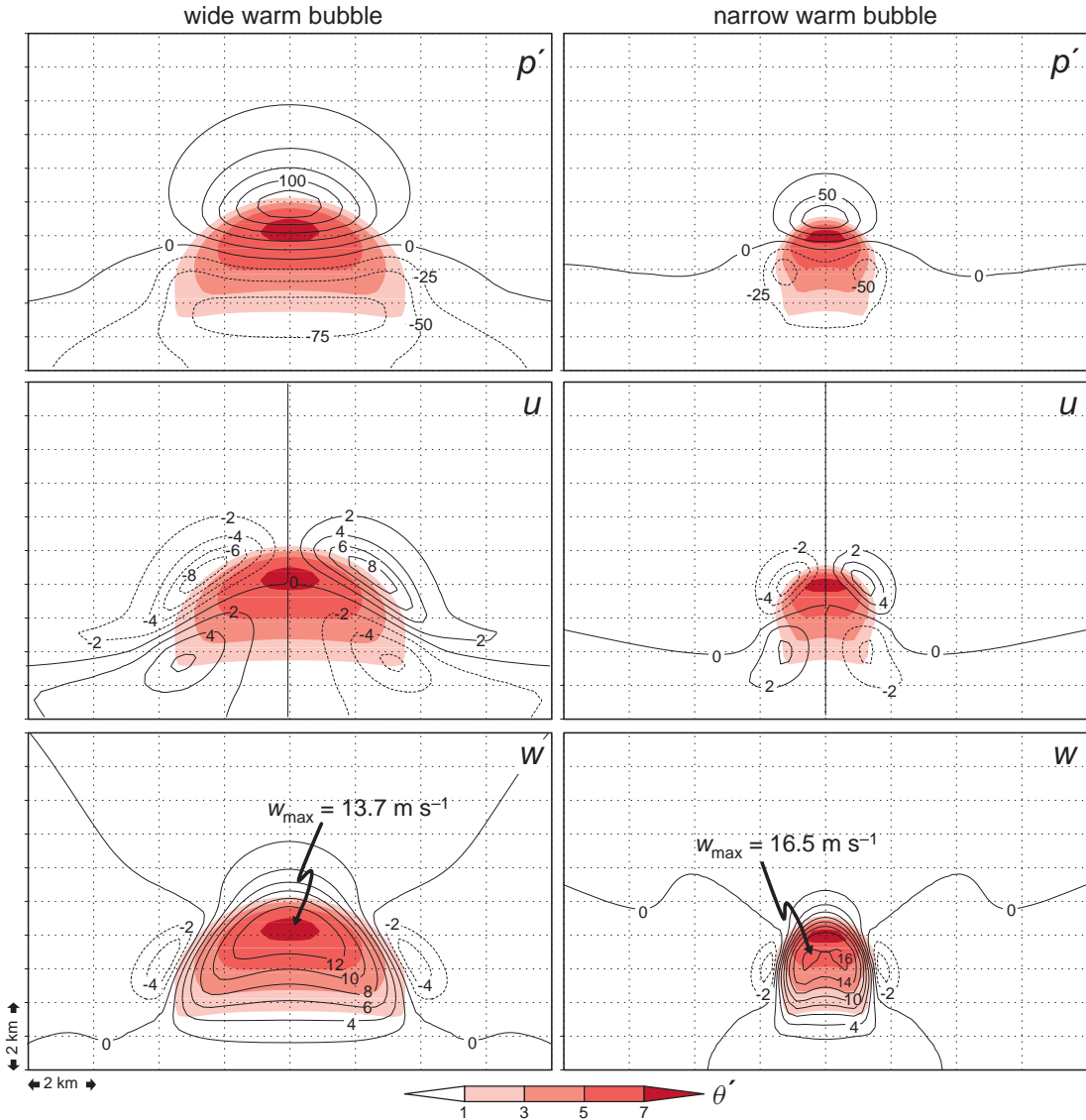


Figure 3.1 A comparison of the perturbation pressure (p') fields and zonal (u) and vertical (w) velocity components for the case of a wide warm bubble (left panels) and a narrow warm bubble (right panels) released in a conditionally unstable atmosphere in a three-dimensional numerical simulation. The contour intervals for p' and the wind components are 25 Pa and 2 m s^{-1} , respectively (dashed contours are used for negative values). Potential temperature perturbations (θ') are shown in each panel (refer to the color scale). The horizontal and vertical grid spacing is 200 m (the domain shown above is much smaller than the actual model domain). Both warm bubbles had an initial potential temperature perturbation of 2 K and a vertical radius of 1.5 km, and were released 1.5 km above the ground. The wide (narrow) bubble had a horizontal radius of 10 km (3 km). In the simulation of the wide (narrow) bubble, the fields are shown 800 s (480 s) after its release. The fields are shown at times when the maximum buoyancies are comparable. Despite the comparable buoyancies, the narrow updraft is 20% stronger owing to the weaker adverse vertical pressure gradient.

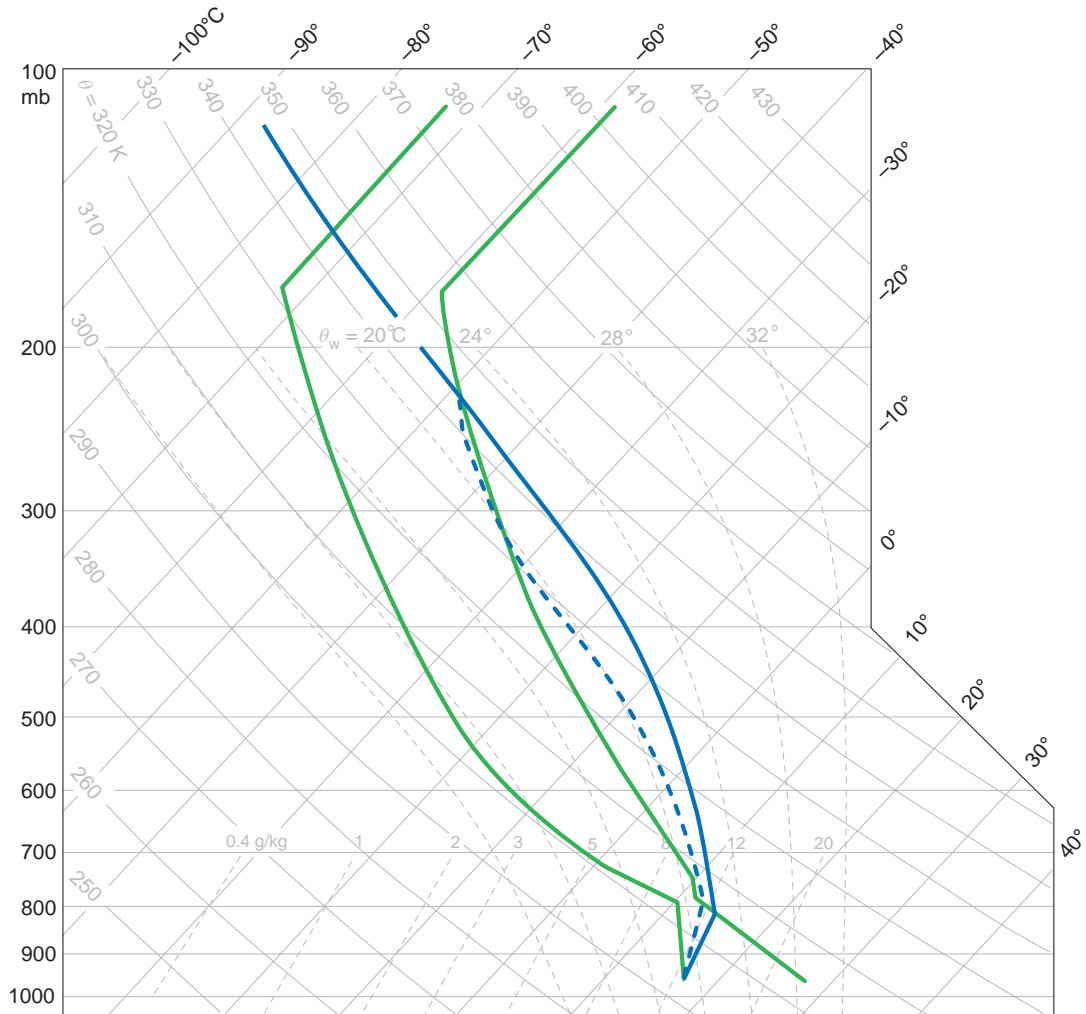


Figure 3.2 A possible parcel process curve (dashed) that might be followed by an updraft parcel on a skew T -log p diagram as a result of the entrainment of environmental air. A parcel process curve (solid) followed by an updraft parcel that ascends undiluted is also shown. Note the implied differences in cloud base (there has been some entrainment below the cloud base, in addition to entrainment over the cloud depth), cloud top, and the realized CAPE.

Because of the aforementioned effects of the vertical perturbation pressure gradient and entrainment, the development and intensity of convection are sensitive to updraft width. This sensitivity is not reflected in the stability analysis or estimate of maximum updraft speed provided by (3.7) and (3.16), respectively. The magnitude of pressure perturbations and the vertical perturbation pressure gradient increases as the width of the displaced parcel increases, whereas the detrimental effects of entrainment decrease as updraft width increases. Convection therefore favors up- and downdrafts having an intermediate width scale that is

large enough to survive the dilution of buoyancy by mixing yet narrow enough that the perturbation pressure gradient force is not too suppressive. In the absence of entrainment, infinitesimally narrow drafts are favored.

In addition to the effects of the vertical perturbation pressure gradient and entrainment, the parcel theory prediction of the vertical acceleration of an air parcel and maximum updraft speed also neglects contributions to buoyancy from the presence of hydrometeors. In deriving (3.7), it was assumed that only temperature perturbations contributed to buoyancy. In deriving (3.17), although it

was not indicated whether or not buoyancy included the effects of hydrometeor loading, buoyancy is virtually always expressed as the temperature or virtual temperature excess of an updraft parcel compared with its environment in the calculation of CAPE [recall (2.148) in Section 2.6], rather than by attempting to account for the condensate acquired within a rising updraft parcel via an expression for buoyancy like that given by (2.79) (large concentrations of hydrometeors can easily contribute the equivalent of a few degrees Celsius of negative buoyancy). In other words, CAPE usually is computed by assuming pseudoadiabatic ascent, such that hydrometeors are assumed to instantly fall out of a rising, saturated parcel such that the condensate mass does not affect the buoyancy. In contrast, in reversible moist adiabatic ascent, all condensate remains within the parcel (recall Figure 2.1). The condensate mass reduces buoyancy, but the condensate also carries heat (these two competing influences usually lead to a net reduction of buoyancy in the lower troposphere and a net increase in buoyancy by the time a lifted parcel reaches the upper troposphere).

Pseudoadiabatic and reversible moist adiabatic ascent are both idealized extremes; the influence of hydrometeors on the buoyancy realized by a real updraft lies somewhere in between. The buoyancy and the associated CAPE realized in pseudoadiabatic ascent are easier to compute than the buoyancy and CAPE assuming reversible moist adiabatic ascent, and are far easier to compute than the actual buoyancy and realized CAPE for a rising parcel. For this reason, CAPE calculations are usually based on the integrated temperature or virtual temperature excess based on pseudoadiabatic ascent (as in Section 2.6).

The freezing of water droplets within updrafts is an additional source of positive buoyancy above the melting level, although it is a much smaller source of buoyancy than condensational heating because the latent heat of fusion is only a small fraction of the latent heat of vaporization. The pseudoadiabatic lapse rate used to calculate CAPE does not consider freezing; thus, the neglect of freezing represents another limitation of parcel theory predictions of vertical velocity, albeit a relatively minor one.

Finally, compensating subsidence within the surrounding air, which can affect the buoyancy and/or the perturbation pressure field depending on how the base state is defined, was ignored in parcel theory, wherein the environment is assumed to be unchanged by the parcel.

3.1.3 Potential instability

A layer in which equivalent potential temperature (or, alternatively, wet-bulb potential temperature) decreases

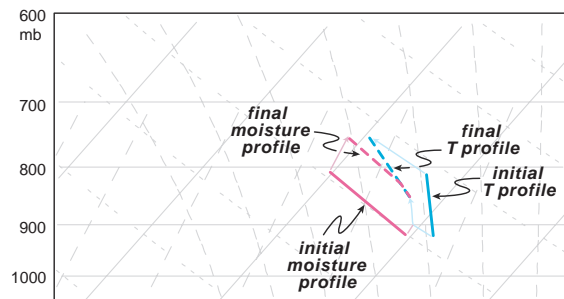


Figure 3.3 Illustration of the concept of potential instability. A potentially unstable layer initially spanning the pressure range of 910–810 mb has been lifted to 850–750 mb. Although destabilization of the layer has occurred, lifting would have cooled the layer (and therefore reduced CIN) regardless of whether or not lifting led to saturation at the bottom of the layer.

with height (i.e., $\partial\theta_e/\partial z < 0$, or, alternatively, $\partial\theta_w/\partial z < 0$) is said to be *potentially unstable* (such layers sometimes are said to be *convectively unstable*). When such a layer is lifted, the bottom of the layer, given sufficiently large relative humidity, becomes saturated before the top of the layer. Thus, the bottom of the layer, upon further lifting, cools at the moist adiabatic lapse rate, while the top of the layer cools at the larger dry adiabatic lapse rate. Since the top of the ascending layer is cooling at a faster rate than the bottom of the layer, destabilization occurs (Figure 3.3). If the layer is lifted sufficiently, the lapse rate can become moist absolutely unstable, regardless of the initial stratification.

The destabilization of layers via the potential instability mechanism is probably important in the formation of mesoscale rainbands within the broader precipitation shields of extratropical cyclones on some occasions, especially when potentially unstable layers are lifted over a front. Potential instability also is often cited as being important in the development of deep moist convection. In the Great Plains of the United States, widely recognized as one of the world's hot spots for severe convection, θ_e usually decreases rapidly with height in convective environments owing to dry midtropospheric air. Despite the common presence of potential instability, however, it usually does not play a role in the destabilization of the atmosphere that precedes the initiation of convection. If the potential instability destabilization mechanism were operating, we might expect to see skies gradually become overcast with stratiform clouds as the potentially unstable layer is bodily lifted, and, only some significant time after this, cumulonimbus might erupt from the stratiform clouds. This evolution is at odds with

what is usually observed, however, where cumulonimbus clouds develop, often explosively, from shallow cumulus and partly cloudy conditions, without any sign of prior widespread lifting of a layer to saturation.

3.2 Centrifugal instability

In this section and in the two that follow (Sections 3.3 and 3.4), we define equilibrium states in which the horizontal forces acting on air parcels are balanced, and then we perturb the parcels to evaluate the stability of the equilibrium states. If an axisymmetric rotating fluid is in *cyclostrophic balance*, such that the centrifugal force and radial pressure gradient force balance each other, then certain distributions of angular momentum may be *centrifugally unstable* such that radially perturbed parcels are accelerated away from their equilibrium position. Although centrifugal instability is not as relevant to most mesoscale phenomena as the other instabilities discussed in this chapter (centrifugal instability is most relevant to vortices such as tornadoes and hurricanes, which can be approximated as being axisymmetric and, if surface friction is neglected, in cyclostrophic balance), we present it as a lead-in to our treatments of *inertial instability* (Section 3.3) and *symmetric instability* (Section 3.4).⁶ The study of inertial and symmetric instabilities originated from the study of centrifugal instability. Centrifugal instability initially was studied by Lord Rayleigh⁷ roughly a century ago.

Consider a cylindrical tank of spinning fluid (Figure 3.4). The equations of horizontal motion in cylindrical coordinates are

$$\frac{du}{dt} = -\alpha_0 \frac{\partial p}{\partial r} + \frac{v^2}{r} \quad (3.19)$$

$$\frac{d(vr)}{dt} = -\alpha_0 \frac{\partial p}{\partial \theta} \quad (3.20)$$

where u is the radial velocity, v is the azimuthal velocity, r is the distance from the axis of rotation, α_0 is a constant specific volume, and θ is the azimuth angle.

By introducing the angular momentum $M = vr$, which is conserved if the pressure field is symmetric about the axis

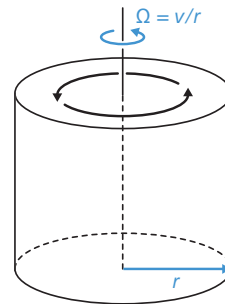


Figure 3.4 A cylindrical tank of spinning fluid, spinning at an angular velocity of $\Omega = v/r$.

of rotation (i.e., if $\partial p / \partial \theta = 0$), we can write the momentum equations as

$$\frac{du}{dt} = -\alpha_0 \frac{\partial p}{\partial r} + \frac{M^2}{r^3} \quad (3.21)$$

$$\frac{dM}{dt} = 0. \quad (3.22)$$

Let us displace a ring of fluid in the r direction and evaluate the new force balance at $r = r_0 + \Delta r$. We displace a ring of fluid rather than an individual parcel because we have assumed symmetry about the axis of rotation in deriving $dM/dt = 0$; an asymmetric disturbance would create $\partial p / \partial \theta \neq 0$. Do the horizontal pressure gradient force and centrifugal force balance each other, and, if not, what is the direction of the net acceleration at $r = r_0 + \Delta r$? (In similar fashion, in the static stability analysis in Section 3.1, a parcel was displaced from $z = z_0$ to $z = z_0 + \Delta z$ and we evaluated the new force balance at $z = z_0 + \Delta z$ to assess whether the acceleration would be upward, downward, or zero.)

Let us define a mean state such that no radial acceleration exists and the horizontal pressure gradient force and centrifugal force balance each other:

$$0 = -\alpha_0 \frac{\partial \bar{p}}{\partial r} + \frac{\bar{M}^2}{r^3}. \quad (3.23)$$

Subtracting (3.24) from (3.22) gives

$$\frac{du}{dt} = -\alpha_0 \frac{\partial p'}{\partial r} + \frac{1}{r^3} (M^2 - \bar{M}^2), \quad (3.24)$$

where $p = \bar{p} + p'$ and $M = \bar{M} + M'$. If we neglect the effects of the perturbation pressure gradient, as is done in parcel theory, we obtain

$$\frac{du}{dt} = \frac{1}{r^3} (M^2 - \bar{M}^2). \quad (3.25)$$

⁶ Centrifugal instability sometimes more generally refers to a broader class of instability that involves a rotating fluid and a restoring force exerted on fluid elements that are perturbed in a plane having a component orthogonal to the axis of rotation. Inertial and symmetric instabilities, as we shall see, fit this broader description.

⁷ John William Strutt (1842–1919), better known as Lord Rayleigh, was a physicist and the third Baron Rayleigh in the peerage of the United Kingdom. He is best known to atmospheric scientists for his work in fluids and radiative transfer. He received a Nobel Prize in 1904 for his co-discovery of argon.

The square of the mean angular momentum at the location of the displaced ring is (using a first-order Taylor series approximation)

$$\bar{M}^2 = M_0^2 + \frac{d\bar{M}^2}{dr} \Delta r, \quad (3.26)$$

where M_0 is the value of \bar{M} at $r = r_0$. Also, because M^2 is conserved, its value for parcels within the displaced ring is

$$M^2 = M_0^2; \quad (3.27)$$

that is, a ring of fluid in equilibrium at r_0 retains its M^2 when displaced to $r_0 + \Delta r$. Therefore, for small Δr , and noting that $du/dt = d(dr/dt)/dt = d^2\Delta r/dt^2$, (3.25) becomes

$$\frac{d^2\Delta r}{dt^2} = \frac{M^2 - \bar{M}^2}{(r_0 + \Delta r)^3} \quad (3.28)$$

$$\approx \frac{M_0^2 - \left(M_0^2 + \frac{d\bar{M}^2}{dr} \Delta r \right)}{r_0^3} \quad (3.29)$$

$$= -\frac{1}{r_0^3} \frac{d\bar{M}^2}{dr} \Delta r. \quad (3.30)$$

The general solution of (3.31) is

$$\Delta r(t) = C_1 e^{i \left[\frac{1}{r_0^3} \frac{d\bar{M}^2}{dr} \right]^{1/2} t} + C_2 e^{-i \left[\frac{1}{r_0^3} \frac{d\bar{M}^2}{dr} \right]^{1/2} t}, \quad (3.31)$$

where C_1 and C_2 are constants that depend on the magnitude and direction of the initial displacement of the ring, as in (3.7). If \bar{M}^2 increases with r (i.e., $d\bar{M}^2/dr > 0$), then the radial acceleration is opposite to Δr and we have a centrifugally stable distribution of angular momentum, resulting in centrifugal waves that oscillate with a frequency of $\left[\frac{1}{r_0^3} \frac{d\bar{M}^2}{dr} \right]^{1/2}$. If \bar{M}^2 decreases with r (i.e., $d\bar{M}^2/dr < 0$), then the radial acceleration is in the same direction as Δr and the distribution of angular momentum is centrifugally unstable.

Centrifugal instability constrains stable vortex characteristics; that is, stable vortices cannot have any arbitrary distribution of angular momentum. The prediction that angular momentum should increase with radius in order to satisfy the stability criterion has been upheld by observations of the wind fields of tornadoes and hurricanes. Angular momentum distributions can also be associated with instabilities in the absence of well-defined vortices such as tornadoes and hurricanes, as is the case with inertial instability and symmetric instability, which are investigated next.

3.3 Inertial instability

Inertial instability is also an instability that leads to horizontal accelerations away from an equilibrium position when parcels are perturbed horizontally.⁸ The equilibrium is that of geostrophic balance, in contrast to the cyclostrophic equilibrium state used to assess centrifugal instability; that is, the Coriolis force and horizontal pressure gradient force balance each other. The instability analysis involves a cross-wise displacement of a tube of parcels aligned with the wind, and then an evaluation of the Coriolis force and horizontal pressure gradient force on the parcels at their new location. Do the two forces still balance each other? If not, in which direction is the net acceleration? The direction of the acceleration dictates stability (a force imbalance accelerates the parcels toward their initial position), instability (a force imbalance accelerates the parcels away from their initial position), or neutrality (if there is no net acceleration acting on the parcels at their new location).

Let us consider the simple case of a zonal geostrophic wind that varies in the north-south (y) direction, that is, $u_g = u_g(y)$ and $v_g = 0$. Using a similar methodology as for the centrifugal stability analysis, we start with the horizontal equations of motion in Cartesian coordinates. In this case, they can be written as

$$\frac{du}{dt} = fv \quad (3.32)$$

$$\frac{dv}{dt} = f(u_g - u). \quad (3.33)$$

The variables u and v are the actual velocity components, which may include an ageostrophic component.

Let us horizontally displace a tube of parcels aligned with the x axis away from their initial position, y_0 , where they are in equilibrium with their environment, that is, $u = u_g = u_0$, where u_0 is the zonal velocity of both the parcels and the environment at the equilibrium position. A *tube* of parcels must be displaced in order to continue satisfying (3.32), which is only valid if no pressure gradient exists along the x axis.⁹ Displacement of a single parcel would generate such

⁸ The American Meteorological Society's *Glossary of Meteorology* defines inertial instability much more broadly as an instability in which only kinetic energy is transferred between the steady state and the disturbance. In this book we have adopted the more restrictive definition requiring negative absolute geostrophic vorticity, as is done in other well-cited dynamics references (e.g., Holton 2004).

⁹ Regarding the displacement of a tube of parcels in the analysis of inertial instability (and, later on, symmetric instability), inertial (and symmetric) instability, as defined, is a two-dimensional instability. As mentioned in Section 3.2, the study of inertial (and symmetric) instability originated with the study of centrifugal instability, in which an axisymmetric rotating flow was considered. Recall that the centrifugal

a gradient and the parcel would likely be accelerated to the velocity of its new surroundings, fundamentally changing our evaluation of the instability. (We also ignored the generation of perturbation pressures when evaluating static instability. In that case, the development of perturbation pressures for a finite buoyant element only alters the rate at which the instability is released (by altering w) rather than whether or not an instability exists at all.)

Because $v \equiv dy/dt$, we can rewrite (3.32) and (3.33) as

$$\frac{du}{dt} = f \frac{dy}{dt} \quad (3.34)$$

$$\frac{d^2\Delta y}{dt^2} = f(u_g - u), \quad (3.35)$$

where Δy is the horizontal displacement distance from the initial position (i.e., $y = y_0 + \Delta y$ at some future time; thus, dy/dt can be written as $d\Delta y/dt$).

If the tube is displaced northward or southward, the new zonal velocity for a parcel within the tube will be, via integration of (3.34),

$$u = u_0 + f\Delta y. \quad (3.36)$$

Most readers are probably familiar with the above result in that it implies that a parcel moving northward (southward) is accelerated eastward (westward) owing to the conservation of angular momentum.

The *geostrophic* wind at the location of the displaced tube will be (using a first-order Taylor series approximation)

$$u_g = u_0 + \frac{\partial u_g}{\partial y} \Delta y. \quad (3.37)$$

where we assume that the initial pressure field and, correspondingly, the geostrophic wind, is not altered by the displacement of the tube. By subtracting (3.36) from the above expression, we obtain

$$u_g - u = \left(\frac{\partial u_g}{\partial y} - f \right) \Delta y, \quad (3.38)$$

and using (3.36), we obtain

$$\frac{d^2\Delta y}{dt^2} + f \left(f - \frac{\partial u_g}{\partial y} \right) \Delta y = 0. \quad (3.39)$$

stability analysis relied on having $M = vr$ be conserved, and M conservation required the axisymmetry assumption (i.e., $\partial p/\partial\theta = 0$) and the displacement of a ring of parcels. Two-dimensional disturbances were retained in theoretical studies of inertial (and symmetric) instability, which extended the earlier studies of centrifugal instability from rotating tanks to the atmosphere (and, in the case of symmetric instability, included the effects of baroclinity).

The term $f - \partial u_g / \partial y$ is the absolute geostrophic vorticity (recall $v_g = 0$, so there is no $\partial v_g / \partial x$ term in the relative vorticity), and the general solution of (3.39) is

$$\Delta y(t) = C_1 e^{i \left[f \left(f - \frac{\partial u_g}{\partial y} \right) \right]^{1/2} t} + C_2 e^{-i \left[f \left(f - \frac{\partial u_g}{\partial y} \right) \right]^{1/2} t}, \quad (3.40)$$

where C_1 and C_2 are constants that depend on the magnitude and direction of the initial displacement, as in the static and centrifugal stability analyses.

The condition for inertial instability is that the absolute geostrophic vorticity must be negative, because when $f - \frac{\partial u_g}{\partial y}$ is negative, $i \left[f \left(f - \frac{\partial u_g}{\partial y} \right) \right]^{1/2}$ is real and Δy exponentially grows in time—a horizontally displaced tube of parcels is accelerated away from y_0 . When $f - \frac{\partial u_g}{\partial y}$ is positive, $i \left[f \left(f - \frac{\partial u_g}{\partial y} \right) \right]^{1/2}$ is imaginary and Δy is oscillatory—stability is present and perturbed parcels oscillate horizontally about y_0 with a frequency of $\left[f \left(f - \frac{\partial u_g}{\partial y} \right) \right]^{1/2}$. The Coriolis force associated with the perturbation wind acts as the restoring force (Figure 3.5). The nature of this restoring force, however, is somewhat different from the case of a parcel that is displaced vertically in a statically stable atmosphere. In the latter case, the restoring force is directed opposite the parcel displacement, whereas in the case of inertial stability, the restoring force is initially at a right angle to the direction of displacement. Though we assess inertial stability versus instability by considering whether Δy grows or decays in time, it is important to realize that a parcel (within the tube) that is horizontally perturbed as in Figure 3.5 is accelerated in *both* horizontal directions, such that the parcels oscillate in clockwise loops superimposed on the mean wind, rather than along a straight line centered on the equilibrium location as is the case for static stability. These *inertial oscillations* are identical to the oscillations that give rise to the nocturnal low-level wind maximum that will be discussed in Section 4.7.

The assumption that the pressure field remains constant during the oscillation is not likely to be valid over a significant period of time. Nonetheless, the inertial instability analysis does provide a useful idealization that explains why, at least on large scales, anticyclonic vorticity centers (i.e., vorticity minima) are limited to a magnitude no larger than f , yet large-scale cyclonic vorticity maxima have no such bound on their intensity. To see why this is so, consider the anticyclonic shear case shown in Figure 3.5a. After the northward displacement, the stronger Coriolis force toward the south is paired with a stronger pressure gradient force toward the north. If the pressure gradient varies only weakly with y , the Coriolis force will end up the dominant force and the parcel will have an acceleration toward its original latitude. However, once a threshold value for the

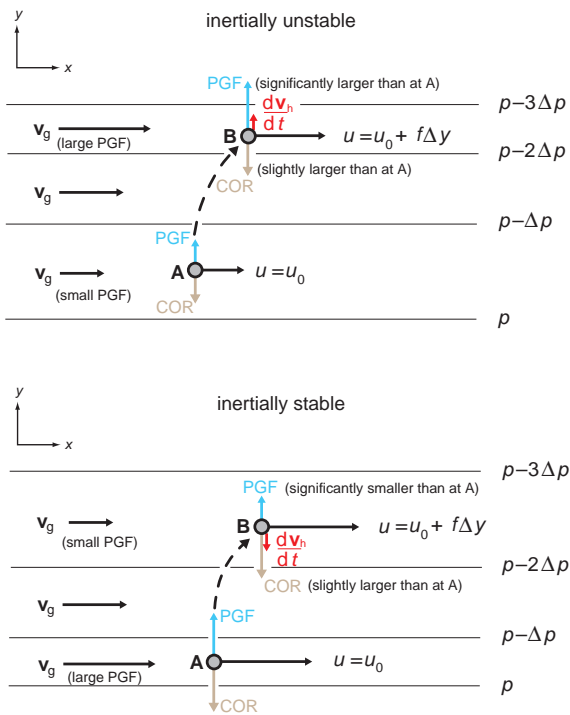


Figure 3.5 Top, the inertially unstable case, as discussed in the text. The parcel has been displaced northward, from point A to point B, as indicated by the dashed arrow. For clarity, only one parcel within the tube of displaced parcels is shown. Bottom, the inertially stable case.

variation in the pressure gradient force with y is exceeded, the pressure gradient will be the dominant force and the parcel will accelerate away from its initial location. In the cyclonic case (Figure 3.5b), however, the stronger Coriolis force is paired with a *weaker* pressure gradient force such that the Coriolis force will always be the dominant force and the parcel will always have a component of acceleration toward its original latitude.

When assessing parcel stability, a conserved variable often can be found such that the stability of a given environment can be assessed by examining the distribution of this variable in a particular direction. For example, we can look at profiles of potential temperature with height to immediately assess static stability. Essentially, by using the temperature a parcel would have if lowered to a standard reference pressure, we are then free to move a parcel from its original level to a new level and simply compare its potential temperature with that of the environment at the new level to assess their actual temperature difference. It then becomes obvious that, when potential temperature decreases with

height, parcels displaced upward will be warmer than their environment and we relate this to an upward buoyant acceleration. This approach is easier than dealing with actual temperatures, in which case the parcel temperature would have to be modified by the dry adiabatic lapse rate before it could be compared with the environmental temperature.

A direct analog exists with regard to inertial instability. When we displaced the parcel to the north (Figure 3.5), we had to adjust its zonal momentum by the rate of gain in zonal momentum due to the Coriolis force before we could compare its new Coriolis force in the y direction (which depends on its total zonal momentum) with the environmental pressure gradient force at the new location. If we note that the environmental pressure gradient force is equal in magnitude to the Coriolis force associated with the (environmental) geostrophic wind, we see that we could alternatively compare the magnitude of the parcel's total zonal momentum (u) at the new location with the zonal momentum of the geostrophic wind (u_g) at that location (assuming f is constant over our entire domain). If $u > u_g$, then the Coriolis force acting on the parcel will be greater than the pressure gradient force and the parcel will accelerate toward its initial latitude. Alternatively, if we displace the parcel to the south, if $u < u_g$, then the Coriolis force (acting toward the south if $u > 0$) is less than the pressure gradient force (acting toward the north), and the parcel also accelerates toward its initial latitude.

We note from (3.36) that the parcel u depends only on its initial (geostrophic) zonal momentum and its displacement in the y direction. Changes in the zonal momentum of a parcel displaced latitudinally are analogous to changes in the temperature of a parcel displaced dry adiabatically in the vertical direction, the latter of which depend only on the initial parcel temperature and the displacement in the z direction. Given the usefulness of potential temperature in that scenario, we foresee the value of determining the ‘potential’ momentum of environmental parcels if they were all moved to a reference y location. This would be a conserved quantity as parcels are moved in the y direction, and a comparison of this quantity between any two parcels at the same y could be used to assess the difference in their momentum. Similarly, the gradient of this quantity in the y direction should be sufficient to assess stability. Thus, we take the zonal momentum values and we adjust them to represent the zonal momentum that parcels would have if moved to $y = 0$, and, following tradition, we define this quantity as the *absolute momentum*¹⁰ (or *pseudoangular*

¹⁰ The *Glossary of Meteorology* defines absolute momentum as the momentum of a parcel as measured in an absolute coordinate system, such that it is the sum of the parcel's momentum relative to the earth and the momentum of the parcel due to the earth's rotation. However, the same term is also commonly defined as $M = u - fy$. Some authors use

momentum), M , where

$$M \equiv u - fy. \quad (3.41)$$

From (3.34), we see that this quantity is conserved following the motion for a purely zonal geostrophic flow (i.e., in the absence of pressure gradients in the x direction) on an f plane. Since our equilibrium state is one of geostrophic balance, we define the *geostrophic absolute momentum* (or *geostrophic pseudoangular momentum*) as

$$M_g \equiv u_g - fy. \quad (3.42)$$

By inspection of (3.41) and noting that

$$-\frac{\partial M_g}{\partial y} = f - \frac{\partial u_g}{\partial y}, \quad (3.43)$$

inertial instability is present when $\partial M_g / \partial y > 0$. In this case, a tube of parcels displaced in the positive y direction reaches its new location with an M value ($=M_g$ at its initial location) smaller than the local M_g value. Since we are comparing these at the same y value, the parcel's zonal momentum is smaller than the geostrophic value at this new location, indicating that the Coriolis force (toward the south) will be weaker than the pressure gradient force (toward the north), yielding an acceleration away from the initial location. The change in M_g with y is sufficient to assess this instability.

Alternatively, we could have written (3.33) as

$$\frac{dv}{dt} = -f[(u - fy) - (u_g - fy)] = -f(M - M_g). \quad (3.44)$$

Further, if we introduce $\bar{M} = M_g$, where $\bar{M} = M - M'$ is the absolute momentum of the equilibrium state, and M' is the deviation of M from the equilibrium state within a displaced parcel, then (3.44) can be written as

$$\frac{dv}{dt} = -f\bar{M}'. \quad (3.45)$$

The horizontal momentum equation above is analogous to the vertical momentum equation written as $\frac{dw}{dt} = g\frac{\theta'}{\theta}$, where θ is the relevant conserved variable. From (3.45) and the fact that M is conserved, if $\frac{\partial M_g}{\partial y} = \frac{\partial \bar{M}}{\partial y} > 0$ and a parcel is displaced northward, conserving its M , then $M' < 0$ and $dv/dt > 0$, resulting in a northward acceleration away from the equilibrium position.

Observations of inertially unstable environments are complicated by the fact that we generally do not observe

$M = v + fx$, which is equally valid. The form one should use depends on whether the environment and disturbance are prescribed to be invariant along the x direction versus the y direction. For any other orientation, the axes may be rotated to fit one of these forms.

equilibrium states, but the wind profile of the equilibrium state is what is relevant. Instead, what we actually observe are motions that represent the sum of a base state and perturbations from the base state. This challenge applies to many other instabilities as well, such as trying to observe environments containing symmetric instability (Section 3.4), or trying to determine whether an observed wind profile is susceptible to shear instability (Section 3.5).

Although we usually cannot know to what extent the observed wind field represents the equilibrium state, regions of negative absolute geostrophic vorticity are generally not observed on the synoptic scale, which suggests that the inertial stability criterion is an important constraint on the wind fields of large-scale troughs and ridges. However, negative absolute geostrophic vorticity observations are much more common on the mesoscale, albeit somewhat transient (Figure 3.6). For example, negative absolute geostrophic vorticity is routinely observed in the upper troposphere on

0000 UTC 20 July 2005

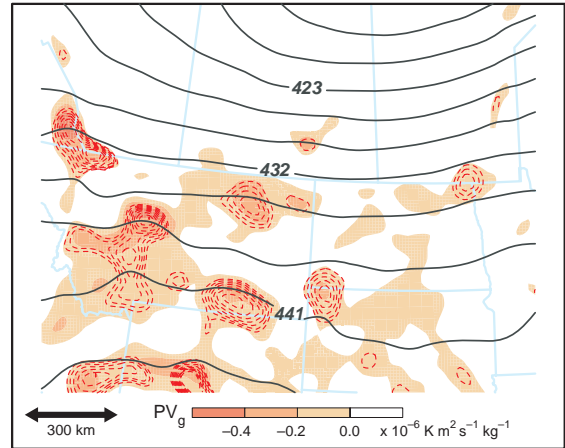


Figure 3.6 Rapid Update Cycle (RUC) initialization at 0000 UTC 20 July 2005. Negative geostrophic potential vorticity (PV_g) over the 600–650 mb layer ($10^{-6} \text{ K m}^2 \text{ kg}^{-1} \text{ s}^{-1}$, shaded according to the scale), negative 600 mb absolute geostrophic vorticity (dashed red contours every $-3 \times 10^{-5} \text{ s}^{-1}$ starting at 0), and 600 mb geopotential height (black contours every 3 dam) are shown. Inertial (symmetric) instability is present where absolute geostrophic vorticity (PV_g) is negative. Several east–west-oriented bands of clouds and generally light rain formed over eastern Montana and the Dakotas. The bands were spaced approximately 150 km apart. Both dry symmetric and inertial instability were present in the region of the bands, which may have accounted for the observed banding. (Adapted from Schultz and Knox [2007].)

the left flank (with respect to the direction of the deep-layer wind shear vector) of a deep convective cloud in an environment of strong vertical wind shear, owing to the upward advection of air having a very different horizontal momentum at low levels than the horizontal momentum of the air in the updraft's upper-level environment.

The structure of circulations resulting from the release of inertial instability are poorly understood. It is probably safe to assume that the instability would manifest itself as wind perturbations that are approximately two-dimensional and aligned with the mean wind. The mechanisms that lead to inertial instability, the details of the atmospheric response to inertial instability, and the possible dynamical role of inertial instability in contributing to precipitating mesoscale phenomena are subjects of ongoing research. For example, the weak inertial instability sometimes observed in the environments of mesoscale convective systems might help enhance their upper-level outflow and longevity (the concept of inertial instability might not be applicable in such cases, however, if the flow is not approximately two-dimensional).

3.4 Symmetric instability

Air parcels can be both statically and inertially stable (i.e., in hydrostatic and geostrophic equilibrium, and therefore in thermal wind balance), but can be unstable to displacements along a path that is slanted with respect to the horizontal for certain distributions of geostrophic momentum and potential temperature. This type of instability is called *symmetric instability*.¹¹ Before embarking on the mathematical derivation of the instability requirement, the instability can be demonstrated conceptually.

First, consider a stable configuration of mean potential temperature ($\bar{\theta}$) surfaces like those in Figure 3.7. In such a case, an upward (downward) displacement of a parcel results in a vertical restoring force that opposes the displacement. If a parcel is displaced upward (downward), it finds itself cooler (warmer) than its surroundings, and the vertical restoring force (i.e., the buoyancy force) accelerates the parcel downward (upward) toward its original $\bar{\theta}$ surface (the parcel will oscillate about its original position too). Similarly, consider a stable configuration of M_g ($= \bar{M}$) surfaces like those in Figure 3.8. If a tube of parcels aligned with a zonal geostrophic wind¹² is displaced northward

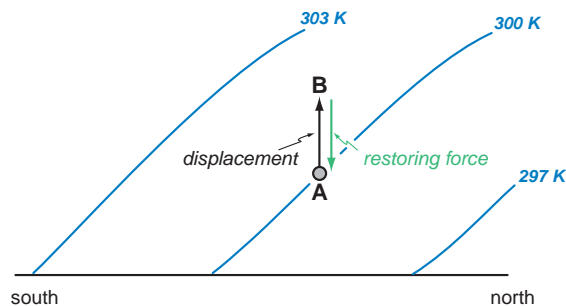


Figure 3.7 Schematic meridional cross-section of $\bar{\theta}$ surfaces in a statically stable atmosphere. A parcel that is displaced from position A toward position B experiences a restoring force that is directed toward its original equilibrium position.

(southward), the parcels are subjected to an acceleration by the horizontal restoring force, that is, the difference between the Coriolis force and horizontal pressure gradient force at their new position, which accelerates the parcels southward (northward) toward their original M_g surface (the parcels will oscillate horizontally about their original position too). The basic idea that you should take from consideration of Figures 3.7 and 3.8 is that, for a *stable* configuration of $\bar{\theta}$ or

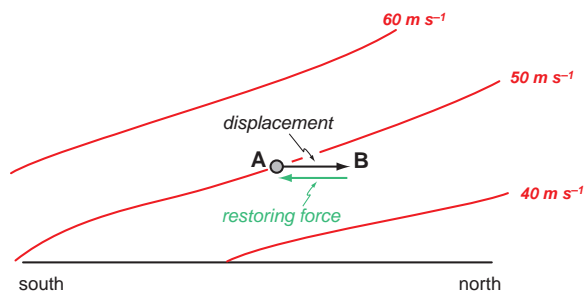


Figure 3.8 Schematic meridional cross-section of geostrophic absolute momentum surfaces in an inertially stable atmosphere. A tube of parcels that is displaced from position A toward position B experiences a restoring force that is directed toward its original equilibrium position.

¹¹ The term *symmetric instability* appears to have originated from studies of centrifugal instability in a rotating tank with baroclinity carried out by H. Solberg (circa 1930). A *symmetric flow* is one in which the base state and perturbations only vary in two dimensions.

¹² We assume here that the geostrophic wind and geostrophic wind shear are zonal, but the theory using $M_g = u - fy$ can be applied to

any geostrophic wind direction as long as the axes are rotated such that x lies along the thermal wind vector (and, thus, the mean-layer isotherms) and y points toward the colder air. The stability criterion in the horizontal requires $\frac{\partial M_g}{\partial y} < 0$. If one uses the form $M_g = v + fx$ then y must lie along the thermal wind and x must point toward the warm air. The corresponding stability criterion in the horizontal for that form requires $\frac{\partial M_g}{\partial x} > 0$. We believe that the former form is more natural for midlatitudes, but the latter form is seen regularly in the literature.

M_g surfaces, a displaced tube of parcels is subjected to restoring forces along each axis that accelerate the parcels back toward their original equilibrium position. The vertical and horizontal restoring forces are proportional to $\theta - \bar{\theta}$ and $M - M_g$ (or $M - \bar{M}$), respectively, where θ and M are the potential temperature and absolute (or pseudoangular) momentum of the displaced parcels, both of which are approximately conserved in the displacement.

But what if we have a configuration of $\bar{\theta}$ and M_g surfaces as in Figure 3.9? The $\bar{\theta}$ surfaces are as they were in Figure 3.7, and the M_g surfaces are as they were in Figure 3.8, that is, the atmosphere is stable with respect to vertical and horizontal displacements of air parcels (i.e., the atmosphere is statically and inertially stable). Consider the displacement of a tube of parcels (extending into and out of the page) along a slantwise path (upward and toward the north) from position A to position B in Figure 3.9. The parcels find themselves below their original $\bar{\theta}$ surface, therefore they are subjected to an upward-directed vertical force. Likewise, they find themselves to the south of their original M_g surface, therefore they are subjected to a northward horizontal force. The resultant acceleration (i.e., the sum of the horizontal and vertical restoring forces) is directed upward and toward the north, in the same direction as the displacement! Thus, the parcels are accelerated away from their original equilibrium position; the equilibrium state is said to be symmetrically unstable. It turns out (this will be proven shortly) that the instability depends on $\bar{\theta}$ surfaces being more steeply sloped than M_g surfaces, and parcel displacements must be at an angle that lies between the slopes of the $\bar{\theta}$ and M_g surfaces.

Symmetric instability involves the displacement of tubes of parcels that are aligned with the thermal wind or

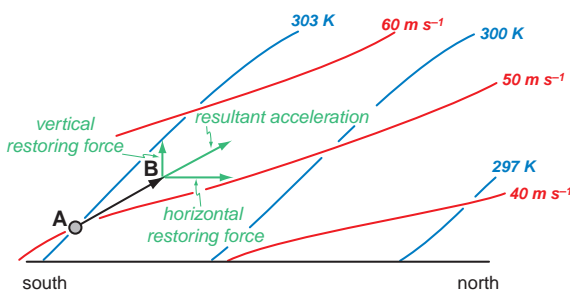


Figure 3.9 Schematic meridional cross-section of isentropic (blue) and geostrophic momentum surfaces (red) in a symmetrically unstable atmosphere. A tube of parcels that is displaced from position A toward position B experiences a resultant acceleration that is directed away from the original equilibrium position.

mean-layer isotherms (in the forthcoming analysis, the geostrophic wind happens to be aligned with the thermal wind). As was the case for inertial instability, the environment must be approximately two-dimensional; that is, the wind and thermal wind can only vary in one horizontal direction and in the vertical. Symmetric instability is perhaps of greater interest than inertial instability owing to the vertical component of the acceleration in the case of symmetric instability, which makes it more likely to lead to precipitation. The release of symmetric instability results in what is often called *slantwise convection*.¹³ For moist convection (i.e., that in which condensation is occurring), the $\bar{\theta}_e^*$ surfaces, representing the θ_e that the environment would have if it were saturated, must be considered rather than the $\bar{\theta}$ surfaces. This is directly analogous to static stability, for which one uses $\bar{\theta}$ to assess dry instability and one uses $\bar{\theta}_e^*$ to assess conditional gravitational instability. Likewise, we can compare the slopes of the $\bar{\theta}_e^*$ surfaces with those of the M_g surfaces to assess the presence of *conditional symmetric instability* (CSI). In most situations, $\bar{\theta}_e^*$ surfaces are more steeply sloped than $\bar{\theta}$ surfaces because cold air tends to be drier than warm air. Finally, we can compare the slope of the $\bar{\theta}_e$ surfaces with those of the M_g surfaces to assess *potential symmetric instability* (PSI).

We shall take a more quantitative look at this instability by first considering the restoring forces in the vertical and horizontal directions for a parcel that experiences no condensation during its slantwise displacement. Then we shall combine the vertical and horizontal restoring forces to examine the restoring force in the slantwise direction. We shall assume that the slantwise displacement occurs in the y - z plane, and that the background geostrophic flow is zonal, but has a y and z dependence (i.e., $u_g = u_g(y, z)$; $v_g = 0$), as in our analysis of inertial instability.

Consider the parcel at position A in Figure 3.10, in equilibrium with its surroundings; i.e., $\theta = \bar{\theta} = \theta_0$ and $u = u_g = u_0$. The potential temperature of a parcel is conserved during its displacement from location A to location B, so

$$\theta = \theta_0 = \bar{\theta}(y_0, z_0). \quad (3.46)$$

The environmental potential temperature at position B, approximated by a first-order Taylor series, is

$$\bar{\theta} = \theta_0 + \frac{\partial \bar{\theta}}{\partial y} \Delta y + \frac{\partial \bar{\theta}}{\partial z} \Delta z. \quad (3.47)$$

¹³ Slantwise convection should not be confused with gravitational convection (i.e., convection that is driven by buoyancy alone) that is tilted by strong vertical wind shear. Gravitational convection having tilted updrafts is associated with slanted streamlines, but the *instability* is in the vertical direction only. In slantwise convection, the instability results in both vertical and horizontal accelerations.

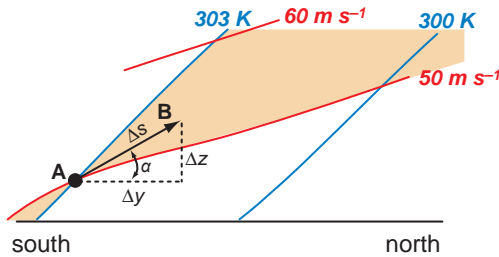


Figure 3.10 Zoomed-in view of Figure 3.9, showing the relationship between α , Δs , Δy , and Δz . Displacements of the parcel at position A to locations within the shaded region (e.g., toward position B) result in acceleration away from position A.

Therefore, the potential temperature difference between the displaced parcel and the environment at location B is (3.46)–(3.47):

$$\theta - \bar{\theta} = -\frac{\partial \bar{\theta}}{\partial y} \Delta y - \frac{\partial \bar{\theta}}{\partial z} \Delta z. \quad (3.48)$$

Thus, the buoyancy force, or net vertical restoring force (F_v), acting on the displaced parcel at location B is

$$F_v = g \frac{\theta - \bar{\theta}}{\bar{\theta}} = -\frac{g}{\bar{\theta}} \frac{\partial \bar{\theta}}{\partial y} \Delta y - \frac{g}{\bar{\theta}} \frac{\partial \bar{\theta}}{\partial z} \Delta z. \quad (3.49)$$

However, there is also a horizontal restoring force on the parcel undergoing a slantwise displacement because the Coriolis force and horizontal pressure gradient force generally will be out of balance at the new position. At location B, the absolute momentum of the displaced tube of parcels will be equal to its initial value [from (3.36)],

$$M = M_0 = M_g(y_0, z_0), \quad (3.50)$$

assuming that no $\partial p'/\partial x$ is generated by the displacement, and f is constant over the domain. The geostrophic absolute momentum at position B is (using a first order Taylor series approximation)

$$M_g = M_0 + \frac{\partial M_g}{\partial y} \Delta y + \frac{\partial M_g}{\partial z} \Delta z. \quad (3.51)$$

The net horizontal restoring force, F_h , is given by (3.44)

$$F_h = -f(M - M_g) \quad (3.52)$$

$$= -f \left(-\frac{\partial M_g}{\partial y} \Delta y - \frac{\partial M_g}{\partial z} \Delta z \right), \quad (3.53)$$

where (3.50) and (3.51) have been used to replace M and M_g .

The equation of motion for the parcel along its direction of slantwise displacement is

$$\frac{d^2 \Delta s}{dt^2} = F_h (\mathbf{j} \cdot \mathbf{s}) + F_v (\mathbf{k} \cdot \mathbf{s}) \quad (3.54)$$

$$= F_h \cos \alpha + F_v \sin \alpha \quad (3.55)$$

$$= -f \left(-\frac{\partial M_g}{\partial y} \Delta y - \frac{\partial M_g}{\partial z} \Delta z \right) \cos \alpha \\ + \left(-\frac{g}{\bar{\theta}} \frac{\partial \bar{\theta}}{\partial y} \Delta y - \frac{g}{\bar{\theta}} \frac{\partial \bar{\theta}}{\partial z} \Delta z \right) \sin \alpha, \quad (3.56)$$

where α is the angle the displacement makes with respect to the horizontal (as indicated in Figure 3.10), \mathbf{s} is a unit vector in the slantwise direction, and Δs represents the displacement along the slantwise direction such that the position along the slant is given by $s = s_0 + \Delta s$, where s_0 is the original location.

Equation (3.56) is a generalized equation for parcel displacements in the y - z plane. Notice that (3.56) reduces to (3.5) for $\Delta y = 0$ and $\alpha = 90^\circ$, and it reduces to (3.44) for $\Delta z = 0$ and $\alpha = 0^\circ$.

We can express (3.56) in terms of the slopes of the M_g and θ surfaces by noting that along a constant M_g surface

$$\Delta M_g = 0 = \frac{\partial M_g}{\partial y} \Delta y + \frac{\partial M_g}{\partial z} \Delta z. \quad (3.57)$$

The slope of an M_g surface is therefore

$$\left(\frac{\Delta z}{\Delta y} \right)_{M_g} = -\frac{\partial M_g / \partial y}{\partial M_g / \partial z} = \frac{f - \frac{\partial u_g}{\partial y}}{\frac{\partial u_g}{\partial z}}. \quad (3.58)$$

Similarly, along a constant $\bar{\theta}$ surface,

$$\Delta \bar{\theta} = 0 = \frac{\partial \bar{\theta}}{\partial y} \Delta y + \frac{\partial \bar{\theta}}{\partial z} \Delta z; \quad (3.59)$$

therefore, the slope of a $\bar{\theta}$ surface is

$$\left(\frac{\Delta z}{\Delta y} \right)_{\bar{\theta}} = -\frac{\partial \bar{\theta} / \partial y}{\partial \bar{\theta} / \partial z}. \quad (3.60)$$

Thus, noting that $\Delta y = \Delta s \cos \alpha$ and factoring this out of all terms, we can write (3.56) as

$$\frac{d^2 \Delta s}{dt^2} = \left\{ f \frac{\partial M_g}{\partial z} \left[\left(\frac{\Delta z}{\Delta y} \right) - \left(\frac{\Delta z}{\Delta y} \right)_{M_g} \right] \cos \alpha \right. \\ \left. + N^2 \left[\left(\frac{\Delta z}{\Delta y} \right)_{\bar{\theta}} - \left(\frac{\Delta z}{\Delta y} \right) \right] \sin \alpha \right\} \Delta s \cos \alpha, \quad (3.61)$$

where $N^2 = \frac{g}{\bar{\theta}} \frac{\partial \bar{\theta}}{\partial z}$.

The sign of $d^2\Delta s/dt^2$, and thus the instability criterion, depends on the slope of the displacement, $\Delta z/\Delta y$, and the slopes of the $\bar{\theta}$ and M_g surfaces. In the case of displacing a parcel from position A to position B in Figure 3.10, acceleration away from position A occurs when $d^2\Delta s/dt^2 > 0$. The slope of the parcel displacement lies between the slopes of the M_g and $\bar{\theta}$ surfaces, so if the slope of the M_g surfaces exceeds the slope of the $\bar{\theta}$ surfaces, then both terms in brackets are positive definite (as are $\sin \alpha$, $\cos \alpha$, N^2 , and f in the northern hemisphere), and $d^2\Delta s/dt^2 < 0$; the parcel is accelerated back to its initial equilibrium position. On the other hand, if the slope of the $\bar{\theta}$ surfaces exceeds the slope of the M_g surfaces, and the parcel displacement lies between its original M_g and $\bar{\theta}$ surfaces, then $d^2\Delta s/dt^2 > 0$ and the parcel is accelerated away from its initial equilibrium position. Thus, a necessary condition for symmetric instability is

$$\left(\frac{\Delta z}{\Delta y}\right)_{\bar{\theta}} > \left(\frac{\Delta z}{\Delta y}\right)_{M_g}, \quad (3.62)$$

when the slope of the parcel displacement lies between the slopes of the M_g and $\bar{\theta}$ surfaces. Depending on the exact slopes of the M_g and $\bar{\theta}$ surfaces and the magnitude of f , N , and $\partial M_g/\partial z$, it still may be possible to have $d^2\Delta s/dt^2 > 0$ (and thus acceleration away from the equilibrium position) for parcel displacements having slopes not between the slopes of the M_g and $\bar{\theta}$ surfaces; however, accelerations away from the equilibrium position are not sustainable for large excursions from the equilibrium position (the reader ought to be able to convince herself or himself of this graphically, adhering to the rule that the acceleration of the displaced parcel in the horizontal and vertical directions is toward the parcel's original M_g and $\bar{\theta}$ surfaces, respectively). The most unstable displacement direction turns out to be nearly along a $\bar{\theta}$ surface.

We note that (3.62) is equivalent to either of the following two tests:

$$\left(\frac{\partial \theta}{\partial z}\right)_{M_g} < 0 \quad (3.63)$$

$$\left(\frac{\partial M_g}{\partial y}\right)_{\bar{\theta}} > 0. \quad (3.64)$$

Thus, one may assess whether $\bar{\theta}$ decreases with increasing height as one follows an M_g surface or whether M_g increases with y as one follows a constant $\bar{\theta}$ surface. Either of these is associated with instability.

Equation (3.61) can be manipulated in other ways to facilitate assessment of symmetric instability. We have not done this here, but we shall merely state that symmetric instability is also present if the absolute geostrophic vorticity on an isentropic surface ($(f - \partial u_g/\partial y)_{\bar{\theta}}$) becomes

negative (analogous to the inertial instability criterion of $f - \partial u_g/\partial y < 0$ on a horizontal surface), or if geostrophic potential vorticity, $PV_g (= \alpha [\nabla \times \mathbf{v}_g + f \mathbf{k}] \cdot \nabla \bar{\theta}$, where $\alpha = 1/\rho$), becomes negative (Figure 3.6). Note that, because PV_g is conserved for adiabatic motions, a stable region ($PV_g > 0$) cannot be rendered unstable by simply rearranging PV_g . Although perhaps not as physically revealing as the comparison of slopes, these three-dimensional criteria are considered more robust as they are not as sensitive to the particular cross-section orientation as is (3.62), where care must be taken to orient the cross-section perpendicular to the thermal wind (or isotherms). However, when using three-dimensional measures, one still must confirm that the underlying flow field satisfies the constraint of approximate two-dimensionality in order for the criterion to represent symmetric stability. It also can be shown that symmetric instability is present if $\frac{Ri}{f} \left(f - \frac{\partial u_g}{\partial y}\right) < 1$, where Ri is the Richardson number $\left(=\frac{g}{\theta} \frac{\partial \bar{\theta}}{\partial z} \left[\frac{\partial u_g}{\partial z}\right]^{-2}\right)$, and is thus favored when static stability is low, vertical shear is strong, and relative vorticity is anticyclonic.

The symmetric instability analysis has not included the effects of saturation. In order to account for the effects of moist adiabatic ascent in the stability analysis, we need only replace θ with the appropriate conservative variable, i.e., θ_e^* or θ_e . Thus, the instability criterion for conditional symmetric instability (CSI) is

$$\left(\frac{\Delta z}{\Delta y}\right)_{\bar{\theta}_e^*} > \left(\frac{\Delta z}{\Delta y}\right)_{M_g}; \quad (3.65)$$

that is, when the slope of $\bar{\theta}_e^*$ surfaces is greater than the slope of M_g surfaces. The criterion for potential symmetric instability (PSI) is

$$\left(\frac{\Delta z}{\Delta y}\right)_{\bar{\theta}_e} > \left(\frac{\Delta z}{\Delta y}\right)_{M_g}. \quad (3.66)$$

Similar substitutions of $\bar{\theta}_e^*$ or $\bar{\theta}_e$ would be made in the three-dimensional forms as well. When applying these criteria, one must confirm they are not identifying regions of conditional gravitational instability or inertial instability, which, by definition, are not areas of symmetric instability.

Qualitatively, environments conducive to slantwise convection bands (i.e., environments containing CSI) have strong vertical wind shear (i.e., a strongly baroclinic atmosphere) and a deep layer that is nearly saturated. The release of CSI is a likely candidate in the formation of mesoscale precipitation bands within extratropical cyclones in many cases, particularly within frontal zones, where

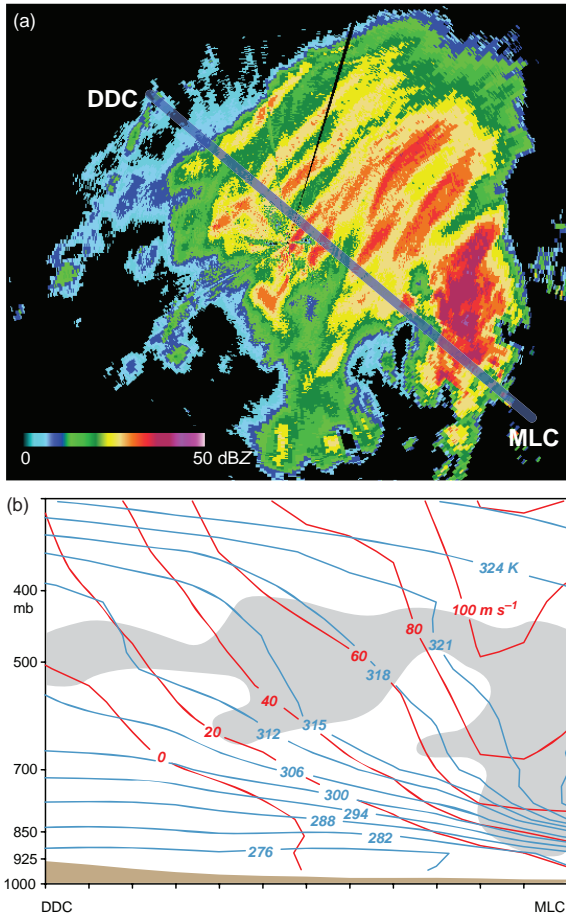


Figure 3.11 (a) Vance Air Force Base (VNX) WSR-88D reflectivity (dBZ) display at 1658 UTC 30 November 2006. The southwest–northeast-oriented precipitation bands are believed to be associated with the release of CSI. (b) A vertical cross-section normal to the bands at 1700 UTC from roughly Dodge City (DDC), KS, to McAllister (MLC), OK (the broad blue line in (a) indicates the cross-section location), shows $\bar{\theta}_e^*$ (K, blue lines) and M_g ($m s^{-1}$, red lines). The gray shaded region is approximately neutral or slightly unstable with respect to CSI.

vertical wind shear is large (Figure 3.11). Precipitation bands due to the release of CSI, sometimes multiple, should be approximately oriented with the thermal wind (Table 3.1). Although parcel displacements are unstable if at an angle between the slope of the M_g and $\bar{\theta}^*$ surfaces, the slope of the updrafts tends to be nearly parallel to $\bar{\theta}^*$ surfaces (in the saturated case, the most unstable displacement direction is nearly along $\bar{\theta}^*$ surfaces). Vertical velocities within the updrafts are of the order of $1 m s^{-1}$, compared

Table 3.1 Characteristics of mesoscale precipitation bands that are related to CSI.

Motion	If the bands are moving, they should be moving with the environmental flow (i.e., bands are advected by the flow; they do not propagate relative to the environmental flow)
Spacing	Believed to be related to the depth of the unstable layer and the slope of the isentropes
Slope of ascent	Should lie between the slopes of $\bar{\theta}_e^*$ and M_g surfaces; when the flow is hydrostatic, the ascent will occur exactly on the isentropic surfaces
Alignment	Nearly along the thermal wind, but can deviate by as much as 15°

with vertical velocities of a few $cm s^{-1}$ on the synoptic scale and $10 m s^{-1}$ within buoyant thunderstorm updrafts. The maximum updraft speed in the slanted direction can be estimated using the *slantwise convective available potential energy* (SCAPE), which can be calculated in a manner similar to how CAPE is computed to assess the potential intensity of gravitational convection, but with the integration of buoyancy performed along a constant M_g surface rather than in the vertical.

Although CSI can be released by growing infinitesimal perturbations, it may also be released by finite-amplitude forcing (analogously, in the case of gravitational convection, the release of conditional instability usually requires the finite lifting of air parcels to their LFC). Thermally direct frontal circulations in response to frontogenesis are believed to be a lifting mechanism that can release CSI, and regions of CSI also are often regions of frontogenesis. Frontogenesis and the ageostrophic vertical circulation that accompanies frontogenesis will be discussed in Section 5.1.

Even if the atmosphere is determined to be stable to moist slantwise and moist gravitational convection, banded clouds and precipitation still can form owing to forced ascent. Thus, not all banded precipitation is the result of CSI. Proving that a particular case was due to CSI requires a rigorous analysis including a comparison with the theoretical environmental conditions necessary for the instability as well as the theoretical behavior of the ensuing convection (Table 3.1). Moreover, as also mentioned at the end of Section 3.3, determining the base state from observations is problematic. For example, in many cases slantwise neutrality is observed rather than large areas of CSI. The slantwise neutrality may be an indication that CSI has been released.



Figure 3.12 Billow clouds, which resemble breaking waves, are a visual manifestation of vertical shear instability (also known as Kelvin–Helmholtz instability) when sufficient moisture is present. Photograph by Brooks Martner.

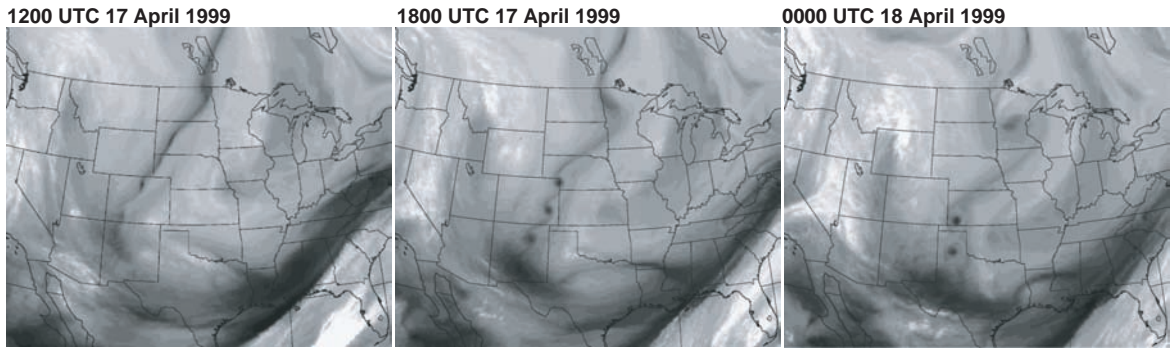


Figure 3.13 Water vapor satellite imagery from 1200–0000 UTC 17–18 April 1999 revealing the development of a series of vortices, most likely as a result of horizontal shear instability. (Adapted from Weinand [2000].)

3.5 Shear instability

The level of interest in the study of the stability of *parallel flows*—flows in which all but one of the mean velocity components are zero—is hard to overstate, as the problem has attracted the likes of Lord Rayleigh, Lord Kelvin, Helmholtz, Heisenberg,¹⁴ and Taylor,¹⁵ going back well over a century. What is loosely referred to as *shear instability* can be present in currents containing vertical or horizontal wind shear.

¹⁴ Werner Heisenberg (1901–1976) was a German theoretical physicist best known for his contributions to quantum mechanics (e.g., the Heisenberg uncertainty principle). He was awarded a Nobel Prize in 1932.

¹⁵ Sir Geoffrey Taylor (1886–1975) was a British physicist and mathematician best known for his work in fluid dynamics, particularly turbulence.

Vertical shear instability in the presence of a statically stable layer, also known as Kelvin–Helmholtz instability, has been invoked to account for observations of *billow clouds* (Figure 3.12), clear-air turbulence, the excitation of gravity waves, and even mammatus clouds. Horizontal shear instability has been invoked to account for observations of vortices along windshift lines (Figure 3.13), kinks or fractures within lines of convection, and even some tornadoes (Figure 3.14).

Shear instability extracts energy from the mean flow. It usually involves the transformation of a corridor of relatively large vorticity, which implies a relative maximum in the wind shear magnitude, into somewhat regularly spaced, nearly circular, discrete patches of vorticity (Figure 3.15). In the limiting case, when the wind shear occurs over an infinitesimal distance, the vorticity becomes infinite along



Figure 3.14 This photograph of multiple waterspouts with a remarkably regular spacing strongly suggests that horizontal shear instability may have played a role in their formation. The image was obtained off the coast of Italy during the early spring of 2001. Photograph by Roberto Giudici.

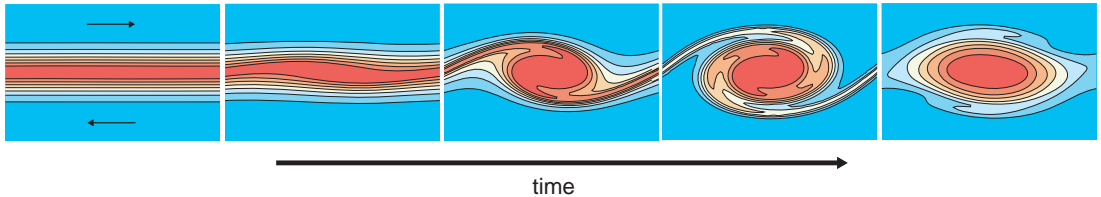


Figure 3.15 Idealized numerical simulation illustrating the effects of inflection-point instability. Time advances from left to right. Shading denotes vorticity magnitude. Warm (cool) colors indicate large (small) vorticity values. The mean wind direction is indicated by the arrows in the first panel. If instability is present and the high-vorticity interface is perturbed, the perturbation amplifies until the interface folds over on itself, leading to wave breaking and a transformation of what was initially a linear corridor of large vorticity into discrete patches of large vorticity. (Adapted from numerical simulation output provided by Brian Fiedler.)

what is known as a *vortex sheet*. Although it is not always obvious how to define a vortex (*vortex* and *vorticity* are not interchangeable), vortices tend to be associated with discrete, nearly circular extrema of vorticity (the presence of a discrete vorticity patch, however, is not a sufficient condition for the presence of a vortex). One approach used to define a vortex is to find a reference frame in which closed streamlines exist (Figure 3.16). If such a reference frame can be found, and if, at a later time, the center of the region of closed streamlines has not moved significantly when viewed from the respective reference frame, then the

region of closed streamlines can be regarded as a vortex.¹⁶ Shear instability is therefore a means by which vortices can arise within a regime of initially straight flow, albeit an initial flow containing vorticity. Vorticity is not created; rather, it is simply redistributed by advection.

For horizontal shear instability, a relative maximum in the horizontal wind shear (vertical vorticity) magnitude is a necessary condition for instability. For Kelvin–Helmholtz instability, although a relative maximum in vertical wind

¹⁶ See Lugt (1979).

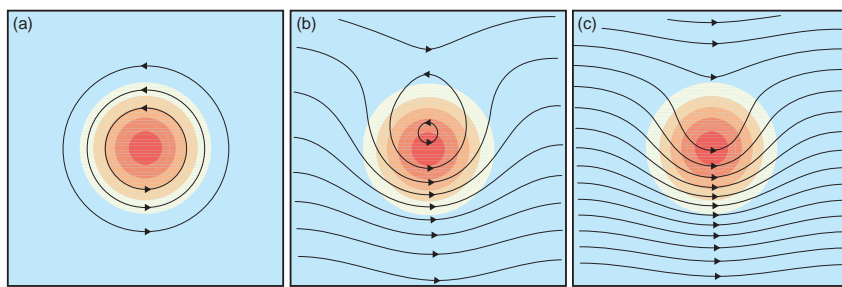


Figure 3.16 The relationship between streamlines (black lines with arrows giving the direction of the wind) and vorticity (shaded, with warm [cool] colors indicating large [small] vorticity values) for a vortex, in this case represented by a circular patch of vorticity, on which (a) no flow is superposed, (b) moderate, uniform westerly flow is superposed, and (c) fast, uniform westerly flow is superposed. The streamlines also are isolines of streamfunction; thus, the distance between streamlines is inversely proportional to the wind speed (the streamfunction contour interval is the same in [a]–[c]). Alternatively, (a)–(c) can be interpreted as the appearance of the wind field if the observer is (a) at rest relative to the vortex, (b) moving at a moderate speed from east to west relative to the vortex, and (c) moving quickly from east to west relative to the vortex. The characteristics of the streamlines associated with a vortex are reference-frame dependent. A vortex is associated with closed streamlines only when viewed in a reference frame moving with the vortex, as in (a). The closed streamlines associated with a vortex can ‘open up’ into waves when viewed from reference frames that are moving relative to the vortex.

shear (horizontal vorticity) magnitude is often present, it will be shown that such a relative maximum is not a requirement for instability. A relative maximum in shear/vorticity magnitude implies that an inflection point is present in the wind profile; that is, the second spatial derivative (with respect to the horizontal or vertical direction, in the case of horizontal or vertical shear instability, respectively) of the wind speed changes sign. For this reason, shear instability is also often termed *inflection-point instability*. Wind profiles that have inflection points, either horizontal wind profiles or vertical wind profiles in the absence of stratification, are often inherently unstable. Lord Rayleigh and Tollmien¹⁷ are usually given credit for identifying the importance of inflection points in wind profiles. For wind profiles that vary directionally with height, one must consider wind speed variations in vertical planes normal to the winds (a range of orientations of the vertical planes must be considered owing to the variation of wind direction with height).

The physical explanation for why inflection points in a wind profile are intrinsically unstable can be obtained by considering the interaction of vortex lines.¹⁸ A plane that intersects vortex lines can be viewed as a field of *point vortices*, that is, point concentrations of vorticity

surrounded by irrotational flow. Given a field of point vortices, the motion of any one is determined by the flow superposed on it by all the other point vortices (Figure 3.17). For example, two vortices of like sign rotate about each

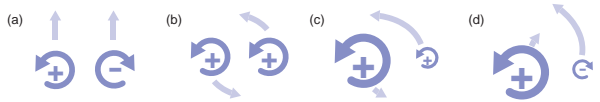


Figure 3.17 Given a field of point vortices, the motion of any one is determined by the flow superposed on it by all the other point vortices. Here we consider simple cases involving two point vortices. The sense of rotation associated with each point vortex is indicated with arrows (+ and – signs also identify the rotation as cyclonic and anticyclonic, respectively), and the size of the arrows is proportional to the strength of the point vortex (vorticity magnitude). Light colored arrows indicate the motion of each point vortex induced by the other point vortex. (a) A pair of vortices having opposite signs and equal strength. The two point vortices move in straight lines parallel to each other. (b) A pair of vortices having the same signs and equal strength rotate around a common center. (c) A weaker vortex rotates around a stronger, like-signed vortex; the weaker vortex induces a small movement of the stronger vortex. (d) As in (c), but for oppositely signed vortices.

¹⁷ Walter Tollmien (1900–1968) was a German engineer best known for his work in fluid dynamics and turbulence.

¹⁸ See Lin (1945) and Brown (1972b).

other¹⁹ (Figure 3.17b), and a weaker vortex rotates around a stronger vortex (Figure 3.17c,d). We shall examine shear instability using this conceptual model.

A two-dimensional parallel flow can be viewed as resulting from a large number of vortex lines (point vortices in the plane containing the two-dimensional flow) moving under the action of each other, such that the flow comprises layers of vortex lines, with vortex lines of equal vorticity being arranged in the same layer. When a fluid element, and the vortex line that passes through the fluid element, is displaced with a component normal to the flow, the vorticity associated with the vortex line is conserved and the vortex line finds itself surrounded by vortex lines associated with either lesser or greater vorticity, depending on the ambient gradient of vorticity. The vortex line (and the fluid element associated with it) is accelerated back to its original layer if the vorticity gradient at the location to which the vortex line was displaced is the same sign as the vorticity gradient

at the original location of the vortex line. The distribution of vorticity within the parallel flow is therefore stable. On the other hand, if the vorticity gradient at the location to which the vortex line was displaced is the opposite sign as the vorticity gradient at the original location of the vortex line, which implies that an inflection point is present in the velocity profile, then the vortex line (and the fluid element associated with it) is accelerated away from its original layer. This is the unstable case.

The reasons for the aforementioned accelerations can be deduced by considering the interactions between the vortex lines. First, let us consider the stable case of a velocity profile having shear but no inflection point (Figure 3.18a). Consider two sheets of vortex lines. Vortex lines within the layer centered at y_1 have a vorticity ζ_1 , while vortex lines within the layer centered at y_2 ($y_2 > y_1$) have a vorticity ζ_2 , and $\zeta_1 > \zeta_2$. Now consider the displacement of a vortex line A from y_1 to y_2 . We do not care how the vortex line got to its new location, and we shall assume that no other vortex lines were affected during the displacement from y_1 to y_2 . However, once vortex line A is at its new location y_2 , the previous balanced state that existed along y_2 is disrupted such that vortex lines are advected toward y_2

¹⁹ This effect is sometimes called the *Fujiwhara effect*, after Sakuhei Fujiwhara (1884–1950), a Japanese meteorologist who is best known for his paper describing the interaction between two proximate cyclonic vortices (Fujiwhara, 1931).

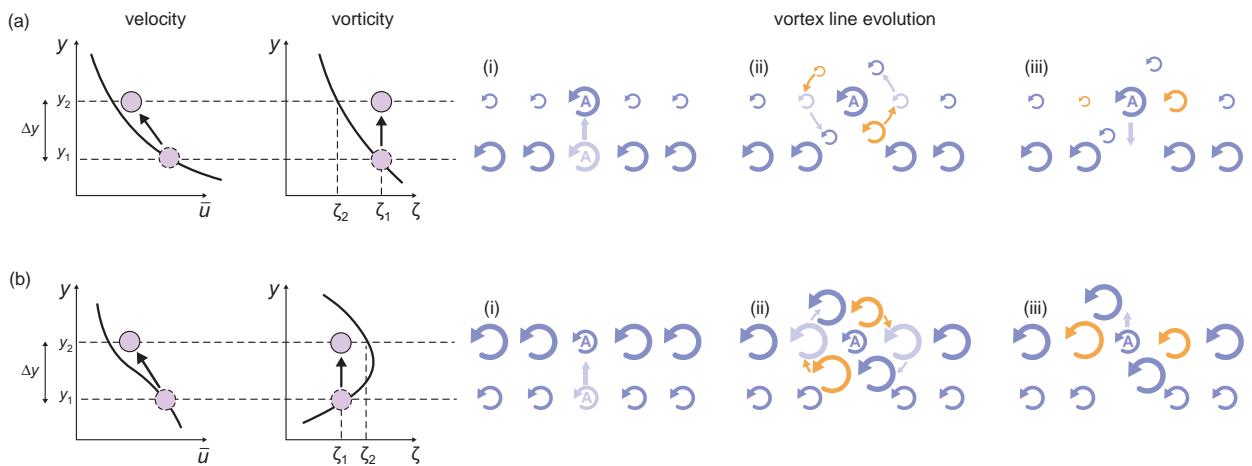


Figure 3.18 Schematic of a displaced vortex line A in a two-dimensional parallel flow (a) without and (b) with an inflection point in the velocity profile. The evolution of vortex lines is shown on the right. The sense of rotation induced by a vortex line is shown with arrows, with the size of the arrows increasing with increasing vorticity magnitude. Frame (i) shows the vortex line distribution immediately after vortex line A has been displaced. The light purple arrows indicate the prior position of vortex line A and the direction of its displacement. Frame (ii) shows the motion of the vortex lines initially at $y = y_2$ induced by vortex line A. The light purple arrows indicate the prior position of the vortex lines and the direction of their motion. The rotation associated with two additional vortex lines influenced by vortex line A, originally at $y = y_1 + \Delta y/2$ and $y = y_2 + \Delta y/2$, is indicated with orange arrows (these vortex lines are not shown in (i) in order to limit clutter). Frame (iii) shows the distribution of vortex lines a little later and the direction toward which vortex line A is accelerated. (Adapted from Brown [1972b] and based on the explanation provided by Lin [1945].)

from above (to the left of A) and below (to the right of A). The vortex lines that end up to the left of A have lesser vorticity than the vortex lines that end up to the right of A, creating a vorticity distribution surrounding A that leads to acceleration in the negative y direction, back toward its original location y_1 .

Next, we shall consider the unstable case of a velocity profile having an inflection point (Figure 3.18b). We shall again consider two layers of vortex lines at y_1 and y_2 having vorticities ζ_1 and ζ_2 , respectively, but in this case, suppose that a relative maximum in vorticity lies between y_1 and y_2 , and that $\zeta_2 > \zeta_1$. We shall again consider the displacement of a vortex line A from y_1 to y_2 . Once again, the new distribution of vorticity is such that additional vortex lines are advected toward y_2 from above and below. In this case, however, the vortex lines that end up to the right of A have weaker vorticity than the vortex lines that end up to the left of A, so the net effect on vortex line A is an acceleration in the positive y direction, away from its original location y_1 . In this case the initial shear profile was unstable when perturbed. Of course, in the case of vertical (as opposed to horizontal) wind shear, the additional presence of stable stratification also affects the net force acting on a displaced fluid element, with static stability suppressing the tendency for fluid elements to be accelerated away from their initial positions.

Given that we have an inflection point in the wind profile, owing to the presence of a vortex sheet or a finite-width shear zone separating two air masses having different velocities, it is not too difficult to grasp physically how initially weak wavelike disturbances introduced along the interface will amplify given that these are simply a series of vortex line displacements along the entire y_2 axis. The interface is a relative maximum in the magnitude of vorticity, as explained earlier. Before the interface is perturbed, winds

blow parallel to the vorticity isopleths and vorticity advection is everywhere zero. When the interface is perturbed sinusoidally, vorticity advection is induced along the interface (Figure 3.19) such that the initial linear corridor of vorticity is transformed into discrete patches of concentrated vorticity (Figure 3.15). Again, in the case of vertical wind shear, the additional presence of a stable stratification inhibits the growth of the disturbance imposed on the interface.

It is generally difficult, if not impossible, to observe a smoking gun that implicates shear instability as a vortex-formation mechanism in the real atmosphere. In the real atmosphere, we typically do not observe an initial, unstable mean state in which a relative maximum in wind shear is devoid of vortices and is characterized by straight flow, such as the initial state used for the numerical simulation depicted in Figure 3.15. Moreover, complicating three-dimensional processes such as vorticity stretching and tilting are usually also present (i.e., nondivergent, rotational flows are generally not observed outside of idealizations of the real atmosphere). It is also difficult, when making observations, to separate the mean state from the perturbations, as is done in the stability analyses in the following two subsections (this point was also raised in Section 3.3). Nonetheless, there is much circumstantial evidence for the importance of shear instability, such as observations of regularly spaced vortices along wind-shift lines, tendencies for the intensity of vortices to increase with increasing mean horizontal shear, and the fact that vorticity structures and evolution in numerical simulations, in which the aforementioned issues can be circumvented, often closely resemble observations.

In Sections 3.1–3.4 we assessed instability by displacing parcels away from locations where they were in equilibrium with their environments to new locations where the

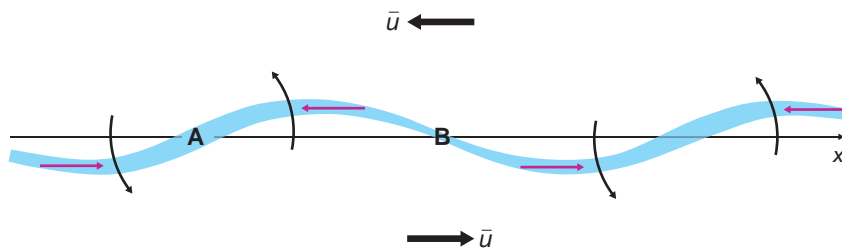


Figure 3.19 Growth of a sinusoidal perturbation on an initially uniform vortex sheet. The local sheet strength is indicated by the thickness of the sheet. The base state wind is indicated with the bold black arrows. The magenta arrows above and below the x axis indicate the direction of the induced vorticity movement along the sheet, concentrating vorticity at points such as A and depleting the vorticity at points such as B. The thick black arrows indicate the sense of rotation associated with the vortices that develop at points such as A. (Adapted from Batchelor [1967].)

parcels experienced a net acceleration. The direction of the acceleration determined whether the environment was stable or unstable. Although we adopted a similar approach above in order to gain physical insight into shear instability, a quantitative assessment of shear instability generally requires us to consider the growth or decay in amplitude of an infinitesimal wavelike perturbation imposed on the mean state.

Below we use what is known as *linear stability analysis* to derive necessary conditions for instability in horizontal and vertical wind profiles. In linear stability analysis, we linearize a dynamical equation or system of dynamical equations; that is, we derive equations for perturbations about a basic state (basic state variables are usually indicated with overbars and perturbation variables are usually indicated with primes; terms involving products of perturbations are assumed to be small and are neglected). Small wavelike perturbations are then introduced, and we assess the conditions under which the perturbations spontaneously amplify. One general limitation of linear stability analysis is that it only predicts the *onset* of instability; it cannot be applied once perturbations have grown large. Moreover, linear stability analysis cannot account for the finite-amplitude disturbances that are often important in triggering instabilities, as was mentioned earlier in this chapter (e.g., in the initiation of both gravitational convection and slantwise convection).

The analyses below strictly apply to inviscid flows (i.e., infinite Reynolds number); the inclusion of viscosity in the forthcoming instability analyses is beyond the scope of this book. Although viscosity usually has a stabilizing influence, it occasionally can destabilize an otherwise stable parallel flow.²⁰

3.5.1 Horizontal shear instability

Let us consider a basic state on an f plane consisting of purely zonal flow in geostrophic balance, that is, $\bar{v} = 0$ and $\bar{u} = \bar{u}(y)$, where

$$\bar{u}(y) = -\frac{1}{f_0} \frac{\partial \bar{\Phi}}{\partial y}, \quad (3.67)$$

and $\Phi = \bar{\Phi} + \Phi' = gz$ is the geopotential, $\bar{\Phi} = \bar{\Phi}(y)$ is the base state geopotential, and Φ' is the geopotential perturbation, the Laplacian of which is associated with a vorticity

²⁰ For example, *parallel instability* is a type of shear instability that does not require an inflection point but requires the Coriolis force and viscosity; that is, an ordinarily stable velocity profile (e.g., a linear one) in a neutral stratification with rotation can be made unstable by the presence of viscosity. Parallel instability may be a factor in the formation of boundary layer convective rolls (Section 4.4).

perturbation. We are interested in the distributions of vorticity that are unstable; thus, let us consider the barotropic vorticity equation (appropriate for two-dimensional, inviscid, horizontal flows),

$$\frac{\partial \zeta}{\partial t} + u \frac{\partial \zeta}{\partial x} + v \frac{\partial \zeta}{\partial y} + v\beta = 0, \quad (3.68)$$

where $\beta = df/dy$. A linearized version of (3.68) is obtained by letting $u = \bar{u} + u' = -\frac{1}{f_0} \frac{\partial \bar{\Phi}}{\partial y} - \frac{1}{f_0} \frac{\partial \Phi'}{\partial y}$, $v = \bar{v} + v' = v' = \frac{1}{f_0} \frac{\partial \Phi'}{\partial x}$, $\zeta = -\partial \bar{u} / \partial y$, $\zeta' = \frac{1}{f_0} \nabla_h^2 \Phi'$, and neglecting products of perturbations:

$$\left(\frac{\partial}{\partial t} + \bar{u} \frac{\partial}{\partial x} \right) \nabla_h^2 \Phi' + \frac{\partial \Phi'}{\partial x} \left(\beta - \frac{\partial^2 \bar{u}}{\partial y^2} \right) = 0. \quad (3.69)$$

Next we impose a Φ' with a wavelike structure²¹ given by

$$\Phi' = \hat{\Phi}(y) e^{ik(x-ct)}, \quad (3.70)$$

where k is the zonal wavenumber ($=2\pi/\lambda_x$, where λ_x is the zonal wavelength) of the geopotential perturbations that are introduced, $\hat{\Phi}(y)$ is the complex amplitude of the geopotential perturbation, and the phase speed of the wavy disturbance, $c = c_r + i c_i$, is also complex. Instability is present when c has an imaginary part, that is, when $c_i \neq 0$ such that there is exponential growth of the disturbance in time. Substituting (3.70) into (3.69) and rearranging terms leads to

$$\frac{\partial^2 \Phi'}{\partial y^2} - k^2 \Phi' + \frac{\left(\beta - \frac{\partial^2 \bar{u}}{\partial y^2} \right)}{\bar{u} - c} \Phi' = 0. \quad (3.71)$$

For the case of $\beta = 0$, (3.71) is known as the *Rayleigh equation*, which is well known in the field of fluid dynamics as a form of the *Orr–Sommerfeld equation*, for the case of infinite Reynolds number.

Again, we are interested in distributions of vorticity that are unstable to small (and wavelike) perturbations. We integrate (3.71) from $y = -L$ to $y = L$ and look for the vorticity distributions that are associated with $c_i \neq 0$. Before integrating, it will be helpful to multiply (3.71) by Φ'^* , the complex conjugate of Φ' , where $\Phi' = \Phi'_r + i\Phi'_i$ and $\Phi'^* = \Phi'_r - i\Phi'_i$. (Note that $\Phi'\Phi'^* = |\Phi'|^2 = \Phi'^2_r + \Phi'^2_i$.) If we assume that $v = 0$ at the boundaries, then the appropriate boundary conditions are $\Phi' = \Phi'^* = 0$ at $y = -L$ and

²¹ Waveform solutions are discussed in greater detail in Chapter 6, which deals with gravity waves.

$y = L$. Multiplying (3.71) by Φ'^* and integrating over y yields

$$\int_{-L}^L \Phi'^* \frac{\partial^2 \Phi'}{\partial y^2} dy - \int_{-L}^L k^2 \Phi' \Phi'^* dy + \int_{-L}^L \Phi' \Phi'^* \frac{\left(\beta - \frac{\partial^2 \bar{u}}{\partial y^2} \right)}{\bar{u} - c} dy = 0. \quad (3.72)$$

Given that, via integration by parts,

$$\begin{aligned} \int_{-L}^L \Phi'^* \frac{\partial^2 \Phi'}{\partial y^2} dy &= \left[\Phi'^* \frac{\partial \Phi'}{\partial y} \right]_{-L}^L - \int_{-L}^L \frac{\partial \Phi'^*}{\partial y} \frac{\partial \Phi'}{\partial y} dy \\ &= - \int_{-L}^L \left| \frac{\partial \Phi'}{\partial y} \right|^2 dy, \end{aligned} \quad (3.73)$$

then (3.72) can be written as

$$\begin{aligned} - \int_{-L}^L \left[\left| \frac{\partial \Phi'}{\partial y} \right|^2 + k^2 |\Phi'|^2 \right] dy + \int_{-L}^L |\Phi'|^2 \frac{\left(\beta - \frac{\partial^2 \bar{u}}{\partial y^2} \right)}{\bar{u} - c} dy = 0. \end{aligned} \quad (3.74)$$

The real and imaginary parts of (3.74) must each equal zero. The imaginary part of (3.74) arises from the second term when c is complex. Given that $c = c_r + i c_i$, then

$$\frac{1}{\bar{u} - c} = \frac{\bar{u} - c^*}{\bar{u} - c^*} \frac{1}{\bar{u} - c} = \frac{\bar{u} - c_r + i c_i}{|\bar{u} - c|^2}, \quad (3.75)$$

where c^* is the complex conjugate of c . The imaginary part of (3.74) therefore can be written as

$$c_i \int_{-L}^L |\Phi'|^2 \frac{\left(\beta - \frac{\partial^2 \bar{u}}{\partial y^2} \right)}{|\bar{u} - c|^2} dy = 0. \quad (3.76)$$

If the base state flow is unstable (i.e., $c_i \neq 0$), then the only way (3.76) can be zero, which is required by (3.74), is if $\beta - \frac{\partial^2 \bar{u}}{\partial y^2}$ changes sign at least once in the open interval $-L \leq y \leq L$. In other words, instability is present when there is a relative maximum in the base state absolute vorticity, $f - \frac{\partial \bar{u}}{\partial y} = f + \bar{\zeta}$. This instability is known as *barotropic instability*. Although (3.76) would not suggest a favored latitude, one might expect that barotropic instability would tend to be more important in the tropics and at high latitudes because baroclinic instability tends

to dominate in midlatitudes where the meridional temperature gradient is maximized. Furthermore, \bar{u} tends to be a maximum in midlatitudes, therefore $\frac{\partial^2 \bar{u}}{\partial y^2}$ tends to be negative in midlatitudes and $\beta - \frac{\partial^2 \bar{u}}{\partial y^2}$ tends to everywhere positive in midlatitudes rather than changing sign. Barotropic instability is believed to play a role in the growth of disturbances south of the core of the African easterly jet. The disturbances propagate westward and can form easterly waves over the Atlantic Ocean, some of which develop into tropical cyclones. Of course, surface heat fluxes and feedbacks between latent heat release and the low-level pressure and wind fields also play a critical role in the genesis of tropical cyclones.

When β is negligible compared with $\frac{\partial^2 \bar{u}}{\partial y^2}$, as is typically the case on the mesoscale, the instability is present when $\frac{\partial^2 \bar{u}}{\partial y^2}$ changes sign, that is, when an inflection point is present in the \bar{u} profile. The requirement of an inflection point is known as *Rayleigh's stability criterion*. It is a necessary but insufficient condition for instability. Fjørtoft later derived a more stringent condition for instability: $\frac{\partial^2 \bar{u}}{\partial y^2}(\bar{u} - \bar{u}_I)$ must be less than zero somewhere in the flow, where \bar{u}_I is the base state zonal wind at the inflection point.²² Fjørtoft's instability criterion requires that the relative maximum in vorticity be away from the boundaries in order for instability to be present (Figure 3.20).

The requirement that the \bar{u} profile has an inflection point is a condition that is commonly satisfied along an interface separating two air masses having different horizontal wind velocities. For a finite-width shear zone, it has been shown theoretically that the spacing between the vortices that result from the manifestation of the inflection-point instability should be approximately 7.5 times the width of the shear zone. Obviously there is nothing special about having a horizontal mean flow. If $\bar{u} = \bar{u}(z)$ and the flow is neutrally stratified ($N^2 = 0$) such that vertical displacements of air are not subjected to a buoyancy force, then the exact same instability criterion applies; i.e., a vertical wind profile having an inflection point (away from the ground, per Fjørtoft's criterion) is unstable. However, if the base state is stably stratified ($N^2 > 0$), then the destabilizing effects of the wind shear must overcome the stabilizing effects of the stratification if instability is to be achieved. This problem is treated in the next section.

3.5.2 Kelvin–Helmholtz instability

Kelvin–Helmholtz instability is similar to horizontal shear instability except that a stable stratification has a

²² See Fjørtoft (1950).

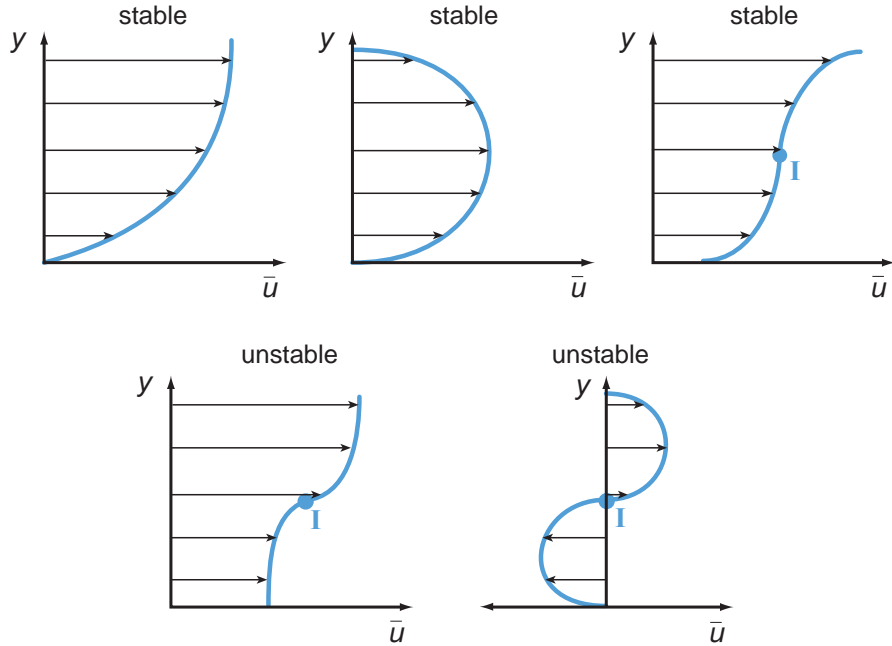


Figure 3.20 Horizontal wind profiles stable and unstable to small perturbations. Inflection points in the wind profiles are denoted with the letter 'I.' (Adapted from Kundu and Cohen [2008].)

suppressing effect on the instability. It was studied extensively by Lord Kelvin and Helmholtz as early as the 1860s. Although Kelvin and Helmholtz only investigated the case of two layers of fluid having different densities, vertical shear instability arising in environments with continuous stratification is also referred to as Kelvin–Helmholtz instability. Kelvin–Helmholtz instability is probably the generating mechanism for much of the gravity wave activity and turbulence in the atmosphere.

We derive a necessary condition for Kelvin–Helmholtz instability below.²³ Consider the linearized, inviscid, Boussinesq, zonal and vertical momentum equations given by

$$\frac{\partial u'}{\partial t} + \bar{u} \frac{\partial u'}{\partial x} + w' \frac{\partial \bar{u}}{\partial z} = -\frac{1}{\rho_0} \frac{\partial p'}{\partial x} \quad (3.77)$$

$$\frac{\partial w'}{\partial t} + \bar{u} \frac{\partial w'}{\partial x} = -\frac{1}{\rho_0} \frac{\partial p'}{\partial z} + g \frac{\theta'}{\bar{\theta}}, \quad (3.78)$$

where $u = \bar{u}(z) + u'$, $w = w'$, $p = \bar{p}(z) + p'$, $\theta = \bar{\theta}(z) + \theta'$, and ρ_0 is a reference density.

Assuming $d\theta/dt = 0$, the linearized thermodynamic equation is

$$\frac{\partial \theta'}{\partial t} + \bar{u} \frac{\partial \theta'}{\partial x} + w' \frac{\partial \bar{\theta}}{\partial z} = 0, \quad (3.79)$$

which can be written as

$$\frac{\partial \theta'}{\partial t} + \bar{u} \frac{\partial \theta'}{\partial x} + w' \frac{\bar{\theta} N^2}{g} = 0, \quad (3.80)$$

where $N^2 = \frac{g}{\bar{\theta}} \frac{\partial \bar{\theta}}{\partial z}$. We can reduce the complexity of the problem by introducing a perturbation streamfunction ψ' , such that $u' = \partial \psi'/\partial z$ and $w' = -\partial \psi'/\partial x$. The momentum and thermodynamic equations given by (3.77), (3.78), and (3.80) then become

$$\frac{\partial^2 \psi'}{\partial z \partial t} + \frac{\partial^2 \psi'}{\partial x \partial z} \bar{u} - \frac{\partial \psi'}{\partial x} \frac{\partial \bar{u}}{\partial z} = -\frac{1}{\rho_0} \frac{\partial p'}{\partial x} \quad (3.81)$$

$$-\frac{\partial^2 \psi'}{\partial x \partial t} - \frac{\partial^2 \psi'}{\partial x^2} \bar{u} = -\frac{1}{\rho_0} \frac{\partial p'}{\partial z} + g \frac{\theta'}{\bar{\theta}} \quad (3.82)$$

$$\frac{\partial \theta'}{\partial t} + \bar{u} \frac{\partial \theta'}{\partial x} - \frac{\bar{\theta} N^2}{g} \frac{\partial \psi'}{\partial x} = 0. \quad (3.83)$$

²³ Our derivation closely follows that of Howard (1961) and Kundu and Cohen (2008).

The coefficients of (3.81)–(3.83) are independent of x and t , which permits us to assume solutions of the form

$$[\theta', p', \psi'] = [\hat{\theta}(z), \hat{p}(z), \hat{\psi}(z)] e^{ik(x-ct)}, \quad (3.84)$$

where $\hat{\theta}$, \hat{p} , and $\hat{\psi}$ are complex amplitudes and $c = c_r + i c_i$ also can be complex. As was the case in Section 3.5.1, the solution is unstable if there exists $c_i \neq 0$. Substituting (3.84) into (3.81)–(3.83) gives

$$(\bar{u} - c) \frac{\partial \hat{\psi}}{\partial z} - \frac{\partial \bar{u}}{\partial z} \hat{\psi} = -\frac{\hat{p}}{\rho_0} \quad (3.85)$$

$$k^2(\bar{u} - c)\hat{\psi} = -\frac{1}{\rho_0} \frac{\partial \hat{p}}{\partial z} + g \frac{\hat{\theta}}{\theta} \quad (3.86)$$

$$(\bar{u} - c)\hat{\theta} - \frac{\bar{\theta}N^2}{g}\hat{\psi} = 0. \quad (3.87)$$

We can eliminate \hat{p} by subtracting (3.86) from $\partial(3.85)/\partial z$, and (3.87) can be used subsequently to eliminate $\hat{\theta}$. The resulting single equation for $\hat{\psi}$ is then

$$(\bar{u} - c) \left(\frac{\partial^2}{\partial z^2} - k^2 \right) \hat{\psi} - \frac{\partial^2 \bar{u}}{\partial z^2} \hat{\psi} + \frac{N^2}{\bar{u} - c} \hat{\psi} = 0. \quad (3.88)$$

Equation (3.88) is a form of the widely known *Taylor–Goldstein equation*. It can be rewritten in what will later be a somewhat more useful form as

$$\begin{aligned} \frac{\partial}{\partial z} & \left[(\bar{u} - c) \frac{\partial \xi}{\partial z} \right] - \left[k^2(\bar{u} - c) + \frac{1}{2} \frac{\partial^2 \bar{u}}{\partial z^2} \right. \\ & \left. + \frac{\frac{1}{4} \left(\frac{\partial \bar{u}}{\partial z} \right)^2 - N^2}{\bar{u} - c} \right] \xi = 0, \end{aligned} \quad (3.89)$$

where $\xi \equiv \hat{\psi}(\bar{u} - c)^{-1/2}$. Following a similar approach as in Section 3.5.1, we multiply (3.89) by ξ^* , the complex conjugate of ξ , and integrate from $z = -H$ to $z = H$. The boundary conditions are $\xi(-H) = \xi(H) = 0$, which imply that $\hat{\psi}(-H) = \hat{\psi}(H) = 0$, which is consistent with assuming that $w'(-H) = w'(H) = 0$ because $w' = -\partial \psi'/\partial x = -ik\hat{\psi}e^{ik(x-ct)}$.

Completing the aforementioned operations leads to

$$\begin{aligned} \int_{-H}^H & (\bar{u} - c) \left(\left| \frac{\partial \xi}{\partial z} \right|^2 + k^2 |\xi|^2 \right) dz + \frac{1}{2} \int_{-H}^H \frac{\partial^2 \bar{u}}{\partial z^2} |\xi|^2 dz \\ & = \int_{-H}^H \frac{N^2 - \frac{1}{4} \left(\frac{\partial \bar{u}}{\partial z} \right)^2}{\bar{u} - c} |\xi|^2 dz. \end{aligned} \quad (3.90)$$

The second term on the lhs of (3.90) is real, but the other two terms in (3.90) have imaginary parts. With the aid of

(3.75), the imaginary part of (3.90) can be written as

$$\begin{aligned} & -c_i \int_{-H}^H \left(\left| \frac{\partial \xi}{\partial z} \right|^2 + k^2 |\xi|^2 \right) dz \\ & = c_i \int_{-H}^H \frac{N^2 - \frac{1}{4} \left(\frac{\partial \bar{u}}{\partial z} \right)^2}{|\bar{u} - c|^2} |\xi|^2 dz. \end{aligned} \quad (3.91)$$

If the mean state is such that $N^2 > \frac{1}{4} \left(\frac{\partial \bar{u}}{\partial z} \right)^2$ everywhere over the interval $-H \leq z \leq H$, then (3.91) implies that the product of c_i and a positive quantity (on the rhs) equals the product of $-c_i$ and a positive quantity (on the lhs; the integral on the lhs is positive definite). This requires that $c_i = 0$, which implies stability. Thus stability is guaranteed if $Ri > 0.25$ everywhere over the interval $-H \leq z \leq H$, where $Ri \equiv N^2 / \left(\frac{\partial \bar{u}}{\partial z} \right)^2$ is the *gradient Richardson number* or *Richardson number*.

Note that the presence of $Ri < 0.25$ somewhere in the flow is a necessary but insufficient condition for instability. In fact, in laboratory experiments the critical Richardson number is often less than 0.25, depending on the boundaries and specific profiles of $\bar{u}(z)$ and $N(z)$. Nonetheless, the $Ri < 0.25$ condition for instability matches quite well with the conditions for which the onset of instability is observed.

Perhaps curiously, an inflection point in the vertical wind profile is not required, in contrast to the stability requirement for horizontal shear instability; e.g., a linear profile of $\bar{u}(z)$ can be unstable. If $N^2 = 0$ and $\beta = 0$, it is obvious that (3.88) takes the form of (3.71), with the difference being $\partial^2/\partial z^2$ instead of $\partial^2/\partial y^2$. Thus, when $N^2 = 0$, instability requires an inflection point in the $\bar{u}(z)$ profile, even though $Ri = 0 < 0.25$. The Richardson number criterion is derived from (3.88), but in the case of $N^2 = 0$ we do not obtain (3.88) in the first place. When $N^2 = 0$, there can be no nonzero θ' , which is inconsistent with the assumed form of θ' given by (3.84) used to derive (3.88). The physical explanation for why an inflection point is needed when $N^2 = Ri = 0$, but not when $N^2 > 0$ and $Ri < 0.25$, is that buoyancy oscillations (present when $N^2 > 0$) play an important part in the development of Kelvin–Helmholtz instability, such that they eliminate the inflection point requirement.

Another approach to determining the instability criterion is to consider the energetics involved in the exchange of two parcels of air. This approach has been presented by Chandrasekhar (1961), Lilly (1986), and Kundu and Cohen (2008). Suppose we have two parcels at heights z_0 and $z_0 + \Delta z$ in a horizontal airflow containing vertical wind shear (Figure 3.21). The parcel at z_0 is moving at a slower speed, $\bar{u} = u_0$, than the parcel at $z_0 + \Delta z$, which is moving at $u_0 +$

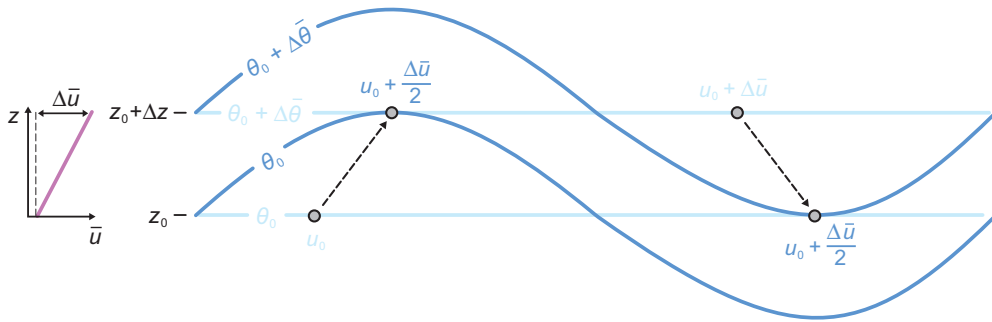


Figure 3.21 An alternative approach to deriving a necessary condition for Kelvin–Helmholtz instability is to examine the energetics involved in the exchange of two parcels of air separated by Δz when the potential temperature surfaces are perturbed in a wavelike manner (light (dark) blue potential temperature surfaces are before (after) the surfaces are perturbed). The vertical profile of mean zonal wind speed (\bar{u}) contains vertical shear (the \bar{u} profile is shown on the far left), and the vertical profile of mean potential temperature ($\bar{\theta}$) is stably stratified. It is assumed that potential temperature is conserved during the exchange. Zonal momentum, however, is not conserved; it is assumed that both parcels have a zonal wind speed of $u_0 + \Delta\bar{u}/2$ after the exchange.

Δu . (The overbars are used to indicate variables that characterize the state of the environment, as was the case in Section 13.1.) We shall also assume a stable stratification such that potential temperature increases with height; the parcel at height z_0 has a potential temperature of $\bar{\theta} = \theta_0$, and the parcel at $z_0 + \Delta z$ has a potential temperature of $\theta_0 + \Delta\theta$.

Next, we interchange the two parcels (we are investigating overturning between two air streams; if a parcel at z_0 rises to $z_0 + \Delta z$, then mass continuity requires that another parcel sink from $z_0 + \Delta z$ to z_0). The exchange of the two parcels requires energy; that is, work must be done against the stratification if the atmosphere is statically stable and this work is equal to the increase in potential energy. The energy comes from the mean wind field as shear is removed by the exchange, leaving a final wind profile with decreased kinetic energy. The total energy (kinetic plus potential energy, both from the mean state and the perturbations) is conserved in the exchange. If more kinetic energy is available from the mean state than is needed to do work against the stratification in exchanging the two air parcels, then the flow is said to be unstable.

First we must calculate the work needed to exchange the parcels. The work required to lift a parcel from z_0 to $z_0 + \Delta z$ (W_{\uparrow}) is just the negative buoyancy ($B = g\theta'/\bar{\theta}$ assumed, where $\theta' = \theta - \bar{\theta}$) integrated from z_0 to $z_0 + \Delta z$, that is,

$$W_{\uparrow} = - \int_{z_0}^{z_0 + \Delta z} B dz = -g \int_{z_0}^{z_0 + \Delta z} \frac{\theta - \bar{\theta}}{\bar{\theta}} dz, \quad (3.92)$$

where θ is the potential temperature of the parcel being moved from z_0 to $z_0 + \Delta z$ and $\bar{\theta}$ is the potential temperature

of the environment. The work can be represented graphically on a thermodynamic diagram as being proportional to the negative area if the denominator in the integral is replaced with its average value in the layer, $\langle \bar{\theta} \rangle$

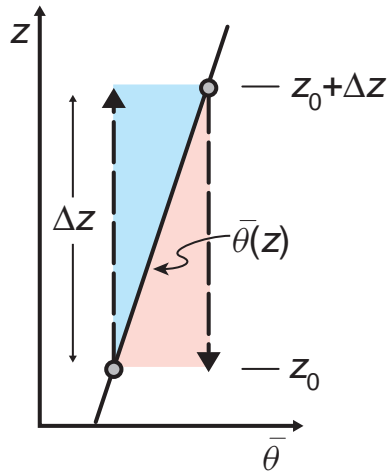


Figure 3.22 Graphical representation of the amount of work required to lift a parcel from z_0 to $z_0 + \Delta z$ (blue) and to force a parcel to sink from $z_0 + \Delta z$ to z_0 (red) in a stable stratification. The environmental potential temperature ($\bar{\theta}$) profile is the solid black line. The dashed lines are the parcel paths on the thermodynamic diagram assuming that the vertical excursions are dry adiabatic.

(Figure 3.22). Letting $\theta = \theta_0$ (assuming that θ is conserved and is equal to θ_0 at z_0) and $\bar{\theta} = \theta_0 + \frac{\partial\theta}{\partial z}(z - z_0)$ gives

$$W_{\uparrow} = -g \int_{z_0}^{z_0+\Delta z} \frac{\theta_0 - \theta_0 - \frac{\partial\bar{\theta}}{\partial z}(z - z_0)}{\theta_0 + \frac{\partial\bar{\theta}}{\partial z}(z - z_0)} dz \quad (3.93)$$

$$= \frac{g}{\langle \bar{\theta} \rangle} \frac{\partial \bar{\theta}}{\partial z} \int_{z_0}^{z_0+\Delta z} (z - z_0) dz, \quad (3.94)$$

where it has been assumed that $\bar{\theta}$ varies linearly with height (i.e., $\partial\bar{\theta}/\partial z$ is a constant). Evaluation of (3.94) gives

$$W_{\uparrow} = \frac{1}{2} \frac{g}{\langle \bar{\theta} \rangle} \frac{\partial \bar{\theta}}{\partial z} (\Delta z)^2 = \frac{1}{2} \frac{g}{\langle \bar{\theta} \rangle} \Delta \bar{\theta} \Delta z, \quad (3.95)$$

where $\Delta \bar{\theta}$ is the potential temperature difference over the vertical distance Δz (Figure 3.21). But thus far we have only considered the work required to lift a parcel from z_0 to $z_0 + \Delta z$. The work required to force a second air parcel to sink from $z_0 + \Delta z$ to z_0 (W_{\downarrow}) is exactly equal to the amount required to lift a parcel over the same distance (Figure 3.22); that is, the total work, W , is

$$W = W_{\downarrow} + W_{\uparrow} = \frac{g}{\langle \bar{\theta} \rangle} \Delta \bar{\theta} \Delta z. \quad (3.96)$$

Equation (3.96) reveals, rather intuitively, that the total work required to exchange the air parcels increases as Δz and $\Delta \theta$ increase.

Now that the amount of work to be done against the stratification has been evaluated, the next step is to ascertain the kinetic energy lost in the exchange, that is, the energy available to do work, which is given by

$$\Delta KE = KE_f - KE_i, \quad (3.97)$$

where the f and i subscripts identify the final and initial states, respectively. The kinetic energy of each parcel changes during the exchange because the parcels are accelerated or decelerated as they join the new air stream above or below their initial level. As stated earlier, if the kinetic energy available for the exchange exceeds the work required for the exchange, then the flow is said to be unstable.

The total kinetic energy before the exchange per unit mass is

$$KE_i = \frac{1}{2} u_0^2 + \frac{1}{2} (u_0 + \Delta \bar{u})^2, \quad (3.98)$$

where $\frac{1}{2} u_0^2$ is the kinetic energy of the parcel initially at z_0 , and $\frac{1}{2} (u_0 + \Delta \bar{u})^2$ is the kinetic energy of the parcel initially at $z_0 + \Delta z$.

Obtaining the total kinetic energy per unit mass after the exchange requires some hand-waving. If we assume that each air parcel acquires the mean wind speed over the layer extending from z_0 to $z_0 + \Delta z$ (in essence, the shear is removed over the layer), then

$$KE_f = \frac{1}{2} \left(u_0 + \frac{\Delta \bar{u}}{2} \right)^2 + \frac{1}{2} \left(u_0 + \frac{\Delta \bar{u}}{2} \right)^2$$

$$= \left(u_0 + \frac{\Delta \bar{u}}{2} \right)^2, \quad (3.99)$$

where $\frac{1}{2} (u_0 + \frac{\Delta \bar{u}}{2})^2$ is the kinetic energy of each of the two parcels after the exchange. The change in kinetic energy per unit mass available for the exchange is therefore obtained by subtracting (3.98) from (3.99),

$$\Delta KE = KE_f - KE_i = -\frac{1}{4} (\Delta \bar{u})^2. \quad (3.100)$$

Note that kinetic energy is always lost by the exchange.

The instability criterion for Kelvin-Helmholtz instability is that the magnitude of the kinetic energy available for the exchange exceeds the work required for the exchange, i.e.,

$$-\Delta KE > W. \quad (3.101)$$

From (3.96) and (3.100),

$$\frac{1}{4} (\Delta \bar{u})^2 > \frac{g}{\langle \bar{\theta} \rangle} \Delta \bar{\theta} \Delta z \quad (3.102)$$

$$\frac{g}{\langle \bar{\theta} \rangle} \frac{\Delta \bar{\theta} \Delta z}{(\Delta \bar{u})^2} < \frac{1}{4}. \quad (3.103)$$

For the linear profiles of \bar{u} and $\bar{\theta}$ assumed, (3.103) becomes

$$\frac{g}{\langle \bar{\theta} \rangle} \frac{\frac{\partial \bar{\theta}}{\partial z}}{\left(\frac{\partial \bar{u}}{\partial z} \right)^2} < \frac{1}{4} \quad (3.104)$$

$$Ri < \frac{1}{4} \quad (3.105)$$

where Ri is the Richardson number.

The earlier assumption that, after the exchange, each air parcel acquires the mean wind speed over the layer extending from z_0 to $z_0 + \Delta z$ results in the maximum available kinetic energy in (3.100) without changing the total momentum. In contrast, for the other two

extremes—(i) both parcels accelerate/decelerate to a speed that matches the environmental wind at the new levels attained by the parcels, or (ii) neither parcel accelerates/decelerates at all during the exchange—the change in kinetic energy is zero. Thus, the instability criterion for Kelvin–Helmholtz instability could actually be stricter than that indicated by (3.105). Furthermore, as also mentioned after the instability analysis involving the Taylor–Goldstein equation, (3.105) should really be regarded as a minimum criterion for Kelvin–Helmholtz instability. Nonetheless, the prediction by (3.105) does seem to fit observations reasonably well and agree with more rigorous theoretical analyses.

Further reading

Buoyancy and gravitational convection

- Bretherton, C. S., and P. K. Smolarkiewicz, 1989: Gravity waves, compensating subsidence and detrainment around cumulus clouds. *J. Atmos. Sci.*, **46**, 740–759.
- Bryan, G. H., and J. M. Fritsch, 2000: Moist absolute instability: The sixth static stability state. *Bull. Amer. Meteor. Soc.*, **81**, 1207–1230.
- Darkow, G. L., 1986: Basic thunderstorm energetics and thermodynamics. *Thunderstorm Morphology and Dynamics*, E. Kessler, Ed., 2d ed., University of Oklahoma Press, 59–73.
- Das, P., 1979: A non-Archimedian approach to the equations of convection dynamics. *J. Atmos. Sci.*, **36**, 2183–2190.
- Davies-Jones, R., 2003: An expression for effective buoyancy in surroundings with horizontal density gradients. *J. Atmos. Sci.*, **60**, 2922–2925.
- Doswell, C. A., and P. M. Markowski, 2004: Is buoyancy a relative quantity? *Mon. Wea. Rev.*, **132**, 853–863.
- Schultz *et al.* (2000).
- Sherwood (2000).
- Warner, J., 1970: On steady-state one-dimensional models of cumulus convection. *J. Atmos. Sci.*, **27**, 1035–1040.

Inertial and symmetric instability

- Bennetts, D. A., and B. J. Hoskins, 1979: Conditional symmetric instability—A possible explanation for frontal rainbands. *Quart. J. Roy. Meteor. Soc.*, **105**, 945–962.
- Bennetts, D. A., and J. C. Sharp, 1982: The relevance of conditional symmetric instability to the prediction of mesoscale frontal rainbands. *Quart. J. Roy. Meteor. Soc.*, **108**, 595–602.
- Blanchard, D. O., W. R. Cotton, and J. M. Brown, 1998: Mesoscale circulation growth under conditions of weak inertial instability. *Mon. Wea. Rev.*, **126**, 118–140.

- Emanuel, K. A., 1979: Inertial instability and mesoscale convective systems. Part I: Linear theory of inertial instability in rotating viscous fluids. *J. Atmos. Sci.*, **36**, 2425–2449.
- Emanuel, K. A., 1983a: The Lagrangian parcel dynamics of moist symmetric stability. *J. Atmos. Sci.*, **40**, 2368–2376.
- Emanuel, K. A., 1983b: On assessing local conditional symmetric instability from atmospheric soundings. *Mon. Wea. Rev.*, **111**, 2016–2033.
- Emanuel, K. A., 1983c: Conditional symmetric instability: A theory for rainbands within extratropical cyclones. *Mesoscale Meteorology—Theories, Observations and Models*, D. K. Lilly and T. Gal-Chen, Eds., Reidel, 231–245.
- Emanuel, K. A., 1988: Observational evidence of slantwise convective adjustment. *Mon. Wea. Rev.*, **116**, 1805–1816.
- Jones, S. C., and A. J. Thorpe, 1992: The three-dimensional nature of ‘symmetric’ instability. *Quart. J. Roy. Meteor. Soc.*, **118**, 227–258.
- Knox, J. A., 2003: Inertial instability. *Encyclopedia of the Atmospheric Sciences*, J. Holton, J. Pyle, and J. Curry, Eds., Academic Press, 1004–1013.
- Novak, D. R., L. F. Bosart, D. Keyser, and J. S. Waldstreicher, 2004: An observational study of cold season-banded precipitation in northeast U.S. cyclones. *Wea. Forecasting*, **19**, 993–1010.
- Novak, D. R., J. S. Waldstreicher, D. Keyser, and L. F. Bosart, 2006: A forecast strategy for anticipating cold season mesoscale band formation within eastern U.S. cyclones. *Wea. Forecasting*, **21**, 3–23.
- Schultz and Knox (2007).
- Schultz, D. M., and P. N. Schumacher, 1999: The use and misuse of conditional symmetric instability. *Mon. Wea. Rev.*, **127**, 2709–2732, Corrigendum, **128**, 1573.
- Stevens, D. E., and P. E. Ciesielski, 1986: Inertial instability of horizontally sheared flow away from the equator. *J. Atmos. Sci.*, **43**, 2845–2856.
- Thorpe, A. J., and K. A. Emanuel, 1985: Frontogenesis in the presence of small stability to slantwise convection. *J. Atmos. Sci.*, **42**, 1809–1824.
- Xu, Q., 1992: Formation and evolution of frontal rainbands and geostrophic PV anomalies. *J. Atmos. Sci.*, **49**, 629–648.
- Xu, Q., and J. H. E. Clark, 1985: The nature of symmetric instability and its similarity to convective and inertial instability. *J. Atmos. Sci.*, **42**, 2880–2883.

Shear instability

- Batchelor, G. K., 1967: *An Introduction to Fluid Dynamics*. Cambridge University Press.
- Brown (1972b).
- Chandrasekhar (1961).

- Drazin, P. G., and W. H. Reid, 2004: *Hydrodynamic Stability*, 2nd edn. Cambridge University Press.
- Howard (1961).
- Kundu and Cohen (2008).
- Kuo, H. L., 1949: Dynamic instability of two-dimensional nondivergent flow in a barotropic atmosphere. *J. Meteor.*, **6**, 105–122.
- Lilly (1986).
- Lin (1945).
- Miles, J. W., 1961: On the stability of heterogeneous shear flows. *J. Fluid Mech.*, **10**, 496–508.
- Miles, J. W., 1986: Richardson's criterion for the stability of stratified flow. *Phys. Fluids*, **29**, 3470–3471.
- Miles, J. W., and L. N. Howard, 1964: Note on heterogeneous shear flow. *J. Fluid Mech.*, **20**, 331–335.

PART II

Lower Tropospheric Mesoscale Phenomena

4

The Boundary Layer

The *boundary layer* is the bottom portion of the troposphere which is strongly influenced by the exchange of momentum, heat, and moisture with the earth's surface. This layer also is commonly referred to as the *atmospheric boundary layer* (ABL) or the *planetary boundary layer* (PBL).¹ The boundary layer flow is dominated by *turbulent eddies* (Figure 4.1) that are the result of surface heating and vertical wind shear. The effects of turbulent eddies often can be safely ignored in the overlying free atmosphere, which does not feel the influences of the surface directly (some noteworthy exceptions are in the vicinity of convective clouds and within sharp frontal zones). In the boundary layer, however, the transfer of momentum, heat, and moisture by eddies must be accounted for in the dynamical equations if we wish to have a realistic portrayal of the evolution of temperature and moisture fields and the relationship between the pressure gradient and wind.

The effects of molecular diffusion, at least above the lowest few millimeters of the boundary layer, where conduction between the air and the ground is important (sometimes called the *viscous sublayer* or *microlayer*), are negligible compared with the mixing effects of turbulent eddies. Having said this, it is important to recognize that, by virtue of molecular viscosity and the fact that the air velocity must vanish at the surface, large vertical wind shear is achieved very near the ground, even when winds are light, and this shear plays a critical role in the generation of mechanically driven turbulent eddies that transfer momentum, heat, and moisture to the lower

boundary layer. Thus, even though molecular viscosity does not directly influence boundary layer motions above a few centimeters, its influence in this thin layer is crucial for the formation of the ubiquitous turbulent eddies that are responsible for mixing throughout the boundary layer. Stated another way, without a surface, where molecular effects are important, there would be no boundary layer!

Before considering the structure and evolution of the boundary layer, it is important to introduce the method by which turbulent motions will be accounted for in the dynamical equations. This method is known as *Reynolds averaging*, and it will lead to the concept of turbulent fluxes, which will be essential in developing an understanding of the morphology and behavior of the boundary layer.

4.1 The nature of turbulent fluxes

4.1.1 Reynolds-averaged equations

Consider two variables χ and ψ . Let us define each variable as comprising a slowly varying mean, $\bar{\chi}$ and $\bar{\psi}$, and a much more rapidly fluctuating perturbation associated with an eddy, χ' and ψ' , respectively:

$$\chi = \bar{\chi} + \chi' \quad (4.1)$$

$$\psi = \bar{\psi} + \psi'. \quad (4.2)$$

The $\overline{(\cdot)}$ operator indicates an average in time or space, for example,

$$\bar{\chi} = \frac{1}{N} \sum_{i=1}^N \chi_i, \quad (4.3)$$

¹ Undergraduate and graduate curricula often devote entire semesters to the boundary layer. For a more comprehensive presentation of the boundary layer, the reader is referred to the textbooks written by Stull (1988), Sorbjan (1989), Garratt (1994), and Arya (2001).

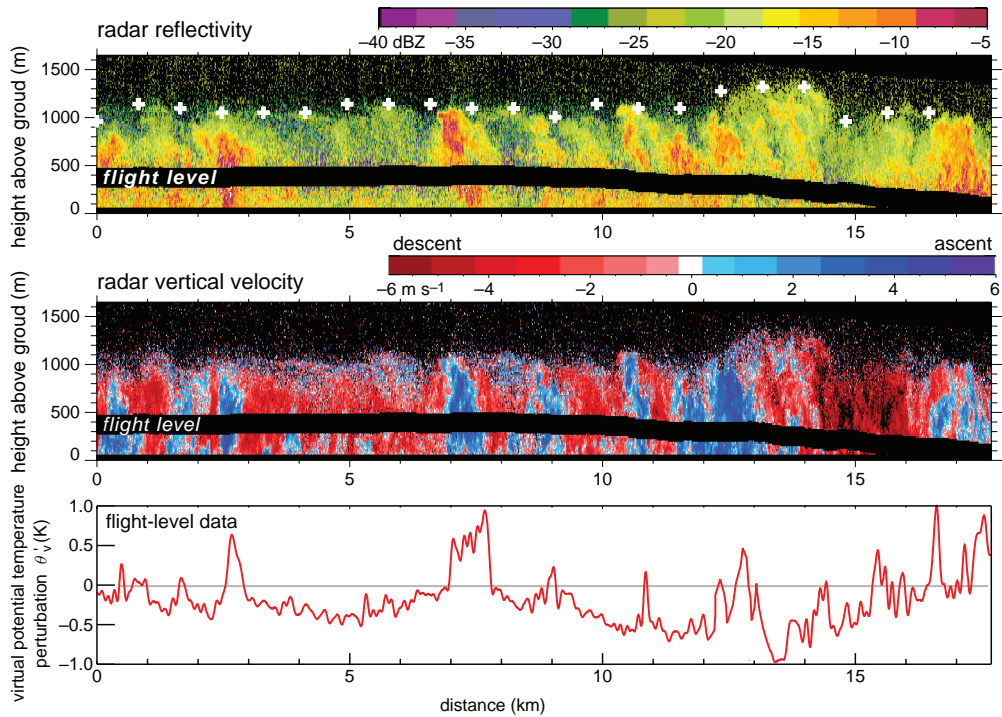


Figure 4.1 Vertical cross-sections of reflectivity (top) and vertical velocity (middle) obtained by a vertically pointing, airborne cloud radar (95 GHz) traveling through a daytime convective boundary layer in northwestern Oklahoma. One minute corresponds to roughly 5 km, so the aspect ratio of both images is about 2:1. White crosses in the top panel indicate the top of the boundary layer. The 200 m deep blind zone contains the aircraft track. The radar echo within the boundary layer is largely the result of insects. Virtual potential temperature perturbations (θ'_v) along the flight track are also shown (bottom). The turbulent nature of the boundary layer is obvious. (Courtesy of B. Geerts; adapted from Geerts and Miao [2005].)

where χ_i is the i th of N observations of χ .² By definition, the average fluctuation about the average must be zero, that is,

$$\bar{\chi}' = \bar{\psi}' = 0. \quad (4.4)$$

Furthermore, the product of a fluctuation with a mean also vanishes when the average is taken; that is,

$$\overline{\chi'\bar{\psi}} = \overline{\chi'}\overline{\bar{\psi}} = 0. \quad (4.5)$$

² Theoretically it is most desirable to define the mean as an *ensemble average* obtained from a large number of realizations of a variable over identical experiments. The ensemble average is rarely used in practice because of the obvious difficulty in repeating a large number of experiments in similar weather conditions. Thus, time and spatial averages are almost always relied upon instead. The time, spatial, and ensemble averages are equal if the turbulence is both homogeneous (the spatial averages do not depend on the direction of the averaging) and stationary (statistically not changing over time).

On the other hand, the average of the product of fluctuating components, called the *covariance*, generally does not vanish; that is,

$$\overline{\chi'\psi'} \neq 0. \quad (4.6)$$

As an example, $\overline{w'\theta'}$ is positive (i.e., w' and θ' are positively correlated) within a daytime convective boundary layer as a result of relatively warm thermals rising ($w' > 0$ when $\theta' > 0$) and relatively cold air sinking ($w' < 0$ when $\theta' < 0$).

In the case of the average of the product of χ and ψ we obtain

$$\begin{aligned} \overline{\chi\psi} &= \overline{(\bar{\chi} + \chi')(\bar{\psi} + \psi')} \\ &= \overline{\bar{\chi}\bar{\psi}} + \overline{\bar{\chi}\psi'} + \overline{\chi'\bar{\psi}} + \overline{\chi'\psi'} \\ &= \overline{\bar{\chi}\bar{\psi}} + \overline{\chi'\psi'} + \overline{\chi'\bar{\psi}} + \overline{\bar{\chi}\psi'} \\ &= \overline{\chi}\overline{\psi} + \overline{\chi'}\overline{\psi'}; \end{aligned} \quad (4.7)$$

that is, the average of the product of two variables is the product of the mean components of each variable plus the average of the product of the fluctuating components. Moreover, when the averaging is applied to a derivative quantity, for example, $\partial \chi / \partial x$, we use the rule $\overline{\partial \chi / \partial x} = \partial \overline{\chi} / \partial x$.

The technique of partitioning variables into mean and perturbation parts and then taking the average, as has been introduced above, is known as *Reynolds averaging*. Reynolds averaging is widely used as a statistical way to account for the effect of turbulent eddies on the mean field. Below we derive Reynolds-averaged momentum, thermodynamic, and moisture equations.

The momentum, thermodynamic, and moisture equations, neglecting the vertical component of the Coriolis force, and making the Boussinesq approximation, which is generally appropriate in the boundary layer, can be expressed as (refer to Chapter 2)

$$\frac{\partial u}{\partial t} = -u \frac{\partial u}{\partial x} - v \frac{\partial u}{\partial y} - w \frac{\partial u}{\partial z} - \frac{1}{\rho_0} \frac{\partial p}{\partial x} + fv + v \nabla^2 u \quad (4.8)$$

$$\frac{\partial v}{\partial t} = -u \frac{\partial v}{\partial x} - v \frac{\partial v}{\partial y} - w \frac{\partial v}{\partial z} - \frac{1}{\rho_0} \frac{\partial p}{\partial y} - fu + v \nabla^2 v \quad (4.9)$$

$$\begin{aligned} \frac{\partial w}{\partial t} = & -u \frac{\partial w}{\partial x} - v \frac{\partial w}{\partial y} - w \frac{\partial w}{\partial z} - \frac{1}{\rho_0} \frac{\partial p}{\partial z} \\ & -g - \frac{\rho'}{\rho_0} g + v \nabla^2 w \end{aligned} \quad (4.10)$$

$$\frac{\partial \theta}{\partial t} = -u \frac{\partial \theta}{\partial x} - v \frac{\partial \theta}{\partial y} - w \frac{\partial \theta}{\partial z} + \frac{q}{c_p} \frac{\theta}{T} + \kappa \nabla^2 \theta \quad (4.11)$$

$$\frac{\partial r_v}{\partial t} = -u \frac{\partial r_v}{\partial x} - v \frac{\partial r_v}{\partial y} - w \frac{\partial r_v}{\partial z} + E - C + \kappa_e \nabla^2 r_v. \quad (4.12)$$

In the above equations, v , κ , and κ_e are the kinematic viscosity, thermal diffusivity, and moisture diffusivity, respectively. The terms involving v , κ , and κ_e represent the effects of molecular diffusion (the terms involving v contributed to the F_u , F_v , F_w terms in (2.54)–(2.56)). In the vertical momentum equation (4.10), ρ' is a density departure from a hydrostatic reference profile of pressure (\bar{p}) and density ($\bar{\rho}$) such that $\frac{\partial \bar{p}}{\partial z} = -\bar{\rho}g$, where $p = \bar{p} + p'$ and $\rho = \bar{\rho} + \rho'$. In the Boussinesq approximation, the $-\frac{1}{\rho} \frac{\partial p'}{\partial z} - \frac{\rho'}{\rho} g$ terms in (2.76) become $-\frac{1}{\rho_0} \frac{\partial p'}{\partial z} - \frac{\rho'}{\rho_0} g$, which can also be written as $-\frac{1}{\rho_0} \frac{\partial p}{\partial z} - g - \frac{\rho'}{\rho_0} g$, as is done above in (4.10).³

³ The reason for writing the vertical momentum equation in this way is to avoid having to introduce either an unprimed density variable that represents a density departure from the hydrostatic base state (this could be potentially confusing because primes ordinarily indicate perturbations), or a double-primed density variable (a perturbation of

The Reynolds-averaged zonal wind equation will be derived first. By multiplying the Boussinesq continuity equation,

$$\frac{\partial u}{\partial x} + \frac{\partial v}{\partial y} + \frac{\partial w}{\partial z} = 0, \quad (4.13)$$

by u and adding the result to (4.8), and using the product rule, we can express (4.8) in *flux form* as

$$\frac{\partial u}{\partial t} = -\frac{\partial uu}{\partial x} - \frac{\partial uv}{\partial y} - \frac{\partial uw}{\partial z} - \frac{1}{\rho_0} \frac{\partial p}{\partial x} + fv + v \nabla^2 u. \quad (4.14)$$

Substituting $u = \bar{u} + u'$, $v = \bar{v} + v'$, $w = \bar{w} + w'$, and $p = \bar{p} + p'$ results in

$$\begin{aligned} \frac{\partial \bar{u}}{\partial t} + \frac{\partial u'}{\partial t} = & -\frac{\partial}{\partial x} (\bar{u} \bar{u} + \bar{u} u' + u' \bar{u} + u' u') \\ & -\frac{\partial}{\partial y} (\bar{u} \bar{v} + \bar{u} v' + u' \bar{v} + u' v') \\ & -\frac{\partial}{\partial z} (\bar{u} \bar{w} + \bar{u} w' + u' \bar{w} + u' w') \\ & -\frac{1}{\rho_0} \frac{\partial \bar{p}}{\partial x} - \frac{1}{\rho_0} \frac{\partial p'}{\partial x} + f \bar{v} + f v' \\ & + v \nabla^2 \bar{u} + v \nabla^2 u'. \end{aligned} \quad (4.15)$$

Taking the Reynolds average of (4.15) yields

$$\begin{aligned} \overline{\frac{\partial \bar{u}}{\partial t}} + \overline{\frac{\partial u'}{\partial t}} = & -\overline{\frac{\partial}{\partial x} (\bar{u} \bar{u} + \bar{u} u' + u' \bar{u} + u' u')} \\ & -\overline{\frac{\partial}{\partial y} (\bar{u} \bar{v} + \bar{u} v' + u' \bar{v} + u' v')} \\ & -\overline{\frac{\partial}{\partial z} (\bar{u} \bar{w} + \bar{u} w' + u' \bar{w} + u' w')} \\ & -\overline{\frac{1}{\rho_0} \frac{\partial \bar{p}}{\partial x}} - \overline{\frac{1}{\rho_0} \frac{\partial p'}{\partial x}} + \overline{f \bar{v}} + \overline{f v'} + \overline{v \nabla^2 \bar{u}} \\ & + \overline{v \nabla^2 u'}. \end{aligned} \quad (4.16)$$

Using the averaging rules given by (4.4), (4.5), and (4.7), we obtain

$$\begin{aligned} \frac{\partial \bar{u}}{\partial t} = & -\frac{\partial \bar{u} \bar{u}}{\partial x} - \frac{\partial \bar{u} \bar{v}}{\partial y} - \frac{\partial \bar{u} \bar{w}}{\partial z} - \frac{1}{\rho_0} \frac{\partial \bar{p}}{\partial x} + f \bar{v} + v \nabla^2 \bar{u} \\ & -\frac{\partial \bar{u}' u'}{\partial x} - \frac{\partial \bar{u}' v'}{\partial y} - \frac{\partial \bar{u}' w'}{\partial z}. \end{aligned} \quad (4.17)$$

the density departure), when a Reynolds-averaged vertical momentum equation is derived later.

Multiplying the Reynolds-averaged continuity equation (4.13),

$$\frac{\partial \bar{u}}{\partial x} + \frac{\partial \bar{v}}{\partial y} + \frac{\partial \bar{w}}{\partial z} = 0, \quad (4.18)$$

by \bar{u} and subtracting it from (4.17) yields the Reynolds-averaged zonal momentum equation,

$$\begin{aligned} \frac{\partial \bar{u}}{\partial t} &= -\bar{u} \frac{\partial \bar{u}}{\partial x} - \bar{v} \frac{\partial \bar{u}}{\partial y} - \bar{w} \frac{\partial \bar{u}}{\partial z} - \frac{1}{\rho_0} \frac{\partial \bar{p}}{\partial x} + f\bar{v} + v\nabla^2 \bar{u} \\ &\quad - \frac{\partial \bar{u}'\bar{u}'}{\partial x} - \frac{\partial \bar{u}'\bar{v}'}{\partial y} - \frac{\partial \bar{u}'\bar{w}'}{\partial z}. \end{aligned} \quad (4.19)$$

The prognostic equation for the mean zonal momentum given by (4.19) is identical to that for the full zonal momentum given by (4.8), except that the variables in (4.8) have been replaced by mean variables and three additional *flux divergence* terms appear: $\frac{\partial \bar{u}'\bar{u}'}{\partial x}$, $\frac{\partial \bar{u}'\bar{v}'}{\partial y}$, and $\frac{\partial \bar{u}'\bar{w}'}{\partial z}$.⁴ As mentioned before, the mean variables can represent averages in either time or space. Numerical models, for instance, use Reynolds-averaged equations in which the variables appearing in the model prognostic equations represent mean values in a grid volume.

Using the same approach as used to derive (4.19), the Reynolds-averaged meridional momentum, vertical momentum, thermodynamic, and moisture equations can be obtained from (4.9)–(4.12):

$$\begin{aligned} \frac{\partial \bar{v}}{\partial t} &= -\bar{u} \frac{\partial \bar{v}}{\partial x} - \bar{v} \frac{\partial \bar{v}}{\partial y} - \bar{w} \frac{\partial \bar{v}}{\partial z} - \frac{1}{\rho_0} \frac{\partial \bar{p}}{\partial y} - f\bar{u} + v\nabla^2 \bar{v} \\ &\quad - \frac{\partial \bar{u}'\bar{v}'}{\partial x} - \frac{\partial \bar{v}'\bar{v}'}{\partial y} - \frac{\partial \bar{v}'\bar{w}'}{\partial z} \end{aligned} \quad (4.20)$$

$$\begin{aligned} \frac{\partial \bar{w}}{\partial t} &= -\bar{u} \frac{\partial \bar{w}}{\partial x} - \bar{v} \frac{\partial \bar{w}}{\partial y} - \bar{w} \frac{\partial \bar{w}}{\partial z} - \frac{1}{\rho_0} \frac{\partial \bar{p}}{\partial z} - g + v\nabla^2 \bar{w} \\ &\quad - \frac{\partial \bar{u}'\bar{w}'}{\partial x} - \frac{\partial \bar{v}'\bar{w}'}{\partial y} - \frac{\partial \bar{w}'\bar{w}'}{\partial z} \end{aligned} \quad (4.21)$$

$$\begin{aligned} \frac{\partial \bar{\theta}}{\partial t} &= -\bar{u} \frac{\partial \bar{\theta}}{\partial x} - \bar{v} \frac{\partial \bar{\theta}}{\partial y} - \bar{w} \frac{\partial \bar{\theta}}{\partial z} + \frac{\bar{q}}{c_p} \frac{\bar{\theta}}{\bar{T}} + \kappa \nabla^2 \bar{\theta} \\ &\quad - \frac{\partial \bar{u}'\bar{\theta}'}{\partial x} - \frac{\partial \bar{v}'\bar{\theta}'}{\partial y} - \frac{\partial \bar{w}'\bar{\theta}'}{\partial z} \end{aligned} \quad (4.22)$$

$$\begin{aligned} \frac{\partial \bar{r}_v}{\partial t} &= -\bar{u} \frac{\partial \bar{r}_v}{\partial x} - \bar{v} \frac{\partial \bar{r}_v}{\partial y} - \bar{w} \frac{\partial \bar{r}_v}{\partial z} + \bar{E} - \bar{C} + \kappa_e \nabla^2 \bar{r}_v \\ &\quad - \frac{\partial \bar{u}'\bar{r}'_v}{\partial x} - \frac{\partial \bar{v}'\bar{r}'_v}{\partial y} - \frac{\partial \bar{w}'\bar{r}'_v}{\partial z}. \end{aligned} \quad (4.23)$$

⁴ Often the overbars are left off of the mean variables, such that (4.19) is written exactly as (4.8), plus the additional flux divergence terms, with the implicit understanding that the variables represent mean quantities.

The $\bar{u}'\bar{u}'$, $\bar{u}'\bar{v}'$, ..., $\bar{w}'\bar{w}'$ terms are components of what is referred to as the *turbulent kinematic momentum flux*. The $\bar{u}'\bar{\theta}'$, $\bar{v}'\bar{\theta}'$, and $\bar{w}'\bar{\theta}'$ terms are the components of the *turbulent kinematic heat flux*. The $\bar{u}'\bar{r}'_v$, $\bar{v}'\bar{r}'_v$, and $\bar{w}'\bar{r}'_v$ terms are the components of the *turbulent kinematic moisture flux*.

The turbulent flux terms represent the effects of turbulent eddies within the boundary layer on the evolution of the mean variables. These eddies are associated with a turbulent transport of heat, moisture, and/or momentum. Note that it is the divergence of the flux that is important to the evolution of the mean. For example, if equal heat is transferred into a volume through one side as leaves the other side, then the mean potential temperature in the volume does not change in time.

4.1.2 Parameterization of turbulent fluxes

In many applications, there is a need to parameterize the turbulent fluxes in terms of mean variables. A comprehensive discussion of the variety of ways by which this can be done is outside the scope of this book, but we shall briefly touch upon the simplest approaches. In many cases, the vertical flux divergences are much larger than the horizontal flux divergences, such that the horizontal flux divergences can be neglected. In such cases, it is the vertical profile of the turbulent flux that assumes greatest importance. Typical vertical profiles of the turbulent fluxes, at least in relatively quiescent conditions (i.e., when mesoscale and synoptic-scale pressure and temperature gradients are relatively weak), are shown in Figure 4.2.

It is often assumed that turbulent eddies act in a manner analogous to molecular diffusion. In other words, the turbulent flux is assumed to be proportional to the local gradient of the mean; for example,

$$\bar{u}'\bar{w}' = -K_m \frac{\partial \bar{u}}{\partial z} \quad (4.24)$$

$$\bar{v}'\bar{w}' = -K_m \frac{\partial \bar{v}}{\partial z} \quad (4.25)$$

$$\bar{w}'\bar{\theta}' = -K_h \frac{\partial \bar{\theta}}{\partial z} \quad (4.26)$$

$$\bar{w}'\bar{r}'_v = -K_e \frac{\partial \bar{r}_v}{\partial z}, \quad (4.27)$$

where K_m , K_h , and K_e are referred to as the *eddy viscosity*, *eddy diffusivity for heat*, and *eddy diffusivity for moisture*, respectively.

The approach outlined above is known as *flux-gradient theory*. The gradients of the mean variables are available

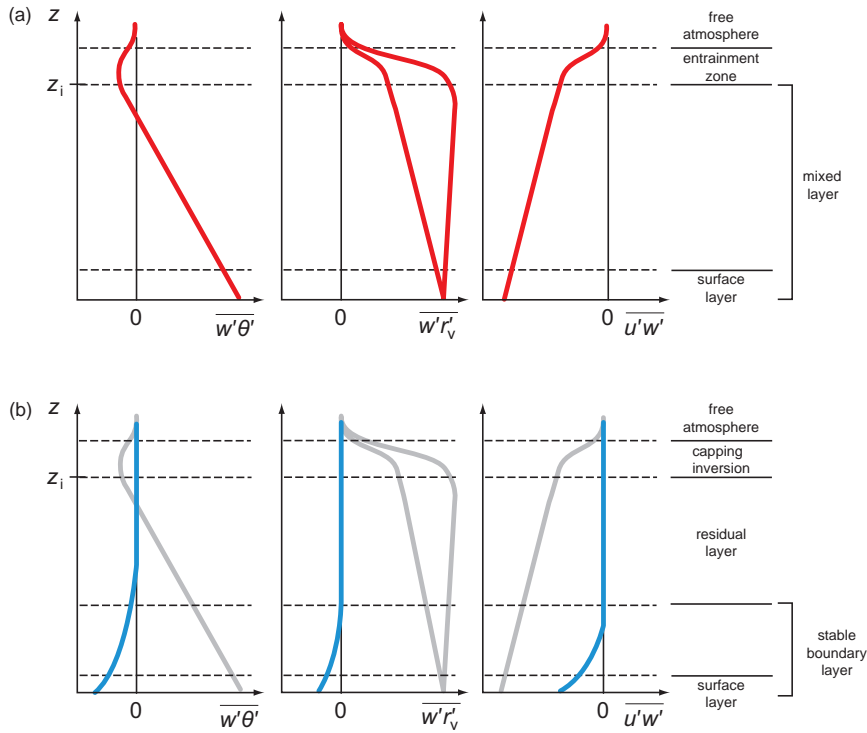


Figure 4.2 Typical vertical profiles of vertical turbulent kinematic heat flux ($\overline{w'\theta'}$), moisture flux ($\overline{w'r'_v}$), and momentum flux ($\overline{u'w'}$); it is assumed that $\overline{u} > 0$) during (a) daytime and (b) nighttime. The daytime profiles also appear in (b) in gray to facilitate day–night comparisons. The layers indicated (e.g., residual layer, mixed layer, etc.) will be defined and discussed in Section 4.3. The height of the inversion at the top of the boundary layer is denoted by z_i . Two daytime $\overline{w'r'_v}$ profiles are shown; a wide range of vertical profiles of $\overline{w'r'_v}$ can be observed, with a $\overline{w'r'_v}$ profile decreasing with height being observed roughly as often as a profile that increases with height. The nighttime $\overline{w'r'_v}$ profile assumes dew formation; in the absence of dew formation, the moisture flux may be positive at the surface and decrease with height to zero at the top of the nocturnal boundary layer (not shown). (Adapted from Stull [1988].)

through the equations governing the dynamics and thermodynamics, but K_m , K_h , and K_e must be prescribed. The simplest way is to treat K_m , K_h , and K_e as constants. More sophisticated techniques parameterize K_m in terms of the mean flow and static stability, and then prescribe K_h and K_e as some function of K_m .

One way to parameterize K_m is to assume that a parcel that is displaced vertically will carry the mean properties from its original level a characteristic distance z' before mixing with its surroundings ($z' > 0$ for upward displacements, $z' < 0$ for downward displacements). We can view z' as being somewhat analogous to a molecular mean free path, a length scale that represents the average distance a molecule travels before colliding with another molecule. If the vertical profiles of mean variables can be assumed to be roughly linear over a distance z' , then a reasonably good

assumption is that

$$u' = -z' \frac{\partial \bar{u}}{\partial z} \quad (4.28)$$

$$v' = -z' \frac{\partial \bar{v}}{\partial z}, \quad (4.29)$$

where u' and v' are the horizontal wind perturbations observed a distance z' away from the original elevation of the rising or sinking air parcel.⁵ From (4.28) and (4.29), it follows that

$$\overline{u'w'} = -\overline{w'z' \frac{\partial \bar{u}}{\partial z}} = -\overline{w'z'} \frac{\partial \bar{u}}{\partial z} \quad (4.30)$$

⁵This approach is attributed to the German physicist Ludwig Prandtl (1875–1953).

$$\overline{v'w'} = -\overline{w'z'} \frac{\partial \bar{v}}{\partial z} = -\overline{w'z'} \frac{\partial \bar{v}}{\partial z}. \quad (4.31)$$

If the horizontal and vertical scales of a turbulent eddy are comparable, then we can assume, using the continuity equation, that the horizontal and vertical velocity perturbations are also of similar magnitude; that is, $|w'| \sim |\bar{v}'|$, where \bar{v}' is the eddy part of the horizontal velocity vector. This assumption also implies, using the fact that $+z'$ must correspond to $+w'$, that $w' \sim z' |\frac{\partial \bar{v}}{\partial z}|$. Thus, (4.30) and (4.31) can be rewritten as

$$\overline{u'w'} = -\overline{z'^2} \left| \frac{\partial \bar{v}}{\partial z} \right| \frac{\partial \bar{u}}{\partial z} = -K_m \frac{\partial \bar{u}}{\partial z} \quad (4.32)$$

$$\overline{v'w'} = -\overline{z'^2} \left| \frac{\partial \bar{v}}{\partial z} \right| \frac{\partial \bar{v}}{\partial z} = -K_m \frac{\partial \bar{v}}{\partial z}, \quad (4.33)$$

where K_m effectively has been parameterized in terms of a mixing length $l = (\overline{z'^2})^{1/2}$, such that

$$K_m = \overline{z'^2} \left| \frac{\partial \bar{v}}{\partial z} \right| = l^2 \left| \frac{\partial \bar{v}}{\partial z} \right|. \quad (4.34)$$

The mixing length can be viewed as the root mean squared parcel displacement over which a parcel carries the mean properties from its original level, and we expect this to be determined by the size of the turbulent eddies. The above parameterization has K_m increasing as eddies get larger and as the vertical wind shear increases. (Other parameterizations express K_m in terms of additional mean velocity gradients, such as the total deformation.) Usually K_m would be replaced by K_h or K_e in the parameterization of heat and moisture fluxes, respectively, as in (4.26)–(4.27), with K_h and K_e being specified as some proportion of K_m . Usually $K_h = K_e$, and values of K_h and K_e are often taken to be larger than K_m by a factor of 1–3. The ratio K_m/K_h is known as the *turbulent Prandtl number*.

All methods for determining K_m , K_h , and K_e have been empirical, with K_m , K_h , and K_e varying depending on the situation, rather than depending on the physical properties of the fluid, as is the case for molecular diffusion. In numerical models, one often relates K_m to the intensity of the turbulence as measured by the turbulent kinetic energy (see Section 4.1.3). Not only is the determination of K_m , K_h , and K_e problematic, but expressing the fluxes as functions of gradients of mean variables might be flawed as well. For example, within much of the mixed layer (the portion of the daytime boundary layer that extends from the surface to the capping inversion⁶ atop the boundary layer, to be

⁶The term “inversion” is used somewhat casually in this context to be consistent with the literature. At times there is a true temperature inversion at the top of the boundary layer, but many times there is simply a lapse rate discontinuity, with an abrupt increase in stability.

described further in Section 4.3), $\partial \bar{\theta} / \partial z = 0$ locally, but $\overline{w'\theta'} > 0$ (Figure 4.2).

Impermeability requires that $w' = 0$ at the lower boundary. This requirement seems at odds with Figure 4.2, which shows that the fluxes tend to have their *maximum* magnitudes at the surface. It turns out that Figure 4.2 presents profiles of what are sometimes referred to as *effective turbulent fluxes*, defined as the sum of the turbulent flux and the molecular flux. Indeed, the turbulent flux does vanish at the surface, but this is where the molecular flux is most important (Figure 4.3). The molecular flux dominates the effective turbulent flux in the lowest few millimeters. Above roughly a centimeter, the effective turbulent flux is, for practical purposes, equivalent to the turbulent flux.

For simplicity, the aforementioned boundary conditions and explanation of effective turbulent fluxes are based on the assumption of an aerodynamically smooth surface. Most real surfaces are rough, however. The height at which the wind and turbulent flux vanish over a rough surface is called the *roughness length*, z_0 . The roughness length is a function of the height and density of *roughness elements* on the surface; z_0 ranges from 10^{-5} m in the case of a calm sea surface to 10^{-1} m for grasslands to 1–100 m in the case of cities, forests, or mountainous terrain.

By introducing effective turbulent flux profiles, we can ignore molecular processes in (4.19)–(4.23) and just use the effective flux written in the same form as turbulent fluxes. The effective turbulent fluxes near the surface (where the effective turbulent fluxes include the molecular fluxes) must be parameterized. In the case of heat we

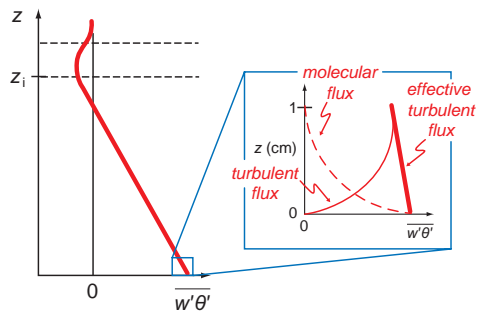


Figure 4.3 The effective turbulent flux is the sum of the turbulent flux and molecular flux. The profiles above are for $\overline{w'\theta'}$ during daytime convective conditions. The profile of effective turbulent flux decreases linearly with height from a maximum at the surface, whereas the turbulent flux goes to zero in approximately the lowest centimeter (the microlayer) and the molecular flux increasingly dominates the effective flux as the surface is approached. (Adapted from Stull [1988].)

must parameterize conduction, and in the case of moisture we must parameterize evaporation and condensation. The most common means of parameterizing fluxes near the surface is as follows:

$$\overline{u'w'}|_0 = -c_d (\overline{u}_a^2 + \overline{v}_a^2)^{1/2} \overline{u}_a \quad (4.35)$$

$$\overline{v'w'}|_0 = -c_d (\overline{u}_a^2 + \overline{v}_a^2)^{1/2} \overline{v}_a \quad (4.36)$$

$$\overline{w'\theta'}|_0 = -c_h (\overline{u}_a^2 + \overline{v}_a^2)^{1/2} (\overline{\theta}_a - \theta_0) \quad (4.37)$$

$$\overline{w'r_v'}|_0 = -c_e (\overline{u}_a^2 + \overline{v}_a^2)^{1/2} (\overline{r}_{va} - r_{vo}) \quad (4.38)$$

where c_d is a drag coefficient, c_h is a bulk transfer coefficient for heat, c_e is a bulk transfer coefficient for moisture, the subscript a indicates the value at anemometer level (often 10 m is assumed as the standard height), and the subscript 0 indicates the value at the height z_0 . The coefficients c_d , c_h , and c_e depend on the static stability, surface roughness, and height of the wind measurement (the coefficients increase as static stability decreases, roughness increases, and the height of the wind measurement decreases). Typical values range from 0.001 to 0.01 for all three coefficients, although c_h and c_e typically are a little larger than c_d , and it is usually assumed that $c_h = c_e$. Hereafter, effective turbulent flux is implied whenever turbulent fluxes are described.

4.1.3 Turbulent kinetic energy

Turbulent kinetic energy (TKE), \bar{e} , is a measure of the intensity of turbulence and is defined as

$$\bar{e} = \frac{1}{2} (\overline{u'^2} + \overline{v'^2} + \overline{w'^2}). \quad (4.39)$$

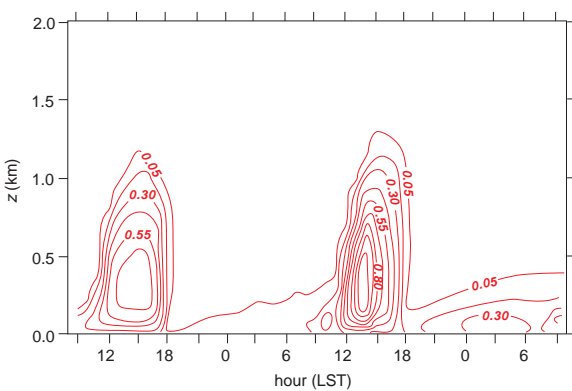


Figure 4.4 Simulation of the time and space variation of TKE ($\text{m}^2 \text{s}^{-2}$) from the Wangara, Australia, boundary layer field experiment. (Adapted from Yamada and Mellor [1975].)

TKE is a maximum during the early afternoon in the middle of the boundary layer, and a minimum during the nighttime hours (Figure 4.4). A prognostic equation for TKE can be derived by subtracting the Reynolds-averaged equations of motion (4.19)–(4.21) from the unaveraged forms (4.8)–(4.10), multiplying the difference equations by the respective zonal, meridional, and vertical eddy wind components, taking the Reynolds average, and then summing. For example, subtracting (4.19) from (4.8), multiplying by u' , and taking the Reynolds average yields

$$\begin{aligned} \frac{\partial}{\partial t} \overline{\left(\frac{u'^2}{2}\right)} &= -\overline{u} \frac{\partial}{\partial x} \overline{\left(\frac{u'^2}{2}\right)} - \overline{v} \frac{\partial}{\partial y} \overline{\left(\frac{v'^2}{2}\right)} - \overline{w} \frac{\partial}{\partial z} \overline{\left(\frac{w'^2}{2}\right)} \\ &\quad - \overline{u'} u' \frac{\partial \overline{u}}{\partial x} - \overline{u'} v' \frac{\partial \overline{u}}{\partial y} - \overline{u'} w' \frac{\partial \overline{u}}{\partial z} \\ &\quad - \frac{\overline{u'}}{\rho_0} \frac{\partial p'}{\partial x} + f \overline{u'v'} + \nu \overline{u' \nabla^2 u'} \\ &\quad - \frac{\partial}{\partial x} \overline{\left(u' \frac{u'^2}{2}\right)} - \frac{\partial}{\partial y} \overline{\left(v' \frac{u'^2}{2}\right)} \\ &\quad - \frac{\partial}{\partial z} \overline{\left(w' \frac{u'^2}{2}\right)}. \end{aligned} \quad (4.40)$$

Similarly, if (4.20) is subtracted from (4.9), multiplied by v' , and Reynolds-averaged, and if (4.21) is subtracted from (4.10), multiplied by w' , and Reynolds-averaged, and then the resulting equations for $\frac{\partial}{\partial t} \overline{\left(\frac{v'^2}{2}\right)}$ and $\frac{\partial}{\partial t} \overline{\left(\frac{w'^2}{2}\right)}$ are summed with (4.40), a prognostic equation for TKE can be obtained,

$$\begin{aligned} \frac{\partial \bar{e}}{\partial t} &= \underbrace{-\overline{u} \frac{\partial \bar{e}}{\partial x} - \overline{v} \frac{\partial \bar{e}}{\partial y} - \overline{w} \frac{\partial \bar{e}}{\partial z}}_{\text{advection}} + \underbrace{\frac{g}{\theta} \overline{w' \theta'}}_{\text{buoyancy generation/consumption}} \\ &\quad - \underbrace{\overline{u'} u' \frac{\partial \overline{u}}{\partial x} - \overline{v'} u' \frac{\partial \overline{v}}{\partial x} - \overline{w'} u' \frac{\partial \overline{w}}{\partial x} - \overline{u'} v' \frac{\partial \overline{u}}{\partial y}}_{\text{shear generation}} \\ &\quad - \underbrace{\overline{v'} v' \frac{\partial \overline{v}}{\partial y} - \overline{w'} v' \frac{\partial \overline{w}}{\partial y} - \overline{u'} w' \frac{\partial \overline{u}}{\partial z} - \overline{v'} w' \frac{\partial \overline{v}}{\partial z} - \overline{w'} w' \frac{\partial \overline{w}}{\partial z}}_{\text{turbulent transport}} \\ &\quad - \underbrace{\frac{1}{\rho_0} \frac{\partial \overline{u'p'}}{\partial x} - \frac{1}{\rho_0} \frac{\partial \overline{v'p'}}{\partial y} - \frac{1}{\rho_0} \frac{\partial \overline{w'p'}}{\partial z}}_{\text{pressure correlation}} \underbrace{-\varepsilon}_{\text{dissipation}} \end{aligned} \quad (4.41)$$

where the various contributions to the TKE budget are indicated above. The Coriolis terms end up summing to

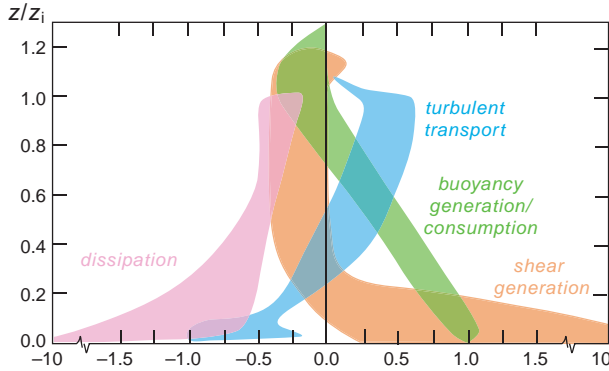


Figure 4.5 Typical ranges of terms in the TKE budget equation (4.41) during daytime, compositized from observations and numerical simulations from a number of investigators. Values have been normalized by w_*^3/z_i , where z_i is the height of the inversion at the top of the boundary layer and w_* is the convective velocity scale defined as $w_* = [(g/\bar{\theta})w'\theta'|_0 z_i]^{1/3}$ (typically, $w_*^3/z_i \sim 6 \times 10^{-3} \text{ m}^2 \text{ s}^{-3}$). (Adapted from Stull [1988].)

zero, which implies that the Coriolis force cannot generate TKE. In deriving the *buoyancy generation/consumption term*, it has been assumed that $-\rho'/\rho_0 \approx \theta'/\bar{\theta}$.⁷ Typical vertical profiles of the terms are shown in Figure 4.5.

The *viscous dissipation* is

$$\begin{aligned}\varepsilon &= -\overline{v u' \nabla^2 u'} - \overline{v v' \nabla^2 v'} - \overline{v w' \nabla^2 w'} \\ &= -\frac{1}{2} \nu \nabla^2 \overline{u' u'} + \nu \overline{(\nabla u')^2} \\ &\quad -\frac{1}{2} \nu \nabla^2 \overline{v' v'} + \nu \overline{(\nabla v')^2} - \frac{1}{2} \nu \nabla^2 \overline{w' w'} + \nu \overline{(\nabla w')^2} \\ &\approx \nu \left[\overline{(\nabla u')^2} + \overline{(\nabla v')^2} + \overline{(\nabla w')^2} \right],\end{aligned}\quad (4.42)$$

where the $\frac{1}{2} \nu \nabla^2 \overline{u' u'}$, $\frac{1}{2} \nu \nabla^2 \overline{v' v'}$, and $\frac{1}{2} \nu \nabla^2 \overline{w' w'}$ terms are negligible compared to the $\nu \overline{(\nabla u')^2}$, $\nu \overline{(\nabla v')^2}$, and $\nu \overline{(\nabla w')^2}$ terms. This term represents the transfer of energy to the molecular scale and always decreases TKE.

The buoyancy generation/consumption term is positive (negative) in statically unstable (stable) conditions and zero in neutral conditions. In unstable (stable) conditions, a rising parcel finds itself warmer (colder) than its surroundings; thus, w' and θ' are positively (negatively)

⁷ We leave it as an exercise for the reader to show that $\frac{\rho'}{\bar{\rho}} \approx \left(1 - \frac{R_d}{c_p}\right) \frac{p'}{\bar{p}} - \frac{\theta_v}{\bar{\theta}_v}$. If moisture variations do not contribute significantly to the buoyancy and if p'/\bar{p} is relatively small, then $\rho'/\bar{\rho} \approx -\theta/\bar{\theta}$. In the Boussinesq approximation, $\bar{\rho}$ is replaced with ρ_0 .

correlated and TKE is generated (consumed). The *shear generation term* (sometimes called *mechanical generation*) represents the production of TKE by velocity gradients. The most important contributions are from the $-\overline{u' w'} \frac{\partial \bar{u}}{\partial z}$ and $-\overline{v' w'} \frac{\partial \bar{v}}{\partial z}$ terms. In statically stable conditions, TKE can be generated only if the shear generation can overcome the damping effects of the buoyancy consumption term. The ratio of these terms is represented by the *flux Richardson number*,

$$\begin{aligned}R_f &= \left[\left(\frac{g}{\bar{\theta}} \right) \overline{w' \theta'} \right] \left(\overline{u' u'} \frac{\partial \bar{u}}{\partial x} + \overline{v' u'} \frac{\partial \bar{v}}{\partial x} + \overline{w' u'} \frac{\partial \bar{w}}{\partial x} + \overline{u' v'} \frac{\partial \bar{u}}{\partial y} \right. \\ &\quad \left. + \overline{v' v'} \frac{\partial \bar{v}}{\partial y} + \overline{w' v'} \frac{\partial \bar{w}}{\partial y} + \overline{u' w'} \frac{\partial \bar{u}}{\partial z} + \overline{v' w'} \frac{\partial \bar{v}}{\partial z} + \overline{w' w'} \frac{\partial \bar{w}}{\partial z} \right)^{-1} \\ &\approx \left[\left(\frac{g}{\bar{\theta}} \right) \overline{w' \theta'} \right] \left(\overline{u' w'} \frac{\partial \bar{u}}{\partial z} + \overline{v' w'} \frac{\partial \bar{v}}{\partial z} \right)^{-1}.\end{aligned}\quad (4.43)$$

Because R_f is a function of turbulent fluxes, which are significant only *after* conditions already have become turbulent, it really is a measure of whether turbulence can be sustained or will subside, rather than a measure of whether a laminar flow will become turbulent. Turbulence tends to be maintained when $R_f < 1$, that is, when the shear production exceeds the damping by buoyancy. For a statically unstable boundary layer, $R_f < 0$, which implies that buoyancy forces are generating TKE rather than suppressing it. Recall the investigation of Kelvin–Helmholtz instability in Section 3.5.2; the stability criterion involved an expression similar to (4.43), called the *gradient Richardson number* or just the *Richardson number*, which contained only mean variables rather than turbulent fluxes.

Regarding the other terms in the TKE equation given by (4.41), the *advection* and *turbulent transport terms* neither create nor destroy turbulence; rather, these terms simply move TKE from one location to another within the boundary layer. The *pressure correlation terms* are often associated with buoyancy oscillations; gravity waves within a stable boundary layer or near the top of a convective boundary layer (possibly excited by thermals impinging on the stable layer at the boundary layer top) are sometimes associated with a net TKE loss from the boundary layer. Lastly, the dissipation term is largest near the surface, where its magnitude approaches the magnitude of the shear production term.

4.1.4 Effect of momentum fluxes on boundary layer winds

If we consider the case of small Rossby number, in which case the total acceleration, $d\mathbf{v}/dt$, is small relative to the

Coriolis acceleration, $-f\mathbf{k} \times \mathbf{v}$, and if the horizontal turbulent flux divergence is neglected and the molecular viscosity is incorporated into the effective turbulent flux, then (4.19) and (4.20) become

$$0 = -\frac{1}{\rho_0} \frac{\partial \bar{p}}{\partial x} + f\bar{v} - \frac{\partial \bar{u}'w'}{\partial z} = f(\bar{v} - \bar{v}_g) - \frac{\partial \bar{u}'w'}{\partial z} \quad (4.44)$$

$$0 = -\frac{1}{\rho_0} \frac{\partial \bar{p}}{\partial y} - f\bar{u} - \frac{\partial \bar{v}'w'}{\partial z} = -f(\bar{u} - \bar{u}_g) - \frac{\partial \bar{v}'w'}{\partial z}, \quad (4.45)$$

where \bar{u}_g and \bar{v}_g are the zonal and meridional geostrophic wind components, respectively. Equations (4.44)–(4.45) reflect a balance between the horizontal pressure gradient force, the Coriolis force, and friction—sometimes referred to as *antitriptic balance*⁸—where the term *friction* describes a drag on the wind attributable to the vertical turbulent momentum flux divergence rather than the direct effects of molecular viscosity. If linear profiles of the turbulent momentum fluxes are assumed (Figure 4.2), with the fluxes vanishing at height z_i , the height of the inversion that caps the boundary layer (at night, the height of the top of the stable boundary layer should be used), and with surface momentum fluxes parameterized via (4.35) and (4.36), then (4.44) and (4.45) can be written as

$$f(\bar{v} - \bar{v}_g) = \frac{c_d |\bar{v}| \bar{u}}{z_i} \quad (4.46)$$

$$-f(\bar{u} - \bar{u}_g) = \frac{c_d |\bar{v}| \bar{v}}{z_i}, \quad (4.47)$$

where $|\bar{v}| = (\bar{u}^2 + \bar{v}^2)^{1/2}$ is the mean wind speed and \bar{u} , \bar{v} , and $|\bar{v}|$ are understood to be at anemometer level. From (4.46) and (4.47) we find that winds become increasingly ageostrophic as the drag coefficient c_d increases; it is also implied that winds are subgeostrophic and blow across isobars toward lower pressure (Figure 4.6). It can be shown that the angle at which the antitriptic wind blows across isobars is equal to $\tan^{-1}(c_d |\bar{v}| / fz_i)$. Geostrophic wind balance is recovered in the case of $c_d = 0$. As a consequence of winds blowing across isobars toward lower pressure within the boundary layer, it is easily shown that boundary layer convergence (divergence) accompanies cyclonic (anticyclonic) geostrophic relative vorticity, where the geostrophic relative vorticity is defined as $\zeta_g = \frac{\partial v_g}{\partial x} - \frac{\partial u_g}{\partial y}$. Thus, mean upward (downward) motion is present when $\zeta_g > 0$ ($\zeta_g < 0$). This is sometimes referred to as *Ekman pumping*.

The vertical profile of horizontal wind within the boundary layer when the vertical profile of the momentum flux is not linear will be considered next. Substituting (4.24) and

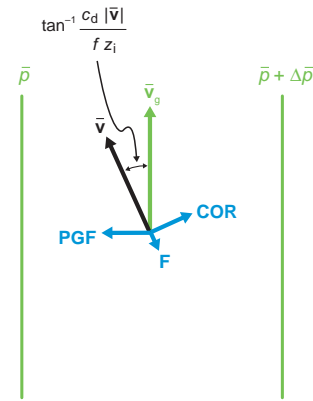


Figure 4.6 Antitriptic wind balance involves a balance among the Coriolis (COR), horizontal pressure gradient (PGF), and friction (F) forces, which are depicted schematically in blue. The geostrophic wind (green) and antitriptic wind (black) are also indicated.

(4.25) into (4.44) and (4.45), respectively, and treating K_m as a constant, gives

$$f(\bar{v} - \bar{v}_g) + K_m \frac{\partial^2 \bar{u}}{\partial z^2} = 0 \quad (4.48)$$

$$-f(\bar{u} - \bar{u}_g) + K_m \frac{\partial^2 \bar{v}}{\partial z^2} = 0, \quad (4.49)$$

which can be solved to determine how departures of \bar{u} and \bar{v} from geostrophy vary with height within the boundary layer. If we assume that $\bar{v}_g = 0$ at all levels, $\bar{u} = \bar{v} = 0$ at $z = 0$, and $\bar{u} = \bar{u}_g$ at $z = \infty$ (idealized as the top of the boundary layer), the following solution is obtained:

$$\bar{u} = \bar{u}_g (1 - e^{-\gamma z} \cos \gamma z) \quad (4.50)$$

$$\bar{v} = \bar{u}_g e^{-\gamma z} \sin \gamma z, \quad (4.51)$$

where $\gamma = (f/2K_m)^{1/2}$ and γz is just a dimensionless height. The solution is plotted as a hodograph in Figure 4.7 and is appropriately named the *Ekman spiral* after the Swedish oceanographer V. Ekman. Note that Figure 4.7 also implies that the horizontal wind crosses isobars toward lower pressure. Recall that the above solution differs from (4.46)–(4.47) because (4.46)–(4.47) were obtained from assuming linear profiles of $\bar{u}'w'$ and $\bar{v}'w'$, in which case $\frac{\partial \bar{u}'w'}{\partial z}$ and $\frac{\partial \bar{v}'w'}{\partial z}$ are independent of height, as is the degree of ageostrophy. The Ekman spiral wind profile, however, can only be obtained if $\frac{\partial \bar{u}'w'}{\partial z}$ and $\frac{\partial \bar{v}'w'}{\partial z}$ vary with height, which implies that $\frac{\partial^2 \bar{u}}{\partial z^2}$ and $\frac{\partial^2 \bar{v}}{\partial z^2}$ are nonzero if the flux-gradient approximation specified by (4.24)–(4.25) is used with constant K_m . The Ekman spiral is generally not observed

⁸ The Coriolis force is sometimes excluded from the definition of antitriptic wind balance.

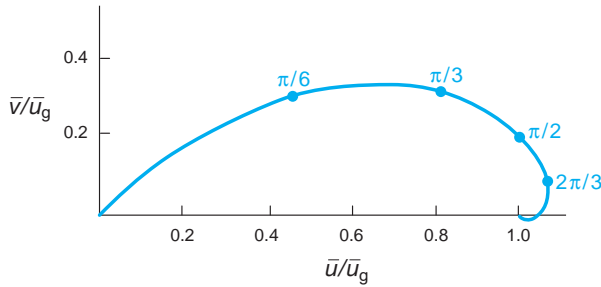


Figure 4.7 The Ekman spiral hodograph in the northern hemisphere. Note that the x and y axes display \bar{u}/\bar{u}_g and \bar{v}/\bar{u}_g , respectively ($\bar{v}_g = 0$). Labels along the hodograph show values of γz .

exactly as it appears in Figure 4.7, although there is often some similarity between observed hodographs and the Ekman spiral, such as the hodographs shown in Figure 2.14, which display veering of the shear vector with height within the boundary layer. One reason the Ekman spiral is not generally observed is that the vertical profiles of $\bar{u}'w'$ and $v'w'$ are (i) usually linear (e.g., Figure 4.2) and (ii) not adequately represented by $-K_m \frac{\partial \bar{u}}{\partial z}$ and $-K_m \frac{\partial \bar{v}}{\partial z}$ with $K_m = \text{constant}$. Usually K_m varies considerably with height near the surface rather than being a constant. Moreover, the Ekman wind profile contains an inflection point and is therefore dynamically unstable (refer to Section 3.5); additional discussion appears in Section 4.4.2.

The lowest part of the boundary layer is referred to as the *surface layer* (this layer will be further discussed in Section 4.3). It is usually considered to occupy roughly the lowest 10% of the boundary layer, where turbulent fluxes can be assumed not to deviate much from their surface values. If the flux profile is linear over the mixed layer depth, then the fluxes within the surface layer would not vary by more than 10% of their surface values. In many boundary layer applications, one of which appears below, it is therefore assumed that the turbulent fluxes can be treated as constant within the surface layer.

Within the surface layer, winds must decrease to zero at the surface from their antitropic velocity at the top of the surface layer. The manner in which winds vary with height within the surface layer can be obtained by assuming that the mixing length is proportional to the distance above the ground within the surface layer, that is, $l = kz$, where k is a constant (essentially we are assuming that the vertical scale of turbulent eddies is limited by their distance above the

ground). Without loss of generality, if we consider the case of $\bar{v} = 0$, (4.24) and (4.34) lead to

$$|\bar{u}'w'|_0 = (kz)^2 \left(\frac{\partial \bar{u}}{\partial z} \right)^2, \quad (4.52)$$

where, as mentioned in the preceding paragraph, the turbulent flux is assumed to be independent of height within the surface layer and well approximated by $|\bar{u}'w'|_0$. Integrating (4.52) with respect to z yields

$$\bar{u} = \frac{u_*}{k} \ln \left(\frac{z}{z_0} \right), \quad (4.53)$$

where $u_*^2 = |\bar{u}'w'|_0$ and z_0 is the previously introduced roughness length (i.e., the height where $\bar{u} = 0$). The velocity u_* is known as the *friction velocity* (u_* typically ranges from 0.03 to 0.30 m s⁻¹, depending on the surface drag). The constant k is often referred to as *von Karman's constant* and has a value of roughly 0.4. The log wind profile specified by (4.53) generally fits wind observations within a statically neutral surface layer reasonably well.

4.2 Surface energy budget

The exchange of heat and moisture between the surface and overlying atmosphere is responsible for the diurnal variations in boundary layer temperature, humidity, and depth, and, as discussed in Section 4.1.3, heat fluxes from the surface play a major role in generating boundary layer turbulence. It is therefore worth devoting some time to examine the energy balance at the surface. It is through this so-called *surface energy budget* that surface heat and moisture fluxes are inescapably tied to the net radiation received at the surface.

The surface receives predominantly short-wave radiation from the sun, with the amount absorbed by the ground dependent on the cloud fraction, solar angle, and surface albedo. The ground also receives predominantly long-wave (infrared) radiation emitted by clouds and the atmosphere. However, the earth's surface also emits radiation at long wavelengths. The net radiation, R_n , is the difference between the incoming short-wave and long-wave radiation and the outgoing long-wave radiation. A complete discussion of the R_n term that will appear in the surface energy budget is obviously beyond the scope of this book, as entire atmospheric sciences courses are devoted to R_n .

One might surmise that the surface heat and moisture fluxes given by (4.37) and (4.38) figure prominently in

the surface energy budget. The expressions for the fluxes must be modified so that their units match the units of R_n (usually W m^{-2}). The resulting expressions for the *sensible heat flux* (Q_h) and *latent heat flux* (Q_e) from the surface are as follows:

$$Q_h = \rho c_p \overline{w' T'}|_0 \quad (4.54)$$

$$Q_e = \rho l_v \overline{w' r'_v}|_0, \quad (4.55)$$

where c_p is the specific heat at constant pressure (the variation of c_p with humidity has been neglected) and l_v is the specific latent heat of vaporization. The parameterization of (4.54)–(4.55), if desired, usually follows the formulation presented in (4.37) and (4.38), although note that T' rather than θ' typically appears in the definition of the sensible heat flux.

The sensible heat flux is related to the heating of the atmosphere from below. Air is largely transparent to incoming solar (short-wave) radiation and therefore is not heated directly by solar radiation; rather, diurnal boundary layer warming occurs via the heat flux convergence term $-\frac{\partial w' \theta'}{\partial z}$ in (4.22), which is intimately tied to (4.37), and therefore (4.54) as well. The latent heat flux, on the other hand, represents the portion of the net radiation used in evaporation, transpiration, or the melting of ice at the surface. There also is a small but non-negligible downward flux of heat into the ground. This *ground heat flux* (Q_g) is usually relatively small compared with the sensible heat flux.

The surface energy budget, that is, the relationship between the net radiation and the sensible, latent, and ground heat fluxes, can be expressed as

$$R_n = Q_h + Q_e + Q_g, \quad (4.56)$$

where R_n is defined to be positive when incoming radiation exceeds outgoing radiation, and the heat fluxes are defined to be positive when directed away from the surface (i.e., Q_h and Q_e are positive when upward directed, and Q_g is positive when downward directed) (Figure 4.8). In words, (4.56) reflects the fact that the sensible, latent, and ground heat fluxes are balanced by net radiation. An additional *storage* term is sometimes included on the rhs of (4.56) if a ground *layer* having a finite depth is considered (above we have considered the surface to be a zero-thickness layer, which works best for flat, barren land surfaces).

The ground heat flux is generally the smallest of the three surface fluxes. Although its exact value depends on the soil type and moisture content, it is usually $\sim 10\%$ of the net radiation. The latent heat flux depends on the amount of available surface moisture, which is a function

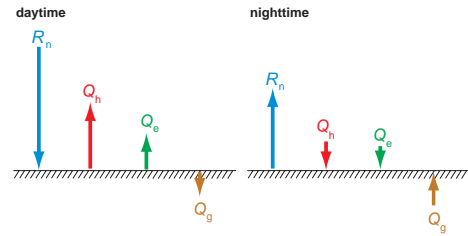


Figure 4.8 Schematic representation of the surface energy budget during daytime and nighttime. Actual magnitudes of the terms depend on the type of surface and its characteristics (e.g., soil type, soil moisture, vegetation), time of year, time of day, and weather.

of vegetation, soil wetness, land use, and near-surface wind speed. It is highly variable in space and time, ranging from roughly zero in a desert to more than 400 W m^{-2} in a jungle. The sensible heat flux depends on the temperature difference between the surface and the air, as well as the wind speed. Daytime sensible heat flux values can range from just a few 10s of W m^{-2} to $> 500 \text{ W m}^{-2}$.

The ratio of the sensible heat flux to the latent heat flux is known as the *Bowen ratio*, $\beta = Q_h/Q_e$. The larger the Bowen ratio, the larger the amount of sensible heating of the lower atmosphere for a given net radiation and ground heat flux. The lowest Bowen ratios are typically found over oceans, where $\beta \sim 0.1$. Over forests $\beta \sim 0.5$, and in arid regions $\beta \sim 3-5$. In deserts or regions of severe drought, $\beta > 10$ has been observed. The Bowen ratio can vary considerably from day to day at a given location, depending on precipitation (e.g., β drops after heavy rains).

4.3 Structure and evolution of the boundary layer

The boundary layer responds rapidly to surface forcings. It is for this reason that the boundary layer has a pronounced diurnal cycle, in contrast to the free atmosphere. On a given day, the depth of the boundary layer is determined by the morning atmospheric profile of temperature, as well as the intensity of the turbulent mixing, which is determined by the amount of insolation and associated sensible heat flux (buoyancy-driven turbulence), as well as the mean vertical wind shear (mechanically driven turbulence). The depth of the boundary layer varies from as shallow as a few tens of meters in strongly stable, nighttime conditions, to as deep

as several kilometers in daytime conditions, when the lower part of the boundary layer is typically superadiabatic and vigorous convective motions dominate. Boundary layer depth also varies spatially, with deeper boundary layers found in warmer, drier climates on average (e.g., desert boundary layer depths frequently exceed 4 km).

Following sunrise, heating of the boundary layer by the ground below, by way of the sensible heat flux, drives the layer of air in contact with the ground toward the dry adiabatic lapse rate ($\partial\theta/\partial z = 0$). Superadiabatic conditions within a shallow layer in contact with the ground induce vertical mixing and turbulence. Because the mixing promotes homogeneity, water vapor concentrations and wind speeds also tend toward constant values with height. Upward-moving thermals overshoot beyond the top of the boundary layer, penetrating the stably stratified atmosphere above, and this *penetrative convection* induces mixing through an even deeper layer, leading to growth of the boundary layer (Figures 4.9 and 4.10). Overshooting thermals generate a capping inversion by causing a small degree of cooling at the top of the mixing layer within the stable region where they overshoot. Additional surface heating leads to more thermals, deeper mixing, and a deepening boundary layer. The boundary layer attains its maximum depth near sunset, when a decreasing sensible heat flux (it typically peaks during the afternoon) eventually undergoes a sign reversal. Surface cooling commences and stability in the near-ground layer increases.

Because of the turbulent motions and their associated mixing effects that typify the daytime boundary layer, the portion of the daytime boundary layer that extends from the surface to the *entrainment zone* atop the boundary layer is often referred to as the *mixed layer*, or a *convective boundary layer* (CBL) or *convectively mixed layer* if there is significant turbulence generation by buoyancy. As mentioned in the preceding paragraph, the vertical profiles of potential temperature, water vapor concentration, and wind speed are roughly constant with height within the daytime mixed layer, except within the lowest 10% of the mixed layer, termed the *surface layer*, where the exchange of heat, moisture, and momentum with the ground is able to overcome the effect of vertical mixing (Figure 4.11a).⁹ As a result, potential temperature may increase by 1–2 K from the top of the daytime surface layer to the ground (i.e., superadiabatic conditions prevail), water vapor mixing ratio may increase slightly as one approaches the ground, and, as discussed in Section 4.1.4, wind speed decreases logarithmically to zero at the ground.

The profiles shown in Figure 4.11a are somewhat idealized. The presence of larger-scale influences, forcings at the top and bottom of the boundary layer, and the fact that mixing is not instantaneous often lead to small departures from

⁹ Some consider the surface layer to be a subset of the mixed layer, whereas others define the bottom of the mixed layer to coincide with the top of the surface layer.

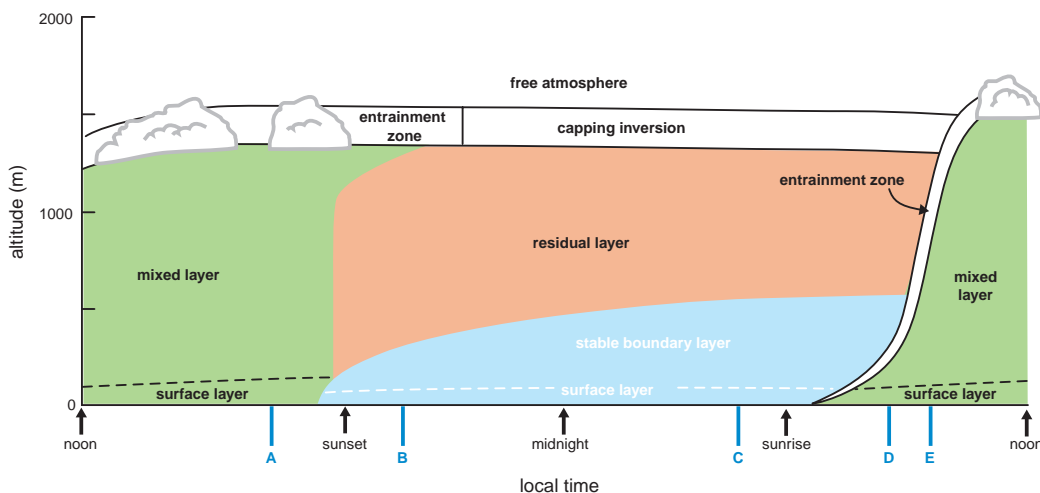


Figure 4.9 The boundary layer in relatively tranquil conditions over land consists of three major parts: a very turbulent mixed layer, a less turbulent residual layer consisting of former mixed-layer air, and a nocturnal stable boundary layer of sporadic turbulence. The letters A–E identify the times of the soundings shown in Figure 4.10. (Adapted from Stull [1988].)

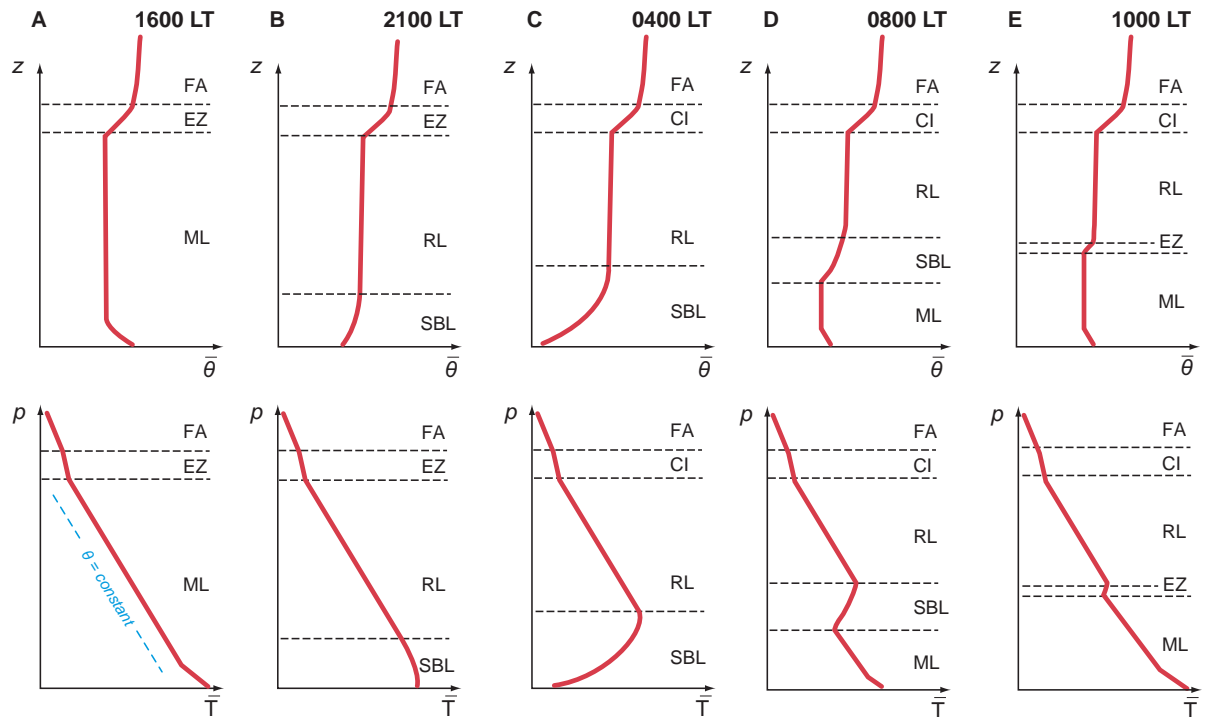


Figure 4.10 Vertical profiles of potential temperature, showing the evolution of the boundary layer during a diurnal cycle starting at about 1600 local time (LT). The letters A–E identify each sounding with a time indicated in Figure 4.9. The free atmosphere (FA), entrainment zone (EZ), capping inversion (CI), mixed layer (ML), residual layer (RL), and stable boundary layer (SBL) are indicated. The top and bottom rows plot the same profiles, but in unskewed $\bar{\theta}$ versus z space and on a skew T -log p diagram, respectively. (Adapted from Stull [1988].)

the profiles in Figure 4.11a. For example, environments supportive of severe thunderstorms tend to be associated with a large thermal wind, and daytime mixed layers in these environments often contain significant vertical wind shear despite vigorous vertical mixing. Another example is the moisture profile; it is not unusual for mean water vapor mixing ratio to decrease slightly with height within the daytime mixed layer as a result of moisture being supplied from below via evaporation, while dry air is being entrained into the top of the mixed layer from the overlying free atmosphere. Moreover, mean potential temperature profiles often have a slight minimum near the middle of the daytime mixed layer; the aforementioned entrainment of warmer air from the free atmosphere into the top of the mixed layer, along with heating from the underlying ground, can lead to this relative minimum.

During daytime convective conditions, turbulent fluxes, with the possible exception of the moisture flux, tend to be a maximum in magnitude at the surface and decrease in

magnitude with height, becoming negligible at the base of the free atmosphere (Figure 4.2a). (The turbulent moisture flux also becomes negligible at the base of the free atmosphere, but its maximum magnitude is sometimes observed significantly above the surface.) The turbulent momentum flux ($\overline{u'w'}$, without loss of generality) tends to be negative because the mean wind typically increases with height; in such mean conditions, rising thermals ($w' > 0$) will be associated with negative wind speed perturbations ($u' < 0$) as they transport lesser momentum upward from below (and compensating sinking motion will be associated with positive wind speed perturbations as they transport higher momentum downward from above). The magnitude of $\overline{u'w'}$ tends to decrease linearly with height from the surface to the top of the mixed layer. Within the entrainment zone, $\overline{u'w'}$ and $\overline{w'\theta'}$ decrease in magnitude rapidly such that they are nearly zero at the top of the entrainment zone. The fact that $\partial \overline{u'w'} / \partial z > 0$ implies a drag on the mean winds within the boundary layer if $\overline{u} > 0$ (when $\overline{u} < 0$, the profile of $\overline{u'w'}$

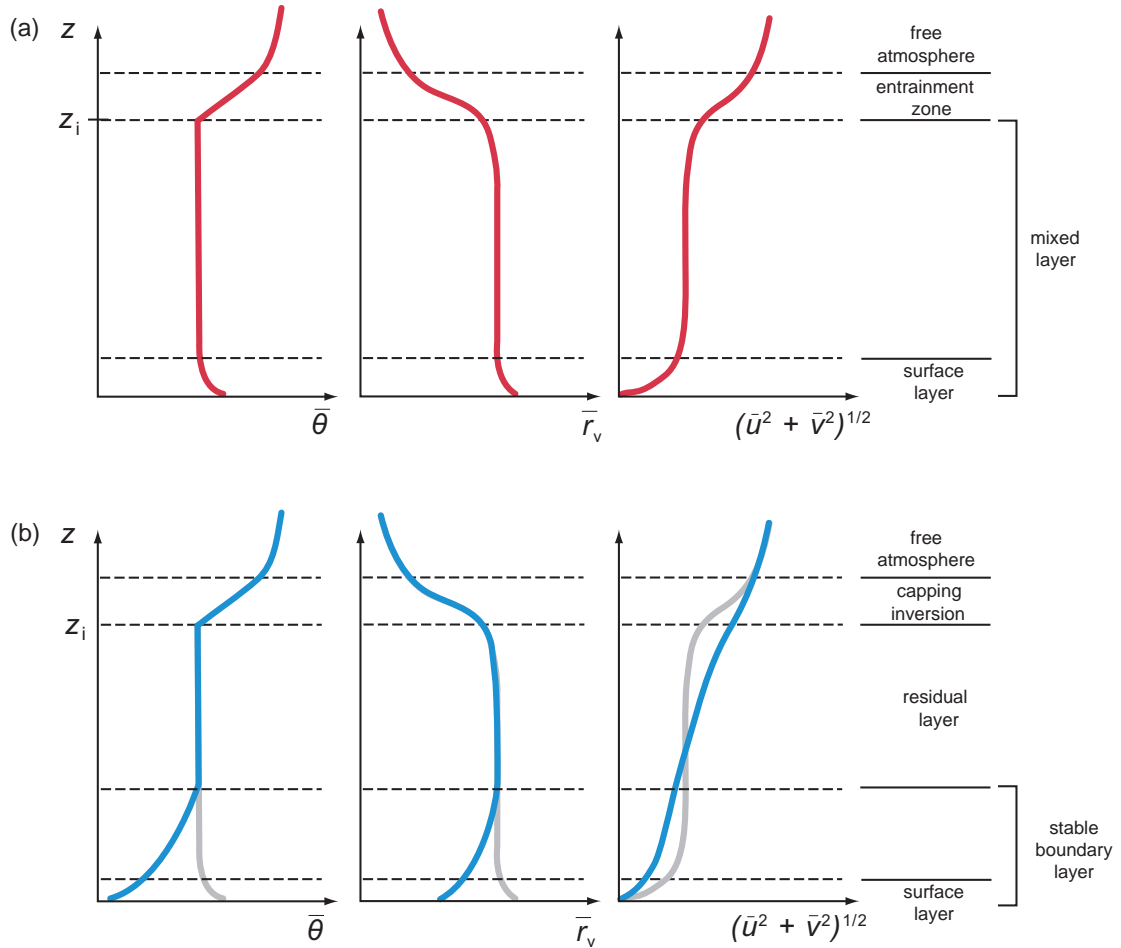


Figure 4.11 Typical vertical profiles of mean potential temperature ($\bar{\theta}$), water vapor mixing ratio (\bar{r}_v), and horizontal wind speed ($(\bar{u}^2 + \bar{v}^2)^{1/2}$) during (a) daytime and (b) nighttime. The daytime profiles also appear in (b) in gray to facilitate day-night comparisons. (Adapted from Stull [1988].)

is such that $\partial \bar{w}' w' / \partial z < 0$, which also implies a drag on the mean winds).

The daytime turbulent heat flux ($\bar{w}' \bar{\theta}'$) is generally positive in the mixed layer as a result of rising air ($w' > 0$) being positively buoyant ($\theta' > 0$). The vertical profile of $\bar{w}' \bar{\theta}'$ tends to decrease linearly with height from the surface to the top of the mixed layer. Within the entrainment zone atop the mixed layer, $\bar{w}' \bar{\theta}'$ tends to be negative and about 10–20% of the magnitude of the flux at the surface, at least in conditions of shear-free convection. Within the mixed layer, $\partial \bar{w}' \bar{\theta}' / \partial z < 0$ implies mean warming; however, mean cooling is implied by $\partial \bar{w}' \bar{\theta}' / \partial z > 0$ within the entrainment zone, where $\bar{w}' \bar{\theta}'$, like $\bar{w}' w'$, also goes to approximately

zero. Boundary layer thermals overshoot their equilibrium levels and are responsible for the cooling in this layer. The vertical profile of turbulent moisture flux ($\bar{w}' \bar{r}'_v$) also tends to be linear (and greater than zero) within the daytime mixed layer, but $\bar{w}' \bar{r}'_v$ can increase or decrease with height (two types of profiles are drawn in Figure 4.2a), depending on the situation, which may imply drying or moistening of the mixed layer. Whether $\partial \bar{w}' \bar{r}'_v / \partial z$ is less or greater than zero depends to a large extent on the surface moisture characteristics. Within the overlying entrainment zone, $\partial \bar{w}' \bar{r}'_v / \partial z < 0$, implying net moistening there.

Neglecting advection and horizontal flux divergences, and assuming linear vertical turbulent flux profiles within

the mixed layer, it is easily shown from (4.22) and (4.23) that

$$\frac{\partial \langle \bar{\theta} \rangle}{\partial t} = \frac{[\overline{w' \theta'}|_0 - \overline{w' \theta'}|_{z_i}]}{z_i} \quad (4.57)$$

$$\frac{\partial \langle \bar{r}_v \rangle}{\partial t} = \frac{[\overline{w' r'_v}|_0 - \overline{w' r'_v}|_{z_i}]}{z_i}, \quad (4.58)$$

where the $\langle \rangle$ brackets indicate a vertical average from the surface to z_i and the subscripts 0 and z_i indicate that the turbulent fluxes are evaluated at $z = 0$ and at $z = z_i$, respectively. It can also be shown that

$$\frac{\partial z_i}{\partial t} = \frac{[\overline{w' \theta'}|_0 - \overline{w' \theta'}|_{z_i}]}{\frac{\partial \bar{\theta}}{\partial z}}, \quad (4.59)$$

where $\partial \bar{\theta} / \partial z$ should be evaluated just above the top of the mixed layer.

The above expressions describe the evolution of the (vertically constant) potential temperature and water vapor mixing ratio within the mixed layer. It is obvious from (4.57) and (4.59) that the rate of boundary layer warming and deepening slows as the day progresses and z_i increases. In principle, if a morning sounding is available, (4.59) can be integrated in time to obtain a prediction of the depth of the mixed layer and (using knowledge of the potential temperature of the initial sounding at z_i and assuming a neutral lapse rate in the final mixed layer) the mean (and surface) temperature associated with that mixed layer depth; $\overline{w' \theta'}|_0$ could be parameterized via (4.37) and $\overline{w' \theta'}|_{z_i}$ is typically 10–20% (assuming shear-free convection) of $-\overline{w' \theta'}|_0$ (Figure 4.2a). (The magnitude of $\overline{w' \theta'}|_{z_i}$ is related to what is sometimes called the *entrainment velocity*.) Of course, horizontal advects often affect the evolution of a boundary layer sounding in nontrivial ways such that they would deviate from this idealization. Another approach would be simply to integrate $\overline{w' \theta'}|_0$ with respect to time, which is just the total heat supplied to a sounding. The initial sounding could then be modified accordingly. On a thermodynamic diagram, for example, area is proportional to energy; thus, the final sounding could be estimated by knowing the total heating and constraining the lapse rate to be dry adiabatic within the mixed layer.

During the nighttime hours, a shallow inversion layer in contact with the surface is created owing to infrared heat loss by the ground (Figures 4.9, 4.10, and 4.11b). This layer, sometimes referred to as a *stable or nocturnal boundary layer*, becomes decoupled from the mixed layer because the inversion inhibits mixing. The remnant mixed layer from the previous day is termed the *residual layer*, and is characterized by nearly constant potential temperature and

water vapor mixing ratio. What is termed the entrainment zone during daytime conditions is usually just generically referred to as a capping inversion at night, because there is not much exchange between the overlying free atmosphere and residual layer during the nighttime hours.

The turbulent momentum, heat, and moisture fluxes tend to be negative within the nocturnal boundary layer (Figure 4.2b). The fluxes have their maximum magnitude (minimum value) at the surface, and the magnitude of the fluxes becomes negligible toward the top of the nocturnal boundary layer. In other words, $\partial \overline{u' w'}/\partial z$, $\partial \overline{w' \theta'}/\partial z$, and $\partial \overline{w' r'_v}/\partial z$ all are greater than zero, implying cooling and drying within the nocturnal boundary layer, as well as an effective drag on the mean wind.

The shallow nocturnal inversion layer grows in steps, which are often interrupted by *turbulent events* (shear-driven turbulent eddies) that deepen the cooled layer and render it less stable. Relative humidity increases within the nocturnal boundary layer, dew may form, and water vapor mixing ratio may decrease at the surface as condensation occurs. The lowest surface air temperatures occur on nights with the strongest net radiational cooling and on nights when turbulent events are limited (e.g., nights with weak winds). On these nights, the nocturnal inversion is strongest and shallowest.

As was the case for the profiles in Figure 4.11a, the profiles in Figure 4.11b are also idealized. For example, the depth of the residual layer relative to the depth of the nocturnal boundary layer is strongly a function of the mean wind shear; on a clear, windless night the nocturnal boundary layer may be only a few tens of meters deep, whereas on a cloudy, windy night the nocturnal boundary layer may be nearly as deep as the daytime mixed layer. Moreover, the surface water vapor mixing ratio may rise or fall after sunset depending on the degree of dew formation (which lowers the surface layer water vapor mixing ratio) versus the degree to which water vapor mixing ratio in the surface layer was lowered during daytime convective conditions because of the downward mixing of dry air (in which case, the surface layer water vapor mixing ratio may rebound after sunset when vertical mixing abates).

Winds at the top of the nocturnal boundary layer and within the residual layer accelerate during the nighttime hours as the effect of surface drag at these levels is effectively ‘shut off’ via decoupling of the nocturnal boundary layer from the overlying residual layer. A nocturnal low-level wind maximum (sometimes called a low-level jet) forms, the dynamics of which is the subject of Section 4.7. At the surface, nocturnal *drainage winds* may arise from the tendency for negatively buoyant air to sink toward the lowest elevations. Such winds are discussed in greater detail in Chapter 11.

4.4 Boundary layer convection

4.4.1 The Rayleigh number

As discussed above, the daytime boundary layer is dominated by convection. Usually the convection is non-precipitating, but on occasion, such as when unusually cold air masses are advected over relatively warm surfaces, boundary layer convection can be intense enough to produce significant precipitation. Lake-effect convection, which is treated in Section 4.5, is a prime example of this form of enhanced boundary layer convection. What is often referred to as deep, moist convection (DMC) is reserved for Part III. This variety of convection involves much larger buoyancy, CAPE, vertical velocities, and vertical displacements than the convection discussed in this chapter; the dynamics and organization of DMC are very different from the much shallower convection discussed below.

In Section 3.1, static instability was reviewed from the perspective of buoyancy forces acting *locally* on a parcel of air. One also can investigate the conditions needed for the onset of convection from a *global* perspective, that is, when buoyancy forces are distributed over a large horizontal area compared with the depth of the overturning layer. The term *thermal instability* is sometimes used to broadly refer to the instability of a fluid layer heated from below.

The conditions under which convective overturning commences were first studied roughly a century ago, both theoretically and experimentally, by Rayleigh and Bénard, respectively.¹⁰ The onset of convection in a thin layer of fluid at rest heated from below occurs when a dimensionless number, called the *Rayleigh number*, exceeds a critical threshold. The Rayleigh number, Ra, is expressed as

$$\text{Ra} = \frac{g \beta \Delta T H^3}{\nu \kappa}, \quad (4.60)$$

where ν and κ are the kinematic viscosity and thermal diffusivity, respectively, β is the coefficient of thermal expansion [$= \frac{1}{\alpha} (\frac{\partial \alpha}{\partial T})_p$ for air, where α is the specific volume, p is pressure, and T is temperature], and ΔT is the temperature difference between two plates separated by a vertical distance H . The Rayleigh number increases as ΔT increases. On the other hand, diffusion has a stabilizing effect; Ra decreases as ν and κ increase.

¹⁰ Henri Bénard (1874–1939) was a French physicist. It is now known that his experiments did not actually demonstrate the same thermal instability as studied by Rayleigh. Because of the thinness of the fluid used, Bénard instead discovered an instability due to surface tension differences that arise when a fluid is unevenly heated.

When $\text{Ra} > \text{Ra}_c$, where Ra_c is the *critical* Rayleigh number, convective motions in the statically unstable layer are able to overcome the stabilizing influence of molecular diffusion and thermal conductivity; thus, convective overturning ensues. It can be shown via linear stability analysis that the minimum Ra_c that must be exceeded for convective overturning to commence is approximately 120, which occurs when the upper and lower boundaries are free-slip and perfectly insulating, and when there is no mean vertical wind shear. The value of Ra_c increases if mean vertical wind shear is present, or if conducting or no-slip boundaries are imposed, which implies that these effects have a suppressing effect on the tendency for convective overturning.

It is reasonable to question the applicability of the aforementioned *Rayleigh-Bénard convection* to the convection observed within the atmospheric boundary layer. For starters, the atmospheric boundary layer is not capped by a rigid lid. Another issue is how the Rayleigh-Bénard convective cells compare with the structures observed in the atmospheric boundary layer. Although structures seen in laboratory experiments of Rayleigh-Bénard convection are qualitatively similar to structures sometimes seen within the atmospheric boundary layer (e.g., hexagonal updraft and downdraft cells), a closer look at the details of these structures reveals that boundary layer convective cells are often much flatter than Rayleigh-Bénard convective cells.

Whether or not Rayleigh-Bénard convection is an appropriate model for the convection observed within the atmospheric boundary layer, thermal instability certainly plays an important role in the development of boundary layer convection and turbulence. One complication in the atmospheric boundary layer is that additional instabilities related to the wind profile are commonly present as well (i.e., the mechanical generation of turbulence can be just as important as the generation of turbulence by buoyancy). Such dynamical instabilities affect the organization of boundary layer convection in ways that differ from the organization that might be expected in the presence of thermal instability alone. Further discussion of the structure of atmospheric boundary layer convection and how it relates to thermal and dynamical instabilities appears below.

4.4.2 Organization of convective motions

Despite the randomness of the motions associated with individual boundary layer eddies, boundary layer convection often exhibits a high degree of organization on scales larger than the scale of individual eddies. Convective motions are often organized into hexagonal cellular patterns when the vertical wind shear is weak

(Figure 4.12). As mentioned in the preceding section, such *mesoscale cellular convection* appears qualitatively similar to Rayleigh-Bénard convective cells. There is no rigorous theory explaining why hexagonal cells should be favored over other geometries such as rectangles or triangles, but some have speculated that hexagons are favored because nature seeks a geometrical configuration that minimizes the perimeter-to-area ratio.¹¹ The horizontal wavelength of Rayleigh-Bénard cells is roughly three times the depth of the overturning layer. Observations of cells in atmospheric boundary layers, however, have revealed much wider cells on occasion, with width-to-height (aspect) ratios at times as large as 30.

Open cellular convection is characterized by walls of cloud surrounding open, cloudless areas, with descent in these central open areas. *Closed* cellular convection comprises rings of open areas surrounding cloudy areas, with upward motion in the center (where the cloud is) and sinking motion in the rings. Cellular convection is most commonly observed over the oceans, and there is some suggestion that open (closed) cells tend to be favored

over warm (cold) water relative to the overlying air. When cellular convection is observed over land, it almost always is open cellular convection. For boundary layers capped by extensive cloudiness, as is often the case when closed cellular convection is observed, radiative cooling at cloud top probably plays an important role in driving the convection. Some laboratory studies of convection also suggest that open (closed) cellular convection depends on the large-scale vertical motion, with open (closed) cellular convection favored when the large-scale vertical velocity is downward (upward).¹² One additional discrepancy between laboratory experiments of Rayleigh-Bénard convection and observations of mesoscale cellular convection is that laboratory experiments of Rayleigh-Bénard convection yield closed cellular convection only when liquids are used and open cellular convection only when gases are used, whereas both types of cellular convection are observed in the atmosphere.

Atmospheric boundary layer convection also is commonly organized as counter-rotating horizontal vortices, called *horizontal convective rolls* (HCRs) (Figures 4.13–4.15). As is the case for convective cells, the vertical scale of HCRs spans the boundary layer. Aspect ratios can range

¹¹ A circle has the smallest perimeter-to-area ratio. The hexagon is the polygon that most closely approximates a circle and can be fitted into an array of elements with common boundaries.

¹² See Krishnamurti (1975b).

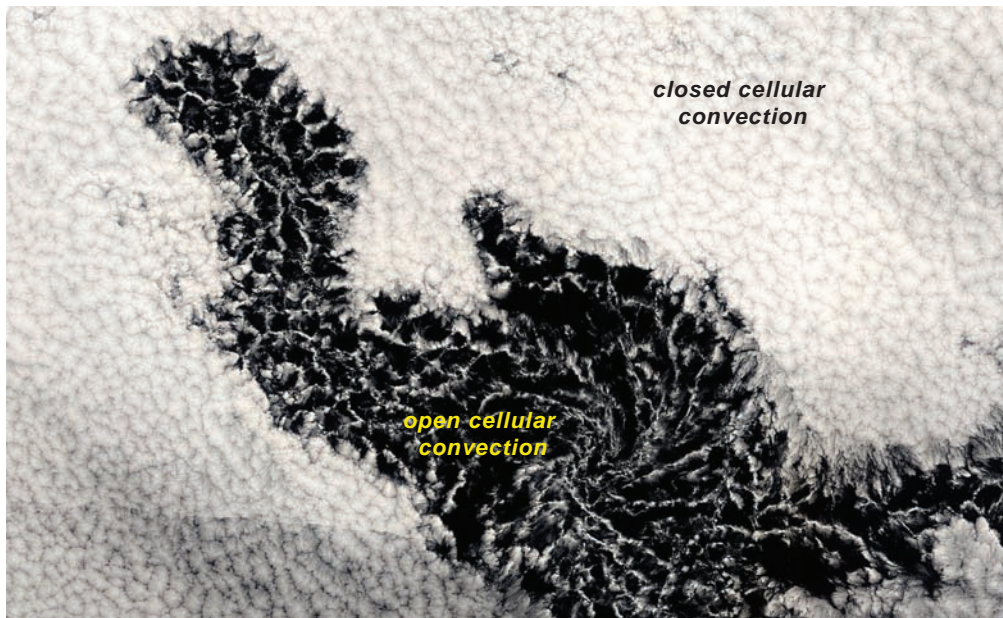


Figure 4.12 Moderate Resolution Imaging Spectroradiometer (MODIS) satellite image showing open and closed cellular convection off the coast of Peru on 30 August 2003. Image courtesy of the MODIS Rapid Response Project at the National Aeronautics and Space Administration (NASA) Goddard Space Flight Center (GSFC).

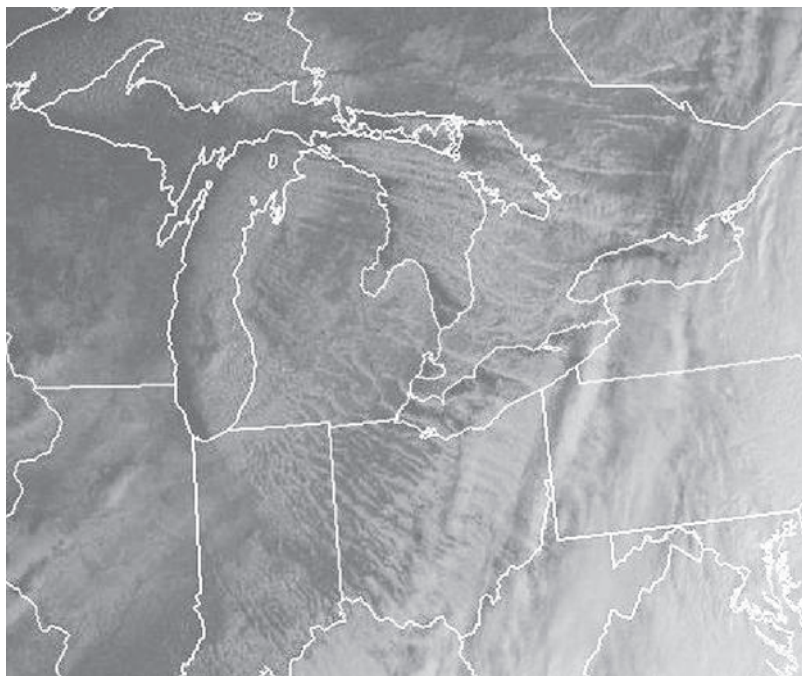


Figure 4.13 HCRs observed in the wake of a cold front in the United States Great Lakes region at 1415 UTC 14 January 2005.



Figure 4.14 Cloud streets (a manifestation of HCRs) viewed from an airplane. Photograph by Joel Gratz.

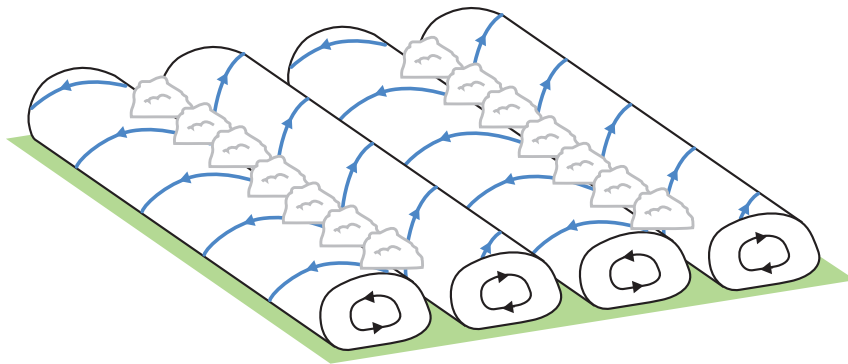


Figure 4.15 Schematic illustration of HCRs in the boundary layer. Black arrows indicate the winds due to the rolls and blue arrows indicate the total wind. Note that the characteristic distance between cloud rows is twice the characteristic width of the convective rolls. (Adapted from Brown [1983].)

from 3 to 10, depending on the dominant forcing for the HCRs, which can vary from case to case (the different instabilities that can give rise to HCRs, which will be discussed below, are associated with different aspect ratios). HCRs produce coherent perturbations in the temperature, humidity, and wind fields because HCRs themselves tend to have coherent updrafts and downdrafts. HCRs also modulate mean surface fluxes and boundary layer depth. HCRs can give rise to the familiar *cloud streets* (Figure 4.14) of nearly unbroken cloud bands within the boundary layer, provided that ample moisture is present in the boundary layer. The ascending branch of the roll circulations is the favored area for the formation of clouds.

The formation of HCRs has been the subject of almost countless modeling and theoretical studies, with some suggestions that they form when a critical value of the buoyancy flux is reached.¹³ Many observations have suggested that HCRs tend to be favored over cells when

$$-\frac{z_i}{L} \lesssim 25, \quad (4.61)$$

where L is the *Obukhov length*, defined as

$$L = -\frac{\overline{\theta} u_*^3}{k g \overline{w' \theta'}|_0}. \quad (4.62)$$

The Obukhov length roughly represents the depth over which the generation of turbulence by the vertical wind shear dominates buoyancy-driven turbulence. In a stable (unstable) surface layer $L > 0$ ($L < 0$), and for a neutral surface layer $L = 0$. Given that both z_i and $\overline{w' \theta'}|_0$ tend to increase from early morning to midday and, as a result

of vertical mixing, the mean vertical wind shear (and thus momentum flux and u_*) tends to decrease from early morning to midday, $-z_i/L$ therefore tends to increase from early morning to midday. This diurnal trend in $-z_i/L$ is consistent with frequent observations of HCRs developing early in the day and transitioning to cellular or disorganized convection later in the day as $-z_i/L$ exceeds 25.¹⁴ In contrast, a number of other studies have failed to document a significant correlation between roll formation and $-z_i/L$, or other parameters involving mean shear, surface fluxes, or static stability. The lack of agreement could be attributable to nonlinear scale interactions between large (roll) and small (subroll) scales,¹⁵ or gravity waves excited by boundary layer convection or processes in the overlying free atmosphere that might interact with boundary layer convection to influence its organization.

HCRs can be driven by a number of instabilities. HCRs driven by thermal instability alone tend to be aligned with the mean vertical wind shear in the boundary layer. Thus, the convective motions are arranged so that the wind shear is minimized along the lines of updrafts and downdrafts.¹⁶ This orientation probably minimizes entrainment and its suppressing effects. Entrainment tends to be maximized upshear and downshear of updrafts, and, by forming lines

¹⁴ See Weckwerth *et al.* (1999).

¹⁵ See Miles and Verlinde (2005).

¹⁶ As mentioned in Section 4.4.1, linear theory finds that R_a increases with increasing mean shear, implying that shear has a stabilizing effect on the onset of Rayleigh-Bénard convection. This might also imply that thermally driven HCRs would align themselves with the mean shear, if the theory of Rayleigh-Bénard convection is at all applicable to atmospheric boundary layer convection, for this orientation would minimize the mean shear present in the plane of the wind perturbations associated with the HCRs.

¹³ See Weckwerth *et al.* (1999).

aligned with the shear, updrafts are somewhat protected from the environment.

It is not clear whether HCRs driven solely by thermal instability exist, however, because wind profiles containing shear frequently are also susceptible to shear instability, as discussed in Section 3.5. *Inflection-point instability*, as the name suggests, is present when a vertical wind profile has an inflection point, that is, $\partial^2 \bar{u} / \partial z^2$ or $\partial^2 \bar{v} / \partial z^2$ changes sign somewhere in the wind profile, and the inflection point in the velocity profile is associated with a relative *maximum* in wind shear (an inflection point alone could be associated with a relative maximum *or* minimum in vertical wind shear). Inflection-point instability generates rolls with axes normal to the wind shear orientation. Thus, for a straight hodograph dominated by speed shear, rolls tend to be normal to the mean wind. For a straight hodograph dominated by directional wind shear, the rolls may be aligned roughly with the mean wind. For a curved hodograph (e.g., the Ekman wind profile), the relationship between the mean wind and roll orientation is not as easy to generalize and depends on the details of how both speed and direction vary with height.

Parallel instability is also a type of shear instability, but in contrast to inflection-point instability, it does not require an inflection point in the vertical wind profile but does require viscosity and the Coriolis force.

The Ekman wind profile defined by (4.50) and (4.51) (Figure 4.7) has been shown to be prone to both inflection-point and parallel instability. The Ekman wind profile is derived from assuming the presence of viscosity and the Coriolis force, so naturally one would expect that parallel instability could be present. Parallel instability has been shown to promote HCRs that are oriented roughly 10–20° to the right of the geostrophic wind when an Ekman mean wind profile is assumed (the geostrophic wind is assumed to be constant with height in deriving the Ekman hodograph). However, the Ekman wind profile also contains an inflection point and is therefore also susceptible to inflection-point instability. Figure 4.16 shows the component of the mean velocity of the Ekman wind profile (Figure 4.7) in vertical planes having a range of orientations relative to the geostrophic wind. Although inflection points are present for all of the wind profiles shown in Figure 4.16, the wind profile associated with the largest growth rate of inflection-point instability is the profile that results from having the vertical plane oriented 10–20° to the left of the geostrophic wind (not shown). In other words, if inflection-point instability is the dominant forcing for HCRs, then we would expect it to produce HCRs oriented 10–20° to the left of the geostrophic wind in the boundary layer.

Given that both inflection-point and parallel instability would lead to HCRs roughly aligned with the boundary

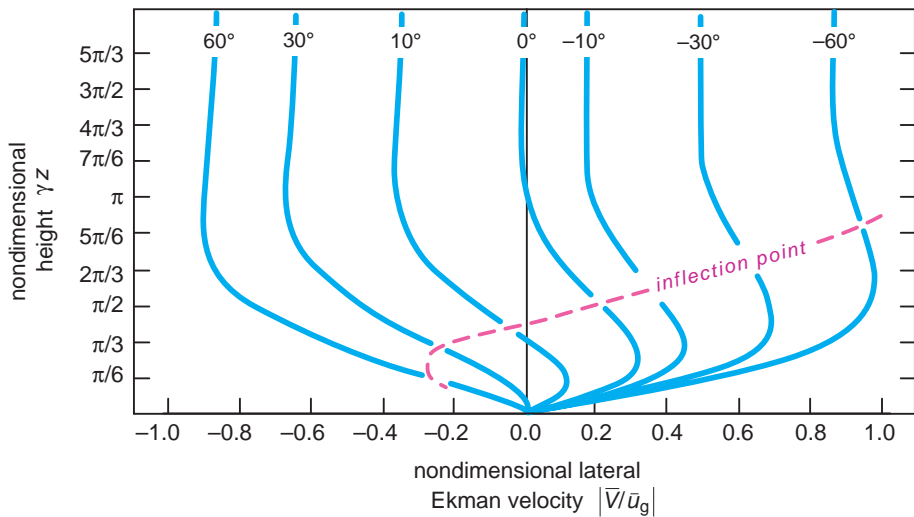


Figure 4.16 Vertical profiles of \bar{V} , the magnitude of the Ekman mean wind profile in a plane normal to a roll. Profiles for rolls oriented at $\pm 10^\circ$, $\pm 30^\circ$, and $\pm 60^\circ$ with respect to \bar{v}_g are shown (positive orientations are to the left of \bar{v}_g). Wind speeds are scaled by the geostrophic wind speed, $|\bar{v}_g| = |\bar{u}_g|$. On the ordinate, γz is just a dimensionless height, where $\gamma = (f/2K_m)^{1/2}$. Also see Figure 4.7. (Adapted from Brown [1972a].)

layer mean wind,¹⁷ historically there has been some difficulty in establishing which instability mechanism might be operating. Because of the larger growth rates associated with inflection-point instability compared with parallel instability, inflection-point instability is believed to be the dominant dynamical instability in most cases. In some situations, however, it is possible that parallel instability would be of greater importance. One situation might be when there is a smooth lower boundary (small c_d), in which case the inflection point in the Ekman hodograph becomes less prominent. The parallel instability mechanism might also be important when the geostrophic wind varies with height, especially in terms of direction, such that the total wind profile, comprising geostrophic and ageostrophic parts (with the ageostrophic part resulting from the effects of surface drag), lacks an inflection point altogether.

On most days on which HCRs are observed, it is likely that both thermal and dynamical instabilities contribute to the formation and orientation of the HCRs. Because of the superpositioning of the various dynamics by which HCRs may form, HCRs may have a wide range of orientations, from being closely aligned with the boundary layer mean wind to deviating from the boundary layer mean wind direction by a large angle. It is probably fair to say, however, that HCRs are usually oriented within 30° of the mean wind in the boundary layer, and, to the extent that the boundary layer hodograph even slightly resembles the Ekman profile, HCRs would also tend to be oriented within 30° of the mean boundary layer shear (the mean boundary layer shear in the Ekman spiral is nearly aligned with the mean boundary layer wind; see Figure 4.7). When strong large-scale temperature advection is occurring, however, the mean wind and mean shear can point in significantly different directions.

Finally, it might be worth mentioning that much shallower convective rolls have also been observed within the surface layer, but these appear to be dynamically different from the HCRs described above. They are usually only 100–200 m deep, have a horizontal wavelength of 300–600 m, and are 500–2000 m long. They are aligned with the surface layer wind and have faster (slower) horizontal wind speeds within their downdrafts (updrafts). They are very likely to be shear driven, but the precise formation mechanisms are still being debated.

¹⁷ Even though the theoretical analyses of the dynamical stability of the Ekman wind profile suggests differences in HCR orientation of 20–40° for the inflection-point versus parallel instability mechanisms, observed mean wind profiles practically never match the Ekman hodograph perfectly. It is therefore difficult to attribute HCRs confidently to one dynamical instability mechanism versus another by simply inspecting the HCR orientation.

4.5 Lake-effect convection

Especially intense boundary layer convection can develop when cold air masses are advected over relatively warm surfaces. In such conditions, the sensible heat flux is greatly enhanced relative to typical magnitudes for a given location and time of day/year. Such augmented boundary layer convection tends to be much more vigorous than the typically nonprecipitating convection discussed in the preceding section, although the basic dynamics are similar for the most part.

The focus in this section will be on boundary layer convection that is enhanced by the advection of cold air over relatively warm water. Although boundary layer convection can occasionally be intense enough to produce precipitation in cold air outbreaks over land, the most spectacular outbreaks of boundary layer convection occur when cold air is advected over relatively warm water and is destabilized by both heat and moisture fluxes from the underlying surface. A cold air mass that is advected over relatively warm land is also destabilized, but the destabilization is much more dramatic in the case of warm water because of the greater thermal inertia of the water and the much greater moisture flux from a water surface compared with that from a land surface. Regarding the thermal inertia of water, it does not cool as rapidly as the land, and thus the temperature difference between the water surface and overlying cold air mass, which drives the sensible heat flux, can be sustained for a long duration.

The aforementioned episodes of precipitating boundary layer convection usually involve lakes, and therefore are often referred to as *lake-effect* precipitation (rain or snow) events, although *ocean-effect* and *bay-effect* precipitation also occurs in various parts of the world. Hereafter we shall just generically refer to all such events as lake-effect events without regard for whether the body of water is an ocean, sea, lake, or bay.

The regions downwind of the Great Lakes of North America are among the best-known locations for lake-effect precipitation (Figures 4.17 and 4.18), with the height of the lake-effect ‘season’ being in the late fall to early winter, when water temperatures are warmest relative to the air masses advected over the lakes (Figure 4.19). Most of the annual snow accumulation in these so-called *snow belts* is attributable to lake-effect snow. Some locales downwind of Lake Ontario average nearly 300 cm per year. In the United States, lake-effect precipitation also occurs downwind of the Great Salt Lake, and even occasionally along the West Coast near the mouth of the Columbia River and downwind of the Chesapeake Bay, Delaware Bay, and Cape Cod Bay. It also is fairly common downwind of many Canadian lakes

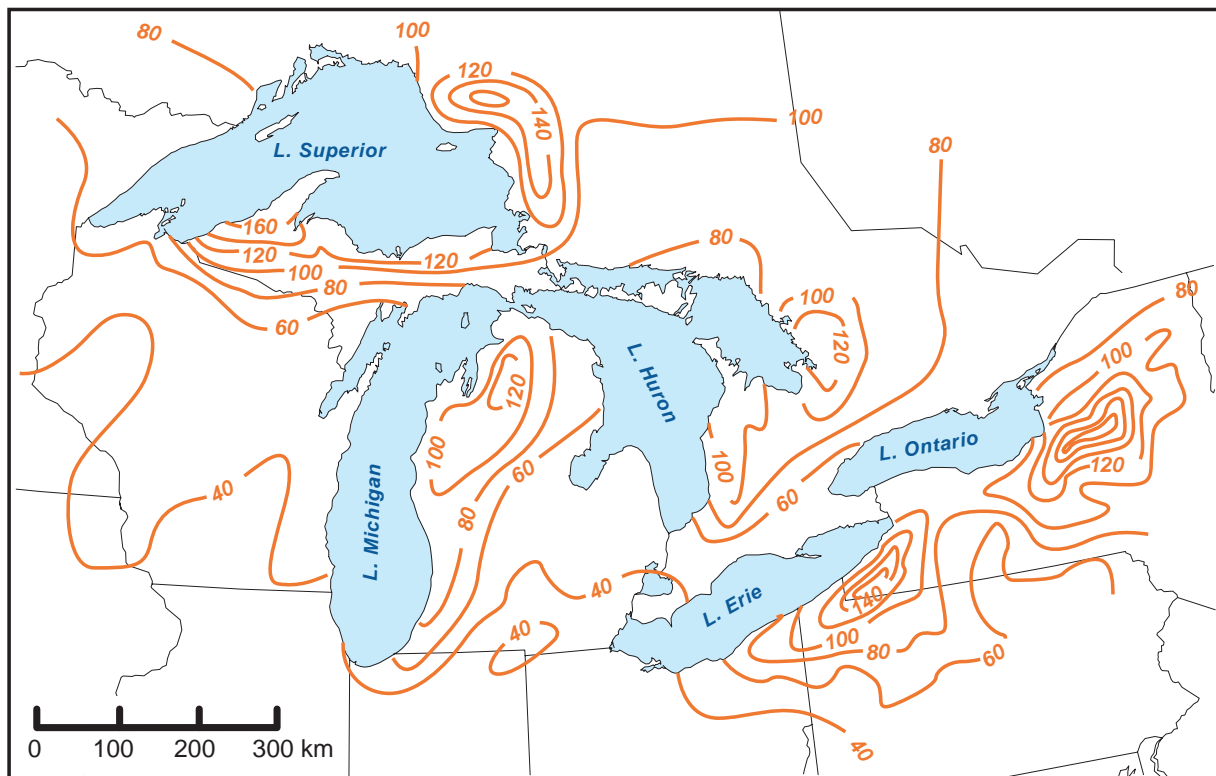


Figure 4.17 Mean annual snowfall (inches) for the Great Lakes region. (Adapted from Eichenlaub [1979].)

(e.g., Lake Winnipeg, Lake Athabasca, Great Slave Lake), as well as in other parts of the world. For example, lake-effect snow occurs in the United Kingdom when easterlies advect cold continental air over the North Sea. Lake-effect precipitation also occurs in the vicinity of the Sea of Japan, Adriatic Sea (affecting parts of Italy), Baltic Sea (affecting parts of Sweden), Aegean Sea (cold northeasterlies called boreas have been associated with heavy lake-effect snows in the vicinity of Athens, Greece), and Black Sea (affecting parts of Turkey and Georgia). By late winter, the surfaces of many bodies of water have frozen, effectively putting an end to the lake-effect season. For high-latitude lakes, such as those in Canada, the lake-effect season may end as early as late fall. For other bodies of water, such as deep lakes (e.g., Lake Ontario; this is principally why the downstream region is the snowiest place in the Great Lakes region) or salt water (e.g., the Great Salt Lake or oceans), the water surface may remain unfrozen all winter long.

The convective clouds associated with lake-effect precipitation can be several kilometers deep with peak vertical velocities as large as 5 m s^{-1} . In the case of lake-effect snow, snowfall rates as large as 30 cm h^{-1} and 75 cm day^{-1} have

been observed, as has lightning in some of the most intense cases. Banded structures are commonly observed and can have a variety of orientations, which is not surprising given the discussion of boundary layer convection structures in Section 4.4. The heaviest precipitation usually falls when linear updrafts are present and exhibit little crosswise movement. More will be said about the organization of the convection later in this section. We shall first touch upon the conditions necessary for its development.

Lake-effect precipitation is driven by the production and subsequent release of CAPE, albeit considerably smaller amounts of CAPE than typically present in the environments of the much deeper warm season convection that is the focus of Part III. As earlier alluded to, the CAPE is generated by modification of continental polar or arctic air by a relatively warm body of water. Thus, the most intense lake-effect snows tend to occur behind strong cold fronts in fall and early winter (by late winter, when many bodies of water prone to lake-effect precipitation have frozen, the surface moisture flux is virtually eliminated, as are the chances for lake-effect precipitation). The passage of relatively cold, dry air over a warm water surface generates large

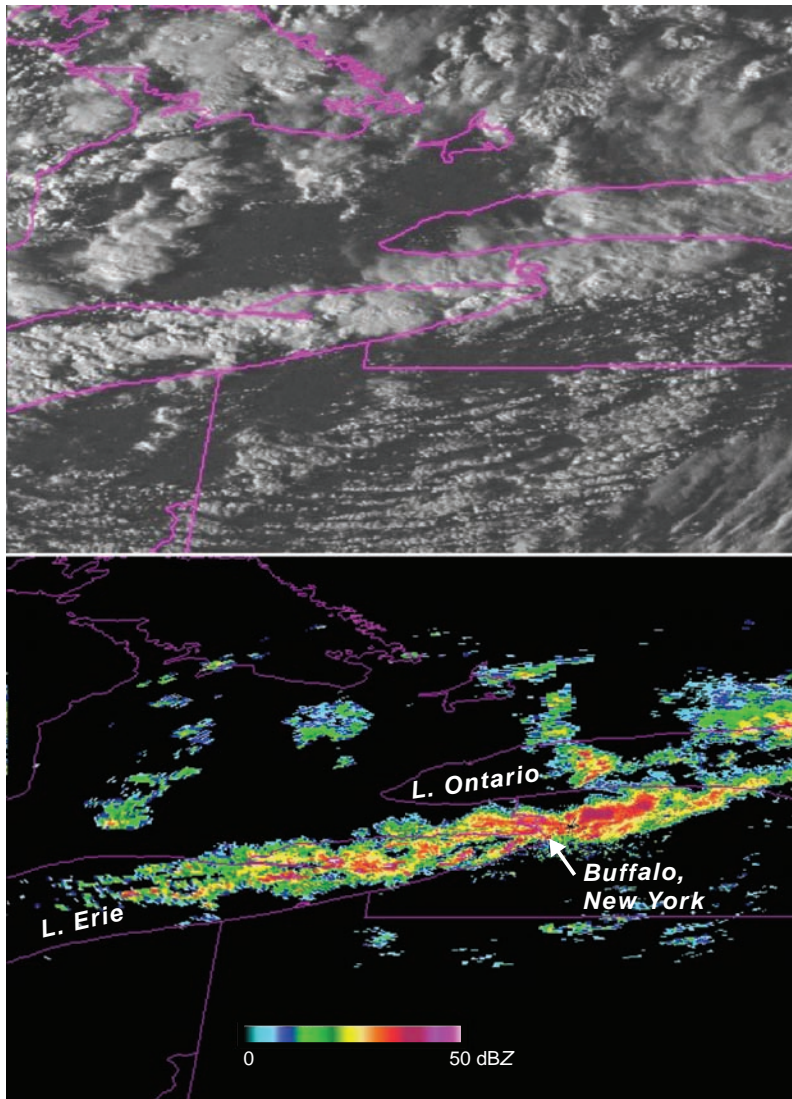


Figure 4.18 (Top) Visible satellite and (bottom) radar reflectivity imagery of an intense lake-effect snow band at 2115 UTC 12 October 2006. As much as 60 cm (two feet) of snow fell in proximity to Buffalo, NY. Cloud tops exceeded 8 km at times (this is extremely unusual, even in strong lake-effect convection episodes), with frequent lightning also observed. A very warm early fall Lake Erie temperature of 17°C, combined with 850 mb temperatures as cold as -7°C, contributed to particularly large low-level instability.

surface sensible and latent heat fluxes (Figure 4.20). For a given wind speed, the larger the temperature difference between the overlying cold air mass and the warm water surface, the larger the sensible and latent heat fluxes and the more dramatic the low-level lapse rate destabilization and moistening. In particularly intense cold-air outbreaks (water-air temperature differentials greater than 30 K and winds at anemometer level greater than 20 m s^{-1}),

the surface sensible and latent heat fluxes can exceed 1000 W m^{-2} .

The rate of warming experienced by an air parcel moving just above the surface (say, at standard anemometer height) as it traverses a warm body of water is given by

$$\frac{d\bar{\theta}_a}{dt} = -\frac{\partial}{\partial z}(\overline{w'\theta'}) \Big|_a, \quad (4.63)$$

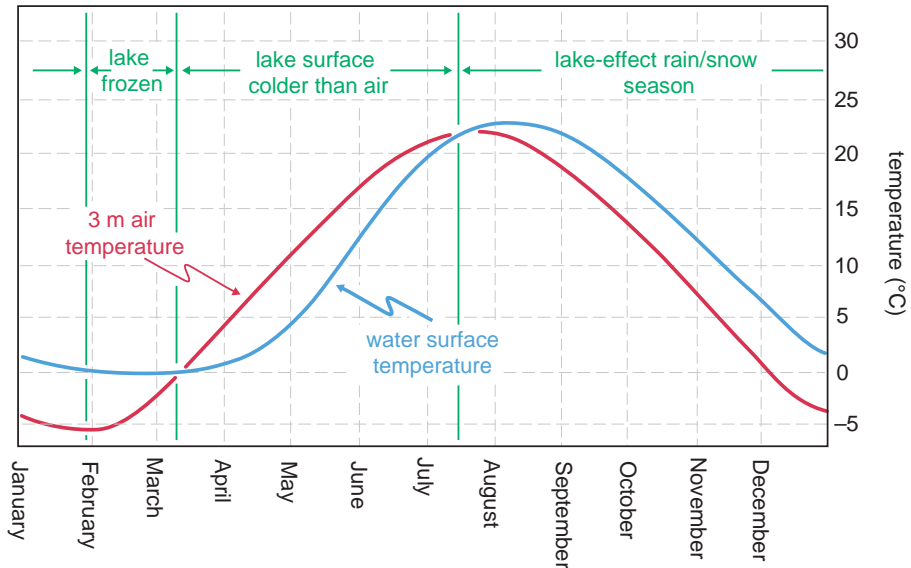


Figure 4.19 Annual cycle of 3 m air temperature and Lake Erie surface temperature. The displacement of the phases of the cycles favors lake-effect convection in the fall and early winter. (Adapted from Niziol *et al.* [1995].)

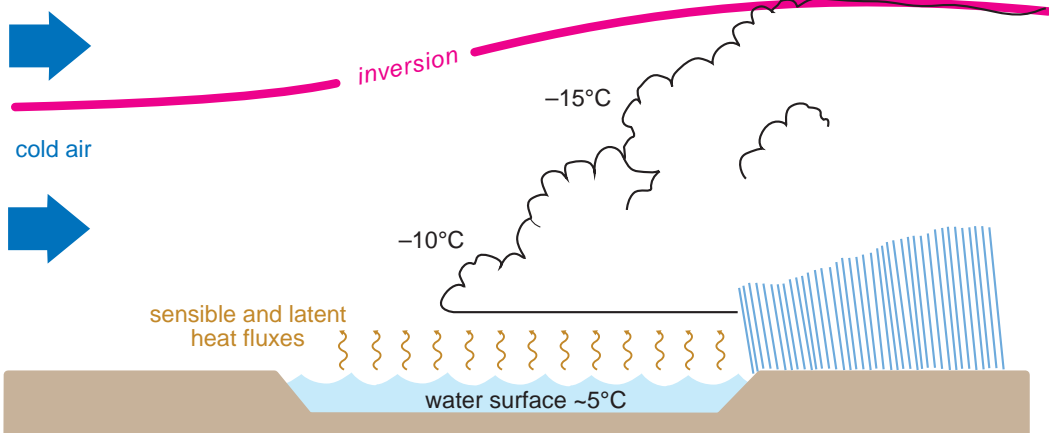


Figure 4.20 Schematic illustrating the polar or arctic air mass modification that leads to the development of lake-effect convection. (Adapted from Davis *et al.* [1968].)

where $\bar{\theta}_a$ is the mean potential temperature of the air at standard anemometer height and the rhs is the vertical heat flux convergence at standard anemometer height. The horizontal flux convergence has been neglected. If we assume a linear vertical profile of $w'\theta'$ (i.e., assume a constant vertical heat flux convergence; see Figure 4.2a), then (4.63) can be written as

$$\frac{d\bar{\theta}_a}{dt} = - \frac{[w'\theta'|_{z_i} - w'\theta'|_0]}{z_i}, \quad (4.64)$$

where z_i is the depth of the mixed layer and $w'\theta'|_{z_i}$ and $w'\theta'|_0$ are the heat fluxes at the top of the mixed layer and at z_0 , respectively. Assuming $w'\theta'|_{z_i} \approx -0.2 w'\theta'|_0$

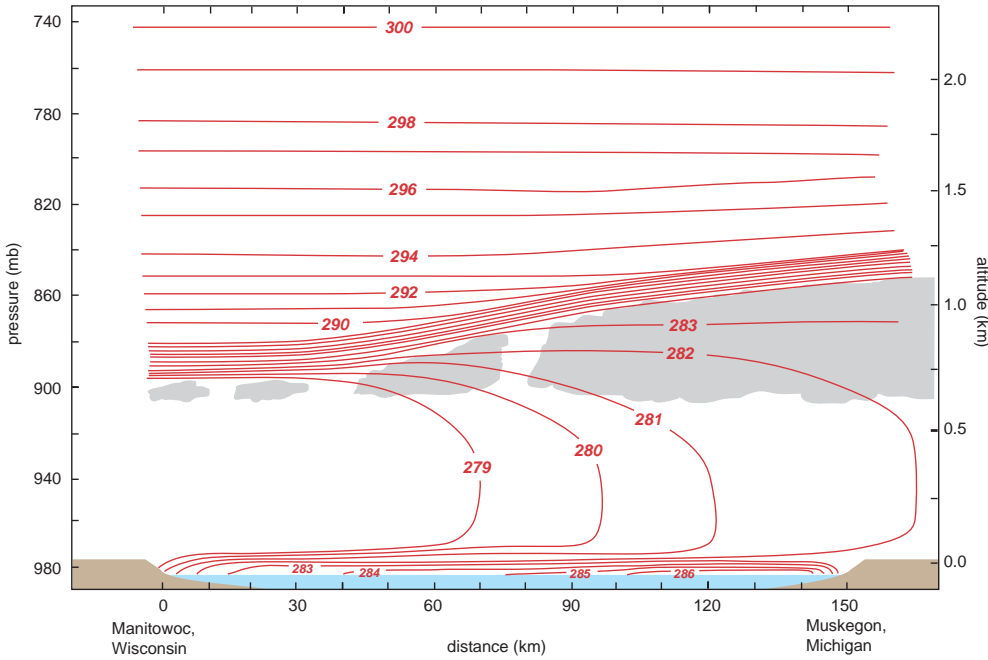


Figure 4.21 Vertical cross-section of potential temperature over Lake Michigan on 5 November 1970 obtained from aircraft transects. The mean wind is from left to right (northwest to southeast). The clouds shown are based on visual observations from the aircraft. (Adapted from Lenschow [1973].)

(Figure 4.2) and parameterizing the surface heat flux using (4.37), we obtain

$$\frac{d\bar{\theta}_a}{dt} \approx \frac{1.2 c_h (\bar{u}_a^2 + \bar{v}_a^2)^{1/2} (\theta_0 - \bar{\theta}_a)}{z_i}, \quad (4.65)$$

where θ_0 is the potential temperature of the water surface in this case. Integrating (4.65) with respect to time gives

$$\Delta\bar{\theta}_a \approx \frac{1.2 c_h (\bar{u}_a^2 + \bar{v}_a^2)^{1/2}}{\bar{z}_i} \frac{(\theta_0 - \bar{\theta}_a)}{\Delta t}, \quad (4.66)$$

where $\Delta\bar{\theta}_a$ is the amount of warming experienced by the parcel moving over the relatively warm surface ($\theta_0 - \bar{\theta}_a > 0$) over a time interval Δt , and the (\cdot) operator acting on z_i , $\theta_0 - \bar{\theta}_a$, and $(\bar{u}_a^2 + \bar{v}_a^2)^{1/2}$ represents an average over Δt (z_i increases with time/distance as cold air is advected over a warm surface, and $\theta_0 - \bar{\theta}_a$ decreases with time/distance).¹⁸ Given that $\Delta t = L/|\bar{\mathbf{v}}|$, where L is the distance traveled over the warm water surface (called the *fetch*) and $|\bar{\mathbf{v}}| = (\bar{u}_a^2 + \bar{v}_a^2)^{1/2}$ is the mean wind speed at

anemometer level averaged over the fetch, (4.66) can be written as

$$\Delta\bar{\theta}_a \approx \frac{1.2 c_h L (\theta_0 - \bar{\theta}_a)}{\bar{z}_i}. \quad (4.67)$$

Note that $\Delta\bar{\theta}_a$ is independent of the mean wind speed $|\bar{\mathbf{v}}|$ in (4.67). (In actuality, c_h weakly depends on $|\bar{\mathbf{v}}|$; thus, $\Delta\bar{\theta}_a$ is probably not entirely independent of $|\bar{\mathbf{v}}|$ as is suggested by the expression above.) For $c_h = 0.002$, $\theta_0 - \bar{\theta}_a = 10$ K, $L = 100$ km, and $\bar{z}_i = 1$ km, (4.67) yields $\Delta\bar{\theta}_a \approx 2.4$ K, which compares favorably with Figure 4.21.

A similar approach can be used to evaluate the moistening of the same air parcel, that is, replacing $\bar{\theta}_a$ in (4.63) with the water vapor mixing ratio of the air at standard anemometer level, \bar{r}_{va} . The vertical profile of $w'r'_v$ within the mixed layer is much less certain than the profile of $w'\theta'$, but observations in lake-effect convection cases indicate that we can assume a linear profile of $w'r'_v$ such that $w'r'_v|_{z_i} \approx 0.6 w'r'_v|_0$. If $w'r'_v|_0$ is parameterized using (4.38), then one obtains

$$\Delta\bar{r}_{va} \approx \frac{0.4 c_e L (r_{v0} - \bar{r}_{va})}{\bar{z}_i}. \quad (4.68)$$

¹⁸ Fleagle and Businger (1980) derive a more complicated expression for the air mass modification that does not require averages over the time interval Δt to be estimated.

Here r_{v0} is the *saturation* water vapor mixing ratio for the temperature of the water surface (it is assumed that the air in the microlayer *above* the water surface is saturated). For $c_e = 0.002$, $(r_{v0} - \bar{r}_{va}) = 4.0 \text{ g kg}^{-1}$, $L = 100 \text{ km}$, and $\bar{z}_i = 1 \text{ km}$, (4.68) yields $\Delta\bar{r}_{va} \approx 0.3 \text{ g kg}^{-1}$, which corresponds to an increase in dewpoint temperature of $\approx 1.5\text{--}2.5 \text{ K}$ at temperatures and pressures typical of the cold season.¹⁹

Figure 4.21 (cf. Figure 4.20) shows a vertical cross-section of potential temperature analyzed from aircraft observations obtained over Lake Michigan during a period of cold-air advection. Lake-effect clouds developed, but they were not deep enough to produce significant lake-effect precipitation. The plot nicely shows the modification of the cold air mass as it is advected over the lake. Approximately 3 K of warming occurs from west to east, and strongly superadiabatic temperature gradients develop just above the water surface. A deepening of the mixed layer from west to east as a direct result of the boundary layer modification also is obvious.

Observations indicate that a necessary condition for significant lake-effect convection is that the low-level (surface to 850 mb) lapse rate becomes at least dry adiabatic ($\approx 10 \text{ K km}^{-1}$) as a result of modification by the water surface. Given the typical height of 850 mb surfaces ($\sim 1300 \text{ m}$), a forecasting rule of thumb is that the 850 mb temperature should be at least 13 K lower than the water surface temperature for the development of significant lake-effect convection. Given that, in most cases, the cold air near the water surface is not warmed to the temperature of the water surface (the air and water temperatures would be most likely to reach equilibrium when the near-surface, upstream air is not much colder than the water surface, and when the fetch is long), in many cases a 13 K differential between the water surface and 850 mb temperatures may not lead to a sufficient destabilization of the cold air mass. Thus, the 13 K guideline should be viewed as a minimum threshold. The longer the fetch of cold air over the lake, the greater the amount of time for surface fluxes to modify the polar or arctic air and sufficiently destabilize the lower atmosphere. Usually the fetch must be at least 75 km in length, which prevents small lakes from being able to produce lake-effect convection.

The warming and moistening estimates obtained above yield an increase in equivalent potential temperature, θ_e , of $\sim 3\text{--}4 \text{ K}$, which is very significant. It can easily be the difference between a sounding having no CAPE and a sounding having enough CAPE to support vigorous

¹⁹ Obviously r_{va} cannot increase to values that exceed the saturation water vapor mixing ratio, but the cold air that is modified in passing over relatively warm water usually starts out so dry that it remains far from saturation even after modification.

lake-effect convection. CAPE would be expected to be a maximum at the downwind shoreline, and values as large as 200 J kg^{-1} can be achieved as a result of the aforementioned air mass modification (Figure 4.22; note that the soundings shown in Figure 4.22 were launched at an inland location and that probably greater CAPE is available to a parcel having the thermodynamic properties of the air immediately offshore, as is suggested by Figure 4.21).²⁰ The equilibrium level for the buoyant updraft parcels is usually no higher than 4–5 km (the 12–13 October 2006 case shown in Figure 4.18 was an exception), where a temperature inversion tends to be observed (Figure 4.22b–e). Lake-effect snows subside when the inversion lowers and intensifies, owing to midlevel subsidence, which also is common in the wakes of departing cold fronts (Figure 4.22f).

Although the air mass modification and destabilization discussed above is fundamentally important for the development of lake-effect precipitation, other mesoscale dynamical processes are important as well and are sensitive to wind direction. The air mass modification over a lake generates a horizontal air temperature gradient directed toward the lake center, approximately normal to the shoreline (Figure 4.23). The baroclinity leads to a thermally direct solenoid that is maximized along the downwind shoreline (this is really just a land-breeze circulation; land breezes will be treated further in Chapter 5). The magnitude of the baroclinity, which determines the strength of the solenoid, is a function of the degree of air mass modification; thus, the strength of the solenoid increases with increasing fetch. Depending on the lake geometry and wind direction, the mesoscale forcing resulting from lake-generated baroclinity can influence the organization of lake-effect convection in important ways. Mesoscale convergence can also be generated on the downwind and right (with respect to the mean wind direction and in the northern hemisphere; left in the southern hemisphere) shorelines as a result of differential surface drag (Figure 4.24), where a larger cross-isobaric wind component is present over the rougher land surface compared with the smoother water surface. Moreover, orographically forced ascent has been found to be important in contributing to the mesoscale ascent that favors the development of significant lake-effect precipitation events (terrain typically slopes upward away from the shoreline), as has large-scale, cyclonic, geostrophic relative vorticity in the boundary layer (i.e., Ekman pumping).

As one would probably surmise, the organization of lake-effect convection is strongly influenced by the wind speeds and vertical wind shear. The shape of the lake and, in the case of highly elliptical lakes (e.g., Lakes Erie and

²⁰ Moist absolutely unstable layers (MAULs) are occasionally observed in simulations of lake-effect convection (Sousounis and Mann, 2000). The effects of such layers on lake-effect convection are not well understood.

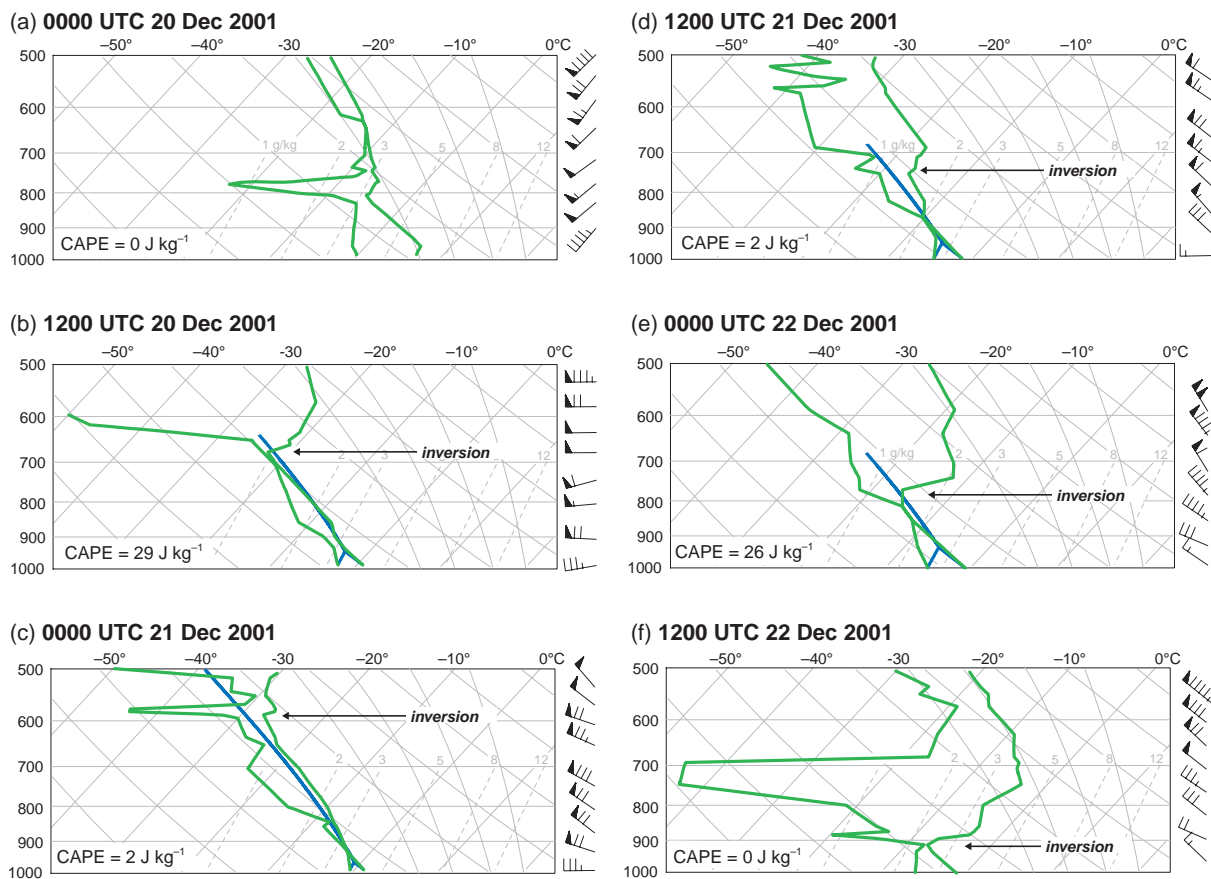


Figure 4.22 Soundings from Buffalo, NY, obtained (a) before, (b)–(e) during, and (f) after a lake-effect snow event downwind of Lake Erie that occurred between 0600 UTC 20 December and 0000 UTC 22 December 2001. Buffalo is located at the eastern end of Lake Erie. The destabilization of the 1000–700 mb layer is evident from 0000–1200 UTC 20 December, as is a rapid lowering of the inversion from 0000 UTC to 1200 UTC 22 December, which was associated with the demise of the lake-effect convection. At times when CAPE is present, the trajectory of a parcel lifted from the surface is also overlaid (undiluted ascent assumed). Note that greater CAPE would probably be available to parcels having the thermodynamic properties of the air immediately offshore, as is suggested by Figure 4.21, which shows that the highly superadiabatic conditions over the lake are absent inland.

Ontario in North America), the angle at which the wind crosses the lake, can also influence the organization of the convection. Lake-effect convection tends to be banded, although it occasionally can be somewhat cellular. When cellular convection is observed, the wind shear tends to be weak, as was discussed in Section 4.4. In the more commonly observed cases of banded precipitation, bands can be either shore parallel (with respect to the downstream shoreline, i.e., approximately perpendicular to the mean wind direction) or approximately aligned with the mean wind and mean wind shear (usually the mean wind and mean wind shear do not vary by more than 20° in the cold-air outbreaks that instigate lake-effect convection).

Figure 4.25 shows a lake-effect snow event in the Great Lakes region in which a wide variety of convective modes are present on different lakes at the same time. These different modes are discussed below.

The heaviest lake-effect precipitation events occur when strong winds ($7\text{--}15 \text{ m s}^{-1}$) blow parallel to the major axis of an highly elliptical lake. In such circumstances the convection can take the form of a single, intense band (e.g., the band that extends off of Lake Ontario in Figure 4.25). Such bands are typically 20–50 km wide and 50–200 km long. It seems that this combination of wind direction and lake shape not only maximize the fetch but also the positive effect of the land-breeze circulation, which, in such cases,

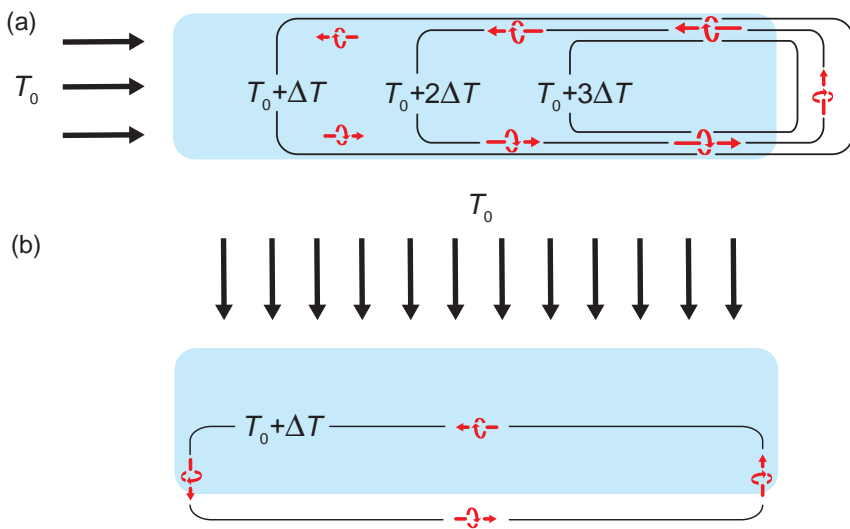


Figure 4.23 The horizontal temperature gradient that arises from the modification of the boundary layer over the relatively warm lake generates thermally direct solenoids, with intensity increasing in the downwind direction (the degree of air mass modification increases downwind). (a) In the case of an elongated lake (blue) with the wind blowing parallel to the major axis of the lake, the solenoids give rise to mesoscale convergence and updraft along the major axis that can promote the formation of an intense, single convective band. The fetch is also maximized, thus the strength of the solenoids is maximized (the horizontal vorticity vectors associated with the solenoids are indicated with red arrows, as is the sense of rotation; the magnitude of the horizontal vorticity is proportional to the size of the vectors). (b) In the case of winds blowing across the same lake parallel to the minor axis, the fetch is minimized. Boundary layer modification is therefore minimized as well, resulting in weaker solenoids. Moreover, the lake geometry relative to the wind direction further reduces the contribution of the solenoids to upward motion over the lake (even if the air mass were somehow equally modified despite the shorter fetch, the horizontal temperature gradient between the shore and lake center would be less than in the case of winds blowing down the major axis of the lake). Mesoscale convergence and updraft are weaker than in (a) and largely confined to the downwind shoreline. In the case of relatively weak mean winds, shore-parallel convective bands can form or, in the case of faster mean winds, HCRs may be observed (by ‘shore-parallel’ bands, we are referring to bands that are parallel to the downstream shoreline, and thus approximately perpendicular to the mean wind, in contrast to HCRs, which tend to be parallel to the mean wind).

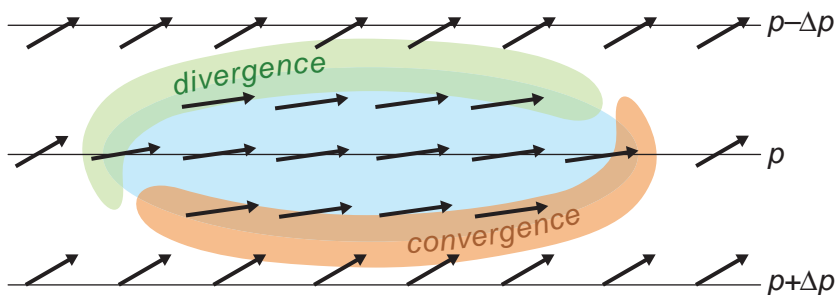


Figure 4.24 Differential surface drag promotes mesoscale convergence (divergence) along the shorelines downwind (upwind) and to the right (left) of the mean wind. The wind–pressure relationship shown above is valid in the northern hemisphere. In the southern hemisphere, the pressure gradient would point toward the north and convergence (divergence) would be found along the shorelines downwind (upwind) and to the left (right) of the mean wind.

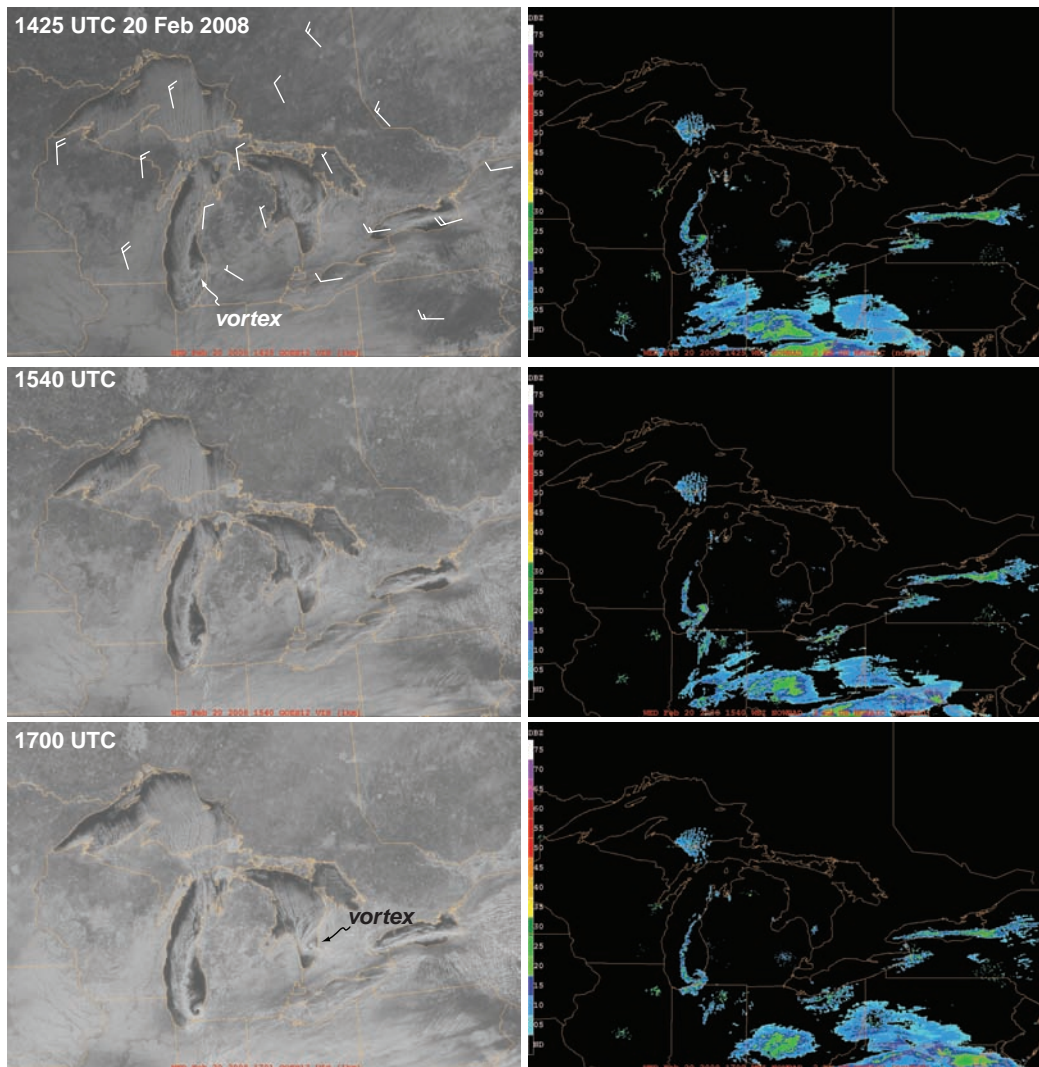


Figure 4.25 Visible satellite and composite radar reflectivity imagery from a cold air outbreak over the Great Lakes region on 20 February 2008. A variety of mesoscale cloud formations are evident: cyclonic vortices over Lake Michigan and Lake Huron (the lakes are identified in Figure 4.17); HCRs over Lake Superior depositing light snow over a broad downwind region; a single, intense snow band streaming off of Lake Ontario; less intense lake-effect snow downwind of Lake Erie (much of the lake is covered with ice at this time), with shore-parallel bands along the southwestern shoreline and disorganized convection in proximity to the eastern shoreline. Wind barbs (knots) at 925 mb from the 1200 UTC 20 February 2008 North American Model (NAM) analysis are overlaid on the 1425 UTC visible satellite.

would act not just on the downwind shoreline but also along the sides of the lake to induce a mesoscale corridor of ascent along the major axis of the lake (Figure 4.23a). In the cases in which a single convective band develops, it is possible for most areas to remain precipitation-free, even experiencing mostly clear conditions, while daily precipitation records are broken at sites beneath the precipitation band.

When strong winds more closely parallel the minor axis of an elliptical lake, not only is the fetch minimized but multiple narrower (5–20 km wide) and less intense convective bands tend to be observed, with the convection taking the form of HCRs (e.g., the convection that is present over Lake Superior in Figure 4.25). It seems that boundary layer roll dynamics dominate in these lake-effect

convection cases, in contrast to the aforementioned case of a single, wide, intense band of convection observed when winds blow along the major axis of an elliptical lake and solenoidal effects figure so prominently. This is not surprising since the reduced fetch would lead to weaker solenoidal circulations (Figure 4.23b). Lesser precipitation accumulations are observed compared with the case of a single band, but the areal coverage is typically greater. As discussed in Section 4.4, the influence of both thermal and dynamical instabilities can lead to HCR orientations that do not exactly coincide with the direction of the mean shear, although the orientation of the HCRs usually does not depart wildly from the direction of the mean wind and mean wind shear.

When wind speeds are weak ($5\text{--}7 \text{ m s}^{-1}$), especially when parallel to the minor axis of the lake, shore-parallel convective bands tend to be observed near the downwind shoreline (e.g., the bands along the southwestern shoreline of Lake Erie in Figure 4.25). In such cases the solenoidal circulation associated with the horizontal temperature differential between the inland air and the modified air seems to play the primary role in organizing the convection, despite the fact that the solenoidal circulation is not as strong as it would be in the case of a longer fetch (Figure 4.23b). Because of the weak winds, shore-parallel bands and their precipitation tend to remain fairly close to the shoreline.

In cases of very weak winds ($<5 \text{ m s}^{-1}$ in the lowest kilometer), lake-effect precipitation is unlikely to be observed inland; however, mesoscale vortices may be observed over the lake (vertical wind shear is also small in such regimes; these conditions tend to be the most likely to be characterized by cellular lake-effect convection). The relative warmth of the air residing over the lake results in hydrostatically lowered pressure (up to a few mb), which in turn gives rise to low-level convergence over the lake. Planetary vorticity and ambient relative vorticity are amplified by this convergence (vorticity stretching), resulting in the cloud swirls seen over Lake Michigan in Figures 4.25 and 4.26. The shape of the shoreline also appears to play a prominent role on the formation of lake vortices, with vortex generation being favored in regions where the shoreline is very curved.

Changes in wind direction with height also have been found to adversely affect the organization of lake-effect convection. When directional wind shear is substantial ($>30^\circ$ over the depth of the boundary layer), lake-effect convection tends to become more disorganized overall (i.e., banded structures such as those described above become less discernible), resulting in relatively light precipitation accumulations over a broad region. In general, lake-effect convection intensity and precipitation accumulations increase as the directional wind shear decreases.

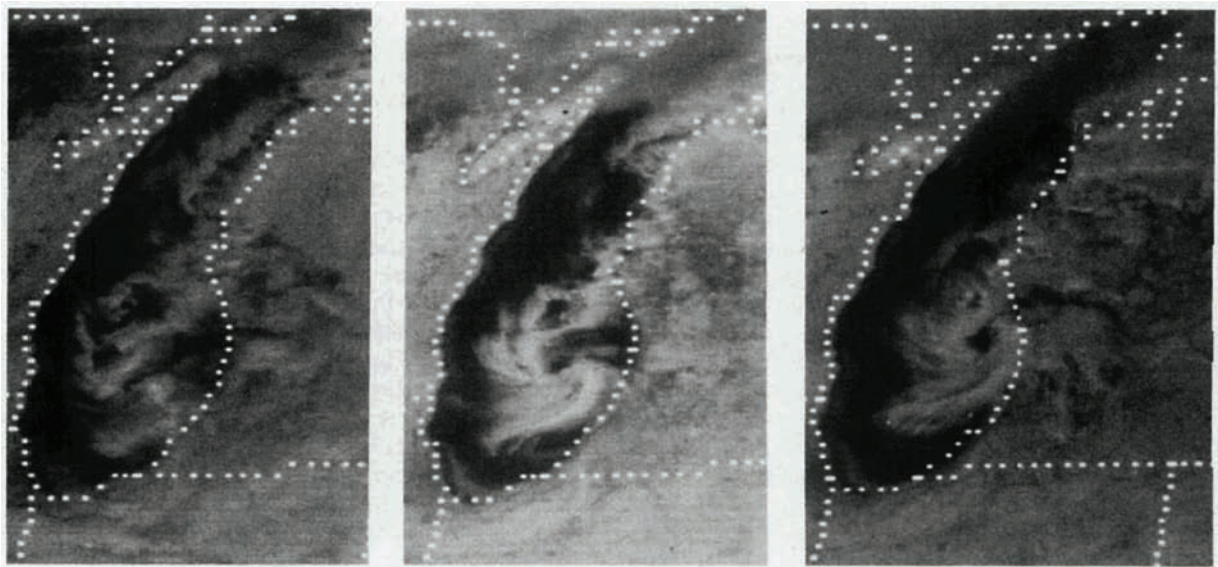


Figure 4.26 Evolution of a lake vortex on 8 January 1981 over Lake Michigan at 1600 UTC (left), 1800 UTC (center), and 2000 UTC (right). (From Forbes and Merritt [1984]. Courtesy of the American Meteorological Society.)

4.6 Urban boundary layers

The radiative, thermodynamic, and aerodynamic characteristics of urban areas differ markedly from rural areas, leading to modifications of local weather and climate. The most documented effect of urbanization on weather has been its effect on temperature, the so-called *urban heat island* effect (Figures 4.27 and 4.28). The annual mean temperature of a large city is typically 2–3 K higher than the surrounding rural areas. On some clear, calm nights, city temperatures may be as much as 10 K higher than those in surrounding rural regions. The warmth created by cities extends vertically to form a dome in light wind conditions, and an *urban heat plume* may extend a significant distance downwind of a city in windy conditions (Figure 4.29). The warm anomaly is also associated with a city-scale updraft. In some cases, the boundary layer convergence associated with this updraft may persist long enough to stretch ambient vertical vorticity to magnitudes sufficient for the low-level streamline pattern to acquire a discernible cyclonic circulation.

The urban heat island phenomenon has been attributed to a number of factors: (i) increased incoming long-wave radiation, owing to the absorption of outgoing long-wave radiation and ‘reemission’ by the radiatively active pollutants in the urban boundary layer; (ii) decreased outgoing long-wave radiation from street canyons owing to a reduction in the fraction of the sky visible in the viewing hemisphere, called the *sky view factor*, by buildings (outgoing long-wave radiation is therefore captured by vertical walls); (iii) increased short-wave radiation absorption owing to the thermal properties of urban materials (e.g., brick, concrete, asphalt) and the fact that the vertical walls in

cities also absorb more incoming short-wave radiation during late afternoon hours due to their geometry; (iv) addition of anthropogenic heat from industrial operations and transportation; (v) decreased evaporation (and hence, latent heat flux) owing to the lack of vegetation and surface waterproofing (leads to runoff into sewers). Basically, all of the components of the surface energy budget in urban areas are modified in a way such that they add to the heat island effect in a positive sense.

Water vapor mixing ratios tend to be slightly smaller in cities than in the surrounding countryside because of smaller evapotranspiration rates (less vegetation is found in cities compared with rural areas). Relative humidity values are also typically smaller in cities than in surrounding areas, owing to smaller water vapor concentrations and higher temperatures. Cloud bases have been found to be several hundred meters higher over cities, on average, than outside of cities. Although relative humidities tend to be slightly smaller in urban areas, average cloud fractions, excluding fog, have been found to be larger than in rural areas. This may be due to the greater concentration of cloud condensation nuclei (CCNs) within cities. Evidence regarding the effect of cities on fog formation is somewhat conflicting. There are some accounts that cities have more occurrences of fog because of the relatively light winds due to increased surface drag along with the presence of elevated concentrations of hygroscopic CCNs. In contrast, other findings have indicated that fog formation is more frequent in rural nocturnal boundary layers because they tend to cool more rapidly at night and thus have a greater likelihood of achieving saturation.

The winds within urban boundary layers also differ from the winds observed in the neighboring countryside.

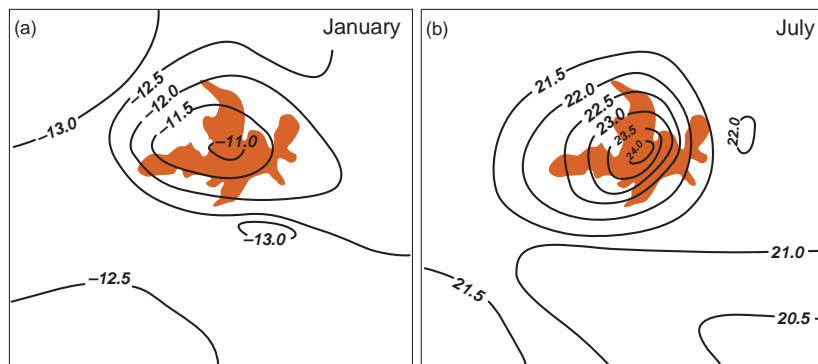


Figure 4.27 Mean (a) January and (b) July surface air temperatures ($^{\circ}\text{C}$) in the Minneapolis-St. Paul area from 1967–1976. Shading indicates the urban area. (Adapted from Winkler *et al.* [1981].)

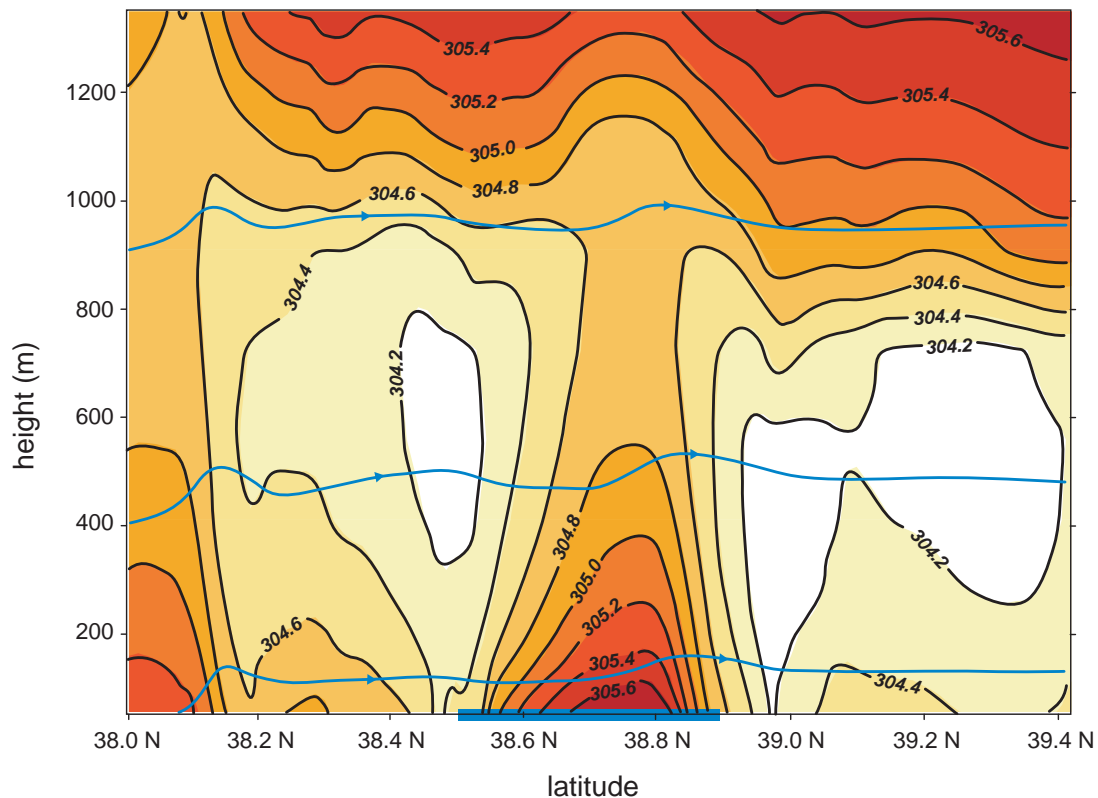


Figure 4.28 North-south vertical cross-section of potential temperature and streamlines from a simulation of the St. Louis heat island. The city of St. Louis is indicated with the bold blue line segment. (Adapted from Rozoff *et al.* [2003].)

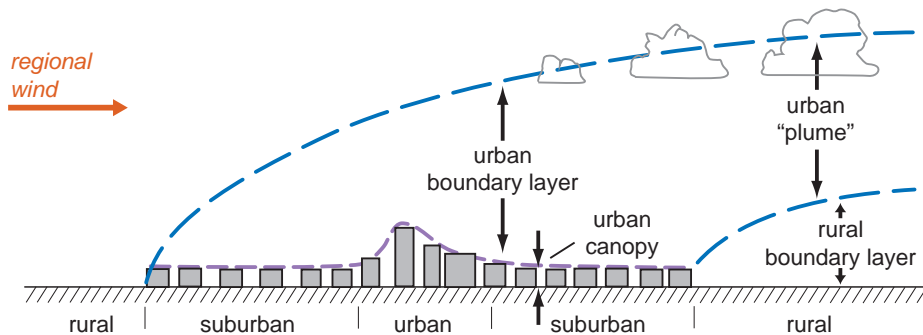


Figure 4.29 Schematic representation of the urban atmosphere illustrating a two-layer classification of urban modification. (Adapted from Oke [1976].)

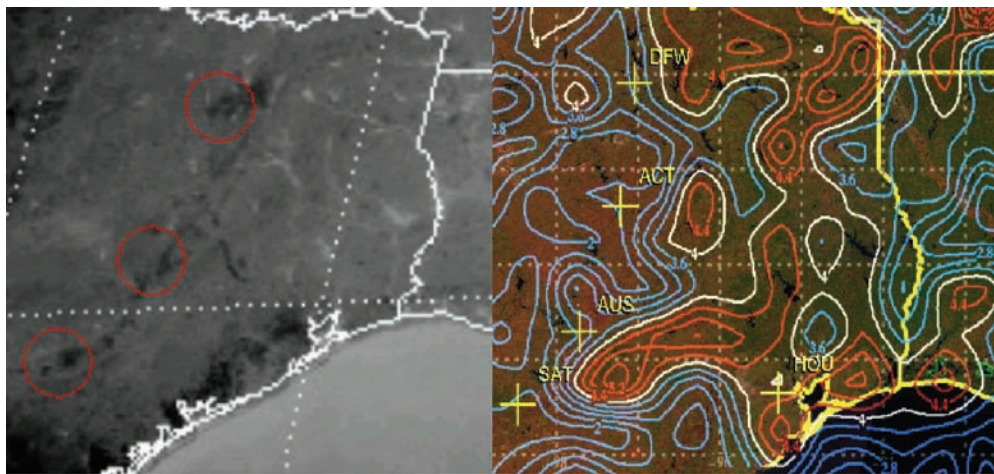


Figure 4.30 (Left) Infrared satellite image showing the heat islands (dark patches) associated with the Dallas–Ft. Worth (DFW), Waco (ACT), Austin (AUS), Houston (HOU), and San Antonio (SAT) metropolitan areas. (Right) Isoleths of the 15 month, warm-season mean rainfall rates at a height of 2 km using 0.5° resolution Tropical Rainfall Measuring Mission (TRMM) precipitation radar data. Values in red are greater than or equal to 4.2 mm h^{-1} . Values in blue are less than or equal to 3.6 mm h^{-1} . (From Shepherd *et al.* [2002]. Courtesy of the American Meteorological Society.)

The buildings within cities enhance surface drag, thereby retarding the low-level winds. Average wind speeds within cities may be $5\text{--}10 \text{ m s}^{-1}$ lower than in rural regions. However, some locations within cities can actually experience much larger localized wind speeds than the surrounding areas as a result of channeling effects between buildings. Microscale vortices may be shed from the corners of buildings, also contributing to wind gusts.

Several studies have reported an increase in precipitation accumulations and mean rainfall rates downwind of cities (Figure 4.30). There may be a propensity for convective storms to be initiated above cities (which later move over downstream areas) by upward motion resulting from the urban heat island circulation associated with cities, that is, the mesoscale circulation resulting from the warm anomaly of the city. The heat island plume and its associated positive buoyancy may be shifted downstream by the prevailing synoptic-scale flow (Figures 4.28 and 4.29), resulting in downstream convection initiation. The CCN distribution may also differ in urban areas compared with rural areas (e.g., urban areas perhaps might have more significant concentrations of very large CCNs), which can also contribute to the elevated downstream precipitation accumulations. It was once thought that the increase in surface drag within cities, and the convergence that would be expected on the upstream side of a city because of this variation in drag, might also contribute to the enhanced frequency of

convection. Recent urban boundary layer studies²¹ cast doubt on whether this effect is a major contributor to the downwind enhancement of convective precipitation.

4.7 The nocturnal low-level wind maximum

4.7.1 Low-level jets versus jet streams

A low-level jet is a fairly commonly observed relative maximum in the vertical profile of wind speed occurring at low levels (i.e., within a few kilometers of the surface). There are two somewhat different phenomena that may each play a role in the formation of low-level jets. The first is a result of the nighttime decoupling of the surface layer from the boundary layer above (it is for this reason that low-level jets are discussed within this chapter). This phenomenon is perhaps most appropriately referred to as the *nocturnal low-level wind maximum*. The second phenomenon is related not to the diurnal cycle but rather to synoptic-scale dynamics, and can be explained using fairly well understood synoptic-scale dynamical principles (e.g., quasigeostrophic theory). This feature might be most appropriately referred to as a *low-level jet stream*.

²¹ For example, see Rozoff *et al.* (2003).

Low-level jets, particularly those that intersect fronts or outflow boundaries or interact with mesoscale convective vortices (Section 9.5), often lead to the initiation and sustenance of long-lived mesoscale convective complexes that produce heavy overnight rains and sometimes flash floods. In the United States, low-level jets play an important role in the transport of Gulf of Mexico moisture northward toward the Great Plains ahead of approaching synoptic-scale disturbances, which may lead to the generation of substantial convective available potential energy. Low-level jets also often increase the low-level vertical wind shear, which may enhance the potential for severe convective storms, including tornadoes. The nocturnal low-level wind maximum, specifically, is believed to be responsible for the observed nighttime maxima in warm-season rainfall accumulations reported by virtually every observing site in the central United States.

4.7.2 Characteristics of the nocturnal low-level wind maximum

During the day, winds near the top of the boundary layer tend to be subgeostrophic, owing to the drag associated with the turbulent momentum flux profile. In other words, during the day, well mixed boundary layers disperse the effects of surface friction throughout the boundary layer. As mentioned previously (Section 4.1.4), a near-balance is achieved among the pressure gradient force, Coriolis force, and frictional force. With the onset of surface cooling at night, the near-ground static stability increases, deep vertical mixing ceases, and the middle and upper portions of the boundary layer become decoupled from the surface layer. This decoupling results in a disruption of the balance among the pressure gradient, Coriolis, and frictional forces in roughly the layer residing 500–1500 m above ground level—basically friction has been turned off in the upper portion of the boundary layer owing to the decoupling from the surface layer. This force imbalance causes an inertial oscillation of the wind about its would-be equilibrium position (geostrophic balance; also refer to Section 3.3). The oscillation leads to supergeostrophic winds and a nocturnal low-level wind maximum in the overnight hours (Figures 4.31–4.33).

4.7.3 Mathematical development

To investigate the dynamics of the nocturnal low-level wind maximum, we begin with the horizontal momentum equations. We include the Coriolis force, because it is needed to produce the observed oscillation. Friction is not included in the equations because we are looking

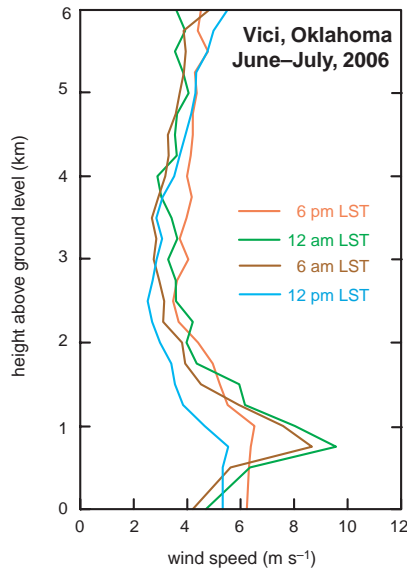


Figure 4.31 Vertical profiles of the mean horizontal wind speed at the Vici, OK, wind profiler at 6 pm, 12 am, 6 am, and 12 pm local standard time in June and July, 2006.

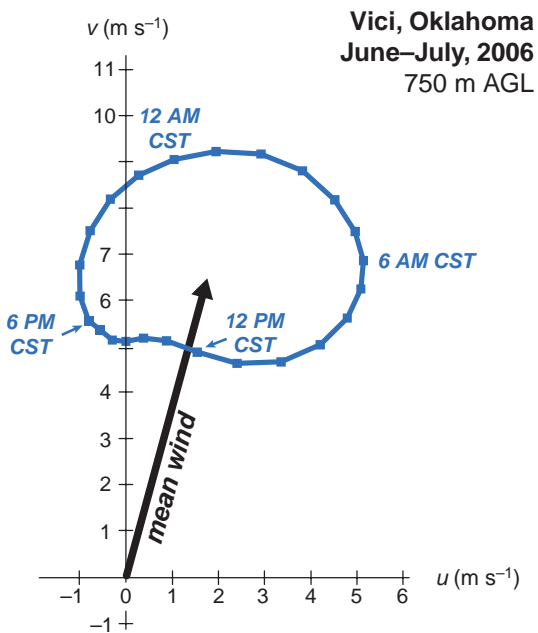


Figure 4.32 Mean diurnal cycle of the horizontal wind velocity components at 750 m above ground level observed by the Vici, OK, wind profiler in June and July, 2006.

at what happens to the low-level flow once it becomes decoupled from the surface layer where friction is present. The horizontal momentum equations are

$$\frac{du}{dt} = -\frac{1}{\rho} \frac{\partial p}{\partial x} + fv \quad (4.69)$$

$$\frac{dv}{dt} = -\frac{1}{\rho} \frac{\partial p}{\partial y} - fu. \quad (4.70)$$

It will be useful to partition the wind into geostrophic (g) and ageostrophic (a) parts:

$$u = u_g + u_a \quad (4.71)$$

$$v = v_g + v_a. \quad (4.72)$$

Substituting the above into (4.69) and (4.70) and assuming²² that $\frac{dv_g}{dt} = 0$, we obtain

$$\frac{du_a}{dt} = -\frac{1}{\rho} \frac{\partial p}{\partial x} + f(v_g + v_a) \quad (4.73)$$

$$\frac{dv_a}{dt} = -\frac{1}{\rho} \frac{\partial p}{\partial y} - f(u_g + u_a). \quad (4.74)$$

By definition,

$$u_g = -\frac{1}{\rho f} \frac{\partial p}{\partial y} \quad (4.75)$$

$$v_g = \frac{1}{\rho f} \frac{\partial p}{\partial x}, \quad (4.76)$$

therefore the momentum equations become

$$\frac{du_a}{dt} = fv_a \quad (4.77)$$

$$\frac{dv_a}{dt} = -fu_a. \quad (4.78)$$

We have two equations and two unknowns. One equation with one unknown can be obtained by taking d (4.77) / dt and using (4.78):

$$\frac{d^2 u_a}{dt^2} = f \frac{dv_a}{dt} = -f^2 u_a \quad (4.79)$$

If we treat f as a constant (the f -plane approximation), then (4.79) is a linear ordinary equation with constant coefficients and has a solution of the form

$$u_a = C_1 \cos ft + C_2 \sin ft, \quad (4.80)$$

²² Because $\mathbf{v}_g = \frac{1}{\rho f} \mathbf{k} \times \nabla_h p$ and $\frac{dv_g}{dt} = \frac{\partial \mathbf{v}_g}{\partial t} + \mathbf{v} \cdot \nabla \mathbf{v}_g$, the assumption that $\frac{dv_g}{dt} = 0$ implies that we are assuming that the horizontal pressure gradient is constant in time, such that $\partial \mathbf{v}_g / \partial t = 0$, and that the horizontal pressure gradient has no derivatives, such that $\nabla(\nabla_h p) = 0$.

where C_1 and C_2 are constants. Also note that

$$v_a = \frac{1}{f} \frac{du_a}{dt} \quad (4.81)$$

$$= \frac{1}{f} (-C_1 f \sin ft) + \frac{1}{f} (C_2 f \cos ft) \quad (4.82)$$

$$= -C_1 \sin ft + C_2 \cos ft. \quad (4.83)$$

At $t = 0$, let us define $u_a = u_{a0}$. Therefore,

$$u_{a0} = C_1 \cos 0 + C_2 \sin 0 \quad (4.84)$$

$$= C_1. \quad (4.85)$$

Similarly, at $t = 0$, let us define $v_a = v_{a0}$. Therefore,

$$v_{a0} = -C_1 \sin 0 + C_2 \cos 0 \quad (4.86)$$

$$= C_2, \quad (4.87)$$

and the equations for the ageostrophic wind are

$$u_a(t) = u_{a0} \cos ft + v_{a0} \sin ft \quad (4.88)$$

$$v_a(t) = v_{a0} \cos ft - u_{a0} \sin ft. \quad (4.89)$$

Using trigonometric identities (e.g., $\sin(\alpha - \beta) = \sin \alpha \cos \beta - \cos \alpha \sin \beta$ and $\cos(\alpha - \beta) = \cos \alpha \cos \beta + \sin \alpha \sin \beta$), we can rewrite (4.88) and (4.89) as

$$u_a(t) = |\mathbf{v}_{a0}| \cos(\psi_0 - ft) \quad (4.90)$$

$$v_a(t) = |\mathbf{v}_{a0}| \sin(\psi_0 - ft), \quad (4.91)$$

where $\mathbf{v}_{a0} = (u_{a0}, v_{a0})$, $|\mathbf{v}_{a0}| = \sqrt{u_{a0}^2 + v_{a0}^2}$, and ψ_0 is the angular constant designating the orientation of the ageostrophic wind at the start of the adjustment process (Figure 4.34).

Equations (4.90) and (4.91) reveal that the ageostrophic wind rotates clockwise (in the northern hemisphere) in a circle (an inertia circle), once the adjustment process begins following the cessation of deep mixing and the decoupling of the boundary layer from the surface layer (usually around $\sim 6-7$ pm local time). A full circle is completed at time $t = 2\pi/f$; thus, it would take a period of $12 \text{ h} / \sin \phi$ for the wind to complete a revolution (where ϕ is latitude). As drawn in Figure 4.34, the ageostrophic wind vector will point north after about a 150° (or $5\pi/6$) rotation. The horizontal wind ($\mathbf{v}_h = \mathbf{v}_g + \mathbf{v}_a$) is supergeostrophic at that time, yielding the maximum nocturnal low-level jet. This is approximately 10 h after the start of the adjustment process for $\phi = 30^\circ$ ($\sim 3-4$ am local time), and about 7 h after the

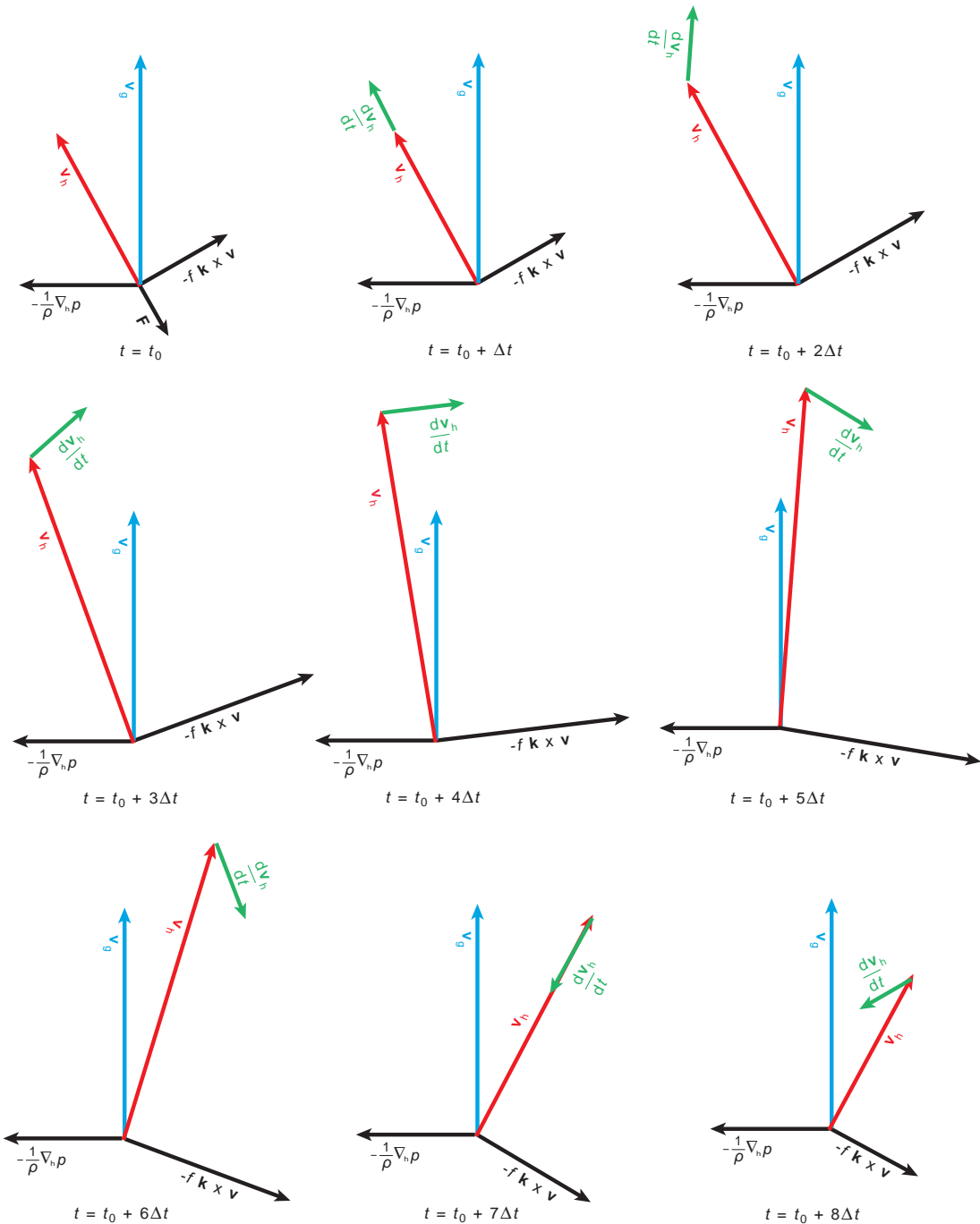


Figure 4.33 Schematic illustrating how the nocturnal low-level wind maximum develops, for the case of a southerly geostrophic wind, without loss of generality. At $t = t_0$ (during the late afternoon), the friction, Coriolis, and pressure gradient forces are in balance; thus, $d\mathbf{v}_h/dt = 0$, where \mathbf{v}_h is the horizontal wind velocity. The removal of the friction force at $t = t_0 + \Delta t$ creates a force imbalance (where $d\mathbf{v}_h/dt = -\frac{1}{\rho} \nabla_h p - \mathbf{f} \mathbf{k} \times \mathbf{v} \neq 0$), which results in net acceleration of the wind vector $t = t_0 + \Delta t$ and $t = t_0 + 8\Delta t$. An inertial oscillation results, with winds becoming supergeostrophic from approximately $t = t_0 + 2\Delta t$ to $t = t_0 + 7\Delta t$.

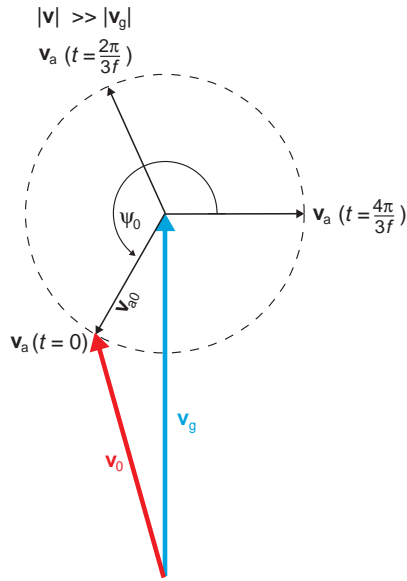


Figure 4.34 Schematic illustrating v_g , $v_a(t)$, v_{a0} , and ψ_0 . The horizontal wind, v_h , is shown at $t = 0$ (v_0), but not at the selected future times in order to maintain clarity.

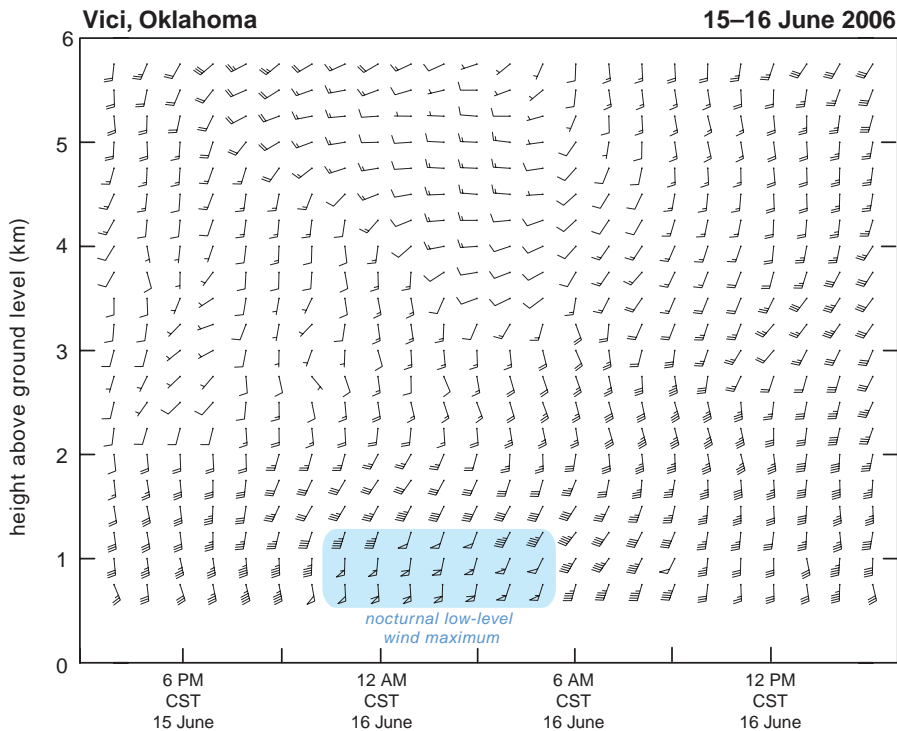
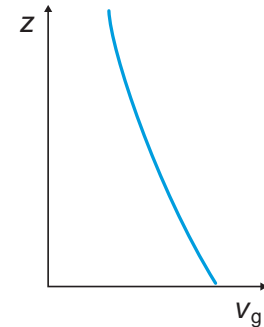
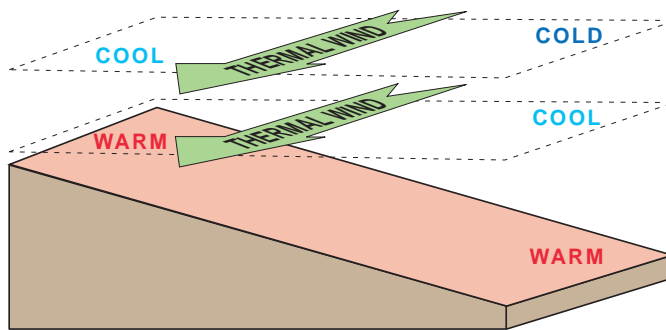


Figure 4.35 Vertical wind profiles observed by the Vici, OK, wind profiler from 4 pm CST 15 June to 3 pm CST 16 June 2006.

(a) daytime



(b) nighttime

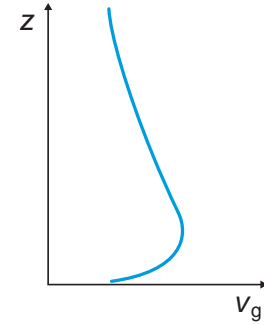
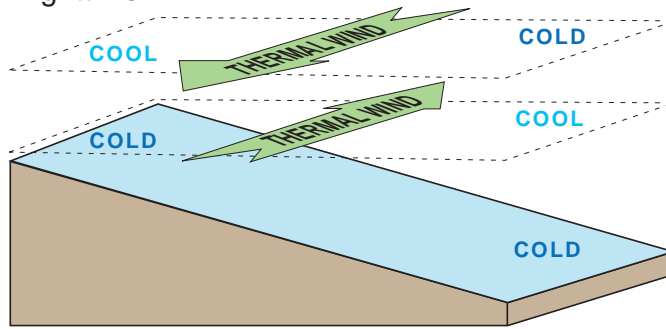


Figure 4.36 Diurnal oscillation of the low-level thermal wind owing to the diurnal heating and cooling of sloped terrain. The northern hemisphere case is shown, such that $|v_g| = v_g$. (a) Daytime conditions. (b) Nighttime conditions. (Adapted from Stull [1988].)

start of the adjustment process for $\phi = 45^\circ$ ($\sim 12\text{--}1$ am local time). The wind is supergeostrophic at these times by an amount that depends on how subgeostrophic it was during the late afternoon. In other words, the strongest amplification of the low-level wind occurs on nights following days during which winds in the upper boundary layer were most retarded by surface friction. These are days associated with abundant insolation, deep mixing, and deep boundary layers.

Figure 4.35 shows a times series of the vertical wind profile at Vici, OK ($\phi \approx 35^\circ$), from the late afternoon of 15 June 2006 through the mid-afternoon of 16 June 2006, which was a period of quiescent synoptic-scale conditions. Note the acceleration and veering of the wind in the $0.75\text{--}1.5$ km layer during the nighttime hours. The nocturnal low-level wind maximum peaked at approximately 1 am CST.

Does the oscillation continue indefinitely? No, because sunrise begins a new day, during which vertical mixing occurs and approximate balance is restored among the

Coriolis, pressure gradient, and friction forces throughout the boundary layer. Furthermore, in studying the process of geostrophic adjustment, one would complete the same derivation as that performed above in order to examine how flow that initially is not in geostrophic balance attempts to restore balance. In this case, the oscillation also does not proceed indefinitely, but might be expected to be damped by a simultaneous adjustment of the mass (pressure) field; that is, realistically, the mass field would not remain static as the wind oscillates.

4.7.4 Enhancement of the nocturnal wind maximum by sloping terrain

The presence of sloping terrain can also contribute to the observed diurnal variability of the low-level wind flow. For example, consider terrain that slopes upward from east to west, as it does on the Great Plains of the United States

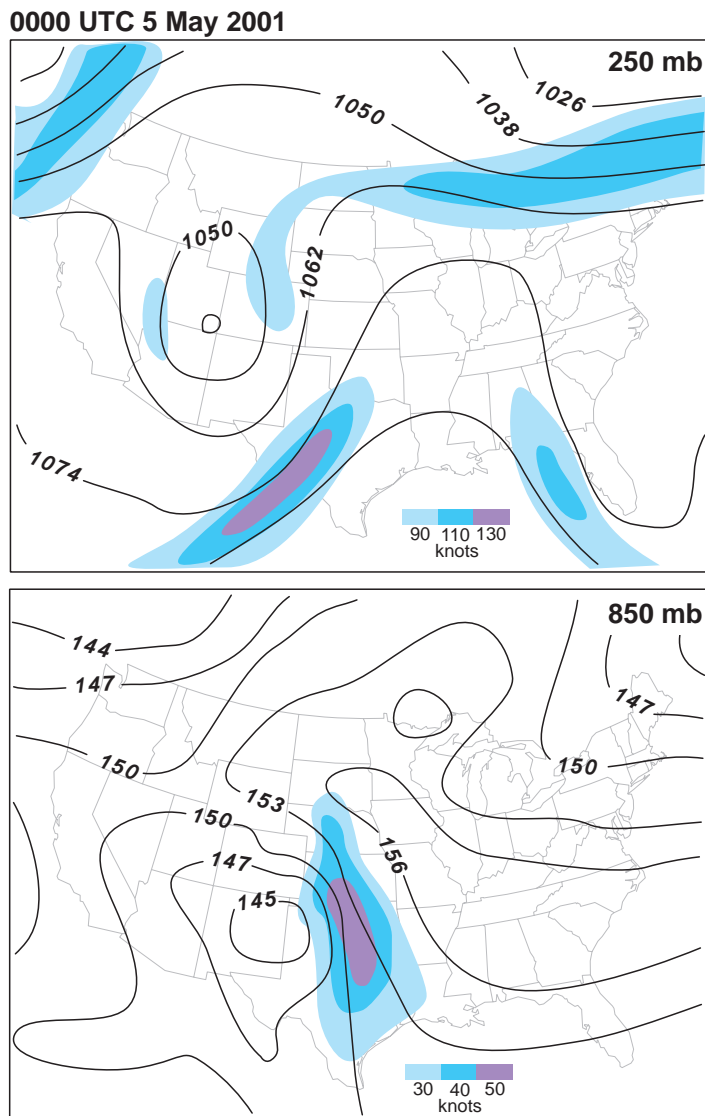


Figure 4.37 Eta model forecast of 250 mb and 850 mb geopotential heights (dam, contoured) and wind speeds (shaded) for 0000 UTC 5 May 2001. The 850 mb low-level jet stream in the southern Great Plains region is coupled with the exit region associated with the 250 mb jet stream.

over a large distance. Let us also consider the case of a poleward geostrophic flow that is constant with height above the boundary layer. Within the boundary layer, in any plane at a constant height above sea level, the higher terrain in the west causes the temperature there to be higher than the temperature in the east during the day. This creates a horizontal temperature gradient directed from east to west, an equatorward thermal wind, and equatorward vertical shear in the geostrophic wind profile over the depth of the

boundary layer (Figure 4.36). Although this vertical profile of the thermal wind, combined with poleward geostrophic winds, would not lead to a relative maximum in the vertical profile of meridional geostrophic wind speed $|v_g|$, surface friction could lead to a relative maximum in the vertical profile of meridional wind speed $|v|$ if the thermal wind above the boundary layer is weak.

At night, the ground cools the adjacent air, but not the air within the upper portions of the boundary layer.

This leads to a reversal of the thermal wind in the lower portion of the boundary layer, but the thermal wind in the upper portion of the boundary layer is largely unaffected. This results in a maximum in the profile of $|v_g|$ above the surface, leading to an even larger relative maximum in the $|v|$ profile than would result from the effects of surface friction alone (Figure 4.36).

Stated another way, in the mathematical treatment of the previous section, we assumed that v_g was a constant in time. The heating and cooling of sloping terrain, however, can lead to $\partial v_g / \partial t \neq 0$, and these diurnal changes in v_g , when superposed upon the inertial oscillation of v_a , can augment the magnitude of the nocturnal low-level wind maximum.

4.7.5 Low-level jet streams as a response to an upper-level jet

Low-level wind speed maxima also can result from processes independent of the diurnal cycle of the boundary layer. The ageostrophic circulations associated with the wind accelerations that accompany an upper-tropospheric wind maximum can extend into the lower troposphere to produce a low-level jet *stream*. The influence of the upper-level jet on low-level accelerations depends on the static stability, with stronger low-level jet streams being coupled to upper-level wind maxima when the static stability is relatively small. *Coupled jets* are common in the central United States when synoptic-scale conditions favor lee cyclogenesis downstream of the Rocky Mountains (i.e., when a mid-upper level trough is present in the western United States with a wind speed maximum rounding the base of the trough) (Figure 4.37). In the warm season, low-level jet streams induced by upper-level jets are commonly present during outbreaks of severe convection in the central United States.

Consider an upper-level westerly jet streak. East of the jet core, the exit region circulation is associated with poleward ageostrophic winds at the base of the transverse circulation. If the static stability is not too strong, the ageostrophic transverse circulation can extend to low levels and the upper-level jet therefore induces a relative maximum in the poleward vertical wind profile at low levels ahead of the upper-level jet (Figure 4.37). West of the jet core, the entrance region circulation is associated with equatorward ageostrophic winds at the base of the transverse circulation, although the enhanced low-level static stability often present in the wake of an extratropical cyclone can limit the coupling of the upper-level jet with the low-level

winds. In such cases, there may be an ‘elevated’ low-level jet stream in the equatorward flow above the frontal inversion associated with the trailing cold front of the extratropical cyclone.

Further reading

General boundary layer resources

- Arya (2001).
 Brown, R. A., 1983: The flow in the planetary boundary layer. *Eolian Sediments and Processes*, M. E. Brookfield and T. S. Ahlbrandt, Eds. Elsevier, 291–310.
 Garratt (1994).
 Sorbjan (1989).
 Stull (1988).

Boundary layer convection

- Agee, E. M., T. S. Chen, and K. E. Dowell, 1973: A review of mesoscale cellular convection. *Bull. Amer. Meteor. Soc.*, **54**, 1004–1011.
 Atkinson, B. W., and J. W. Zhang, 1996: Mesoscale shallow convection in the atmosphere. *Rev. Geophys.*, **34**, 403–431.
 Brown, R. A., 1972a: On the inflection point instability of a stratified Ekman boundary layer. *J. Atmos. Sci.*, **29**, 850–859.
 Brown, R. A., 1972b: On the physical mechanism of the inflection point instability. *J. Atmos. Sci.*, **29**, 984–986.
 Conzemius, R. J., and E. Fedorovich, 2008: A case study of convective boundary layer development during IHOP_2002: numerical simulations compared to observations. *Mon. Wea. Rev.*, **136**, 2305–2320.
 Deardorff, J. W., 1974: Three-dimensional numerical study of the height and mean structure of a heated planetary boundary layer. *Bound. Layer Meteor.*, **7**, 81–106.
 Etling, D., and R. A. Brown, 1993: Roll vortices in the planetary boundary layer: a review. *Bound. Layer Meteor.*, **65**, 215–248.
 Krishnamurti, R., 1975a: On cellular cloud patterns. Part 1: Mathematical model. *J. Atmos. Sci.*, **32**, 1353–1363.
 Krishnamurti (1975b).
 Krishnamurti, R., 1975c: On cellular cloud patterns. Part 3: Applicability of the mathematical and laboratory models. *J. Atmos. Sci.*, **32**, 1373–1383.
 Kuettner, J. P., 1971: Cloud bands in the earth’s atmosphere: observation and theory. *Tellus*, **23**, 404–425.

- LeMone, M. A., 1973: The structure and dynamics of horizontal roll vortices in the planetary boundary layer. *J. Atmos. Sci.*, **30**, 1077–1091.
- LeMone, M. A., 1976: Modulation of turbulent energy by longitudinal rolls in an unstable boundary layer. *J. Atmos. Sci.*, **33**, 1308–1320.
- Lilly, D. K., 1966: On the instability of Ekman boundary flow. *J. Atmos. Sci.*, **23**, 481–494.
- Moeng, C.-H., and P. P. Sullivan, 1994: A comparison of shear- and buoyancy-driven planetary boundary layer flow. *J. Atmos. Sci.*, **51**, 999–1022.
- Shirer, H. N., 1980: Bifurcation and stability in a model of moist convection in a shearing environment. *J. Atmos. Sci.*, **37**, 1586–1602.
- Stensrud, D. J., and H. N. Shirer, 1988: Development of boundary layer rolls from dynamic instabilities. *J. Atmos. Sci.*, **45**, 1007–1019.
- Weckwerth, T. M., T. W. Horst, and J. W. Wilson, 1999: An observational study of the evolution of horizontal convective rolls. *Mon. Wea. Rev.*, **127**, 2160–2179.
- Weckwerth, T. M., J. W. Wilson, R. M. Wakimoto, and N. A. Crook, 1997: Horizontal convective rolls: Determining the environmental conditions supporting their existence and characteristics. *Mon. Wea. Rev.*, **125**, 505–526.
- Young, G. S., D. Kristovich, M. Hjelmfelt, and R. Foster, 2002: Rolls, streets, waves, and more: a review of quasi-two-dimensional structures in the atmospheric boundary layer. *Bull. Amer. Meteor. Soc.*, **83**, 997–1001.
- Lake-effect precipitation**
- Byrd, G. P., R. A. Anstett, J. E. Heim, and D. M. Usinski, 1991: Mobile sounding observations of lake-effect snowbands in western and central New York. *Mon. Wea. Rev.*, **119**, 2323–2332.
- Cooper, K. A., M. R. Hjelmfelt, R. G. Derickson, D. A. R. Kristovich, and N. F. Laird, 2000: Numerical simulation of transitions in boundary layer convective structures in a lake-effect snow event. *Mon. Wea. Rev.*, **128**, 3283–3295.
- Forbes and Merritt (1984).
- Hjelmfelt, M. R., 1990: Numerical study of the influence of environmental conditions on lake-effect snowstorms over Lake Michigan. *Mon. Wea. Rev.*, **118**, 138–150.
- Hjelmfelt, M. R., 1992: Orographic effects in simulated lake-effect snowstorms over Lake Michigan. *Mon. Wea. Rev.*, **120**, 373–377.
- Kelly, R. D., 1984: Horizontal roll and boundary layer interrelationships over Lake Michigan. *J. Atmos. Sci.*, **41**, 1816–1826.
- Laird, N. F., 1999: Observation of coexisting mesoscale lake-effect vortices over the western Great Lakes. *Mon. Wea. Rev.*, **127**, 1137–1141.
- Laird, N. F., J. E. Walsh, and D. A. R. Kristovich, 2003: Model simulations examining the relationship of lake-effect morphology to lake shape, wind direction, and wind speed. *Mon. Wea. Rev.*, **131**, 2102–2111.
- Lavoie, R. L., 1972: A mesoscale numerical model of lake-effect storms. *J. Atmos. Sci.*, **29**, 1025–1040.
- Lenschow (1973).
- Miner, T. J., and J. M. Fritsch, 1997: Lake-effect rain events. *Mon. Wea. Rev.*, **125**, 3231–3248.
- Niziol, T. A., W. R. Snyder, and J. S. Waldstreicher, 1995: Winter weather forecasting throughout the eastern United States. Part IV: Lake effect snow. *Wea. Forecasting*, **10**, 61–77.
- Schultz, D. M., 1999: Lake-effect snowstorms in northern Utah and western New York with and without lightning. *Wea. Forecasting*, **14**, 1023–1031.
- Sousounis and Mann (2000).
- Steenburgh, W. J., S. Halvorson, and D. J. Onton, 2000: Climatology of lake-effect snowstorms of the Great Salt Lake. *Mon. Wea. Rev.*, **128**, 709–727.

Urban boundary layers

- Baik J.-J., Y. H. Kim, and H. Y. Chun, 2001: Dry and moist convection forced by an urban heat island. *J. Appl. Meteor.*, **40**, 1462–1475.
- Changnon S. A., Jr., R. G. Semonin, and F. A. Huff, 1976: A hypothesis for urban rainfall anomalies. *J. Appl. Meteor.*, **15**, 544–560.
- Dabberdt W. F., and Coauthors, 2000: Forecast issues in the urban zone: Report of the 10th prospectus development team of the U.S. Weather Research Program. *Bull. Amer. Meteor. Soc.*, **81**, 2047–2064.
- Hildebrand, P. H., and B. Ackerman, 1984: Urban effects on the convective boundary layer. *J. Atmos. Sci.*, **41**, 76–91.
- Huff F. A., 1973: Precipitation modification by major urban areas. *Bull. Amer. Meteor. Soc.*, **54**, 1220–1232.
- Ochs H. T., III, and R. G. Semonin, 1979: Sensitivity of a cloud microphysical model to an urban environment. *J. Appl. Meteor.*, **18**, 1118–1129.
- Rozoff, C. M., W. R. Cotton, and J. O. Adegoke, 2003: Simulation of St. Louis, Missouri, land use impacts on thunderstorms. *J. Appl. Meteor.*, **42**, 716–738.
- Shepherd *et al.* (2002).

Nocturnal low-level wind maximum

Blackadar, A. K., 1957: Boundary layer wind maxima and their significance for the growth of nocturnal inversions. *Bull. Amer. Meteor. Soc.*, **38**, 283–290.

Bonner, W. D., 1968: Climatology of the low-level jet. *Mon. Wea. Rev.*, **96**, 833–850.

Holton, J. R., 1967: The diurnal boundary layer wind oscillation above sloping terrain. *Tellus*, **19**, 199–205.

Hoxit, L. R., 1975: Diurnal variations in planetary boundary-layer winds over land. *Bound.-Layer Meteor.*, **8**, 21–38.

Mahrt, L., 1974: Time dependent integrated planetary boundary layer flow. *J. Atmos. Sci.*, **31**, 457–464.

Stensrud, D. J., 1996: Importance of low-level jets to climate: A review. *J. Climate*, **9**, 1698–1711.

5

Air Mass Boundaries

Air masses and fronts are among the main features of the long-standing Norwegian cyclone model developed in the early part of the 20th century. Fronts are transition zones separating air masses having different origins, within which the horizontal temperature (and density) gradient is greatly enhanced relative to the larger-scale meridional temperature gradient associated with the meridional variation of net radiation. The cross-front horizontal scale typically is on the order of 100 km or less, in contrast to the along-front scale, which can be as large as a few thousand kilometers. The cross-front scale is therefore decidedly mesoscale, whereas the along-front scale can be synoptic scale. Owing to their along-front dimension, and also because these air mass boundaries were originally analyzed on early synoptic maps (Chapter 1), we shall sometimes refer to these boundaries as *synoptic fronts* in order to distinguish them from the other air mass boundaries that will be discussed in this chapter, some of which share similarities with synoptic fronts (Figure 5.1).

The characteristics and formation of synoptic fronts are considered first. We next discuss air mass boundaries known as *drylines* that separate warm maritime air from warm continental air. Drylines can also have a synoptic-scale along-boundary dimension, but are not regarded as fronts because the direction of the horizontal density gradient associated with a dryline typically reverses itself from day to night.¹ Both synoptic fronts and drylines form as a result of large-scale geostrophic deformation (often manifest as confluent air streams) enhancing initially broad

gradients of temperature and moisture, respectively (both fronts and drylines can be enhanced by other effects, as will be shown later).

This chapter also deals with smaller-scale air mass boundaries that are mesoscale even in the along-front dimension. In contrast to synoptic fronts, the formation of these *mesoscale air mass boundaries* (or just *mesoscale boundaries*), as we define them, does not require geostrophic deformation (e.g., confluence) acting on a preexisting density gradient. Mesoscale boundaries have a variety of origins. They most commonly arise from horizontally differential latent heating/cooling (e.g., outflow boundaries associated with deep convection) or the differential heating/cooling of the earth's surface (e.g., sea-breeze fronts). Much of the theory developed for synoptic fronts cannot be readily applied to mesoscale boundaries because thermal-wind balance may not apply owing to significant nonhydrostatic pressure perturbations, and also because the along-boundary winds can be ageostrophic.

Accurate weather forecasts often require a detailed knowledge of the presence and motion of air mass boundaries given that meteorological conditions can vary tremendously across them. Air mass boundaries can be sites for the initiation of deep convection that subsequently can produce heavy rain and severe weather. Convective storms that interact with air mass boundaries away from the region of convection initiation occasionally undergo sudden increases or decreases in intensity, depending on the characteristics of the air masses separated by the boundary. Not only are synoptic fronts and their associated baroclinity important for the development of larger-scale extratropical cyclones, but in some situations even mesoscale boundaries can influence larger-scale extratropical cyclones.

¹ Under some circumstances, the horizontal density gradient associated with a front can also be reversed over time (see, e.g., Doswell and Haugland, 2007), but this evolution of the density field is not routinely observed with fronts as is the case with drylines.

2100 UTC 16 July 1980

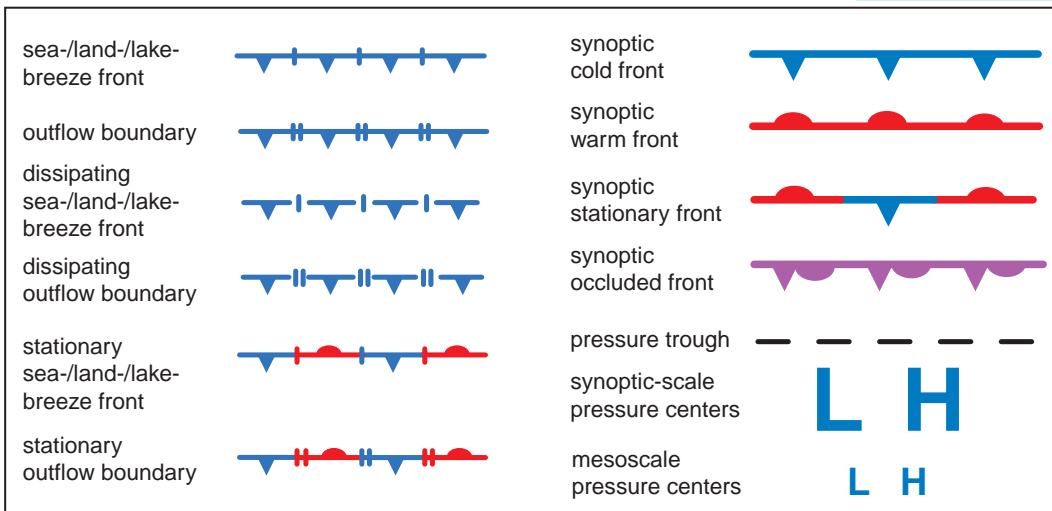
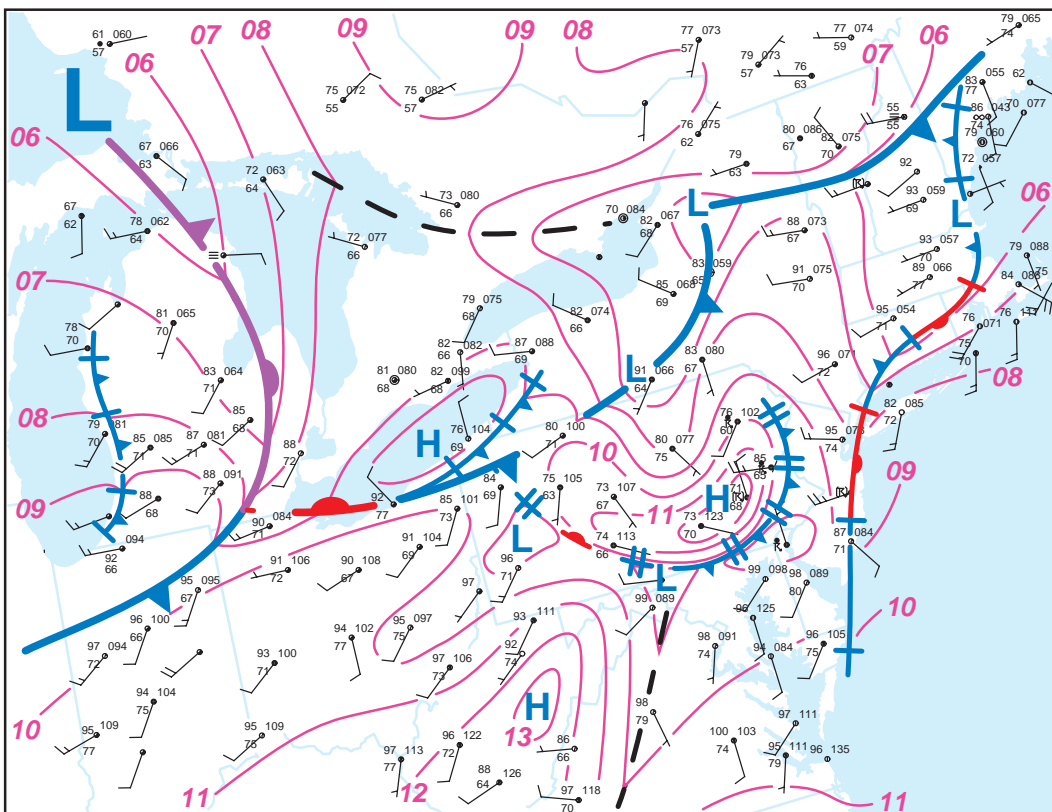


Figure 5.1 Mesoanalysis at 2100 UTC 16 July 1980 depicting a variety of air mass boundaries, such as lake-breeze fronts, a sea-breeze front, an outflow boundary, and synoptic fronts, following the conventions proposed by Young and Fritsch (1989). Isobars are drawn at 1 mb intervals (the leading '10' is dropped). The symbols used to indicate synoptic fronts and pressure centers are larger than those used to indicate mesoscale boundaries and pressure centers. (Adapted from Young and Fritsch [1989].)

Our focus is on air mass boundaries observed at the surface. Upper-tropospheric fronts, which form from *tropopause folding*—the tilting of the large vertical potential temperature gradient along the tropopause into the horizontal by the secondary circulations associated with jet streaks, are not discussed herein, nor are jet streaks, which are inescapably tied to all baroclinic zones in a quasigeostrophic atmosphere by way of the thermal-wind relation. In our experience these topics tend to be covered fairly thoroughly in synoptic meteorology references, even though there are certainly mesoscale aspects of jet streaks and upper-tropospheric fronts. We refer the reader to synoptic meteorology references (e.g., Bluestein, 1993; Carlson, 1998; Davies, 1999; Keyser, 1999; Martin, 2006) for a more extensive treatment of these topics.

5.1 Synoptic fronts

5.1.1 General characteristics

Synoptic fronts, hereafter referred to as fronts within this section (in subsequent sections, mesoscale air mass boundaries associated with significant temperature gradients will be distinguished from fronts as sea-breeze fronts, land-breeze fronts, gust fronts, coastal fronts, etc.), are usually defined as elongated zones of strong horizontal temperature gradient, where the magnitude of the horizontal temperature gradient is at least an order of magnitude larger than the typical synoptic-scale meridional temperature gradient of ~ 10 K (1000 km) $^{-1}$. Fronts are also corridors of enhanced cyclonic vertical vorticity (implied by the wind shifts and pressure troughs that accompany them), vertical wind shear, and usually static stability, with the latter due to the fact that frontal zones tend to be tilted over the cold air mass (Figure 5.2a–c) by the ageostrophic vertical circulation that accompanies frontogenesis (to be discussed in Section 5.1.6). The ageostrophic wind field is also responsible for the largest temperature gradient usually being observed on the cold side of the wind shift associated with the surface pressure trough.

The Rossby number is relatively small ($\ll 1$) in the along-front direction because the along-front length scale is large; however, the cross-front length scale is much smaller, therefore the Rossby number is relatively large ($\gtrsim 1$) and quasigeostrophic theory is inadequate to describe frontal processes in the cross-front direction. This shortcoming of quasigeostrophic theory is the basis for what is known as *semigeostrophic theory* (Section 5.1.6), where the advection of geostrophic momentum and temperature by the ageostrophic wind is considered, in addition to the advectons of geostrophic momentum and temperature by the geostrophic wind that quasigeostrophic theory considers.

5.1.2 Types of fronts

Fronts are identified as *cold fronts* (Figures 5.2a,b) when the cold air mass advances relative to the warm air mass, usually with an equatorward and eastward component (exceptions are what are sometimes called *back-door cold fronts*, which have a westward component to their motion, opposite the typical progression of midlatitude disturbances). Fronts are identified as *warm fronts* (Figure 5.2c) when the warm air mass advances relative to the cold air mass, usually with a poleward and eastward component (*back-door warm fronts*, like back-door cold fronts, have a westward component to their motion and are sometimes observed when warm air is wrapped around the poleward side of an extratropical cyclone). Fronts that exhibit little or no motion are termed *stationary fronts*. Many cold fronts slow to a halt, become stationary fronts, and then retreat as warm fronts. Other fronts are identified as cold fronts along a portion of the air mass boundary, and as stationary or warm fronts along other parts of the same air mass boundary. Sometimes a near-discontinuity in the temperature field is observed (e.g., Figure 5.2b); such intense fronts, which are virtually always cold fronts, have characteristics similar to those of density currents (to be discussed in Section 5.3.2).

Warm fronts are usually less steeply sloped than cold fronts, probably at least partly as a result of surface drag, which tends to steepen cold fronts by retarding the motion of the frontal zone at the ground. Because the isentropic surfaces tilt over the cold air, retardation of the frontal zone at the ground makes the isentropic surfaces more vertical near the ground. In the case of warm fronts, surface drag has the opposite effect because the motion of the front is in the same direction as the tilt of the isentropic surfaces. The difference in warm versus cold front slopes also is likely the result of differences in surface fluxes between the cold side of warm fronts and the cold side of cold fronts (recall that the magnitude of the sensible heat flux from the surface to the overlying atmosphere increases as the temperature difference between the surface and overlying atmosphere increases, with a relatively warm surface resulting in a positive (upward-directed) sensible heat flux). Warm (cold) air overruns a relatively cold (warm) surface in the case of a warm (cold) front, thereby contributing to a negative (positive) surface heat flux (the surface heat flux during daytime conditions is usually positive, but we would expect the surface heat flux to be less positive in a warm-frontal zone than in a cold frontal zone as a result of the aforementioned effect). The stronger surface heat flux in the cold frontal zone promotes stronger, deeper vertical mixing, which makes the isentropes more vertical, thereby increasing the slope of the front. Differences in surface fluxes between cold and

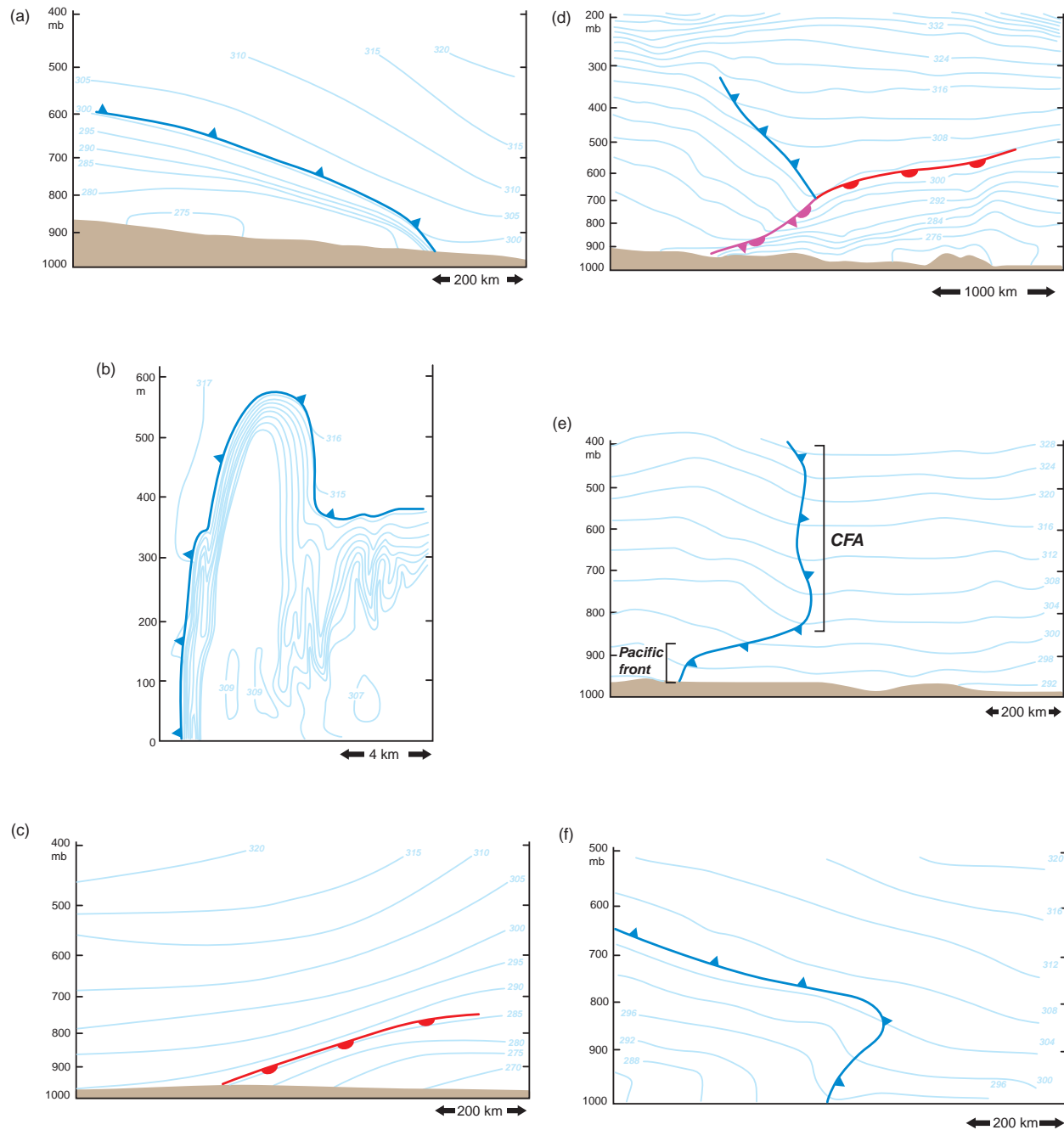


Figure 5.2 Examples of synoptic fronts as seen in approximately front-normal vertical cross-sections of potential temperature (blue contours). (a) Cold front analyzed by Sanders (1955) using rawinsonde observations. (b) Strong cold front analyzed by Shapiro *et al.* (1985) based on observations obtained from an instrumented tower (observations were time-to-space converted). (c) Warm front analyzed by Bluestein (1993) using rawinsonde observations. (d) A warm occlusion as revealed in a model analysis by Stoelinga *et al.* (2002). (e) Cold front aloft (CFA) and Pacific cold front in a model analysis by Locatelli *et al.* (2002). (f) Forward-tilting cold front in a simulation by Schultz and Steenburgh (1999).

warm-frontal zones can also be attributable to differences in cloud cover and precipitation; greater insolation and associated low-level destabilization generally might be favored behind cold fronts rather than ahead of warm fronts.

The wind shift along warm fronts is often not as pronounced as along cold fronts, which is related to the fact that warm fronts also tend to be have weaker temperature gradients and vertical circulations than cold fronts (discussed further in Section 5.1.6). Some warm fronts form when air crosses a mountain range, and the downsloping, adiabatically warming air advances in the lee of the mountain range. This evolution is somewhat common east of the Rocky Mountains in the United States, where such warm fronts are called *chinook fronts*.

Although they have been analyzed on weather maps since the development of the Norwegian cyclone model, the formation of *occluded fronts* (Figure 5.2d) has historically been controversial and remains a topic of ongoing research.² In the Norwegian cyclone model, the cold front moves faster than the warm front, eventually overtaking it, resulting in *occlusion* of the extratropical cyclone, with the occluded front being the surface boundary along which the cold front has overtaken the warm front. Although a number of observational and numerical modeling studies support this basic evolution, some other mechanisms for occluded front formation have been identified that depart from the classical occlusion process (in fact, for a number of years there was considerable skepticism that occluded fronts were ever produced by cold fronts catching up to warm fronts). For example, occluded fronts can form when a low deepens on the cold side of a front, independent of a narrowing of the warm sector by a cold front outrunning a warm front. Along similar lines, a low initially located at the ‘peak’ of the warm sector often propagates into the cold air as it deepens, thereby separating itself from the junction of the warm and cold fronts—an occluded front develops as a result, joining the surface low with the junction of the warm and cold fronts. Upper-tropospheric fronts, which are outside of the scope of this book, can also interact with surface fronts and play a role in the formation of thermodynamic structures that resemble occluded fronts in vertical cross-sections.

The Norwegian cyclone model distinguished between *cold occlusions* and *warm occlusions*. In cold occlusions, the advancing cold air mass that overtakes the warm front is colder than the retreating cold air mass on the cold side of

the warm front, such that the warm front and retreating cold air mass are lifted over the advancing cold front and the denser air mass behind it (i.e., the cold front undercuts the warm front). In warm occlusions, the advancing cold air mass that overtakes the warm front is warmer than the retreating cold air mass on the cold side of the warm front, such that the advancing cold front rides up and over the warm front and the denser air mass on its cold side (i.e., the warm front undercuts the cold front).

More recently it has been shown that the type of occlusion depends on the difference in static stability within the cold air masses straddling the narrowing warm sector, rather than by which of the cold air masses is denser.³ A cold occlusion results when the statically more stable air is behind the cold front, and a warm occlusion results when the statically more stable air lies ahead of the warm front. Warm occlusions are virtually always observed⁴ (e.g., Figure 5.2d), which is consistent with the static stability differences, rather than density differences, being associated with occlusion type. Though there is no strong tendency for either the air mass behind the cold front or the air mass ahead of the warm front to be colder than the other, statically less stable conditions behind the cold front relative to the stability ahead of the warm front appear to be a ubiquitous characteristic of midlatitude cyclones, as discussed earlier. One must be careful in assigning cause and effect; though lesser (greater) static stability behind the cold front (ahead of the warm front) is *associated with* warm occlusions, this does not necessarily imply that the stability differences *cause* warm occlusions to be favored over cold occlusions.⁵

Thermodynamic structures similar to those associated with warm occluded fronts can occur anytime a cold front encounters prefrontal air that is more stably stratified than the air mass behind the cold front. For example, on the western Great Plains of the United States, a *Pacific cold front* (so called because the cold front ushers in maritime polar air originating over the Pacific Ocean) may overtake a dryline. As the cold front descends the lee slope of the Rocky Mountains to the west of the Great Plains, the cold

³ See Stoelinga *et al.* (2002).

⁴ Schultz and Mass (1993) were unable to find a single case of a cold occlusion documented in the literature in their review of occluded fronts.

⁵ Schultz and Mass (1993) and Stoelinga *et al.* (2002) raised the possibility that the occlusion process perhaps can be viewed as a convergence of a cold front and warm front into what would otherwise be a vertically oriented occluded front, but with background vertical wind shear generally tilting the occluded front forward with height such that a warm occlusion structure is observed.

² Schultz and Mass (1993) and Stoelinga *et al.* (2002) provide nice reviews of occluded fronts.

air mass is warmed, dried, and develops a deep mixed layer. Upon encountering the western edge of a moist air mass that has been advected northward from the Gulf of Mexico (i.e., a dryline), the modified maritime polar air mass overrides the moist air mass (the static stability at the top of the moist layer is much larger than the static stability within the modified polar air mass). The undercutting of the modified maritime polar air mass results in a *cold front aloft* (CFA) that may lead the surface trough by a few hundred kilometers as both air mass boundaries advance to the east under the influence of a migrating extratropical cyclone (Figure 5.2e). The surface trough can be analyzed as either a dryline or a Pacific cold front depending on whether a significant temperature gradient is associated with the surface trough.

The CFA is not to be confused with an upper-tropospheric front, defined more by dynamics at the tropopause than by its interaction with an underlying layer of increased static stability in the lower troposphere, nor a *split front*, which also leads a surface front but is associated more with a horizontal humidity gradient than a horizontal density gradient.⁶ A CFA sometimes generically refers to *any* boundary associated with cold advection above the surface that leads the cold advection at the surface. That is, CFAs would be an aspect of warm occluded fronts, Pacific cold fronts that override drylines, and *forward-tilting cold fronts*—cold fronts that encounter a stable prefrontal layer not associated with a warm front or dryline (Figure 5.2f).⁷

5.1.3 Motion of fronts

The motion of surface fronts is strongly dependent upon the front-normal isallobaric gradient. For example, rising

⁶ The split front model originated with Browning and Monk (1982). Split fronts represent the leading edge of the dry slot of an extratropical cyclone. Cross-sections depicting split fronts in the literature, virtually without exception, plot wet-bulb potential temperature rather than potential temperature. It is therefore not clear whether split fronts really are associated with any true baroclinity. The passage of a split front above the surface is accompanied by drying and a drop in wet-bulb potential temperature, which results in the generation of potential instability. The potential instability might play a role in the formation of some mesoscale rainbands that develop within the dry slot.

⁷ Schultz and Steenburgh (1999) documented a forward-tilting cold front case in which an upper-tropospheric front interacted with a surface cold front; thus, at least in some cases, it appears as though the development of forward-tilting frontal boundaries, whether it involves warm occlusions, Pacific fronts overriding drylines, or forward-tilting cold fronts, might be more complicated than simply the result of interactions between surface fronts separating air masses with different stratifications. Some overlap might exist between the development of CFAs and upper-tropospheric fronts.

(falling) pressure on the cold (warm) side of a cold front causes the low-pressure trough associated with the front to move toward the warm air. Because the temperature gradient is usually largest on the cool side of a front, frontal movement tends to be highly correlated with the wind direction, and thus temperature advection, on the cold side of a front. Cold fronts have cold advection (which contributes to rising pressure) on their cold sides and warm fronts have warm advection (which contributes to falling pressure) on their cold sides. Cold fronts tend to move faster than warm fronts because the ageostrophic vertical circulation along fronts (Section 5.1.6) is usually thermally direct. Thus, the vertical circulation is responsible for low-level ageostrophic cold air advection within the frontal zone, thereby accelerating (decelerating) cold (warm) fronts relative to the forward speed that could be attributed to the isallobaric gradient resulting from geostrophic temperature advection alone.

For fronts having along-front winds and an along-front length scale such that the Rossby number is relatively large (~ 1), their motion is more a function of the temperature differential across the front, which is associated with a horizontal pressure gradient, rather than temperature advection on either side of the front contributing to surface pressure tendencies. Frontal motion can also be influenced by diabatic effects such as latent cooling resulting from the evaporation of precipitation (latent cooling influences the surface pressure field and therefore also affects the isallobaric gradient) and surface fluxes (e.g., strong vertical mixing in sunny conditions can erode the shallow edge of a cold air mass). These processes occasionally can promote discontinuous frontal motion, such that a front appears to ‘jump.’

5.1.4 Slope of fronts

The simplest model of a front is that of a *zero-order* temperature (density) discontinuity, such that the temperature gradient is confined to an infinitesimally thin interface between the air masses (Figure 5.3a). The early theoretical studies on fronts used this model in order to derive expressions for the slope of a front and the vertical velocity of air moving over a front.

Consider a zonally oriented front separating relatively dense (cold) air to the north having density ρ_c , and less dense (warmer) air to the south having density ρ_w . Although density is assumed to be a constant within each air mass, pressure varies three dimensionally; the pressures on the cold and warm sides of the front are $p_c(x, y, z)$ and $p_w(x, y, z)$, respectively. Pressure is assumed to be continuous along the front even though density is discontinuous. Thus, $p_c = p_w$ along the front, which

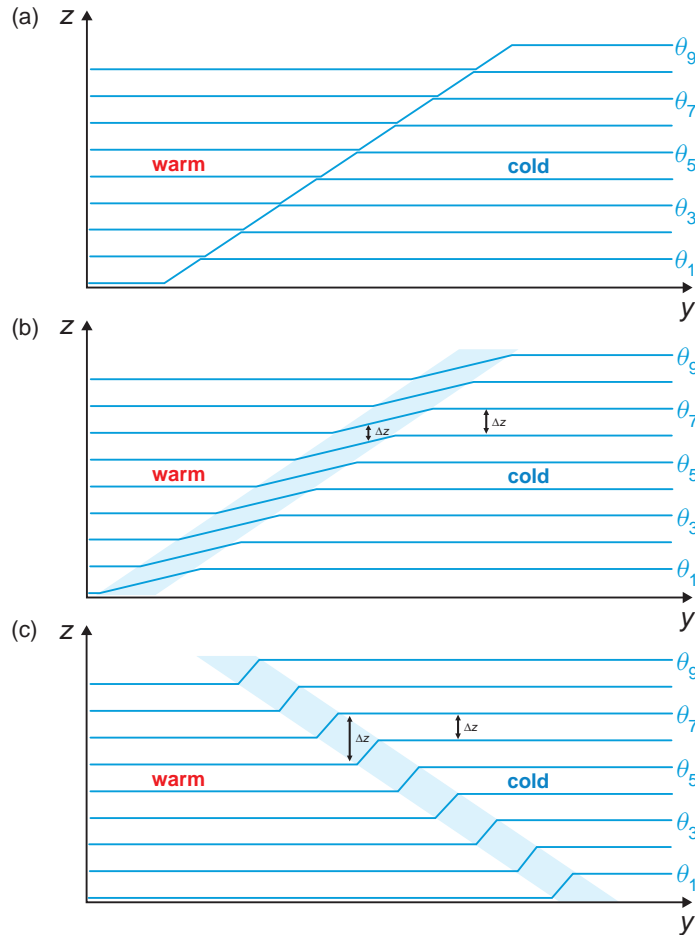


Figure 5.3 Idealized vertical cross-sections of potential temperature for (a) a front that is tilted over the cold air and represented as a zero-order discontinuity in temperature, (b) a front tilted over the cold air and represented as a first-order discontinuity in temperature, and (c) a front tilted over the warm air and represented as a first-order discontinuity in temperature. In all three panels, $\theta_9 > \theta_7 > \theta_5 > \theta_3 > \theta_1$. The shaded regions in (b) and (c) represent the frontal zone. Notice that the frontal zone is a region of enhanced static stability when it tilts over the cold air in (b), but is a region of reduced static stability when it tilts over the warm air in (c). (Adapted from Bluestein [1986].)

implies that the differential $d(p_c - p_w)$ vanishes at the front, that is,

$$\begin{aligned} d(p_c - p_w) &= \left[\left(\frac{\partial p}{\partial x} \right)_c - \left(\frac{\partial p}{\partial x} \right)_w \right] dx \\ &\quad + \left[\left(\frac{\partial p}{\partial y} \right)_c - \left(\frac{\partial p}{\partial y} \right)_w \right] dy \\ &\quad + \left[\left(\frac{\partial p}{\partial z} \right)_c - \left(\frac{\partial p}{\partial z} \right)_w \right] dz = 0 \quad (5.1) \end{aligned}$$

where dx , dy , and dz represent components of an incremental distance along the sloping frontal surface. As one

moves in the x direction (i.e., parallel to the front) on opposite sides of the front, the pressures on the opposite sides of the front must remain equal in order for pressure to be continuous across the front. Thus, $\left(\frac{\partial p}{\partial x} \right)_c = \left(\frac{\partial p}{\partial x} \right)_w$, and we can rearrange (5.1) to obtain

$$\frac{dz}{dy} = - \frac{\left(\frac{\partial p}{\partial y} \right)_c - \left(\frac{\partial p}{\partial y} \right)_w}{\left(\frac{\partial p}{\partial z} \right)_c - \left(\frac{\partial p}{\partial z} \right)_w}, \quad (5.2)$$

where dz/dy is the slope of the front. The slope must be positive in order for the density distribution to be statically

stable (negative dz/dy implies that relatively dense air overlies less dense air). Given that pressure decreases more rapidly with height in the cold air mass than in the warm air mass (i.e., $\left(\frac{\partial p}{\partial z}\right)_c < \left(\frac{\partial p}{\partial z}\right)_w$), (5.2) requires that

$$\left(\frac{\partial p}{\partial y}\right)_c > \left(\frac{\partial p}{\partial y}\right)_w, \quad (5.3)$$

which is ensured if the front lies within a pressure trough. Isobars must therefore be kinked along the front, which also implies a wind shift across the front and an attendant relative maximum in cyclonic vorticity.

Using the equation of state, and assuming hydrostatic and geostrophic conditions in each air mass (i.e., $\left(\frac{\partial p}{\partial z}\right)_c = -\rho_c g$, $\left(\frac{\partial p}{\partial z}\right)_w = -\rho_w g$, $u_{gc} = -\frac{1}{\rho_c} \left(\frac{\partial p}{\partial y}\right)_c$, and $u_{gw} = -\frac{1}{\rho_w} \left(\frac{\partial p}{\partial y}\right)_w$, where u_{gc} and u_{gw} are the along-front geostrophic wind components in the cold and warm air mass, respectively), (5.2) can be written as

$$\frac{dz}{dy} = \frac{f\bar{T}}{g} \frac{u_{gw} - u_{gc}}{T_w - T_c}, \quad (5.4)$$

where $T_w - T_c$ is the temperature difference across the front, $u_{gw} - u_{gc}$ is a measure of the cyclonic wind shear across a front, and \bar{T} is some representative temperature (though it is not necessarily the average of T_w and T_c , for computational purposes, the average works well enough). The above expression for the slope of a front is commonly known as *Margules' formula*.

Despite the crude assumptions about the characteristics of the front (e.g., the front was represented as a zero-order density discontinuity), Margules' formula provides an estimate of the slope that is the right order of magnitude. For $T_w - T_c \sim 10$ K, $u_{gw} - u_{gc} \sim 10$ m s⁻¹, $f \sim 10^{-4}$ s⁻¹, and $\bar{T} \sim 300$ K, we obtain a slope of $\sim 1/300$, which compares favorably with the slope of the warm front in Figure 5.2c. The slope along the leading edge of a cold front (e.g., Figure 5.2a,b) is often much steeper than what Margules' formula would predict owing to surface drag and possibly surface heat fluxes, as discussed before. Nonhydrostatic effects are probably significant in many cases of intense fronts having a temperature gradient that approaches that of a zero-order discontinuity (e.g., Figure 5.2b), so we also cannot naively expect Margules' formula to be most applicable to fronts that resemble zero-order discontinuities. We also cannot assume that strong fronts (i.e., large $T_w - T_c$) are more gently sloped than weak fronts, because $u_{gw} - u_{gc}$ tends to increase as $T_w - T_c$ increases. Moreover, for a given cyclonic shear and temperature differential, low-latitude fronts are predicted to be more gently sloped than midlatitude fronts.

A more realistic model of a front is that of a discontinuity in temperature *gradient* rather than a discontinuity in temperature (alternatively, the temperature field might be said to have a *first-order* discontinuity). In other words, the temperature gradient spans a *frontal zone* having a finite width (Figure 5.3b,c). It can be shown that the tilt of the frontal zone is

$$\frac{dz}{dy} = \frac{\left(\frac{\partial \theta}{\partial y}\right)_c - \left(\frac{\partial \theta}{\partial y}\right)_w}{\left(\frac{\partial \theta}{\partial z}\right)_w - \left(\frac{\partial \theta}{\partial z}\right)_c} \quad (5.5)$$

where the subscripts c and w indicate that the derivatives are to be taken on the immediate cold and warm sides of the front, respectively (the front is usually on the warm side of the zone of enhanced horizontal temperature gradient).⁸ The numerator on the rhs of (5.5) is always negative; therefore, the sign of the slope of the front is determined only by the denominator on the rhs of (5.5), that is, only by the static stability change across the front.

In contrast to the case of a zero-order temperature discontinuity, (5.5) implies that a frontal zone can tilt over the warm air while remaining statically stable (Figure 5.3c). Such forward-tilting frontal zones are characterized by a relative minimum in static stability rather than a relative maximum in static stability, as is the case within the more common rearward-tilting frontal zones. The aforementioned frontal structures, such as warm occluded fronts in which the coldest air is behind the cold front (Figure 5.2d) and forward-tilting cold fronts (Figure 5.2f), are only possible when fronts are viewed (correctly) as first-order temperature discontinuities.

5.1.5 Kinematics of frontogenesis

Frontogenesis refers to an increase in the magnitude of the horizontal density gradient, whereas *frontolysis* refers to a decrease in the magnitude of the horizontal density gradient. In assessing changes in the intensity of a front, it is helpful to rotate the coordinate axes so that the x axis is parallel to the front and the +y direction points toward the cold air. Thus, the strength of a front can be defined as $-\partial \theta / \partial y$ (the negative sign appears because θ decreases in the +y direction), where it is assumed that horizontal density gradients are proportional to horizontal θ gradients (one reason that frontogenesis is not usually evaluated in terms of changes in the horizontal density gradient is because density is not conserved, even for dry adiabatic motions). If significant horizontal moisture gradients are

⁸ See Stoelinga et al. (2002).

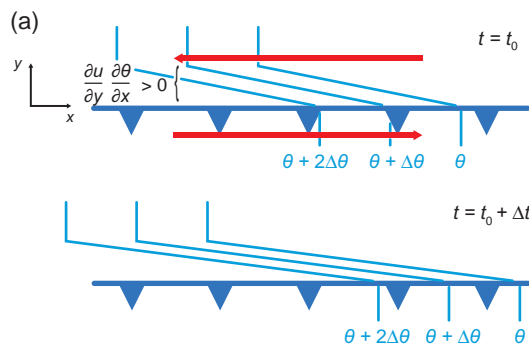
present, then horizontal θ_v gradients would be a better proxy for horizontal air density gradients.

We begin with the thermodynamic equation (2.9) written as

$$\frac{d\theta}{dt} = \frac{q\theta}{c_p T}, \quad (5.6)$$

where q is the diabatic heating rate per unit mass, which can result from latent or radiative heating or cooling. By differentiating (5.6) with respect to y , we obtain an equation for the time rate of change of the strength of the baroclinity along a front,

$$F = \frac{d}{dt} \left(-\frac{\partial \theta}{\partial y} \right) = \frac{\partial u}{\partial y} \frac{\partial \theta}{\partial x} + \frac{\partial v}{\partial y} \frac{\partial \theta}{\partial y} + \frac{\partial w}{\partial y} \frac{\partial \theta}{\partial z} - \frac{\partial}{\partial y} \left(\frac{q\theta}{c_p T} \right), \quad (5.7)$$



where F is the *scalar frontogenetical function* or *accumulation* of the potential temperature gradient.⁹ More generally, for any orientation of coordinate axes and for cases in which an along-front potential temperature gradient is present, $F = d|\nabla_h \theta|/dt$. The terms on the rhs of (5.7) represent the kinematic effects of horizontal shear, confluence, tilting of the vertical potential temperature gradient into the horizontal, and the horizontal variation of diabatic heating, respectively (Figure 5.4). Of course, for boundaries defined by gradients of quantities other than temperature, other conservative variables can be used in (5.7) in place of θ or θ_v . Moreover, (5.7) is scale-independent and can be applied to any boundary. For example, one could derive a similar expression for water vapor mixing ratio gradients in order to diagnose the kinematics of dryline formation (the

⁹ See Saucier (1955, p. 363).

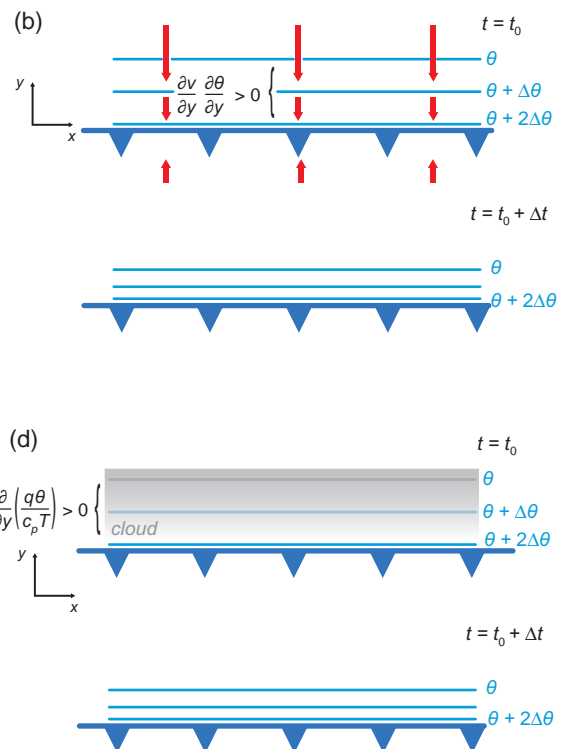


Figure 5.4 Schematic examples of frontogenesis as a result of (a) horizontal shear, (b) confluence, (c) tilting, and (d) a horizontal gradient in diabatic heating. A ‘before’ ($t = t_0$) and ‘after’ ($t = t_0 + \Delta t$) illustration is provided for each case. The red arrows in (a)–(c) indicate wind vectors in the plane of the drawings, with the lengths of the vectors being proportional to the magnitudes of the vectors. The gray shading in (d) represents cloud, and daytime conditions are assumed, so that the horizontal gradient of sky conditions is frontogenetic; the optical thickness of the cloud increases toward the north. In (a), (b), and (d), a cold front is analyzed on the warm side of the largest horizontal temperature gradient without loss of generality. It does not matter what type of front is present, nor whether a front is analyzed at all.

diabatic heating term would have to be replaced by a term that represents sources/sinks of water vapor, e.g., a surface moisture flux).

Note that F defines the rate of change of the magnitude of the horizontal potential temperature gradient following a parcel's motion, that is,

$$\frac{d}{dt} \left(-\frac{\partial \theta}{\partial y} \right) = \frac{\partial}{\partial t} \left(-\frac{\partial \theta}{\partial y} \right) + \mathbf{v} \cdot \nabla \left(-\frac{\partial \theta}{\partial y} \right). \quad (5.8)$$

The quantity $\frac{\partial}{\partial t} \left(-\frac{\partial \theta}{\partial y} \right)$ is due in part to frontal ground-relative motion and in part to true strengthening of the front in time. To assess the latter, we rewrite (5.8) in a reference frame moving with the front at velocity \mathbf{c} as

$$\left[\frac{\partial}{\partial t} \left(-\frac{\partial \theta}{\partial y} \right) \right]_{fr} = \frac{d}{dt} \left(-\frac{\partial \theta}{\partial y} \right) - (\mathbf{v} - \mathbf{c}) \cdot \nabla \left(-\frac{\partial \theta}{\partial y} \right), \quad (5.9)$$

where the 'fr' subscript indicates the front-relative reference frame, $\mathbf{v} - \mathbf{c}$ is the front-relative wind, and $-(\mathbf{v} - \mathbf{c}) \cdot \nabla \left(-\frac{\partial \theta}{\partial y} \right)$ is advection of the potential temperature gradient by the front-relative wind. Although the Lagrangian form of (5.7) might suggest the need for a complete trajectory analysis of air parcels to assess changes in frontal strength, the advection of the potential temperature gradient by the front-relative winds is frequently small within a frontal zone where, by definition, $-\partial \theta / \partial y$ is a maximum; thus, the second term on the rhs of (5.9) frequently can be ignored and changes in frontal strength can be evaluated fairly accurately using the terms on the rhs of (5.7), which are useful for physically describing frontogenetical processes.

If the effects of tilting and differential diabatic heating can be neglected (e.g., tilting goes to zero at the surface), then (5.7) can be written as

$$F = \frac{d}{dt} |\nabla_h \theta| = \frac{|\nabla_h \theta|}{2} (D \cos 2\beta - \delta), \quad (5.10)$$

where β is the angle between the isentropes and the *axis of dilatation*, $\delta = \frac{\partial u}{\partial x} + \frac{\partial v}{\partial y}$ is the horizontal divergence, and D is the *resultant or total deformation*, which is defined as

$$D = (D_1^2 + D_2^2)^{1/2} = \left[\underbrace{\left(\frac{\partial u}{\partial x} - \frac{\partial v}{\partial y} \right)^2}_{D_1} + \underbrace{\left(\frac{\partial v}{\partial x} + \frac{\partial u}{\partial y} \right)^2}_{D_2} \right]^{1/2}, \quad (5.11)$$

where D_1 is known as the *stretching deformation* and D_2 is known as the *shearing deformation*. The x and y axes are unrotated, unlike the case in the expression given by (5.7) (δ is rotationally invariant, but D_1 and D_2 are not).

The axis of dilatation is the axis along which a fluid element is stretched in a flow containing deformation; the relationships between idealized wind fields and the axis of dilatation are evident in Figure 5.5. The axis of dilatation is at an angle α counterclockwise from the x axis given by $\alpha = \frac{1}{2} \tan^{-1} \left(\frac{D_2}{D_1} \right)$. We observe from (5.10) that frontogenesis occurs whenever a nonzero horizontal potential temperature gradient coincides with convergence ($\delta < 0$), and whenever the total deformation field acts upon isentropes that are oriented within 45° of the axis of dilatation (Figure 5.5a). For angles between isentropes and the axis of dilatation that are between 45° and 90° , frontolysis occurs (Figure 5.5b). Divergence ($\delta > 0$) also contributes to frontolysis. Vorticity does not contribute directly to frontogenesis or frontolysis, but can affect frontogenesis or frontolysis by rotating the isentropes, thereby changing the angle between the isentropes and the axis of dilatation, which affects F .

5.1.6 Dynamics of frontogenesis and the vertical circulation at fronts

In the intensification (weakening) of synoptic fronts, a positive feedback loop involving the ageostrophic wind accelerates frontogenesis (frontolysis). Although the details of this dynamical feedback are not evident from the purely kinematic perspective discussed above, (5.10) suggests a significant contribution to frontogenesis from ageostrophic motions because only ageostrophic motions contribute significantly to δ . In short, the magnitude of the confluence acting on a temperature gradient increases with the magnitude of the temperature gradient itself; that is, in (5.7), $|\partial v / \partial y|$ increases with increasing $|\partial \theta / \partial y|$, with the contribution of the ageostrophic wind to $|\partial v / \partial y|$ being the culprit. This is explained in detail below.

One way to view the feedback loop is to regard the atmosphere as being in thermal wind balance, with geostrophic temperature (and vorticity) advection tending to drive the atmosphere away from thermal wind balance, but with vertical motions and associated ageostrophic winds being a response that maintains thermal wind balance in spite of the geostrophic forcings. Frontogenesis and frontolysis by the geostrophic part of the wind field are unavoidably accompanied by horizontal temperature advection (e.g., cold advection on the cold side of a front and warm advection on the warm side of a front would be associated with frontogenesis). In the case of frontogenesis, horizontal temperature advection leads to an increased thickness on the warm side of the front, with increased (decreased) heights of constant pressure surfaces at upper (lower) levels. The opposite occurs on the cold side (Figure 5.6).

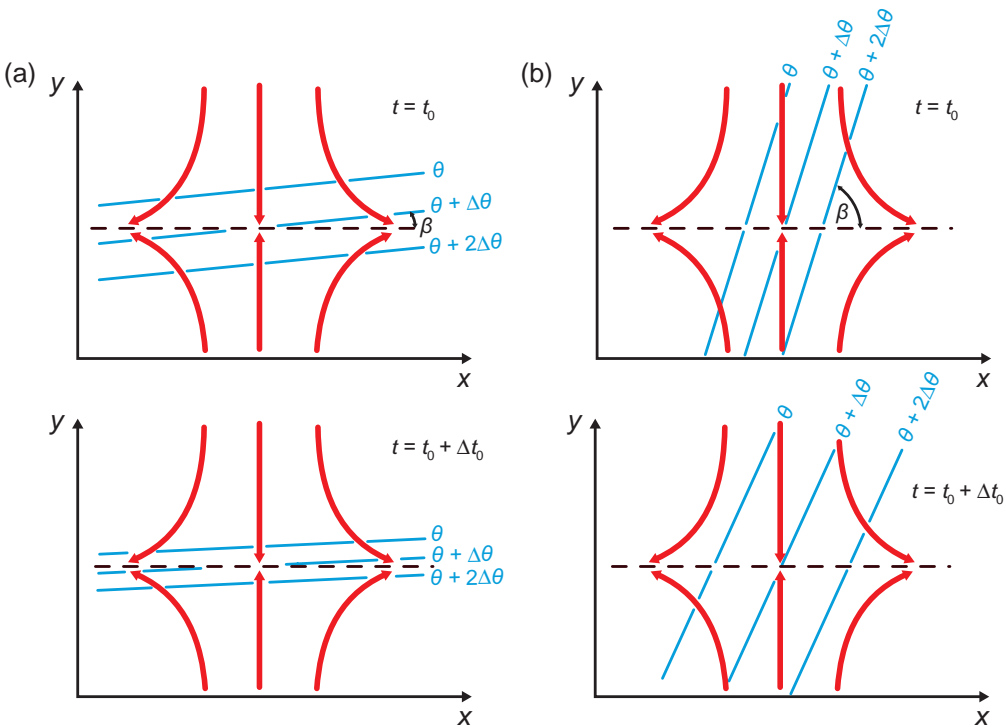


Figure 5.5 Schematic illustration of the relationship between isentropes (blue contours) and an idealized wind field dominated by deformation (red streamlines) in a situation of (a) frontogenesis ($0^\circ < \beta < 45^\circ$) and (b) frontolysis ($45^\circ < \beta < 90^\circ$). The axis of dilatation (black dotted line) and angle β (see text) are also indicated. (The isentropes rotate slightly clockwise in both cases.)

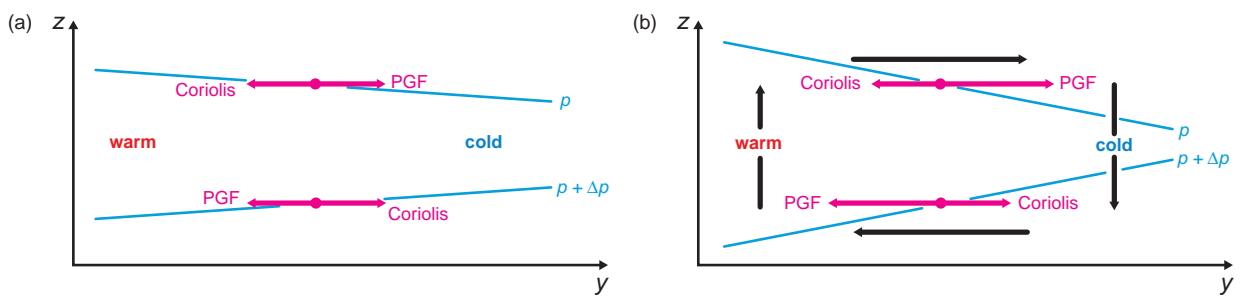


Figure 5.6 Illustration of the adjustment that occurs when a horizontal temperature gradient is increased through the action of geostrophic deformation, resulting in a thermally direct ageostrophic vertical circulation. Isobars (blue), forces (magenta vectors), and ageostrophic winds (black vectors) are shown. (a) Initial state of thermal wind balance. (b) Imbalance of forces following an increase in the horizontal temperature gradient, such that the thickness between pressure levels p and $p + \Delta p$ has been increased (decreased) hydrostatically on the left (right) side of the figure. (Adapted from Bluestein [1986].)

The pressure tendencies created in this process lead to an ageostrophic wind at upper (lower) levels in the positive (negative) y direction. As the Coriolis force acts on these ageostrophic winds, the vertical shear increases, as necessary to maintain thermal wind balance in the presence of an increasing temperature gradient. The ageostrophic winds also create a divergence/convergence pattern associated with rising (sinking) motion on the warm (cold) side of the front (i.e., a thermally direct circulation), with the attendant adiabatic cooling (warming) opposing the effects of the horizontal temperature advection by the geostrophic wind. Similar ageostrophic winds are associated with the geostrophic advection of momentum that must occur in a confluent geostrophic flow. The ageostrophic horizontal winds that accompany the vertical motion field further enhance $|\partial\theta/\partial y|$, which then requires even stronger vertical motions and ageostrophic winds, leading to a continued enhancement of $|\partial v/\partial y|$ and $|\partial\theta/\partial y|$. In the case of frontolysis, the process works in reverse via the same feedback loop.

The aforementioned effects of the ageostrophic wind field on frontogenesis cannot be represented using the quasigeostrophic approximation, wherein only advectives of geostrophic momentum and temperature by the geostrophic wind are considered. Instead, we use the momentum equations subject to what is sometimes called the *geostrophic momentum approximation*, where we include the advection of geostrophic momentum and temperature by the ageostrophic wind (and vertical velocity). The advection of ageostrophic momentum (by either the geostrophic or ageostrophic wind) remains neglected. The equations subject to the geostrophic momentum approximation are also sometimes referred to as *semigeostrophic* equations.

The semigeostrophic zonal momentum equation and thermodynamic equations are, respectively, in rotated (the x axis is parallel to the front and the y axis points toward the cold air), isobaric coordinates,

$$\frac{\partial u_g}{\partial t} + u_g \frac{\partial u_g}{\partial x} + u_a \frac{\partial u_g}{\partial x} + v_g \frac{\partial u_g}{\partial y} + v_a \frac{\partial u_g}{\partial y} + \omega \frac{\partial u_g}{\partial p} = f v_a \quad (5.12)$$

$$\frac{\partial \theta}{\partial t} + u_g \frac{\partial \theta}{\partial x} + u_a \frac{\partial \theta}{\partial x} + v_g \frac{\partial \theta}{\partial y} + v_a \frac{\partial \theta}{\partial y} + \omega \frac{\partial \theta}{\partial p} = \frac{q\theta}{c_p T}, \quad (5.13)$$

where u_g and v_g are the along-front and cross-front geostrophic wind components, respectively, and u_a and v_a are the along-front and cross-front ageostrophic wind components, respectively. On the rhs of (5.12), note that $f v_a = -\frac{\partial \phi}{\partial x} + fv$, where $\phi = gz$ is the geopotential height. The reason for expressing the above equations in isobaric coordinates is that we shall soon make use of the

thermal-wind relation, which has a much simpler expression in isobaric coordinates than in height coordinates. It is frequently assumed that $u_a = 0$, that is, that the ageostrophic circulation is confined to the $y-p$ plane.

Not only does semigeostrophic frontogenesis proceed faster than quasigeostrophic frontogenesis as a result of the added contribution of $\partial v_a/\partial y$ to the frontogenetical forcing (through both the deformation and divergence), but the advection of temperature by the ageostrophic circulation in semigeostrophic frontogenesis tilts the front rearward over the cold air mass (Figure 5.7b). The axis of dilatation associated with the total wind field (geostrophic plus ageostrophic parts) shifts to the warm side of the front, that is, to the warm side of the axis of dilatation associated with the geostrophic part of the wind field. Without the deformation, divergence, and advectives associated with the ageostrophic circulation, quasigeostrophic frontogenesis proceeds too slowly, the tilt of the frontal zone is unrealistic, and statically unstable conditions develop on the warm side of the front (also unrealistic) (Figure 5.7a).

The structure of the vertical circulation associated with frontogenesis or frontolysis can be obtained by subtracting $\frac{RT}{f_0 p \theta} \cdot \frac{\partial}{\partial y}$ (5.13) from $\frac{\partial}{\partial p}$ (5.12), which, with some effort, can be written as

$$\begin{aligned} & -2 \frac{R}{f_0 p} \frac{T}{\theta} \left(\frac{\partial \theta}{\partial y} \frac{\partial v_g}{\partial y} + \frac{\partial \theta}{\partial x} \frac{\partial u_g}{\partial y} \right) \\ & + \frac{R}{f_0 p} \frac{T}{\theta} \frac{\partial}{\partial y} \left(-v_a \frac{\partial \theta}{\partial y} - \omega \frac{\partial \theta}{\partial p} \right) \\ & + \frac{\partial}{\partial p} \left[-v_a \left(f - \frac{\partial u_g}{\partial y} \right) + \omega \frac{\partial u_g}{\partial p} \right] = -\frac{R}{c_p f_0 p} \frac{\partial q}{\partial y}. \end{aligned} \quad (5.14)$$

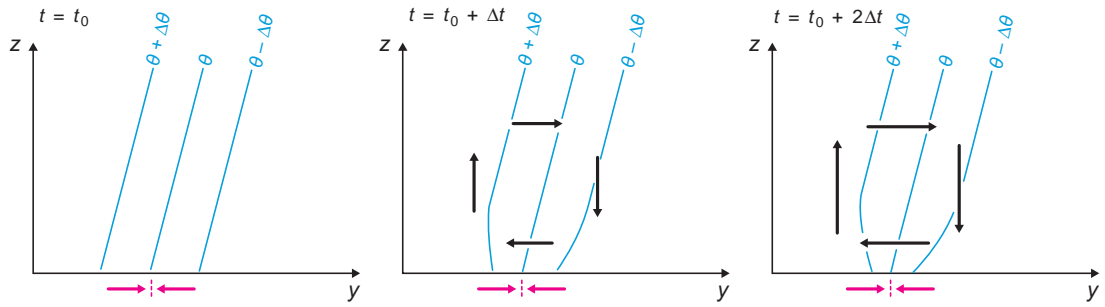
In obtaining the above expression, we have assumed that the ageostrophic circulation is confined to the $y-p$ plane (i.e., $u_a = 0$). We have also replaced f with a constant f_0 (the f -plane approximation) in the geostrophic wind relations, allowing us to exploit the fact that the geostrophic wind is nondivergent on an f plane (i.e., $\frac{\partial u_g}{\partial x} = -\frac{\partial v_g}{\partial y}$). The thermal wind relations on an f plane have also been used (thus, hydrostatic conditions are also assumed), where [cf. (2.67)]

$$\frac{\partial \theta}{\partial x} = -\frac{f_0 p}{R} \frac{\theta}{T} \frac{\partial v_g}{\partial p} \quad (5.15)$$

$$\frac{\partial \theta}{\partial y} = \frac{f_0 p}{R} \frac{\theta}{T} \frac{\partial u_g}{\partial p}. \quad (5.16)$$

We next introduce a streamfunction ψ in order to express v_a and ω in terms of the gradient of a single variable. We define $v_a \equiv -\partial \psi / \partial p$ and $\omega \equiv \partial \psi / \partial y$. Substitution

(a) quasigeostrophic frontogenesis



(b) semigeostrophic frontogenesis

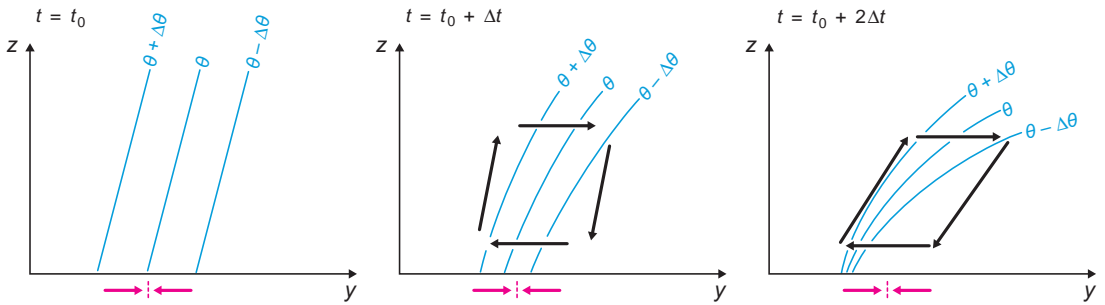


Figure 5.7 Comparison of (a) quasigeostrophic and (b) semigeostrophic frontogenesis. In (a), the isentropes (blue contours) are advected by the geostrophic winds (magenta vectors indicate the front-normal geostrophic wind components; the axis of dilatation for the geostrophic wind field is indicated with a dashed magenta line) but the ageostrophic wind field (black vectors; the lengths of vectors are proportional to the wind speed) that develops in response to the changing horizontal potential temperature gradient does not contribute to the advection of the isentropes. In (b), the ageostrophic circulation that develops in response to the changing potential temperature gradient feeds back to the evolution of the isentropes. Notice that the strength of the ageostrophic circulations increases in time, but a stronger ageostrophic circulation develops in the semigeostrophic case. The semigeostrophic case exhibits faster frontogenesis, a stronger front, and a more realistic tilt of the frontal zone than the quasigeostrophic case. Static instability also develops on the warm side of the front in the quasigeostrophic case. (Adapted from Bluestein [1986].)

into (5.14) yields what is commonly referred to as the *Sawyer-Eliassen equation*,

$$\begin{aligned} \frac{\partial^2 \psi}{\partial y^2} \left(-\frac{\partial \theta}{\partial p} \frac{RT}{f_0 p \theta} \right) + \frac{\partial^2 \psi}{\partial y \partial p} \left(2 \frac{\partial u_g}{\partial p} \right) + \frac{\partial^2 \psi}{\partial p^2} \left(f - \frac{\partial u_g}{\partial y} \right) \\ = 2 \frac{RT}{f_0 p \theta} \left(\frac{\partial u_g}{\partial y} \frac{\partial \theta}{\partial x} + \frac{\partial v_g}{\partial y} \frac{\partial \theta}{\partial y} \right) - \frac{R}{c_p f_0 p} \frac{\partial q}{\partial y}, \end{aligned} \quad (5.17)$$

where we have neglected horizontal variations of static stability (i.e., $\frac{\partial^2 u_g}{\partial p^2} \propto \frac{\partial}{\partial y} \left(\frac{\partial \theta}{\partial p} \right) = 0$ assumed) and have assumed that the strength of the baroclinity as measured by $\partial \theta / \partial y$ is a constant within the frontal zone (i.e., $\frac{\partial}{\partial y} \left(\frac{\partial u_g}{\partial p} \right) \propto \frac{\partial^2 \theta}{\partial y^2} = 0$ assumed).

The Sawyer-Eliassen equation is a linear, second-order partial differential equation that relates the streamfunction for the two-dimensional ageostrophic vertical circulation (ψ) to the static stability ($-\partial \theta / \partial p$), inertial stability ($f - \partial u_g / \partial y$), horizontal temperature gradient (through $\partial u_g / \partial p$), and frontogenetical forcing by the geostrophic wind and differential diabatic heating. It is a partial differential equation of the form

$$a \frac{\partial^2 \psi}{\partial y^2} + b \frac{\partial^2 \psi}{\partial y \partial p} + c \frac{\partial^2 \psi}{\partial p^2} = d; \quad (5.18)$$

such equations are classified as *elliptic*, *parabolic*, or *hyperbolic* depending on the discriminant $b^2 - 4ac$ (here a , b ,

and c are related to the static stability, baroclinity, and inertial stability, respectively). If $b^2 - 4ac < 0$ everywhere, (5.17) is an elliptic equation and ψ is uniquely determined by d , which is referred to as a *forcing function*. The ellipticity condition is met if

$$\left(\frac{\partial u_g}{\partial p}\right)^2 + \left(\frac{RT}{f_0 p \theta}\right) \frac{\partial \theta}{\partial p} \left(f - \frac{\partial u_g}{\partial y}\right) < 0. \quad (5.19)$$

It can be shown that (5.17) is hyperbolic if the atmosphere is either statically, inertially, or symmetrically unstable somewhere in the domain in which we are solving (5.17), in which case non-unique solutions arise from the release of the instability and the ageostrophic motions cannot be related to the frontogenetical forcing.

Despite its appearance, qualitative interpretations from the Sawyer-Eliassen equation are rather straightforward. The solution of (5.17) is a field of generally elliptical streamlines, although more complicated streamlines can result if frontogenetical forcing by the geostrophic wind field is combined with latent heat release (latent heating tends to introduce sharp gradients of forcing for ψ , thereby leading to more complicated ψ patterns). Positive

(negative) forcing on the rhs of (5.17) is associated with a thermally direct (indirect) vertical circulation (Figure 5.8). The intensity of the circulation is proportional to the magnitude of the rhs of (5.17). Cold fronts often have stronger vertical circulations than warm fronts, as well as sharper temperature gradients, because both deformation terms on the rhs of (5.17) are usually frontogenetic, whereas the $\frac{\partial u_g}{\partial y} \frac{\partial \theta}{\partial x}$ term is often negative along warm fronts.

The eccentricity of the ageostrophic circulation (i.e., the relative strengths of the horizontal and vertical branches of the circulation) is controlled by the relative magnitudes of the coefficients of the $\partial^2 \psi / \partial y^2$ and $\partial^2 \psi / \partial p^2$ terms (a and c , respectively), that is, the relative strength of the static stability compared with the inertial instability. When the static stability is large relative to the inertial stability [$a \gg c$ in (5.18)], vertical motions are suppressed relative to horizontal motions and the streamlines that define the ageostrophic circulation are ‘squashed’ in the vertical (e.g., Figures 5.8b,d). Conversely, when the inertial stability is large relative to the static stability [$a \ll c$ in (5.18)], horizontal motions are suppressed relative to vertical motions and the streamlines that define the ageostrophic circulation are ‘squashed’ in the horizontal (e.g., Figures 5.8a,c).

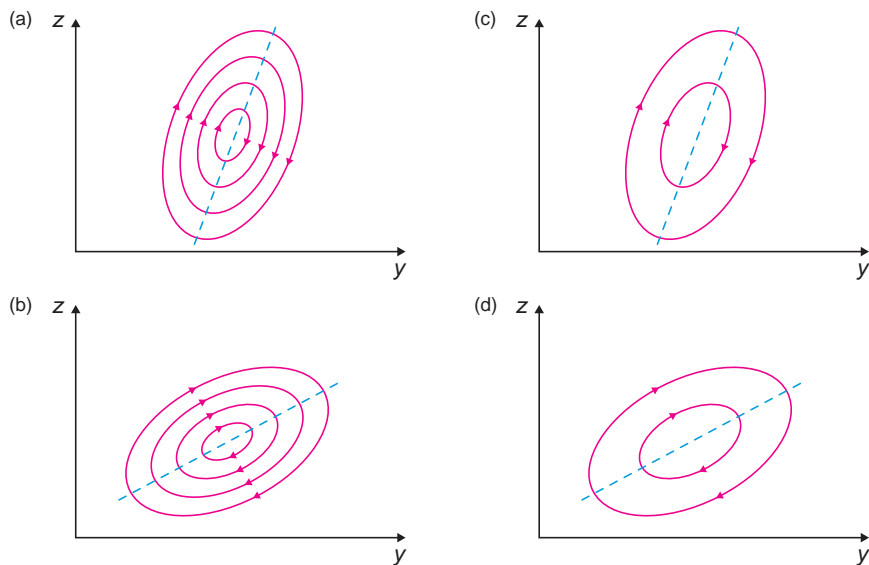


Figure 5.8 Schematic streamfunction contours depicting ageostrophic circulations (arrows indicate the wind direction) in cases of (a) strong geostrophic frontogenetical forcing, relatively strong inertial stability, relatively weak static stability, and steeply sloped M_g surfaces, (b) strong geostrophic frontogenetical forcing, relatively weak inertial stability, relatively strong static stability, and gently sloped M_g surfaces, (c) weak geostrophic frontogenetical forcing, relatively strong inertial stability, relatively weak static stability, and steeply sloped M_g surfaces, and (d) weak geostrophic frontogenetical forcing, relatively weak inertial stability, relatively strong static stability, and gently sloped M_g surfaces. The tilt of the circulations is indicated with dashed blue lines. The cold air is to the right.

The tilt of the ageostrophic circulation can be deduced by expressing the Sawyer-Eliassen equation in *geostrophic coordinates* (X, Y, P, T),¹⁰ where

$$X = x + v_g/f \quad (5.20)$$

$$Y = y - u_g/f, \quad (5.21)$$

and the vertical coordinate and time variable in real space are the same as in geostrophic space, that is, $P = p$ and $T = t$. In geostrophic space, the Sawyer-Eliassen equation describes an ageostrophic circulation in the $Y-P$ plane. In contrast to (5.17), a cross-derivative term involving $\partial^2\psi/\partial Y \partial P$ is absent in geostrophic space. Thus, the ageostrophic circulation is not tilted in the $Y-P$ plane, which implies that one of the axes (it turns out to be the major axis) of the ageostrophic circulation is parallel to a constant- Y surface. Because $Y = -M_g/f$, where $M_g = u_g - fy$ is the geostrophic absolute momentum (Section 3.3), M_g surfaces are parallel to Y surfaces; therefore, the tilt of the ageostrophic circulation is equal to the tilt of M_g surfaces (Figure 5.8). (If a quasigeostrophic version of (5.17) is derived by neglecting the momentum and temperature advectons by v_a and ω in (5.12) and (5.13), the resulting partial differential equation for ψ does not contain a $\partial^2\psi/\partial y \partial p$ term either, which is consistent with the earlier discussion about the importance of ageostrophic advectons in tilting the frontal zone over the cold air.)¹¹

The slope of M_g surfaces is given by (3.59) and is dependent on the relative magnitudes of the geostrophic absolute vorticity and the baroclinity (by way of the thermal wind relation); for a given geostrophic absolute vorticity, the slope of an M_g surface decreases as the horizontal temperature gradient increases. Recall that Margules' formula given by (5.2) also indicates, for a given horizontal shear of the geostrophic wind, that the slope of a front decreases as the horizontal temperature gradient increases. It might be somewhat surprising that Margules' formula, derived solely from kinematic relationships and assuming that fronts are zero-order density discontinuities, predicts essentially the same slope of a front as the Sawyer-Eliassen equation, which was derived from semigeostrophic momentum and thermodynamic equations.

One can view frontogenetical geostrophic deformation acting on a preexisting temperature gradient as 'jump

starting' the frontogenesis process by driving a secondary circulation that, as discussed above, enhances frontogenesis. In this regard, semigeostrophic frontogenesis is similar to an instability, in that a positive feedback is present. Mixing (both vertical and horizontal) limits the ultimate intensity of a front, preventing the magnitude of the horizontal temperature gradient from becoming infinitely large. The small-scale processes responsible for limiting front intensity remain poorly understood.

The feedback between the ageostrophic circulation and geostrophic frontogenetical forcing is probably not applicable to most of the air mass boundaries studied in the remainder of this chapter, in general (drylines are a possible exception), because the formation of mesoscale air mass boundaries, at least as we have defined them, does not rely on geostrophic deformation acting on a preexisting horizontal temperature gradient. Furthermore, strong fronts (e.g., Figure 5.2b) and many of the mesoscale air mass boundaries discussed in subsequent sections of this chapter (e.g., outflow boundaries, sea-breeze fronts, etc.) can have large nonhydrostatic pressure perturbations and large departures from geostrophic balance; thus, their circulations are not exactly in thermal wind balance and cannot be fully described by the Sawyer-Eliassen equation. In those cases, the tilt and intensity of the narrow updraft along the leading portion of the boundary must be predicted using a different approach. We revisit this topic in Chapter 9 (Section 9.3) because it has been most frequently studied in the context of the lifting by a gust front of potentially buoyant air parcels to their level of free convection in order to maintain mesoscale convective systems.

5.1.7 Frontal rainbands

Fronts are commonly associated with mesoscale rainbands that can be found ahead of, along, or behind the surface boundary. The ensuing discussion focuses on *narrow cold-frontal rainbands*, *wide cold-frontal rainbands*, *warm-frontal rainbands*, and *warm-sector rainbands* (Figure 5.9). Narrow cold-frontal rainbands are decidedly convective, whereas wide cold-frontal and warm-frontal rainbands represent enhancements of stratiform precipitation¹² within the larger-scale frontal precipitation region. Warm-sector rainbands occur ahead of the surface trough, cold front, or dryline that extends equatorward from the surface low, sometimes by a few hundred kilometers, outside of the

¹⁰ See Hoskins (1975).

¹¹ In geostrophic space, the dynamical equations subject to the geostrophic momentum approximation are transformed into equations having an appearance similar to the dynamical equations subject to the quasigeostrophic approximation. Sometimes the term *semigeostrophic equations* is restricted to dynamical equations subject to the geostrophic momentum approximation and transformed to geostrophic space.

¹² Houze (1993) defines stratiform precipitation as precipitation produced by upward vertical motions that are small compared with the fall speed of ice crystals and snow. Typical fall speeds for snow are $1-3 \text{ m s}^{-1}$.

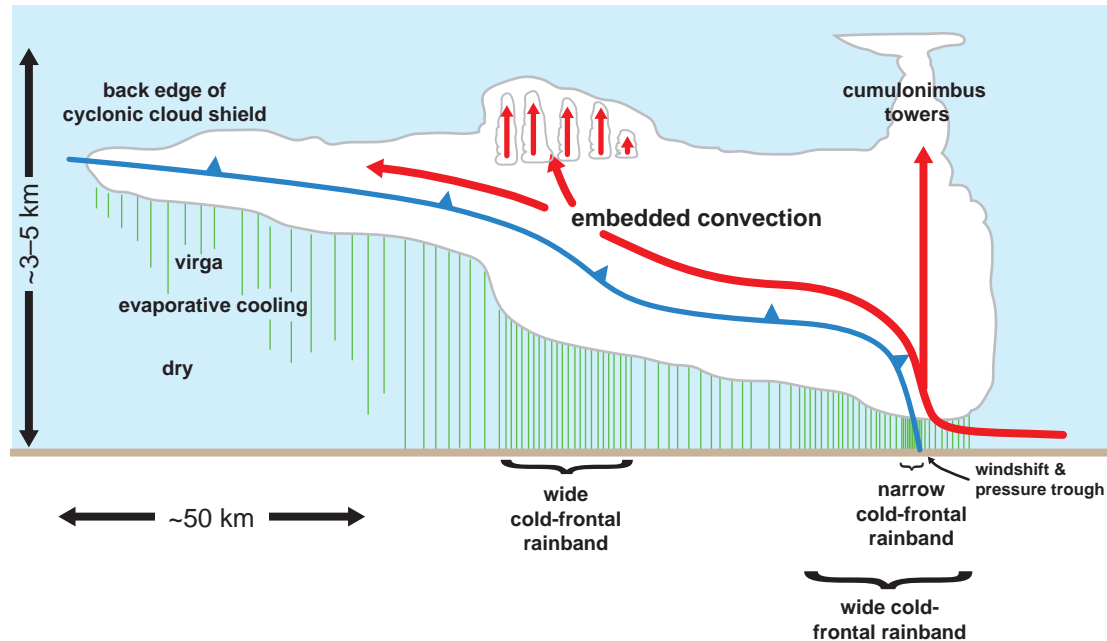


Figure 5.9 Schematic of the clouds, precipitation, and relative air motions associated with a cold front (motion is from left to right) documented by Matejka *et al.* (1980). Narrow and wide cold-frontal rainbands were observed within the precipitation shield. The density of the green hatching is proportional to the rain rate. (Adapted from Matejka *et al.* [1980].)

envelope of the frontal precipitation region. They can be convective or stratiform.

Narrow cold-frontal rainbands (Figures 5.10 and 5.11) are observed along the surface front at the location of the wind shift (Figure 5.9). They are often extraordinarily narrow, with a line-normal dimension sometimes as small as 1–2 km (Figure 5.10). The updrafts can be intense, occasionally exceeding 10 m s^{-1} at altitudes as low as 1 km. The most severe narrow cold-frontal rainbands even can spawn tornadoes.¹³

Narrow cold-frontal rainbands ought to be regarded as a form of convection, albeit forced convection (the distinction between *free* and *forced* convection was made in Section 3.1). Although their structure, maintenance, and impact share many similarities with those of squall lines, narrow cold-frontal rainbands tend to be much shallower than the forms of (free) deep, moist convection explored in Part III. The rainbands are driven principally by vertical perturbation pressure gradients (vertical gradients of both dynamic and buoyancy pressure perturbations, p'_d and p'_b , respectively) associated with the vertical circulation along the front (Section 5.1.6) rather than the

release of CAPE. Despite the lack of CAPE, their environments tend to be nearly (moist) neutrally stratified so that little work must be done against the stratification by the updrafts (Figure 5.11b). In strongly stratified environments that cannot support rainbands, sometimes a shallow, forced, laminar *rope cloud* is observed along the front instead.

Some investigators¹⁴ have found that the maintenance of narrow cold-frontal rainbands depends on a balance between the horizontal vorticity associated with the wind shear in the prefrontal air mass and the vertical circulation along the leading portion of the cold air mass. Similar arguments have been applied to squall lines, wherein the balance is between environmental horizontal vorticity and the circulation driven by evaporatively cooled outflow. This theory is discussed in greater detail in Chapter 9.

The rainbands and their attendant updrafts often develop kinks and breaks, sometimes called a *core-and-gap structure*, as a result of meso-γ-scale vortices along the line (Figure 5.12; similar structures are visible within the rainband shown in Figure 5.11a). These are very likely the same vortices that are occasionally amplified to

¹³ Carbone (1982, 1983) documented a tornadic rainband.

¹⁴ For example, see Parsons (1992).

1454 UTC 16 November 2005

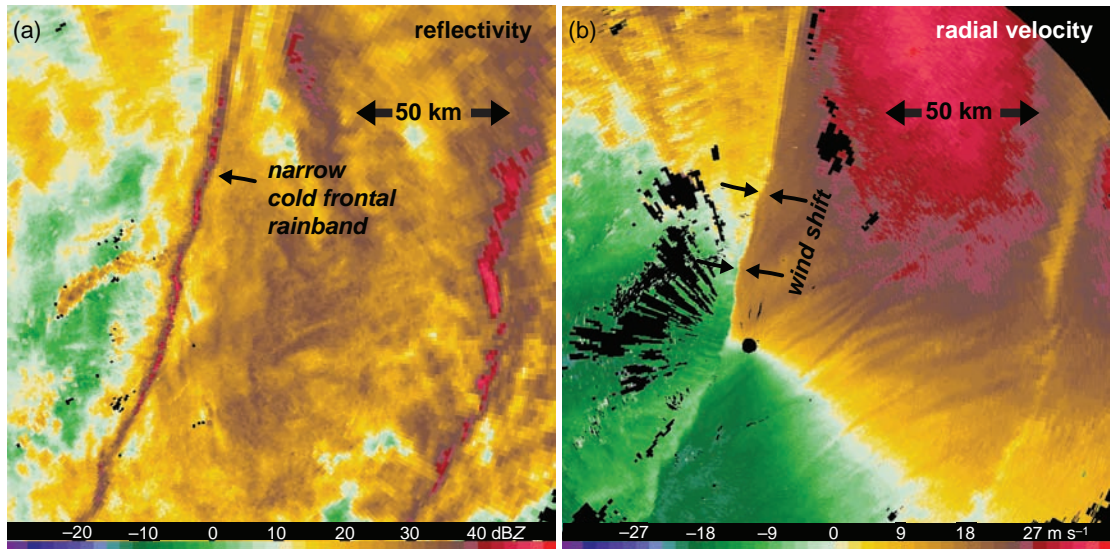
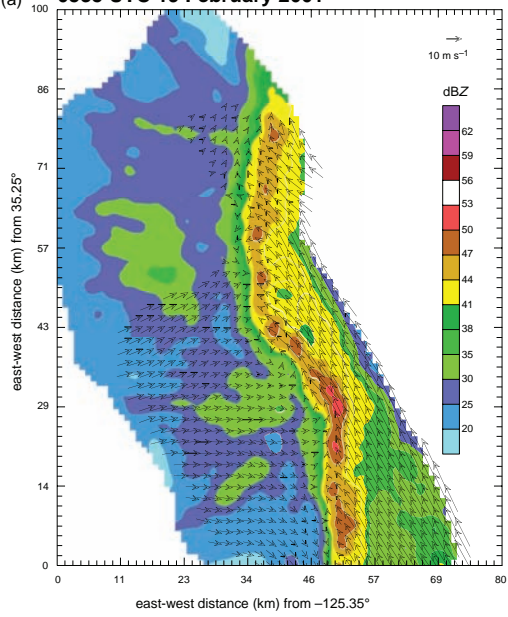


Figure 5.10 (a) Reflectivity (dBZ) and (b) radial velocity (m s^{-1}) imagery of a narrow cold-frontal rainband in central Pennsylvania at 1454 UTC 16 November 2005. A wide cold-frontal rainband is also visible farther east.

(a) 0535 UTC 19 February 2001



(b)

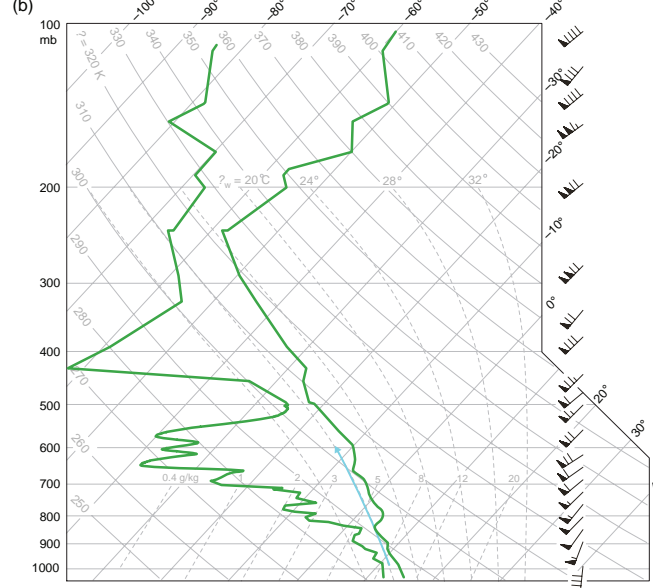


Figure 5.11 (a) Pseudo-dual-Doppler analysis of a narrow cold-frontal rainband on 19 February 2001. Horizontal wind vectors at 1 km are overlaid on radar reflectivity at the same altitude. (b) Composite sounding believed to represent the environment of the cold-frontal rainband. The path taken by a parcel lifted from the surface is indicated in blue. (Adapted from Jorgensen *et al.* [2003].)

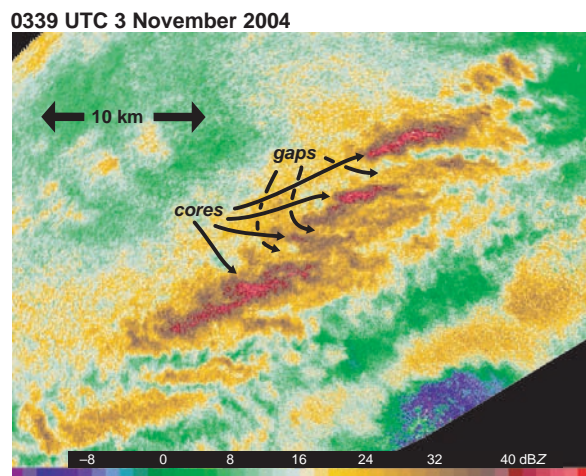


Figure 5.12 Narrow cold-frontal rainband exhibiting a core-and-gap reflectivity structure observed by a Doppler On Wheels (DOW) radar in central Pennsylvania on 3 November 2004.

tornado strength, in the rare cases when tornadoes are observed within rainbands. The small-scale vortices within cold-frontal rainbands (and along all fronts possessing sharp wind-shifts) probably arise from the instability of horizontal wind shear discussed in Section 3.5. The vortices ‘fracture’ the frontal updraft, leading to alternating precipitation cores and gaps in the line. Small-scale along-line variability in the updrafts along a front (with or without sufficient moisture to support rainbands) can also be the result of a front interacting with prefrontal boundary layer convective structures (e.g., cells, rolls, and less coherent structures).

In contrast to narrow cold-frontal rainbands, wide cold-frontal rainbands are only indirectly tied to processes near the surface (Figure 5.9). Their motion is independent of the motion of the front, unlike that of narrow cold-frontal rainbands, which are driven by strong vertical pressure gradients in the vicinity of the surface front. Wide cold-frontal rainbands move with the winds in the layer of enhanced vertical motion that defines the rainbands; wide cold-frontal rainbands frequently move ahead of the cold front and may overtake and move ahead of the narrow cold-frontal rainband (Figure 5.10). A cold front may be associated with multiple wide cold-frontal rainbands, whereas only a single narrow cold-frontal rainband is present, if one exists at all, at the location of the surface front (Figure 5.9).

Wide cold-frontal rainbands are associated with a local steepening of the frontal surface (Figure 5.9), although it is not clear whether the steepened frontal surface is

a cause or an effect of the rainbands. Some wide cold-frontal rainbands may be attributable to the release of conditional symmetric instability (CSI) (Figure 5.13). As discussed in Section 3.4, regions of CSI are also often regions of frontogenesis, and the ageostrophic vertical circulation that accompanies frontogenesis is believed to be a lifting mechanism that can release CSI.

Warm-frontal rainbands occur within and above the warm-frontal zone, on the poleward side of the surface warm front. As was the case for some wide cold-frontal rainbands, many warm-frontal rainbands can also be attributable to the release of CSI (Figure 5.13). Some warm-frontal rainbands also likely result from the destabilization that accompanies the lifting of a potentially unstable layer over a warm-frontal surface. Ducted gravity waves (Chapter 6) are probably also responsible for warm-frontal rainbands in some instances.

Warm-sector rainbands, as their name suggests, can develop within the warm sector of an extratropical cyclone, well ahead of the cold front (or dryline or surface trough). Many of these rainbands are likely associated with a CFA or split front. In the case of a CFA, the upward velocities have been explained in terms of a response to frontogenesis aloft via the Sawyer-Eliassen equation. In the case of a split front, the relatively drier air behind a split front would be associated with the development of midtropospheric potential instability, although it remains somewhat unclear whether frontogenetical forcing is present in order to release the potential instability, as many, perhaps most, split fronts are not associated with nearly as significant a horizontal temperature gradient as their humidity gradient.

5.2 Drylines

5.2.1 General description

Air mass boundaries separating moist, maritime tropical air from dry, continental tropical air commonly develop in the western Great Plains of the United States during spring and summer. These boundaries have been referred to as *dry fronts*, *dewpoint fronts*, and, most popularly, *drylines* (Figure 5.14a).¹⁵ The relatively large horizontal moisture gradients associated with drylines arise from the large-scale

¹⁵ It is not obvious why these boundaries are called *drylines* and not *moistlines*. Perhaps it is because during the day, as will be discussed later, the dry air mass typically advances from west to east (the identification of fronts as cold or warm fronts is based on which air mass is advancing). On the other hand, at night, drylines typically retreat to the west, yet they are still called drylines rather than moistlines, despite the fact that moist air is advancing from the east. We do not similarly refer to warm fronts as retreating cold fronts.

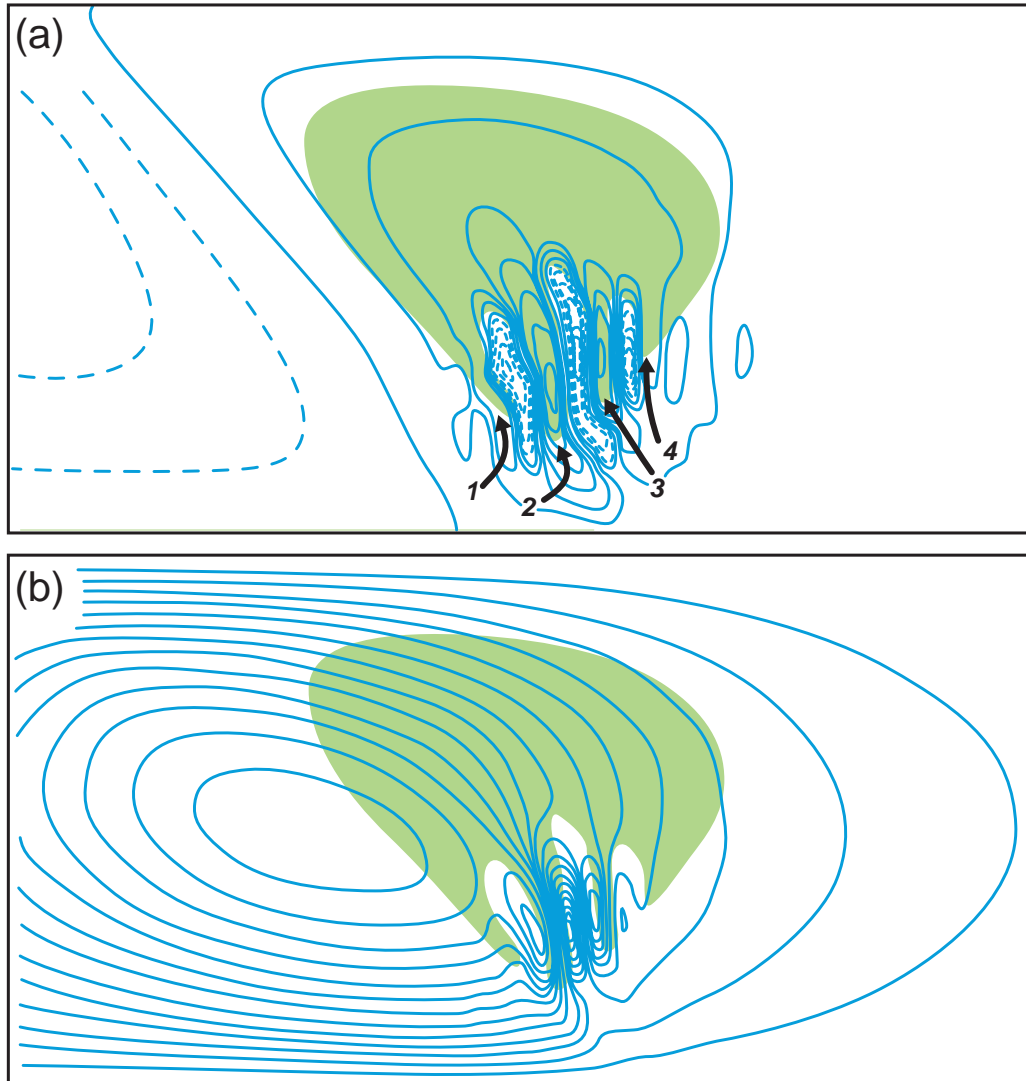


Figure 5.13 Vertical cross-sections of (a) vertical velocity and (b) streamfunction in an idealized numerical simulation of frontogenesis in an environment possessing CSI. The cross-sections are normal to the front, and the cold air is to the left. The vertical velocity contours in (a) are drawn with power increasing intervals (dashed contours are negative) of $\pm 2^n \times 0.5 \text{ cm s}^{-1}$ (i.e., 0, ± 1 , ± 2 , ± 4 , $\pm 8 \text{ cm s}^{-1}$, ...). A thermally direct circulation associated with frontogenesis is evident, as are stronger, smaller-scale motions that have resulted from the release of CSI. The saturated region is shaded green. Four rainbands are evident within the ascending branch of the frontal circulation. (Adapted from Xu [1992].)

confluence of air coming from different source regions. In other words, large-scale geostrophic deformation plays an important role in dryline formation, just as large-scale geostrophic deformation is crucial to the formation of synoptic fronts. Drylines are observed in other parts of the world, such as northern India, eastern China, and Spain. Our focus will be on United States drylines, although

similar dynamics can be applied to drylines elsewhere, at least midlatitude drylines.¹⁶

¹⁶ Drylines behave differently at low latitudes (e.g., northern India), where deep easterly flow is present, than those in midlatitudes, where vertical mixing generally transports westerly momentum to the surface.

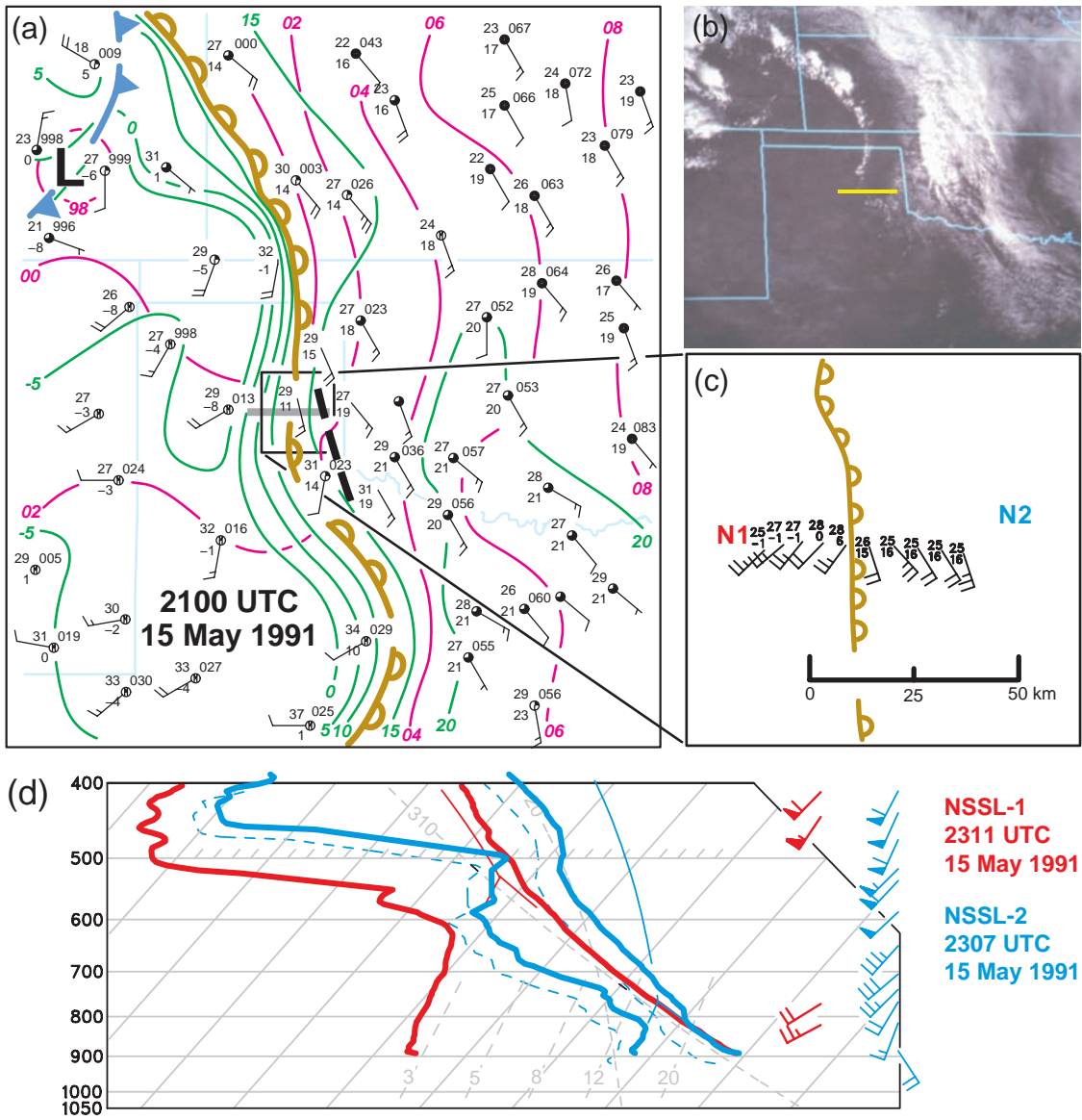


Figure 5.14 Surface, visible satellite, and sounding observations on 15 May 1991. (a) Manual analysis at 2100 UTC of mean sea level pressure (magenta contours every 2 mb; the leading '9' or '10' is dropped) and surface dewpoint (green contours every 5°C). The dryline is indicated with the brown, open-scalloped line. A low-pressure trough is indicated with a dashed black contour. A cold front is indicated with a heavy blue barbed line. Station models display temperature (°C), dewpoint (°C), mean sea level pressure (tenths of mb with the leading '9' or '10' dropped), sky conditions, and wind barbs (kt). The heavy gray line indicates the approximate location of aircraft transects used to construct the vertical cross-sections shown in Figure 5.18. (b) Visible satellite image at 2100 UTC. The yellow line indicates the approximate location of the aforementioned aircraft transects. (c) Close-up of surface observations in the immediate vicinity of the dryline obtained by mobile instrumentation (the enlarged region is shown in (a)). The station models display temperature (°C), dewpoint (°C), and wind (kt). The locations of two mobile sounding units (NSSL-1 and NSSL-2, respectively) positioned on opposite sides of the dryline are also indicated (N1 and N2, respectively). (d) Soundings obtained west and east of the dryline by NSSL-1 (red) and NSSL-2 (blue), respectively. The thin contours show the paths of a lifted surface parcel for each of the two soundings on the thermodynamic diagram. Winds are also shown for each sounding. (Adapted from Ziegler and Rasmussen [1998].)

In the United States, the moist air east of a dryline originates from the Gulf of Mexico, whereas the dry air west of a dryline originates from the arid regions of the southwestern United States and high plateau of Mexico. Horizontal land-use, vegetation, and soil moisture differences can also play significant roles in the generation and maintenance of drylines. Soil moisture and vegetation decrease from east to west in the Great Plains region; thus, the latent heat flux tends to decrease as one travels from east to west, thereby contributing to the zonal dewpoint gradient. Dewpoint temperature gradients in the vicinity of a dryline exceeding 10 K (1 km)^{-1} have been observed. On other days, the gradients are more diffuse, for example, $10\text{ K (100 km)}^{-1}$. Surface pressure troughs are sometimes associated with drylines, although many drylines do not reside within pressure troughs. A wind-shift line is also usually located near, but not necessarily within, the largest moisture gradient. Winds typically have a westerly component on the dry side and a small easterly component on the moist side. Drylines in the Great Plains region are generally oriented meridionally, with dry (moist) air to the west (east).

The dry air mass west of a dryline typically has a larger diurnal temperature cycle than the moist air mass east of a dryline. The differences in diurnal cycle are partly a result of differences in water vapor absorption of longwave radiation between the dry and moist air mass and differences in cloud cover (the moist air mass east of a dryline is often capped by stratus, stratocumulus, or cumulus clouds; Figure 5.14b). Because of the aforementioned westward decrease in soil moisture and vegetation in the Great Plains region, the sensible heat flux tends to be increasingly dominant in the surface energy budget as one travels from east to west (i.e., the Bowen ratio generally increases toward the west), thereby also promoting larger diurnal cycles on the west (dry) side of a dryline compared with the east (moist) side. As a result of the diurnal cycle differences, the dry side tends to be cooler than the moist side at night and warmer than the moist side during the day (Figure 5.14d). For this reason, drylines are not classified as cold fronts or warm fronts, which generally do not have a diurnal reversal of the direction of the temperature gradient.

5.2.2 Dryline formation

As mentioned above, synoptic-scale processes play an important role in regulating dryline formation and intensity. Dryline strength is highly correlated with the strength of the large-scale confluence, which itself is a function of strength of lee troughing downstream of the Rocky Mountains. Lee troughs are surface pressure troughs that form downwind of mountain ranges in situations where winds blow across the mountains with a substantial cross-ridge

component. In the United States, lee troughs are common to the east of the Rocky Mountains. Lee trough formation can be explained thermodynamically as being the result of adiabatic compression and warming of sinking air on the lee slope, or dynamically in terms of the vertical stretching of columns of air that descend the lee slope, wherein the stretching is associated with horizontal convergence and a spin-up of relative vorticity (the dynamical perspective is also commonly explained in terms of potential vorticity conservation, which requires that the vertical stretching of the columns be compensated by an increase in relative vorticity). The lee troughs downstream of the Rockies draw moist air northwestward from the Gulf of Mexico and dry air northeastward from the southwestern United States or northern Mexico (Figure 5.15c). Stronger lee troughs, stronger confluence, and stronger drylines (i.e., larger horizontal moisture gradients) are observed downstream of short-wave troughs in the mid- to upper-level westerlies (Figures 5.15a,c), whereas mid- to upper-level ridging in the upstream westerlies is characterized by weaker lee troughing, weaker confluence, and weaker drylines (Figures 5.15b,d).¹⁷

Although sloping terrain is what promotes lee troughing, the sloping terrain of the Great Plains (terrain slopes upward from east to west) contributes to dryline formation in another way as well. That the north-south orientation typical of most United States drylines is approximately normal to the terrain-height gradient is not a coincidence, because drylines essentially represent the intersection of the top of the maritime tropical boundary layer with the ground (Figure 5.16). Suppose a moist layer extends from the ground up to some fixed pressure level. Then the moist layer is relatively deep to the east at lower elevations and relatively shallow to the west at higher elevations (Figures 5.16 and 5.17). At some longitude, the top of the moist layer intersects the ground, and this intersection is a dryline. Vertical mixing promotes a dryline boundary that is nearly upright from the ground to an altitude of approximately $1.0\text{--}1.5\text{ km}$, and the dryline boundary then turns quasihorizontally to the east (Figure 5.18). Relatively cool, moist air is capped east of the dryline by a layer of large static stability at the top of the boundary layer. A warm, dry layer with large lapse rates, which overlies the inversion to the east (this layer is often referred to as an *elevated mixed layer* owing to its development originally as a mixed layer over higher terrain), is present from the surface to the middle troposphere to the west of the dryline.

Although the above-cited factors of lee troughing and sloping terrain, along with zonal variations in surface heat fluxes, are important for dryline development, these

¹⁷ See Schultz *et al.* (2007).

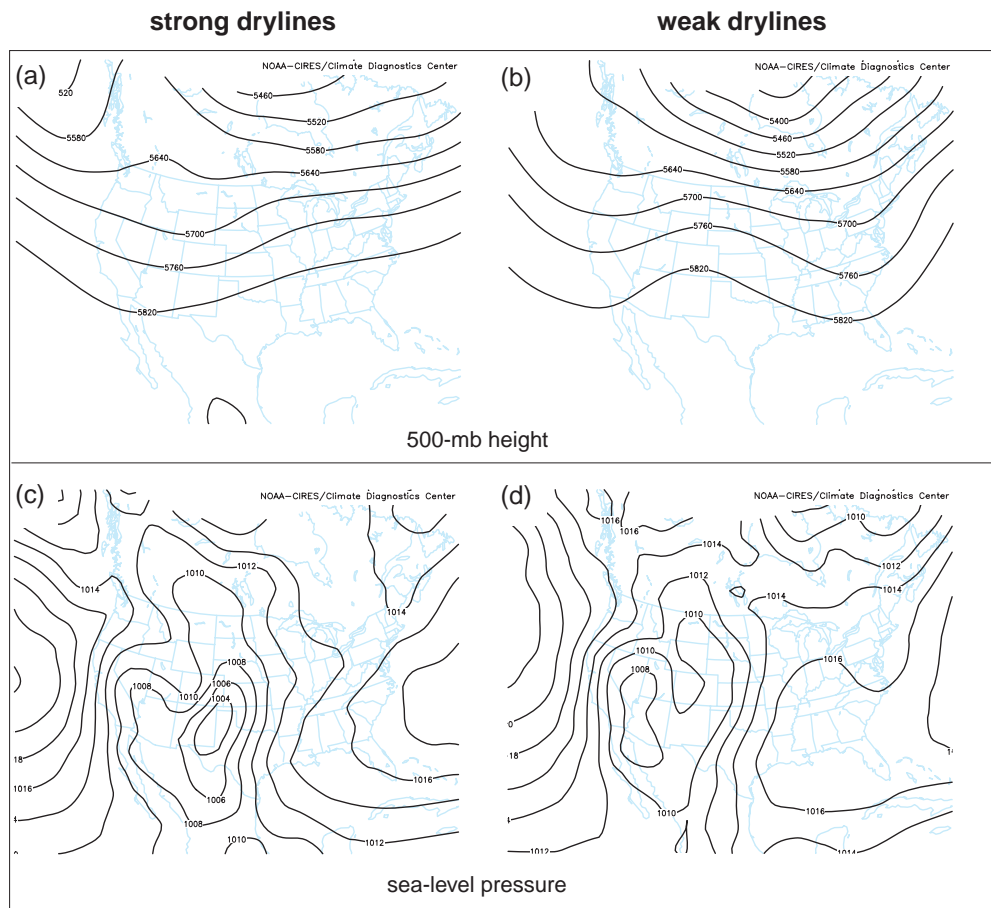


Figure 5.15 Composites of synoptic-scale conditions in cases of (left) strong drylines and (right) weak drylines: (a), (b) 500 mb geopotential height (contoured every 60 m); (c), (d) sea level pressure (contoured every 2 mb). (Adapted from Schultz *et al.* [2007].)

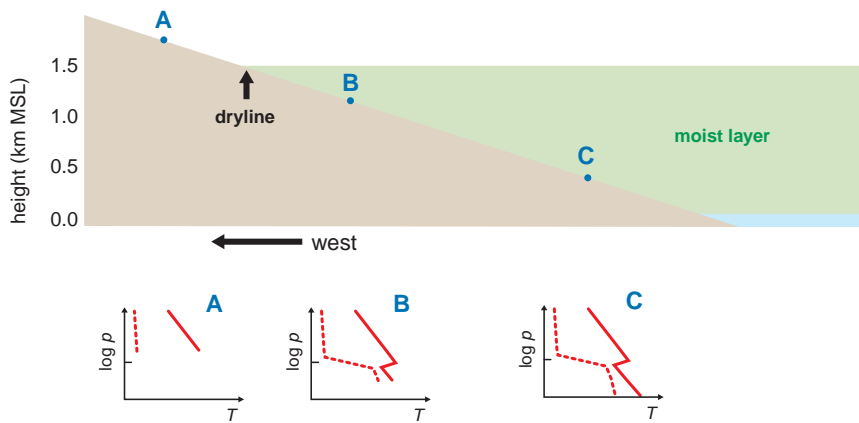


Figure 5.16 Schematic vertical cross-section of the dryline and its relation to topography. Idealized soundings at points A, B, and C represent the conditions west, just east, and far east of the dryline. (Adapted from Bluestein [1993].)

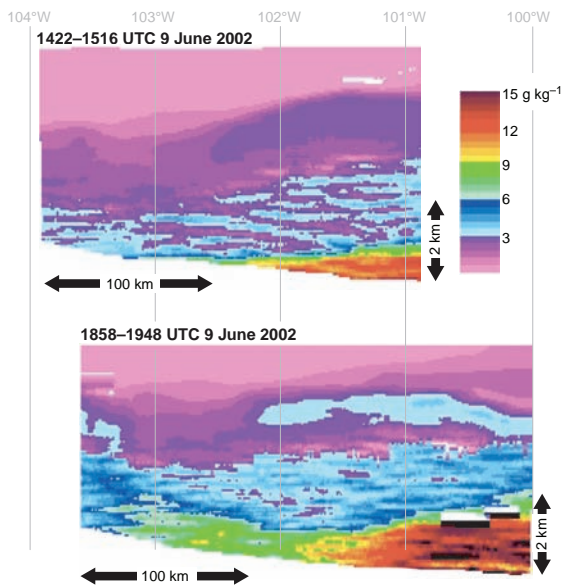


Figure 5.17 Cross-sections of mixing ratio obtained from west–east traverses of a downward-pointing airborne water vapor lidar over the southern United States Great Plains during the International H₂O Project (the aircraft was flying at approximately 37°N latitude). The top cross-section was obtained during the mid-morning, and the bottom cross-section was obtained during the early afternoon. Note how the moist layer intersects the sloping terrain at the location of the surface dryline. Also note the differences in the moisture distribution between the morning and afternoon traverses. (Imagery courtesy of the National Center for Atmospheric Research Earth Observing Laboratory.)

factors alone probably cannot account for the occasional observations of extreme moisture gradients (e.g., dewpoint gradients $>10\text{ K } (10\text{ km})^{-1}$; Figure 5.14c). On the other hand, ‘frontogenetical’ dryline dynamics can quickly intensify horizontal moisture gradients. Horizontal temperature gradients, although not as large as the moisture gradients, can increase the moisture gradients by way of a solenoidally forced vertical circulation at the dryline (Figure 5.18). Beneath the ascending branch of this circulation, convergence and frontogenesis (with respect to both temperature *and* moisture) are present. A positive feedback likely exists between the frontogenetical forcing of the horizontal moisture gradient ($d|\nabla_h r_v|/dt$) and the temperature gradient that usually accompanies a dryline’s moisture gradient, such as that described in Section 5.1.6 in the discussion of the vertical circulations of fronts. Another mechanism for locally increasing the moisture gradient along a dryline

is by way of differential vertical mixing. Deeper vertical mixing on the west (dry) side of a dryline can increase the westerly momentum transported to the ground on the west (dry) side, thereby increasing low-level convergence at the dryline, which, in turn, increases the moisture gradient. The variation in the depth of the mixing across a dryline and the magnitude of the horizontal temperature gradient associated with a dryline are probably related; differences in the depth of vertical mixing across a dryline would be expected to be most prominent when a significant temperature contrast exists across the dryline (and associated vertical circulation).

5.2.3 Dryline motion

Under the influence of strong synoptic-scale forcing, such as a migrating extratropical cyclone, a dryline can translate far to the east and exhibit no diurnal component to its motion. In the absence of strong synoptic-scale forcing, however, dryline motion has a strong diurnal component, with eastward motion during the day and a westward retreat at night. Daytime dryline motion in such instances of weak large-scale forcing is attributable to the cross-dryline variation in vertical mixing. Because the moist-layer depth (i.e., the height of the stable layer above the ground) decreases toward the west, the amount of surface sensible heating needed to destabilize the stable layer (some casually refer to this as ‘mixing out’ the moisture) increases from west to east. The general eastward decrease of the Bowen ratio further increases the amount of net radiation required to eradicate the capping inversion from below. The static stability is reduced until the lapse rate becomes dry adiabatic just to the east of the dryline, after which the dry air from above the stable layer is mixed with the moist air below, the surface dewpoint drops, westerly momentum is mixed to the ground, and the dryline propagates eastward. Here, *propagates* is used deliberately because dryline movement is not necessarily continuous. Dryline *jumping* (i.e., discontinuous motion) is fairly commonly observed. For example, drylines often jump across fairly flat areas, when the capping inversion is eliminated and dry air is mixed to the surface from aloft simultaneously over a wide area having roughly the same elevation, to a location where the terrain abruptly drops and the moist layer depth abruptly increases.

During the evening hours, the air west of a dryline typically cools faster than the air east of a dryline, and a radiation inversion forms. The increasing near-ground stability ends the process of vertical mixing, and surface winds slow and back in response to the pressure gradient force associated with the lee trough. Low-level moisture is

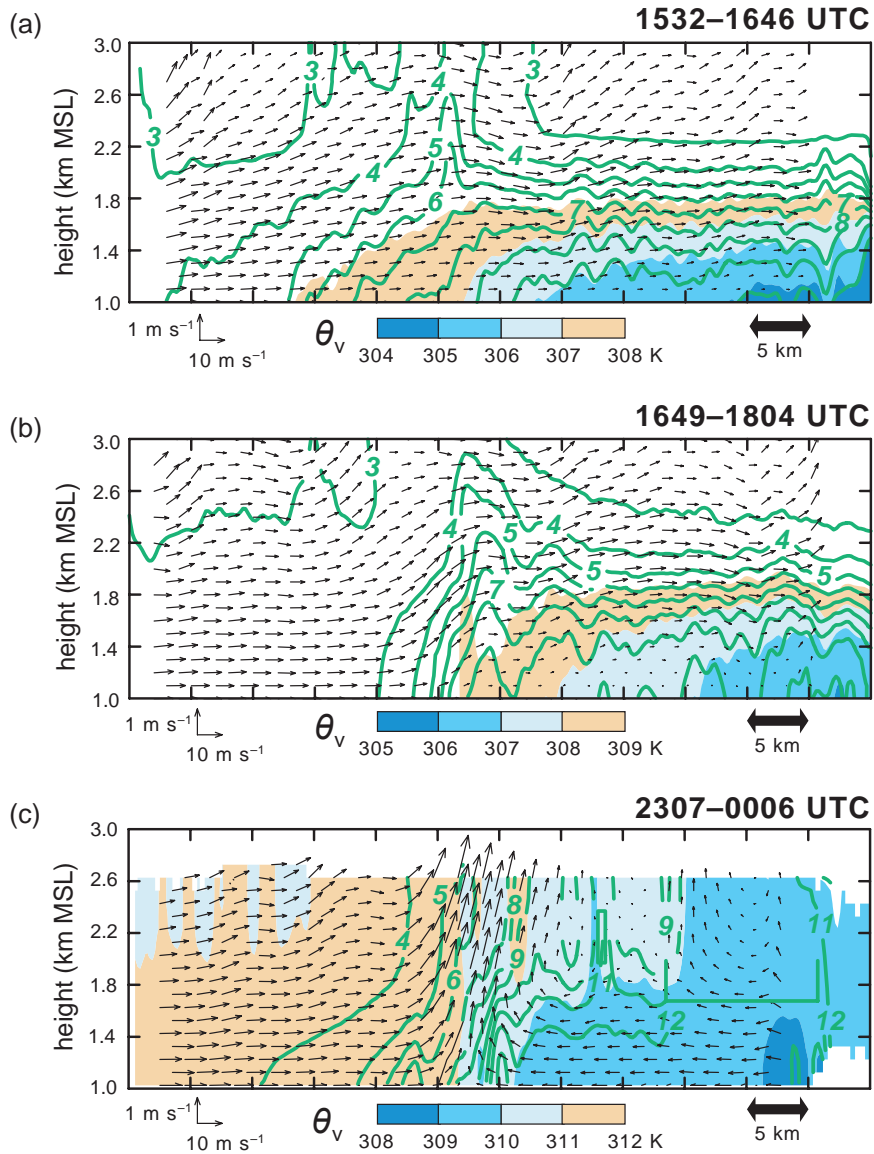


Figure 5.18 Vertical cross-sections of virtual potential temperature (θ_v ; shaded), water vapor mixing ratio ($g\text{ kg}^{-1}$; green contours), and wind (see scale) obtained from stepped aircraft traverses across a dryline between (a) 1532 and 1646 UTC, (b) 1649 and 1804 UTC, and (c) 2307 and 0006 UTC 15–16 May 1991. The location of the traverses is indicated in Figure 5.14a, 5.14b. (Adapted from Ziegler and Rasmussen [1998].)

adverted westward, as is the dryline. A retreating dryline initially may be morphologically similar to a density current (Section 5.3.2) in early evening, during the time when mixing has ceased and the air east of the dryline is still relatively cool compared with the air west of the dryline. Later in the evening, if the dry air mass becomes cooler than the moist air, a retreating dryline may act like a warm front.

5.2.4 Capping inversions and convection initiation

Drylines are among the most important air mass boundaries in the United States Great Plains region during the spring and early summer, owing to the convective storms that are frequently initiated along them (the Great Plains region

has the greatest frequency of severe convective weather worldwide). Storms often form in the dry air mass just west of the dryline, where the ascending branch of the thermally direct circulation is situated, and then move east onto the moist side of the dryline, where the convection can subsequently intensify as a result of the large θ_e values in the moist sector, or weaken owing to the presence of a strong cap east of the dryline. On other occasions, storms are initiated *east* of a dryline by a cold front aloft (sometimes >100 km east of a dryline), or perhaps by gravity waves excited by the dryline updraft impinging on the stable layer atop the boundary layer.¹⁸

Although fronts or favored topographic features (e.g., mountain crests) are probably the most common locations of thunderstorm initiation worldwide, drylines probably are at least as important, if not more so, in the initiation of warm-season severe convection in the Great Plains region. Because drylines so often precede cold fronts in the warm season in this region, cold fronts often do not get the opportunity to encroach upon conditionally unstable maritime tropical air masses, but often instead end up lifting post-dryline air that is considerably less potentially buoyant. Toward the latter part of the warm season, cold frontal passages themselves, especially through the southern Great Plains, become increasingly infrequent. Another aspect of drylines is that they seem to be more prone to initiate isolated thunderstorms rather than solid lines of storms as cold fronts often do. The relatively isolated storms are usually the ones that end up being the most prolific tornado producers. It is probably fair to say that most of the major tornado outbreaks in the central United States involve drylines.

As discussed in Section 5.2.2, drylines are closely related to capping inversions, also sometimes referred to as *caps* or *lids*, as a result of the dryline marking the intersection of the top of the moist air mass with the ground; a capping inversion is found atop the moist layer as a result of a continental tropical (i.e., relatively warm and dry) boundary layer being advected over the maritime tropical boundary layer to the east (Figure 5.16). In other words, the surface dryline marks the leading edge of the continental tropical air mass at the surface, but the continental tropical air aloft typically spreads east beyond the dryline, giving rise to the often-observed cap on Plains moist sector soundings (e.g., Figure 2.9). The base of a capping inversion generally lies between 900 and 800 mb, but can be found higher or lower if synoptic-scale vertical motions

are upward or downward. Capping inversions prevent the release of CAPE until the CIN associated with boundary layer air parcels can be overcome. Thus, capping inversions allow for the generation of large CAPE values and subsequent explosive thunderstorm development. Boundary layer θ_e values generally increase during the day beneath a cap due to the suppression of deep mixing by the large static stability associated with the cap, along with latent heat fluxes and sometimes positive horizontal moisture advection. Without a cap, CAPE tends to be released shortly after it is generated, so that it is released when CAPE values are relatively small, as is usually the case in the tropics. Because days with strong capping inversions are often days with large CAPE, the days with the greatest severe weather potential, by virtue of the presence of large CAPE, are frequently also the days with the greatest potential for failed forecasts of convection initiation, by virtue of the large CIN.

5.2.5 Other aspects of drylines

Drylines occasionally exhibit complicated structures. Some dryline passages are followed by stepwise decreases in dewpoint rather than monotonic decreases. Multiple drylines are sometimes analyzed on surface weather maps in such cases. Their spacing, when observed, is usually 10–50 km. It seems as though the air masses residing between such multiple dryline boundaries, at least in some cases, represent mixtures of air from the other sides of the dryline boundaries. Why multiple drylines are observed on some days and only single, better-defined drylines occur on other days is not well understood.

Meso- β -scale bulges or waves sometimes develop along drylines (Figure 5.19). The dryline bulges or waves can be associated with locally enhanced convergence, particularly on the poleward side of the apices of the bulges or waves. The cause of dryline bulges and waves is also not well understood. The downward mixing of locally faster wind speeds aloft could conceivably lead to a dryline bulge. Such a region of locally larger momentum aloft is often found within jet streaks, and the ageostrophic motions and transverse circulation associated with the exit region of a jet streak could be why dryline bulges are often associated with increased low-level convergence and a propensity for severe storm formation poleward of a bulge (the region poleward of a dryline bulge is often in the left exit region of a jet streak). A relative maximum in sensible heat flux can promote a locally deeper boundary layer and therefore also contribute to some dryline bulges if the locally deeper boundary layer taps stronger westerly momentum aloft that is subsequently mixed downward.

¹⁸ Wakimoto *et al.* (2006a) concluded that a gravity wave propagating eastward on top of the moist boundary layer east of a dryline was responsible for convection initiation in a case that was observed during the International H₂O Project (IHOP).

2300 UTC 22 May 2007

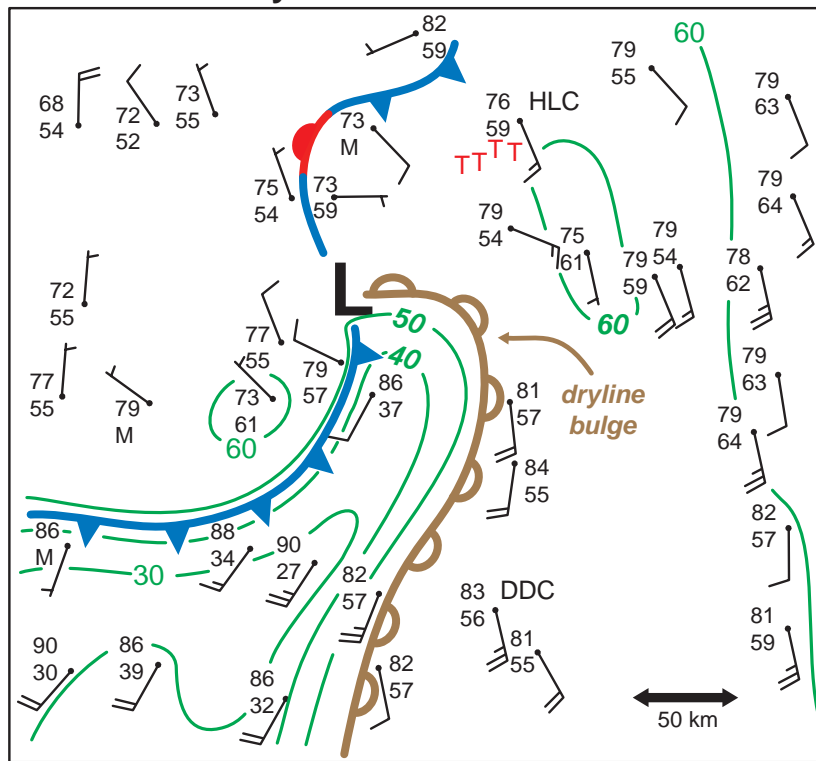


Figure 5.19 Surface analysis at 2300 UTC 22 May 2007 in western Kansas. Isodrosotherms are drawn at 10°F intervals. Station models display temperature (°F), dewpoint (°F), and wind barbs (knots). A dryline bulge is evident. A number of tornadoes occurred between 2300 and 0100 UTC. Their approximate locations are indicated with a letter 'T.' The cities of Hill City and Dodge City are labeled as 'HLC' and 'DDC,' respectively.

5.3 Outflow boundaries

5.3.1 General description

Outflow boundaries are among the most common meso-scale boundaries, particularly in the warm season. Even the casual weather observer is familiar with the relatively cool, refreshing outflow produced by showers or thunderstorms as rain falls into subsaturated air and evaporates. The relatively cool air tends to sink and spread outward, away from its source, upon reaching the surface, and for this reason this air is called *outflow*. Because the outflow is denser than the ambient air mass it displaces, the outflow is associated hydrostatically with locally higher pressure, sometimes called a *mesohigh* or *bubble high*. Downdrafts and outflow can also be generated by dry air impinging on a thunderstorm updraft aloft, leading to evaporation and subsequent cooling aloft, followed by the descent of this cool air to the

ground by virtue of its negative buoyancy. The melting and sublimation of ice hydrometeors (snow, graupel, and hail) can contribute to the negative buoyancy of outflow as well. As a result of the entrainment of midlevel low- θ_e air from the environment in the formation of downdrafts, θ_e within convective outflows also tends to be lower than ambient values (Figure 5.20).

The leading edge of the outflow is called an *outflow boundary*, and the portion of the outflow boundary in close proximity to the progenitor convection is commonly referred to as a *gust front*. Outflow boundaries are commonly detectable in radar reflectivity data as *fine-lines*¹⁹

¹⁹ Mesoscale boundaries often appear as fine-lines in radar reflectivity data largely owing to the presence of insects that are locally more concentrated in the convergence zones along the boundaries, or lofted by updrafts along the boundaries to a height where the insects can be detected by radar. Occasionally the refractive index differences across

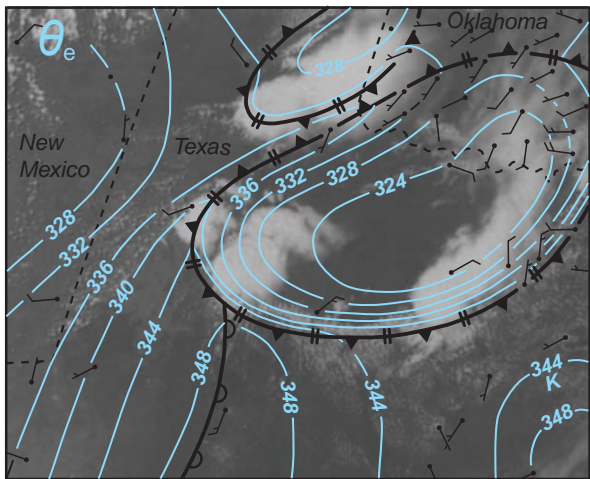


Figure 5.20 Visible satellite image of convective outflow from 2000 UTC 31 May 1995, with θ_e contours overlaid. Outflow boundaries are indicated using the symbology introduced in Figure 5.1. A dryline (Section 5.2) is also analyzed using unfilled scallops. (Adapted from Wakimoto *et al.* [2004b].)

(Figure 5.21) and are easily identifiable in visible satellite imagery when middle and high clouds do not obscure the view of low clouds (Figure 5.20). Outflows are typically on the order of 1 km deep, although outflows as shallow as a few hundred meters and as deep as 4 km can occasionally be observed. The depth depends in large part on the age of the parent convection, with the deepest outflows generally being observed in convection that has persisted the longest. Air forced to ascend along the leading edge of the outflow sometimes forms long *arcus* or *shelf clouds* (Figure 5.22).

The magnitude of the temperature deficits within outflow depends on the vertical profiles of environmental temperature and relative humidity, as well as on the height from which air descends to the surface. Decreasing environmental temperatures aloft lead to colder outflow, and the cooling produced by the evaporation of rain increases with decreasing environmental relative humidity. On the other hand, less hail melting occurs in dry environments compared with humid environments. Thus, for a given condensate mass produced by a convective storm, how cold the outflow will be is difficult to generalize because of the sensitivity to the microphysical traits of the parent storm. An additional complication is that the condensate mass that may contribute to latent cooling is itself dependent on the environmental relative humidity.

a boundary, due to air density differences, may also make a boundary visible in radar reflectivity data.

For example, a dry mid-tropospheric environment tends to weaken updrafts and decrease the condensate mass that subsequently can be evaporated, melted, or sublimated to chill the air. For a fixed boundary layer relative humidity, numerical simulations indicate that convective storms actually produce colder outflow as the midlevel relative humidity in the storm environment increases.²⁰ Thus, even though the entrainment of dry environmental air is a crucial part of downdraft formation, outflow does not necessarily become colder as the relative humidity of the midlevel environment is reduced. Notwithstanding the sensitivities of outflow characteristics to the midlevel environmental relative humidity, the coldest outflow tends to be produced by high-based thunderstorms that rain into very dry boundary layers, such as the storms that develop in the western United States during the middle to late summer (temperature deficits can exceed 25 K in the coldest outflows). Conversely, small temperature deficits (just a few kelvin) are most often observed in tropical environments in which the boundary layer has a large relative humidity.

Wind shifts are typically present across outflow boundaries. Moreover, although most of the pressure excess associated with outflow can be regarded as having hydrostatic origins (i.e., is due to an increase in the weight of the air; see Section 2.5), the pressure excess that is observed right along the outflow boundary is a result of nonhydrostatic or dynamic effects (Figure 5.23; again, see Section 2.5 and also Figure 2.6). The relatively high pressure is required with the deflection of ambient air up and over the outflow. A second area of nonhydrostatic high pressure can be found within the outflow beneath the strongest downdraft (Figure 5.23) and is associated with the deceleration of downdraft air as it approaches the ground. Note that there are some differences between Figures 2.6 and 5.23; for example, the nonhydrostatic pressure excess beneath the strongest downdraft in Figure 5.23 is absent from Figure 2.6. This is probably because the density current shown in Figure 2.6 was initialized using a block of cold air independent of an overlying thunderstorm.

Over time, particularly in the mature and decaying stages of a mesoscale convective system, a region of low pressure typically develops within the trailing portion of the outflow (Figure 5.24). This low is referred to as a *wake low* or *wake depression*. This feature is a result of unsaturated descent in the trailing region of the convective system (additional discussion appears in Chapter 9). In a hydrostatic atmosphere, surface pressure is proportional to the integral of density over the entire depth of the column overhead. In other words, surface pressure changes reflect density changes *throughout* the column; thus, even

²⁰ See James and Markowski (2008).

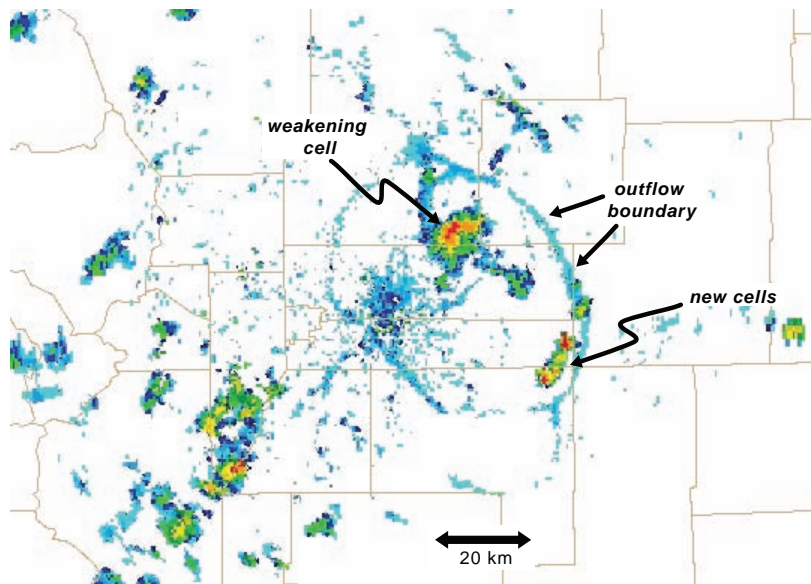


Figure 5.21 Radar reflectivity image showing a nearly circular outflow boundary produced by storms east of Denver, CO, manifested as a reflectivity fine-line.

though the low-level air mass is usually cold owing to the presence of rain-cooled outflow, surface pressure can fall as subsidence and warming occur at midlevels.

5.3.2 Density current dynamics

Outflow boundaries often behave like *density currents*, also known as *gravity currents*. A density current is the flow of a relatively dense fluid embedded within a lighter fluid (Figures 5.25 and 5.26). Density current motion is by



Figure 5.22 Photograph of a shelf cloud along the leading edge of an outflow boundary. Photograph by Eric Nguyen.

way of the horizontal pressure gradient force that exists across the density interface because of hydrostatic pressure differences associated with the density differences between the two fluids. Synoptic fronts generally do not behave like density currents because the horizontal pressure gradient is usually counteracted by the Coriolis force on large scales (exceptions are some intense cold fronts such as that shown in Figure 5.2b). Furthermore, density currents behave as material surfaces; that is, air parcels do not pass through the interface separating the air of differing densities. Synoptic fronts cannot usually be regarded as material surfaces, however. For example, if we assume adiabatic motion such that a parcel's motion is confined to an isentropic surface, a parcel often will pass *through* a frontal boundary such as those idealized in Figure 5.3, whereas a parcel will pass *over* a density current as in the case of the intense cold front shown in Figure 5.2b, which has a structure similar to that of a density current.

Density currents typically have a head (deeper portion) on their leading edge, sometimes twice the depth of the fluid far behind the leading edge of the density current. The depth of the lifting along the leading edge of the density current depends on the magnitude of the density differential, ambient wind shear, and whether a relative headwind or tailwind exists. Furthermore, the top interface of the density current may become unstable and break down into billows as a result of Kelvin–Helmholtz

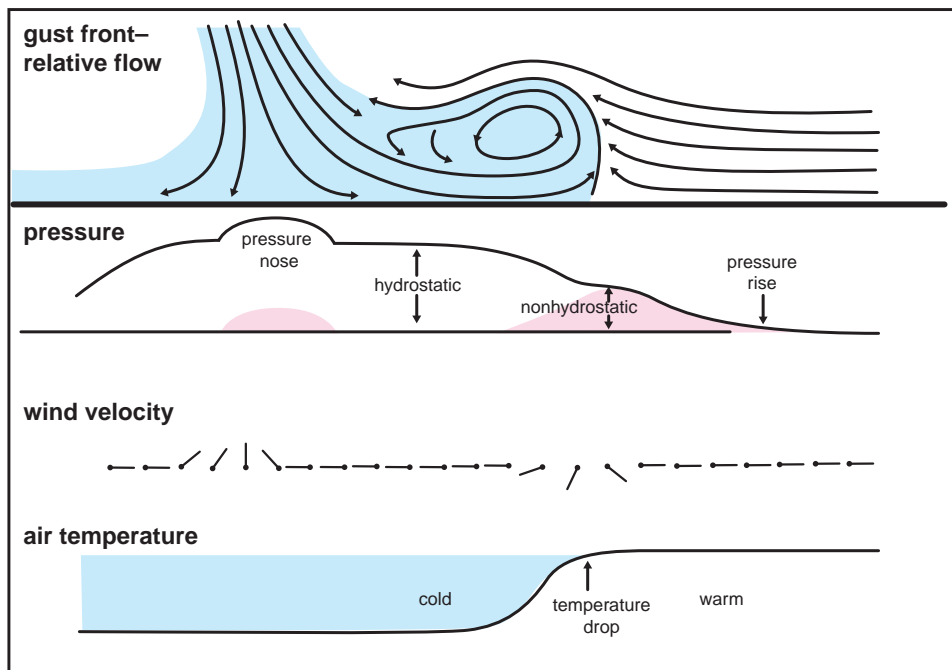


Figure 5.23 Conceptual model of surface observations during the passage of a gust front in its mature stage. Note that part of the pressure excess is due to nonhydrostatic effects (cf. Figure 2.6). (Adapted from Wakimoto [1982].)

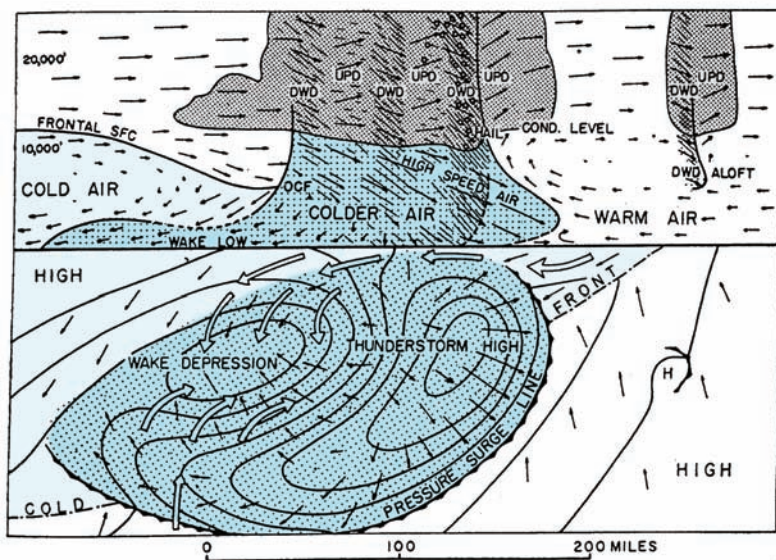


Figure 5.24 Fujita's early model of squall-line circulation, showing high- and low-pressure regions at the surface. (Adapted from Fujita [1955].)

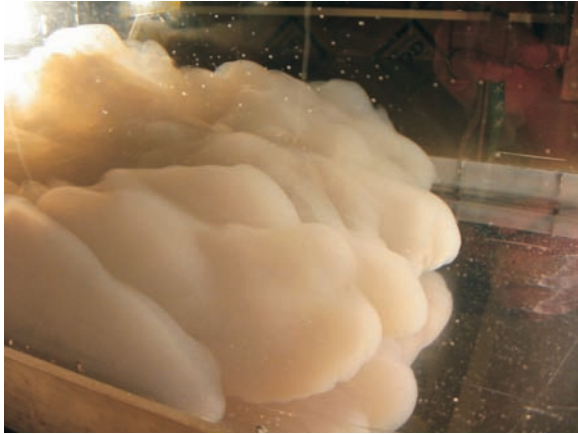


Figure 5.25 A density current in a laboratory tank. (Photograph courtesy of Jerome Neufeld and the Experimental Nonlinear Physics Group at the University of Toronto.)

instability (Section 3.5.2). The leading edge of the density current often acquires lobes and clefts as a result of *lobe and cleft instability* (Figure 5.27), which results when static instability arises on the leading edge of the density current as a density current tilts forward with height in a shallow layer near the ground. The interaction of the density current with the ground leads to the forward tilt; the speed of the dense fluid is retarded by drag at the surface. Infinitesimal density (temperature) perturbations within the statically unstable layer are all that is needed to lead to convective overturning at the leading edge of the density current.

Density current dynamics are fairly well understood, from both laboratory experiments and numerical simulations. For this reason, we shall spend some time discussing their dynamics here. We shall solve for the forward speed of a density current in terms of its depth and density excess (the hydrostatic pressure excess within the dense fluid depends on the magnitude and depth of the density excess). Consider the ambient air to have a density ρ_1 . Consider the density current to have a depth H and density ρ_2 . See Figure 5.28. The buoyancy in the ambient environment is zero, the lower boundary is assumed to be flat, and the lower boundary condition is free-slip (i.e., no surface drag). Also, in the reference frame of the density current, air flows toward the density current at speed c .

First we shall compute the pressure perturbation at the surface in the dense (cold) air at $x = -\infty$. To do this, we shall use the hydrostatic equation (Boussinesq form) written as

$$\alpha_0 \frac{\partial p'}{\partial z} = B, \quad (5.22)$$

where α_0 is a constant specific volume characterizing the mean conditions. Integrating (5.22) at $x = -\infty$ from $z = 0$ to $z = H$ gives

$$\int_{p'(0)}^{p'(H)} \alpha_0 \, dp' = \int_0^H B \, dz \quad (5.23)$$

$$\alpha_0 p'(H) - \alpha_0 p'(0) = -gH \frac{\rho_2 - \rho_1}{\rho_1} \quad (5.24)$$

$$\alpha_0 p' = \alpha_0 p'(H) + gH \frac{\rho_2 - \rho_1}{\rho_1} \text{ at } x = -\infty \quad (5.25)$$

where p' will be understood to be the pressure perturbation at the surface.

To obtain an expression for the forward speed of a density current, we shall employ a simplified form of the x equation of motion at $z = 0$. If we assume inviscid, Boussinesq, and steady conditions (assuming the density current is steady as viewed in a reference frame moving with the density current), the x -equation of motion at $z = 0$ is

$$u \frac{\partial u}{\partial x} + \alpha_0 \frac{\partial p'}{\partial x} = 0, \quad (5.26)$$

which we can write as

$$\frac{\partial}{\partial x} \left(\frac{1}{2} u^2 + \alpha_0 p' \right) = 0. \quad (5.27)$$

Integrating (5.27) from $-\infty$ to ∞ yields

$$\int_{-\infty}^{\infty} \frac{\partial}{\partial x} \left(\frac{1}{2} u^2 + \alpha_0 p' \right) \, dx = 0 \quad (5.28)$$

$$\frac{1}{2} u^2 \Big|_{-\infty}^{\infty} + \alpha_0 p' \Big|_{-\infty}^{\infty} = 0. \quad (5.29)$$

In the reference frame moving with the density current, $u(\infty) = -c$ and $u(-\infty) = 0$; therefore, (5.29) becomes

$$\frac{1}{2} c^2 + \alpha_0 p' \Big|_{-\infty}^{\infty} = 0. \quad (5.30)$$

Far upstream ($x = \infty$), p' is defined to be zero. At $x = -\infty$, substitution of (5.25) yields

$$\frac{1}{2} c^2 - \alpha_0 p'(H) - gH \frac{\rho_2 - \rho_1}{\rho_1} = 0. \quad (5.31)$$

For $p'(H) = 0$, we obtain

$$c = \sqrt{2gH \frac{\rho_2 - \rho_1}{\rho_1}}, \quad (5.32)$$

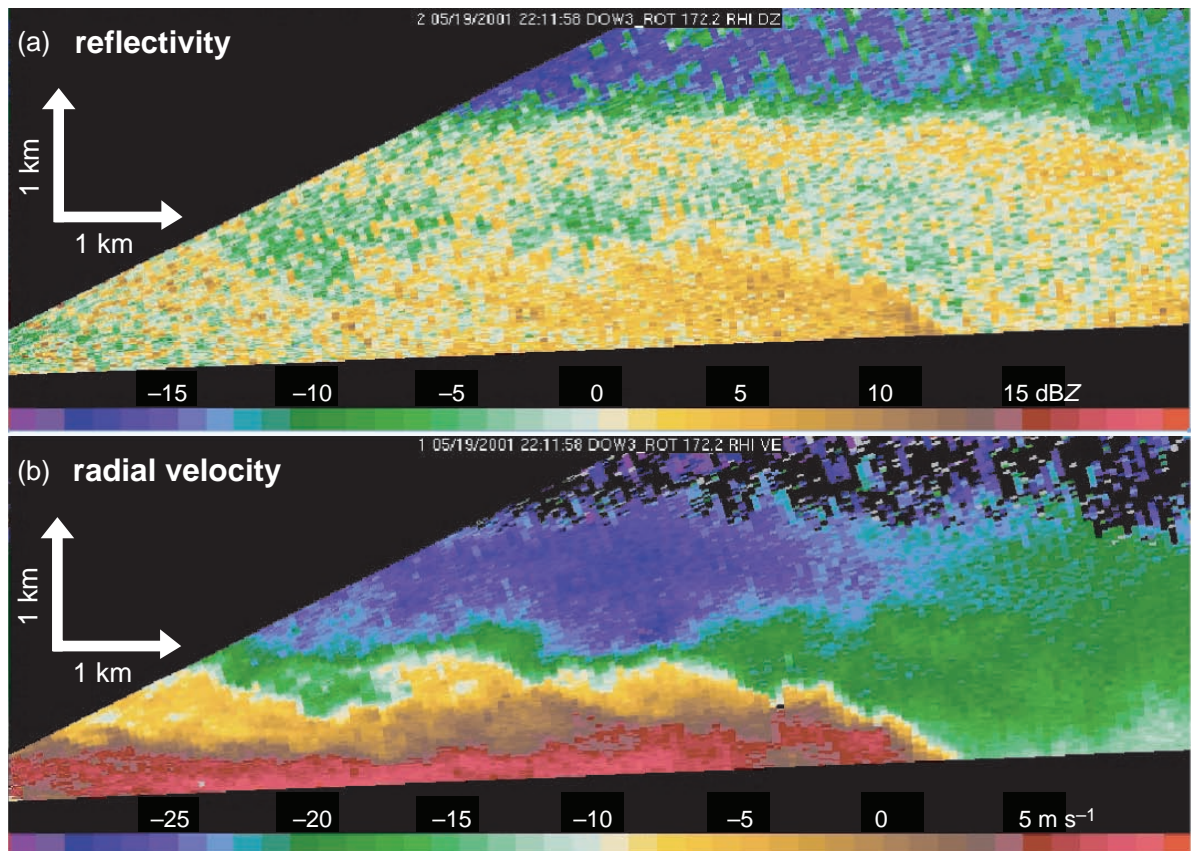


Figure 5.26 Radar observations of a gust front (moving from left to right) having density current characteristics. The data were obtained by the Doppler On Wheels (DOW) radar. (a) Reflectivity factor (reflectivities are uncalibrated) in dBZ. (b) Radial velocity in m s^{-1} .

where c is the forward speed of the density current. The expression given by (5.32) is sometimes written as

$$c = k \sqrt{gH \frac{\rho_2 - \rho_1}{\rho_1}}, \quad (5.33)$$

where k is a constant. From (5.32), it would seem that $k = \sqrt{2}$. However, because real atmospheric density currents often have $p'(H) \neq 0$, and because some mixing typically occurs along the leading edge of a density current, values of k tend to be closer to unity, ranging from approximately 0.7 to 1.3. Friction between the density current and the ground also reduces k below its theoretical value.

The speed of a density current can be viewed as the speed an approaching air parcel must have so that its kinetic energy is exhausted while doing work against the

nonhydrostatic pressure gradient force ahead of the leading edge of the density current. In order for pressure to be continuous across the density current interface, a nonhydrostatic pressure gradient force must arise ahead of the density current so that the sum of the hydrostatic and nonhydrostatic pressure ahead of the density current interface is equal to the hydrostatic pressure behind the density current interface.

An alternative way to derive the speed of a density current is to integrate the inviscid, two-dimensional, meridional horizontal vorticity equation given by

$$\frac{d\eta}{dt} = -\frac{\partial B}{\partial x}, \quad (5.34)$$

where η is the meridional vorticity component and B is the buoyancy force. This approach will be useful to introduce now because the same approach will be used again in

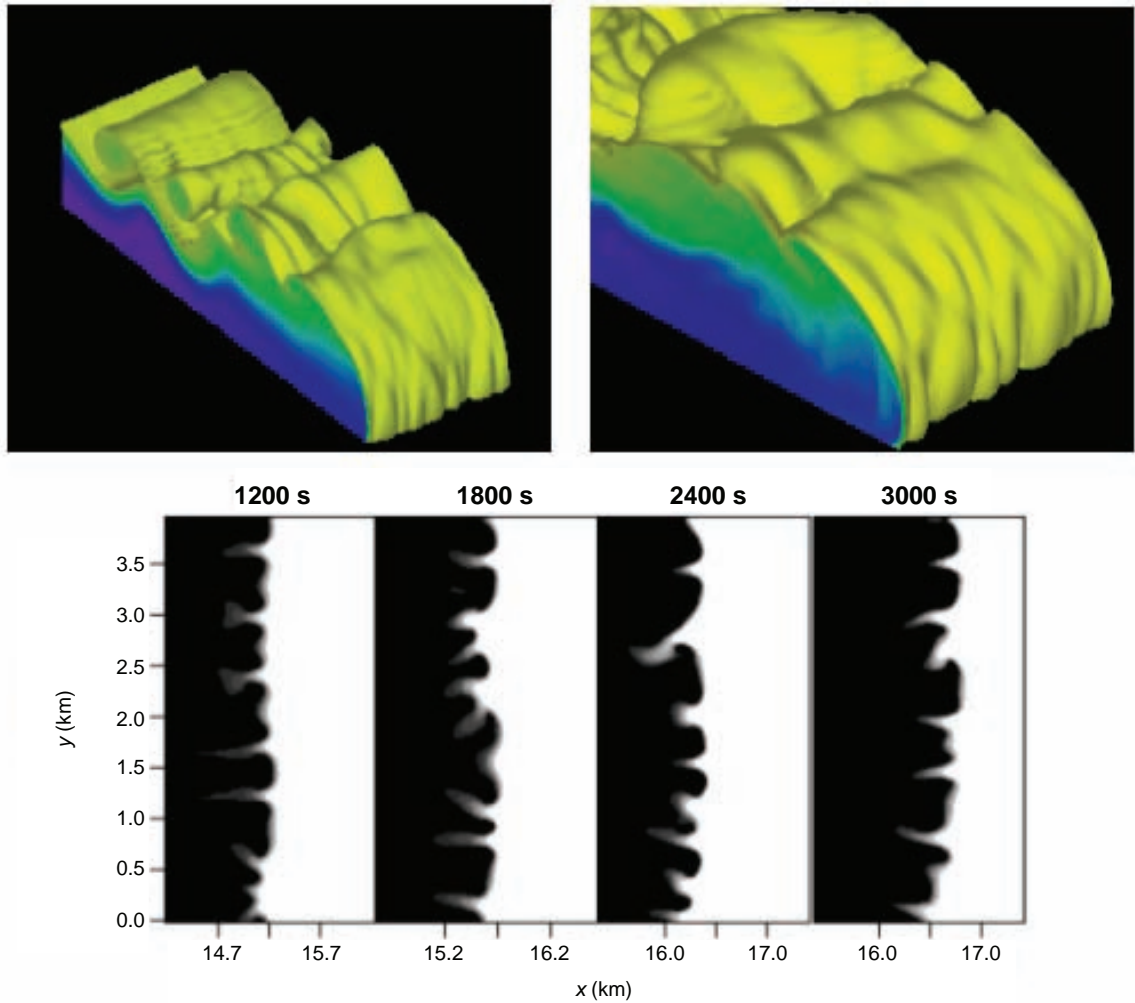


Figure 5.27 Numerical simulation of a density current presenting structures resulting from lobe and cleft instability (top, isosurfaces of potential temperature colder than the ambient potential temperature; bottom, top view of the simulated density current at four select times). Lobe and cleft structures are also evident in the density current shown in Figure 5.25. (Adapted from Lee and Finley [2002].)

Chapter 9 in order to describe the characteristics of updrafts along the gust fronts of squall lines. In order to derive an expression for the speed of a density current, we integrate (5.34) over a *control volume* that extends horizontally from well ahead of the leading edge of the density current to a location well behind the leading edge, and vertically from the ground to an altitude well above the top of the density current (Figure 5.29). The winds *relative to the density current* at the top right, bottom right, top left, and bottom left corners of the control volume will be denoted as $u_{R,d}$, $u_{R,0}$, $u_{L,d}$, and $u_{L,0}$, respectively, where the first subscript indicates the x position (L for left and R for right) and the

second subscript indicates the z position (0 for the ground and d for the top of the control volume). Note that if we can deduce $u_{R,0}$, then we shall have also deduced the speed of the density current, because $u_{R,0}$ is the wind relative to the density current at the ground, out ahead of the density current.

Expanding $d\eta/dt$ in (5.34) into a local time derivative and advection, and using the Boussinesq continuity equation multiplied by the horizontal vorticity,

$$\eta \frac{\partial u}{\partial x} + \eta \frac{\partial w}{\partial z} = 0, \quad (5.35)$$

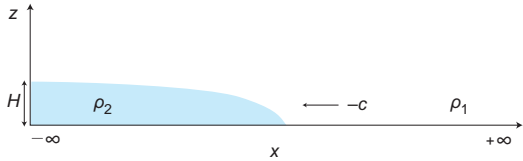


Figure 5.28 Schematic cross-section through a density current. Variables are as defined in the text.

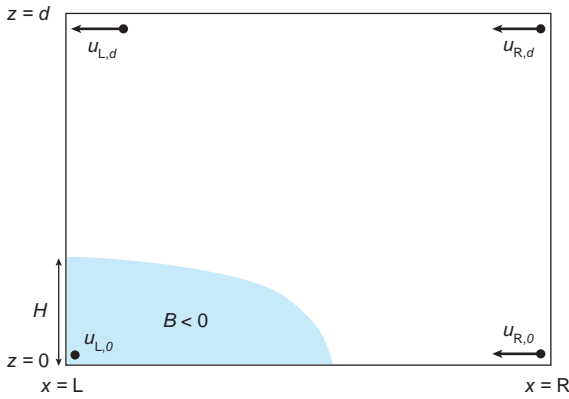


Figure 5.29 Schematic of the relationship between a density current and the control volume described in the text. All winds are relative to the density current.

we can write (5.34) in flux form as

$$\frac{\partial \eta}{\partial t} = -\frac{\partial(u\eta)}{\partial x} - \frac{\partial(w\eta)}{\partial z} - \frac{\partial B}{\partial x}. \quad (5.36)$$

Integrating (5.36) over the control volume gives

$$\begin{aligned} \frac{\partial}{\partial t} \int_0^d \int_L^R \eta \, dx \, dz &= - \int_0^d \int_L^R \frac{\partial(u\eta)}{\partial x} \, dx \, dz \\ &\quad - \int_L^R \int_0^d \frac{\partial(w\eta)}{\partial z} \, dz \, dx \\ &\quad - \int_0^d \int_L^R \frac{\partial B}{\partial x} \, dx \, dz \end{aligned} \quad (5.37)$$

$$\begin{aligned} &= - \int_0^d [(u\eta)_R - (u\eta)_L] \, dz \\ &\quad - \int_L^R [(w\eta)_d - (w\eta)_0] \, dx \\ &\quad - \int_0^d (B_R - B_L) \, dz. \end{aligned} \quad (5.38)$$

Because $w = 0$ at the ground, and if we define the reference temperature such that $B_R = 0$, then (5.39) becomes

$$\begin{aligned} \frac{\partial}{\partial t} \int_0^d \int_L^R \eta \, dx \, dz &= \int_0^d (u\eta)_L \, dz - \int_0^d (u\eta)_R \, dz \\ &\quad - \int_L^R (w\eta)_d \, dx + \int_0^d B_L \, dz. \end{aligned} \quad (5.39)$$

Moreover, we can assume that $\eta = \frac{\partial u}{\partial z} - \frac{\partial w}{\partial x} \approx \frac{\partial u}{\partial z}$ at $x = L$ and $x = R$ because the boundaries of the control volume are far away from the leading edge of the density current where w and $\partial w/\partial x$ are large, and, if we also set $\partial/\partial t = 0$ because we are interested in the steady, balanced state, then

$$0 = \int_0^d u_L \, du_L - \int_0^d u_R \, du_R - \int_L^R (w\eta)_d \, dx + \int_0^H B_L \, dz \quad (5.40)$$

$$\begin{aligned} &= \left(\frac{u_{L,d}^2}{2} - \frac{u_{L,0}^2}{2} \right) - \left(\frac{u_{R,d}^2}{2} - \frac{u_{R,0}^2}{2} \right) - \int_L^R (w\eta)_d \, dx \\ &\quad + \int_0^H B_L \, dz, \end{aligned} \quad (5.41)$$

where we have modified the upper limit of integration of B_L because the density current depth is H and $B_L = 0$ above the density current. If we define the left boundary of the control volume judiciously such that the dense fluid at $x = L$ is stagnant relative to the leading edge of the density current, then $u_{L,0} = 0$. Furthermore, if there is no shear in the ambient air ahead of the density current at $x = R$, then $u_{R,d} = u_{R,0}$. Last, if we judiciously place the top of the control volume at a sufficiently high altitude that the presence of the density current does not perturb the flow at this high level (i.e., streamlines are horizontal at this level), then

$$\int_L^R (w\eta)_d \, dx = 0. \quad (5.42)$$

Given these conditions, (5.41) reduces to

$$u_{L,d}^2 = -2 \int_0^H B_L \, dz \equiv c^2, \quad (5.43)$$

where c is now regarded as the net buoyant generation of vorticity by the cold pool. The greater the depth and/or negative buoyancy of the density current, the greater the rate of circulation generation by the horizontal buoyancy gradient found along its leading edge. Recall that we had chosen d to be at a sufficiently high altitude that the flow at $z = d$ was not perturbed by the presence of the density current below. In this case, not only does (5.42) hold, but

$u_{L,d} = u_{R,d}$, and, because we also assumed no vertical wind shear, then $u_{L,d} = u_{R,0}$ as well. Thus, (5.43) can be written as

$$u_{R,0}^2 = -2 \int_0^H B_L dz \quad (5.44)$$

$$u_{R,0} = -\sqrt{-2 \int_0^H B_L dz}, \quad (5.45)$$

where the negative root of $u_{R,0}$ has been taken because the flow is from the east relative to the density current in the configuration considered in Figure 5.29. Because $u_{R,0}$ is the wind speed at the ground relative to the density current, it follows that the rhs of (5.45) is the speed of the density current relative to the ambient air. If the negative buoyancy decreases linearly with height within the density current, with the minimum buoyancy B_{min} found at the ground, then

$$-\sqrt{-2 \int_0^H B_L dz} = \sqrt{-B_{min} H} = \sqrt{-\frac{\theta'_{\rho_{min}}}{\bar{\theta}_v} g H}, \quad (5.46)$$

where $\theta'_{\rho_{min}}$ is the density potential temperature perturbation at the surface and $\bar{\theta}_v$ is the mean virtual potential temperature in the ambient air mass at the surface. For $\theta'_{\rho_{min}} = -10$ K, $\bar{\theta}_v = 300$ K, and $H = 1000$ m, we obtain $u_{R,0} = 18$ m s⁻¹. Figure 5.30 shows how a control volume might be positioned with respect to an actual density current; from the figure it is apparent that our assumptions that went into deriving (5.45) are reasonably well justified.

If we define the wind speed at the ground *relative to the ground* in the ambient air as $U_{R,0}$ and the density current

speed relative to the ground as U_c , then by definition $u_{R,0} = U_{R,0} - U_c$. Therefore

$$U_c = U_{R,0} + \sqrt{-2 \int_0^H B_L dz} \quad (5.47)$$

is the speed of the density current relative to the ground. It depends on the ambient wind at the ground and the depth and magnitude of the negatively buoyant air.

Equations (5.32) and (5.45) are the simplest possible expressions for the speed of a density current. Note that (5.45) is a more general expression of (5.32) for the case of a continuously stratified atmosphere. In other words, (5.45) becomes (5.32) for the case of a constant density within the cold pool and within the ambient air mass. Surface friction has been neglected in the derivations of (5.32) and (5.45), and we assumed no environmental wind shear. Not only does wind shear having a component parallel (or antiparallel) to the density current motion alter the speed at which a density current moves, but the presence of shear profoundly affects the structure of the head of a density current, and thereby the strength and depth of the lifting that occurs there. When environmental shear is present and points in the direction of density current motion, the motion of the density current is slowed relative to the environmental air and the density current develops a deeper head (Figure 5.31a). Lifting at the leading edge of the density current tends to be more intense, with a vertical jet of air often erupting upward there. Just the opposite occurs when environmental shear is present and directed opposite the direction of density current motion

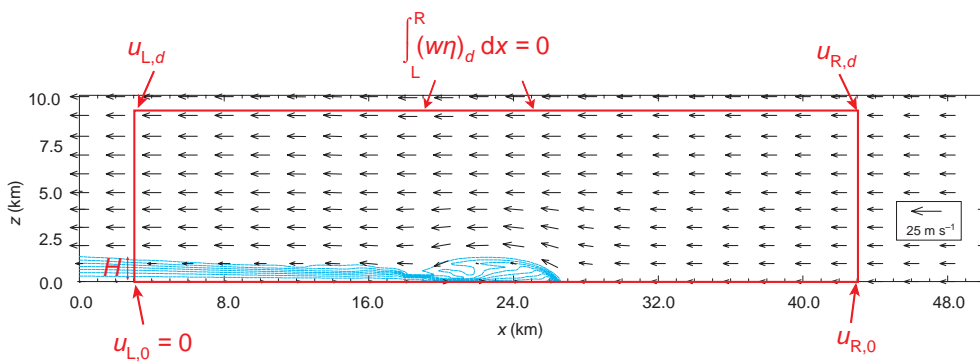


Figure 5.30 Numerical simulations of an eastward-moving density current in an environment containing no ambient wind shear. A control volume is overlaid in red. Potential temperature perturbations are contoured at 1 K intervals within the cold pool, starting at -1 K. Wind vectors are relative to the density current ($U_c \approx 11$ m s⁻¹). It should be apparent that the assumptions that went into the derivation of (5.45) are reasonably well justified; for example, $u_{L,0} = 0$ m s⁻¹, $u_{L,d} = u_{R,d} = u_{R,0}$, and $\int_L^R (w\eta)_d dx = 0$.

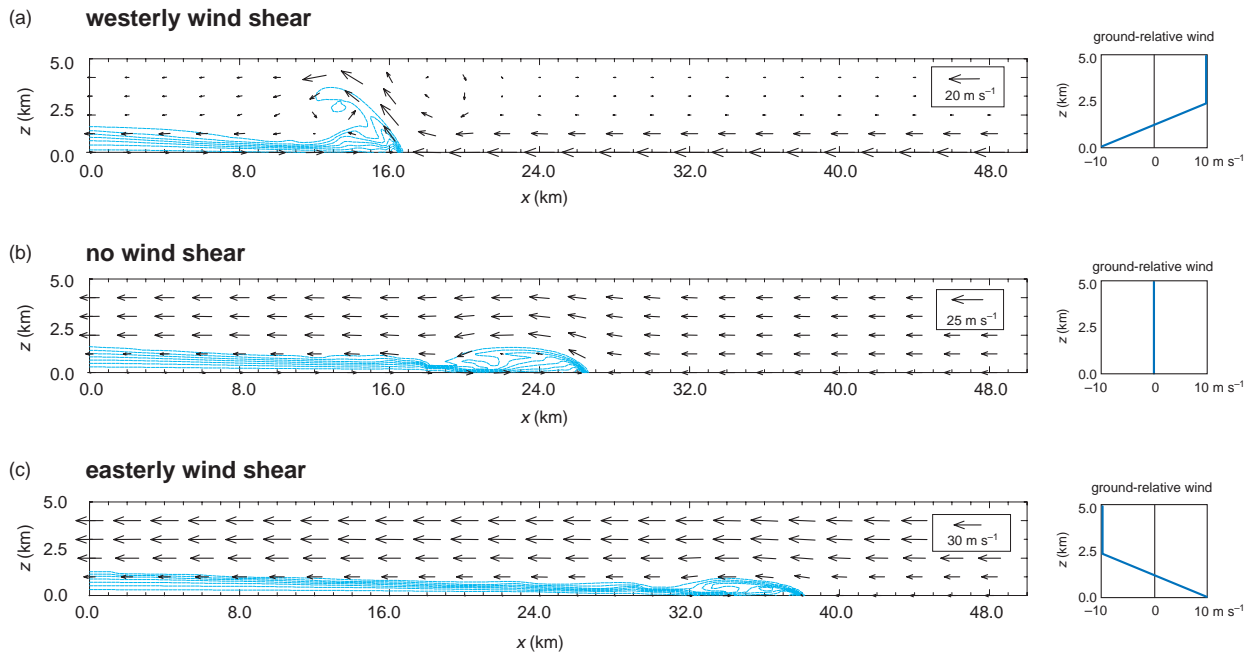


Figure 5.31 Numerical simulation of an eastward-moving density current in an environment containing (a) westerly wind shear, (b) no wind shear, and (c) easterly wind shear. (The no-shear case is identical to that which appears in Figure 5.30.) Potential temperature perturbations are contoured at 1 K intervals within the cold pool, starting at -1 K . Wind vectors are relative to the density current ($U_c \approx 19, 11, \text{ and } 8\text{ m s}^{-1}$ in the easterly shear, no shear, and westerly shear cases, respectively). The ground-relative vertical wind profiles are shown for each case on the right. All three cases have the same mean wind speed ($=0\text{ m s}^{-1}$) in the lowest 2.5 km. The model domain extends to 10 km; only the lowest 5 km of the model domain is shown.

(Figure 5.31c). The changes in the strength and depth of lifting forced by an outflow boundary when shear is present have important implications for the initiation, propagation, and maintenance of convective storms, the dynamics of which are intimately tied to how the gust front interacts with the conditionally unstable environment.

We do not consider the circulations that arise from the heating and cooling of sloped terrain, such as mountain and valley circulations, which usually do not involve dramatic wind shifts and temperature gradients along the surface. Thermally driven orographic circulations are treated in Chapter 11 instead.

5.4 Mesoscale boundaries originating from differential surface heating

Horizontal differences in the diabatic heating of the earth's surface can give rise to significant horizontal air temperature gradients. The horizontal air temperature gradients generate vertical circulations and therefore are often of interest to forecasters. Differential surface heating can be produced by horizontally inhomogeneous surface characteristics or by insolation variations that are independent of surface characteristics. Some examples are discussed below.

5.4.1 Sea- and land-breeze fronts

Sea- and land-breeze fronts are probably the best-known mesoscale boundaries that can be attributed to differential surface heating. Large temperature contrasts can develop in the proximity of coastlines along large bodies of water owing to heat capacity differences between soil and water. The land is heated and cooled with a frequency of $2\pi\text{ day}^{-1}$, whereas the water can be assumed to have an approximately constant temperature over the course of a diurnal cycle.²¹ During the day, the inland air is warmer than the air over

²¹ Theoretical studies have shown that, in the absence of friction, the characteristics of sea and land breezes are very different when the heating

the cooler water surface, and the horizontal temperature gradient generates a thermally direct circulation via (2.104) such that onshore winds develop along the surface, with compensating offshore winds blowing in the upper portion of the boundary layer. The onshore winds are known as a *sea breeze* when they originate over an ocean (or a *lake* or *river breeze* in the case of a large lake or river), and the mesoscale convergence zone where the sea breeze and ambient inland winds meet is known as a *sea-breeze* (or *lake-breeze* or *river-breeze*) *front* (Figures 5.32 and 5.33).

At night, the inland boundary layer typically becomes cooler than the offshore boundary layer, owing to the same horizontal heat capacity differences that gave rise to the opposite temperature gradient during the day. A thermally direct circulation having the opposite sense of rotation can develop, with the cooler inland air advancing offshore as a *land breeze*. (Recall the role of land breezes in enhancing lake-effect convection discussed in Section 4.5; in those instances, the land breezes develop not as a result of the diurnal cycle but instead as a result of the modification of a cold air mass moving over a warm water surface.) The mesoscale convergence zone that arises at the interface of the land breeze and the ambient offshore winds is known as a *land-breeze front*. The land-breeze front is not simply a retreating sea-breeze front, and vice versa. During the mid-morning hours of some days, a sea-breeze front can be observed inland at the same time that a land-breeze front, remaining from the previous night, is observed offshore.

Sea breezes and land breezes are most likely to be observed during periods of relatively quiescent weather (e.g., light winds). When the large-scale, ambient winds are very strong, sea- and land-breeze circulations are less prominent or may not be observed at all. For example, an empirical predictor of sea-breeze likelihood is the ratio of the geostrophic wind speed squared to the temperature

and cooling frequency $\omega = 2\pi \text{ day}^{-1}$ exceeds the Coriolis parameter $(\omega > f)$ at latitudes $< 30^\circ$, compared with when $\omega < f$ (latitudes $> 30^\circ$). When $\omega < f$, the atmospheric response to the development of an onshore-offshore horizontal temperature gradient is to produce a thermally direct circulation having a horizontal scale of $NH(f^2 - \omega^2)^{-1/2}$, where N is the Brunt-Väisälä frequency and H is the vertical scale of the onshore-offshore horizontal temperature gradient. When $\omega > f$, however, inertia-gravity waves result, with the wind field not looking at all like the wind fields observed in conjunction with sea-/land-breeze (a thermally direct circulation is absent and inertia-gravity waves radiate outward and upward from the coastline). When friction is added, however, the sensitivity of the sea- and land-breeze circulations to latitude is practically absent, with the sea- and land-breeze circulations being more similar to the case of $\omega < f$; i.e., a thermally direct circulation having elliptical streamlines is obtained, which closely matches observations of actual sea/land breezes. The reader is referred to Rotunno (1983) for further details.

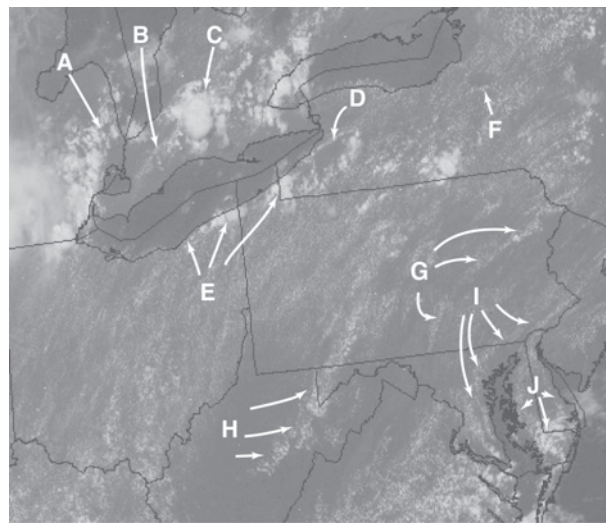


Figure 5.32 Visible satellite image of the northeastern US at 1815 UTC 23 July 2001 showing several examples of boundaries owing to differential heating. A, lake-breeze front associated with Lake Huron; B, colliding boundaries produced by Lake Erie and Lake Huron; C, incipient cumulonimbus cloud initiated at the intersection of the colliding boundaries in B; D, outflow boundary associated with dissipating rain showers; E, towering cumulus clouds on a lake-breeze front on the south shore of Lake Erie; F, lake-breeze front surrounding Lake Oneida; G and H, lines of cumulus associated with the heating of long, nearly continuous mountain ridges; I, sea-breeze front due to the Chesapeake Bay; J, ring-shaped sea-breeze front, with the western portion due to the Chesapeake Bay and the eastern portion due to the Atlantic Ocean.

difference between the sea surface and the land surface, that is, $|\mathbf{v}_g|^2 / \Delta T$. Sea-breeze formation is likely when this parameter is less than approximately 5.

Sea- and land-breeze circulations are typically 500–1000 m deep (Figure 5.33b) and have horizontal wind perturbations of 5–10 m s⁻¹ (this compares well with the wind speeds estimated using Bjerknes' circulation theorem in Section 2.4.3, where we assumed a 10 K (30 km)⁻¹ horizontal temperature gradient in the demonstration calculation). Theory predicts that the horizontal and vertical velocity perturbations associated with sea- and land-breeze circulations are proportional to N^{-1} and N^{-3} , respectively. The stability dependence is a result of the influence of static stability on the rising and sinking branches of the sea-/land-breeze circulations. As the stability increases, more work must be done against the stratification to force air to rise/sink. Because of the static stability dependence of sea-/land-breeze intensity and the typical diurnal cycle

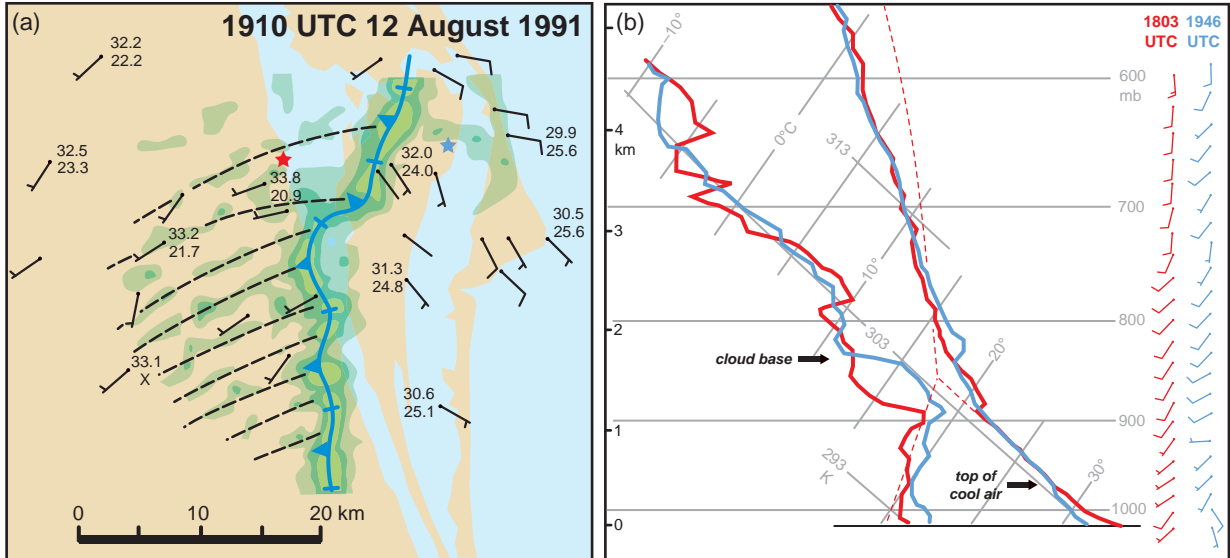


Figure 5.33 (a) Analysis of a sea-breeze front on the east coast of Florida on 12 August 1991 during the Convection and Precipitation/Electrification Experiment (CaPE). Station models display temperature and dewpoint in °C, and wind barbs in knots. Three levels of radar reflectivity are shaded; the thresholds are 0, 4, and 8 dBZ. The locations of updrafts associated with horizontal convective rolls are indicated with black dashed lines. (b) Soundings launched on opposite sides of the sea-breeze front depicted in (a). The blue (red) sounding was obtained in the cool (warm) air mass at the location of the blue (red) star in (a). The trajectory followed by a lifted inland parcel is also shown, as is the photogrammetrically determined cloud base. (Adapted from Wakimoto and Atkins [1994].)

of N , sea-breeze circulations tend to be stronger and deeper than land-breeze circulations. The relative strengths of sea- and land-breeze circulations also obviously depend on the magnitude of the horizontal temperature gradient, which varies with the time of year. For example, the temperature differential across a sea-breeze front is typically larger than the differential across a land-breeze front in the spring months when the daily mean air temperature over land is warmer than the water temperature, which implies that the difference between the nighttime minimum air temperature over land and the water temperature is smaller than the difference between the daytime maximum air temperature over land and the water temperature.

Bjerknes' circulation theorem can be written as (Section 2.4.3)

$$\frac{dC}{dt} = - \oint \frac{dp}{\rho} - 2\Omega \frac{dA_e}{dt} = -R_d \ln \left(\frac{p_b}{p_t} \right) (\bar{T}_w - \bar{T}_c) - 2\Omega \frac{dA_e}{dt}, \quad (5.48)$$

where C is the circulation, p is pressure, ρ is density, Ω is the angular rotation rate of the earth, dA_e/dt is the rate of

change of the area that the circuit projects on the equatorial plane, p_b and p_t are the pressures along the bottom and top of the circuit along which circulation is evaluated, respectively, \bar{T}_w and \bar{T}_c are the log-pressure-weighted mean virtual temperatures along the vertical segments of the circuit on the warm and cold side of the circuit, respectively, and viscosity has been neglected. The first term on the lhs of (5.48) is associated with the generation of circulation as long as a horizontal temperature differential exists between the land and water. The second term on the rhs is a result of the Coriolis force.

Neglecting the effect of the Coriolis force, $|dC/dt|$ would be a maximum at the times of maximum or minimum inland temperature (which corresponds to the largest horizontal temperature differential between the inland and offshore air masses); therefore, $|C|$ would be a maximum at the times when the inland and offshore air masses have the same temperature (i.e., when $dC/dt = 0$), which typically would be a few hours after sunset and sunrise. However, the inclusion of the Coriolis force leads to a different result.

The contribution to dC/dt from the Coriolis force opposes the baroclinic generation of circulation. As the sea- and land-breeze circulations mature, the Coriolis force

causes the winds to develop a component parallel to the coast, with the onshore branch of the circulation being deflected in the opposite direction as the offshore branch. The inland (offshore) penetration of a sea (land) breeze therefore increases with decreasing f . The along-shore wind components grow at the expense of the offshore and

onshore wind components, thereby weakening the circulation. In terms of the Coriolis term on the rhs of (5.48), the projection on the equatorial plane of the material circuit along which C is computed evolves in time such that there is an increasingly negative contribution to the magnitude of C . For example, consider the case of a north-south

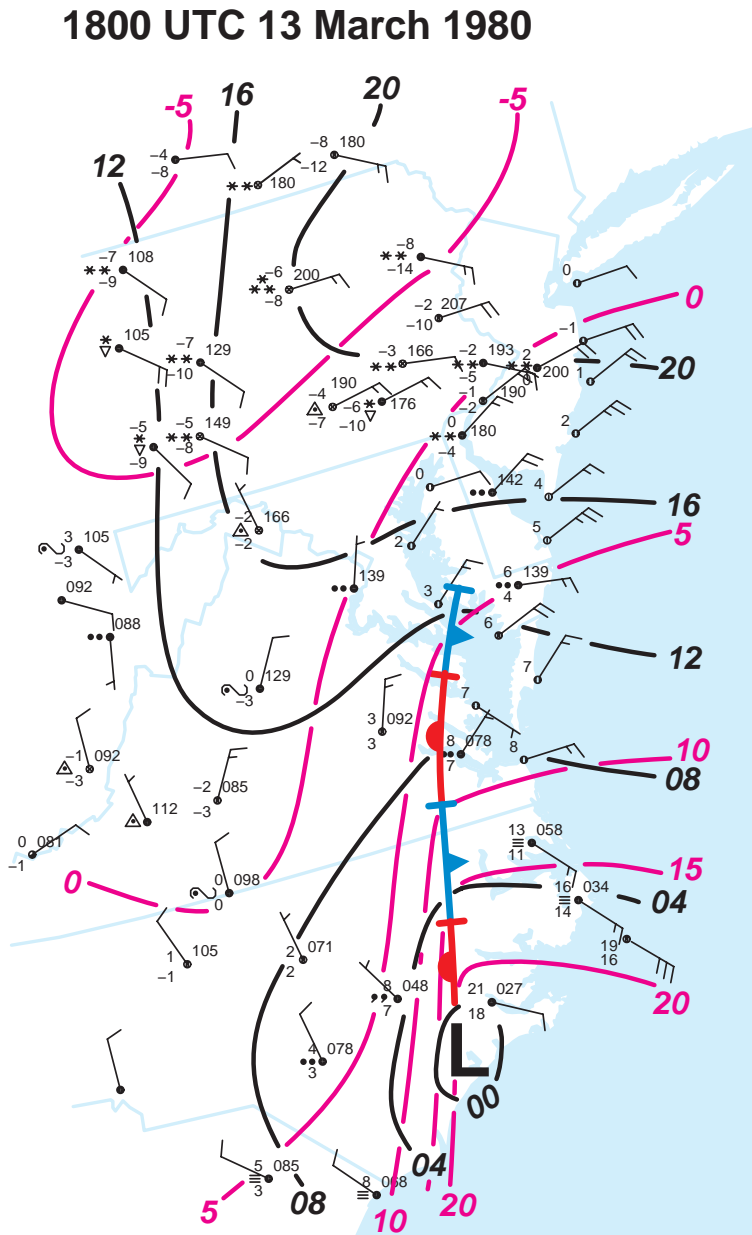


Figure 5.34 Analysis of a coastal front on 13 March 1980. Mean sea level pressure (mb; black contours; the leading '10' has been dropped) and temperature ($^{\circ}\text{C}$; magenta contours) are analyzed. (Adapted from Bluestein [1993].)

oriented coastline in the northern hemisphere, with cold (warm) air to the west (east), such that positive (counter-clockwise if looking in the positive y direction) circulation would be generated baroclinically about a vertical circuit normal to the coastline (e.g., Figure 4.24). Over time, the lower, offshore (upper, onshore) branch of the circulation develops a northerly (southerly) wind component, which tips the circuit such that its projection onto the equatorial plane is increased. Thus, $dA_e/dt > 0$, which results in a negative contribution to the circulation tendency.

The overall effect of the opposing contributions to circulation tendency from the Coriolis and baroclinic generation terms in (5.48) is that the strength of the sea- (and land-) breeze circulation does not lag the diurnal cycle of the magnitude of the horizontal temperature gradient, as one would expect if considering the baroclinic generation term alone. Instead, the maximum sea- and land-breeze circulations are observed during the afternoon and predawn hours, respectively (i.e., near the times when the maximum and minimum inland temperatures are observed).

5.4.2 Coastal fronts

Coastal fronts are low-level baroclinic zones prevalent in the late fall and winter that separate relatively warm maritime air originating over the ocean from cold continental air originating from an anticyclone over land (Figure 5.34). They are usually less than 1 km deep, and are frequently only a few hundred meters deep. Horizontal temperature gradients are frequently on the order of $10 \text{ K } (10 \text{ km})^{-1}$, although gradients as large as $5 \text{ K } \text{km}^{-1}$ have been observed on occasion.

Although coastal fronts have solenoidal circulations similar to land-breeze fronts, coastal fronts are not referred to as land-breeze fronts because coastal fronts are observed inland rather than offshore. Coastal fronts cannot be viewed as sea-breeze fronts either because the temperature gradient associated with coastal fronts is directed offshore, opposite the orientation for sea-breeze fronts. Coastal fronts are observed inland despite an offshore-directed temperature gradient, which implies that they are regulated in important ways by the synoptic scale, unlike land-breeze fronts. In addition to the requirement of a substantial land–sea temperature contrast, a large-scale onshore flow is necessary for coastal front formation, else the fronts would tend to be driven offshore via density current dynamics. Despite the importance of synoptic-scale influences, coastal frontogenesis often occurs in the absence of synoptic-scale geostrophic frontogenesis. It is for this reason that coastal fronts are generally regarded as mesoscale boundaries rather than synoptic fronts. Surface friction changes

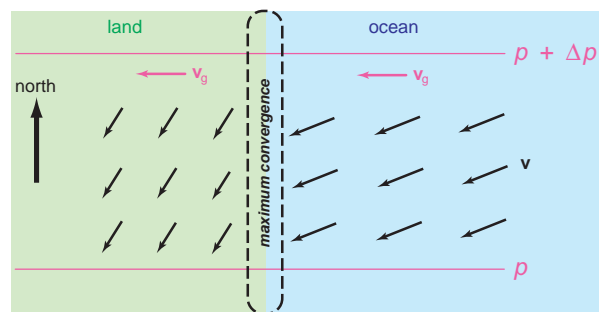


Figure 5.35 Illustration of the effect of differential friction along a coastline. For easterly geostrophic wind (as shown), a north–south-oriented corridor of convergence is generated by larger surface drag over land than over water, which creates a larger cross-isobaric wind component over land than water. The convergence acts on the west–east temperature gradient between the land and ocean to promote frontogenesis. The wind-pressure relationship shown above is valid for the northern hemisphere, but the frontogenetic effect of differential surface drag is hemisphere independent. (Also see Figure 4.24.)

across the land–sea interface can also contribute to coastal frontogenesis (Figure 5.35).

Coastal fronts are common along the Gulf Coast and the East Coast of the United States. In the Gulf Coast region, cold-season outbreaks of severe convection often occur when a zonally oriented coastal front migrates northward under the influence of an approaching extratropical cyclone, allowing anomalously warm and moist air to penetrate inland and interact with the cyclone and its associated large vertical wind shear and large-scale ascent. Coastal fronts tend to be observed along the East Coast of the United States, particularly in the Northeast and Mid-Atlantic region, when a cold high-pressure cell is located at the surface in New England or eastern Canada and an upper-level trough is approaching from the west or southwest, resulting in strong onshore winds to the south of the high. This synoptic pattern is similar to that associated with cold-air damming east of the Appalachian Mountains (to be discussed in Section 13.2); thus, cold-air damming is often observed inland on days when coastal fronts are observed along the East Coast. The Appalachian Mountains often mark the western extent of the surface cold air mass originating from the high-pressure cell to the northeast, whereas the coastal front marks the eastern interface of the cold air.

In some cases coastal fronts behave similarly to warm fronts or stationary fronts, such that when they interact with extratropical cyclones most of the precipitation falls on the

cold side of the boundary. Coastal fronts often separate frozen precipitation from liquid precipitation during cold-season precipitation episodes. Coastal fronts occasionally play a role in rapid, intense cyclogenesis driven by baroclinic instability. For example, weak surface depressions sometimes move along East Coast coastal fronts, and the isotherms within and around these features can resemble the opening and closing of a zipper. For this reason, these disturbances have been referred to as *zipper lows* (Figures 5.36 and 5.37). Ahead of a zipper low deformation strengthens the temperature gradient, whereas in the wake of the zipper low the temperature gradient remains stronger than it was initially. Thus, the net effect of zipper lows may be to precondition the atmosphere for more intense cyclogenesis by increasing the environmental baroclinicity, vorticity, convergence, and low- to midlevel moisture.

5.4.3 Boundaries generated by clouds or horizontal gradients of vegetation characteristics, surface moisture, or albedo

Mesoscale boundaries can also arise from differential heating due to horizontal gradients in cloud cover, vegetation, soil moisture, and surface albedo—essentially, any effect that modifies the surface energy budget (either net radiation or sensible, latent, or ground heat fluxes) is capable of producing horizontal temperature gradients. These boundaries and their associated thermally direct circulations

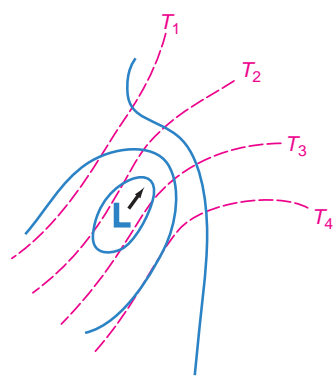


Figure 5.36 Schematic illustration of a zipper low and attendant pressure and temperature fields. Solid lines represent schematic isobars. Dashed lines denote schematic isotherms ($T_4 > T_3 > T_2 > T_1$). The bold arrow indicates the direction of the low movement.

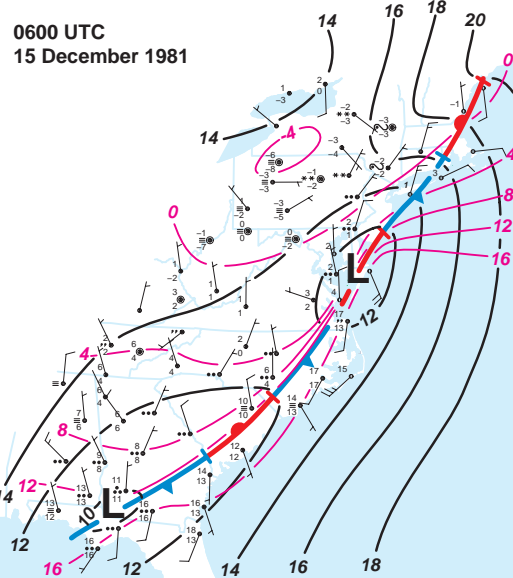


Figure 5.37 Surface analysis for 0600 UTC 15 December 1981, revealing a zipper low near the Delmarva Peninsula and a second low in southwestern Georgia. Mean sea level pressure (mb; black contours; the leading '10' has been dropped) and temperature ($^{\circ}\text{C}$; magenta contours) are analyzed. The second low would intensify into a 'bomb' during the next 12 h, and it was responsible for a crippling snowstorm in the Middle Atlantic and New England regions. The coastal front has been analyzed as well. (Adapted from Keshishian and Bosart [1987].)

are sometimes generically referred to as *inland sea-breeze fronts/circulations* and are usually most recognizable in conditions characterized by weak large-scale flow, as is also the case for sea and land breezes.

Clouds are most likely to lead to the formation of discernible mesoscale boundaries when they are optically thick and have a well defined edge separating regions of nearly solid overcast from regions receiving substantial insolation. Patches of low stratus clouds that linger after sunrise can lead to the formation of boundary layer cold pockets having roughly the same shape as the patches of lingering cloudiness. The stratus clouds limit surface heating by way of their large albedo and absorption of incoming short-wave radiation. The cooler air beneath the cloudy region spreads out beneath the cloudy region against the relatively warmer surroundings, leading to regions of convergence and upward motion along the periphery of the cloudy region. Compensating descent within the cloudy

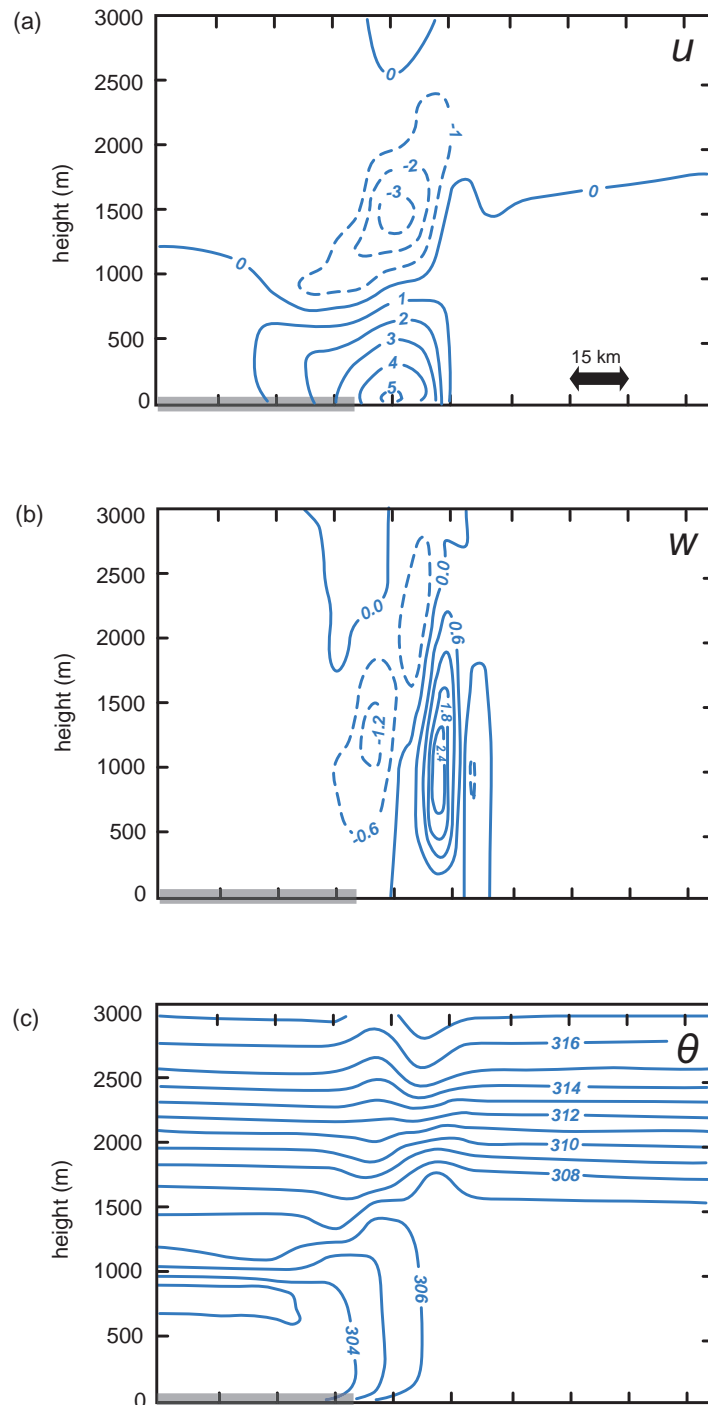


Figure 5.38 Idealized simulation of a mesoscale circulation produced by differential heating across the edge of a cloud deck. Vertical cross-sections of (a) u (m s^{-1}), (b) w (m s^{-1}), and (c) θ (K) are shown. The cloud layer spans the horizontal region indicated with the heavy, gray line. (Adapted from Segal *et al.* [1986].)

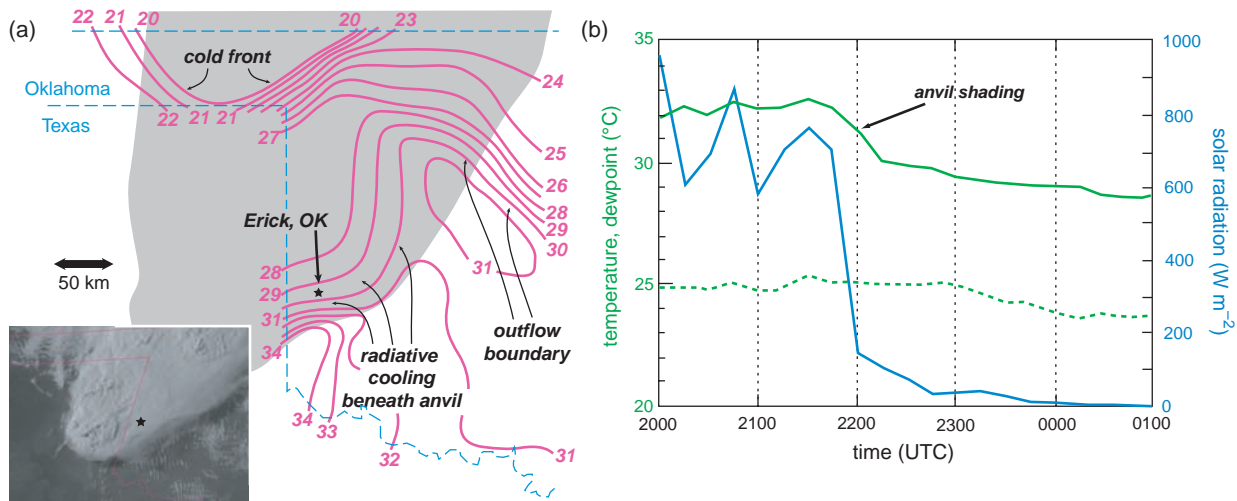


Figure 5.39 (a) Surface temperatures (contoured at 1°C intervals) at 2300 UTC 8 June 1995. The anvil canopy associated with a line of thunderstorms (see inset visible satellite image) is shaded gray. (b) Time series of temperature (solid green) and dewpoint (dashed green), both in °C, and solar radiation (solid blue), in W m^{-2} , from 2000 to 0100 UTC 8–9 June 1995 at Erick, OK (its location is indicated in [a]). (Adapted from Markowski *et al.* [1998].)

region may accelerate the dissipation of the lingering cloudy region. Hence, by mid-morning or early afternoon, patches of stratus clouds can give way to rings of convection surrounding a clear hole where the stratus has dissipated (see ‘F’ in Figure 5.32; also see Figure 5.38).

Mesoscale boundaries have also been observed along the edges of thunderstorm anvil shadows. Strong insolation outside of the shadow, coupled with surface cooling of 3–5 K beneath the cirrus canopy as a result of the drop in incoming solar radiation, can result in the formation of horizontal temperature gradients along the periphery of the anvil shadow (Figure 5.39). The effects of these baroclinic zones on storm dynamics are not yet fully understood, although numerical simulations have shown that cloud shading can significantly influence the gust front structure and low-level vertical vorticity in severe thunderstorms.

Heterogeneities in the vegetation and soil type can be associated with significant horizontal variations in net radiation (via albedo differences) and sensible, latent, and ground heat fluxes. If the horizontal sensible heat flux gradient, which is coupled to the horizontal gradients of net radiation and latent and ground heat fluxes via the surface energy budget, is sufficiently large, then the differential heating can produce horizontal temperature and pressure

gradients large enough to affect mesoscale air motions. For example, where plant growth is dense or soil moisture is high, more incoming solar radiation is used to evaporate moisture from plants or the soil than in regions devoid of vegetation or having dry soil, resulting in a smaller sensible heat flux and lower air temperatures, all else being equal (Figure 5.40). Locations where heavy rainfall has recently occurred are slower to warm than adjacent regions, leading to the formation of a thermal boundary roughly along a corridor where rainfall isohyets are closely packed.

Even large hailswaths (corridors of crop damage due to hail) have been found to be capable of generating horizontal temperature gradients sufficiently large to produce noticeable mesoscale wind perturbations.²² Warm anomalies arise within the hailswaths during the day as a result of an enhanced Bowen ratio. Albedo differences between regions covered by a fresh snowfall and surrounding regions receiving no snow have also been observed on occasion to produce a mesoscale cold pool and high-pressure anomaly (Figure 5.41). The sensible heat flux is also reduced in the snow-covered region because some of the absorbed solar energy is used to melt the snow (i.e., the latent heat flux is enhanced at the expense of the sensible heat flux).

²² See Parker *et al.* (2005).

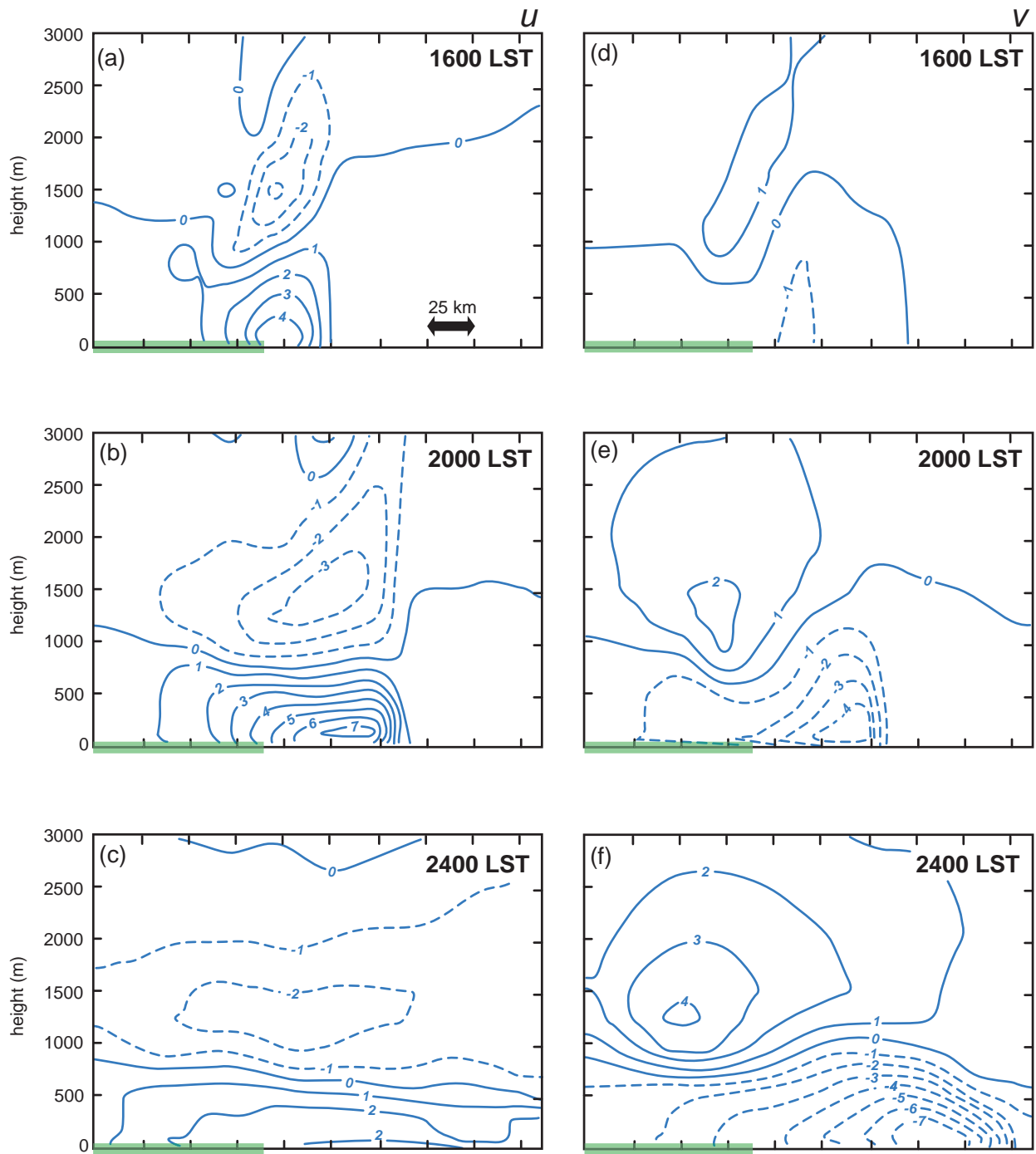


Figure 5.40 Idealized simulation of a mesoscale circulation attributable to soil moisture differences. Vertical cross-sections of (a)–(c) u (m s^{-1}) and (d)–(f) v (m s^{-1}) are shown at three different times. The wet soil is indicated with the heavy green line. The u -wind (v -wind) component becomes less (more) perturbed in time owing to the Coriolis force. (Adapted from Oookouchi *et al.* [1984].)

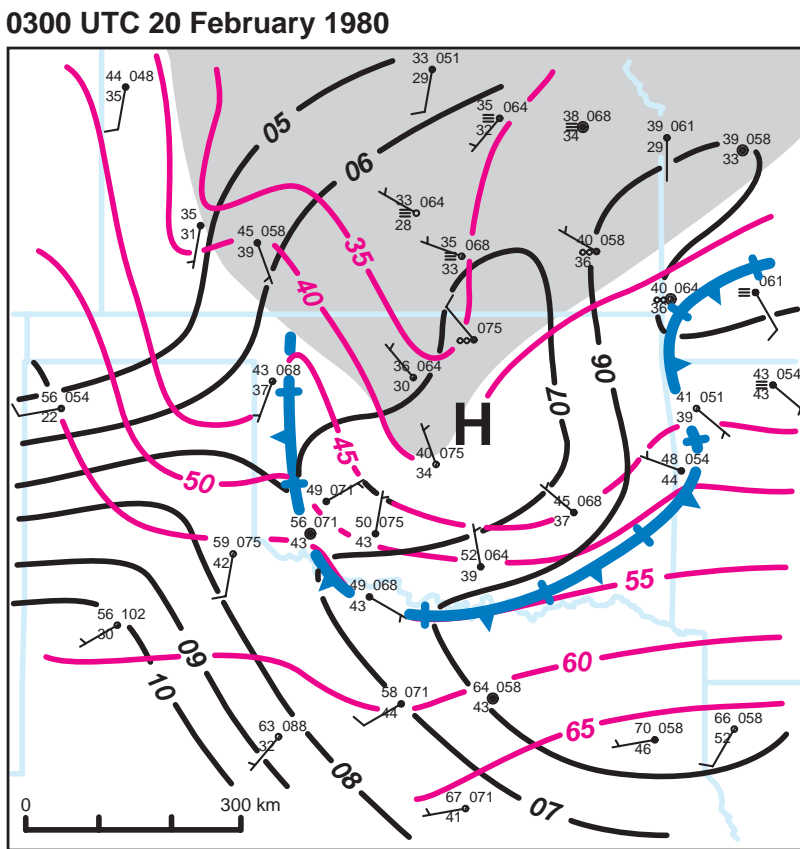


Figure 5.41 Surface analysis (isobars [mb; the leading '10' is dropped] are magenta, isotherms ($^{\circ}$ F) are black) at 0300 UTC 20 February 1980 showing a mesoscale air mass boundary and surface mesohigh induced by differential heating as a result of a snow cover. Gray shading indicates approximate snow cover. (Adapted from Bluestein [1982].)

Further reading

Frontal rainbands

- Brown, M. J., J. D. Locatelli, and P. V. Hobbs, 1998: Organization of precipitation along cold fronts. *Quart. J. Roy. Meteor. Soc.*, **124**, 649–652.

Browning, K. A., and R. Reynolds, 1994: Diagnostic study of a narrow cold-frontal rainband and severe winds associated with a stratospheric intrusion. *Quart. J. Roy. Meteor. Soc.*, **120**, 235–257.

Carbone (1982).

Carbone (1983).

Chen, C., C. H. Bishop, G. S. Lai, and W.-K. Tao, 1997: Numerical simulations of an observed narrow cold-frontal rainband. *Mon. Wea. Rev.*, **125**, 1027–1045.

Crook, N. A., 1987: Moist convection at a surface cold front. *J. Atmos. Sci.*, **44**, 3469–3494.

Jorgensen, D. P., Z. Pu, P. O. G. Persson, and W.-K. Tao, 2003: Variations associated with cores and gaps of a Pacific narrow cold frontal rainband. *Mon. Wea. Rev.*, **131**, 2705–2729.

Lamaitre, Y., G. Scialom, and P. Amayenc, 1989: A cold frontal rainband observed during the LANDES-FRONTES 84 experiment: Mesoscale and small-scale structure inferred from dual-Doppler radar analysis. *J. Atmos. Sci.*, **46**, 2215–2235.

Locatelli, J. D., J. E. Martin, and P. V. Hobbs, 1995: Development and propagation of precipitation cores on cold fronts. *Atmos. Res.*, **38**, 177–206.

Parsons (1992).

Parsons, D. B., and P. V. Hobbs, 1983: The mesoscale and microscale structure and organization of clouds and precipitation in midlatitude cyclones. Part XI: Comparisons between observational and theoretical aspects of rainbands. *J. Atmos. Sci.*, **40**, 2377–2397.

- Parsons, D. B., C. G. Mohr, and T. Gal-Chen, jcit 1987: A severe frontal rainband. Part III: Derived thermodynamic structure. *J. Atmos. Sci.*, **44**, 1613–1631.
- Roux, F., V. Marécel, and D. Hauser, 1993: The 12/13 January 1988 narrow cold-frontal rainband observed during MFDP/FRONTS 87. Part I: Kinematic and thermodynamics. *J. Atmos. Sci.*, **50**, 951–974.
- Wakimoto, R. M., and B. L. Bosart, 2000: Airborne radar observations of a cold front during FASTEX. *Mon. Wea. Rev.*, **128**, 2447–2470.

Drylines

- Atkins, N. T., R. M. Wakimoto, and C. L. Ziegler, 1998: Observations of the finescale structure of a dryline during VORTEX 95. *Mon. Wea. Rev.*, **126**, 525–550.
- Beebe, R. G., 1958: An instability line development as observed by the tornado research airplane. *J. Meteor.*, **15**, 278–282.
- Buban, M. S., C. L. Ziegler, E. N. Rasmussen, and Y. P. Richardson, 2007: The dryline on 22 May 2002 during IHOP: ground-radar and in situ data analyses of the dryline and boundary layer evolution. *Mon. Wea. Rev.*, **135**, 2473–2505.
- Carlson, T. N., S. G. Benjamin, G. S. Forbes, and Y.-F. Li, 1983: Elevated mixed layers in the regional severe storm environment: conceptual model and case studies. *Mon. Wea. Rev.*, **111**, 1453–1474.
- Crawford, T. M., and H. B. Bluestein, 1997: Characteristics of dryline passage during COPS-91. *Mon. Wea. Rev.*, **125**, 463–477.
- Fujita, T. T., 1958: Structure and movement of a dry front. *Bull. Amer. Meteor. Soc.*, **39**, 574–582.
- Hane, C. E., 2004: Quiescent and synoptically-active drylines: a comparison based upon case studies. *Meteor. Atmos. Phys.*, **86**, 195–211.
- Hane, C. E., H. B. Bluestein, T. M. Crawford, M. E. Baldwin, and R. M. Rabin, 1997: Severe thunderstorm development in relation to along-dryline variability: a case study. *Mon. Wea. Rev.*, **25**, 231–251.
- Jones, P. A., and P. R. Bannon, 2002: A mixed-layer model of the diurnal dryline. *J. Atmos. Sci.*, **59**, 2582–2593.
- McCarthy, J., and S. E. Koch, 1982: The evolution of an Oklahoma dryline. Part I: A meso- and subsynoptic-scale analysis. *J. Atmos. Sci.*, **39**, 225–236.
- Schaefer, J. T., 1986: The dryline. *Mesoscale Meteorology and Forecasting*. P. S. Ray, Ed., Amer. Meteor. Soc., 549–572.
- Schultz *et al.* (2007).
- Shaw, B. L., R. A. Pielke, and C. L. Ziegler, 1997: A three-dimensional numerical simulation of a Great Plains dryline. *Mon. Wea. Rev.*, **125**, 1489–1506.
- Ziegler, C. L., and C. E. Hane, 1993: An observational study of the dryline. *Mon. Wea. Rev.*, **121**, 1134–1151.
- Ziegler, C. L., W. J. Martin, R. A. Pielke, and R. L. Walko, 1995: A modeling study of the dryline. *J. Atmos. Sci.*, **52**, 263–285.

Density currents and convective outflows

- Benjamin, T. B., 1968: Gravity currents and related phenomena. *J. Fluid Mech.*, **31**, 209–248.
- Bryan, G. H., and R. Rotunno, 2008: Gravity currents in a deep anelastic atmosphere. *J. Atmos. Sci.*, **65**, 536–556.
- Charba, J., 1974: Application of the gravity current model to analysis of squall-line gust fronts. *Mon. Wea. Rev.*, **102**, 140–156.
- Goff, C. R., 1976: Vertical structure of thunderstorm outflows. *Mon. Wea. Rev.*, **104**, 1429–1440.
- Johnson (2001).
- Klemp, J. B., R. Rotunno, and W. C. Skamarock, 1994: On the dynamics of gravity currents in a channel. *J. Fluid Mech.*, **269**, 169–198.
- Klinge, D. L., D. R. Smith, and M. M. Wolfson, 1987: Gust front characteristics as detected by Doppler radar. *Mon. Wea. Rev.*, **115**, 905–918.
- Mahoney, W. P., III, 1988: Gust front characteristics and the kinematics associated with interacting thunderstorm outflows. *Mon. Wea. Rev.*, **116**, 1474–1491.
- Maxworthy, T., J. Leilich, J. E. Simpson, and E. H. Meiburg, 2002: The propagation of a gravity current into a linearly stratified fluid. *J. Fluid Mech.*, **453**, 371–394.
- Mueller, C. K., and R. E. Carbone, 1987: Dynamics of a thunderstorm outflow. *J. Atmos. Sci.*, **44**, 1879–1898.
- Rotunno, R., J. B. Klemp, and M. L. Weisman, 1988: A theory for strong, long-lived squall lines. *J. Atmos. Sci.*, **45**, 463–485.
- Sasaki, Y. K., and T. L. Baxter, 1986: The gust front. *Thunderstorm Morphology and Dynamics*, E. Kessler, Ed., 2nd edn. University of Oklahoma Press, 187–196.
- Simpson, J. E., 1987: *Gravity Currents*. Ellis Horwood.
- Ungarish, M., 2006: On gravity currents in a linearly stratified ambient: a generalization of Benjamin's steady-state propagation results. *J. Fluid Mech.*, **548**, 49–68.
- Wakimoto (1982).
- Xue, M., 2000: Density currents in two-layer shear flows. *Quart. J. Roy. Meteor. Soc.*, **126**, 1301–1320.
- Xue, M., 2002: Density currents in shear flows: effects of rigid lid and cold-pool internal circulation, and application to squall line dynamics. *Quart. J. Roy. Meteor. Soc.*, **128**, 47–73.

Sea breezes

- Anthes, R. A., and H. Yan, 1987: The effect of latitude on the sea breeze. *Mon. Wea. Rev.*, **115**, 936–956.
- Arritt, R. W., 1993: Effects of the large-scale flow on characteristic features of the sea breeze. *J. Appl. Meteor.*, **32**, 116–125.
- Atkins, N. T., and R. M. Wakimoto, 1995: Observations of the sea-breeze front during CaPE. Part II: Dual-Doppler and aircraft analysis. *Mon. Wea. Rev.*, **123**, 944–969.
- Dailey, P. S., and R. G. Fovell, 1999: Numerical simulation of the interaction between the sea-breeze front and horizontal convective rolls. Part I: Offshore ambient flow. *Mon. Wea. Rev.*, **127**, 858–878.
- Dalu, G., and R. A. Pielke, 1989: An analytical study of the sea breeze. *J. Atmos. Sci.*, **46**, 1815–1825.
- Fovell, R. G., and P. S. Dailey, 2001: Numerical simulation of the interaction between the sea-breeze front and horizontal convective rolls. Part II: Alongshore ambient flow. *Mon. Wea. Rev.*, **129**, 2057–2072.
- Pearson, R. A., 1973: Properties of the sea breeze front as shown by a numerical model. *J. Atmos. Sci.*, **30**, 1050–1060.
- Pielke, R. A., 1974: A three-dimensional numerical model of the sea breezes over south Florida. *Mon. Wea. Rev.*, **102**, 115–139.

- Rotunno (1983).
- Wakimoto and Atkins (1994).

Other mesoscale boundaries

- Bluestein (1982).
- Johnson, R. H., G. S. Young, J. J. Toth, and R. M. Zehr, 1984: Mesoscale weather effects of variable snow cover over northeast Colorado. *Mon. Wea. Rev.*, **112**, 1141–1152.
- Keshishian and Bosart (1987).
- Ookouchi *et al.* (1984).
- Pielke R. A., and M. Segal, 1986: Mesoscale circulations forced by differential terrain heating. *Mesoscale Meteorology and Forecasting*, P. S. Ray, Ed. Amer. Meteor. Soc., 516–548.
- Segal, M., and R. W. Arritt, 1992: Nonclassical mesoscale circulations caused by surface sensible heat-flux gradients. *Bull. Amer. Meteor. Soc.*, **73**, 1593–1604.
- Segal, M., J. H. Cramer, R. A. Pielke, J. R. Garratt, and P. Hildebrand, 1991: Observational evaluation of the snow breeze. *Mon. Wea. Rev.*, **119**, 412–424.
- Segal *et al.* (1986).
- Young and Fritsch (1989).

6

Mesoscale Gravity Waves

Gravity waves are ubiquitous in the atmosphere.¹ The equations that govern atmospheric flow allow wave solutions of all sorts, and gravity waves (or buoyancy oscillations) are possible under statically stable conditions. Waves can be generated by airflow over mountains, the penetration of stable layers by convection, density impulses, vertical shear instabilities, and the disruption of balanced flow. Gravity waves influence the general circulation of the atmosphere through their transport and deposition of momentum, and are important in the adjustment of the atmosphere toward a balanced state through their adjustments of the mass and momentum fields.

Gravity waves typically transfer much of their energy upward, and therefore usually lose much of their amplitude by the time they have traveled even a few wavelengths horizontally from their source. However, when the static stability or the wind shear change with height, upward-propagating wave energy can be reflected, allowing gravity waves to travel large distances horizontally from their source before surrendering most of their energy. These large-amplitude, ‘ducted’ gravity waves, sometimes referred to as *mesoscale* gravity waves (or *solitary* waves, if only one dominant waveform is present), can occasionally have a significant impact on weather by producing bands of enhanced precipitation within larger-scale regions of precipitation (Figures 6.1 and 6.2). In unsaturated environments, ducted gravity waves of sufficient amplitude can lift air parcels to saturation, or even to their level of free convection, if one exists (Figure 6.3) (see Chapter 7). Ducted waves generally occur in the lower atmosphere in a deep stable layer; therefore, we consider them lower-tropospheric

phenomena, and they are the focus later in this chapter. Before we can understand ducted waves, however, we must first understand basic internal gravity waves, which also are crucial in Chapter 12, wherein mountain-generated waves are considered.

6.1 Basic wave conventions

Atmospheric phenomena often appear as wavelike patterns on weather maps, in the sense that they involve periodic variations of quantities such as temperature and wind. Also, we know from Fourier analysis that any continuous function can be constructed through the superpositioning of waveforms. For these reasons, it is common in meteorology to assume a wave solution for atmospheric variables and then use these assumed solutions to assess properties of the flow. This type of analysis is most useful when the final equation set is linear (i.e., it does not contain terms involving multiplication of perturbations from a base state). The most common waveforms we tend to think of are simple sine and cosine functions along one direction, expressed as, for example,

$$f = A \cos \left[\frac{2\pi}{\lambda_x} (x - ct) \right] \quad (6.1)$$

where λ_x is the wavelength in the x direction, c is the phase speed, and A is the amplitude. From (6.1), we see that, as x increases from 0 to λ_x at $t = 0$, the function f varies from $\cos 0$ to $\cos 2\pi$ and thus completes a full wave cycle. For positive values of c , the wave will move toward positive x with time. It is often more convenient to express the rhs of (6.1) in terms of wavenumber, k , and angular

¹ Strictly speaking, we are referring to internal gravity waves, because there are no free surfaces in the atmosphere.

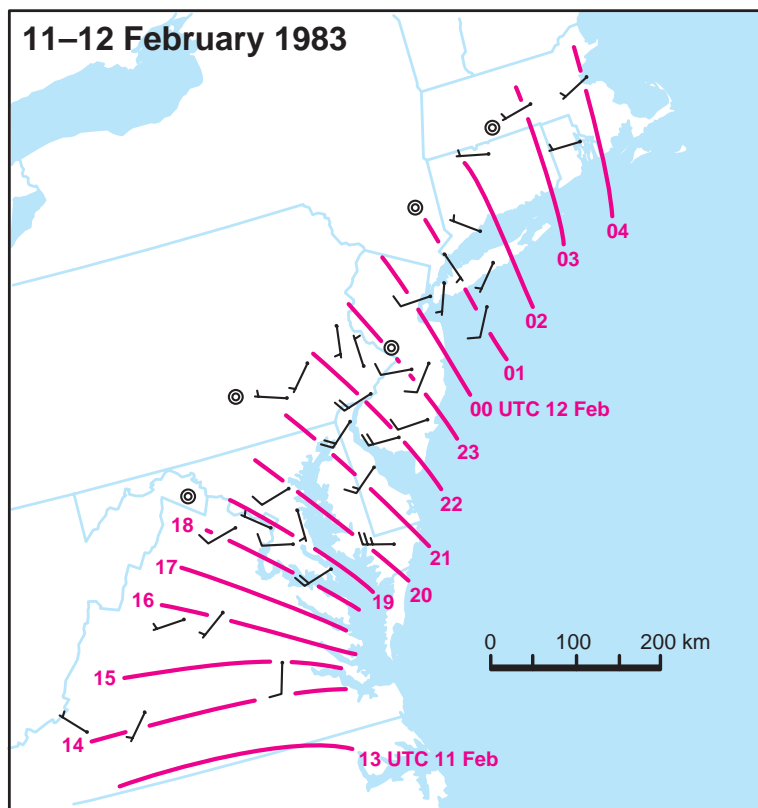


Figure 6.1 Isochrones (UTC) of a large-amplitude gravity wave crest on 11–12 February 1983, during one of the heaviest snowstorms ever to strike the Northeast US major cities. Wind barbs indicate the vector wind shift associated with the wave passage. (Adapted from Bosart and Sanders [1986].)

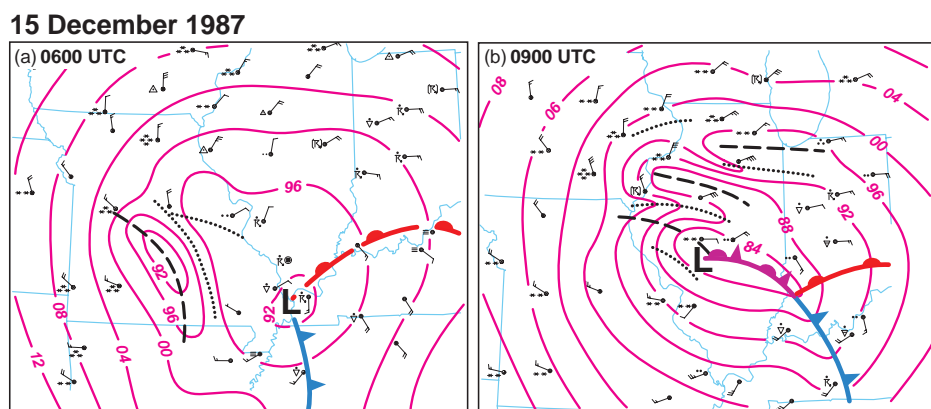


Figure 6.2 Surface pressure analyses (mb; the leading '9' or '10' is dropped) for (a) 0600 UTC and (b) 0900 UTC on 15 December 1987. Pressure troughs (ridges) associated with mesoscale gravity waves are indicated with dashed (dotted) lines. (Adapted from Schneider [1990].)

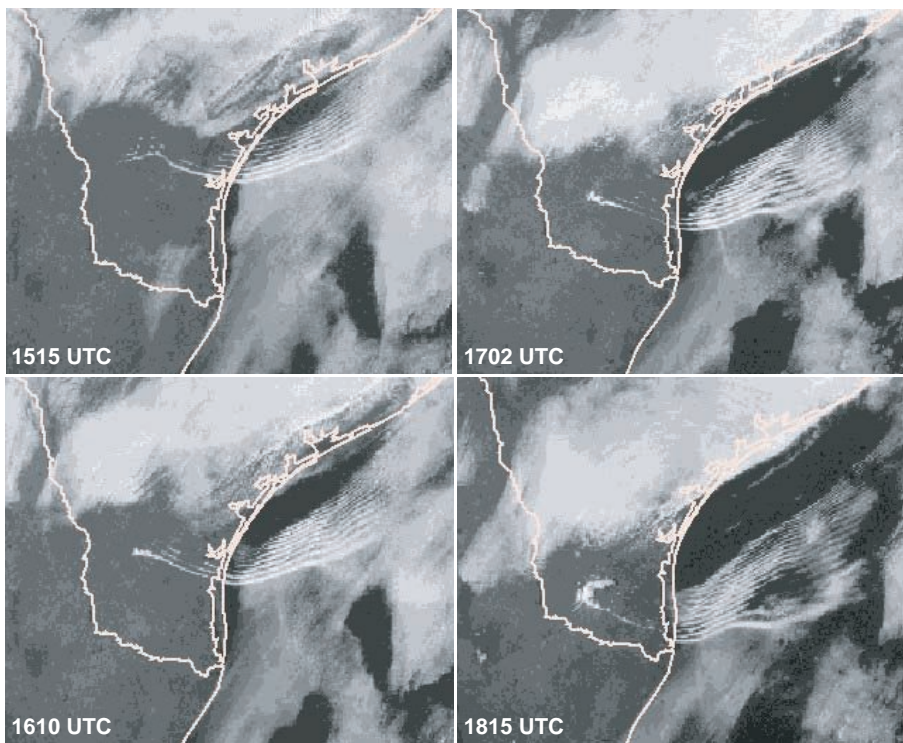


Figure 6.3 Series of visible satellite images from 14 March 1997 (1515, 1610, 1702, and 1815 UTC), showing a soliton (a train of amplitude-ordered solitary waves) and the subsequent initiation of a thunderstorm in southern Texas. The storm went on to produce 4.5 inch diameter hail. (Courtesy of the Storm Prediction Center.)

frequency, ω , using the definitions $k = 2\pi/\lambda_x$ and $\omega = ck$ for a one-dimensional wave. Then (6.1) becomes

$$f = A \cos(kx - \omega t). \quad (6.2)$$

For a function having a wave structure in the x and z directions (Figure 6.4), we modify (6.2) to include the second direction such that it becomes

$$f = A \cos(kx + mz - \omega t) \quad (6.3)$$

where $m = 2\pi/\lambda_z$ and λ_z is the vertical wavelength. For notational convenience and to allow for cosine as well as sine solutions, we shall often express our assumed wave solutions in the form

$$f = \Re \left\{ A e^{i(kx + mz - \omega t)} \right\} \quad (6.4)$$

where A is now a complex amplitude (i.e., $A = A_r + iA_i$), $e^{i(kx + mz - \omega t)}$ expands to $\cos(kx + mz - \omega t) + i \sin(kx + mz - \omega t)$.

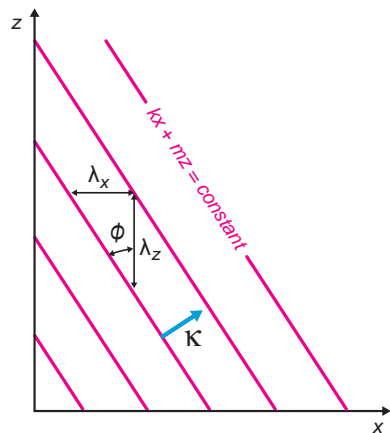


Figure 6.4 Basic wave properties. Lines indicate constant phase for a plane wave; λ_x (k) and λ_z (m) are the wavelengths (wavenumbers) in the x and z directions, respectively, ϕ is the angle between the phase lines and the vertical, and κ is the wave vector.

$+mz - \omega t$), and the \Re operator indicates that we retain only the real part of the quantity in brackets.

At any particular time, the quantity $kx + mz - \omega t$ is described as the *phase* of the wave, and lines of constant phase are called *wavefronts*, which are perpendicular to the *wave vector* (also sometimes called the *wavenumber vector*) $\kappa = ki + mk$. We can write (6.3) using the wave vector and a position vector, $\mathbf{r} = xi + zk$, to obtain

$$f = A \cos(\kappa \cdot \mathbf{r} - \omega t). \quad (6.5)$$

The wave propagates along the direction of κ with a phase speed c . This speed corresponds to the $d|\mathbf{r}|/dt$ one must have in order to keep the phase constant in time. In other words, we can find c by setting $d(\kappa \cdot \mathbf{r} - \omega t)/dt = 0$ and solving for $|d\mathbf{r}/dt|$. Thus, we find, following a line of constant phase,

$$\frac{d(\kappa \cdot \mathbf{r} - \omega t)}{dt} = \kappa \cdot \frac{d\mathbf{r}}{dt} - \omega = 0, \quad (6.6)$$

and the magnitude of the phase speed is given by

$$c = \frac{d|\mathbf{r}|}{dt} = \frac{\omega}{|\kappa|} = \frac{\omega}{\sqrt{k^2 + m^2}}. \quad (6.7)$$

At times, we shall be interested in the speed of the wavefronts along a particular direction, such as the horizontal or the vertical. We find these speeds using an identical procedure to that used in finding (6.7), but we hold one of the directions (e.g., z) constant in order to find the phase speed along the other direction (e.g., x). Following a line of constant phase and holding z constant yields

$$\frac{d(kx + mz - \omega t)}{dt} = k \frac{dx}{dt} - \omega = 0, \quad (6.8)$$

from which we obtain the phase speed in the x direction, given by

$$c_x = \frac{dx}{dt} = \frac{\omega}{k}. \quad (6.9)$$

The equivalent procedure for the z direction yields

$$c_z = \frac{\omega}{m}. \quad (6.10)$$

It is important to note that the phase velocity has a magnitude given by c and a direction given by a unit vector along the direction of κ . It does not behave like a vector in the sense that $c \neq \sqrt{c_x^2 + c_z^2}$. Rather, from Figure 6.4, the phase speed along either the x or the z directions is greater than that along κ , because wavefronts take a shorter time

to traverse a given distance along these directions than they do along κ .

When waves occur within a fluid having an ambient wind, the frequency will experience a *Doppler shift* along the wind direction with a magnitude given by the wind speed multiplied by the wavenumber for that direction (i.e., $\bar{u}k$ for an environmental wind \bar{u} along the x direction). We define the *intrinsic* frequency, Ω , as that which the wave would experience in the absence of an ambient wind. Thus,

$$\omega = \Omega + \bar{u}k \quad (6.11)$$

in the case of an ambient wind in the x direction. From (6.9), we can use (6.11) to determine the phase speed in the x direction as

$$c_x = \frac{\Omega}{k} + \bar{u} \quad (6.12)$$

The quantity Ω/k is the intrinsic phase speed, and it represents the phase speed measured by an observer moving with the ambient wind. Equation (6.12) indicates that the ground-relative phase speed along a particular direction is shifted from its intrinsic value by an amount equal to the component of the ambient wind along that direction.

In the atmosphere, waves do not extend indefinitely in space as would be implied by (6.3), but instead occur in the form of *wave packets* (Figure 6.5), which are limited regions within which waves have appreciable amplitude. These packets are the result of superpositioning multiple waves of the form given by (6.3) with slightly different

energy and phase propagation of a wave packet

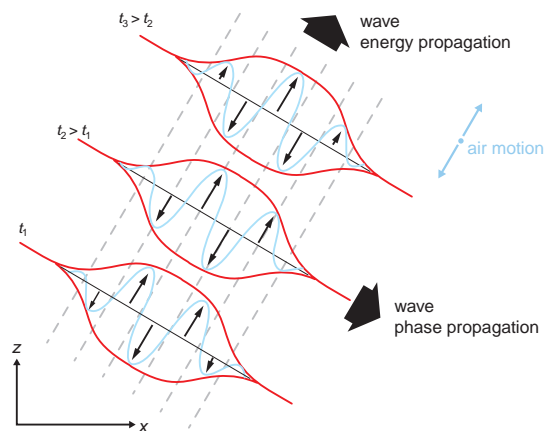


Figure 6.5 Relationship between wavefronts, phase velocity, and group velocity for an internal gravity wave. (Adapted from Hooke [1986].)

frequencies and wavenumbers. The classic example of this effect involves superpositioning two one-dimensional waves with equal amplitudes, A , but slightly different wavenumbers, $k_0 \pm \delta k$, and frequencies, $\omega_0 \pm \delta\omega$. When these waves are added together, the resulting waveform is given by

$$\begin{aligned} f = & A \cos [(k_0 + \delta k)x - (\omega_0 + \delta\omega)t] \\ & + A \cos [(k_0 - \delta k)x - (\omega_0 - \delta\omega)t]. \end{aligned} \quad (6.13)$$

Using standard trigonometric identities, this can be written as

$$f = 2A \cos(\delta kx - \delta\omega t) \cos(k_0 x - \omega_0 t) \quad (6.14)$$

from which we see that the superpositioning of the two wave modes has created an *amplitude envelope* given by $2A \cos(\delta kx - \delta\omega t)$. The movement of this amplitude envelope determines the speed and direction of the flow of wave energy. In analogy to (6.7), we can determine that the speed of the amplitude envelope (called the *group velocity*, c_g) is given by

$$c_{gx} = \frac{\delta\omega}{\delta k}. \quad (6.15)$$

In the limit of small δk and $\delta\omega$, and assuming that $\delta\omega$ and δk are not independent [i.e., $\omega = \omega(k)$], this becomes

$$c_{gx} = \frac{\partial\omega}{\partial k}. \quad (6.16)$$

In the example given here for a one-dimensional wave, the group velocity and the phase velocity are in the same (x) direction, as is typical for external waves. If ω has a simple relationship with k , such that ω is equal to a constant multiplying k , then (6.9) and (6.16) indicate that the phase speed and the group velocity speed will be equal and constant (i.e., not a function of wavenumber). In this case, the waveform produced through superpositioning waves with different wavelengths does not change shape as it moves, because all wavelengths travel at the same speed. In general, ω often has a more complicated relationship with k such that we obtain different phase speeds for different wavelengths, causing individual waves to move faster or slower than the amplitude envelope created by superposition. For internal waves, we shall find that the group and phase velocities are not in the same direction.

For two-dimensional waves, the analysis can be extended to find that the group velocity in the z direction is given by

$$c_{gz} = \frac{\partial\omega}{\partial m}. \quad (6.17)$$

The group velocity often provides a critical boundary condition on the wave solution, as energy is always required to travel away from the source of wave activity.

6.2 Internal gravity wave dynamics

For most of us, our experience with waves is founded on those that appear on a water surface such as a lake or ocean. Waves such as these, forming along the interface between two fluids of very different densities and having their maximum amplitude at this interface (the external surface of the lower, generally homogeneous and incompressible, fluid), are referred to as *surface waves* or *external waves*. In contrast, *internal waves* are found in a fluid with continually varying density and have their maximum amplitude within the fluid. Unfortunately, the two types of waves behave very differently, such that our intuitive understanding of external waves does little to aid our understanding of waves in the atmosphere which are internal. Thus, we must use the equations of motion to develop our understanding of these waves.

Most interesting aspects of gravity wave behavior are retained even when the perturbations associated with the waves are assumed to be small compared with the mean flow. Thus, we linearize the equations of motion by assuming that flow variables consist of a mean part, which we assume is either constant or varies only in the vertical, and a smaller-amplitude fluctuating part that varies in both space and time and is designated with a prime (e.g., $u = \bar{u} + u'$). We substitute these into the equations of motion and ignore any terms containing multiples of primed variables. By ignoring the nonlinear terms, we remove some of the interesting physics of waves, such as nonlinear steepening, by which sharp gradients in the flow can develop, but we retain sufficient information to explain their basic behavior.

To simplify our analysis, we assume two-dimensional waves varying in only the x and z directions. Thus, we start with the two-dimensional equations of motion in the x and z directions ($v = 0$, $\partial/\partial y = 0$), the continuity equation, and a thermodynamic equation. We neglect the Coriolis force and viscosity. Unlike most atmospheric phenomena, wave motions can extend over a great depth even though individual parcel excursions remain relatively shallow. In order to keep the problem tractable, we assume that motions are adiabatic and ignore the changes in density following a parcel in our mass continuity equation. However, because the wave may propagate over a significant depth, we retain the variation of the mean state density with height in the momentum equations (i.e., we assume $\rho = \bar{\rho}(z)$ in the pressure gradient terms). We also approximate the

buoyancy as $g\theta'/\bar{\theta}$, where $\bar{\theta} = \bar{\theta}(z)$ is the base state potential temperature and $\theta = \bar{\theta} + \theta'$. The equations of motion are then

$$\frac{\partial u}{\partial t} + u \frac{\partial u}{\partial x} + w \frac{\partial u}{\partial z} = -\frac{1}{\bar{\rho}} \frac{\partial p'}{\partial x} \quad (6.18)$$

$$\frac{\partial w}{\partial t} + u \frac{\partial w}{\partial x} + w \frac{\partial w}{\partial z} = -\frac{1}{\bar{\rho}} \frac{\partial p'}{\partial z} + g \frac{\theta'}{\bar{\theta}} \quad (6.19)$$

$$\frac{\partial u}{\partial x} + \frac{\partial w}{\partial z} = 0 \quad (6.20)$$

$$\frac{\partial \theta}{\partial t} + u \frac{\partial \theta}{\partial x} + w \frac{\partial \theta}{\partial z} = 0 \quad (6.21)$$

where p' is the departure of pressure from a hydrostatic base state defined by $\partial \bar{p}/\partial z = -\bar{\rho}g$.

As mentioned previously, the easiest way to demonstrate wave solutions will be to linearize the above equations. We shall assume that $w = w'$, $\theta = \bar{\theta}(z) + \theta'$, and the base state zonal wind profile (\bar{u}) is a function of z , such that $u = \bar{u}(z) + u'$. We ignore any terms containing multiplications of perturbation (primed) quantities. All of the above assumptions lead to a simpler system of equations:

$$\frac{\partial u'}{\partial t} + \bar{u} \frac{\partial u'}{\partial x} + w' \frac{\partial \bar{u}}{\partial z} = -\frac{1}{\bar{\rho}} \frac{\partial p'}{\partial x} \quad (6.22)$$

$$\frac{\partial w'}{\partial t} + \bar{u} \frac{\partial w'}{\partial x} = -\frac{1}{\bar{\rho}} \frac{\partial p'}{\partial z} + g \frac{\theta'}{\bar{\theta}} \quad (6.23)$$

$$\frac{\partial u'}{\partial x} + \frac{\partial w'}{\partial z} = 0 \quad (6.24)$$

$$\frac{\partial \theta'}{\partial t} + \bar{u} \frac{\partial \theta'}{\partial x} + w' \frac{\partial \bar{\theta}}{\partial z} = 0. \quad (6.25)$$

We seek one equation in one unknown², w' . We first multiply all equations by $\bar{\rho}$ and eliminate p' by taking $\frac{\partial}{\partial z}$ (6.23) - $\frac{\partial}{\partial z}$ (6.22) and eliminating like terms to obtain

$$\begin{aligned} \bar{\rho} \left(\frac{\partial}{\partial t} + \bar{u} \frac{\partial}{\partial x} \right) \left(\frac{\partial w'}{\partial x} - \frac{\partial u'}{\partial z} - \frac{1}{\bar{\rho}} \frac{d\bar{\rho}}{dz} u' \right) \\ - w' \frac{d\bar{\rho}}{dz} \frac{d\bar{u}}{dz} - w' \bar{\rho} \frac{d^2 \bar{u}}{dz^2} - \bar{\rho} \frac{g}{\bar{\theta}} \frac{\partial \theta'}{\partial x} = 0. \end{aligned} \quad (6.26)$$

where we have replaced partial derivatives with respect to z with ordinary derivatives for those variables that depend only on z . We now take $\partial(6.26)/\partial x$ and use (6.24) to eliminate all $\partial u'/\partial x$ terms. This yields

² It would be equally valid to solve this system of equations by assuming a waveform for all perturbation variables, substituting these assumed solutions into the equations, performing all differentiations, and then solving the resulting set of equations using the methods of linear algebra.

$$\begin{aligned} \bar{\rho} \left(\frac{\partial}{\partial t} + \bar{u} \frac{\partial}{\partial x} \right) \left(\frac{\partial^2 w'}{\partial x^2} + \frac{\partial^2 w'}{\partial z^2} + \frac{1}{\bar{\rho}} \frac{d\bar{\rho}}{dz} \frac{\partial w'}{\partial z} \right) \\ - \frac{d\bar{\rho}}{dz} \frac{d\bar{u}}{dz} \frac{\partial w'}{\partial x} - \bar{\rho} \frac{d^2 \bar{u}}{dz^2} \frac{\partial w'}{\partial x} - \bar{\rho} \frac{g}{\bar{\theta}} \frac{\partial^2 \theta'}{\partial x^2} = 0. \end{aligned} \quad (6.27)$$

Next, we divide (6.27) by $\bar{\rho}$ and eliminate θ' by applying $(\frac{\partial}{\partial t} + \bar{u} \frac{\partial}{\partial x})$ to (6.27) and combining with (6.25), which gives

$$\begin{aligned} \left(\frac{\partial}{\partial t} + \bar{u} \frac{\partial}{\partial x} \right)^2 \left(\frac{\partial^2 w'}{\partial x^2} + \frac{\partial^2 w'}{\partial z^2} + \frac{1}{\bar{\rho}} \frac{d\bar{\rho}}{dz} \frac{\partial w'}{\partial z} \right) \\ - \left(\frac{\partial}{\partial t} + \bar{u} \frac{\partial}{\partial x} \right) \left(\frac{1}{\bar{\rho}} \frac{d\bar{\rho}}{dz} \frac{d\bar{u}}{dz} + \frac{d^2 \bar{u}}{dz^2} \right) \frac{\partial w'}{\partial x} \\ + \frac{g}{\bar{\theta}} \frac{d\bar{\theta}}{dz} \frac{\partial^2 w'}{\partial x^2} = 0 \end{aligned} \quad (6.28)$$

We assume a solution for w' given by

$$w' = \Re \left\{ \sum_k w'_k \right\} = \Re \left\{ \sum_k \tilde{w}_k e^{i(kx - \omega_k t)} \right\}, \quad (6.29)$$

where \tilde{w}_k is a complex amplitude (i.e., $\tilde{w}_k = \tilde{w}_{kr} + i\tilde{w}_{ki}$) that is a function of height, the \Re operator indicates that we keep only the real part of the quantity in brackets, and ω_k is the frequency corresponding to the k th mode. Note that the complex amplitude is necessary in order to fit any arbitrary initial and boundary conditions (e.g., our boundary conditions can be accommodated whether they are sine functions or cosine functions because the real part of (6.29) expands to $w'_k = \tilde{w}_{kr} \cos(kx - \omega_k t) - \tilde{w}_{ki} \sin(kx - \omega_k t)$). From this point forward, it will be assumed that only the real part of the final expanded solution for a variable is of physical interest without explicitly writing the \Re operator.

We now substitute (6.29) into (6.28), noting that $\partial w'_k/\partial x = ikw'_k$ and $\partial w'_k/\partial t = -i\omega_k w'_k$ for each k . This yields the following expression:

$$\begin{aligned} \sum_k \left[(-i\omega_k + \bar{u}ik)^2 \left(i^2 k^2 \tilde{w}_k + \frac{d^2 \tilde{w}_k}{dz^2} + \frac{1}{\bar{\rho}} \frac{d\bar{\rho}}{dz} \frac{d\tilde{w}_k}{dz} \right) \right. \\ \left. - (-i\omega_k + \bar{u}ik) \left(ik \frac{d^2 \bar{u}}{dz^2} + \frac{1}{\bar{\rho}} \frac{d\bar{u}}{dz} \frac{d\bar{\rho}}{dz} ik \right) \tilde{w}_k \right. \\ \left. + N^2 i^2 k^2 \tilde{w}_k \right] e^{i(kx - \omega_k t)} = 0, \end{aligned} \quad (6.30)$$

where $N^2 = \frac{g}{\bar{\theta}} \frac{d\bar{\theta}}{dz}$. At this point, it is helpful to recall that the *intrinsic* frequency, that which the wave would have if observed in a reference frame moving with the mean wind, is given by $\Omega = \omega - \bar{u}k$, which we substitute into (6.30)

and then divide each term by Ω^2 . We note that the modes being summed in (6.30) are linearly independent (i.e., they do not cancel with one another no matter what their amplitudes, just as one could not change the amplitude of orthogonal vectors and cause them to cancel), such that the only way the summation can be equal to zero is if the term in brackets is zero for *each of the modes separately*. Thus, we can write (6.30) for an individual mode k , and we hereafter neglect the k subscripts on the amplitude and frequency. Also, recognizing that $i^2 = -1$, the bracketed term in (6.30) becomes

$$\frac{d^2\tilde{w}}{dz^2} + \frac{1}{\bar{\rho}} \frac{d\bar{\rho}}{dz} \frac{d\tilde{w}}{dz} + \left(\frac{k}{\Omega} \frac{d^2\bar{u}}{dz^2} + \frac{k}{\Omega} \frac{1}{\bar{\rho}} \frac{d\bar{\rho}}{dz} \frac{d\bar{u}}{dz} + \frac{k^2 N^2}{\Omega^2} - k^2 \right) \tilde{w} = 0. \quad (6.31)$$

If we make the common assumption of an exponentially decreasing density profile, such that $\frac{1}{\bar{\rho}} \frac{d\bar{\rho}}{dz} = -\frac{1}{H}$, where H is the scale height, we obtain

$$\frac{d^2\tilde{w}}{dz^2} - \frac{1}{H} \frac{d\tilde{w}}{dz} + \left(\frac{k}{\Omega} \frac{d^2\bar{u}}{dz^2} - \frac{k}{\Omega H} \frac{d\bar{u}}{dz} + \frac{k^2 N^2}{\Omega^2} - k^2 \right) \tilde{w} = 0. \quad (6.32)$$

By (6.32), the amplitude will vary with height based partly on the density profile. We can incorporate this part of the height dependence by expressing our equation in terms of a new variable, \hat{w} , such that

$$\tilde{w} = e^{z/2H} \hat{w}. \quad (6.33)$$

We note from (6.33) that the effect of decreasing density with height is to amplify the wave (i.e., $|\tilde{w}|$ increases with height if \hat{w} is constant), leading to important effects in the stratosphere and mesosphere that will not be discussed herein. Substituting (6.33) into (6.32), applying the product rule when performing the differentiations with respect to z , and canceling like terms yields the Taylor-Goldstein equation³

$$\frac{d^2\hat{w}}{dz^2} + \left(\frac{k^2 N^2}{\Omega^2} + \frac{k}{\Omega} \frac{d^2\bar{u}}{dz^2} - k^2 - \frac{k}{\Omega H} \frac{d\bar{u}}{dz} - \frac{1}{4H^2} \right) \hat{w} = 0. \quad (6.34)$$

³ See Taylor (1931) and Goldstein (1931).

The Taylor-Goldstein equation shows that the gravity wave structure with height depends on the environmental static stability (quantified by N^2) and the vertical wind profile, as well as the distribution of density with height (as manifested in the H terms). For any given profiles of N and \bar{u} , the solution to (6.34) can be obtained numerically through direct simulation or analytically using the WKB⁴ technique, for which the term in brackets must be slowly varying such that it does not change significantly over one vertical wavelength. The WKB method is outside the scope of this book, but the reader is referred to Nappo (2002) for a review of this method. For our purposes, we shall assume hereafter that the term in brackets is constant within a layer of the atmosphere. Furthermore, if density is constant with height, H is effectively infinite; thus, the terms with $1/H$ go to zero and $\tilde{w} = \hat{w}$. Even if density is not constant, the $1/H$ terms may be ignored if the vertical wavelength is much less than H , and this will be assumed to be the case for the remainder of our discussion. Thus, from this point forward we simplify the Taylor-Goldstein equation as

$$\frac{d^2\hat{w}}{dz^2} + \left(\frac{k^2 N^2}{\Omega^2} + \frac{k}{\Omega} \frac{d^2\bar{u}}{dz^2} - k^2 \right) \hat{w} = 0, \quad (6.35)$$

which can also be written as

$$\frac{d^2\hat{w}}{dz^2} + \left[\frac{N^2}{(c_x - \bar{u})^2} + \frac{1}{(c_x - \bar{u})} \frac{d^2\bar{u}}{dz^2} - k^2 \right] \hat{w} = 0, \quad (6.36)$$

where we have used the relationship $c_x = \omega/k = \Omega/k + \bar{u}$.

Given (6.36), each mode of \hat{w} has a solution of the form

$$\hat{w} = A e^{imz} + B e^{-imz} \quad (6.37)$$

such that

$$w' = A e^{i(kx+mz-\omega t)} + B e^{i(kx-mz-\omega t)} \quad (6.38)$$

with

$$m = \sqrt{\frac{N^2}{(c_x - \bar{u})^2} + \frac{1}{(c_x - \bar{u})} \frac{d^2\bar{u}}{dz^2} - k^2}, \quad (6.39)$$

and A, B representing constant complex wave amplitudes. The z dependence of w is determined by whether m is real or imaginary, which depends on whether the bracketed term in (6.36) is positive or negative. Fundamentally different solutions are obtained for the two cases. If m is real, the solution is a two-dimensional wave with propagation in both the horizontal and vertical directions. If m is

⁴ Named after the physicists G. Wentzel, H. A. Kramers, and L. Brillouin. The WKB technique was originally applied in the field of quantum mechanics.

imaginary, we make the substitution $m = i\mu$, where μ is a real number, such that (6.38) becomes

$$w' = Ae^{-\mu z}e^{i(kx-\omega t)} + Be^{\mu z}e^{i(kx-\omega t)}. \quad (6.40)$$

When $B = 0$ in (6.40), as it must in order to prevent physically unreasonable solutions that grow unbounded with height, the solution for w exhibits exponential decay with height and is referred to as an *evanescent* solution. In this case, waves are unable to propagate vertically. To better understand conditions that favor propagating waves over evanescent solutions, we now consider some simplified environments.

6.2.1 Environments with constant wind and static stability

When $\bar{u} = u_0$ and N are both constant, (6.39) leads to

$$m^2 = -k^2 + \frac{k^2 N^2}{\Omega^2}, \quad (6.41)$$

and we find that wave solutions (i.e., those with $m^2 > 0$) are possible when $\Omega^2 < N^2$. If $\Omega^2 > N^2$, only evanescent solutions ($m^2 < 0$) are possible. In order to understand physically why the solution behavior changes so dramatically when Ω exceeds N , we must think a bit more deeply about the types of oscillations due to buoyancy that the atmosphere is able to support. In Section 3.1, it was shown that vertical motions due to buoyancy in a stable atmosphere have an oscillation frequency equal to N . Parcels within internal gravity waves do not follow a strictly vertical path, but, nonetheless, are also driven by buoyancy. If buoyancy is the sole force acting in the direction of parcel oscillation (i.e., if perturbation pressures are constant along the direction of oscillation, as we shall see is the case for internal gravity waves), then the oscillation frequency can be derived in the same manner as is done for vertical displacements, with the full buoyancy, B , replaced by its component along the direction of oscillation, $B \cos \phi$, where ϕ is the angle with respect to the vertical along which the oscillation occurs. The frequency of this oscillation will be given by $N \cos \phi$. Thus, with buoyancy as the restoring force, the atmosphere can support oscillations with frequencies less than or equal to N for angles with respect to the vertical varying between 90° (purely horizontal) and 0° (purely vertical). Oscillations with a frequency greater than N cannot be supported. We like to think of this as analogous to a child's paddle toy with a ball on a string. Given a particular length of string, there is a preferred oscillation frequency at which one naturally drives the paddle in order to keep the ball in motion. This

frequency could be altered by changing the length of the string (analogous to oscillating along a slanted, rather than vertical, path in the atmosphere). However, if the paddle is driven at a frequency greater than the natural oscillation frequency, the ball will not undergo organized oscillatory motions.

The oscillation frequency for wave solutions is given by the *dispersion relation*, obtained using the ω from (6.41). Thus,

$$\begin{aligned} \omega &= u_0 k + \Omega = u_0 k \pm \frac{kN}{(k^2 + m^2)^{1/2}} \\ &= u_0 k \pm \frac{\lambda_z N}{(\lambda_x^2 + \lambda_z^2)^{1/2}} = u_0 k \pm N \cos \phi, \end{aligned} \quad (6.42)$$

where $\lambda_x = 2\pi/k$ and $\lambda_z = 2\pi/m$ are the wavelengths in the horizontal and vertical directions, respectively. This important relationship indicates that the intrinsic oscillation frequency (Ω) of internal gravity waves depends only on the static stability and the angle at which the oscillation occurs with respect to the vertical, as we deduced above based on physical arguments. Any combination of k and m resulting in the same angle for the wave vector will therefore have the same intrinsic oscillation frequency. (Note that this is in contrast to surface waves for which the oscillation frequency is a function of the *magnitude* of the wave vector.) According to (6.42), internal gravity waves are dispersive, with each wavelength having a different phase speed. The physics of an individual problem will often determine whether the positive or negative branch is relevant in (6.42).

Considering only the positive branch of (6.42), the phase speeds in the x and z directions are given by

$$c_x = \frac{\omega}{k} = u_0 + \frac{\Omega}{k} = u_0 + \frac{N}{(k^2 + m^2)^{1/2}} \quad (6.43)$$

$$c_z = \frac{\omega}{m} = u_0 \frac{k}{m} + \frac{\Omega}{m} = u_0 \frac{k}{m} + \frac{kN}{m(k^2 + m^2)^{1/2}}. \quad (6.44)$$

Dispersion causes waves of different wavelengths to go in and out of phase as they travel, creating an envelope of amplitude that travels at the group velocity, c_g , given by [again considering only the positive branch of (6.42)]

$$c_g = \left(\frac{\partial \omega}{\partial k}, \frac{\partial \omega}{\partial m} \right) \quad (6.45)$$

with

$$c_{gx} = u_0 + \frac{Nm^2}{(k^2 + m^2)^{3/2}} \quad (6.46)$$

and

$$c_{gz} = -\frac{Nkm}{(k^2 + m^2)^{3/2}} \quad (6.47)$$

which indicate the direction of energy transfer in the x and z directions, respectively. We note that c_z and c_{gz} have opposite signs, indicating upward (downward) transport of energy for downward (upward) phase propagation (Figure 6.5). This is true whether we choose the positive or negative branch of (6.42).

The above result can seem somewhat counterintuitive. How can energy go in a different direction than that in which the wave is going? The difficulty in understanding this perhaps stems from thinking in terms of a single wave mode for which the amplitude is constant spatially and the magnitude of the function at any point is a function only of phase, with troughs and ridges denoting the locations of maximum absolute value. Once we add in additional wave modes with wavelengths slightly different from the original one, however, this picture is no longer valid. Now the amplitude is tied to the sum of the values of all of the waves rather than the particular phase of any one wave. In essence, the presence of multiple wavelengths breaks the link between the magnitude of the function and the phase of any one mode. Thus, it should not be surprising that the phase speed and the group velocity, which is determined by the movement of the energy-containing amplitude envelope, can be in completely different directions. This implies that individual crests and troughs move through the amplification envelope with their amplitudes changing according to their location within the packet.

We also note that, for $u_0 = 0$, the slope of the group velocity vector with respect to the horizontal is $c_{gz}/c_{gx} = -k/m$ such that the group velocity is perpendicular to the phase velocity, which lies along the wave vector having a slope with the horizontal given by m/k . To understand why the two are perpendicular, recall that ω is constant for parcel oscillations at a given angle from the vertical and that parcel oscillations are along the wavefronts, perpendicular to the phase velocity. Thus, the phase velocity vector (along κ) defines a line of parcels having equal ω . We can rotate our coordinates such that, rather than having a k component along x and an m component along z , we have a k' component along κ and an m' component perpendicular to κ . If we express the group velocity in terms of these two components, we see that the component along the phase velocity will be zero since ω is constant (i.e., not a function of wavenumber) along that line. Thus, the only surviving component of group velocity is perpendicular to the phase velocity, along the phase lines and parallel to the parcel oscillations. The fact that $c_g = 0$ along the line of constant

parcel ω does not imply there is not interference between waves of different wavelengths along that direction. In fact, a constant value for ω implies varying phase speeds for varying wavelengths, creating an amplitude envelope. However, given the constant value for ω along this direction, the amplitude envelope remains stationary along κ as the individual waves move through it.

We can use (6.22)–(6.25) to derive expressions for u' , θ' , and p' in relation to w' , by assuming solutions for each of them that are of the same form as (6.29) (replacing the $(\tilde{\ })$ variables with $(\hat{\ })$ variables given our previous assumptions) and substituting these into (6.22)–(6.25) to obtain the *polarization equations*:

$$-i\omega\hat{u} + iku_0\hat{u} = -ik\frac{\hat{p}}{\bar{\rho}} \quad (6.48)$$

$$-i\omega\hat{w} + iku_0\hat{w} = -\frac{1}{\bar{\rho}}\frac{\partial\hat{p}}{\partial z} + g\frac{\hat{\theta}}{\bar{\theta}} \quad (6.49)$$

$$ik\hat{u} + \frac{dw}{dz} = 0 \quad (6.50)$$

$$-i\omega\hat{\theta} + iku_0\hat{\theta} + \hat{w}\frac{d\bar{\theta}}{dz} = 0. \quad (6.51)$$

Solving for each variable in terms of \hat{w} using (6.37) with $B = 0$, yields

$$\hat{u} = -\frac{m}{k}\hat{w} \quad (6.52)$$

$$\hat{p} = -\frac{\bar{\rho}m(\omega - u_0k)}{k^2}\hat{w} = -\frac{\bar{\rho}m\Omega}{k^2}\hat{w} \quad (6.53)$$

$$\hat{\theta} = -\frac{i}{(\omega - u_0k)}\frac{d\bar{\theta}}{dz}\hat{w} = -\frac{i}{\Omega}\frac{d\bar{\theta}}{dz}\hat{w}. \quad (6.54)$$

For the special case in which $u_0 = 0$ (Figure 6.6), from (6.52), we see that the slope of the parcel motions (w'/u') is equal to $-k/m$, which indicates that the parcel motions are in the same direction as the group velocity, along the phase lines and perpendicular to the phase velocity. From (6.53), we see that pressure is in phase with w' when m is negative and 180° out of phase with w' when m is positive (note that both k and m are negative in Figure 6.6). Perturbation pressure also is constant along a phase line, consistent with our assumption when using physical arguments to determine the oscillation frequency. Finally, the i on the rhs of (6.54) indicates that θ' is 90° out of phase with w' (i.e., if w' contains $\cos(kx + mz - \omega t)$, θ' contains $\sin(kx + mz - \omega t)$). These relationships can be used to distinguish features due to gravity waves from those due to buoyant convection, for which w' and θ' are in phase. In Figure 6.6, the wavefronts move downward and to the left. We can see why this is the

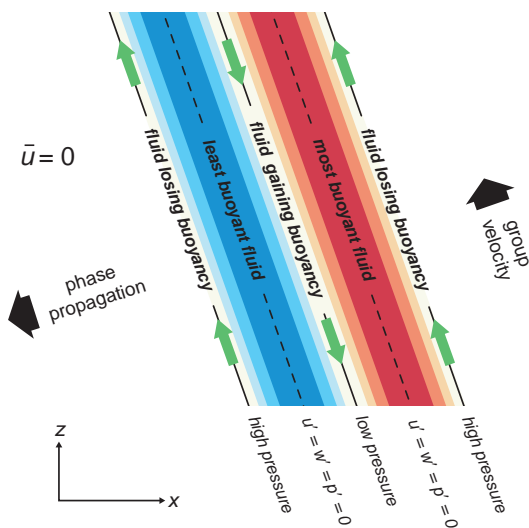


Figure 6.6 Relationship between potential temperature, velocity, and pressure perturbations for an internal gravity wave with $\bar{u} = 0$. (Adapted from Durran [1990].)

case by considering, for example, the perturbation potential temperature. The location between the most buoyant fluid (largest positive θ') and the least buoyant fluid (largest negative θ') is collocated with negative vertical velocity, which leads to increasing buoyancy following a parcel in a stable atmosphere. Thus, the region of most buoyant fluid moves toward this direction. It is in this manner that the phase lines propagate in the direction shown, exactly as predicted by (6.43) and (6.44).

6.3 Wave reflection

When the static stability and/or winds vary with height in such a way that they are relatively constant within particular layers, waves may experience refraction and/or reflection at the interface between these layers, in a similar manner to optical rays passing through layers of varying density. In the case of reflection, for each upward-propagating wave a downward-propagating wave is produced. This can have an interesting effect on the waveforms, as the upward- and downward-propagating waves interact. This interaction can be either constructive, leading to an increase in wave amplitude, or destructive, leading to decreased amplitude. Constructive interference leads to the trapping of wave energy within the lower layer, which is then referred to as a *wave duct*.

We first consider the simple case of reflection at the interface between two layers in the absence of any ambient

wind (i.e., $u_0 = 0$).⁵ To begin with, we must know what is required to happen at the interface (i.e., we must know the boundary conditions to apply). The atmosphere does not support infinite accelerations caused by discontinuous pressures; thus, one of our boundary conditions is that pressure be continuous across the interface. This is known as the *dynamic* boundary condition.⁶ Next, we prevent a solution in which the layers separate from one another. This is the *kinematic* boundary condition, and if density is continuous across the interface, this boundary condition becomes a simple matching of the vertical velocity on each side of the boundary. We can combine the kinematic and dynamic boundary conditions into one, and at the same time eliminate the wave amplitude from the boundary condition, by taking the ratio of the pressure and the mass flux. This new quantity, known as the *impedance*, is given by

$$Z = \frac{p}{\rho w}. \quad (6.55)$$

Thus, Z for each fluid is required to match at the height of the interface (z_r), such that $Z_1 = Z_2$, where the subscripts 1 and 2 indicate a lower and upper layer, respectively. We consider the case in which the value of ω is greater than N in the upper layer (N_2), but is smaller than N in the lower layer (N_1). In this case, the wave would be transmitted in the lower layer but evanescent in the upper layer, such that

$$w'_2 = A_2 e^{-\mu_2(z-z_r)} e^{i(kx-\omega t)} \quad (6.56)$$

and, from an equation similar to (6.53) derived for $m = i\mu_2$,

$$p'_2 = -i \frac{\overline{\rho} \mu_2 \omega}{k^2} A_2 e^{-\mu_2(z-z_r)} e^{i(kx-\omega t)}, \quad (6.57)$$

leading to

$$Z_2 = -i \frac{\omega \mu_2}{k^2}. \quad (6.58)$$

In the lower layer, the incident waves are propagating upward with an amplitude A_1 while the reflected waves are propagating downward with an amplitude B_1 . Defining the *reflection coefficient*, $R = B_1/A_1$, the full w_1 field can be expressed as

$$w'_1 = A_1 [e^{im_1(z-z_r)} + R e^{-im_1(z-z_r)}] e^{i(kx-\omega t)}. \quad (6.59)$$

⁵ The derivation in this section closely follows that of Nappo (2002).

⁶ This boundary condition applies to the total pressure, but is automatically satisfied for the base state part of the pressure. Thus, we need only enforce it for the perturbation pressure.

The perturbation pressure is then obtained from the polarization equations, (6.48)–(6.51), and is given by

$$p'_1 = -\frac{\bar{\rho}m_1\omega}{k^2}A_1 \left[e^{im_1(z-z_r)} - R e^{-im_1(z-z_r)} \right] e^{i(kx-\omega t)}, \quad (6.60)$$

such that the impedance in the lower layer is

$$Z_1 = -\frac{\omega m_1}{k^2} \left[\frac{e^{im_1(z-z_r)} - R e^{-im_1(z-z_r)}}{e^{im_1(z-z_r)} + R e^{-im_1(z-z_r)}} \right]. \quad (6.61)$$

If we apply the boundary condition, $Z_1 = Z_2$ at $z = z_r$, we find

$$R = \frac{m_1 - i\mu_2}{m_1 + i\mu_2}. \quad (6.62)$$

Interestingly, the magnitude of R , given by $\sqrt{RR^*}$, where R^* is the complex conjugate of R , is equal to one, indicating perfect reflection of the wave and causing its energy to be trapped in the lower layer. This example illustrates the essence of wave reflection due to variations in the static stability, but the assumptions used are far too idealized for the real atmosphere, as they require two layers of infinite thickness. In the real atmosphere, multiple layers of finite thickness exist and reflection of the downward propagating waves off of the ground must also be considered. When the distance between the reflecting layer and the ground is such that all of the resultant waves are in phase, resonance occurs and the amplitude can grow in time when there is a continuous source of wave energy, such as when there is flow over a mountain (see Section 12.1). The layer containing the trapped wave is referred to as a *duct*. To see when resonance would occur in our simple model above, we consider a lower boundary at the base of the ducting layer and we look for a case in which the amplitude of the resultant wave goes to infinity. This can be thought of as the resonance case for waves continually forced at the bottom boundary, or as the case in which waves experiencing no continued forcing (*free waves*) would have large amplitude and persist as they travel horizontally. To find this solution, we set w'_1 from (6.59) equal to a constant forcing at the lower boundary given by $w_0 e^{i(kx-\omega t)}$, such that

$$A_1 = \frac{w_0}{e^{-im_1 z_r} + R e^{im_1 z_r}}, \quad (6.63)$$

which yields

$$w' = w_0 \left[\frac{e^{im_1(z-z_r)} + R e^{-im_1(z-z_r)}}{e^{-im_1 z_r} + R e^{im_1 z_r}} \right] e^{i(kx-\omega t)}. \quad (6.64)$$

From this expression, we see that the amplitude will go to infinity when the denominator goes to zero, which

occurs when $R = -e^{-i2m_1 z_r}$. Setting the R from (6.62) equal to this value, after multiplying the numerator and denominator by $(m_1 + i\mu_2)$, rearranging, and taking the square root of both sides leads to

$$ie^{im_1 z_r} = \frac{m_1 + i\mu_2}{(m_1^2 + \mu_2^2)^{1/2}}, \quad (6.65)$$

which can be expanded as

$$i \cos m_1 z_r - \sin m_1 z_r = \frac{m_1}{(m_1^2 + \mu_2^2)^{1/2}} + \frac{i\mu_2}{(m_1^2 + \mu_2^2)^{1/2}}. \quad (6.66)$$

Equating the real and imaginary parts, we obtain two equations,

$$\cos m_1 z_r = \frac{\mu_2}{(m_1^2 + \mu_2^2)^{1/2}} \quad (6.67)$$

$$\sin m_1 z_r = -\frac{m_1}{(m_1^2 + \mu_2^2)^{1/2}}. \quad (6.68)$$

We can combine (6.67) and (6.68) into one expression,

$$\tan m_1 z_r = -\frac{m_1}{\mu_2}, \quad (6.69)$$

which is a transcendental equation that can be solved graphically or numerically and yields a family of possible ducted modes. The wave with the longest vertical wavelength (called the *fundamental mode*) is less susceptible to dissipation than the shorter wavelength modes and is, therefore, the mode most likely to be observed.

Although we obtained this result assuming a wave with continuous forcing at the surface, we can obtain the same expression for a free wave with $w_0 = 0$ at the surface if we consider a two-layer atmosphere in which the static stability is constant within the lower layer and is zero above the reflection level; in this case we refer to the layer of trapped waves as a *temperature duct*. In this case, waves again propagate in the lower layer but are forced to satisfy the lower boundary condition $w_0 = 0$. In the upper layer, the solution is forced to decay with height. Thus, the solutions for the wave amplitudes in the two layers are given by

$$\hat{w}_1 = A \sin m_1 z \quad (6.70)$$

$$\hat{w}_2 = B e^{-\mu(z-z_r)}. \quad (6.71)$$

Applying the kinematic boundary condition at the interface (z_r) requires that

$$A \sin m_1 z_r = B. \quad (6.72)$$

The dynamic boundary condition can be derived by substituting (6.70) and (6.71) into the polarization

equations (6.48)–(6.50) to obtain the perturbation pressure amplitude at z_r for each layer,

$$\hat{p}_1 = i \frac{\omega m_1 A \rho_0}{k^2} \cos m_1 z_r, \quad (6.73)$$

$$\hat{p}_2 = -i \frac{\omega \mu B \rho_0}{k^2}, \quad (6.74)$$

which are then set equal to one another to obtain

$$\mu B = -m_1 A \cos m_1 z_r. \quad (6.75)$$

Dividing (6.72) by (6.75) yields the relationship that must be satisfied for waves to survive within the duct,

$$\tan m_1 z_r = -\frac{m_1}{\mu} \quad (6.76)$$

This condition, indeed, is the same as that for forced waves given by (6.69). It should be noted that our analysis of wave reflection has been performed using a single mode and examining reflection of this mode between layers. In reality, we are more concerned with the propagation of wave packets and the reflection of energy associated with these packets. As noted previously, these packets move in the opposite vertical direction to the individual waves. For the simple conditions used here, analysis of the reflection of individual waves versus reflection of wave packets does not affect the conclusions as no energy is transferred in the upper level. In more sophisticated multi-layer models, one must be careful to assess energy reflection and ensure the correct direction for energy propagation within the top layer (if it allows propagation).

Note that, according to (6.36), reflection also could occur owing to changes in the mean wind profile with height rather than changes in static stability (i.e., a layer exhibiting significant curvature of the wind speed profile with height, such as would be associated with a jet, could lead to a real value for m in a layer surrounding the jet, whereas m is imaginary in layers above and below the jet where the curvature of the wind profile is insignificant). In that case, the layer in which the waves are confined is referred to as a *wind duct*. Ducting due to curvature in the wind profile was found to occur in several observations of the *Morning Glory*, an impressive solitary wave, generally accompanied by an extensive roll cloud, observed in Australia.⁷

The examples given above have pleasing analytic solutions for wave trapping and require only that (6.69) or (6.76) be satisfied and that the oscillation frequency of the given wave lies between that of the upper level and that of the lower level, such that the wave propagates in the lower

level and decays in the upper level. However, in reality the conditions for trapping are more stringent than those given here because the upper evanescent layer does not extend to infinity and energy can be lost to a layer of wave propagation lying above the evanescent layer. In this case, wave reflection associated with the existence of a *critical level*, where the wind speed is equal to the phase speed, becomes important for wave trapping when the Richardson number is less than 0.25. Interesting behavior ensues as waves approach a critical level, and we discuss these important levels next.

6.4 Critical levels

Inspection of (6.36) reveals that a level at which the phase speed (c) is equal to the wind speed (\bar{u}) represents a singularity in the Taylor-Goldstein equation. A complete derivation of wave behavior near the critical level is outside the scope of this book, but a description of the results is useful. It is possible to write the Taylor-Goldstein equation in terms of the Richardson number at the critical level,

$$Ri = \frac{N^2}{\left| \frac{d\bar{u}}{dz} \right|^2} \quad (6.77)$$

and show that the wave stress ($-\rho_0 \bar{u} \bar{w}$), a measure of wave amplitude, is reduced by $e^{-2\pi\sqrt{Ri-0.25}}$ as a wave crosses the critical level.⁸ Thus, waves are nearly completely absorbed for values of $Ri > 0.25$. When nonlinear effects are included, one obtains results similar to those for the linear case when $Ri > 2.0$, but a greater amount of reflection occurs for $0.25 < Ri < 2.0$.⁹

Figure 6.7 shows the change in a gravity wave packet as it approaches a critical level with $Ri > 0.25$. As the gravity wave nears the critical level, the phase lines become horizontal and the vertical group velocity goes to zero such that the wave packet never actually reaches the critical level. In addition, $u \rightarrow \infty$ theoretically, but we do not observe infinite velocities, because the wave *breaks* and becomes turbulent before this happens. *Wave-breaking* involves the overturning of isentropes and development of static instability; the overturning of phase lines becoming horizontal as the critical level is approached. Recall from (6.32) that wave amplitude increases with height in a compressible atmosphere in which density decreases with height; wave-breaking also can result from this effect in the upper troposphere or stratosphere if wave amplification is sufficiently large. The destruction of waves from wave-breaking leads to *momentum deposition*

⁷ See Crook (1988).

⁸ See Booker and Bretherton (1967).

⁹ See Breeding (1971).

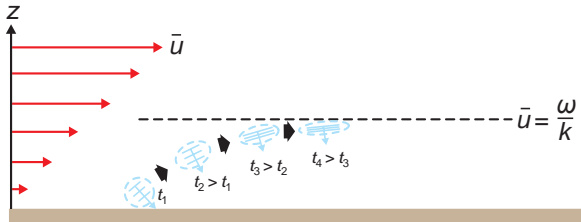


Figure 6.7 An internal gravity wave approaching a critical level. (Adapted from Hooke [1986], based on the theory by Booker and Bretherton [1967].)

within the layer underlying the critical level, where the upward momentum flux decreases with height to zero, resulting in momentum flux convergence. In some cases, wave-breaking can excite waves absent from the original spectrum.

Although we tend to think of critical levels as places in which the wind velocity matches a set phase speed for a wave, we can alternatively think of them as a location where the intrinsic frequency goes to zero such that the phase speed is determined solely by the wind speed. Figure 6.7 indicates a change in the tilt of the phase lines and the associated intrinsic frequency with height, as expected (assuming N is constant over the entire depth) in order that the phase speed in the x direction remain constant in the presence of varying u_0 . As the wave packet approaches the critical layer, the restoring force $B \cos \phi$ becomes increasingly small as parcel oscillations become increasingly horizontal, such that the wave simply becomes part of the mean wind.

When $Ri < 0.25$, fundamentally different behavior occurs, as perhaps expected given our discussion of Kelvin-Helmholtz instability (Section 3.5.2). In this case, the layer is unstable to perturbations, and a wave encountering this level is able to extract energy from the mean flow. In this case, the reflection coefficient can exceed one, a condition referred to as *overreflection*. Overreflection figures prominently in the analysis of wave trapping by Lindzen and Tung (1976, hereafter LT76), who outlined the necessary conditions for the ducting of internal gravity waves. This process is discussed in the next section.

6.5 Structure and environments of ducted mesoscale gravity waves

LT76 examined the reflection and transmission of waves in a three-layer model of the atmosphere (Figure 6.8), with the bottom two layers similar to those we used to examine reflection (i.e., a stable layer—the duct—topped by a less stable layer) and the top layer representing an additional

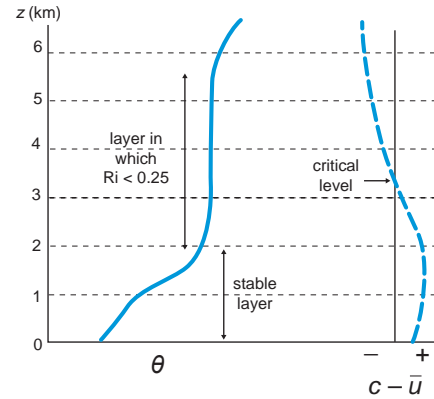


Figure 6.8 Schematic representation of the typical environmental conditions for ducted gravity waves.

stable layer in which wave energy propagation can occur. Note that the addition of the stable layer aloft changes the results compared with our two-layer model, in which the evanescent region was presumed to be infinite, because it provides a mechanism for energy loss to the system. Thus, the reflection coefficient between the lowest two layers in the three-layer model has a magnitude less than one. When the reflection coefficient has a magnitude less than one, it is impossible to make the denominator in (6.53) vanish, and the atmosphere is unable to support free waves for which there is no forcing. However, if the reflection coefficient is close to unity, LT76 showed that the response to a small forcing will be large (enabling *almost free waves*) if

$$1 + \cos(4\pi D/\lambda_z) \approx 0 \quad (6.78)$$

where D is the depth of the duct, λ_z is the vertical wavelength, and it was also assumed that there is little phase shift between the incident and reflected waves. From (6.78), we see that the depth of the duct needed depends on the vertical wavelength according to

$$\frac{D}{\lambda_z} = \frac{1}{4} + \frac{1}{2}n, \quad n = 0, 1, 2, \dots \quad (6.79)$$

As stated previously, waves with relatively short wavelengths are more prone to dissipation, so we expect the longest (i.e., $n = 0$) wave of those in (6.79) to dominate, which indicates that for an observed value of λ_z a corresponding duct must have a depth of $\lambda_z/4$. Though this is an important result, it is not practical to apply because the exact value of λ_z is normally not revealed in standard observations. However, horizontal phase speeds are readily observed by tracking pressure anomalies. We can relate the depth

requirement to an observed phase speed by noting that, for long wavelengths (i.e., small aspect ratios) characteristic of these hydrostatic waves, $k^2 \ll m^2$ such that, from (6.41),

$$m^2 = \left(\frac{2\pi}{\lambda_z} \right)^2 \approx \frac{N^2}{(c - \bar{u})^2}, \quad (6.80)$$

where c is now the horizontal phase speed and \bar{u} is the component of the environmental wind in the direction of wave propagation. Solving for λ_z ,

$$\lambda_z \approx \frac{2\pi(c - \bar{u})}{N}, \quad (6.81)$$

which, combining (6.79) and (6.81) for the $n = 0$ mode, yields an intrinsic phase speed

$$c - \bar{u} = \frac{2ND}{\pi}. \quad (6.82)$$

This provides a useful test when assessing the likelihood that an observed pressure pattern is due to a ducted wave. For an intrinsic phase speed of 25 m s^{-1} and average values of N for a stable layer, one can deduce that the corresponding duct would have to be approximately 3 km deep. If no stable layer of this depth exists, the observed phenomenon is not a ducted wave. Note that we are unable to specify the horizontal wavelength as we have removed k owing to the hydrostatic approximation. The conditions for a duct as outlined by LT76 may be summarized as follows:

- The duct must be statically stable.
- The duct must be sufficiently thick to accommodate one-quarter of the vertical wavelength of the wave. This criterion is usually tested using the observed phase speed and deducing the corresponding vertical wavelength.
- The duct must be below a layer with significant reflection (e.g., $>85\%$ for the $n = 0$ mode) such that a wave can be sustained for at least two cycles.
- The duct cannot contain a critical layer as this would lead to absorption of the wave within the stable layer of the duct.

The criteria above tell us only the characteristics of a ducting layer, and do not specify the atmospheric conditions leading to sufficient reflection in the layer above. Given our prior discussions of reflection, we can assume that at the very least good reflection for a particular wavelength requires that the waves be evanescent in the layer above. If the evanescent layer extends to infinity, this is sufficient for perfect reflection. For a finite evanescent layer, the reflection due to the change in stability alone would be less than one

but is greatly enhanced if the layer contains a critical level with $\text{Ri} < 1/4$, in which case over-reflection can occur. Even if the flow speed does not quite produce a critical level but does get close to $c - \bar{u} = 0$ when $\text{Ri} < 1/4$, the reflectivity is enhanced.¹⁰ In order to achieve a small Ri , the layer must have shear and small values of static stability. For an unsaturated atmosphere, this requires that N is small. If the environment is saturated, the moist Brunt-Väisälä frequency, N_m , should be used. LT76 assume that perturbations in a conditionally unstable and approximately saturated environment will experience a stability due to a mean of the dry and saturated stabilities, which is generally much lower than the dry stability alone. An observed sounding associated with a case of a large-amplitude ducted gravity wave is shown in Figure 6.9. The sounding contains all of the necessary conditions specified by LT76 for ducting, and a fairly reasonable match between the expected and observed phase speed was noted.¹¹

Figure 6.10 shows the structure of a hydrostatic ducted mesoscale gravity wave which results from the superpositioning of upward and downward propagating wave modes and corresponding resonance in the absence of ambient flow.¹² The largest upward vertical velocities and low-level convergence are a quarter of a wavelength downstream of the wave crest, whereas surface pressure is highest directly beneath the wave crest, as expected hydrostatically. Surface pressure is lowest beneath the troughs of the waves, which lag the region of largest downward vertical velocities by a quarter of a wavelength. The strongest surface winds relative to the moving gravity wave are found beneath the ridge and trough. Large-amplitude gravity waves have pressure perturbations of several millibars, in contrast to the everyday small-amplitude gravity waves which are associated with

¹⁰ Numerical experiments (Wang and Lin, 1999) indicate that the LT76 criteria may represent a subset of possible ducted modes due in part to the assumption made by LT76 of zero phase shift during reflection, which may not be a valid assumption when the stability in the middle layer is not close to neutral. In particular, nonlinear simulations indicate that ducting may occur over a broader range of Ri in the presence of a critical level when the reflection coefficient is close to one and the ducting layer has a thickness close to the optimal value, and a critical level may not be necessary when a stable layer of thickness $(0.25 + n/2)D$ is capped by a thick nearly neutral layer with $0.01 < \text{Ri} < 100$. The success of LT76 in comparison with observations is likely due to the fact that shear and stability profiles outside those they considered are not as commonly observed. For example, reflection without a critical level requires a very deep neutral layer, whereas reflection with a critical layer but large Ri implies a very deep weak-shear layer. Wang and Lin (1999) state that ‘the criteria proposed by LT76 is still useful in explaining the maintenance of some long-lasting waves in the real atmosphere, although it does not cover all possible observed cases’.

¹¹ See Bosart and Sanders (1986).

¹² For a discussion of gravity wave structure in the presence of ambient flow including vertical shear, see Koch and Gorus (1988).

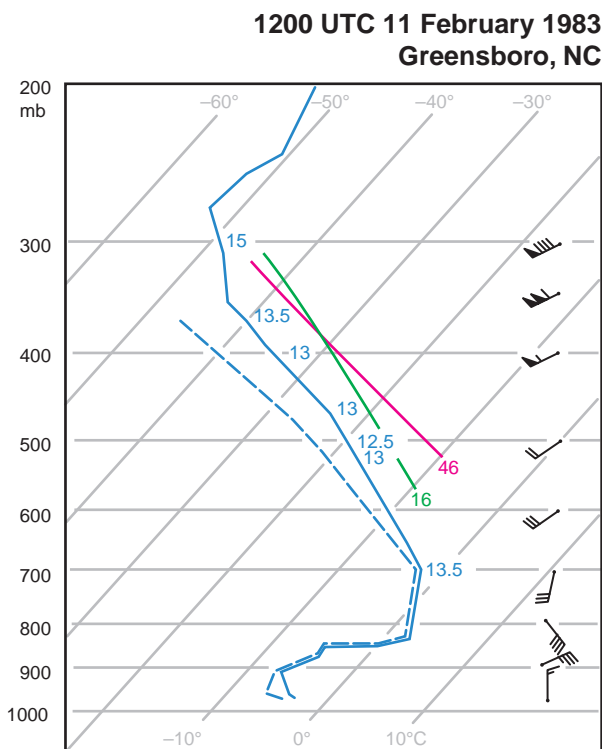


Figure 6.9 Sounding from Greensboro, NC, during the event shown in Figure 6.1. Numbers plotted along the sounding are the θ_w values in $^{\circ}\text{C}$, and the two curves labeled '16' and '46' are the moist adiabat for $\theta_w = 16^{\circ}\text{C}$ and the 46°C dry adiabat, respectively. (Adapted from Bosart and Sanders [1986].)

pressure perturbations of just a fraction of a millibar. Fluctuations as large as 10 mb have been observed in extreme cases, with pressure tendencies as large as 10 mb h^{-1} (in extreme cases, forecasters have wrongly attempted to ‘correct’ model forecasts of cyclone tracks after being fooled by surface isallobar fields heavily influenced by mesoscale gravity waves). Moreover, the horizontal wavelengths tend to be much larger than those of typical gravity waves (e.g., meso- α scale [100–400 km] rather than meso- β or meso- γ scale). A single crest of a ducted gravity wave can often be tracked for several hours as shown in Figure 6.1.

In a study of several ducted gravity wave cases, Uccellini and Koch (1987) identified common synoptic settings for their cases (Figure 6.11). The common features in these settings include a low-level inversion associated with a front and an upper-level jet streak propagating toward a ridge axis. The low-level inversion is important for serving as a duct, and the upper-level conditions are associated with flow imbalance, which initiates inertia-gravity waves (i.e., gravity waves for which the effect of the Coriolis force is not negligible).¹³ Thus, both the energy source for the waves and a mechanism for trapping the wave energy exist in this scenario.

6.6 Bores

Bores are just gravity waves that have been triggered by the intrusion of a density current into a low-level stable layer

¹³ See Zhang *et al.* (2001) and Koch *et al.* (2005) for in-depth discussions and examples of the generation of gravity waves as a result of flow imbalance.

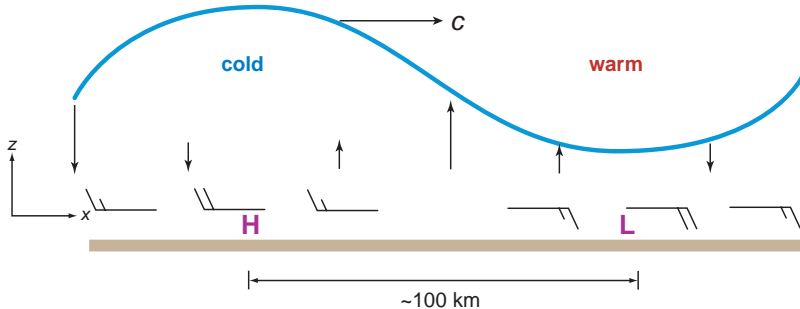


Figure 6.10 Idealized vertical cross-section of a linear plane gravity wave, with no basic current, propagating toward the right at speed c . The heavy sinusoidal line is a representative isentropic surface or a temperature inversion. Cold and warm anomalies are indicated, as are a surface pressure maximum ('H') and minimum ('L'). (Adapted from Bosart and Sanders [1986] and Eom [1975].)

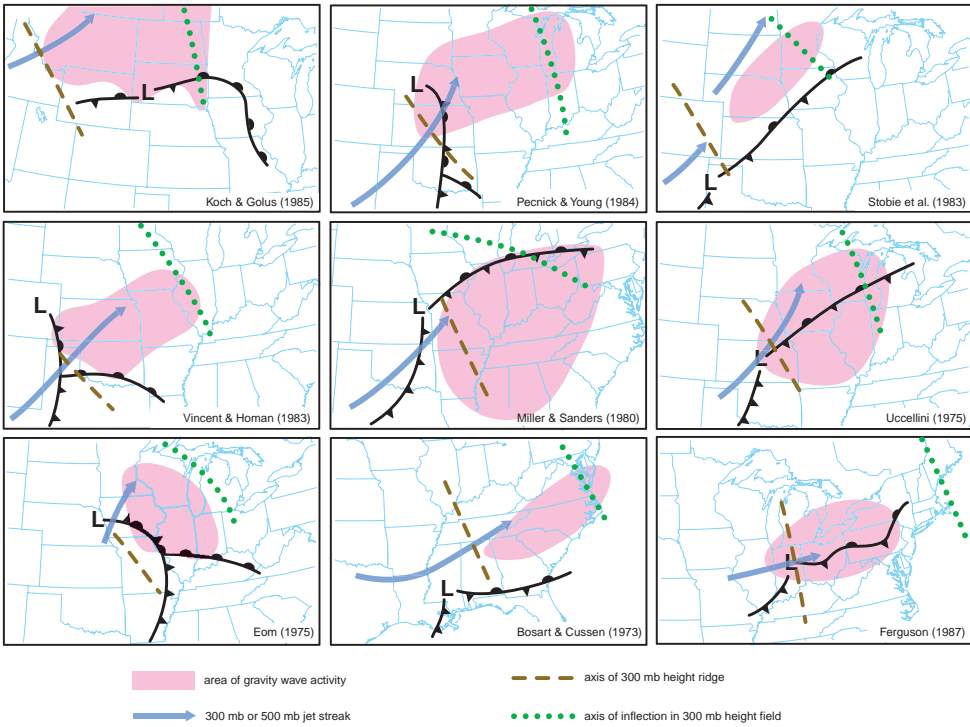


Figure 6.11 A compilation of synoptic settings in which significant mesoscale gravity waves have been documented. (Adapted from Uccellini and Koch [1987].)

(Figures 6.12–6.15; it is not a coincidence that the bore in Figure 6.15 was observed at night). Bores may evolve into a train of amplitude-ordered solitary waves (soliton), which maintain their form owing to a balance between nonlinear effects, which tend to steepen a waveform, and dispersion, which tends to spread out a waveform. Observations of solitons indicate an impressive alteration of the low-level atmospheric structure due to their passage (Figure 6.15).¹⁴

Laboratory experiments show that three different types of bores can be produced when a solid obstacle is moved along the surface in a two-layer fluid, with the mixing behavior between the two fluids depending on the strength of the bore as measured by h_1/h_0 , the ratio of the mean bore depth to the pre-bore inversion depth (Figures 6.12 and 6.13).¹⁵ Undular (smooth) bores, with very little mixing between the two fluids, are found to occur when $1 < h_1/h_0 < 2$. In this case, undulations are produced by flow over the obstacle and move upstream relative to the obstacle. When $2 < h_1/h_0 < 4$, the bore exhibits similar undulations but there is increased mixing between the two

fluids due to shear instability at the interface. For even greater bore strength, $h_1/h_0 > 4$, the bore appearance is like that of a density current, with mixing along the interface, rather than smooth undulations, dominating the form behind the leading edge. For internal bores (i.e., those in a environment with a significant change in density across the interface but no free surface), the mixing process results in a deepened mixed layer in the wake of the bore as it moves forward. In this manner, a bore can significantly influence the final height of an inversion layer as well as the depth of a moist layer (Figure 6.15), both of which have implications for convection initiation.

The speed of the bore based on hydraulic theory is given by

$$\frac{C}{\sqrt{g'h_0}} = \left[\frac{1}{2} \frac{h_1}{h_0} \left(1 + \frac{h_1}{h_0} \right) \right]^{1/2} \quad (6.83)$$

where C is the bore speed in a reference frame for which the fluid upstream of the bore is at rest, and $g' = g(\rho_1 - \rho_2)/\rho_1$.¹⁶ Owing to the theoretical assumptions upon which it is based, (6.83) is found to work well in the absence of

¹⁴ See Koch *et al.* (2008).

¹⁵ See Rottman and Simpson (1989).

¹⁶ See Rottman and Simpson (1989).

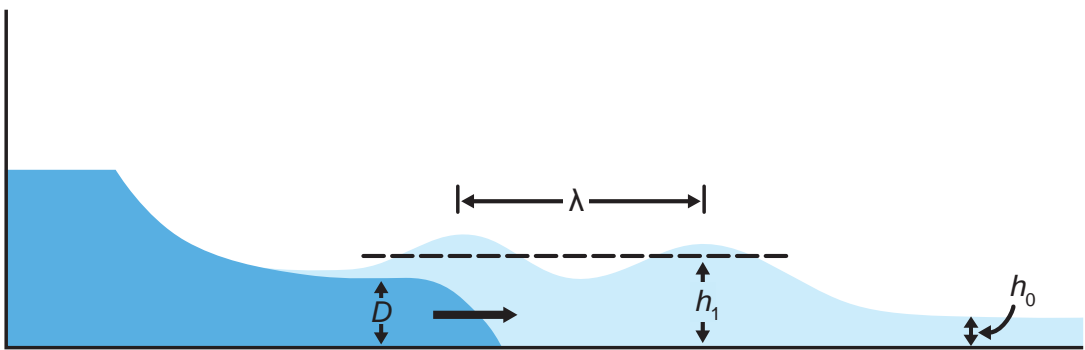


Figure 6.12 Generation of a bore of depth h_1 , by an advancing density current of depth D , intruding into a stable layer of depth h_0 . Shading indicates the density of the fluid, with darker shading indicating denser fluid. (Adapted from Rottman and Simpson [1989].)

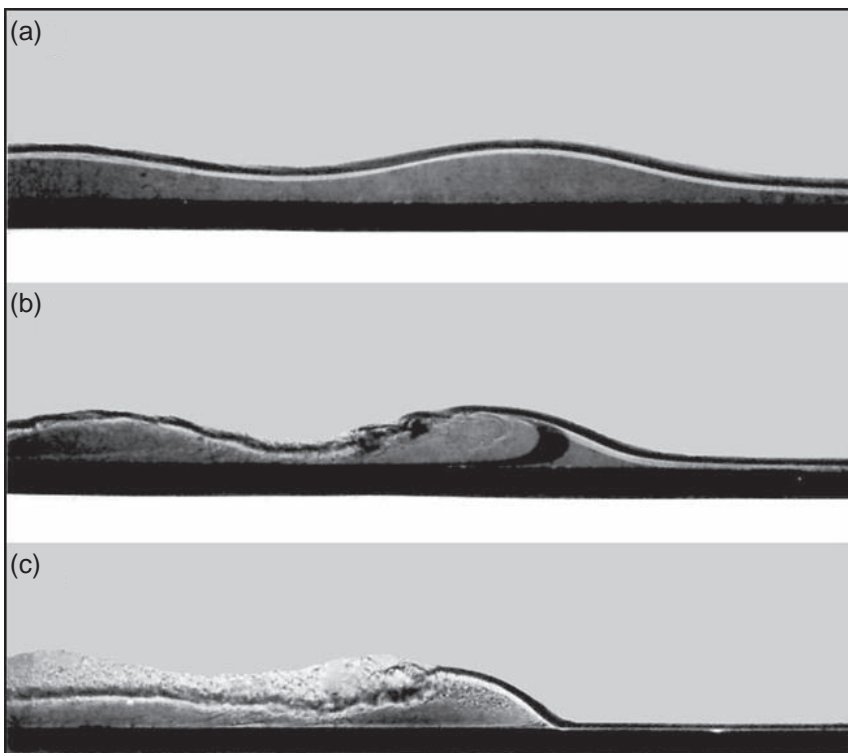


Figure 6.13 Photographs of three types of bore generated by towing an obstacle through a two-layer fluid. (a) A smooth, undular bore obtained when $1 < h_1/h_0 < 2$. (b) A bore with some mixing downstream of the first crest, obtained when $2 < h_1/h_0 < 4$. (c) A bore with the appearance of a gravity wave, obtained when $h_1/h_0 > 4$. (From Rottman and Simpson [1989].)

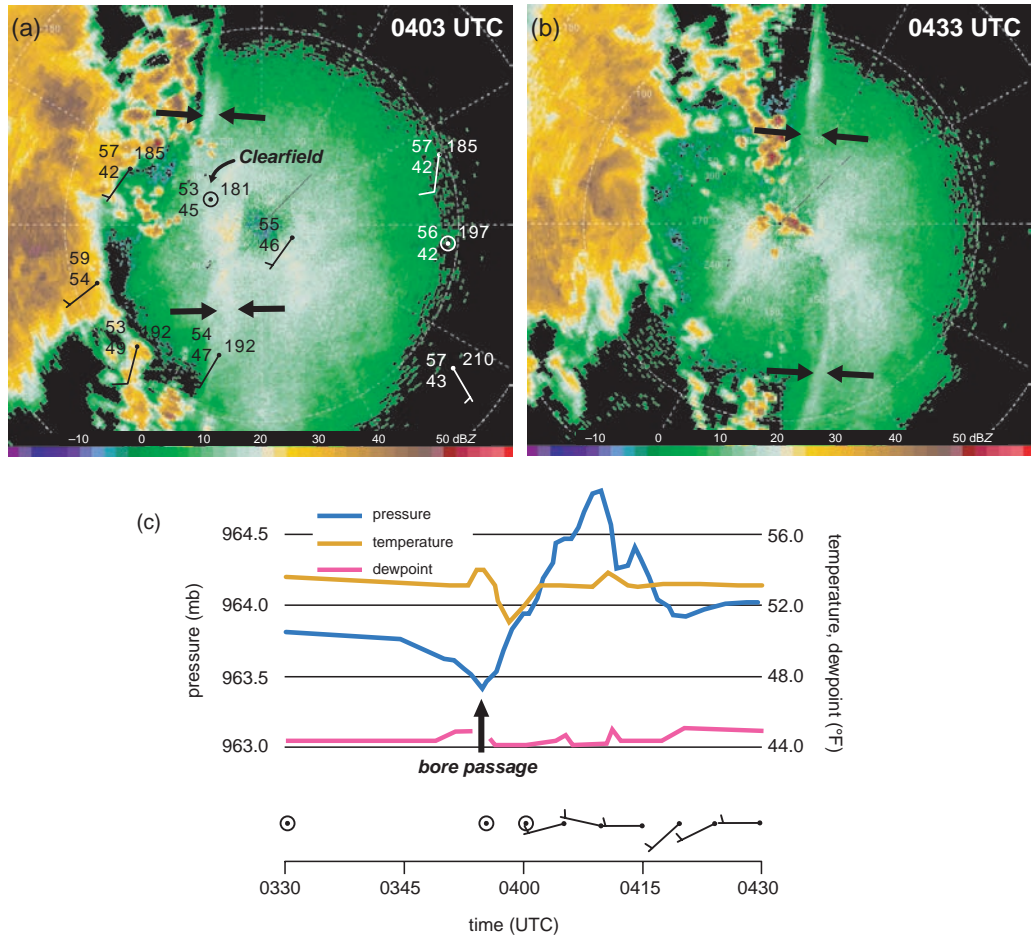


Figure 6.14 Reflectivity display of the State College, PA, WSR-88D (KCCX) at (a) 0403 UTC and (b) 0433 UTC on 14 May 2005. Range rings are every 50 km. A bore, evident as a reflectivity fineline, passes from west to east over the radar during this time period. The location of the bore is indicated with arrows. Surface observations from 0400 UTC are overlaid in (a); station models show temperature ($^{\circ}$ F), dewpoint ($^{\circ}$ F), mean sea level pressure (tenths of mb, with the leading '10' dropped), and winds (knots). (c) 1-min surface observations at Clearfield, PA. The location of Clearfield is indicated in (a). Notice the pressure jump associated with the bore passage, as well as the fact that, after the initial pressure jump, the post-bore pressure remained ~ 0.2 mb higher than the pre-bore pressure. The surface temperature and dewpoint remained relatively constant as the bore passed by. The surface winds were calm prior to the arrival of the bore (winds were missing from 0335 to 0350 UTC), but acquired a westerly component following the arrival of the bore.

mixing (i.e., for undular bores as in Figure 6.13a), but for $h_1/h_0 > 2$ (Figure 6.13b,c) the bore speed is better described as the speed of a density current with head height h_1 .¹⁷ For bores with $h_1/h_0 > 4$, the bore speed may be nearly equal to that of the density current such that the bore remains in the same position relative to the density current. In contrast,

the undular bores have a speed higher than that of the density current and are found to take a bit of the density current fluid with them in a shedding process that disrupts the density current front temporarily.¹⁸

In surface observations, the passage of a bore can be distinguished from the passage of a density current by

¹⁷ See Wood and Simpson (1984).

¹⁸ See Rottman and Simpson (1989).

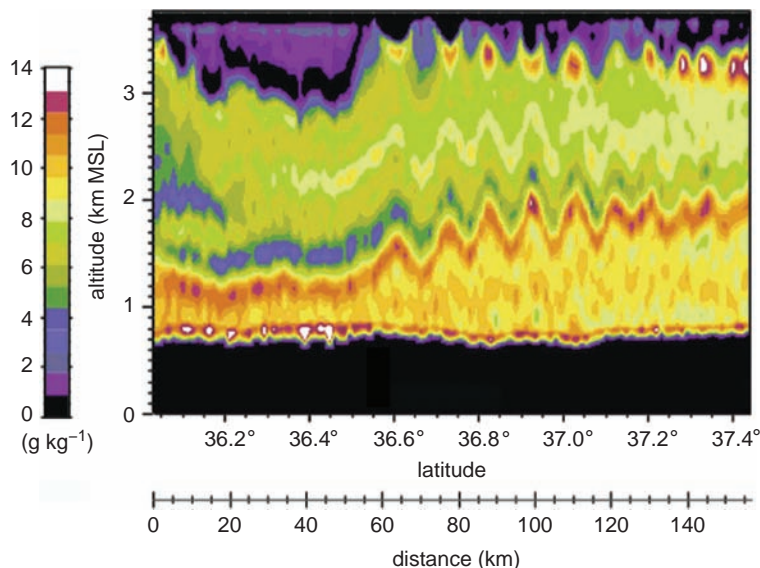


Figure 6.15 Vertical cross-section of the water vapor mixing ratio field observed by an airborne downward-pointing DIAL lidar (LEANDRE II) during the International H₂O Project (IHOP) from 0555 to 0616 UTC 20 June 2002. The waves apparent in the moisture field originated from a bore–soliton system. Lifting by the soliton has created an oscillatory, nearly saturated layer at 3.4 km MSL as well as an increased height for the low-level inversion. The lack of wave tilt with height is consistent with trapping of wave energy, in this case thought to be the result of curvature in the wind profile associated with a strong low-level jet. (From Koch *et al.* [2008].)

analyzing the temperature trace. As shown in Section 5.3, a density current is associated with a significant hydrostatic pressure jump due to the cold air behind the leading edge. Bores are also associated with a hydrostatic pressure jump due to cooling in the overlying column, but the cooling is above the surface and due to adiabatic ascent rather than the advection of cold air near the surface. Thus, the surface temperature falls after the passage of a density current, but no appreciable surface temperature change accompanies the passage of a bore (Figure 6.14).

Further reading

- Booker and Bretherton (1967).
 Bosart and Sanders (1986).
 Bosart L. F., and A. Seimon, 1988: A case study of an unusually intense atmospheric gravity wave. *Mon. Wea. Rev.*, **116**, 1857–1886.
 Bretherton, F. P., 1966: The propagation of groups of internal gravity waves in a shear flow. *Quart. J. Roy. Meteor. Soc.*, **92**, 466–480.
 Crook (1988).
 Hooke (1986).
 Jones, W. L., Ducting of internal gravity waves on a stable layer with shear. *J. Geophys. Res.*, **77**, 3879–3885.
 Koch, S. E., and R. E. Golus, 1988: A mesoscale gravity wave event observed during CCOPE. Part I: Multiscale statistical analysis of wave characteristics. *Mon. Wea. Rev.*, **116**, 2527–2544.
 Koch, S. E., and C. O’Handley, 1997: Operational forecasting and detection of mesoscale gravity waves. *Wea. Forecasting*, **12**, 253–281.
 Koch, S. E., B. D. Jamison, C. Lu, T. L. Smith, E. I. Tollerud, C. Girz, N. Wang, T. P. Lane, M. A. Shapiro, D. D. Parrish, and O. R. Cooper, 2005: Turbulence and gravity waves within an upper-level front. *J. Atmos. Sci.*, **62**, 3885–3908.
 Koch *et al.* (2008).
 Lin, Y.-L., 2007: *Mesoscale Dynamics*. Cambridge University Press.
 Lindzen and Tung (1976).
 Miller, D. A., and F. Sanders, 1980: Mesoscale conditions for the severe convection of 3 April 1974 in the east-central United States. *J. Atmos. Sci.*, **37**, 1041–1055.
 Nappo (2002).
 Rottman and Simpson (1989).

- Schneider (1990).
Uccellini and Koch (1987).
Wang and Lin (1999).
Wood and Simpson (1984).
Zhang, F., 2004: Generation of mesoscale gravity waves in upper-tropospheric jet-front systems. *J. Atmos. Sci.*, **61**, 440–457.

Zhang, F., S. E. Koch, C. A. Davis, and M. L. Kaplan, 2001: Wavelet analysis and the governing dynamics of a large-amplitude mesoscale gravity wave event along the East Coast of the United States. *Quart. J. Roy. Meteor. Soc.*, **127**, 2209–2245.

PART III

Deep Moist Convection

7

Convection Initiation

7.1 Requisites for convection initiation and the role of larger scales

What we shall refer to as *deep moist convection* (DMC) arises when air is lifted to saturation and subsequently achieves positive buoyancy, such that it may rise to great heights. In other words, the initiation of DMC, which we shall simply refer to as *convection initiation*, requires that air parcels reach their level of free convection (LFC) and subsequently remain positively buoyant over a significant upward vertical excursion. Thus, convective available potential energy (CAPE) is a necessary, albeit insufficient, condition for convection initiation.

The location and timing of convection initiation is of acute interest to forecasters owing to the obvious association between convective storms and severe weather, in addition to less obvious impacts, such as the effects of convection on energy demand, future numerical weather predictions, and subsequent convective storm development. Dramatic warm season weather forecast failures are often the result of an inability to anticipate the initiation of DMC, or forecasting DMC that fails to develop. Convection initiation forecasting skill arguably has advanced at a slower rate than our ability to anticipate convective storm type, organization, and associated severe weather threats. As we shall see, there is much more to the problem than assessing parameters derived from thermodynamic diagrams. Pinpointing where and when convective storms are likely to be initiated is a complex function of vertical motions ranging from the scale of thermals to the synoptic scale, mesoscale temperature and moisture inhomogeneities, and the mean stratification that largely results from synoptic-scale processes.

The presence of an LFC and CAPE requires a relatively large lower to middle tropospheric lapse rate (larger than the moist adiabatic lapse rate, on average) and lower tropospheric moisture (Figure 7.1; see also Figure 2.9). The difficulty in accurately predicting convection initiation stems from the fact that the presence of CAPE is not a sufficient condition for convection initiation. Air typically requires some forced ascent in order to reach the LFC, owing to the presence of at least some convective inhibition (CIN) on most environmental soundings. Deep moist convection is commonly initiated along air mass boundaries such as synoptic fronts, drylines, outflow boundaries, and sea breezes (Figure 7.2). Convective storms can also be initiated by orographic circulations driven by the heating of elevated or sloped terrain, and by forced lifting by ducted gravity waves.

Synoptic-scale dynamics often prime the mesoscale environment for convection initiation by way of large-scale mean ascent, which tends to reduce CIN and deepen the low-level moist layer. On the other hand, synoptic-scale dynamics also can discourage convection initiation by way of mean subsidence, which has the opposite effects. Large-scale vertical motions arguably can be anticipated reasonably well from pattern recognition and application of synoptic meteorology principles (e.g., quasigeostrophic theory), in conjunction with numerical model guidance. Synoptic-scale processes typically cannot be overlooked in making forecasts of convection initiation (Figure 7.3), despite the fact that convection initiation is a distinctly mesoscale process.

7.1.1 Lapse rate tendency equation

Although the process of getting parcels to their LFC is an intrinsically mesoscale process, the large scale sets the stage

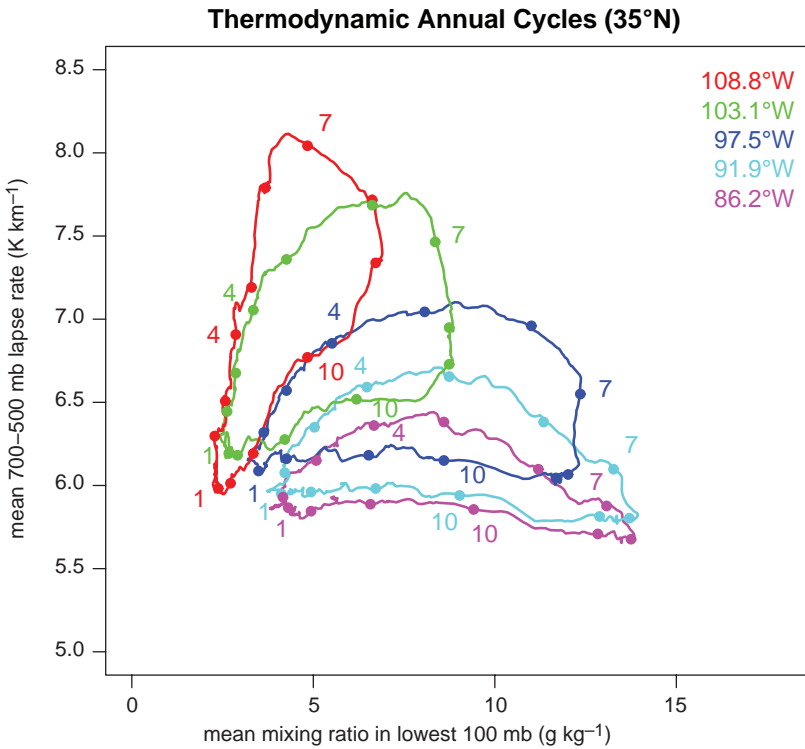


Figure 7.1 Annual cycles of midlevel (700–500 mb) lapse rates versus the mean water vapor mixing ratio in the lowest 100 mb, derived from North American reanalysis data, at five locations in a west-east line located at latitude 35°N, running from approximately northwestern New Mexico (108.8°W) to south central Tennessee (86.2°W). Filled circles along each loop indicate the first day of the month (January, April, July, and October are labeled with the numbers 1, 4, 7, and 10, respectively). CAPE is maximized when rich low-level moisture is overrun by large midlevel lapse rates. This generally occurs in the spring and summer months. Note the differences in the cycles from west to east. The cycles in the western United States are dominated by lapse rate changes from winter to summer, whereas the eastern United States cycles are dominated by moisture changes from winter to summer. Courtesy of Harold Brooks.

by modulating the CAPE and CIN, accomplished in part by modifications of the lapse rate. Below we investigate the processes by which the environmental lapse rate may be altered.

We begin with the first law of thermodynamics written as

$$q = c_p \frac{dT}{dt} - \alpha \frac{dp}{dt}, \quad (7.1)$$

where q is the heating rate per unit mass, p is pressure, T is absolute temperature, $\alpha = \rho^{-1}$ is the specific volume, and c_p is the specific heat at constant pressure. All variables are understood to represent the large-scale environment. Assuming hydrostatic conditions, it follows that

$$q = c_p \left(\frac{\partial T}{\partial t} + \mathbf{v}_h \cdot \nabla_h T + w \frac{\partial T}{\partial z} \right) + gw, \quad (7.2)$$

where \mathbf{v}_h is the horizontal wind velocity and w is the vertical velocity component. Differentiating (7.2) with respect to z and multiplying both sides by -1 gives

$$\begin{aligned} -\frac{\partial q}{\partial z} &= c_p \left[\frac{\partial}{\partial t} \left(-\frac{\partial T}{\partial z} \right) + \mathbf{v}_h \cdot \nabla_h \left(-\frac{\partial T}{\partial z} \right) \right. \\ &\quad \left. + w \frac{\partial}{\partial z} \left(-\frac{\partial T}{\partial z} \right) - \frac{\partial \mathbf{v}_h}{\partial z} \cdot \nabla_h T - \frac{\partial w}{\partial z} \frac{\partial T}{\partial z} \right] \\ &\quad - g \frac{\partial w}{\partial z}, \end{aligned} \quad (7.3)$$

where we have neglected the effects of moisture on c_p (i.e., c_p is treated as a constant). Making use of the definitions $\gamma \equiv -\partial T / \partial z$ and $\Gamma_d \equiv g / c_p$, where γ and Γ_d are the lapse rate of environmental temperature and the dry adiabatic lapse rate, respectively, and solving for $\partial \gamma / \partial t$, gives the result

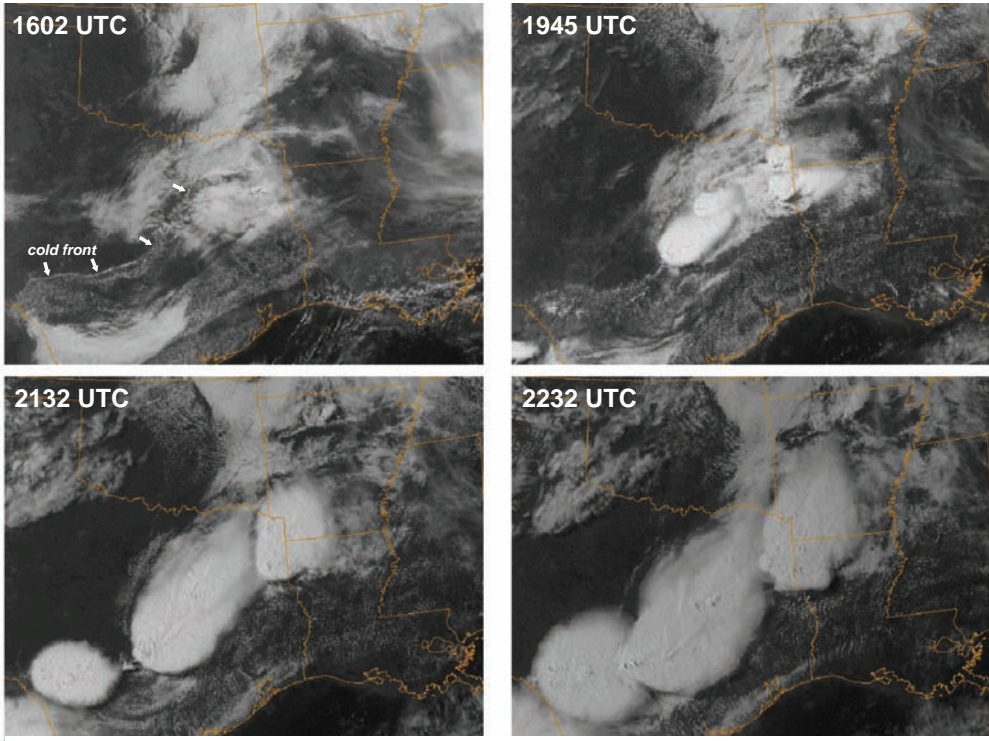


Figure 7.2 In the absence of favored topographic features that act as elevated buoyancy sources, DMC tends to be initiated along air mass boundaries, which are usually accompanied by a wind shift and convergence. This allows forecasters to enjoy at least modest predictability with regard to anticipating the location of convection initiation, for such boundaries are fairly easily observable in routinely available synoptic surface observations and radar and satellite data. The sequence of visible satellite images shows the development of a line of severe thunderstorms along a cold front on 27 May 1997. The town of Jarrell, TX, was devastated by a tornado during this event.

$$\frac{\partial \gamma}{\partial t} = -\mathbf{v}_h \cdot \nabla_h \gamma - w \frac{\partial \gamma}{\partial z} + \frac{\partial \mathbf{v}_h}{\partial z} \cdot \nabla_h T \quad \text{I} \quad \text{II} \quad \text{III}$$

$$+ \frac{\partial w}{\partial z} (\Gamma_d - \gamma) - \frac{1}{c_p} \frac{\partial q}{\partial z}. \quad \text{IV} \quad \text{V}$$
(7.4)

Terms I and II are the horizontal and vertical lapse rate advection (Figures 7.4 and 7.5), respectively. Term III, when combined with the horizontal lapse rate advection (term I), represents the effects of differential temperature advection (Figure 7.6):

$$\frac{\partial \mathbf{v}_h}{\partial z} \cdot \nabla_h T - \mathbf{v}_h \cdot \nabla_h \gamma = -\frac{\partial}{\partial z} (-\mathbf{v}_h \cdot \nabla_h T). \quad (7.5)$$

(Note that only the vertical shear of the ageostrophic wind contributes to $\frac{\partial \mathbf{v}_h}{\partial z} \cdot \nabla_h T$ because $\frac{\partial \mathbf{v}_g}{\partial z} \cdot \nabla_h T = 0$.)

Term IV is sometimes called the *stretching* term. When $\partial w / \partial z > 0$ (as would be the case below the level of nondivergence when rising motion is present) and $\gamma < \Gamma_d$, the term acts to increase the environmental lapse rate (Figure 7.7). The term vanishes when $\gamma = \Gamma_d$ because the vertical advection of temperature cancels the temperature changes owing to adiabatic expansion/compression both above and below the level of interest, allowing the level to maintain a dry adiabatic lapse rate. Term V represents differential diabatic heating. If diabatic heating decreases (increases) with height, the lapse rate is increased (decreased) (Figure 7.8), with the opposite being true for diabatic cooling. On the synoptic scale, terms I–V typically have magnitudes of $10^{-7} \text{ K m}^{-1} \text{ s}^{-1}$, $10^{-8} \text{ K m}^{-1} \text{ s}^{-1}$, $10^{-8} \text{ K m}^{-1} \text{ s}^{-1}$, $10^{-8} \text{ K m}^{-1} \text{ s}^{-1}$, and $10^{-9} \text{ K m}^{-1} \text{ s}^{-1}$, respectively. Thus the largest contribution tends to be from the horizontal advection of lapse rate. On the mesoscale, terms II–V easily

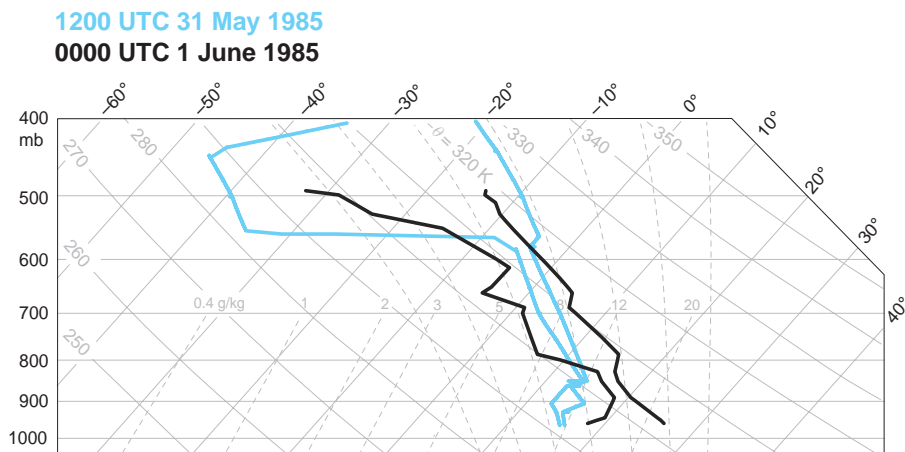


Figure 7.3 Soundings from Pittsburgh, PA, at 1200 UTC 31 May 1985 (blue) and 0000 UTC 1 June 1985 (black). Between 1200 and 0000 UTC, the mean tropospheric lapse rate has undergone significant changes, probably as the result of a number of large-scale processes acting in unison (e.g., insolation, lapse rate advection/differential temperature advection, stretching effect, etc.). The low-level moisture also increased by several g kg^{-1} during the same 12 h period, primarily as a result of moisture advection. The increase in lapse rate and low-level moisture between 1200 and 0000 UTC led to the development of large CAPE (the lifted index decreased from +3 to -7; the lifted index is the temperature difference between the environmental 500 mb temperature and the temperature of an air parcel that has been lifted to 500 mb from the surface, with negative indices indicating that the lifted parcel is warmer than the environment at 500 mb). (Large vertical wind shear also accompanied the large instability; the worst tornado outbreak in the history of Pennsylvania was in progress not far from Pittsburgh at 0000 UTC.)

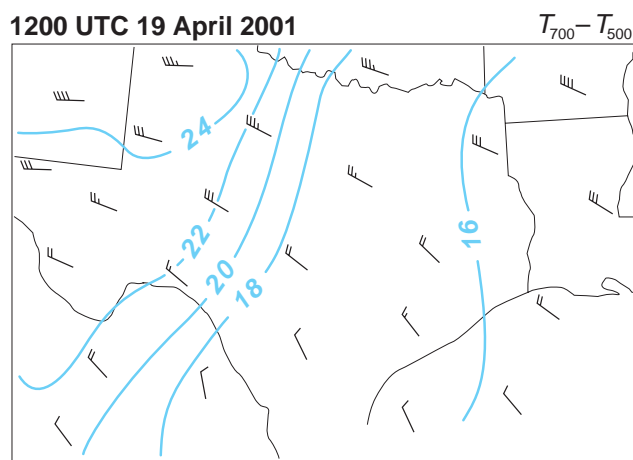


Figure 7.4 Analysis of the environmental temperature difference between 500 and 700 mb (K), which is a bulk measure of the midlevel lapse rate (a temperature difference of 27 K between 500 and 700 mb corresponds to an approximately dry adiabatic environmental temperature profile), revealing the presence of horizontal lapse rate advection. Wind barbs depict the mean wind in the 500–700 mb layer. Large lapse rates from the high terrain of northern Mexico and eastern New Mexico are being advected toward the southern Great Plains of the United States. This common warm season phenomenon leads to the formation of the elevated mixed layer that caps soundings in the Great Plains region.

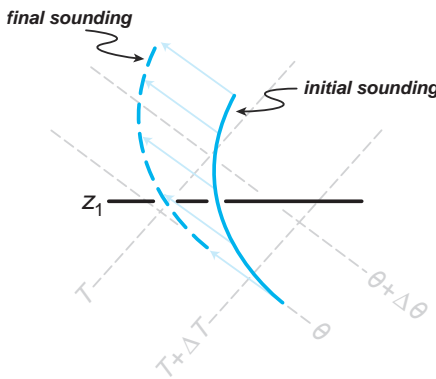


Figure 7.5 Schematic thermodynamic diagram illustrating the effect of vertical lapse rate advection. The light blue arrows indicate dry adiabatic parcel displacements. At level z_1 , $\partial\gamma/\partial z < 0$, so when upward motion is imposed ($w > 0$ but $\partial w/\partial z = 0$, so that all of the parcels are displaced upward by the same distance) larger lapse rates are advected from below z_1 upward to z_1 , increasing the lapse rate there. Note that this process occurs adiabatically, so that cooling has occurred at z_1 in addition to increasing the lapse rate there. This cooling associated with upward motion is typically more important for cap removal and thunderstorm initiation than just the increasing lapse rate. For example, dry adiabatic large-scale ascent always leads to cooling (and cap weakening) when lapse rates are less than dry adiabatic, but lapse rate changes resulting from large-scale ascent may or may not be significant, depending on the initial γ , $\partial\gamma/\partial z$, and $\partial w/\partial z$.

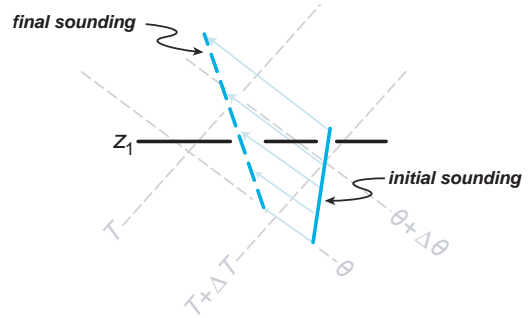


Figure 7.7 Schematic thermodynamic diagram illustrating the stretching effect on lapse rate. In this example, $\Gamma_d > \gamma$ and $\partial w/\partial z > 0$, therefore the lapse rate at level z_1 increases in time. The light blue arrows indicate dry adiabatic upward parcel displacements (because $\partial w/\partial z > 0$, the displacements increase with height).

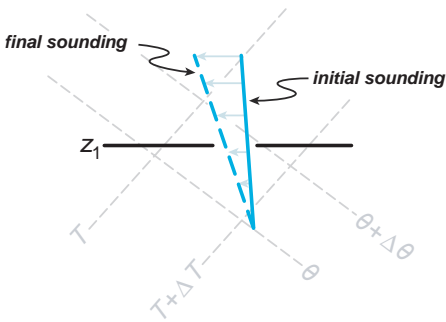


Figure 7.6 Schematic thermodynamic diagram illustrating the effect of differential horizontal temperature advection (by the ageostrophic wind) on the lapse rate (temperature changes are indicated by the light blue arrows). Cold advection increases with height at level z_1 , which leads to an increase in the lapse rate at that level. This effect is really the same effect as illustrated in Figure 7.4.

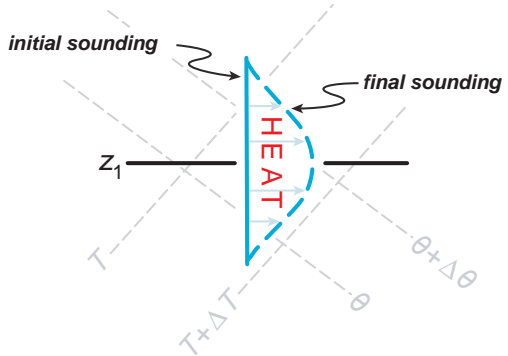


Figure 7.8 Schematic thermodynamic diagram illustrating the effects of differential diabatic heating on lapse rate (temperature changes are indicated by the light blue arrows). The maximum latent heating occurs at level z_1 , where $\partial q/\partial z = 0$ and the lapse rate is unchanged. The lapse rate increases above the level of maximum heating ($z > z_1$) and decreases below the level of maximum heating ($z < z_1$).

can be an order of magnitude larger than their synoptic-scale magnitudes.

7.1.2 Large-scale modifications of CAPE and CIN that are independent of lapse rate tendency

Although changes in the tropospheric lapse rate can have an important effect on the CAPE and CIN, it is worth

noting that important modifications to the CAPE and CIN can result even if the lapse rate changes are only modest or absent. There is some danger that the above analysis of the lapse rate tendency might overemphasize the importance of lapse rate changes, especially when they are confined to the middle troposphere. For example, the most spectacular changes in CIN and CAPE often result from dramatic increases in low-level moisture, independent of lapse rate changes. The significant destabilization of the sounding shown in Figure 7.3 (from an available energy standpoint), for example, was as much a result of low-level moistening as it was a result of middle tropospheric lapse rate changes. Furthermore, whether or not mean ascent increases with height (such that $\partial w/\partial z > 0$), mean ascent is associated with adiabatic cooling; thus, mean large-scale ascent *always* reduces CIN. Although synoptic-scale vertical motions are negligible in magnitude compared with the vertical motions associated with boundary layer thermals, if they persist for hours even vertical velocities of just a few cm s^{-1} can have a significant impact on the environmental sounding. CIN also typically decreases from morning to afternoon owing to the warming of the boundary layer, yet the boundary layer lapse rate tends to remain fairly constant (neutral)

as the boundary layer deepens. Strictly speaking, lapse rate changes are occurring in this case, but the lapse rate changes are confined to the very top of the boundary layer; the more important factor in the diurnal reduction of CIN is the fact that parcels lifted from the surface are warmer later in the day. Figure 7.9 illustrates these effects, all of which can be occurring simultaneously on a given day, in addition to the processes described in Section 7.1.1 that can alter lapse rates more generally.

The presence of potential instability (a layer in which $\partial\theta_e/\partial z < 0$, or alternatively, $\partial\theta_w/\partial z < 0$) is frequently cited as being important in the initiation of DMC. In terms of (7.4), the potential instability mechanism would increase lapse rates via the differential diabatic heating term. As discussed in Section 3.1.3, although θ_e (and θ_w) commonly decrease with height in the environments that support DMC, the removal of CIN by the potential instability mechanism does not appear to operate in most cases involving convection initiation along an air mass boundary. DMC that develops along air mass boundaries such as cold fronts and drylines is not usually preceded by the widespread formation of stratiform clouds that might suggest large-scale layer-lifting to saturation. Potential instability need not be

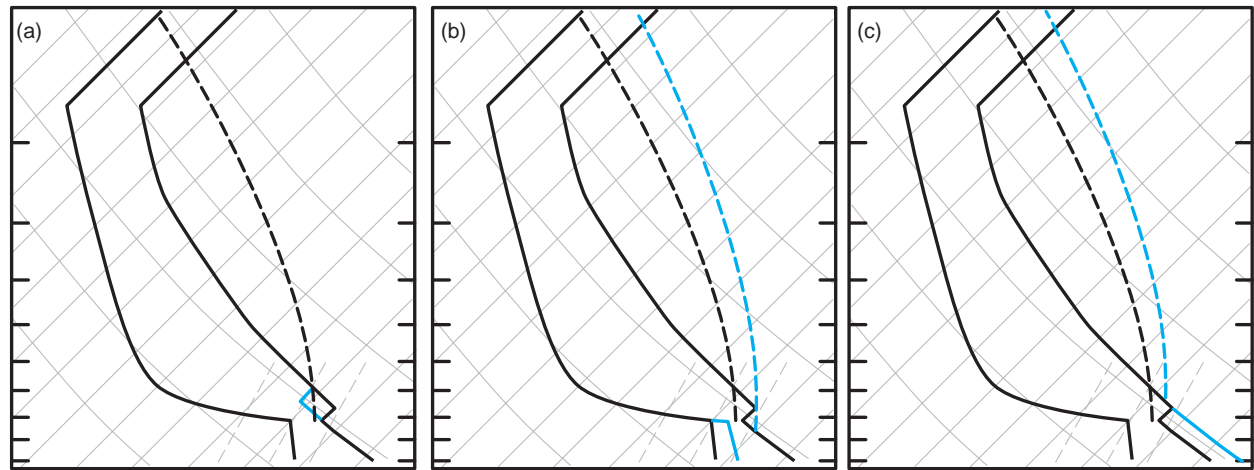


Figure 7.9 CIN can be reduced by (a) large-scale rising motion, (b) low-level moistening (e.g., moisture advection), and (c) low-level warming (e.g., insolation), despite the fact that the CIN modifications may not be accompanied by lapse rate changes, at least not over a significant depth. In (a)–(c), the isotherms and isentropes are solid gray lines, the constant mixing ratio lines are gray dashed lines, the sounding and trajectory taken by an air parcel lifted from the surface are solid and dashed black curves, respectively, and the modified sounding and parcel trajectory are blue solid and dashed curves, respectively. In (a), for clarity, only the temperature profile has been modified (the moisture profile has not been modified in accordance with the vertical motion that has been imposed in the layer of the capping inversion). Note that (b) and (c) are also accompanied by increases in CAPE. Conversely, CIN is augmented by large-scale descent, boundary layer cooling (although this would typically not occur without a concurrent stabilization of the lapse rate), and boundary layer drying (not shown).

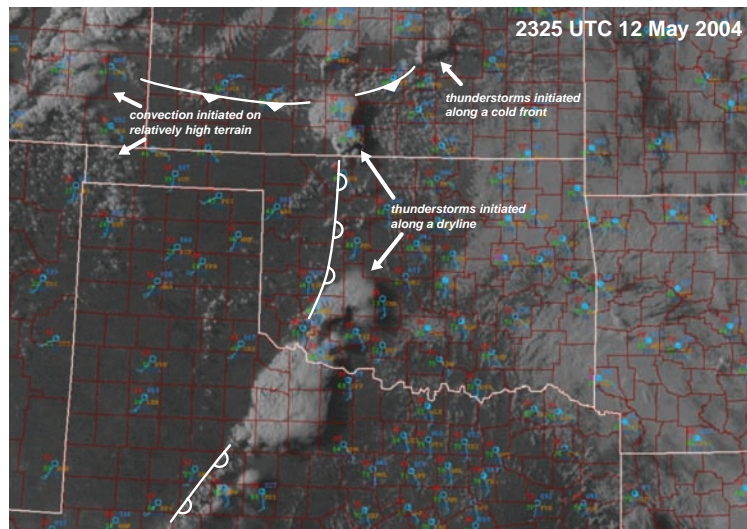


Figure 7.10 Example of convection initiation along only short segments of air mass boundaries. The visible satellite image is from 2325 UTC 12 May 2004 and shows the initiation of scattered thunderstorms along a dryline (line with open scallops) and cold front (line with filled barbs) in the southern Great Plains region. What conditions or processes have enabled air parcels to reach their LFC at these favored locations, though not elsewhere along the air mass boundaries? Additional thunderstorms developed over the higher terrain of southeastern Colorado, in the absence of any obvious boundaries. Could their initiation have been anticipated skillfully?

present in order for lifting to lead to cap removal. Lifting of a cap (i.e., a relatively warm layer) leads to cooling and cap weakening, no matter what the θ_e profile and regardless of whether or not saturation is achieved in part of the layer as it is lifted (Figure 7.9a). Stated another way, CIN reduction does not require lapse rate increases within the layer that is lifted.

7.2 Mesoscale complexities of convection initiation

Although convection often is initiated along relatively easily identifiable air mass boundaries in the presence of CAPE and relatively small CIN, particularly when large-scale ascent is also present (the large-scale ascent reduces CIN as discussed above), convection initiation forecasting is complicated by a number of mesoscale processes. For example, although air mass boundaries are relatively easy to identify using operational observing systems, rarely does convection develop along the entire length of such boundaries. Instead, convective storms typically are initiated along only limited segments of boundaries (Figure 7.10).

At least in some cases, it seems likely that kinematic inhomogeneities along air mass boundaries play a role in

favoring some segments of a boundary over other segments. For example, convective storms have been observed to develop where horizontal convective rolls intersect air mass boundaries (e.g., Figure 7.11). Small-scale (<4 km diameter) vertical vortices, sometimes called *mesocyclones*, have also been identified in close proximity to many growing cumulonimbi (Figure 7.12). Such vortices, which are naturally favored along wind shift lines owing to the dynamical instability associated with the horizontal shear of the wind (Section 3.5), enhance convergence along some segments of an air mass boundary, usually between vortices, while weakening convergence along other segments, usually within the cores of the vortices (Figure 7.13). The structure of the convergence field often resembles the core-and-gap structure of narrow cold-frontal rainbands (Section 5.1), probably for identical dynamical reasons. In other cases, it seems plausible that thermodynamic inhomogeneities encountered by an air mass boundary may favor or preclude convection initiation along select segments of the boundary. The episodes of convection initiation ‘failure’ that are probably least understood are when parcels surpass their LFC yet still fail to develop into sustained, precipitating DMC (Figure 7.14). It is difficult to know to what extent processes within the boundary layer versus above the boundary layer contribute to this failure mode.

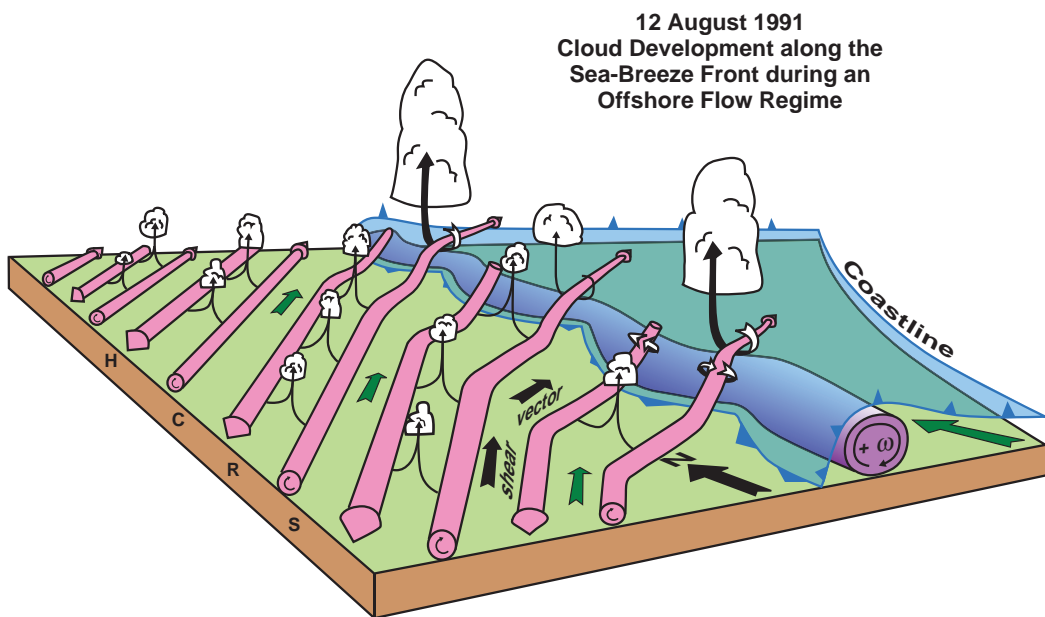


Figure 7.11 Schematic diagram showing the interaction between the sea-breeze front and horizontal convective rolls and how it related to cloud development on 12 August 1991 during the Convection and Precipitation/Electrification Experiment (CaPE). The sea-breeze front is delineated by the heavy blue barbed line. The circulation along the leading portion of the sea-breeze front is shaded purple. The horizontal vorticity vectors associated with the counter-rotating roll circulations are also shown, as are clouds along the horizontal convective rolls and at the intersection points along the front. The shear vector and low-level winds are indicated with black and green arrows, respectively. This is the same case as shown in Figure 5.33. (Adapted from Atkins and Wakimoto [1995].)

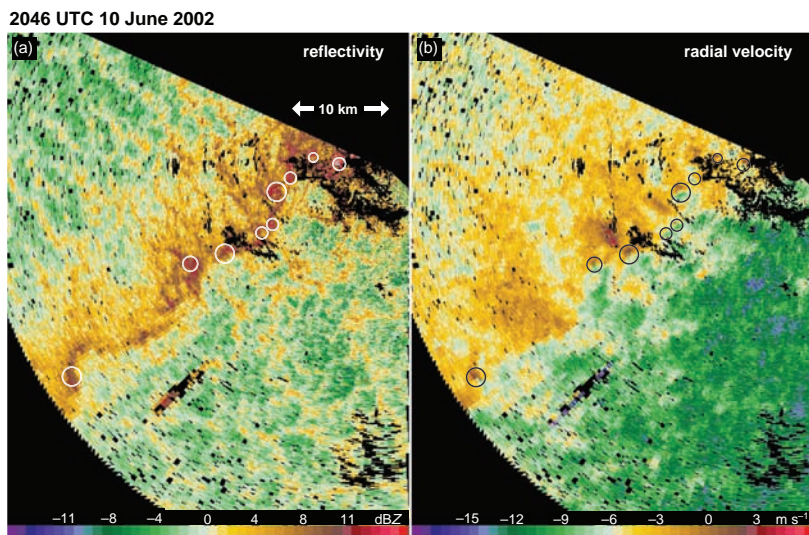


Figure 7.12 Misocyclones (circled) along a non-precipitating cold front evident in (a) reflectivity (dBZ; reflectivity values are uncalibrated) and (b) radial velocity (m s⁻¹) data obtained by the Doppler On Wheels (DOW) radar in western Kansas on 10 June 2002 (0.5° elevation angle). The reflectivity is mainly attributable to insects. Horizontal shear instability likely played a role in the formation of the vortices.

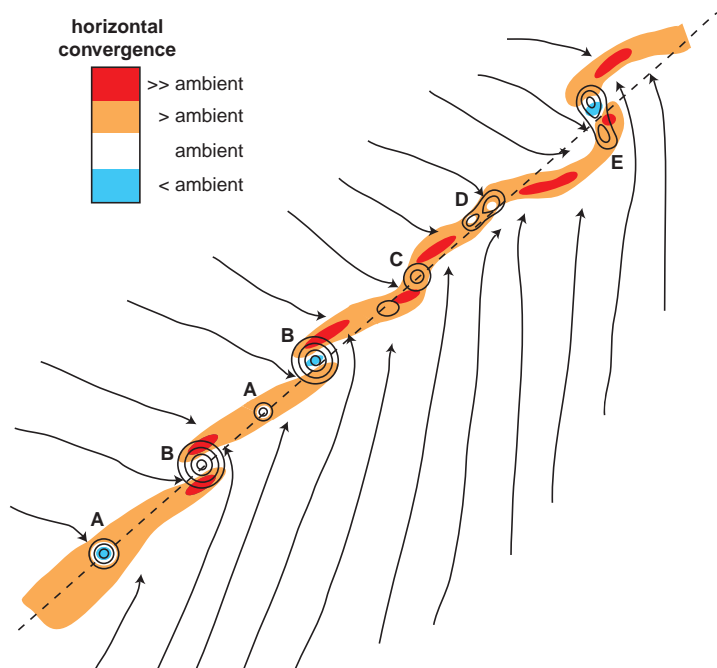


Figure 7.13 Conceptual model of misocyclones (vertical vorticity, ζ , greater than the ambient value is contoured), horizontal convergence (shaded), and streamlines based on a sample of air mass boundaries observed during the International H₂O Project (IHOP), one of which was the case shown in Figure 7.12. The misocyclones at both A positions are small relative to the average width of the mesoscale convergence zone. The misocyclones at both B positions are large compared with the width of mesoscale convergence zone. The misocyclone at position C has a width similar to that of the convergence zone. Merging misocyclones aligned with the boundary and oriented perpendicular to the boundary are located at positions D and E, respectively. (From Marquis *et al.* [2007].)



Figure 7.14 A photograph of *turkey towers*, which develop when air parcels surpass their LFC, rise to high altitudes, and produce anvils, yet the DMC fails to sustain itself and reach maturity (i.e., develop precipitation-induced cold pools). Photograph courtesy of Roger Edwards/Insojourn.

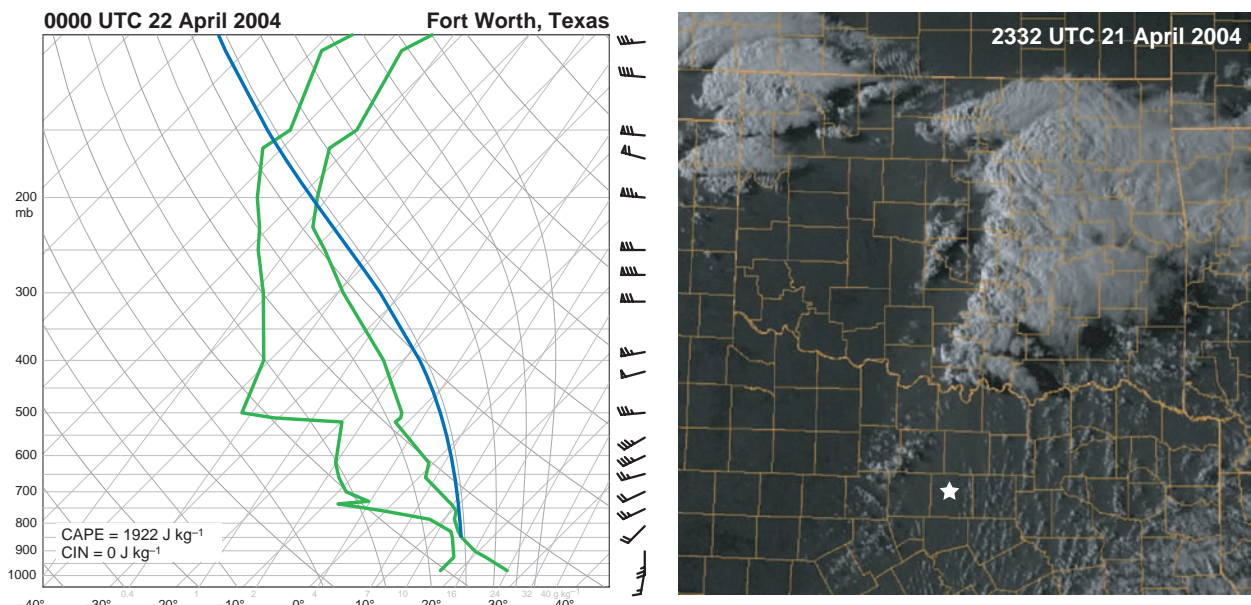


Figure 7.15 Example of convection initiation ‘failure’ in the absence of CIN on 21 April 2004. The Fort Worth, TX, sounding (left) has no CIN and appreciable CAPE, yet the only thunderstorms that developed were over 150 km north of the 0000 UTC sounding location, indicated by the star in the 2332 UTC visible satellite image (right). The CIN is zero, even neglecting virtual temperature effects.

7.2.1 The insufficiency of CIN removal for convection initiation

One might reasonably expect that DMC would commence when the *convective temperature*¹ is reached, or when the CIN is eliminated. (The effects of water vapor should really be included in the CIN calculation; as shown in Section 2.6, water vapor can have a significant influence on CIN calculations. Neglecting moisture can also limit the utility of the convective temperature as an indicator that the CIN has been eliminated.) In some cases, CIN is observed to be entirely absent, yet DMC still fails to develop (Figure 7.15). In other cases, DMC is initiated despite nearby soundings indicating that significant CIN remains. On some occasions there are almost certainly issues pertaining to sounding

representativeness—the inhomogeneities in the temperature and moisture fields mentioned above are not generally observed in real time and often cannot even be resolved in *ex post facto* studies (Figures 7.16 and 7.17). Or perhaps it is the assumptions made in using soundings to assess the likelihood of convection that are problematic. Thus, convection initiation is not as simple as reaching the convective temperature or eliminating CIN, although reducing CIN is certainly one aspect of creating an environment favorable for convection initiation.

One common method of computing CIN is to lift a parcel from the surface (often the parcel possessing the largest CAPE and smallest CIN) to its LCL and LFC. Water vapor mixing ratio (r_v) and potential temperature (θ) are assumed to be conserved for the dry adiabatic part of the ascent from the surface to the LCL, and equivalent potential temperature (θ_e) (or, alternatively, wet-bulb potential temperature [θ_w]) is assumed to be conserved for the moist adiabatic part of the ascent from the LCL to the LFC. As previously stated, soundings sometimes have zero CIN in environments *without* DMC (e.g., Figure 7.15). What has gone wrong?

One possibility is that the assumption of conserving water vapor mixing ratio and potential temperature for the ascent of the parcel from the surface to the LCL and LFC was inappropriate. Mixing (entrainment) of dry environmental

¹ The convective temperature, T_c , is the surface temperature that must be reached so that an air parcel can rise from the surface dry-adiabatically to its lifting condensation level (LCL) without ever being colder than the environment. The convective temperature can be determined from a sounding by following a line upward from the surface dewpoint, parallel to a constant water vapor mixing ratio line, until it intersects the temperature profile of the sounding (this height is known as the *convective condensation level*, or CCL), and then proceeding downward along a dry adiabat to the surface pressure. For soundings having only one LFC for a parcel lifted from the surface, surface-based CIN is removed when the convective temperature is reached.

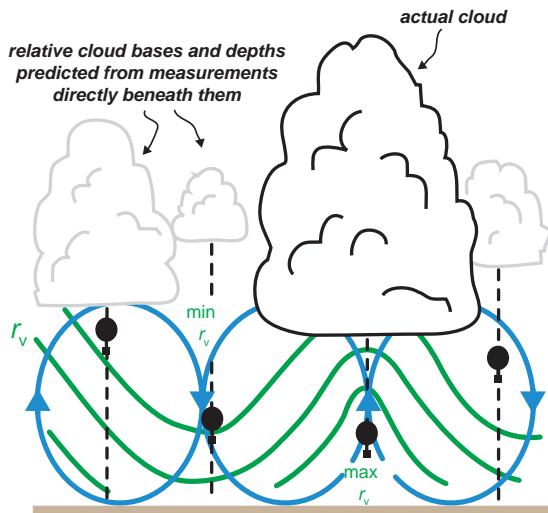


Figure 7.16 Schematic showing the effect of boundary layer roll circulations on the moisture profiles measured by soundings. A sounding that ascends through the updraft of a roll samples larger water vapor concentrations than a sounding that ascends through the downdraft of a roll. Thus, the LCL height based on a sounding that has ascended through a downdraft might be overestimated compared with the bases of the observed clouds, which generally reside within boundary layer updrafts. CAPE and CIN values computed from a sounding would also be sensitive to whether the sounding ascended through an updraft or a downdraft. (Adapted from Weckwerth *et al.* [1996].)

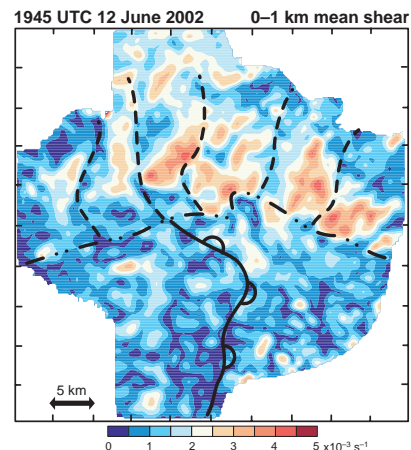


Figure 7.17 Horizontal cross-section of the mean vertical wind shear in the 0–1 km AGL layer at 1945 UTC 12 June 2002, obtained from a dual-Doppler wind synthesis. The dashed lines are gravity wave phase fronts, the dash-dot line is an outflow boundary, and the line with open scallops is a dryline. Note the remarkable variability of the vertical wind shear field, partly due to thermals and partly as a result of the mesoscale boundaries (e.g., the mean shear is larger on the north side of the outflow boundary). It is tempting to wonder whether the spatial distribution of CIN, if it could ever be observed with the same level of detail, might have similar complexity. If so, it would be very difficult to anticipate convection initiation based on the characteristics of a single sounding alone. (Adapted from Markowski and Richardson [2007].)

air into an ascending parcel dilutes the buoyancy and θ_e of the ascending parcel, usually raising the LCL and LFC of that parcel. Another way to compute CIN is to lift a parcel having the *mean* water vapor mixing ratio and potential temperature of the lowest 50–100 mb, or sometimes the entire depth of the boundary layer. This usually is done to account for the mixing that was neglected in the first CIN calculation (Figures 7.18 and 7.19). Still again, there are sometimes soundings lacking both CIN and DMC, despite the fact that CIN was computed by lifting a parcel having the mean boundary layer water vapor mixing ratio and potential temperature. What has gone wrong in *those* cases?

By approximating the amount of ‘thermodynamic dilution’ within the lifted surface parcel using the mean potential temperature and water vapor mixing ratio over the lowest, say, 50–100 mb, we have assumed implicitly that the entrainment rate is a constant between the surface and a level 50–100 mb above the surface. Although this

assumption sometimes works well (perhaps best when wind shear is weak), it certainly does not work well all of the time. In general, the degree to which the temperature and moisture perturbations of a lifted parcel are reduced by mixing increases with the ambient vertical wind shear and the tilt of the updraft (either above or below the LCL) (Figures 7.20 and 7.21); that is, strong environmental wind shear has an inhibiting effect on convection initiation, unless the environmental shear can somehow be offset by the wind field locally induced by an air mass boundary. (This balance between the environmental shear and the shear induced locally by an outflow boundary, for example, will be shown in Chapter 9 to be important in the maintenance of mature convective systems.)

The degree to which the temperature and moisture of a lifted parcel are reduced by mixing is also a function of the characteristics of the environmental air entrained into the lifted parcel. For example, the drier the environmental air that is entrained by the lifted parcel, the greater the loss of

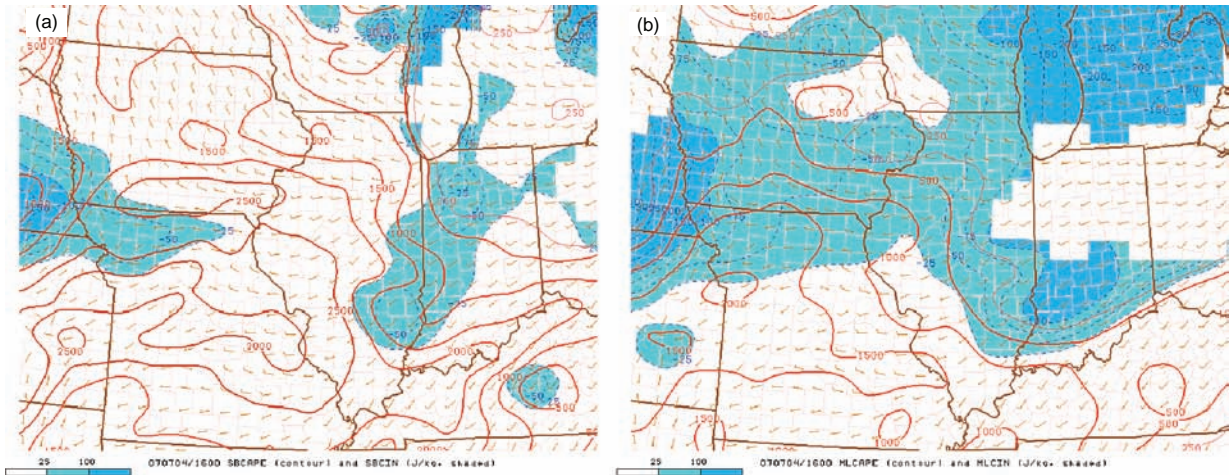


Figure 7.18 Comparison of CAPE (red contours; J kg^{-1}) and CIN values (blue shading; J kg^{-1}) computed by lifting (a) a parcel from the surface, assuming no mixing, and (b) a parcel having the mean potential temperature and water vapor mixing ratio of the lowest 100 mb, which crudely attempts to account for mixing that occurs en route to the LFC. CAPE (CIN) values are typically smaller (larger) when a parcel is lifted having the mean properties of the lowest 100 mb (or some layer of roughly similar depth), as is the case above, except perhaps at night or on the cold side of a front, where a shallow layer of relatively cool air might be found near the surface. (Courtesy of the Storm Prediction Center.)

potential buoyancy² that may be realized by the parcel—in fact, the lifted parcel may not even reach its LCL or LFC at all. One reason why air mass boundaries are favored corridors for the initiation of DMC is probably the persistent convergence and vertical motion along air mass boundaries, which can locally deepen the moist layer, thereby reducing the hostility of the environment to parcels that subsequently might rise from the surface to their LCL and LFC. However, even if parcels do reach their LFC, they still must survive the effects of entrainment in a potentially hostile environment above the LFC in order to develop DMC (Figure 7.14).

Another common assumption is that convection will be initiated if the CIN becomes smaller than the kinetic energy of the boundary layer updraft that provides the forcing. Using parcel theory (Section 3.1), one can show that the minimum vertical velocity needed by a parcel, such that the parcel will have sufficient momentum to pass through a layer of CIN en route to its LFC, is

$$w_{\min} = \sqrt{2 \text{ CIN}}, \quad (7.6)$$

² By *potential* buoyancy, we are referring to the buoyancy that *may* be realized above the LFC, if the LFC can be reached. This buoyancy can be reduced by the entrainment of dry air into rising parcels that occurs well below the LFC (and LCL); the drying can reduce θ_e significantly, and thus the buoyancy that eventually might be realized above the LFC, which is strongly dependent on the latent heat release (θ_e is a measure of the potential warming from latent heat release).

which is very similar to the form of (3.17). From the forecasting perspective, it is problematic that the proximity soundings used to assess the CIN are typically no closer than a few tens to a few hundreds of kilometers from the area of boundary layer convergence, thus far enough removed from the area of highest convective potential to be unrepresentative. Moreover, boundary layer updrafts that initiate DMC are often associated with mesoscale convergence zones, rather than bubbles of high initial vertical momentum that may be invoked to locally break through the capping inversion or exceed the residual CIN. In other words, the effects of the pressure field are often important and can limit the usefulness of (7.6).

In summary, convection initiation is much more complex than simply reaching the convective temperature. It involves all sorts of mesoscale and cloud-scale circulations that we generally are unable to resolve, mixing rates and humidity along ascending plumes, and the three-dimensional structure of these plumes. For example, parcel residence time within a mesoscale updraft also is important, with DMC possible only if the time required to cross the updraft in the horizontal exceeds the time necessary to reach the LFC. Although CIN and its removal is related to the probability of convection initiation, it is only part of the story. Perhaps the most practical forecasting strategy for predicting convection initiation, assuming CAPE is present, is to be vigilant for regions

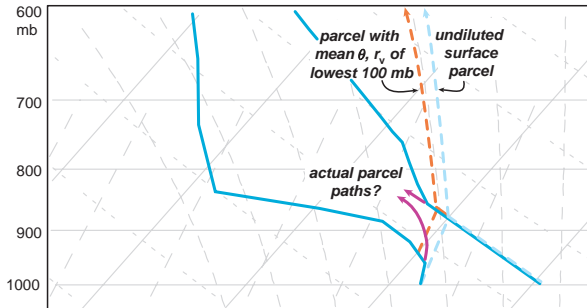


Figure 7.19 In this sounding, convective temperature has been reached and no CIN is present, either for an undiluted surface parcel (light blue dashed path), or for a parcel having the mean potential temperature (θ) and water vapor mixing ratio (r_v) of the lowest 100 mb (orange dashed path). Convection initiation is still not guaranteed, however. For example, the actual path a parcel follows on a thermodynamic diagram can deviate significantly from the paths associated with the undiluted parcel and the parcel assumed to be lifted with the mean thermodynamic characteristics of the lowest 100 mb, depending on the trajectory that the parcel takes as it rises through the boundary layer. The trajectory that a parcel takes—and the mixing that occurs along this route—is sensitive to the ambient vertical wind profile and the depth of the convergence along an air mass boundary, if one exists. For example, a parcel following the magenta path represented on the skew T -log p diagram may or may not reach its LCL, and it would have to overcome significant negative area in order to attain its LFC. Though the above example highlights the adverse effects of entrainment below the LCL, as mentioned elsewhere, entrainment above the LCL (and LFC) also is important, especially for the sounding above, which contains a very dry layer of air above the LCL.

of persistent low-level convergence where CIN values are small (or inferred to be small, based on comparisons of observed surface conditions with whatever sounding data might be available). Visible satellite imagery, particularly imagery having a high temporal resolution (<15 min), is also valuable for nowcasting convection initiation.

7.3 Moisture convergence

A quantity known as the *moisture convergence*, $-\nabla \cdot (r_v \mathbf{v}_h)$, often is used as a forecasting tool for convection initiation. It also is occasionally invoked as an explanation for the generation of local maxima in water vapor mixing ratios (a phenomenon sometimes referred to as *moisture pooling*). However, moisture convergence alone cannot produce a

relative maximum in water vapor concentration. Local water vapor mixing ratio changes are governed by

$$\frac{\partial r_v}{\partial t} = -\mathbf{v} \cdot \nabla r_v - C + E, \quad (7.7)$$

where $-\mathbf{v} \cdot \nabla r_v$ is the moisture advection, C is a water vapor sink due to condensation, and E is a water vapor source due to evaporation (either from falling precipitation or via a surface moisture flux). In the absence of evaporation, water vapor mixing ratios can only increase locally owing to advection, but advection cannot generate local extrema.

So where does moisture convergence come in? If we combine (7.7) with the Boussinesq mass continuity equation multiplied by r_v ,

$$r_v \nabla \cdot \mathbf{v}_h + r_v \frac{\partial w}{\partial z} = 0, \quad (7.8)$$

we obtain

$$\frac{\partial r_v}{\partial t} = -\nabla \cdot (r_v \mathbf{v}_h) - \frac{\partial (r_v w)}{\partial z} - C + E, \quad (7.9)$$

where moisture convergence appears on the rhs of (7.9). For $-\nabla \cdot (r_v \mathbf{v}_h) > 0$, $\partial r_v / \partial t > 0$ —but when $-\nabla \cdot (r_v \mathbf{v}_h) > 0$, $-\partial (r_v w) / \partial z < 0$, which contributes to $\partial r_v / \partial t < 0$; that is, $-\partial (r_v w) / \partial z$ and $-\nabla \cdot (r_v \mathbf{v}_h)$ always oppose each other. A part of $-\nabla \cdot (r_v \mathbf{v}_h)$ exactly cancels $-\partial (r_v w) / \partial z$, and the part of $-\nabla \cdot (r_v \mathbf{v}_h)$ that remains is just moisture advection, which cannot generate extrema, only translate preexisting extrema.

So if moisture convergence or moisture pooling cannot produce local moisture maxima, then what does? After all, we frequently observe locally large water vapor mixing ratios within persistent convergence zones along air mass boundaries. Moisture convergence is well correlated with horizontal velocity convergence ($-\nabla \cdot \mathbf{v}_h$), which is associated with upward motion. Thus, moisture convergence is associated with a *deepening* of boundary layer moisture. The deepening of boundary layer moisture reduces the dilution of rising parcels as they ascend from near the surface to the LCL and LFC. Thus, regions of locally deeper moisture may be more favorable for convection initiation than surrounding areas. Updrafts in such regions also realize larger CAPE owing to less θ_e reduction as surface parcels rise to the LFC.

Returning to our original question at the start of the previous paragraph, increased moisture depth means that vertical mixing results in a smaller drop (or no drop) in the moisture concentration at the surface compared with surrounding shallow-moisture areas, where vertical mixing can lead to significant decreases in the moisture concentration at the surface; thus, local maxima in water vapor

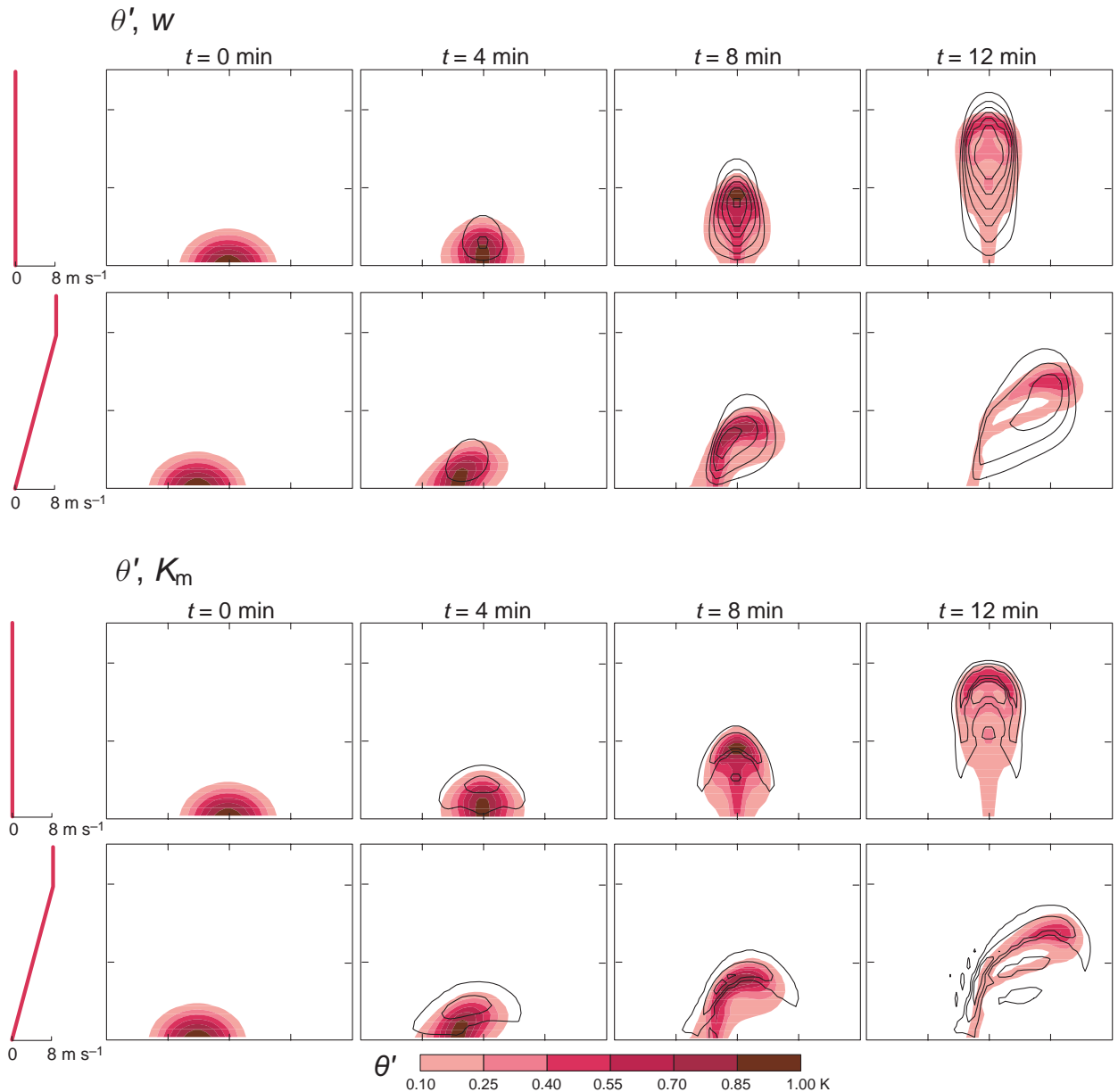


Figure 7.20 Output from a pair of simulations of a thermal rising through a neutrally stratified boundary layer, with and without vertical wind shear. The top two rows show cross-sections in the x - z plane of the potential temperature perturbation, θ' (red shades), and the vertical velocity, w (contoured at 1 m s^{-1} intervals starting at 1 m s^{-1}), for the simulation without vertical wind shear (top row) and the simulation with constant westerly wind shear in the lowest 2 km (second row from top). Tick marks are drawn on the axes every 2 km. The vertical profiles of the westerly wind component are shown to the left of the panels displaying the model output. The bottom two rows show cross sections of θ' (red shades) and eddy viscosity, K_m (contoured at $2 \text{ m}^2 \text{ s}^{-1}$ intervals starting at $2 \text{ m}^2 \text{ s}^{-1}$), for the simulation without vertical wind shear (third row from top) and the simulation with constant westerly wind shear in the lowest 2 km (bottom row).



Figure 7.21 In general, the detrimental effects of entrainment increase as the tilt of the updraft increases. In the above sequence, an updraft is tilted away from the vertical by strong wind shear and eventually dissipates (a small funnel is visible in the bottom image as the cloud dissipates). Paradoxically (to be discussed in Chapter 8), vertical wind shear can have an enhancing effect on mature convection if the convection can survive the generally detrimental effects of wind shear during the early stages of development. Photographs by Eric Nguyen.

concentration can occur at the surface in regions where boundary layer moisture is deeper than adjacent regions. In mathematical terms, such local moisture maxima are produced by horizontal differences in the vertical advection of water vapor. The maxima created by this process, however, do not exceed the largest values of r_v originally present in the water vapor field.

7.4 Elevated convection

Although it has not been stated explicitly, the focus up to this point has been on the initiation of *surface-based* DMC, that is, DMC that draws its inflow from air that is in contact with the surface in close proximity to the updraft (though not necessarily directly beneath the updraft because gust fronts commonly lead the updraft by a short distance, say a few kilometers, even in cases of severe, long-lived DMC). Surface-based convection requires that air in contact with the surface can be lifted to the LFC. In boundary layers characterized by large CIN, it might not be possible for air parcels to be lifted to their LFC from the surface, if they even have an LFC. On the other hand, air parcels lifted from above a low-level stable layer might possess relatively little CIN and significant CAPE. Such parcels can support what is known as *elevated* DMC.

In contrast to surface-based DMC, elevated DMC is situated atop stable boundary layers and draws its inflow from a layer not in contact with the surface in close proximity to the storm. Elevated DMC most often occurs at night above nocturnal boundary layers and poleward of warm fronts, especially when a low-level jet rides up and over a warm front. In the latter example, air parcels ride up the frontal surface until they reach their LFC, sometimes more than 100 km from the source region of the potentially buoyant air. Figure 7.22 shows a typical sounding obtained within an environment associated with elevated DMC poleward of a warm front. Notice that a parcel lifted from the surface has no CAPE at all; however, a parcel lifted from the top of the stable boundary layer has little CIN and CAPE on the order of 1000 J kg^{-1} . DMC is occasionally initiated by a cold front aloft (CFA; Section 5.1), sometimes as far as a few hundred kilometers ahead of a surface front or dryline. In these situations, the DMC is initially elevated but can become surface-based once low-level outflow is produced if the outflow can force surface air parcels to their LFC.

Perhaps a better term for elevated DMC would be *non-surface-based* DMC, because the cloud base of elevated DMC need not be high, as the term ‘elevated’ implies. In contrast, surface-based convection can be high based (but not ‘elevated’) in relatively dry environments, as it often is in the southwestern United States, where LCLs associated

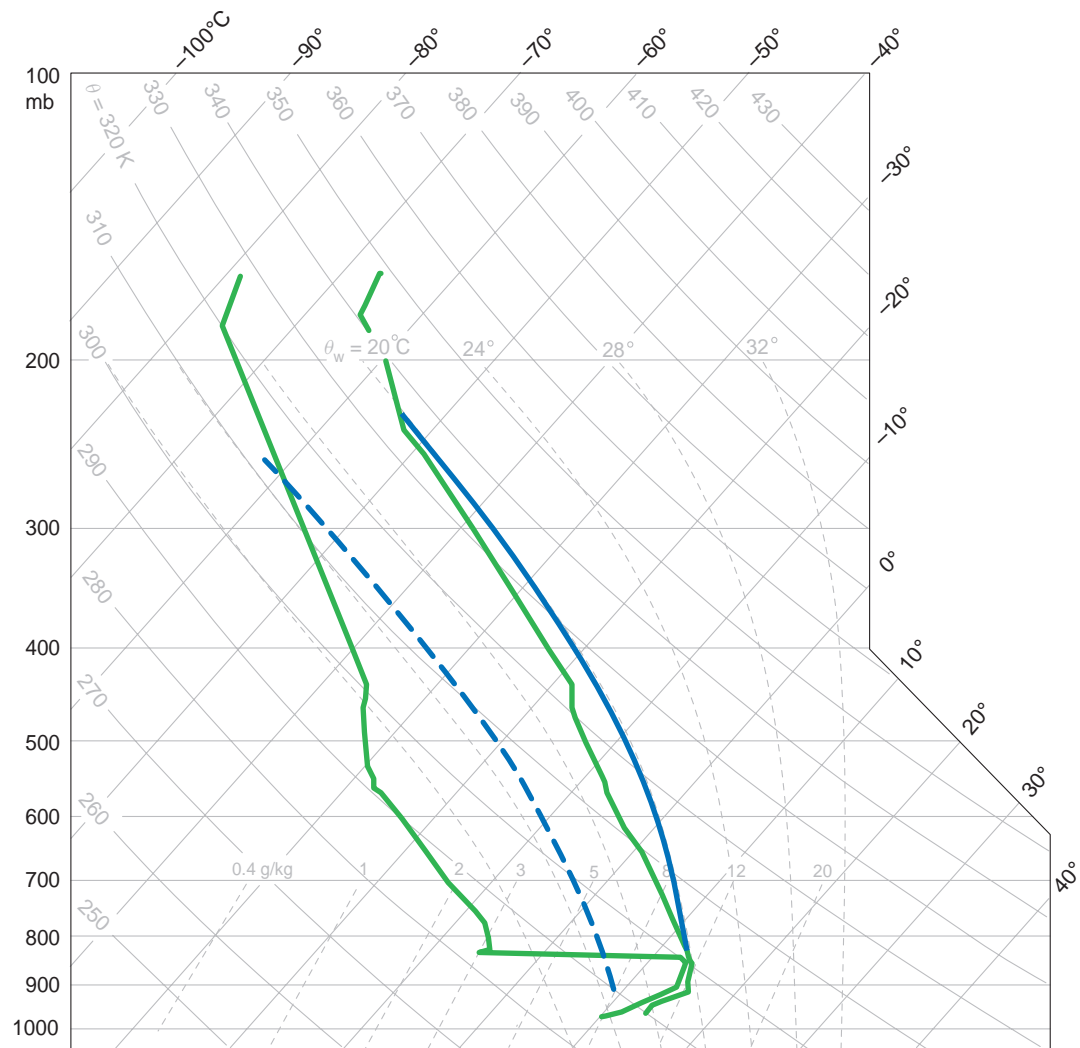


Figure 7.22 Example of a sounding containing elevated CAPE but no surface-based CAPE. A parcel of air lifted from the surface follows the dashed blue trajectory, whereas an air parcel lifted from the top of the stable boundary layer follows the solid blue trajectory.

with surface-based convection in the warm season are routinely above 3 km. Elevated DMC is widely assumed to pose a lesser high wind threat (e.g., tornadoes, damaging straight-line winds) compared with surface-based DMC. The primary threats from elevated DMC tend to be large hail and flooding. Damaging surface winds are less likely in elevated DMC because downdrafts are less able to penetrate a stable low-level air mass (the negative buoyancy of a downdraft is reduced when stable low levels are encountered; damaging straight-line winds are discussed in more detail

in Chapter 10). Tornadoes also are rarely associated with elevated convection, for perhaps related reasons (as also discussed in Chapter 10, downdrafts are well known to be associated with tornadoes, and if these downdrafts are inhibited then tornadogenesis may be less likely). In general, the most intense convection is surface-based, because usually the highest possible parcel temperature excesses over the environment (i.e., buoyancy) may be realized when near-surface air is lifted, for this air tends to have the largest θ_e . Furthermore, the boundary layer tends to be the

layer in which wind shear is largest, owing to the influence of surface drag on the low-level wind—convective storms that do not process inflow from the boundary layer cannot take advantage of the large wind shear that is often present there.

Further reading

- Arnott, N. R., Y. P. Richardson, J. M. Wurman, and E. N. Rasmussen, 2006: Relationship between a weakening cold front, mesocyclones, and cloud development on 10 June 2002 during IHOP. *Mon. Wea. Rev.*, **134**, 311–335.
- Banacos, P. C., and D. M. Schultz, 2005: The use of moisture flux convergence in forecasting convective initiation: Historical and operational perspectives. *Wea. Forecasting*, **20**, 351–366.
- Crook, N. A., and J. B. Klemp, 2000: Lifting by convergence lines. *J. Atmos. Sci.*, **57**, 873–890.
- Doswell, C. A., III, 1987: The distinction between large-scale and mesoscale contribution to severe convection: A case study example. *Wea. Forecasting*, **2**, 3–16.
- Droegemeier, K. K. and R. B. Wilhelmson, 1985: Three-dimensional numerical modeling of convection produced by interacting thunderstorm outflows. Part I: Control simulation and low-level moisture variation. *J. Atmos. Sci.*, **42**, 2381–2403.
- Farrell, R. J., and T. N. Carlson, 1989: Evidence for the role of the lid and underrunning in an outbreak of tornadic thunderstorms. *Mon. Wea. Rev.*, **117**, 857–871.
- Jorgensen, D. P., and T. M. Weckwerth, 2003: Forcing and organization of convective systems. *Radar and Atmospheric Science: a Collection of Essays in Honor of David Atlas*, Meteor. Monogr., No. 52, 75–104.
- Kingsmill, D. E., 1995: Convection initiation associated with a sea-breeze front, a gust front, and their collision. *Mon. Wea. Rev.*, **123**, 2913–2933.
- Koch, S. E., 1984: The role of an apparent mesoscale frontogenetical circulation in squall line initiation. *Mon. Wea. Rev.*, **112**, 2090–2111.
- Lee, B. D., and R. B. Wilhelmson, 1997a: The numerical simulation of non-supercell tornadogenesis. Part I: Initiation and evolution of pretornadic mesocyclone circulations along a dry outflow boundary. *J. Atmos. Sci.*, **54**, 32–60.
- Markowski, P. M., C. Hannon, and E. Rasmussen, 2006: Observations of convection initiation ‘failure’ from the 12 June 2002 IHOP deployment. *Mon. Wea. Rev.*, **134**, 375–405.
- Marquis *et al.* (2007).
- Wakimoto, R. M., H. V. Murphrey, E. V. Browell, and S. Ismail, 2006: The ‘triple point’ on 24 May 2002 during IHOP. Part I: Airborne Doppler and LASE analyses of the frontal boundaries and convection initiation. *Mon. Wea. Rev.*, **134**, 231–250.
- Weckwerth, T. M., and D. B. Parsons, 2006: A review of convection initiation and motivation for IHOP_2002. *Mon. Wea. Rev.*, **134**, 5–22.
- Wilson, J. W., and W. E. Schreiber, 1986: Initiation of convective storms at radar-observed boundary-layer convergence lines. *Mon. Wea. Rev.*, **114**, 2516–2536.
- Wilson, J. W., G. B. Foote, N. A. Crook, J. C. Fankhauser, C. G. Wade, J. D. Tuttle, and C. K. Mueller, 1992: The role of boundary-layer convergence zones and horizontal rolls in the initiation of thunderstorms: a case study. *Mon. Wea. Rev.*, **120**, 1785–1815.
- Ziegler, C. L., and E. N. Rasmussen, 1998: The initiation of moist convection at the dryline: forecasting issues from a case study perspective. *Mon. Wea. Rev.*, **125**, 1001–1026.
- Ziegler, C. L., T. J. Lee, and R. A. Pielke, 1997: Convection initiation at the dryline: a modeling study. *Mon. Wea. Rev.*, **125**, 1001–1026.

8

Organization of Isolated Convection

Convective storms can be organized in a variety of ways. Some occur as discrete and somewhat isolated cells, whereas others occur within large complexes or lines. The organization of convective storms, to a considerable degree, influences the threats they pose (e.g., damaging straight-line winds, large hail, flash floods, tornadoes). Perhaps ironically, determining whether, where, and when convective storms will be initiated is often more difficult than determining the range of likely storm types in the event that convective storms are initiated.

Much of our understanding of the relationship between storms and their environments has been obtained from numerical modeling studies in which the characteristics of the environment can be controlled. The earliest three-dimensional thunderstorm modeling studies initiated convection by placing a warm bubble into the low levels of a conditionally unstable environment. The warm bubble initiated a sustained updraft, and the subsequent evolution was dependent on parameters such as the vertical wind shear and CAPE of the environment, among others.

In this chapter we explore the relationship between the parent environment and isolated convection like that which might develop in an idealized simulation from a warm bubble, or in nature by localized convergence. Larger-scale convective systems, which can be initiated from less localized forcing (e.g., widespread lifting of air over a frontal surface to the LFC) or when the outflows produced by initially isolated updrafts merge to produce one large outflow, are the focus of Chapter 9. A more targeted consideration of the hazards associated with DMC appears in Chapter 10.

8.1 Role of vertical wind shear

The organization of DMC can be affected by the vertical wind shear, CAPE, relative humidity, and the vertical

distributions of each of these variables, among other things. Of these parameters, the vertical wind shear probably exerts the greatest influence on storm type. Vertical wind shear tends to promote storm organization and longevity, although excessive vertical shear can be detrimental to weak updrafts in environments of marginal instability, just as strong shear can be detrimental to convection initiation by increasing entrainment.

Although there are many measures of vertical wind shear (and its associated horizontal vorticity), one parameter that works fairly well for quantifying vertical shear and predicting storm type is simply the magnitude of the 0–6 km vector wind difference, which often casually is referred to as the 0–6 km shear, even though it does not have units of shear (Figure 8.1).¹ Values of

¹ In practice, the 0–6 km shear typically is computed from the vector difference between the wind at 6 km and the wind at the lowest wind observation level, which is usually a few meters above the ground rather than at $z = 0$ m (the horizontal wind goes to zero at $z = 0$ m; it is not known what effect, if any, the vertical shear in the lowest few meters has on a storm). The characterization of the vertical wind shear using a bulk measurement such as the magnitude of the 0–6 km vector wind difference, in contrast to some others (e.g., hodograph length), is insensitive to the kinks and inflections common in observed hodographs. ‘Small-scale’ hodograph details are quite possibly important for some sorts of prediction (e.g., the intensification of near-ground rotation in simulated storms can be sensitive to small hodograph changes), but for anticipating storm type, small-scale hodograph details do not appear to be as critical. The magnitude of the 0–6 km vector wind difference is easy to compute, because it requires no integrations or calculations of mean winds. We note that evaluating the shear over the lowest 6 km is more of a historical tradition than any indication of something special about the 0–6 km layer. Skillful forecasts of the organization of DMC probably also could be made using the magnitudes of the 0–5 km, 0–7 km, or 0–8 km vector wind differences, etc., with, of course, different thresholds.

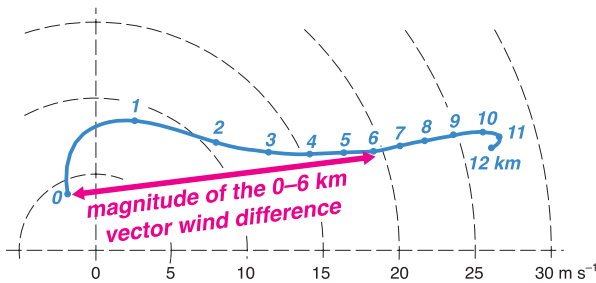


Figure 8.1 Relationship between the magnitude of the 0–6 km vector wind difference, or ‘0–6 km shear’, and a hodograph. Numerals along the hodograph indicate altitudes above ground level. In this figure and in others in this chapter depicting hodographs, the point on the hodograph labeled “0” is the lowest altitude where the wind is measured, which typically is a few meters above the ground rather than at $z = 0$ m. The magnitude of the 0–6 km vector wind difference discriminates among storm types reasonably well.

0–6 km shear less than 10 m s^{-1} are usually regarded as weak, 0–6 km shear of $10\text{--}20 \text{ m s}^{-1}$ is usually regarded as moderate, and 0–6 km shear $>20 \text{ m s}^{-1}$ is usually regarded as strong.

A parameter that combines shear and CAPE, known as the *bulk Richardson number* (BRN), also has been used to forecast storm type. The BRN is defined as

$$\text{BRN} = \frac{\text{CAPE}}{\frac{1}{2}U^2}, \quad (8.1)$$

where U is the magnitude of the vector difference between the 0–6 km mean wind and the 0–500 m mean wind. Though CAPE is obviously a measure of potential updraft strength, CAPE has also been assumed to be a proxy for the strength of the outflow produced by the evaporation, melting, and sublimation of hydrometeors within a storm, with larger CAPE associated with stronger cold pools.² (Outflow strength only increases with CAPE when the vertical profile of environmental relative humidity is held constant. Downdraft and outflow strength, in general, as will be discussed in Chapter 10, depend on a number of factors, with the condensate mass produced by an updraft being only one of them.) Regarding the denominator, if

² See Weisman and Klemp (1982).

the 0–6 km mean wind is a crude proxy for the storm motion, then U approximates the 0–500 m storm-relative wind, and $\frac{1}{2}U^2$ is therefore a measure of the storm-relative inflow kinetic energy. The greater the storm-relative inflow kinetic energy, the greater the degree to which the outflow is restrained. Thus, the basic idea behind the BRN is that it gives a rough measure of the balance between inflow and outflow, assuming that outflow strength is well-predicted by CAPE, and that this balance should at least partly be related to storm organization, longevity, and severity. Inflow and outflow tend to be relatively well-matched for a small ($\lesssim 50$) BRN, perhaps leading to longer-lived, more severe storms. On the other hand, a large BRN ($\gtrsim 50$) implies that outflow might overwhelm the inflow and undercut the updraft, leading to relatively short-lived cells, although, depending on other aspects of the environment, new cells might be able to be triggered successively by the storm’s gust front, thereby leading to a convective system that outlives the shorter-lived individual cells. The wind shear appearing in the denominator of the BRN is also a measure of the ability of an updraft to acquire rotation via tilting of horizontal vorticity. Thus, a low BRN can imply that updrafts will develop significant rotation. Storms having strong updraft rotation are known as *supercells* and are responsible for a disproportionate fraction of severe weather reports.

Although the BRN was found to account for much of the variance in storm type within numerical simulations exploring the CAPE-shear parameter space, forecasters usually just examine the wind shear magnitude because storm type is a stronger function of vertical wind shear than CAPE. Observations suggest that the *product* of CAPE and shear, rather than the quotient of CAPE and shear, may be a better predictor of storm type anyway, at least for some types of storms. For example, the rate of vertical vorticity development in supercells from the tilting of horizontal vorticity is proportional to the vertical shear times the updraft speed, and the updraft speed is proportional to $\text{CAPE}^{1/2}$, at least within the confines of parcel theory.

The reasons why vertical wind shear tends to enhance the organization, longevity, and severity of DMC are twofold. The first reason is that the degree to which precipitation and outflow interfere with an updraft is reduced as the vertical shear over the updraft depth increases (we sometimes will refer to this as the *deep-layer* shear). Where precipitation falls relative to the low-level updraft depends on the horizontal momentum of air relative to the updraft when it enters

the updraft, the horizontal accelerations air experiences over the vertical excursion that grows hydrometeors to precipitation size (the horizontal accelerations can result from horizontal gradients in either p'_b or p'_d), and the *storm-relative* wind field through which the precipitation falls on the way to the ground. In spite of all of the complexities, there is a tendency for the distance precipitation falls from its parent updraft to increase with increasing deep-layer shear and upper-level storm-relative winds, and the precipitation tends to fall on the downwind side of the updraft with respect to the direction of the upper-level storm-relative winds (and the radar echoes associated with isolated convective storms therefore tend to be elongated in the direction of the upper-level storm-relative winds).

The strength of the upper-level (and low-level) storm-relative winds tends to increase with the magnitude of the deep-layer wind shear; that is, strong-shear environments also tend to have strong storm-relative winds (Figure 8.2). Furthermore, strong storm-relative winds at low levels restrain the motion of the gust front relative to the updraft, thereby limiting the tendency for rain-cooled outflow to undercut the updraft (Figures 8.3b–c versus 8.3e–g, 8.4).

The second reason why vertical wind shear can have an important enhancing effect on DMC is by the development of dynamic vertical pressure gradients. Low-level

shear, as we shall see, has a significant influence on the lifting along a gust front (the strength of this lifting ultimately is tied to the strength of the vertical gradients of both p'_d and p'_b), and thereby has significant control over the ability of the gust front to trigger new cells, which in turn affects how DMC is organized. In weak-shear environments, the lifting of environmental air by the gust front is relatively weak; thus, new cells generally fail to be initiated, at least in any systematic, predictable way (if the environmental CIN is very small then even weak lifting by the gust front could generate new cells). The result is relatively short-lived, disorganized convection that sometimes is referred to as *single-cell* convection (this is the mode of convection identified in simulations initialized with a high-BRN environment). In moderate-shear environments, the lifting of environmental air along the gust front is enhanced along a preferred flank (e.g., we shall later find that lifting is enhanced on the downshear flank of the outflow in the case of fairly straight hodographs), leading to the repeated triggering of new cells and so-called *multicell* convection (this is the mode of convection identified in simulations initialized with a moderate-BRN environment).

As mentioned earlier, large-shear environments are conducive to supercells. Not only does the tilting of horizontal vorticity lead to storm rotation, but the dynamic vertical pressure gradients that accompany large-shear

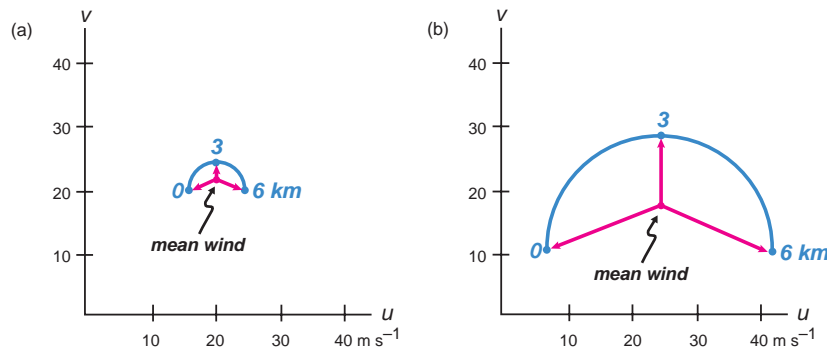


Figure 8.2 Relationship between vertical wind shear and storm-relative winds. The hodograph in (a) depicts a vertical wind profile having weak shear relative to the hodograph in (b); notice that the length of the hodograph in (a) is much shorter than that in (b). Storm-relative wind vectors (magenta) are overlaid at 0, 3, and 6 km for the two cases, assuming a storm motion approximately equal to the mean wind defined by each hodograph. The length of the storm-relative wind vectors is proportional to the magnitude of the storm-relative winds. Numerals along the hodographs indicate altitudes above ground level.

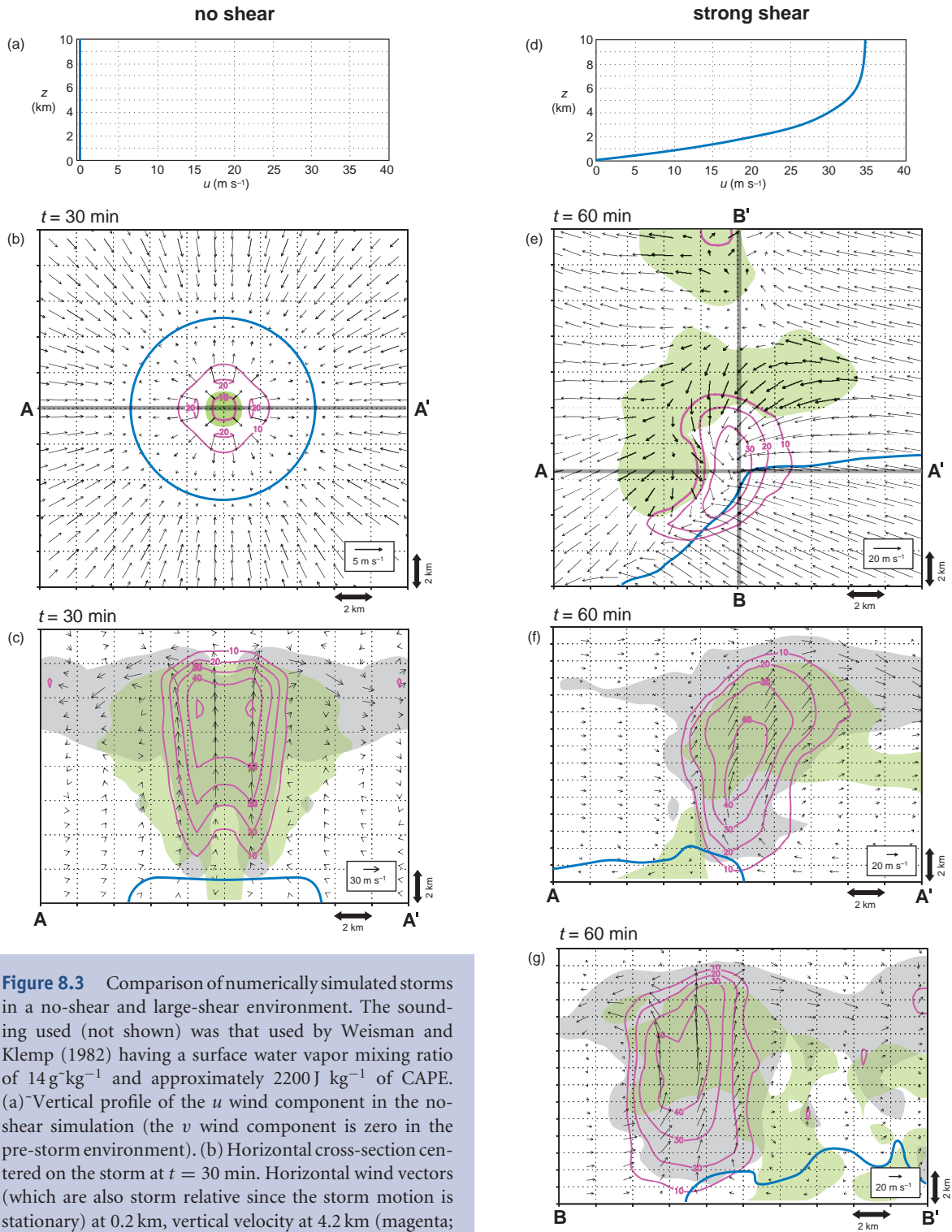


Figure 8.3 Comparison of numerically simulated storms in a no-shear and large-shear environment. The sounding used (not shown) was that used by Weisman and Klemp (1982) having a surface water vapor mixing ratio of 14 g kg^{-1} and approximately 2200 J kg^{-1} of CAPE. (a)~Vertical profile of the u wind component in the no-shear simulation (the v wind component is zero in the pre-storm environment). (b)~Horizontal cross-section centered on the storm at $t = 30$ min. Horizontal wind vectors (which are also storm relative since the storm motion is stationary) at 0.2 km , vertical velocity at 4.2 km (magenta; 10 m s^{-1} interval starting at 10 m s^{-1}), interval starting at 10 m s^{-1}), rainwater concentration at 1.0 km (green;

environments, especially if the shear is distributed over a significant fraction of the cloud depth, can also enhance updrafts at altitudes high above the gust front. The propagation of such storms is driven by deep-layer vertical pressure gradient forces independent of the gust front (this is the mode of convection identified in simulations initialized with a low-BRN environment). Figure 8.5 summarizes the relationship between the spectrum of storm types and the vertical wind shear.³

Some sources attribute increases in storm organization, longevity, and severity to updraft tilt, arguing that shear promotes a tilted updraft such that hydrometeors can fall out of the updraft without falling through the updraft, but many severe storms occurring in large-shear environments have fairly erect updrafts (see, e.g., Figure 8.3f, g). In fact, updrafts that are tilted are more adversely affected by entrainment and, as will be discussed in Chapter 9, by the vertical gradient of buoyancy perturbation pressure ($\partial p'_b / \partial z$). Updraft tilt depends on the vertical shear and the strength of the updraft, the latter of which, as discussed above (and in much more detail later in this chapter), can itself be intensified by the vertical shear; that is, vertical shear can actually promote *more upright* updrafts. This is especially true once storms develop extensive rain-cooled outflow, as will be shown in Chapter 9. Indeed, some long-lived, severe convective storms do have fairly tilted updrafts. The fact that long-lived DMC sometimes does and sometimes does not have tilted updrafts is evidence that the tilt of an updraft is not a good predictor of storm longevity (or severity). The ability of the gust

front or midlevel updraft to lift air to the LFC is what matters.

The characteristics and environments of single-cell, multicell, and supercell storms are described in the next sections. It is worth noting that the aforementioned numerical modeling studies, upon which much of our present understanding of the organization of DMC is based, simulated environments that were horizontally homogeneous and time invariant. A growing body of observational evidence and idealized numerical simulations suggest that spatial inhomogeneities in the environment can lead to profound changes in convective storm morphology and behavior. Furthermore, synoptic and mesoscale conditions are rarely, if ever, unchanging in time. We have only recently begun to consider what happens when convection initiated in weak shear finds itself in much stronger shear hours later. Idealized simulations suggest, perhaps somewhat intuitively, that convection can be transformed fairly readily from supercellular to multicellular convection if the vertical wind shear weakens while the convection is ongoing, but that multicellular, cold-pool-driven convection is not as easily transformed into supercellular, non-cold-pool-driven convection if the vertical wind shear strengthens while convection is ongoing. It seems as though cold pools provide a sort of ‘dynamical inertia’ that makes it difficult to change the behavior of a cold-pool-driven convective system. Simulated storms are also initiated, somewhat necessarily, with highly idealized forcing (e.g., isolated warm bubbles). The organization of DMC can be sensitive, however, to the means by which it is initiated (e.g., by an initial warm bubble versus a cold pool in a numerical model, and with potentially a range of horizontal and vertical dimensions, or perhaps, in the real atmosphere, depending on whether convection is initiated by a dryline or cold front, or the orientation of a mesoscale boundary relative to the mean wind direction). We do not yet possess a mature understanding of the sensitivity of DMC organization to the processes responsible for its initiation.

³ Elevated convection (Section 7.4) can be single-celled, multicellular (including large, long-lived mesoscale convective systems), or supercellular, depending on the magnitude of the vertical wind shear in the *cloud-bearing layer*. In elevated convection environments, strong shear is frequently present in the lowest ~ 1 km, especially on the immediate cool side of an air mass boundary, but if this air is very stable and is not feeding the convection, then the presence of strong shear in the layer is irrelevant.

Figure 8.3 (continued) $>2 \text{ g kg}^{-1}$ shaded), and the gust front at 0.2 km (-0.2 K potential temperature perturbation blue contour) are shown. (c) Vertical cross-section from A to A' (refer to [b]). Storm-relative wind vectors in the plane of the cross-section: the cloud field (gray; cloud ice and cloud water concentration greater than 1 g kg^{-1}), large hydrometeors (rainwater plus graupel plus snow; green; $>2 \text{ g kg}^{-1}$ shaded), vertical velocity (magenta; 10 m s^{-1} interval starting at 10 m s^{-1}), and the gust front (-0.2 K potential temperature perturbation blue contour) are shown. (d) As in (a), but for the large-shear simulation (the v wind component is zero in the pre-storm environment). The storm motion subtracted from the wind in order to obtain the storm-relative winds is $(20, -5) \text{ m s}^{-1}$. (e) As in (b), but for the large-shear simulation and at $t = 60 \text{ min}$. (f) and (g) Zonal and meridional vertical cross-sections as in (c) from A to A' and B to B' (refer to [e] for the locations of the cross-sections).

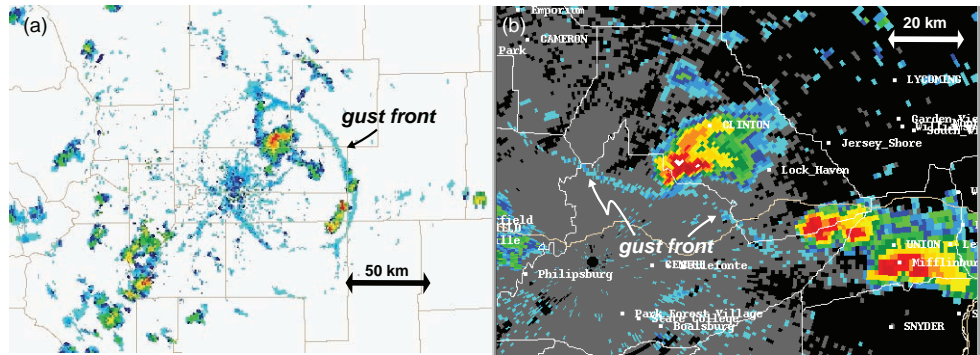


Figure 8.4 Radar reflectivity comparison of gust fronts associated with convection in (a) weak shear and (b) strong shear. In environments containing weak vertical wind shear, the gust front moves well beyond the radar echo (and the updraft that produces the precipitation that is responsible for the echo). Conversely, in environments containing strong vertical wind shear, the gust front tends to be closely attached to the echo, indicating that the updrafts are not being undercut by outflow. Also refer to Figure 8.3b, d.

8.2 Single-cell convection

Single-cell convection is the term for the variety of deep moist convection that consists of only one updraft and does not initiate subsequent convection in any organized manner. The lifting along gust fronts in weak-shear environments is weak and shallow; thus, it is difficult for the gust front produced by any individual cell to trigger

new cells. However, there are typically a number of discrete cells initiated by whichever mesoscale forcing initiates DMC on a particular day. Subsequent cells are often initiated by colliding outflows that provide much stronger forced lifting than any single gust front would. However, this evolution should be distinguished from the evolution typically associated with so-called *multicellular convection*, wherein new cells are triggered repeatedly, usually on a

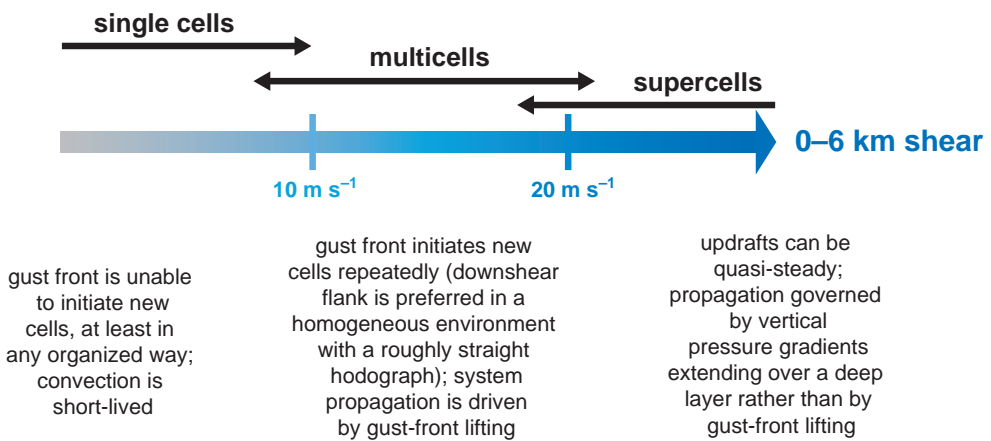


Figure 8.5 Spectrum of storm types as a function of vertical wind shear. Although the vertical shear exerts the greatest influence on storm type, other secondary factors can also affect the mode of convection (e.g., vertical distribution of buoyancy, moisture, and shear, as well as the means by which storms are initiated); thus, some overlap among storm types exists in this simple single-parameter depiction. The relationship between vertical wind shear magnitudes and the nature of cell regeneration/propagation is also shown.



Figure 8.6 Photographs of DMC in environments containing weak vertical wind shear. Note the location of the precipitation shafts relative to the updrafts (upper left, right) and the fairly symmetrical, circular anvils (lower left). Photograph credits: Jim LaDue (upper left), Roger Edwards/Insoujourn (lower left), Thomas Sävert (right).

preferred flank of the initial cell, such that a *highly organized* cluster or line of cells is maintained for a much longer period of time than the typical lifetime of an individual cell.

The weak vertical wind shear of single-cell convection environments usually implies weak synoptic-scale forcing; that is, the development of soundings that support single-cell convection is usually dominated by the diurnal cycle of the boundary layer rather than by large-scale ascent and/or advection of temperature or moisture. Thus, single-cell convection tends to occur near and shortly after the time of maximum daytime heating (when CIN is smallest and CAPE is largest) and tends to dissipate quickly after sunset. It only occasionally produces hail or wind gusts that could be characterized as severe. When severe weather is produced, it is generally of the *pulse* variety—short lived, usually marginal (e.g., a brief wind gust above 25 m s^{-1}), and difficult to issue warnings for. Although CAPE can range from just a few hundred J kg^{-1} to $>2000 \text{ J kg}^{-1}$ in single-cell environments, pulse severe weather events are usually limited to environments having large ($>2000 \text{ J kg}^{-1}$) CAPE. Peak updraft speeds also are highly variable and probably a strong function of the CAPE, though this does not imply that updraft speeds closely match those predicted by parcel theory. Maximum updraft speeds might be as

small as 5 m s^{-1} in low-CAPE, tropical, weak-shear environments, and in excess of 40 m s^{-1} in high-CAPE, midlatitude, weak-shear environments. Photographs of single-cell convection appear in Figure 8.6. Examples of single-cell convection in visible satellite and radar images appear in Figure 8.7.

Although we have classified DMC as single-cell, multicell, and supercell up to this point (refer to the previous section), alternatively, cells have also been classified either as *ordinary* cells or supercells. The updraft of an ordinary cell is driven virtually solely by buoyancy, whereas the updraft of a supercell is driven by both buoyancy and dynamic vertical pressure gradient forces that are comparable in magnitude. Single-cell convection is therefore viewed as comprising a single ordinary cell, and multicell convection is viewed as comprising multiple ordinary cells (the gust front of a multicellular convective system lifts air to the LFC via dynamic vertical pressure gradient forces on a preferred flank, but buoyancy still dominates the vertical acceleration above the LFC).

The lifetime of an ordinary cell, τ , can be approximated as the time it takes air to ascend from the surface to the equilibrium level (approximately H , the scale height of the atmosphere) divided by the average updraft speed (w_0), plus the time it takes for the precipitation produced by the

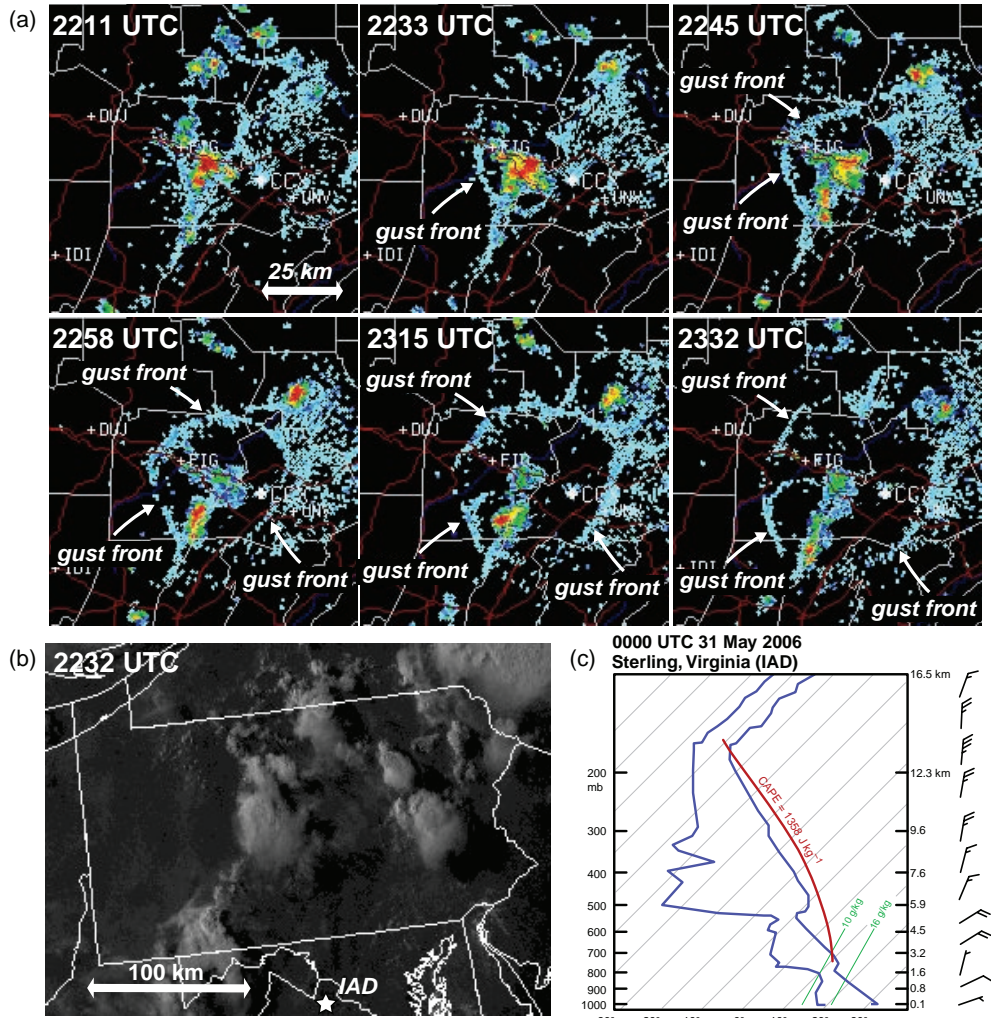


Figure 8.7 (a) Sequence of radar reflectivity images (0.5° elevation angle) from the State College, PA, WSR-88D on 30 May 2006 from 2211 to 2332 UTC showing the evolution of single-celled convection (*disorganized convection* would perhaps be more appropriate terminology in this case). (b) Visible satellite image at 2232 UTC. (c) Sounding from Sterling, VA (IAD; the location is indicated with a star in [b]) at 0000 UTC 31 May 2006. Note the weak vertical wind shear (the magnitude of the 0–6 km vector wind difference is approximately 5 m s^{-1}).

ascent to fall to the ground, which can be approximated as H/v_t , where v_t is the mean terminal fall speed of the precipitation:

$$\tau \approx \frac{H}{w_0} + \frac{H}{v_t}. \quad (8.2)$$

For $H \simeq 10 \text{ km}$, $w_0 \simeq 5\text{--}10 \text{ m s}^{-1}$, and $v_t \simeq 5\text{--}10 \text{ m s}^{-1}$, the lifetime is roughly 30–60 minutes.

The lifecycle of an ordinary cell begins with the towering cumulus stage. In this stage, only an updraft exists (Figure 8.8). The towering cumulus stage is followed by

the mature stage, which commences with the production of precipitation particles large enough to fall through the updraft (Figure 8.8). At this time, an anvil also begins to form. The precipitation formed by the rising air currents within the updraft falls through the updraft rather than being deposited away from the updraft, and the associated hydrometeor loading reduces updraft buoyancy. The falling precipitation and subsequent evaporation of precipitation induce a downdraft, which spreads laterally upon reaching the surface. The leading edge of the downdraft marks the gust front.

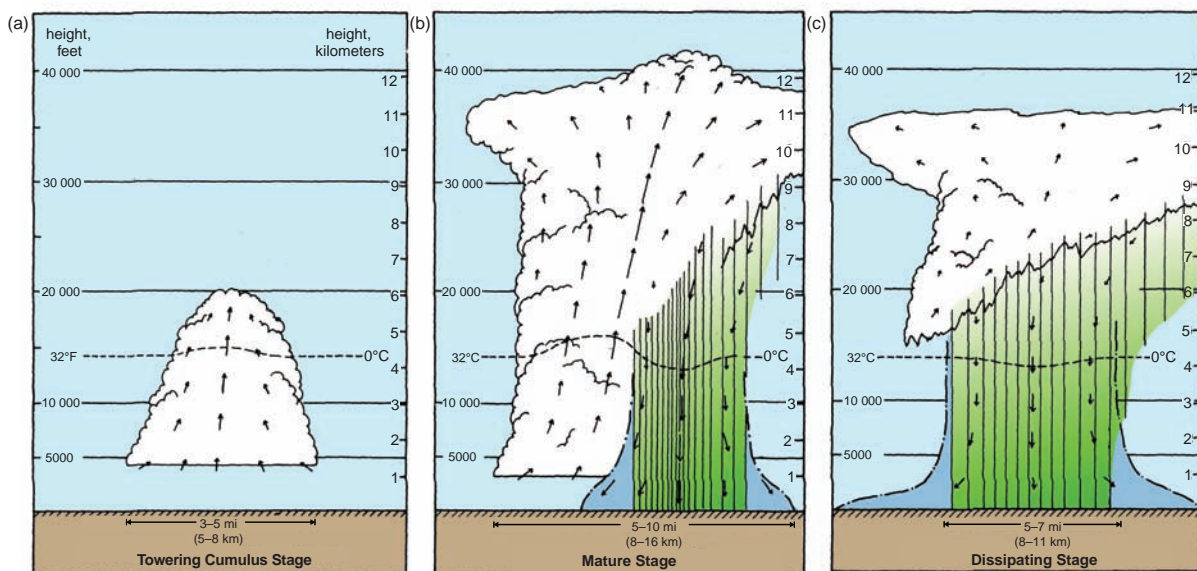


Figure 8.8 The three stages of an ordinary cell: (a) towering cumulus stage, (b) mature stage, and (c) dissipating stage. (Adapted from Byers and Braham [1949] and Doswell [1985].)

Eventually the downdraft completely dominates the cell, at which time the dissipating stage begins (Figure 8.8). During this stage, the rain-cooled air spreads far from the updraft; the updraft is cut off from potentially buoyant inflow and cannot be maintained. New cells may or may not be initiated by the gust front, depending on the environmental CIN and the vertical motion associated with the gust front. Eventually the old convective cloud is reduced to an *orphan anvil* composed entirely of ice crystals. The anvil slowly sublimates into oblivion (this can take many hours). If severe weather occurs, it usually occurs near the transition from the mature to dissipating stages, or about the time when the maximum fallout of precipitation occurs. Severe wind gusts are most likely when precipitation falls through relatively dry subcloud layers, where evaporative cooling and generation of negative buoyancy is substantial.

8.3 Multicellular convection

Multicellular convection probably is the most common form of convection in midlatitudes. In contrast to single-cell convection, multicellular convection is characterized by the repeated development of new cells along the gust front, where the forced ascent is sufficient to lift parcels to the LFC. The regular initiation of new cells enables the

survival of a larger-scale convective system, one that can be regarded as being composed of ordinary cells (Figure 8.8), despite the fact that each individual cell persists for only 30–60 minutes. The most severe forms of multicellular convection can last for hours and produce large swaths of damaging straight-line winds and hail up to the size of golf balls. Multicellular convection can be organized as meso- β -scale clusters of cells (see, e.g., Figures 8.9 and 8.10), or as meso- α -scale convective systems, which often take the form of nearly unbroken lines. Our scope is limited in this section to the smaller-scale form of multicellular convection, for example, that which can arise in a numerical simulation initialized with a single warm bubble. Larger-scale convective systems initiated by broad regions of mesoscale ascent, or by the merging of outflows produced by initially isolated updrafts, are treated separately in Chapter 9.

The environments of multicell convection are characterized by a moderate degree of vertical wind shear (the magnitude of the 0–6 km vector wind difference is usually in the 10–20 m s⁻¹ range). CAPE can be relatively small or large. Figure 8.11 presents a vertical cross-section of a typical evolution. In the top panel, Cell 1 is entering its dissipative stage (dominated by downdraft) and Cell 2 is in its mature stage. Cell 3 is just reaching the stage where precipitation is beginning to form (it is dominated by updraft at this time). The altitude of the first radar echo can provide



Figure 8.9 Photograph of a multicellular thunderstorm cluster. New updrafts are being forced on the left and old, dissipating updrafts are located on the right. Photograph by Al Moller.

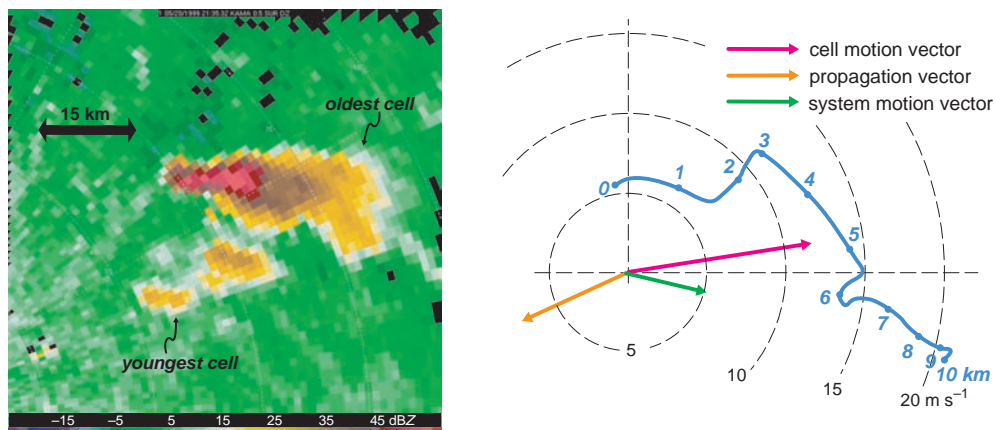


Figure 8.10 (a) Multicellular convection on 20 May 1999 as seen in reflectivity data obtained by the Amarillo, TX, WSR-88D. Range rings are drawn every 15 km. (b) Hodograph obtained from a wind profiler located approximately 100 km east of the convection in Vici, OK. The magnitude of the 0–6 km vector wind difference is 16 m s^{-1} . Vectors indicating cell motion, propagation, and overall system motion are also shown. It is evident that the (southwestward) propagation was not in the direction of the low-level shear (directed toward the east); thus, the observed propagation appears to be the result of environmental inhomogeneity (e.g., interaction with the dryline that was responsible for convection initiation in the first place, or perhaps CIN variations).

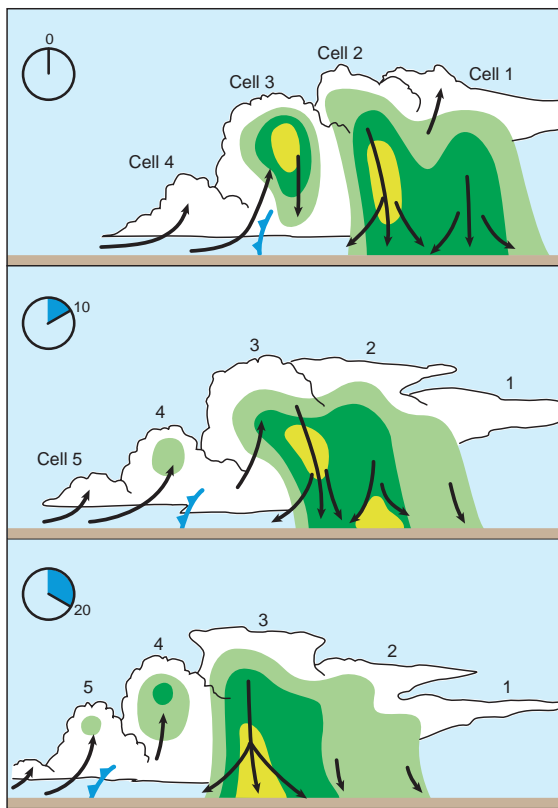


Figure 8.11 Schematic of the evolution of multicellular convection. Refer to the text for details. (Adapted from Doswell [1985].)

an indication of the updraft strength, with the altitude of the initial echo increasing with updraft strength. Cell 4 is only beginning to ascend toward the equilibrium level. In the middle panel of Figure 8.11, which is ~ 10 min after the top panel, the heavy precipitation produced by Cell 2 has reached the ground and its updraft is weakening. Cell 1 has almost completely dissipated. The top of Cell 3 has passed through its equilibrium level and is decelerating, which forces it to spread out horizontally into an anvil. Cell 4 continues to develop, and a new Cell 5 has been initiated. In the bottom panel of Figure 8.11, which is another ~ 10 min later, Cell 1 and Cell 2 have nearly dissipated, Cell 3 is dominated by downdrafts and has begun to weaken, Cell 4 is approaching the equilibrium level and is nearing maturity, and Cell 5 continues to grow (the first echo has appeared aloft). This cycle repeats itself—Cell 3 replaces Cell 2, Cell 4 replaces Cell 3, Cell 5 replaces Cell 4, and so on. Individual ordinary cells tend to move with the velocity of the mean wind averaged over their depth. This movement, combined with the repeated development

of new cells on a preferred flank, leads to a propagation of the multicell system that can be slower or faster than the mean wind, and often in a different direction than the mean wind (Figure 8.10b). We are careful to distinguish between *movement* and *propagation*. The movement of the multicell system (as well as the mesoscale convective systems in Chapter 9) is regarded as the sum of individual cell movement and propagation. The movement of individual cells is viewed as resulting from the *advection* of cells by the mean wind over the depth of the cell, whereas *propagation* refers to movement independent of advection.

There is a strong tendency for new cells to be initiated on the downshear flank of the outflow, because lifting by a gust front is enhanced where the environmental shear over approximately the depth of the outflow points in the opposite direction to the density gradient associated with the outflow (Figure 8.12; also refer to Figure 5.31). Lifting is enhanced (suppressed) on the downshear (upshear) flank of the outflow because this is where the baroclinically generated horizontal vorticity opposes (adds to) the horizontal vorticity associated with the low-level vertical wind shear in the environment. Gust front-relative streamlines originating in the environment turn upward most abruptly and lifting tends to be deepest along the portion of the gust front where the environmental and outflow-induced horizontal vorticity cancel most; air parcels lifted by this portion of the gust front have an excellent chance of reaching their LFC (Figure 8.12). Conversely, where the environmental and outflow-induced horizontal vorticity are in the same direction, lifting along the gust front is shallow and updrafts are highly tilted; air parcels are rapidly accelerated horizontally over the cold air as they rise above the ground, greatly limiting the chance that they will reach their LFC (Figure 8.12). The relationship between the tilt of the gust front updraft and the balance between outflow-induced horizontal vorticity and the environmental horizontal vorticity will be explored in greater detail in Chapter 9.

The environmental storm-relative (and therefore gust front-relative) winds at low levels, which are a function of storm motion and therefore depend on the wind profile over the entire depth of the storm (and therefore depend on the deep-layer shear), also play a role in the initiation of new cells. In addition to being influenced by the low-level vertical wind shear in the environment, the vertical motion along a gust front is also influenced by the strength of the storm-relative headwind encountered by the gust front (stronger headwinds are associated with stronger horizontal convergence and vertical motion). In the case of a straight hodograph, the strongest headwinds are encountered by the gust front on its downshear flank; that is, the influence of the low-level, environmental vertical wind shear and storm-relative winds on the vertical motion along the gust

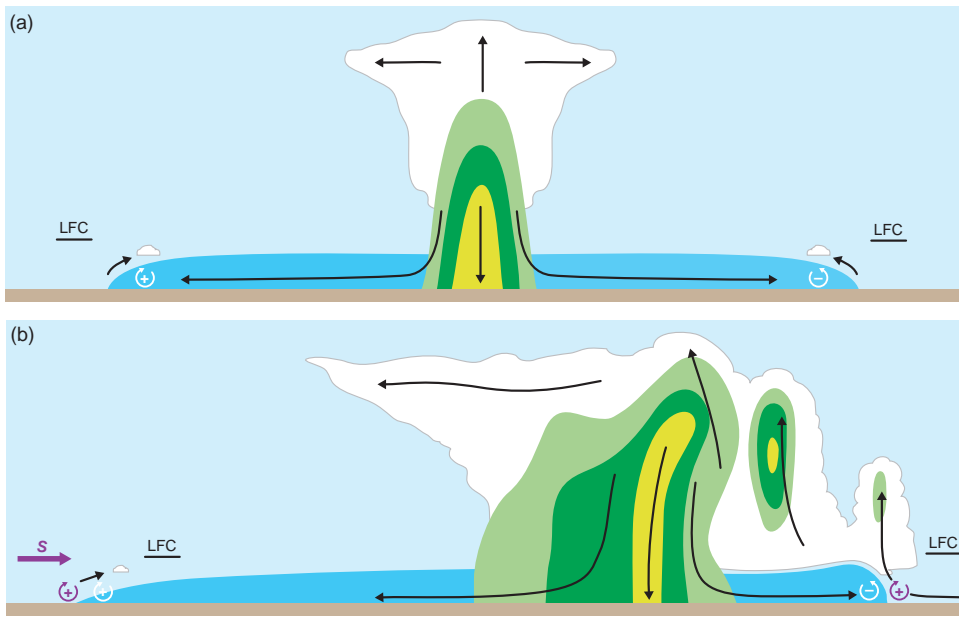


Figure 8.12 Comparison of lifting by the gust front in (a) a no-shear, single-cell environment and (b) a moderate-shear, multicell environment (the shear is westerly). Rain and hail are schematically indicated by the green and yellow shading. Evaporatively cooled outflow is shaded dark blue. Cloud is white. Some select storm-relative streamlines are shown as black arrows. The LFC is also indicated. The sense of the horizontal vorticity induced by the cold pools is indicated with white circular arrows. In (b), the sense of the horizontal vorticity associated with the environmental vertical wind shear is indicated with purple circular arrows. Moreover, the modification of the depth and slope of the leading portions of the cold pool by its interaction with the environmental shear, along with the effect on the nature of the lifting along the gust front, is also reflected in (b). Compare the depths of the western and eastern outflow heads in (b) to each other, as well as to those drawn in (a).

front are both maximized on the downshear flank of the outflow, which promotes downshear propagation. When the hodograph is curved, however, the strongest headwind may not be on the downshear flank of the gust front. For example, consider the multicell simulation shown in Figure 8.13, in which the hodograph turns through 90° . Over the depth of the cold pool ($\sim 1 \text{ km}$), the mean low-level environmental shear points toward the north-northeast, whereas the mean low-level environmental storm-relative wind points toward the west-southwest (Figure 8.13a). New cells develop along the gust front in an arc that extends from the northern flank to the eastern flank, leading to an overall propagation toward the northeast (Figures 8.13b–d).

Although the orientation of the shear and storm-relative winds affect the propagation of multicellular convection in important ways, multicell propagation can also be influenced by environmental heterogeneities. One common example is the influence of a mesoscale boundary or synoptic front, or possibly even terrain, which can interact with convective outflow in order to initiate new

cells in a way that defies what one would expect in a homogeneous environment when only the characteristics of the environmental wind profile can modulate the lifting by the gust front. Occasionally such heterogeneities lead to *backbuilding* multicellular convection, in which case the system propagation is in the opposite direction to individual cell motions. Variability of CIN within the environment also can affect the propagation of the convection. When CIN varies within the ambient environment, new cell generation and thus system propagation depend on where the superpositioning of gust front lifting and weak CIN is optimal (this is just a simple consequence of the fact that convection initiation depends on both the vertical motion and CIN). Multicellular convection has a propagation component toward smaller CIN when CIN gradients exist in the environment (Figure 8.14).

Supercells, which arise when the vertical wind shear is large, are treated in the next section. Significant dynamic vertical pressure gradient forces act over large depths within supercells, and these lifting forces are largely independent of

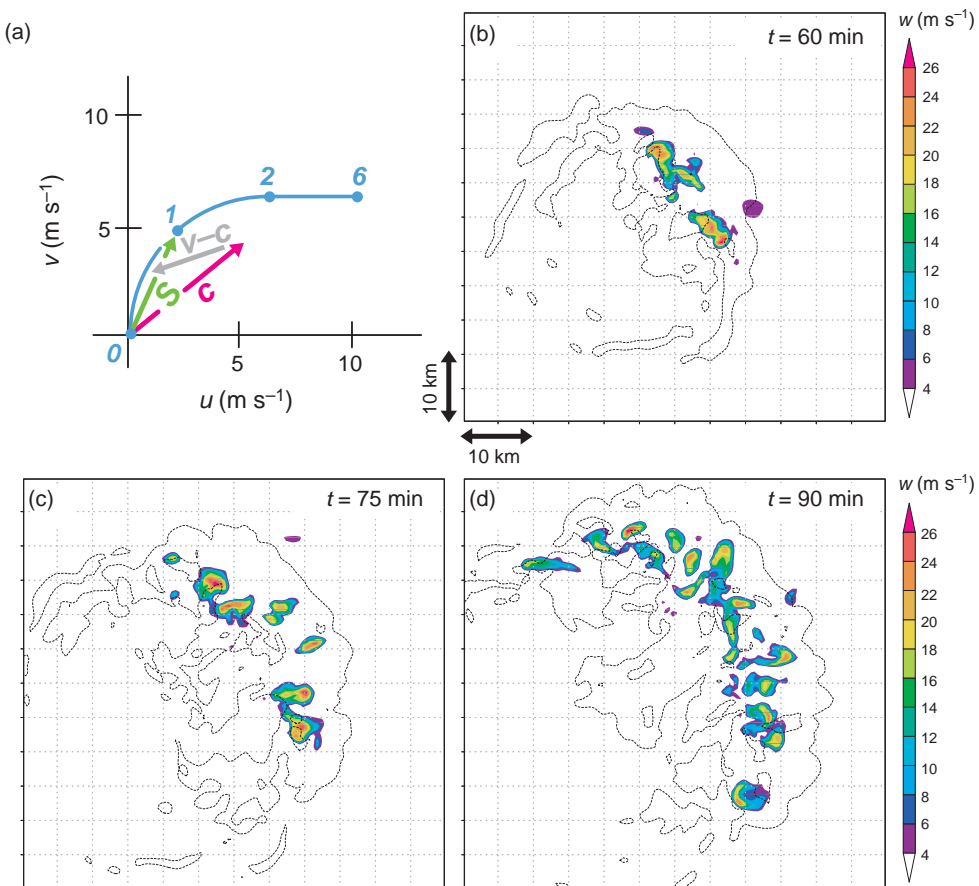


Figure 8.13 Simulation of multicellular convection in which the hodograph is curved. The hodograph is shown in (a); the blue numerals indicate heights above ground level in kilometers. The magenta, gray, and green vectors indicate the cell motion (c), the mean 0–1 km storm-relative wind ($v - c$), and the 0–1 km vector wind difference (S). In (b)–(d), horizontal cross-sections show updraft at a height of 5 km (color shading; see the legend) and the -1 K potential temperature contour (approximately the location of the outflow boundary) at 60, 75, and 90 min, respectively.

the gust front. As a result, supercell propagation tends not to be driven by the gust front. Supercells sometimes propagate nearly continuously, in contrast to the discrete propagation that typifies the motion of multicellular convection.

8.4 Supercellular convection

8.4.1 Definition of a supercell and characteristics of supercell environments

Supercells are probably the least common storm type worldwide, but they nonetheless are responsible for a disproportionately large fraction of severe weather reports. Almost all

reports of hail having a diameter of 5 cm or larger are associated with supercell storms, as are virtually all strong and violent tornadoes.⁴ Supercells can also produce extremely high lightning flash rates, with rates exceeding 200 flashes per minute possible. Supercells are frequently long-lived (1–4 h lifetimes are common, and some have been observed to persist as long as 8 h); in fact, this is probably one reason why they were originally called supercells. The consensus now seems to favor a dynamical criterion in place of a longevity criterion for classification of a storm as a supercell.

⁴ Tornadoes are classified as *strong* if they have an enhanced Fujita (EF) scale rating of EF2 or EF3 (estimated winds of 111–165 mph), and *violent* if they are rated EF4 or EF5 (>166 mph). Tornadoes are discussed in greater detail in Section 10.2.

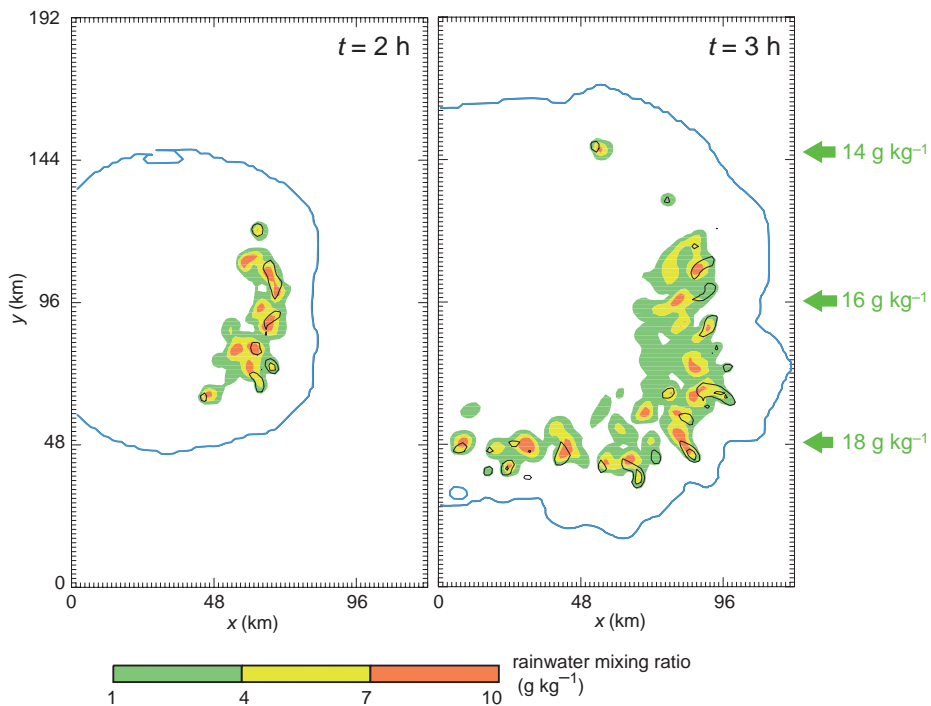


Figure 8.14 Example of propagation of multicellular convection in a numerical simulation in which the environment contains horizontally varying moisture. The moisture gradient points toward the south; the base state water vapor mixing ratios at the surface as a function of latitude are indicated on the far right. The environmental shear is westerly at all levels. The rainwater (see legend) and vertical velocity (5 and 15 m s^{-1} isotachs) fields are shown at 4.6 km AGL at $t = 2\text{ h}$ and $t = 3\text{ h}$ in order to provide a sense of the locations of convective cells. The -1 K potential temperature contour at the lowest grid level is highlighted in blue to indicate the gust front location. In a horizontally homogeneous environment, the convection would propagate toward the east, resulting in a system motion at a speed faster than the mean wind, which is also westerly. However, the environmental moisture gradient in this case is associated with a CIN gradient, with lesser (greater) CIN to the south (north) where moisture is above (below) average. Thus, the propagation of the convection has an additional component toward the south, resulting in an overall system motion toward the southeast. (From Richardson [1999].)

The widely accepted dynamical criterion is the presence of a persistent, deep *mesocyclone* within the updraft. A mesocyclone is a region of vertical vorticity with a characteristic width of $3\text{--}8\text{ km}$ and magnitude of $O(10^{-2})\text{ s}^{-1}$. The mesocyclone should persist long enough for an air parcel to pass through the entire updraft ($\sim 20\text{ min}$), and the mesocyclone should extend over at least half the depth of the updraft. In other words, small-scale, shallow, and transient vortices—for example, those that are routinely observed along gust fronts, probably as a result of shear instability—are typically not identified as mesocyclones. As discussed in Section 8.1, supercells can also be distinguished dynamically from nonsupercells by way of their propagation, which, in contrast to nonsupercells, is not dominated by the triggering of new cells by the gust front.

Supercells occur in environments containing large vertical wind shear. In other words, long hodographs typify supercell environments (Figure 8.15). Hodographs are often also curved, although hodograph curvature is not required for supercell storms. Curiously, the motion of supercells tends to deviate significantly from the mean wind, with cyclonically (anticyclonically) rotating supercells having a propagation component to the right (left) of the mean wind shear. The horizontal vorticity associated with the large vertical wind shear in supercell environments is the source of vertical vorticity for the midlevel mesocyclone by way of the tilting term in the vorticity equation. The vertical wind shear present in supercell environments tends to extend over a significant depth of the troposphere (Figure 8.15), rather than being confined to

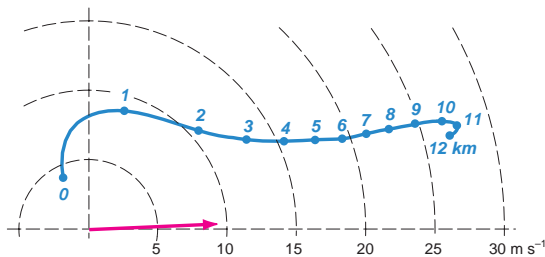


Figure 8.15 Composite hodograph based on a nationwide sample of over 400 proximity soundings in the environments of cyclonically rotating supercell thunderstorms in the United States. The proximity soundings were obtained from Rapid Update Cycle analyses. The mean storm motion is indicated by the magenta arrow. Notice that it lies not just to the right of the mean wind, but to the right of *all* of the winds that define the hodograph. (Adapted from Markowski *et al.* [2003].)

the lowest kilometer or two, which is the case in some multicell storm environments such that the magnitude of 0–6 km shear might otherwise suggest that sufficient shear is present for supercells (recall the overlap between storm types in Figure 8.5). The fact that the vertical shear in supercell environments tends to span a significant depth of the troposphere results in significant storm-relative winds throughout most of the troposphere (Figure 8.15). The advantages of strong storm-relative winds at low levels and upper levels were discussed in Section 8.1. Dynamically induced vertical pressure gradients arising from the interaction of an updraft with vertical wind shear, as well as dynamical effects associated with the mesocyclone, can also enhance the updraft in significant ways. It is in this way that supercells differ from ordinary cells, which are driven almost solely by buoyancy. Although CAPE tends to be significant ($>1000 \text{ J kg}^{-1}$) in supercell environments, extreme amounts of CAPE are not necessary for supercells.

8.4.2 Structure of supercells

Visual and radar appearance

Supercells are characterized by a single dominant updraft, which can have a quasi-steady appearance, depending on the temporal frequency of observations. An attendant *flanking line* of updrafts also can occasionally be seen, typically located on the right-rear flank (with respect to storm motion) and shallower than the dominant updraft closer to the core of heaviest precipitation (Figure 8.16). Vertical velocities can exceed 50 m s^{-1} within the most intense supercell updrafts. The main updraft of a supercell

and its associated mesocyclone are often visually stunning (Figure 8.17). In Doppler radar velocity data, the mesocyclone is associated with a couplet of inbound and outbound radial velocities (Figure 8.18). A locally lowered cloud base called a *wall cloud* is often present at the base of the updraft, where humid, rain-cooled air originating from the precipitation regions is drawn into the updraft, reaching saturation at a lower altitude than the height at which ambient environmental air becomes saturated via lifting (Figure 8.16). A pair of schematics generalizing the airflow in supercells is presented in Figures 8.19 and 8.20.

The updraft of a supercell is typically associated with a reflectivity minimum in radar data, called the *bounded weak-echo region* or *BWER* (Figure 8.21). The BWER is assumed to signify a region of updraft too strong to allow the descent of hydrometeors and/or a region in which the Lagrangian timescales are insufficient for precipitation formation. At low levels, the BWER may not be ‘bounded’, in which case a *weak-echo region* or *WER* exists. The downward extension of the rear side of the *echo overhang* that caps the BWER (Figure 8.21) forms a pendant-shaped *hook echo* in radar imagery at low elevations (Figure 8.18). The hook echo is the best-recognized reflectivity feature associated with a supercell storm. Although conventional wisdom suggests that the advection of hydrometeors out of the main echo core by the mesocyclone plays a major role in the formation of the hook echo, hook echo formation in many cases is complicated by precipitation processes occurring within flanking line cells and the general fact that hydrometeors are not good tracers of the airflow because of their large fall speeds.

Downdraft regions

Supercells contain two main downdraft regions. The first is associated with the hook echo region to the rear of the storm. This downdraft is referred to as the *rear-flank downdraft* or *RFD* (Figure 8.22). It has long been surmised that the RFD forms when dry mid- and upper-level winds impinge upon the backside of the updraft, leading to evaporative chilling and negative buoyancy, and ensuing downward accelerations (Figure 8.20). However, downward-directed vertical pressure gradient forces on the upshear flank of the storm might also play a role in dynamically driving the RFD, and the extent to which RFDs are thermodynamically versus dynamically forced is not yet fully understood. If low- θ_e air at midlevels is entrained into the RFD, low θ_e values would likely be observed at the surface (θ_e deficits of 10–20 K have been observed, depending on θ_e values aloft and the degree of entrainment). If the RFD is driven predominantly by precipitation loading and/or dynamic effects, then θ_e deficits within the RFD can

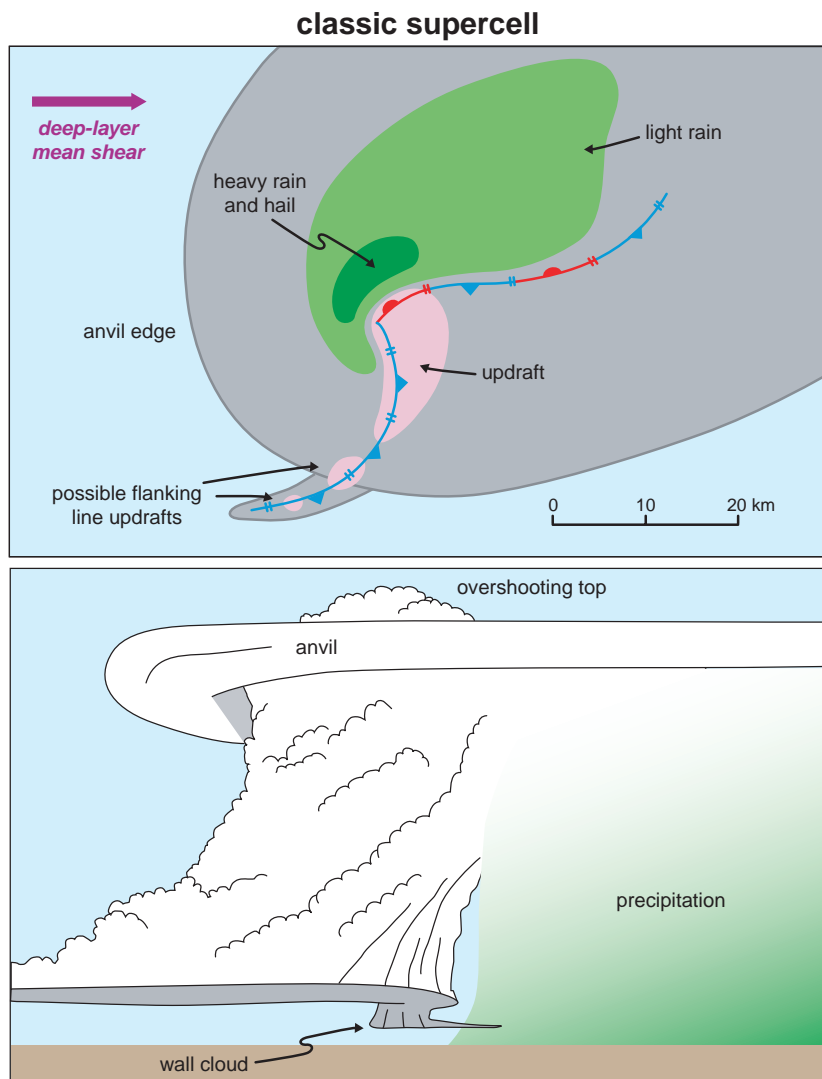


Figure 8.16 Structure of what is sometimes termed a *classic supercell* (other classes of supercells will be introduced later in this section). Top, horizontal cross-section of low-level radar structure and cloud features. Bottom, schematic of the visual appearance from the viewpoint of an observer located to the south of the storm. (Adapted from Doswell and Burgess [1993].)

be considerably smaller (θ_e deficits as small as just a few kelvins are sometimes observed). Temperature deficits in the RFD vary considerably from one supercell to another (temperature deficits can range from near zero to 10 K), with the differences among storms likely depending on the concentration and distribution of hydrometeors within the RFD, environmental relative humidity, and the degree of entrainment.

As a result of the deep-layer wind shear and upper-level storm-relative winds, the bulk of the hydrometeors

are deposited on the forward flank of the updraft. Evaporation of rain and the melting and sublimation of ice lead to the development of negative buoyancy and a downdraft in this forward-flank region. This downdraft is appropriately referred to as the *forward-flank downdraft* or FFD (Figure 8.22). As was the case for the RFD, temperature deficits within the FFD also vary significantly from one storm to another (temperature deficits can range from 2 to 10 K), depending largely on the low-level relative humidity, and probably also depending on factors such as



Figure 8.17 A midlevel mesocyclone is the defining visual characteristic of a supercell storm. Little imagination is needed to sense the cyclonic vertical vorticity associated with the storm updraft. Photograph by Herb Stein (the Dopper On Wheels radar is in the foreground).

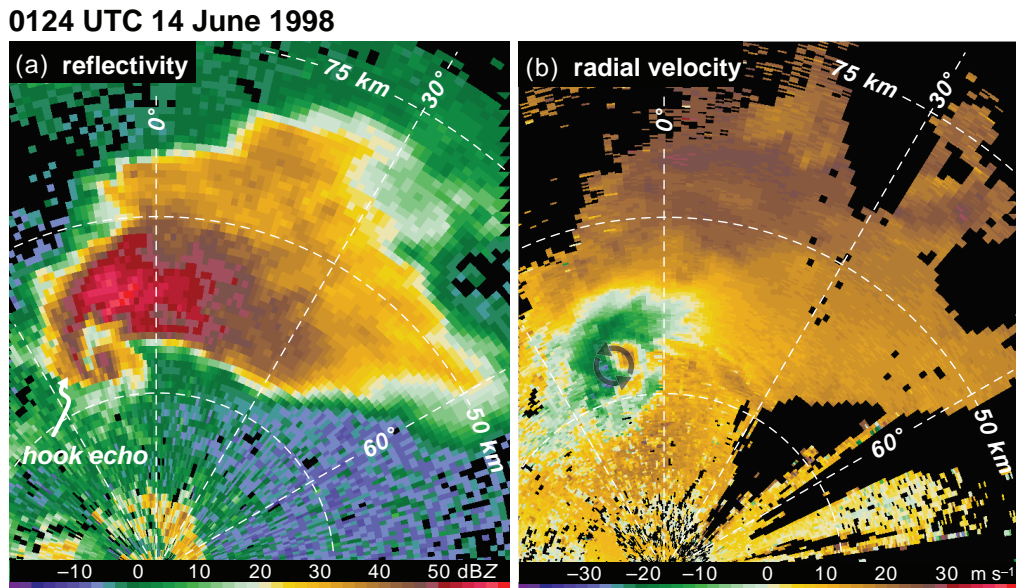


Figure 8.18 A hook echo in reflectivity data and an inbound–outbound couplet in radial velocity data are the defining radar characteristics of supercells in low-altitude radar scans. The images are (a) reflectivity and (b) radial velocity from the Oklahoma City, OK, radar at 0124 UTC 14 June 1998. The inbound–outbound radial velocity couplet is oriented such that the zero contour is approximately parallel to the radials, with inbound (outbound) velocities to the west (east), thereby implying cyclonic vertical vorticity.

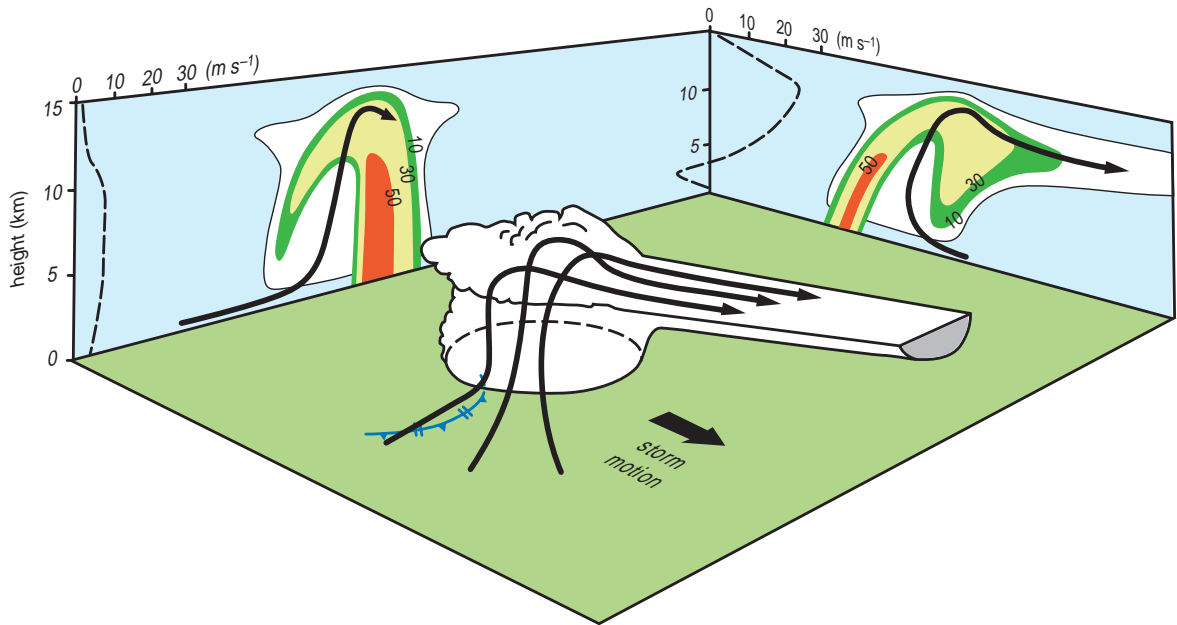


Figure 8.19 Perspective view of a supercell depicting storm-relative airflow and reflectivity structure. The reflectivity contours are 10, 30, and 50 dBZ. The rear-flank gust front also is shown. (Adapted from Chisholm and Renick [1972].)

the midlevel entrainment of environmental air. The FFD and RFD collectively produce a surface gust front structure that resembles, at least kinematically, the frontal structure associated with a midlatitude extratropical cyclone (Figure 8.22).

During the intensification of near-ground rotation in a supercell, if it occurs, a small-scale downdraft known as an *occlusion downdraft* may develop in close proximity to the updraft. Occlusion downdrafts can be viewed as a localized intensification of the RFD, as occlusion downdrafts are usually embedded within the broader RFD. They are driven by a downward-directed dynamic vertical pressure gradient force in association with the amplification of vertical vorticity near the ground. Recall that low pressure is associated with fluid rotation (Section 2.5.3). If a vertical gradient of rotation develops, as is the case when vertical vorticity rapidly amplifies near the ground and exceeds the vertical vorticity aloft, then so does a vertical gradient of dynamic perturbation pressure (the resulting acceleration is downward if low-level rotation exceeds midlevel rotation).

Inflow lows

The inflow into a supercell updraft is commonly strong, and can be damaging occasionally, with speeds greater than

20 m s⁻¹ possible. The inflow region is associated with a dynamic pressure minimum of 1–3 mb called an *inflow low*. A similar pressure minimum also can be observed within the forward-flank outflow (Figure 8.23)—even though this air is precipitation-cooled and referred to as outflow, some of this air is ‘recycled’ by the updraft as inflow despite the negative buoyancy of the air (recall that the dynamic lifting of this cooler, humidified air is what forms the wall cloud). The strong dynamic vertical pressure gradient force of a supercell updraft (Section 8.4.5) enables it to process more negatively buoyant air than nonsupercells would ordinarily be able to process.

Because the assumption that $\nabla^2 p' \propto -p'$ (Section 2.5) loses credibility near rigid boundaries, surface pressure perturbations are best assessed using a Bernoulli equation. For example, in the case of steady flow,

$$\frac{\rho v^2}{2} + p = \text{constant} \quad (8.3)$$

where p , ρ , and v are the air pressure, density, and wind speed, respectively, along a horizontal streamline. The lhs of (8.3) is conserved along streamlines, so where flow is fast, pressure is low, and vice versa. Thus, low pressure occurs in the inflow region of intense convective storms, where flow accelerates toward the updraft base. Using (8.3),

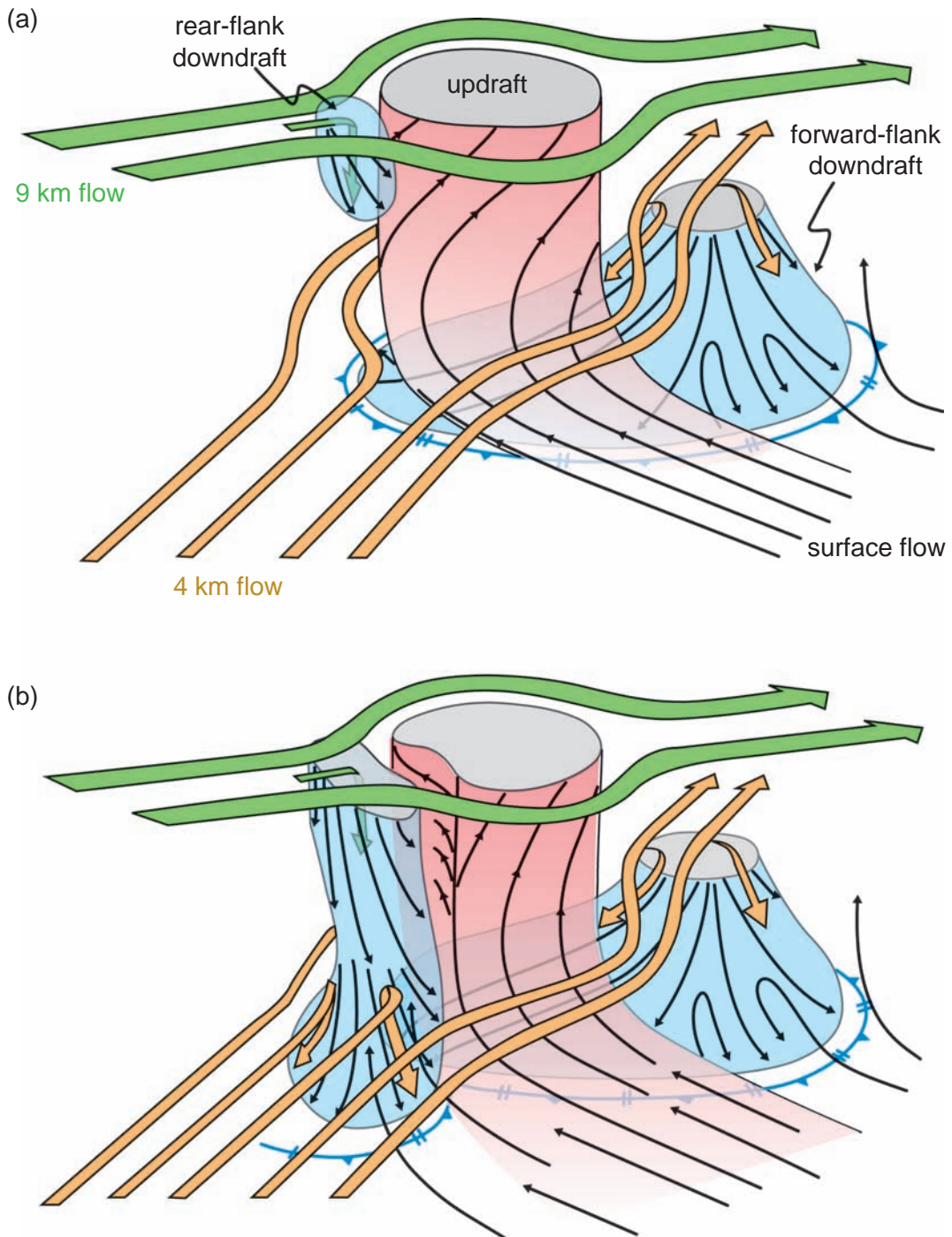


Figure 8.20 Schematic three-dimensional depiction of updraft and downdraft structure in a supercell storm (a) early in the lifetime and (b) during the mature stage, as proposed by Lemon and Doswell (1979). One aspect of this conceptual model that should probably not be taken too literally is the implied descent of air from high altitudes all the way to the surface. (The original figure caption by Lemon and Doswell in fact warns against literal interpretation of the arrows as actual streamlines or trajectories.) (Adapted from Lemon and Doswell [1979].)

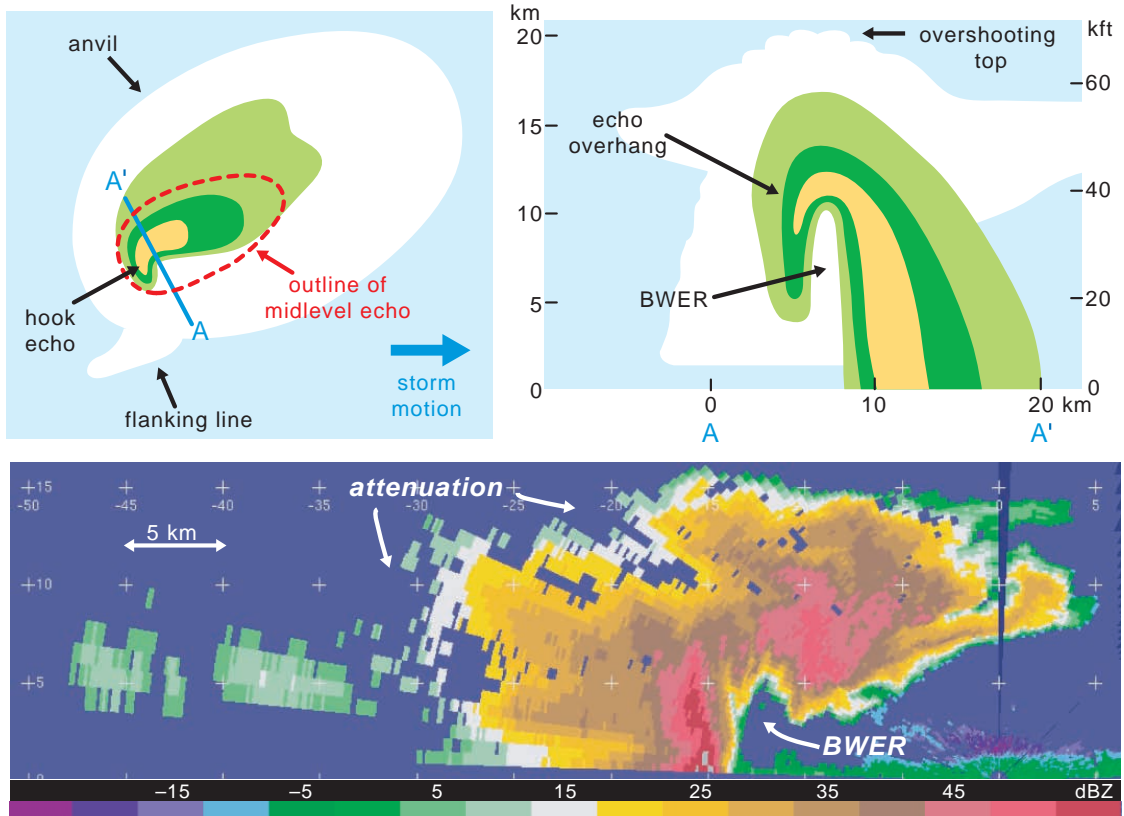


Figure 8.21 Top, schematic of the reflectivity structure of a supercell, showing the relationship between the bounded weak echo region (BWER), overshooting top, and hook echo. The green and yellow shading indicates weak, moderate, and high radar reflectivity visible at low levels (top left) and in a vertical cross-section (top right). Bottom, actual quasi-vertical cross-section of radar reflectivity factor in a supercell thunderstorm obtained from a helically scanning radar mounted in the tail of an aircraft at 2306 UTC 16 May 1995 during the Verification of the Origin of Rotation in Tornadoes Experiment (VORTEX).

the pressure drop, Δp , associated with inflow accelerations is

$$\Delta p = \frac{\rho}{2} (v^2 - v_\infty^2), \quad (8.4)$$

where v is the wind speed near the storm and v_∞ is the wind speed far from the storm. For $\rho \approx 1 \text{ kg m}^{-3}$, inflow that accelerates from 5 to 20 m s^{-1} generates an inflow low having a pressure deficit slightly in excess of 2 mb, consistent with observations.

Supercell spectrum

The spatial distribution of precipitation within supercells can vary significantly across what is sometimes called the *supercell spectrum*. Supercells having precipitation

characteristics that are similar to the precipitation characteristics originally documented in supercells are now referred to as *classic* (CL) supercells (e.g., Figure 8.22). Whereas classic supercells have most of their precipitation on the forward flank, with only a small amount within the hook echo at the rear of the updraft, *low-precipitation* (LP) supercells have nearly all of their precipitation far displaced from the updraft in the forward region of the storm, where much of it evaporates before reaching the surface (Figure 8.24). LP storms can appear visually spectacular (Figure 8.25), but their radar appearance often exhibits only weak echo ($< 45 \text{ dBZ}$) without a hook-shaped appendage. Downdrafts tend to be weak, and the RFD can be absent entirely. Tornadoes are rare in such storms. On the other hand, *heavy-* or *high-precipitation* (HP) supercells have a large amount

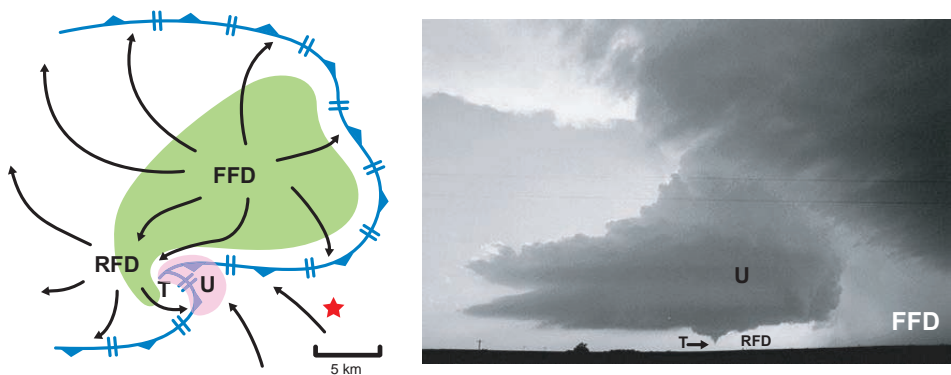


Figure 8.22 (Left) Schematic representation of a supercell thunderstorm, adapted from the conceptual model presented by Lemon and Doswell (1979). The green shading approximates the precipitation region as viewed by radar (e.g., radar reflectivity factor $>30 \text{ dBZ}$). Within this region, the locations of the forward-flank downdraft (FFD) and rear-flank downdraft (RFD) are indicated. The pink shading approximates the main updraft region (U). The typical location of a tornado, if one occurs, is also indicated (T). The outflow boundary is indicated by the barbed contour. A few storm-relative streamlines are drawn. The star indicates the approximate vantage point of the photograph appearing on the right. (Right) Photograph of a tornadic supercell that closely resembles the schematic shown on the left. The labels in the photograph correspond to the same features depicted in the schematic. Photograph courtesy of Erik Rasmussen.

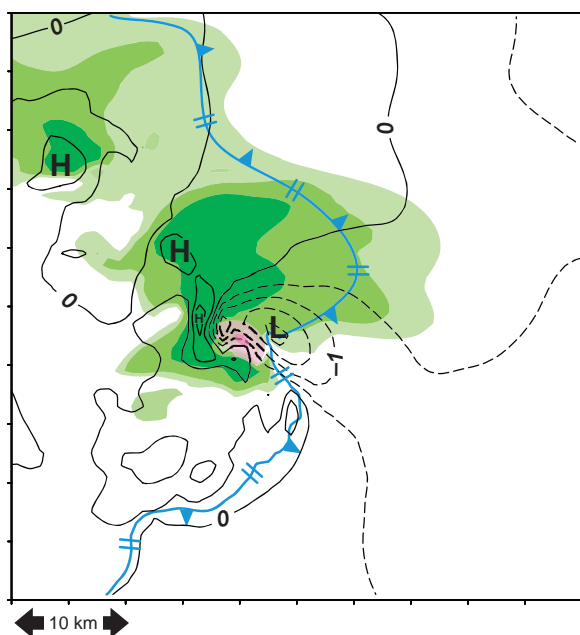


Figure 8.23 Pressure perturbations at the lowest grid level ($z = 125 \text{ m}$) in a numerical simulation of a supercell. Contours are every 0.5 mb; dashed contours are used for negative values. The gust front is indicated with a blue barbed line (the gust front follows the -1 K potential temperature perturbation contour). The three green levels indicate rainwater concentrations of $1\text{--}3 \text{ g kg}^{-1}$, $3\text{--}5 \text{ g kg}^{-1}$, and $>5 \text{ g kg}^{-1}$, respectively, at $z = 1125 \text{ m}$. The two pink levels indicate where updraft speeds are $8\text{--}12 \text{ m s}^{-1}$ and $>12 \text{ m s}^{-1}$, respectively, at $z = 1125 \text{ m}$. Note the prominent pressure minimum immediately east of the updraft; the pressure minimum is in a region of strong easterly winds flowing toward the updraft.

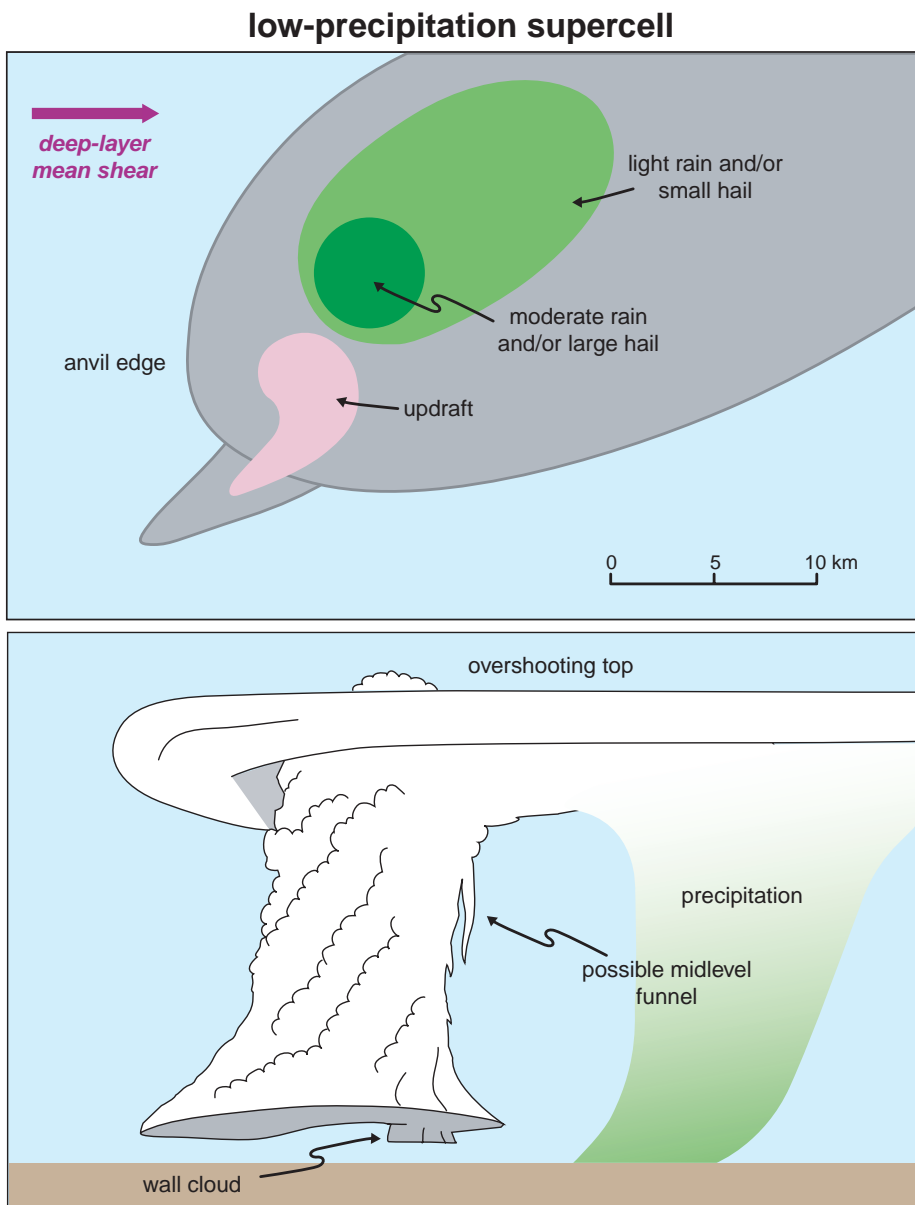


Figure 8.24 As in Figure 8.16, but for a low-precipitation (LP) supercell. (Adapted from Doswell and Burgess [1993].)

of precipitation within the hook echo region and on the backside of the storm (Figure 8.26). Visually, the updraft may be difficult to see if it is engulfed in rain, and on radar HP storms can take on a kidney-bean appearance. Downdrafts can be intense. Tornadoes are not as common in HP supercells as in classic supercells, perhaps because the downdrafts are so strong that they repeatedly undercut the

updraft with cold outflow (the importance of downdrafts in tornadogenesis is discussed in Section 10.2.2). Large hail and damaging downburst winds are common with HP supercells, however.

The classification of supercells is rather subjective, in part because storms may visually appear to fall into one class, but the radar appearance may suggest another class.



Figure 8.25 Photographs of an LP (top) and HP (bottom) supercell. Photographs by Eric Nguyen.

The LP-CL-HP supercell classes should be viewed as a continuum. The part of the continuum that appears to pose the most dangerous tornado threat is the LP-CL transition region. It has been found that supercell type, at least in the case of isolated storms, is a strong function of the upper-level storm-relative winds near the level of the anvil (e.g., at 9–12 km).⁵ When upper-level storm-relative winds are weak (approximately $< 18 \text{ m s}^{-1}$), hydrometeors tend to fall near the updraft, with a substantial amount

of precipitation wrapping around the updraft, therefore favoring an HP supercell. When upper-level storm-relative winds are strong (approximately $> 28 \text{ m s}^{-1}$), hydrometeors are deposited far downstream of the updraft, and very little falls near the updraft, therefore favoring an LP supercell. Classic supercells tend to occur for a middle range of upper-level storm-relative winds (roughly $18\text{--}28 \text{ m s}^{-1}$). In the case of multiple storms, precipitation originating in one storm may fall into and seed nearby storms, tending to push them toward the HP end of the spectrum.

⁵ See Rasmussen and Straka (1998).

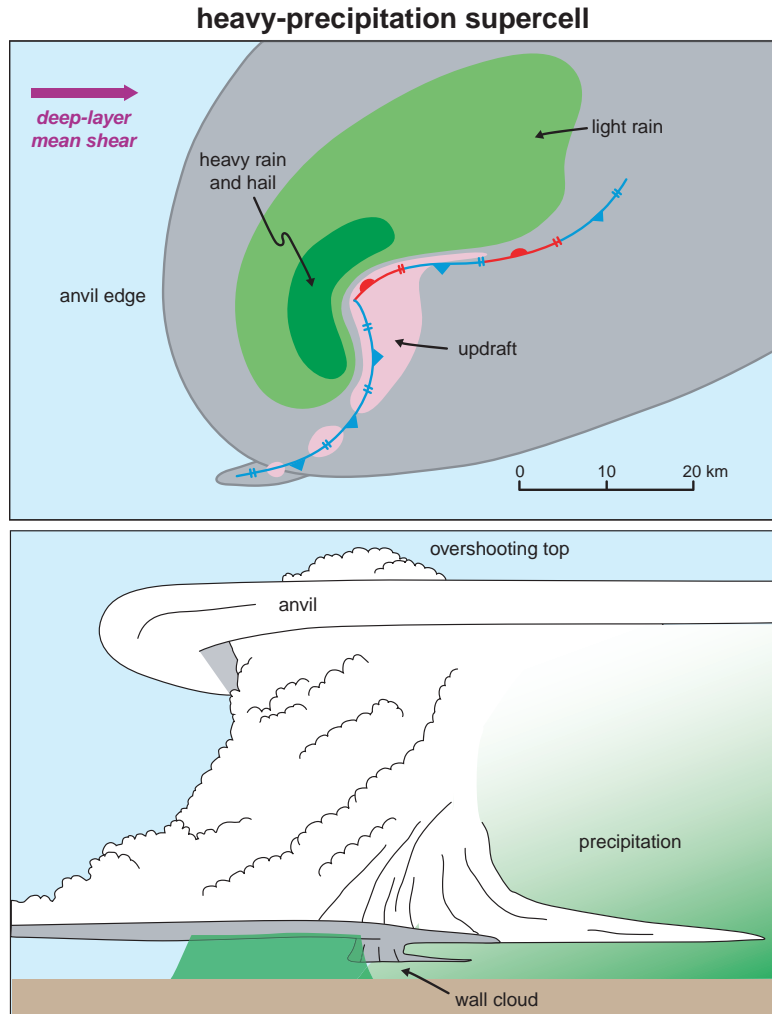


Figure 8.26 As in Figure 8.16, but for a heavy-precipitation (HP) supercell. (Adapted from Doswell and Burgess [1993].)

8.4.3 Origins of midlevel rotation

Linear theory of midlevel mesocyclogenesis

The origin of midlevel rotation in supercells is relatively well understood. As we shall see later, the development of rotation near the surface involves additional factors, principally the development of downdrafts. In examining the development of midlevel rotation within an updraft, we begin with the vertical vorticity equation written as

$$\frac{\partial \zeta}{\partial t} = -\mathbf{v} \cdot \nabla \zeta + \boldsymbol{\omega} \cdot \nabla w \quad (8.5)$$

$$= -u \frac{\partial \zeta}{\partial x} - v \frac{\partial \zeta}{\partial y} - w \frac{\partial \zeta}{\partial z} + \xi \frac{\partial w}{\partial x} + \eta \frac{\partial w}{\partial y} + \zeta \frac{\partial w}{\partial z}$$

$$\begin{aligned}
 &= \underbrace{-u \frac{\partial \zeta}{\partial x} - v \frac{\partial \zeta}{\partial y} - w \frac{\partial \zeta}{\partial z}}_{\text{advection}} \\
 &\quad + \underbrace{\left(\frac{\partial w}{\partial y} - \frac{\partial v}{\partial z} \right) \frac{\partial w}{\partial x} + \left(\frac{\partial u}{\partial z} - \frac{\partial w}{\partial x} \right) \frac{\partial w}{\partial y}}_{\text{tilting}} \\
 &\quad + \underbrace{\left(\frac{\partial v}{\partial x} - \frac{\partial u}{\partial y} \right) \frac{\partial w}{\partial z}}_{\text{stretching}}
 \end{aligned}$$

where $\boldsymbol{\omega} = (\xi, \eta, \zeta)$ is the three-dimensional relative vorticity vector, and we have neglected the Coriolis force and

baroclinic generation of vertical vorticity, which do not contribute to $\partial\zeta/\partial t$ in a major way.⁶

A linearized vertical vorticity equation is sufficient to account for mesocyclogenesis. Substituting $u = \bar{u}(z) + u'$, $v = \bar{v}(z) + v'$, $w = w'$, and $\zeta = \zeta'$ into (8.5) and neglecting the products of perturbations yields⁷

$$\frac{\partial\zeta'}{\partial t} = -\underbrace{\bar{u}\frac{\partial\zeta'}{\partial x} - \bar{v}\frac{\partial\zeta'}{\partial y}}_{\text{advection}} + \underbrace{\frac{\partial\bar{u}}{\partial z}\frac{\partial w'}{\partial y} - \frac{\partial\bar{v}}{\partial z}\frac{\partial w'}{\partial x}}_{\text{tilting}}, \quad (8.6)$$

which can be written as

$$\frac{\partial\zeta'}{\partial t} = \underbrace{-\bar{\mathbf{v}} \cdot \nabla_h \zeta'}_{\text{advection}} + \underbrace{\mathbf{S} \times \nabla_h w' \cdot \mathbf{k}}_{\text{tilting}}, \quad (8.7)$$

where the mean vertical wind shear is $\mathbf{S} = \partial\bar{\mathbf{v}}/\partial z$. Note that the mean velocity vector $\bar{\mathbf{v}}$ only has horizontal components ($\bar{\mathbf{v}} = \bar{u}\mathbf{i} + \bar{v}\mathbf{j}$). Hereafter mean variables will be taken to represent the environment.

It is easier to interpret (8.7) if it is rewritten so that $\partial\zeta'/\partial t$ is considered in the moving reference frame of the updraft. If the updraft moves with a constant velocity \mathbf{c} , then

$$\left(\frac{\partial\zeta'}{\partial t}\right)_{\text{sr}} = \underbrace{-(\bar{\mathbf{v}} - \mathbf{c}) \cdot \nabla_h \zeta'}_{\text{advection}} + \underbrace{\mathbf{S} \times \nabla_h w' \cdot \mathbf{k}}_{\text{tilting}}, \quad (8.8)$$

where $\bar{\mathbf{v}} - \mathbf{c}$ is the *storm-relative* wind and $(\partial\zeta'/\partial t)_{\text{sr}}$ is the vertical vorticity tendency in the storm-relative reference frame. The second term on the rhs of (8.8) is responsible for generating ζ' by way of tilting of horizontal

⁶ It can be shown that the vertical vorticity production due to the convergence of f is small compared with the production of vertical vorticity by tilting if $fD/SL \ll 1$, where D is the updraft depth scale, L is the updraft horizontal length scale, and S is the vertical wind shear magnitude. In supercell environments, $fD/SL \sim 0.01$. Regarding the baroclinic generation of ζ , it is also small (it vanishes if the Boussinesq approximation is made). Baroclinic vorticity generation can be important indirectly, as we shall see later, by generating horizontal vorticity that subsequently can be tilted to produce vertical vorticity.

⁷ Note that $\bar{\zeta} = 0$ if \bar{u} and \bar{v} are functions of z only.

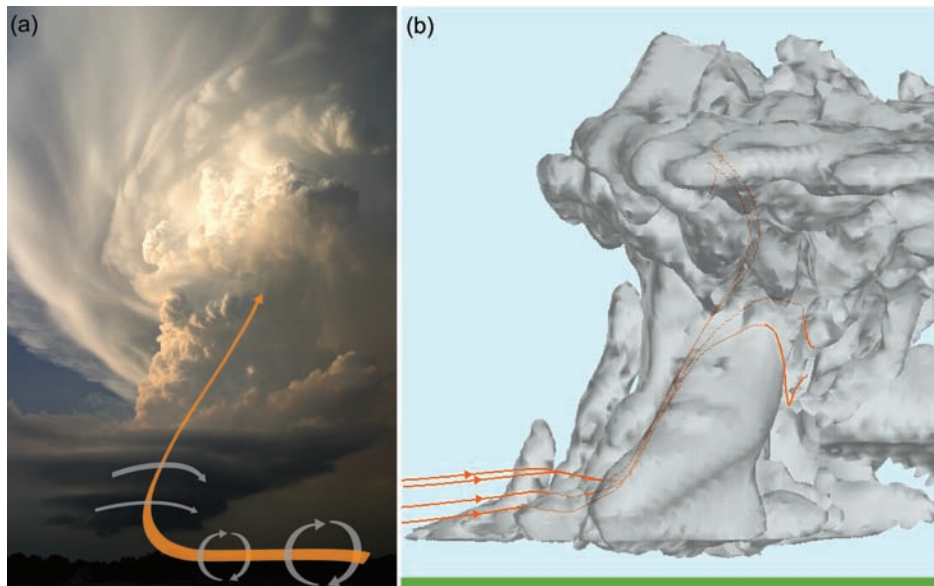


Figure 8.27 Vertical vorticity is acquired by supercells via tilting of horizontal vorticity associated with the vertical shear of the environmental wind profile. (a) Photograph of a supercell updraft. A schematic vortex line has been overlaid. The striated, laminar appearance in the lower portion of the updraft is a visual manifestation of negatively buoyant air being forcibly lifted by a strong, upward-directed, dynamic perturbation pressure gradient force. Such forces arise when buoyant convection develops in environments containing significant vertical wind shear (Section 8.4.5). Photograph courtesy of Eric Nguyen. (b) Numerically simulated supercell updraft (the gray isosurface is the cloud boundary) with actual vortex lines drawn. The vortex lines originate in the low-level inflow and pass through the midlevel mesocyclone. (The model output was displayed using the Vis5D visualization software.)



Figure 8.28 Sometimes when cumulus clouds dissipate in environments containing strong vertical wind shear, a *horseshoe vortex* is observed. The horseshoe vortex can be thought of as a visual manifestation of a vortex tube that has been tilted and deformed by the small-scale updraft associated with the cumulus cloud. Photograph by Charles Edwards.

vorticity associated with the mean vertical wind shear by vertical velocity gradients (Figures 8.27 and 8.28). The first term on the rhs of (8.8) represents advection of ζ' by the storm-relative wind. This term shifts the ζ' field horizontally within the updraft once ζ' has developed. Note that only the tilting term can lead to the development of ζ' because the advection term is zero when ζ' is everywhere zero. As an updraft intensifies, vorticity that has been tilted into the vertical is also amplified substantially by stretching ($\zeta' \partial w'/\partial z$), which is a nonlinear effect absent from (8.8).

A more detailed examination of (8.8) reveals that the tilting term produces a vorticity couplet that straddles the location of maximum updraft (w_{\max}), with $\zeta' > 0$ ($\zeta' < 0$) on the right (left) side of w_{\max} , if looking downshear (Figure 8.29). (Use the right-hand rule to convince yourself that the above relationship is correct—the vorticity couplet produced by tilting is aligned orthogonally with respect to the shear direction.)

Now consider more carefully the advection term in (8.8). Note that $\nabla_h \zeta'$ points 90° to the right of \mathbf{S} , that is, in the *opposite* direction to the environmental horizontal

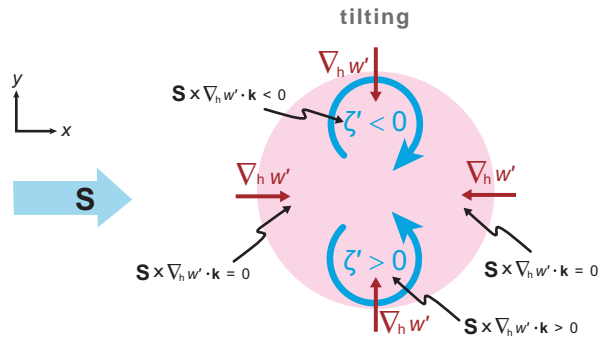


Figure 8.29 Evaluation of $(\partial \zeta' / \partial t)_{sr}$ via the tilting term ($S \times \nabla_h w' \cdot k$) in (8.8). The illustration shows the horizontal cross-section of an updraft (pink) at midlevels, indicating the relationship among ζ' (the sense of rotation is given by the curved blue arrows), S , and $\nabla_h w'$.

vorticity, $\bar{\omega}_h$ (Figure 8.30). When $\bar{\mathbf{v}} - \mathbf{c}$ points in the direction normal to $\bar{\omega}_h$, we have what is termed *crosswise vorticity*, in contrast to *streamwise vorticity*, which is present when $\bar{\mathbf{v}} - \mathbf{c}$ points in the same direction as $\bar{\omega}_h$ (recall Section 2.7.4). The sense of rotation for parcels containing mainly crosswise vorticity is like that of an American football rotating end over end, whereas for parcels containing mainly streamwise vorticity, the sense of rotation is like that of a football thrown as a spiral. When the vorticity is crosswise, $-(\bar{\mathbf{v}} - \mathbf{c}) \cdot \nabla_h \zeta' = 0$ at the location of maximum updraft (Figure 8.30a). Therefore, $(\partial \zeta' / \partial t)_{sr} = 0$ at the location of maximum updraft (assumed to be the center of the updraft in Figures 8.29 and 8.30), which implies that there is no shifting of the vorticity couplet within the updraft in the cross-shear direction. The vorticity couplet straddles the updraft maximum, although the vorticity couplet is shifted slightly downshear because of nonzero advection of ζ' by the storm-relative wind in the along-shear direction (Figures 8.30a and 8.31a).

At the other extreme, when $\bar{\mathbf{v}} - \mathbf{c}$ points in the same direction as $\bar{\omega}_h$ (i.e., the vorticity is purely streamwise), $-(\bar{\mathbf{v}} - \mathbf{c}) \cdot \nabla_h \zeta' > 0$ at the location of maximum updraft (Figure 8.30b). Therefore, $(\partial \zeta' / \partial t)_{sr} > 0$ at the location of maximum updraft, which shifts the cyclonic vortex ($\zeta' > 0$) toward the maximum updraft (i.e., the maximum updraft becomes collocated with cyclonic vorticity) (Figures 8.30b and 8.31b). The anticyclonic vortex ($\zeta' > 0$) is shifted outside of the updraft into a proximate downdraft. Also see Figure 8.32, which illustrates the dynamics in terms of lifting of vortex lines by flow over an isentropic (i.e., $\theta = \text{constant}$) hill.

The downshear shift of the ζ' couplet in the crosswise vorticity case is not as large as the cross-shear shift in the

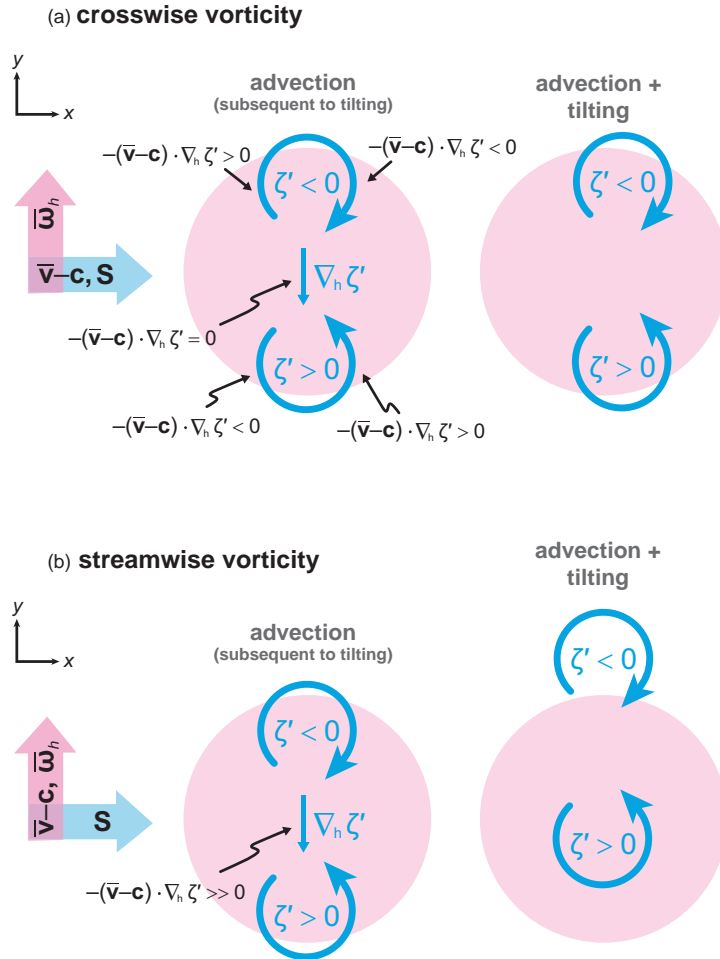


Figure 8.30 Evaluation of $(\partial \zeta'/\partial t)_{sr}$ via the advection term $-(\bar{v} - c) \cdot \nabla_h \zeta'$ in (8.8), based on the fact that the tilting term leads to a couplet of vertical vorticity straddling the updraft and oriented normal to the shear vector (cf. Figure 8.29), for the cases of (a) crosswise vorticity and (b) streamwise vorticity. The relationship between the vertical vorticity and vertical velocity fields resulting from the sum of the advection and tilting terms is also shown. As in Figure 8.29, the illustration shows the horizontal cross-section of an updraft (pink) at midlevels and the relationship among ζ' (its sense is given by the curved blue arrows), S , $\bar{\omega}_h$, $\bar{v} - c$, and $\nabla_h \zeta'$. The lateral shifting of the ζ' field within the updraft cross-section depends on the orientation of $\bar{v} - c$ with respect to $\bar{\omega}_h$ (and $\nabla_h \zeta'$, which points in the opposite direction to $\bar{\omega}_h$). This orientation is related to whether the environmental horizontal vorticity is streamwise or crosswise.

ζ couplet in the streamwise vorticity case, because $|\nabla_h \zeta'|$ is larger between the cyclonic and anticyclonic vorticity centers than it would be upshear or downshear of either vorticity center (a larger ζ' differential exists between a negative and a positive ζ' extremum than between a location where $\zeta' = 0$ and either a negative or positive ζ' extremum; Figure 8.31a). Furthermore, the midlevel cyclonic vorticity in the streamwise vorticity case is stronger than the midlevel anticyclonic vorticity owing to positive stretching (Figure 8.31b). For the same reason, the midlevel cyclonic

vorticity in the streamwise vorticity case is stronger than the midlevel cyclonic vorticity in the crosswise vorticity case (cf. Figures 8.31a and 8.31b).

The degree to which the vertical vorticity and vertical velocity maxima are correlated (i.e., whether a vertical vorticity maximum is nearly collocated with the vertical velocity maximum or whether a pair of counter-rotating vortices straddle the vertical velocity maximum) can be quantified in terms of the relative magnitudes of the environmental streamwise and crosswise vorticity, ω_s and ω_c ,

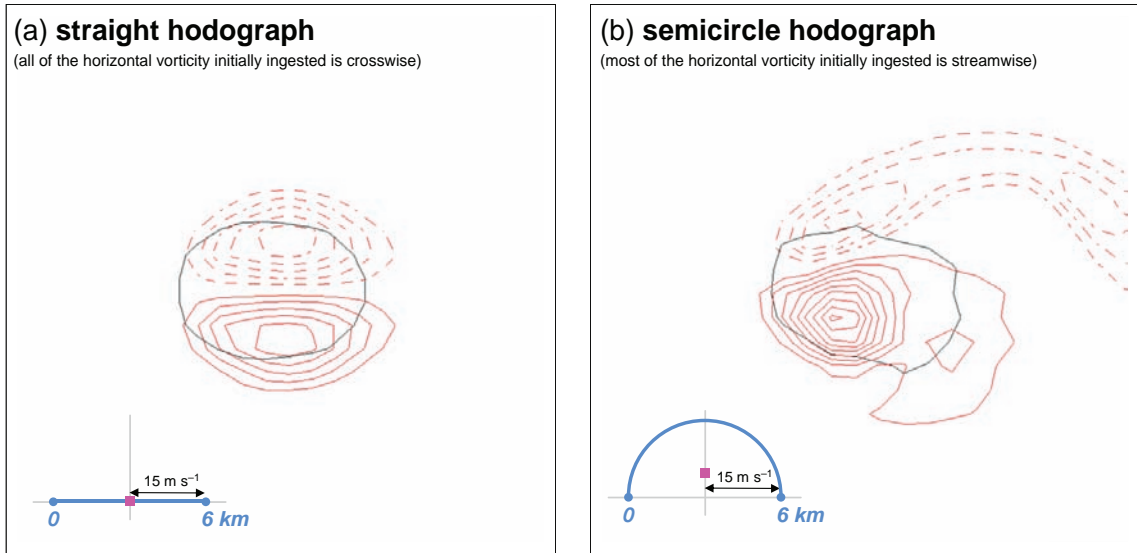


Figure 8.31 Vertical vorticity fields at $z = 5 \text{ km}$ at $t = 25 \text{ min}$ in numerical simulations in which an isolated storm is initiated using a warm bubble in an environment having (a) a straight hodograph and (b) a semicircular hodograph. Vertical vorticity contours are drawn every $2.5 \times 10^{-3} \text{ s}^{-1}$. Solid (dashed) contours indicate positive (negative) values, and the zero contour is suppressed. The thin black contour encloses the region where the vertical velocity exceeds 5 m s^{-1} . The sounding had approximately 2500 J kg^{-1} of CAPE. The hodographs are shown in each of the two panels; the magenta square indicates the mean updraft motion in the first 25 min of the simulations. In the straight-hodograph environment, the horizontal vorticity ingested in the early stages of storm development is purely crosswise. Note that the updraft is straddled by a couplet of cyclonic and anticyclonic vorticity of equal magnitude. In the semicircular-hodograph environment, the updraft acquires net cyclonic rotation and the anticyclonic vorticity is predominantly within a downdraft.

respectively. The correlation coefficient r between ζ' and w' , to a good approximation, is⁸

$$\begin{aligned} r &\approx \frac{\omega_s}{(P^2 + 1)^{1/2}(\omega_s^2 + \omega_c^2)^{1/2}} = \frac{(\bar{\mathbf{v}} - \mathbf{c}) \cdot \bar{\boldsymbol{\omega}}_h}{(P^2 + 1)^{1/2}|\bar{\mathbf{v}} - \mathbf{c}| |\bar{\boldsymbol{\omega}}_h|} \\ &= \frac{|\bar{\mathbf{v}} - \mathbf{c}| |\bar{\boldsymbol{\omega}}_h| \cos \phi}{(P^2 + 1)^{1/2} |\bar{\mathbf{v}} - \mathbf{c}| |\bar{\boldsymbol{\omega}}_h|} = \frac{\cos \phi}{(P^2 + 1)^{1/2}}, \end{aligned} \quad (8.9)$$

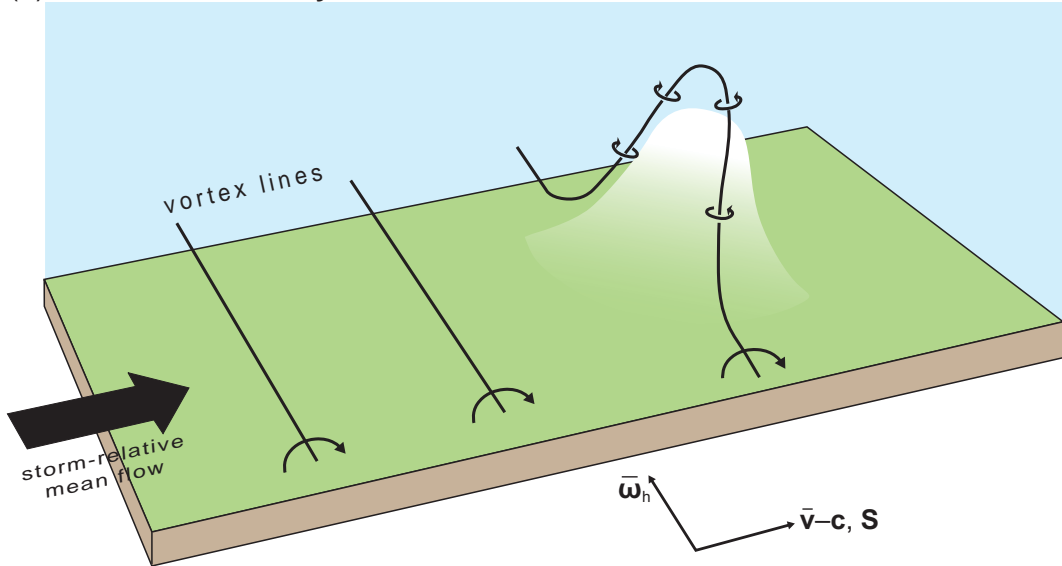
where $P = \sigma L / |\bar{\mathbf{v}} - \mathbf{c}|$, σ is the growth rate of an isentropic surface, L is a length scale across the updraft, ϕ is the angle between $\bar{\mathbf{v}} - \mathbf{c}$ and $\bar{\boldsymbol{\omega}}_h$, and $\cos \phi$ is sometimes referred to as the *relative helicity*, which can be viewed as the fraction of the horizontal vorticity that is streamwise. When $\cos \phi \approx 0$ (vorticity in the storm inflow is purely crosswise), a vorticity couplet straddles the updraft, as discussed above (Figures 8.30a, 8.31a, and 8.32a), yielding no *net* rotation if ζ' is averaged over the entire updraft (i.e., $r = 0$). When $\cos \phi \approx 1$ and P is small owing to a small growth rate and

large storm-relative wind speeds, the w' and ζ' fields nearly coincide (i.e., a nearly purely cyclonically rotating updraft results; Figures 8.30b and 8.32b). Because of buoyancy (i.e., $\sigma \neq 0$), which promotes positive vertical velocity over the entire isentropic hill, the correlation between vertical vorticity and vertical velocity can never be exactly unity (e.g., Figure 8.31b).

Summarizing the development of midlevel rotation within a thunderstorm updraft, initially a vorticity couplet develops owing to the tilting of environmental horizontal vorticity. This is immediately advected by the storm-relative winds such that, depending on the degree to which the horizontal vorticity has a streamwise component, the rotation and updraft can become more in phase. The relative magnitudes of the streamwise versus crosswise vorticity components are sensitive to storm motion. For example, once deviate storm motion commences (recall that cyclonically [anticyclonically] rotating supercells propagate to the right [left] of the mean wind), the horizontal vorticity typically becomes more streamwise with respect to the

⁸ See Davies-Jones (1984).

(a) crosswise vorticity



(b) streamwise vorticity

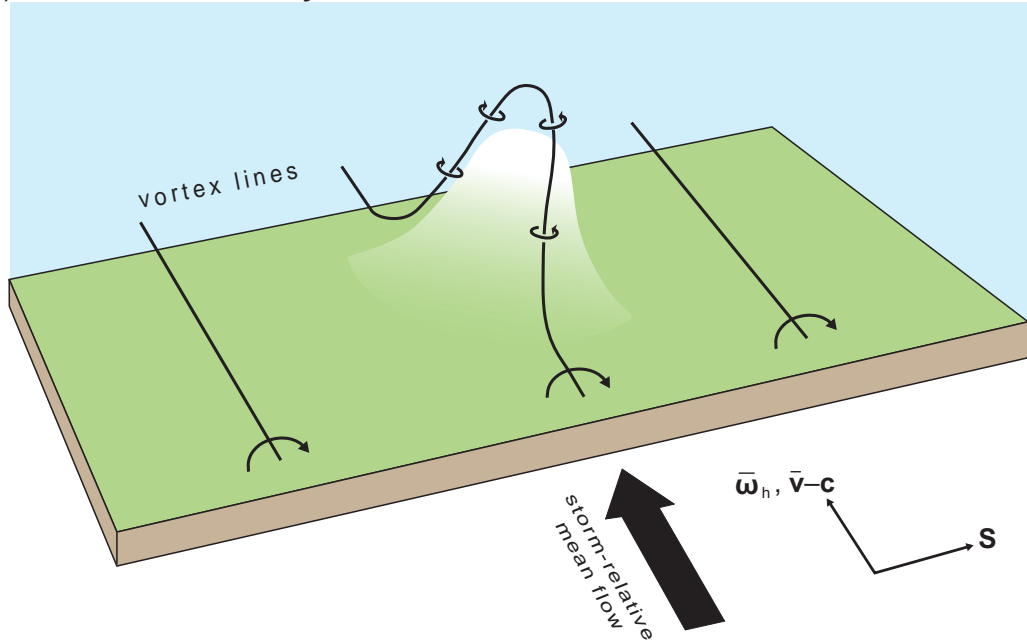


Figure 8.32 Tilting of environmental horizontal vorticity along a hill of constant entropy produces vertical vorticity, whereas storm-relative flow leads to positive (negative) vertical motion on the uphill (downhill) side of the isentropic hill and growth of the hill contributes to positive vertical motion everywhere on the hill. The correlation between w' and ζ' depends on the orientation of the horizontal vorticity $\bar{\omega}_h$ relative to the storm-relative mean wind, $\bar{v} - c$. (a) Tilting of purely crosswise vorticity by an isentropic hill leads to a vortex couplet with zero correlation between w' and ζ' . (b) Tilting of purely streamwise vorticity by an isentropic hill leads to a correlation between w' and ζ' of nearly unity. (Adapted from Davies-Jones [1984].)

deviate motion. We shall soon find that the rotation that develops within supercells leads to pressure perturbations and gradients of pressure perturbations, which in turn affect the motion of updrafts themselves. In other words, updraft rotation and propagation are related to each other. The nature of this relationship is explored further in Section 8.4.5.

Application of potential vorticity conservation to midlevel mesocyclogenesis

Another means by which the tilting process can be conceptualized is by way of Ertel's potential vorticity conservation (Section 2.4.5),

$$\frac{d}{dt} \left(\frac{\boldsymbol{\omega} \cdot \nabla \theta_e}{\rho} \right) = 0, \quad (8.10)$$

where θ_e is an appropriate conservative variable for dry and moist adiabatic motions and the Coriolis force has been neglected. Because θ_e is not a state variable for dry adiabatic motions, (8.10) is only approximately correct in subsaturated regions.⁹

In most environments, $\nabla \theta_e$ points approximately downward toward the ground (i.e., θ_e typically decreases with height much more rapidly than it varies horizontally). In supercell environments, the horizontal vorticity components (ξ and/or η) are typically one to two orders of magnitude larger than the vertical component ($\sim 10^{-2} \text{ s}^{-1}$ versus $\sim 10^{-3} - 10^{-4} \text{ s}^{-1}$) (recall that we assumed $\zeta = 0$ in deriving (8.8)). Therefore, $\boldsymbol{\omega}$ is oriented quasihorizontally, or roughly perpendicular to $\nabla \theta_e$, and $\boldsymbol{\omega} \cdot \nabla \theta_e \approx 0$. In this situation, conservation of Ertel's potential vorticity requires that $\boldsymbol{\omega} \cdot \nabla \theta_e \approx 0$ for all time. Because $\boldsymbol{\omega} \cdot \nabla \theta_e \approx 0$, vortex lines lie within θ_e surfaces for all time (in the absence of mixing). In a thunderstorm, θ_e surfaces bulge upward (downward) within the updraft (downdraft), along with the environmental vortex lines (Figure 8.27). Vertical vorticity is present where θ_e surfaces are sloped. Whereas (8.8) applies only to linear flows, (8.10) applies to fully nonlinear flows (e.g., those that contain significant vorticity stretching).

Storm-relative helicity

Helicity is a measure of the degree to which the direction of fluid motion is aligned with the vorticity of the fluid.

⁹ To be exact, the rhs of (8.10) should be $-\alpha J(B, \theta_e)$, where $\alpha = 1/\rho$, B is buoyancy, and J is the Jacobian operator. When air is saturated, $B = B(\theta_e, z)$ and $-\alpha J(B, \theta_e) = 0$. When air is unsaturated (e.g., for dry adiabatic motions), $-\alpha J(B, \theta_e)$ is nonzero but remains relatively small, so that (8.10) is reasonably accurate for both dry and moist adiabatic motions. See Rotunno and Klemp (1985).

Helicity is therefore closely related to streamwise vorticity. Flows that are said to be highly helical are dominated by streamwise vorticity. Mathematically, helicity, \mathcal{H} , is the covariance or dot product of the velocity and vorticity vectors,

$$\mathcal{H} = \mathbf{v} \cdot \boldsymbol{\omega} = \mathbf{v} \cdot \nabla \times \mathbf{v}. \quad (8.11)$$

Obviously, $\mathcal{H} = 0$ when the velocity vector is normal to the vorticity vector. Flows in which the velocity is everywhere parallel to the vorticity are called *Beltrami flows*.

Although the concept of helicity originates in the field of fluid dynamics, it has also been applied to supercell storms because, as will be shown, it is related to streamwise vorticity and also possibly the longevity of supercells. Helical flows tend to suppress turbulence, and some have hypothesized that the helical updrafts of supercells may partly explain their longevity.

In its application to convective storms, it is customary to integrate the helicity associated with the environmental wind ($\bar{\mathbf{v}}$) and vorticity ($\bar{\boldsymbol{\omega}}$) over some depth d that is roughly taken to be the depth of a storm's inflow (1–3 km depths are most commonly assumed), that is,

$$\mathcal{H} = \int_0^d \bar{\mathbf{v}} \cdot \bar{\boldsymbol{\omega}}_h dz \quad (8.12)$$

where $\bar{\boldsymbol{\omega}} = \bar{\boldsymbol{\omega}}_h = \bar{\xi} \mathbf{i} + \bar{\eta} \mathbf{j}$ if $\bar{\mathbf{u}} = \bar{\mathbf{u}}(z)$ and $\bar{\mathbf{v}} = \bar{\mathbf{v}}(z)$, as was assumed before. Assuming $\bar{w} = 0$, then

$$\bar{\boldsymbol{\omega}}_h = \left(-\frac{\partial \bar{v}}{\partial z}, \frac{\partial \bar{u}}{\partial z} \right) = \mathbf{k} \times \mathbf{s}. \quad (8.13)$$

Only the helicity in the storm-relative reference frame is relevant because the moving updraft of the storm is the tilting mechanism. From (8.12) and (8.13), it follows that the *storm-relative helicity* (SRH) of the environment [SRH derived from a sounding sometimes is referred to as storm-relative *environmental helicity* (SREH)] is

$$\begin{aligned} \text{SRH} &= \int_0^d (\bar{\mathbf{v}} - \mathbf{c}) \cdot \bar{\boldsymbol{\omega}}_h dz = \int_0^d |\bar{\mathbf{v}} - \mathbf{c}| \omega_s dz \\ &= - \int_0^d \mathbf{k} \cdot (\bar{\mathbf{v}} - \mathbf{c}) \times \mathbf{s} dz. \end{aligned} \quad (8.14)$$

SRH can be evaluated graphically from a hodograph. The magnitude of the SRH is equal to twice the area bounded by a hodograph and the tip of the storm motion vector (Figure 8.33).¹⁰ The SRH is positive (negative) if the area is associated with streamwise (antistreamwise) vorticity. Moreover, given a vertical profile of N wind observations,

¹⁰ The relationship between SRH and the area bounded by the hodograph and storm motion can be derived by applying Green's theorem to (8.14).

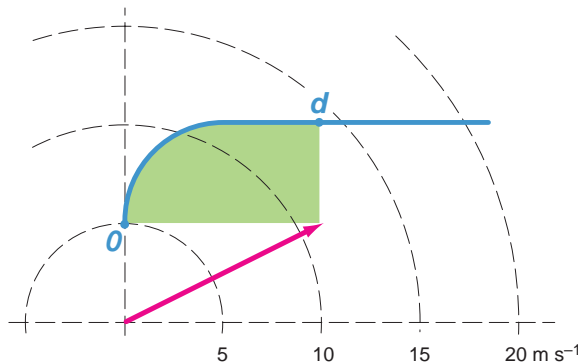


Figure 8.33 Illustration of the graphical relationship between SRH and the hodograph. The shaded area represents half of the SRH present in the layer from $z = 0$ to $z = d$ for the given storm motion (magenta vector), which results in streamwise vorticity for the given wind profile. The green shaded region comprises a quarter circle of radius 5 m s^{-1} plus a square having dimensions $5 \text{ m s}^{-1} \times 5 \text{ m s}^{-1}$. Thus, the area of the green region is $(5 \text{ m s}^{-1})^2\pi/4 + (5 \text{ m s}^{-1})^2 \approx 45 \text{ m}^2 \text{ s}^{-2}$, which gives an SRH of $\approx 90 \text{ m}^2 \text{ s}^{-2}$ (the SRH is positive in this case because the horizontal vorticity is streamwise for the given storm motion).

the SRH can be computed via¹¹

$$\text{SRH} = \sum_{n=1}^{N-1} [(u_{n+1} - c_x)(v_n - c_y) - (u_n - c_x)(v_{n+1} - c_y)], \quad (8.15)$$

where $\mathbf{c} = (c_x, c_y)$.

In addition to the 0–6 km vertical shear, SRH is also often used to forecast the likelihood of supercells. Values of 0–3 km SRH greater than approximately $150 \text{ m}^2 \text{ s}^{-2}$ indicate a potential for supercells (strictly speaking, SRH should probably be regarded as a mesocyclone predictor, but, then again, mesocyclones are the defining characteristic of supercells). Although the magnitude of the 0–6 km vector wind difference and SRH are seemingly independent of each other, in reality they tend to be somewhat correlated such that, with few exceptions, magnitudes of the 0–6 km vector wind difference suggestive of supercells

(i.e., $>15\text{--}20 \text{ m s}^{-1}$) also tend to be associated with SRH values that favor mesocyclones. In outbreaks of supercells and tornadoes, 0–3 km SRH values exceeding $400 \text{ m}^2 \text{ s}^{-2}$ are occasionally observed. The SRH in the shallower 0–1 km layer can discriminate between tornadic and nontornadic supercells. More will be said on this matter in Section 10.2.

8.4.4 Baroclinically generated horizontal vorticity and its effect on the mesocyclone

As shown above, the presence of large environmental wind shear and its implied environmental horizontal vorticity are critical for mesocyclogenesis. However, the outflow that unavoidably accompanies mature storms generates additional horizontal vorticity via horizontal buoyancy gradients. The outflow that is usually most relevant is the outflow associated with the FFD, because a significant fraction of the low-level inflow tends to pass through this region en route to the updraft (Figure 8.22). As discussed earlier, it is the lifting of this cooler, humidified air that gives rise to the cloud lowering known as the wall cloud (Figure 8.16).

This storm-scale, *internally generated* horizontal vorticity from the FFD outflow can augment the horizontal vorticity present in the ambient environment, leading to larger overall horizontal vorticity available for tilting, at least if the environmental horizontal vorticity and storm-generated horizontal vorticity have components in the same direction (Figure 8.34). Indeed, the mean supercell hodograph shown in Figure 8.15 implies that, on average, the environmental horizontal vorticity and storm-generated horizontal vorticity would tend to add to each other. Easterly low-level storm-relative winds are implied by the hodograph in Figure 8.15, as is approximately easterly environmental low-level horizontal vorticity (\mathbf{S} points toward the north at low levels). Thus, the low-level environmental vorticity has a large streamwise component. If the precipitation falls in an elongated west–east zone (recall from Section 8.1 that hydrometeors tend to be distributed in the direction of the deep-layer wind shear and upper-level storm-relative winds, which roughly point toward the east in Figure 8.15), then easterly inflow to the updraft passing along the southern flank of the cold pool will have a significant velocity component parallel to the approximately zonally oriented low-level isentropes (Figures 8.22 and 8.34). Any horizontal vorticity generated baroclinically would point toward the west if the cold air is to the north. The baroclinic vorticity would therefore have a large streamwise component and also point in approximately the same direction as the low-level environmental vorticity, thereby adding to it.

¹¹ Observing platforms really measure u and v rather than \bar{u} and \bar{v} . Thus, calculations of SRH and other prognostic variables must usually utilize u and v observations, which can vary significantly in space and time as a result of boundary layer dry convection (recall Figure 7.17) or the influence of an air mass boundary. Although such heterogeneity can make the representativeness of the wind observations from a single sounding questionable, there is usually no way to extract \bar{u} and \bar{v} from single-sounding observations of u and v .

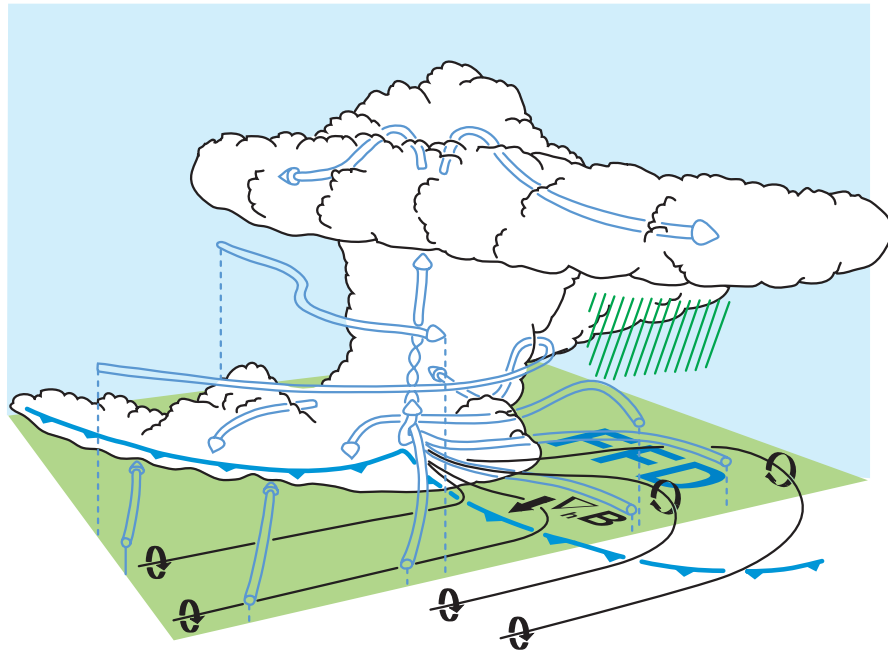


Figure 8.34 Schematic of a supercell thunderstorm in westerly mean shear, viewed from the southeast, at a stage when low-level rotation is intensifying. The cylindrical arrows depict the storm-relative winds. The black lines are vortex lines, with the sense of rotation indicated by the circular arrows. The blue barbed line marks the gust front. The orientation of the horizontal buoyancy gradient, $\nabla_h B$, is also indicated. (Adapted from Klemp [1987].)

Numerical simulations have demonstrated that the magnitude of the baroclinic horizontal vorticity generated along the immediate cool side of the FFD gust front can be comparable to or exceed the magnitude of the environmental horizontal vorticity. This result is not surprising given the following scale analysis, where the change in horizontal vorticity following an air parcel moving parallel to the buoyancy isopleths, $\Delta\omega_s$, is [cf. (2.94)]

$$\Delta\omega_s = \frac{g}{\theta_v} \frac{\partial\theta_\rho}{\partial n} \frac{\Delta s}{v_s}, \quad (8.16)$$

where s and n represent directions parallel and perpendicular to the flow, respectively, ω_s is the streamwise vorticity component, θ_ρ is the density potential temperature, and v_s is the storm-relative wind speed in the baroclinic zone. For $\partial\theta_\rho/\partial n \simeq 1 \text{ K km}^{-1}$ and $v_s \simeq 15 \text{ m s}^{-1}$, a streamwise horizontal vorticity $\Delta\omega_s \simeq 10^{-2} \text{ s}^{-1}$ is generated over a distance $\Delta s \simeq 5 \text{ km}$.

For a given horizontal vertical velocity gradient $\nabla_h w$, the tilting rate increases with increasing horizontal vorticity ω_h via (8.5). Tilting of the baroclinically enhanced

low-level horizontal vorticity therefore produces more significant vertical vorticity at low altitudes than does the tilting of environmental vorticity alone (as in early stages of supercell development). Thus, the formation of *low-level* mesocyclones usually awaits the development of an extensive forward-flank precipitation region and outflow. As discussed above, although baroclinic vorticity generated within the FFD outflow might generally be expected to augment environmental horizontal vorticity, in some situations the environmental horizontal vorticity is not predominantly streamwise, nor is it necessarily always in the same direction as the baroclinic vorticity that is generated (Figure 8.15 shows only a *mean* hodograph obtained from supercell environments). Some numerical simulations have suggested that the orientation of the low-level environmental vorticity and the orientation of the baroclinically generated vorticity to the low-level environmental vorticity can influence the intensity and longevity of low-level mesocyclones, with stronger and more persistent low-level rotation developing when low-level environmental vorticity is streamwise and the baroclinically generated vorticity points in the same

direction as the low-level environmental vorticity. The spatial distribution of precipitation, controlled in large part by the deep-layer shear and storm-relative winds, affects the spatial distribution of negative buoyancy and baroclinic vorticity generation, and therefore also likely exerts a significant influence on the characteristics of low-level mesocyclones.

The presence of a low-level mesocyclone is not a sufficient condition for tornadogenesis, nor does the likelihood of tornadogenesis necessarily increase with increasing low-level mesocyclone intensity or longevity.¹² The generation of vertical vorticity at the surface—a requisite for tornadogenesis—requires that a downdraft be involved in the tilting process, at least if there is no significant preexisting vertical vorticity at the surface. Because air parcels rise away from the ground as they experience vorticity tilting by an updraft alone (the vertical advection of vertical vorticity offsets the generation of vertical vorticity from tilting), tilting by an updraft alone can never lead to vertical vorticity at the surface. If a downdraft in proximity to an updraft is also involved in the tilting process, however, air can descend toward the surface as tilting generates positive vertical vorticity. The vertical velocity gradients associated with the FFD are usually an order of magnitude weaker than the vertical velocity gradients at the interface between the updraft and RFD (the RFD tends to be more intense and smaller in scale; both of these factors lead to larger $\nabla_h w'$ in the vicinity of the RFD). Thus, the RFD is likely to be of more direct importance in tornadogenesis than the FFD. The importance of the FFD is in the production of horizontal vorticity by horizontal buoyancy gradients within the FFD outflow; that is, it is the baroclinity of the FFD outflow that is being emphasized rather than vorticity tilting by the FFD. A much more detailed discussion appears in Section 10.2.2, where tornadogenesis is treated separately.

8.4.5 Supercell propagation

Dynamic perturbation pressures

To investigate the dynamics that give rise to supercell propagation, we begin by recalling the relationship between the pressure field and the three-dimensional wind and buoyancy fields. It was shown in Section 2.5 that a diagnostic pressure equation can be obtained by taking the

¹² Field experiment observations, albeit only obtained in a relatively limited number of supercells, have shown that tornadic supercells actually tend to have weaker forward-flank baroclinity than nontornadic supercells (Shabbott and Markowski, 2006). More will be said of this curious result in Section 10.2.2.

divergence ($\nabla \cdot$) of the momentum equations. Let us begin by writing (2.137) as

$$\begin{aligned} p' \propto & \underbrace{\left[\left(\frac{\partial u'}{\partial x} \right)^2 + \left(\frac{\partial v'}{\partial y} \right)^2 + \left(\frac{\partial w'}{\partial z} \right)^2 \right]}_{\text{fluid extension terms}} \\ & + 2 \left(\frac{\partial v'}{\partial x} \frac{\partial u'}{\partial y} + \frac{\partial w'}{\partial x} \frac{\partial u'}{\partial z} + \frac{\partial w'}{\partial y} \frac{\partial v'}{\partial z} \right) \\ & \underbrace{+ 2 \mathbf{S} \cdot \nabla_h w'}_{\text{nonlinear dynamic pressure perturbation, } p'_{\text{dnl}}} - \underbrace{\frac{\partial B}{\partial z}}_{\text{buoyancy pressure term, } p'_b}. \end{aligned} \quad (8.17)$$

The terms in square brackets on the rhs of (8.17) are sometimes called *fluid extension terms*.

The nonlinear dynamic pressure perturbation can be simplified if some assumptions are made. Let us suppose that we are interested only in the interior of a strongly rotating updraft, such that the following components of the deformation can be neglected to a reasonable approximation,

$$\frac{\partial v'}{\partial x} + \frac{\partial u'}{\partial y} = \frac{\partial w'}{\partial y} + \frac{\partial v'}{\partial z} = \frac{\partial w'}{\partial x} + \frac{\partial u'}{\partial z} = 0, \quad (8.18)$$

which implies that

$$\frac{\partial v'}{\partial x} = -\frac{\partial u'}{\partial y} \quad \frac{\partial w'}{\partial y} = -\frac{\partial v'}{\partial z} \quad \frac{\partial w'}{\partial x} = -\frac{\partial u'}{\partial z}. \quad (8.19)$$

If horizontal vorticity is also negligible, then

$$\frac{\partial w'}{\partial y} - \frac{\partial v'}{\partial z} = \frac{\partial u'}{\partial z} - \frac{\partial w'}{\partial x} = 0, \quad (8.20)$$

which implies that

$$\frac{\partial w'}{\partial y} = \frac{\partial v'}{\partial z} \quad \frac{\partial u'}{\partial z} = \frac{\partial w'}{\partial x}. \quad (8.21)$$

From (8.19) and (8.21), it can be deduced that

$$\frac{\partial u'}{\partial z} = \frac{\partial v'}{\partial z} = \frac{\partial w'}{\partial x} = \frac{\partial w'}{\partial y} = 0. \quad (8.22)$$

At this point only the nonlinear dynamic term $2 \frac{\partial v'}{\partial x} \frac{\partial u'}{\partial y}$ remains. Because we have assumed that $\frac{\partial v'}{\partial x} = -\frac{\partial u'}{\partial y}$ [from (8.19)], the remaining nonlinear dynamic term $2 \frac{\partial v'}{\partial x} \frac{\partial u'}{\partial y}$ can

be written as

$$\begin{aligned} 2 \frac{\partial v'}{\partial x} \frac{\partial u'}{\partial y} &= -\frac{1}{2} \left(-\frac{\partial v'}{\partial x} \frac{\partial u'}{\partial y} - 2 \frac{\partial v'}{\partial x} \frac{\partial u'}{\partial y} - \frac{\partial v'}{\partial x} \frac{\partial u'}{\partial y} \right) \\ &= -\frac{1}{2} \left(\frac{\partial v'}{\partial x} \frac{\partial v'}{\partial x} - 2 \frac{\partial v'}{\partial x} \frac{\partial u'}{\partial y} + \frac{\partial u'}{\partial y} \frac{\partial u'}{\partial y} \right) \\ &= -\frac{1}{2} \left(\frac{\partial v'}{\partial x} - \frac{\partial u'}{\partial y} \right)^2 \\ &= -\frac{1}{2} \zeta'^2 \end{aligned} \quad (8.23)$$

Using (8.22) and (8.23), we can write (8.17) as

$$\begin{aligned} p' \propto & \underbrace{\left[\left(\frac{\partial u'}{\partial x} \right)^2 + \left(\frac{\partial v'}{\partial y} \right)^2 + \left(\frac{\partial w'}{\partial z} \right)^2 \right]}_{\text{fluid extension terms}} \underbrace{-\frac{1}{2} \zeta'^2}_{\text{spin term}} \\ & \text{nonlinear dynamic pressure perturbation, } p'_{\text{dnl}} \\ + & \underbrace{2 \mathbf{S} \cdot \nabla_h w'}_{\text{linear dynamic pressure perturbation, } p'_{\text{dl}}} \underbrace{- \frac{\partial B}{\partial z}}_{\text{buoyancy pressure perturbation, } p'_{\text{b}}} \end{aligned} \quad (8.24)$$

Although all of the terms on the rhs of (8.24) can contribute equally to p' , our focus hereafter is on the contribution of the dynamic vertical perturbation pressure gradient force ($-\alpha \partial p'_d / \partial z$; also known as *dynamic forcing*) to the vertical acceleration (dw/dt). Thus, we shall not consider the buoyancy pressure perturbation ($\propto -\partial B / \partial z$) further. Moreover, in supercell updrafts, the fluid extension terms do not contribute to $\partial p'_d / \partial z$ as much as the ζ'^2 and $\mathbf{S} \cdot \nabla_h w'$ terms. Therefore, we shall assume that

$$-\frac{\partial p'_d}{\partial z} \propto \underbrace{\frac{1}{2} \frac{\partial \zeta'^2}{\partial z}}_{\text{nonlinear dynamic forcing}} \underbrace{-2 \frac{\partial}{\partial z} \mathbf{S} \cdot \nabla_h w'}_{\text{linear dynamic forcing}}, \quad (8.25)$$

where the contribution to the vertical acceleration is upward (downward) when the terms on the rhs are positive (negative).

In supercells, unlike ordinary cells, the contribution to dw/dt from $-\alpha \partial p'_d / \partial z$ has the same order of magnitude as the contribution to dw/dt from $-\alpha \partial p'_b / \partial z + B$ (also known as *buoyancy forcing*). Below cloud base, upward-directed dynamic forcing, due to both the linear and nonlinear terms appearing above, is responsible for forcing negatively buoyant air to the LFC. This forced lifting of stable air often gives rise to visually spectacular, laminar, striated low-level clouds in supercells (Figures 8.17 and 8.27a).

The effects of nonlinear dynamic forcing

Let us take a closer look at the nonlinear dynamic forcing term in (8.25). It may seem strange that we are examining the nonlinear term before looking at the linear term, but nonlinear effects often play an important role in the early evolution of a supercell updraft.

The nonlinear dynamic forcing term promotes *updraft splitting* at early stages in storm evolution, at least in cases when significant crosswise vorticity is present (Figure 8.35b). Tilting of crosswise vortex lines leads to a couplet of counter-rotating vortices that straddle the midlevel updraft (Figure 8.36). Low pressure is found where $|\zeta'|$ is large, regardless of the sign of ζ' (i.e., elevated pressure minima are produced in both the cyclonic and anticyclonic members of the vortex couplet). Because $|\zeta'|$ is a maximum on the midlevel updraft flanks, p' is a minimum on the midlevel updraft flanks, and an upward-directed dynamic vertical perturbation pressure gradient force arises on the flanks below the level of maximum $|\zeta'|$ (the maximum is usually found 4–8 km above the ground). The upward-directed dynamic pressure gradient forces on the opposing flanks cause the updraft to split (Figures 8.37 and 8.38). The splitting process, when it occurs, is observed within approximately 30–60 minutes of storm initiation, and can occur multiple times. Splitting is also encouraged by rainwater and associated downdraft formation along the axis of the initial updraft, but a rainy downdraft is not required for splitting.

Updraft splitting leads to the formation of right- and left-moving storms, sometimes called *right movers* and *left movers*, respectively. Right and left are defined with respect to the direction of the deep-layer wind shear vector rather than the mean wind, although in most cases a storm moving to the right (left) of the deep-layer shear vector also moves to the right (left) of the mean wind. The lateral updraft propagation (at right angles to the shear vector) that follows storm splitting increases the streamwise (antistreamwise) vorticity ingested by the right-moving (left-moving) updraft.

Consider the case of a straight hodograph with westerly shear. An updraft initially moves at approximately the mean wind velocity; therefore, the updraft motion in early stages lies on the hodograph (recall from Section 2.7 that the mean wind lies on the hodograph in the case of a straight hodograph). Therefore, the updraft initially ingests purely crosswise vorticity because the storm-relative winds are orthogonal to the horizontal vorticity at all levels. In terms of SRH, the SRH is zero because there is no area on the hodograph diagram between the storm motion and the hodograph if the storm motion lies on a straight hodograph.

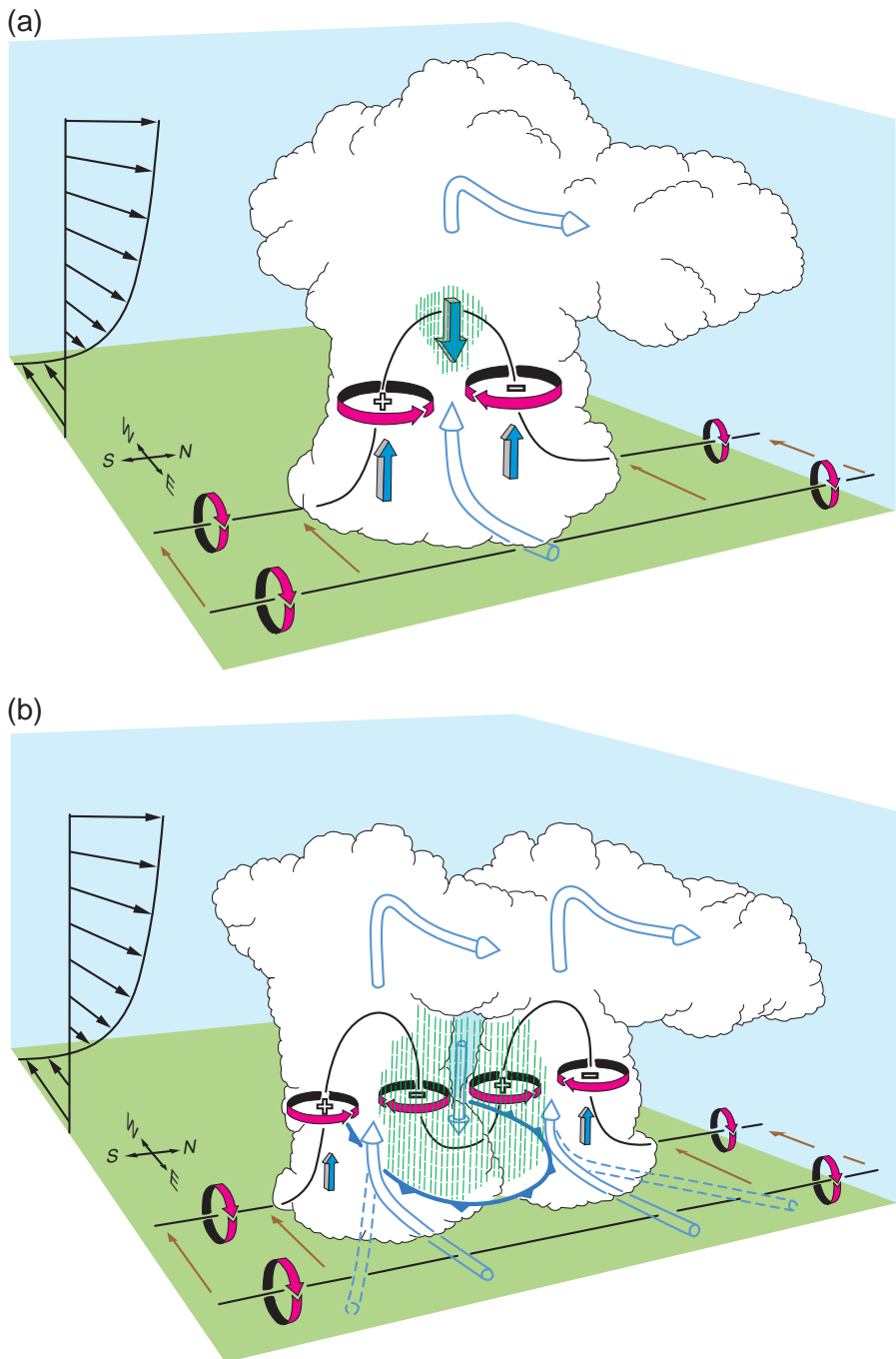


Figure 8.35 The splitting of cells and the subsequent development of rotation through vortex line tilting in the case of a straight hodograph. (a) In the early stage a vortex pair forms through tilting of the horizontal vorticity associated with the mean shear, creating vertical perturbation pressure gradient forces (blue shaded arrows) on the flanks. (b) As rainy downdrafts form and the cell splits, vortex lines are tilted downward, and the original updraft-centered vortex pair is transformed into two vortex pairs. The updraft of the rightward (facing downshear) moving member propagates toward the positive vorticity on the right flank, and thus a correlation between updraft and positive vorticity develops. In (a) and (b), the transparent blue arrows indicate storm-relative trajectories. In (b), the dashed transparent blue arrows indicate storm-relative trajectories after storm splitting. (Adapted from Klemp [1987].)

Nonlinear Contribution to Dynamic Pressure Perturbations

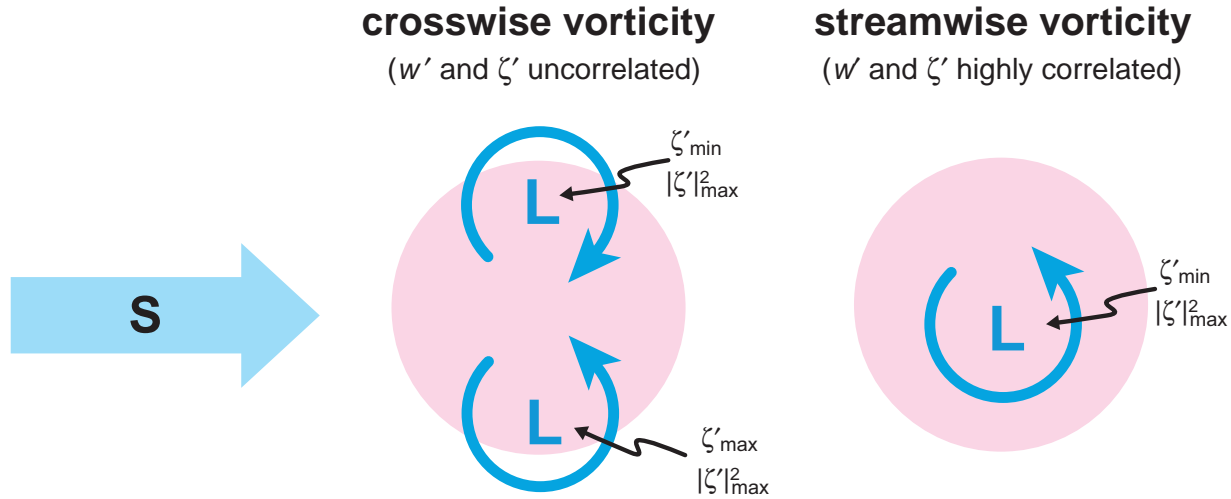


Figure 8.36 Schematic horizontal cross-sections through the midlevel updraft (pink) of a supercell showing the locations of vorticity centers and pressure minima for the cases of purely crosswise vorticity and purely streamwise vorticity. When the vorticity ingested by the updraft is purely crosswise, the $-\frac{1}{2}\zeta'^2$ term in the diagnostic pressure equation leads to an upward-directed dynamic vertical pressure gradient force on the storm flanks below the level of maximum $|\zeta'|$ and minimum p' . In the limit of purely streamwise vorticity being ingested by the updraft, the ζ' and w' fields are approximately in phase; thus, the $-\frac{1}{2}\zeta'^2$ term cannot lead to a significant off-axis, upward-directed, dynamic vertical pressure gradient force.

Following storm splitting, right- and left-moving updrafts acquire a lateral propagation such that their motions no longer lie on the hodograph. Thus, the storm-relative winds in the reference frame of the right-moving (left-moving) updraft have a southerly (northerly), that is, streamwise (antistreamwise) component. In a graphical sense, there is now an area on the hodograph diagram between the hodograph and the storm motions of both the right- and left-moving updrafts, corresponding to positive (negative) SRH, respectively, and a positive (negative) correlation between ζ' and w' develops. The right-moving (left-moving) updraft acquires net positive (negative) vorticity.

Vertical vorticity is constantly produced by tilting on the updraft flanks, where $\nabla_h w'$ is largest, which leads to continuous lateral propagation as the right-moving (left-moving) updraft is continuously forced on its right (left) flank. The nonlinear dynamic forcing term promotes lateral updraft propagation as long as ζ' and w' are not collocated—the updraft can never ‘catch up’ to

the dynamic uplift because the uplift remains off-axis as long as a crosswise vorticity component is present. Even though splitting increases the streamwise (antistreamwise) vorticity tilted by the right-moving (left-moving) updrafts, sufficient crosswise vorticity can be present after splitting that subsequent splitting occurs (e.g., sometimes a right-moving updraft ‘sheds’ multiple left-moving updrafts). At the other extreme, if a hodograph has substantial curvature, the initial updraft moving at the mean wind speed (recall from Section 2.7 that the mean wind lies on the concave side of a curved hodograph) may tilt predominantly streamwise vorticity from the start. In such cases, storm splitting may be suppressed entirely because the midlevel pressure minimum resulting from ζ'^2 is located close to the updraft axis rather than on each updraft flank (Figure 8.36). Although the nonlinear dynamic forcing cannot promote lateral updraft propagation for a perfectly curved hodograph, lateral propagation still occurs as a result of the linear dynamic forcing. We discuss linear dynamic forcing next.

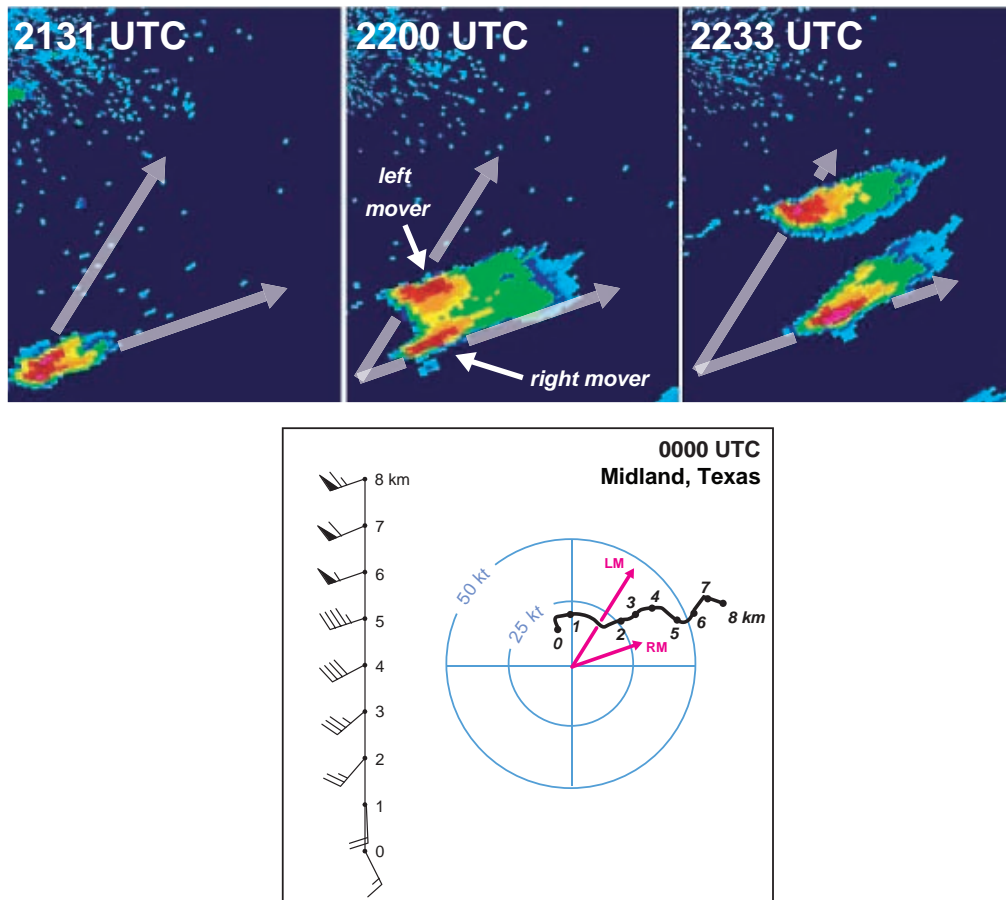


Figure 8.37 Sequence of radar reflectivity images from the Clovis, NM, WSR-88D on 19 April 2004, depicting a developing supercell storm splitting into right- and left-moving supercells. The vertical wind profile and hodograph from Midland, TX, at 0000 UTC 20 April are displayed as well. Numerals along the hodograph indicate altitudes above ground level in kilometers, and the storm motions are also indicated on the hodograph ('RM' and 'LM' are the motion vectors of the right- and left-moving supercells, respectively). The hodograph is fairly straight overall. It is therefore not surprising that the right- and left-moving supercells that developed from the splitting process were comparable in intensity.

The effects of linear dynamic forcing

Now let us take a closer look at the linear dynamic forcing term in (8.25). High pressure is found upshear (not *upwind*) of the updraft and low pressure is found downshear (not *downwind*) of the updraft (Figure 8.39). In other words, the couplets of high and low pressure at any level are aligned *with* the shear vector at that level (recall that the vorticity couplets produced by tilting were aligned *normal* to the shear).

When the vertical wind shear is unidirectional (i.e., the hodograph is straight), the high- and low-pressure perturbations are vertically stacked (Figure 8.40a).

Upward- and downward-directed vertical perturbation pressure gradients arise, but they cannot force lateral updraft propagation. As discussed above, the nonlinear dynamic forcing leads to storm splitting, after which mirror-image, symmetrical right- and left-moving storms are produced, which propagate off the hodograph by way of continued forcing by the midlevel pressure minima on the updraft flanks (Figure 8.41; see also Figure 8.37). On the other hand, when the shear vector veers with height (i.e., the hodograph turns clockwise with height), the high–low-pressure couplets become stacked such that an upward-directed dynamic vertical pressure gradient force exists on the right flank of an updraft



Figure 8.38 Photograph of splitting storms. A rainshaft can also be seen between the two distinct updraft towers. Photograph by Chuck Doswell.

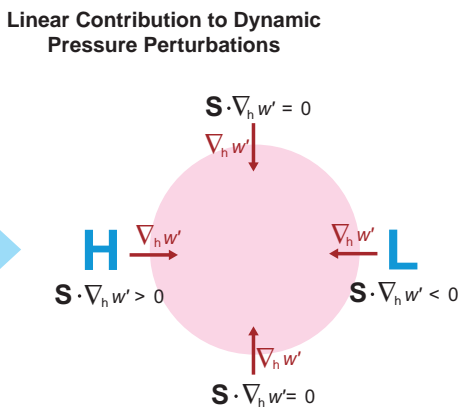


Figure 8.39 Pressure perturbations arising from the linear dynamic term, $2\mathbf{S} \cdot \nabla_h w'$. A couplet of high and low p' is aligned with the shear vector and straddles the updraft at any particular altitude. The magnitude of p' is proportional to the horizontal w' gradient (strong updrafts tend to also have large $\nabla_h w'$) and the strength of the vertical wind shear.

and a downward-directed dynamic vertical pressure gradient force exists on the left flank of an updraft (Figure 8.40b). Thus, the linear dynamic forcing suppresses the left-moving storm and enhances the right-moving storm (Figures 8.41 and 8.42). When the hodograph turns counterclockwise with height, the opposite is true—the left-mover is favored and the right-mover is suppressed. As previously stated, storm-splitting may not be observed in environments exhibiting substantial hodograph curvature; significant clockwise (counterclockwise) turning of the shear vector with height can suppress the left- (right-) moving storm altogether. Also note that the vertical perturbation pressure gradients are larger in magnitude in the curved hodograph case than in the straight hodograph case because vertical variations in the magnitude and direction of \mathbf{S} and magnitude of $\nabla_h w'$ all contribute to $|\partial p'_d / \partial z|$ in the curved hodograph case, whereas only vertical variations in the magnitude of \mathbf{S} and $\nabla_h w'$ contribute to $|\partial p'_d / \partial z|$ in the straight hodograph (Figure 8.40).

Recall that there is a large correlation between w' and ζ' when the horizontal vorticity has a large streamwise component. In the limit of an updraft tilting purely streamwise

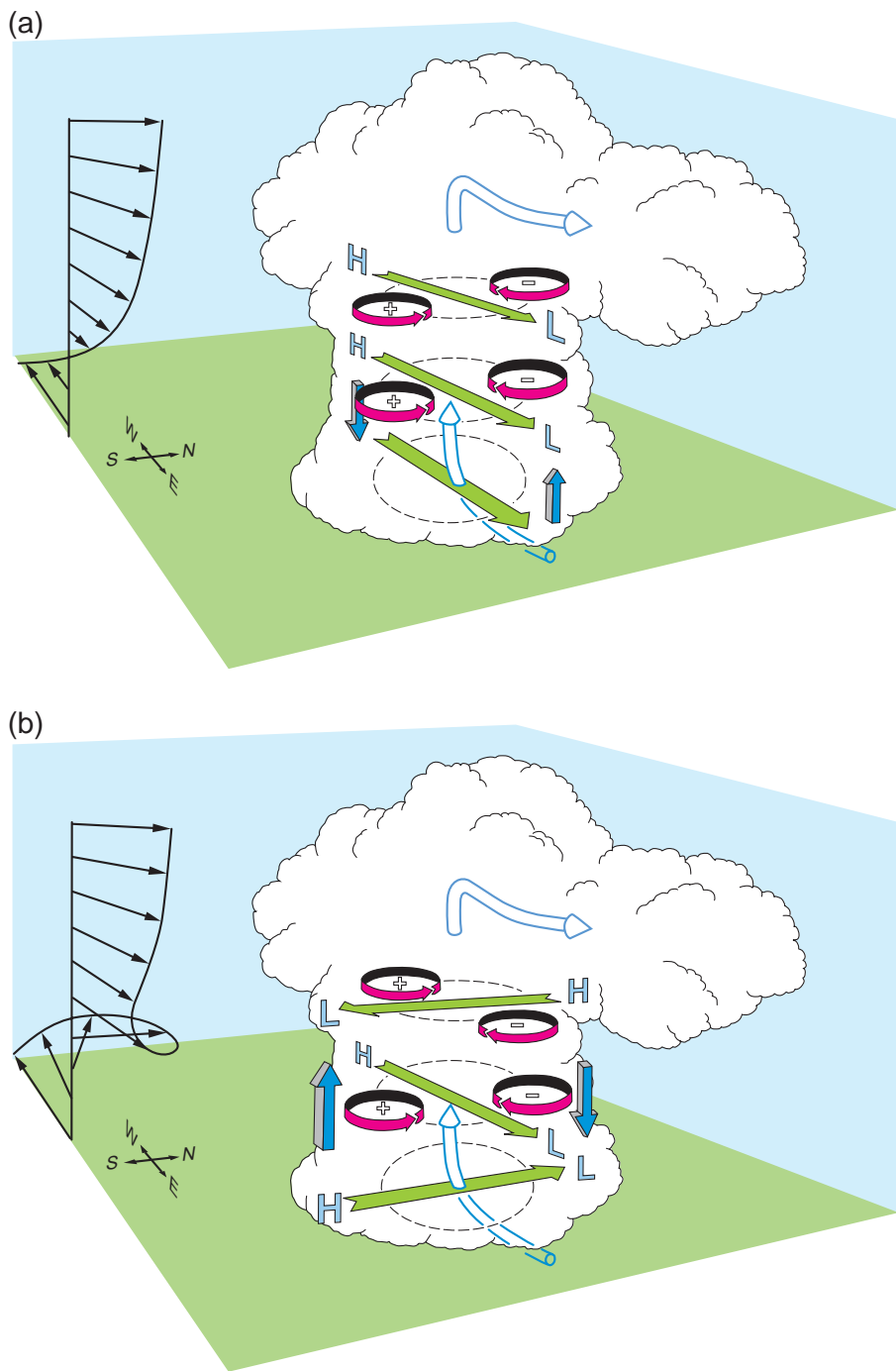


Figure 8.40 Pressure perturbations arising as an updraft interacts with an environmental wind shear that (a) does not change with height and (b) turns clockwise with height. The high (H) to low (L) horizontal pressure gradients parallel to the shear vectors (green flat arrows) are labeled. The dark blue shaded arrows indicate the implied vertical pressure gradient force, which favors the right flank in the curved hodograph case. (Adapted from Klemp [1987].)

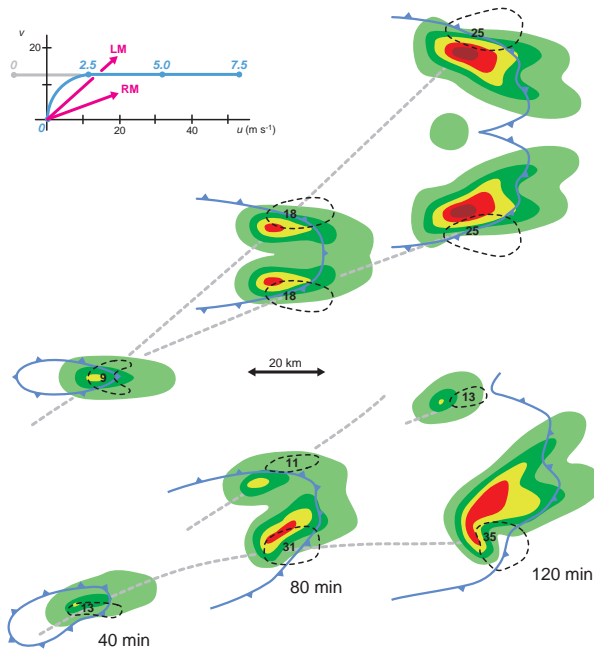


Figure 8.41 Plan views of cloud-model-produced, low-level rainwater fields for two simulations using, respectively, a straight hodograph (gray in lowest 2.5 km, blue above; numerals along the hodograph indicate altitude in km) and one with low-level clockwise hodograph curvature (blue). The straight hodograph produces storms with mirror-image symmetry, whereas the curved hodograph enhances the right-moving storm. The left- and right-moving storm motions are indicated on the hodographs with magenta arrows and are labeled 'LM' and 'RM', respectively. The dashed black contours enclose the regions of significant midlevel updraft, and the numerals indicate the location and magnitude of the maximum vertical velocity (m s^{-1}). Gust fronts are also shown. The gray dashed lines indicate storm motions. (Adapted from Klemp [1987].)

vorticity (i.e., there is no crosswise vorticity component and the relative helicity is unity), the w' and ζ' fields are nearly collocated [recall from (8.9) that they are not exactly coincident because of buoyancy within the updraft] (Figure 8.30a). Therefore, the nonlinear dynamic forcing cannot promote lateral updraft propagation because the upward-directed forcing is a maximum near the updraft axis. Instead, linear dynamic forcing is directed upward on the right flank; that is, the right-mover is enhanced on its right flank by the turning of the shear vector with height, and rightward propagation occurs. In summary, dynamic perturbation pressure gradients promote lateral updraft propagation in both straight and curved

hodograph environments. For a straight hodograph, lateral updraft propagation is due to the nonlinear dynamic forcing in (8.25). For a curved hodograph, lateral updraft propagation is due to the linear dynamic forcing in (8.25). A summary comparison of supercell updraft properties appears in Table 8.1.

Empirical predictions of supercell motion

Part of the motion of a supercell updraft is attributable to advection of the updraft by the vertically averaged winds (mean flow), but part of the motion is also a function of lateral propagation due to the dynamic forcing on the updraft flanks (both linear and nonlinear forcing can contribute) as investigated above. The movement of the storm's own outflow and gust front, although not the primary factors in influencing propagation as is the case for nonsupercellular convection, can influence storm motion in a minor way (perhaps more so for HP supercells than for classic or LP supercells), as can external boundaries, like fronts, outflow boundaries from earlier or adjacent storms, and even terrain.

Some algorithms for predicting supercell motion express the motion as some function of the mean wind speed and direction. For example, some older techniques predict supercell motion as being 75–80% of the mean wind speed, at an angle 25–30° to the right of the mean wind. One issue with these methods is that they are not Galilean invariant; that is, the relationship between storm motion and the hodograph depends on the mean wind implied by the hodograph. Other methods predict a supercell motion with respect to a shear vector. Such methods are preferable to those mentioned above because they are Galilean invariant; that is, the relationship between the predicted storm motion and the hodograph is *independent* of the mean wind on the hodograph. For example, one popular method predicts supercell motion to be 7.5 m s^{-1} orthogonal to the right of the shear vector drawn between the 0–500 m mean wind and the 0–6 km mean wind.¹³ A similar method predicts supercell motion to be 8.7 m s^{-1} orthogonal to the right of a location 60% of the distance from the tail to the head of the shear vector drawn between the 0–500 m mean wind and the 4 km wind (Figure 8.43).¹⁴ These techniques are least accurate for HP storms, perhaps because their cold pools are substantial enough to influence storm propagation significantly. The algorithms that are based on the wind shear

¹³ See Bunkers *et al.* (2000). In the southern hemisphere, the cyclonic storm motion would be 7.5 m s^{-1} to the left of the shear vector.

¹⁴ See Rasmussen and Blanchard (1998). In the southern hemisphere, the cyclonic storm motion would be 8.7 m s^{-1} to the left of the shear vector.

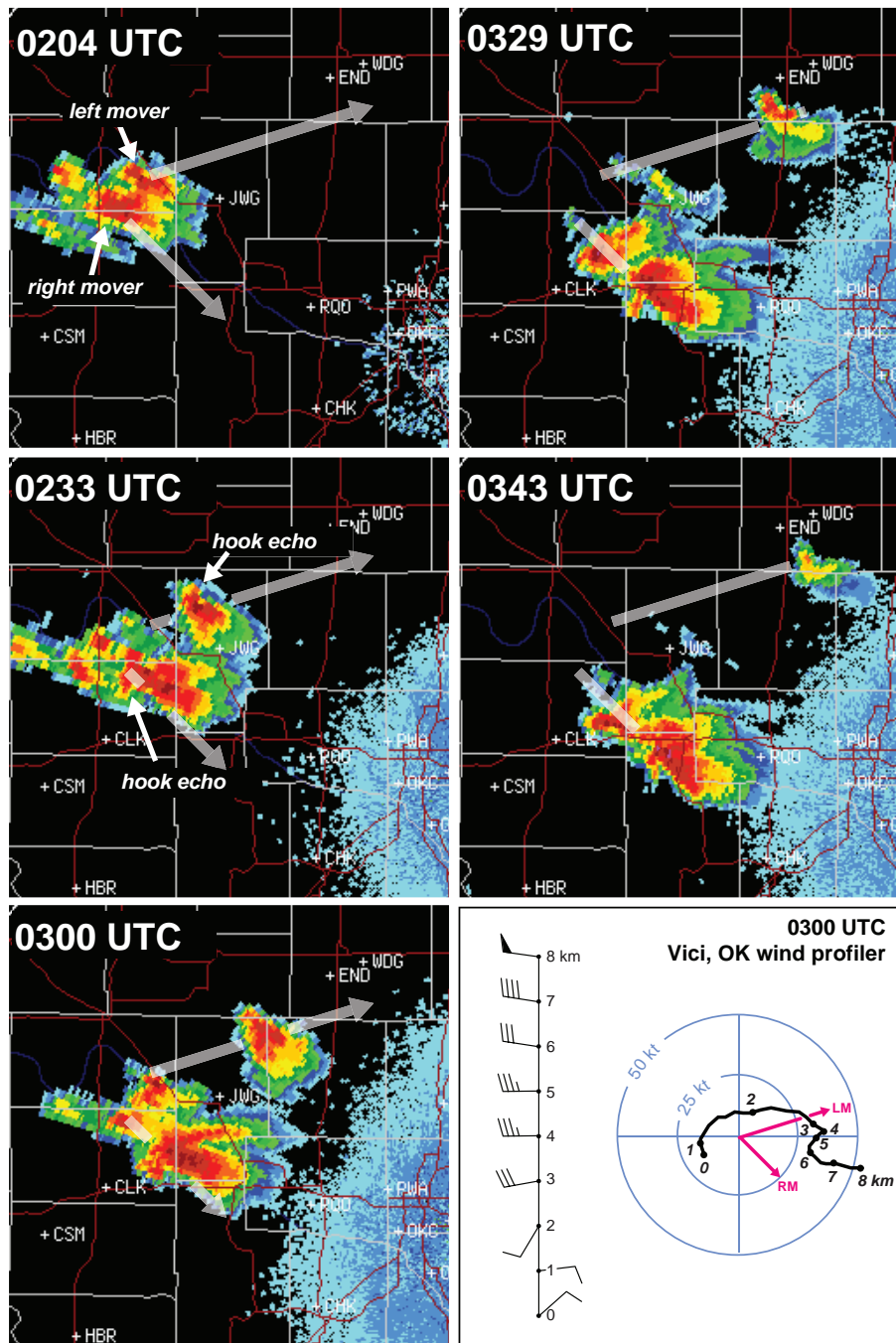


Figure 8.42 Left- and right-moving supercells following an episode of storm-splitting on 1 June 2008 in western Oklahoma. Note the intensification (weakening) of the right- (left-) mover following the splitting of the original cell. The broad gray arrows indicate the storm motions. The vertical wind profile and hodograph from the nearby Vici, OK, wind profiler are displayed in the bottom right panel. Numerals along the hodograph indicate altitudes above ground level in kilometers, and the storm motions are also indicated on the hodograph ('RM' and 'LM' are the motion vectors of the right- and left-movers, respectively). The hodograph has substantial curvature, such that the shear vector veers with height in the lowest 4 km. It is therefore not surprising that the right-mover was dominant in this case.

Table 8.1 Comparison of the properties of supercells in environments with nearly straight hodographs and with strongly curved hodographs that turn clockwise with height. It is assumed that the environments have roughly similar CAPE and vertical wind shear. (From Davies-Jones *et al.* [2001].)

Property	(Nearly) straight hodograph	Strongly curved hodograph
Symmetry of left and right movers	Yes (for straight hodograph, neglecting f)	No
Net updraft rotation in initial storm	No	Yes
Cyclonic vortex in initial storm	On the right side of the updraft	In strong updraft
Anticyclonic vortex in initial storm	On the left side of the updraft	In downdraft or weak updraft
Storm splitting	Highly significant	Insignificant or absent
Time to first mesocyclone	Slower	Faster
Low and midlevel mesocyclone intensity	Generally less intense	Generally more intense
Mesoanticyclone	In left mover	Generally absent
Maximum updraft strength	Weaker	Stronger
Direction of low-level environmental vorticity versus baroclinically generated horizontal vorticity	Very different (roughly orthogonal)	In roughly same direction
Lateral updraft propagation	Via nonlinear dynamic forcing	Via linear dynamic forcing

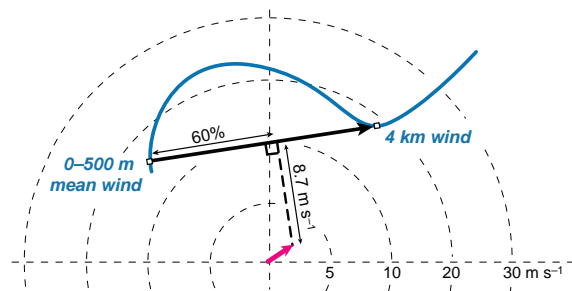


Figure 8.43 The Rasmussen and Blanchard (1998) method for forecasting supercell motion predicts a motion 8.7 m s^{-1} orthogonal to the right of a location 60% of the distance from the tail to the head of the shear vector drawn between the 0–500 m mean wind and the 4 km wind. In the hodograph, the magenta arrow indicates the predicted supercell motion.

somewhat implicitly assume that supercell propagation is driven primarily by dynamic forcing associated with the wind shear profile.

Further reading

Organization of DMC

Browning, K. A., 1986: Morphology and classification of mid-latitude thunderstorms. *Thunderstorm Morphology and Dynamics*, E. Kessler, Ed., 2nd edn. University of Oklahoma Press, 133–152.

Doswell, C. A., III, 2001: Severe convective storms—an overview. *Severe Local Storms, Meteor. Monogr.*, No. 50, 1–26.

Johnson, R. H., and B. E. Mapes, 2001: Mesoscale processes and severe convective weather. *Severe Local Storms, Meteor. Monogr.*, No. 50, 71–122.

Jorgensen, D. P., and T. M. Weckwerth, 2003: Forcing and organization of convective systems. *Radar and Atmospheric Science: a Collection of Essays in Honor of David Atlas, Meteor. Monogr.*, No. 52, 75–104.

Richardson, Y. P., K. K. Droegemeier, and R. P. Davies-Jones, 2007: The influence of horizontal environmental variability on numerically simulated convective storms. Part I: Variations in vertical shear. *Mon. Wea. Rev.*, 135, 3429–3455.

Schaefer, J. T., L. R. Hoxit, and C. F. Chappell, 1986: Thunderstorms and their mesoscale environment. *Thunderstorm Morphology and Dynamics*, E. Kessler, Ed., 2nd edn. University of Oklahoma Press, 113–131.

Weisman and Klemp (1982).

Weisman, M. L., and J. B. Klemp, 1984: The structure and classification of numerically simulated convective storms in directionally varying wind shears. *Mon. Wea. Rev.*, 112, 2479–2498.

Weisman, M. L., and J. B. Klemp, 1986: Characteristics of isolated convective storms. *Mesoscale Meteorology and Forecasting*, P. S. Ray, Ed. Amer. Meteor. Soc., 331–358.

Multicell storms

- Fovell, R. G., and Y. Ogura, 1989: Effect of vertical wind shear on numerically simulated multicell storm structure. *J. Atmos. Sci.*, **46**, 3144–3176.
- Fovell, R. G., and P. S. Dailey, 1995: The temporal behavior of numerically simulated multicell-type storms. Part I: Modes of behavior. *J. Atmos. Sci.*, **52**, 2073–2095.
- Fovell, R. G., and P.-H. Tan, 1998: The temporal behavior of numerically simulated multicell-type storms. Part II: The convective cell life cycle and cell regeneration. *Mon. Wea. Rev.*, **126**, 551–577.
- Marwitz, J. D., 1972b: The structure and motion of severe hailstorms. Part II: Multicell storms. *J. Appl. Meteor.*, **11**, 180–188.
- Wilhelmsen, R. B., and C.-S. Chen, 1982: A simulation of the development of successive cells along a cold outflow boundary. *J. Atmos. Sci.*, **39**, 1466–1483.
- Yang, M.-J., and R. A. Houze, Jr., 1995: Multicell squall-line structure as a manifestation of vertically trapped gravity waves. *Mon. Wea. Rev.*, **123**, 641–660.

Supercell storms

- Adlerman, E. J., K. K. Droegemeier, and R. P. Davies-Jones, 1999: A numerical simulation of cyclic mesocyclogenesis. *J. Atmos. Sci.*, **56**, 2045–2069.
- Beatty, K., E. N. Rasmussen, J. M. Straka, and L. R. Lemon, 2008: The supercell spectrum. Part I: A review of research related to supercell precipitation morphology. *E. J. Severe Storms Met.*, **3**.
- Brandes, E. A., 1993: Tornadic thunderstorm characteristics determined with Doppler radar. *The Tornado: its Structure, Dynamics, Prediction, and Hazards*, Geophys. Monogr., No. 79, Amer. Geophys. Union, 143–159.
- Brooks, H. E., C. A. Doswell III, and R. P. Davies-Jones, 1993: Environmental helicity and the maintenance and evolution of low-level mesocyclones. *The Tornado: its Structure, Dynamics, Prediction, and Hazards*, Geophys. Monogr., No. 79, Amer. Geophys. Union, 97–104.
- Brooks, H. E., C. A. Doswell III, and R. B. Wilhelmsen, 1994: The role of midtropospheric winds in the evolution and maintenance of low-level mesocyclones. *Mon. Wea. Rev.*, **122**, 126–136.
- Browning, K. A., and F. H. Ludlam, 1962: Airflow in convective storms. *Quart. J. Roy. Meteor. Soc.*, **88**, 117–135.
- Browning, K. A., 1964: Airflow and precipitation trajectories within severe local storms which travel to the right of the winds. *J. Atmos. Sci.*, **21**, 634–639.
- Davies-Jones (1984).
- Davies-Jones *et al.* (2001).
- Doswell and Burgess (1993).

Klemp (1987).

Klemp, J. B., and R. B. Wilhelmsen, 1978: Simulations of right-and left-moving storms produced through storm splitting. *J. Atmos. Sci.*, **35**, 1097–1110.

Klemp, J. B., R. B. Wilhelmsen, and P. S. Ray, 1981: Observed and numerically simulated structure of a mature supercell thunderstorm. *J. Atmos. Sci.*, **38**, 1558–1580.

Klemp, J. B., and R. Rotunno, 1983: A study of the tornadic region within a supercell thunderstorm. *J. Atmos. Sci.*, **40**, 359–377.

Lemon and Doswell (1979).

Lilly, D. K., 1986a: The structure, energetics, and propagation of rotating convective storms. Part I: Energy exchange with the mean flow. *J. Atmos. Sci.*, **43**, 113–125.

Lilly, D. K., 1986b: The structure, energetics, and propagation of rotating convective storms. Part II: Helicity and storm stabilization. *J. Atmos. Sci.*, **43**, 126–140.

Markowski, P. M., 2002: Hook echoes and rear-flank down-drafts: a review. *Mon. Wea. Rev.*, **130**, 852–876.

Markowski, P. M., J. M. Straka, and E. N. Rasmussen, 2002: Direct surface thermodynamic observations within the rear-flank downdrafts of nontornadic and tornadic supercells. *Mon. Wea. Rev.*, **130**, 1692–1721.

Marwitz, J. D., 1972a: The structure and motion of severe hailstorms. Part I: Supercell storms. *J. Appl. Meteor.*, **11**, 166–179.

Rasmussen and Straka (1998).

Ray, P. S., B. C. Johnson, K. W. Johnson, J. S. Bradberry, J. J. Stephens, K. K. Wagner, R. B. Wilhelmsen, and J. B. Klemp, 1981: The morphology of several tornadic storms on 20 May 1977. *J. Atmos. Sci.*, **38**, 1643–1663.

Rotunno, R., 1981: On the evolution of thunderstorm rotation. *Mon. Wea. Rev.*, **109**, 577–586.

Rotunno, R., and J. B. Klemp, 1982: The influence of the shear-induced pressure gradient on thunderstorm motion. *Mon. Wea. Rev.*, **110**, 136–151.

Rotunno, R., and J. B. Klemp, 1985: On the rotation and propagation of simulated supercell thunderstorms. *J. Atmos. Sci.*, **42**, 271–292.

Thompson, R., R. Edwards, J. Hart, K. Elmore, and P. Markowski, 2003: Close proximity soundings within supercell environments obtained from the Rapid Update Cycle. *Wea. Forecasting*, **18**, 1243–1261.

Wakimoto, R. M., C. Liu, and H. Cai, 1998a: The Garden City, Kansas, storm during VORTEX 95. Part I: Overview of the storm life cycle and mesocyclogenesis. *Mon. Wea. Rev.*, **126**, 372–392.

Wakimoto, R. M., and C. Liu, 1998b: The Garden City, Kansas, storm during VORTEX 95. Part II: The wall cloud and tornado. *Mon. Wea. Rev.*, **126**, 393–408.

- Wakimoto, R. M., and H. Cai, 2000: Analysis of a nontornadic storm during VORTEX 95. *Mon. Wea. Rev.*, **128**, 565–592.
- Wicker, L. J., and R. B. Wilhelmson, 1995: Simulation and analysis of tornado development and decay within a three-dimensional supercell thunderstorm. *J. Atmos. Sci.*, **52**, 2675–2703.
- Elevated convection**
- Colman, B. R., 1990a: Thunderstorms above frontal surfaces in environments without positive CAPE. Part I: A climatology. *Mon. Wea. Rev.*, **118**, 1103–1122.
- Colman, B. R., 1990b: Thunderstorms above frontal surfaces in environments without positive CAPE. Part II: Organization and instability mechanisms. *Mon. Wea. Rev.*, **118**, 1123–1144.
- Horgan, K. L., D. M. Schultz, J. E. Hales Jr., S. F. Corfidi, and R. H. Johns, 2007: A five-year climatology of elevated severe convective storms in the United States east of the Rocky Mountains. *Wea. Forecasting*, **22**, 1031–1044.
- Moore, J. T., A. C. Czarnetzki, and P. S. Market, 1998: Heavy precipitation associated with elevated thunderstorms formed in a convectively unstable layer aloft. *Meteor. Appl.*, **5**, 373–384.

9

Mesoscale Convective Systems

9.1 General characteristics

The American Meteorological Society's *Glossary of Meteorology* defines a *mesoscale convective system* (MCS) as any ensemble of thunderstorms producing a contiguous precipitation area on the order of 100 km or more in horizontal scale in at least one direction (Figure 9.1). This length scale is approximately the scale at which the Coriolis acceleration becomes significant (i.e., the perturbations produced by the Coriolis force approach the same order of magnitude as the original wind); $V/f \sim 100$ km, where V is the characteristic wind speed ($V \sim 10 \text{ m s}^{-1}$ assumed) and f is the Coriolis parameter ($f \sim 10^{-4} \text{ s}^{-1}$ assumed).¹

MCSs can evolve from convection that is somewhat isolated early in its life. After several hours have elapsed, outflows that might have originated from widely separated areas of initial convective development tend to merge into a single, large cold pool capable of initiating new cells along most of its length. Such evolution is often termed *upscale growth* of convection. It is accelerated in environments in which the deep-layer wind shear, and also usually the environmental system-relative winds at upper levels, have a large component parallel to the convection-initiating boundary. In such an environment, hydrometeor fallout is primarily in the along-line direction, thereby providing a source of latent cooling in the along-line direction (Figure 9.2). In other cases, MCSs develop almost immediately following convection initiation, perhaps as a result of widespread, strong forcing along an air mass boundary in a

weakly capped environment, or perhaps as a result of strong isentropic upglide over a synoptic-scale front, particularly if a low-level jet is involved. The latter breed of MCS has been referred to as a *Type 1* MCS, whereas those driven by their own cold pools are sometimes referred to as *Type 2* MCSs.² Type 2 MCSs are the most likely to produce severe weather given their greater potential coupling to the boundary layer, although both types of MCS can produce heavy rain.

Most MCSs probably can be regarded as multicellular convection, in the sense that new cells are repeatedly triggered by the gust front in order to maintain a system of cells that long outlives the life of any individual cell. Thus, the structure of many MCSs (many Type 2 MCSs, specifically) can be represented schematically by Figure 8.12b by simply extending the figure infinitely into and out of the page. We might allow for the possibility that in a rare case the vertical wind profile could lead to an ordinary cell motion that exactly matches the forward speed of the gust front, such that cells are not repeatedly undercut by the gust front as in multicellular convection, although such unicellular behavior is not observed to our knowledge, nor is it seen in numerical simulations of MCSs (Figure 9.3) unless some components of the precipitation processes are unrealistically turned off (e.g., evaporation and precipitation loading).

When the shear is strong and deep, an MCS may comprise a line of supercells, but perhaps only for some particular orientations of the deep-layer shear to the line of forcing. For example, if the deep-layer shear is strong but oriented at roughly a 90° angle with respect to the initiating boundary, the splitting of cells along the line may result in

¹ The length scale V/f comes from assuming $\Delta V/\Delta t = fV$, and when ΔV is as large as V , this becomes $1/\Delta t = f$. If this time interval is related to a horizontal distance L that is traveled by an air parcel at speed V , that is, $\Delta t = L/V$, then $L = V/f$.

² Note that an MCS can be cold pool driven (i.e., Type 2) even if it moves along the cold side of a synoptic front.

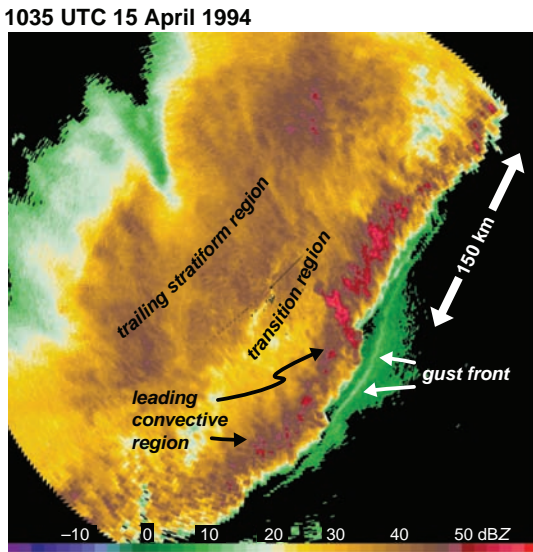


Figure 9.1 Radar reflectivity (dBZ) from the St. Louis, MO, radar at 1035 UTC 15 April 1994 showing a mesoscale convective system (MCS). A quasi-linear, narrow band of high reflectivity is associated with the leading convective towers and is trailed by a much broader region of weak to moderate reflectivity. The gust front also is evident.

left- and right-movers colliding with each other, resulting in a rapid upscale growth into a two-dimensional MCS (e.g., in the northern hemisphere, a northeastward-moving left-mover that results from storm-splitting can collide with southeastward-moving right-mover that results from a different storm-splitting occurrence farther north). On the other hand, if the deep-layer shear is strong and oriented at roughly a 45° angle with respect to the initiating boundary, the left-movers that result from storm-splitting tend to move roughly parallel to the initiating boundary, whereas the right-movers can move at an angle roughly orthogonal to the initiating boundary, allowing them to avoid cell collisions and maintain their three-dimensionality.³ We also shall see (Section 9.4) that a type of MCS or sub-MCS structure (both are possible) known as a *bow echo* can evolve from supercells, particularly HP supercells. In general, however, this chapter will not consider lines of supercells that, on occasion, technically can satisfy the definition of an MCS. Instead, our emphasis is on MCSs that exhibit multicellular behavior. An exploration of MCSs has been postponed until this chapter because of the role that the Coriolis force and associated meso- α -scale circulations play in the maintenance of many MCSs.

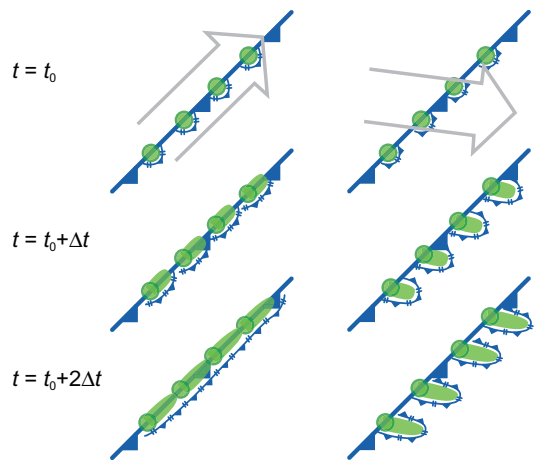


Figure 9.2 Schematic illustrating why the upscale growth of convection is accelerated in environments in which the deep-layer shear has a large component parallel to the convection-initiating boundary (a cold front in this case, without loss of generality). In the left column, the cold pools (gust fronts are indicated by the thin, hatched barbed lines, precipitation areas are shaded green) grow in the along-boundary direction over the time interval $2\Delta t$, following convection initiation shortly before $t = t_0$, as a result of the deep-layer wind shear (direction indicated with the gray arrow) promoting hydrometeor fallout in the along-line direction. By $t = t_0 + 2\Delta t$, one contiguous cold pool has formed, which promotes the formation of an unbroken convective line along its entire length. In the right column, the deep-layer shear vector crosses the convection-initiating boundary at a relatively large angle, which retards the formation of a single, large cold pool and thus allows for the maintenance of relatively discrete cells for a longer time period, assuming that the initial convective development is somewhat discrete. The severe weather threats posed by discrete cells versus a line can differ tremendously (the former might be associated with a greater tornado threat, whereas the latter might be associated with a greater threat from damaging straight-line winds). It follows that storm structure and evolution (and the attendant hazards) depend on more than just the hodograph and sounding, but also on external factors such as the orientation of the vertical shear vector with respect to the initiating boundary, as is the case in the schematic above. Identical hodographs and soundings can be associated with very different types of weather. An additional complication not easily depicted in the schematics above is that in strong shear, storm-splitting and subsequent storm collisions can occur; for example, when the deep-layer shear crosses the initiating boundary at a very large angle (e.g., 90°), upscale growth also can result.

³ See Bluestein and Weisman (2000).

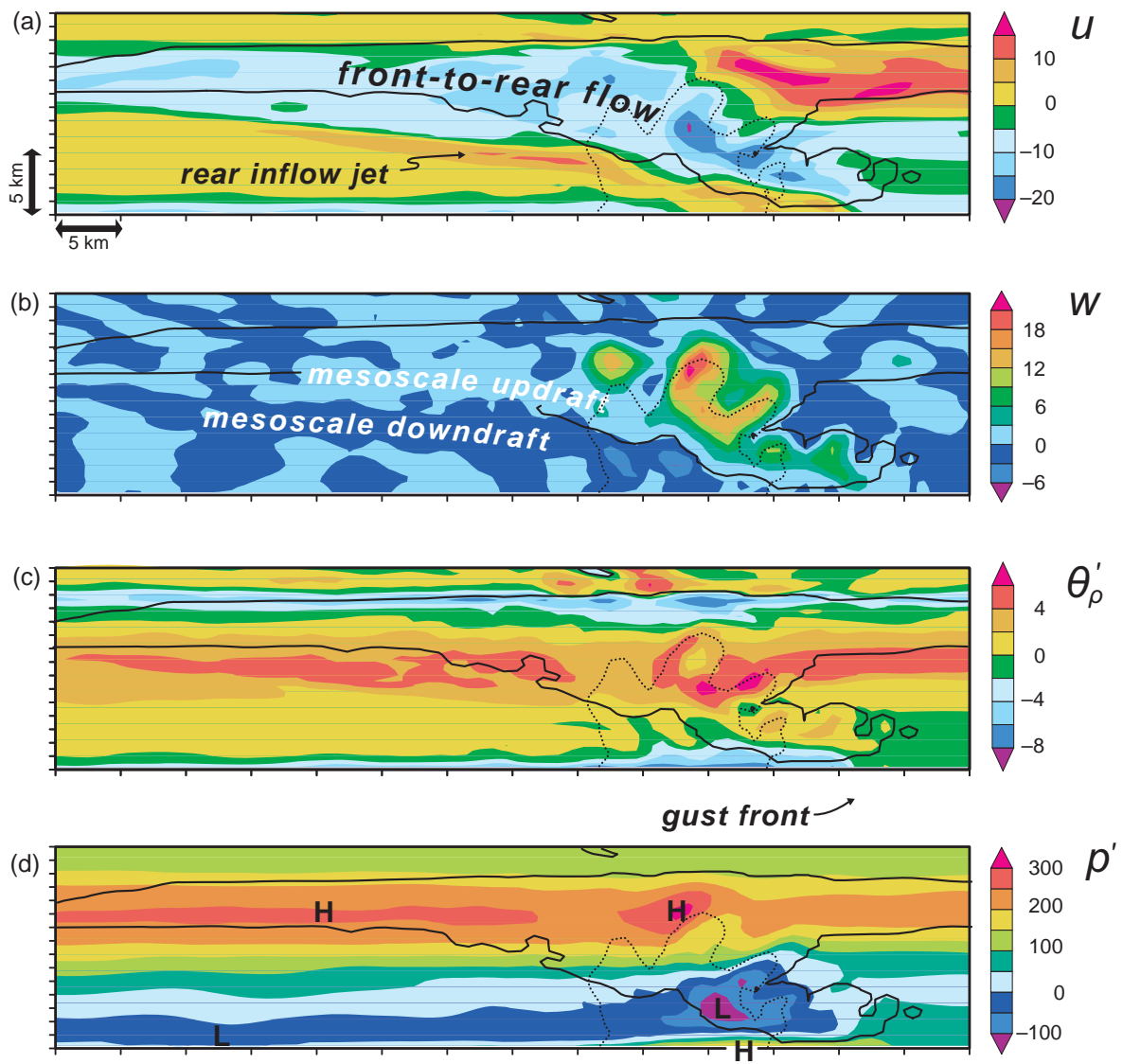


Figure 9.3 Output from a numerical simulation of a squall line in an environment using the sounding and wind profile used by Rotunno *et al.* (1988) (the sounding contains a little more than 2000 J kg^{-1} of CAPE and the unidirectional, westerly wind shear of 10 m s^{-1} is confined to the lowest 2.5 km). The squall line is shown 2.5 h after its initiation. The convection was initiated using a line of warm bubbles; small (0.1 K) random temperature perturbations were also added to the initial warm bubbles. The microphysics parameterization includes ice. The zonal vertical cross-sections display the following fields: (a) zonal wind u (m s^{-1} ; the system motion has been subtracted); (b) vertical velocity w (m s^{-1}); (c) density potential temperature perturbation θ'_ρ (K); (d) total pressure perturbation p' (Pa); (e) buoyancy pressure perturbation p'_b (Pa); (f) dynamic pressure perturbation p'_d (Pa). The retrieved p'_b and p'_d fields are only known to within a constant (see Section 2.5.3 and Figures 2.6–2.7). The cloud boundary (rain and hail region) is outlined with a solid (dotted) black line in each panel. Note the multicellular nature (as evidenced by the multiple updraft maxima), the differences in the depth and slope of the cold pool on the downshear (east) versus upshear (west) flanks, and the two major air streams (front to rear and rear to front) comprising the line. Relative pressure minima and maxima are labeled with the letters ‘L’ and ‘H’, respectively, in (d)–(f).

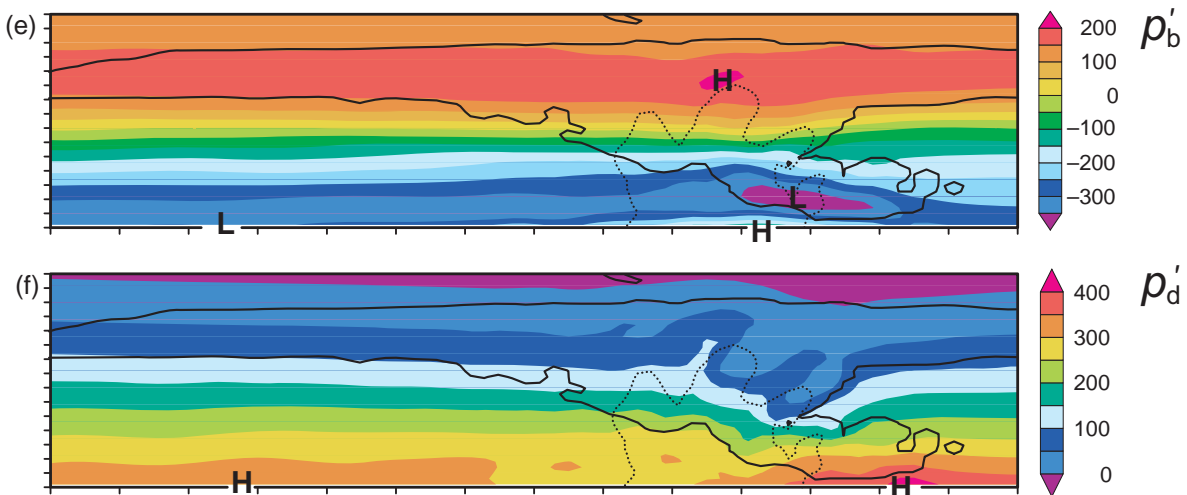


Figure 9.3 *Continued*

MCSs tend to be more common at night. One possible reason for the nocturnal maximum is the simple fact that, at least for MCSs that develop from the gradual upscale growth of initially isolated convective cells over several hours, the initiation of the isolated convection usually does not occur until the late afternoon or evening hours. Others have linked the nocturnal maximum in MCS activity to the nocturnal low-level wind maximum (Section 4.7). Of course, daytime MCSs also can be observed, particularly in the presence of strong forcing for convection initiation (e.g., strong convergence along an air mass boundary) and small CIN, as mentioned above.

MCSs are subclassified in a number of ways (Figure 9.4). *Squall lines* or *quasi-linear convective systems* (QLCSs) are MCSs that have a linear radar reflectivity appearance, as the name suggests (Figure 9.1). *Bow echoes*, introduced above, are arc-shaped or bowing radar reflectivity structures within squall lines. Sometimes an entire MCS is bow shaped (Figure 9.5a), whereas in other cases the bow echo is a decidedly sub-squall-line structure (Figure 9.5b). Multiple bows embedded within a single line form a *line-echo wave pattern* (LEWP; Figure 9.5b). *Mesoscale convective complexes* are yet another subclassification of MCSs; the classification requires that the anvil be fairly circular (Figure 9.6), regardless of the radar appearance (i.e., some squall lines can have sufficiently circular anvils to be classified as MCCs as well).

MCSs can be observed over a wide range of vertical wind shears. MCCs can occur in relatively weak-shear environments ($0\text{--}6\text{ km shear } \sim 10\text{ m s}^{-1}$), in contrast to environments that support bow echoes, which often contain

sufficient vertical wind shear for supercells ($0\text{--}6\text{ km shear } > 20\text{ m s}^{-1}$, and occasionally even the $0\text{--}2\text{ km shear exceeds } 20\text{ m s}^{-1}$). CAPE values also have a wide range, often less than 500 J kg^{-1} in cold-season squall line environments accompanied by strong synoptic-scale dynamics, or in excess of 5000 J kg^{-1} in some warm-season bow echo events.

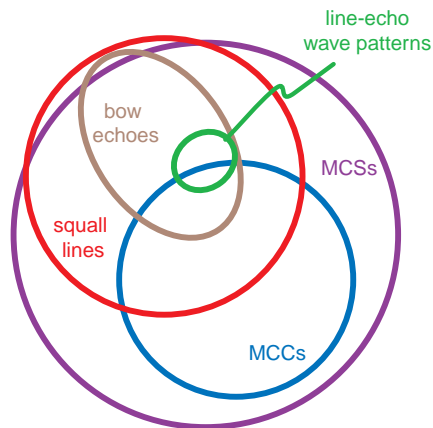


Figure 9.4 Venn diagram of MCS classifications. The position and overlap of the circles and ellipses only indicates relationships among the classifications; the sizes of the circles and ellipses should not be taken too literally to infer the relative frequencies of the various types of MCS. A small fraction of squall lines and bow echoes is not classified as MCSs because their horizontal length scale is less than 100 km.

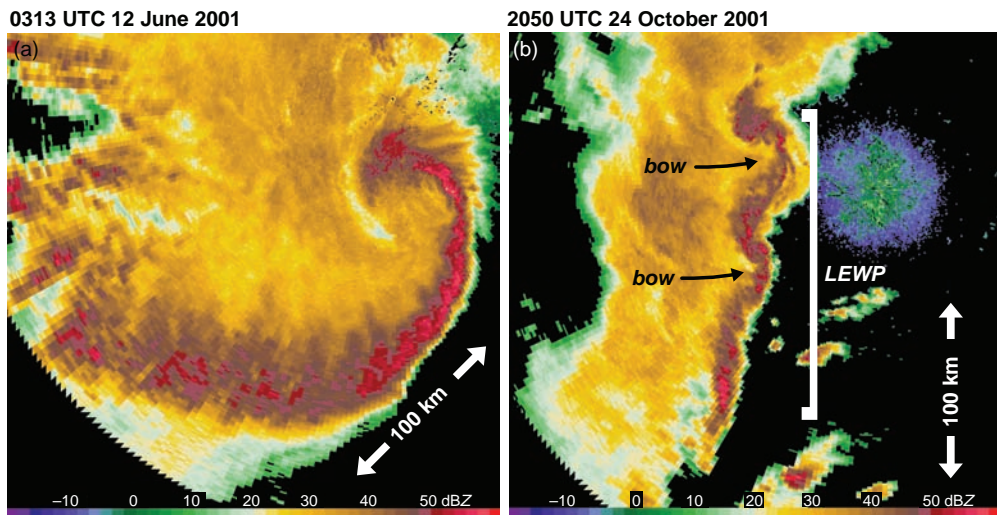


Figure 9.5 Examples of bow echoes. The radar reflectivity displays (dBZ) are from (a) Green Bay, WI, at 0313 UTC 12 June 2001 and (b) Fort Wayne, IN, at 2050 UTC 24 October 2001. Note the difference in the horizontal scales of the bow echoes. Multiple bow echoes embedded within a single line, as in (b), form a line-echo wave pattern (LEWP).

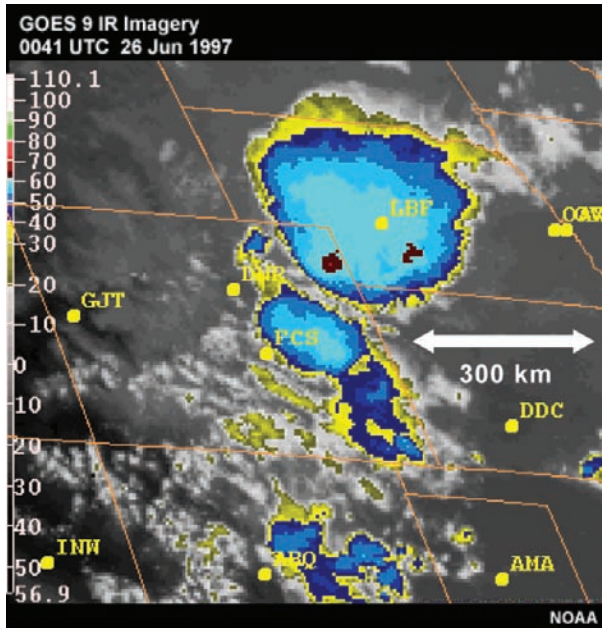


Figure 9.6 Infrared satellite image of a mesoscale convective complex (MCC) over Nebraska on 26 June 1997. Note the fairly circular cirrus shield. Image courtesy of the Cooperative Program for Operational Meteorology, Education, and Training (COMET).

In the remainder of this chapter, our attention is devoted to squall line structure and maintenance, bow echoes, which have perhaps been the most studied squall line derivative owing to their propensity for producing severe weather, and MCCs, for which larger, meso- α -scale circulations play an important role in maintenance.

9.2 Squall line structure

A conceptual model of a squall line is shown in Figure 9.7 (cf. Figures 9.1 and 9.3). The convective towers and most intense radar echoes usually are confined to the leading edge of the system, with a second, larger region of enhanced radar reflectivity associated with a *trailing stratiform precipitation* region commonly found to the rear of the convective line.⁴ The trailing stratiform region is separated from the leading convective towers by a region of lesser reflectivity often referred to as a *transition region* (Figures 9.1 and 9.7). The squall line generalized in Figure 9.7 and appearing in Figures 9.1 and 9.3 is that which occurs when the vertical wind profile is dominated by line-normal rather than along-line wind shear, and when the wind shear is largely confined to low levels. There is some tendency for squall lines to orient themselves normal to the low-level shear owing to

⁴ Stratiform precipitation is defined as in Section 5.1.7, that is, precipitation produced by upward vertical motions that are small compared with the fall speed of ice crystals and snow.

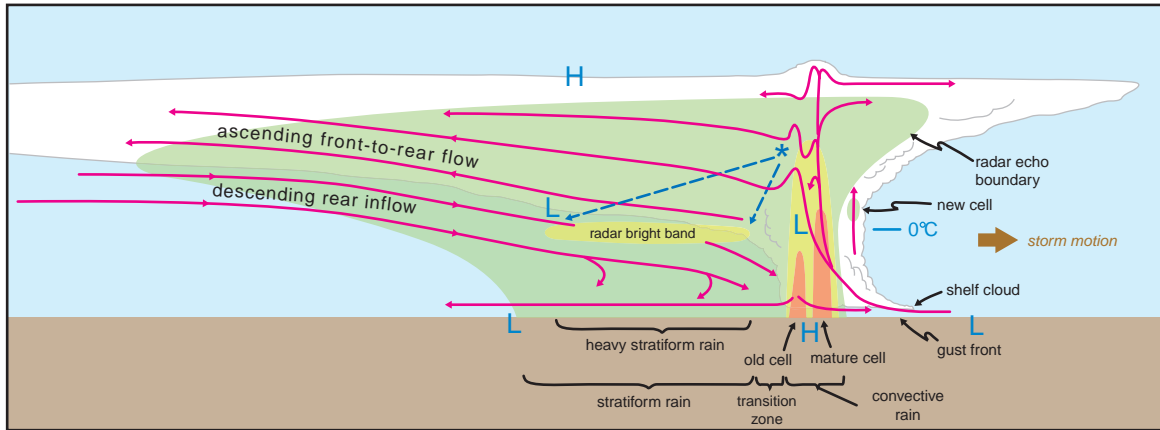


Figure 9.7 Conceptual model of a squall line with trailing stratiform area viewed in a vertical cross-section oriented perpendicular to the convective line (cf. Figures 9.1 and 9.3). The green shading indicates the region of precipitation-sized hydrometeors, i.e., where radar echo is present. The yellow and orange shading indicates more intense radar echoes. Pressure minima and maxima are also indicated, as is the height of the melting level, which is located just above the height at which a radar bright band is observed. (Adapted from Houze *et al.* [1989].)

the fact that the formation of new cells is more likely on the downshear flank of the outflow, as discussed in Section 8.3.

For a squall line in an environment dominated by line-normal, rear-to-front, low-level shear, hydrometeors are deposited to the rear of the squall line by a front-to-rear flow through the system (Figure 9.3). Low-level inflow approaches the squall line from the front, is lifted to its LFC by the gust front, and retains much of its front-to-rear momentum as it ascends through the leading convective updraft, and after it has exited the leading updraft (Figure 9.3a). After exiting the leading updraft, the front-to-rear air stream sometimes descends over a short distance within the transition region before ascending once again within the trailing stratiform region (Figure 9.7). The ascent of the front-to-rear air stream within the trailing stratiform region is gradual, occurring over several tens of kilometers and being associated with upward vertical velocities generally less than 0.5 m s^{-1} . It is beneath this *mesoscale updraft* that the trailing stratiform rain is observed.

The enhanced reflectivity in the trailing stratiform region is a result of both a secondary maximum in precipitation rate and the radar bright-band effect due to melting.⁵ The reason for the secondary maximum in precipitation rate involves *size-sorting* of hydrometeors, such that the

hydrometeors with appreciable fall speeds ($>5 \text{ m s}^{-1}$) descend near the updrafts within the leading convective zone, whereas small, slowly falling ice particles are advected rearward and through the mesoscale updraft. Within the mesoscale updraft the ice particles grow via vapor deposition. The upward air motions are large enough to condense significant amounts of water vapor but are sufficiently small so that the ice particles can fall. The growth of the ice particles takes time, thus precipitation rates and reflectivity are enhanced only well rearward of the leading convective region, thereby contributing to the relative minimum in precipitation rate and reflectivity in the transition region.

The environmental system-relative winds tend to be front-to-rear at all levels in squall line environments dominated by low-level wind shear, such as in the example described above (Figure 9.8). However, the midtropospheric environmental winds to the rear of the updrafts experience significant accelerations as a result of the convection, resulting in the development of rear-to-front flow, or *rear inflow*, at midlevels (Figure 9.9; rear inflow is also apparent in the simulation output shown in Figure 9.3a) as a result of internal dynamical processes (to be discussed in Section 9.4). The magnitude of the rear inflow, in general, is related to the intensity of the squall lines, with the most intense squall lines (which tend to form in environments of large CAPE and low-level wind shear) having the most intense rear inflow. The rear inflow gradually descends as it approaches the leading edge of the squall line, and the descent within this *mesoscale downdraft* is accompanied by

⁵ Although radar observations of an MCS would not typically display a 360° ring surrounding the radar (see Figure A.16 in Section A.3 of the appendix) unless the radar were situated within the trailing stratiform region, much of the enhanced reflectivity in the trailing stratiform region can still be attributed to the same bright-band effect.

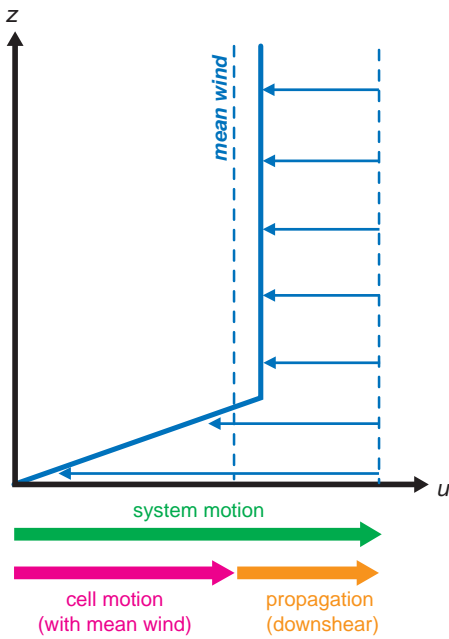


Figure 9.8 Illustration of why front-to-rear system-relative environmental winds are favored when the environmental wind profile (solid blue line) is characterized by unidirectional shear, with the shear largely confined to low levels. The system motion (green vector), which is the summation of downshear propagation (orange vector) and cell motion (magenta vector) that is approximately at the speed of the mean wind, results in front-to-rear (east-to-west) system-relative winds (thin blue vectors).

adiabatic warming that reduces surface pressure hydrostatically. In the wake of the squall line, this effect may be larger than the pressure-increasing (hydrostatic) effect of the rain-cooled air in the stratiform region; thus, a *wake low* may be observed at the surface to the rear of the mesohigh found within the region of heaviest precipitation and largest evaporative cooling rates (Figures 9.7 and 9.10).

In a translating squall line, the divergence center is slightly behind the mesohigh center at the surface (Figure 9.10). Similarly, the convergence center slightly lags the wake low center at the surface. There are regions where the flow is actually toward higher pressure. These oddities result from translation of the pressure field and air parcels being exposed to pressure gradients and accelerations for only short periods of time (i.e., large isallobaric effects). Compensating subsidence and its associated adiabatic warming ahead of a squall line can result in hydrostatically lowered pressure in the inflow of the convection (Figure 9.10). It has been suggested that the low pressure

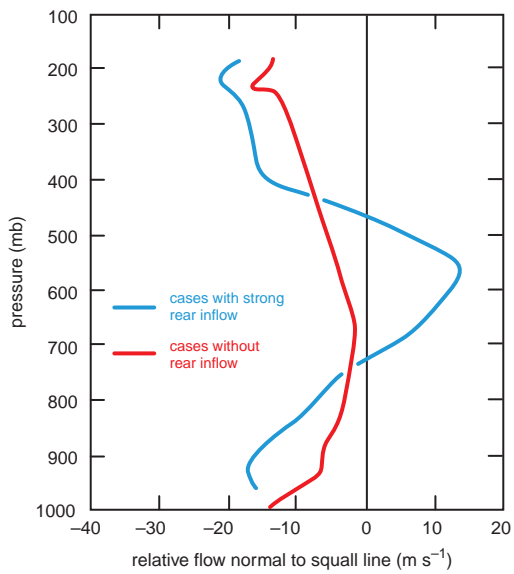


Figure 9.9 Profiles of system-relative winds from soundings taken to the rear of squall lines. (Adapted from Smull and Houze [1987].)

in the inflow increases convergence, leading to a positive feedback between the convection and low pressure.⁶ As the convergence intensifies, the convection may intensify, leading to increased compensating subsidence, increased adiabatic warming, and increased hydrostatic pressure falls.

Although the majority of squall lines adhere to the conceptual model described on the preceding pages, hereafter referred to as *trailing stratiform* (TS) squall lines, squall line environments frequently contain significant along-line or rear-to-front wind shear in the middle to upper levels. These squall lines must be treated somewhat differently than those conceptualized in Figures 8.12b and 9.7. In such cases, the bulk of the precipitation may not fall to the rear of the leading updraft. When the deep-layer shear has a strong rear-to-front component, hydrometeors are deposited ahead of the convective towers, leading to a *leading stratiform* (LS) squall line (Figures 9.11b and 9.12a). When the deep-layer shear has a strong along-line component, hydrometeors are deposited in the direction parallel to the orientation of the updrafts, leading to a *parallel stratiform* (PS) squall line (Figures 9.11c and 9.12b). It is estimated that approximately 10–20% of squall lines are of the LS variety and 10–20% are of the PS variety, whereas 60–80% of squall lines are the TS type.⁷

⁶ See Hoxit *et al.* (1976) and Fritsch and Chappell (1980).

⁷ See Parker and Johnson (2000).

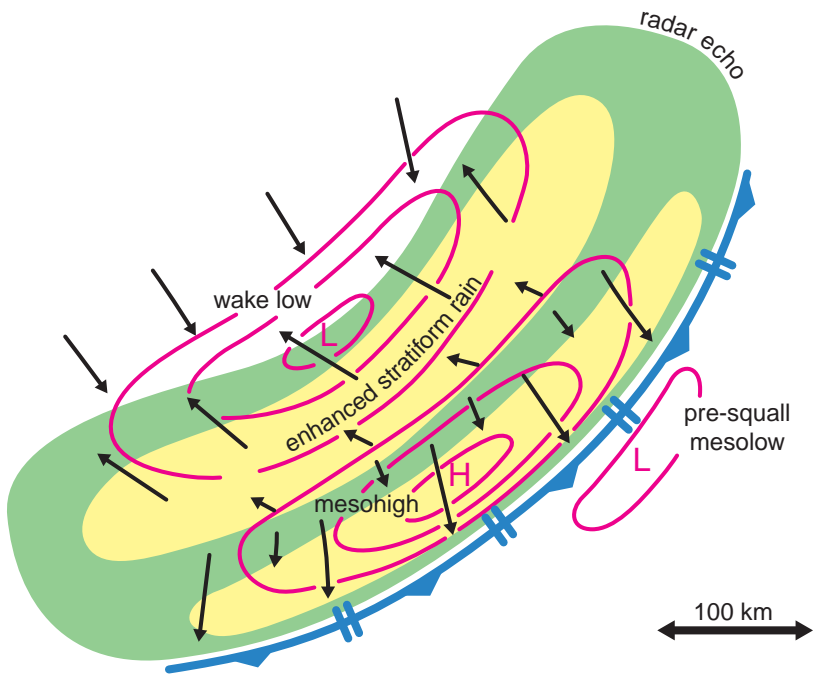


Figure 9.10 Schematic surface pressure, wind, and precipitation fields during the mature stage of a squall line. Arrows indicate actual (as opposed to system-relative) winds. (Adapted from Johnson and Hamilton [1988].)

It is tempting to think that squall lines with parallel, and especially leading stratiform precipitation, would be difficult to maintain because their precipitation falls into their own inflow. However, although the low-level inflow does tend to be latently cooled in LS systems, and to a lesser degree in PS systems, the atmosphere is not stabilized because the low-level cooling is matched by latent cooling aloft as well. In fact, the midlevel and low-level evaporation, melting, and sublimation of hydrometeors falling ahead of the line of updrafts in a squall line has actually been shown to destabilize the atmosphere ahead of the line, thereby actually promoting the maintenance of the lines rather than fostering their demise.⁸ In some LS systems, the inflow at low levels is actually from the rear to the front.⁹ In these cases, the precipitation does not fall into the inflow at all.

The structure of the updraft region of squall lines is known to vary considerably as well. Although *line* implies a fair degree of two-dimensionality, and indeed many squall line radar presentations do suggest an unbroken,

quasi-two-dimensional updraft region (e.g., Figure 9.13a), some squall lines have updraft regions that display significant three-dimensionality (e.g., Figure 9.13b). The three-dimensionality tends to be found a few kilometers above the ground at altitudes well above the top of the gust front (the gust front updraft tends to be contiguous even in cases when the midlevel draft structure is more cellular). *Slab-like* (i.e., quasi-two-dimensional) versus *cellular* (i.e., three-dimensional) updraft regions in squall lines seem to depend, in part, on the environmental relative humidity. Relatively dry low-level environments favor strong cold-pool development, leading to upshear-tilted, slab-like convection (the relationship between tilt and cold-pool strength will be discussed in detail in the next section). Conversely, high relative humidity in the environment at low levels leads to weak cold pools and downshear-tilted convective systems, with primarily cell-scale three-dimensionality in the convective region. The presence of two- versus three-dimensional squall line updraft structure also seems to have some sensitivity to the depth and magnitude of moist absolutely unstable layers (MAULs)¹⁰ that commonly form ahead of squall lines as a result of intense lifting (the forced lifting by vertical perturbation pressure gradients is strong enough to

⁸ See Parker and Johnson (2004b, 2004c).

⁹ A much publicized example was the MCS that led to the severe flooding in Johnstown, PA, on 19–20 July 1977 (Bosart and Sanders, 1981; Zhang and Fritsch 1986, 1987, 1988).

¹⁰ See Bryan and Fritsch (2000).

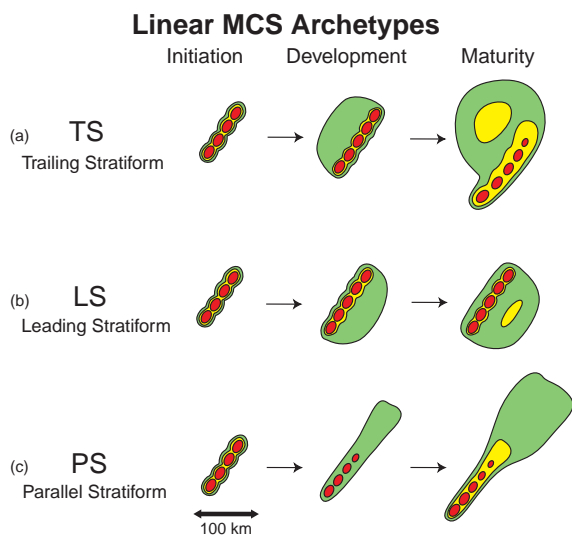


Figure 9.11 Schematic reflectivity drawing of idealized life cycles for three linear MCS archetypes: (a) TS, (b) LS, and (c) PS. Approximate time intervals between phases: for TS 3–4 h; for LS 2–3 h; for PS 2–3 h. Levels of color shading roughly correspond to 20, 40, and 50 dBZ. (From Parker and Johnson [2000].)

maintain the MAULs, even though one might surmise that the layers would tend to overturn quickly at the expense of the unstable stratification that results from the lifting).¹¹ The presence of a prominent MAUL has been found to be associated with an updraft structure that is more slab-like than cellular.

9.3 Squall line maintenance

One of the most often cited and debated theories related to convective storms is what is referred to as *RKW theory*, which is attributed to the study of squall line maintenance by R. Rotunno, J. Klemp, and M. Weisman.¹² RKW theory postulates that the mechanism for maintaining a long-lived squall line is a balance between the horizontal vorticity produced by the buoyancy gradient across the gust front and the horizontal vorticity associated with the environmental low-level vertical wind shear.

Recall (5.41), which was obtained in deriving the speed of a density current (the reader may wish to revisit Section

¹¹ MAULs require the lifting of a potentially unstable layer, i.e., a layer in which $\partial\theta_e/\partial z < 0$ (Section 3.1.3). Vertical profiles of θ_e such that θ_e decreases with height are typical of the environments of DMC, particularly in the central United States, where moist boundary layers tend to be capped by dry, low- θ_e elevated mixed layers.

¹² See Rotunno *et al.* (1988).

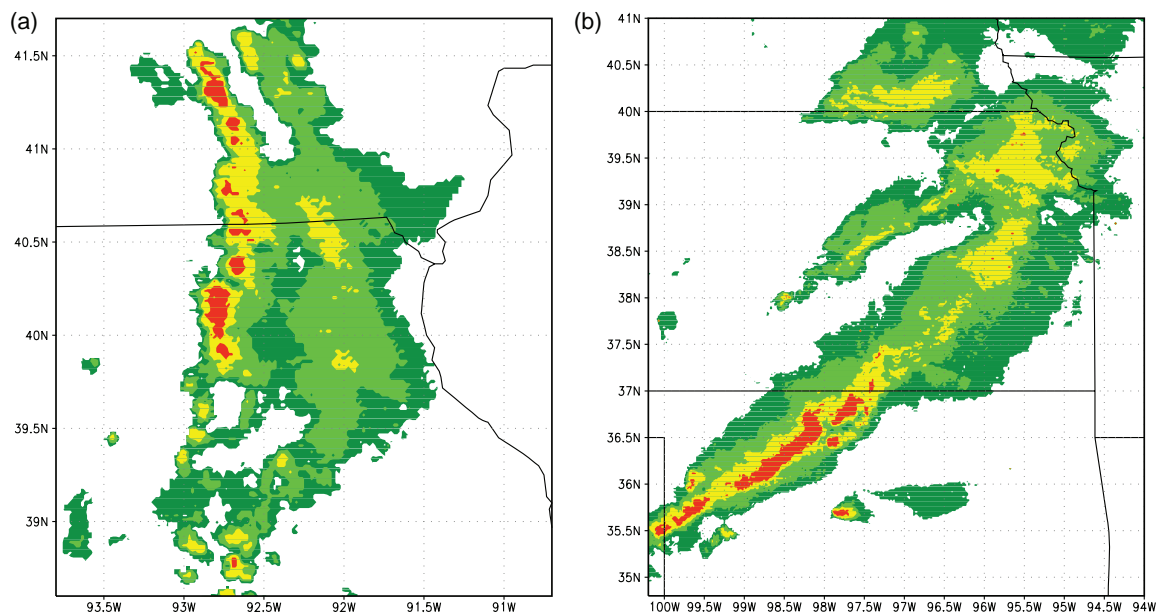


Figure 9.12 Composited radar reflectivity imagery illustrating (a) an LS MCS and (b) a PS MCS. (From Parker and Johnson [2000].)

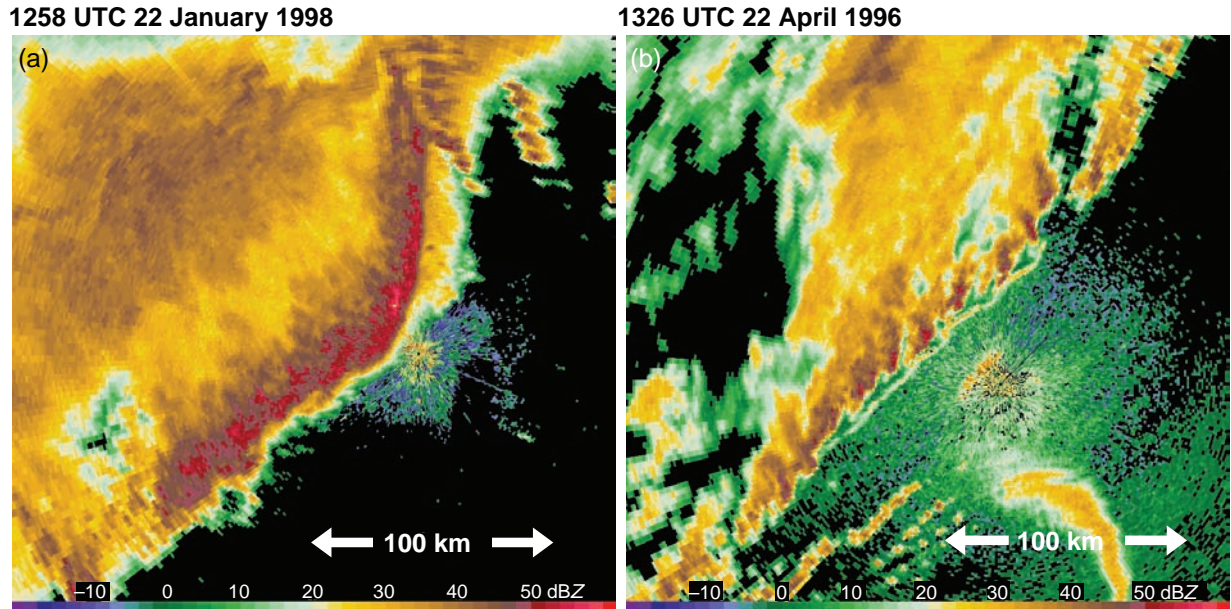


Figure 9.13 Radar reflectivity images of mesoscale convective systems characterized by (a) a slab-like, virtually unbroken line of updraft and high reflectivity (1258 UTC 22 January 1998; Mobile, AL, radar), and (b) a leading portion composed of discrete, cellular reflectivity elements (1326 UTC 22 April 1996, Memphis, TN, radar). (Adapted from Bryan and Fritsch [2000].)

5.3; also refer to Figures 5.29 and 5.30):

$$0 = \left(\frac{u_{L,d}^2}{2} - \frac{u_{L,0}^2}{2} \right) - \left(\frac{u_{R,d}^2}{2} - \frac{u_{R,0}^2}{2} \right) - \int_L^R (w\eta)_d dx + \int_0^H B_L dz. \quad (9.1)$$

The winds *relative to the density current* at the top right, bottom right, top left, and bottom left corners of a control volume that encapsulates the leading portion of the density current are $u_{R,d}$, $u_{R,0}$, $u_{L,d}$, and $u_{L,0}$, respectively. The above relationship among the wind speeds in the corners of the control volume was obtained by integrating the inviscid, Boussinesq horizontal vorticity equation over a control volume in the x - z plane and assuming a steady state. An expression for the speed of a density current was obtained by judiciously placing the boundaries of the control volume in locations where assumptions could be made about the relationships among $u_{R,d}$, $u_{R,0}$, $u_{L,d}$, and $u_{L,0}$ (e.g., the placement of the boundaries of the control volume allowed us to assume that $u_{L,0} = 0$, $u_{L,d} = u_{R,d}$, and $\int_L^R (w\eta)_d dx = 0$).

In deriving the speed of a density current (5.45), we assumed that there was no wind shear in the environment

ahead of the density current (i.e., $u_{R,d} = u_{R,0}$). On the other hand, in the environments of long-lived convective systems, there is virtually always significant wind shear in the environment (i.e., $u_{R,d} \neq u_{R,0}$). In the absence of an evaporatively driven cold pool (the melting and sublimation of ice also contribute to the cold pool), such as early in the lifecycle of a cumulonimbus cloud, environmental shear tilts an updraft in the downshear direction (Figure 9.14c). In the absence of environmental wind shear, the development of an evaporatively driven cold pool tilts the updraft rearward over the cold pool (Figure 9.14b). In the presence of both environmental shear *and* an evaporatively driven cold pool, a balanced state may exist such that the lifting by the cold pool is nearly upright (Figure 9.14d).

RKW theory presupposes that squall line intensity and longevity are a function of updraft tilt. Updrafts that are significantly tilted away from the vertical tend to have their buoyancy reduced more by entrainment compared with an erect updraft, resulting in a weaker overall system (Figure 9.15). Moreover, increasing updraft tilt is associated with an increasing adverse vertical gradient of perturbation pressure due to buoyancy ($\partial p'_b / \partial z$).¹³ In other words, for a

¹³ The authors thank M. Parker for pointing out this aspect of RKW theory.

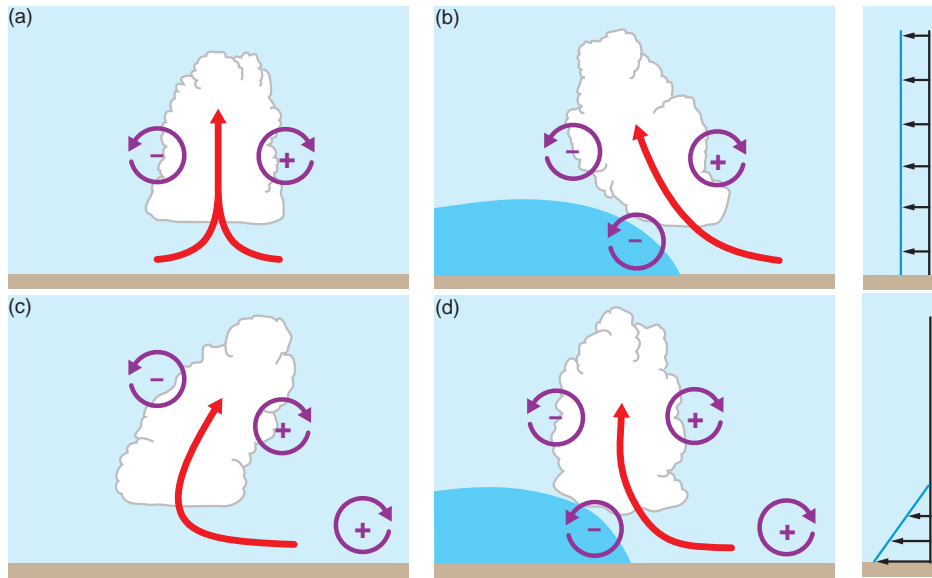


Figure 9.14 Schematic diagram showing how a buoyant updraft may be influenced by environmental wind shear and/or a cold pool. (a) With no environmental shear and no cold pool, the axis of the updraft produced by the thermally created, symmetric vorticity distribution is vertical. (b) With a cold pool, the distribution is biased by the negative vorticity of the underlying cold pool, causing the updraft to tilt over the cold pool. (c) With environmental shear and no cold cool, the distribution is biased toward positive vorticity, causing the updraft to lean downshear. (d) With both a cold pool and shear, the two effects may negate each other and promote an erect updraft. (Adapted from Rotunno *et al.* [1988].)

given positive buoyancy, the downward-directed buoyancy pressure gradient force increases as an updraft becomes more tilted, thereby resulting in a smaller upward acceleration (Figure 9.16). The aspect ratio (depth divided by width) of the buoyant region is minimized when the buoyant column is tilted into the horizontal. Recall from Section 3.1 (also see Figure 3.1) that the vertical acceleration for a given buoyancy decreases as the aspect ratio decreases. The hydrostatic limit ($dw/dt = 0$) is reached as the aspect ratio vanishes.

RKW theory proposes a relationship among the variables in (9.1) that must exist if an updraft is to be upright along the gust front. RKW theory assumes that such an updraft is necessary for a long-lived squall line.¹⁴ With regard to the control volume variables, because $u_{R,d} \neq u_{R,0}$, the control volume must be defined slightly differently than was done

in the derivation of the speed of a density current in a shear-free environment given by (5.45).

Figure 9.17 shows output from the simulation of a density current in which strong westerly shear is encountered by an eastward-moving density current, such that an intense, erect updraft is present along the leading edge of the density current. Notice that at an altitude slightly above the altitude of the mean density current depth, at least at some x locations, there exist locations where both $u_{R,d} \approx 0$ and $u_{L,d} \approx 0$. We may cleverly place the top of the control volume at this altitude (note that this is a significantly lower altitude than in Figure 5.30). Furthermore, let us assume that the stagnation condition exists within the density current at the left boundary of the control volume (i.e., $u_{L,0} \approx 0$). Finally, if we assume a priori that an erect updraft is present along the leading edge of the gust front (after all, we are seeking to find the relationship among $u_{R,d}$, $u_{R,0}$, etc. that is associated with the presence of an erect updraft), then $\int_L^R (w\eta)_d dx = 0$ because the flux of positive horizontal vorticity through the top of the control volume is exactly canceled by the flux of negative horizontal vorticity (Figure 9.18). There is no net flux of horizontal vorticity through the top of the control volume in the case

¹⁴ RKW theory also has been found to account for differences in the structure and intensity of simulated narrow cold frontal rainbands, such that the maintenance and tilt of the rainband's updraft are determined by a balance between the wind shear in the pre-frontal air mass and the circulation driven by the cold front rather than convective outflow (Parsons, 1992).

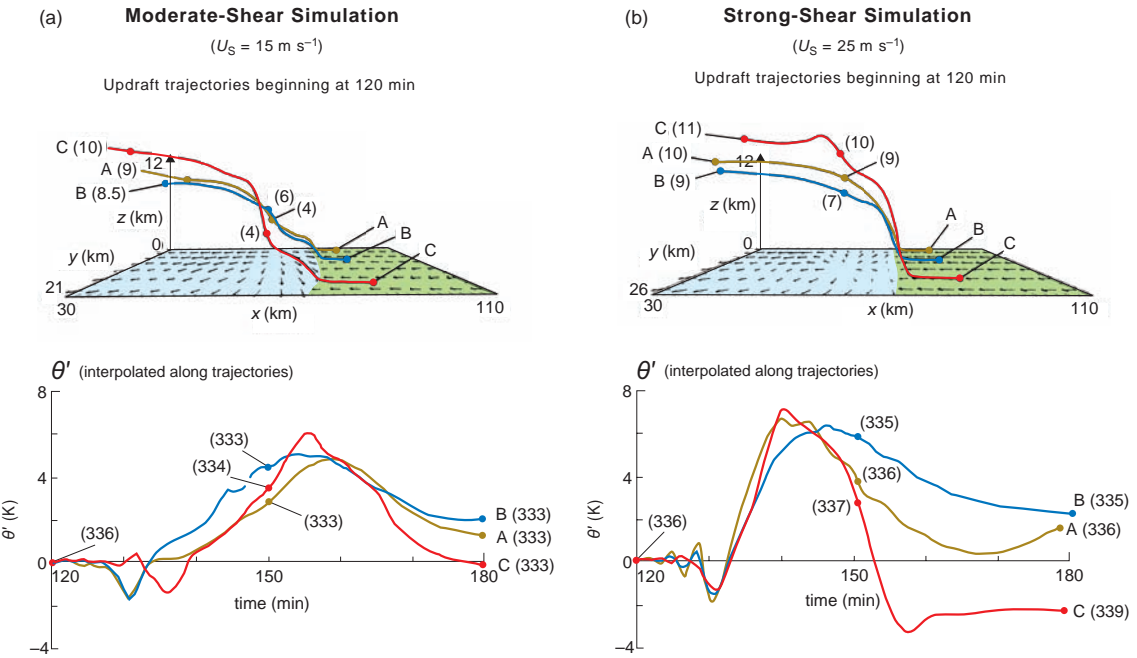


Figure 9.15 Characteristic updraft trajectories and potential temperature perturbations along the trajectories in numerical simulations of a squall line in (a) moderate (15 m s^{-1}) low-level wind shear and (b) strong (25 m s^{-1}) low-level wind shear. Each trajectory originates at 350 m above the surface and about 10 km ahead of the cold pool (blue shading) and is traced for 60 min. The height of each trajectory is indicated in parentheses at 30-min intervals. Numerals in parentheses at 30-min intervals along the potential temperature perturbation traces indicate potential temperatures. Note how the trajectories are more steeply sloped in the strong-shear simulation than in the moderate-shear simulation, and that less buoyancy dilution has occurred along the trajectories in the strong-shear simulation compared with the moderate-shear simulation. (Adapted from Weisman [1992].)

of an erect updraft, but for tilted updrafts there is a nonzero net flux of horizontal vorticity.

Setting $u_{L,d} = u_{R,d} = u_{L,0} = \int_L^R (w\eta)_d \, dx = 0$ in (9.1) yields

$$0 = \frac{u_{R,0}^2}{2} + \int_0^H B_L \, dz; \quad (9.2)$$

thus,

$$u_{R,0}^2 = -2 \int_0^H B_L \, dz = c^2 \quad (9.3)$$

$$u_{R,0} = -c, \quad (9.4)$$

where c is the strength of the cold-pool circulation. The reason for taking the negative root in (9.4) will be apparent below. Because $u_{R,d} = 0$, (9.4) can be written as

$$\Delta u = c, \quad (9.5)$$

where $\Delta u = u_{R,d} - u_{R,0}$ is the magnitude of the vertical shear over the depth of the control volume, which is a bit

greater than the mean depth of the density current. RKW theory refers to the condition given by (9.5) as the *optimal condition* for squall line longevity. Physically, it implies that an erect gust front updraft will be present when the horizontal vorticity associated with the environmental wind shear is equal and opposite the horizontal vorticity that is baroclinically generated by the horizontal density gradient along the leading edge of the outflow. If we had chosen the positive root in (9.4), then we would have selected the case in which the vorticity associated with the environmental shear is the same sign and magnitude as the baroclinic vorticity in the outflow; that is, the vorticity associated with the environmental shear would have the wrong sign for balancing the vorticity in the outflow (e.g., Figure 5.31c). Moreover, the positive root in (9.4) corresponds to the case of $w(x, d) = 0$, that is, the degenerate case of no vorticity flux anywhere through the top of the control volume.

When $c < \Delta u$, the gust front updraft tilts downshear (*downshear* is with respect to the environmental shear).

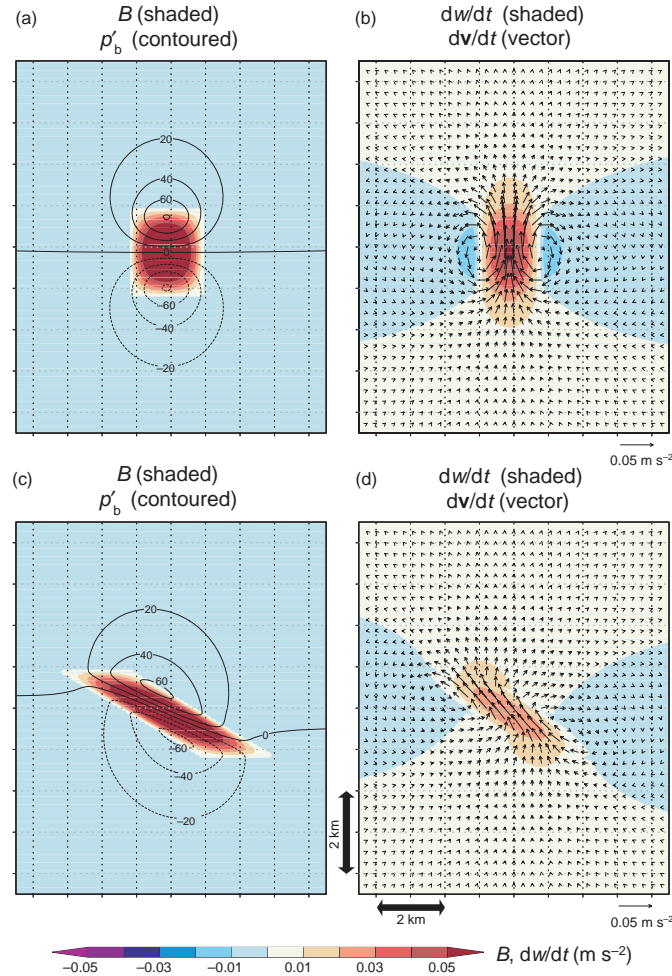


Figure 9.16 The relationship among the tilt of a buoyant column, the buoyancy perturbation pressure field (p'_b), vertical acceleration (dw/dt), and total acceleration (dv/dt). (a) Buoyancy (shaded) and buoyancy perturbation pressure (contours every 20 Pa) fields associated with an upright column of warm air. (b) Vertical acceleration (shaded) and total acceleration (vectors) for the buoyant column shown in (a). (c), (d) As in (a), (b), but the region of positive buoyancy is tilted. The maximum buoyancy in (c) is the same as in (a), but the downward-directed gradient of p'_b is larger within the buoyant column, resulting in a smaller vertical acceleration in (d) compared with (b). Courtesy of Matt Parker.

When $c > \Delta u$, the gust front updraft tilts upshear (i.e., rearward over the cold pool). The shear Δu is perhaps most appropriately measured over approximately the lowest 2.5 km, which corresponds to the depth of the control volume used to obtain (9.5), although it would be foolish to define the depth over which Δu is computed very rigidly [this is one difficulty in applying (9.5) in a forecasting setting—it is not clear that the 0–2.5 km shear is generally more appropriate to use than, for example, the 0–2.0 km or 0–3.0 km shear]. For most thunderstorm outflows, RKW theory implies an optimal shear of $17\text{--}25 \text{ m s}^{-1}$. Note that

Δu is the line-normal shear; thus, one must know the squall line orientation in order to evaluate $c/\Delta u$ properly. Another complication in determining the optimal condition is that c is not generally a constant in time (Figure 9.19a). As a convective system matures, c typically increases owing to a deepening of the cold pool and the development of a more extensive trailing precipitation region. Thus, environmental shear that is optimal early in the life of a squall line may very well become *suboptimal* as the squall line matures, leading to a progressively more rearward-tilting updraft as time goes on. The rearward tilt of a buoyant updraft is

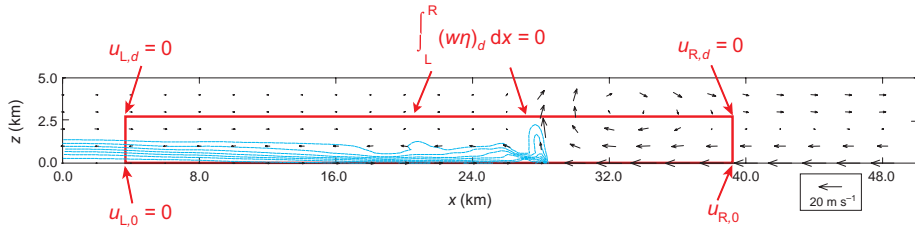


Figure 9.17 Numerical simulation of an eastward-moving density current in an environment containing westerly vertical wind shear such that the circulation associated with the environmental shear approximately balances the circulation associated with the density current (i.e., the environment approximately satisfies RKW theory's optimal state). The result is an erect updraft along the leading edge of the density current. The control volume considered in the derivation of the optimal shear is overlaid in red. Potential temperature perturbations are contoured at 1°C intervals within the cold pool starting at -1°C . Wind vectors are relative to the density current ($U_c \approx 8 \text{ m s}^{-1}$). The model domain extends to 10 km; only the lowest 5 km of the model domain are shown.

precisely what generates rear inflow and can lead to bow echoes when the system is not strictly 2-D (Section 9.4).

As an alternative to the RKW vorticity argument, the tilt of the gust front updraft, which is determined by the trajectories of rising air parcels, can be explained in terms of the horizontal accelerations experienced by the rising parcels. The horizontal acceleration experienced by a rising parcel, and thus the trajectory of the parcel, is principally governed by the horizontal gradients of the linear dynamic perturbation pressure, p'_{dl} , and the buoyancy perturbation pressure, p'_b (the nonlinear contribution to the dynamic perturbation pressure field, p'_{dnl} , does not tend to have a significant horizontal gradient across the updraft). In the case of an air parcel approaching a gust front from the east in an environment containing westerly low-level shear, the parcel is initially slowed and deflected upward by what is largely a p'_{dnl} excess associated with the convergence at the gust front (recall from Section 2.5 that convergence is associated with nonlinear rather than linear dynamic perturbation pressure; this pressure excess is also apparent in the total dynamic perturbation pressure [p'_d] field of the density current simulation output shown in Figure 2.6). Once the parcel has begun rising, its horizontal acceleration is primarily influenced by the horizontal gradients of p'_{dl} and p'_b . Because relatively high (low) p'_{dl} is found upshear (downshear) of the updraft core, the rising parcel experiences a downshear-directed horizontal gradient of p'_{dl} . On the other hand, a relative minimum in p'_b is present along the top of the cold pool where $\partial B / \partial z > 0$ ($p'_b \propto -\partial B / \partial z$); thus, the rising parcel experiences an upshear-directed horizontal gradient of p'_b . The relative strengths of the two competing accelerations determine whether the parcel experiences a net rearward or forward acceleration as it ascends. The forward acceleration increases with increasing westerly shear,

and the rearward acceleration increases with increasing cold-pool strength ($\partial B / \partial z$ increases with the strength of the cold pool). Updraft trajectories are vertical when the two competing horizontal accelerations cancel each other.

RKW theory has been the subject of some controversy,¹⁵ in large part because climatologies of the environments associated with severe straight-line winds show that the environments tend to have wind shears significantly weaker than required by RKW theory's optimal condition (see, e.g., Figure 9.20). There are several possibilities for the discrepancy. One possibility that has been argued is that the optimal condition need not be met in order for severe weather to occur; however, one might then question the practical forecasting utility of evaluating whether the optimal condition is actually met. Another possibility is that the occurrence of severe straight-line winds in a squall line is not a reliable indication that the squall line has an erect updraft. Squall lines that produce damaging winds generally might be suboptimal from the perspective of RKW theory. A significant upshear tilt is, in fact, observed in many severe squall lines. For example, the development of an upshear tilt is important in the formation of bow echoes (discussed in the next section), which are responsible for the most extreme high-wind events. These systems develop a strong rear-inflow jet, which further alters the vorticity balance by counteracting part of the cold-pool circulation.

It is also not clear whether *severity* should be defined by the strength of the surface winds or the maximum updraft speed; the strength of the surface winds, which are responsible for wind damage, are not well correlated with

¹⁵ See Coniglio and Stensrud (2001), Evans and Doswell (2001), Coniglio *et al.* (2004, 2006), Weisman and Rotunno (2004, 2005), and Stensrud *et al.* (2005).

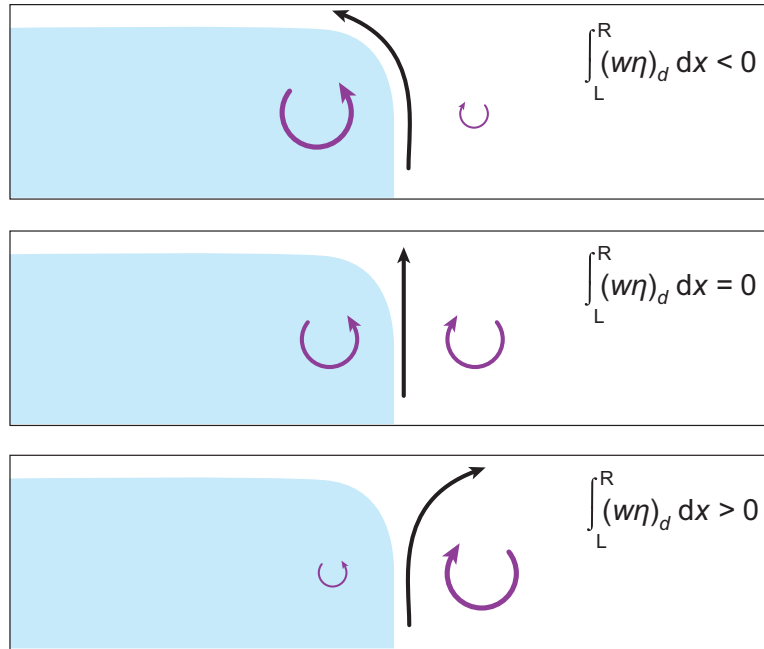


Figure 9.18 Schematic showing the relationships between the net flux of horizontal vorticity through the top of the control volume, $\int_L^R (w\eta)_d dx$, and updraft tilt. (a) The cold-pool horizontal vorticity (defined to be negative) dominates the horizontal vorticity associated with the mean low-level shear (defined to be positive); air lifted by the cold pool is accelerated rearward and exits the top of the control volume at an angle, and there is a net flux of negative vorticity through the top of the volume. (b) The cold-pool horizontal vorticity balances the horizontal vorticity associated with the mean low-level shear; the updraft at the leading edge of the cold pool is not tilted and there is no net flux of vorticity through the top of the volume. (c) The horizontal vorticity associated with the mean low-level shear dominates the cold-pool horizontal vorticity; air lifted by the cold pool is accelerated forward and exits the top of the control volume at an angle, and there is a net flux of positive vorticity through the top of the volume.

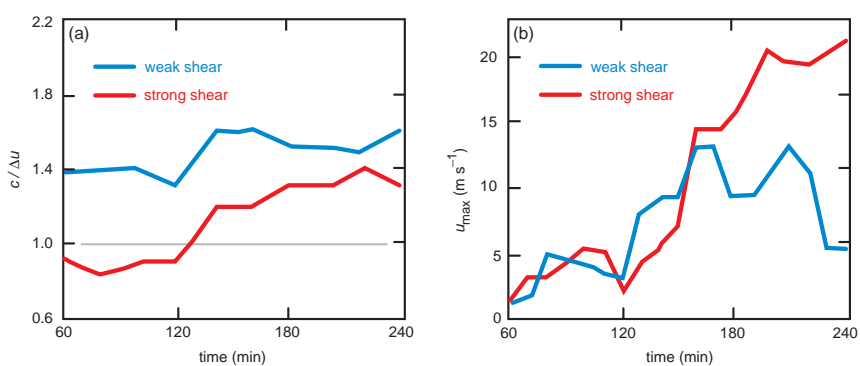


Figure 9.19 Time series of (a) $c/\Delta u$ and (b) maximum midlevel rear inflow strength in a pair of numerical simulations of squall lines in which the environment has relatively weak (15 m s^{-1}) low-level wind shear and relatively strong (25 m s^{-1}) low-level wind shear. (Adapted from Weisman [1992].)

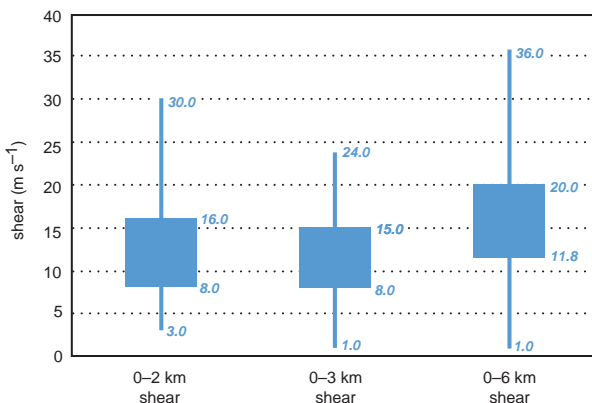


Figure 9.20 Box-and-whiskers plots of 0–2 km, 0–3 km, and 0–6 km shear vector magnitudes in environments associated with extreme convective windstorms (environments that evidently supported long-lived MCSs). Most of the distributions of shear magnitudes are significantly less than the optimal shear predicted by RKW theory for typical cold-pool strengths ($\sim 20\ m\ s^{-1}$ in the lowest 2.5 km). (Adapted from Evans and Doswell [2001].)

updraft speed. The severity of straight-line winds within squall lines is much better correlated with the forward speed of the squall line. The forward speed of the convective system is maximized when advection of cells by the mean wind and the system propagation are aligned, which is favored when the mean wind is large and aligned with the environmental shear.¹⁶

Another likely reason for the discrepancy between the observations of severe winds in squall lines and the wind shears characterizing these environments is that RKW theory only strictly applies to the tilt of the *gust front updraft*. The overall tilt of the updraft, which typically extends to the tropopause, depends on more than the interaction of the outflow with the environmental low-level shear. Stated another way, there is much more to the overall characteristics of a squall line than just the gust front updraft. The gust front updraft is certainly part of the story, but the larger-scale structure and evolution of a squall line also is very likely to depend on the magnitude and orientation of mid- and upper-tropospheric vertical wind shear (i.e., dynamical effects occurring well above the control volume depicted in Figure 9.17).¹⁷ Strong mid- and upper-tropospheric wind shear directed from rear to front

¹⁶ Cohen *et al.* (2007) found that severe, long-lived MCSs are fast moving and are favored over slower-moving, nonsevere MCSs when both the deep-layer shear vector and the mean deep-layer wind are large and nearly parallel.

¹⁷ See Coniglio *et al.* (2006).

accelerates parcels downshear (i.e., forward) in mid- to upper levels, and can therefore prevent an updraft from being severely tilted over its own outflow in the event that the low-level shear is overwhelmed by the circulation of the cold pool. The effects of mid- and upper-tropospheric wind shear can also be understood in terms of vorticity (Figure 9.21). We do not wish to mislead the reader into thinking that the characteristics of the environmental wind profile alone, even when considered over a deep layer, are sufficient to account for all aspects of squall line structure, or even just the tilt of the system. For example, in the case of a rearward- or upshear-leaning updraft, additional rearward accelerations in mid- to upper levels can be driven by a rearward-directed buoyancy pressure gradient (Figure 9.3e).

Although RKW theory improved our understanding of the interaction of density currents with ambient wind shear (little work had been done in that area at the time), RKW theory probably places too much emphasis on the importance of the tilt of the gust front updraft in attempting to explain squall line longevity. If the dome of isentropes associated with the cold pool is sufficiently deep to lift air to its LFC, RKW theory becomes irrelevant to the longevity of a squall line. Perhaps RKW theory is more applicable to the issue of convection *initiation* than convection maintenance, for the convection initiation problem—in other words, getting air parcels to their LFC—is largely confined to low levels where the tilt of a low-level updraft (along an air mass boundary like a dryline, for instance) might assume a much larger relative importance than in the case of a mature convective system that spans the depth of the troposphere.

9.4 Rear inflow and bow echoes

As discussed in Section 9.2, rear inflow is a very common, if not virtually ubiquitous, trait of TS squall lines (Figures 9.3a and 9.7), despite the fact that the system-relative environmental wind in squall lines is usually from front to rear at midlevels (Figure 9.8). This suggests a tendency for squall lines to induce system-scale, midlevel, rear-to-front accelerations. Such accelerations occur when updrafts tilt rearward over their cold pools.

Recall that the development of a rearward tilt in time is a somewhat natural evolution of a squall line, because c typically increases in time as squall lines mature and cold pools deepen (Figure 9.19). A rearward-tilting updraft induces a midlevel pressure minimum above the cold pool largely as a result of hydrostatics (Figure 9.22). The pressure minimum also can be viewed as a reflection of the vertical buoyancy gradient ($\partial B/\partial z$) term in the pressure equations given by (2.134) and (8.24); relatively low pressure is found where $\partial B/\partial z > 0$ (Figure 9.3c–e). The elevated pressure

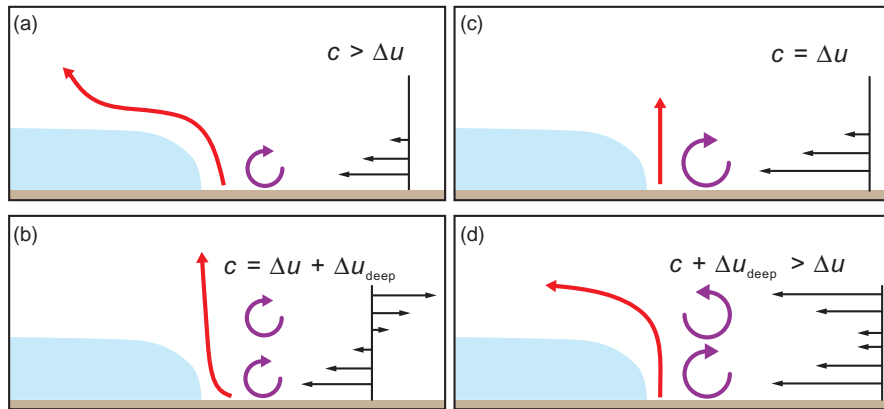


Figure 9.21 Environmental shear over a deep layer (Δu_{deep}) can prevent an updraft from being severely tilted over its own outflow in the event that the low-level shear (Δu) is overwhelmed by the circulation of the cold pool. Rising air parcels are accelerated downshear by the linear dynamic perturbation pressure field; shear present above the cold pool also affects the trajectories of rising air parcels. The effects of the shear also can be understood in terms of vorticity, as illustrated above. (a) The environmental low-level shear is relatively weak (the magnitude of the environmental horizontal vorticity is proportional to the size of the curved arrows) and no environmental shear is present above the cold pool. The horizontal vorticity of the cold pool dominates the horizontal vorticity of the approaching air parcels; therefore, the air parcels are accelerated rearward over the cold pool (the parcel trajectory is indicated with the red arrow). (b) The environmental low-level shear is weak, but significant deep-layer shear is present. The sum of the horizontal vorticity associated with the low-level shear and deep-layer shear is comparable to the horizontal vorticity of the cold pool, resulting in a more vertical updraft. (c) Shear is absent above the cold pool but strong low-level shear and associated horizontal vorticity in the environment balance the horizontal vorticity of the cold pool, leading to an upright updraft; this is RKW theory's optimal state. (d) Strong low-level environmental shear is present and associated with horizontal vorticity that would otherwise be balanced by the horizontal vorticity of the cold pool, but environmental shear above the cold pool is directed rearward over the cold pool. Air parcels are accelerated rearward over the cold pool upon encountering the rearward-directed shear. (Adapted from an image provided by the Cooperative Program for Operational Meteorology, Education, and Training [COMET].)

minimum accelerates air into the convective system from the rear (Figure 9.19b). The magnitude of the elevated pressure deficit, and thus the strength of the rear inflow, increase with increasing CAPE.

The rear-to-front acceleration also can be explained using vorticity arguments. The rear portion of the cold pool induces a vertical circulation that acts to accelerate air up and over the rear portion of the cold pool. Once the updraft tilts rearward over the cold pool, the aforementioned cold-pool-induced acceleration is augmented by the circulation induced along the rear flank of the buoyant updraft (Figure 9.22).

The formation of these *rear-inflow jets* also has been invoked to explain how upshear-tilted, suboptimal squall lines reestablish an erect gust front updraft (Figure 9.23). In the absence of a rear-inflow jet, RKW theory predicts an erect gust front updraft when c matches Δu . Over time, c exceeds Δu , thereby promoting the upshear tilt and acceleration of rear inflow discussed above. However,

the horizontal vorticity associated with the rear-inflow jet, when added to the horizontal vorticity associated with the environmental shear, Δu , may permit a new balance to exist (Figure 9.23), such that

$$\Delta u^2 + \Delta u_j^2 = c^2, \quad (9.6)$$

where Δu_j is the wind shear associated with the rear-inflow jet. Equation (9.6) comes from allowing $u_{L,d}$ and $u_{L,0}$ in (9.1) to be nonzero, where

$$\Delta u_j^2 = u_{L,d}^2 - u_{L,0}^2. \quad (9.7)$$

When the system has ends (i.e., is not purely two-dimensional), a bow echo may form, in which a couplet of vertical vorticity straddles the rear-inflow jet, with the most intense vorticity concentrated in *bookend vortices* (Figures 9.24–9.26). In a mature bow echo, bookend vortices are the result of vortex lines being

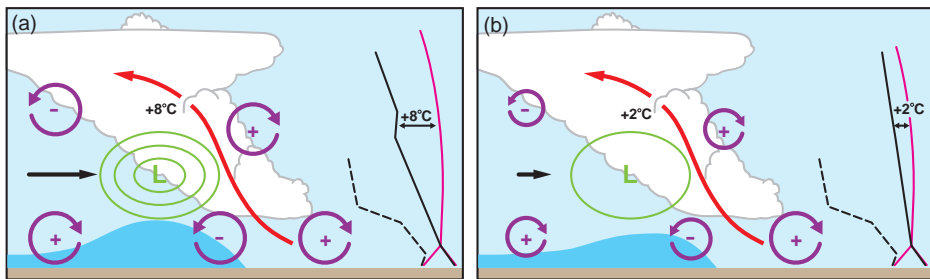


Figure 9.22 Illustration of how a tilted updraft induces midlevel rear inflow in an (a) high-CAPE and (b) low-CAPE environment. The low pressure is largely a consequence of hydrostatics, which also implies that the magnitude of the midlevel pressure deficit, and thus the rear inflow, increase as the updraft buoyancy (a function of environmental CAPE) increases. Purple arrows indicate the senses of the horizontal vorticity at various locations. Soundings are schematically presented along the right-hand side of each panel. (Adapted from an image provided by the Cooperative Program for Operational Meteorology, Education, and Training [COMET].)

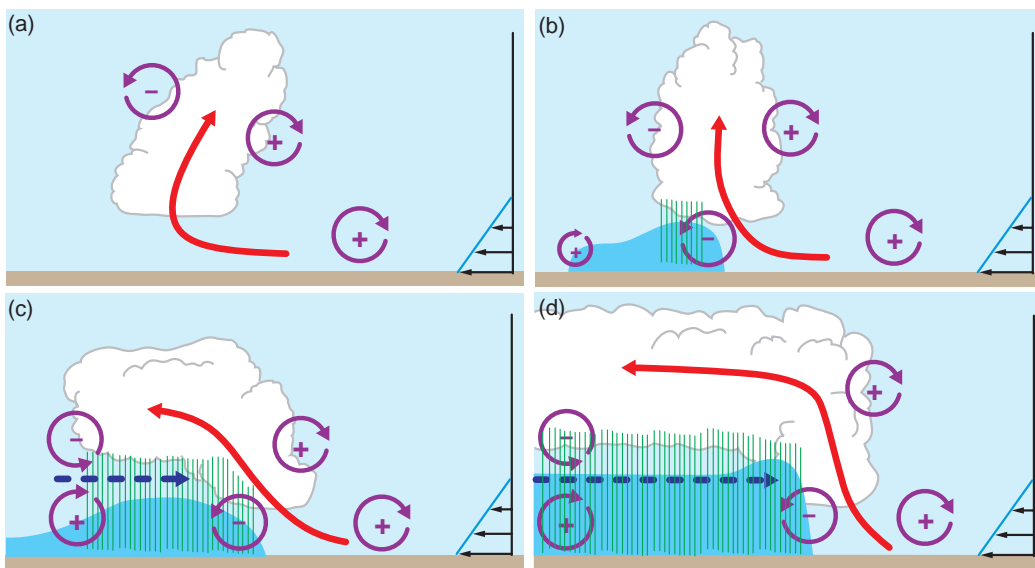


Figure 9.23 Four stages in the evolution of an idealized bow echo. (a) An initial updraft leans downshear in response to the environmental vertical wind shear, which is shown on the right. (b) The circulation generated by the storm-induced cold pool balances the horizontal vorticity associated with the environmental shear, and the system becomes upright. (c) The cold-pool circulation overwhelms the horizontal vorticity associated with the environmental shear, and the system tilts upshear, producing a rear-inflow jet. (d) A new steady state is achieved such that the circulation of the cold pool is balanced by both the horizontal vorticity associated with the environmental shear and the elevated rear-inflow jet. The updraft current is denoted by the red arrow, and the rear-inflow current in (c) and (d) is denoted by the dashed blue arrow. The purple arrows depict the most significant sources of horizontal vorticity, which either are associated with the environmental shear or are generated within the convective system. Regions of rainfall are indicated by the green vertical lines. (Adapted from Weisman [1993].)

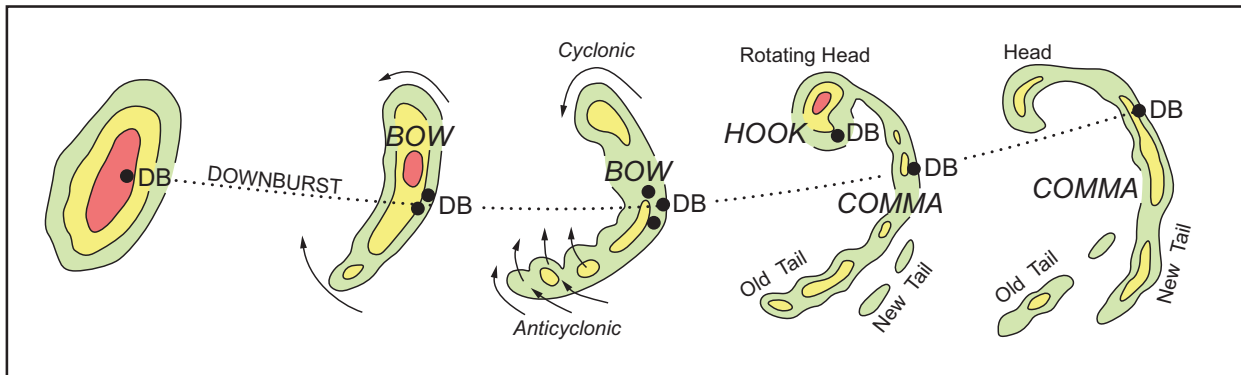


Figure 9.24 Fujita's conceptual model of a bow echo. Black dots labeled 'DB' are downburst locations. Colors are radar echo intensity. (Adapted from Fujita [1978].)

1848 UTC 5 May 1996

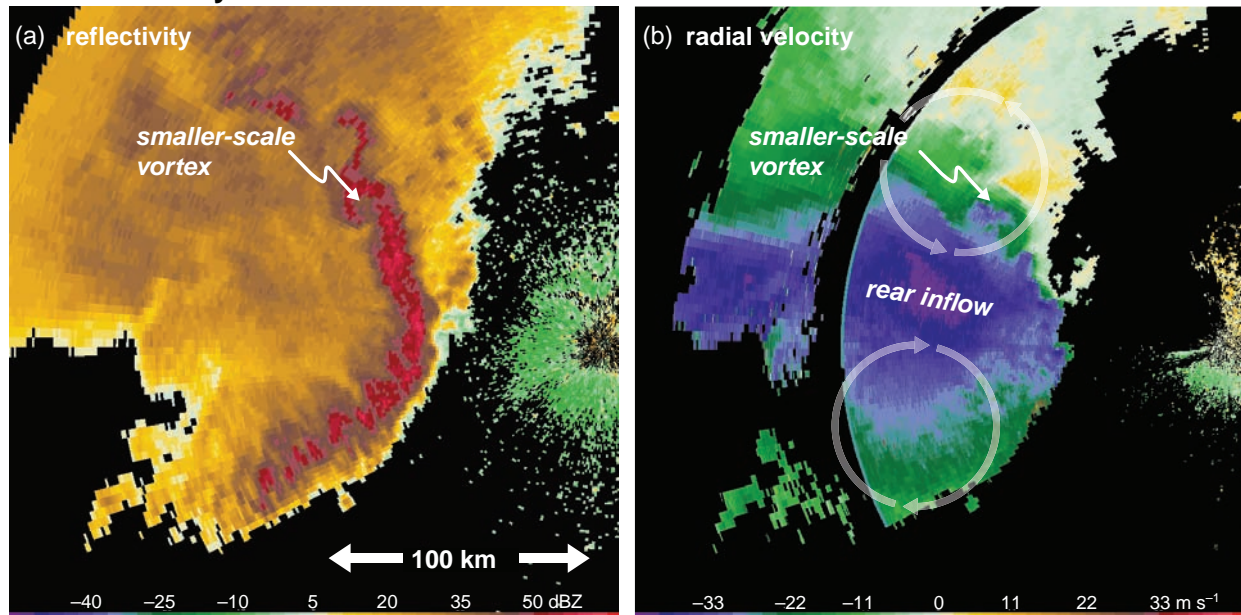


Figure 9.25 (a) Reflectivity factor and (b) radial velocity from the Paducah, KY, radar at 1848 UTC 5 May 1996, showing a mature bow echo. The rear inflow is rather obvious in the velocity imagery. Broad arrows in (b) indicate the sense of rotation associated with the bookend vortices (note that the radial velocities are ground relative, however). A smaller-scale vortex is also evident at the northern end of the bow echo in both the reflectivity and velocity data.

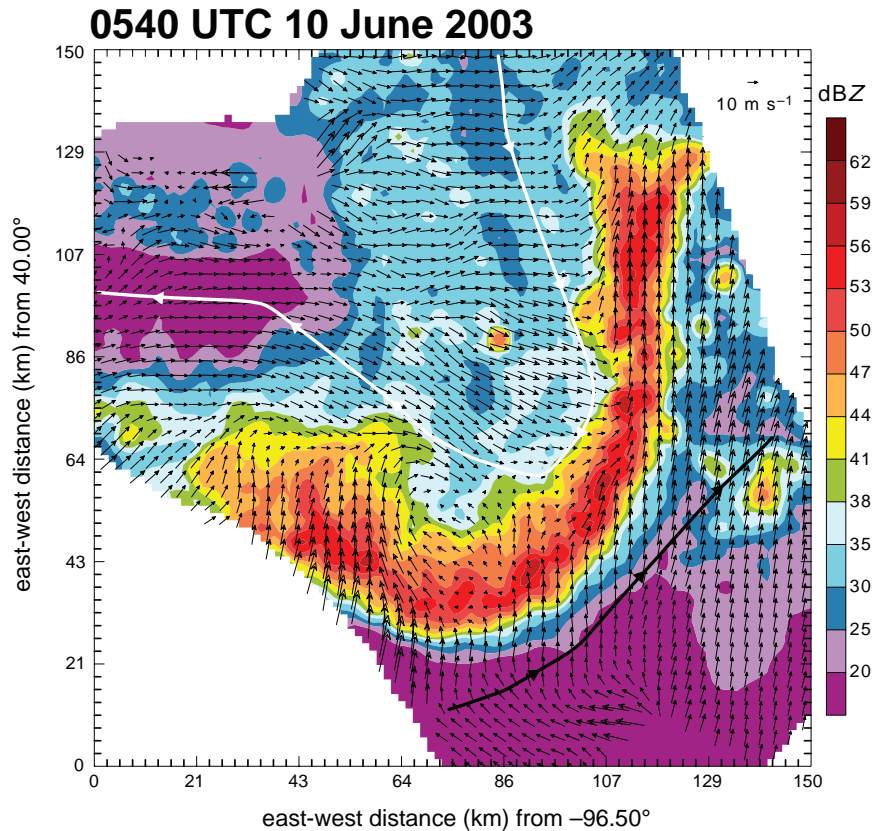


Figure 9.26 Pseudo-dual-Doppler analysis of a bow echo observed by a pair of airborne Doppler radars at 0540 UTC on 10 June 2003 during the Bow Echo and MCV Experiment (BAMEX). The wind vectors are system relative. The aircraft flight tracks are indicated with the white and black bold lines. (Adapted from Davis *et al.* [2004].)

generated baroclinically in the cold pool of the squall line and subsequently being drawn upward by the leading updraft, which yields counter-rotating line-end vortices (Figure 9.27). (When environmental horizontal vorticity is large, tilting of environmental vortex lines, rather than vortex lines generated in the cold pool, can dominate the production of vertical vorticity early in the system's lifetime, and even at later times in strong cells near the ends of convective lines in the same way that supercell thunderstorm updrafts acquire vertical vorticity.) The bookend vortices enhance the rear-inflow jet and initiate the bowing process. At early stages in their evolution, the cyclonic and anticyclonic bookend vortices are of similar strengths. After several hours, by which time the accumulated effect of the Coriolis force has become significant, the cyclonic vortex usually dominates, giving the convective system a comma-shaped appearance (Figure 9.24).

As mentioned in Section 9.1, bow echoes can have a wide range of horizontal scales, ranging from 20 to 200 km

in the along-line dimension (Figures 9.5, 9.25, and 9.26). Damaging winds are often found near the apex of the bow, particularly when a rear-inflow jet descends to the surface (Figure 9.24). Many rear-inflow jets remain elevated, however, and are not associated with such destructive surface winds. The differences between bow echoes in which severe winds reach the surface and those that are not associated with severe surface winds are an active area of research today. Meso- γ -scale vortices along the gust front also seem to play an important role in the development of localized damaging winds within bow echoes and MCSs in general. Additional aspects of damaging, nontornadic winds in squall lines are presented in Chapter 10.

Bow echo environments tend to have larger CAPE and low-level shear than ordinary squall line environments. The environments of the most prolific severe-weather-producing bow echoes occasionally have CAPE in excess of 5000 J kg^{-1} and 0–2 km shear (and 0–6 km shear as well) as large as 25 m s^{-1} . It may not be entirely obvious

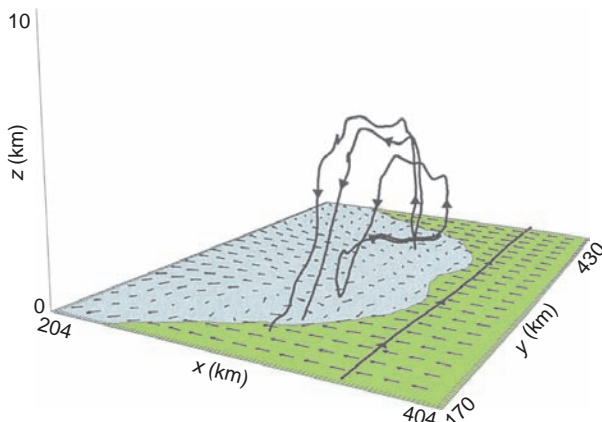


Figure 9.27 Vortex-line structure in a numerical simulation of a quasi-linear convective system with line-end vortices. The vortex lines are denoted by the thick solid lines, with the direction of the vorticity vector indicated by the arrow heads. Vectors denote the surface wind flow. The surface cold pool (potential temperature perturbations less than -1 K) is shaded blue. (Adapted from Weisman and Davis [1998].)

why large shear would favor bow echoes, especially since bow echoes form after convection begins to tilt rearward, and the rearward tilt requires $c/\Delta u > 1$ in the context of RKW theory. It seems that the shear creates a zone of preferred lifting in the downshear direction, leading to a focused area of updraft necessary for tilting the vortex lines into arches. In addition, greater vertical shear is associated with increased midlevel updraft buoyancy by promoting an erect updraft and therefore less buoyancy reduction via entrainment (Figure 9.15), thus leading to a larger midlevel pressure deficit as the updraft is eventually tilted rearward (presumably the rearward tilting takes longer in a strong-shear environment compared with a weak-shear environment). In other words, strong shear might delay the onset of rear inflow development, but strong shear may make rear inflow more intense when it finally does develop. Another possibility is that a strong cold pool is nearly unavoidable in such large-CAPE environments, so strong shear might be needed to balance the strong cold-pool circulation in order to maintain strong, deep lifting along the leading edge.

Given that bow echo and supercell environments are both characterized by strong shear,¹⁸ it is not entirely surprising that bow echoes can also evolve from supercells, specifically HP supercells. The differences in whether one strong-shear environment spawns mainly supercells

versus another spawning a bow echo may lie in the subtleties of the initiation mechanism, cell interactions, or higher-order details of the environment, for example the vertical distribution of CAPE and shear, midlevel relative humidity, etc.

As is probably evident from the presentation above, most bow echo research has investigated the favorable ranges of CAPE and wind shear. Bow echo formation almost certainly depends on other aspects of the environment as well. For example, bow echo formation in numerical simulations is sensitive to small changes in the low-level relative humidity of the environment. As discussed in Section 9.1, the characteristics of the gust front lifting along a convective line are sensitive to the environmental low-level relative humidity, such that quasi-two-dimensional, slab-like lifting is favored in relatively dry conditions and three-dimensional, cellular structures are favored in relatively moist conditions. Numerically simulated bow echoes occur in an intermediate low-level moisture regime, and it is somewhat troubling that relative humidity changes corresponding to water vapor mixing ratio modifications of only a couple of grams per kilogram are sufficient to go from the slab regime to the cellular regime.¹⁹ It is not easy to evaluate whether actual squall line formation is this sensitive to the environmental humidity, but the sensitivity in simulations might account for some of the difficulty in forecasting bow development in real time.

9.5 Mesoscale convective complexes

Mesoscale convective complexes (MCCs) are a subset of MCSs that are defined by the characteristics of their anvils. MCCs exhibit a large, circular, long-lived, cold cloud shield (Figure 9.6).²⁰ Beneath the nearly circular cirrus canopy, the organization of the convection may be much more linear in terms of its radar appearance. Thus, many squall lines and bow echoes can also be classified as MCCs (and therefore MCCs also tend to have rear inflow, a mesohigh, a wake low, etc.).

MCC structure and evolution are probably more dependent on the synoptic-scale pattern than other types of MCS. Synoptic weather patterns that favor MCCs usually feature broad middle- and upper-tropospheric ridging; MCCs are

¹⁸ See Doswell and Evans (2003).

¹⁹ See James *et al.* (2006).

²⁰ MCCs are rather strictly defined in terms of the characteristics of their cloud shields. The cloud shield with infrared temperature $\leq -32^\circ\text{C}$ must have an area $\geq 10^5 \text{ km}^2$, and the interior cold cloud region with temperature $\leq -52^\circ\text{C}$ must have an area $\geq 5 \times 10^4 \text{ km}^2$. The size criteria must be met for a period $\geq 6 \text{ h}$. Moreover, the eccentricity (minor axis divided by major axis) of the anvil must be ≥ 0.7 at the time of maximum extent. The reader is referred to Maddox *et al.* (1986) for additional details.

¹⁸ See Doswell and Evans (2003).

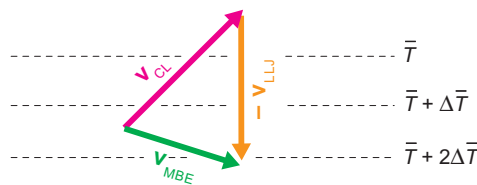


Figure 9.28 Conceptual model of MBE movement (v_{MBE} ; green) within an MCC (assuming it is a Type 1 MCC) as the vector sum of the mean flow in the cloud layer (v_{CL} ; magenta) and the propagation component (v_{PROP} ; orange). The magnitude and direction of v_{PROP} are assumed to be equal and opposite to those of the low-level jet (v_{LLJ}). The isotherms (black dashed contours) display mean temperature in the 850–300 mb layer. (Adapted from Corfidi *et al.* [1996].)

prone to develop when a short-wave trough moves through the longer-wavelength ridge, although the large-scale ascent that precedes MCC development tends to be primarily a reflection of strong low-level warm advection rather than differential cyclonic vorticity advection.²¹ There is probably an even greater nocturnal bias of MCC activity than the nocturnal bias for MCSs in general. MCCs tend to be initiated on the cold side of synoptic fronts and draw their inflow from above the stable nocturnal boundary layer, especially if a low-level jet (whether it takes the form of the nocturnal low-level wind maximum or whether it is associated with the synoptic-scale pressure gradient, or both)

²¹ See Maddox and Doswell (1982).

overruns a front; that is, MCCs can usually be regarded as Type 1 MCSs. Initiation also tends to be near sunset, when the low-level jet begins its nighttime acceleration. Middle and upper tropospheric winds are often relatively weak; in these situations, MCC movement is slow and the flash flood threat is high.

The motion of MCCs (assuming they are Type 1) tends to be parallel to fronts, although individual cells may have a component of their movement toward colder air. Empirically, the motion of individual *meso-β-scale convective elements* (MBEs; v_{MBE}), which produce the heaviest rainfall, has been shown to be well-predicted by the sum of the cloud layer mean wind (v_{CL}) and the system propagation (v_{PROP}), the latter of which is assumed to be equal and opposite to the low-level jet (v_{LLJ}); i.e., $v_{MBE} = v_{CL} + v_{PROP} = v_{CL} - v_{LLJ}$ (Figure 9.28). The vertical wind shear in MCC environments at middle and upper levels is generally weak, but the low-level vertical shear may be significant, owing to strong warm advection and the corresponding thermal wind.

Because of their size and duration, MCCs generate *warm-core*, meso- α -scale circulations that are organized on a much larger scale than the individual convective elements. Near the tropopause (i.e., above the level of maximum convective heating), MCCs generate a mesohigh and divergent, anticyclonic outflow, once the accumulated effect of the Coriolis acceleration becomes significant, that is, a few hours after initiation (Figure 9.29b).²² Below the level of

²² Any large and long-lived MCS, even one that does not meet all of the MCC criteria, will obviously generate similar circulations.

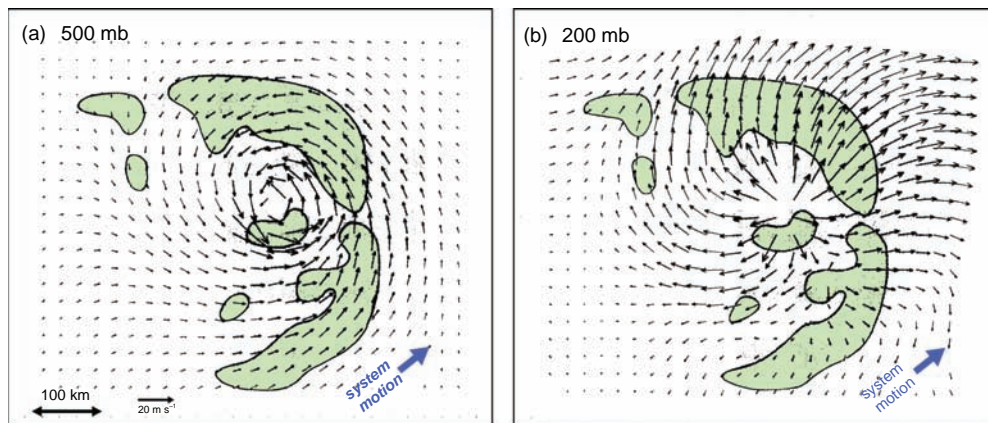


Figure 9.29 Mesoscale model output showing cyclonic vorticity at 500 mb and anticyclonic vorticity at 200 mb in the wake of a midlatitude mesoscale convective complex. Winds are system-relative. Green shading denotes regions of convective precipitation. (Adapted from Chen and Frank [1993].)

maximum convective heating, a low-pressure perturbation and convergent, cyclonic eddy is produced, called a *mesoscale convective vortex* (MCV; Figure 9.29a). Both the cyclonic and anticyclonic circulations are often apparent in cloud debris (Figure 9.30) and occasionally in the radar appearance of the convective complex (Figure 9.31). The superpositioning of the upper-tropospheric anticyclone on the background synoptic wind field often leads to the formation of a mesoscale jet streak on the northwestern flank of the MCC (Figures 9.29b and 9.32).

As was the case in the explanation of the development of a midlevel pressure minimum and rear inflow in a mature squall line (Section 9.4), the pressure perturbations associated with the anticyclonic and cyclonic circulations can be explained by the sign of $\partial B/\partial z$; relatively high (low) pressure is found where $\partial B/\partial z < 0$ ($\partial B/\partial z > 0$). The wind and temperature perturbations that accompany the pressure perturbations can be viewed as a reflection of potential vorticity anomalies. In a statically stable environment (i.e., $\partial \theta/\partial z > 0$), diabatic heating depresses isentropes downward. As a result, above (below) the level of maximum heating, $\partial \theta/\partial z$ is reduced (increased); therefore, the potential vorticity, PV, is also reduced (increased) above (below) the level of maximum convective heating, where

$$PV = \frac{(\omega + f\mathbf{k}) \cdot \nabla \theta}{\rho} \approx \frac{\zeta + f}{\rho} \frac{\partial \theta}{\partial z}, \quad (9.8)$$

$\omega = (\xi, \eta, \zeta)$ is the three-dimensional relative vorticity vector, and the Coriolis acceleration has been approximated as $f\mathbf{k}$ (Figure 9.33).

The mesoscale potential vorticity anomalies and associated mesoscale circulations induced by the convective

heating are an intrinsic characteristic of MCCs and play an important role in MCC maintenance. In what is known as the *potential vorticity thinking* framework, in the presence of shear, vortex-relative environmental flow rides up the isentropic surface as it approaches the positive, lower tropospheric potential vorticity anomaly from the downshear side. This air reaches its LFC, with the subsequent latent heat release maintaining the potential vorticity anomalies (Figure 9.34a). The presence of wind shear implies tilted isentropic surfaces via the thermal wind relation, and lifting induced by the cyclonic potential vorticity anomaly is favored on the downshear flank of the circulation where southerlies induced by the potential vorticity anomaly ride up the isentropic surfaces (Figure 9.34b).

MCCs are maintained as long as they have a supply of moist, conditionally unstable inflow (often aided by the presence of a low-level jet), which is helped to its LFC by the aforementioned dynamics associated with the MCV. The lifting resulting from the interaction of MCVs and environmental wind shear occurs over a deep layer; not only does inflow glide up isentropic surfaces until it reaches its LFC, but the deep layer-lifting associated with the MCV reduces CIN and increases CAPE, thereby making the LFC more easily attainable and increasing the subsequent convective heating that is important for the maintenance of the MCV.²³ The lifting can also form MAULs. Dissipation of an MCC usually occurs when the MCC moves away from its source of conditionally unstable air or forced ascent is unable to continue to lift parcels to the LFC.

²³ See Davis and Trier (2007) and Trier and Davis (2007); these papers report recent MCV observations made during the Bow Echo and MCV Experiment (BAMEX).

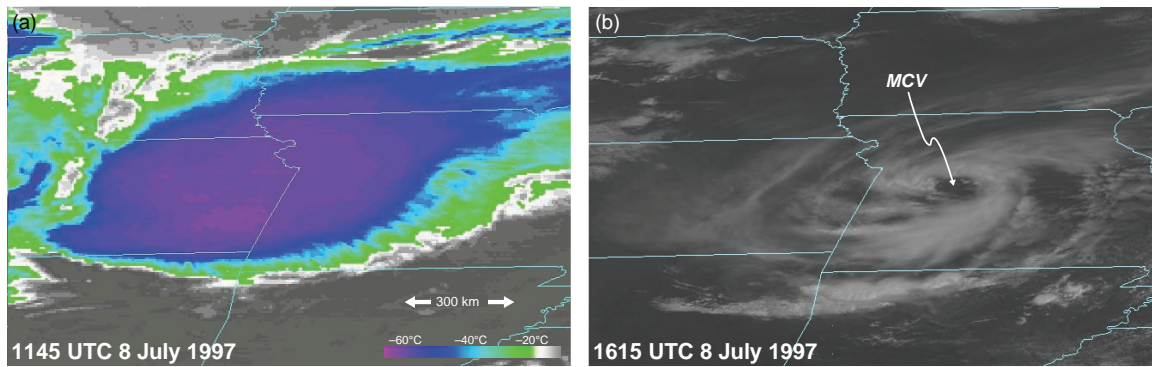


Figure 9.30 (a) Infrared satellite image of a weakening MCC at 1145 UTC 8 July 1997. (b) Visible satellite image of an MCV at 1615 UTC 8 July 1997. The circulation was produced by the MCC in (a).

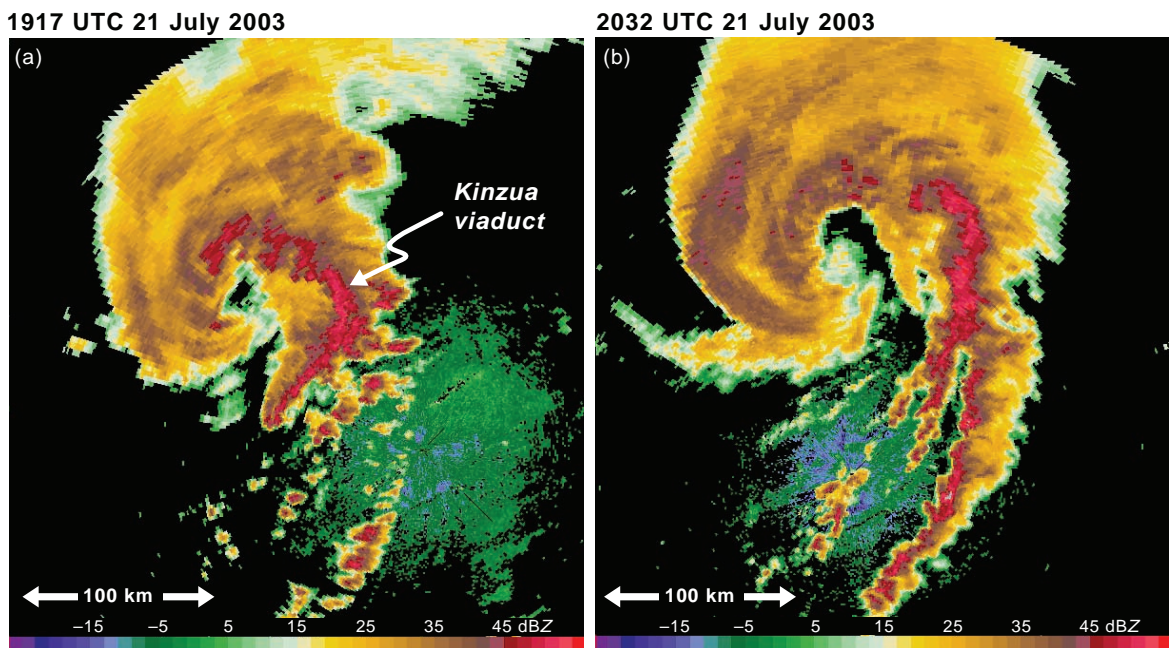


Figure 9.31 MCS on 21 July 2003 visible in the State College, PA, radar reflectivity imagery. The MCS was initiated by an MCV generated upstream on the previous day. The MCS subsequently intensified the MCV (the meso- α -scale cyclonic reflectivity pattern is obvious). A number of mesovortices and tornadoes were embedded within the line. A tornado destroyed the Kinzua Viaduct, built in 1882, which was the longest and tallest railroad bridge ever built at the time and was advertised as the 'Eighth Wonder of the World'.

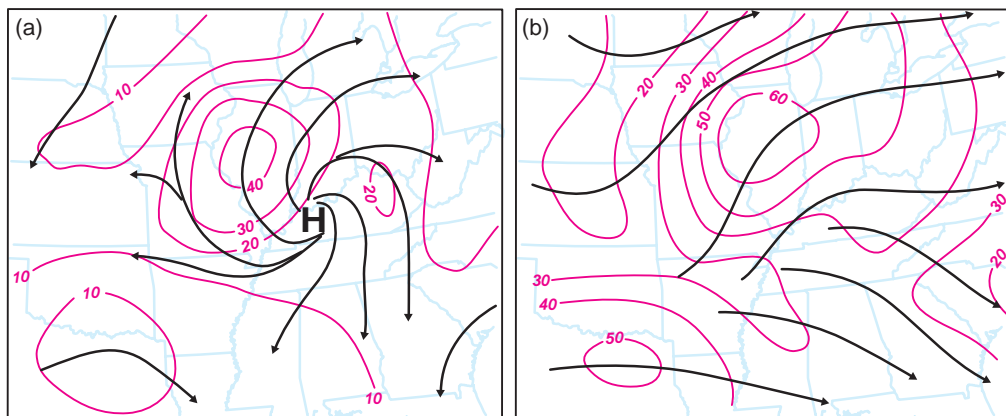


Figure 9.32 (a) Wind field ($m s^{-1}$) at 200 mb at 0600 UTC 25 April 1975, with the synoptic-scale basic flow subtracted, associated with a mesoscale convective complex. (b) The same as (a), but the total wind field is shown. (Adapted from Maddox *et al.* [1981].)

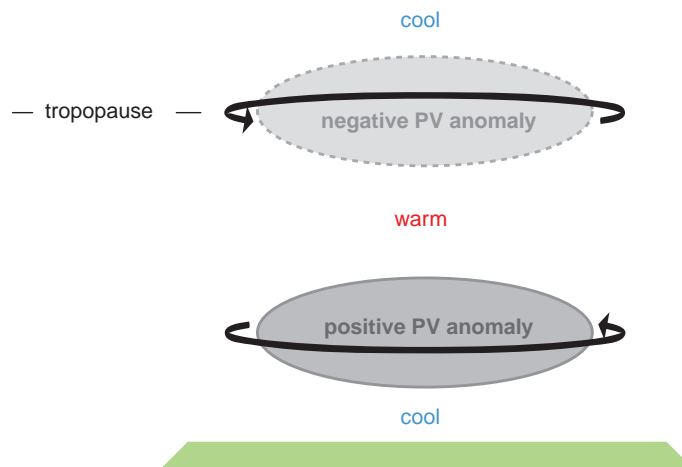


Figure 9.33 Structure of potential vorticity anomalies produced by a region of deep moist convection and the associated modifications of the temperature and wind fields. A cyclonic circulation develops around the lower tropospheric positive potential vorticity anomaly, and an anticyclonic circulation develops around the upper tropospheric negative potential vorticity anomaly, as indicated by the arrows. (Adapted from Raymond and Jiang [1990].)

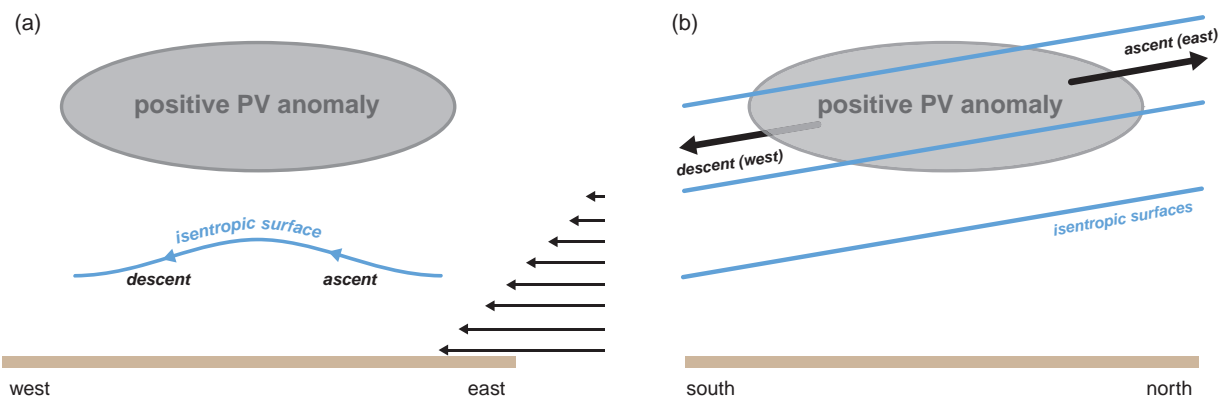


Figure 9.34 Illustrations of the mechanisms by which ascent can occur in the presence of a potential vorticity anomaly in shear. The environmental shear is westerly in the illustration and only shown below the positive potential vorticity anomaly for clarity. (a) In a frame of reference moving with the potential vorticity anomaly, the relative environmental wind causes flow on the perturbation isentropic surface caused by the potential vorticity anomaly, with ascent (descent) upwind (downwind) of the anomaly. (b) The potential vorticity anomaly, as viewed from the east. The tilted isentropic surfaces are associated with the environmental westerly wind shear indicated in (a). The cyclonic circulation around the potential vorticity anomaly causes ascent (descent) in the southerlies (northerlies) east (west) of the anomaly. (Adapted from Raymond and Jiang [1990].)

The above discussion of the role of potential vorticity anomalies and isentropic ascent in the maintenance of MCCs implies that localized gust front lifting (and therefore the presence of strong environmental low-level shear in order to counteract the circulation induced by a cold pool) is probably less crucial in the maintenance of MCCs than in other MCSs. MCCs usually form as elevated storms above a nocturnal boundary layer or stable air mass on the cold side of a synoptic-scale front—in which case the horizontal buoyancy gradients associated with the gust fronts tend to be suppressed—or their outflows undercut the surface-based initial storms and they become elevated over their own cold pools. In addition to the aforementioned MCV dynamics, lifting by gravity waves (bores, more precisely) can also be important in the maintenance of nocturnal MCSs in strongly stratified low-level environments.²⁴

MCVs can persist much longer than the buoyant convection itself, occasionally even several days.²⁵ MCVs can also be important for the initiation of new convection on subsequent days (Figures 9.30 and 9.31), usually on their downshear flanks as described above, and the new convection can perpetuate the MCV by way of latent heat release, which generates/maintains the cyclonic (anticyclonic) potential vorticity anomalies via pressure falls (rises) and convergence (divergence) below (above) the level of maximum heating. MCVs are most likely to survive beyond their parent MCC when the environmental vertical wind shear is weak, which is often the case in the synoptic-scale pattern that accompanies MCCs. Some maritime MCCs eventually develop into tropical cyclones, which may not be surprising given that the warm-core dynamical structure of an MCC resembles that of a tropical disturbance.

Further reading

Mesoscale convective systems and squall lines

- Bernardet, L. R., and W. R. Cotton, 1998: Multiscale evolution of a derecho-producing mesoscale convective system. *Mon. Wea. Rev.*, **126**, 2991–3015.
- Biggerstaff, M. I., and R. A. Houze, Jr., 1991: Kinematic and precipitation structure of the 10–11 June 1985 squall line. *Mon. Wea. Rev.*, **119**, 3035–3065.

²⁴ See Schmidt and Cotton (1990) and Parker (2008).

²⁵ Fritsch *et al.* (1994) documented an MCC that formed, underwent five convective redevelopments, tripled its detectable size, and survived for three days as it traveled from Colorado to Quebec.

- Biggerstaff, M. I., and R. A. Houze, Jr., 1993: Kinematic and microphysics of the transition zone of the 10–11 June 1985 squall line. *J. Atmos. Sci.*, **50**, 3091–3110.
- Bluestein, H. B., and M. H. Jain, 1985: Formation of mesoscale lines of precipitation: Severe squall lines in Oklahoma during spring. *J. Atmos. Sci.*, **42**, 1711–1732.
- Coniglio *et al.* (2004).
- Coniglio *et al.* (2006).
- Davis, C. A., and M. L. Weisman, 1994: Balanced dynamics of mesoscale vortices produced in simulated convective systems. *J. Atmos. Sci.*, **51**, 2005–2030.
- Evans and Doswell (2001).
- Fovell, R. G., and P. S. Dailey, 1995: The temporal behavior of numerically simulated multicell-type storms. Part I: Modes of behavior. *J. Atmos. Sci.*, **52**, 2073–2095.
- Fovell, R. G., and Y. Ogura, 1988: Numerical simulation of a midlatitude squall line in two dimensions. *J. Atmos. Sci.*, **45**, 3846–3879.
- Fovell, R. G., and P.-H. Tan, 1998: The temporal behavior of numerically simulated multicell-type storms. Part II: The convective cell life cycle and cell regeneration. *Mon. Wea. Rev.*, **126**, 551–577.
- Fritsch, J. M., and G. S. Forbes, 2001: Mesoscale convective systems. *Severe Local Storms, Meteor. Monogr.*, No. 50, 323–358.
- Fujita, T. T., 1955: Results of detailed synoptic studies of squall lines. *Tellus*, **4**, 405–436.
- Hane, C. E., 1986: Extratropical squall lines and rainbands. *Mesoscale Meteorology and Forecasting*, P. S. Ray, Ed., Amer. Meteor. Soc., 359–389.
- Houze, R. A., Jr., 2004: Mesoscale convective systems. *Rev. Geophys.*, **42**, RG4003.
- Houze, R. A., Jr., M. I. Biggerstaff, S. A. Rutledge, and B. F. Smull, 1989: Interpretation of Doppler weather radar displays of midlatitude mesoscale convective systems. *Bull. Amer. Meteor. Soc.*, **70**, 608–619.
- Hoxit *et al.* (1976).
- Knievel, J. C., and R. H. Johnson, 2002: The kinematics of a midlatitude, continental mesoscale convective system and its mesoscale vortex. *Mon. Wea. Rev.*, **130**, 1749–1770.
- Lafore, J., and M. W. Moncrieff, 1989: A numerical investigation of the organization and interaction of the convective and stratiform regions of tropical squall lines. *J. Atmos. Sci.*, **46**, 521–544.
- Parker and Johnson (2000).
- Parker, M. D., and R. H. Johnson, 2004a: Structures and dynamics of quasi-2D mesoscale convective systems. *J. Atmos. Sci.*, **61**, 545–567.
- Parker and Johnson (2004b).

- Parker and Johnson (2004c).
- Raymond, D. J., and H. Jiang, 1990: A theory for long-lived mesoscale convective systems. *J. Atmos. Sci.*, **47**, 3067–3077.
- Rotunno *et al.* (1988).
- Skamarock, W. C., M. L. Weisman, and J. B. Klemp, 1994: Three-dimensional evolution of simulated long-lived squall lines. *J. Atmos. Sci.*, **51**, 2563–2584.
- Smull, B. F., and R. A. Houze, Jr., 1985: A midlatitude squall line with a trailing region of stratiform rain: Radar and satellite observations. *Mon. Wea. Rev.*, **113**, 117–133.
- Smull and Houze (1987).
- Thorpe, A. J., M. J. Miller, and M. W. Moncrieff, 1982: Two-dimensional convection in non-constant shear: A model of mid-latitude squall lines. *Quart. J. Roy. Meteor. Soc.*, **108**, 739–762.
- Trapp, R. J., and M. L. Weisman, 2003: Low-level mesovortices within squall lines and bow echoes. Part II: Their genesis and implications. *Mon. Wea. Rev.*, **131**, 2804–2823.
- Trier, S. B., W. C. Skamarock, and M. A. LeMone, 1997: Structure and evolution of the 22 February 1993 TOGA COARE squall line: Organization mechanisms inferred from numerical simulation. *J. Atmos. Sci.*, **54**, 386–407.
- Weisman, M. L., J. B. Klemp, and R. Rotunno, 1988: Structure and evolution of numerically simulated squall lines. *J. Atmos. Sci.*, **45**, 1990–2013.
- Weisman and Rotunno (2004).
- Weisman, M. L., and R. J. Trapp, 2003: Low-level mesovortices within squall lines and bow echoes. Part I: Overview and dependence on environmental shear. *Mon. Wea. Rev.*, **131**, 2779–2803.
- Yang, M.-J., and R. A. Houze, Jr., 1995: Multicell squall-line structure as a manifestation of vertically trapped gravity waves. *Mon. Wea. Rev.*, **123**, 641–660.
- Yuter, S. E., and R. A. Houze, Jr., 1995a: Three-dimensional kinematic and microphysical evolution of Florida cumulonimbus. Part I: Spatial distribution of updrafts, downdrafts, and precipitation. *Mon. Wea. Rev.*, **123**, 1921–1940.
- Yuter, S. E., and R. A. Houze, Jr., 1995b: Three-dimensional kinematic and microphysical evolution of Florida cumulonimbus. Part II: Frequency distributions of vertical velocity, reflectivity, and differential reflectivity. *Mon. Wea. Rev.*, **123**, 1941–1963.
- Zipser, E. J., 1977: Mesoscale and convective-scale down-drafts as distinct components of squall-line structure. *Mon. Wea. Rev.*, **105**, 1568–1589.
- Bow echoes**
- Atkins, N. T., C. S. Bouchard, R. W. Przybylinski, R. J. Trapp, and G. Schmocker, 2005: Damaging surface wind mechanisms within the 10 June 2003 Saint Louis bow echo during BAMEX. *Mon. Wea. Rev.*, **133**, 2275–2296.
- Burke, P. C., and D. M. Schultz, 2004: A 4-yr climatology of cold-season bow echoes over the continental United States. *Wea. Forecasting*, **19**, 1061–1074.
- Johns, R. H., 1993: Meteorological conditions associated with bow echo development in convective storms. *Wea. Forecasting*, **8**, 294–299.
- Jorgensen, D. P., and B. F. Smull, 1993: Mesovortex circulations seen by airborne Doppler radar within a bow-echo mesoscale convective system. *Bull. Amer. Meteor. Soc.*, **74**, 2146–2157.
- Wakimoto, R. M., H. V. Murphrey, C. A. Davis, and N. T. Atkins, 2006: High winds generated by bow echoes. Part II: The relationship between the mesovortices and damaging straight-line winds. *Mon. Wea. Rev.*, **134**, 2813–2829.
- Weisman, M. L., 1992: The role of convectively generated rear-inflow jets in the evolution of long-lived mesoconvective systems. *J. Atmos. Sci.*, **49**, 1826–1847.
- Weisman, M. L., 1993: The genesis of severe, long-lived bow echoes. *J. Atmos. Sci.*, **50**, 645–670.
- Weisman, M. L., 2001: Bow echoes: A tribute to T. T. Fujita. *Bull. Amer. Meteor. Soc.*, **82**, 97–116.
- Weisman and Davis (1998).
- Mesoscale convective complexes and mesoscale convective vortices**
- Bartels, D. L., and R. A. Maddox, 1991: Midlevel cyclonic vortices generated by mesoscale convective systems. *Mon. Wea. Rev.*, **119**, 104–118.
- Davis and Trier (2007).
- Fritsch *et al.* (1994).
- Maddox, R. A., 1981: Satellite depiction of the life cycle of a mesoscale convective complex. *Mon. Wea. Rev.*, **109**, 1583–1586.
- Maddox, R. A., 1983: Large-scale meteorological conditions associated with midlatitude, mesoscale convective complexes. *Mon. Wea. Rev.*, **111**, 1475–1493.
- Maddox *et al.* (1986).
- Maddox *et al.* (1981).
- Menard, R. D., and J. M. Fritsch, 1989: A mesoscale convective complex-generated inertially stable warm core vortex. *Mon. Wea. Rev.*, **117**, 1237–1260.
- Trier and Davis (2007).

- Trier, S. B., C. A. Davis, and W. C. Skamarock, 2000: Long-lived mesoconvective vortices and their environment. Part II: Induced thermodynamic destabilization in idealized simulations. *Mon. Wea. Rev.*, **128**, 3396–3412.
- Trier, S. B., C. A. Davis, and J. D. Tuttle, 2000: Long-lived mesoconvective vortices and their environment. Part I: Observations from the central United States. *Mon. Wea. Rev.*, **128**, 3376–3395.
- Zhang, D.-L., and J. M. Fritsch, 1987: Numerical simulation of the meso- β scale structure and evolution of the 1977 Johnstown flood. Part II: Inertially stable warm-core vortex and the mesoscale convective complex. *J. Atmos. Sci.*, **44**, 2593–2612.

10

Hazards Associated with Deep Moist Convection

Simply taking the product of the CAPE and vertical wind shear magnitude yields a reasonably good first guess of the possibility of severe weather on any given day (Figure 10.1), assuming convection is able to develop. Severe weather is hereby defined using the terminology of the United States National Weather Service, that is, wind gusts exceeding 25 m s^{-1} (50 kt), hail diameter exceeding 19 mm (0.75 inches), or a tornado. Severe weather becomes more likely as the product of CAPE and shear increases. One might wonder why the product of CAPE and shear is more relevant than just the shear. After all, the vertical wind shear was the principal factor in controlling the organization of convective storms (e.g., single-cell versus multicell versus supercell storms). Although storm type influences the likelihood of severe weather occurrence, the maximum updraft speed is also an important factor in whether or not a convective storm will produce severe weather. Thus, although severe weather tends to be more widespread when large shear accompanies significant CAPE, less organized, single-cell storms with briefly intense updrafts also can produce severe weather (of the pulse variety) in high-CAPE, weak-shear environments.

In this chapter we explore the formation mechanisms and prediction of the hazards associated with DMC. Flash floods are included as well, even though they present additional challenges that go beyond simply using CAPE and shear to predict severe weather potential. In most parts of the world, the United States included, flash floods

present a greater threat to human life than lightning, damaging straight-line winds, hail, and tornadoes.¹ Finally, our discussion of convection-related hazards excludes lightning. Although we do not wish to downplay the dangers of lightning, the charging of cumulonimbus clouds is outside the scope of this book, as we consider it more of a precipitation microphysics topic than a mesoscale meteorology topic.²

10.1 Tornadoes

10.1.1 General characteristics

Tornadoes are violently rotating columns of air, usually associated with a swirling cloud of debris or dust near the ground and a funnel-shaped cloud extending downward from the base of the parent cumulonimbus updraft. Most tornadoes have winds of less than 50 m s^{-1} , although the strongest 1%, which is the fraction of tornadoes that is rated EF4 or EF5 (3-s wind gusts exceeding 75 m s^{-1}),

¹ According to the National Weather Service, the 30-year average (1977–2006) annual death toll from floods in the United States is 99 (most of these result from flash floods). This compares with a 30-year average of 61 deaths for lightning, 54 for tornadoes, and 21 for nontornadic straight-line winds and hail combined.

² Readers interested in cloud electrification are referred to the textbook written by MacGorman and Rust (1998).

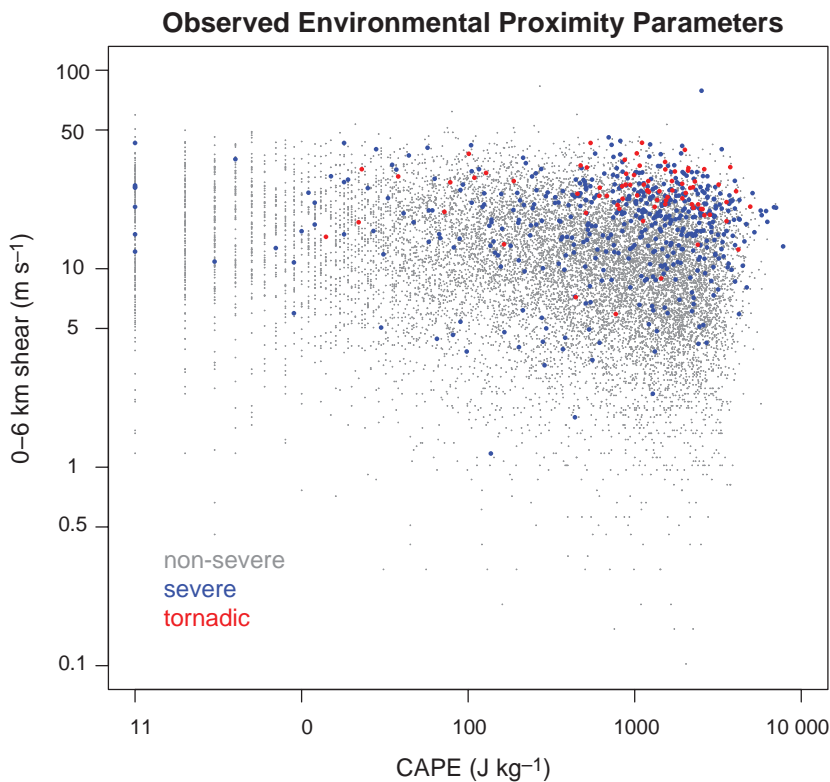


Figure 10.1 Relationship between severity of observed thunderstorms and the CAPE and vertical wind shear of the environments, as determined by proximity soundings. Red dots indicate tornado reports. Green dots indicate nontornadic damaging wind and/or large hail reports. Black dots indicate nonsevere thunderstorm reports. Courtesy of Harold Brooks, adapted from a figure originally appearing in Brooks *et al.* (2003).

account for a disproportionate fraction ($\sim 70\%$) of the fatalities.³ Vertical vorticity has magnitudes on the order

³ T. Fujita developed a wind speed scale (circa 1970) to assess tornado damage and estimate the maximum tornado intensity. Called the *F-scale*, it was designed to link the Beaufort wind scale with the Mach scale. A Beaufort force of 12 (minimal hurricane force winds) was equal to F1, and F12 was equal to Mach 1 (the speed of sound). The minimum wind speed (v_{\min} in mph) of any F-scale range (F) was $v_{\min} = 14.1(F + 2)^{\frac{3}{2}}$. In 2007, the *enhanced Fujita scale* (EF-scale) was adopted in the United States. It was designed to improve the accuracy of wind speed estimates derived from observed damage, in part, by attempting to account for the quality of construction. Tornadoes rated EF0–EF1, EF2–EF3, and EF4–EF5 are referred to as weak, strong, and violent tornadoes, respectively. Examples of damage from an EF0 (65–85 mph 3-s gusts) tornado include damage to chimneys, broken tree branches, and damage to sign boards. Examples of EF1 (86–110 mph 3-s gusts) tornado damage include destroyed garages or barns and peeled-off roofs. An EF2 (111–135 mph 3-s gusts) tornado, however, might tear roofs off frame houses, obliterate mobile homes, and snap or uproot large trees. EF3 (136–165 mph 3-s gusts) tornadoes destroy interior walls of well-constructed homes. EF4 (166–200 mph 3-s gusts) tornadoes are

of 1 s^{-1} , given typical tornado diameters on the order of 100 m. Vertical velocities also may be intense, especially just above the shallow inflow layer of the tornado (probably 5–50 m deep), with updrafts greater than 75 m s^{-1} possible. Radial inflow velocities typically range from $20\text{--}60 \text{ m s}^{-1}$. Most tornadoes persist less than 10 min, although some are known to have persisted for as long as an hour or more. Tornado diameter and longevity generally increase with intensity, although enough exceptions are observed that it

capable of completely leveling a well-built home. An EF5 ($>200 \text{ mph}$ 3-s gusts) tornado strips clean the foundation of a well-built structure and is capable of throwing automobiles over 100 m. Any estimation of tornado strength based on damage is error-prone for a number of reasons, including variations in the duration of extreme winds and debris loading within a tornado, not to mention the fact that many tornadoes do not strike man-made structures. Furthermore, EF-scale (and F-scale) ratings are based on the *maximum* damage observed. Even the most intense tornado that one might expect to be able to observe, an EF5, typically only contains EF5 winds within a region occupying less than 10% of the total path area.

is unwise to infer tornado intensity from size and longevity alone. Although tornadoes can be associated with any form of DMC, most significant tornadoes (EF2 and stronger) and practically all violent tornadoes (EF4 and EF5) are associated with supercell storms (supercells can and often do produce weak tornadoes as well).

Tornadoes are known to occur on every continent except Antarctica. The United States Great Plains region is the most favorable region for tornadoes, at least tornadoes spawned by supercells, which are the tornadoes having the greatest potential for casualties (Figure 10.2). This region is favorable owing to its proximity to the warm waters of the Gulf of Mexico to the south and the Rocky Mountains and high-altitude deserts to the west. The warm water to the south is a source of high- θ_e low-level air, and the heating of elevated terrain to the west produces large lapse rates that are subsequently advected eastward, overrunning the aforementioned high- θ_e air that is advected northward

from the Gulf of Mexico. The superpositioning of large midtropospheric lapse rates and high boundary layer θ_e gives rise to substantial CAPE. The vertical wind shear in the Great Plains region in spring is also regularly large and thus favorable for supercells and tornadoes, in part because there are no terrain barriers between the Gulf of Mexico and North Pole. The absence of terrain barriers means that fronts and their attendant baroclinity, which is associated with vertical wind shear via the thermal wind relation, make regular intrusions. The climatologically favorable wind shear in the Great Plains region is also probably related to the presence of elevated terrain to the west. Lee troughs and drylines routinely form in the western Great Plains region as a result of westerly midtropospheric winds blowing over the terrain (recall Section 5.2). These pressure troughs, as well as the more significant extratropical cyclones that they may spawn, are often accompanied by strong horizontal wind accelerations and therefore

Annual Mean Tornadic Environment Periods (1970–1999)

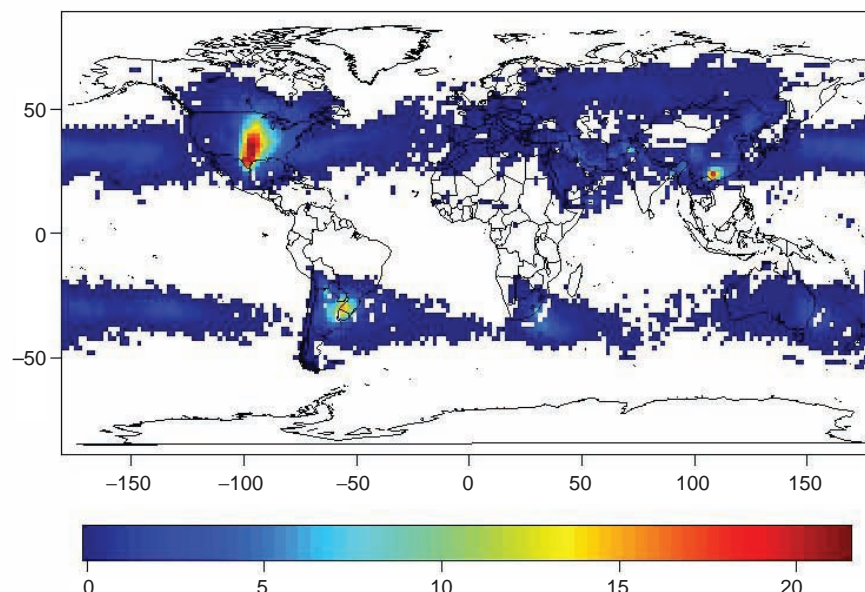


Figure 10.2 Average number of days per year having environments favorable for tornadic supercells were convection to form. Such conditions include the presence of strong shear over a deep tropospheric layer and CAPE (these are the conditions required for supercells), as well as strong low-level shear and high boundary layer relative humidity (these parameters, as will be discussed later in this section, are associated with an enhanced probability of tornadogenesis within supercells). The above synthetic climatology of tornadic supercell days, which is based on analyses obtained from the global reanalysis program, is shown instead of actual tornadic supercell or tornado reports because of the lack of reliable reports over the vast majority of the earth. (From Brooks *et al.* [2003].)

large ageostrophic winds and wind shear (wind shear that significantly exceeds the magnitude of the geostrophic wind shear attributable to the large-scale meridional temperature gradient; ageostrophic shear also contributes curvature to the hodograph).⁴ Other relative maxima in supercell and tornado frequency, albeit less anomalous than in the central United States, are found elsewhere in the world downstream of major mountain barriers and poleward of relatively warm bodies of water. Examples include southeastern China (north of the South China Sea and east of the Tibetan Plateau), Bangladesh (north of the Bay of Bengal and southeast of the Himalayas), southern Brazil (east of the Andes and northwest of the southern Atlantic Ocean), and parts of northern Italy, Slovenia, and Croatia (north of the Adriatic Sea and southeast of the Alps). There are also tornado hot spots around the world where supercells are not typically observed; for example, waterspouts are common in the Florida Keys and downwind of several Mediterranean islands.

Although the stretching of the earth's vorticity is small relative to the magnitude of the tilting and stretching of relative vorticity in tornado environments, the vast majority of tornadoes are cyclonic. The Coriolis force has an indirect role in this bias by way of supercell updraft dynamics. Cyclonic tornadoes are favored because right-moving (left-moving), cyclonically rotating supercell updrafts tend to be favored over left-moving (right-moving), anticyclonically rotating supercell updrafts in typical northern (southern) hemisphere supercell environments, owing to clockwise-turning (counterclockwise-turning) hodographs. Hodographs tend to turn clockwise (counterclockwise) with height in the northern (southern) hemisphere at low levels at least partly because of the influence of surface drag and the Coriolis force (the Ekman spiral, introduced in Section 4.1.4, is a curved hodograph that can be derived analytically when surface drag and rotation effects are considered).

10.1.2 Tornadogenesis

By definition, tornadogenesis requires that large vertical vorticity arises at the ground. If preexisting vertical

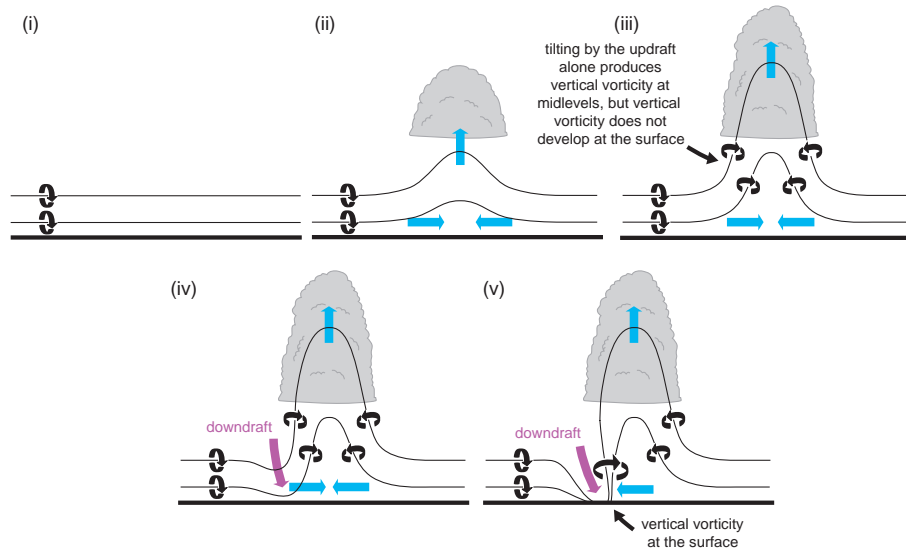
⁴ Banacos and Bluestein (2004) found that the geostrophic wind shear of hodographs, at least for idealized baroclinic waves, is generally straight; therefore, ageostrophic winds appear to be important in the development of hodographs with significant clockwise curvature, as are typically observed in supercell environments (e.g., Figure 8.15). Clearly much of the ageostrophy and hodograph curvature can be attributable to boundary layer drag, but other ageostrophic effects not related to friction, e.g., isalobaric contributions associated with migrating or deepening cyclones, likely also contribute to hodograph curvature in important ways.

vorticity is negligible near the ground, then vorticity stretching near the ground is initially negligible and vertical vorticity must first arise either from the tilting of horizontal vorticity or from advection toward the surface from aloft. Tilting by the horizontal vertical velocity gradients associated with an updraft alone is not effective at producing vertical vorticity near the surface because air is rising away from the surface as horizontal vorticity is tilted into the vertical. However, if a downdraft is involved in the tilting process, then vertical vorticity can be advected toward the surface as it is produced via tilting, where it can subsequently be stretched to form a tornado. For these reasons, it has been argued that a downdraft is needed for tornadogenesis when preexisting rotation is absent near the ground (Figure 10.3a). This argument depends on eddies being too weak to transport vertical vorticity downward against the flow. Furthermore, once a tornado is established, tilting of surface-layer horizontal vorticity by the extreme vertical velocity gradient associated with the tornado updraft itself probably contributes to the near-ground vertical vorticity in a significant way. However, such abrupt upward turning of streamlines, strong pressure gradients, and large vertical velocities are not present next to the ground prior to tornadogenesis; therefore, tilting by an updraft alone cannot be invoked to explain the amplification of near-ground vertical vorticity that results in tornadogenesis.

The aforementioned theoretical arguments for the importance of downdrafts in tornadogenesis have been verified in numerical simulations, and nearly countless observations exist of rear-flank downdrafts (RFDs), hook echoes, and *clear slots* in close proximity to tornadoes (Figure 10.4). Furthermore, trajectory analyses in a limited number of observed supercells as well as in numerical simulations indicate that at least some of the air entering the tornadoes (or, in the case of simulations, intense vortices that appear tornadolike) passes through the RFD prior to entering the tornado (Figure 10.5).

Analyses of vortex lines in the vicinity of low-level mesocyclones reveal that vortex lines form arches that join counter-rotating vortices (one of which is the cyclonic vortex associated with the tornado parent circulation) on opposite sides of the RFD (Figures 10.6 and 10.7), rather than vortex lines that are depressed downward as in Figure 10.3a, as would happen if a downdraft advects environmental vortex lines as material lines. The arching vortex line structures are also consistent with the notion of a downdraft playing a fundamental role in the generation of rotation near the ground. In fact, the arching vortex line structure bears a striking resemblance to the structure of the vortex lines that pass through the line-end vortices of bow echoes (Figure 9.27). In bow echoes

(a) vertical vorticity is initially negligible at the surface



(b) preexisting vertical vorticity at the surface

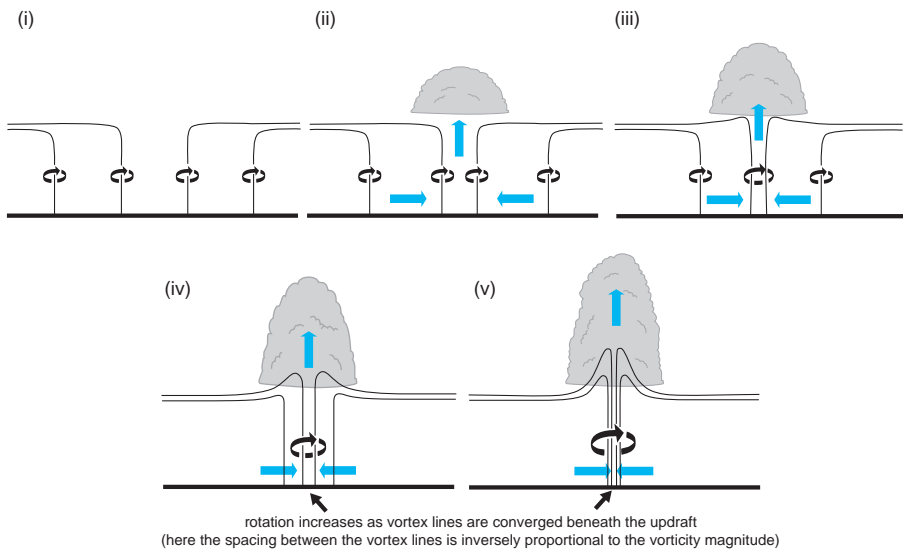


Figure 10.3 (a) Simple vortex line demonstration of why a downdraft is needed in order for significant vertical vorticity to develop at the ground beneath a thunderstorm in the absence of preexisting vertical vorticity at the surface. There is assumed to be no baroclinic vorticity generation; thus, the vortex lines are assumed to be frozen in the fluid. This is obviously an oversimplification, for there must be baroclinity at least somewhere or else a buoyant updraft could not exist in the first place (rainy downdrafts and their associated baroclinity, even if it is just a result of hydrometeor loading, are also a virtual certainty at least somewhere in the vicinity of a thunderstorm updraft). Nonetheless, the basic conclusion reached from considering only a purely barotropic redistribution is not changed: if tilting of vortex lines is accomplished by only an updraft, significant vertical vorticity cannot arise at the ground because air is rising away from the ground as it is tilted. On the other hand, if a downdraft is involved, a positive contribution to the vertical vorticity tendency can arise from tilting even as air is sinking toward the ground. (b) Simple vortex line demonstration of how a tornado can arise from convergence alone, in the absence of a downdraft, when preexisting vertical vorticity is present at the ground.

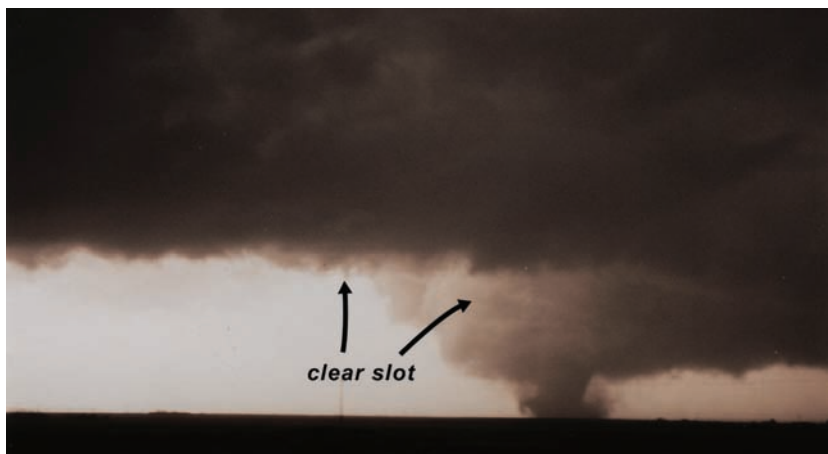


Figure 10.4 A clear slot like that shown above near the Dimmitt, TX, tornado on 2 June 1995 is a visual manifestation of sinking air, probably in what ought to be regarded as an *occlusion downdraft* (defined in Section 8.4 as a local, dynamically driven intensification of sinking motion within the larger-scale RFD). Photograph by Paul Markowski.

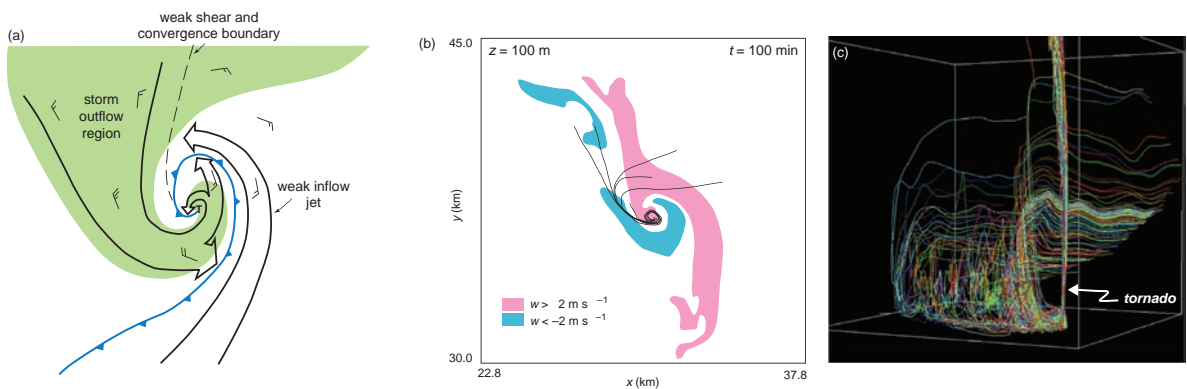


Figure 10.5 Observations and numerical simulations indicate that the air that enters tornadoes, tornado parent circulations, or nontornadic, near-ground circulations in supercells typically enters the circulations from the outflow air mass, rather than directly from the inflow. Such findings are consistent with the notion of downdrafts being important in the generation of rotation near the ground in supercells. (a) Trajectories in the RFD region composited from dual-Doppler observations of supercell thunderstorms (adapted from Brandes [1978]); (b) backward trajectories computed from the near-ground vertical vorticity maximum in a supercell simulation (adapted from Wicker and Wilhelmson [1995]); (c) a three-dimensional perspective from the southeast of trajectories entering a tornado that developed within a supercell simulation (from Xue [2004]; courtesy of Ming Xue).

(Section 9.4), baroclinically generated vortex lines within the outflow are lifted out of the outflow along the outflow's leading edge, leading to the counter-rotating, line-end vortices. It is tempting to wonder whether similar dynamics are at work in the RFD region of supercell thunderstorms—that is, a baroclinic process (Figure 10.8) rather than simply a redistribution of environmental

vorticity (Figure 10.3a)—as is suggested by the vortex line configuration evident in Figure 10.6.

When there is preexisting rotation at the surface, a downdraft such as the RFD is not needed for tornadogenesis (Figure 10.3b). In these cases, near-ground convergence alone can amplify vertical vorticity to tornado intensity. It seems as though nonmesocyclonic tornadoes and perhaps

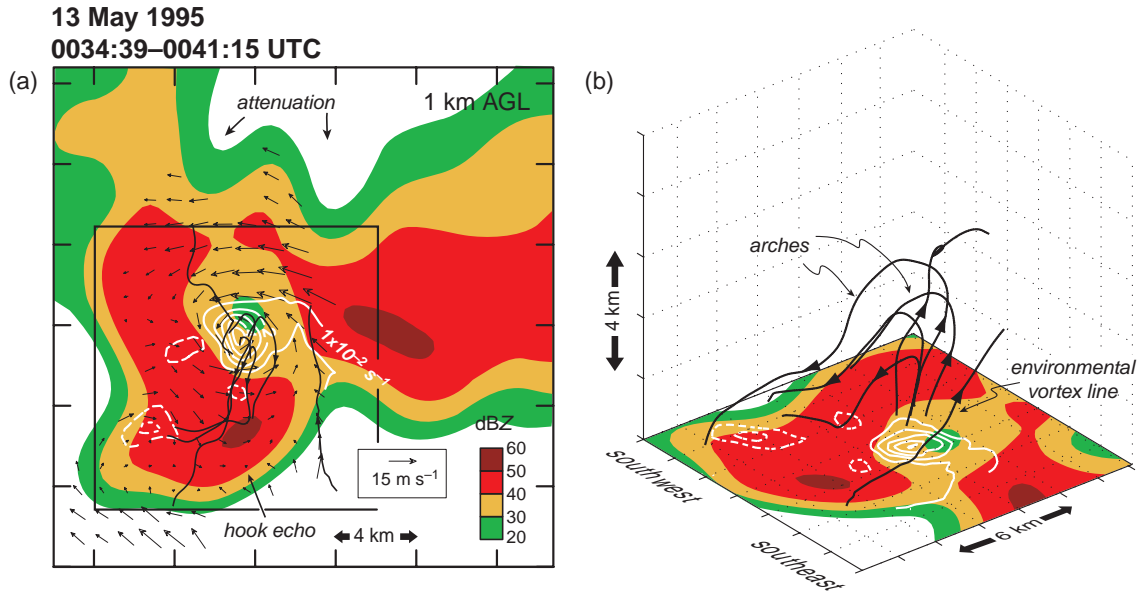


Figure 10.6 (a) Radar reflectivity factor (dBZ; shaded) at 1.0 km AGL at 0034:39–0041:15 UTC 13 May 1995. Dual-Doppler-derived, storm-relative wind vectors and vertical vorticity (white) contours (10^{-2} s^{-1} contour interval; the zero contour is suppressed and negative contours are dashed) at the same altitude are also overlaid, as are projections of select vortex lines (bold solid lines) onto the ground. The direction of the vorticity vector is indicated by the arrowheads. Five of the vortex lines pass through points centered on and surrounding the vertical vorticity maximum at 1.0 km. A sixth vortex line originates in the environment ahead of the gust front. The region enclosed by the square is shown in (b). (b) A three-dimensional perspective of the vortex lines emanating from the low-level mesocyclone center. For purposes of clarity, the reflectivity and vertical vorticity fields at 1.0 km AGL are displayed at the bottom of the three-dimensional domain. (Adapted from Markowski *et al.* [2008].)

most other geophysical vortices commonly arise in this manner. Nonmesocyclonic tornadoes are treated next.

10.1.3 Nonmesocyclonic tornadoes

Some vortices satisfy the definition of a tornado, in that they are connected to a deep convective cloud base and are capable of damage at the surface, yet these vortices do not form by way of processes unique to supercells, such as those described earlier that likely involve the reorientation and generation of vorticity within a downdraft in close proximity to the storm's main updraft. These *nonmesocyclonic tornadoes* do not require the presence of a downdraft and usually arise from the intensification of small-scale vortices at the surface, sometimes called *misocyclones*, that preexist the overlying convection (misocyclones were introduced in Section 7.2, as they can also influence convection initiation). Nonmesocyclonic tornadoes are often referred to as *nonsupercell tornadoes*, but we prefer the former terminology because supercells can produce

tornadoes by mechanisms similar to those of nonsupercells, as well as tornadoes in close association with the mesocyclone.

Nonmesocyclonic tornadoes most commonly develop along air mass boundaries with large wind shifts and therefore locally large horizontal wind shear and vertical vorticity. Such corridors of anomalously large vertical vorticity tend to break down into discrete patches of vorticity as a result of horizontal shear instability (Figure 10.9; also refer to Section 3.5). The transformation of a corridor of relatively large vorticity found along a wind-shift line into patches of large vorticity is associated with the formation of vortices. If DMC subsequently develops or passes over one of these vortices, vorticity stretching can amplify the vortex to tornado strength (Figure 10.3b).

Nonmesocyclonic tornadoes commonly referred to as *landspouts* and *waterspouts*, depending on whether they develop over land or water, form beneath growing cumulus congestus clouds, most commonly in environments characterized by weak vertical wind shear (Figure 10.10).

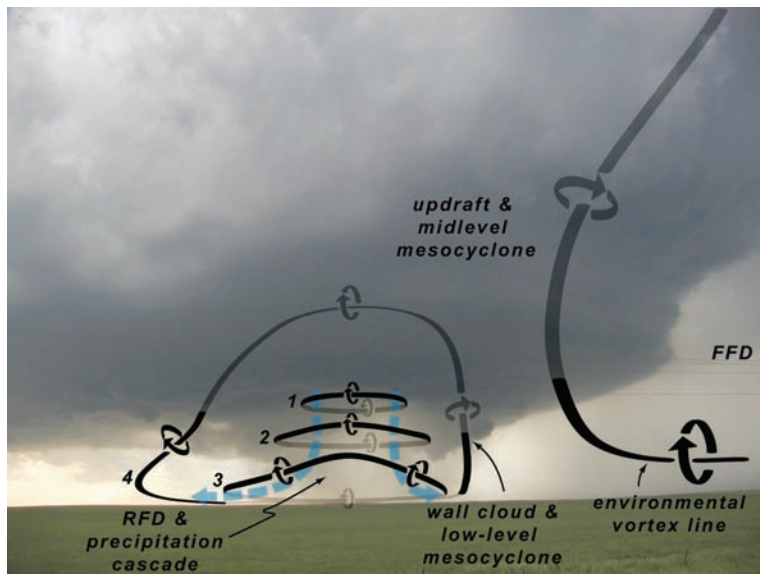


Figure 10.7 Idealized evolution of vortex rings and arches inferred from the sample of supercells analyzed by Markowski *et al.* [2008], superimposed on a photograph of a supercell thunderstorm (courtesy of Jim Marquis; the view is from the south). The numerals 1–4 can indicate either a single vortex line seen at four different times in a sequence, or four different vortex lines at a single time but in different stages of evolution. An environmental vortex line is also shown.

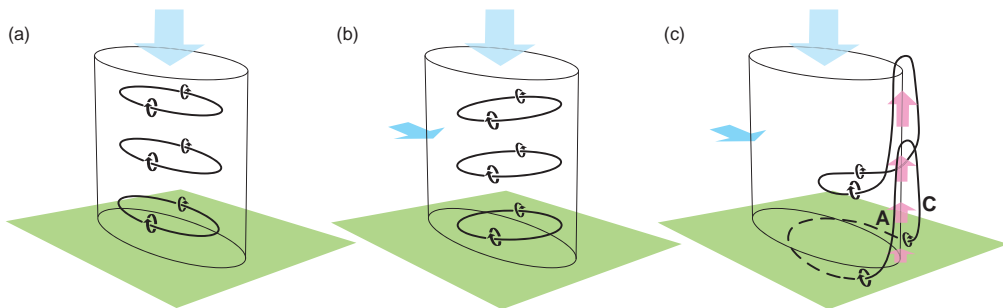


Figure 10.8 One possible way in which vertical vorticity can be produced at the surface by a purely baroclinic process in an environment containing no preexisting vertical vorticity at the surface (actually, in this idealization there is no preexisting vorticity—neither horizontal nor vertical—anywhere; the final vorticity field is solely a result of baroclinic vorticity generation and subsequent rearrangement of the baroclinically-generated vortex lines). (a) Baroclinically generated vortex rings encircle a buoyancy minimum that extends throughout a vertical column (such a region of negative buoyancy might be found in the hook echo/RFD region of a supercell, for example); the presence of negative buoyancy causes the vortex rings to sink toward the ground as they are generated. (b) If the vortex rings are swept forward as they descend toward the ground owing to the additional presence of rear-to-front flow through the buoyancy minimum, the vortex rings become tilted upward on their downstream sides (a vertical velocity gradient is present within the column because buoyancy is a minimum in the center of the column and increases with increasing distance from the center of the column). (c) If the leading edge of the vortex rings can be lifted by an updraft in close proximity to the buoyancy minimum (an updraft is typically found in close proximity to the hook echo/RFD region of a supercell, for example), then the vortex rings can be tilted further and stretched upward, leading to arching vortex lines and a couplet of cyclonic ('C') and anticyclonic ('A') vertical vorticity that straddles the buoyancy minimum and associated downdraft. (Adapted from Straka *et al.* [2007]).

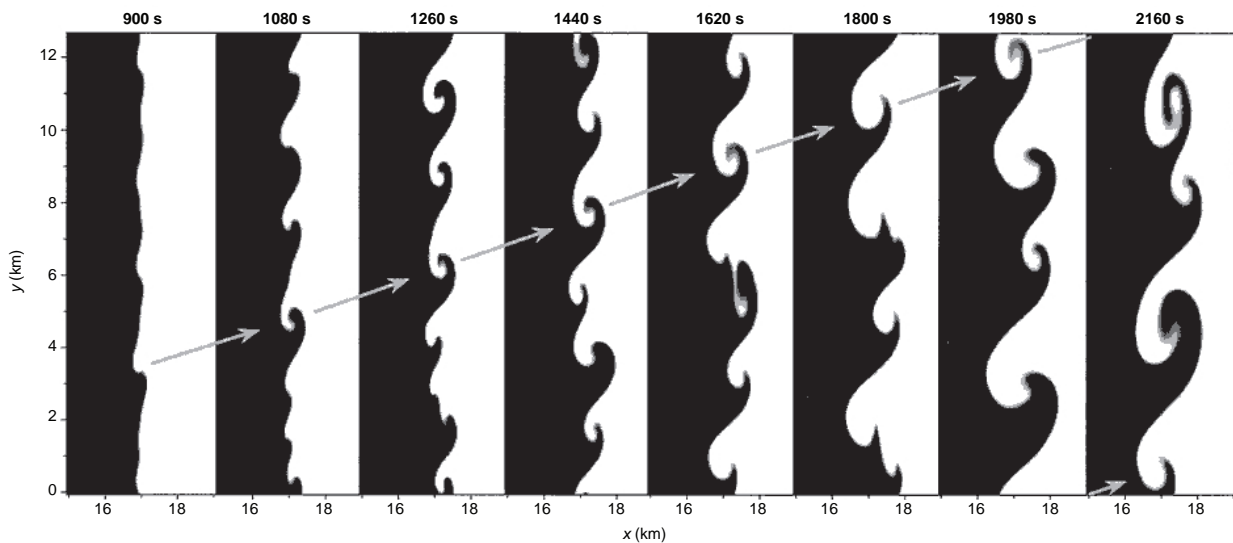


Figure 10.9 Horizontal cross-section through the leading edge of a simulated outflow boundary at $z = 0.55$ km showing the development of misocyclone circulations as a result of horizontal shear instability. The abrupt shading change denotes the approximate -3 K perturbation potential temperature. (From Lee and Wilhelmson [1997a].)



Figure 10.10 Landspouts near Lazbuddie, TX, on 4 June 1995. Photograph by Peter Blottman.

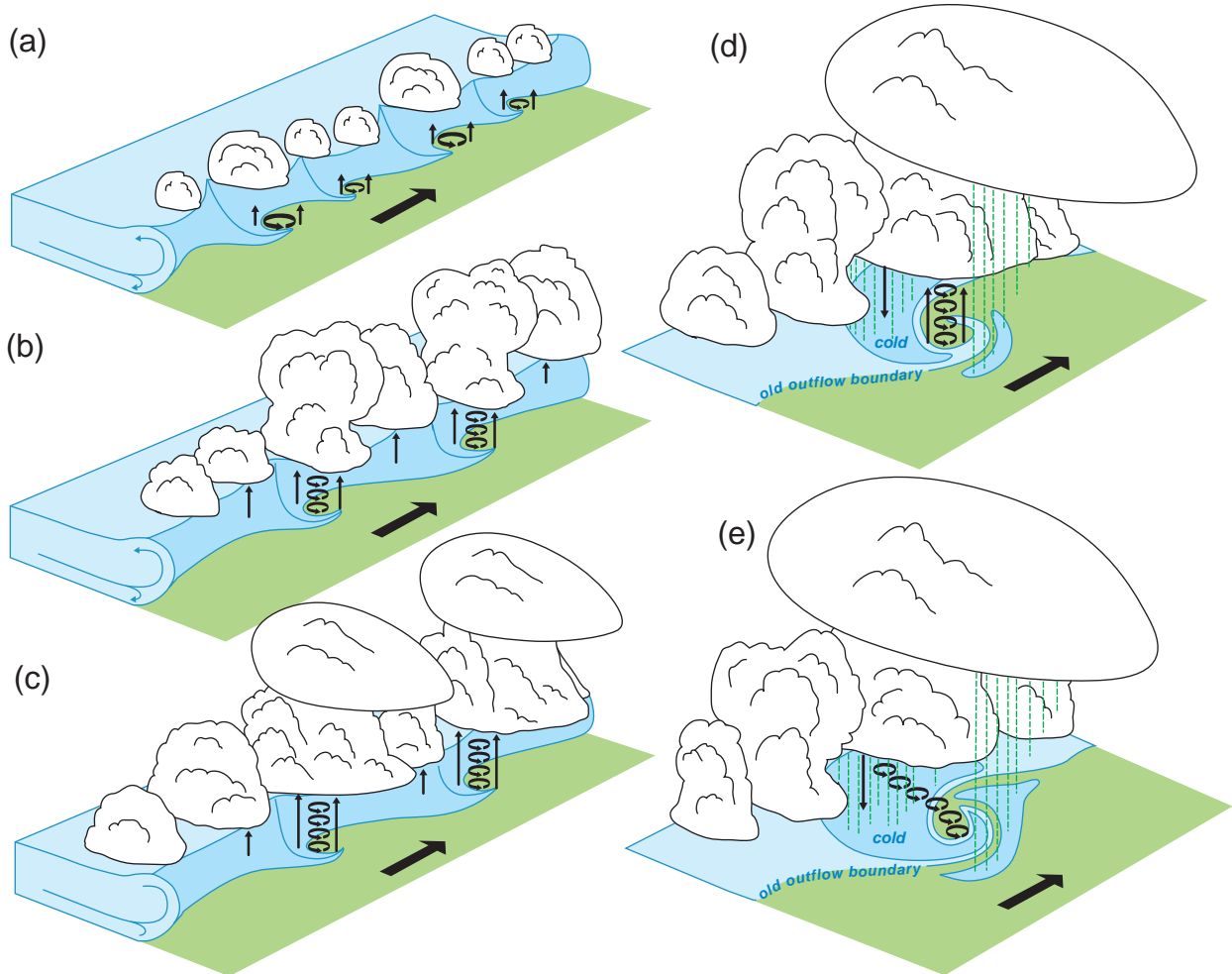


Figure 10.11 Schematic presentation of the lifecycle stages of landspouts. The viewing perspective is from an elevated position looking northwest. See the text for details. The bold arrow indicates the ambient wind direction ahead of the air mass boundary. The diagrams for stages iv and v focus on just one member of the landspout family. (Adapted from Lee and Wilhelmson [1997b].)

The genesis of landspouts and waterspouts often accompanies the convection initiation process itself. The weak shear probably maximizes the duration that the overlying updrafts can remain over the misocyclones and intensify them via stretching. The preexisting vertical vorticity source for waterspouts may be land breezes that are located a few miles offshore during late morning, when waterspouts are most common. The preexisting vertical vorticity source for landspouts is often an outflow boundary, colliding boundaries, or a mesoscale eddy, such as the *Denver convergence and vorticity zone* (DCVZ), where probably more landspouts develop than anywhere else in the United

States.⁵ Landspouts are also occasionally observed beneath the flanking lines of supercells.

The lifecycle of a typical landspout is depicted in Figure 10.11 (this is also applicable to a waterspout).⁶ In the vortex development stage (i), a corridor of relatively large vertical vorticity is present along a mesoscale

⁵ The DCVZ develops in conjunction with the *Denver cyclone*, a mesoscale eddy that can form downwind of the Palmer Divide, located in central Colorado, on days with southeasterly low-level winds. This and other mesoscale lee vortices are discussed in Section 13.3.

⁶ The discussion of the lifecycle is based on the work of Lee and Wilhelmson (1997a, b).

boundary. The corridor of large vertical vorticity is transformed into a series of regularly spaced vortices along the mesoscale boundary by horizontal shear instability; the release of the instability is triggered by wind perturbations along the mesoscale boundary that can be the result of lobe and cleft instability (Section 5.3.2), horizontal convective roll intersections with the mesoscale boundary, natural variations in surface roughness, or naturally occurring temperature variations within either air mass. In the misocyclone interaction and merger stage (ii), the vertical vorticity along the mesoscale boundary is concentrated by preferential vorticity advection induced by the horizontal shear instability. Interactions among vortices (e.g., vortices of similar strength rotate around each other and often coalesce, and sometimes a stronger vortex extrudes the vorticity from its weaker neighbor[s]) increase the spacing between misocyclones, as well as the circulation of the misocyclones which may then be subjected to strong vorticity stretching (in two-dimensional theory, when two misocyclones merge, the circulation of the resultant misocyclone represents the sum of the circulations of each misocyclone prior to the merger). The larger misocyclones may produce an asymmetric pattern of forcing for deep convection along the mesoscale boundary, as discussed in Section 7.2.

As the young storms rapidly develop, vertical vorticity is redistributed from the boundary layer to the storm midlevels through vertical advection. The early mature stage of the formation of the landspouts (iii) occurs as low-level stretching intensifies the misocyclone circulations to tornado intensity. Concurrently, deep convection occurring above the circulations further supports tornado intensification by inducing subcloud convergence and vortex stretching throughout the depth of the boundary layer. Multiple landspouts are often observed simultaneously (Figure 10.10), and with somewhat regular spacing, which is hardly surprising given that the progenitor misocyclones are often regularly spaced along air mass boundaries. The most intense phase, the late mature stage of a landspout (iv), occurs at the same time that precipitation-induced cold pools develop. Cold air surrounds the tornado, increasing the low-level convergence and significantly increasing vortex stretching on the periphery of the tornado. Eventually downdrafts and negatively buoyant air surround the landspout, bringing about its dissipation (v). The tornado may become sharply tilted if its lower portion is advected by an advancing gust front.

Nonmesocyclonic tornadoes can also form within squall lines, although occasionally a supercell merges with a squall line and subsequently produces tornadoes within the squall line that are associated with the mesocyclone of

the embedded supercell. Nonmesocyclonic tornadoes that form within squall lines are usually associated with meso- γ -scale vortices embedded within the lines, which are sometimes generically referred to as *mesovortices*. (Damaging straight-line winds within squall lines also tend to be associated with mesovortices, as we shall discuss in Section 10.2.) Only in rare cases do strong (EF2 or EF3) tornadoes occur within squall lines, and violent (EF4 or EF5) tornadoes are even less common.⁷ The rare cases when strong or violent tornadoes occur usually involve a supercell becoming entrained into the squall line. Such tornadoes should probably not be regarded as nonmesocyclonic, however.

Although the details of tornadogenesis within squall lines are not well understood (less well understood than tornadogenesis in supercells), it is possible that downdrafts within squall lines could play a similar role in tornadogenesis as the downdrafts in supercells, whatever the details of that role might be. In an environment lacking preexisting vertical vorticity at the surface, a downdraft is required for tornadogenesis, regardless of whether or not the parent convection is a supercell or a larger-scale convective system.

Gustnadoes are relatively shallow and transient vortices that occur along thunderstorm gust fronts (Figure 10.12). They are rarely responsible for significant damage. Gustnadoes presumably arise from the same shear instability mechanism that gives rise to landspouts and waterspouts, but it is likely that gustnadoes do not attain the same intensities as the former vortices because the gust fronts along which gustnadoes develop tend to race ahead of the overlying deep updrafts, thereby limiting the vorticity stretching that can occur. In contrast to landspouts and waterspouts, gustnadoes are rarely, if ever, connected to an overlying cloud base. The American Meteorological Society's *Glossary of Meteorology* defines a tornado as a 'violently rotating column of air, in contact with the ground, either pendant from a cumuliform cloud or underneath a cumuliform cloud'. Although a gustnado fits this definition, gustnadoes are typically excluded from tornado logs because they are a nearly ubiquitous aspect of thunderstorms, at least storms having strong outflow.⁸ It does not seem to matter whether the gust front is produced by single-cell, multicell, or supercell convection, or convective systems. Gustnado sightings are most common in dry, dusty locations owing to the fact that gustnadoes are not typically strong enough to loft heavy debris.

⁷ An unfortunate exception was the F4 bow echo tornado that struck West Bend, WI, on 4 April 1981.

⁸ In our view, the *Glossary's* definition of a tornado should be narrowed to exclude vortices that are not connected to the base of a deep convective cloud.



Figure 10.12 Photograph of a gustnado. Photograph taken by Chuck Doswell.

10.1.4 Forecasting and nowcasting tornadoes

Most strong (EF2–EF3) and virtually all violent (EF4–EF5) tornadoes are associated with supercells. Although supercells might be regarded as being relatively easy to anticipate, predicting which supercells will spawn tornadoes is one of the most challenging tasks facing forecasters and researchers alike. Even *detecting* tornadic supercells is not an easy task. Except in rare circumstances, radars only detect tornado parent circulations (i.e., mesocyclones)—they cannot resolve tornadoes themselves. Perhaps surprisingly, tornadoes are relatively infrequent even within supercells; only about a quarter of all radar-detected mesocyclones are associated with tornadoes, using fairly stringent mesocyclone detection criteria⁹ (some studies using more liberal mesocyclone detection criteria have found that as few as 5–10% of mesocyclones are associated with tornadoes). Moreover, the strongest midlevel mesocyclones are not necessarily the ones associated with tornadoes. Tornadoes occur over a broad range of midlevel mesocyclone intensities, with some of the most intense mesocyclones ever documented being observed in nontornadic supercells.¹⁰

One of the most fruitful strategies undertaken in the United States for improving tornado warnings has been

to combine real-time radar data with observations of the near-storm environment. Two parameters seem to offer the most promise in discriminating between nontornadic and tornadic supercells: (1) boundary layer relative humidity and (2) low-level vertical wind shear. Boundary layers with large relative humidity and low-level vertical shear (relative to the average supercell environment) are most favorable for tornadic supercells (Figure 10.13). There is growing evidence that strong cold pools and excessive negative buoyancy are detrimental to tornadogenesis (Figure 10.14), and these findings are consistent with supercell proximity sounding climatologies showing that tornadic supercells are favored in environments having a low cloud base (environments with a low cloud base, i.e., large boundary layer relative humidity, can limit the production of exceptionally cold outflow).

Occasionally boundary layer relative humidity and low-level wind shear are favorable for tornadic supercells on the meso- α scale. These are the days on which outbreaks of supercells and tornadoes are most likely to be observed. More commonly, tornadoes seem to occur as ‘mesoscale accidents’, that is, there seems to be a strong random element to tornado formation within supercells. Some of the apparent randomness is probably due to localized, meso- β -scale enhancements of boundary layer

⁹ See Trapp *et al.* (2005).

¹⁰ The mesocyclone of a nontornadic supercell documented by Wakimoto *et al.* (2004a) near Superior, NE, was extraordinarily large and

intense. It had a diameter of 9 km and a 118 m s⁻¹ radial velocity differential, and is believed to be the strongest mesocyclone ever documented.

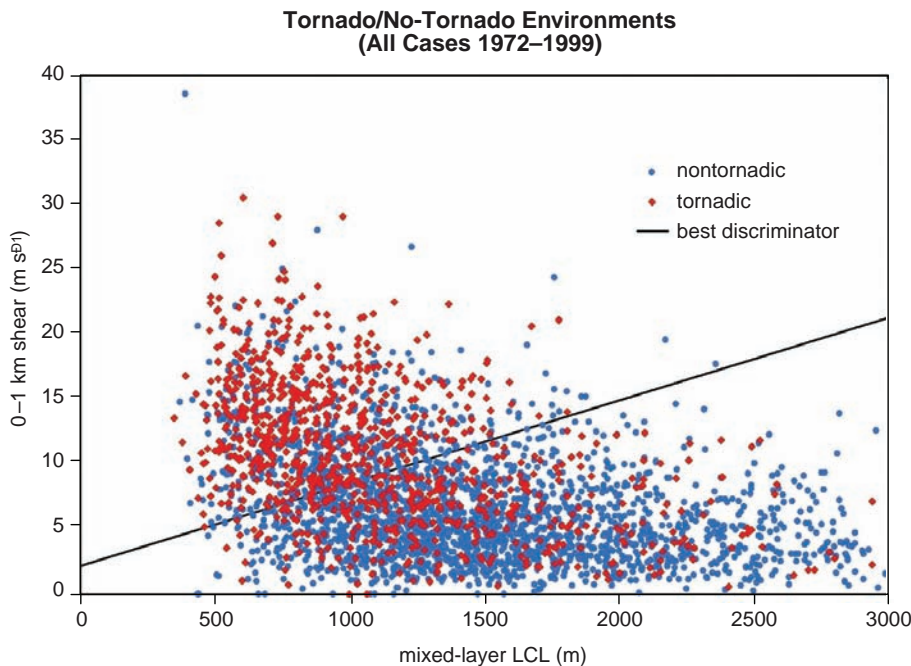
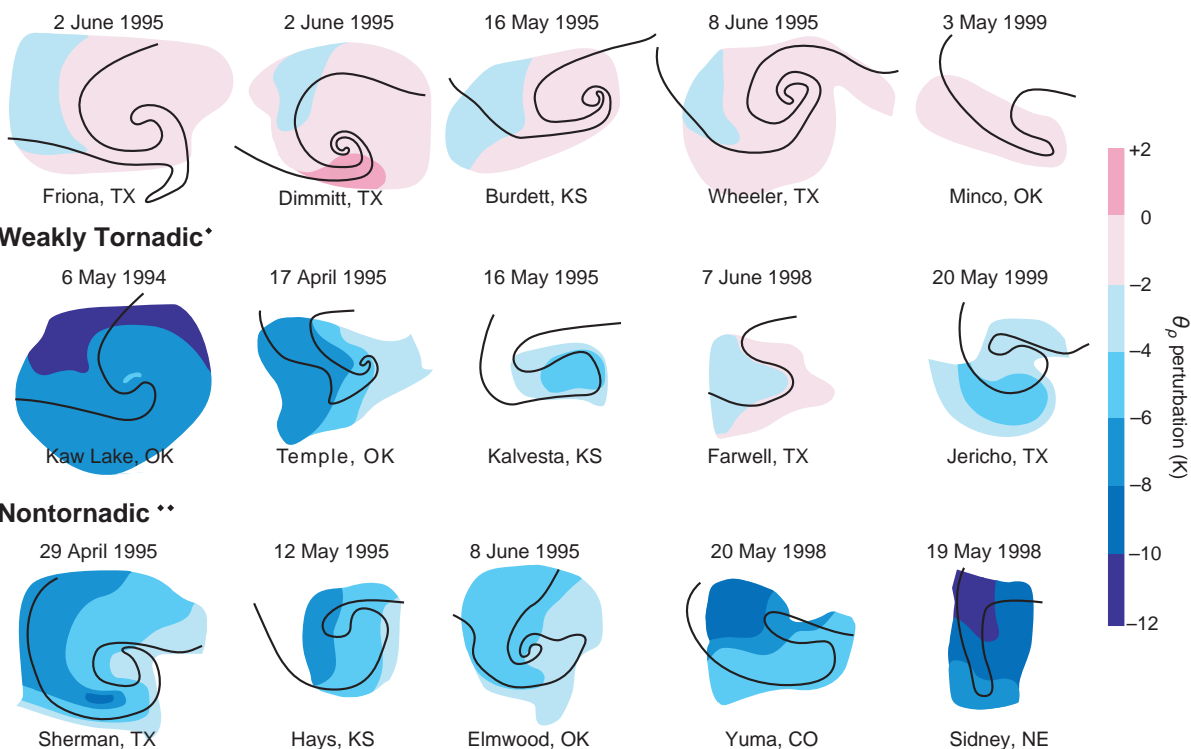


Figure 10.13 Observations of tornadic versus nontornadic supercells as a function of low-level shear and mean boundary layer relative humidity of the environment (what is actually displayed on the axes is the magnitude of the 0–1 km vertical wind shear vector and the LCL computed by lifting an air parcel having the mean potential temperature and water vapor mixing ratio of the lowest 100 mb). Tornadoes are favored in environments containing large low-level relative humidity and low-level wind shear. Although this combination of environmental parameters has been found to be the most promising to date, much overlap still exists between the tornadic and nontornadic occurrences (the overlap is somewhat reduced if weak tornadoes are filtered). Courtesy of Harold Brooks, based on a figure originally appearing in Craven and Brooks (2004).

relative humidity and/or low-level wind shear that may or may not be detectable by the observation network (Figure 10.15). When such enhancements in the environment are detectable, they are often associated with air mass boundaries like outflow boundaries, warm fronts, inland sea breezes, etc., and may be visible in satellite imagery as lines of cumulus clouds or in radar data as fine-lines. The horizontal density gradients that tend to be associated with such boundaries generate horizontal vorticity baroclinically [via (2.96)], which can augment the larger-scale environmental wind shear. Mean boundary layer relative humidity is also occasionally enhanced along mesoscale boundaries owing to the convergence and attendant deepening of the moist layer there. One nowcasting challenge, however, is that not all storm-boundary interactions are favorable. Many result in rapid storm weakening. Whether or not a storm-boundary interaction is likely to result in storm intensification versus weakening likely depends on the characteristics of the ‘new’ air mass that a storm finds itself in; for example, a storm that crosses a boundary into

air that possesses little or no CAPE and large CIN will almost certainly weaken, regardless of the degree to which the vertical shear might be enhanced there.

Despite the above understanding, there is no shortage of case examples in which supercells fail to produce tornadoes in seemingly very favorable tornado environments, and others in which a supercell is a prolific tornado producer in a seemingly marginal tornado environment. The differences from one storm to the next clearly must originate from at least slight differences in the storm environments. Our ability to observe storms and their environments will always have limits. Nonetheless, we know that the environments of deep, moist convection have considerable kinematic and thermodynamic variability, even down to the scale of boundary layer thermals (recall Figure 7.17). We do not yet know what effect, if any, such small-scale variability has on storms. When mesoscale accidents (or conversely, mesoscale ‘failures’) lead to (or prevent) tornadoes, it is sometimes tempting to wonder what nonlinear impact small-scale environmental variability might have had.

Significantly Tornadic*

*Sampled within 5 min of tornadogenesis

**Sampled within 5 min of strongest rotation on lowest tilt of nearest WSR-88D

Figure 10.14 Surface density potential temperature perturbations measured by mobile mesonets (instrumented automobiles) within the hook-echo and RFD regions of supercells. The black contours outline the 40 dBZ radar echoes of the storms in order to emphasize the hook echoes. Regions left unshaded represent regions that were not sampled by the mobile mesonets. Supercells that spawned significant tornadoes were associated with warmer RFD outflow, on average, compared with nontornadic or weakly tornadic supercells. (Adapted from Markowski *et al.* [2002] and Markowski and Richardson [2009].)

It seems as though tornadic supercells might benefit from large low-level horizontal vorticity that is not accompanied by large negative buoyancy; strong cold pools have a tendency to either undercut updrafts and/or suppress vorticity stretching beneath the updraft. When the environmental horizontal vorticity is relatively marginal, then perhaps tornadogenesis requires significant enhancement of the environmental horizontal vorticity. Such enhancement is unlikely without strong storm-induced baroclinity (which is suppressed by large environmental low-level relative humidity), but strong baroclinity tends to be accompanied by strong cold pools.

Although forecasting tornadoes within supercells is challenging, forecasting nonmesocyclonic tornadoes is even more difficult, in large part because nonsupercellular

convection is much more common than supercellular convection (a much smaller fraction of nonsupercells produces tornadoes compared with supercells). Many nonmesocyclonic tornadoes are associated with growing cumulus towers that do not even exhibit a low-level radar echo. As discussed in Section 10.1.3, a wind-shift line is typically present beneath the overlying convective cloud, but there is no clear way to identify which wind-shift lines and cumulus congestus will be associated with nonmesocyclonic tornadogenesis. Regarding nonmesocyclonic tornadoes occurring in squall lines, there is some indication that CAPE and shear tend to be larger in the environments of tornado-producing squall lines than in nontornadic squall lines (Figure 10.16). This is not entirely surprising, given that bow echoes and LEWPs

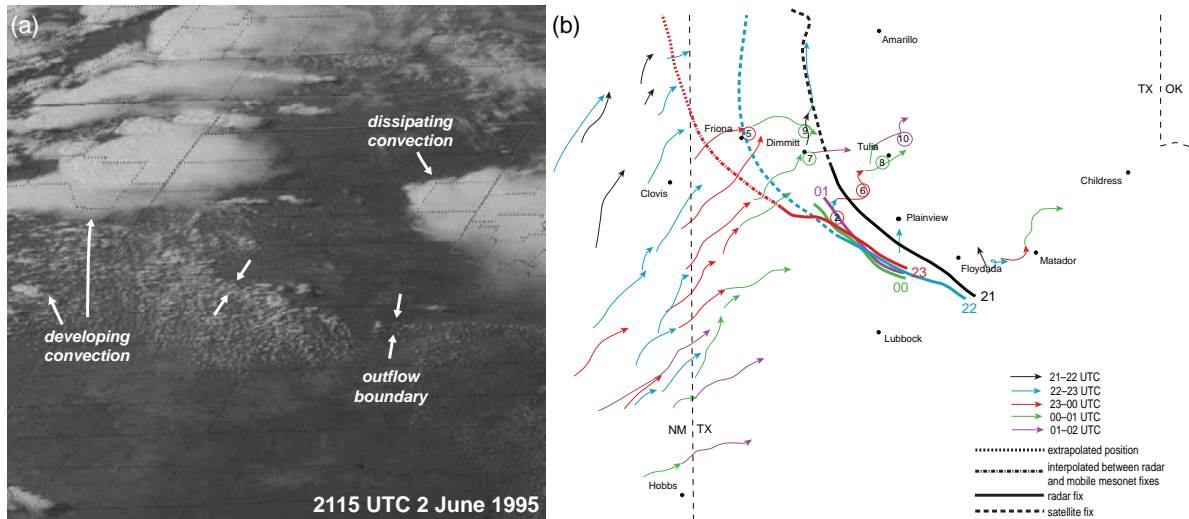


Figure 10.15 (a) Visible satellite image at 2115 UTC 2 June 1995, showing an outflow boundary in the wake of dissipating convection, and new convection forming to the west. Many of the new storms developed into supercells, and of these, those that tracked across the outflow boundary produced by the earlier convection were more likely to produce tornadoes. Both low-level relative humidity and low-level shear were enhanced on the immediate cool side of the outflow boundary. Despite the fact that it was cool within the outflow relative to the air mass south and west of the outflow, the outflow air mass had been substantially modified by late afternoon such that the atmosphere along the immediate cool side of the outflow boundary actually possessed more CAPE and less CIN than the ambient air mass to the south and west. (b) Echo centroid tracks for five 1 h periods on 2 June 1995, depicted with the various line types shown in the legend. Thick lines represent outflow boundary positions according to the symbols in the legend, and apply to the start of the 1 h periods. Circled numerals indicate tornado reports. Note that tornado occurrence was favored shortly after the storms crossed the outflow boundary into the more favorable low-level shear and moisture. (Adapted from Rasmussen *et al.* [2000].)

are also favored when CAPE and shear are larger than in the average squall line environment (Section 9.4), and tornadoes, when they occur in squall lines, tend to be associated with bow echo and LEWP structures.

10.1.5 Tornado structure and dynamics

Flow regions

Our present understanding of the morphology and dynamics of tornadoes has been gained from photogrammetric studies (e.g., Figure 10.17), laboratory experiments, and numerical simulations (e.g., Figure 10.18). The flow in tornadoes can be partitioned into five regions¹¹ (Figure 10.19):

Outer region (I): The outer region comprises inward spiraling air that approximately conserves its angular momentum, therefore air spins faster as it approaches the tornado axis.

Core (II): The core region extends outward from the tornado axis to the radius of maximum winds. It often contains a funnel cloud and a column of dust and debris from the ground. Because of the intense rotation in this region, air parcels are approximately in cyclostrophic balance; i.e., the apparent centrifugal force owing to the large curvature and high speed of the flow is balanced by a horizontal pressure gradient force directed inward toward the axis. Moreover, the region is strongly centrifugally stable; thus, the resistance to radial displacements results in there being almost no entrainment into the core.

Corner (III): The corner region is the part of the boundary layer where the flow turns upward from a primarily horizontal direction to a primarily vertical direction (the flow ‘turns the corner’).

Boundary layer flow (IV): The tornado’s boundary layer is anywhere from 10 to 100 m deep and is turbulent owing to the interaction of the flow with the ground. Friction precludes cyclostrophic balance, and radial

¹¹ See Snow (1982) and Davies-Jones (1986).

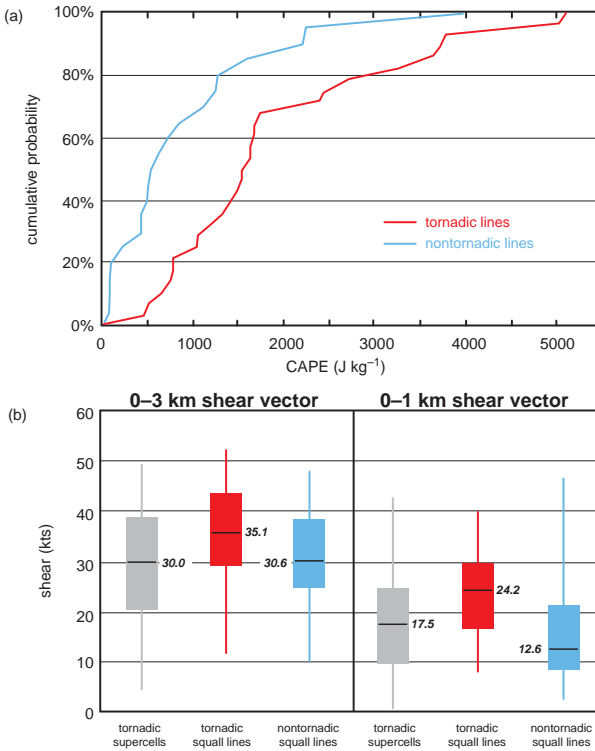


Figure 10.16 (a) Cumulative probability distribution of CAPE in squall lines that contain tornadoes and those that do not (CAPE was computed by lifting a parcel having the average potential temperature and water vapor mixing ratio of the lowest 100 mb). (b) Box-and-whiskers plots of the magnitude of the 0–1 km and 0–3 km vertical wind shear vectors in the environments of tornadic supercells, tornadic squall lines, and nontornadic squall lines. (Adapted from Godfrey *et al.* [1996].)

inflow toward the axis is produced. The radial inflow and convergence of angular momentum give rise to intense wind speeds. Thus, paradoxically, the presence of friction can actually intensify the vortex.

Rotating updraft (V): This is the larger-scale, parent updraft situated above the tornado.

Wind and pressure profile

The simplest idealization of the wind field of a tornado is that of a *Rankine vortex*; that is, constant angular velocity (v/r , where v is the tangential wind speed and r is the distance from the tornado center) is found within the radius of maximum tangential winds, and angular momentum (vr) is constant outside the radius of maximum winds,

such that,

$$v = \begin{cases} v_{\max}r/r_{\max}, & r \leq r_{\max} \\ v_{\max}r_{\max}/r, & r > r_{\max} \end{cases} \quad (10.1)$$

where r_{\max} is the radius of the maximum tangential wind speed, v_{\max} . The purely azimuthal wind profile of a Rankine vortex implies cyclostrophic balance. The Rankine wind profile is therefore most applicable above the boundary layer of the tornado (the strong radial inflow within the boundary layer implies a large departure from cyclostrophic balance there).

In the case of cyclostrophic balance, the momentum equation in natural coordinates (or the tangential momentum equation in cylindrical coordinates) can be written as

$$\frac{\rho v^2}{r} = \frac{\partial p'}{\partial r}. \quad (10.2)$$

To obtain the pressure, we integrate (10.2), assuming p' is a function of r only,

$$\int_{p'(r)}^{p'_{\infty}} dp' = \int_r^{\infty} \frac{\rho v^2}{r} dr, \quad (10.3)$$

where $p'(r)$ is the pressure perturbation at radius r from the vortex center and p'_{∞} is the pressure perturbation far away from the vortex. Assuming a constant density, $p'_{\infty} = 0$, and using (10.1), the pressure field for $r > r_{\max}$ is

$$p'(r) = - \int_r^{\infty} \rho \left(\frac{v_{\max}r_{\max}}{r} \right)^2 \frac{dr}{r} \quad (10.4)$$

$$= -\rho v_{\max}^2 r_{\max}^2 \left[-\frac{1}{2r^2} \right]_r^{\infty} \quad (10.5)$$

$$= -\frac{1}{2} \rho v_{\max}^2 \frac{r_{\max}^2}{r^2} \quad \text{for } r > r_{\max}. \quad (10.6)$$

For $r \leq r_{\max}$, again, assuming constant density, $p'_{\infty} = 0$, and using (10.1), the pressure field is given by

$$p'(r) = - \int_r^{r_{\max}} \rho \left(\frac{v_{\max}r}{r_{\max}} \right)^2 \frac{dr}{r} - \int_{r_{\max}}^{\infty} \rho \left(\frac{v_{\max}r_{\max}}{r} \right)^2 \frac{dr}{r} \quad (10.7)$$

$$= -\frac{\rho v_{\max}^2}{r_{\max}^2} \left[\frac{r^2}{2} \right]_r^{r_{\max}} - \rho v_{\max}^2 r_{\max}^2 \left[-\frac{1}{2r^2} \right]_{r_{\max}}^{\infty} \quad (10.8)$$

$$= -\rho v_{\max}^2 \left(1 - \frac{1}{2} \frac{r^2}{r_{\max}^2} \right) \quad \text{for } r \leq r_{\max}. \quad (10.9)$$

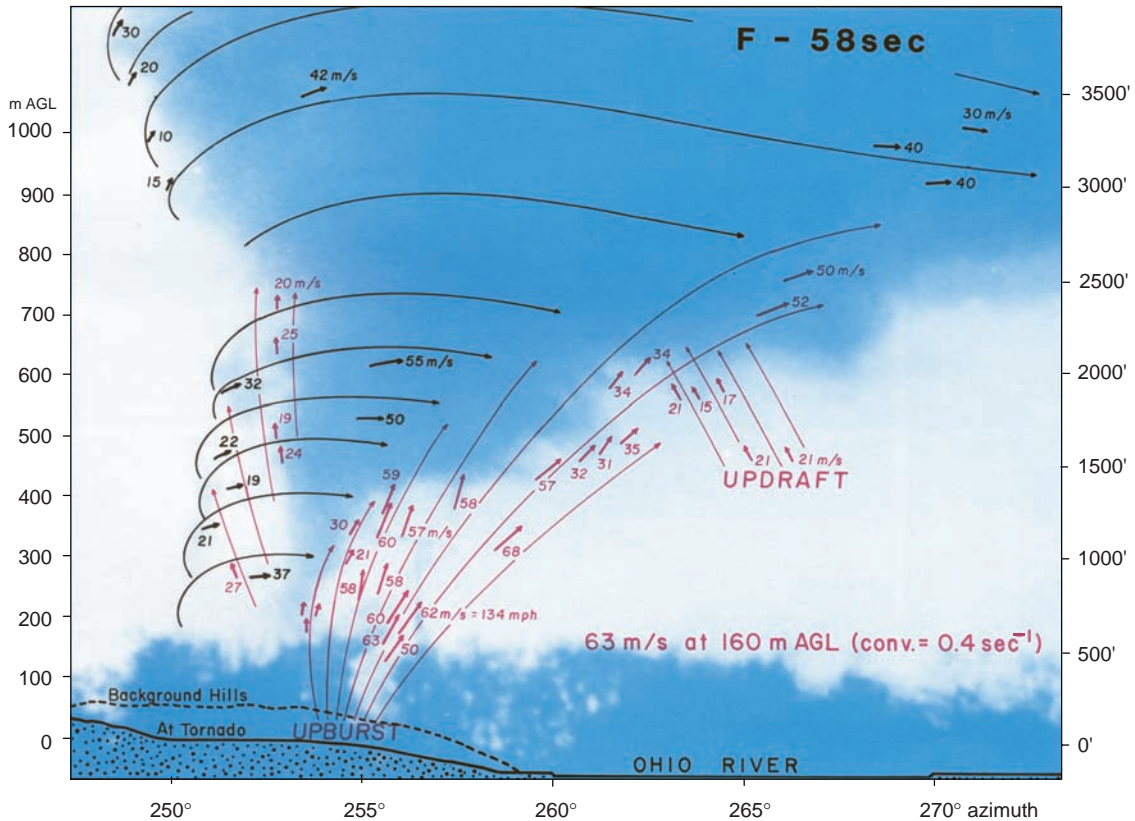


Figure 10.17 Fujita's photogrammetric analysis of wind velocities in the Sayler Park, OH, tornado of 3 April 1974. Winds are in m s^{-1} . (From Fujita [1992].)

The minimum pressure is found at the vortex center ($r = 0$):

$$p'_{\min} = -\rho v_{\max}^2. \quad (10.10)$$

For $\rho \sim 1 \text{ kg m}^{-3}$ and a weak tornado ($v_{\max} \sim 25 \text{ m s}^{-1}$), $p'_{\min} \sim 6 \text{ mb}$. This pressure deficit is only enough to lower the cloud base by approximately 60 m. In such cases a debris cloud might be present at the surface, but only a short funnel cloud would be visible aloft. If the tornado intensifies to $v_{\max} = 100 \text{ m s}^{-1}$, (10.10) predicts $p'_{\min} \sim 100 \text{ mb}$, and the cloud base lowers by $\sim 1000 \text{ m}$, which would likely be near the ground. The funnel cloud is not a material surface; rather, it descends even as air is continually flowing upward through it.

The *Burgers-Rott vortex* is another idealized vortex model that has been applied to tornadoes. It is more realistic than the Rankine vortex because it also specifies radial and vertical flow. The Burgers-Rott vortex takes the

following form:

$$u = -ar \quad (10.11)$$

$$v = \frac{C}{2\pi r} \left(1 - e^{-\frac{ar^2}{2\nu}} \right) \quad (10.12)$$

$$w = 2az. \quad (10.13)$$

Here u , v , and w are the radial, tangential, and vertical velocity components, respectively, C is the circulation, ν is viscosity (eddy viscosity would be more appropriate than molecular viscosity), and a determines the strength of the updraft. The tangential wind profile of the Burgers-Rott vortex is similar to that of the Rankine vortex but has the advantage of smoothing out the unrealistic cusp found at the radius of maximum wind in the Rankine vortex model. Some obvious unrealistic aspects of the Burgers-Rott vortex, as applied to tornadoes, are that the vertical velocity increases linearly with height without bound and that the strength of the circulation, C , is uncoupled from the radial and vertical flow.

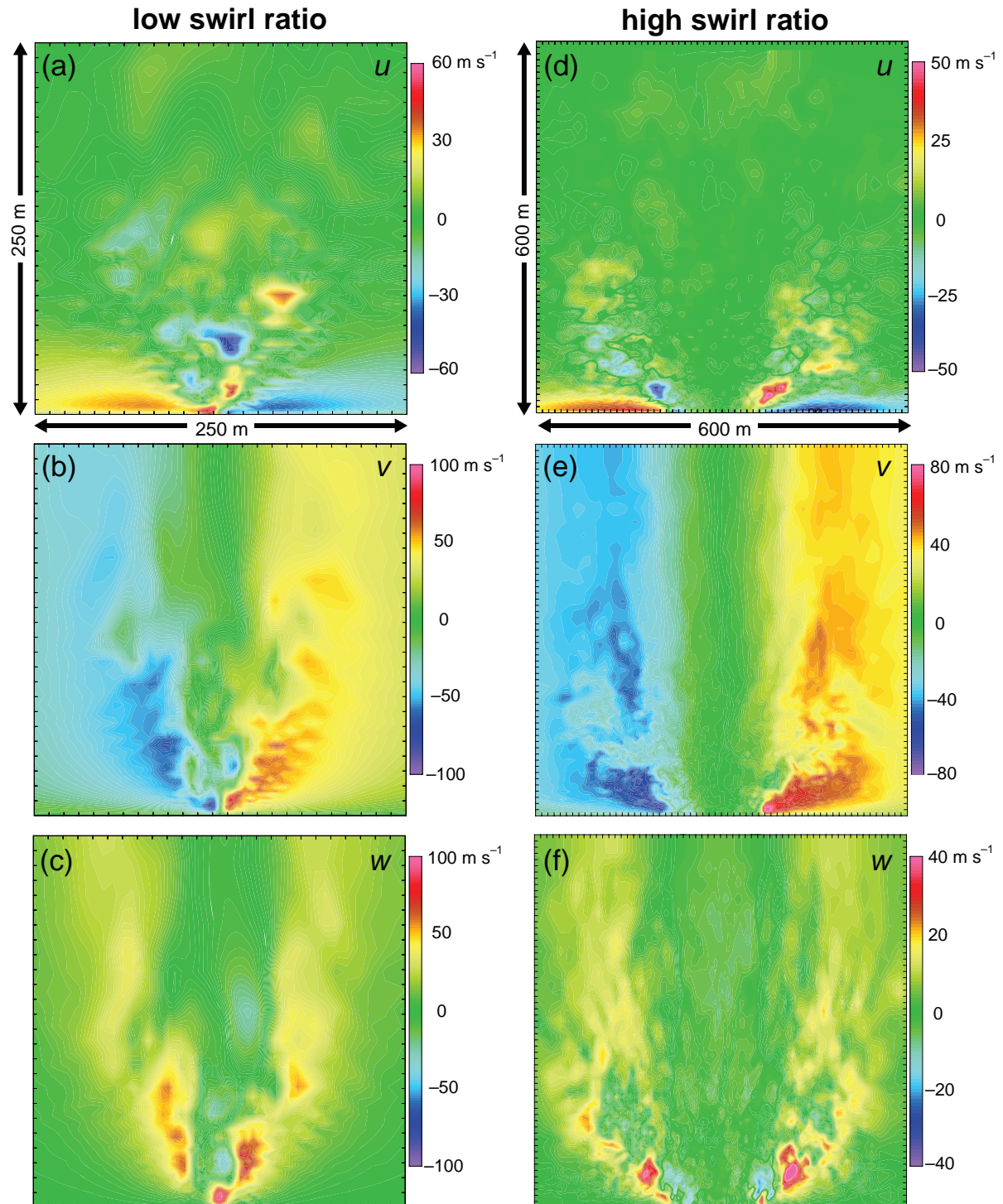


Figure 10.18 (a)–(c) Vertical cross-sections of instantaneous radial (u), tangential (v), and vertical (w) velocities in a three-dimensional numerical simulation of a tornado having a low swirl ratio. The cross-sections are taken through the center of the tornado. (d)–(f) As in (a)–(c), but for a simulated tornado having a high swirl ratio. Courtesy of Dave Lewellen.

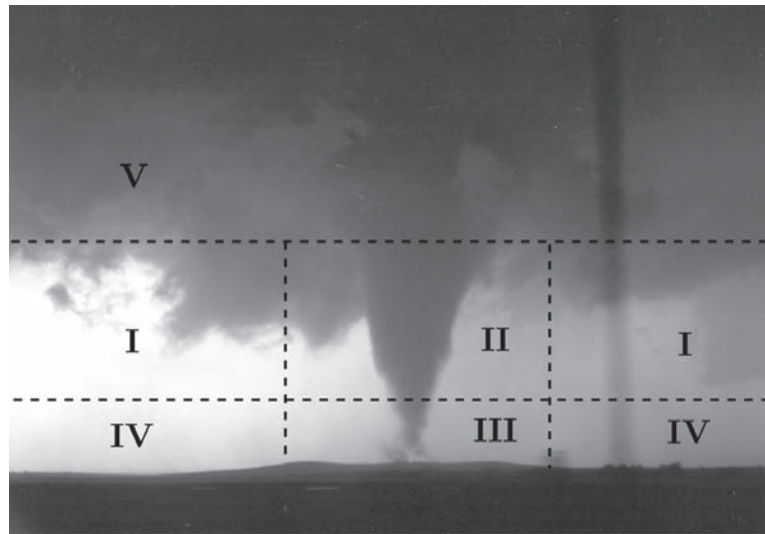


Figure 10.19 The five regions of a tornado vortex. See the text for descriptions. Photograph by Paul Markowski.

Another vortex model, the Sullivan vortex, will not be discussed in detail here. In brief, it is more realistic, and thus necessarily more complex, than the Burgers-Rott vortex. The radial, tangential, and vertical velocity fields are coupled, and the Sullivan vortex even prescribes an axial downdraft, as is commonly observed in real tornadoes.

Swirl ratio

Laboratory vortex experiments have shown that the structure of the vortices strongly depends on a dimensionless parameter called the swirl ratio, S ,

$$S = \frac{r_0 C}{2Q} = \frac{v_0}{w_0}, \quad (10.14)$$

where C is the circulation about the central axis at a radius of r_0 , Q is the rate of volume flow through the top of the tornado chamber, v_0 is the tangential velocity at r_0 , and w_0 is the mean vertical velocity at the top of the chamber.

For small values of S (e.g., <1), the flow is dominated by updraft rather than by rotation. At any given level above the boundary layer of the tornado, the pressure rises as the flow approaches the axis because the air parcels must decelerate. Thus, the boundary layer ‘separates’ and any rotation that exists in the approaching stream is carried aloft before reaching the axis (Figure 10.20a).¹² As S is increased, the rotation in the outer flow makes the pressure gradient in the direction of the flow favorable so that surface flow

can penetrate to the axis, resulting in a *one-celled* vortex. One-celled refers to the fact that the vortex contains an updraft throughout (Figures 10.18a–c and 10.20b). As S is increased further (Figures 10.18d–f and 10.20c, d), a central downdraft forms and a *two-celled* vortex results. The large swirl ratio (e.g., >2) is associated with a low-level pressure deficit that is large enough to induce a net axial downflow. Two-celled refers to the fact that a central downdraft is surrounded by updraft in this case.

The transition from a one-celled vortex to a two-celled vortex is termed *vortex breakdown*. When S is very large, the central downdraft reaches the ground. The interface between the rapidly rotating inflow and weakly rotating downdraft air at the surface is unstable, and multiple vortices are formed (Figures 10.20e and 10.21). The multiple vortices rotate about the parent vortex circulation. Many tornadoes, and perhaps most strong tornadoes, are observed to evolve from one-celled to two-celled tornadoes and exhibit vortex breakdown and ultimately subvortices (Figures 10.21 and 10.22). Subvortices can be associated with localized intense damage within the broader debris swath of the tornado owing to the superposition of the velocity field associated with the small-scale subvortex and the larger-scale tornado.

Numerical simulations of tornadoes, which have largely replaced laboratory experiments, demonstrate a similar sensitivity of tornado structure to the swirl ratio. However, depending on the design of the numerical model, it can be a challenge to define the appropriate values of v_0 and w_0 ; e.g., it is often not obvious what radius and level are the most appropriate to use to obtain v_0 and w_0 , respectively. The

¹² See Rotunno (1986).

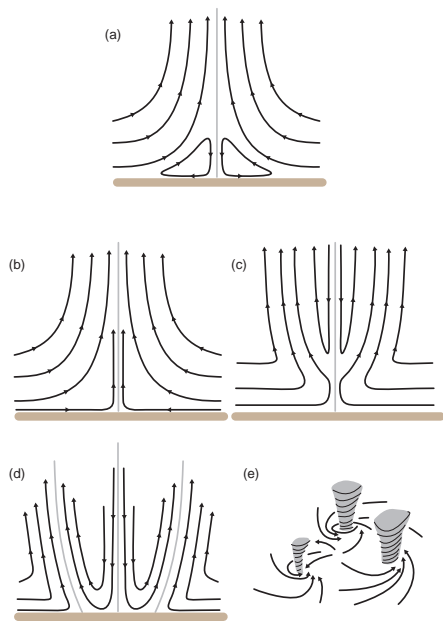


Figure 10.20 Types of vortices produced in a vortex chamber as swirl ratio increases: (a) weak swirl—boundary layer separates and flow passes around the lower corner; (b) one-celled vortex; (c) one-celled vortex over the lower portion, two-celled vortex over the upper portion, separated by vortex breakdown; (d) two-celled vortex; and (e) multiple vortices. (Adapted from Davies-Jones [1986].)

same challenges apply to assessing relationships between observed tornado structure and swirl ratio. Sometimes a *local* swirl ratio is used instead, computed inside the core region in the surface layer, which is less sensitive to the precise radial or vertical location at which v_0 and w_0 are measured.¹³ However, the local corner flow swirl ratio does not really replace the aforementioned *outer* swirl ratio. The two swirl ratios measure different physical properties of the tornado flow.

10.2 Nontornadic, damaging straight-line winds

Damaging straight-line winds within convective storms are almost always associated with the precipitation-cooled (via evaporation, melting, or sublimation) outflow. An exception is that, in rare cases, supercell updrafts can be so intense that they induce inflow winds capable of doing damage. This exception aside, outflow-related damaging winds are usually produced by either meso- γ -scale

downdrafts, termed *downbursts*, that strike the ground and subsequently create strong, often highly divergent horizontal winds there, or by meso- β -scale cold pools associated with horizontal pressure gradients large enough to produce damaging winds in the absence of strong downdrafts. The latter events tend to arise after numerous thunderstorms' outflows have merged, leading to a deepening of the outflow and corresponding rise in surface pressure within the outflow; vortices that form along the outflow boundary also can contribute to high winds. Regarding downbursts, high winds can be due to either intense downdrafts or lesser downdrafts that carry large momentum from aloft (e.g., the descent of a rear-inflow jet to the surface within an MCS).

In the case of isolated cells, forecasting damaging straight-line winds usually amounts to identifying environments conducive to the formation of intense downdrafts. Forecasting damaging straight-line winds within MCSs involves anticipating the formation of long-lived MCSs, which can produce damaging winds if their rear-inflow jet descends to the surface, or simply owing to their deep meso- β -scale cold pools, especially where vortices locally enhance the outflow winds. Supercells can also produce damaging straight-line winds. For example, the winds in the most intense RFDs can be stronger than those in a weak tornado.¹⁴ Damaging straight-line winds can also occur within low-topped (perhaps even non-thundering) squall lines or rainbands in low-CAPE (or zero-CAPE) environments having strong synoptic-scale gradient winds, as is often the case in the cold season. The high winds in these events result from the downward transport of high-speed air from above the surface by system-scale downdrafts.

A *derecho* is a widespread damaging wind event associated with long-lived DMC. The extreme winds can be the result of any of the aforementioned mechanisms. Often people whose homes are damaged by straight-line winds, which can exceed 50 m s^{-1} in extreme cases, falsely attribute the damage to tornadoes. However, the damage pattern from downbursts is highly divergent (Figure 10.27), in contrast to the convergent flow associated with tornadoes. Through aerial surveillance of damage, Fujita was the first to recognize these differing patterns and distinguish between the two.

10.2.1 Damaging winds resulting from downdrafts

Downbursts are defined to have horizontal dimensions less than 10 km. If a downburst is particularly small in

¹³ See Lewellen *et al.* (2000).

¹⁴ The Doppler On Wheels radar scanned a tornado on 29 May 2004 that had peak winds of $\sim 40 \text{ m s}^{-1}$ while the radar truck was being slammed by RFD winds in excess of 50 m s^{-1} .

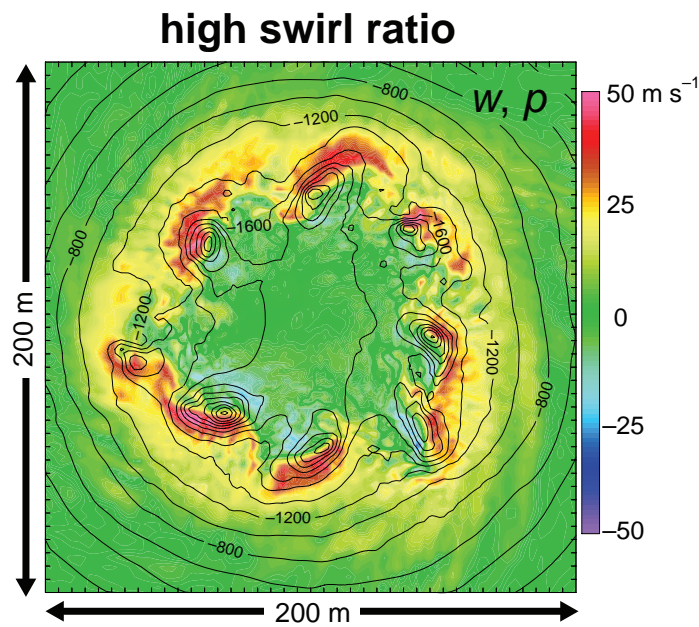


Figure 10.21 Horizontal cross-section at $z = 50$ m of vertical velocity (w ; color shading, see scale) and pressure perturbations (p ; contours every 200 Pa) in a three-dimensional numerical simulation of a tornado having a high swirl ratio. Numerous subvortices (there are eight of them) are evident. Courtesy of Dave Lewellen.



Figure 10.22 Video frame of a multiple-vortex tornado near Mountain View, OK, on 9 October 2001. Courtesy of Amos Magliocco.



Figure 10.23 Photograph of a wet microburst, with the gust front position and a couple of schematic streamlines drawn. A cloud is situated on the leading edge of the outflow (indicated by the cold frontal symbols) where air is being forced upward. Photograph courtesy of the National Oceanic and Atmospheric Administration (NOAA).

2224 UTC 2 June 2005

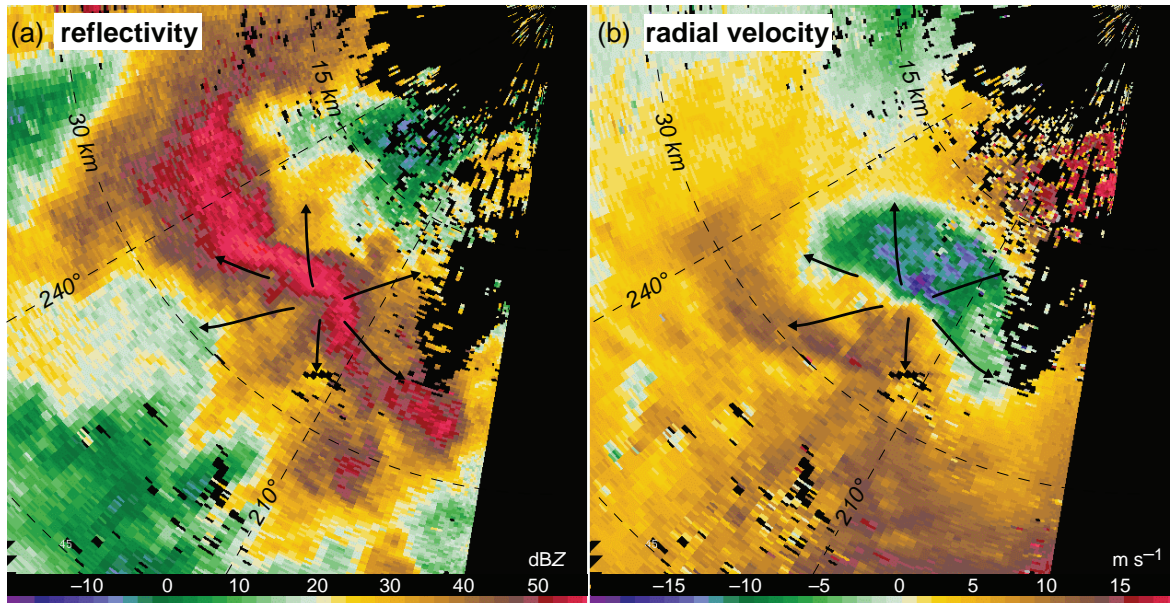


Figure 10.24 A downburst as seen in (a) radar reflectivity (dBZ) and (b) radial velocity ($m s^{-1}$) imagery obtained at 2224 UTC 2 June 2005 by the Colorado State University CHILL radar in northeastern Colorado (0.5° elevation angle). The radial velocity signature of a downburst on low-altitude scans is an inbound–outbound velocity couplet oriented such that the zero contour is approximately normal to the radials, with inbound (outbound) velocities closer to (farther from) the radar, thereby implying radial divergence.

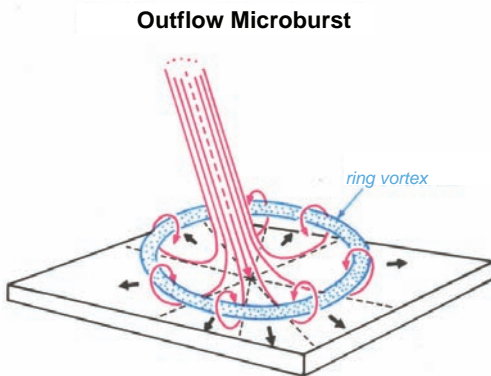


Figure 10.25 Fujita's conceptual model of a microburst, which can be viewed as an intense vortex ring intercepting the ground. (From Fujita [1985].)

its horizontal dimensions (less than 4 km on a side), it is also known as a *microburst* (Figures 10.23–10.27).¹⁵ These classifications are based rather arbitrarily on horizontal scales rather than on the governing dynamics. Downbursts are produced by a downdraft, by definition. Below we focus on the development of strong downdrafts, rather than on damaging winds that principally result from large horizontal momentum being transported to the surface, independent of downdraft strength.

The vertical momentum equation can be written as

$$\frac{dw}{dt} = \underbrace{-\frac{1}{\rho} \frac{\partial p'_d}{\partial z}}_{\text{dynamic forcing}} + \underbrace{\left(-\frac{1}{\rho} \frac{\partial p'_b}{\partial z} + B \right)}_{\text{thermodynamic forcing}}, \quad (10.15)$$

where w is the vertical velocity, ρ is the air density, $p' = p'_d + p'_b$ is the total pressure perturbation, p'_d is the dynamic pressure perturbation, p'_b is the buoyancy pressure perturbation, and B is the buoyancy [refer to the diagnostic pressure equation (2.133) in Section 2.5]. The first term on the rhs is the *dynamic forcing*, whereas the buoyancy and the vertical gradient of the buoyancy pressure perturbation are considered together as the *thermodynamic or buoyancy forcing*. Although both forcings can be important, the thermodynamic forcing is probably dominant in most downburst cases.¹⁶

Downbursts are associated with relatively high pressure at the surface, as are all downdrafts; the high pressure is necessary to deflect downward-directed streamlines horizontally. Recall that the high pressure at the surface situated

beneath downbursts has both hydrostatic and nonhydrostatic origins; that is, there is high pressure both because the column of air tends to be relatively cool and because the requirement that air decelerate as it approaches the ground is unavoidably associated with fluid strain. An estimate of the magnitude of (positive) p' at the surface beneath a downdraft can be obtained using a Bernoulli equation,

$$p' \approx \bar{\rho} \left(\frac{v^2}{2} + \text{DCAPE} \right), \quad (10.16)$$

where v is the downdraft velocity evaluated a few kilometers above the surface, at a height where p' is small; $\bar{\rho}$ is the mean air density between this altitude and the surface, and the DCAPE is the integrated negative buoyancy realized by the downdraft parcel between this altitude and the surface (Figure 10.28). For $v \sim 10 \text{ m s}^{-1}$, $\bar{\rho} \sim 1 \text{ kg m}^{-3}$ (as might be the case for a parcel descending from a height of $\sim 2 \text{ km}$), and DCAPE $\sim 200 \text{ m}^2 \text{ s}^{-2}$, (10.16) yields $p' \sim 2.5 \text{ mb}$.

The application of parcel theory (Section 3.1.1) to a downdraft predicts that

$$w_{\min} = -\sqrt{2 \text{ DCAPE}}, \quad (10.17)$$

where w_{\min} is the *maximum* downdraft speed. However, whereas CAPE is clearly defined as the integral of positive buoyancy from the level of free convection to the equilibrium level, the upper level from which DCAPE should be integrated is not as clear (Section 2.6). This limits its usefulness as a quantitative predictor of downdraft strength, in addition to limits imposed by parcel theory. Downdrafts entrain environmental air, just as updrafts do. Moreover, the effects of $\partial p'/\partial z$ are clearly important because air cannot descend through the ground. Without a vertical perturbation pressure gradient force (usually involving both p'_d and p'_b) opposing the downward-directed buoyancy force, downdraft speeds would be a maximum at the surface. Another difficulty in predicting downdraft speeds from DCAPE is that downdraft parcels are often unsaturated for part of their excursions (i.e., parcels may not follow a pseudoadiabat all the way to the ground; Figure 10.28); DCAPE calculations are usually based on the negative area between the environmental temperature profile on a sounding and the pseudoadiabat followed by a downdraft parcel.

Thermodynamic effects

The thermodynamic forcing for downdrafts is related to the generation of negative buoyancy, which can be produced by two mechanisms: latent cooling and hydrometeor loading. We turn our attention to latent cooling first.

¹⁵ The terms *downburst* and *microburst* were coined by T. Fujita.

¹⁶ The most common exception may be the occlusion downdraft of supercell thunderstorms (Section 8.4.2).

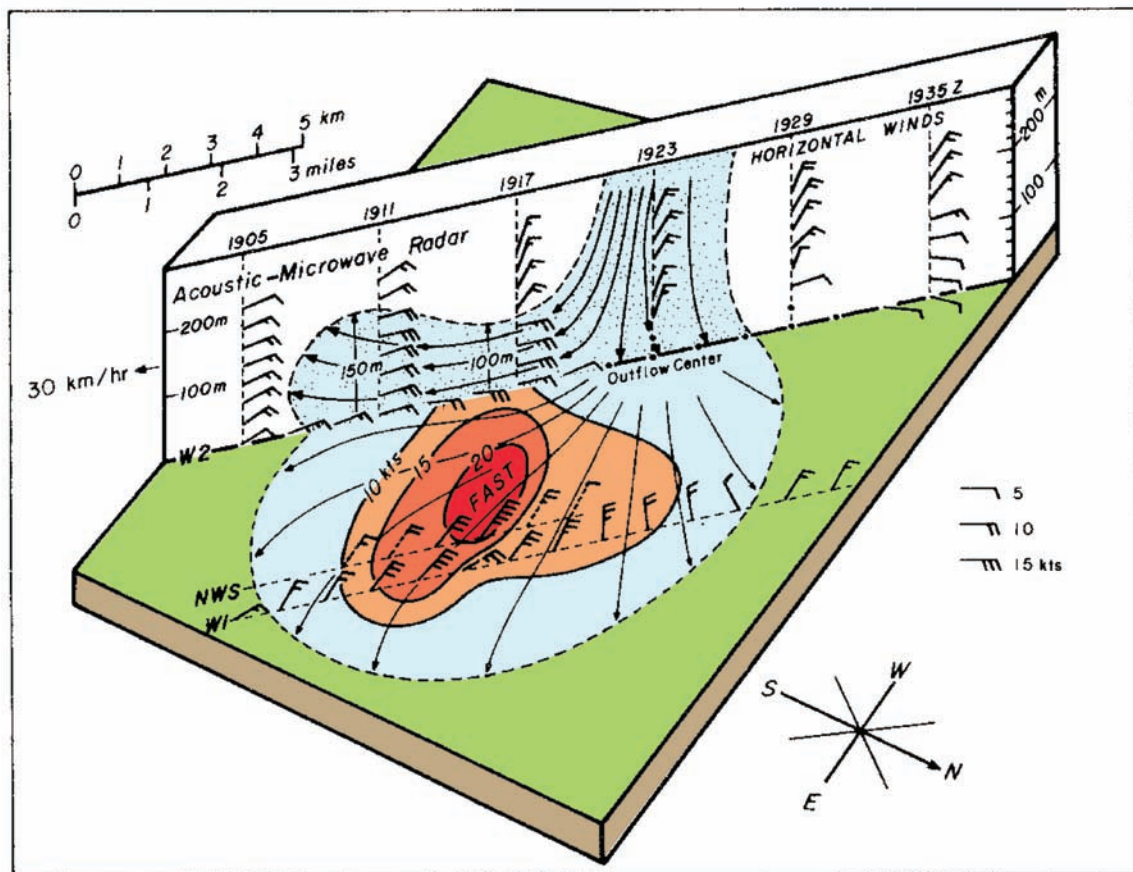


Figure 10.26 Cross-section of a microburst. (Adapted from Fujita [1978].)

Latent cooling is due to the evaporation of liquid water (raindrops and cloud droplets; Figure 10.29a, b), melting of ice (hail, graupel, and snow; Figure 10.29c, d, g, h), and sublimation of ice (mainly snow; Figure 10.29e, f). Evaporation and melting are more important in the lower troposphere below the melting level, whereas the cooling effects of sublimation are confined to higher altitudes. All three effects can contribute to the negative buoyancy that supports downdrafts.

Boundary layers that are dry (i.e., relative humidity is small, cloud bases are high) are favorable for the generation of significant negative buoyancy via evaporation as raindrops fall from cloud base into a deep, unsaturated layer of air. Even if the boundary layer is not particularly dry, the entrainment of dry midlevel environmental air into a storm can produce negative buoyancy aloft, leading to downdraft formation. Midlevel entrainment generally increases with vertical wind shear and storm-relative winds. Recall from Section 5.3.1, however, that, although evaporation

is important in the initiation of downdrafts, downdraft intensity does not necessarily increase with increasing environmental dryness (for a given CAPE), owing to the weakening of updrafts and the associated reduction in condensate that is available to be evaporated (Figure 10.29a, b). Stated another way, for a given liquid water content, the cooling due to evaporation increases as the relative humidity decreases, but the liquid water content available for evaporation is itself affected by the environmental relative humidity.

As for ice, some simulations suggest that the sublimation and especially melting of ice can be a significant source of negative buoyancy and is even necessary to produce downbursts in environments with greater low-level stability. The sublimation rate increases as the environmental relative humidity decreases (Figure 10.29e, f). On the other hand, melting rates increase as environmental relative humidity increases (Figure 10.29c, d, g, h). (This is another reason why downdraft intensity does not

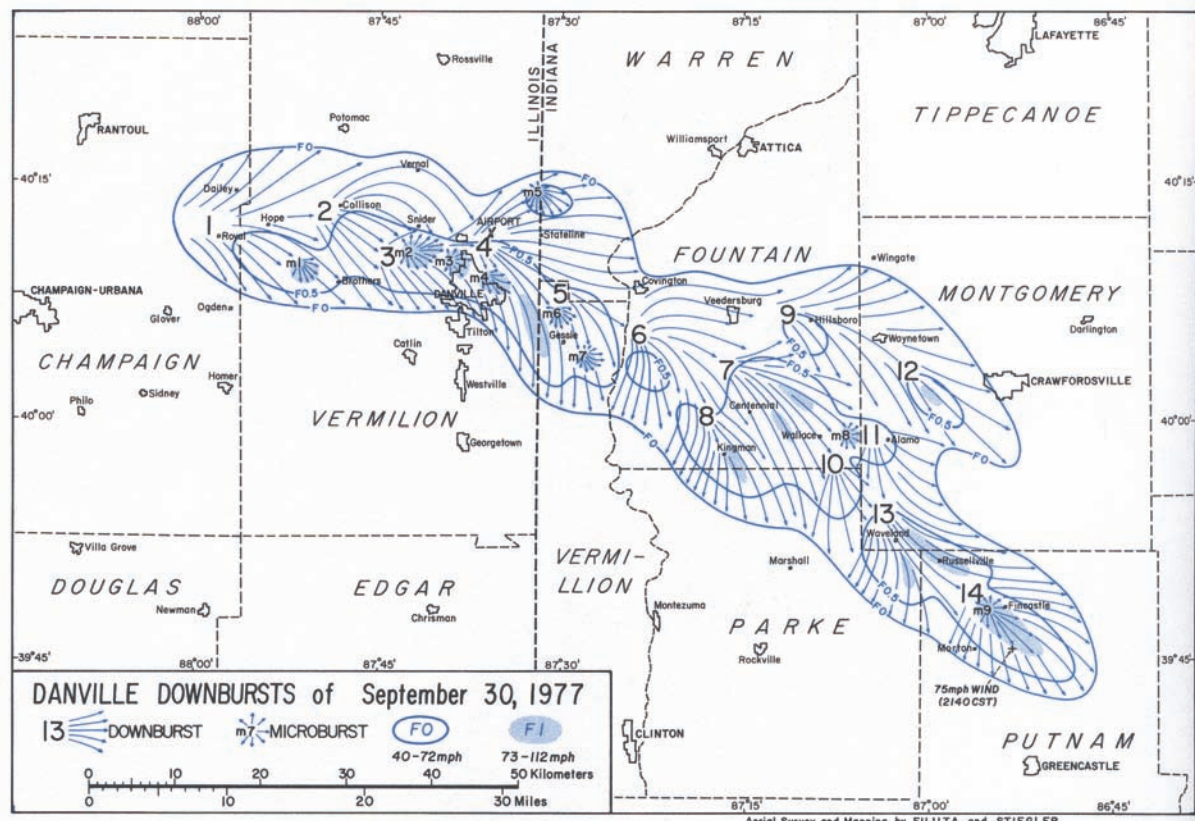


Figure 10.27 Streamline analysis of a series of downbursts and microbursts on 30 September 1977. (From Fujita [1978].)

necessarily increase with increasing environmental dryness.) Because the air temperature near the surface of a hydrometeor is approximately equal to the wet-bulb temperature, T_w , melting does not occur until ice encounters wet-bulb temperatures above freezing. As the environmental relative humidity increases, hailstones maintain a higher temperature owing to less evaporation of the meltwater; thus, there is increased melting. Furthermore, the altitude at which $T_w = 0^\circ\text{C}$ (known as the *wet-bulb-zero level* to forecasters; Figure 10.30) is lower in dry environments than in moist environments, in addition to its obvious dependence on temperature (the wet-bulb-zero level is higher in warm environments than cool environments). Thus, in dry environments, less time is available for melting as ice falls to the ground; therefore, less cooling via melting occurs.

The latent cooling resulting from evaporation, melting, or sublimation can be quantified using the first law of thermodynamics. From the first law, the potential temperature change of an air parcel at constant pressure,

$\delta\theta$, produced by latent cooling is

$$\delta\theta = \frac{\theta}{T} \frac{l}{c_p} \delta r_h \quad (10.18)$$

where θ is the potential temperature, T is the absolute temperature, c_p is the specific heat at constant pressure, l is either the specific latent heat of vaporization (l_v), fusion (l_f), or sublimation (l_s), and r_h is the hydrometeor mass (kg per kg of air) that is either evaporated, melted, or sublimated ($r_h = r_c + r_r + r_i$, where r_c , r_r , and r_i are the cloud water, rain water, and ice (cloud ice, graupel, hail, and snow) mixing ratios, respectively). For every 1 g kg⁻¹ of hydrometeor mass that is evaporated/melted/sublimated, θ cools by approximately 2.5/0.3/2.8 K.

We now revisit the effects of hydrometeor loading. Recall from Section 2.3 that the downward acceleration due to the mass of hydrometeors is gr_h . The density increase within a parcel attributable to the condensate weight can therefore be accounted for in the buoyancy term of the vertical

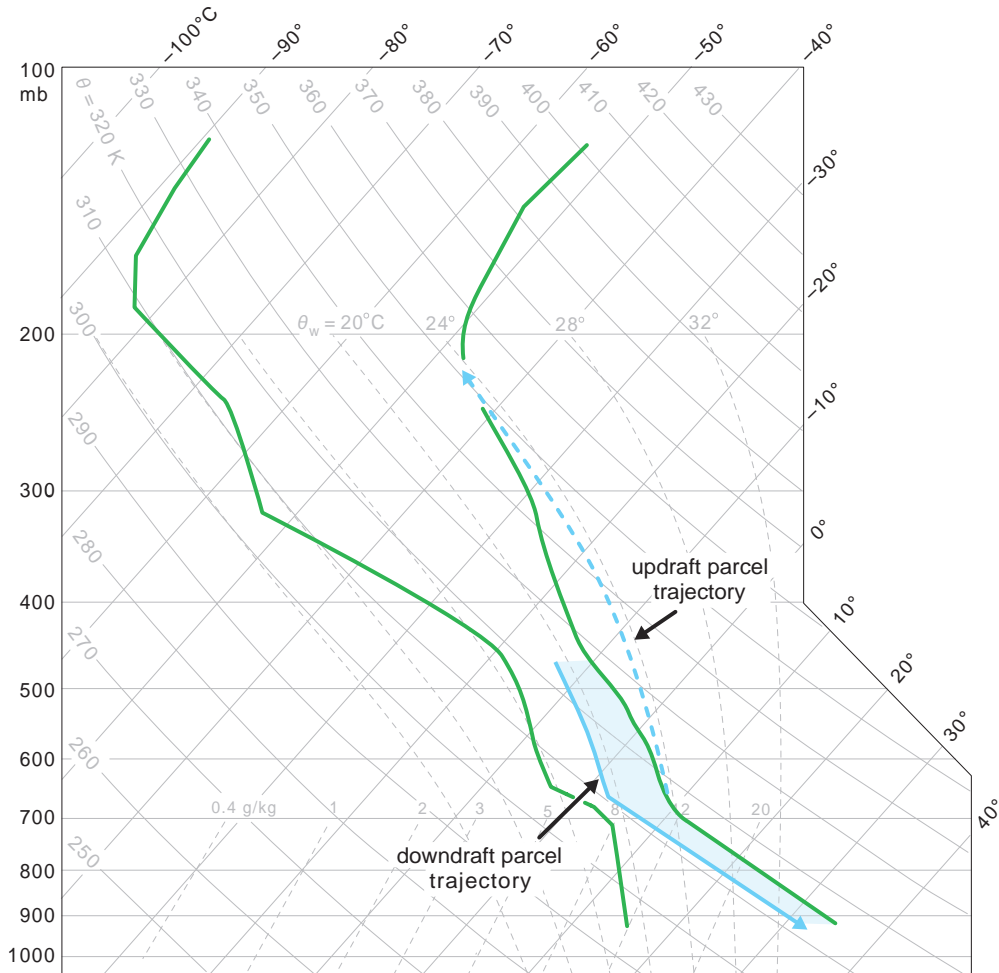


Figure 10.28 Downburst air parcels commonly undergo both moist and dry adiabatic descent en route to the ground. The kinetic energy realized by a downdraft parcel, and, in part, the surface pressure perturbation associated with the downdraft, are proportional to the area that is shaded blue.

momentum equation. Including the weight of condensate, in addition to the contribution of water vapor perturbations, recall that the buoyancy of an air parcel may be written as

$$B \approx g \frac{\theta'_\rho}{\bar{\theta}_\rho} \approx g \left(\frac{\theta'}{\bar{\theta}} + 0.61r'_v - r_h \right), \quad (10.19)$$

where r'_v is the water vapor mixing ratio perturbation relative to the ambient water vapor mixing ratio and $\theta_\rho = \bar{\theta}_\rho + \theta'_\rho = \theta(1 + 0.61r_v - r_h)$ is the density potential temperature.¹⁷ For $r_h = 10 \text{ g kg}^{-1}$, the contribution

to B is the same as from a -3 K potential temperature perturbation. Hydrometeor loading is often crucial in initiating the downdraft, after which the other effects also become important.

Dynamic effects

Dynamic effects, more specifically, dynamic pressure perturbations and their vertical gradients, are most likely to be significant in environments containing large vertical wind shear (e.g., supercell environments). Relatively high p'_{dl} (the linear contribution to p'_d) is found aloft upshear of the updraft, and is a maximum at the level where the product of updraft speed and environmental

¹⁷ Recall from Section 2.3.3 that $B = g\theta'_\rho/\bar{\theta}_\rho$ if the vertical pressure gradient force in the vertical momentum equation is written in terms of θ_ρ and π' .

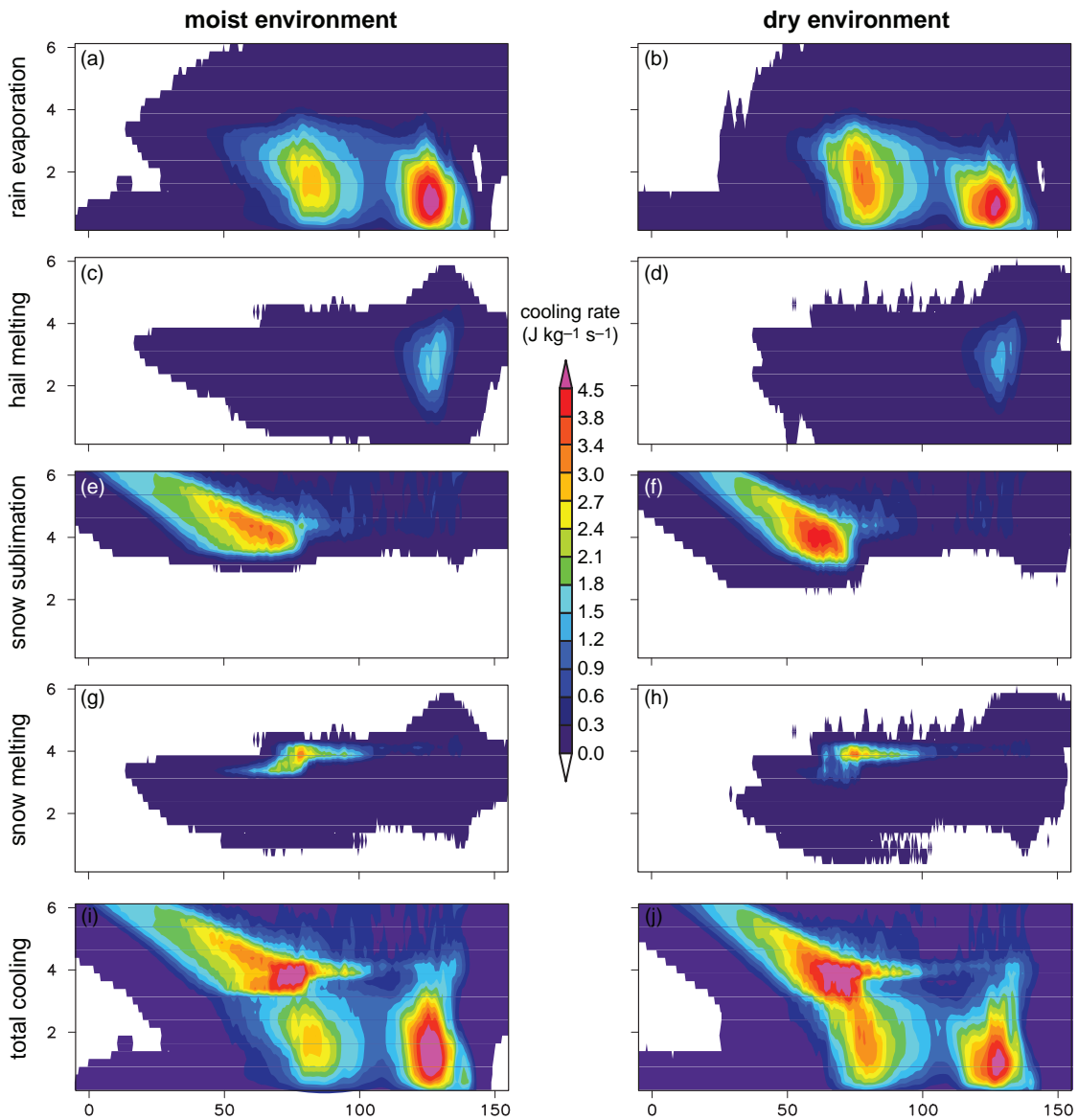


Figure 10.29 Vertical cross-sections of line-averaged latent cooling rates in a pair of numerical simulations of a long-lived MCS. The panels in the left column (a, c, e, g, i) are from a simulation in which the environment has a relatively high relative humidity throughout the troposphere (the relative humidity decreases from 95% at the top of the boundary layer to 50% at the tropopause), whereas the panels in the right column (b, d, f, h, j) are from a simulation in which the midtropospheric environment has a 1.5 km-deep dry layer with relative humidity of only 10%. The CAPE in both simulations is 4000 J kg^{-1} . The melting level in both simulations is at approximately 4 km. The x and z axis labels are in kilometers. The latent cooling rates ($\text{J kg}^{-1} \text{ s}^{-1}$) from (a, b) rain evaporation, (c, d) hail melting, (e, f) snow sublimation, and (g, h) snow melting are shown 4 h into the simulations, as is (i, j) the total latent cooling rate. The evaporative cooling (and total latent cooling) in the moist environment immediately behind the gust front (the gust front is at $x = 150 \text{ km}$) exceeds that in the dry environment (the domain-wide evaporative cooling and total latent cooling are also greater in the moist environment, although this is not as obvious from the panels above). Image courtesy of Richard James.

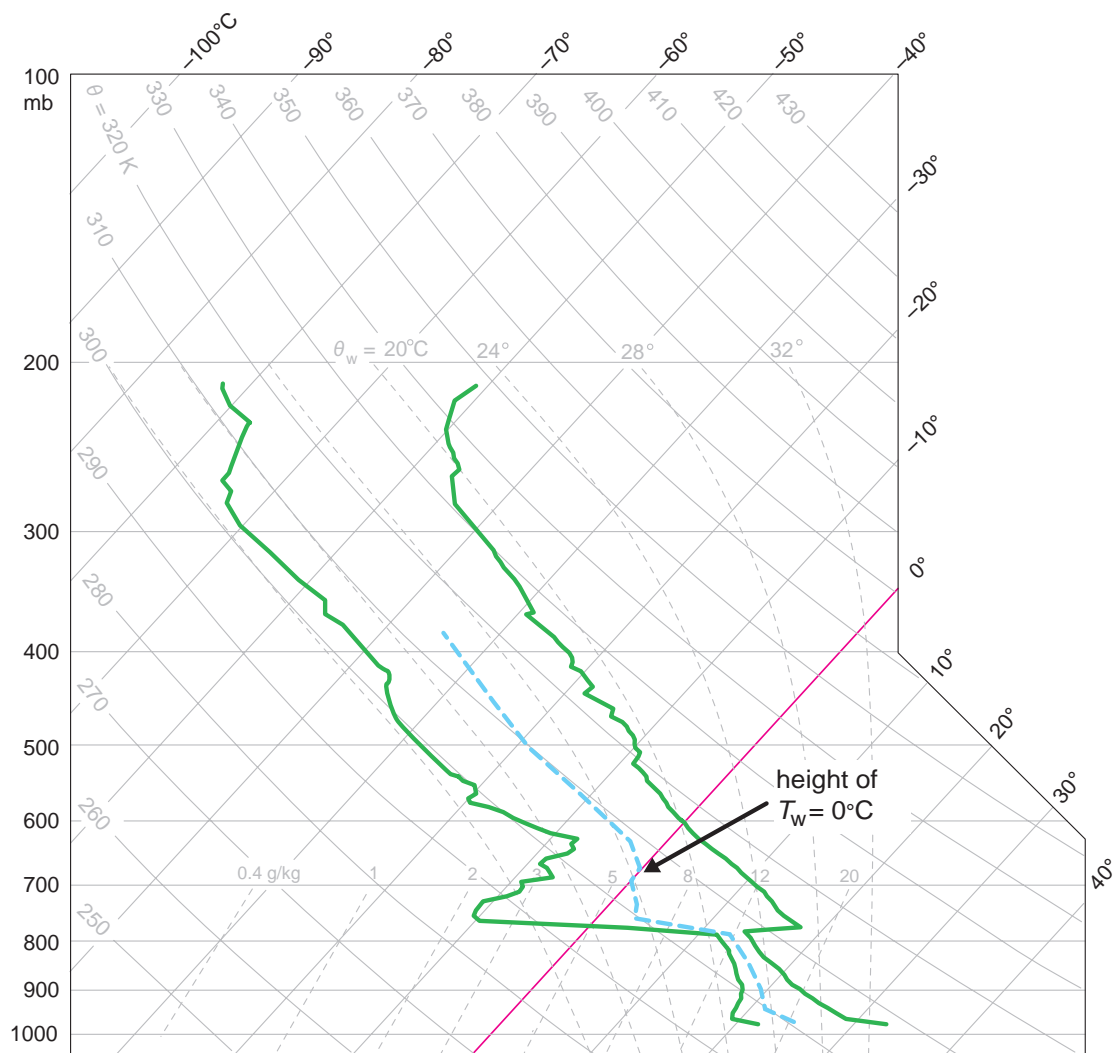


Figure 10.30 A typical *loaded gun* sounding with the vertical profile of wet-bulb temperature (T_w) indicated with a dashed blue line. The 0°C isotherm is highlighted.

shear is largest, assuming that the magnitude of the horizontal vertical velocity gradient is proportional to the vertical velocity. Below this level, $-\partial p'_{\text{dl}}/\partial z < 0$, which contributes to downward accelerations. Air that is not negatively buoyant may be forced to descend. Another example is when vertical vorticity decreases with height, implying that p'_{dnl} ($\propto -\zeta^2$; the nonlinear contribution to p_{dv}) increases with height. Such conditions give rise to subsidence along the axis of a tornado and to the occlusion downdraft in a supercell.

Subclasses of downbursts/microbursts

Events termed *dry microbursts* are those in which precipitation, except perhaps for a few sprinkles (one definition specifies rainfall $<0.25 \text{ mm}$ and radar reflectivity $<35 \text{ dBZ}$), fails to reach the ground. Negative buoyancy is generated by the evaporation of rain below cloud base. Dry microbursts are common in the High Plains region of the United States on days with deep boundary layers and high (e.g., $>3 \text{ km}$) cloud bases (Figures 10.31 and 10.32).

Microburst Composite Sounding Denver, Colorado

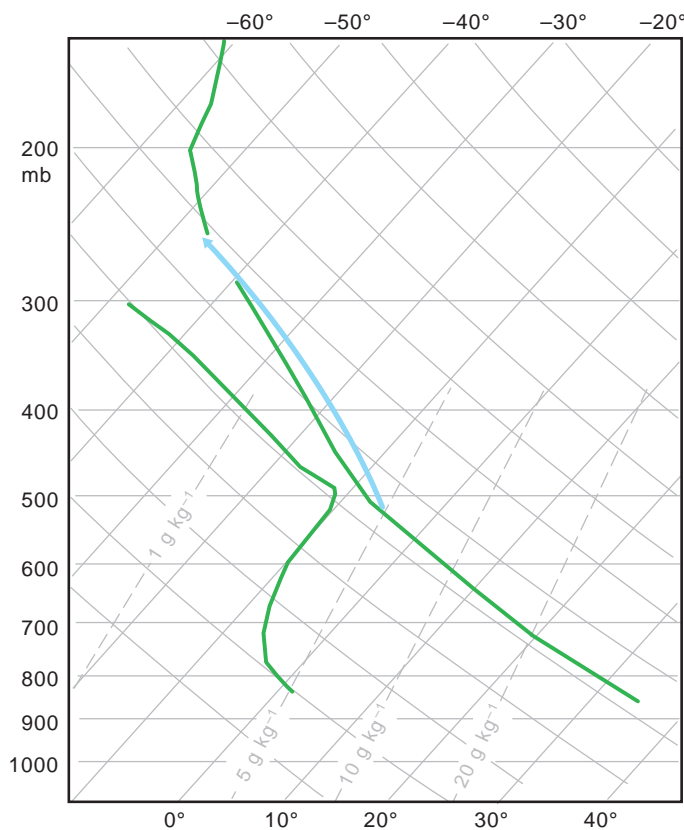


Figure 10.31 Composite skew T -log p diagram for Denver, CO, on dry microburst-producing days. Such a sounding is sometimes referred to as an *inverted V* sounding. The blue line represents the trajectory followed by a parcel lifted from the surface. (Adapted from Brown *et al.* [1982].)



Figure 10.32 Photographs of dry microbursts. Photos by (left) Fred Caracena and (right) Marisa Ferger. The photograph on the right was taken from the upper deck of Coors Field in Denver, CO, during a Colorado Rockies baseball game. The base of the parent cumulus cloud is visible near the top of the image, above the blowing dust.

They often occur in conjunction with fairly shallow clouds that might not look much more threatening than shallow cumulus convection. Typically virga is observed beneath dry microburst-spawning convection (the virga is an indication of the evaporation that generates the negative buoyancy). Conversely, *wet microbursts* are those in which extensive precipitation reaches the ground. These are the most common class of microburst and are largely forced by a combination of hydrometeor loading, evaporation, and hail melting (Figure 10.23).

Events termed *mid-air microbursts* do not penetrate to the ground because they encounter a low-level stable

layer, which slows and ultimately halts their descent. These phenomena are still a danger to aircraft, however. *Heat bursts* occur when downbursts penetrate through a shallow stable layer near the surface. These are similar to mid-air microbursts, but the downdraft succeeds in reaching the ground. Typically the stable layer is shallower than in the mid-air microburst case, so downdrafts have sufficient downward momentum to overshoot their equilibrium level and reach the ground (Figures 10.33 and 10.34). As their name suggests, sudden, intense warming (and often drying) at the surface accompanies a heat burst.

0440 UTC 24 June 1985 Russell, Kansas

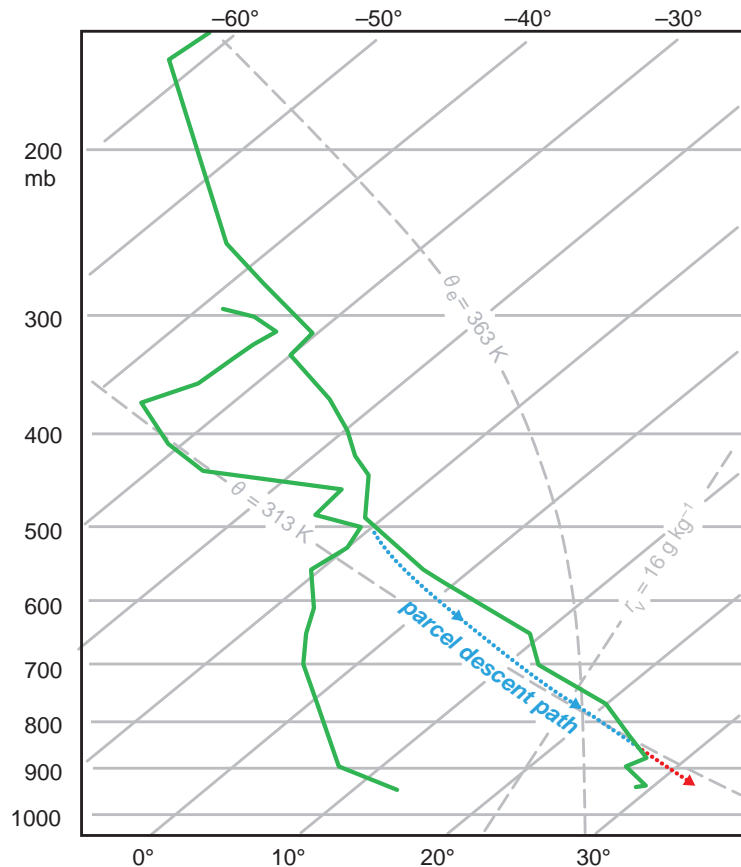


Figure 10.33 Skew T -log p diagram for Russell, KS, at 0440 UTC 24 June 1985. The expected heat-burst parcel trajectory is shown and colored blue (red) for the portions of the trajectory that are negatively (positively) buoyant. (Adapted from Johnson *et al.* [1989].)

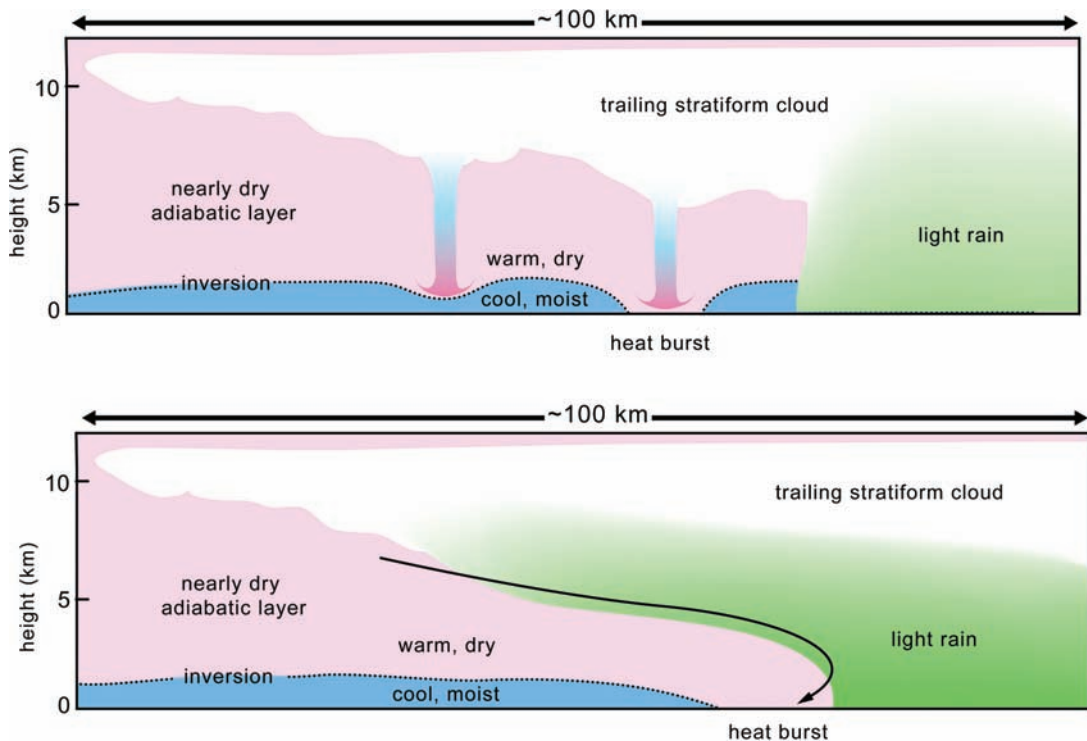


Figure 10.34 Depictions of two possible heat-burst mechanisms associated with the trailing stratiform regions of mesoscale convective systems: top, microbursts penetrating a shallow surface inversion, and bottom, descending rear inflow penetrating a surface inversion. Heat bursts can also occur in association with downdrafts from isolated thunderstorms penetrating a surface inversion (not shown). (Adapted from Johnson [2001].)

10.2.2 Damaging winds occurring in the absence of a strong downdraft

Many nontornadic damaging wind events occur in the absence of a nearby intense downdraft. Such is commonly the case within MCSs, wherein meso- β -scale cold pools can be associated with horizontal pressure gradients large enough to produce severe winds in the absence of intense meso- γ -scale downdrafts.¹⁸ Damaging winds also can result from the descent of a rear-inflow jet to the surface, that is, a relatively weak downdraft transports large horizontal momentum to the surface. Both mechanisms

tend to make the apex of a bow echo a favored location for high winds.

Recent field observations and numerical simulations¹⁹ have revealed that wind damage within squall lines also frequently coincides with the tracks of meso- γ -scale vortices embedded within the lines (Figure 10.35), sometimes referred to simply as *mesovortices* (Figure 10.36; also recall the small-scale vortex in Figure 9.24). The vortices can have a variety of origins. Some form in the same manner as the bookend vortices of bow echoes form: that is, from the lifting of vortex lines generated baroclinically within the cold pool by an updraft (see, e.g., Figure 9.27). Others may arise from horizontal shear instability along the gust front, although the horizontal wind shear implies vertical vorticity, and the vertical vorticity can only arise along the gust front if vorticity tilting is involved, assuming that the environment does not contain significant vertical vorticity.

¹⁸ It is not clear whether Fujita intended to restrict the usage of the term *downburst* to damaging wind events associated with intense meso- γ -scale downdrafts, as we have. Fujita's bow echo conceptual model (Figure 9.23) includes downbursts, even though it seems likely that the notion of a relatively small-scale (<10 km), intense downdraft producing the severe winds at the surface might not always be applicable in bow echo high-wind events.

¹⁹ Much of the understanding summarized in this paragraph is derived from the Bow Echo and MCV Experiment (BAMEX), which was conducted in the central Great Plains of the United States in 2003.

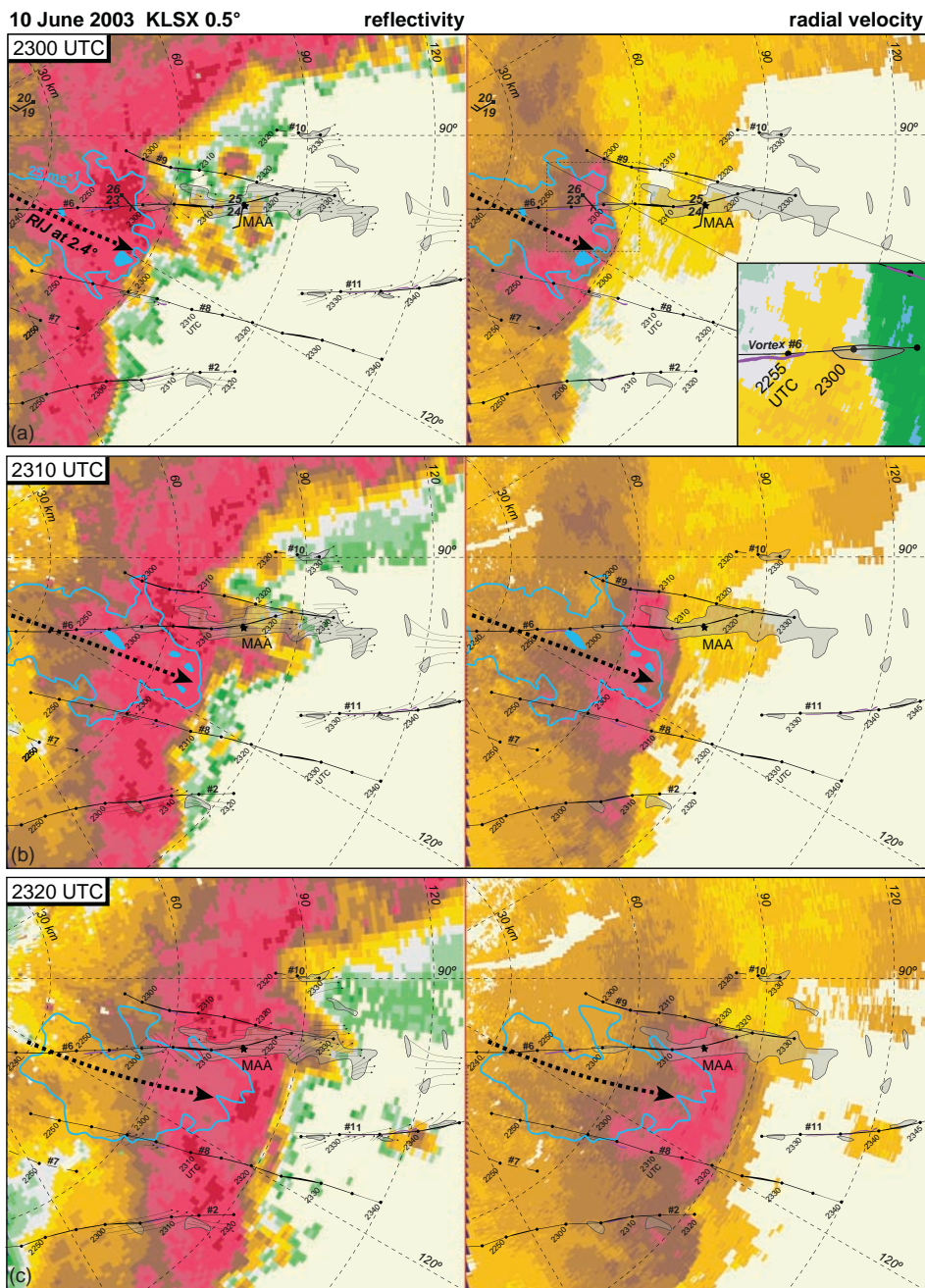


Figure 10.35 Damage survey from 10 June 2003 superimposed on 0.5° radar reflectivity data (dBZ) and ground-relative radial velocities (m s^{-1} ; cool [warm] colors are flow toward [away] from the radar) from the St. Louis (KLSX) radar at (a) 2300, (b) 2310, and (c) 2320. In all panels, the positions of tornadic and nontornadic mesovortices are shown as solid and dashed black lines, respectively. Couplet locations and time stamps are indicated along the mesovortex tracks. Tornado paths are colored purple. The blue contour represents the 25 m s^{-1} radial velocity isopleth observed at 2.4° with values greater than 30 m s^{-1} filled. The gray shaded regions are where wind damage was observed. The thick-dashed line represents the approximate location of a rear-inflow jet. Thin-dashed lines are the range–azimuth grid lines for the KLSX radar. Surface data are also plotted in (a), showing the winds, temperature, and dewpoint. The starred location is MidAmerica Airport (MAA). The inset diagram in (a) displays storm-relative radial velocities in the area of the dashed box. (From Atkins *et al.* [2005]. Courtesy of the American Meteorological Society.)

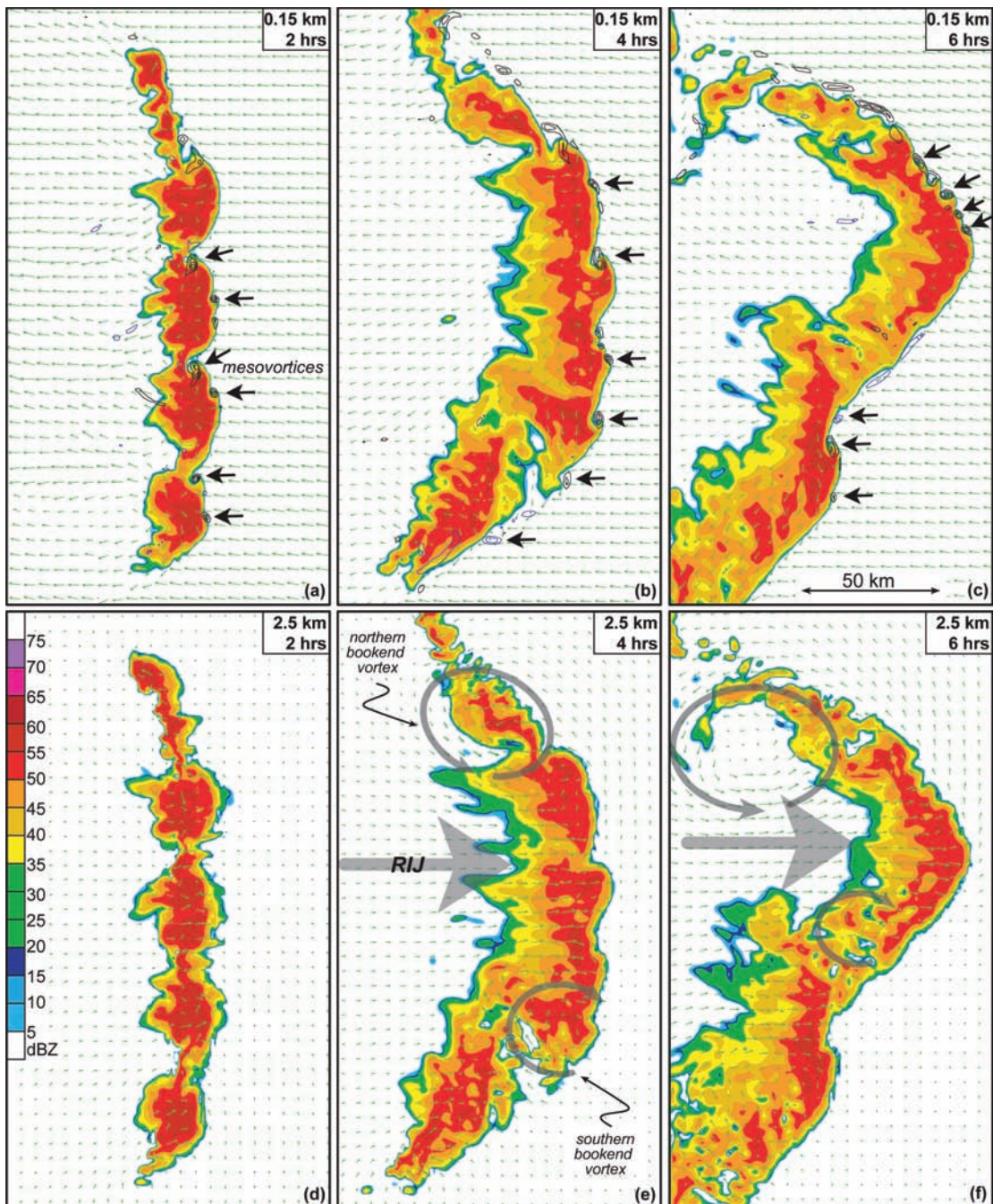


Figure 10.36 Simulation of a bow echo, depicting radar reflectivity (dBZ) in color, along with storm-relative winds (m s^{-1} , green) and vertical vorticity ($\times 10^{-3} \text{ s}^{-1}$, black) at 2, 4, and 6 h. Data at 0.15 km and 2.5 km are shown in (a)–(c) and (d)–(f), respectively. Locations of prominent mesovortices at 0.15 km are shown with black arrows. 'RIJ' indicates the rear-inflow jet, and additional broad gray arrows indicate the circulations associated with bookend vortices. (From Atkins and Cunningham [2006]. Courtesy of the American Meteorological Society.)

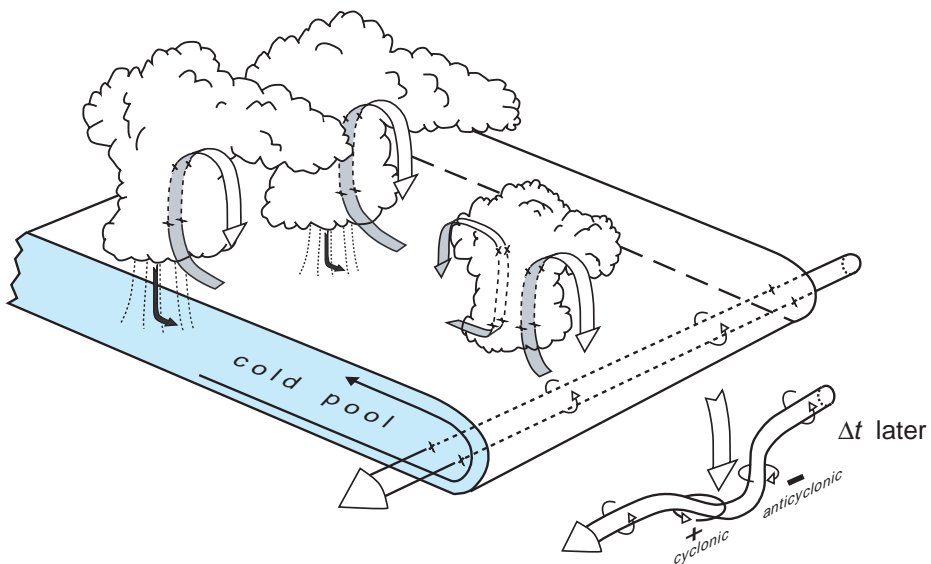


Figure 10.37 Schematic model illustrating the origin of vortex couples along the outflow boundary of the bow echo studied by Wakimoto *et al.* [2006b]. The diagram at the bottom right represents the distortion of the vortex tube with increasing time. Also note the similarity with Figure 10.3a. (Adapted from Wakimoto *et al.* [2006b].)

Other mesovortices are believed to form from the *downward* tilting of vortex lines within the cold pool (Figure 10.37). In numerical simulations, the Coriolis force also influences the development of mesovortices in nontrivial ways, with MCSs developing stronger cyclonic mesovortices when the Coriolis force is included.²⁰ Regardless of how the details of mesovortex formation vary from one mesovortex to another, the basic idea is that the horizontal winds within the outflow are enhanced by the superpositioning of the wind fields of the mesovortices and the outflow. For westerly outflow winds and a cyclonic mesovortex, the strongest winds would be observed on the equatorward flank of the mesovortex, where the two wind fields add constructively. The presence of shallow stable layers in the environment reduces the threat of damaging straight-line winds. Such stable layers prevent the rear-inflow jet from reaching the surface. Ongoing research continues to explore the roles of ambient stratification and the variety of means by which mesovortices may form.

10.3 Hailstorms

10.3.1 Hail formation and growth

The growth of hailstones depends on the complicated interaction between the airflow within a deep convective

²⁰ See Weisman and Trapp (2003) and Trapp and Weisman (2003).

cloud and precipitation particles. Hailstones primarily grow by collection of supercooled cloud droplets and raindrops. A few ice particles are present in the storm updraft because of the presence of freezing nuclei; however, most of the hydrometeors in the updraft remain as supercooled liquid (cloud droplets and raindrops can remain unfrozen down to temperatures as low as -40°C). After approximately 5–10 minutes of ice crystal growth via vapor deposition, ice crystals acquire sufficient mass to descend relative to the supercooled cloud droplets, which freeze immediately upon contact with the ice particles. The collection of supercooled cloud droplets leads to the formation of nearly spherical graupel particles (the original ice crystals that grew by way of vapor deposition are aspherical) having diameters of a few millimeters.

The growing ice particles become larger, fall faster relative to the air, and consequently sweep out more supercooled droplets because of a larger cross-sectional area, leading to an even faster growth rate. Continued growth due to the collection of individual droplets that freeze on contact leads to a layer of low density ice that looks opaque under a microscope. Once the growth rate becomes large, the hailstone temperature may be above 0° owing to the increased energy transferred to the ice in the fusion process, such that collected supercooled droplets may not freeze immediately on contact but instead first flow across the hailstone surface, filling in gaps within the

stone between earlier freezing sites, thereby increasing the hailstone density and forming a layer of clear ice. The hailstone density in such layers may ultimately approach that of pure ice. As the hailstone continues collection growth, its fall speed continues to increase, and the rate of growth also continues increasing as long as the hailstone remains in a region where supercooled liquid water content is large.

The final size that the hailstone can achieve is a function of the liquid water concentration and the time that the hailstone can reside in the region of high supercooled liquid water content. The total residence time of the hailstone in the region of large supercooled liquid water content depends on the updraft strength and hailstone fall speed, as well as the ability of the hailstone to make multiple excursions through the updraft. The fall speed of an ice hydrometeor, v_t , depends on the air density, ice density, size, shape, and smoothness via

$$v_t = \sqrt{\frac{4g\rho_i D}{3c_d\rho}}, \quad (10.20)$$

where ρ_i is the ice density (0.9 g cm^{-3} is a typical density), ρ is the air density, D is the diameter of the ice hydrometeor, and c_d is a dimensionless drag coefficient that accounts for air resistance (c_d is a function of the shape and smoothness of the hydrometeor; typical values of c_d range from 0.4 to 1.0). Dozens of studies have derived empirical relationships between fall speeds and hail size. One such empirical relationship for ice hydrometeors having diameters in the $0.1\text{--}8 \text{ cm}$ range (such particles are referred to as graupel until they reach a diameter of 0.5 cm , at which point they are referred to as hail) and an air density of $\approx 1 \text{ kg m}^{-3}$ is

$$v_t \approx 9D^{0.8}, \quad (10.21)$$

where v_t is in m s^{-1} and D is in cm (Figure 10.38).²¹

The ideal conditions for hail growth are when hailstone fall speeds nearly match the updraft velocity when the ice particles enter the portion of the updraft where the supercooled liquid water concentration is large. In this scenario, hailstones remain suspended in a region of high liquid water content for a long period of time. The hailstones can grow to diameters of 10 cm or larger if the updraft is intense, and ultimately the hailstones descend when their fall speeds exceed the updraft speed. If the fall speed of growing ice particles is only a few m s^{-1} and the updraft is especially strong (say, $>35 \text{ m s}^{-1}$), then the ice particles may simply ascend rapidly through the updraft and be ejected into the anvil, thereby missing out on the long growth period that is possible if the ice particles can remain in the

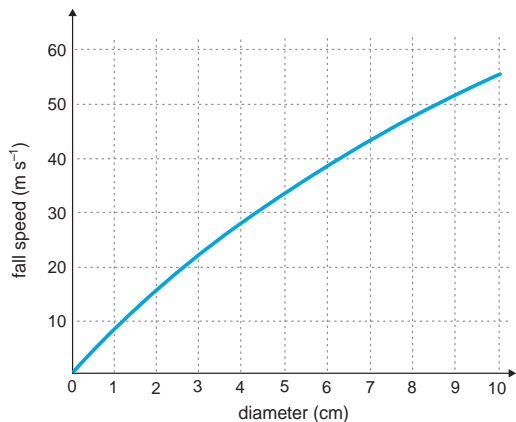


Figure 10.38 Hailstone terminal fall speed as a function of diameter assuming $v_t = 9D^{0.8}$. (Particles less than 0.5 cm in diameter are referred to as graupel.)

region of high supercooled liquid water content for a longer time period. When the updraft is tilted, hailstone fall speeds can stay matched with the updraft speed as the hailstone grows by having the hailstone drop progressively closer to the updraft core where vertical motion is the strongest. If the hailstone is ejected aloft, certain trajectories will allow it to fall back into the updraft below it and repeat the growth process until its fall speed finally exceeds even the strongest updraft speeds. Hailstones experiencing repeated vertical excursions often have alternating layers of clear and cloudy ice owing to their residence in regions of varying liquid water content during each trip. In summary, the development of a hailstone from a small embryo to a giant hailstone depends on complex interactions between the airflow and microphysics. If the updraft is too strong when the stone is small, it can be ejected high in the anvil. If the updraft is too weak to hold the stone aloft as it grows, it falls out prematurely.

The size of the hailstone that reaches the ground also depends on the amount of melting occurring during the hailstone descent. If the in-cloud freezing level within the updraft is at a high elevation and hailstones fall back *through* the updraft rather than being ejected *from* the updraft, a significant amount of melting may occur before the hailstone even emerges from the cloud. Less melting occurs when hailstones fall outside of the buoyant updraft, where hailstones are exposed to drier air and a lower melting level. As discussed in Section 10.2.1, the lower the height of the wet-bulb-zero level, the lower the amount of hail melting en route to the ground. For hailstones that descend through environmental air, the total melting decreases as the environmental moisture decreases. Hailstones also may

²¹ See Pruppacher and Klett (1997).

fall through downdrafts. In that case, hailstones reach the ground faster and are therefore larger, all else being equal, because less time is available for melting en route to the ground.

10.3.2 Forecasting hail size

Based on the above discussion, it is apparent that predicting the size of hailstones reaching the surface requires knowledge of many unobservable processes, at least in a forecasting setting. All that is remotely predictable is a rough estimate of the maximum updraft speed (based on the environmental CAPE and shear) and the degree of melting once a hailstone exits the cloud (based on the wet-bulb-zero level). As noted above, even intense updrafts are no guarantee of large hailstones because of the importance of favorable hailstone trajectories and high supercooled liquid water content. And even if large hailstones *do* form, there is no guarantee that large hailstones will reach the surface, owing to melting within and outside of the cloud.

CAPE and the height of the wet-bulb-zero level are among the most popular parameters that have been used to predict the likelihood of severe hail. Unfortunately, observed hail size is poorly correlated with both parameters. The correlations are presumably so small because of all of the complexities described in Section 10.3.1. Furthermore, CAPE is not always a good predictor of updraft strength; its predictive utility for the maximum

updraft speed decreases as the conditions deviate further from parcel theory. Although CAPE and the wet-bulb-zero height (and vertical wind shear) are individually of limited utility for hail size forecasting, considering CAPE, wet-bulb zero height, and wind shear together is probably the best strategy for predicting large hail. A large CAPE–shear product and low wet-bulb-zero height favors the largest hail.

Once a storm is detected by radar, the presence of large hail can sometimes be inferred from observation of a *hail spike* in reflectivity data, also known as a *flare echo* or *three-body scattering signature*. The hail spike is found along a radial, immediately behind a region of large hail (Figure 10.39). The signature is the result of the radar transmission being scattered by airborne large hail toward the ground (which may be covered with hail), back to the airborne large hail, and then finally back to the radar. The radar's receiver detects the backscattered power that has taken this circuitous route and, owing to the time delay associated with the extra path length, the radar interprets the range of the signal incorrectly, erroneously displaying weak echo at ranges beyond the range to the large hail but along the same radial. The anomalous velocity data within the hail spike signature are an additional clue that the reflectivity signature is indeed the result of this 'extra' scattering. The maximum reflectivity within a radar echo is generally not a good indicator of hail size. On the other hand, dual-polarimetric radar data (see the Appendix), if available, can provide the most accurate estimates of hail size.

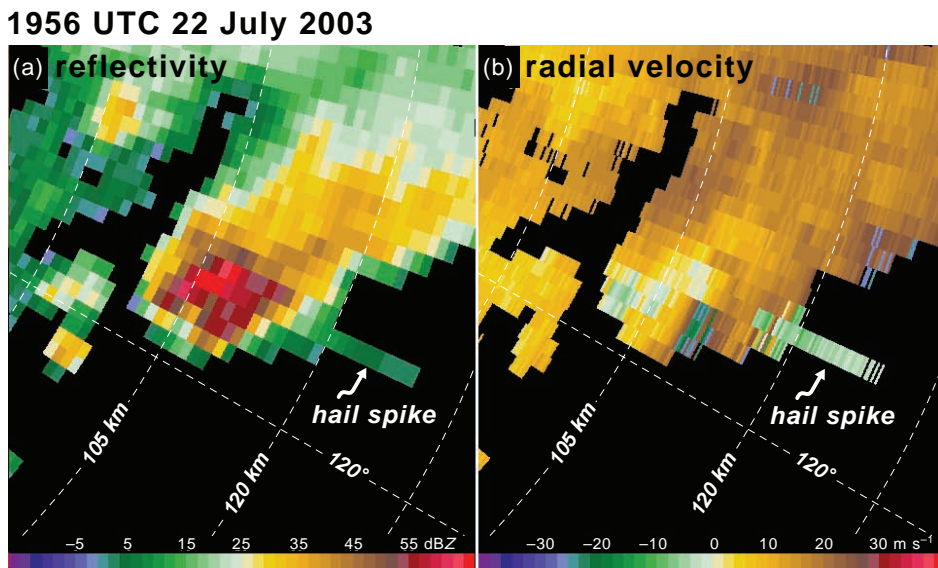


Figure 10.39 An example of a flare echo (hail spike) as viewed in (a) reflectivity (dBZ) and (b) radial velocity (m s^{-1}) data. The data were obtained from the 2.4° elevation scan of the State College, PA, radar at 1956 UTC 22 July 2003.

10.4 Flash floods

Flash floods are the deadliest hazard associated with convection worldwide. While tornado- and hurricane-related deaths have decreased steadily over the last 50 years, at least in the United States, no doubt owing to better warnings and technology, flash-flood-related casualties have not decreased comparably. The nature of the flash flood forecasting problem is complicated by the interaction of meteorology with hydrology. For example, a given rainfall's chances to produce a flash flood are substantially affected by factors such as antecedent precipitation amounts, the size of the drainage basin, the topography of the drainage basin, the amount of urban use within the basin, dam failures, etc. Although our focus is on the meteorological aspects of flash flooding, we do not wish to imply that hydrological aspects cannot be equally as important.

If \bar{R} is the average rainfall rate and D is the duration of the rainfall, then the total accumulation of precipitation, P , is

$$P = \bar{R}D; \quad (10.22)$$

that is, the greatest precipitation accumulations occur where it rains the hardest for the longest.²² In general, rainfall duration increases with decreasing storm translation speeds and thus as mean wind speed decreases, or, in the case of MCSs, rainfall duration is maximized when *cell motion* is opposed by the *propagation* of the convective system, in which case the *system motion* can be quasi-stationary (Figure 10.40). This situation is most often observed when a warm front or stationary front interacts with a low-level jet, such that new cells are repeatedly triggered on the rear flank of the MCS, leading to a *backbuilding* MCS. Convective cells and their associated high rainfall rates can move repeatedly over the same areas, a phenomenon known as (*radar*) *echo training*. In these events, the low-level wind shear tends to be roughly perpendicular to the front, and midlevel wind shear tends to be approximately parallel to the front. In general, leading stratiform (LS) MCSs tend to move more slowly than parallel stratiform (PS) and trailing stratiform (TS) MCSs, and are therefore more prone to produce extreme rainfall accumulations. In LS MCSs the propagation (which depends on how the gust front or synoptic front interacts with the environmental wind shear) tends to oppose the cell motion (approximately equal to the mean wind in the cloud layer), or at least not have a direction that coincides with the cell motion, whereas in TS MCSs the ground-relative propagation and cell motion tend to be in the same direction (Figure 9.8). The duration of heavy precipitation at a fixed location also depends on the structure of the convection;

²² This relationship is sometimes known as the *first law of quantitative precipitation forecasting* (QPF). The term has been attributed to C. F. Chappell (Doswell et al. 1996).

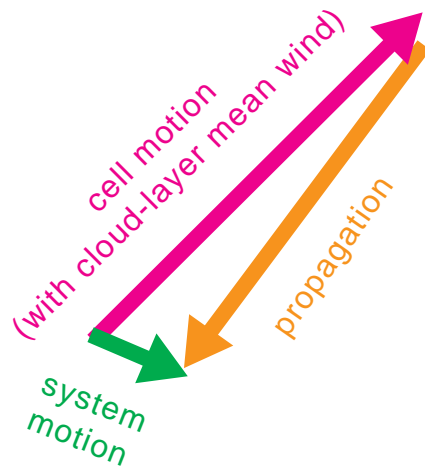


Figure 10.40 Schematic showing a near-cancellation between cell motion (magenta) and propagation (orange). The system motion (green) is very slow toward the southeast. (Adapted from Doswell et al. [1996].)

for example, an MCS with a large stratiform precipitation region poses a greater threat than an MCS with a small stratiform precipitation region, all else being equal.

The instantaneous rainfall rate, R , at a particular location is proportional to the (upward) vertical moisture flux, wr_v , where w is the vertical velocity and r_v is the water vapor mixing ratio of the rising air. Thus, for significant precipitation, rising air should have a large water vapor content and a rapid ascent rate. However, not all of the water vapor entering a cloud falls out as precipitation. The amount that falls out depends on the *precipitation efficiency*—the ratio of the measured precipitation rate at the ground to the water vapor flux through the cloud base. In other words, we can express the instantaneous rainfall rate as

$$R = Ewr_v, \quad (10.23)$$

where E is the precipitation efficiency.

Some investigators have found an inverse relationship between the precipitation efficiency of observed convective storms and the vertical wind shear of the environment (Figure 10.41), whereas numerical simulations of storms have suggested a somewhat more complicated relationship (Figure 10.42). Only in environments of small to moderate CAPE ($<2000\text{ J kg}^{-1}$) do the precipitation efficiencies of simulated storms decrease with increasing shear, in agreement with observations. In environments having higher CAPE, the precipitation efficiency of simulated storms has been found to increase with increasing shear. We are unaware of any more recent reconciliation of these seemingly conflicting past findings. On one hand,

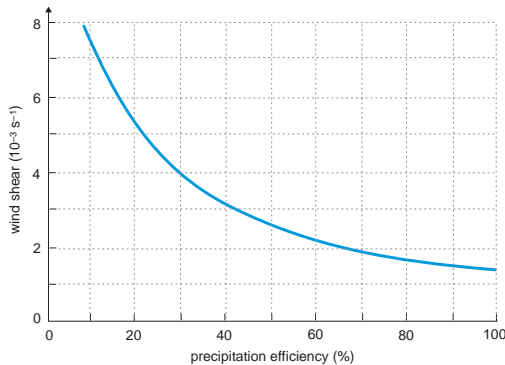


Figure 10.41 Relationship between precipitation efficiency and vertical wind shear derived from studies of 14 High Plains thunderstorms. (Adapted from Marwitz [1972] and Browning [1977].)

determining the precipitation efficiency in observed storms is somewhat error-prone because of the challenges of measuring rainfall reaching the surface and the amount of water vapor entering a cloud. On the other hand, the numerical simulations cited above utilized a simple, warm-rain microphysics parameterization. This simple microphysics parameterization might not be adequate for conducting a reliable precipitation efficiency study. It is somewhat intuitive that precipitation efficiency would decrease with

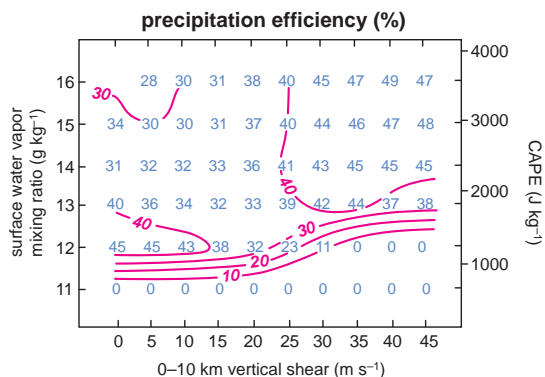


Figure 10.42 Relationship between precipitation efficiency and vertical wind shear in the numerical simulation study conducted by Weisman and Klemp (1982). The abscissa displays the magnitude of the 0–10 km shear, although nearly all of the shear was located in the 0–6 km layer. The ordinate displays water vapor mixing ratio at the surface, as well as CAPE (the vertical temperature profile was held constant; thus, CAPE depended only on the surface mixing ratio).

increasing shear as shown in Figure 10.41, owing to the fact that the entrainment of environmental air tends to increase with increasing shear. The entrainment of typically dry, environmental air leads to evaporation of hydrometeors and downdraft production, both of which reduce the amount of precipitation that reaches the surface (within downdrafts, compressional warming results in evaporation). Furthermore, in large-shear (and large-storm-relative-wind) environments, precipitation might be expected to fall farther from the updraft and be exposed to more environmental air and evaporation during its descent to the surface, further reducing the precipitation efficiency.

Strong vertical wind shear may not always be detrimental to heavy precipitation, however, even if it turns out that shear generally does reduce precipitation efficiency. As discussed in Chapter 8, convection tends to be better organized and thus potentially longer lived in environments containing significant wind shear. Long-lived convective storms might lead to a greater total precipitation accumulation than might have otherwise occurred, even though the instantaneous precipitation efficiency might not necessarily be large. For example, slow-moving HP supercells are occasionally responsible for extreme rainfall and flooding.²³

As the environmental relative humidity increases, precipitation efficiency increases because the evaporation rate decreases, even if a nontrivial amount of entrainment occurs. Moreover, an isolated updraft is more likely to experience substantial entrainment than an updraft embedded within a larger cloud system, since the environment of the latter is much more nearly saturated than the environment in the vicinity of the isolated updraft.

Although the environmental wind shear and environmental relative humidity might be fairly well known from soundings or numerical model guidance in a real-time forecasting setting, precipitation efficiency is influenced by other factors that are virtually impossible for a forecaster to assess, such as microphysical processes within clouds. For example, clouds with a large depth below the freezing level may be more efficient heavy rain producers owing to increased warm rain processes compared with clouds in which a significant depth is located above the freezing level. Cell mergers promote increased precipitation efficiency, not just because of a reduction of entrainment, but also because of the possible merging of two different drop-size distributions, which may increase the collision and coalescence rates within the updraft formed by the merger.

In summary, the worst flash floods resulting from DMC tend to occur when a number of ingredients conspire to maximize precipitation accumulations: slow storm motion or system motion (increases D ; generally associated with

²³ See Smith *et al.* (2001).

weak mean winds or, in the case of an MCS, cell motion that is nearly cancelled by propagation), large low-level water vapor concentration in the presence of strong updrafts (increases wr_v and therefore R), large environmental relative humidity (increases E), a significant cloud depth below the freezing level (increases E), and perhaps weak vertical wind shear (probably increases E ; weak shear also tends to be correlated with weak mean winds). It is probably safe to say that precipitation efficiency is high enough in almost all episodes of DMC that it would not be the difference-maker in terms of whether or not an extreme rainfall event occurs. In the worst flash floods, larger mesoscale effects are usually involved, such as cell mergers, backbuilding convection along slow-moving or stalled fronts, backbuilding due to lifting by a convectively

generated gravity wave,²⁴ or topographic effects that influence the evolution of the convection or the runoff of its precipitation (interactions between conditionally unstable, moist airstreams and fronts, convectively generated gravity waves, or mountainous terrain are usually required in order to have a near-cancellation between the cell motion and the system propagation). All of the aforementioned sounding and wind profile characteristics, as well as topographic influences, were present in two of the worst flash flood events in United States history: the 31 July 1976 Big Thompson Canyon, CO, flood and the 9 June 1972 Black Hills, SD, flood.²⁵ Figure 10.43 summarizes the large-scale

²⁴ See Schumacher and Johnson (2008).

²⁵ See Maddox *et al.* (1978).

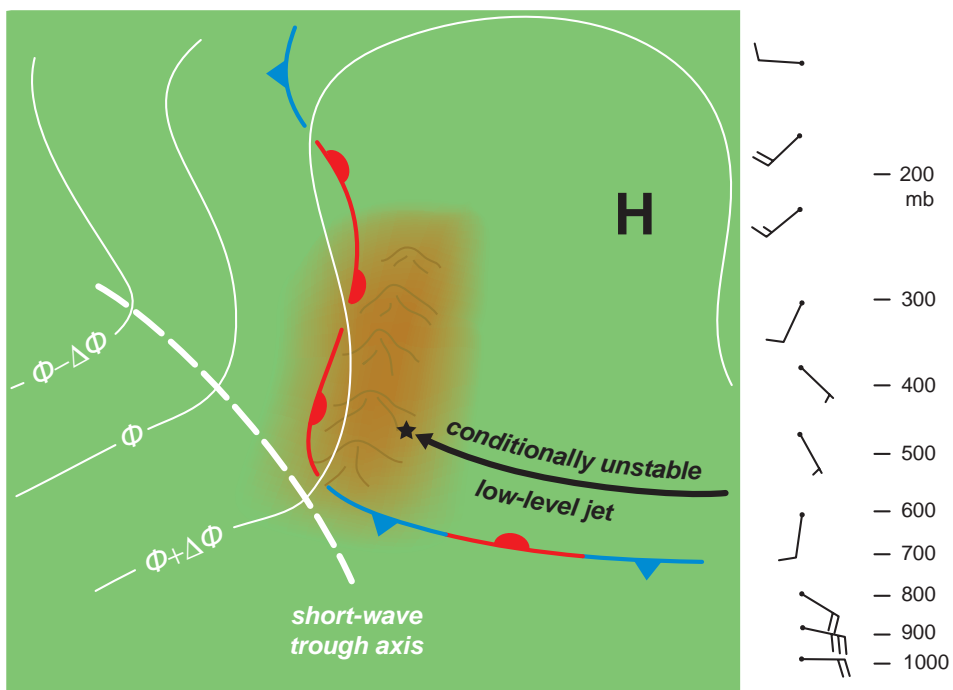


Figure 10.43 Composite illustration of typical synoptic-scale conditions associated with severe orographic flash flood events. The worst flooding occurs in the vicinity of the star, which also marks the location represented by the vertical wind profile shown on the right (wind barbs are in knots). The flood-producing convection tends to be initiated downstream of a negatively tilted, midtropospheric short-wave trough (white midlevel height contours are indicated schematically) in an environment of weak southerly winds and divergence aloft. The short-wave trough contributes to the destabilization of the environment and advection of midlevel moisture into the threat area. At the surface, the most prominent feature is a large high-pressure system (the center of the high is indicated with a black letter 'H') downstream of a midtropospheric ridge axis. A slow-moving or stalled front is typically found to the south, and a postfrontal band of strong, conditionally unstable, moist easterly winds flows upslope and initiates new cells repeatedly over approximately the same area. Slow updraft motions, nearly stationary convective system motion as a result of the new cell generation being tied to the terrain, a moist and warm sounding, and weak vertical wind shear all contribute to the heavy precipitation accumulations. (Adapted from Pontrelli *et al.* [1999].)

conditions associated with the worst flash flood events, including the Big Thompson Canyon and Black Hills cases.

Further reading

Tornadoes

- Atkins, N. T., M. L. Weisman, and L. J. Wicker, 1999: The influence of preexisting boundaries on supercell evolution. *Mon. Wea. Rev.*, **127**, 2910–2927.
- Brandes (1978).
- Brandes, E. A., 1981: Finestructure of the Del City–Edmond tornadic mesocirculation. *Mon. Wea. Rev.*, **109**, 635–647.
- Brooks *et al.* (2003).
- Davies-Jones (1986).
- Davies-Jones, R. R. J. Trapp, and H. B. Bluestein, 2001: Tornadoes and tornadic storms. *Severe Local Storms, Meteor. Monogr.*, No. 50, 167–221.
- Doswell, C. A., III, and D. W. Burgess, 1993: Tornadoes and tornadic storms: a review of conceptual models. *The Tornado: its Structure, Dynamics, Prediction, and Hazards*, Geophys. Monogr., No. 79, Amer. Geophys. Union, 161–172.
- Fiedler, B. H., 1993: Numerical simulation of axisymmetric tornadogenesis in forced convection. *The Tornado: its Structure, Dynamics, Prediction, and Hazards*, Geophys. Monogr., No. 79, Amer. Geophys. Union, 41–48.
- Howells, P. A. R. Rotunno, and R. K. Smith, 1988: A comparative study of atmospheric and laboratory-analogue numerical tornado-vortex models. *Quart. J. Roy. Meteor. Soc.*, **114**, 801–822.
- Klemp, J. B., and R. Rotunno, 1983: A study of the tornadic region within a supercell thunderstorm. *J. Atmos. Sci.*, **40**, 359–377.
- Lee and Wilhelmson (1997a).
- Lee and Wilhelmson (1997b).
- Leslie, L. M., and R. K. Smith, 1978: The effect of vertical stability on tornadogenesis. *J. Atmos. Sci.*, **35**, 1281–1288.
- Maddox, R. A. L. R. Hoxit, and C. F. Chappell, 1980: A study of tornadic thunderstorm interactions with thermal boundaries. *Mon. Wea. Rev.*, **108**, 322–336.
- Markowski, P. M. E. N. Rasmussen, and J. M. Straka, 1998: The occurrence of tornadoes in supercells interacting with boundaries during VORTEX-95. *Wea. Forecasting*, **13**, 852–859.
- Markowski, P. M. J. M. Straka, and E. N. Rasmussen, 2003: Tornadogenesis resulting from the transport of circulation by a downdraft: idealized numerical simulations. *J. Atmos. Sci.*, **60**, 795–823.

Markowski, P. M. J. M. Straka, E. N. Rasmussen, R. P. Davies-Jones, Y. Richardson, and J. Trapp, 2008: Vortex lines within low-level mesocyclones obtained from pseudo-dual-Doppler radar observations. *Mon. Wea. Rev.*, **136**, 3513–3535.

Rotunno, R., 1986: Tornadoes and tornadogenesis. *Mesoscale Meteorology and Forecasting*, P. S. Ray, Ed. Amer. Meteor. Soc., 414–436.

Trapp, R. J., 1999: Observations of non-tornadic low-level mesocyclones and attendant tornadogenesis failure during VORTEX. *Mon. Wea. Rev.*, **127**, 1693–1705.

Trapp, R. J., 2000: A clarification of vortex breakdown and tornadogenesis. *Mon. Wea. Rev.*, **128**, 888–895.

Walko, R. L., 1993: Tornado spin-up beneath a convective cell: required basic structure of the near-field boundary layer winds. *The Tornado: its Structure, Dynamics, Prediction, and Hazards*, Geophys. Monogr., No. 79, Amer. Geophys. Union, 89–95.

Downbursts

- Betts, A. K., and M. F. Silva Dias, 1979: Unsaturated downdraft thermodynamics in cumulonimbus. *J. Atmos. Sci.*, **36**, 1061–1071.
- Fujita (1978).
- Fujita, T. T., 1981: Tornadoes and downbursts in the context of generalized planetary scales. *J. Atmos. Sci.*, **38**, 1511–1534.
- Fujita (1985).
- Fujita, T. T., and F. Caracena, 1977: An analysis of three weather-related aircraft accidents. *Bull. Amer. Meteor. Soc.*, **58**, 1164–1181.
- Hjelmfelt, M. R., 1988: Structure and life cycle of microburst outflows observed in Colorado. *J. Climate Appl. Meteor.*, **27**, 900–927.
- Kingsmill, D. E., and R. M. Wakimoto, 1991: Kinematic, dynamic, and thermodynamic analysis of a weakly sheared severe thunderstorm over northern Alabama. *Mon. Wea. Rev.*, **119**, 262–297.
- Mahoney, W. P., III, and A. R. Rodi, 1987: Aircraft measurements on microburst development from hydrometeor evaporation. *J. Atmos. Sci.*, **44**, 3037–3051.
- Proctor, F. H., 1988: Numerical simulations of an isolated microburst. Part I: Dynamics and structure. *J. Atmos. Sci.*, **45**, 3137–3160.
- Srivastava, R. C., 1985: A simple model of evaporatively driven downdrafts: application to microburst downdraft. *J. Atmos. Sci.*, **42**, 1004–1023.
- Srivastava, R. C., 1987: A model of intense downdrafts driven by melting and evaporation of precipitation. *J. Atmos. Sci.*, **44**, 1752–1773.

- Wakimoto, R. M., 2001: Convectively driven high wind events. *Severe Local Storms, Meteor. Monogr.*, No. 50, 255–298.
- Wakimoto, R. M. C. J. Kessinger, and D. E. Kingsmill, 1994: Kinematic, thermodynamic, and visual structure of low-reflectivity microbursts. *Mon. Wea. Rev.*, **122**, 72–92.
- Wilson, J. W., and R. M. Wakimoto, 2001: The discovery of the downburst: T. T. Fujita's contribution. *Bull. Amer. Meteor. Soc.*, **82**, 49–62.
- Hailstorms**
- Edwards, R., and R. L. Thompson, 1998: Nationwide comparisons of hail size with WSR-88D vertically integrated liquid water and derived thermodynamic sounding data. *Wea. Forecasting*, **13**, 277–285.
- Heymsfield, A. J. A. R. Jameson, and H. W. Frank, 1980: Hail growth mechanisms in a Colorado storm. Part II: Hail formation processes. *J. Atmos. Sci.*, **37**, 1779–1807.
- Jameson, A. R., and A. J. Heymsfield, 1980: Hail growth mechanisms in a Colorado storm. Part I: Dual-wavelength radar observations. *J. Atmos. Sci.*, **37**, 1763–1778.
- Kennedy, P. C., and A. G. Detwiler, 2003: A case study of the origin of hail in a multicell thunderstorm using *insitu* aircraft and polarimetric radar data. *J. Appl. Meteor.*, **42**, 1679–1690.
- Knight, C. A., and N. C. Knight, 2001: Hailstorms. *Severe Local Storms, Meteor. Monogr.*, No. 50, 223–254.
- List, R., 1986: Properties and growth of hailstones. *Thunderstorm Morphology and Dynamics*, E. Kessler, Ed., 2nd edn. University of Oklahoma Press, 259–276.
- Morgan, G. M., Jr., and P. W. Summers, 1986: Hailfall and hailstorm characteristics. *Thunderstorm Morphology and Dynamics*, E. Kessler, Ed., 2nd edn. University of Oklahoma Press, 237–257.
- Ziegler, C. L. P. S. Ray, and N. C. Knight, 1983: Hail growth in an Oklahoma multicell storm. *J. Atmos. Sci.*, **40**, 1768–1791.

Flash floods

- Chappell, C. F., 1986: Quasi-stationary convective events. *Mesoscale Meteorology and Forecasting*, P. S. Ray, Ed., Amer. Meteor. Soc., 289–310.
- Davis, R. S., 2001: Flash flood forecast and detection methods. *Severe Local Storms, Meteor. Monogr.*, No. 50, 481–525.
- Doswell *et al.* (1996).
- Lamb, D., 2001: Rain production in convective storms. *Severe Local Storms, Meteor. Monogr.*, No. 50, 299–321.
- Maddox, R. A. C. F. Chappell, and L. R. Hoxit, 1979: Synoptic and meso- α scale aspects of flash flood events. *Bull. Amer. Meteor. Soc.*, **60**, 115–123.
- Maddox *et al.* (1978).
- Pontrelli *et al.* (1999).
- Schumacher, R. S., and R. H. Johnson, 2005: Organization and environmental properties of extreme-rain-producing mesoscale convective systems. *Mon. Wea. Rev.*, **133**, 961–976.
- Schumacher, R. S., and R. H. Johnson, 2006: Characteristics of U.S. extreme rain events during 1999–2003. *Wea. Forecasting*, **21**, 69–85.

PART IV

Orographic Mesoscale Phenomena

11

Thermally Forced Winds in Mountainous Terrain

Part IV treats orographic mesoscale phenomena. In this chapter we consider the diurnally varying winds generated by the heating and cooling of sloped terrain, or by the differences in the diurnal temperature ranges within valleys compared with surrounding plains. Sometimes generically referred to as *mountain-valley wind systems* or just *mountain winds*, these thermally forced circulations do not require the presence of ambient winds and large-scale pressure gradients. Mesoscale phenomena that arise from interactions between ambient winds and terrain, such as gravity waves, severe downslope winds, trapped cold-air surges, gap winds, and wake vortices, are the foci of Chapters 12 and 13.

Most of the early studies on mountain-valley wind systems originated in Germany and Austria, and investigated the effects of the complex Alpine topography. Mountain-valley wind systems are characterized by a reversal of wind direction twice each day and develop over a wide range of scales. The circulations tend to be most significant when the large-scale wind is weak and the diurnal cycle has its greatest amplitude, that is, when nights are clear and days are sunny. The main components of the mountain-valley wind system are *slope winds*, which are upslope during the day and downslope at night, and *valley winds*, which are upvalley during the day and downvalley at night.¹ Slope winds and valley winds are discussed separately in greater detail in the following sections.

¹ Sometimes the term *valley winds* refers to upvalley winds, and sometimes the term *mountain winds* refers to downvalley winds.

11.1 Slope winds

Slope winds are driven by the horizontal buoyancy gradients that arise between air in contact with a heated or cooled sloped surface and air at the same altitude that is far enough away from the surface that it is relatively unaffected by the heating and cooling of the surface. The daytime heating of a mountain slope induces upslope or *anabatic* winds, and the night-time radiative cooling of a mountain slope generates downslope or *katabatic* winds. The momentum equations in a coordinate system oriented along and perpendicular to a slope of constant inclination angle α are²

$$\frac{\partial u}{\partial t} + u \frac{\partial u}{\partial s} + w \frac{\partial u}{\partial n} = -\frac{1}{\rho} \frac{\partial p'}{\partial s} + B \sin \alpha - \frac{\partial \bar{u}'w'}{\partial n} \quad (11.1)$$

$$\frac{\partial w}{\partial t} + u \frac{\partial w}{\partial s} + w \frac{\partial w}{\partial n} = -\frac{1}{\rho} \frac{\partial p'}{\partial n} + B \cos \alpha \approx 0, \quad (11.2)$$

where s and n are the upslope and slope-normal (i.e., perpendicular to the mountainside) directions, respectively, u and w are the upslope and slope-normal wind components, respectively, B is buoyancy, p' is the perturbation pressure, and $\partial \bar{u}'w' / \partial n$ is the turbulent momentum flux divergence (turbulent friction). The other turbulent momentum fluxes in (11.1) have been neglected, as have all of the turbulent fluxes in (11.2). The Coriolis force also has been neglected. Note that the rhs of (11.2) is approximately zero if the slope flow is in hydrostatic balance normal to the slope (sometimes called *quasi-hydrostatic* balance).

² See Mahrt (1982) and Haiden (2003).

The driving force for an upslope (downslope) wind in (11.1) is the buoyancy force B , which is generated by warming (cooling) the layer of air adjacent to the slope. Alternatively, the essence of slope winds can be explained using the horizontal vorticity equation (2.90), where the heating and cooling of a sloped surface leads to horizontal buoyancy gradients and baroclinic vorticity generation. The baroclinically generated vorticity field implies upslope (downslope) winds adjacent to a heated (cooled) slope (Figures 11.1 and 11.2).

Regarding the perturbation pressure field ($p' = p'_h + p'_{nh}$, where p'_h is the hydrostatic pressure perturbation and p'_{nh} is the nonhydrostatic pressure perturbation; recall Section 2.5.4), for gentle slopes (i.e., small α) p' is dominated by p'_h . Thus, the magnitude of p' largely depends on the magnitude and depth of the temperature perturbation associated with the slope wind. In the case of a downslope wind, the depth of the relatively cool slope flow layer typically increases with decreasing elevation; thus, $p' (>0)$ increases in the downslope direction and the downward acceleration driven by the buoyancy force is opposed by an adverse (directed opposite the wind velocity, i.e., upslope in this case) pressure gradient force ($\partial p'/\partial s < 0$). In the case of a relatively warm upslope wind, which typically deepens in the upslope direction, $p' (< 0)$ decreases in the upslope direction and the upward acceleration driven by the buoyancy force is augmented by an upslope-directed pressure gradient force ($\partial p'/\partial s < 0$) (Figure 11.3). Thus, daytime anabatic winds tend to be stronger than nighttime katabatic winds. If the terrain is steeply sloped, then a significant part of the pressure perturbation may be from the nonhydrostatic part; in these situations, both upslope and downslope winds may experience an adverse pressure gradient force that opposes the acceleration due to buoyancy.

Thermally driven upslope winds usually attain their maximum a few hours after sunrise, when the temperature contrast between the sunlit slopes and the valley atmosphere is largest. Peak speeds of $1-5 \text{ m s}^{-1}$ at a height of $10-20 \text{ m}$ above the surface are typical. Thermally driven downslope winds tend to be a maximum near sunset when slopes are first shaded. Peak speeds are usually $1-4 \text{ m s}^{-1}$ and at a height of $1-3 \text{ m}$. Both upslope and downslope winds are characterized by a significant degree of intermittency.

Although the depth of slope winds varies with elevation and time of day/night, the depth of upslope (downslope) flows ranges from 50 to 150 m ($10-40 \text{ m}$) on average. The depth of upslope winds tends to increase with increasing elevation, as mentioned above, as well as time of day, with the latter result attributable to the effects of decreasing static stability. Conversely, the depth of downslope winds increases with decreasing elevation (see, e.g., Figure 11.2), with a reasonable estimate of the depth of the downslope flow at any particular location along the slope being roughly 5% of the drop in elevation from the crest of the ridge (e.g., 100 m below the crest, one might expect a 5 m deep downslope flow).³ Downslope winds also tend to decrease in depth as the night progresses as a result of increasing static stability.

The evolution of isentropic surfaces and the low-level wind field from the pre-dawn to afternoon hours in the vicinity of a mountain with an extended region of sloped terrain, similar to the terrain of the Front Range of the Rocky Mountains and the High Plains that extend to the east, is shown in Figure 11.4. An ambient westerly wind also is present. In the early morning hours, upslope flow develops within the developing mixed layer east of the highest terrain (Figure 11.4b). The mixing of westerly

³ See Whiteman (2000).

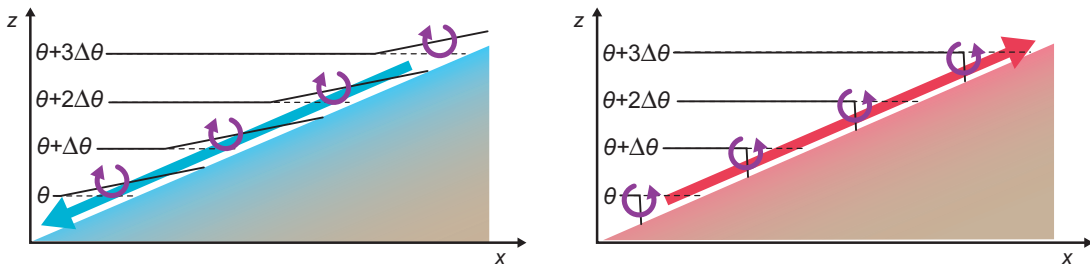


Figure 11.1 Illustration of the generation of (left) downslope and (right) upslope winds by the cooling and heating of sloped terrain, respectively. The thick solid black contours are isentropes that have been modified by surface cooling and heating, respectively. The dashed black lines are unmodified isentropes. The purple arrows indicate the sense of the horizontal vorticity production by the horizontal buoyancy gradient. The broad blue and red arrows indicate the sense of downslope and upslope flow along the surface, respectively, implied by the baroclinic horizontal vorticity generation.

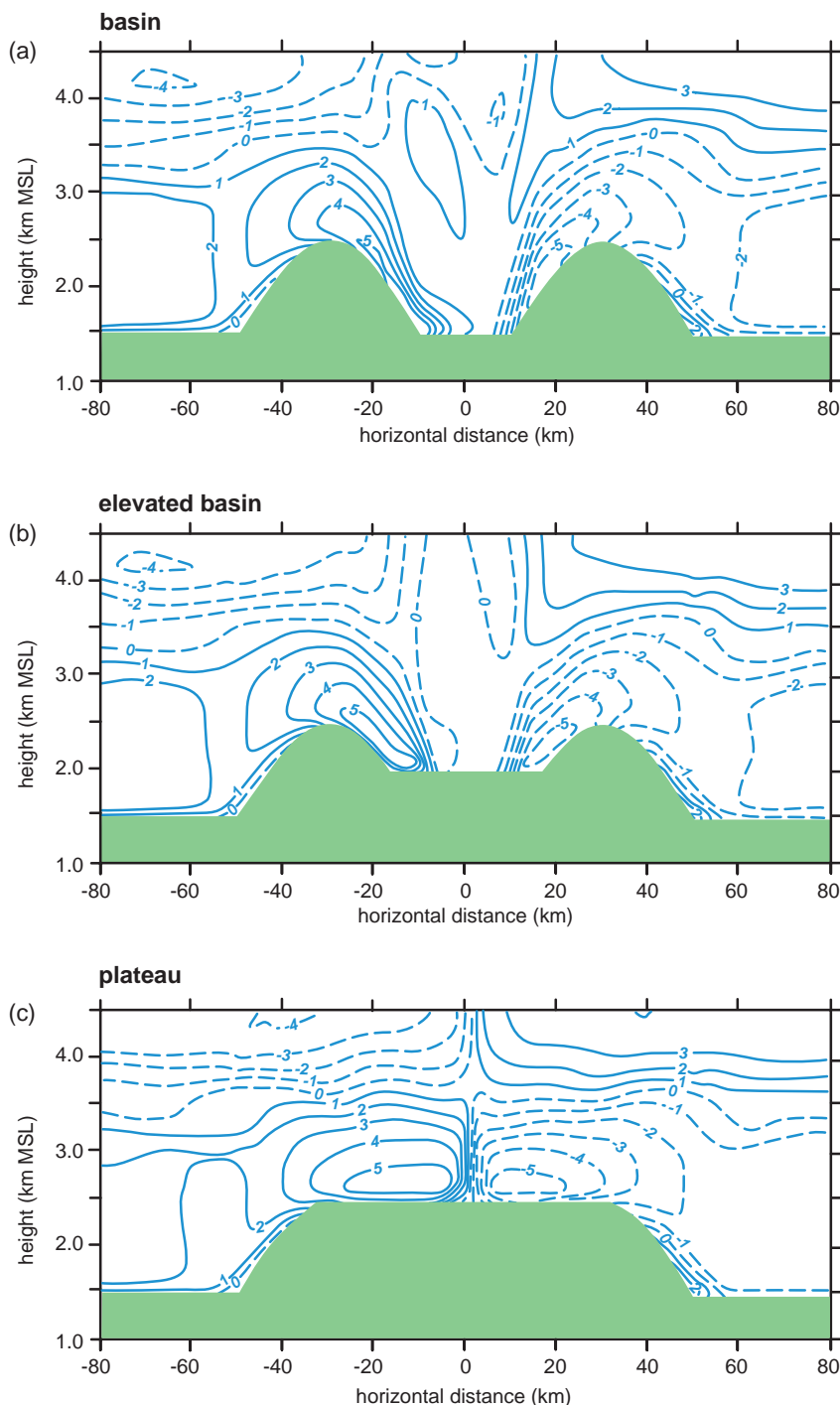


Figure 11.2 The early evening (2000 LST) zonal wind component (m s^{-1}) in a suite of idealized, two-dimensional numerical simulations involving diurnally varying radiative forcing, simple topography, and no ambient wind. In addition to obvious downslope winds, there are larger-scale winds that have also been thermally forced by the valley wind generation mechanism. (Adapted from de Wekker *et al.* [1998].)

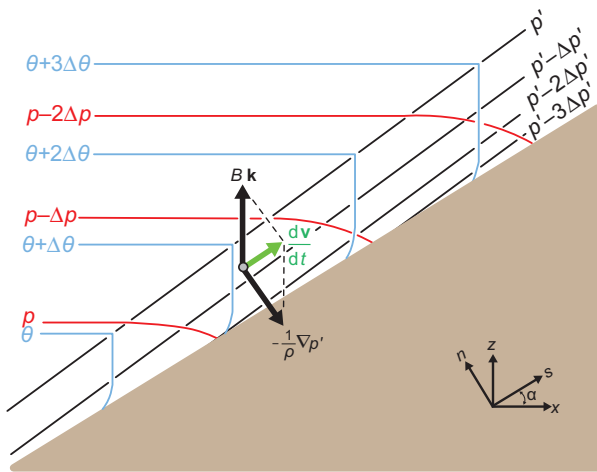


Figure 11.3 Force diagram in the case of a daytime, thermally driven upslope flow in which the depth of the temperature perturbation increases in the upslope direction. Isentropes are blue, perturbation pressure contours are black, and full pressure contours are red. The perturbation pressure gradient gives a small positive contribution to upslope acceleration in this case. Perpendicular to the slope, the flow is quasi-hydrostatically balanced. In the special case of along-slope thermal homogeneity, the perturbation pressure contours would be parallel to the slope and the perturbation pressure gradient would be exactly perpendicular to the terrain. (Adapted from Haiden [2003].)

momentum from aloft into the developing mixed layer is inhibited by the remnant stable layer that caps the mixed layer. The depth of the mixed layer having upslope winds grows in time (Figure 11.4c). It is also apparent from Figure 11.4 (as evidenced by the closed θ_1 contour atop the mountain in Figs. 11.4b,c) why the first cumulus clouds of the day (and showers and thunderstorms, if the atmosphere is sufficiently unstable) tend to be found over mountain tops. In the presence of an ambient wind, as in the case depicted in Figure 11.4, the plume of greatest buoyancy is shifted downwind.

A region of horizontal convergence is present in the wind field near the upslope side of the maximum horizontal potential temperature (and buoyancy) gradient, and the convergence maximum shifts downslope as the day progresses. Convective clouds, including thunderstorms, also can be initiated within this convergence maximum on occasion, and convection that develops over the mountain summit often is invigorated if and when it reaches this convergence zone and the enhanced moisture to its east (this convection can develop into large convective

systems that persist well into the night-time hours).⁴ By afternoon, at least on relatively quiescent days on which convective storms do not develop, the inversion layer is completely eroded, which allows westerly winds aloft to be mixed downward to the surface on the eastern plain. The downward mixing of westerly momentum destroys the low-level upslope flow (Figure 11.4d). As one might expect, the duration of the low-level upslope flow is lengthened (shortened) as the westerly winds aloft decrease (increase). Westerly, downslope winds continue after sunset, although these winds are a result of slope wind dynamics rather than the downward mixing of westerly momentum from aloft (Figure 11.4a).

11.2 Valley winds

Valley winds, also sometimes referred to as *valley breezes*, blow parallel to the longitudinal axis of a valley and arise from temperature differences that form within a valley or between a valley and a nearby plain, assuming that the valley eventually widens to a degree where it can be considered a plain. Winds blow upvalley (i.e., toward the direction of the mountains from the direction of the plains) during the day and downvalley (i.e., from the direction of the mountains toward the direction of the plains) at night (Figure 11.5), although the valley floor need not be sloped in order for valley winds to arise. The driving mechanism for valley winds is a difference in the amplitude of the diurnal temperature cycle along the axis of the valley, or between the valley, which typically has sloped sidewalls, and the surrounding plains (Figures 11.6 and 11.7). During the day, the air in the interior of the valley warms more than an equivalent vertical column of air over the adjacent plains, leading to a hydrostatically produced horizontal pressure gradient force directed from the plains toward the valley; thus, air flows upvalley (Figure 11.8). At night, the atmosphere in the valley interior cools more than the atmosphere over the plains, leading to a reversal of the horizontal pressure gradient and a downvalley flow (Figure 11.8). The combined airflow of nocturnal downvalley and downslope winds is sometimes referred to as a *drainage wind*.

Upvalley winds typically begin in the morning within a few hours after sunrise and persist until shortly after sunset, after which time they are replaced by downvalley winds. The downvalley winds, in turn, persist until being replaced by upvalley winds the next morning. Peak speeds attained by up- and downvalley winds can reach $5-10 \text{ m s}^{-1}$. Mature

⁴ The interaction of this slope-flow-induced convergence zone with mountain-induced gravity waves can also contribute significantly to the development of the convective systems. See Tripoli and Cotton (1989a, b).

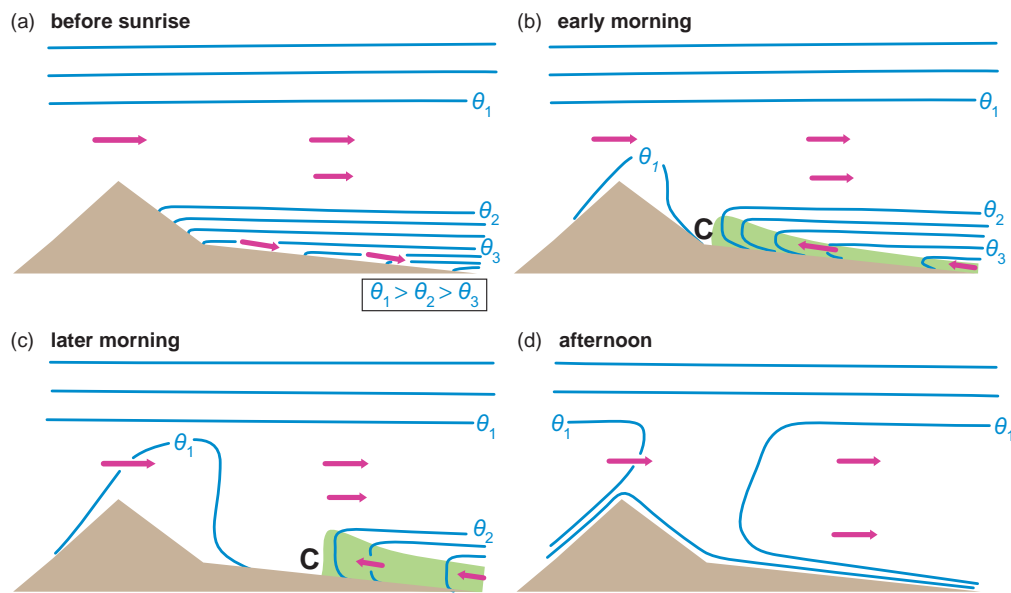


Figure 11.4 Evolution of potential temperature and winds from (a) before sunrise to (b) early morning to (c) late morning to (d) afternoon as a result of the development of a thermally forced anabatic wind (the previous night's katabatic wind is evident in [a]). An ambient wind also is present, blowing from left to right. The shaded region indicates a shallow mixed layer that contains the upslope flow, and the C at the upwind edge indicates the convergence zone. (Adapted from Banta [1990].)

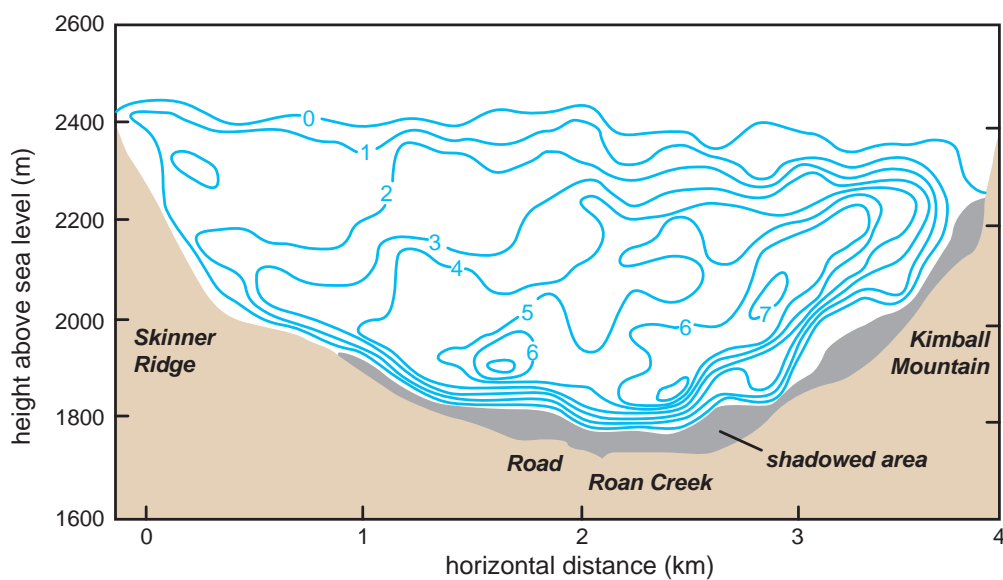


Figure 11.5 Vertical cross-section of downvalley nocturnal drainage winds as viewed by a Doppler lidar. The isotachs indicate wind speeds out of the page ($m s^{-1}$). (Adapted from Neff [1990].)

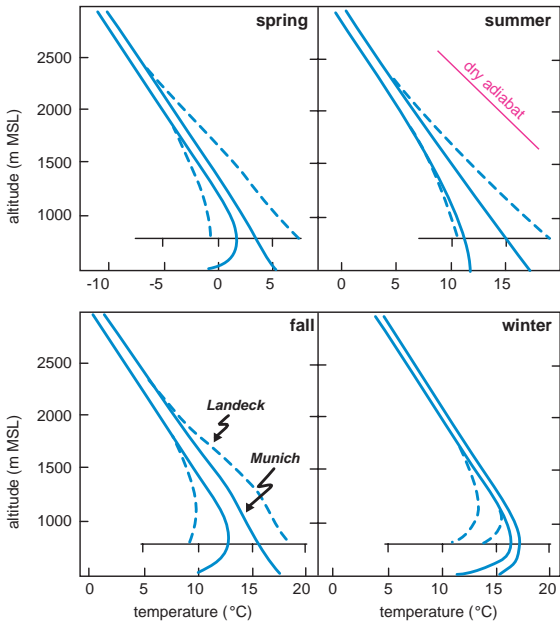


Figure 11.6 Schematic vertical temperature profiles for a valley location (dashed lines, Landeck, Germany, at 821 m MSL in the Inn Valley) and for a location on the adjacent plain (solid lines, Munich, Germany, at 529 m MSL) at 0600 and 1500 UTC for spring, summer, fall, and winter. (Adapted from Whiteman [1990], whose figure was adapted from Nickus and Vergeiner [1984].)

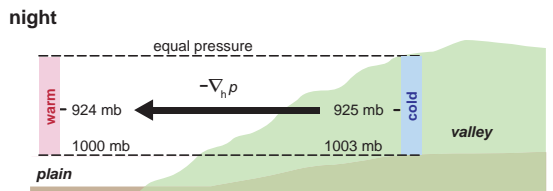
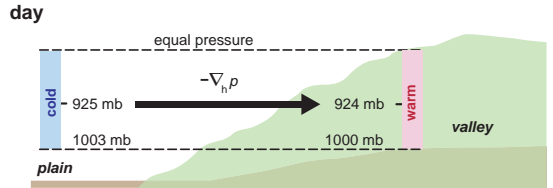


Figure 11.8 Illustration of the origin of the horizontal pressure gradient that drives valley winds. (Adapted from Whiteman [1990], whose figure was adapted from a paper by Hawkes [1947].)

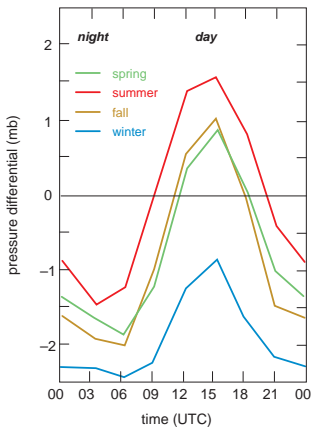


Figure 11.7 Daily evolution of the horizontal pressure differential at 550 m MSL between a location on the plains (Munich, Germany) and a deep valley station (Innsbruck, Austria) on sunny days. (Adapted from Whiteman [1990], whose figure was adapted from Nickus and Vergeiner [1984].)

up- and downvalley flows tend to span the depth of the valley. On rare occasions the valley flows are shallower and overrun by a significant return flow called an *antiwind*. Such return flows are usually not observed directly because they tend to lie above the crests of the surrounding terrain. When the return flow occurs at such heights, it is usually too weak to detect because it is not confined to a channel like the lower branch of the circulation.

As indicated above, the primary forcing for valley winds is the horizontal pressure gradient that ultimately results from a more pronounced diurnal cycle within the valley compared with the surrounding plains. The differences in the diurnal temperature cycle are most often explained by way of the first law of thermodynamics, which, in the case of $dp/dt = 0$, can be written as

$$Q = C_p \frac{dT}{dt} = \rho c_p V \frac{dT}{dt}, \quad (11.3)$$

where Q is the heating rate [J K^{-1}]; this ultimately results from the sensible heat flux, which results from an imbalance between the net radiation incident at the surface and the latent and ground heat fluxes via (4.56)], C_p is the heat capacity at constant pressure, c_p is the specific heat at constant pressure, ρ is the air density, V is the volume of air, and dT/dt is the rate of temperature change. From (11.3) it is apparent that the same solar radiation flux through equal areas topping a valley and a plain results in greater warming of the smaller volume of valley air. Similarly, a smaller valley air volume will cool more at night than the surrounding plain. Thus, valleys have amplified diurnal temperature cycles.

The amplification of the diurnal temperature cycle is often quantified in terms of the *topographic amplification factor* (TAF), where

$$\text{TAF} = \frac{\left[\frac{A_{xy}(h)}{V_{\text{valley}}} \right]}{\left[\frac{A_{xy}(h)}{V_{\text{plain}}} \right]} = \frac{V_{\text{plain}}}{V_{\text{valley}}}, \quad (11.4)$$

where $A_{xy}(h)$ is the horizontal area through which solar radiation enters the tops of the volumes at height $z = h$ above the valley floor or plain, and V_{valley} and V_{plain} are the underlying volumes of the valley and plain, respectively. Note that $V_{\text{plain}} = hA_{xy}(h)$.

For a simple, unit-thickness, vertical cross-section through a valley, the TAF can be defined as

$$\text{TAF} = \frac{\left[\frac{W}{A_{xz_{\text{valley}}}} \right]}{\left[\frac{W}{A_{xz_{\text{plain}}}} \right]} = \frac{A_{xz_{\text{plain}}}}{A_{xz_{\text{valley}}}}, \quad (11.5)$$

where W is the width at the top of the cross-section, and $A_{yz_{\text{valley}}}$ and $A_{yz_{\text{plain}}}$ are the areas of the vertical cross-sections taken in the valley and adjacent plain, respectively. The numerator and denominator of (11.5) are the area-to-volume ratios for the valley and plain, respectively. In summary, the TAF is just a ratio, computed solely from the topography, of the amplitude of the diurnal temperature cycle in a valley compared with that at the same altitude over the adjacent plain (Figure 11.9).

Although the amplified diurnal temperature cycle within valleys has been identified as the primary driving force for valley winds, other effects have also been shown to contribute to valley winds, such as along-valley elevation changes (which produce upslope and downslope accelerations as discussed in Section 11.1), along-valley variations in the surface energy budget, and vertical motions associated with slope and valley wind circulations. With respect to along-valley variations in the surface energy budget, it is not difficult to imagine that albedo could vary in the along-valley direction if there is a glacier at the head of a valley and a forest at the base of the valley, or that soil moisture and thus the sensible heat flux could vary longitudinally within a valley (it conceivably could be drier near the higher-altitude head of the valley than at the lower-altitude base). Regarding the effect of vertical motions, the compensating subsidence within a valley occurring during the day as a result of upslope winds along valley sidewalls (i.e., the *cross-valley circulation*) has been found to enhance the relative pressure minimum within the valley that drives the upvalley flow.

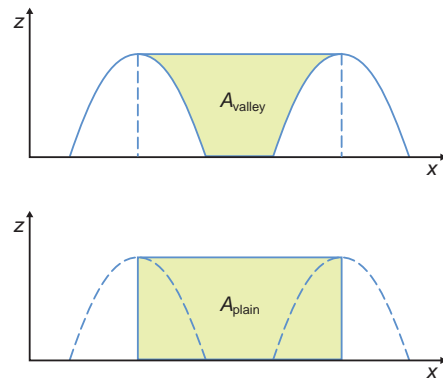


Figure 11.9 Illustration of the topographic amplification factor concept. For this idealized valley topography, the topographic amplification factor is simply the ratio of the areas of the shaded cross-sections over the plains (A_{plain}) and the valley (A_{valley}). (Adapted from de Wekker *et al.* [1998].)

Similarly, the convergence of nocturnal downslope winds in a valley is associated with rising motion in the valley interior (above the surface), and the resultant adiabatic cooling has been shown to contribute to the relative pressure excess in the valley that drives the downvalley flow. In summary, even if the sidewalls of a valley were vertical, the slope winds and compensating vertical motions would still be capable of generating temperature and (hydrostatic) pressure perturbations, horizontal pressure gradients, and valley winds.

Although slope and valley winds have been treated somewhat separately above, together they produce an intrinsically three-dimensional mountain-valley wind system. Slope and valley winds can influence each other, as touched upon above in the discussion of how compensating vertical motions in the cross-valley plane can contribute to valley winds. Figure 11.10 depicts the basic characteristics of slope and valley winds in a typical diurnal cycle; this figure is reproduced in a number of reviews on slope and valley winds. The superpositioning of slope and valley winds leads to a clockwise (counterclockwise) turning of the wind in time on the left (right) side of a valley if looking upvalley (Figure 11.11).

One final issue that has been ignored up to this point is the fact that opposing valley sidewalls are unavoidably heated unequally during much of the day (e.g., eastward-facing slopes are warmer than westward-facing slopes in the morning).⁵ The *cross-valley winds* that result from

⁵ The surface energy budget at any particular location in an actual valley depends on the fraction of the sky visible in the viewing hemisphere, called the *sky view factor*. The distribution of sky view factors leads to complicated spatial variations in downward longwave and diffuse solar radiation that are outside the scope of this book.

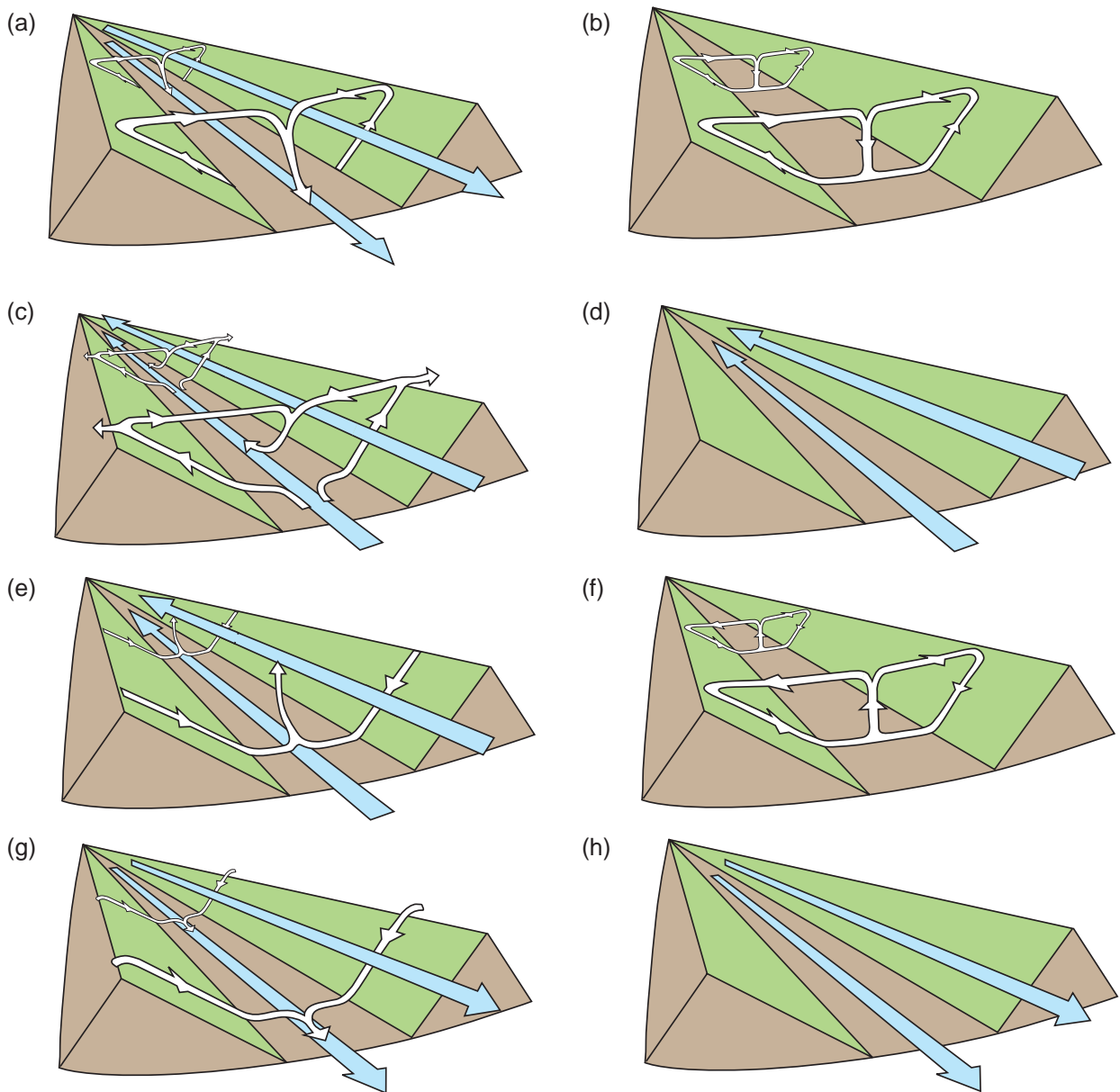


Figure 11.10 Diurnal cycle of valley and slope winds (after Defant [1951]). (a) Sunrise: onset of upslope winds (white arrows) and continuation of downvalley winds (blue arrows) from the previous night. The valley is colder than the plain. (b) Mid-morning (approximately 0900 LST): strong slope winds, transition from downvalley to upvalley wind. The valley is the same temperature as the plain. (c) Noon and early afternoon: diminishing slope winds; fully developed upvalley wind. The valley is warmer than the plain. (d) Late afternoon: slope winds have ceased, the upvalley wind continues. The valley is still warmer than the plain. (e) Evening: onset of downslope winds, diminishing upvalley wind. The valley is slightly warmer than the plain. (f) Early night: well developed downslope winds, transition from upvalley wind to downvalley wind. The valley and plain are at same temperature. (g) Middle of the night: downslope winds continue, the downvalley wind is fully developed. The valley is colder than the plain. (h) Late night to morning: downslope winds have ceased and the downvalley wind fills the valley. The valley is colder than the plain.

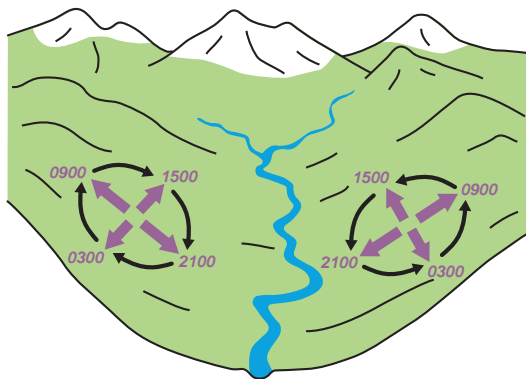


Figure 11.11 Winds on the left (right) side of a valley turn clockwise (counterclockwise) over the course of a day owing to the combined effects of slope and valley winds. Times are local standard time. (Adapted from Whiteman [1990], whose figure was adapted from a paper by Hawkes [1947].)

this differential heating can also contribute to the overall thermally forced mountain wind system, although cross-valley winds are usually weaker (typically $\leq 2 \text{ m s}^{-1}$) than slope winds and valley winds. Cross-valley winds blow from the colder valley sidewall toward the warmer valley sidewall at low levels, with a compensating flow in the opposite direction at higher altitudes within the valley. The exact magnitude of the cross-valley wind depends on the valley width and cross-valley temperature gradient; the strength of the flow increases with decreasing valley width and increasing temperature differences between the valley sidewalls.

Further reading

Banta, R. M., 1990: The role of mountains in making clouds. *Atmospheric Processes over Complex Terrain*, Meteor. Monogr., No. 45, 229–283.

- Defant, F., 1951: Local winds. *Compendium of Meteorology*, T. M. Malone, Ed. Amer. Meteor. Soc., 655–672.
- de Wekker, S. F. J., S. Zhong, J. D. Fast, and C. D. Whiteman, 1998: A numerical study of the thermally driven plain-to-basin wind over idealized basin topographies. *J. Appl. Meteor.*, **37**, 606–622.
- Egger, J., 1990: Observations of thermally developed wind systems in mountainous terrain. *Atmospheric Processes over Complex Terrain*, Meteor. Monogr., No. 45, 43–58.
- Haiden, T., 2003: On the pressure field in the slope wind layer. *J. Atmos. Sci.*, **60**, 1632–1635.
- Horst, T. W., and J. C. Doran, 1986: Nocturnal drainage flow on simple slopes. *Bound.-Layer Meteor.*, **34**, 263–286.
- Mahrt, L., 1982: Momentum balance of gravity flows. *J. Atmos. Sci.*, **39**, 2701–2711.
- McKee, T. B., and R. D. O’Neal, 1989: The role of valley geometry and energy budget in the formation of nocturnal valley winds. *J. Appl. Meteor.*, **28**, 445–456.
- Nickus, U., and I. Vergeiner, 1984: The thermal structure of the Inn Valley atmosphere. *Arch. Meteor. Geophys. Bioklim.*, **A33**, 199–215.
- Orville, H. D., 1964: On mountain upslope winds. *J. Atmos. Sci.*, **21**, 622–633.
- Rampanelli, G., D. Zardi, and R. Rotunno, 2004: Mechanisms of up-valley winds. *Mon. Wea. Rev.*, **61**, 3097–3111.
- Steinacker, R., 1984: Area–height distribution of a valley and its relation to the valley wind. *Contrib. Atmos. Phys.*, **57**, 64–71.
- Whiteman, C. D., 1990: Observations of thermally developed wind systems in mountainous terrain. *Atmospheric Processes over Complex Terrain*, Meteor. Monogr., No. 45, 5–42.
- Whiteman, C. D., 2000: *Mountain Meteorology: Fundamentals and Applications*. Oxford University Press.

12

Mountain Waves and Downslope Windstorms

In this chapter, our attention turns toward orographically induced wave motions, as these are perhaps the best understood and most common phenomena induced by air flowing over varying terrain. Orographically induced waves can propagate significant distances upward as well as downstream, depending on the environmental wind and temperature profiles. When sufficient moisture is present, such waves may lead to the formation of laminar lenticular clouds (Figures 12.1 and 12.2). Under the right conditions, wave energy originating from the terrain can propagate upward to the top of the troposphere. In other words, even relatively small mountains may affect the airflow a considerable distance above the ground. Under other atmospheric conditions, most of the wave energy may be trapped in a layer near the surface extending downstream from the mountain. Readers who are not already familiar with gravity wave dynamics are encouraged to read Chapter 6.

We first explore small-amplitude gravity waves triggered by topography using linear theory, as is traditionally done. Here we consider the simplest case first: flow over terrain that is two-dimensional in the x and z directions (i.e., mountain ridges that are infinite in length in the y direction). We then extend our analysis to isolated three-dimensional mountains. Finally, we investigate downslope windstorms, which can be hazardous to aviation.

12.1 Internal gravity waves forced by two-dimensional terrain

We start with the results for two-dimensional gravity waves obtained in Chapter 6. We assume our terrain varies in the

x direction such that waves are produced in the x - z plane. We assume a steady state ($\partial/\partial t = \omega = c = 0$) solution, because the forcing for the gravity waves is stationary (i.e., as the flow develops, after an initial transient period of adjustment, the solution should no longer change in time).¹ Owing to the steady-state assumption, our presumed solution for w' is

$$w' = \Re \left\{ \sum_k \hat{w}_k e^{ikx} \right\} \quad (12.1)$$

where \hat{w}_k is a complex amplitude that contains the z dependence, and the \Re operator indicates that we keep only the real part of the quantity in brackets (as in Chapter 6, we drop the \Re operator from this point forward and assume we are interested in only the real portion of any final variable). Note that the complex amplitude is necessary in order to fit a free-slip lower-boundary condition given any arbitrary terrain profile. This lower-boundary condition requires the flow to be tangential to the terrain (i.e., there is no flow in a direction perpendicular to the ground) such that the lower-boundary condition is $w'(x, 0) = \bar{u} \partial h_t / \partial x$, where $h_t(x)$ is the height of the terrain. At the upper boundary, we require that the flux of energy due to the perturbed flow either goes to zero as $z \rightarrow \infty$ or is directed upward from the surface (i.e., no source at infinity is allowed to propagate energy into the domain).

¹ The steady-state assumption has proved appropriate for capturing most aspects of mountain-wave dynamics except when the waves are very nonlinear, or when considering momentum flux (Chen *et al.*, 2005).

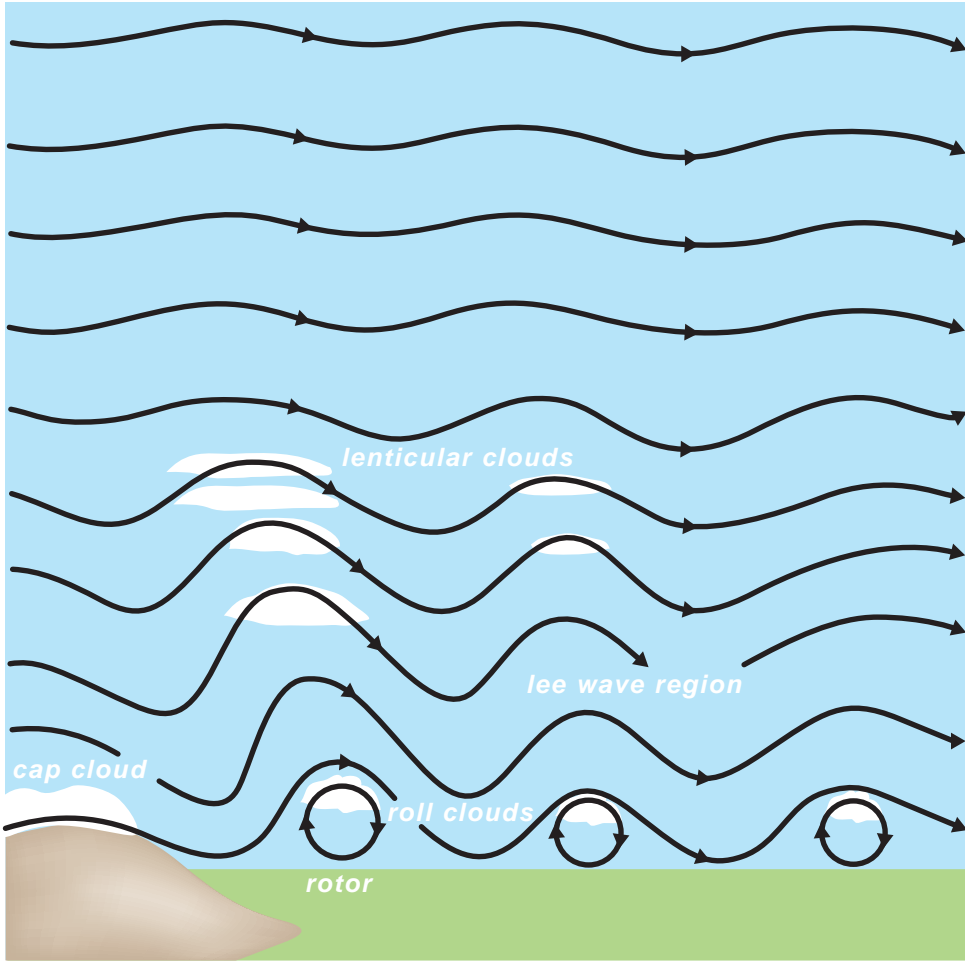


Figure 12.1 Trapped waves and associated clouds in the lee of a mountain ridge. (Adapted from an image provided by the Cooperative Program for Operational Meteorology, Education, and Training [COMET].)

The solution for \hat{w} for each mode is determined by the Taylor-Goldstein equation (6.36), which can be written as

$$\frac{d^2\hat{w}}{dz^2} + \left(\frac{N^2}{\bar{u}^2} - \frac{1}{\bar{u}} \frac{d^2\bar{u}}{dz^2} - k^2 \right) \hat{w} = \frac{d^2\hat{w}}{dz^2} + (\ell^2 - k^2) \hat{w} = 0, \quad (12.2)$$

where $\ell = \sqrt{\frac{N^2}{\bar{u}^2} - \frac{1}{\bar{u}} \frac{d^2\bar{u}}{dz^2}}$ is the *Scorer parameter*. As in Chapter 6, we obtain fundamentally different solutions depending on whether the term in parentheses is positive or negative (i.e., depending on whether $\ell^2 > k^2$). We shall look at solutions for several simplified environments.

12.1.1 Series of ridges with constant zonal wind and static stability

In our first simplified scenario, we consider a series of ridges separated by a distance L_x that defines a particular wavenumber $k = 2\pi/L_x$ of the terrain. We assume that the environmental wind is zonal with a constant speed, u_0 , and the static stability is constant such that N is constant. Under these conditions, $\ell^2 - k^2$ reduces to $N^2/u_0^2 - k^2$ and is constant, so the solution to (12.1), using (12.2), can be expressed

$$w' = A e^{i(kx+mz)} + B e^{i(kx-mz)}, \quad (12.3)$$



Figure 12.2 Photograph of a lenticular cloud associated with a vertically propagating gravity wave forced by topography.
Photograph by Marisa Ferger.

with $m = \sqrt{N^2/u_0^2 - k^2}$ and A, B representing constant complex amplitudes.

If m is real (i.e., $N^2 > u_0^2 k^2$), the solution is a plane wave in the x - z plane. To understand why we might expect a wave solution in this case, let us remind ourselves of the dispersion relation (6.42) under these conditions,

$$\begin{aligned}\omega &= u_0 k + \Omega = u_0 k \pm \frac{Nk}{(k^2 + m^2)^{1/2}} \\ &= u_0 k \pm N \cos \phi = 0,\end{aligned}\quad (12.4)$$

where ω is the ground-relative oscillation frequency, Ω is the intrinsic oscillation frequency, and ϕ is the angle of the oscillation with respect to the vertical. We shall assume that u_0 and k are both positive, so we choose the negative branch of (12.4). From the first equality, the only way that ω can be zero is if the intrinsic frequency, Ω , is equal to $-u_0 k$. This is a reasonable result, as we would expect that the intrinsic oscillation frequency should be forced by the flow over the terrain. The greater the wind velocity, the faster the oscillation as the flow follows the peaks and valleys. Similarly, as the wavenumber increases for a given wind speed, the peaks and valleys are encountered

at a faster rate, forcing a faster intrinsic oscillation frequency.

As long as the intrinsic frequency is less than N , the oscillation can be supported along an angle $\phi = \cos^{-1}(u_0 k / N)$ from the vertical. Thus, the wavefronts will tilt with height, having a negative slope for the A solution in (12.3) and a positive slope for the B solution (see Chapter 6). We need the upper boundary condition to determine which of these solutions to keep. Because this is a wave solution in the vertical, the amplitude will not go to zero with height, so the proper upper boundary condition instead requires that energy propagation be directed away from the energy source at the surface. The vertical group velocity for the A solution, which must then be positive (upward) in order to satisfy the upper boundary condition, is given by

$$c_{gz} = \frac{\partial \omega}{\partial m} = \frac{Nkm}{(k^2 + m^2)^{3/2}} > 0,\quad (12.5)$$

where we again have used the negative branch of (12.4). For the B solution, c_{gz} would be negative. Thus, we retain only the A solution, and our phase lines have a negative slope, whereby they tilt westward (upstream) with height.

The form for A can be determined from the lower-boundary condition to ensure that $w'(z = 0) = u_0 \partial h_t / \partial x$. For example, if our terrain profile is given by

$$h_t(x) = h_m \sin kx, \quad (12.6)$$

where h_m is the amplitude of the terrain profile, then we must have

$$w'(z = 0) = u_0 kh_m \cos kx. \quad (12.7)$$

Thus, referring to (12.3), $A = u_0 kh_m$, and our final solution when m is real is given by

$$w' = u_0 kh_m \cos(kx + mz). \quad (12.8)$$

Waves of this form are shown in Figure 12.3a.

On the other hand, if m is imaginary (i.e., $N^2 < u_0^2 k^2$), we substitute $m = i\mu$, where μ is a real number, and (12.3) then becomes

$$w' = Ae^{ikx} e^{-\mu z} + Be^{ikx} e^{\mu z}. \quad (12.9)$$

In this case, our upper boundary condition prohibits solutions that are unbounded with height, so the B solution

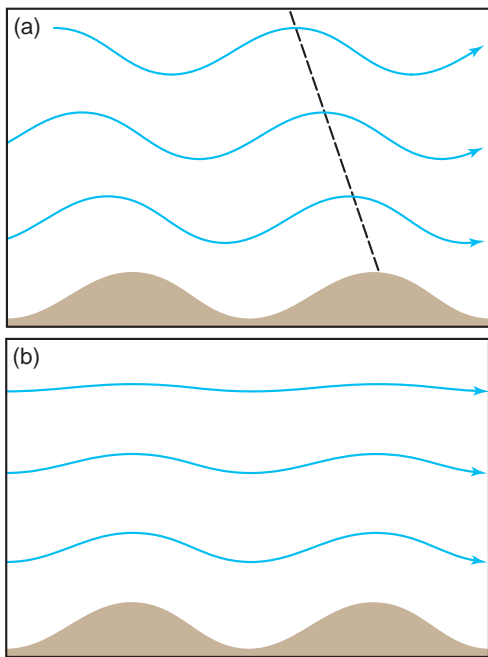


Figure 12.3 Streamlines in steady flow over an infinite series of sinusoidal ridges (a) for the case where $N^2 > u_0^2 k^2$ and (b) for the case where $N^2 < u_0^2 k^2$. The dashed line in (a) shows the phase of maximum upward displacement, which tilts westward with height. (Adapted from Durran [1990].)

is not viable. The lower-boundary condition leads to $A = u_0 kh_m$ such that the full solution is

$$w' = u_0 kh_m e^{-\mu z} \cos kx. \quad (12.10)$$

Evanescent waves of this type are shown in Figure 12.3b.

The physical reasoning behind these two solutions is exactly as described in Section 6.2.1. With buoyancy as the restoring force, the atmosphere can support oscillations with frequencies less than or equal to N for angles with respect to the vertical varying between 90° (purely horizontal) and 0° (purely vertical). Oscillations with a frequency greater than N cannot be supported. To relate this to the mountain wave problem, we must realize that the flow over the terrain is driving an oscillation at a frequency with a magnitude equal to $u_0 k$. As long as this frequency is less than N , we can find a slanted path along which the oscillation can be supported. Once the frequency exceeds N , no such path is possible and the waves simply decay with height.

12.1.2 Isolated ridge with constant zonal wind and static stability

The theory presented in the previous section leads to an easy interpretation of gravity wave behavior based on a single forced frequency of oscillation due to flow over a series of equally spaced ridges. However, an endless series of ridges is not a common form of topography (except perhaps in central Pennsylvania!). More often, the topography consists of an isolated mountain or a single mountain chain, approximated as a single two-dimensional ridge. In this section, we extend the results of the previous section to such an isolated ridge. The flow remains two-dimensional but is somewhat more complicated, as many different wavelengths are now associated with the topography.

Because the topography is no longer represented by a single wave mode, we must perform a Fourier transform of the topographic profile to reveal the relevant wavenumbers. We then solve for the vertical velocity corresponding to each mode in wavenumber space and perform an inverse Fourier transform to obtain $w'(x, z)$, with the weights for each wavenumber determined by the Fourier transform of the topography.² One commonly assumed profile is the ‘Witch of Agnesi’³ profile given by

$$h_t(x) = \frac{h_m a^2}{x^2 + a^2}, \quad (12.11)$$

² See Durran (2003a).

³ The name for this function was originally the *curve of Agnesi*, named after Maria Agnesi, in Italian. A misreading of the name resulted in the conversion of *curve* to *witch* in English.

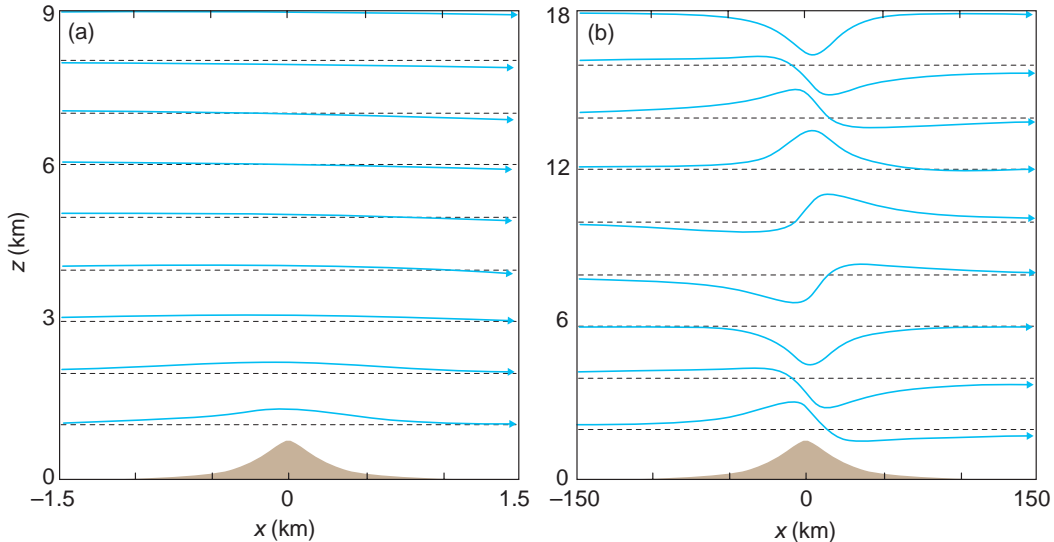


Figure 12.4 Streamlines in steady airflow over an isolated ridge when (a) $u_0 a^{-1} \gg N$ and (b) $u_0 a^{-1} \ll N$. (Adapted from Durran [1986a].)

which has the desirable properties of asymptotically approaching zero as $x \rightarrow \infty$ and having a width that is easily tuned by varying a , the shape parameter. The horizontal wavelengths associated with the terrain will be determined by the value of a , with longer wavelengths (i.e., wider mountains) for larger values of a . Thus, for the same environmental conditions, we can anticipate that the larger (smaller) we make a , the more (less) likely the solution will contain wavenumbers that satisfy $u_0^2 k^2 < N^2$, such that waves propagate vertically (Figure 12.4). In the hydrostatic limit, $k^2 \ll m^2$ and the horizontal group velocity becomes

$$c_{gx} = u_0 - \frac{Nm^2}{(k^2 + m^2)^{3/2}} \rightarrow u_0 - \frac{N}{m}. \quad (12.12)$$

However, (12.4) implies that for steady waves (i.e., $\omega = 0$) in the hydrostatic limit, $u_0 \rightarrow N/m$, such that $c_{gx} \rightarrow 0$, and very little energy will be transferred horizontally away from the mountain; thus, we expect to observe hydrostatic waves near the mountain only (Figure 12.4b). Waves appearing downstream from the mountain are nonhydrostatic, but even these generally transport their energy to the upper levels before traveling very far downstream, unless special conditions prevail to confine the energy to low levels, leading to *trapped lee waves*. We now investigate the conditions leading to these interesting waves.

12.1.3 Variations in zonal wind and stability with height: trapped waves

In the previous section, we used linearized, steady equations, with a constant horizontal flow containing no vertical wind shear. We also assumed that N^2 was constant with height and that the flow was two-dimensional (i.e., an infinitely long ridge in the y direction). Our first modification to this idealization is to consider the case in which either the zonal wind or the stability varies with height such that we have two layers of fluid with different Scorer parameter values ℓ_U and ℓ_L for the upper and lower layers, respectively. Assuming $\ell_U < \ell_L$, this creates a situation in which waves whose wavenumbers fall between the two ℓ values will propagate vertically in the lower layer but decay with height in the upper layer. For these waves, the interface (at $z = z_r$) between the two fluids acts as a perfect reflector of wave energy, that is, $R = 1$, and, as shown in Section 6.3, if the flow satisfies

$$\mu \tan m_1 z_r = -m_1, \quad (12.13)$$

the waves satisfy $w_0 = 0$ at the surface but have a large response for a finite forcing due to constructive interference between the upward- and downward-moving waves. This interference also causes the waves to exhibit no tilt in the vertical. When both sides of (12.13) are plotted as a

function of $m_1 z_r$, the number of intersection points, n , is governed by

$$\left[\frac{(2n-1)\pi}{2z_r} \right]^2 < \ell_L^2 - \ell_U^2 < \left[\frac{(2n+1)\pi}{2z_r} \right]^2. \quad (12.14)$$

Thus, at least one solution exists if $\ell_L^2 - \ell_U^2 > \pi^2/4z_r^2$ and $\ell_L > k > \ell_U$.⁴ Note that the variation in ℓ could be due to a variable vertical profile of N , curvature in the wind profile with height, or both. The resonant wavelength depends on the atmospheric properties downstream of the mountain rather than depending on the width of the mountain.

Linear theory is expected to produce accurate results when the *nondimensional mountain height* ($=Nh_m/\bar{u}$, a measure of the nonlinearity produced in the flow) is much less than one. Even when the nondimensional mountain height is not small, in cases with constant \bar{u} and N the difference between the linear prediction and the fully nonlinear solution is small unless waves break. However, the difference between linear and nonlinear solutions is sometimes dramatic for environments with variable \bar{u} and N that produce trapped lee waves (Figure 12.5). Indeed, numerical simulations of lee waves show that linear theory can usefully predict wave amplitude only when the ratio of lee wavelength to mountain width is greater than one.⁵ In linear theory, the forcing at a particular wavelength is obtained by

⁴ See Scorer (1949).

⁵ See Vosper (2004).

the Fourier transform of the mountain and, therefore, very little forcing is produced at the resonant wavelength if the mountain is very wide in comparison with that wavelength. Thus, the nonlinear wave amplitude when resonant wavelengths are short compared with the mountain width is due to the enhancement of shorter wavelengths through nonlinear wave interactions rather than through direct forcing by the terrain, and this interaction is excluded from linear theory.

Vertical parcel displacements within the waves may be sufficient for transporting parcels to their lifting condensation level (LCL), resulting in stunning bands of clouds parallel to the mountain (Figure 12.6). Lee waves also transport energy downstream from downslope windstorms (see Section 12.3).

12.2 Gravity waves forced by isolated peaks

Flow over isolated peaks also can produce gravity waves, but parcel and wave motions are not confined to only the x and z directions, as they were in Section 12.1. It can be shown that the analogous form of (6.41) for the case of an isolated peak with zero phase speed is

$$k^2 + \left(\frac{k^2}{k^2 + l^2} \right) m^2 = \frac{N^2}{\bar{u}^2}, \quad (12.15)$$

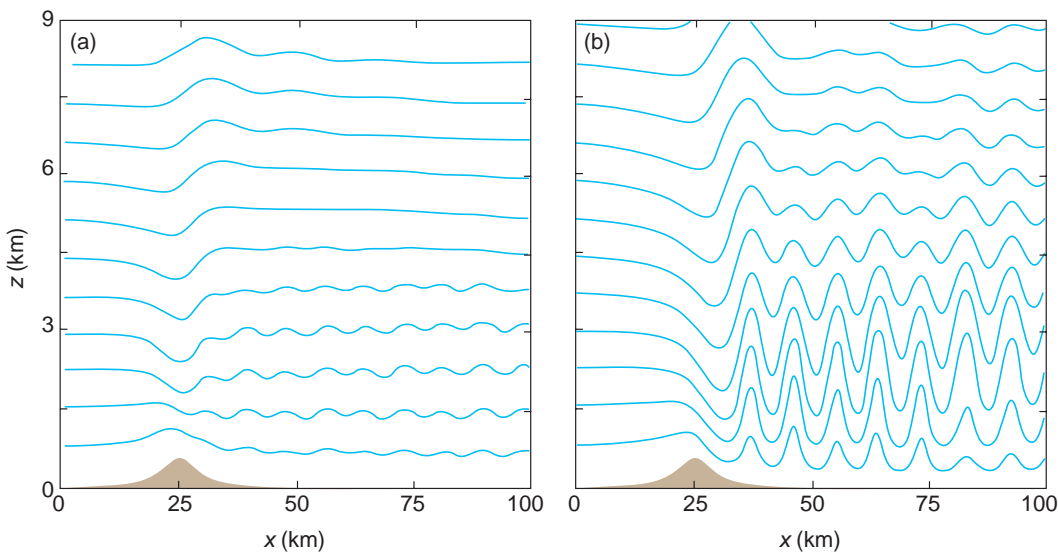


Figure 12.5 Streamlines in air flow over a mountain for (a) steady flow subject to the linear approximation and (b) the fully nonlinear and unsteady solution. (Adapted from Durran [2003a].)

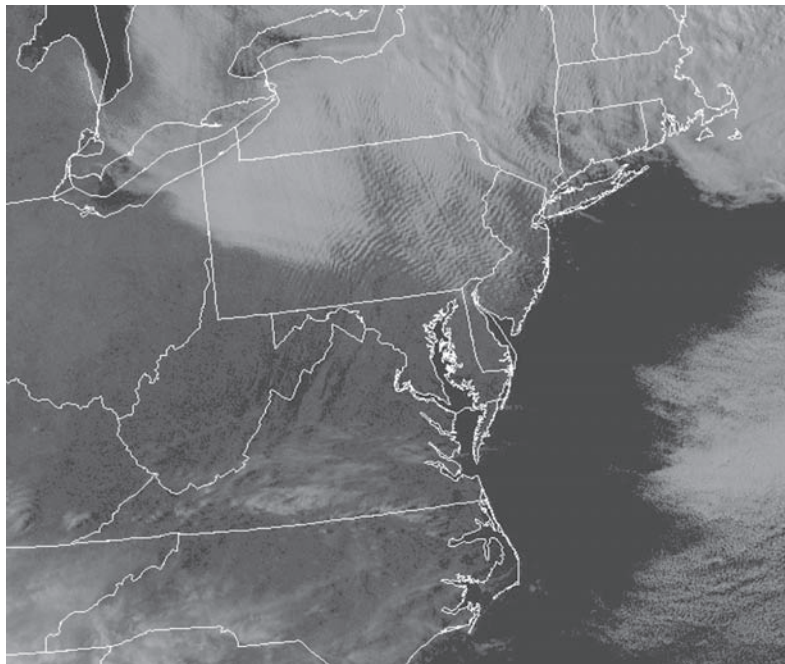


Figure 12.6 Trapped lee waves triggered by the series of mountain ridges in Pennsylvania observed in visible satellite imagery at 2045 UTC 30 March 2009.

where l is the wavenumber in the y direction (depends on the wavelength of the terrain in the y direction), and the incident flow is zonal (from the $-x$ direction). Thus, m depends on l as well as k . As in the two-dimensional case, waves can propagate vertically if $N^2 > (\bar{u}k)^2$, because then $m^2 > 0$ and m is real. The $k^2/(k^2 + l^2)$ factor in (12.15) gives the waves a herringbone structure, as in Figure 12.7.

12.3 Downslope windstorms

Sometimes the flow experiences substantial acceleration as it passes over a barrier. In this section, we consider high-amplitude gravity waves, wave-breaking, and the formation of downstream hydraulic jumps that can be hazardous to the public, especially aviation interests, as they can be associated with downslope *windstorms*, rotors, and other forms of severe clear-air turbulence in the lee of major mountain ridges, particularly those with a steep lee slope. The downslope winds discussed here typically are distinguished from the *katabatic winds* treated in Chapter 11, which usually refer to shallow density currents produced by the cooling of sloped terrain. The downslope winds discussed in this chapter form when a deep layer of air is forced over a terrain barrier, usually with a strong stable layer present near the crest of the barrier and/or a critical level aloft. The diabatic

cooling of air in contact with sloping terrain is not needed for the generation of this variety of downslope winds.

Strong, dynamically forced downslope winds are known to occur at many midlatitude locations worldwide. Examples include the Rocky Mountain chinook (Boulder, CO, is particularly notorious for its windstorms, perhaps in large part due to the collocation of the National Center for Atmospheric Research; Figures 12.8–12.10), southern California Santa Ana, Alpine foehn, Croatian bora, and Argentine zonda. The most severe downslope windstorms may contain winds exceeding hurricane strength (32 m s^{-1}). In most cases, the downsloping winds result in leeside warming. The most notable exception is the bora, in which the upstream air that spills over the mountain is so cold that, even with compressional warming, leeside cooling is observed. The dynamics appear to be similar regardless of the upwind temperatures and the temperature change, if any, experienced in the lee of the barrier.

The basic characteristics of downslope windstorms are analogous to hydraulic jumps, whose behavior is explained using the nonlinear shallow water equations; this is the approach taken in Section 12.3.1. We then discuss efforts to transfer the results of shallow-water theory to the real atmosphere and consider theories based on wave reflection and subsequent wave resonance.

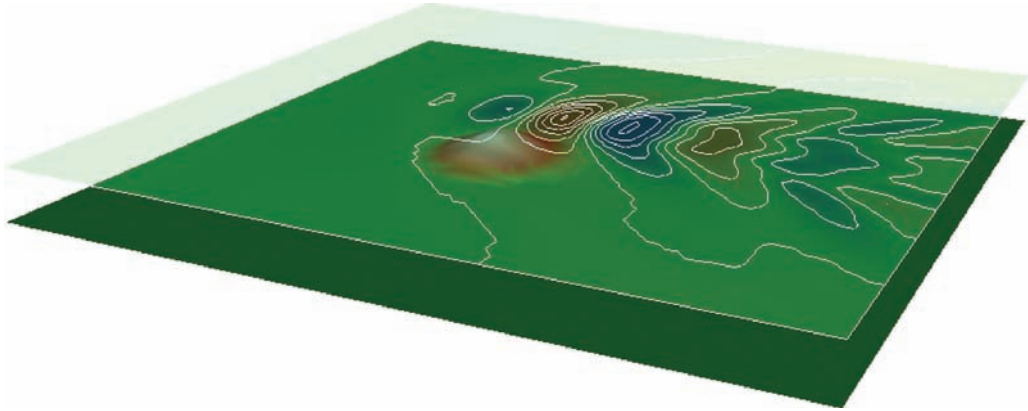


Figure 12.7 Simulation of gravity waves triggered by westerly flow over an isolated peak, as viewed from the southeast. Contours of vertical velocity are shown at an altitude of 6 km at 1 m s^{-1} intervals. Blue (red) shading indicates negative (positive) vertical velocities.

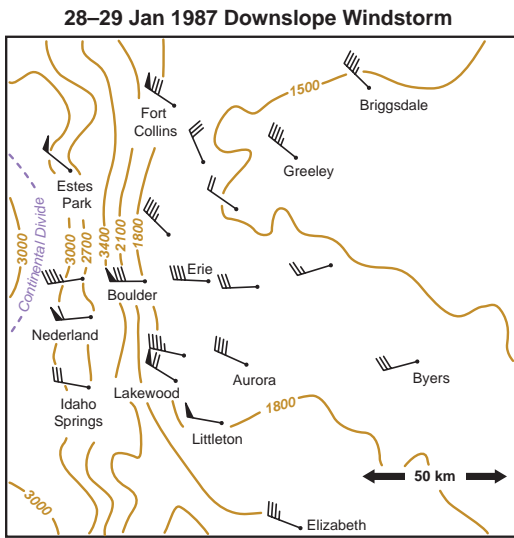


Figure 12.8 Maximum wind gusts observed during a downslope windstorm in the lee of the Colorado Rockies on the night of 28–29 January 1987. Smoothed elevation contours (m) also are shown. (Adapted from Neiman *et al.* [1988].)

12.3.1 Amplified leeside winds in shallow-water theory

Atmospheric fields (e.g., isentropes) during downslope wind events bear a striking resemblance to those predicted

in hydraulic jumps, features that are understood most easily in the context of shallow-water theory. Although not directly applicable to the stratified atmosphere associated with downslope windstorms, using shallow-water theory will allow us to develop some intuition regarding the possible flow regimes for air traversing a barrier.

Let us assume that we have a layer of fluid with density ρ . The top of the layer is a free surface (i.e., a boundary between two homogeneous fluids; the real atmosphere does not have free surfaces). The terrain height is h_t and the perturbation fluid depth is D , such that the height of the free surface is $D + h_t$ (Figure 12.11). Also note that the vertical velocity at the lower boundary is $w(x, h_t) = u \partial h_t / \partial x$, and at the free surface it is $w(x, D + h_t) \approx u \partial (D + h_t) / \partial x$.

The nonlinear, steady-state equations for momentum in the x direction and for mass continuity applicable to an inviscid, hydrostatic fluid in a nonrotating reference frame are

$$u \frac{\partial u}{\partial x} + \frac{1}{\rho} \frac{\partial p}{\partial x} = 0 \quad (12.16)$$

$$\frac{\partial u}{\partial x} + \frac{\partial w}{\partial z} = 0. \quad (12.17)$$

It is helpful to eliminate p and w from equations (12.16) and (12.17) in favor of D and h_t , so that the flow accelerations following a parcel can be related to changes in the depth of the fluid and to the slope of the terrain. The pressure gradient force, $-\frac{1}{\rho} \frac{\partial p}{\partial x}$, in (12.16) can be written as $-g \frac{\partial (D + h_t)}{\partial x}$, assuming hydrostatic balance. The continuity

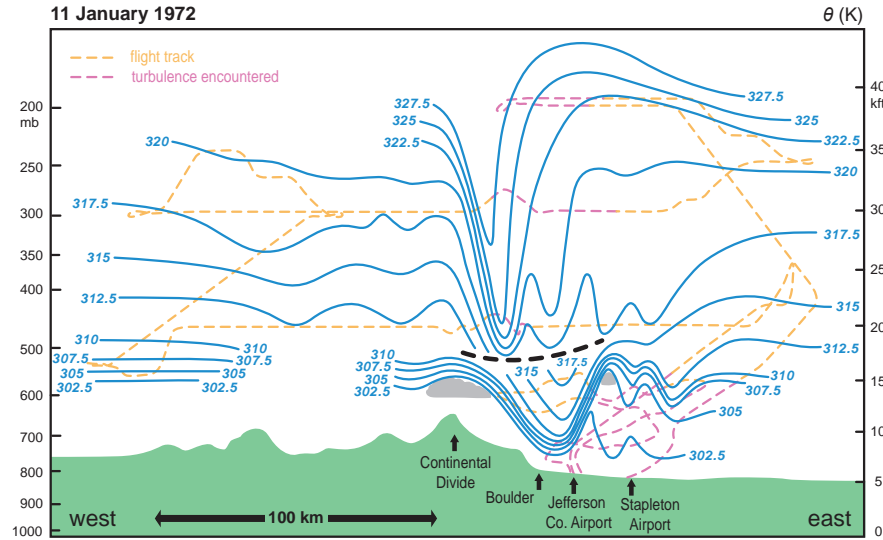


Figure 12.9 Analysis of potential temperatures (blue contours; K) from aircraft flight data (aircraft flight tracks are indicated with dashed lines) and rawinsondes on 11 January 1972 during a downslope windstorm near Boulder, CO. The heavy dashed line separates data taken by the Queen Air at lower levels before 2200 UTC from that taken by the Sabreliner aircraft in the middle and upper troposphere after 0000 GMT (12 January). The aircraft flight tracks were made along an approximate 130° – 310° azimuth, but the distances shown are along the east–west projection of these tracks. (Adapted from Lilly [1978].)

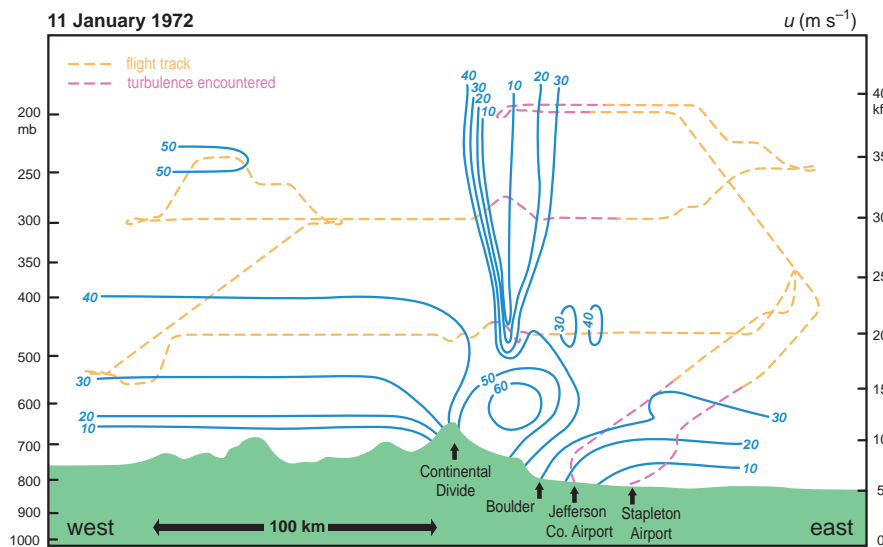


Figure 12.10 Analysis of the westerly wind component (blue contours; m s^{-1}) on 11 January 1972 during the downslope windstorm near Boulder, CO, shown in Figure 12.9. The analysis below 500 mb was partially obtained from vertical integration of the continuity equation, assuming two-dimensional steady-state flow. (Adapted from Klemp and Lilly [1975].)

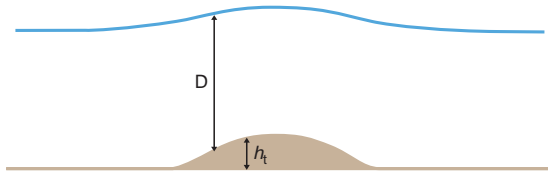


Figure 12.11 Relationship between free surface height, depth (D), and terrain height (h_t).

equation can be integrated with respect to z over the fluid depth to obtain

$$\int_{h_t}^{D+h_t} \frac{\partial u}{\partial x} dz + \int_{h_t}^{D+h_t} \frac{\partial w}{\partial z} dz = 0 \quad (12.18)$$

$$\frac{\partial u}{\partial x}(D + h_t - h_t) + w(D + h_t) - w(h_t) = 0 \quad (12.19)$$

$$\frac{\partial u}{\partial x}D + u \frac{\partial(D + h_t)}{\partial x} - u \frac{\partial h_t}{\partial x} = 0. \quad (12.20)$$

We were able to pull the $\partial u / \partial x$ term out of the integral because u is independent of z for all time if it starts so initially, owing to its dependence on the pressure gradient force in (12.16), which depends only on the fluid depth and, therefore, is independent of z . Thus, the nonlinear x momentum and continuity equations from (12.16) and (12.17) can be written

$$u \frac{\partial u}{\partial x} + g \frac{\partial D}{\partial x} = -g \frac{\partial h_t}{\partial x} \quad (12.21)$$

$$\frac{\partial}{\partial x}(uD) = 0. \quad (12.22)$$

According to equation (12.21), the steady-state condition is achieved through a balance between horizontal advection and the horizontal pressure gradient force. Mass is conserved, according to (12.22), by requiring a constant mass flux in the x direction. (If the mass flux varied, the divergence of the mass flux would not allow a steady-state solution.) This implies that thickening of the fluid is associated with deceleration following a parcel, whereas thinning of the fluid is associated with acceleration, a simple relationship that is not possible in the absence of a free surface.

To combine (12.21) and (12.22) into one equation relating all of the relevant flow variables, we use (12.22) to substitute for $\partial u / \partial x$ in (12.21). This yields

$$-\frac{u^2}{D} \frac{\partial D}{\partial x} + g \frac{\partial D}{\partial x} = -g \frac{\partial h_t}{\partial x}. \quad (12.23)$$

We now divide by g to obtain

$$\left(1 - \frac{u^2}{gD}\right) \frac{\partial D}{\partial x} = -\frac{\partial h_t}{\partial x}. \quad (12.24)$$

The intrinsic shallow-water gravity wave speed is defined as $c^2 \equiv gD$, therefore we can write (12.24) as

$$\left(1 - \frac{u^2}{c^2}\right) \frac{\partial D}{\partial x} = -\frac{\partial h_t}{\partial x} \quad (12.25)$$

or

$$(1 - Fr^2) \frac{\partial D}{\partial x} = -\frac{\partial h_t}{\partial x}, \quad (12.26)$$

where $Fr^2 = u^2/c^2$, and Fr is the *Froude number* for shallow-water theory. The Froude number is the ratio of the mean flow to the gravity wave phase speed. When $Fr > 1$, gravity waves are unable to propagate upstream relative to the mean flow, and the fluid is unable to produce perturbation pressure gradients of sufficient magnitude to balance nonlinear advection.

The Froude number can be used to identify three distinct flow regimes. Based on inspection of (12.26), if $Fr > 1$ and $\partial h_t / \partial x > 0$, then $\partial D / \partial x > 0$ such that the fluid thickens going in the uphill direction, achieving its maximum thickness at the peak of the mountain (Figure 12.12a). On the lee slope, where $\partial h_t / \partial x < 0$, the fluid thins. As the thickness of the fluid changes, the zonal velocity also changes in accordance with the constant zonal mass flux prescribed by the continuity equation. Thus, when $Fr > 1$, we find a minimum in the wind speed at the top of the mountain where the fluid is thickest. Considering a parcel embedded in a westerly wind, the parcel will decelerate as it passes over the mountain and return to its original speed at the leeward base of the mountain (ignoring any frictional effects). This flow behavior represents a transfer of energy from kinetic to potential and back to kinetic, and is the behavior most in line with our natural intuition for the behavior of, for example, a ball rolling up a hill. This type of flow, for which $Fr > 1$, is termed *supercritical flow*.

In contrast, when $Fr < 1$, termed *subcritical flow*, (12.26) predicts that the fluid will thin ($\partial h_t / \partial x < 0$) as the terrain height increases ($\partial h_t / \partial x > 0$) (Figure 12.12b). Accompanying this thinning is an increase in the zonal wind speed, reaching a maximum value at the top of the mountain where the fluid is thinnest. The behavior associated with subcritical flow as a parcel traverses a mountain is not in line with our usual arguments regarding the simple transfer of energy from kinetic to potential, and we must break with our conceptual model of an isolated ball rolling up a hill. An individual air parcel is not isolated from the surrounding parcels; it feels their presence

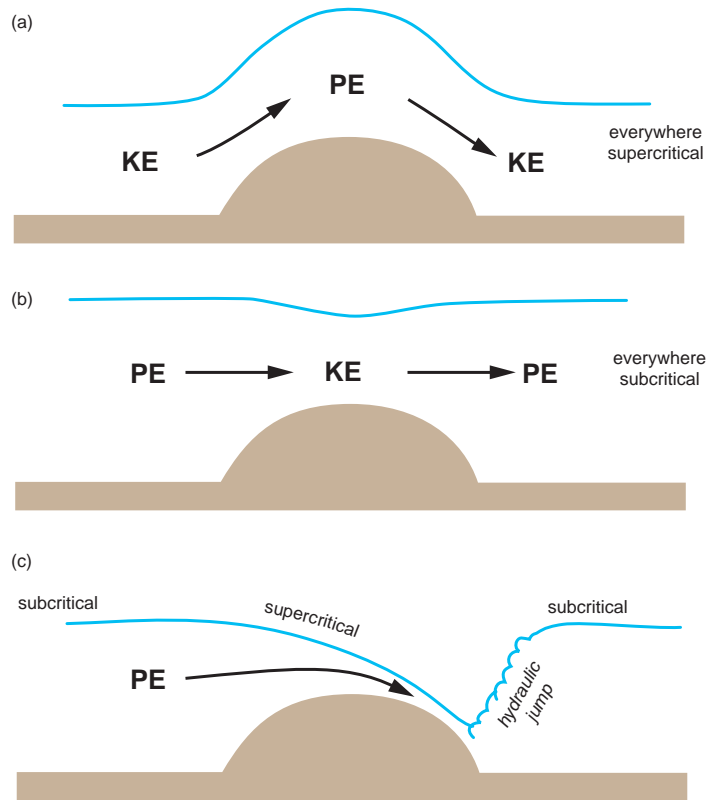


Figure 12.12 Flow over an obstacle for the simple case of a single layer of fluid having a free surface. (a) Supercritical flow ($Fr > 1$) everywhere. (b) Subcritical flow ($Fr < 1$) everywhere. (c) Supercritical flow on the windward side with adjustment to subcritical flow at a hydraulic jump near the base of the obstacle. (From Durran [1990].)

through the influence of the pressure gradient force. Thus, the acceleration a parcel attains depends on the difference between the pressure gradient force arising from changes in the fluid depth [the second term in (12.21)] versus the amount of work (i.e., conversion of kinetic energy to potential energy) associated with climbing the terrain. In subcritical flow, the pressure gradient force dominates and leads to a net positive acceleration following the parcel as it ascends. On the lee side, the fluid thickens and returns to its original depth as the parcel decelerates to its original speed.

So far we have explored two very different behaviors depending on Fr , but the net result for both is a return to the original zonal wind speeds when the parcel reaches the lee side. How then do we get winds on the lee side that greatly exceed their original value? In other words, how can we accelerate along the entire path from windward side to leeward side? To see how this acceleration pattern can be achieved, we notice that accelerations on the windward side occur for subcritical flow, whereas accelerations on

the leeward side occur for supercritical flow. Thus, to achieve acceleration along the entire path, the flow must undergo a transition from subcritical on the windward side to supercritical as it crests the mountain. In other words, the acceleration on the windward side must cause u to cross the threshold from subcritical to supercritical flow, which is likely to happen only if the flow has a Fr close to unity at the start. The transition from subcritical to supercritical results in leeward wind speeds that exceed their original value on the windward side. In accordance with the increasing speeds, the fluid thickness will decrease over the entire path, causing the free surface to drop sharply on the leeward side, analogous to the descending isentropes during downslope wind events, and resulting in what is called a *hydraulic jump*. Hydraulic jumps are very turbulent, and large amounts of energy are dissipated within them.⁶

⁶ One of the best examples of a hydraulic jump is when water spills over a dam. A hydraulic jump forms at the base of the dam.

12.3.2 More realistic treatment of downslope windstorms

The preceding analysis gives an easily understood analogue to downslope windstorms. However, free surfaces do not exist in the real atmosphere, which is continuously stratified, so the extension of shallow-water theory to the atmosphere in a quantitative manner is not straightforward. In particular, calculating a value for Fr appropriate to the atmosphere is especially challenging as there is no obvious layer depth.

When low-level inversions are specified at a height z_i , authors have used $\text{Fr} = \bar{u}/\sqrt{g' z_i}$, to develop relationships between Fr and simulated flow characteristics. In this expression, g' is the *reduced gravity* given by $g' = g \Delta\theta/\theta_0$, where $\Delta\theta$ is the potential temperature difference across the inversion. This expression has been widely used in applying shallow-water theory to atmospheric flows, a practice that dates back at least to Freeman (1948) and Long (1954). However, both practical experience with observed downslope windstorms and theoretical studies⁷ suggest that the resulting Fr cannot always be used to obtain accurate quantitative models of atmospheric flows below elevated inversions. Although interesting results are obtained in simulations by varying Fr, it is somewhat unclear how to apply these results to observed cases for which \bar{u} and z_i may not have obvious values.

It also is not clear that it is appropriate to expect the low-level pressure to be determined by the height of the inversion in the free atmosphere, as it was by the height of the free surface in shallow-water theory. In addition to the lack of a free surface, the atmosphere differs from shallow-water theory in that internal waves play an important role in the energy transfer within a stratified environment, but they are absent from shallow-water theory. Thus, two lines of thought emerge regarding downslope windstorms, one that looks at them as an atmospheric form of a hydraulic jump, and one that is based on the presence of waves, seeking conditions that lead to their reflection and amplification.

There are three predominant situations in which downslope windstorms are observed: (1) when standing waves in a deep cross-mountain flow overturn and break, (2) when standing waves break and dissipate at a critical level in shallow cross-mountain flow, and (3) when a layer having strong static stability exists near the mountaintop with a layer of lesser stability above (Figure 12.9).⁸

When standing waves overturn and break, which occurs only if they reach sufficient amplitude, a region of low static stability and reversed flow with a critical level can

develop. These features allow one to specify boundary conditions along a *dividing streamline*, which descends sharply as the flow traverses the mountain and is the lower boundary of the well-mixed region. In particular, Smith (1985), who developed the theory presented herein, assumes that potential temperature is constant and pressure perturbations are small in the well-mixed layer between the split streamlines. The latter assumption requires a critical level to prohibit wave propagation through the well-mixed region. Below the dividing streamline, the flow is assumed to be smooth, nondissipative, hydrostatic, Boussinesq, and steady, whereas the upstream flow is assumed to have constant speed u_0 and stability N_0 . Under these conditions, the governing equation developed by Long (1955) is

$$\frac{\partial^2 \delta}{\partial z^2} + l^2 \delta = 0, \quad (12.27)$$

where $\delta(x, z) = z - z_0$ is the displacement of an arbitrary streamline, and z_0 is the upstream altitude of the streamline through the point (x, z) (Figure 12.13). Assuming that the air between the split streamlines is hydrostatic with constant potential temperature, a Bernoulli equation along the lower branch of the split streamlines indicates that the zonal velocity is constant and equal to its original value along that

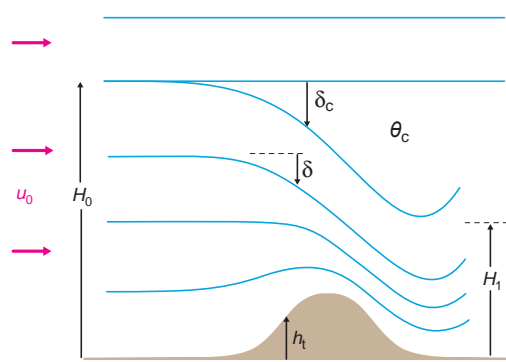


Figure 12.13 Schematic of the idealized high-wind-speed flow configuration, derived from aircraft observations and numerical simulations. A certain critical streamline divides and encompasses a region of uniform potential temperature. H_0 is the original height of the dividing streamline, θ_c is the potential temperature in the well-mixed region between the split streamlines, δ is the displacement of an arbitrary streamline, δ_c is the displacement of the dividing streamline, and H_1 is the nadir of the lower dividing streamline. (From Smith [1985].)

⁷ See Durran (2000).

⁸ This discussion is based upon the presentation of Durran (2003b).

streamline. This provides an important boundary condition for the solution of (12.27), allowing one to predict δ_c , the displacement of the dividing streamline. The solutions are given by a family of curves for δ_c versus h_t , with a different curve for each upstream height of the dividing streamline (normalized using the vertical wavelength). Behavior analogous to hydraulics is possible when the undisturbed height of the dividing streamline is between $(1/4 + n)\lambda_z$ and $(3/4 + n)\lambda_z$. For these optimal values of H_0 , and a sufficiently high mountain, the dividing streamline will descend on both the windward and leeward sides of the mountain in a manner resembling that of shallow water flow that transitions from supercritical to subcritical when passing over the mountain. Accompanying this descent is a significant increase in wind speed.

The phenomenon of wave amplification due to wave breaking was originally interpreted as a form of resonance

due to reflection of wave energy at the level of the overturned layer.⁹ As stated previously, the layer in which breaking occurs is presumed to have a low Richardson number and often reversed flow such that a critical level is generated by the breaking (this has been referred to in the literature as a *self-induced* critical level; because the phase speed for mountain waves is zero, the cross-mountain component of the flow is zero in a critical level). As discussed in Section 6.4, linear waves encountering a critical level can experience over-reflection when the Richardson number is less than one-quarter. The over-reflected waves will interfere with the incident waves, with resonance possible only for critical level heights of $\frac{1}{4}, \frac{3}{4}, \frac{5}{4}, \dots$ vertical wavelengths above the ground. This is a valid mechanism for wave amplification, but some simulations suggest that the critical level heights

⁹ See Clark and Peltier (1984) and Peltier and Clark (1983).

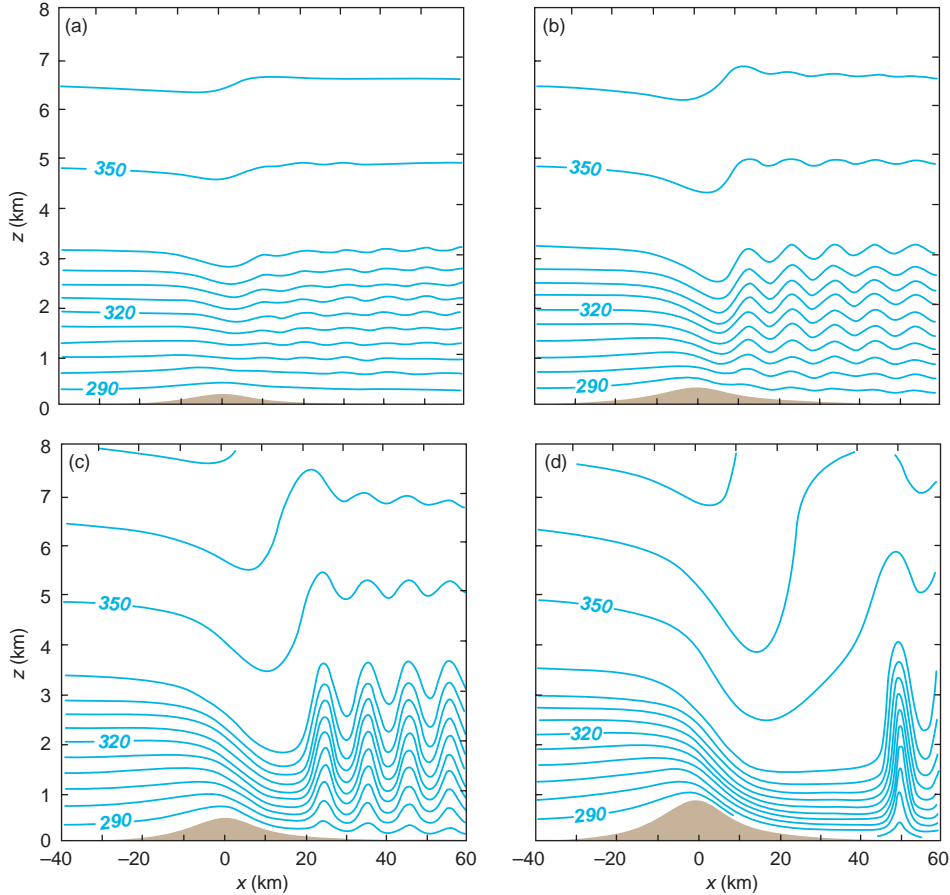


Figure 12.14 Isentropes for the airflow in a two-layer atmosphere when the interface is fixed at 3000 m, and the mountain height is (a) 200, (b) 300, (c) 500, and (d) 800 m. (From Durran [1986b].)

leading to significant wave amplification are better matched with those predicted by the hydraulic jump analog than with those predicted by the wave-resonance theory.¹⁰ The wave-resonance theory depends on the existence of high-amplitude waves such that wave breaking occurs. At that point, it may be that the nonlinear effects, which are included in the hydraulic jump analog, are essential. Similar zonal wind amplification will occur if the *mean* wind profile contains a critical level.

In the final observed situation, that of a layer with strong static stability below a layer with lesser stability, the displacement of the interface will influence the pressure gradient, although not as directly as this displacement does when the interface represents a true density, rather than stability, discontinuity. An analytic expression can be

¹⁰ See Durran and Klemp (1987).

developed for the contribution to the total perturbation pressure owing to the displacement of the interface, and simulations suggest that as the flow becomes more nonlinear [for example, as the mountain height is increased (Figure 12.14)] this contribution to the pressure gradient on the lee side becomes dominant, suggesting the flow is then governed by the hydraulic analog.¹¹

When the flow is in a regime analogous to shallow-water theory, we expect the depth of the stable layer, analogous to the depth of the shallow water fluid, to play a large role in determining the flow properties. Indeed, simulations suggest that varying the depth of the stable layer has an influence similar to varying the fluid depth in the two-layer model for shallow-water theory (Figure 12.15). As the stable layer depth increases, the isentropes transition from

¹¹ See Durran (1986b).

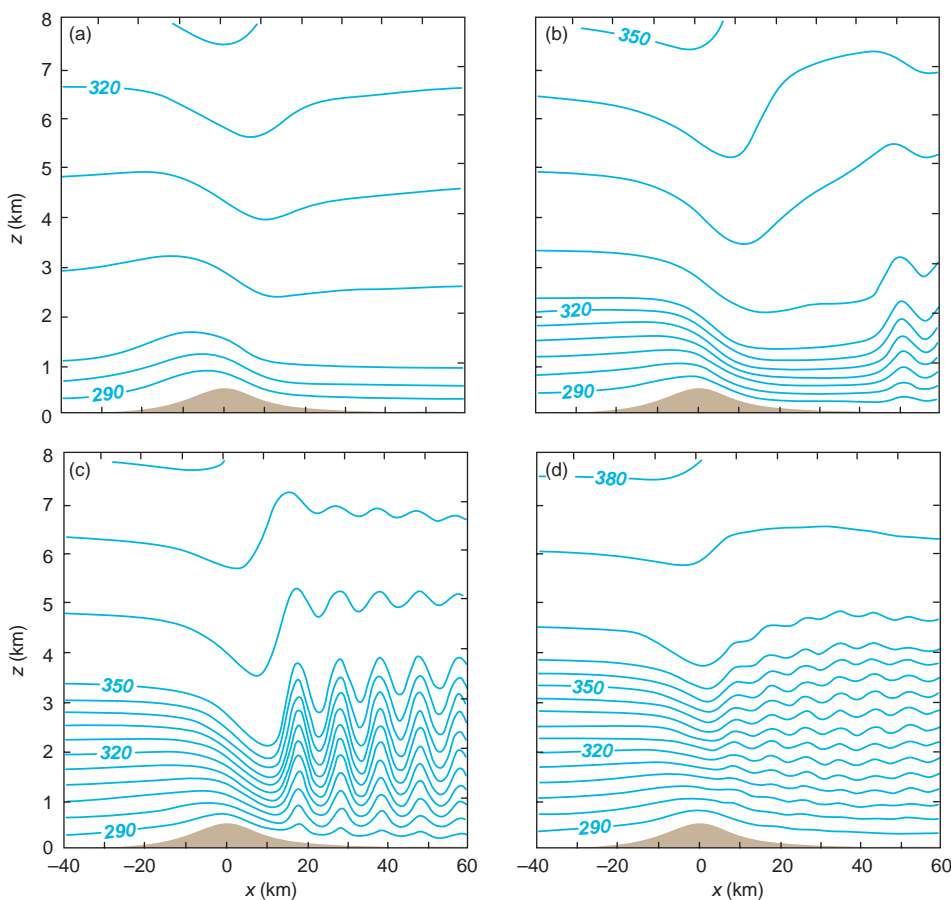


Figure 12.15 Isentropes for the airflow in a two-layer atmosphere when the mountain height is fixed at 500 m, and the interface is at (a) 1000 m, (b) 2500 m, (c) 3500 m, and (d) 4000 m. (From Durran [1986b].)

a regime with thickening of the stable layer as the flow traverses the mountain to a regime with a clear hydraulic jump. We see that strong lee waves form downstream of the jump and radiate energy away from the mountain. Finally, as the depth is increased further, the isentrope behavior is similar to the shallow water free surface in the subcritical regime, with a decrease in the stable layer depth as the flow crosses the mountain but a gentle return of the stable layer to its original depth on the lee side, rather than the development of a hydraulic jump. Thus, even without a pre-existing layer across which the density changes rapidly (i.e., an inversion), phenomena that are *qualitatively* very similar to those in shallow-water theory can be produced in two-layer fluids with high static stability in the lower layer. As testament to the importance of the low-level stable layer, when this layer was artificially removed in the simulation of an observed case, strong winds did not develop on the lee side.¹²

When multiple layers of varying stability exist, partial wave reflection is possible at the interfaces of the layers, and, when the stability structures of these layers is tuned to maximize the positive interference of the reflected and incident waves, wave amplification may be anticipated to be important. The theory for the partial reflection of long, hydrostatic waves shows that maximum amplification of

the surface velocity in a three-layer model having strong, weak, and strong stability in the three layers, respectively, occurs when the lower two layers each have a thickness equal to one-fourth of the vertical wavelength valid for that layer. This implies a relatively thin, low-level inversion with a thicker, less stable troposphere aloft.¹³ When compared with observations, the predicted structure is often validated. The partial wave reflection theory, which is based on linear theory, rapidly breaks down as the mountain height becomes noninfinitesimal in cases with high static stability in the lower level. It is possible that this mechanism promotes the initial growth of wave amplitude, leading eventually to wave breaking and the associated effects discussed above for that phenomenon.

Putting all of this together, here are some of the conditions that forecasters look for when predicting downslope windstorms:

- an asymmetric mountain with a gentle windward slope and a steep lee slope
- strong cross-mountain geostrophic winds ($>15 \text{ m s}^{-1}$) at and just above mountain-top level associated with surface high pressure upstream and surface low pressure downstream

¹² See Durran (1986b).

¹³ See Klemp and Lilly (1975).



Figure 12.16 Photograph of a rotor cloud taken during the Terrain-Induced Rotor Experiment (T-REX). Courtesy of Vanda Grubisic, Boro Grubisic, Brian Billings, and Ivana Stiperski.

- an angle between the cross-mountain flow and the ridge that is greater than $\sim 60^\circ$
- a stable layer near or just above the mountain top, and a layer of lesser stability above
- a level that exhibits a wind direction reversal or where the cross-barrier flow simply goes to zero (the mean state critical level); the existence of weak, vertical wind shear or reverse shear is more favorable than forward shear
- situations of cold advection and anticyclonic vorticity advection, which promote downward synoptic motion to generate and reinforce the vertical stability structure
- absence of a deep, cold, stable layer in the lee of mountains, which may keep the downslope flow from penetrating to the surface.

12.4 Rotors

Intense horizontal vortices called *rotors* (Figures 12.12 and 12.16) can form in the lee of mountains under a wide range of conditions, with the most intense rotors forming near hydraulic jumps; that is, in conditions similar to

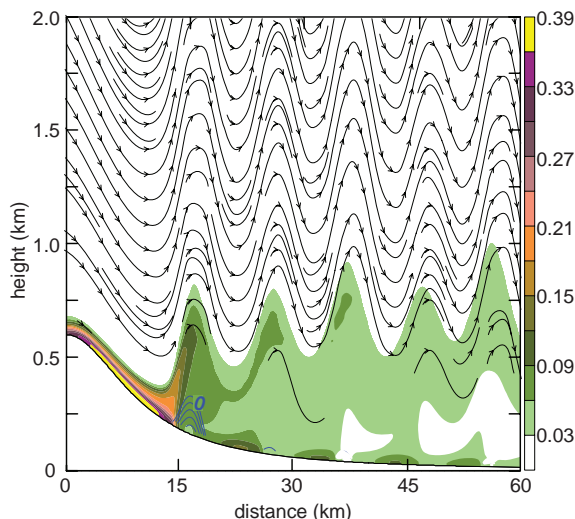


Figure 12.17 Streamlines and horizontal vorticity (colored, s^{-1}) in a numerical simulation using a no-slip lower-boundary condition. Horizontal wind speeds less than or equal to zero are shown using blue isolachs (every $2 m s^{-1}$). (From Doyle and Durran [2002].)

those that favor downslope windstorms (e.g., supercritical flow on the lee side). Rotors can be dangerous to aircraft because of the large wind shears and turbulence associated with them.

Rotors form owing to flow separation in the wake of ridge-tops (Figure 12.17). Strong horizontal vorticity is created by surface friction as flow descends the mountain toward a region of trapped lee waves. The adverse pressure gradient associated with the first lee wave aids in the separation of this high-vorticity region from the surface. The vortex sheet is then advected into the lee wave train and transported downstream, with a portion captured below the wave crest leading to the formation of a rotor (Figure 12.17; note that the blue contours indicate the reversed flow associated with rotors beneath the first two lee waves).¹⁴ Thus, lee waves and surface friction both play an integral part in the formation of rotors.

Further reading

- Chen *et al.* (2005).
Clark, T. L., and W. R. Peltier, 1977: On the evolution and stability of finite-amplitude mountain waves. *J. Atmos. Sci.*, **34**, 1715–1730.
Clark and Peltier (1984).
Durran (1986b).
Durran (1990).
Durran (2000).
Durran, D. R., 2003a: Lee waves and mountain waves. In *Encyclopedia of the Atmospheric Sciences*, J. Holton, J. Curry and J. Pyle, Eds. Academic, 1161–1169.
Durran, D. R., 2003b: Downslope winds. In *Encyclopedia of the Atmospheric Sciences*, J. Holton, J. Curry and J. Pyle, Eds. Academic, 644–650.
Durran and Klemp (1987).
Freeman (1948).
Hertenstein, R. F., 2009: The influence of inversions on rotors. *Mon. Wea. Rev.*, **137**, 433–446.
Klemp and Lilly (1975).
Long (1954).
Neiman *et al.* (1988).
Reed, R. J., 1981: A case study of a bora-like windstorm in western Washington. *Mon. Wea. Rev.*, **109**, 2383–2393.
Scorer (1949).
Smith (1985).
Smith, R. B., 1987: Aerial observations of the Yugoslavian bora. *J. Atmos. Sci.*, **44**, 269–297.
Vosper (2004).

¹⁴ See Doyle and Durran (2002).

13

Blocking of the Wind by Terrain

13.1 Factors that govern whether air flows over or around a terrain obstacle

In Chapter 12 we investigated phenomena that result from air flowing over mountains. In this chapter we explore phenomena that result from the blocking of winds by terrain. Whether an air parcel approaching a mountain goes over or around the mountain depends on the height of the parcel relative to the height of the mountain, the slope and dimensions (height and width) of the mountain, the static stability, and the strength of the upstream horizontal winds directed at the mountain. As the stratification increases, an air parcel has an increasing tendency to go around rather than over a mountain. A similar tendency is observed as the speed at which a parcel approaches a mountain decreases, and as the distance that must be climbed by a parcel increases.

In assessing the potential for blocking, it is tempting to compare the kinetic energy of an upstream air parcel to the work that must be done against the stratification to lift the parcel over a barrier (thereby increasing the parcel's potential energy), where the work is proportional to the negative area on a thermodynamic diagram acquired by lifting a parcel in a stably stratified environment. However, such an analysis neglects pressure perturbations, and pressure perturbations are a leading-order influence on the flow over a barrier, as was apparent in Chapter 12 (particularly Section 12.3). In order to include the effects of pressure perturbations, we shall make use of a Bernoulli equation.¹ (In the treatment of downslope windstorms

using hydraulic theory [Section 12.3.1], we combined the effects of the pressure gradient force and the ascent of an obstacle, but it is harder to combine these effects in the case of an internally stratified fluid.)

Let us consider a streamline in steady flow that passes over a hill or mountain like that shown in Figure 13.1. The streamline is at a height z_0 far upstream ($x = -\infty$), and the streamline is displaced upward to a height $z = z_0 + \delta$ in the vicinity of the barrier, where δ is the vertical displacement. We shall assume that parcel motions are dry adiabatic, in which case the streamlines lie within surfaces of constant potential temperature, that is, $\theta = \theta_0$ is a constant along a streamline.

For steady flow, Bernoulli's equation can be written as [cf. (2.146)]

$$\pi + \frac{u^2}{2c_p\theta_0} + \frac{gz}{c_p\theta_0} = \text{constant} \quad (13.1)$$

along a streamline, where $\pi = (p/p_0)^{R/c_p}$ is the Exner function (nondimensional pressure) and c_p is the specific heat at constant pressure, hereafter assumed to be a constant (the contribution of water vapor to c_p will be neglected).

Far upstream at $x = -\infty$, Bernoulli's equation is

$$\pi_0 + \frac{u_0^2}{2c_p\theta_0} + \frac{gz_0}{c_p\theta_0} = \text{constant}, \quad (13.2)$$

where π_0 and u_0 are, respectively, the nondimensional pressure and component of the wind perpendicular to the barrier far upstream where the streamline is at height z_0 . If we define $\pi' = \pi(z) - \bar{\pi}(z)$ to be the difference between the nondimensional pressure at some height z on a streamline, $\pi(z)$, and the nondimensional pressure at a point at the same elevation far upstream, $\bar{\pi}(z)$, then (13.1)

¹ The ensuing analysis closely follows the approach undertaken by Smith (1990).

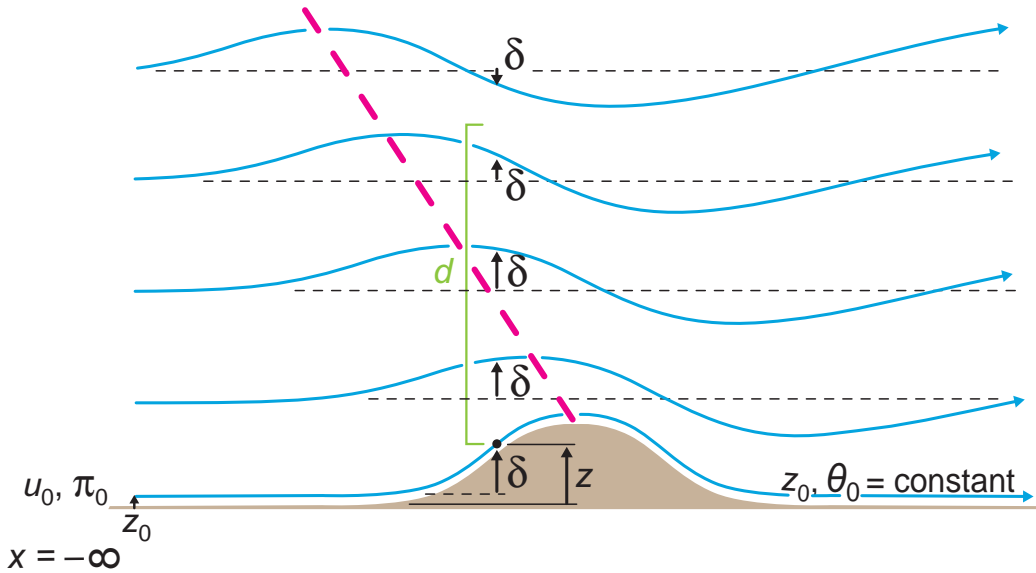


Figure 13.1 A schematic illustration of streamlines (blue; coincident with isentropes for inviscid, dry adiabatic motion), passing over a mountain, along which the Bernoulli equation applies. The relationships among u_0 , π_0 , z_0 , z , and θ_0 are indicated along the lowest streamline; δ is indicated for all of the streamlines at the location of the black dot (d is the height over which positive displacements exist above the location of the black dot). The dashed magenta line indicates the upwind phase tilt, which gives rise to large positive values of I_δ on the windward slope. (Adapted from Smith [1990].)

and (13.2) can be combined and written as

$$\pi' + \bar{\pi} + \frac{u^2}{2c_p\theta_0} + \frac{gz}{c_p\theta_0} = \pi_0 + \frac{u_0^2}{2c_p\theta_0} + \frac{gz_0}{c_p\theta_0}. \quad (13.3)$$

Because $-\rho^{-1} \partial p / \partial z = -c_p \theta \partial \pi / \partial z$, for hydrostatic upstream conditions,

$$\bar{\pi}(z) = \pi_0 - \frac{g}{c_p} \int_{z_0}^z \frac{dz}{\bar{\theta}}, \quad (13.4)$$

where $\bar{\theta}(z)$ is the upstream potential temperature profile. Assuming that the upstream stratification is independent of height, then

$$\bar{\theta}(z) = \theta_0 + \frac{\partial \bar{\theta}}{\partial z}(z - z_0) = \theta_0 \left(1 + \frac{N^2 \delta}{g}\right), \quad (13.5)$$

where $\delta = z - z_0$, and $N^2 = \frac{g}{\theta_0} \frac{\partial \bar{\theta}}{\partial z}$ is the upstream Brunt-Väisälä frequency at z_0 . Substituting (13.5) into (13.4) and assuming $\left(1 + \frac{N^2 \delta}{g}\right)^{-1} \approx 1 - \frac{N^2 \delta}{g}$ gives

$$\bar{\pi}(z) = \pi_0 - \frac{g\delta}{c_p\theta_0} + \frac{N^2 \delta^2}{2c_p\theta_0}, \quad (13.6)$$

and substitution of (13.6) into (13.3) leads to

$$u^2 = u_0^2 - 2c_p\theta_0\pi' - N^2\delta^2. \quad (13.7)$$

If $\pi' = 0$, then

$$u^2 = u_0^2 - N^2\delta^2, \quad (13.8)$$

which indicates that air slows down as it ascends a mountain (i.e., u decreases as δ increases) in stably stratified conditions. Equation (13.8) predicts that an air parcel can rise no more than

$$\delta_{\max} = \frac{u_0}{N} \quad (13.9)$$

without *stagnating*, that is, having $u \rightarrow 0$. Air flowing along the surface will not be able to pass over terrain taller than u_0/N , regardless of the shape of the terrain. The dividing streamline is the streamline that separates flow passing around the sides of the obstacle from flow passing over the obstacle.

Equations (13.8) and (13.9) are the basis for the popular forecasting criterion for blocking in terms of the *mountain Froude number*, $Fr_m = u_0/Nh_m$, where h_m is the height of the mountain (recall from Chapter 12 that Nh_m/u_0 is

sometimes called the nondimensional mountain height) and $\text{Fr}_m < 1$ implies that at least some depth of the flow will be blocked by the terrain. But there is more to the blocking problem than the value of Fr_m , as we shall see below. For example, (13.8) predicts that the minimum wind speeds will be at the mountain crest. On the contrary, air parcels generally do not simply slow down as they ascend a mountain. The slowest winds are often observed roughly halfway up the windward slope. At the crest, the wind is often the same speed as the wind far upstream at the same height. Furthermore, observations and numerical simulations reveal that both the slope and the aspect ratio of a mountain (the crosswise dimension divided by the streamwise dimension) affect the tendency for blocking, with blocking being more likely for a given upstream wind speed and stratification as the slope and aspect ratio of the terrain increase.

The discrepancies between the implications of (13.8) and actual observations and numerical simulations of wind accelerations in the vicinity of a terrain barrier are a result of pressure perturbations. Pressure perturbations are not only important, but sometimes play a dominant role in the acceleration of air parcels approaching a barrier. Our next step is to develop an expression for u that does not assume $\pi' = 0$ as was done in obtaining (13.8).

If the mountain or hill is not too steeply sloped, then dw/dt is sufficiently small that the pressure perturbation can be obtained by integrating the hydrostatic equation. This leads to

$$\pi' = -\frac{g}{c_p} \int_z^\infty \frac{\theta'}{\theta_0^2} dz = \frac{N^2}{c_p \theta_0} \int_z^\infty \delta dz, \quad (13.10)$$

where $\theta' = \theta_0 - \bar{\theta}(z)$ is the potential temperature perturbation, which is proportional to the displacement $\delta(x, y, z)$, and $\pi' = \pi'_h$ is the nondimensional hydrostatic pressure perturbation.² The obvious challenge in using (13.10) with (13.7) is that (13.10) involves an integration over some depth (the lower limit of integration varies as the height of the streamline changes), whereas (13.7) is valid along a streamline. We shall attempt to get around this problem by expressing δ in terms of (x, y, z_0) , where $z_0(\theta)$ is the upstream height of each potential temperature surface. Because $z = z_0 + \delta$, then $dz = dz_0 + d\delta$, which allows us

² Recall from Section 2.5 that the hydrostatic pressure perturbation, p'_h , is obtained by integrating (2.123). In order to obtain the nondimensional hydrostatic pressure perturbation, one uses the vertical momentum equation in terms of the vertical gradient of nondimensional pressure perturbation and buoyancy, where, neglecting the contribution of water vapor and hydrometeors to the density of air, $\frac{dw}{dt} = -c_p \theta \frac{\partial \pi'}{\partial z} + g \frac{\theta'}{\theta}$. By letting $dw/dt = 0$, one obtains $\partial \pi'_h / \partial z = g \theta' / c_p \bar{\theta} = g \theta' / c_p \bar{\theta} \theta_0 \approx g \theta' / c_p \theta_0^2$, which is integrated to yield (13.10).

to write (13.10) as

$$\pi' = \frac{N^2}{c_p \theta_0} \left(\int_{z_0}^\infty \delta dz_0 + \int_\delta^0 \delta d\delta \right), \quad (13.11)$$

where we have assumed that $\delta \rightarrow 0$ as $z_0 \rightarrow \infty$ (in the case of vertically propagating gravity waves, δ can be significant high above the underlying terrain).

If we define I_δ to be the integral of the displacement, that is,

$$I_\delta = \int_{z_0}^\infty \delta dz_0, \quad (13.12)$$

then (13.11) can be written as

$$\pi' = \frac{N^2}{c_p \theta_0} \left(I_\delta - \frac{\delta^2}{2} \right) \quad (13.13)$$

and (13.7) becomes

$$u^2 = u_0^2 - 2N^2 I_\delta. \quad (13.14)$$

Equation (13.14) is a diagnostic expression relating the wind speed to the vertical displacement field, which not only can be used to assess low-level blocking, but can also be applied to streamlines far above the ground in order to predict stagnation aloft, which leads to gravity wave breaking. The wind speed is controlled by the *integral* of the vertical displacements above a point, I_δ , rather than the local displacement δ (note that the displacement field tilts upstream with height; Figure 13.1). Note that I_δ depends on the structure of the overlying topographically generated gravity waves (e.g., the tilt of the phase lines and how their amplitude varies with height). An upstream tilting of phase lines with height (e.g., Figure 13.1) shifts the maximum in I_δ (and therefore π') away from the mountain crest, down the windward slope, leading to an upslope-directed pressure gradient force along at least part of the windward slope. In this situation, the slowest wind speeds are found on the windward slope rather than at the mountain crest.

The greater the integrated upward displacements, the greater the negative buoyancy in the overlying column, and the greater the resulting (hydrostatic) pressure perturbation. Stagnation (i.e., $u = 0$) occurs where

$$I_\delta = \frac{u_0^2}{2N^2}. \quad (13.15)$$

At a given height, the slowest flow occurs where there is a local maximum of $I_\delta(x, y, z_0)$. At such a maximum,

$$\frac{\partial I_\delta}{\partial z_0} = \frac{\partial}{\partial z_0} \int_{z_0}^\infty \delta dz_0 = 0; \quad (13.16)$$

therefore, $\delta = 0$ where wind speed is a minimum.

One must estimate I_δ in order to predict the critical height of a mountain such that the approaching flow will be blocked. This is no easy task, and in the event of steep terrain and nontrivial nonhydrostatic pressure perturbations the prediction of the wind speed along a streamline is further complicated. Figure 13.2 displays predictions for the onset of flow stagnation, based on calculations of I_δ derived from linear theory, as a function of the nondimensional mountain height and aspect ratio of the mountain. As mentioned earlier and as one would probably guess, the tendency for blocking increases as the aspect ratio of the terrain increases for a given nondimensional mountain height (i.e., terrain that is much wider in the crosswise direction than in the streamwise direction is more likely to block the oncoming air). Another interesting observation from Figure 13.2 is that stagnation begins when the nondimensional mountain height attains a value of ~ 1 for mountains having a large aspect ratio; therefore, for these terrain geometries, the mountain Froude number criterion for blocking (such that blocking is favored when $Fr_m < 1$) turns out to be a reasonably good predictor of blocking. In practice, Fr_m usually is computed using the upstream wind at the surface and by averaging N over the depth of the mountain. Ambiguity often exists in determining what velocity u to use (terrain-induced

pressure perturbations can influence u well ahead of the crest of a mountain; it is sometimes unclear how far upstream one should look to obtain the appropriate value of u) and whether to use the moist Brunt-Väisälä frequency (air often adiabatically cools to its saturation temperature as it ascends a terrain barrier), N_m , given by (3.9), instead of N , where $N_m < N$.

A second nondimensional number, known as the *Burger number*, also is used to assess blocking potential. The Burger number is defined as $Bu = Ro/Fr_m = Nh_m/L_m f$, where L_m is the half-width of the mountain in the streamwise direction, f is the Coriolis parameter, and h_m/L_m is the slope of the terrain. Thus, the Burger number considers the effects of both the steepness of the terrain [if the terrain is steeply sloped, pressure perturbations might not be well predicted by (13.10)] and the effects of rotation (also not considered above). Blocking can occur when $Bu > 1$, even if $Fr_m > 1$; such barriers are said to be *hydrodynamically steep*. In such situations, the ascent forced by the steep terrain results in a strong adverse pressure gradient force.

13.2 Orographically trapped cold-air surges

Phenomena known generically as *orographically trapped cold-air surges* occur when low-level winds are blocked by a quasi-two-dimensional topographic barrier. The winds are deflected and tend to blow along the barrier toward lower pressures, being trapped by the terrain to the right (left), with respect to the deflected wind direction, in the northern (southern) hemisphere. Such surges are common on the west coast of North America, east of the front ranges of the Rocky Mountains and Appalachian Mountains in the western and eastern United States, respectively, along the coast of South Africa, southeastern Australia (where they are referred to as *southerly busters* or *bursters*), and west of the Andes Mountains in Chile. It is probably safe to assume that orographically trapped surges occur near most terrain barriers worldwide. In some cases, the temperature gradient associated with the leading portion of orographically trapped surges is so strong that the surges are effectively trapped density currents. It has been proposed that orographically trapped surges can be explained using trapped Kelvin wave³ dynamics, but, in many if not most cases, surges seem to occur without evidence of a wave-like disturbance propagating through the pressure and wind fields adjacent to the barrier.

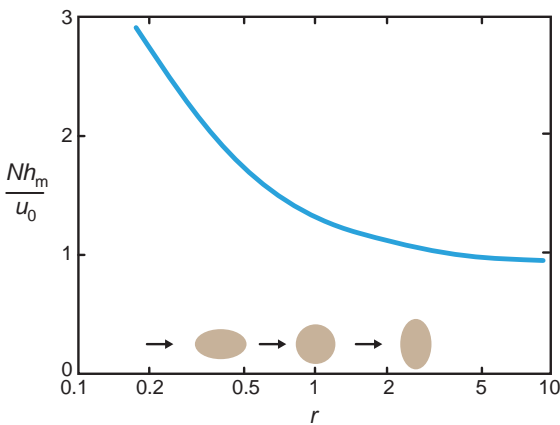


Figure 13.2 The nondimensional mountain height Nh_m/u_0 at which (13.15) is met, that is, where stagnation begins, as a function of the aspect ratio of the mountain r (crosswise dimension divided by streamwise dimension) for an air parcel moving along the surface. For a particular r , one can consider higher and higher mountains by moving upward on the diagram until the stagnation curve is reached. The stagnation curve was estimated based on linear theory calculations of I_δ . (Adapted from Smith [1990].)

³A Kelvin wave is a gravity wave trapped by a horizontal boundary (or the equator). The winds and wave propagation are parallel to the boundary.

When such surges occur along coastlines, in locations where there are mountain ranges near the coast, the surges are often referred to as *coastal surges*. In the western United States, coastal surges are most common in the warm season and are associated with an abrupt shift in wind from northerly to southerly, rapid decreases in temperature (as much as 10°C or more), increases in pressure, and a transition from cloud-free to low overcast sky conditions (e.g., Figure 13.3). In the eastern United States, northerly surges of cold air down the east side of the Appalachian Mountains are commonly observed in winter on the south side of a surface anticyclone, where winds having an easterly geostrophic wind component are directed from offshore toward the mountains, and are blocked and deflected southward by the mountains. This type of orographically trapped cold-air surge is locally referred to as *cold-air damming* (Figures 13.4–13.6). Cold-air damming occurs in virtually every significant East Coast freezing and frozen precipitation event. Ageostrophic cold advection and hydrostatic pressure rises associated with the damming offset geostrophic warm advection and pressure falls in advance of extratropical cyclones approaching from the west or southwest. Secondary cyclogenesis along the coast is partly related to the inability of cyclones to be maintained as they pass over the low-level, stable, dammed air mass.

In most cases of orographically trapped cold-air surges, the low-level atmosphere satisfies

$$h_m > \frac{u}{N} \rightarrow Fr_m < 1, \quad (13.17)$$

where u is the barrier-normal wind component at the surface upstream of the barrier and N is the average Brunt-Väisälä frequency over the depth of the barrier. For cases in which the flow is blocked over a significant depth, Fr_m is significantly less than unity (Fr_m is often in the range of 0.1–0.5 in trapped surge events).

It is apparent from (13.17) that orographically trapped surges are favored in strongly stratified environments, which is why the phenomena most often involve relatively cold low-level air masses. The presence of clouds on the upwind side of the mountains, especially those that precipitate into a dry boundary layer, further enhances the potential for trapping or damming. In some cases Fr_m is initially marginal or unsupportive of trapping or damming, but the evaporation of precipitation almost by itself increases the low-level static stability and decreases Fr_m . These ‘bootstrap’ cases are sometimes referred to as *diabatic damming* cases, in contrast to *dynamic damming* cases in which small Fr_m is present owing to the prevailing large-scale conditions (i.e., cases in which evaporation and subsequent diabatic cooling are not necessary in order for damming to occur).

In the case of low-level air approaching a mountain barrier from the west (east), winds are deflected poleward (equatorward), resulting in a large poleward (equatorward) ageostrophic wind component west (east) of the barrier. A ridge of high pressure builds poleward (equatorward) as a hydrostatic consequence of the trapped cold air mass. The width of the pressure ridge attributable to the trapped cold air mass is well approximated by the *Rossby radius of deformation*,

$$L_R = \frac{Nh}{f}, \quad (13.18)$$

where f is the Coriolis parameter, h is the scale height of the flow that is perturbed by the terrain, and N should be representative of the average static stability over h . When $Fr_m < 1$, an appropriate scale height is $h = h_I = u/N$, where h_I is known as the *inertial height scale* or *gravity height scale*. In this case, (13.18) becomes

$$L_R = \frac{u}{f} = L_{Rm} Fr_m, \quad (13.19)$$

where $L_{Rm} = Nh_m/f$ is sometimes called the *mountain Rossby radius*.⁴

In the case of an abrupt change of air mass in the vertical, such as in the case of a layer of warm subsiding air overlying a cool marine layer, with the two air masses being separated by a strong inversion (as is observed in many coastal surge events), conditions approach a two-layer fluid system and (13.18) can be well approximated as

$$L_R = \frac{\sqrt{g'H}}{f}, \quad (13.20)$$

where $g' = g\Delta\theta/\bar{\theta}$ is sometimes called the *reduced gravity*, H is the depth of the lower (relatively cold) layer, $\bar{\theta}$ is the mean potential temperature of the lower layer, and $\Delta\theta$ is the potential temperature jump across the inversion separating the two layers. For $f = 10^{-4} \text{ s}^{-1}$, $H = 1 \text{ km}$, $\Delta\theta = 5 \text{ K}$, and $\bar{\theta} = 290 \text{ K}$, (13.20) yields $L_R = 130 \text{ km}$.

Regarding the deflection of air, without loss of generality, consider a low-level parcel of air moving approximately westward toward a north–south-oriented mountain range (Figure 13.7), as might be the case in an episode of cold-air damming east of the Appalachian Mountains when an anticyclone is positioned to the north of the parcel. Far upstream of the mountains, the parcel experiences no net acceleration owing to a balance among the pressure gradient, Coriolis,

⁴ In the case of $Fr_m > 1$, the appropriate scale height h is the mountain height h_m ; thus, $L_R = Nh_m/f = L_{Rm}$. The dimensionless quantity u/fL_{Rm} is sometimes called the *mountain Rossby number*. See Overland and Bond (1995).

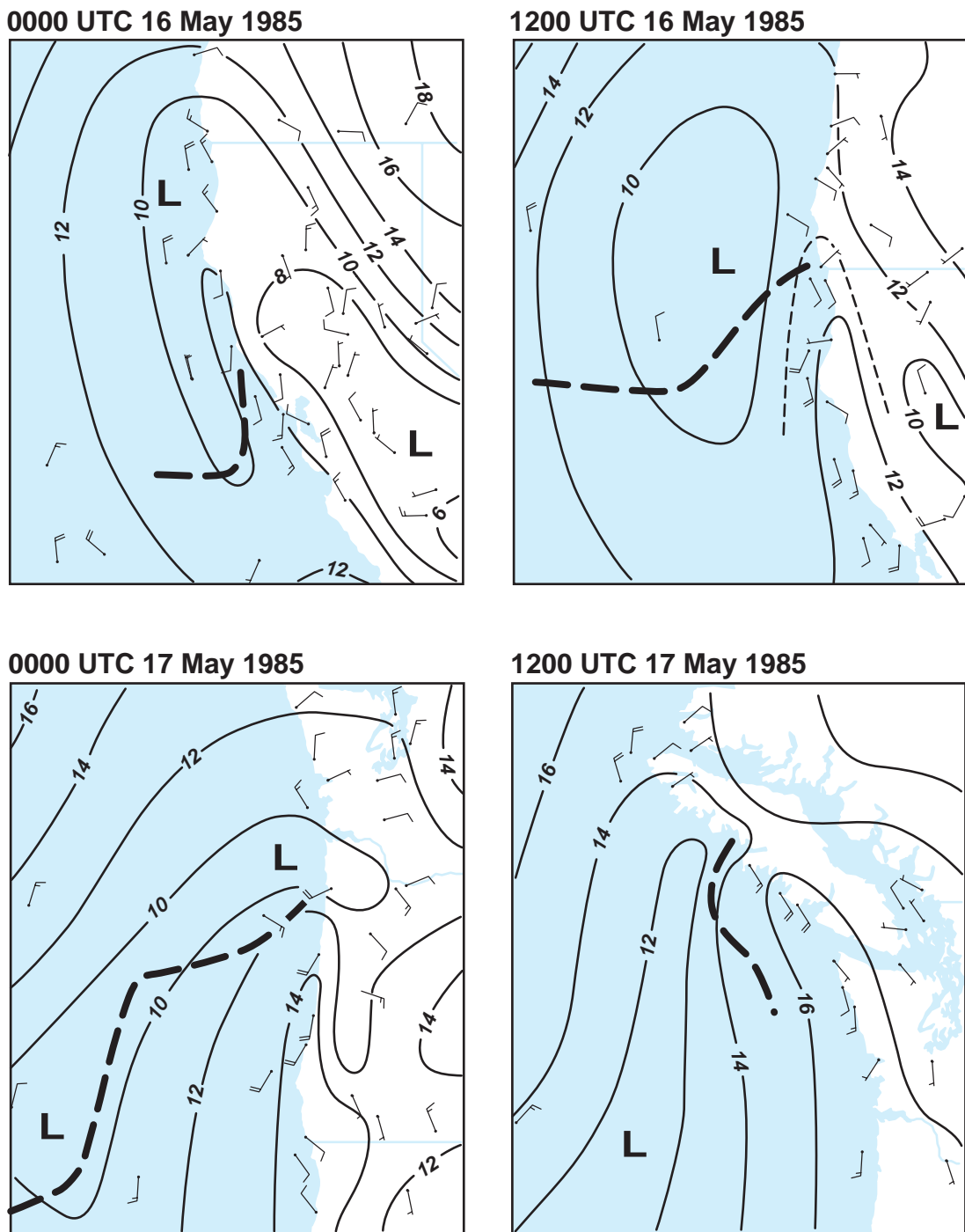


Figure 13.3 Sea-level pressure analyses and surface winds depicting a northward propagating coastal surge along the West Coast of the United States on 16–17 May 1985. Isobars are contoured every 2 mb (the leading '10' is omitted) with solid lines; an intermediate isobar is drawn as a thin dashed line in the 1200 UTC 16 May analysis. The bold dashed line in each panel indicates the northern boundary of stratus clouds based on satellite imagery. Wind barbs are in knots. (Adapted from Mass and Albright [1987].)

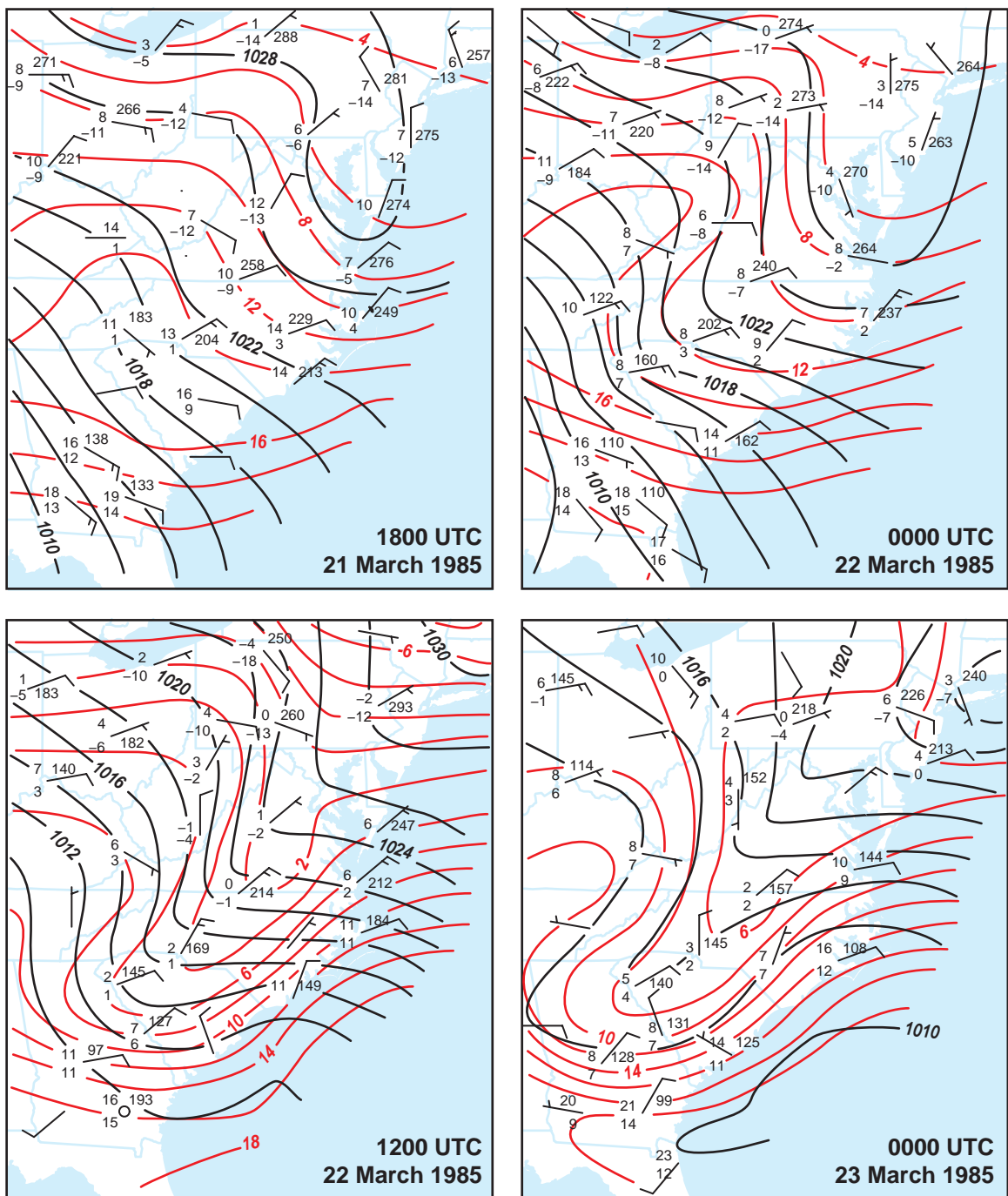


Figure 13.4 Cold-air damming example along the Appalachian Mountains during the period 21–23 March 1985. Black contours are altimeter settings in mb (2 mb intervals), red contours are surface potential temperatures in °C (2°C intervals), and station models display temperature (°C), dewpoint (°C), sea-level pressure (tenths of mb; the leading '10' and decimal are omitted), and wind barbs (knots). The pressure ridge extends almost to the coast, which is approximately a distance of one Rossby radius from the mountain crest. (Adapted from Bell and Bosart [1988].)

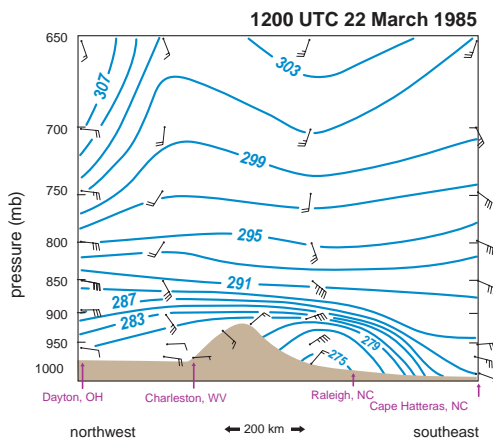


Figure 13.5 Vertical cross-section normal to the Appalachian Mountains for the case shown in Figure 13.4 at 1200 UTC 22 March 1985. Potential temperatures are contoured with units of K. (Adapted from Bell and Bosart [1988].)

2015 UTC 18 April 2003

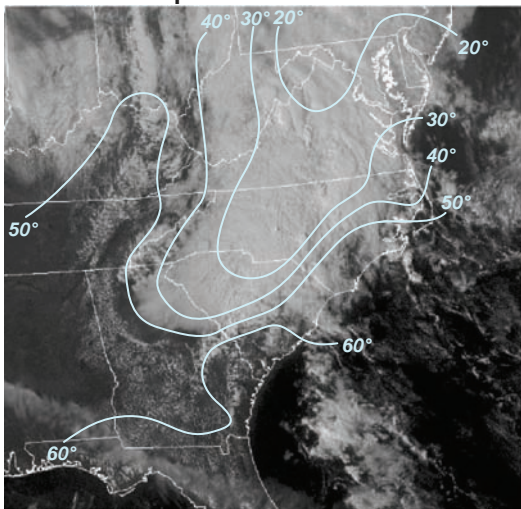


Figure 13.6 Visible satellite image showing a dramatic example of cold-air damming at 2015 UTC 18 April 2003, in which the cold-air mass was advancing southward as a trapped density current. Isotherms ($^{\circ}$ F) are overlaid.

and friction forces. Once the parcel reaches the mountain slope and begins ascending, the parcel begins decelerating as a result of the effects described in Section 13.1. The deceleration of the parcel is associated with a weakening of the northward-directed Coriolis force, resulting in a

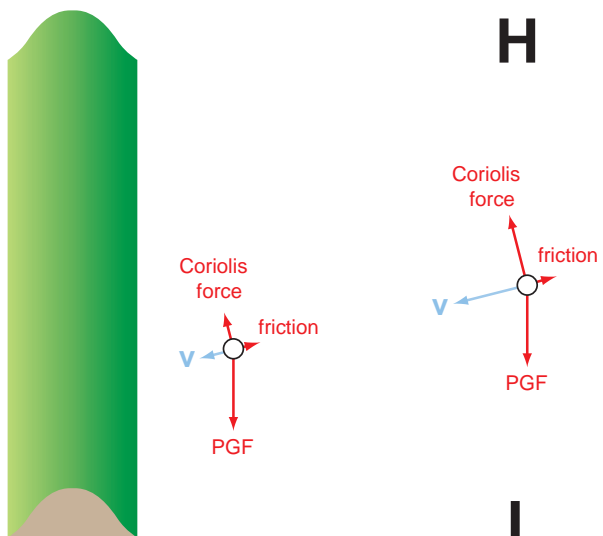


Figure 13.7 Force diagrams for an air parcel approaching a northern hemisphere mountain range in a situation with $Fr_m < 1$. Far away from the mountain range, a balance exists among the pressure gradient, Coriolis, and friction forces. If the atmosphere is stably stratified, the parcel decelerates as it nears and ascends the mountain range. If the pressure gradient force is the same near the mountain range as it is a large distance from the mountains, then the upstream balance among the pressure gradient, Coriolis, and friction forces cannot be maintained as higher terrain is encountered. The parcel experiences a net acceleration in the direction of the pressure gradient force (toward the south). Also see Figure 13.8.

southward deflection (to the left of the parcel's initial motion) by the large-scale pressure gradient force. Once air has been diverted southward, the Coriolis force keeps the cold air trapped against the mountains (Figure 13.8). Farther upstream within the cold-air mass, but close to the mountains, where northerly winds are approximately steady and blowing roughly along the elevation contours, the pressure gradient force is directed downslope and is in approximate balance with the upslope-pointing Coriolis force and friction (Figure 13.8).

In many cold-air surge cases, the deflection of air by the terrain produces a *barrier jet* on the upslope side of the barrier. Barrier jets can attain wind speeds of $15\text{--}30 \text{ m s}^{-1}$ and are usually centered at an altitude roughly half the height of the mountain crest (Figure 13.9). In addition to being seen in cases of cold-air damming east of the Appalachian Mountains in the eastern United States, barrier jets have been

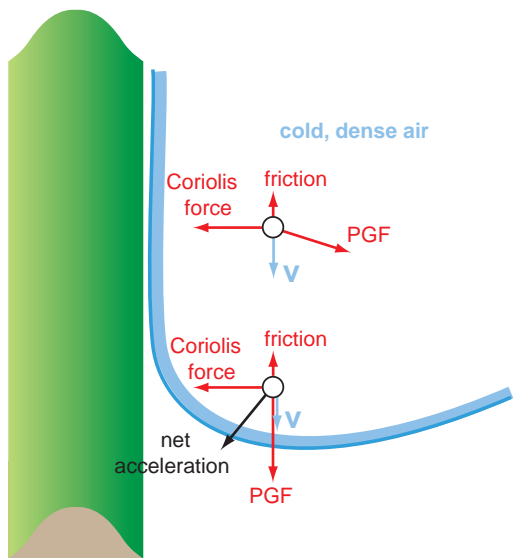


Figure 13.8 Schematic illustration of the damming of cold air against a mountain range in the northern hemisphere. Within the leading portion of the cold-air surge, an along-mountain pressure gradient force is present, the Coriolis force points (upslope) to the right of a parcel's velocity (v), and the net force traps air parcels against the terrain. Farther upstream within the cold-air mass, the pressure gradient force is directed downslope and is in approximate balance with the upslope-pointing Coriolis force.

observed along the Sierra Nevada in California, the Brooks Range in Alaska, the southern coast of Alaska (Figure 13.10), and the Transantarctic Mountains and Antarctic Peninsula in Antarctica. It can be shown that the approximate scale of the velocity increase in the direction parallel to the coast or mountain range is $\Delta v \approx N^2 h_f^2 / f L_{Rm} = u^2 / f L_{Rm}$, where v is the coast- or mountain-parallel wind component.⁵ The strongest barrier jets are therefore observed when there is a strong mountain-normal wind and small mountain Rossby radius, and thus small N and h_m , but not so small (nor u so large) that Fr_m exceeds unity.

13.3 Lee vortices

Counter-rotating vortices are commonly observed in the lee of an isolated terrain obstacle when the flow is strongly stratified and forced to pass around the obstacle. On some occasions a single pair of oppositely signed vertical vorticity extrema is observed in the wake of the obstacle

(Figure 13.11), whereas on other occasions a long series of alternating cyclonic and anticyclonic vortices—a *von Karman vortex street*—extends downwind of the obstacle (Figure 13.12). Wake vortices can form from fundamentally different dynamical processes, depending on the mountain Froude number. The time and space scales of wake vortices are relatively small (hours and 10–100 km, respectively); thus, the rotation of the Earth does not play a major role in their development.

Though it is tempting to presume that all wake vortices form as a result of the separation of a viscous boundary layer from an obstacle, numerical simulations in which a free-slip lower boundary condition (i.e., no surface drag) is employed also contain wake vortices (e.g., Figure 13.11), despite viscous stress being entirely absent at the lower boundary.⁶ These simulated vortices actually decrease in intensity when surface friction is added. This variety of wake vortices, at least in numerical simulations, is confined to a range of Fr_m between 0.1 and 0.5. This range of Fr_m is fairly typical of cases in which wake vortices are observed in the real atmosphere.

In the case of wake vortices that form as a result of a purely inviscid mechanism, baroclinic vorticity generation is key; these wake vortices form even when there is no vorticity, either horizontal or vertical, in the upstream flow. On the upwind side of an obstacle, upsloping winds cause isentropes to bulge upward, resulting in a region of negative buoyancy, horizontal buoyancy gradients, and generation of horizontal vorticity (vortex rings encircle the buoyancy minimum). Horizontal advection of vorticity displaces the vortex rings downwind from the buoyancy minimum. (In the absence of horizontal advection of vorticity, the vortex rings would be collocated with the buoyancy contours, although this limiting case cannot actually be achieved here because the negative buoyancy is a direct result of a horizontal airstream ascending the obstacle in a stable atmosphere.) Furthermore, isentropes are depressed in the wake of the obstacle, leading to a region of positive buoyancy immediately downstream of the obstacle. The horizontal buoyancy gradients associated with the buoyancy maximum generate vortex rings having the opposite sense of rotation as the vortex rings generated upwind as a result of the buoyancy minimum. Like the upwind-generated vortex rings, these vortex rings are also shifted downwind of the warm anomaly owing to horizontal advection. Negative vertical velocities are found downwind of the obstacle, and the interaction of the baroclinically generated vortex rings with the horizontal gradients of vertical velocity on the immediate downstream side of the obstacle produce vertical vorticity by way of tilting. A pair of

⁵ See Overland and Bond (1995).

⁶ See Smolarkiewicz and Rotunno (1989, 1990).

0000 UTC 14 January 1980
mountain-parallel wind component

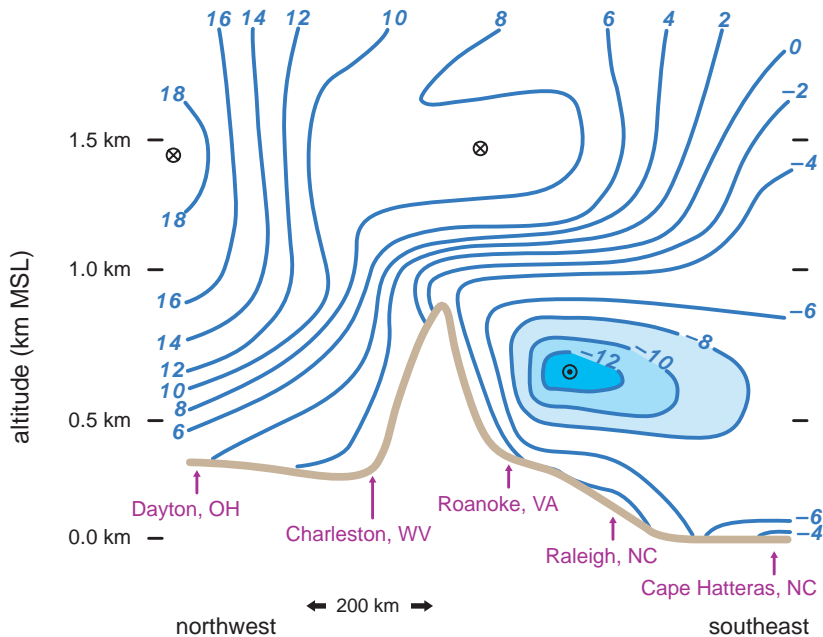


Figure 13.9 Components of the winds parallel to the Appalachian Mountains in a cold-air damming case at 0000 UTC 14 January 1980. Wind speeds are in m s^{-1} , and negative values indicate northeasterly wind components (out of the page). A barrier jet is evident east of the mountains below the crest of the mountains (wind speeds less than -8 m s^{-1} shaded). (Adapted from Forbes *et al.* [1987].)

counter-rotating vortices straddles the minimum vertical velocity immediately downstream of the obstacle.⁷

It is admittedly difficult to conceptualize the dynamics described above. Perhaps the easiest way is by consideration of Ertel's potential vorticity conservation (Section 2.4.5), which was also used in Section 8.4 to provide an alternative perspective on mesocyclogenesis in supercell

⁷ The interaction of stratified flow with the obstacle results in gravity waves, which were discussed in Chapter 12. When the gravity waves are generated by an isolated obstacle, the downstream vertical velocity pattern has a herringbone structure (Section 12.2), which also is evident in Figure 13.13. Thus, the wake vortices described herein can also be viewed as the result of three-dimensional gravity wave dynamics. Gravity wave breaking and the overturning of isentropic surfaces have also been found in numerical simulations to contribute to regions of large vertical vorticity in the wake of obstacles (see, e.g., Crook *et al.* 1990). Even in these more complicated situations, however, the baroclinic generation of horizontal vorticity, followed by tilting via the vertical velocity gradients in the wake of the obstacle, remains as the fundamental process by which vertical vorticity is generated in the first place.

thunderstorms. From Ertel's theorem, an inviscid, adiabatic fluid conserves its potential vorticity, that is,

$$\frac{d}{dt} \left(\frac{\boldsymbol{\omega} \cdot \nabla \theta}{\rho} \right) = 0, \quad (13.21)$$

where the Coriolis force has been neglected and $\boldsymbol{\omega} \cdot \nabla \theta = 0$ upstream of the obstacle; therefore, potential vorticity must remain zero at all times along parcel trajectories. For adiabatic motion, this implies that vortex lines must lie in isentropic surfaces. Furthermore, for steady flow around the obstacle, streamlines and trajectories are identical and the difficult issue of displaying a complicated three-dimensional flow is made a little easier in that we can look at a two-dimensional analysis of the wind on isentropic surfaces. For example, see Figure 13.13. Vertical vorticity is implied where vortex lines cross contours of isentrope displacement height. For a given strength of vorticity along a vortex line, vertical vorticity is largest in magnitude where a vortex line crosses closely spaced

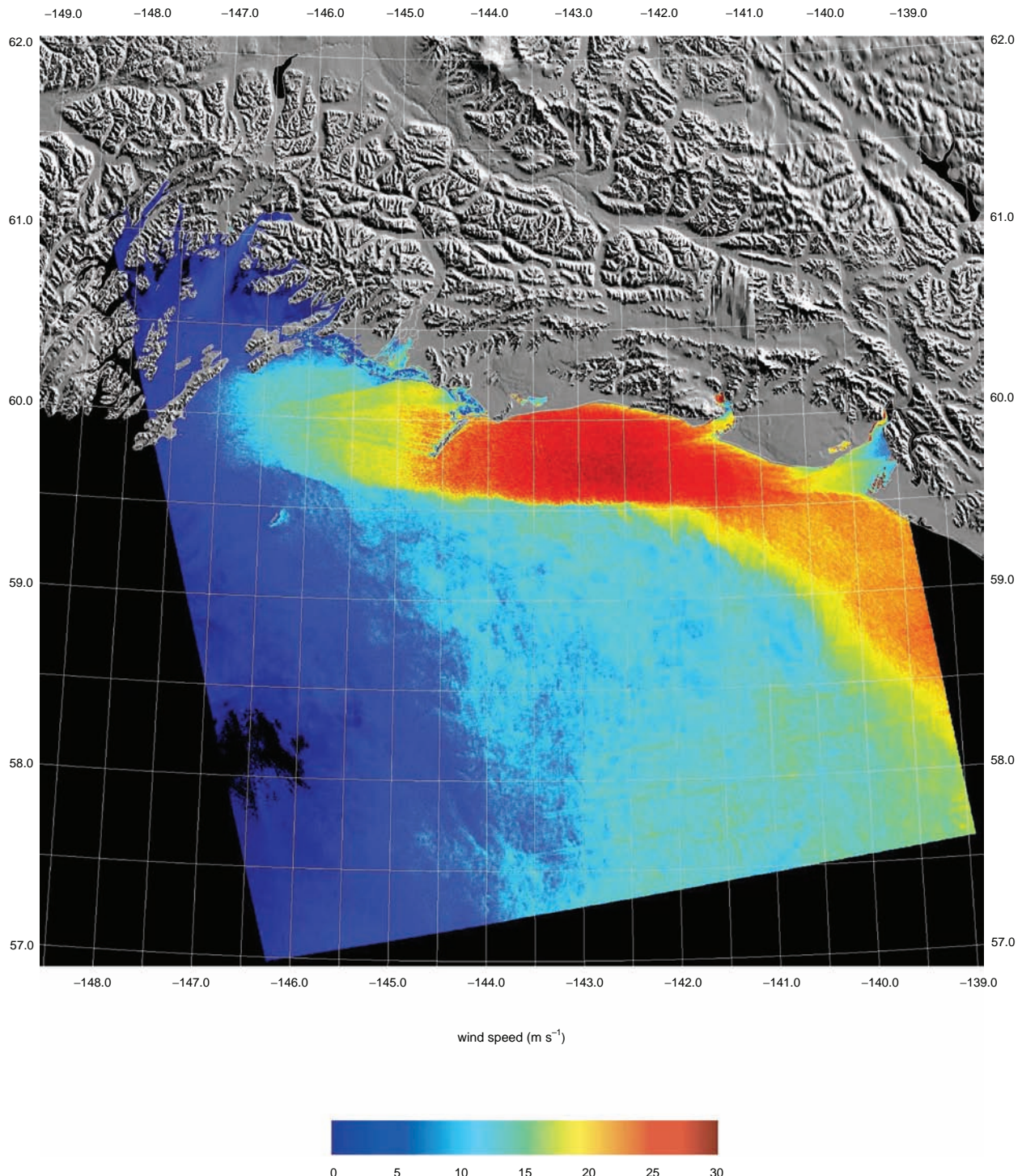


Figure 13.10 Synthetic aperture radar imagery of an easterly barrier jet (peak winds are well in excess of 25 m s^{-1}) resulting from the deflection of southerly winds approaching the southern coast of Alaska. Courtesy of Nathaniel Winstead.

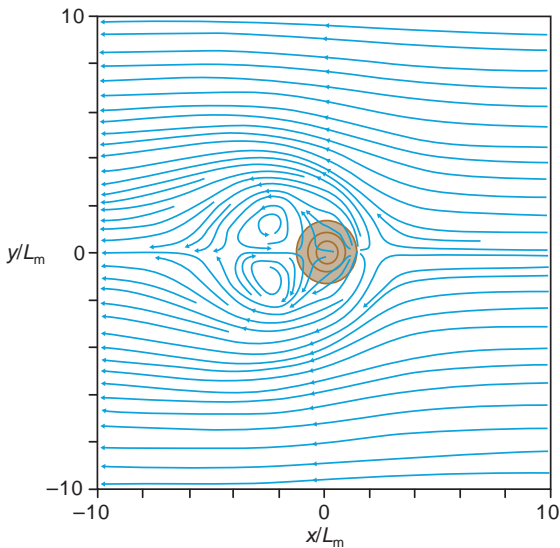


Figure 13.11 Example of a pair of counter-rotating vortices in the wake of an isolated mountain peak in a numerical simulation. Streamlines along the ground are shown (the lower boundary is free-slip), and the concentric brown shaded contours in the center of the domain represent the height of the mountain with a contour interval of $0.25 h_m$, where h_m is the height of the mountain. The axes are nondimensionalized by L_m , the radius of the mountain. The mountain Froude number Fr_m is 0.22. (Adapted from Smolarkiewicz and Rotunno [1989].)

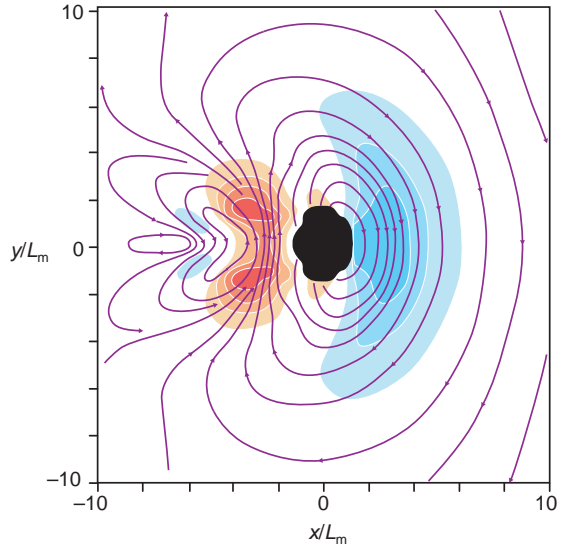


Figure 13.13 Vortex lines on the isentropic surface of undisturbed height for the numerical simulation shown in Figure 13.11. The shaded regions show the displacement field of the isentropic surface (warm shades indicate downward displacements of $-3.33, -6.66, -10$, and $-13.33 \times 10^{-5} h_m$, where h_m is the mountain height; cold shades indicate upward displacements of $3.33, 5.00$, and $6.66 \times 10^{-5} h_m$). The axes are nondimensionalized by L_m , the radius of the mountain. (Adapted from Smolarkiewicz and Rotunno [1989].)

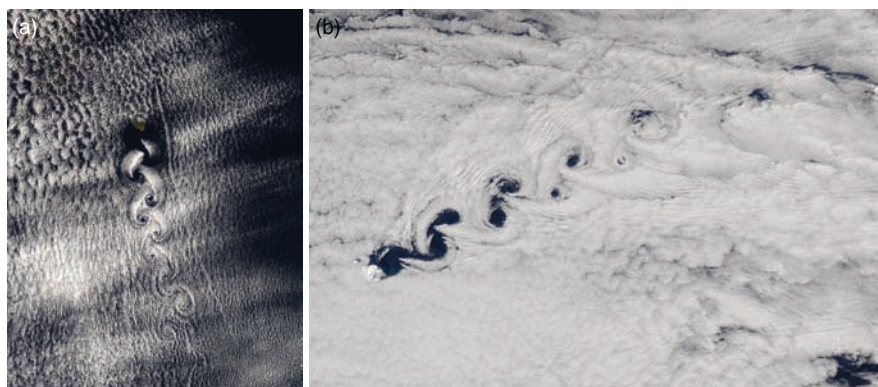


Figure 13.12 Moderate Resolution Imaging Spectroradiometer (MODIS) satellite imagery of von Karman vortex streets in a strongly stratified atmosphere downwind of (a) the Revillagigedo Archipelago in the north Pacific Ocean (13 May 2004) and (b) Heard Island in the south Indian Ocean (30 September 2004). Images courtesy of the MODIS Rapid Response Project at the National Aeronautics and Space Administration (NASA) Goddard Space Flight Center (GSFC).

contours of isentrope displacement height at a large angle (we cannot infer the strength of the vorticity along the vortex lines in Figure 13.13, but vortex lines cross displacement height contours at significant angles in the wake of the obstacle). The sign of the vertical vorticity is given by whether the vortex line points up or down the isentropic surface. Note that the general pattern of the vortex lines in Figure 13.13 is that the vortex lines form rings with shapes that roughly match the shape of the upwind displacement field (and are shifted downstream by a dimensionless distance of roughly $2\text{--}3 L_m$ in this particular simulation, where L_m is the radius of the obstacle), which corresponds to the buoyancy field on a horizontal surface. Again, the pattern of the horizontal projection of vortex lines is due to the combined effects of baroclinic generation by buoyancy gradients plus horizontal advection. A three-dimensional perspective of wind vectors, vortex lines, and temperature anomalies is presented in Figure 13.14.

Some caution should be used in applying Ertel's theorem to the problem of wake vortices, since Ertel's theorem

assumes inviscid flow.⁸ An initially inviscid flow may undergo a transition into a dissipative regime if wave breaking occurs. Potential vorticity is not conserved in such dissipative regimes, and in fact (nonzero) potential vorticity zones, called *potential vorticity banners*, are typically found in the wakes of obstacles. This complication notwithstanding, *surface friction is unnecessary for the formation of wake vortices*.

In idealized numerical simulations of wake vortices resulting from the baroclinic effects described above, the width of the vortices and the distance between the obstacle and the vortices decrease as Fr_m increases within the range of 0.1–0.5. The intensity and depth of the vortices does not vary appreciably within this range of Fr_m . The shedding of vortices, like that evident in Figure 13.12, can occur if there is asymmetry in the shape of the obstacle, such as an isolated elliptical obstacle that is turned at a slight angle to the mean flow. Vortex shedding can also occur from

⁸ See Smith (1989) and Schar and Smith (1993a, 1993b).

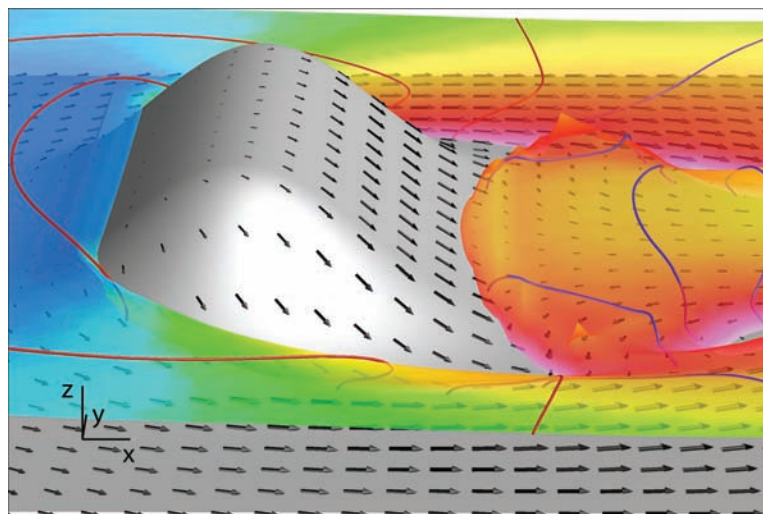


Figure 13.14 Numerical simulation of the flow of a stratified layer past a three-dimensional obstacle. The isosurface of potential temperature with an initial undisturbed height of 0.8 times the initial depth of the stratified layer is shown. Coloring of the isosurface indicates buoyancy (or equivalently vertical displacement), with red colors representing positive buoyancy (downward displacement) and blue colors negative (upward displacement). The thin purple and red tubes show selected vortex lines running approximately tangent to the isosurface. The direction of the vortex lines is such that the red tubes circle in the clockwise direction as viewed from above, while the purple tubes circle counterclockwise. Note that this implies positive vertical vorticity on the right-hand side of the wake (as viewed from upstream) and negative vertical vorticity on the left-hand side. Vectors show the total velocity at the surface of the terrain. The figure has been stretched by a factor of 12 in the vertical for ease of visual interpretation. (From Epifanio and Rotunno [2005]. Courtesy of the American Meteorological Society.)

a symmetric obstacle if the oncoming flow is horizontally non-uniform or if the Coriolis force is included.

For Fr_m outside of the range of 0.1–0.5, wake vortices are not observed to form as a result of purely inviscid processes, at least not in numerical simulations. When wake vortices are observed outside of this range of Fr_m , it is likely that the separation of the viscous boundary layer from the obstacle has played the dominant role in their formation. Our emphasis has been on the inviscid baroclinic mechanism because wake vortices are usually observed in an environment characterized by low Fr_m .

The baroclinic vorticity generation mechanism is believed to be responsible for the formation of a number of well known mesoscale eddies in the United States.

Examples include the *Santa Cruz eddy* over the Monterey Bay (California) (Figure 13.15) and the *Denver Cyclone* (Colorado) (Figure 13.16). In the case of the Denver Cyclone, the west–east ridge known as the Palmer Divide is the source of baroclinic vorticity generation (Figure 13.17). The Palmer Divide extends eastward onto the plains from the approximately north–south-oriented Rocky Mountains. The Denver Cyclone forms in regimes of southerly to southeasterly low-level flow and low mountain Froude number. Only a cyclonic vortex is generated because the obstacle is ‘one sided’ in the sense that the Palmer divide connects with higher, north–south-oriented terrain to the west. Narrow shear zones are also commonly found to arise within the Denver Cyclone, and these shear

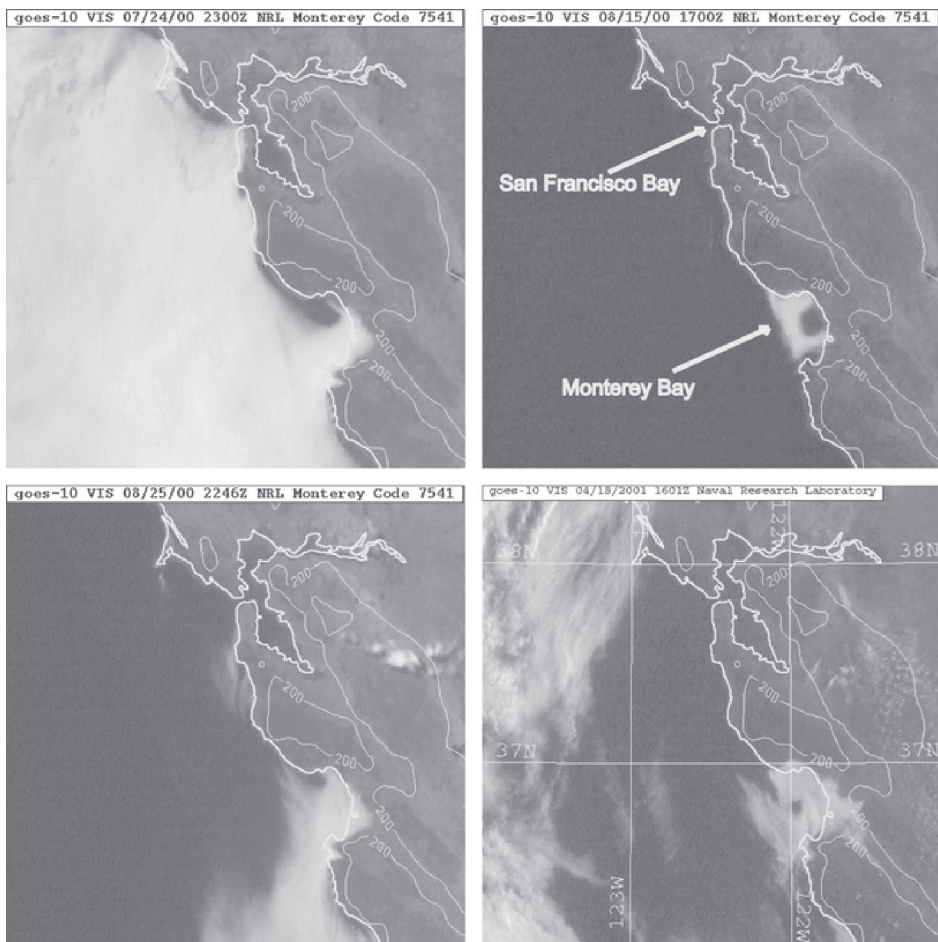


Figure 13.15 GOES-10 visible satellite images (1 km resolution) of San Francisco Bay and Monterey Bay, showing several examples of cyclonically rotating stratus clouds associated with Santa Cruz eddies: (a) 2300 UTC (1600 PDT) 24 Jul 2000; (b) 1700 UTC (1000 PDT) 15 Aug 2000; (c) 2246 UTC (1546 PDT) 25 Aug 2000; (d) 1600 UTC (0900 PDT) 18 Apr 2001. (From Archer and Jacobson [2005]. Courtesy of the American Meteorological Society.)

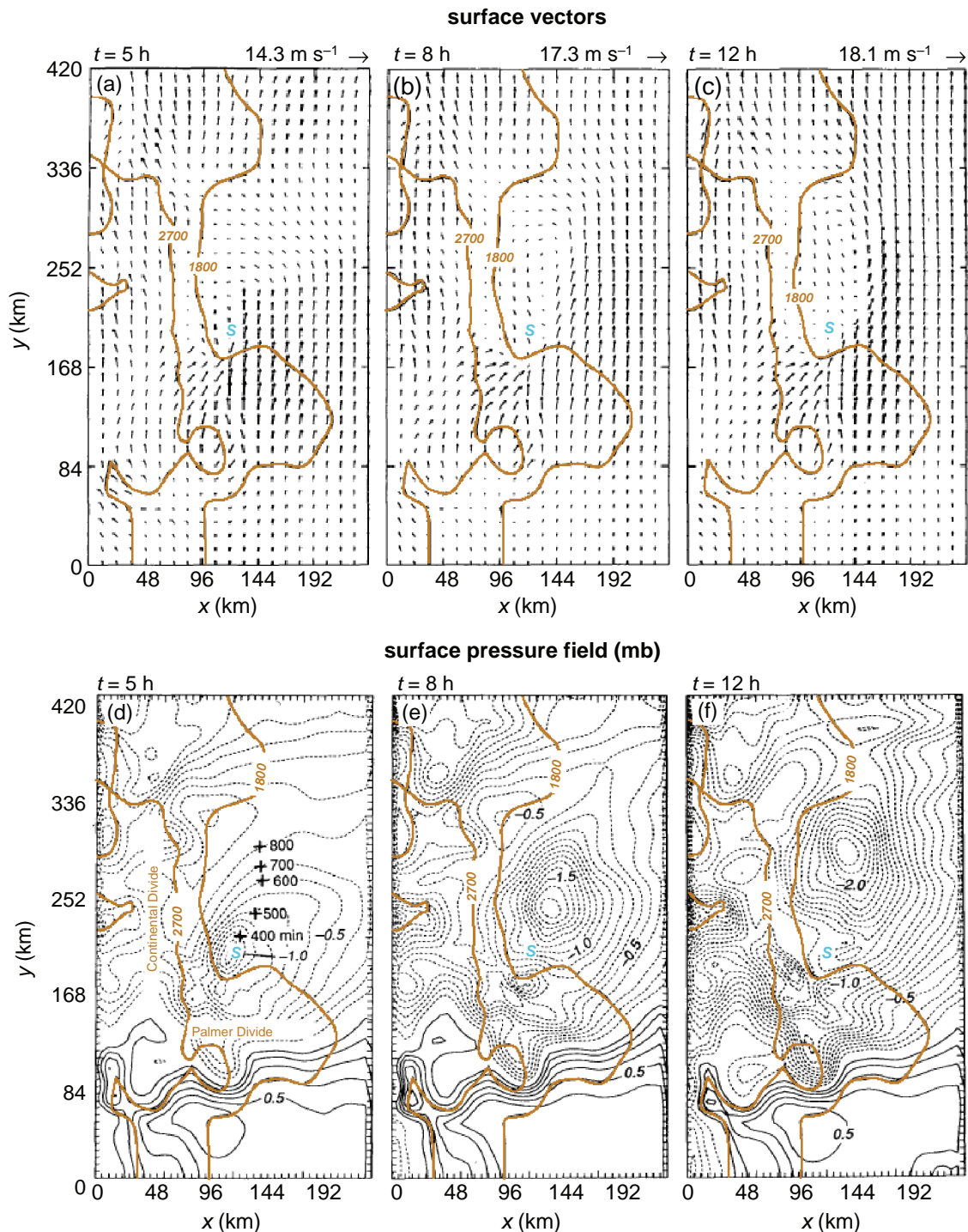


Figure 13.16 Surface wind vector field in an idealized numerical simulation of the Denver Cyclone in which the ambient wind is from the south and $\text{Fr}_m = 0.48$ at (a) $t = 5 \text{ h}$, (b) $t = 8 \text{ h}$, and (c) $t = 12 \text{ h}$. The contour interval of topography is 900 m. 'S' marks the position of Stapleton Airport. Surface perturbation pressure field at (d) $t = 5 \text{ h}$, (e) $t = 8 \text{ h}$, and (f) $t = 12 \text{ h}$. The track of the surface low at intervals of 100 min is shown in (d). (Adapted from Crook *et al.* [1990].)

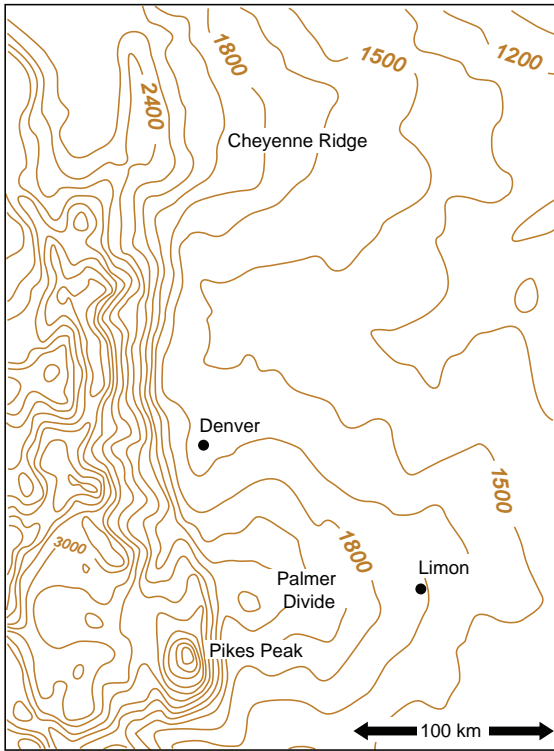


Figure 13.17 The terrain of eastern Colorado (contour interval 150 m).

zones seem to be the vorticity source of nonmesocyclonic tornadoes that frequently develop in the vicinity of the Denver Cyclone (Section 10.2).

13.4 Gap flows

When winds approach a terrain barrier that contains a gap, anomalously high wind speeds can be observed as air is forced through the gap. Such *gap flows* are associated with along-gap pressure gradient forces, the origins of which are most commonly the larger-scale flow regime. Even when the large-scale wind field is fairly stagnant (implying a weak large-scale pressure gradient force), however, gap flows can arise from significant low-level temperature differences in the air masses on each side of the barrier. Gap flows perhaps most often occur in conjunction with cold-air surges, when significant cross-barrier temperature differences and cross-barrier winds may both be present. Gap flows have been

well documented in the Columbia River Gorge and the Strait of Juan de Fuca in the northwestern United States (Figure 13.18), the Howe Sound and Dixon Entrance in British Columbia (Figure 13.19), between the Aleutian Islands and within the Shelikof Strait of Alaska, the Strait of Gibraltar between Spain and Morocco, the Chivela Pass of Mexico (Figure 13.20), and the Cook Strait of New Zealand. In the case of corridors of enhanced wind observed between islands, the relatively fast gap winds are mainly a consequence of winds on either side of the gap being slowed by the enhanced surface drag of the upstream terrain compared with the water. In this section the focus is on gap wind *accelerations*.

In the case of a long narrow gap, the *cross-gap Rossby number*, Ul/fL^2 (where U is the along-gap wind speed, f is the Coriolis parameter, and l and L are the cross- and along-gap length scales, respectively), is usually much less than unity, implying a nearly geostrophic balance in the cross-gap direction. In the along-gap direction there is a three-way ageostrophic ‘balance’ among the acceleration, pressure gradient force, and drag forces owing to surface friction and entrainment atop the gap flow, although there is usually a point within a long gap at which antitriptic balance between the drag and pressure gradient forces is attained in the along-gap direction. The strength of the gap flow increases with the strength of the along-gap pressure gradient force. In strong gap flow cases, winds can easily exceed 25 m s^{-1} with accompanying pressure differentials of 5 mb or more from the gap entrance to exit.

In general, the fastest winds are not observed within the gap, as one might anticipate based on the Venturi effect, from which we would expect that the fastest flow would occur where the terrain constriction is greatest (i.e., the lowest pressure is typically not observed in the gap, but instead an along-gap pressure gradient typically exists over the length of the gap). Instead, in the most intense examples of gap winds, the fastest winds are found in the gap exit regions (Figures 13.21b, 13.21c and 13.22b, c). As stated above, typically cooler air is present on one side of the gap, with warmer air on the other side, and an inversion is often present at a height below the crest of the terrain barrier so that the cold air is forced through the gap rather than simply passing over the barrier. The mountain Froude number of the upstream flow tends to be less than unity, although when Fr_m becomes much less than unity the fastest along-gap winds are found near the center of the gap, or perhaps are even slightly shifted toward the entrance region of the

1700 UTC 9 December 1995



Figure 13.18 Surface analysis from 1700 UTC 9 Dec 1995 during a gap flow event in the Strait of Juan de Fuca. Flight-level data from the NOAA P-3 aircraft are plotted every 2 min between 1658 and 1718 UTC. The aircraft was situated at three different altitudes above MSL denoted by the boxed numbers; the flight track is indicated by the white dashed line. The contour interval for sea level pressure is 2 mb (the leading '10' is dropped). (Adapted from Colle and Mass [2000].)

gap (Figures 13.21d and 13.22d). As one might expect, for large Fr_m (i.e., >1), there is almost no enhancement of the gap winds (Figures 13.21a and 13.22a).

The fact that the winds typically do not attain their maximum speed within the gap itself implies that the flow through the gap cannot be strictly horizontal. On the contrary, air parcels above the surface but below the crest of the

terrain barrier typically descend as they pass through a gap. The relationship between vertical motion and gap winds is evident from the potential temperature contours in the vertical cross-sections shown in Figure 13.23 (for motions that are steady, inviscid, and dry adiabatic, the isentropes in the vertical cross-sections are also streamlines). The vertical motion field is the result of gravity waves generated by the

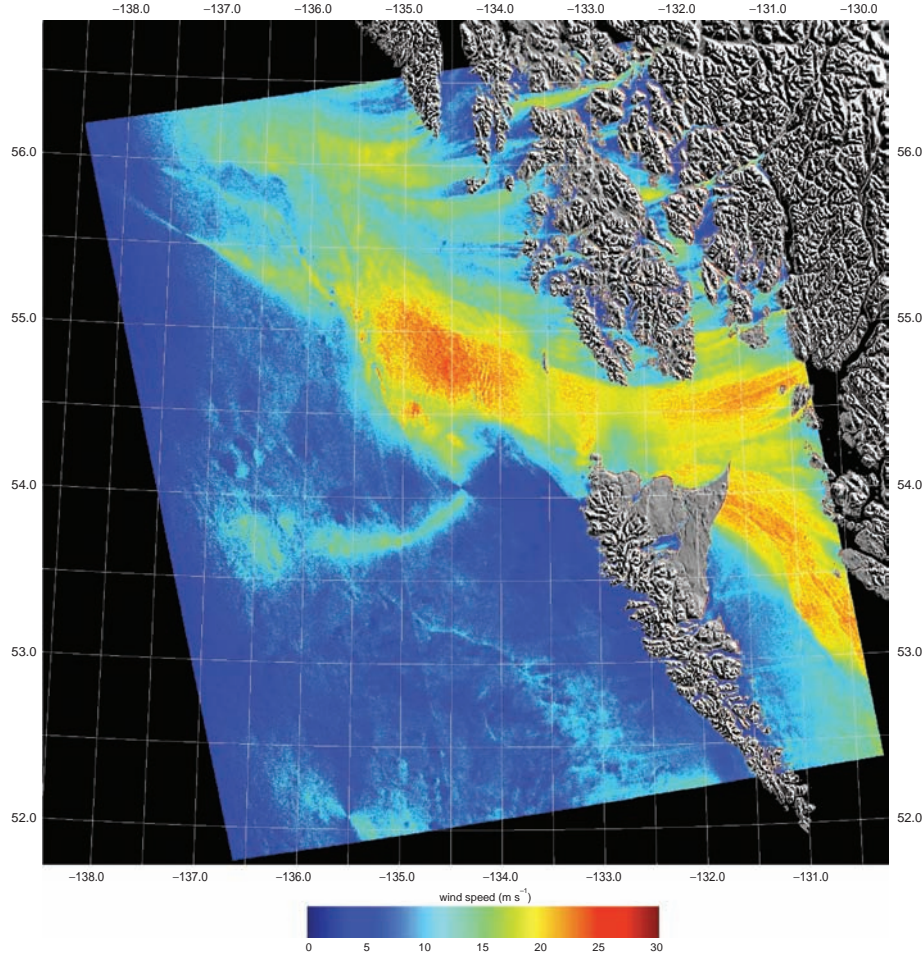


Figure 13.19 Gap winds observed by synthetic aperture radar in the Dixon Entrance between Graham Island, British Columbia, and Prince of Wales Island, Alaska. Image courtesy of Nathaniel Winstead.

barrier; that is, gravity waves are ultimately responsible for the shift of the region of maximum low-level horizontal wind speed to the exit region of the gap. Vertical momentum transport associated with gravity wave breaking plays an important role in the formation of the strongest gap winds. In the case of very small Fr_m , vertical motions are suppressed and the maximum low-level winds occur nearer to the location of greatest flow constriction within the gap (e.g., Figure 13.23d; in Figure 13.23d the fastest winds are actually shifted slightly toward the gap entrance region).

The fact that faster gap winds can be obtained when air descends as it flows through the gap is also easily demonstrated via the Bernoulli equation for steady compressible flow [refer to Section 2.5 and Equation (2.146)],

$$\frac{v^2}{2} + c_p T + gz = \text{constant}, \quad (13.22)$$

where v is the wind speed, T is absolute temperature, and the lhs is conserved along a trajectory in the absence

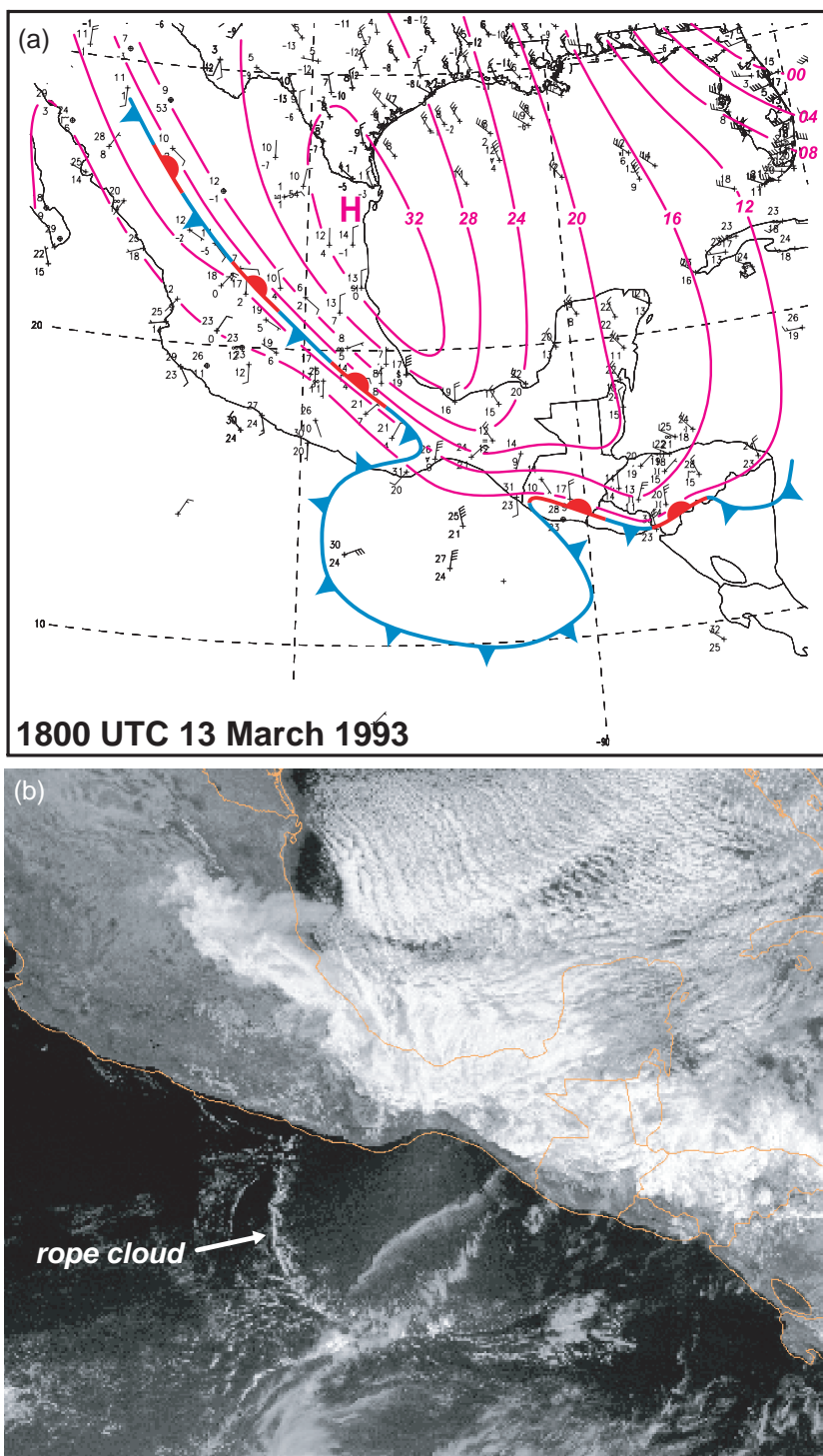


Figure 13.20 (a) Manually analyzed surface map from 1800 UTC 13 March 1993 during a gap flow event through the Chivela Pass of Mexico. Magenta contours are isobars (mb; the leading '10' is dropped). (b) GOES-7 visible satellite imagery at 1801 UTC 13 March showing a rope cloud at the leading edge of the polar air mass. (Adapted from Steenburgh *et al.* [1998].)

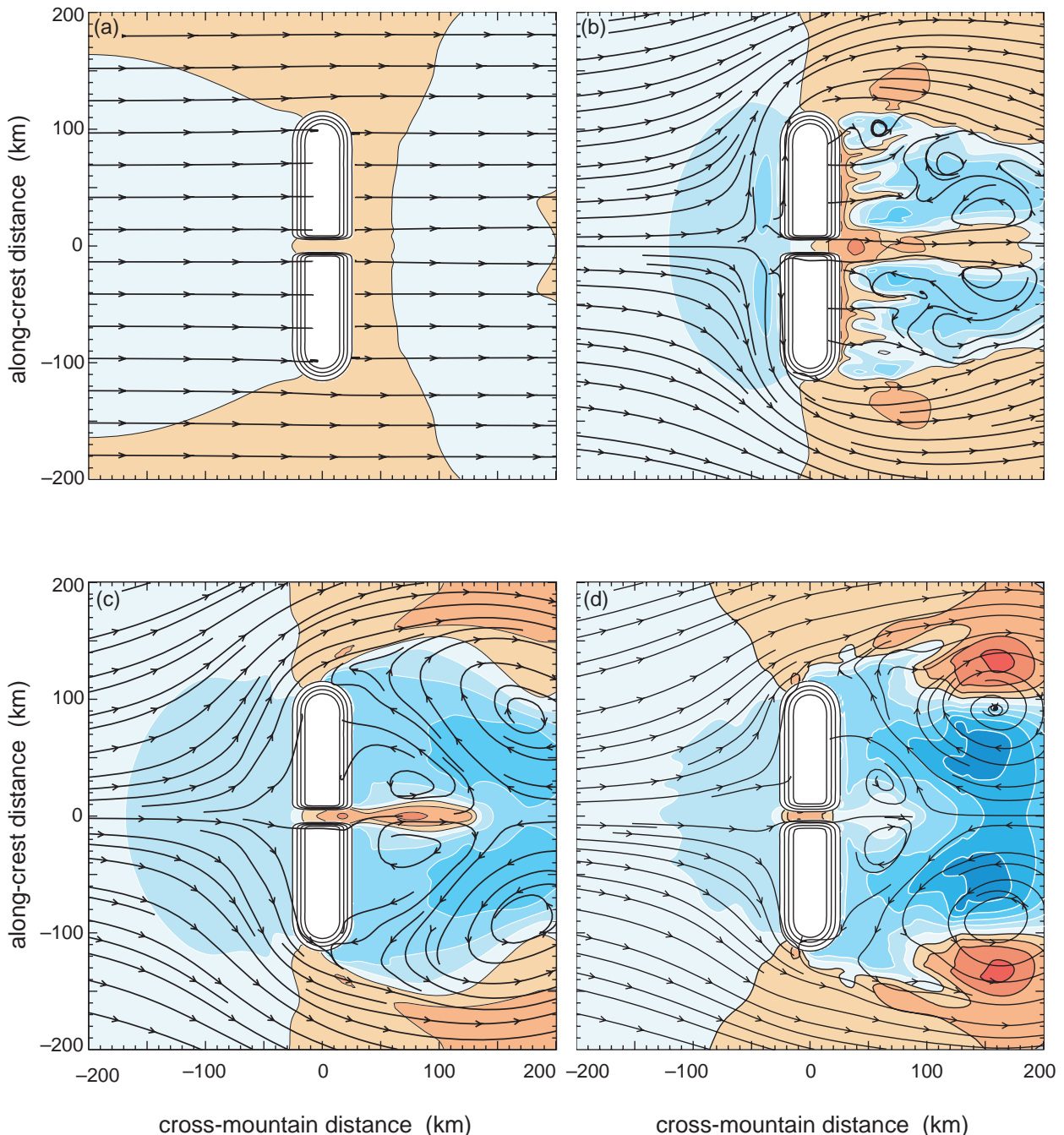


Figure 13.21 Idealized numerical simulation of westerly winds encountering a ridge with a gap when the F_{rm} is equal to (a) 4.0, (b) 0.7, (c) 0.4, and (d) 0.2. Horizontal streamlines and normalized perturbation velocity ($((u - U)/U)$, where u is the zonal wind speed and U is the zonal wind speed far upstream; shaded contours) at $z = 300$ m are shown. The contour interval is 0.5; warm (cold) color shading corresponds to positive (negative) values. Terrain contours are every 300 m. Notice how (a) and (b)–(d) represent flow-over and flow-around regimes, respectively, as would be expected from the differences in F_{rm} . The simulation does not include the Coriolis force. (Adapted from Gaberšek and Durran [2004].)

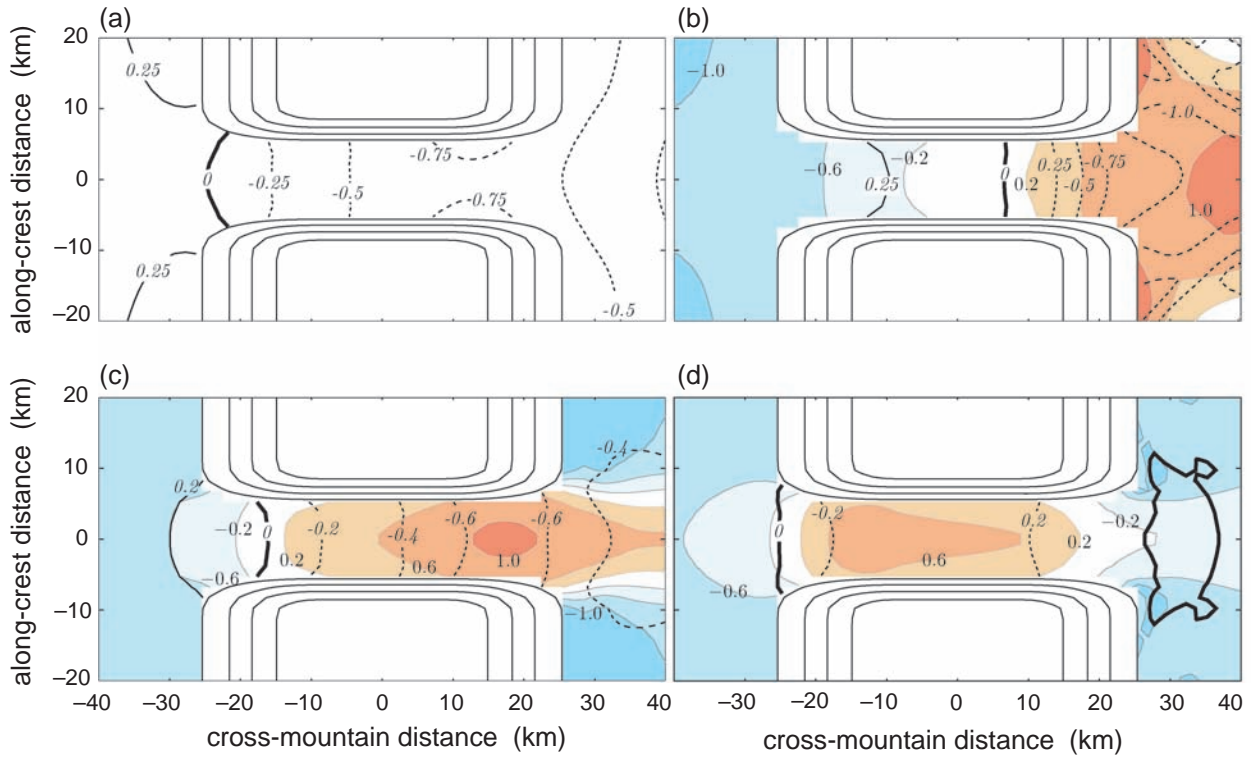


Figure 13.22 Close-up view of the simulated gap flows shown in Figure 13.21. Normalized pressure perturbation ($(p/\text{Fr}_m/\rho_0 U^2)$; solid black lines for positive, dashed black lines for negative values, thick solid line represents zero perturbation) and normalized perturbation velocity ($((u - U)/U)$; shaded contours) at $z = 300$ m are shown when Fr_m is equal to (a) 4.0, (b) 0.7, (c) 0.4, and (d) 0.2. The contour interval for pressure perturbation (italics) is 0.25 in (a) and (b) and 0.2 in (c) and (d). For the velocity perturbation, the contour interval is 0.4; warm (cold) color shading corresponds to positive (negative) values; speeds in the interval $[-0.2, 0.2]$ are unshaded. Terrain contours are every 300 m. (Adapted from Gaberšek and Durran [2004].)

of mixing. In gap flows where both the wind speed and temperature increase downstream, as is typically the case, trajectories must be descending, provided the flow is steady and dry adiabatic.

The width of the gap determines how rapidly the flow transitions to the ambient conditions near the gap exit region. For wide gaps having a width scale l

equal to or greater than the mountain Rossby radius, $L_{\text{Rm}} = Nh_m/f$, there is a gradual transition to the ambient conditions in the gap exit region. Conversely, for narrow gaps having $l < L_{\text{Rm}}$, such as the case simulated in Figures 13.21–13.23, the transition to the ambient conditions is more rapid and can involve hydraulic jumps.

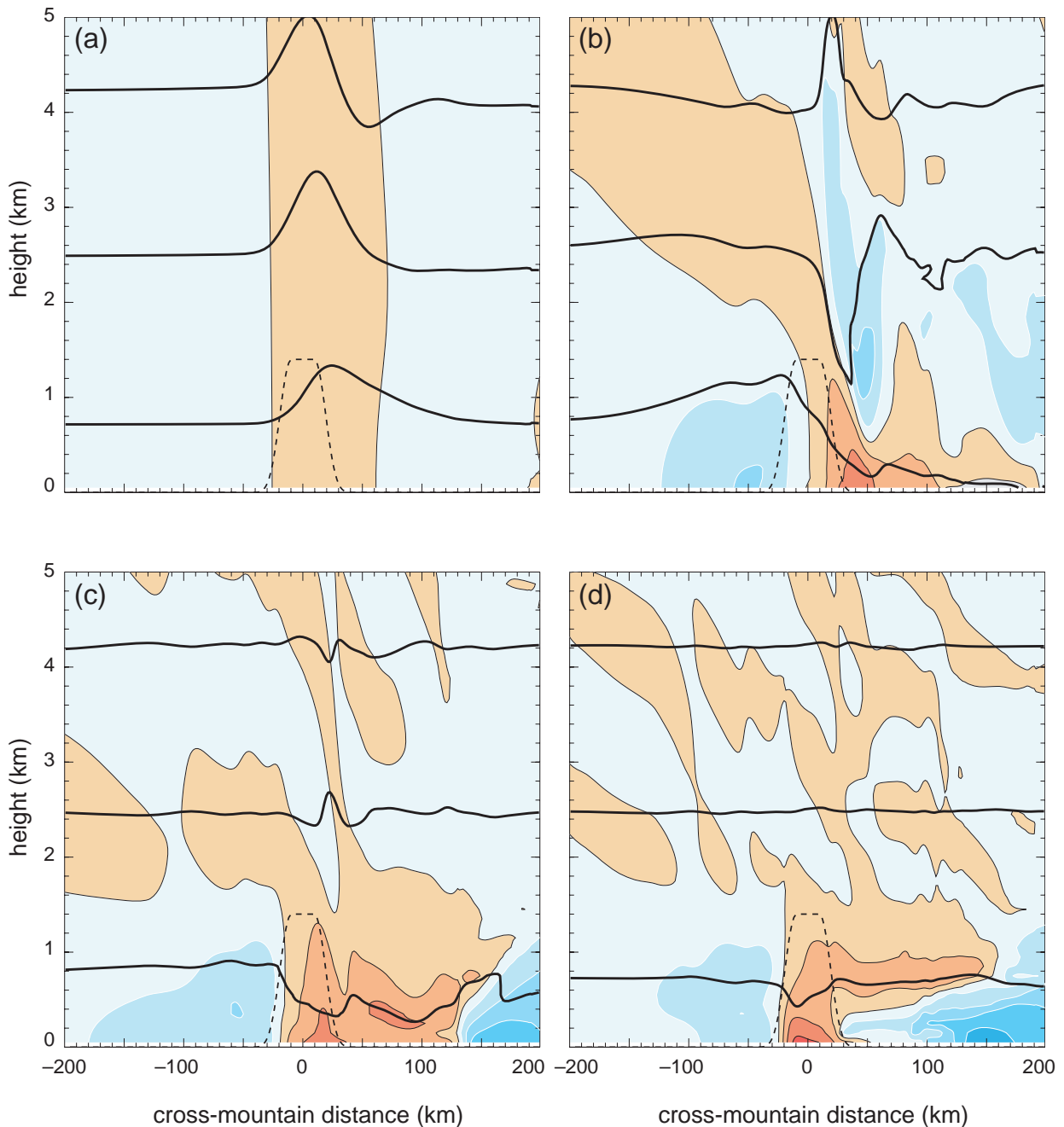


Figure 13.23 Potential temperature and horizontal velocity in the y - z plane along the centerline of the gap for the numerical simulation shown in Figures 13.21 and 13.22 for the case of Fr_m equal to (a) 4.0, (b) 0.7, (c) 0.4, and (d) 0.2. The heavy lines are the 275, 280, and 285 K isentropes; the normalized perturbation velocity field is contoured every 0.5 and shaded as in Figure 13.21. The dashed line shows the profile of the adjacent ridge. (Adapted from Gaberšek and Durran [2004].)

Further reading

General resources

- Baines, P. G., 1979: Observations of stratified flow past three-dimensional barriers. *J. Geophys. Res.*, **84**, 7834–7838.
- Baines, P. G., 1995: *Topographic Effects in Stratified Flows*. Cambridge University Press.
- Pierrehumbert, R. T., and B. Wyman, 1985: Upstream effects of mesoscale mountains. *J. Atmos. Sci.*, **42**, 977–1003.
- Smith, R. B., 1979: The influence of mountains on the atmosphere. *Advances in Geophysics*, Vol. **21**, Academic Press, 87–230.
- Smith, R. B., 1989a: Hydrostatic airflow over mountains. *Advances in Geophysics*, Vol. **31**, Academic Press, 1–41.
- Smith, R. B., 1989b: Mountain induced stagnation points in hydrostatic flow. *Tellus*, **41A**, 270–274.
- Smith (1990).
- Snyder, W. H., R. S. Thompson, and R. E. Eskridge, 1985: The nature of strongly stratified flow over hills: dividing streamline concept. *J. Fluid Mech.*, **152**, 249–288.

Orographically trapped cold-air surges

- Bell, G. D., and L. F. Bosart, 1988: Appalachian cold-air damming. *Mon. Wea. Rev.*, **116**, 137–161.
- Forbes, G. S., R. A. Anthes, and D. W. Thomson, 1987: Synoptic and mesoscale aspects of an Appalachian ice storm associated with cold-air damming. *Mon. Wea. Rev.*, **115**, 564–591.
- Mass and Albright (1987).
- Overland, J. E., 1984: Scale analysis of marine winds in straits and along mountainous coasts. *Mon. Wea. Rev.*, **112**, 2530–2534.
- Overland and Bond (1995).
- Stauffer, D. R., and T. T. Warner, 1987: A numerical study of Appalachian cold-air damming and coastal frontogenesis. *Mon. Wea. Rev.*, **115**, 799–821.

Wake vortices

- Crook *et al.* (1990).
- Crook, N. A., T. L. Clark, and M. W. Moncrieff, 1991: The Denver Cyclone. Part II: Interaction with the convective boundary layer. *J. Atmos. Sci.*, **48**, 2109–2126.
- Epifanio, C. C., and D. R. Durran, 2002a: Lee-vortex formation in free-slip stratified flow over ridges. Part I: Comparison of weakly nonlinear inviscid theory and fully nonlinear viscous simulations. *J. Atmos. Sci.*, **59**, 1153–1165.
- Epifanio, C. C., and D. R. Durran, 2002b: Lee-vortex formation in free-slip stratified flow over ridges. Part II: Mechanisms of vorticity and PV formation in nonlinear viscous wakes. *J. Atmos. Sci.*, **59**, 1166–1181.
- Epifanio, C. C., and R. Rotunno, 2005: The dynamics of orographic wake formation in flows with upstream blocking. *J. Atmos. Sci.*, **62**, 3127–3150.
- Rotunno, R., and P. K. Smolarkiewicz, 1991: Further results on lee vortices in low-Froude-number flow. *J. Atmos. Sci.*, **48**, 2204–2211.
- Schär, C., and D. R. Durran, 1997: Vortex formation and vortex shedding in continuously stratified flow past isolated topography. *J. Atmos. Sci.*, **54**, 534–554.
- Schär and Smith (1993a).
- Schär and Smith (1993b).
- Smolarkiewicz, P. K., and R. Rotunno, 1989: Low Froude number flow past three-dimensional obstacles. Part I: Baroclinically generated lee vortices. *J. Atmos. Sci.*, **46**, 1154–1166.
- Smolarkiewicz, P. K., and R. Rotunno, 1990: Low Froude number flow past three-dimensional obstacles. Part II: Upwind flow reversal zone. *J. Atmos. Sci.*, **47**, 1498–1511.
- Thomson, R. E., J. F. R. Gower, and N. W. Bowker, 1977: Vortex streets in the wake of the Aleutian Islands. *Mon. Wea. Rev.*, **105**, 873–884.

Gap flows

- Colle, B. A., and C. F. Mass, 1998a: Windstorms along the western side of the Washington Cascade Mountains. Part I: A high-resolution observational and modeling study of the 12 February 1995 event. *Mon. Wea. Rev.*, **126**, 28–52.
- Colle, B. A., and C. F. Mass, 1998b: Windstorms along the western side of the Washington Cascade Mountains. Part II: Characteristics of past events and three-dimensional idealized simulations. *Mon. Wea. Rev.*, **126**, 53–71.
- Colle and Mass (2000).
- Gaberšek and Durran (2004).
- Gaberšek, S., and D. R. Durran, 2006: Gap flows through idealized topography. Part II: Effects of rotation and surface friction. *J. Atmos. Sci.*, **63**, 2720–2739.
- Jackson, P. L., and D. Steyn, 1994a: Gap winds in a fjord. Part I: Observations and numerical simulations. *Mon. Wea. Rev.*, **122**, 2645–2665.

- Jackson, P. L., and D. Steyn, 1994b: Gap winds in a fjord. Part II: Hydraulic analog. *Mon. Wea. Rev.*, **122**, 2666–2676.
- Lackmann, G. M., and J. E. Overland, 1989: Atmospheric structure and momentum balance during a gap-wind event in Shelikof Strait, Alaska. *Mon. Wea. Rev.*, **117**, 1817–1833.
- Mass, C. F., S. Businger, M. D. Albright, and Z. A. Tucker, 1995: A windstorm in the lee of a gap in a coastal mountain barrier. *Mon. Wea. Rev.*, **123**, 315–331.
- Overland, J. E., and B. A. Walter, 1981: Gap winds in the Strait of Juan de Fuca. *Mon. Wea. Rev.*, **109**, 2221–2233.
- Pan, F., and R. B. Smith, 1999: Gap winds and wakes: SAR observations and numerical simulations. *J. Atmos. Sci.*, **56**, 905–923.
- Steenburgh *et al.* (1998).

PART V

Appendix

A

Radar and Its Applications

A.1 Radar basics

Radar are arguably the most important mesoscale meteorological observing systems. It is virtually impossible to study mesoscale phenomena observationally without analyzing radar data at some point. Recall from Chapter 1 that the first use of the term *mesoscale* was in a radar paper highlighting observations of subsynoptic-scale meteorological phenomena.

A weather radar works by transmitting electromagnetic waves (microwaves) that interact with hydrometeors as the waves propagate through the atmosphere. The radar's *transmitter* produces power at a known frequency (3–10 GHz for most weather radars), and the transmitted waves are focused into a beam (typically 1–2° wide) by an *antenna*. When the radar beam intercepts a particle, called a *target*, some of the energy is absorbed and some is scattered. The amount that is scattered depends on the shape and dielectrical properties of the scatterer (i.e., its *refractive index*) and on the ratio of the wavelength of the transmitted energy to the size of the scatterer. When the diameter of the target (e.g., a raindrop) is very small compared with the wavelength, the scattered energy is proportional to the sixth power of the diameter of the target. This is sometimes referred to as the *Rayleigh scattering regime*. In contrast, when the target diameter is large relative to the wavelength, sometimes called the *Mie scattering regime*, the relationship between the scattered energy and target diameter is considerably more complicated and cannot be expressed as a simple function of target size.

Only a small fraction of the energy transmitted by the radar is backscattered by targets to the radar's antenna; most of the scattering is in directions that do not intersect

the antenna. The radar's *receiver* detects, amplifies, and converts the reflected signal into a low-frequency signal. The receiver must be very sensitive—the transmitted power of a radar is typically between 250 and 1000 kW, yet the backscattered power that reaches the receiver may only be $\sim 10^{-16}$ kW, that is, 18 orders of magnitude less than was transmitted!¹¹ Furthermore, the receiver must be able to detect a wide range of backscattered power. The backscattered power can vary by nine orders of magnitude, depending on whether the radar is observing large hail or dust.

The most popular quantity related to returned power probably is the *logarithmic reflectivity factor*,

$$Z = 10 \log_{10} \left(\frac{z}{1 \text{ mm}^6/\text{m}^3} \right), \quad (\text{A.1})$$

where z is the *reflectivity factor*, which has units of $\text{mm}^6 \text{ m}^{-3}$ (z is the summation over a volume of the sixth power of target diameters), and Z is measured in units of dBZ (i.e., decibels relative to a reflectivity factor of $1 \text{ mm}^6 \text{ m}^{-3}$).

The reflectivity factor is related to the *received backscattered power*, P_r , via

$$z = C P_r r^2, \quad (\text{A.2})$$

where C , known as the *radar constant*, depends on the attributes of the radar (e.g., wavelength, antenna characteristics, losses of power in the radar, etc.) and r is the distance to the target. Therefore, the reflectivity factor

¹¹ It is hard for most of us to grasp just how large a span of 18 orders of magnitude is. It represents the difference between the diameter of a dime ($\sim 10^{-2}$ m) and the distance to the nearest star outside of our solar system ($\sim 10^{16}$ m), which itself is hard for most of us to grasp.

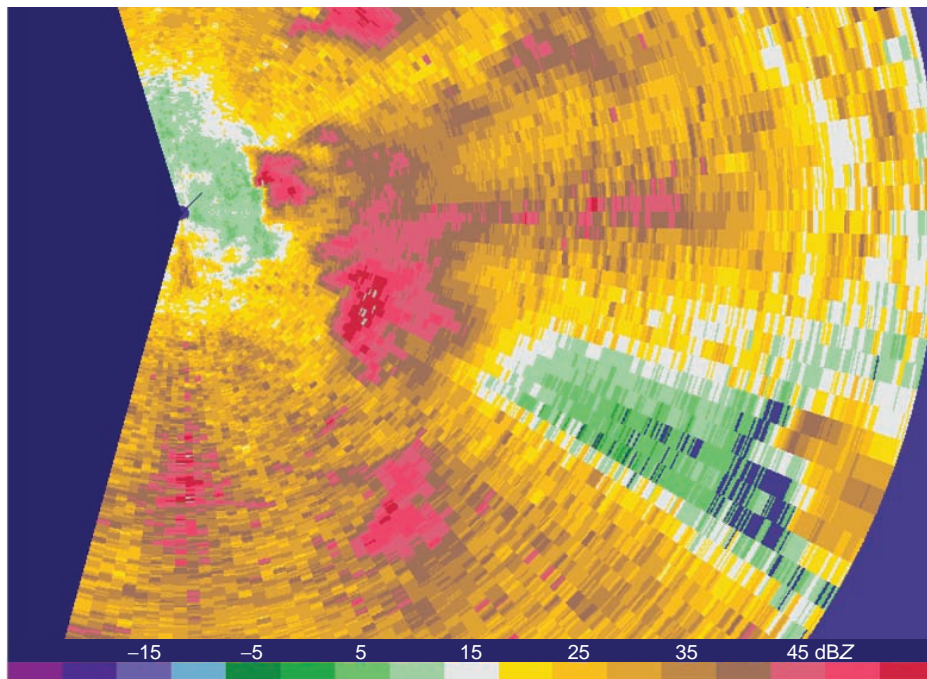


Figure A.1 When relatively short wavelengths are used, both scattering and absorption are significant, and attenuation can be severe. In this example, a 5-cm radar mounted in the tail section of an aircraft is scanning a broken line of severe thunderstorm from the west. Significant loss of power is occurring within the heavy precipitation core (which likely contains large hail) located southeast of the radar; thus, the reflectivity at ranges beyond this heavy precipitation core has been underestimated.

can be viewed as a range-corrected measure of received power (there is an r^{-2} reduction in the power that is backscattered to the radar).

In addition to being sensitive to the size of the targets, the logarithmic reflectivity factor (hereafter referred to as *reflectivity*²) depends on the number of targets encountered by the electromagnetic pulse (high reflectivity implies heavier precipitation, if all else is equal). As the transmitted or backscattered radiation passes through the air, cloud, rain, etc., some of the energy is absorbed or scattered in other directions. This loss of power along the path of the radar beam is called *attenuation*, and it is most pronounced for radar using wavelengths less than 10 cm (Figure A.1).

To detect returns at various radar ranges, the returned signals are ‘gated’ (i.e., sampled periodically), usually approximately every 0.1–1 μ s, to obtain information

roughly every few tens or hundreds of meters in range. This sampling can go on until it is time to transmit the next pulse. The frequency at which pulses are transmitted by the radar is called the *pulse repetition frequency*, or PRF. Most radars have a PRF on the order of 1000 Hz. For a PRF of 1000 Hz, it is possible to acquire 1000 1- μ s samples between pulses. A sample point in time is called a *range gate*.

The factors that govern the choice of a wavelength to be used in a particular radar include the radar’s desired sensitivity (i.e., the ability to detect weak targets at long range), the radar’s ability to resolve small features, the types of targets to be studied, and the effect of the intervening atmosphere on the transmitted energy (i.e., attenuation). Other factors must also be considered, such as the cost, size, and weight of the radar. Most weather radars have wavelengths that range from 0.8–10.0 cm. Short-wavelength radars are generally smaller and less expensive to build. Furthermore, at short wavelengths (e.g., 3–5 cm or smaller), a narrow beam (1° or less) can be produced by a smaller antenna. As wavelength increases, antenna size also increases if the beamwidth is held fixed. However, the shorter the

² Even though reflectivity and logarithmic reflectivity factor are two different things as defined above, the use of the term *reflectivity* in place of *logarithmic reflectivity factor* has become so commonplace that most assume *logarithmic reflectivity factor* is implied when the term *reflectivity* is used, unless it is otherwise obvious from the context.

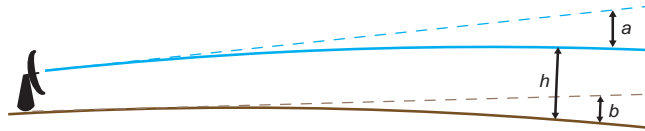


Figure A.2 Effect of Earth's curvature and refraction on the height of distant targets above the ground. The solid blue line is the path of the transmitted and reflected beam, and the solid brown line is the Earth's surface (the curvature is somewhat exaggerated for illustrative purposes). The dashed blue line is the path that the beam would take in the absence of refraction. The dashed brown line represents the line tangent to the Earth's surface at the location of the radar. The Earth's radius and oblateness determine a , and the variation of static stability along the beam determines b (usually a standard atmosphere is assumed). The height of targets above the ground (h) is known if a and b are known.

wavelength, the greater the attenuation. Short-wavelength radars are more effective in detecting small particles such as cloud droplets and drizzle droplets; however, as mentioned above, attenuation becomes more severe than when longer wavelengths are used, owing to scattering *and* absorption. Thus, it may be difficult to accurately measure the intensity of backscattered energy from distant targets. The main advantage of using longer wavelengths is that absorption by the intervening particles is drastically reduced. For example, the Weather Surveillance Radar-1988 Doppler (WSR-88D) used by the United States National Weather Service operates with a 10-cm wavelength, which is relatively immune to substantial attenuation.

The radar needs three pieces of information to determine the location of a target: azimuth angle (the angle of the radar beam with respect to north), elevation angle (the angle of the beam with respect to the horizon), and the distance from the radar to the target. The distance to the target is determined by measuring the time it takes for the pulse to complete a round trip from the radar to the target and back, that is,

$$r = \frac{ct}{2}, \quad (\text{A.3})$$

where c is the speed of light ($3 \times 10^8 \text{ m s}^{-1}$), which is the speed at which the radar pulses travel, and t is the time that elapses between the transmission of the pulse and the reception of backscattered energy from the target.

One must account for the curvature of the Earth when determining the altitude of a target. Distant targets that are close to the ground cannot be seen by a radar because they will be below the horizon. The height of a distant target that is above the horizon will be underestimated if the curvature of the Earth is not considered.

Refraction also affects the path that transmitted electromagnetic energy takes as it propagates through the atmosphere. The degree to which the radar beam is bent depends on how the refractive index, which is a strong

function of the air density, varies with height.³ In most situations the refractive index decreases with height, which causes the radar beam to be deflected downward. Usually a standard atmosphere temperature profile is assumed when computing beam height; thus, departures from this stratification lead to errors in the vertical placement of targets. In extreme cases, such as when a strong temperature inversion is present, the radar beam can be bent downward so much that it intersects the ground. This effect is called *anomalous propagation*, and it results in the appearance of ground targets on the radar display that would not normally appear.

A.2 Doppler radar principles

A.2.1 Radial velocity and spectrum width

In Doppler radars, the phase of the backscattered signal is detected, and, when it is compared with the returned phase of the previous pulse, a *radial velocity*—the component of the target's velocity parallel to the radar beam—can be computed. A phase shift is observed between subsequent pulses if a target is moving. The phase shift, $\Delta\phi$, is a result of differences in the distance a wave must travel from one pulse to the next. It can be shown that

$$\Delta\phi = \frac{4\pi\Delta r}{\lambda}, \quad (\text{A.4})$$

where $\Delta\phi$ is measured in radians, Δr is the distance the target travels between pulses (positive (negative) if the target is moving away from (toward) the radar), and λ is the wavelength of the radar. The radial velocity, v_R , is

³ The refractive index, n , is often expressed in terms of *refractivity*, N , where $N = (n - 1) \times 10^6$. For example, $n = 1.0003$ corresponds to $N = 300$; N varies from ~ 400 near the surface to ~ 200 in the middle troposphere in typical warm-season conditions.

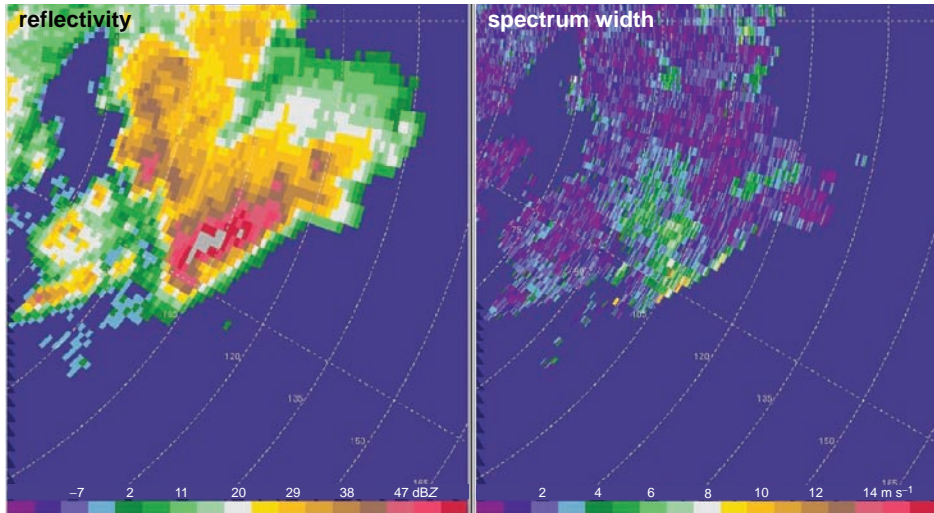


Figure A.3 Example of spectrum width imagery (right; reflectivity is on the left) of a supercell thunderstorm in central Pennsylvania. Here the spectrum width, or the standard deviation of the radial velocity measurements within a sample volume (scale has units of m s^{-1}), can be used to make inferences about the turbulence within the storm and its near environment. The inflow region of the storm (to the east-northeast) is characterized by low spectrum width values, implying fairly laminar flow, which is what might be expected in a region of horizontal accelerations, which increase helicity and suppress turbulence. The hook echo region (where the rear-flank downdraft is located), on the other hand, is characterized by large spectrum width values, implying larger turbulence there. This also might be anticipated, owing to the fact that downdrafts are driven, at least in part, by entrainment, which tends to promote turbulence.

related to the phase shift via

$$v_R = \frac{\Delta r}{\Delta t} = \frac{\lambda}{4\pi} \frac{\Delta\phi}{\Delta t}, \quad (\text{A.5})$$

where Δt is the time between pulses, known as the *pulse repetition time*, or PRT, where $\text{PRT} = \text{PRF}^{-1}$. Motion of a target toward (away from) a radar has a negative (positive) radial velocity.

When one views a radial velocity display, it is the mean velocities in the radar sample volumes that are being displayed. The variance of the radial velocity measurements in a sample volume is related to the *spectrum width*, which is a function of the spread of the terminal fall speeds of scatterers, turbulence within the sample volume, and shear of the wind along or across the beam. Spectrum width is also often used as a measure of data quality; spectrum width is falsely large when the returned signals are weak. Spectrum width imagery of a supercell thunderstorm is shown in Figure A.3.

A.2.2 Range and velocity folding

The pulses of transmitted energy are separated in space by a distance R , which is related to the PRF by $R = c/\text{PRF}$.

When radiation is backscattered off a far-away target and received at the radar *after* radiation from the next pulse has been sent, *range-folding* occurs, and it is not known whether the radar echo represents a target nearby or far away (Figures A.4 and A.5). The maximum range

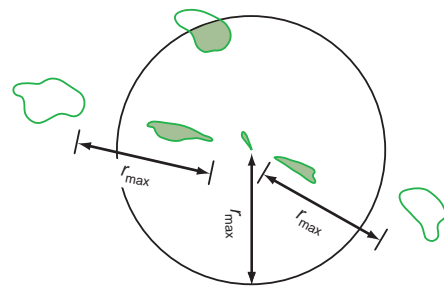


Figure A.4 Illustration of range-folding. Radar echoes beyond the maximum unambiguous range (r_{\max}) (unshaded echoes) are *folded* back into the area within the maximum unambiguous range. Echoes actually located within the maximum unambiguous range, as well as folded echoes, are both shaded.

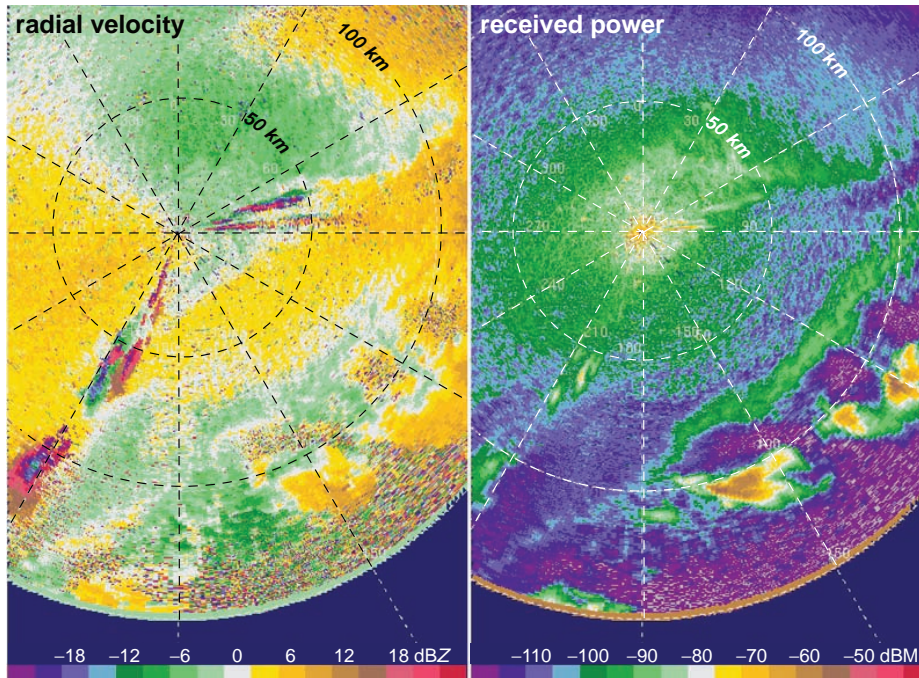


Figure A.5 Example of range-folding in imagery obtained by the National Center for Atmospheric Research (NCAR) S-POL radar on 12 June 2002 during the International H₂O Project (IHOP). Radial velocity (m s⁻¹) is displayed on the left and received power (dBm; dBm = 10 log₁₀(P_r/1 mW)) is displayed on the right. A trio of thunderstorms is unambiguously detected to the southeast of the radar. These thunderstorms developed along a northeast–southwest-oriented mesoscale convergence line. Additional thunderstorms developed along the line farther to the northeast and southwest (the extreme northern edge of one is barely visible at approximately 190° near the maximum range of 150 km), but beyond the radar’s maximum unambiguous range. These echoes are displayed as second-trip echoes near 200° and 210° at approximately 70–80 km range, near 215° at a range of approximately 110 km, and at 75–85° at ranges of approximately 20–50 km. Note the anomalous radial velocities in the region of range-folded echoes, in addition to the unusually elongated shapes of the range-folded echoes.

at which the location of echoes may be determined unambiguously is

$$r_{\max} = \frac{c}{2 \text{ PRF}}. \quad (\text{A.6})$$

Echoes at a range of $r_{\max} + nc/2\text{PRF}$ (where n is a positive integer) are received by the receiver at the same time as echoes at r_{\max} . Distant, *second-trip* echoes (echoes located between $r = r_{\max}$ and $r = 2r_{\max}$) can be distinguished by their elongated appearance since their angular width is preserved when displayed at their apparent, incorrect range.⁴ Range-folding can be identified (and removed

algorithmically) by interlacing signals having different PRFs. When the PRF changes, range-folded echoes appear to move, whereas *first-trip* echoes (echoes located at range $r < r_{\max}$) remain stationary.

The sampling rate of the returned signal (i.e., the PRF) is important in detecting the phase shift of the signal. If the sampling rate (PRF) is too slow, a large phase shift can be aliased (i.e., it will appear to have a much smaller phase shift than it actually has, resulting in an incorrect radial velocity value). Thus, a maximum unambiguous velocity also exists. It is related to the PRF and wavelength by

$$v_{R\max} = \pm \frac{(\text{PRF}) \lambda}{4}. \quad (\text{A.7})$$

All velocities exceeding these bounds are aliased or *folded* onto other portions of the velocity spectrum (Figure A.6).

⁴ Third-trip echoes (echoes located between $r = 2r_{\max}$ and $r = 3r_{\max}$) are rare because the radar beam usually overshoots echoes at such long ranges.

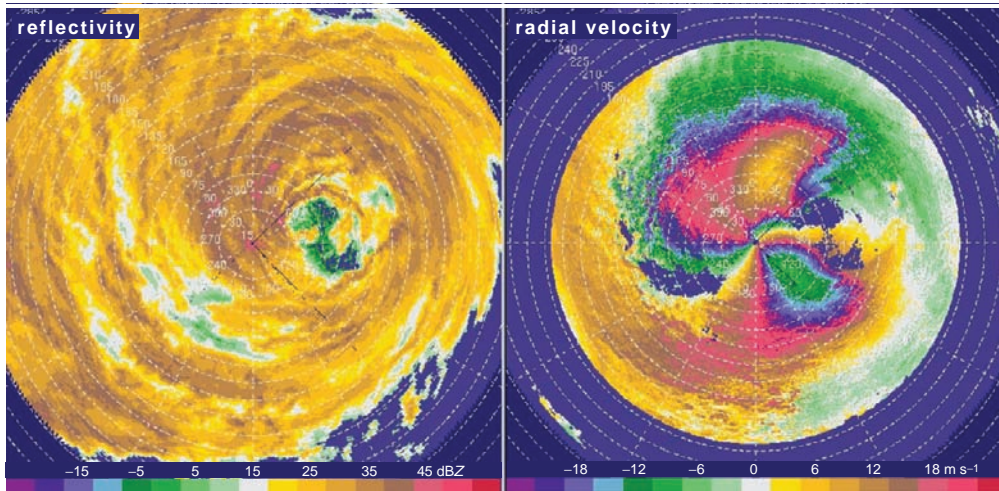


Figure A.6 Example of velocity aliasing during the landfall of Hurricane Isabel (2003) along the coast of North Carolina. Reflectivity is displayed on the left, and radial velocity is displayed on the right. Range rings are at 15 km intervals and azimuth spokes are at 30° intervals. The eye of the hurricane is approximately 75 km east of the radar, and the strong northerly winds at the radar have been aliased in the regions ~60 km north of the radar (where yellow outbounds are erroneously displayed) and ~60 km south-southeast of the radar (where green inbounds are erroneously displayed).

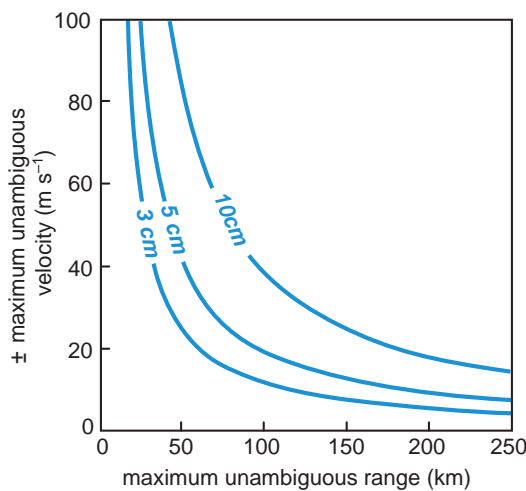


Figure A.7 Relationship between maximum unambiguous range and maximum unambiguous Doppler velocity for radars transmitting at wavelengths of 3, 5, and 10 cm.

The interval given by (A.7) is also called the *Nyquist interval*, with $v_{R\max}$ also sometimes called the *Nyquist velocity*.

Increasing the PRF to extend $v_{R\max}$ decreases r_{\max} . This limitation is popularly referred to as the *Doppler dilemma*.

We can combine (A.6) and (A.7) to illustrate this:

$$v_{R\max} r_{\max} = \pm \frac{\lambda c}{8}. \quad (\text{A.8})$$

From (A.8) and Figure A.7 we see that the PRF and wavelength must be chosen carefully. In addition, the wavelength must not be too long, or else precipitation and clouds will not be detected owing to weak backscattering. On the other hand, if the wavelength is too small, attenuation will limit range.

A.3 Applications

A.3.1 Clear-air returns

When a radar transmits energy, part of it may be intercepted by targets on the ground, such as buildings, trees, power lines, or other objects. This *ground clutter* interferes with the detection of meteorological targets because ground targets are large and typically produce high reflectivity. Ground clutter can result even if the main radar beam is above ground targets, because part of the energy radiated from the antenna is emitted off the beam axis in what are known as *sidelobes*. Backscattered energy from the sidelobes is interpreted by the radar processor to come from the main lobe; thus, ground targets hit by one of the sidelobes

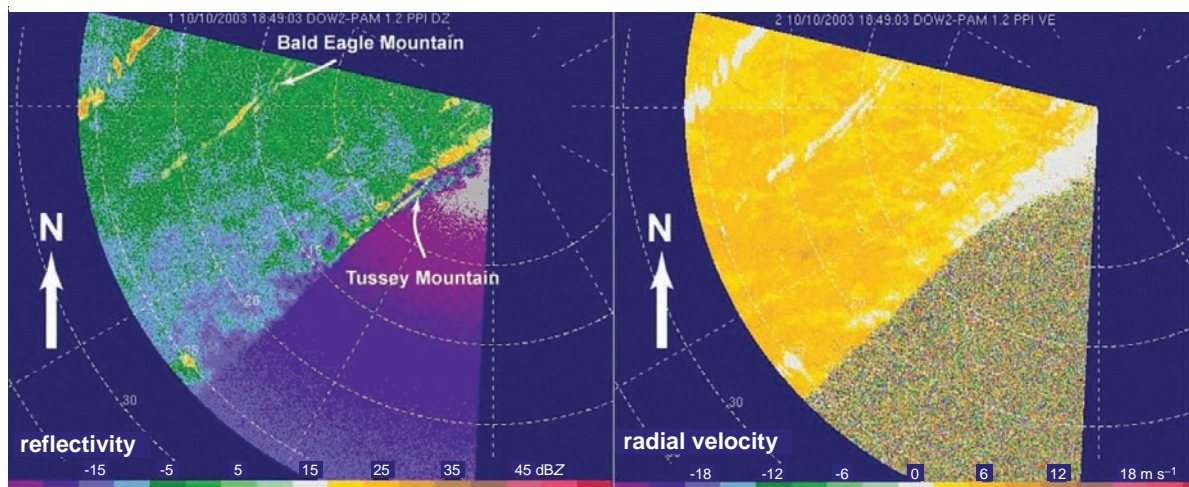


Figure A.8 Example of ground clutter in radar imagery obtained by the Doppler On Wheels (DOW) radar southwest of State College, PA. Reflectivity is displayed on the left and radial velocity is displayed on the right. Range rings are at 5 km intervals and azimuth spokes are at 30° intervals. At locations where the radar beam intersects mountains, reflectivities are large and radial velocities are approximately zero. The echoes from the valley between the two mountain ridges are largely from insects.

appear to a radar user in the same relative position in the main lobe.

Ground clutter is usually worst within about 20 km of the radar, where the beam is still close to the earth's surface. Farther from the radar, the beam is higher owing to both its elevation angle and the curvature of the earth (Figure A.2). Ground clutter is easily identified with a Doppler radar because the radial velocity measured by the Doppler radar is approximately zero (most ground targets are stationary; Figure A.8). The radial velocity may not be exactly zero because moving targets within the beam, such as birds, airborne insects, and raindrops, also contribute to the total power returned to the radar.

Airborne insects, which are commonly detected by weather radars during the warm season, are among the most important clear-air returns. They are excellent tracers of air motion because, on average, airborne insects move with the wind (Figures A.8). The echoes from insects can reveal convergence zones (e.g., drylines, outflow boundaries, fronts) as reflectivity fine-lines, where deep convection may be most likely to be initiated or where existing storms could interact with a zone of enhanced wind shear (Figure A.9). Clear-air returns can also be obtained from regions containing fluctuations in the refractive index of the air due to turbulence. This is called Bragg scattering.

A.3.2 Interpreting Doppler velocity patterns

To understand Doppler radial velocity patterns, one first has to consider the geometry of a radar scan. Normally the radar beam is pointed at an elevation angle greater than zero so that the beam height increases with range. Because of this geometry, radar returns originating from targets near the radar detect the low-level wind field, whereas returns from distant targets detect the wind field at higher levels. To determine the horizontal wind at a particular elevation above the radar, one can examine the radial velocities on a constant-range ring encircling the radar. The elevation represented by a particular constant-range ring depends upon the elevation angle of the radar beam.

In the examples that follow, idealized Doppler radial velocity patterns were constructed assuming simple vertical wind profiles. These simplified radial velocity patterns can serve as a starting point from which inferences can be made from observations of more complicated patterns. Doppler velocity patterns (right) correspond to vertical wind profiles (left), where the wind barbs indicate wind speed and direction from the ground up to 8 km. Negative Doppler velocities (blue shades) are toward the radar and positive (red shades) are away. The radar location is at the center of the display.

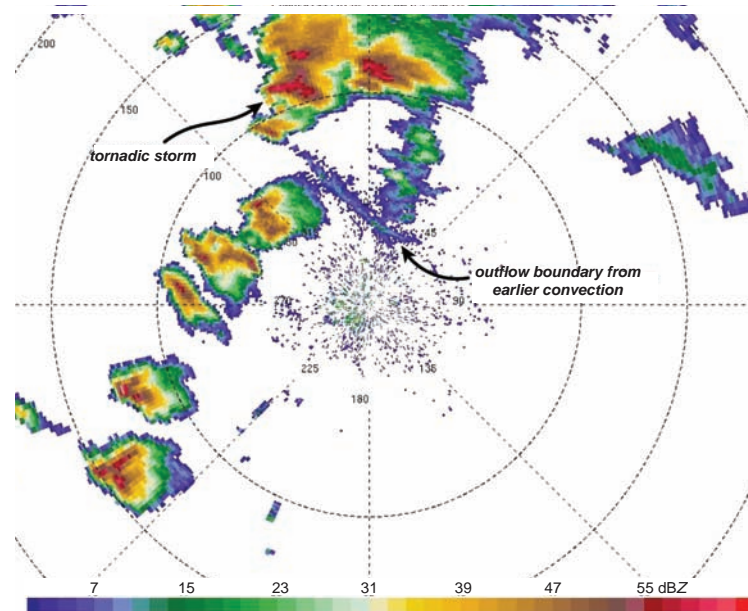


Figure A.9 Lowest-elevation-angle reflectivity from the Lubbock, TX, radar at 0102 UTC 3 June 1995. A reflectivity fine-line is associated with an outflow boundary produced by convection occurring a few hours earlier. Many of the subsequent storms that crossed this outflow boundary became tornadic. Vertical wind shear and low-level humidity were enhanced along and on the immediate cool side of the outflow boundary. This is the same case as shown in Figure 10.15.

In Figure A.10a, wind direction is constant with height, but wind speed increases from 10 kt at the ground to 40 kt at 8 km. Note that the maximum inbound velocity is to the west and maximum outbound velocity is to the east. The radar measures zero radial velocity to the north and south because the winds are perpendicular to the radar beam when the beam is directed toward the north or south. In Figure A.10b, the winds increase from 10 to 40 kt between the surface and 4 km, and then decrease again to 10 kt at 8 km. The wind direction is again constant with height. The radar beam intersects the 4 km level at a range of approximately 50 km, where the maximum inbound and outbound velocities are observed.

Figure A.11a displays the Doppler velocity field for the case of winds that back from northerly at the ground to westerly at 8 km; wind speed is a constant with height. Note the characteristic backward ‘S’ shape of the zero-velocity line. In Figure A.11b, the interpretation is exactly the opposite of that in Figure A.11a. The winds veer with height and the zero line takes the shape of a forward ‘S.’ In Figure A.12, winds veer with height to 4 km and then back with height to 8 km, resulting in a forward ‘S’ pattern within 50 km range and a backward ‘S’ beyond 50 km range.

When the wind field is horizontally uniform, the radial velocity sampled along a constant range ring varies sinusoidally with azimuth. However, the wind field commonly is not horizontally uniform; in such instances, the radial velocity sampled along a constant range ring does not vary sinusoidally with azimuth. There may even be rather pronounced asymmetries in the radial velocity field, especially if an abrupt wind shift (e.g., along a front) is sampled by the radar. Figure A.13 presents idealized Doppler velocity displays for the cases of a difluent wind field, a confluent wind field, and a front associated with a 90° wind shift.

Nonuniformity in the wind field may exist on much smaller scales as well; for example, in an isolated thunderstorm there may be locally strong low-level convergence and/or divergence (e.g., beneath the updraft or within a microburst, respectively), or perhaps a mesocyclone. Figure A.14 displays what a uniform westerly wind field would look like in a subdomain of the regions displayed in Figures A.10–A.13. Figure A.15 displays idealized Doppler velocity patterns for the case of a mesocyclone having cyclonic vorticity (Figure A.15a), a purely convergent wind field (Figure A.15b), and a wind field consisting of roughly equal amounts of cyclonic vorticity and

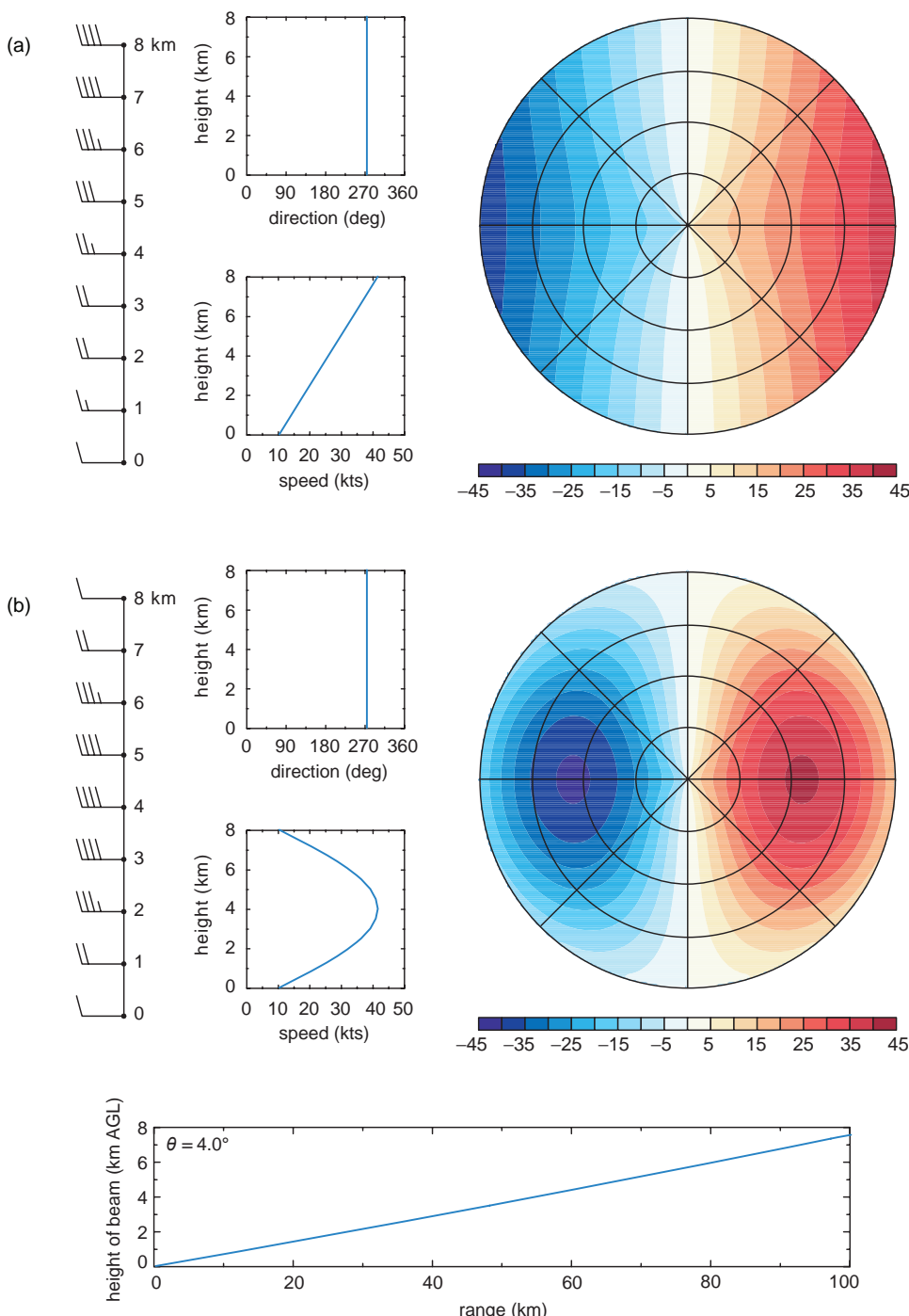


Figure A.10 (a) A velocity display in the presence of linear, unidirectional, westerly wind shear given an elevation angle of 4° . Range rings are drawn every 25 km and azimuth spokes are drawn every 45° . (b) As in (a), but for the case of unidirectional wind shear with a sinusoidal wind speed profile. The beam height versus range is displayed beneath (a) and (b).

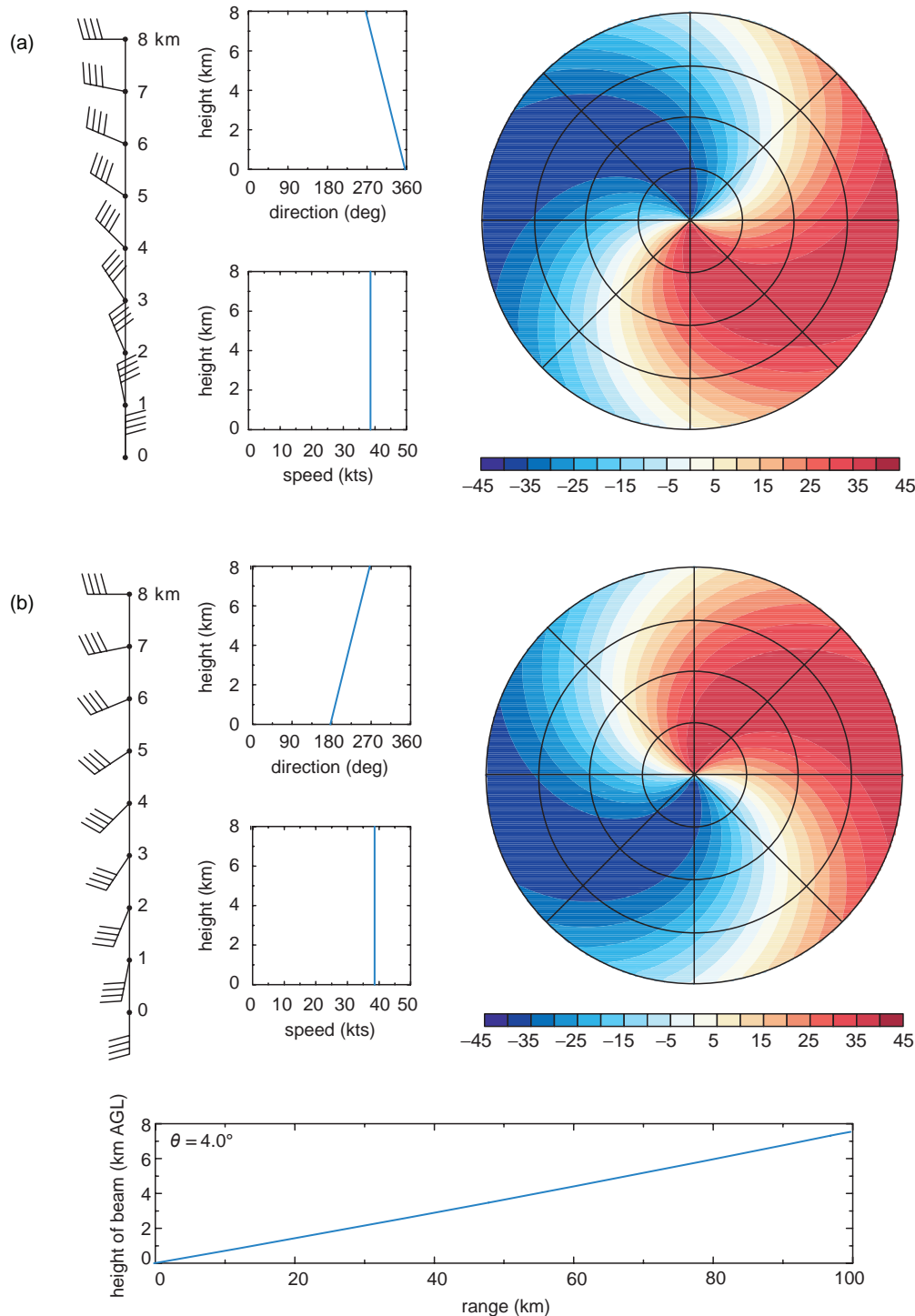


Figure A.11 (a) A velocity display in the presence of backing winds with height. As in Figure A.10, the elevation angle of the radar beam is 4° . Range rings are drawn every 25 km and azimuth spokes are drawn every 45° . (b) As in (a), but for the case of veering winds with height.

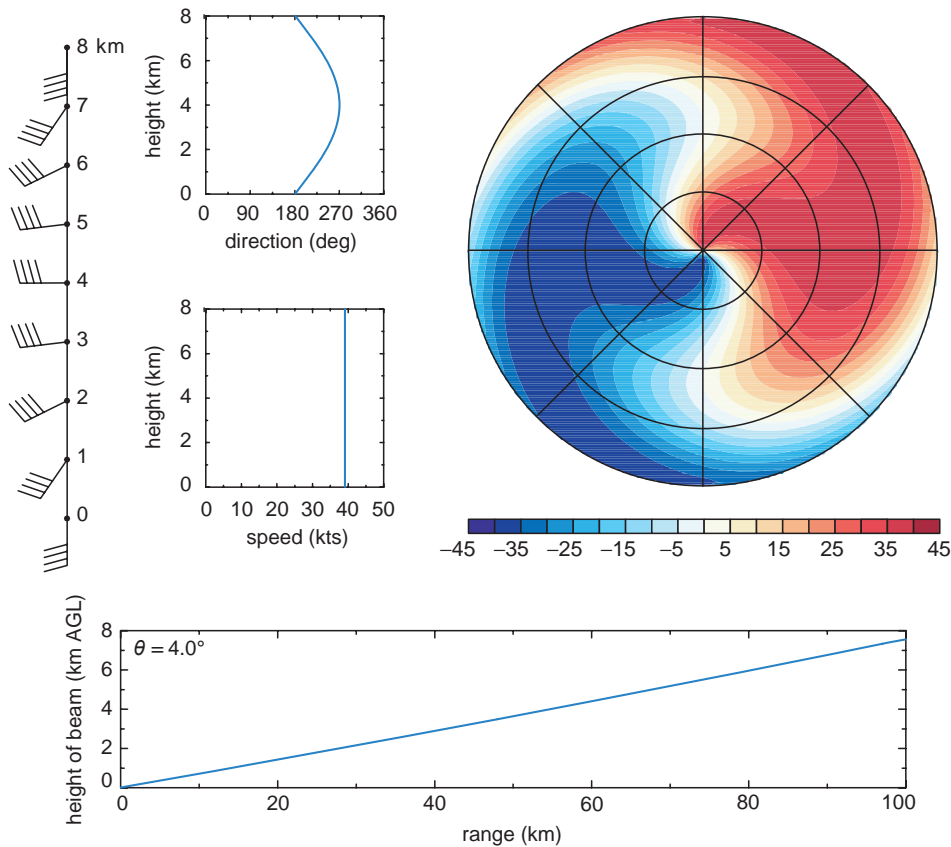


Figure A.12 As in Figure A.11, but for the case of veering winds with height overlain by a layer of backing winds with height.

convergence (Figure A.15c). Convergence/divergence and vorticity centers result in inbound-outbound radial velocity couplets, and the orientation of the couplets (i.e., the orientation of the zero radial velocity contour, or isodop, that separates the inbound and outbound velocities) relative to the radials is a function of the relative magnitudes of convergence and vorticity. Regions of high vorticity result in an inbound-outbound couplet that has its zero isodop oriented parallel to the radial that passes through the center of the couplet (Figure A.15a). Regions of purely convergent or divergent flow result in an inbound-outbound couplet that has its zero isodop normal to the radial that passes through the center of the couplet (Figure A.15b). A flow field that is both vortical and divergent/convergent has an inbound-outbound couplet with a zero isodop oriented at some intermediate angle with respect to the radial that passes through the center of the couplet (Figure A.15c).

A.3.3 Estimating rainfall

Z-R relationships

The so-called *Z-R method*, which relates the logarithmic reflectivity factor Z to the rainfall rate R , is the simplest and most common way to estimate rainfall, because only measurements of reflectivity are needed. This technique assumes

$$Z = A R^B, \quad (\text{A.9})$$

where A and B are constants. The method is simple but prone to large errors, because the parameters A and B depend on the drop size distribution, which is generally not known with great accuracy. As an example, in stratiform precipitation, assuming a Marshall-Palmer drop size distribution leads to $Z = 200R^{1.6}$.

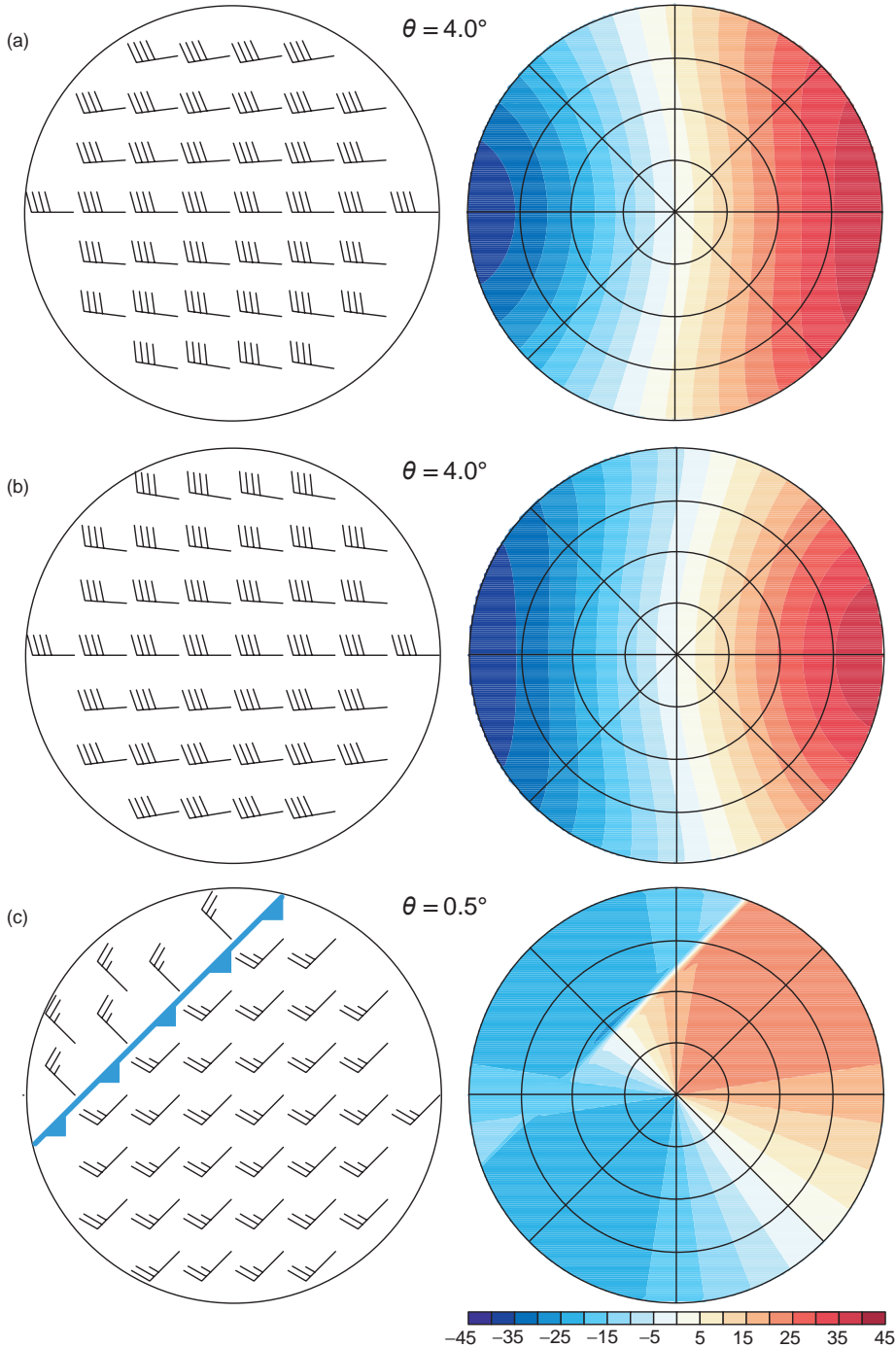


Figure A.13 Idealized Doppler velocity displays in the presence of horizontal inhomogeneity in the wind field. (a) A difluent wind field (left; horizontal cross-section is at 8 km) and its corresponding radial velocity display (right) for a 4° elevation angle. The wind speed increases linearly with height as in Figure A.10a. (b) The same as (a), but for a confluent wind field. (c) The case of a cold front approaching the radar from the northwest. Wind barbs in the horizontal cross-section (left) are at 0.5 km, and the corresponding radial velocity display (right) is based on a 0.5° elevation angle.

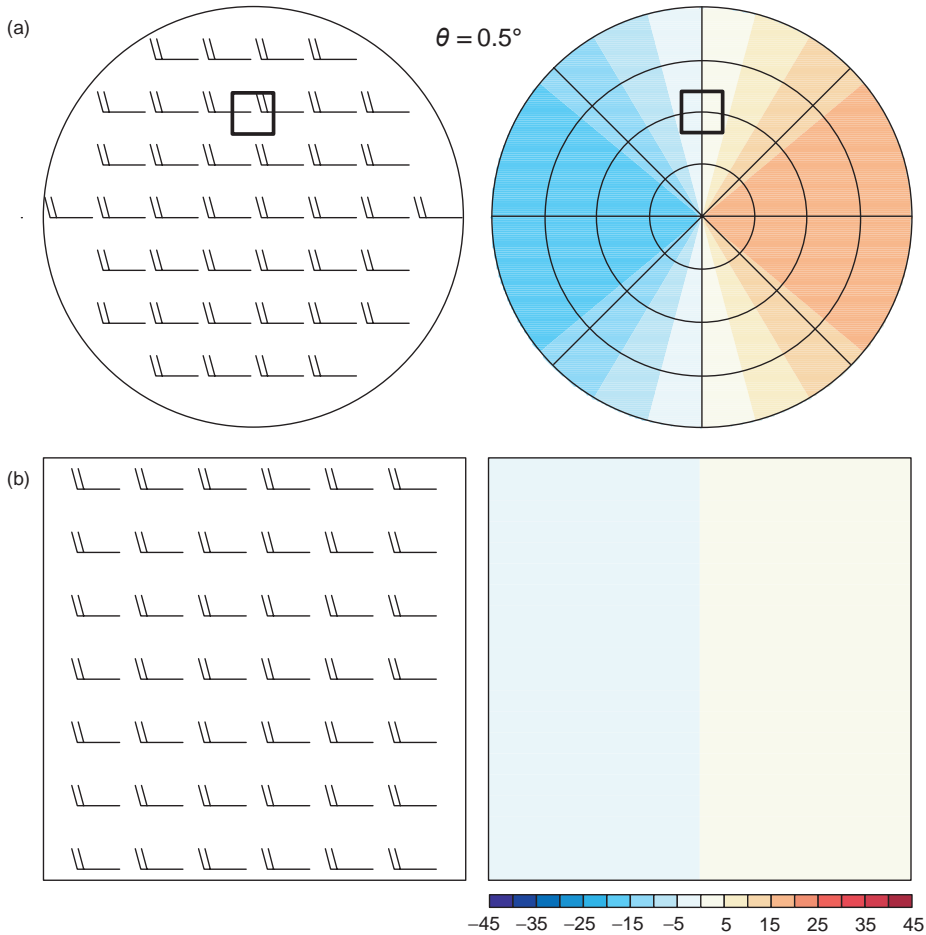


Figure A.14 (a) Idealized Doppler velocity display in the presence of uniform westerly low-level winds. On the left is a horizontal cross-section at 0.5 km, and on the right is its corresponding radial velocity display (0.5° elevation angle). (b) The region enclosed by the box in (a) is cropped and enlarged. The enlarged region is 18×18 km and is centered 50 km north of the radar.

One fundamental challenge in using $Z-R$ relationships to estimate rain accumulations is that Z is proportional to the sixth power of the drop diameter, whereas R is proportional to the cube of the drop diameter (i.e., drop volume), such that there is no simple formula to relate the two quantities without knowing the size distribution of the hydrometeors. In addition to the uncertainty in knowing A and B , errors can also arise owing to the inability of the radar to make measurements near the ground beyond the radar horizon, calibration errors, incomplete beam filling, rainfall rate gradients, the presence of hail (large hail can invalidate the Rayleigh scattering approximation) or *bright bands* (Figure A.16), evaporation below cloud base, and the presence of strong updrafts (which suspend rainfall aloft).

When ice is present (either hail or bright bands), differences in the dielectric constant of liquid water compared with ice (liquid water is about nine times more reflective than ice at microwave wavelengths) can also contribute to the errors in precipitation estimation.

Dual-polarization radar

The polarization of an electromagnetic wave is defined by the orientation of the electric field wave crests. Conventional weather radars transmit and receive energy with a single, horizontal polarization; that is, the electric field wave crests are horizontal. *Dual-polarization* radars, on the other hand, transmit and receive both horizontally and

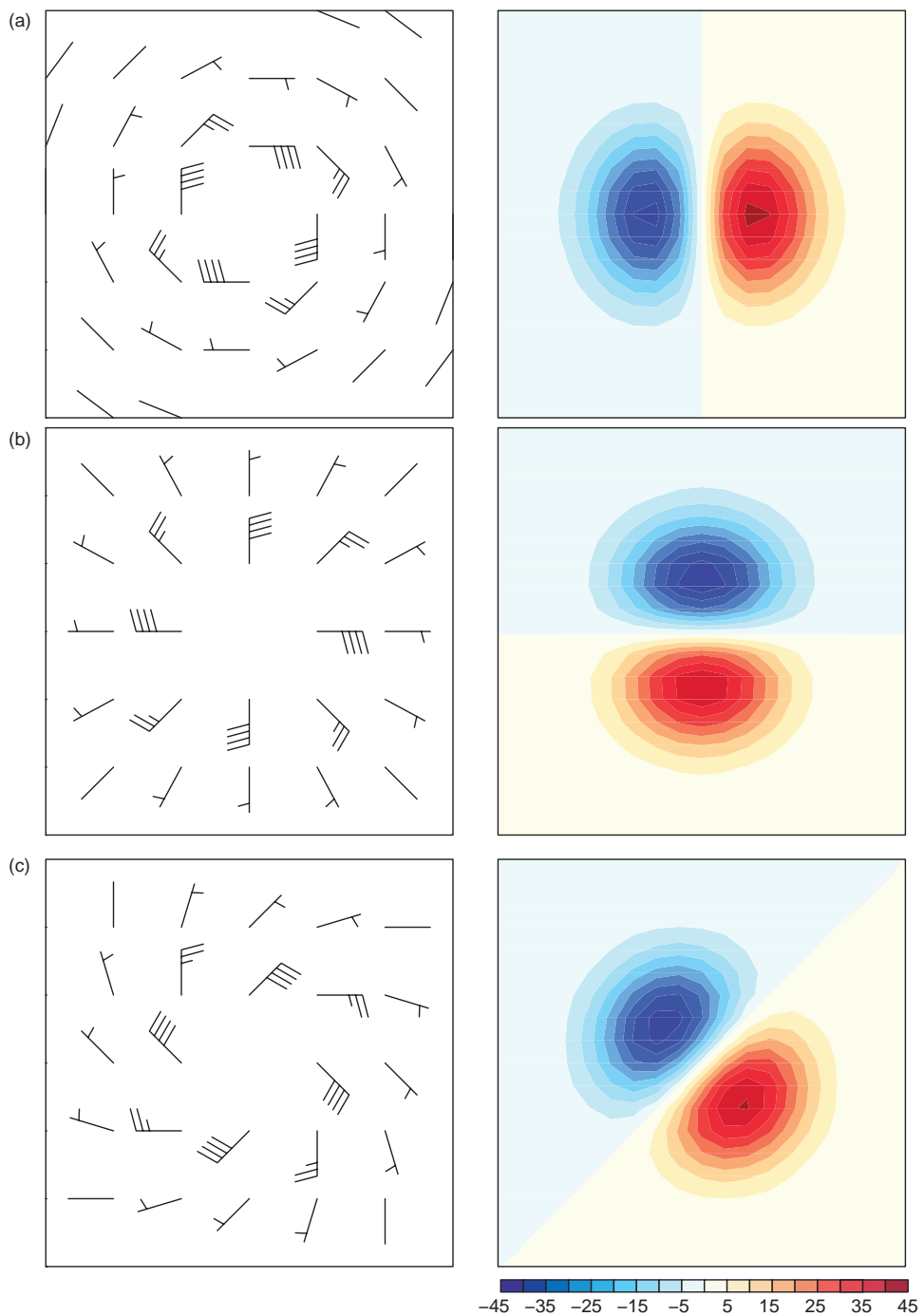


Figure A.15 (a) Idealized Doppler velocity display for the case of a mesocyclone having cyclonic vorticity (the radar is located to the south, e.g., the domain might be in the same location relative to the radar as the domain shown in Figure A.14). The elevation angle of the radar beam is 0.5° . Wind barbs are shown on the left and the Doppler velocity display is shown on the right. (b) As in (a), but for a purely convergent wind field. (c) As in (a), but for a wind field consisting of equal amounts of cyclonic vorticity and convergence.

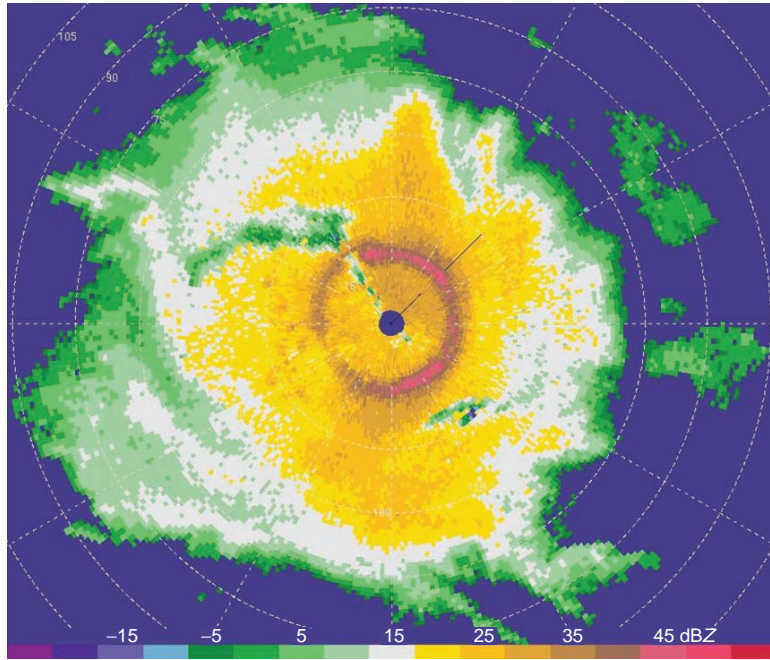


Figure A.16 As ice crystals form aloft and fall toward the surface, they collect each other to form large snowflakes. When the snowflakes start to melt upon reaching the melting level, they initially develop a water coating. Liquid water is about nine times more reflective than ice at microwave wavelengths, so these large wet snowflakes produce high reflectivity. Snowflakes with wet edges also readily clump together, forming large and highly reflective aggregates. As the flakes continue to fall and melt, they collapse into rain drops. The rain drops are smaller and fall faster, so both the size of the particles and their concentration are reduced, reducing the radar reflectivity. All of these processes lead to the formation of a narrow annulus of high reflectivity—a bright band—near the melting level that surrounds a radar scanning 360°.

vertically polarized pulses. Such radars can allow inferences to be made about the microphysical characteristics of precipitation regions (e.g., the drop size distribution) by way of differences between the horizontally and vertically polarized backscattered pulses. For example, reflectivity differences, or *differential reflectivity* (Z_{DR} ; measured in dB), can be used to estimate hydrometeor shape and therefore drop size, where

$$Z_{DR} = 10 \log_{10} \left(\frac{Z_{hh}}{Z_{vv}} \right) = Z_{hh} - Z_{vv}. \quad (\text{A.10})$$

The h (v) subscripts indicate reflectivity factors associated with the horizontally (vertically) polarized pulses, and the first (second) subscript refers to the polarization of the transmitted (received) pulse. Hail and drizzle are nearly spherical and therefore backscatter the horizontally and vertically polarized transmitted pulses roughly equally, resulting in Z_{DR} values ~ 0 dB. Rain is associated

with Z_{DR} values ~ 2 dB. Snow is associated with Z_{DR} values ~ 1 dB. Melting bands are associated with Z_{DR} values ≥ 3.5 dB. Conical graupel particles that are oriented vertically as they fall may be associated with negative Z_{DR} values. Information about the hydrometeor species can yield much better rainfall estimates than are possible with Z-R algorithms.

Other variables measured by dual-polarimetric radars are listed below.

Linear depolarization ratio The linear depolarization ratio (LDR) is the ratio of the power received in the channel that is orthogonal to the transmission channel, to the power received in the transmission channel. For example,

$$\text{LDR} = 10 \log_{10} \left(\frac{Z_{hv}}{Z_{hh}} \right) = Z_{hv} - Z_{hh}. \quad (\text{A.11})$$

LDR depends on the shape of the scatterer, among other things. LDR values typically range from approximately

–15 to –40 dB for meteorological targets (LDR approaches negative infinity for perfect spheres, but in real radars LDR values for small spheres are typically limited to roughly –40 dB owing to antenna limitations). LDR values can distinguish between rain, small hail, large hail, or a mixture of hydrometeor types. Large LDR, for example, suggests heavy rain mixed with hail.

Specific differential phase The specific differential phase (K_{DP}) is the difference in the phase shift of the horizontally and vertically polarized waves owing to changes in the speed of the pulses as they travel through hydrometeors. Large K_{DP} values ($>4^\circ \text{ km}^{-1}$) may indicate the presence of rain mixed with hail.

Co-polar correlation coefficient The co-polar coefficient (ρ_{hv}) is the pulse-by-pulse correlation between the

returned power of the horizontally and vertically polarized transmissions. In hail, ρ_{hv} is typically 0.90–0.95, although it can be >0.95 (<0.90) in small, dry hail (large, especially wet hail). In rain, ρ_{hv} is usually very large, often as large as 0.99; the exception is very light rain or drizzle, where a low signal-to-noise ratio can result in ρ_{hv} as low as 0.90. In mixed precipitation (including bright bands), ρ_{hv} is typically 0.90–0.95.

Dual-polarimetric variables are used collectively to develop hydrometeor classification algorithms (HCAs; Figure A.17). Not only do hydrometeor retrievals improve rainfall or snowfall estimates, but dual-polarimetric radar data show promise in large-hail and tornado detection as well (debris lofted by tornadoes has a unique

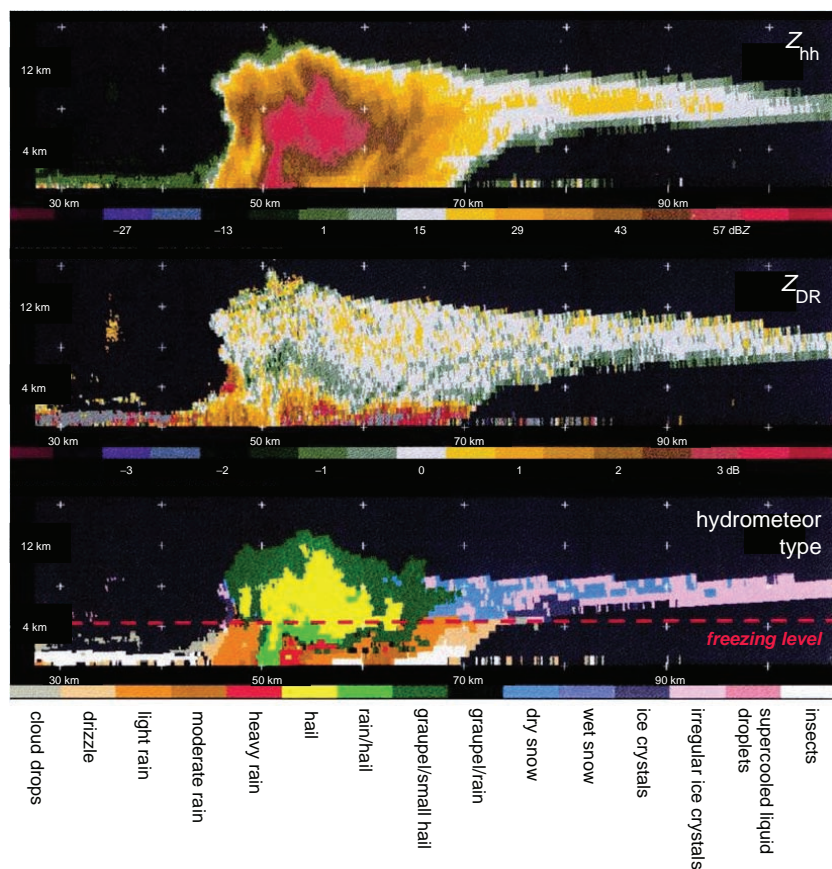


Figure A.17 Example of hydrometeor classification in a vertical cross-section of a thunderstorm using data from a dual-polarization radar (c); images (a) and (b) are reflectivity and differential reflectivity, respectively. Such classifications can improve rainfall estimations and perhaps warnings for severe hail and tornadoes as well. (From Vivekanandan *et al.* [1999]. Courtesy of the American Meteorological Society.)

dual-polarimetric radar signature). It is anticipated that the WSR-88D network in the United States will be upgraded to a dual-polarization radar network in the next decade.

A.3.4 Dual-Doppler analysis

If two radars sample the same region quasi-simultaneously from different angles, the two-dimensional wind field can be retrieved (Figure A.18), and using a continuity equation, the full three-dimensional wind field can be retrieved. A wind synthesis obtained using two Doppler radars is referred to as a *dual-Doppler analysis* (Figure A.19).

The radar does not actually measure the wind motion at a point; rather, it measures the average speed of the hydrometeors toward or away from the radar in each sample volume. The fall speeds of hydrometeors therefore contribute to the measured radial velocity. Fall speeds are typically removed (somewhat crudely) by parameterizing the fall speeds in terms of the reflectivity. The resulting three-dimensional wind synthesis (and derivatives of the wind field, such as convergence and vorticity) can be adversely affected by the uncertainty associated with hydrometeor fall speeds.

The radial velocity v_R measured by one radar is

$$v_R = u \cos \phi \sin \theta + v \cos \phi \sin \theta + W \sin \phi, \quad (\text{A.12})$$

where ϕ is the elevation angle of the radar, θ is the azimuth angle of the radar, u and v are the horizontal wind components, and W is the sum of the actual vertical

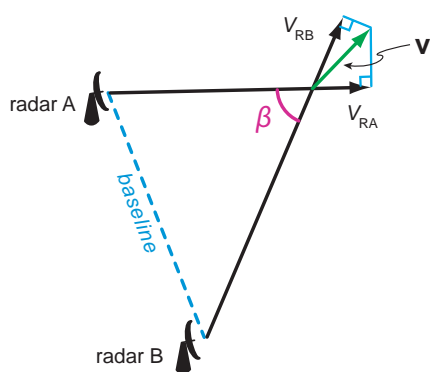


Figure A.18 Relationship between the radial wind components at radar A (v_{RA}) and radar B (v_{RB}), the baseline (dashed line), the between-beam angle (β), and the component of the wind velocity v in the plane defined by the radar radials.

velocity (w) plus some contribution from hydrometeor fall speeds (v_t).

The above expression contains three unknowns: u , v , and W . A three-dimensional wind synthesis is possible with two radars because two radars scanning the same location provide two independent radial velocity measurements at that location, and the use of the continuity equation, which couples the horizontal and vertical wind components, provides the third constraint on the three-dimensional wind (i.e., there are thus three knowns and three unknowns at each location scanned by two radars). Without becoming overly detailed, u , v , and w are obtained iteratively in regions scanned by two radars by computing the horizontal divergence, integrating the continuity equation, and parameterizing fall speeds in terms of Z . Solutions cannot be obtained along the line joining the two radars, referred to as the *baseline*, because the radial velocity measurements from the two radars are not independent at points along the baseline (i.e., the viewing angles of the radars are parallel along the baseline). Wind synthesis errors are typically unacceptably large wherever the between-beam angle (Figure A.18) is less than $20\text{--}30^\circ$ or greater than $150\text{--}160^\circ$; the three-dimensional wind retrieval is most accurate where the between-beam angle is 90° . Errors also are large when the elevation angle of either of the radars is too high (higher than $\sim 20\text{--}30^\circ$), or when the radial velocity data obtained by each radar are highly non-simultaneous (dual-Doppler data collection usually involves coordination between radars so that scanning is synchronized, i.e., both radars are scanning the same elevation at the same times at the target of interest.). With three or more radars, errors are reduced by fitting the synthesized wind field to the radial velocity observations in a least squares sense (this is sometimes called an *over-determined* dual-Doppler analysis).⁵

A.3.5 Thermodynamic retrieval

If three-dimensional, dual-Doppler wind syntheses are available at multiple times, temperature and pressure perturbations can be retrieved via a *thermodynamic retrieval*, sometimes simply called a *dynamic retrieval*. The horizontal

⁵ With three or more radars, it is possible to obtain u , v , and W simultaneously, without iteration, and without the aid of the continuity equation. This approach is rarely used in practice, however, at least in the case of ground-based radars, because such radars scan at low elevation angles, which means that the radars sample the horizontal wind components much better than the vertical wind component. Such 'direct' multi-Doppler wind syntheses work best when each of the three velocity components is sampled well by at least one of the radars.

0031 UTC 6 June 2001

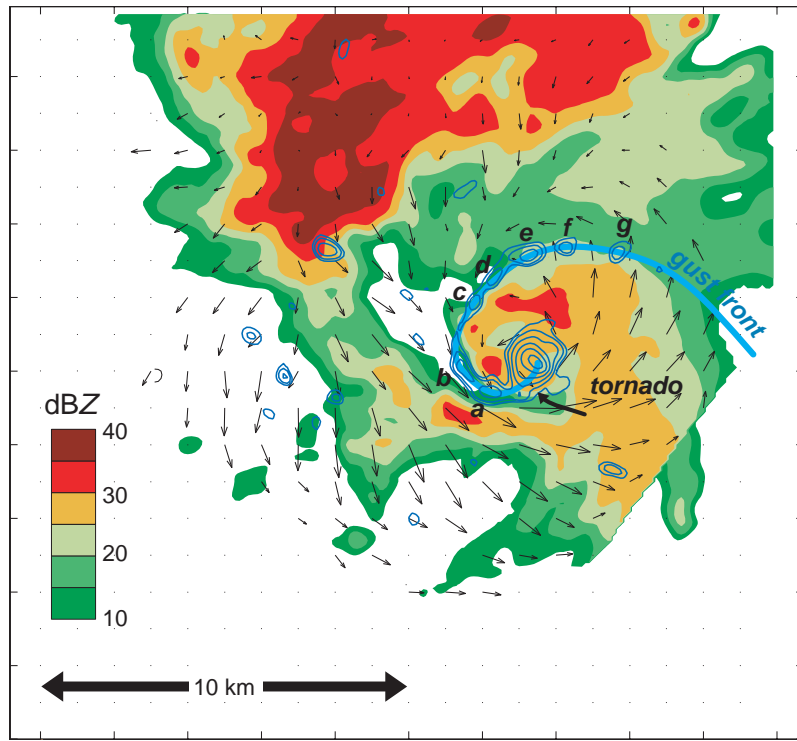


Figure A.19 Dual-Doppler wind synthesis based on Doppler On Wheels (DOW) observations of a tornadic supercell thunderstorm in south central Kansas at 0031 UTC 6 June 2001. Reflectivity (uncalibrated) is shown using the color shading. Isoverts at $z = 100$ m are blue, and the rear-flank gust front is indicated with a bold blue line. Horizontal wind vectors at $z = 100$ m are black. Vortices are evident along the rear-flank gust front (labeled a–g). The vortices were likely a result of horizontal shear instability, although vorticity stretching also likely contributed to the vorticity tendency significantly. Courtesy of Jim Marquis.

momentum equations can be written as

$$-\frac{\partial p'}{\partial x} = \bar{\rho} \left(\frac{du}{dt} - fv - F_u \right) \quad (\text{A.13})$$

and

$$-\frac{\partial p'}{\partial y} = \bar{\rho} \left(\frac{dv}{dt} + fu - F_v \right), \quad (\text{A.14})$$

where u and v are the zonal and meridional wind components, p' is the pressure perturbation, $\bar{\rho} = \bar{\rho}(z)$ is a reference density profile, f is the Coriolis parameter, F_u and F_v represent the effects of turbulent drag, and $d/dt = \partial/\partial t + \mathbf{v} \cdot \nabla$. At each vertical level, the Coriolis, momentum advection, and turbulent drag terms (via parameterization) can be obtained from the dual-Doppler wind synthesis. The local accelerations $\partial u/\partial t$ and $\partial v/\partial t$ can be estimated

from a series of three-dimensional wind syntheses. The reference density profile can be obtained from a nearby sounding.

Because the rhs of (A.13) and (A.14) is known, the horizontal pressure gradients $\partial p'/\partial x$ and $\partial p'/\partial y$ are therefore also known; p' can be obtained at each level by taking $\partial(\text{A.13})/\partial x + \partial(\text{A.14})/\partial y$ and inverting $\nabla_h^2 p' = \partial^2 p'/\partial x^2 + \partial^2 p'/\partial y^2$, usually applying Neumann boundary conditions on the horizontal boundaries of the dual-Doppler domain. If Neumann boundary conditions are used, then the retrieved p' field is not unique. However, the horizontal gradients of p' , which are unique, are typically of greater interest than p' itself.

It can be shown that the field of $p' - \langle p' \rangle$ is unique, where $\langle p' \rangle$ is the horizontal average of the retrieved p' at each level. If $p' - \langle p' \rangle$ is vertically differentiated, it can be

used to retrieve information about the buoyancy field via

$$B - \langle B \rangle = \left(\frac{dw}{dt} - F_w \right) - \left\langle \frac{dw}{dt} - F_w \right\rangle + \frac{1}{\rho} \frac{\partial}{\partial z} (p' - \langle p' \rangle), \quad (\text{A.15})$$

where w is the vertical velocity, B is the buoyancy, F_w is turbulent drag, $\langle B \rangle$ is the average of the retrieved buoyancy at a given level, and $\langle \frac{dw}{dt} - F_w \rangle$ is the average $\frac{dw}{dt} - F_w$ at a given level. Equation (A.15) is obtained by subtracting the horizontally averaged vertical momentum equation from the unaveraged vertical momentum equation. At each vertical level, $\frac{dw}{dt} - F_w$ and $\langle \frac{dw}{dt} - F_w \rangle$ can be obtained from the dual-Doppler wind syntheses. Because all of the terms on the rhs are unique, $B - \langle B \rangle$ on the lhs is also unique. However, B is not unique, as was the case for the retrieved p' field. Nonetheless, the *pattern and gradients* of the retrieved B field on a horizontal plane are unique (B and $B - \langle B \rangle$ differ only by a constant on a horizontal plane), which is often of significant value. Ambiguities regarding the uniqueness of the B field can be resolved if independent *in situ* observations are available at each level.

Thermodynamic retrievals commonly are performed in mesoscale observational studies when high-quality multiple-Doppler radar data are available. They can be valuable because *in situ* measurements of temperature and pressure often cannot be obtained easily, especially above the ground. However, there are limits to the quality of the retrieved pressure and buoyancy fields. The retrieved pressure and buoyancy fields are intrinsically less accurate than the synthesized wind fields because of all of the differentiations involved (the buoyancy retrieval involves one more differentiation than the pressure retrieval; therefore, the retrieved buoyancy field is usually less reliable than the pressure field). Moreover, poor temporal resolution (e.g., several minutes may elapse between volume scans of a storm) leads to errors in the estimation of $\partial v / \partial t$, and the parameterization of

turbulent drag also introduces uncertainty. In the end, even decent-looking dual-Doppler-derived horizontal wind fields can result in poor buoyancy fields. Thus, direct measurements of temperature and pressure are virtually always important components of mesoscale observational studies.

Further reading

- Bluestein, H. B., and R. M. Wakimoto, 2003: Mobile radar observations of severe convective storms. *Radar and Atmospheric Science: a Collection of Essays in Honor of David Atlas*, Meteor. Monogr., No. 52, 105–138.
- Burgess, D., and P. S. Ray, 1986: Principles of radar. *Mesoscale Meteorology and Forecasting*, P. S. Ray, Ed. Amer. Meteor. Soc., 85–117.
- Chandrasekar, V., R. Meneghini, and I. Zawadzki, 2003: Global and local precipitation measurements by radar. *Radar and Atmospheric Science: a Collection of Essays in Honor of David Atlas*, Meteor. Monogr., No. 52, 215–236.
- Doviak, R. J., D. Sirmans, and D. S. Zrnic, 1988: Weather radar. *Instruments and Techniques for Thunderstorm Observation and Analysis*, E. Kessler, Ed., 2nd edn. University of Oklahoma Press, 137–169.
- Doviak, R. J., and D. S. Zrnic, 1993: *Doppler Radar and Weather Observations*. Academic Press, 562 pp.
- Hane, C. E., C. L. Ziegler, and P. S. Ray, 1988: Use of velocity field from Doppler radars to retrieve other variables in thunderstorms. *Instruments and Techniques for Thunderstorm Observation and Analysis*, E. Kessler, Ed., 2nd edn. University of Oklahoma Press, 215–234.
- Raghavan, S., 2004: *Radar Meteorology*. Springer, 537 pp.
- Rinehart, R. E., 20xx: *Radar for Meteorologists*, Fourth Edition. Rinehart, 428 pp.
- Sauvageot, H., 1992: *Radar Meteorology*. Artech House, 384 pp.
- Vivekanandan *et al.* (1999).

References

Highlighted references appear in the ‘Further reading’ lists at the end of each chapter.

- Agee, E. M., J. T. Snow, and P. R. Clare, 1976: Multiple vortex features in the tornado cyclone and the occurrence of tornado families. *Mon. Wea. Rev.*, **104**, 552–563.
- Archer, C. L., and M. Z. Jacobson, 2005: The Santa Cruz eddy. Part I: Observations and statistics. *Mon. Wea. Rev.*, **133**, 767–782.
- *Arya, S. P., 2001: *An Introduction to Micrometeorology*, 2nd edn. Academic.
- Atkins, N. T., C. S. Bouchard, R. W. Przybylinski, R. J. Trapp, and G. Schmocker, 2005: Damaging surface wind mechanisms within the 10 June 2003 Saint Louis bow echo during BAMEX. *Mon. Wea. Rev.*, **133**, 2275–2296.
- Atkins, N. T., and J. J. Cunningham, 2006: The influence of low-level stable layers on damaging surface winds within bow echoes. Preprints, *23rd Conf. on Severe Local Storms*, St. Louis, MO, Amer. Meteor. Soc.
- Atkins, N. T., and R. M. Wakimoto, 1995: Observations of the sea-breeze front during CaPE. Part II: Dual-Doppler and aircraft analysis. *Mon. Wea. Rev.*, **123**, 944–969.
- Banacos, P. C., and H. B. Bluestein, 2004: Hodograph variability within analytically modeled, synoptic-scale, baroclinic systems. *Mon. Wea. Rev.*, **132**, 1448–1461.
- Banta, R. M., 1990: The role of mountains in making clouds. *Atmospheric Processes over Complex Terrain*, Meteor. Monogr., No. 45, 229–283.
- Batchelor, G. K., 1967: *An Introduction to Fluid Dynamics*. Cambridge University Press.
- Bell, G. D., and L. F. Bosart, 1988: Appalachian cold-air damming. *Mon. Wea. Rev.*, **116**, 137–161.
- *Bluestein, H. B., 1982: A wintertime mesoscale cold front in the Southern Plains. *Bull. Amer. Meteor. Soc.*, **63**, 178–185.
- Bluestein, H. B., 1986: Fronts and jet streaks: a theoretical perspective. *Mesoscale Meteorology and Forecasting*, P. S. Ray, Ed. Amer. Meteor. Soc., 173–215.
- Bluestein, H. B., 1993: *Synoptic-Dynamic Meteorology in Midlatitudes. Vol. II, Observations and Theory of Weather Systems*. Oxford University Press.
- *Bohren, C. F., and B. A. Albrecht, 1998: *Atmospheric Thermodynamics*. Oxford University Press.
- Bolton, D., 1980: The computation of equivalent potential temperature. *Mon. Wea. Rev.*, **108**, 1046–1053.
- *Booker, J. R., and F. P. Bretherton, 1967: The critical layer for internal gravity waves in a shear flow. *J. Fluid Mech.*, **27**, 513–539.
- Bosart, L. F., and J. P. Cussen, Jr., 1973: Gravity wave phenomena accompanying east coast cyclogenesis. *Mon. Wea. Rev.*, **101**, 446–454.
- Bosart, L. F., and F. Sanders, 1981: The Johnstown Flood of July, 1977: a long-lived convective system. *J. Atmos. Sci.*, **38**, 1616–1642.
- *Bosart, L. F., and F. Sanders, 1986: Mesoscale structure in the megalopolitan snowstorm of 11–12 February 1983. Part III: a large-amplitude gravity wave. *J. Atmos. Sci.*, **43**, 924–939.
- *Brandes, E. A., 1978: Mesocyclone evolution and tornadogenesis: some observations. *Mon. Wea. Rev.*, **106**, 995–1011.
- Breeding, R. J., 1971: A nonlinear investigation of critical levels for internal atmospheric gravity waves. *J. Fluid Mech.*, **50**, 545–563.
- *Brooks, H. E., J. W. Lee, and J. P. Craven, 2003: The spatial distribution of severe thunderstorm and tornado environments from global reanalysis data. *Atmos. Res.*, **67–68**, 73–94.
- Brown, R. A., 1972a: On the inflection point instability of a stratified Ekman boundary layer. *J. Atmos. Sci.*, **29**, 850–859.
- *Brown, R. A., 1972b: On the physical mechanism of the inflection point instability. *J. Atmos. Sci.*, **29**, 984–986.

- Brown, R. A., 1983: The flow in the planetary boundary layer. *Eolian Sediments and Processes*, M. E. Brookfield and T. S. Ahlbrandt, Eds. Elsevier, 291–310.
- Brown, J., K. R. Knupp, and F. Caracena, 1982: Destructive winds from shallow, high-based cumulonimbi. *Preprints, 12th Conf. on Severe Local Storms*, Boston, MA, Amer. Meteor. Soc., 272–275.
- Browning, K. A., 1977: The structure and mechanisms of hailstorms. *Hail: a Review of Hail Science and Hail Suppression*, Meteor. Monogr., No. 16, Amer. Meteor. Soc., 1–43.
- Browning, K. A., and G. A. Monk, 1982: A simple model for the synoptic analysis of cold fronts. *Quart. J. Roy. Meteor. Soc.*, **108**, 435–452.
- Bryan, G. H., and M. J. Fritsch, 2000: Moist absolute instability: The sixth static stability state. *Bull. Amer. Meteor. Soc.*, **81**, 1207–1230.
- Bunkers, M. J., B. A. Klimowski, J. W. Zeitler, R. L. Thompson, and M. L. Weisman, 2000: Predicting supercell motion using a new hodograph technique. *Wea. Forecasting*, **15**, 61–79.
- Byers, H. R., 1959: Outline of synoptic analysis. *General Meteorology*, 3rd edn. McGraw-Hill, 363–367.
- Byers, H. R., and R. R. Braham, 1949: *The Thunderstorm*. Report of the Thunderstorm Project, U.S. Weather Bureau, Dept. of Commerce.
- *Carbone, R. E., 1982: A severe frontal rainband. Part I: Stormwide hydrodynamic structure. *J. Atmos. Sci.*, **39**, 258–279.
- *Carbone, R. E., 1983: A severe frontal rainband. Part II: Tornado parent vortex circulation. *Mon. Wea. Rev.*, **111**, 2639–2654.
- Carlson, T. N., 1998: *Mid-Latitude Weather Systems*. American Meteorological Society.
- *Chandrasekhar, S., 1961: *Hydrodynamic and Hydromagnetic Stability*. Oxford University Press.
- *Chen, C. C., D. R. Durran and G. J. Hakim, 2005: Mountain wave momentum flux in an evolving synoptic-scale flow. *J. Atmos. Sci.*, **62**, 3213–3231.
- Chen, S. S., and W. M. Frank, 1993: A numerical study of the genesis of extratropical convective mesovortices. Part I: Evolution and dynamics. *J. Atmos. Sci.*, **50**, 2401–2426.
- Chisholm, A. J., and J. H. Renick, 1972: The kinematics of multicell and supercell Alberta hailstorms. Research Council of Alberta Hail Studies Report 72-2, 24–31.
- *Clark, T. L., and W. R. Peltier, 1984: Critical level reflection and the resonant growth of nonlinear mountain waves. *J. Atmos. Sci.*, **41**, 3122–3134.
- Cohen, A. E., M. C. Coniglio, S. F. Corfidi, and S. J. Corfidi, 2007: Discrimination of mesoscale convective system environments using sounding observations. *Wea. Forecasting*, **22**, 1045–1062.
- *Colle, B. A., and C. F. Mass, 2000: High-resolution observations and numerical simulations of easterly gap flow through the Strait of Juan de Fuca on 9–10 December 1995. *Mon. Wea. Rev.*, **128**, 2398–2422.
- Coniglio, M. C., and D. J. Stensrud, 2001: Simulation of a progressive derecho using composite initial conditions. *Mon. Wea. Rev.*, **129**, 1593–1616.
- *Coniglio, M. C., D. J. Stensrud, and M. B. Richman, 2004: An observational study of derecho-producing convective systems. *Wea. Forecasting*, **19**, 320–337.
- *Coniglio, M. C., D. J. Stensrud, and L. J. Wicker, 2006: Effects of upper-level shear on the structure and maintenance of strong quasi-linear mesoscale convective systems. *J. Atmos. Sci.*, **63**, 1231–1252.
- Corfidi, S. F., J. H. Merritt, and J. M. Fritsch, 1996: Predicting the movement of mesoscale convective complexes. *Wea. Forecasting*, **11**, 41–46.
- *Craven, J. P., and H. E. Brooks, 2004: Baseline climatology of sounding derived parameters associated with deep, moist convection. *Nat. Wea. Digest*, **28**, 13–24.
- *Crook, N. A., 1988: Trapping of low-level internal gravity waves. *J. Atmos. Sci.*, **45**, 1533–1541.
- *Crook, N. A., T. L. Clark, and M. W. Moncrieff, 1990: The Denver Cyclone. Part I: Generation in low Froude number flow. *J. Atmos. Sci.*, **47**, 2725–2742.
- Davies, H. C., 1999: Theories of frontogenesis. *The Life Cycles of Extratropical Cyclones*, M. A. Shapiro and S. Grønas, Eds. Amer. Meteor. Soc., 215–238.
- *Davies-Jones, R. P., 1984: Streamwise vorticity: the origin of updraft rotation in supercell storms. *J. Atmos. Sci.*, **41**, 2991–3006.
- *Davies-Jones, R. P., 1986: Tornado dynamics. *Thunderstorm Morphology and Dynamics*, E. Kessler, Ed., 2d edn. University of Oklahoma Press, 197–236.
- *Davies-Jones, R., R. J. Trapp, and H. B. Bluestein, 2001: Tornadoes and tornadic storms. *Severe Local Storms*, Meteor. Monogr., No. 50, 167–221.
- Davis, C., N. Atkins, D. Bartels, L. Bosart, M. Coniglio, G. Bryan, W. Cotton, D. Dowell, B. Jewett, R. Johns, D. Jorgensen, J. Knievel, K. Knupp, W.-C. Lee, G. Mcfarquhar, J. Moore, R. Przybylinski, R. Rauber, B. Smull, R. Trapp, S. Trier, R. Wakimoto, M. Weisman, and C. Ziegler, 2004: The Bow Echo and MCV Experiment: observations and opportunities. *Bull. Amer. Meteor. Soc.*, **85**, 1075–1093.
- *Davis, C. A., and S. B. Trier, 2007: Mesoscale convective vortices observed during BAMEX. Part I: Kinematic and thermodynamic structure. *Mon. Wea. Rev.*, **135**, 2029–2049.

- Davis, L. G., R. L. Lavoie, J. I. Kelley, and C. L. Hosler, 1968: Lake-effect studies. Final Report to Environ. Sci. Serv. Adm., Contract No. E22-80-67(N), Dept. of Meteorology, Pennsylvania State University.
- Defant, F., 1951: Local winds. *Compendium of Meteorology*, T. M. Malone, Ed. Amer. Meteor. Soc., 655–672.
- de Wekker, S. F. J., S. Zhong, J. D. Fast, and C. D. Whitteman, 1998: A numerical study of the thermally driven plain-to-basin wind over idealized basin topographies. *J. Appl. Meteor.*, **37**, 606–622.
- Doswell, C. A., III, 1985: *The operational meteorology of convective weather. Vol. 2: Storm scale analysis*. NOAA Tech. Memo. ERL ESG-15.
- Doswell, C. A., III, 1987: The distinction between large-scale and mesoscale contribution to severe convection: a case study example. *Wea. Forecasting*, **2**, 3–16.
- *Doswell, C. A., III, 1991a: A review for forecasters on the application of hodographs to forecasting severe thunderstorms. *Natl. Wea. Dig.*, **16**, 2–16.
- Doswell, C. A., 1991b: A point of clarification about area and energy on common thermodynamic diagrams. *Wea. Forecasting*, **6**, 299–301.
- *Doswell, C. A., III, H. E. Brooks, and R. A. Maddox, 1996: Flash flood forecasting: An ingredients-based methodology. *Wea. Forecasting*, **11**, 560–581.
- *Doswell, C. A., III, and D. W. Burgess, 1993: Tornadoes and tornadic storms: A review of conceptual models. *The Tornado: Its Structure, Dynamics, Prediction, and Hazards*, Geophys. Monogr., No. 79, Amer. Geophys. Union, 161–172.
- Doswell, C. A., III, and J. S. Evans, 2003: Proximity sounding analysis for derechos and supercells: An assessment of similarities and differences. *Atmos. Res.*, **67–68**, 117–133.
- Doswell, C. A., III, and M. J. Haugland, 2007: A comparison of two cold fronts: Effects of the planetary boundary layer on the mesoscale. *E. J. Severe Storms Met.*, **2**(4), 1–12.
- Doswell, C. A., III, and P. M. Markowski, 2004: Is buoyancy a relative quantity? *Mon. Wea. Rev.*, **132**, 853–863.
- Doswell, C. A., and E. N. Rasmussen, 1994: The effect of neglecting the virtual temperature correction on CAPE calculations. *Wea. Forecasting*, **9**, 625–629.
- Doyle, J. D., and D. R. Durran, 2002: The dynamics of mountain-wave-induced rotors. *J. Atmos. Sci.*, **59**, 186–201.
- Durran, D. R., 1986a: Mountain waves. *Mesoscale Meteorology and Forecasting*, P. S. Ray, Ed. Amer. Meteor. Soc., 472–492.
- *Durran, D. R., 1986b: Another look at downslope windstorms. Part I: On the development of supercritical flow in an infinitely deep, continuously stratified fluid. *J. Atmos. Sci.*, **43**, 2527–2543.
- *Durran, D. R., 1990: Mountain waves and downslope winds. *Atmospheric Processes over Complex Terrain*, B. Blumen, Ed. American Meteorological Society, 59–81.
- *Durran, D. R., 2000: Small-amplitude coastally trapped disturbances and the reduced-gravity shallow-water approximation. *Quart. J. Roy. Meteor. Soc.*, **126**, 2671–2689.
- Durran, D. R., 2003a: Lee waves and mountain waves. In *Encyclopedia of the Atmospheric Sciences*, J. Holton, J. Curry and J. Pyle, Eds. Academic, 1161–1169.
- Durran, D. R., 2003b: Downslope winds. In *Encyclopedia of the Atmospheric Sciences*, J. Holton, J. Curry and J. Pyle, Eds. Academic, 644–650.
- Durran, D. R., and J. B. Klemp, 1982: On the effects of moisture on the Brunt–Väisälä frequency. *J. Atmos. Sci.*, **39**, 2152–2158.
- *Durran, D. R., and J. B. Klemp, 1987: Another look at downslope winds. Part II: Nonlinear amplification beneath wave-overturning layers. *J. Atmos. Sci.*, **44**, 3402–3412.
- Eichenlaub, V. L., 1979: *Weather and Climate of the Great Lakes Region*. University of Notre Dame Press.
- Emanuel, K. A., 1994: *Atmospheric Convection*. Oxford University Press.
- Eom, J. K., 1975: Analysis of the internal gravity wave occurrence of 19 April 1970 in the Midwest. *Mon. Wea. Rev.*, **103**, 217–226.
- Epifanio, C. C., and R. Rotunno, 2005: The dynamics of orographic wake formation in flows with upstream blocking. *J. Atmos. Sci.*, **62**, 3127–3150.
- *Evans, J. S., and C. A. Doswell III, 2001: Examination of derecho environments using proximity soundings. *Wea. Forecasting*, **16**, 329–342.
- Ferguson, H. L., 1967: Mathematical and synoptic aspects of a small-scale wave disturbance over the lower Great Lakes area. *J. Appl. Meteor.*, **6**, 523–529.
- Fjørtoft, R., 1950: Application of integral theorems in deriving criteria of stability of laminar flow and for the baroclinic circular vortex. *Geophys. Publ.*, **17**, 1–52.
- Fleagle, R. G., and Businger, J. A., 1980: *An Introduction to Atmospheric Physics*, 2nd edn. Academic.
- Forbes, G. S., R. A. Anthes, and D. W. Thomson, 1987: Synoptic and mesoscale aspects of an Appalachian ice storm associated with cold-air damming. *Mon. Wea. Rev.*, **115**, 564–591.
- *Forbes, G. S., and J. M. Merritt, 1984: Mesoscale vortices over the Great Lakes in wintertime. *Mon. Wea. Rev.*, **112**, 377–381.

- *Freeman, J.C., Jr., 1948: An analogy between equatorial easterlies and supersonic gas dynamics. *J. Meteorol.*, **5**, 138–146.
- Fritsch, J. M., and C. G. Chappell, 1980: Numerical prediction of convectively driven mesoscale pressure systems. Part II: Mesoscale model. *J. Atmos. Sci.*, **37**, 1734–1762.
- *Fritsch, J. M., J. D. Murphy and J. S. Kain, 1994: Warm core vortex amplification over land. *J. Atmos. Sci.*, **51**, 1781–1806.
- Fujita, T. T., 1955: Results of detailed synoptic studies of squall lines. *Tellus*, **7**, 405–436.
- *Fujita, T. T., 1978: Manual of downburst identification for Project NIMROD. SMRP Research Paper 156, University of Chicago.
- *Fujita, T. T., 1981: Tornadoes and downbursts in the context of generalized planetary scales. *J. Atmos. Sci.*, **38**, 1511–1534.
- *Fujita, T. T., 1985: The downburst. Satellite and Mesometeorology Research Project (SMRP), Dept. of Geophysical Sciences, University of Chicago.
- Fujita, T. T., 1992: The mystery of severe storms. Wind Research Laboratory Research Paper 239, Department of Geophysical Sciences, University of Chicago.
- Fujiwhara, S., 1931: Short note on the behavior of two vortices. *Proc. Phys.-Math. Soc. Japan*, **13**, 106–110.
- *Gaberšek, S., and D. R. Durran, 2004: Gap flows through idealized topography. Part I: Forcing by large-scale winds in the nonrotating limit. *J. Atmos. Sci.*, **61**, 2846–2862.
- *Garratt, J. R., 1994: *The Atmospheric Boundary Layer*. Cambridge University Press.
- Geerts, B., and Q. Miao, 2005: The use of millimeter Doppler radar echoes to estimate vertical air velocities in the fair-weather convective boundary layer. *J. Atmos. Oceanic Technol.*, **22**, 225–246.
- Godfrey, E., R. J. Trapp, and H. E. Brooks, 2004: A study of the pre-storm environment of tornadic quasilinear convective systems. Preprints, 22nd Conf. on Severe Local Storms, Amer. Meteor. Soc., Hyannis, MA.
- Goldstein, S., 1931: On the stability of superposed streams of fluid of different densities. *Proc. Roy. Soc. A*, **132**, 524–548.
- Goodstein, D. L., and J. R. Goodstein, 1996: *Feynman's Lost Lecture*. Norton.
- Haiden, T., 2003: On the pressure field in the slope wind layer. *J. Atmos. Sci.*, **60**, 1632–1635.
- Hawkes, H. B., 1947: Mountain and valley winds—with special reference to the diurnal mountain winds of the Great Salt Lake region. Ph.D. dissertation, Ohio State University.
- Holton, J. R., 2004: *An Introduction to Dynamic Meteorology*, 4th edn. Elsevier.
- *Hooke, W. H., 1986: Gravity waves. *Mesoscale Meteorology and Forecasting*. P. S. Ray, Ed. Amer. Meteor. Soc., 272–288.
- Hoskins, B. J., 1975: The geostrophic momentum approximation and the semi-geostrophic equations. *J. Atmos. Sci.*, **32**, 233–242.
- *Hoxit, L. R., C. F. Chappell, and J. M. Fritsch, 1976: Formation of mesolows or pressure troughs in advance of cumulonimbus clouds. *Mon. Wea. Rev.*, **104**, 1419–1428.
- Houze, R. A., Jr., 1993: *Cloud Dynamics*. Academic.
- Houze, R. A., Jr., M. I. Biggerstaff, S. A. Rutledge, and B. F. Smull, 1989: Interpretation of Doppler weather radar displays of midlatitude mesoscale convective systems. *Bull. Amer. Meteor. Soc.*, **70**, 608–619.
- *Howard, L. N., 1961: Note on a paper of John. W. Miles. *J. Fluid Mech.*, **13**, 158–160.
- James, R. P., and P. M. Markowski, 2008: A numerical investigation of the effects of dry air aloft on quasilinear convective systems. Preprints, 24th Conf. on Severe Local Storms, Savannah, GA, Amer. Meteor. Soc.
- James, R. P., P. M. Markowski, and J. M. Fritsch, 2006: Bow echo sensitivity to low-level moisture. *Mon. Wea. Rev.*, **134**, 950–964.
- Johnson, R. H., 2001: Surface mesohighs and mesolows. *Bull. Amer. Meteor. Soc.*, **82**, 13–31.
- Johnson, R. H., S. Chen, and J. J. Toth, 1989: Circulations associated with a mature-to-decaying midlatitude mesoscale convective system. Part I: Surface features, heat bursts and mesolow development. *Mon. Wea. Rev.*, **117**, 942–959.
- Johnson, R. H., and P. J. Hamilton, 1988: The relationship of surface pressure features to the precipitation and airflow structure of an intense midlatitude squall line. *Mon. Wea. Rev.*, **116**, 1444–1473.
- Jorgensen, D. P., Z. Pu, P. O. G. Persson, and W.-K. Tao, 2003: Variations associated with cores and gaps of a Pacific narrow cold frontal rainband. *Mon. Wea. Rev.*, **131**, 2705–2729.
- *Keshishian, L. G., and L. F. Bosart, 1987: A case study of extended East Coast frontogenesis. *Mon. Wea. Rev.*, **115**, 100–117.
- Keyser, D., 1999: On the representation and diagnosis of frontal circulations in two and three dimensions. *The Life Cycles of Extratropical Cyclones*, M. A. Shapiro and S. Grønås, Eds. Amer. Meteor. Soc., 239–264.
- Kirshbaum, D. J., and D. R. Durran, 2004: Factors governing cellular convection in orographic precipitation. *J. Atmos. Sci.*, **61**, 682–698.
- *Klemp, J. B., 1987: Dynamics of tornadic thunderstorms. *Ann. Rev. Fluid Mech.*, **19**, 369–402.
- *Klemp, J. B., and D. R. Lilly, 1975: The dynamics of wave-induced downslope winds. *J. Atmos. Sci.*, **32**, 320–339.

- *Koch, S. E., C. Flamant, J. W. Wilson, B. M. Gentry, and B.D. Jamison, 2008: An atmospheric soliton observed with Doppler radar, differential absorption lidar, and a molecular Doppler lidar. *J. Atmos. Oceanic Technol.*, **25**, 1267–1287.
- Koch, S. E., and R. E. Golus, 1985: Observed interactions between strong convection and internal gravity waves. Preprints, *14th Conf. on Severe Local Storms*, Indianapolis, IN, Amer. Meteor. Soc., 198–201.
- Koch, S. E., and C. O’Handley, 1997: Operational forecasting and detection of mesoscale gravity waves. *Wea. Forecasting*, **12**, 253–281.
- Koch, S. E., B. D. Jamison, C. Lu, T. L. Smith, E. I. Tollerud, C. Girz, N. Wang, T. P. Lane, M. A. Shapiro, D. D. Parrish, and O. R. Cooper, 2005: Turbulence and gravity waves within an upper-level front. *J. Atmos. Sci.*, **62**, 3885–3908.
- Koch, S. E., and R. E. Golus, 1988: A mesoscale gravity wave event observed during CCOPE. Part I: Multiscale statistical analysis of wave characteristics. *Mon. Wea. Rev.*, **116**, 2527–2544.
- *Krishnamurti, R., 1975b: On cellular cloud patterns. Part 2: Laboratory model. *J. Atmos. Sci.*, **32**, 1364–1372.
- *Kundu, P. K., and I. M. Cohen, 2008: *Fluid Mechanics*, 4th edn. Academic.
- Lalas, D. P., and F. Einaudi, 1974: On the correct use of the wet adiabatic lapse rate in the stability criteria of a saturated atmosphere. *J. Appl. Meteor.*, **13**, 318–324.
- Lee, B. D., and C. A. Finley, 2002: High resolution numerical simulations of thunderstorm outflow boundaries. Preprints, *21st Conf. on Severe Local Storms*, San Antonio, TX, Amer. Meteor. Soc.
- *Lee, B. D., and R. B. Wilhelmson, 1997a: The numerical simulation of non-supercell tornadogenesis. Part I: Initiation and evolution of pre tornadic mesocyclone circulations along a dry outflow boundary. *J. Atmos. Sci.*, **54**, 32–60.
- *Lee, B. D., and R. B. Wilhelmson, 1997b: The numerical simulation of non-supercell tornadogenesis. Part II: Evolution of a family of tornadoes along a weak outflow boundary. *J. Atmos. Sci.*, **54**, 2387–2415.
- *Lemon, L. R., and C. A. Doswell III, 1979: Severe thunderstorm evolution and mesocyclone structure as related to tornadogenesis. *Mon. Wea. Rev.*, **107**, 1184–1197.
- *Lenschow, D. H., 1973: Two examples of planetary boundary layer modification over the Great Lakes. *J. Atmos. Sci.*, **30**, 568–581.
- Lewellen, D. C., W. S. Lewellen, and J. Xia, 2000: The influence of a local swirl ratio on tornado intensification near the surface. *J. Atmos. Sci.*, **57**, 527–544.
- Ligda, M. G. H., 1951: Radar storm observation. *Compendium of Meteorology*, T. F. Malone, Ed. Amer. Meteor. Soc., 1265–1282.
- Lilly, D. K., 1978: A severe downslope windstorm and aircraft turbulence event induced by a mountain wave. *J. Atmos. Sci.*, **35**, 59–77.
- *Lilly, D. K., 1986: Instabilities. *Mesoscale Meteorology and Forecasting*, P. S. Ray, Ed. Amer. Meteor. Soc., 259–271.
- *Lin, C. C., 1945: On the stability of two-dimensional parallel flows. *Q. Appli. Math.*, **3**, 117f, 218f, 277f.
- *Lindzen, R. S., and K.-J. Tung, 1976: Banded convective activity and ducted gravity waves. *Mon. Wea. Rev.*, **104**, 1602–1617.
- Locatelli, J. D., R. D. Schwartz, M. T. Stoelinga, and P. V. Hobbs, 2002: Norwegian-type and cold front aloft-type cyclones east of the Rocky Mountains. *Wea. Forecasting*, **17**, 66–82.
- *Long, R. R., 1954: Some aspects of the flow of stratified fluids II. Experiments with a two-fluid system. *Tellus*, **6**, 97–115.
- Long, R. R., 1955: Some aspects of the flow of stratified fluids: III. Continuous density gradients. *Tellus*, **7**, 341–357.
- Lugt, H. J., 1979: The dilemma of defining a vortex. *Recent Developments in Theoretical and Experimental Fluid Mechanics*, U. Muller, K. G. Roesner, and B. Schmidt, Eds. Springer, 309–321.
- MacGorman, D. R., and W. D. Rust, 1998: *The Electrical Nature of Storms*. Oxford University Press.
- *Maddox, R. A., 1980: An objective technique for separating macroscale and mesoscale features in meteorological data. *Mon. Wea. Rev.*, **108**, 1108–1121.
- Maddox, R. A., and C. A. Doswell III, 1982: An examination of the jet stream configurations, 500 mb vorticity advection, and low-level thermal advection patterns during extended periods of intense convection. *Mon. Wea. Rev.*, **110**, 184–197.
- *Maddox, R. A., K. W. Howard, D. L. Bartels, and D. M. Rogers, 1986: Mesoscale convective complexes in the middle latitudes. *Mesoscale Meteorology and Forecasting*, P. S. Ray, Ed. Amer. Meteor. Soc., 390–413.
- *Maddox, R. A., L. R. Hoxit, C. F. Chappell, and F. Caracena, 1978: Comparison of meteorological aspects of the Big Thompson and Rapid City flash floods. *Mon. Wea. Rev.*, **106**, 375–389.
- *Maddox, R. A., D. J. Perkey, and J.M. Fritsch, 1981: Evolution of upper tropospheric features during the development of a mesoscale convective complex. *J. Atmos. Sci.*, **38**, 1664–1674.
- Mahrt, L., 1982: Momentum balance of gravity flows. *J. Atmos. Sci.*, **39**, 2701–2711.

- Markowski, P. M., C. Hannon, J. Frame, E. Lancaster, A. Pietrycha, R. Edwards, and R. Thompson, 2003: Characteristics of vertical wind profiles near supercells obtained from the Rapid Update Cycle. *Wea. Forecasting*, **18**, 1262–1272.
- Markowski, P. M., E. N. Rasmussen and J. M. Straka, 2002: Direct surface thermodynamic observations within the rear-flank downdrafts of nontornadic and tornadic supercells. *Mon. Wea. Rev.*, **130**, 1692–1721.
- Markowski, P. M., E. N. Rasmussen, J. M. Straka and D. C. Dowell, 1998: Observations of low-level baroclinity generated by anvil shadows. *Mon. Wea. Rev.*, **126**, 2942–2958.
- Markowski, P. M., and Y. P. Richardson, 2006: On the classification of vertical wind shear as directional shear versus speed shear. *Wea. Forecasting*, **21**, 242–247.
- Markowski, P. M., and Y. P. Richardson, 2007: Observations of vertical wind shear heterogeneity in convective boundary layers. *Mon. Wea. Rev.*, **135**, 843–861.
- Markowski, P. M., and Y. P. Richardson, 2009: Tornadogenesis: our current understanding, forecasting considerations, and questions to guide future research. *Atmospheric Research*, **88**.
- Markowski, P. M., J. M. Straka, E. N. Rasmussen, R. P. Davies-Jones, Y. Richardson, and J. Trapp, 2008: Vortex lines within low-level mesocyclones obtained from pseudo-dual-Doppler radar observations. *Mon. Wea. Rev.*, **136**, 3513–3535.
- *Marquis, J. N., Y. P. Richardson, and J. M. Wurman, 2007: Kinematic observations of misocyclones along boundaries during IHOP. *Mon. Wea. Rev.*, **135**, 1749–1768.
- Martin, J. E., 2006: *Mid-Latitude Atmospheric Dynamics: a First Course*. Wiley.
- Marwitz, J. D., 1972: Precipitation efficiency of thunderstorms on the High Plains. *J. Rech. Atmos.*, **6**, 367–370.
- *Mass, C. F., and M. D. Albright, 1987: Coastal southerlies and alongshore surges of the west coast of North America: Evidence of mesoscale topographically trapped response to synoptic forcing. *Mon. Wea. Rev.*, **115**, 1707–1738.
- Matejka, T. J., R. A. Houze, Jr., and P. V. Hobbs, 1980: Microphysics and dynamics of clouds associated with mesoscale rainbands in extratropical cyclones. *Quart. J. Roy. Met. Soc.*, **106**, 29–56.
- Miles, N. L., and J. Verlinde, 2005: Observations of transient linear organization and nonlinear scale interactions in lake-effect clouds. Part II: Nonlinear scale interactions. *Mon. Wea. Rev.*, **133**, 692–706.
- Miller, D. A., and F. Sanders, 1980: Mesoscale conditions for the severe convection of 3 April 1974 in the east-central United States. *J. Atmos. Sci.*, **37**, 1041–1055.
- *Nappo, C. J., 2002: *An Introduction to Atmospheric Gravity Waves*. Academic.
- Neff, W. D., 1990: Remote sensing of atmospheric processes over complex terrain. *Atmospheric Processes over Complex Terrain*, B. Blumen, Ed. American Meteorological Society, 173–228.
- *Neiman, P. J., R. M. Hardesty, M. A. Shapiro, and R. E. Cupp, 1988: Doppler lidar observations of a downslope windstorm. *Mon. Wea. Rev.*, **116**, 2265–2275.
- Nickus, U., and I. Vergeiner, 1984: The thermal structure of the Inn Valley atmosphere. *Arch. Meteor. Geophys. Bioklim.*, **A33**, 199–215.
- Nizioł, T. A., W. R. Snyder, and J. S. Waldstreicher, 1995: Winter weather forecasting throughout the eastern United States. Part IV: Lake effect snow. *Wea. Forecasting*, **10**, 61–77.
- Ogura, Y., 1963: A review of numerical modeling research on small-scale convection in the atmosphere. *Meteor. Monogr.*, No. 27, Amer. Meteor. Soc., 65–76.
- *Ogura, Y., and N. A. Phillips, 1962: Scale analysis of deep and shallow convection in the atmosphere. *J. Atmos. Sci.*, **19**, 173–179.
- Oke, T. R., 1976: The distinction between canopy and boundary layer urban heat islands. *Atmosphere*, **14**, 268–277.
- *Ookouchi, Y., M. Segal, R. C. Kessler, and R. A. Pielke, 1984: Evaluation of soil moisture effects on the generation and modification of mesoscale circulations. *Mon. Wea. Rev.*, **112**, 2281–2292.
- *Orlanski, I., 1975: A rational subdivision of scales for atmospheric processes. *Bull. Amer. Meteor. Soc.*, **56**, 527–530.
- *Overland, J. E., and N. A. Bond, 1995: Observations and scale analysis of coastal wind jets. *Mon. Wea. Rev.*, **123**, 2934–2941.
- Parker, M. D., 2008: Response of simulated squall lines to low-level cooling. *J. Atmos. Sci.*, **65**, 1323–1341.
- *Parker, M. D., and R. H. Johnson, 2000: Organizational modes of midlatitude mesoscale convective systems. *Mon. Wea. Rev.*, **128**, 3413–3436.
- Parker, M. D., and R. H. Johnson, 2004a: Structures and dynamics of quasi-2D mesoscale convective systems. *J. Atmos. Sci.*, **61**, 545–567.
- *Parker, M. D., and R. H. Johnson, 2004b: Simulated convective lines with leading precipitation. Part I: Governing dynamics. *J. Atmos. Sci.*, **61**, 1637–1655.
- *Parker, M. D., and R. H. Johnson, 2004c: Simulated convective lines with leading precipitation. Part II: Evolution and maintenance. *J. Atmos. Sci.*, **61**, 1656–1673.
- Parker, M. D., I. C. Ratcliffe, and G. M. Henebry, 2005: The July 2003 Dakota hailswaths: Creation, characteristics, and possible impacts. *Mon. Wea. Rev.*, **133**, 1241–1260.

- *Parsons, D. B., 1992: An explanation for intense frontal updrafts and narrow cold-frontal rainbands. *J. Atmos. Sci.*, **49**, 1810–1825.
- Pecnick, M. J., and J. A. Young, 1984: Mechanics of a strong subsynoptic gravity wave deduced from satellite and surface observations. *J. Atmos. Sci.*, **41**, 1850–1862.
- Peltier, W. R., and T. L. Clark, 1983: Nonlinear mountain waves in two and three spatial dimensions. *Quart. J. Roy. Met. Soc.*, **109**, 527–548.
- Petterssen, S., 1956: Convective clouds and weather. *Weather Analysis and Forecasting*, 2nd edn. McGraw-Hill, 133–195.
- *Pontrelli, M. D., G. Bryan, and J. M. Fritsch, 1999: The Madison County, Virginia, flash flood of 27 June 1995. *Wea. Forecasting*, **14**, 384–404.
- Pruppacher, H. R., and J. D. Klett, 1997: *Microphysics of Clouds and Precipitation*. Kluwer.
- Rasmussen, E. N., and D. O. Blanchard, 1998: A baseline climatology of sounding-derived supercell and tornado forecast parameters. *Wea. Forecasting*, **13**, 1148–1164.
- Rasmussen, E. N., S. J. Richardson, J. M. Straka, P. M. Markowski, 2000: The association of significant tornadoes with a baroclinic boundary on 2 June 1995. *Mon. Wea. Rev.*, **128**, 174–191.
- *Rasmussen, E. N., and J. M. Straka, 1998: Variations in supercell morphology. Part I: Observations of the role of upper-level storm-relative flow. *Mon. Wea. Rev.*, **126**, 2406–2421.
- Raymond, D. J., and H. Jiang, 1990: A theory for long-lived mesoscale convective systems. *J. Atmos. Sci.*, **47**, 3067–3077.
- Richardson, Y. P., 1999: The influence of horizontal variations in vertical shear and low-level moisture on numerically simulated convective storms. Ph.D. dissertation, School of Meteorology, University of Oklahoma.
- *Rottman, J.W., and J. E. Simpson, 1989: The formation of internal bores in the atmosphere: a laboratory model. *Quart. J. Roy. Meteor. Soc.*, **115**, 941–963.
- *Rotunno, R., 1983: On the linear theory of the land and sea breeze. *J. Atmos. Sci.*, **40**, 1999–2009.
- *Rotunno, R., J. B. Klemp, and M. L. Weisman, 1988: A theory for strong, long-lived squall lines. *J. Atmos. Sci.*, **45**, 463–485.
- Rotunno, R., 1993: Tornadoes and tornadogenesis. *Mesoscale Meteorology and Forecasting*, P. S. Ray, Ed. Amer. Meteor. Soc., 414–436.
- Rozoff, C. M., W. R. Cotton, and J. O. Adegoke, 2003: Simulation of St. Louis, Missouri, land use impacts on thunderstorms. *J. Appl. Meteor.*, **42**, 716–738.
- Sanders, F., 1955: An investigation of the structure and dynamics of an intense surface frontal zone. *J. Atmos. Sci.*, **12**, 542–552.
- Saucier, W. J., 1955: *Principles of Meteorological Analysis*. Dover.
- *Schär, C., and R. B. Smith, 1993a: Shallow-water flow past isolated topography. Part I: Vorticity production and wake formation. *J. Atmos. Sci.*, **50**, 1373–1400.
- *Schär, C., and R. B. Smith, 1993b: Shallow-water flow past isolated topography. Part II: Transition to vortex shedding. *J. Atmos. Sci.*, **50**, 1401–1412.
- Schmidt, J. M., and W. R. Cotton, 1990: Interactions between upper and lower tropospheric gravity waves on squall line structure and maintenance. *J. Atmos. Sci.*, **47**, 1205–1222.
- *Schneider, R. S., 1990: Large-amplitude mesoscale wave disturbances within the intense Midwest extratropical cyclone of 15 December 1987. *Wea. Forecasting*, **5**, 533–558.
- *Schultz, D. M., and J. A. Knox, 2007: Banded convection caused by frontogenesis in a conditionally, symmetrically, and inertially unstable environment. *Mon. Wea. Rev.*, **135**, 2095–2110.
- Schultz, D. M., and C. F. Mass, 1993: The occlusion process in a midlatitude cyclone over land. *Mon. Wea. Rev.*, **121**, 918–940.
- *Schultz, D. M., P. N. Schumacher, and C. A. Doswell, III, 2000: The intricacies of instabilities. *Mon. Wea. Rev.*, **128**, 4143–4148.
- Schultz, D. M., and W. J. Steenburgh, 1999: The formation of a forward-tilting cold front with multiple cloud bands during Superstorm 1993. *Mon. Wea. Rev.*, **127**, 1108–1124.
- *Schultz, D. M., C. C. Weiss, and P. M. Hoffman, 2007: The synoptic regulation of dryline intensity. *Mon. Wea. Rev.*, **135**, 1699–1709.
- Schumacher, R. S., and R. H. Johnson, 2008: Mesoscale processes contributing to extreme rainfall in a midlatitude warm-season flash flood. *Mon. Wea. Rev.*, **136**, 3964–3986.
- *Scorer, R., 1949: Theory of waves in the lee of mountains. *Quart. J. Roy. Meteor. Soc.*, **75**, 41–56.
- *Segal, M., J. F. W. Purdom, J. L. Song, R. A. Pielke and Y. Mahrer, 1986: Evaluation of cloud shading effects on the generation and modification of mesoscale circulations. *Mon. Wea. Rev.*, **114**, 1201–1212.
- Shabbott, C. J., and P. M. Markowski, 2006: Surface in situ observations within the outflow of forward-flank down-drafts of supercell thunderstorms. *Mon. Wea. Rev.*, **134**, 1422–1441.
- Shapiro, M. A., T. Hampel, D. Rotzoll, and F. Mosher, 1985: The frontal hydraulic head: a micro- α -scale (~ 1 km) triggering mechanism for mesoconvective weather systems. *Mon. Wea. Rev.*, **113**, 1166–1183.

- *Shepherd, J. M., H. Pierce, and A. J. Negri, 2002: Rainfall modification by major urban areas: Observations from spaceborne rain radar on the TRMM satellite. *J. Appl. Meteor.*, **41**, 689–701.
- *Sherwood, S. C., 2000: On moist instability. *Mon. Wea. Rev.*, **128**, 4139–4142.
- Smith, J. A., M. L. Baeck, Y. Zhang, and C. A. Doswell III, 2001: Extreme rainfall and flooding from supercell thunderstorms. *J. Hydrometeor.*, **2**, 469–489.
- *Smith, R. B., 1985: On severe downslope winds. *J. Atmos. Sci.*, **42**, 2597–2603.
- Smith, R. B., 1989: Comment on ‘Low Froude number flow past three-dimensional obstacles. Part I: Baroclinically generated lee vortices.’ *J. Atmos. Sci.*, **46**, 3611–3613.
- *Smith, R. B., 1990: Why can’t stably stratified air rise over high ground? *Atmospheric Processes over Complex Terrain*, B. Blumen, Ed. American Meteorological Society, 105–107.
- Smolarkiewicz, P. K., and R. Rotunno, 1989: Low Froude number flow past three-dimensional obstacles. Part I: Baroclinically generated lee vortices. *J. Atmos. Sci.*, **46**, 1154–1166.
- Smolarkiewicz, P. K., and R. Rotunno, 1990: Low Froude number flow past three-dimensional obstacles. Part II: Upwind flow reversal zone. *J. Atmos. Sci.*, **47**, 1498–1511.
- *Smull, B. F., and R. A. Houze, 1987: Dual-Doppler radar analysis of a midlatitude squall line with a trailing region of stratiform rain. *J. Atmos. Sci.*, **44**, 2128–2149.
- Snow, J. T., 1982: A review of recent advances in tornado vortex dynamics. *Rev. Geophys. Space Phys.*, **20**, 953–964.
- *Sorbian, Z., 1989: *Structure of the Atmospheric Boundary Layer*. Prentice-Hall.
- *Sousounis, P. J., and G. E. Mann, 2000: Lake-aggregate mesoscale disturbances. Part V: Impacts on lake-effect precipitation. *Mon. Wea. Rev.*, **128**, 728–745.
- *Steenburgh, J. W., D. M. Schultz, and B. A. Colle, 1998: The structure and evolution of gap outflow over the Gulf of Tehuantepec, Mexico. *Mon. Wea. Rev.*, **126**, 2673–2691.
- Stensrud, D. J., M. C. Coniglio, R. P. Davies-Jones, and J. S. Evans, 2005: Comments on ‘“A theory for strong long-lived squall lines” revisited.’ *J. Atmos. Sci.*, **62**, 2989–2996.
- Stobie, J. G., F. Einaudi, and L. W. Uccellini, 1983: A case study of gravity wave-convective storms interaction: 9 May 1979. *J. Atmos. Sci.*, **40**, 2804–2830.
- Stoelinga, M. T., J. T. Locatelli, and P. V. Hobbs, 2002: Warm occlusions, cold occlusions, and forward-tilting cold fronts. *Bull. Amer. Meteor. Soc.*, **83**, 709–721.
- Straka, J. M., E. N. Rasmussen, R. P. Davies-Jones, and P. M. Markowski, 2007: An observational and idealized numerical examination of low-level counter-rotating vortices toward the rear flank of supercells. *E. J. Severe Storms Met.*, **2**(8), 1–22.
- *Stull, R. B., 1988: *An Introduction to Boundary Layer Meteorology*. Kluwer.
- Taylor, G. I., 1931: Effect of variation of density on the stability of superposed streams of fluid. *Proc. Roy. Soc. A*, **132**, 499–523.
- Tepper, 1959: Mesometeorology—the link between macroscale atmospheric motions and local weather. *Bull. Amer. Meteor. Soc.*, **40**, 56–72.
- Trapp, R. J., and M. L. Weisman, 2003: Low-Level Mesovortices within Squall Lines and Bow Echoes. Part II: Their Genesis and Implications. *Mon. Wea. Rev.*, **131**, 2804–2823.
- Trapp, R. J., G. J. Stumpf, and K. L. Manross, 2005: A reassessment of the percentage of tornadic mesocyclones. *{\it Wea. Forecasting}*, **20**, 680–687.
- *Trier, S. B., and C. A. Davis, 2007: Mesoscale convective vortices observed during BAMEX. Part II: Influences on secondary deep convection. *Mon. Wea. Rev.*, **135**, 2051–2075.
- Tripoli, G. J., and W. R. Cotton, 1989a: Numerical study of an observed orogenic mesoscale convective system. Part I: Simulated genesis and comparison with observations. *Mon. Wea. Rev.*, **117**, 273–304.
- Tripoli, G. J., and W. R. Cotton, 1989b: Numerical study of an observed orogenic mesoscale convective system. Part II: Analysis of governing dynamics. *Mon. Wea. Rev.*, **117**, 305–328.
- Uccellini, L. W., 1975: A case study of apparent gravity wave initiation of severe convective storms. *Mon. Wea. Rev.*, **103**, 497–513.
- *Uccellini, L. W., and S. E. Koch, 1987: The synoptic setting and possible energy sources for mesoscale wave disturbances. *Mon. Wea. Rev.*, **115**, 721–729.
- Vincent, D. G., and J. H. Homan, 1983: Mesoscale analysis of pressure and precipitation patterns during AVE-SESAME 1979, 10–11 April. *Bull. Amer. Meteor. Soc.*, **64**, 23–28.
- *Vivekanandan, J., S. M. Ellis, R. Oye, D. S. Zrnic, A. V. Ryzhkov, and J. Straka, 1999: Cloud microphysics retrieval using S-band dual-polarization radar measurements. *Bull. Amer. Meteor. Soc.*, **80**, 381–388.
- *Vosper, S. B., 2004: Inversion effects on mountain lee waves. *Quart. J. Roy. Met. Soc.*, **130**, 1723–1748.
- *Wakimoto, R. M., 1982: The life cycle of thunderstorm gust fronts as viewed with Doppler radar and rawinsonde data. *Mon. Wea. Rev.*, **110**, 1060–1082.
- *Wakimoto, R. M., and N. T. Atkins, 1994: Observations of the sea-breeze front during CaPE. Part I: Single-Doppler, satellite, and cloud photogrammetry analysis. *Mon. Wea. Rev.*, **122**, 1092–1114.

- Wakimoto, R. M., H. Cai, and H. V. Murphrey, 2004a: The Superior, Nebraska, supercell during BAMEX. *Bull. Amer. Meteor. Soc.*, **85**, 1095–1106.
- Wakimoto, R. M., H. V. Murphrey, E. V. Browell, and S. Ismail, 2006a: The ‘triple point’ on 24 May 2002 during IHOP. Part I: Airborne Doppler and LASE analyses of the frontal boundaries and convection initiation. *Mon. Wea. Rev.*, **134**, 231–250.
- Wakimoto, R. M., H. V. Murphrey, and H. Cai, 2004b: The San Angelo, Texas, supercell of 31 May 1995: Visual observations and tornadogenesis. *Mon. Wea. Rev.*, **132**, 1269–1293.
- Wakimoto, R. M., H. V. Murphrey, C. A. Davis, and N. T. Atkins, 2006b: High winds generated by bow echoes. Part II: The relationship between the mesovortices and damaging straight-line winds. *Mon. Wea. Rev.*, **134**, 2813–2829.
- Walko, R. L., 1993: Tornado spin-up beneath a convective cell: Required basic structure of the near-field boundary layer winds. *The Tornado: Its Structure, Dynamics, Prediction, and Hazards*, Geophys. Monogr., No. 79, Amer. Geophys. Union, 89–95.
- *Wang, T.-A., and Y.-L. Lin, 1999: Wave ducting in a stratified shear flow over a two-dimensional mountain. Part I: General linear criteria. *J. Atmos. Sci.*, **56**, 412–436.
- Weckwerth, T.M., J. W. Wilson, and R. M. Wakimoto, 1996: Thermodynamic variability within the convective boundary layer due to horizontal convective rolls. *Mon. Wea. Rev.*, **124**, 769–784.
- Weinand, B. J., 2000: Mesoscale shear eddies in the upper troposphere. *Mon. Wea. Rev.*, **128**, 4126–4130.
- Weisman, M. L., 1992: The role of convectively generated rear-inflow jets in the evolution of long-lived mesoconvective systems. *J. Atmos. Sci.*, **49**, 1826–1847.
- Weisman, M. L., 1993: The genesis of severe, long-lived bow echoes. *J. Atmos. Sci.*, **50**, 645–670.
- *Weisman, M. L., and C. A. Davis, 1998: Mechanisms for the generation of mesoscale vortices within quasi-linear convective systems. *J. Atmos. Sci.*, **55**, 2603–2622.
- *Weisman, M. L., and J. B. Klemp, 1982: The dependence of numerically simulated convective storms on vertical wind shear and buoyancy. *Mon. Wea. Rev.*, **110**, 504–520.
- *Weisman, M. L., and R. Rotunno, 2004: ‘A theory for strong, long-lived squall lines’ revisited. *J. Atmos. Sci.*, **61**, 361–382.
- Weisman, M. L., and R. Rotunno, 2005: Reply to ‘Comments on “A theory for strong long-lived squall lines” revisited.’ *J. Atmos. Sci.*, **62**, 2997–3002.
- Weisman, M. L. and R. F. Trapp, 2003: Low-Level Mesovortices within Squall Lines and Bow Echoes. Part I: Overview and Dependence on Environmental Shear *Mon. Wea. Rev.*, **131**, 2779–2803.
- Weisman, M. L., and H. B. Bluestein, 2000: The interaction of numerically simulated supercells initiated along lines. *Mon. Wea. Rev.*, **128**, 3128–3149.
- Whiteman, C. D., 1990: Observations of thermally developed wind systems in mountainous terrain. *Atmospheric Processes over Complex Terrain*, Meteor. Monogr., No. 45, 5–42.
- Whiteman, C. D., 2000: *Mountain Meteorology: Fundamentals and Applications*. Oxford University Press.
- Wicker, L. J., and R. B. Wilhelmson, 1995: Simulation and analysis of tornado development and decay within a three-dimensional supercell thunderstorm. *J. Atmos. Sci.*, **52**, 2675–2703.
- Winkler, J. A., R. H. Skaggs, and D. G. Baker, 1981: Effect of temperature adjustments on the Minneapolis–St. Paul urban heat island. *J. Appl. Meteor.*, **20**, 1295–1300.
- *Wood, I. R., and J. E. Simpson, 1984: Jumps in layered miscible fluids. *J. Fluid Mech.*, **140**, 329–342.
- Xu, Q., 1992: Formation and evolution of frontal rainbands and geostrophic PV anomalies. *J. Atmos. Sci.*, **49**, 629–648.
- Xue, M., 2004: Tornadogenesis within a simulated supercell storm. Preprints, 22nd Conf. on Severe Local Storms, Hyannis, MA, Amer. Meteor. Soc.
- Yamada, T., G. Mellor, 1975: A simulation of the Wangara atmospheric boundary layer data. *J. Atmos. Sci.*, **32**, 2309–2329.
- *Young, G. S., and J. M. Fritsch, 1989: A proposal for general conventions in analyses of mesoscale boundaries. *Bull. Amer. Meteor. Soc.*, **70**, 1412–1421.
- Zhang, D.-L., and J. M. Fritsch, 1986: Numerical simulation of the meso- β -scale structure and evolution of the 1977 Johnstown Flood. Part I: Model description and verification. *J. Atmos. Sci.*, **43**, 1913–1944.
- Zhang, D.-L., and J. M. Fritsch, 1987: Numerical simulation of the meso- β -scale structure and evolution of the 1977 Johnstown Flood. Part II: Inertially stable warm-core vortex and the mesoscale convective complex. *J. Atmos. Sci.*, **44**, 2593–2612.
- Zhang, D.-L., and J. M. Fritsch, 1988: Numerical simulation of the meso- β -scale structure and evolution of the 1977 Johnstown Flood. Part III: Internal gravity waves and the squall line. *J. Atmos. Sci.*, **45**, 1252–1268.
- Zhang, F., S. E. Koch, C. A. Davis, and M. L. Kaplan, 2001: Wavelet analysis and the governing dynamics of a large-amplitude mesoscale gravity wave event along the East Coast of the United States. *Quart. J. Roy. Meteor. Soc.*, **127**, 2209–2245.
- Ziegler, C. L., and E. N. Rasmussen, 1998: The initiation of moist convection at the dryline: Forecasting issues from a case study perspective *Wea. Forecasting*, **13**, 1106–1131.

Index

- ABL, *See* atmospheric boundary layer
absolute circulation, *See* circulation, absolute
absolute instability, *See* instability, static
absolute momentum, *See* momentum, absolute
absolute vorticity, *See* vorticity, absolute
adiabatic process, 13–14, *See also* dry adiabatic process; moist adiabatic process; pseudoadiabatic process; reversible moist adiabatic process
advection, 11
ageostrophic, 129
differential temperature, 185–186
geostrophic, 126, 129
moisture, 41, 139, 186, 188, 195
temperature, 36, 41, 93, 120, 124, 126, 129, 185–187
vorticity, 62, 124, 266, 283, 342
aerodynamic drag, 78, 103
ageostrophic momentum,
See momentum, ageostrophic
ageostrophic wind, 4–5, 8, 18, 107, 112, 117, 124–127, 276
air mass boundaries, 115–158, *See also* front; dryline; mesoscale boundaries
characteristics of, 117
types of, 117
air mass thunderstorm, *See* single-cell convection
albedo, 82, 154–158
amplitude, *See* wave, amplitude of
anabatic wind, 317–318, 321
anelastic approximation, *See* continuity equation, anelastic form
angular momentum, *See* momentum, angular
antitropic wind, 82
antiwind, 322
anvil cloud, 156, 191, 207–209, 211, 216, 220, 222–224, 246, 265, 307
approximation
anelastic, *See* continuity equation, anelastic form
Boussinesq, *See* continuity equation, Boussinesq form
geostrophic momentum, 126, 129
hydrostatic, 8, 18
quasigeostrophic, 8, 126, 129
arcus cloud, 141
area
negative, 33–35, 67, 195, 295, 343,
See also convective inhibition
positive, 33–34, *See also* convective available potential energy
aspect ratio, 9, 19, 74, 89, 255, 345–346
atmospheric boundary layer (ABL),
See boundary layer
attenuation, *See* radar, attenuation of axis of dilatation, 124–127
backbuilding, 212, 309, 311
back-door cold front, 117
back-door warm front, 117
balanced flow, 18–19, *See also* geostrophic wind; gradient wind
band-pass filter, 5, 7
baroclinic instability, *See* instability, baroclinic
baroclinic vorticity generation,
See vorticity, baroclinic generation of baroclinic zone, *See* air mass boundaries
baroclinity, 36, 50, 53, 98, 115, 120, 233, 277, 286
barotropic instability, *See* instability, barotropic
barrier jet, 8–11
baseline, *See* dual-Doppler analysis, baseline of
bay-effect precipitation, *See* lake-effect precipitation
Beaufort scale, 274
Beltrami flow, 230
Bernoulli equation, 32, 43, 218, 295, 338, 343–344, 360
billow cloud, 58
Bjerknes' circulation theorem,
See circulation, Bjerknes' theorem
blocking of wind by terrain, 343–364,
See also mountain Froude number; nondimensional mountain height
bookend vortex, *See* bow echo, bookend vortex of
bora, 333
bore, 176–179
boundaries, *See* air mass boundaries
boundary condition, 170
dynamic, 170–171
kinematic, 170–171
boundary layer, 73, 88–89, 91, *See also* convective boundary layer; mixed layer; residual layer; stable boundary layer; surface layer
dry convection within, 88–93
evolution of, 83–87
structure of, 73–74, 83–87
bounded weak-echo region (BWER), 215,
See also supercell
Boussinesq approximation, *See* continuity equation, Boussinesq form
bow echo, 260–265
bookend vortex of, 261–262
development of, 260, 264
environment of, 261–262, 264
Bowen ratio, 83, 135, 137, 156
Bragg scattering, 375
breaking (of gravity waves), *See* gravity wave, breaking
bright band, 250, 381, 383–384
BRN, *See* bulk Richardson number
Brunt-Väisälä frequency, 5, 42, 150, 174, 344, 346–347, *See also* moist Brunt-Väisälä frequency

- bubble high, *See* mesohigh
 bulk Richardson number (BRN),
See Richardson number, bulk
 bulk transfer coefficient
 for heat, 79
 for moisture, 79
 buoyancy
 force, 19–20, 24, 41, 43–44
 frequency, *See* Brunt-Väisälä frequency
 generation of horizontal vorticity,
See vorticity, baroclinic
 generation of
 generation of turbulent kinetic energy,
See turbulent kinetic energy,
 buoyant generation of
 hydrometeor loading, 20, 47
 oscillations, 42, 61, *See also* gravity wave
 pressure perturbation, *See* pressure,
 buoyancy perturbation
 retrieval, *See* dual-Doppler analysis,
 thermodynamic retrieval derived
 from
 Burger number, 346
 Burgers-Rott vortex, *See* vortex,
 Burgers-Rott
 bursters, *See* southerly buster
 BWER, *See* bounded weak-echo region
 cap, *See* capping inversion
 CAPE, *See* convective available potential
 energy
 capping inversion, 77–78, 84–87,
 137–139, *See also* convection
 initiation
 cavitation, *See* gravity wave, cavitation
 CBL, *See* convective boundary layer
 CCL, *See* convective condensation level
 centrifugal force, 17, 19, 48, 287
 centrifugal instability, *See* instability,
 centrifugal
 centripetal acceleration, 5, 19
 CFA, *See* cold front aloft
 chinook front, 119
 chinook wind, 333
 CIN, *See* convective inhibition
 circulation
 absolute, 23
 ageostrophic, 112, 126–129
 Bjerknes' theorem, 22–24, 150–151
 Helmholtz' theorem, 25
 Kelvin's theorem, 23, 25
 solenoidal, 22, 102, 137, 153
 Stokes' theorem, 22
 thermally direct, 41, 57, 126, 133, 139,
 150, 154
 thermally indirect, 128
 transverse, 112, 139
 classic supercell, 216, 220, 222–223,
See also supercell
 Clausius-Clapeyron equation, 12, 14, 32
 clear-air returns, 374–375
 clear slot, 276, 278
 cloud street, 90–91
 closed cellular convection, 89
 coastal front, 153–154
 coastal surge, *See* orographically trapped
 cold-air surges
 cold-air damming, 153, 347, 349–350, 352
 cold front, 117–119, 120, 255
 cold front aloft (CFA), 118, 120, 139, 197
 conditional instability, *See* instability,
 conditional
 conditional symmetric instability (CSI),
See instability, conditional symmetric
 continuity equation
 anelastic form, 16
 Boussinesq form, 9, 16, 75
 for incompressible fluid, *See* continuity
 equation, Boussinesq form
 control volume, 146–148, 254–258, 260
 convection initiation, 138–139, 183–198
 convective available potential energy
 (CAPE), 33, 42, 43, 57, 106, 183
 convective boundary layer (CBL),
 74, 80, 84
 convective condensation level (CCL), 192
 convective inhibition (CIN), 33, 42,
 43, 183
 convective system, *See* mesoscale
 convective system
 convective temperature, 192, 194–195
 co-polar correlation coefficient, 384
 core-and-gap structure, 130, 189
 Coriolis parameter, 5–6, 18, 150, 245,
 346–347, 358
 f-plane approximation for, 107, 126
 coupled jets, 112
 covariance, 74, 230
 critical level, 172–173
 self-induced, 339
 cross-gap Rossby number, 358
 cross-valley circulation, 323
 cross-valley wind, 323, 325
 CSI, *See* conditional symmetric instability
 cumulus congestus cloud, 279
 cyclostrophic balance, 19, 48, 287–288
 damming, *See* cold-air damming
 DCVZ, *See* Denver Convergence and
 Vorticity Zone
 decoupling, 87, 105–107
 deformation
 geostrophic, 115, 125, 129, 133
 resultant, *See* deformation, total
 shearing, 124
 stretching, 124
 three-dimensional, *See* deformation
 tensor
 total, 124
 deformation tensor, 28
 density current
 dynamics of, 142–149
 motion of, 142, 148
 density potential temperature,
 See temperature, density potential
 density temperature, *See* temperature,
 density
 Denver Convergence and Vorticity Zone
 (DCVZ), 282
 Denver Cyclone, 282, 356–358
 derecho, 292
 dewpoint temperature, *See* temperature,
 dewpoint
 diabatic damming, 347
 diabatic heating, 26, 123–124, 127, 149,
 185, 187–188, 267
 differential
 heating, 115, 150, 154–156, 158, 325
 reflectivity, 383–384
 temperature advection, 185–186
 diffusivity
 moisture, 75
 thermal, 75, 88
 discontinuous propagation, 137, *See also*
 propagation, of convective storms
 dispersion of gravity waves, *See* gravity
 wave, dispersion
 dispersion relation, *See* gravity wave,
 dispersion relation
 dissipation, *See* viscous dissipation
 dividing streamline, 338–339, 344
 Dalton's Law, 12
 Doppler radar, 215, 263, 371, *See also*
 radar
 aliasing, 374
 Doppler dilemma, 374
 Downburst, 292, 294–300, 303, *See also*
 microburst
 downdraft, 33, 91, 215, 292, 300, *See also*
 forward-flank downdraft; mesoscale
 convective system, mesoscale
 downdraft of; occlusion downdraft;
 rear-flank downdraft
 dynamic forcing for, 295
 thermodynamic forcing for, 295
 downdraft convective available potential
 energy, 33
 downslope windstorms, 327–342, *See also*
 bora; chinook; foehn; Santa Ana;
 zonda
 drag coefficient, 79, 81, 307

- drainage wind, 87, 320–321
dry adiabatic lapse rate, *See* lapse rate, dry adiabatic
dry adiabatic process, 12, 16, 33
dry convection, 231
dryline, 115, 132–140
 characteristics of, 132–135
 formation of, 135–137
 motion of, 137–138
dryline bulge, 139–140
dry microburst, *See* microburst
dual-Doppler analysis, 385
 baseline of, 385
 thermodynamic retrieval derived from, 385–387
dual-polarization radar, 381–385
ducted gravity wave, *See* gravity wave
dynamic pressure perturbation, 28, 247, 295, 298
linear dynamic pressure perturbation, 30, 233, 258, 261
nonlinear dynamic pressure perturbation, 233
echo overhang, 215, 220
echo training, 309
eddy, *See* turbulent eddy
eddy diffusivity
 for heat, 76
 for moisture, 76
eddy viscosity, 17, 76, 196, 289
EF-scale, *See* enhanced Fujita scale
effective turbulent flux, 78–79, 81, *See* turbulent, effective flux
Ekman pumping, 81, 98
Ekman spiral, 36, 81–82, 276
elevated convection, 197–199, 205
elevated mixed layer, 135, 186, 253
energy, *See* convective available potential energy; downdraft convective available potential energy; internal energy; kinetic energy; potential energy; work
enhanced Fujita scale (EF-scale), *See* Fujita scale, enhanced Fujita scale
ensemble average, 74
entrainment (in cumulonimbi), 44, 46, 192–195, 197, 201, 205, 215–216, 218, 255, 264, 296, 310, 358
entrainment velocity, 87, *See also* boundary layer
entrainment zone, 84–87, *See also* boundary layer
equation of state, 11, 20, 32, 122
 for water vapor, 12
equilibrium level, 33–34, 43, 86, 98, 207, 211, 295, 302
equivalent potential temperature,
 See temperature, equivalent potential equivalent temperature, *See* temperature, equivalent
evanescent wave, *See* gravity wave, evanescent
evapotranspiration, 103
Ertel's potential vorticity, *See* potential vorticity, Ertel's
Exner function, 20, 32, 343
external wave, *See* gravity wave, external fetch, 97–102, *See also* lake-effect convection
FFD, *See* forward-flank downdraft
filter, 5, *See also* band-pass filter; high-pass filter; low-pass filter
fine-line, 140, 142, 285, 375–376
first law of thermodynamics, 11–12, 14, 32, 184, 297, 322
Fjørtoft's shear instability criterion, 64, *See also* instability, shear
flanking line, 215–216, 220, 282, *See also* supercell
flare echo, 308
flash flood, 273, 309–312
flood, *See* flash flood
fluid extension, 233–234
flux
 divergence of, 336
 effective turbulent, *See* turbulent flux, effective
ground heat, 83, 154, 156, 322
latent heat, 83, 95–96, 103, 135, 139, 156
sensible heat, 83–84, 93, 117, 135, 139, 156, 322–323
turbulent, *See* turbulent flux
 vorticity, *See* vorticity, flux of
flux form of equation, *See* equation, flux form of
flux-gradient theory, 76
flux Richardson number, *See* Richardson number, flux
foehn, 333
forced convection, 41, 130
forward-flank downdraft (FFD), 216, 219, 221, *See also* supercell
forward-tilting cold front, 118, 120, 122
free convection, 41
frequency
 of radar transmitter, 308, 374
 of wave, *See* wave, frequency of
friction, 81, 106, 108, 149, 350
 molecular, 81
 turbulent, 81
friction velocity, 82
front, 115–132, *See also* back-door cold front; back-door warm front; chinook front; cold front; cold front aloft; forward-tilting cold front; occluded front; Pacific cold front; split front; stationary front; upper-tropospheric front; warm front
definition of, 115
isobars, kinked along, 122
movement of, 120
slope of, 117, 120–122
temperature discontinuity, as, 122
temperature-gradient discontinuity, as, 122
frontal rainbands, *See* rainbands
frontal zone, *See* front
frontogenesis, 122–129, *See also* front; frontogenetical function
deformation, effect on, 125
diabatic heating, effect on, 123
divergence, effect on, 124, 126
dynamics of, 124–129
kinematics of, 122–124
quasigeostrophic, 126–127
semigeostrophic, 126–127, 129
tilting, effect on, 123–124
vorticity, effect on, 124
frontogenetical function, 123
frontolysis, 122, 124–126, *See also* frontogenesis
Froude number, 336, *See also* mountain Froude number
Fujita scale, 3
 Enhanced, 274
Fujiwhara effect, 61
fundamental mode, *See* gravity wave, fundamental mode
Galilean invariance, 240
gap wind, 349, 358–360
gas constant, 11–12
geopotential, 18, 52, 63, 111, 126, 136
geostrophic absolute momentum,
 See momentum, geostrophic absolute
geostrophic adjustment, 5, 110
geostrophic balance, *See* geostrophic wind
geostrophic coordinates, 129
geostrophic momentum, *See* momentum, geostrophic
geostrophic momentum approximation, 126, 129
geostrophic pseudoangular momentum,
 See momentum, geostrophic absolute
geostrophic space, *See* geostrophic coordinates

- geostrophic wind, 18–19, 50, 53, 81, 92, 276, 347
- gradient Richardson number,
See Richardson number, gradient
- gradient wind, 19, 135
- gradient wind balance, *See* gradient wind
- gravitational convection, 41, 54, 57, 63
- gravitational instability, *See* instability, static
- gravity current, *See* density current
- gravity height scale, 347
- gravity wave, 4–5, 42, 161–179, *See also* wave
- breaking, 345, 352, 360
 - dispersion relation, 168
 - dispersion, 168, 176
 - duct, 170–175
 - evanescent, 168, 170, 172–174
 - external, 165
 - forced by isolated peaks, 332–333
 - forced by two-dimensional terrain, 327–332
 - fundamental mode, 171
 - generation, 175
 - group velocity, 164–165, 168–170, 172, 329, 331
 - impedance, 170–171
 - intrinsic frequency, 164, 166, 173, 329, 336
 - momentum deposition, 172
 - overreflection, 173
 - polarization equations, 169, 171
 - reflection, 170–172, 333, 338–339, 341
 - refraction, 170
 - surface waves, *See* gravity wave, external temperature duct, 171
 - trapping, 170, 172–173, 175, 179, 327–328, 331–333, 342
 - vertical propagation, 164, 167, 172, 327–332
 - wind duct, 172
- graupel, 140, 205, 296–297, 306–307, 383–384
- ground clutter, 374–375
- ground heat flux, *See* flux, ground heat
- group velocity, *See* gravity wave, group velocity
- gust front, 140, 203, 205–208, 247, 260
- gustnado, 283–284
- hail, 140, 212, 216, 222, 273
- forecasting, 308
 - formation of, 306–308
 - terminal fall speed of, 307
- hail spike, *See* flare echo
- HCRs, *See* horizontal convective rolls
- heat, *See* diabatic heating; urban heat island effect; specific heat; sensible heat flux
- heat burst, 302–303
- heat island, *See* urban heat island effect; urban plume
- heavy-precipitation (HP) supercell, *See* high-precipitation (HP) supercell
- helicity, *See also* Beltrami flow
- relative, 228, 240
 - storm-relative, 40, 201, 230–231
- Helmholtz' theorem, *See* circulation, Helmholtz' theorem
- high-pass filter, 5
- high-precipitation (HP) supercell, 220, 224, *See also* supercell
- hodograph, 34–40, *See also* Ekman spiral
- fundamentals of, 34–36
 - horizontal vorticity and vertical shear implied by, 35–36, 40
 - mean wind derived from, 36–37
 - storm-relative winds derived from, 36–37
- hook echo, 215, 217, 220, 241, 276, 279–280, 286, *See also* supercell
- horizontal convective rolls (HCRs), 89, 151, 189–190, 283
- horizontal shear instability, *See* instability, horizontal shear
- horseshoe vortex, 226
- HP supercell, *See* heavy-precipitation/ high-precipitation (HP) supercell
- hydraulic jump, 333–334, 337–338, 340–342, 363
- hydrometeor loading, *See* buoyancy, hydrometeor loading
- hydrostatic equation, 8, 18–19, *See also* quasihydrostatic balance
- hydrostatic height tendency, 26
- hydrostatic pressure tendency, 26
- hypsometric equation, 18, 26
- ideal gas law, *See* equation of state
- impedance, *See* gravity wave, impedance
- incompressible approximation,
- See* Boussinesq approximation
- inertial height scale, *See* gravity height scale
- inertial instability, *See* instability, inertial inflection-point instability, *See* instability, inflection-point
- inland sea breeze, 154, 285
- instability
- absolute, *See* instability, static
 - baroclinic, 5, 41, 64, 154
 - barotropic, 5, 64
 - centrifugal, 48–49, 53
- conditional, 43, 57
- conditional symmetric, 54, 56, 132
- gravitational, *See* instability, static
- horizontal shear, 58–59, 63–64, 190, 279, 281, 283, 303, *See also* Fjørtoft's shear instability criterion, Rayleigh stability criterion
- Rayleigh stability criterion
- inertial, 49–53
- inflection-point, 59–60, 64, 92–93, *See also* Fjørtoft's shear instability criterion, Rayleigh stability criterion
- Kelvin-Helmholtz, 64–69
- lobe and cleft, 144, 146
- moist absolute, 43
- parallel, 63, 92–93
- potential, 47–48, 120, 132, 188
- potential symmetric, 54, 56
- shear, 58–69
- static, 41–48
- symmetric, 53–58
- thermal, 5, 88, 91–92, *See also* Rayleigh-Bénard convection
- intrinsic frequency, 42, 164, 166, 173, 329
- isallobaric wind, 120, 276
- isobaric process, 14
- jet
- barrier, *See* barrier jet
 - coupled, *See* coupled jet
 - low-level, *See* low-level jet
- jet streak, 36, 112, 117, 139, 267
- K-theory, *See* flux-gradient theory
- katabatic wind, 317–318, 321, 333
- Kelvin's circulation theorem,
- See* circulation, Kelvin's theorem
- Kelvin-Helmholtz, instability *See* instability, Kelvin-Helmholtz
- Kelvin wave, 346
- kinematic viscosity, 17, 75, 88
- kinetic energy, 68–69, 298
- lake breeze, 150, *See also* sea breeze
- lake-effect convection, 93–102
- lake-effect precipitation, *See* lake-effect convection
- land breeze, 98–99, 149–153
- landspout, 279, 281–283
- lapse rate
- dry adiabatic, 12, 42, 47, 51, 84, 184–185
 - environmental, 42–43, 184–185
 - moist adiabatic, 14, 42–43, 47, 183

- moist neutral, 43, 130
 neutral, 87
 pseudoadiabatic, 14, 47
 reversible moist adiabatic, 14
 superadiabatic, 84, 98–99
 lapse rate tendency, 183–187
 latent heat
 of fusion, 47
 of sublimation, 296
 of vaporization, 47
 latent heat flux, *See* flux, latent heat
 LDR, *See* linear depolarization ratio
 lee wave, 332, 341–342
 lenticular cloud, 327–329
 level of free convection (LFC), 33–34, 43, 129, 161, 183, 295
 level of neutral buoyancy, *See* equilibrium level
 LEWP, *See* line-echo wave pattern
 LFC, *See* level of free convection
 lid, *See* capping inversion
 linear depolarization ratio (LDR), 383
 line-echo wave pattern (LEWP), 248–249
 lifting condensation level (LCL), 15, 33–34, 192, 332
 linear stability analysis, 63, 88
 loaded gun sounding, 300
 lobe and cleft instability, *See* instability, lobe and cleft
 low-level jet, 105–106, *See also* coupled jets; low-level jet stream; nocturnal low-level wind maximum
 low-level jet stream, 105, 111–112
 low-pass filter, 5, 7
 low-precipitation (LP) supercell, 220, 222, *See also* supercell
 LP supercell, *See* low-precipitation (LP) supercell
 Margules' formula, 122, 129, *See also* front, slope of
 mass conservation, *See* continuity equation
 material derivative, 11
 maximum unambiguous range, *See* range, maximum unambiguous
 maximum unambiguous velocity, *See* velocity, maximum unambiguous
 MCC, *See* mesoscale convective complex
 MCS, *See* mesoscale convective system
 MCV, *See* mesoscale convective vortex
 mesoanalysis, 116
 mesocyclone, 214–215, 231–233, 242, 284, *See also* supercell
 mesohigh, 27, 140, 158, 251, 265–266
 mesolow, 252, *See also* wake low
 mesoscale boundaries, 115–116, 140, 149–158, *See also* coastal front; gust front; inland sea breeze; lake breeze; land breeze; outflow boundary; river breeze; sea breeze
 characteristics of, 115–116
 mesoscale cellular convection, 89, *See also* closed cellular convection; open cellular convection
 mesoscale convective complex (MCC), 106, 248, 265–269
 characteristics of, 245–248
 environment of, 246
 maintenance of, 246
 motion of, 250, 266
 mesoscale convective system (MCS), 245–269, *See also* bow echo; line-echo wave pattern; squall line; mesoscale convective complex
 characteristics of, 245–248
 classification of, 248
 leading stratiform MCS, 251–253
 maintenance of, 246, 267, 270
 mesoscale downdraft of, 250
 mesoscale updraft of, 250
 parallel stratiform MCS, 251, 253
 rear inflow of, 250–251, 260–265
 trailing stratiform MCS, 253
 trailing stratiform precipitation of, 249
 transition region of, 246, 249–250
 Type 1, 245, 266
 Type 2, 245
 mesoscale convective vortices (MCV), 106, 267
 mesoscale gravity wave, *See* gravity wave
 mesovortex, 304, 306
 microburst, 295, 300–302
 microlayer, *See* viscous sublayer
 mid-air microburst, *See* microburst
 Mie scattering, 369
 misocyclone, 189–191, 279, 281–283
 mixed layer, 78, 84–87, *See also* boundary layer
 mixing length, 78, 82
 mixing ratio
 for ice, 290–291
 for hydrometeors, 13
 for total water, 13
 for water vapor, 12, 42
 moist absolute instability, *See* instability, moist absolute
 moist absolutely unstable layer (MAULs), 98, 252
 moist adiabatic lapse rate, *See* lapse rate, moist adiabatic
 moist adiabatic process, 13–14, 16
 moist Brunt-Väisälä frequency, 42, 174, 346, *See also* Brunt-Väisälä frequency
 moist neutral lapse rate, *See* lapse rate, moist neutral
 moisture convergence, 195–197
 moisture diffusivity, *See* diffusivity, moisture
 momentum
 absolute, 51, 52–53, 55
 ageostrophic, 126
 angular, 48–50, 287–288
 conservation of, *See* momentum equation
 deposition, 172
 geostrophic, 53–54, 117, 126, 129
 geostrophic absolute, 52–53, 55
 momentum equation
 in Cartesian coordinates, 17–18
 in cylindrical coordinates, 48, 288
 flux form, 75
 in natural coordinates, 19, 288
 in pressure coordinates, 18
 in vector form, 17–18
 Morning Glory, 172, *See also* bore
 mountain Froude number, 344, 346, 351, 356, 358, *See also* Froude number; nondimensional mountain height
 mountain Rossby number, 347, *See also* Rossby number
 mountain Rossby radius of deformation, 347, 351, 363, *See also* Rossby radius of deformation
 mountain-valley wind systems, 317
 mountain wind, 317, 325
 multicellular convection, 209–213
 characteristics of, 213–215
 environment of, 213–215
 propagation of, 212
 narrow cold-frontal rainbands, *See* rainbands, narrow cold-frontal
 negative area, *See* area, negative
 net radiation, 82–83, 115, 137, 154, 156, 322
 neutral lapse rate, *See* lapse rate, neutral
 nocturnal boundary layer, *See* stable boundary layer
 nocturnal low-level wind maximum, 105–112
 nondimensional mountain height, 332, 345–346, *See also* mountain Froude number
 nonmesocyclonic tornado, *See* tornado, nonmesocyclonic
 nonsupercell tornado, *See* tornado, nonmesocyclonic

nontornadic damaging straight-line wind, 292–306
 nontornadic supercell, 231, 233, 284–285
 Norwegian cyclone model, 3, 115, 119
 Nyquist velocity, 374, *See also* Doppler radar, aliasing

Obukhov length, 91
 occluded front, 116, 119–120, 122,
See also occlusion
 occlusion (of an extratropical cyclone)
 cold, 119
 warm, 118–120
 occlusion downdraft, 218, 278, 295, 300
 ocean-effect precipitation, *See* lake-effect convection
 one-celled vortex, *See* vortex, one-celled open cellular convection, 89
 ordinary cell, 207–209, 211, *See also* single-cell convection, multicellular convection
 orphan anvil, 209
 orographically trapped cold-air surges, 346–350
 Orr-Sommerfeld equation, 63
 oscillation
 buoyancy, 5, 42, 66, 80, 161, *See also* Brunt-Väisälä frequency
 centrifugal, 49
 inertial, 5, 50, 106, 108, 112
 outflow boundary, 140, 376
 overreflection of gravity wave, *See* gravity wave, overreflection

Pacific cold front, 118–120
 parallel flow, 58, 61, 63
 parallel instability, *See* instability, parallel parcel theory, 41
 limitations of, 44–47
 PBL, *See* planetary boundary layer
 penetrative convection, 84
 phase speed (velocity), *See* wave, phase speed (or velocity) of
 planetary boundary layer (PBL),
See boundary layer
 point vortex, *See* vortex, point
 Poisson's equation, 12
 polarization equations, *See* gravity wave, polarization equations
 positive area, *See* area, positive
 potential energy, 67, 337
 potential instability, *See* instability, potential
 potential symmetric instability (PSI),
See instability, potential symmetric
 potential temperature, *See* temperature, potential

potential vorticity
 conservation of, 25, 230, 352, 358–359, 362–364
 geostrophic, 52, 56
 Ertel's, 25, 230, 352
 potential vorticity banner, 355
 precipitation efficiency, 309–310
 pressure
 buoyancy perturbation, 25–32, 205, 256, 259
 diagnostic equation for, 28
 dynamic perturbation, 27–32, 218, 233–234, 240, 258, 261
 hydrostatic perturbation, 25–27
 linear dynamic perturbation, 30–31, 258, 261
 nonhydrostatic perturbation, 27
 nonlinear dynamic perturbation, 30, 233–234
 saturation vapor, 12, 15
 vapor, 12, 15
 pressure retrieval, *See* dual-Doppler analysis, thermodynamic retrieval derived from
 pressure tendency, *See* hydrostatic pressure tendency
 propagation
 of convective storms, 149
 of gravity waves, 139
 pseudoadiabatic lapse rate, *See* lapse rate, pseudoadiabatic
 pseudoadiabatic process, 14, 16, 32
 pseudoangular momentum,
See momentum, absolute
 pseudomoist adiabatic lapse rate, *See* lapse rate, pseudoadiabatic
 pseudomoist adiabatic process,
See pseudoadiabatic process
 pseudoequivalent potential temperature,
See temperature, pseudoequivalent potential
 PSI, *See* potential symmetric instability
 pulse repetition frequency, 370, *See also* Doppler radar; radar
 pulse repetition time, 372, *See also* Doppler radar; radar
 pulse severe weather, 207
 QLCSs, *See* quasilinear convective systems
 quasigeostrophic approximation, 8, 126, 129
 quasigeostrophic frontogenesis,
See frontogenesis, quasigeostrophic
 quasihydrostatic balance, 317, 320
 quasilinear convective system (QLCS),
See squall line

radar, 369–387, *See also* Doppler radar;
 dual-Doppler analysis; Z-R relationship
 applications using, 374–387
 attenuation of, 220, 279, 370–371, 374
 backscattered power received by, 308
 basics of, 369–371
 dual-polarization, 381–383
 estimating rainfall using, 379–385
 interpreting Doppler velocity patterns observed by, 375–385
 radial velocity measured by, 371–372
 reflectivity factor measured by, 369
 spectrum width measured by, 371–372
 thermodynamic retrieval, 385–387
 radial velocity, *See* radar, radial velocity measured by
 rainbands
 narrow cold-frontal, 129–132, 189
 warm-frontal, 129, 132
 warm-sector, 129, 132
 wide cold-frontal, 129–132
 rainfall rate, 379, 381
 range
 maximum unambiguous, 372–374,
See also Doppler radar; Doppler dilemma
 range folding, 372–373
 Rankine vortex, *See* vortex, Rankine rate-of-strain tensor, *See* deformation tensor
 Rayleigh-Bénard convection, 88–89, 91,
See also instability, thermal
 Rayleigh equation, 63
 Rayleigh number, 88
 Rayleigh scattering, 369, 381
 Rayleigh stability criterion, 64, *See also* instability, shear
 rear-flank downdraft (RFD), 215, 219, 221, 276, 372, *See also* supercell
 received power, *See* radar, backscattered power received by
 reduced gravity, 338, 347
 reflection of gravity wave, *See* gravity wave, reflection
 reflectivity, *See* radar, reflectivity factor measured by
 refraction
 of gravity wave, *See* gravity wave, refraction
 of radar beam, 371
 relative humidity, 87, 141, 296, 299
 residual layer, 77, 84–87, *See also* boundary layer

- retrieval of three-dimensional wind field
from Doppler radar data,
See dual-Doppler analysis
- reversible moist adiabatic lapse rate,
See lapse rate, reversible moist
adiabatic
- reversible moist adiabatic process,
13–14
- Reynolds-averaged equation, 73–76
- Reynolds number, 17, 63
- Reynolds averaging, 73, 75, *See also*
boundary layer
- RFD, *See* rear-flank downdraft
- Richardson number
bulk, 201
flux, 80
gradient, 66, 80
- river breeze, 150
- RKW theory, 253–257, 254, 255, 258, 260,
261, 265, *See also* mesoscale
convective system, maintenance of
- rope cloud, 130, 361
- Rossby radius of deformation, 5, 347,
See also mountain Rossby radius of
deformation
- Rossby number, 8, 80, 117, 120, *See also*
cross-gap Rossby number; mountain
Rossby number
- rotor, 328, 333, 342
- roughness element, 78
- roughness length, 78, 82
- Santa Ana, 333
- Santa Cruz eddy, 356
- saturated adiabatic process, *See* moist
adiabatic process
- saturation point, 33
- saturation temperature, *See* temperature,
saturation
- Sawyer-Eliassen equation, 127–129, 132
- scale height, 167, 347
- SCAPE, *See* slantwise convective available
potential energy
- Scorer parameter, 328, 331
- sea breeze, 150–151, *See also* land breeze
- semigeostrophic equations, 126, 129
- semigeostrophic frontogenesis,
See frontogenesis, semigeostrophic
- semigeostrophic theory, 117
- sensible heat flux, *See* flux, sensible heat
- shallow water equations, *See* shallow
water theory
- shallow water theory, 333–336, 338,
340–341
- shear
directional, 37–40
horizontal, 58, 63
- one-directional or unidirectional,
37, 251
- speed, 37–40
- thermal wind, *See* thermal wind
- vertical, 201–203, 205–206, 215,
See also hodograph
- shear instability, *See* instability, shear
- shelf cloud, 141
- single-cell convection, 206–209
characteristics of, 205
- environment of, 205
- lifecycle of, 208
- skew T -log p diagram,
See thermodynamic diagram
- sky view factor, 103, 323
- slantwise convection, 41, 54, 56, 63
- slantwise convective available potential
energy (SCAPE), 57
- slope wind, 318, 320
- snow belt, 93
- solenoidal circulation, 102, 153
- solenoidal vorticity generation,
See vorticity, baroclinic generation of
- solitary wave, 161, 163, 172, 176, *See also*
bore
- soliton, 163, 176, 179, *See also* bore
- southerly buster, 346
- specific differential phase, 384
- specific heat, 11, 13–14, 42, 83, 184, 297,
322, 343
- specific humidity, 83, *See also* relative
humidity
- spectrum width, *See* radar, spectrum
width measured by
- split front, 120, 132
- squall line, 248–261, *See also* mesoscale
convective system
- SRH, *See* storm-relative helicity
- stable boundary layer, 77, 80–81, 84–86,
197, *See also* boundary layer
- stagnation, 345–346, 255
- state variable, 25, 63, 230
- static instability, *See* instability, static
- static stability, 119–122, 127–128, 137,
168–170, 328–330, *See also*
Brunt-Väisälä frequency
- static stability parameter, 26
- stationary front, 117, 153, 309
- Stokes' theorem, 22
- storm-relative helicity (SRH), *See* helicity,
storm-relative
- storm-relative wind, 36–37, 203, 212, 310
- storm-splitting, 238, 241, *See also*
supercell, dynamic vertical pressure
gradients in
- streamfunction, 60, 65, 126–128, 133
- subcritical flow, 336–337
- Sullivan vortex, *See* vortex, Sullivan
- superadiabatic lapse rate, *See* lapse rate,
superadiabatic
- supercell, 213–242, *See also* classic
supercell; flanking line hook echo;
helicity; high-precipitation (HP)
supercell; low-precipitation (LP)
supercell; storm-splitting
characteristics of, 213–215
definition of, 213–215
dynamic vertical pressure gradients in,
203, 207, 212, 218, 236–238
- environment of, 215
- inflow low of, 218–220
- mesocyclogenesis in, 224–225, 230
- motion of, 214, 240
- supercritical flow, 336–337, 342
- surface energy budget, 82–83, *See also*
ground heat flux; latent heat flux; net
radiation; sensible heat flux
- surface flux, 83, 91, 98, 117, 120, *See also*
ground heat flux; latent heat flux;
sensible heat flux
- surface layer, 82, 84, 87, *See also* boundary
layer
- surface wave, *See* gravity wave; external
wave
- swirl ratio
local, 292
outer, 292
- symmetric flow, 53
- symmetric instability, *See* instability,
symmetric
- synoptic front, *See* front
- synoptic map, 3, 115
- synoptic scale, 5–10
- TAF, *See* topographic amplification factor
- Taylor-Goldstein equation, 66, 69, 167,
172, 328
- temperature
density, 13
- density potential, 13, 20, 148, 232, 247,
286, 298
- dewpoint, 13, 98, 135
- equivalent, 14
- equivalent potential, 14–16, 43, 47, 98,
192
- potential, 12–13, 51, 53–54, 166,
192–195, 297, 321, 364
- pseudoequivalent potential, 16
- saturation, 14, 346
- virtual, 13, 19–20, 23–24, 26, 33
- virtual potential, 13, 33, 74, 138, 148
- wet-bulb, 13, 15, 33, 297, 300
- wet-bulb potential, 13, 15, 47,
120, 192

- temperature advection, 36, 41, 93, 120, 124, 126, 129, 185–187, *See also* advection
 differential, 185–186
 temperature duct, *See* gravity wave, temperature duct
 terminal fall speed (or velocity), *See* velocity, terminal fall
 thermal buoyancy, 28, *See also* buoyancy
 thermal diffusivity, *See* diffusivity, thermal
 thermal instability, *See* instability, thermal
 thermal wind, 19, 37, 54, 110–111
 thermally direct circulation, *See* circulation, thermally direct
 thermally indirect circulation, *See* circulation, thermally indirect
 thermodynamic diagram, 15, 32–35, 301–302
 thermodynamic equation, 16, 65, 123, 126, 129, 165
 thermodynamic retrieval, *See* dual-Doppler analysis; thermodynamic retrieval derived from
 thermodynamic speed limit, 43
 three-body scattering signature, *See* flare echo
 topographic amplification factor (TAF), 323
 tornado, 273–292
 dynamics of, 287–292
 flow regions of, 287–288
 forecasting and nowcasting, 284–287
 formation of, 276–283
 general characteristics of, 273–276
 nonmesocyclonic, 279–284
 pressure profile in, 288–291
 wind profile in, 288–291
 tornadogenesis, *See* tornado, formation of trapped cold-air surges, *See* orographically trapped cold-air surges
 trapped gravity waves, *See* gravity waves, trapping
 tropopause folding, 117
 turbulent eddy, 73, 78–79
 turbulent flux
 effective, 78–79, 81
 of heat, 76, 78, 83
 of moisture, 75–76
 of momentum, 80–82
 parameterization of, 76–79
 turbulent kinematic heat flux, *See* turbulent flux, of heat
 turbulent kinematic moisture flux, *See* turbulent flux, of moisture
 turbulent kinematic momentum flux, *See* turbulent flux, of momentum
 turbulent kinetic energy, 79–80
 buoyant generation of, 79–80
 dissipation of, 80
 shear generation of, 80
 turbulent transport of, 80
 turbulent Prandtl number, 78
 turkey tower, 191, *See also* convection initiation
 two-celled vortex, *See* vortex, two-celled
 upper-tropospheric front, 117, 119, 120
 upright convection, *See* gravitational convection
 upscale growth (of deep moist convection), 245–246
 urban heat island effect, 103
 urban heat plume, 103
 urban plume, 104
 valley wind, 319, 323
 vapor pressure, 12, 15
 velocity
 maximum unambiguous, 372–374
 phase, *See* wave, phase speed (or velocity) of
 terminal fall, 208, 307, 372
 velocity aliasing (or folding), 374, *See also* Doppler radar, aliasing
 vertical propagation of gravity waves, *See* gravity wave, vertical propagation
 virtual potential temperature, *See* temperature, virtual potential
 virtual temperature, *See* temperature, virtual
 viscosity
 eddy, *See* eddy viscosity
 kinematic, *See* kinematic viscosity
 viscous dissipation, 80
 viscous sublayer, 73
 von Karman constant, 82
 von Karman vortex street, 351, 354
 vortex
 Burgers-Rott, 289
 mesoscale convective, *See* mesoscale convective vortex
 one-celled, 291–292
 point, 60
 Rankine, 288–289
 Sullivan, 291
 two-celled, 291–292
 vortex breakdown, 291–292
 vortex lines, 24–25, 60, 229–230
 vortex sheet, 59, 62, 342
 vorticity
 absolute, 50, 64, 129
 baroclinic generation of, 25, 225, 233, 277, 280, 318, 351, 356
 crosswise, 40, 226–229, 236
 flux of, 22, 255, 256, 259
 horizontal, 40, 60, 211–212, 228–230, 259, 352
 potential, 25, 135, 267, 269, 352, 355
 relative, 50, 56, 135, 276
 streamwise, 40, 226–227, 229–232, 236, *See also* helicity
 stretching of, 21, 276
 tilting of, 202–203, 225, 228–229, 235, 276–277, 306
 vorticity equation, 21, 24, 214, *See also* vorticity
 horizontal, 24, 145, 254, 318
 vector, 24, 230, 265, 279
 vertical, 59, 225, 228, 230, 236, 261, 274, 276, 352
 wake low, 141, 251, 265
 wall cloud, 215–216, 218, 222, 224, 231, *See also* supercell
 wake depression, *See* wake low
 warm front, 117–120, 122, 128–129, 132, 132, 135, 197, 285, 309
 warm-frontal rainbands, *See* rainbands, warm-frontal
 warm-sector rainbands, *See* rainbands, warm-sector
 wide cold-frontal rainbands, *See* rainbands, wide cold-frontal
 waterspout, 59, 276, 279, 282–283
 water vapor
 contribution of, 343, 345
 mixing ratio, *See* mixing ratio, for water vapor
 wave, 327–342, *See also* gravity wave
 amplitude of, 63, 167, 171
 frequency of, 42, 172
 phase speed (or velocity) of, 63, 165, 168–169, 173–174, 336
 wavelength of, 330–333
 wavenumber of, 328–331, 333
 wavenumber vector, *See* wave vector
 wave vector, 163–164, 168–169
 weak-echo region, 215, *See also* supercell
 wet-bulb potential temperature, *See* temperature, wet-bulb potential
 wet-bulb temperature, *See* temperature, wet-bulb
 wet-bulb-zero level, 297, 307
 wet microburst, *See* microburst
 wide cold-frontal rainband, *See* rainband, wide cold-frontal
 wind
 ageostrophic, *See* ageostrophic wind
 anabatic, *See* anabatic wind

- antitriptic, *See* antitriptic wind
duct, *See* gravity wave, wind duct
gap, *See* gap wind
geostrophic, *See* geostrophic
wind
gradient, *See* gradient wind
- isallobaric, *See* isallobaric wind
katabatic, *See* katabatic wind
radius of maximum,
 287–289
thermal, *See* thermal wind
witch of Agnesi, 330
- work, 48, 58, 60, 67–68, 385, *See also*
potential energy
Z-R relationship, 379–381
zipper low, 154
zonda, 333